

Nitin Afzalpulkar · Vishnu Srivastava
Ghanshyam Singh · Deepak Bhatnagar
Editors

Proceedings of the International Conference on Recent Cognizance in Wireless Communication & Image Processing

ICRCWIP-2014

Proceedings of the International Conference
on Recent Cognizance in Wireless Communication
& Image Processing

Nitin Afzalpulkar · Vishnu Srivastava
Ghanshyam Singh · Deepak Bhatnagar
Editors

Proceedings
of the International
Conference on Recent
Cognizance in Wireless
Communication & Image
Processing

ICRCWIP-2014

 Springer

Editors

Nitin Afzalpulkar
Asian Institute of Technology
Bangkok
Thailand

Vishnu Srivastava
Microwave Tubes Division
Central Electronics Engineering Research
Institute
Pilani, Rajasthan
India

Ghanshyam Singh
Department of Electronics and Technology
Malaviya National Institute of Technology
Jaipur
India

Deepak Bhatnagar
Department of Physics
University of Rajasthan
Jaipur
India

ISBN 978-81-322-2636-9

ISBN 978-81-322-2638-3 (eBook)

DOI 10.1007/978-81-322-2638-3

Library of Congress Control Number: 2016930278

© Springer India 2016

This work is subject to copyright. All rights are reserved by the Publisher, whether the whole or part of the material is concerned, specifically the rights of translation, reprinting, reuse of illustrations, recitation, broadcasting, reproduction on microfilms or in any other physical way, and transmission or information storage and retrieval, electronic adaptation, computer software, or by similar or dissimilar methodology now known or hereafter developed.

The use of general descriptive names, registered names, trademarks, service marks, etc. in this publication does not imply, even in the absence of a specific statement, that such names are exempt from the relevant protective laws and regulations and therefore free for general use.

The publisher, the authors and the editors are safe to assume that the advice and information in this book are believed to be true and accurate at the date of publication. Neither the publisher nor the authors or the editors give a warranty, express or implied, with respect to the material contained herein or for any errors or omissions that may have been made.

Printed on acid-free paper

This Springer imprint is published by Springer Nature
The registered company is Springer (India) Pvt. Ltd.

Preface

The 1st International Conference on Recent Cognizance in Wireless Communication & Image Processing (ICRCWIP-2014) was held in the campus of Poornima Institute of Engineering & Technology Jaipur during 16–17 January 2015. A total of 400 participants, 175 of whom were students, attended the conference. The participants had fruitful scientific and technical discussions and exchanges that made the conference a complete success.

The overall response to the conference was quite encouraging. A large number of papers were received. After careful review, 173 papers were chosen for presentation during the conference. After the conference, an additional round of review was carried out. Among the presented papers, 110 papers were selected for inclusion in the conference proceedings. A very informative panel discussion was also organized during the conference. The aim of the panel discussion was to discuss the advancements in wireless communication, optical communication, circuit design and image processing, and their effects on humans. The discussion was planned to give faculty, academicians, delegates, and students a platform where they can discuss issues and share problems and solutions with each other in a healthy and knowledgeable environment.

The papers appearing in the proceedings belong to these major clusters:

CLUSTER-I Image processing and its application

CLUSTER-II Wireless and microwave communication

CLUSTER-III Nanoelectronics and industry application

CLUSTER-IV Optoelectronics and photonic devices

CLUSTER-V Analog circuit design and its application

These papers represent the most recent research on the respective subject areas. The editors would like to thank all the authors, reviewers, panelists, local organizers, and the session chairs for paying attention to the quality of the publications. Partial financial support for publishing the conference proceedings is received from DRDO.

The contents of this proceedings reveal the breadth of current activities in different themes related to wireless communications and image processing. We hope these will form a useful starting point for beginners as well as practitioners in this discipline.

Nitin Afzalpulkar
Vishnu Srivastava
Ghanshyam Singh
Deepak Bhatnagar

About the Conference

The International Conference on Recent Cognizance in Wireless Communication & Image Processing-ICRCWIP-2015 was organized by the Department of Electronics & Communication and Department of Electrical Engineering, Poornima Institute of Engineering and Technology, Jaipur, India. The conference was held during Jan 16–17, 2015 in Jaipur, India. ICRCWIP-2015 aims at bringing together researchers, engineers, and students to review the latest development in the area of wireless communication and image processing. The conference comprised of technical sessions and plenary lectures by invited experts. The core vision of ICRCWIP is to disseminate new knowledge about technology for the benefit of everyone in the community ranging from the academic and professional research communities to industry practitioners. The conference covers a range of topics in electronics and communication engineering, including electrical and communication security, mobile and wireless networking, and wireless communication systems. It also provided a venue for high-caliber researchers, Ph.D. students, and professionals to submit ongoing research and developments in these areas. Another goal of the conference was to promote exchange of scientific information between researchers, developers, engineers, students, and practitioners working across the globe. The conference was intended to be an annual event to provide a distinct platform for people to share views and experiences in the areas of information, telecommunication, computing, mobile techniques, and related areas.

Committee

Steering Committee

Chief Patron

Dr. S.M. Seth, Chairman, Poornima Foundation, Chairperson, Poornima University, Jaipur, Former Director, National Institute of Hydrology, Roorkee, India

Patron

Shri Shashikant Singhi, Director General, Poornima Foundation, Jaipur, India

General Chair

Dr. Ghanshyam Singh, Associate Professor, MNIT, Jaipur, India

Conference Chair

Dr. Ajay Kumar Bansal, Director, Poornima Institute of Engineering and Technology, Jaipur, India

Convener

Mr. Sachin Chauhan, Head of Department, Department of ECE, Poornima Institute of Engineering and Technology, Jaipur, India

Mr. Anil Boyal, Head of Department, Department of EE, Poornima Institute of Engineering and Technology, Jaipur, India

Co-convener

Mr. Ankur Saharia, Associate Professor, Department of ECE, Poornima Institute of Engineering and Technology, Jaipur, India

Section Oversight Committee

Dr. Naomi Chavez, Senior Director, Optical Society, Washington, DC, USA

Dr. Michael Anthony Elliott, Division Assistant, Optical Society, Washington, DC, USA

Technical Program Committee

Chairs

Track-1: (CS/IT) Dr. Lalit Kr. Awasthi, Dean, Himachal Pradesh Technical University, Hamirpur, India

Track-2: (ECE) Dr. R.P. Yadav, MNIT, Jaipur, India

Track-3: (EE) Dr. Rajesh Kumar, MNIT, Jaipur, India

Members

Dr. Ajeet Kumar, Delhi Technical University

Dr. Annelise E. Barron, University of Texas, USA

Dr. Annie Vilcot, Institute of Technology, France

Dr. Anshuman Kalla, JNU, Jaipur

Dr. Balaji S. Prabhakar, Stanford University, USA

Dr. Bernd Girod, Professor, University of Texas

Dr. Blandin Jean, Grenoble Institute of Technology, France

Dr. D. Bhatnagar, University of Rajasthan, Jaipur

Dr. D.K. Raghuvanshi, NIT, Bhopal

Dr. Dheerendra Mathur, GEC, Ajmer

Dr. Dheerendra Singh, BITS, Pilani

Dr. Fox, California Technical University, USA

Dr. Ghanshyam Singh, Jaypee University of Information Technology, Solan

Dr. Ghanshyam Singh, Malviya National Institute of Technology, Jaipur

Dr. H.D. Mathur, BITS, Pilani

Dr. Jitender Kumar Chhabra, National Institute of Technology, Kurukshetra

Dr. Jitendra Kumar Deegwal, CEG, Government of India

Dr. K.K. Sharma, Malviya National Institute of Technology, Jaipur

Dr. Lokesh Tharani, RTU, Kota

Dr. M.C. Govil, Malviya National Institute of Technology, Jaipur

Dr. M.M. Sharma, Principal, GEC, Ajmer

Dr. Mantosh Biswas, National Institute of Technology, Kurukshetra

Dr. Michael Anthony Elliott, Optical Society, Washington, DC, USA

Dr. Mithlesh Kumar, RTU, Kota

Dr. Mohammad Salim, Malviya National Institute of Technology, Jaipur

Dr. Naomi Chavez, Optical Society, Washington, DC, USA

Dr. Nick W McKeown, Stanford University, USA

Dr. Nitin Afzalpulkar, Asian Institute of Technology, Bangkok, Thailand

Dr. O.P. Vyas, JIET, Jodhpur

Dr. O.P. Meena, NIT, Bhopal

Dr. P.K. Singhal, MITS, Gwalior

Dr. R.L. Yadav, Galgotia University, Noida

Dr. R. Nath, Department of Physics, IIT, Roorkee

Dr. R.K. Sarin, NIT, Jalandhar

Dr. R.P. Yadav, Malviya National Institute of Technology, Jaipur

Dr. R.P. Tiwari, ISTE, Jaipur
Dr. Rajeev Gupta, RTU, Kota
Dr. Rajesh Kumar, Malviya National Institute of Technology, Jaipur
Dr. Ritu Sharma, Malviya National Institute of Technology, Jaipur
Dr. R.S. Saxena, PWD, Jaipur
Dr. Samar Ansari, Malviya National Institute of Technology, Jaipur
Dr. Sandeep Sancheti, Manipal University, Jaipur
Dr. Sanjay Kumar, IETE, Jaipur
Sh. Sanjeev Agarwal, Malviya National Institute of Technology, Jaipur
Dr. Sarabjeet Singh, NIT, Jalandhar
Dr. Shashi B. Rana, Guru Nanak Dev University, Gurdaspur
Dr. Sheila K. Shull, Computing and Mathematical Sciences, California Technical University, USA
Dr. Sumit Srivastava, Manipal University
Sh. Tarun Verma, Malviya National Institute of Technology, Jaipur
Dr. Trilok Mathur, BITS, Pilani
Dr. U.S. Modani, Government College, Ajmer
Dr. Veron Muriel, Grenoble Institute of Technology, France
Dr. Vijay Janyani, Malviya National Institute of Technology, Jaipur
Dr. Vineet Sahula, Malviya National Institute of Technology, Jaipur
Dr. Vipul Rastogi, Associate Professor, Department of Physics, IIT, Roorkee
Dr. Virender Ranga, National Institute of Technology, Kurukshetra
Dr. Seema Verma, Banasthali University, Jaipur, India
Dr. Buta Singh, Guru Nanak Dev University
Dr. Harjit Pal Singh, CT Institute of Engineering, Management and Technology
Dr. Suyeb Ahmed Khan, Shiv Shankar Institute of Engineering and Technology
Dr. Subir Sarkar, University of Kolkata
Dr. Preetam Kumar, IIT, Patna
Dr. Kalpana Dhaka, IIT, Gawhati
Dr. Seema Verma, Banasthali University, Jaipur
Dr. Manish Tiwari, REC, Jaipur

Review Panel

Members

Dr. Ajay Kr. Bansal, Poornima Institute of Engineering and Technology, Jaipur
Dr. Ajeet Kumar, Delhi Technical University
Dr. Archana Agrawal, Institute of Technology and Management, Bhilwara
Dr. Avinash Sharma, Advait Vedanta Institute of Technology, Jaipur
Dr. C. Periasamy, Malviya National Institute of Technology, Jaipur
Dr. C.K. Babulal, Thiagarajar College of Engineering, Madurai
Dr. Deepak Bhatnagar, University of Rajasthan, Jaipur
Dr. Deepak Jhanwar, Government Engineering College, Ajmer

Dr. Devesh Kumar, Manipal University, Jaipur
 Dr. Dheeraj Palwelia, Rajasthan Technical University, Kota
 Dr. Dharendra Mathur, Government Engineering College, Ajmer
 Dr. E.S. Pilli, Malviya National Institute of Technology, Jaipur
 Dr. Ghanshyam Singh, JUIT, Solan
 Dr. H.S. Parihar, Central University, Kishangarh
 Dr. Harjeet Singh, NIT, Jalandhar
 Dr. Jayashri Vajpai, MBM, Jodhpur
 Dr. Jitendra Chhabra, NIT, Kurukshetra
 Dr. Jitendra Kr. Tripathi, Rajarshi Rananjay Sinh Institute of Management and Technology, Amethi (UP)
 Dr. Kumud Ranjan Jha, Shri Mata Vaishno Devi University, Katra
 Dr. Lokesh Tharani, Rajasthan Technical University, Kota
 Dr. Mahesh Bunde, Poornima University, Jaipur
 Dr. Manoj Gupta, Poornima University, Jaipur
 Dr. Manoj Kuri, Engineering College, Bikaner
 Dr. Mantosh Bishwas, NIT, Kurukshetra
 Dr. Mushtaq Ahmed, Malviya National Institute of Technology, Jaipur
 Dr. Narendra Singh Yadav, Balaji College
 Dr. Neeta Nain, Malviya National Institute of Technology, Jaipur
 Dr. O.P. Sharma, Poornima College of Engineering, Jaipur
 Dr. O.P. Vyas, JIET, Jodhpur
 Dr. Om Prakash Rishi, Central University, Kishangarh
 Dr. P.K.Singhal, MITS, Gwalior
 Dr. Poonam Saini, PEC University of Technology, Chandigarh
 Dr. R.C. Poonia, Amity, Noida
 Dr. R.P. Yadav, Malviya National Institute of Technology, Jaipur
 Dr. Ravi Kr. Madilla, Malviya National Institute of Technology, Jaipur
 Dr. Renu Kumawat, Manipal University, Jaipur
 Dr. Ritu Sharma, Malviya National Institute of Technology, Jaipur
 Dr. S.K. Bishnoi, Engineering College, Bikaner
 Dr. Sajavir Singh, Jaypee, Noida
 Dr. Samar Ansari, Malviya National Institute of Technology, Jaipur
 Dr. Sandeep Joshi
 Dr. Sanjeev Methya, Rajasthan College of Engineering for Women, Jaipur
 Dr. Satyasai J. Nanda, Malviya National Institute of Technology, Jaipur
 Dr. Seema Verma, Banasthali Vidyapith
 Dr. Shashi B. Rana, Guru Nanak Dev University, Gurdaspur
 Dr. Shruti Jain, JUIT, Solan
 Dr. Sujata Pandey, Amity, Noida
 Dr. Sumit Srivastava, Manipal University, Jaipur
 Dr. Suyeb Ahmed Khan, NIT, Jalandhar
 Dr. Uma Shankar Modani, Government Engineering College, Ajmer
 Dr. Umesh Kr. Dwivedi, Amity University, Jaipur
 Dr. Vineet Khanna, Rajasthan College of Engineering for Women, Jaipur

Dr. Vinod Yadav, Maharana Pratap University, Udaipur
Dr. Viranjay Srivastava, South Africa
Dr. Virendra Sangtani, Anand International College of Engineering, Jaipur
Dr. Vivekanand Tiwari, Manipal University, Jaipur
Mr. Aditya, Jaipur National University, Jaipur
Mr. Ajay Khunteta, Poornima College of Engineering, Jaipur
Mr. Alok Jhaldiyal, Indian Institute of Remote Sensing, ISRO, Dehradun
Mr. Anshuman Kalla, Jaipur National University, Jaipur
Mr. Arvind Kr. Upadhyay, Jaipur National University, Jaipur
Mr. Devendra Soni, Arya Institute of Engineering and Technology, Jaipur
Mr. Kalyan Acharjya, Jaipur National University, Jaipur
Mr. Manish Singhal, Poornima College of Engineering, Jaipur
Mr. Manish Tiwari, Rajdhani Engineering College, Jaipur
Mr. Navneet Kumar Verma, Jaipur National University, Jaipur
Mr. Rahul Mishra, Galgotia College of Engineering and Technology, Greater Noida
Mr. Rahul Srivastava, Arya Institute of Engineering and Technology, Jaipur
Mr. Rajesh Sangla, NIT, Jalandhar
Mr. Ritu Raj, Government Engineering College, Bikaner
Mr. Santosh Kumar Vipparthi, Malviya National Institute of Technology, Jaipur
Mr. Tanuj Chauhan, Jaypee Institute of Information Technology, Noida
Ms. Jasmin Saini, Jaypee, Noida
Ms. Rekha Mehra, Government Engineering College, Ajmer
Prof. Dr. Mithilesh Kumar, Rajasthan Technical University, Kota
Prof. Dr. R.L. Yadava, Galgotia College of Engineering and Technology, Greater Noida

Acknowledgments

The editors wish to extend their heartfelt acknowledgment to the authors, peer-reviewers, committee members, and production staff whose diligent work put shape to the ICRCWIP-2014 proceedings. We especially thank our dedicated team of peer-reviewers who volunteered for the arduous and tedious step of quality checking and critiquing on submitted manuscripts. We congratulate campus Director Dr. Ajay Kumar Bansal and the faculty team at the Department of EC & Electrical Engineering, PIET, Jaipur especially to Mr. Sachin Chauhan, Mr. Anil Boyal, and Mr. Ankur Saharia for extending their enormous assistance during the reviewing and editing process of the conference documentation. The time spent by all of them and midnight oil burnt is greatly appreciated. Lastly, we would like to thank Springer for publishing the ICRCWIP-2014 conference proceedings. Especially the efforts of Swati Meherishi, Senior Editor, Applied Sciences and Engineering and Aparajita Singh, Editorial Assistant, for their help in the publishing process are worth mentioning.

Contents

A Novel Image Zooming Technique Using Wavelet Coefficients.	1
Himanshu Jindal, Singara Singh Kasana and Sharad Saxena	
Analysis of Operational Transformation Algorithms.	9
Santosh Kumawat and Ajay Khunteta	
A Digital Image Watermarking Technique Using Cascading of DCT and Biorthogonal Wavelet Transform	21
Arvind Kumar, Pragma Agarwal and Ankur Choudhary	
Multi-domain Image Enhancement of Foggy Images Using Contrast Limited Adaptive Histogram Equalization Method	31
Garima Yadav, Saurabh Maheshwari and Anjali Agarwal	
Comparison of Various Reliability Measures of a Computer System with the Provision of Priority.	39
Ashish Kumar and Monika Saini	
Dual-Band Filter Using DGS for X-Band Applications	51
Suman Kumari, Amit Singh Bhadouria and Mithilesh Kumar	
A Review on Performance Evaluation of Routing Protocols in MANET	59
Shruti Thapar and Anshuman Kalla	
Retinal Nerve Fiber Layer Analysis in Digital Fundus Images: Application to Early Glaucoma Diagnosis.	69
Dharmanna Lamani, T.C. Manjunath, M. Mahesh and Y.S. Nijagunarya	
Design, Development of MC-CDMA, and Reduction of ISI for Different Modulation Techniques	81
Arun Kumar and Manisha Gupta	

A Compact Dual Wide Band Patch Antenna with Modified Ground Plane	93
Priyanka Jain, Shagun Maheshwari and Archana Agarwal	
Contention Sensitive Routing for Mobile Ad Hoc Networks.	99
Richa Sharma, Neha Janu and Chhagan Doot	
An Analytical Approach for Accurate Design of MSPA Using Dielectric Constant Engineering (DCE).	107
Monika Mathur, Ghanshyam Singh and S.K. Bhatnagar	
Design of CAN-Based Enhanced Event Data Recorder and Evidence Collecting System.	115
Pankaj H. Chandankhede and M.M. Khanapurkar	
Detection of Brain Tumor in MRI Images, Using Fuzzy C-Means Segmented Images and Artificial Neural Network.	123
Parveen and Amritpal Singh	
Multiple Inputs Combinational Logic Minimization by Minterms Set	133
Sahadev Roy, Rajesh Saha and Chandan Tilak Bhunia	
Design and Simulation of 16 × 8 Synchronous SRAM in 90 nm CMOS Technology	141
Vipul Bhatnagar, Pradeep Kumar and Sujata Pandey	
A Voltage-Mode Nonlinear-Synapse Neural Circuit for Bi-partitioning of Graphs.	151
Mohd Samar Ansari	
CNFET-Based Resistive Sensor Interface with Voltage/Current-Mode Readouts	159
Mohd Samar Ansari and S.K. Tripathi	
Design of CMOS Ring Oscillators with Low Phase Noise and Power Dissipation for Data Transmission in RF Range	167
Dhruba Ghosh, Malay Ranjan Tripathy and Sujata Pandey	
A Novel Hybrid Method for Segmentation of Ultrasound Images	175
Yogendra Singh Poonia, Ramesh Kumar Sunkaria, Deepti Mittal and Dipesh Kumar Patidar	
Temperature Sensor Using a SMF-PCF-SMF Heterostructure.	187
Rekha Mehra and Heena Shahani	
Investigation of Channel Drop Filter Based on Two Dimensional Photonic Crystal Structure	193
Ritu Sharma, Mayur Kumar Chhipa and Lalit Kumar Dusad	

Design and Analysis of a Nano-Fiber with All-Normal and Flat Dispersion for Supercontinuum Generation 201
 Than Singh Saini, Ajeet Kumar and Ravindra Kumar Sinha

Investigation of Semiconductor Optical Amplifier for DWDM System with 50 GHz Channel Spacing 209
 Aruna Rani and Sanjeev Dewra

Automatic License Plate Recognition System Using Raspberry Pi 217
 Vijayaraghavan Sundararaman, T.G. Vijayalakshmi, G.V. Swathi and Sambit Mohapatra

Multiple Sink Data Aggregation. 223
 Krishna Joshi, T.P. Sharma, Shadab Siddiqui and Shahin Fatima

Handwritten Devnagari Script Database Development for Off-Line Hindi Character with Matra (Modifiers) 233
 Maninder Singh Nehra, Neeta Nain and Mushtaq Ahmed

Part-of-Speech Tagging of Hindi Corpus Using Rule-Based Method . . . 241
 Deepa Modi and Neeta Nain

A Survey on Security Analysis in Cloud Computing 249
 Suryambika, Abhishek Bajpai and Shruti Singh

Copper Nanofilm Antenna Design and Development: For X-Band Wireless Sensor Applications 263
 Rajendra R. Patil, R.M. Vani and P.V. Hunagund

Vein Biometric Template Security Using Overlapped Shares Accounting for Minimum Storage 271
 Ruchika Solanki, Saurabh Maheshwari, Vineet Khanna and Kalpana Sharma

Miniaturization of MEMs-Based Smart Patch Antennas for Biomedical Applications. 279
 Shankar Bhattacharjee and Santanu Maity

Authentication of Primary User at Physical Layer Through Approximation in Cognitive Radio. 287
 Muzzammil Hussain and Suditi Choudhary

Data-Based Correlation Scheme. 297
 Krishna Joshi, Shadab Siddiqui and Shahin Fatima

A Comparative Analysis of Different LFSR-Based Ciphers and Parallel Computing Platforms for Development of Generic Cipher Compatible on both Hardware and Software Platforms. 305
 Trishla Shah, Darshana Upadhyay and Priyanka Sharma

Generation of Automatic Variable Key to Make Secure Communication.	317
Bishal Kumar Singh, Subhasish Banerjee, Manash P. Dutta and C.T. Bhunia	
Vector Evaluated Genetic Algorithm-Based Distributed Query Plan Generation in Distributed Database.	325
Vikash Mishra and Vikram Singh	
A Novel MEMS-Based Frequency Tunable Rectangular Patch Antenna	339
Rajesh Saha, Santanu Maity and Lipi Sarkar	
Design and Optimization of Band-Stop Filter Using Metamaterial Structures for K-Band Applications.	347
Ngasepam Monica Devi and Santanu Maity	
Low-Cost Crash Protection System for Heavy Motor Vehicles.	353
Vishwajit Nandi, Rijita Poddar, Rajesh Saha and Sahadev Roy	
Effect of Parasitic Elements on Non-inverting Buck-Boost Converter Used in PV System	359
Subramanya Bhat and H.N. Nagaraja	
Effective Medium Approximation for Defining the Unavoidable Resistance of Solar Cell Front Contact.	367
S. Maity, P. Chakraborty, R. Raushan, C.T. Bhunia and P.P. Sahu	
A Novel Low-Power Design Approach to Exploit the Power Usage of AMBA APB Bridge.	373
Kiran Rawat, Kanika Sahni, Sujata Pandey and Ziauddin Ahmad	
Solar Wind and Diesel Hybrid Energy System: A Review.	381
R.A. Gupta, Bhim Singh and Bharat Bhushan Jain	
Analysis and Optimization of Stability for 6T SRAM Cell Using 180 nm Technology	391
Nidhi Tiwari, Srishti Gusain, Surabhi Chakravorty, Ankita Nirankari and Apoorva Khandelwal	
Harvesting Electric Field Energy for Powering Wireless Sensors of Smart Grid.	399
Anil Boyal, Akanksha Deo, Amit Kr. Pandey and Amit Limba	
Chalcogenide (LiGaSe₂, LiGISE, LiGaS₂): A Perfect Material to Design Highly Nonlinear PCFs for Supercontinuum Generation	409
Sandeep Vyas, Manish Tiwari, Takasumi Tanabe and Ghanshyam Singh	

Mach–Zehnder Interferometer: A Review of a Perfect All-Optical Switching Structure. 415
 A.I. Stanley, Ghanshyam Singh, James Eke and Hiroyuki Tsuda

Design and Analysis of Different Decoders for SAC-OCDMA Systems 427
 Soma Kumawat and M. Ravi Kumar

An Efficient Trust-Based Routing Scheme by Max-Min Composition of Fuzzy Logic for MANET. 435
 Joydeep Kundu, Koushik Majumder and Debashis De

Modified D-Latch Enabled BEC1 Carry-Select Adder with Low Power-Delay Product and Area Efficiency. 441
 Sakshi Bhatnagar, Harsh Gupta and Swapnil Jain

Identification of Devanagari Script from Bilingual Printed Text Documents 451
 Ranjana S. Zinjore and R.J. Ramteke

Ultra-Wideband Equal Power Divider Using Stepped-Impedance Technology. 463
 Atul Kumar Agrawal and Deepak Bhatia

Implementation and Performance Analysis of Enhanced SHA-192. 471
 Harshita and Sarvesh Tanwar

Human Object Detection in Images Using Shift-Invariant Stationary Wavelet Transform. 481
 Om Prakash, Manish Khare, Nguyen Thanh Binh and Ashish Khare

A Novel Framework for Extracting GeoSpatial Information Using SPARQL Query and Multiple Header Extraction Sources. 489
 Poonam Malpani, Paras Bassi, Mehul Mahrishi and Vipin Jain

Secure Data Sharing with Data Integrity in Public Clouds Using Mediated Certificate-Less Encryption. 501
 Atesh Kumar, Saurabh Mishra, Priyank Dubey and Niraj Kumar

K-N Secrete Sharing Scheme of Visual Cryptography for Hiding Image Using 2×2 Blocks Replacement. 511
 Ashish Sharma and Devesh Kumar Srivastava

Stepping Stone Detection Techniques: Classification and State-of-the-Art 523
 Rahul Kumar and B.B. Gupta

CBIR Feature Extraction Using Neuro-Fuzzy Approach. 535
 Ajay Kumar Bansal and Swati Mathur

Multiband and Wideband Antenna for Wi-Fi, WLAN, X-Band and Space Research Applications	543
Goswami Siddhant Arun, Deepak C. Karia and Bhushan Dhengale	
Triple Band Slotted Antenna for Wireless Applications.	559
Ankur Dalmiya and Om Prakash Sharma	
A Compact Design of Modified E-shaped Ground Plane Patch Antenna for Broadband Applications	567
Sanjay Sharma and Sanyog Rawat	
Frequency Switching in Coupled Microstrip Line Loaded with Split-Ring Resonator	573
Gurwinder Singh, Rajni and Anupma Marwaha	
A New Compact Dual Band Microstrip BPF for GSM (1.8GHz) and WiMAX Using Asymmetric Stepped Impedance Resonators	581
Tasher Ali Sheikh, Janmoni Borah, Sahadev Roy and Abhishek Kumar Pandey	
Performance Analysis of ZigBee Mesh Networks Under Nodes Failure	589
Jashan Preet Kaur, Rajdeep Kaur and Gurpreet Singh Mann	
Probabilistic-Based Energy Efficient Dynamic Route Discovery in MANET's.	599
Madan Mohan Agarwal, M.C. Govil and Anuj Kumar Jhankal	
A Survey Paper on Computational Intelligence Approaches	609
S. Taruna and Nidhi Bhartiya	
Simulation of p-GaN/i-In_aGa_(1-a)N/n-GaN Solar Cell for Maximum Efficiency	619
Manoj Thosar, R.K. Khanna and Ashwini Joshi Thosar	
Assessing the Severity of Attacks in Wireless Networks.	627
Jeril Kuriakose, V. Amruth, R. Jaya Krishna and Devesh Kumar Srivastava	
SD and TCH Blocking KPI Improvement Without Adding TRX Unit in BTS in GSM Network.	635
Jitendra Vaswani and Gaurav Sharma	
Design and Analysis of Right-Angled EBG Structure	645
Ajay Yadav, Dinesh Sethi, Priyanka Rahi and R.K. Khanna	
High-Speed Packet Encoded Error Correction Technique for Wireless HD Video Streaming	657
C.P. Latha, M.B. Manjunatha and A. Mohsin Khan	

Review of Circular Polarization Techniques for Design of Microstrip Patch Antenna 663
 Madhuri Sahal and V.N. Tiwari

A Proposed Modification Over Learning Vector Quantization and K-Means Algorithms for Performance Enhancement 671
 Shirish Nagar and Ajay Khunteta

Taxonomy of Recent DDoS Attack Prevention, Detection, and Response Schemes in Cloud Environment 683
 Omkar P. Badve and B.B. Gupta

Design of Compact Concentric Circular Ring Patch Antenna with Defected Ground Plane 695
 Neelam Choudhary, Ajay Tiwari, Brajraj Sharma, J.S. Saini and D. Bhatnagar

On the Bandwidth Enhancement of Modified Star-Triangular Fractal Antenna 703
 Simarpreet Kaur, Rajni and Gurwinder Singh

A Simple Miniaturized Dual Band Antenna for WiMAX/WLAN Applications 711
 Nirma Kumawat and Krishna Rathore

Fault Detection for the Cluster-Based System in Wireless Sensor Networks 719
 Rimpi Goyal and Sukhwinder Singh Sran

Gain and Bandwidth Enhancement of Single-Layered Slotted Triangular-Shaped Microstrip Patch Antenna with Stub for WLAN Applications 729
 Dheeraj Bhardwaj, Gitansh Gulati, Lakshit Bhardwaj and Komal Sharma

Design of Dual Resonator Broadband Multilayer Electromagnetically Coupled Microstrip Antenna for X-Band Applications 741
 Dheeraj Bhardwaj, Aayush Dwivedi, Nidhi Jain and Komal Sharma

An Environment Aware Frequency Selective Headset 751
 Sambit Mohapatra, G.V. Swathi and Vijayaraghavan Sundararaman

Performance Analysis and Optimization of 40 Gbps Transmission System over 4000 km with FBG 759
 Mukesh Kumar Gupta, Jyoti Agarwal, Anila Dhingra and Ghanshyam Singh

Broadband Modified U-Shaped Patch Antenna for Wireless Communication. 767
 Devendra Mehra and Sanyog Rawat

Performance Improvement of Epidemic Routing Protocol of Delay Tolerant Networks Using Improved Buffer Management.	773
Harminder Singh Bindra	
Elliptically Slotted Self-affine 8-Shaped Fractal Multiband Antenna.	783
Rohit Gurjar, Ravi Singh and Saurabh Kumar	
Design of Compact Triangular Patch Antenna for WiMax Applications	791
Manisha Gupta and Vinita Mathur	
Post-accident Assistance Using On-Board Diagnostics and Smartphones	797
Arghya Biswas and Abhishek Pal	
Digital Image Forensics and Counter Anti-forensics	805
Neha Singh and Sandeep Joshi	
Can We Use Mass-Based Similarity Measure in Classification?	813
Ashish Kumar, Roheet Bhatnagar and Sumit Srivastava	
CNT-Based Biomedical Sensor for Cancer Detection.	821
Argha Sarkar, B. Madhuri, Shivam Kumar and Santanu Maity	
Effective Role of Thrashing in Load Balancing During VM Live Migration.	829
Pradeep Kumar Tiwari and Sandeep Joshi	
Real-Time Abandoned Object Detection Using Video Surveillance.	837
Aditya Gupta, V.R. Stapute, K.D. Kulat and Neeraj Bokde	
Request Allocation and Resource Management Techniques in Cloud Computing	845
Swati Khemka and Mehul Mahrishi	
Blind Image Watermarking of Variable Block Size for Copyright Protection	853
Amit M. Joshi, Monica Bapna and Manisha Meena	
Compact Goblet-Shaped Single Band-Notched UWB Antenna.	861
Rajesh Kumar Raj, Krishna Rathore, Bhavana Peswani, Roopkishor Sharma and H.R. Chaudhary	
An Application of Firefly Algorithm for Clustering in Wireless Sensor Networks	869
Arshad Nadeem, T. Shankar, Rakesh Kumar Sharma and Sourabh K. Roy	
Microstrip Antenna with Defected Ground Structure (DGS) for Multiband Operation	879
Vinay Sharma and Rajesh Kumar Vishwakarma	

Design of a Compact Novel Planar Dual Band-Notched UWB Antenna 889
 Sanjiv Tomar and Ajay Kumar

X-Band and Ku-Band Patch Antenna for Radio Location Applications 897
 Amit Singh Bhadouria, Suman Kumari and Mithilesh Kumar

Procuring Wireless Sensor Actuator Network Security 905
 Jasminder Kaur Sandhu and Sharad Saxena

Performance Analysis of VoIP over WiMAX Networks Under Nodes Failure 917
 Jinia and Jarnail Singh

Design of Reduced Order Controller for Mechanical System 925
 Jyoti Kataria, Manish Kumar Madhav and Sunny Kumar Verma

A Survey on Black Hole Attack in MANET 933
 Shruti Singh, Abhishek Bajpai and Suryambika

Area-Efficient FPGA Model of LMS Filtering Algorithm 943
 Devendra Goyal and Manish Singhal

An Efficient Hybrid-Cascaded Framework for Emission Computed Tomography Using OSEM Image Reconstruction Algorithm 953
 Shailendra Tiwari and Rajeev Srivastava

A Review of Energy-Efficient Routing Protocols in Wireless Sensor Networks 963
 Simerjeet Kaur, Rajni and Barinder Paul Singh

A Study of Phase Shifting Surface 973
 Neha Singh and Kamal Kishor Choure

Review on Student Attendance Maintenance System: A Discontentment 987
 Anshuman Kalla and Dileep Kumar Tiwari

Author Index 999

About the Editors



Dr. Nitin Afzalpulkar started his research in the late 80s focusing on robotics, especially parallel robotic architectures and their implementations on transputer networks. He published several journal papers in this area and received a best conference paper award in 1989 in New Zealand. In the mid-90s his research interests turned to computer vision and its application for robotics. Here his initial work was on stereo vision algorithms and its implementation on robotic platforms. Currently, one main area of his research is still computer vision with focus on tracking and identification of human, emotion and gesture recognition,

application of machine vision for electronics industry. He has published extensively in international journals and conferences with two international best paper awards (Germany and Croatia) and has received three US patents in this area. In early 2000, he started research on microelectromechanical systems (MEMS) which forms a major area of his current research. He has published several papers in top journals in MEMS area and his book titled “Microfluidics and BioMEMS: Design, Fabrication and Applications” was published in 2009.



Dr. Vishnu Srivastava is presently working as Chief Scientist and Head of the Microwave Tubes Division, CSIR-Central Electronics Engineering Research Institute (CSIR-CEERI), Pilani (Rajasthan), India, and as Professor of Ac-SIR (Academy for Scientific and Innovative Research, New Delhi). He received the M.Sc. degree in Physics from Rajasthan University, Jaipur, in 1975, and the Ph.D. degree in Engineering from Lancaster University, UK in 1987. He was a commonwealth scholar from 1984 to 1987 in the UK, and was Junior Research Fellow at Rajasthan

University during 1975. He joined CSIR-CEERI, Pilani, in January 1976. At CEERI, he was involved with the design and development of various types of high power vacuum microwave devices for communication and radars. He developed X-band 200 kW tunable coaxial magnetron for ECCM radars. He developed space-qualified C-band 60 W TWT and Ku-band 140 W TWT for satellite communication. He developed SUNRAY-codes for small-signal and large signal analysis of beam-wave interaction in TWTs. His successfully developed SUNRAY-1D software code for multi-signal analysis of beam-wave interaction in TWTs, was exported to UK., and was also purchased by MTRDC (DRDO), Bangalore. He developed technologies for the successful development of high efficiency vacuum microwave amplifiers (Space TWTs) for satellite communication. Presently, he is associated with the design and development of vacuum microelectronic devices for THz communication—requiring innovations in MEMS technologies (UV LIGA processes) for such devices. He has more than 120 research publications in different national and international journals, and has already guided 8 Ph.D. students and more than 60 ME/MTech students. He received IETE—JC Bose memorial awards for best engineering paper and best project team . He is a fellow of IETE and VEDA Society, and senior member of IEEE, CSI, IPA, IVS, PSI, and IFTA. Recently, he was awarded Honorary Fellowship of Society for Education & Research Development (SERD), New Delhi. His present interests are in the design and development of high efficiency, high power vacuum microelectronic devices for mm- and sub-mm-wave frequencies.



Dr. Ghanshyam Singh has more than 15 years of teaching and research experience and is currently Associate Professor in the Department of Electronics & Communication Engineering at Malaviya National Institute of Technology, Jaipur, India. He obtained his Bachelor's degree in Electronics & Communication Engineering from National Institute of Technology, Silchar, Assam, India and his Master's and Ph.D. degrees in Electronics & Communication Engineering from Malaviya National Institute of Technology, Jaipur, India. He has guided more than 20 master's theses and is presently guiding 6 Ph.D. research

scholars. His areas of research interest include optical communication engineering, optical switches, optical logic gates & circuits, photonic crystal fibers, nano-photonics, nano-optical structures, RF & microwave devices, microstrip and smart antennas. He has worked with the Optics group at the Department of Physics, Herriot Watt University, Edinburgh, UK, under the research grant from TEQIP, Government of India. He had also been a recipient of CIMO fellowship from Government of Finland to work with photonics groups at Nanofabrication Laboratory, Department of Physics and Mathematics, University of Eastern Finland, Joensuu, Finland. He has been a Visiting Professor at Tsuda Labs,

Department of EEE, KEIO University, Hiyoshi Campus, Japan and participated in IKSS, Krutyn Poland. He is presently engaged in a DST-JSPS sponsored research project with Prof. Hiroyuki Tsuda & Group, KEIO University, Japan (Period: 2014–2016). He is presently a member of IEEE Photonic Society, SPIE, Optical Society of America (OSA), Optical Society of India (OSI), Indian Laser Society (ILA), Broadcast Engineering Society of India (BESI), IETE India, Institute of Engineers India, and Indian Society for Technical Education (ISTE).



Dr. Deepak Bhatnagar He obtained his Master's and Ph.D. degrees from university of Rajasthan Jaipur in 1981 and 1986 respectively. Presently he is working as Professor in Department of Physics, University of Rajasthan and Director, Center for Converging Technologies. He is heading Microwave and Communication Group in Department of Physics, University of Rajasthan, Jaipur. His main area of research interest is design of antennas for mobile, wireless and satellite communication systems. Till date 20 students have obtained their Ph.D. degree under his supervision. He has produced nearly 200

research papers in international and national journals and proceedings of various international and national conferences. He is author of six books for under graduate students of Rajasthan state. He has successfully completed five major research projects sanctioned by ISRO, Bangalore, UGC, New Delhi, DST, New Delhi and DIT, New Delhi. He is senior member of IEEE, USA and Fellow of IETE (India).

A Novel Image Zooming Technique Using Wavelet Coefficients

Himanshu Jindal, Singara Singh Kasana and Sharad Saxena

Abstract The objective of getting a good quality of image plays an important role in applications related to image processing. To achieve this, the quality of image should be monitored dynamically and by applying optimized algorithms. Thus, the zoomed image got using algorithms is sharper compared to other methods. Hence keeping all this in mind on this source of information, discrete wavelet transform (DWT) with various interpolation techniques had been applied upon variances to obtain their values. The proposed method gives better *PSNR* compared to other methods. Thus in this paper, an algorithmic approach is used to zoom a given image in wavelet domain and to get a sharper image using various interpolation techniques.

Keywords DWT · Interpolation · MSE · PSNR

Introduction

The image formed on the surface either through reflection or refraction is the visualized analogous form of the rays coming from object image. The main work in image zooming is interpolating new pixels that surround the original pixels. There are several ways of zooming an image, which include:

Himanshu Jindal (✉) · S.S. Kasana · Sharad Saxena
School of Mathematics and Computer Applications, Thapar University,
Patiala 147004, Punjab, India
e-mail: himanshu.jindal@thapar.edu

S.S. Kasana
e-mail: singara@thapar.edu

Sharad Saxena
e-mail: sharad.saxena@thapar.edu

- *Pixel replication*—This method is used to zoom an image so that it would be easily displayed on screen considering the initial pixel values available for an image.
- *Interpolation*—The process of calculating the values of unknown pixels by using the values of known data is called interpolation. This process is applied in the same manner as constructing new data values. There are various interpolation techniques used for image zooming, which are as follows:
- *Beeline*—This is the easiest approach for assessment of anonymous values among the avowed values.
- *Bilinear*—It is used for interpolating the functions of two variables. The bilinear interpolation is the reassembling process of the pixels. It produces real images.
- *Bicubic*—It is used for interpolating pixel values in a multidimensional lattice. The bicubic takes 16 pixels instead of 4 pixels for interpolation. Thus, the image formed with bicubic interpolation is undisturbed and has less issues of distortion.
- *Nearest neighbor*—It is the simplest form of multiformity of the pixels in more than one dimension. It takes only one pixel which is close to the interpolated point. This technique easily zooms the image by expanding each pixel size.

Related Work

In this section, various existing techniques are reviewed which have explored the various studies that have been done to understand the properties of an image through various operations. The two keen phases are identified for image processing [1]. The first phase is rendering phase and is based on edge direction which maps low resolution images to high resolution by using filtering process in second phase which is correction and thus performing linear interpolation and correction among the filtered output. This phase prevents interpolation across edges providing efficacy to the applied interpolation. The *DCT*-stationed exaggeration measures that can evaluate proportion and contour exaggeration quantitatively that are computationally efficient were introduced further for getting better images [2, 3]. Edge-counseled bicubic involution and edge-adaptive interpolation were also proposed for enhancing the image efficacy [4, 5]. These researches were given to get a quality image. Some researchers worked on partial differential equations and new interpolation technique using exponential B-spline to show effectiveness and reliability of the proposed using the above-said methodology [6, 7]. Most examined various interpolation methods for getting neighboring pixels for accessing RGB colors and grayscale of an individual image [8–11]. Demosaicking methods using directional or adaptive color methods were used to get sharper images [12–14]. As the image we get after zooming has issues of blurring, noise, and distortion of pixels, in order to remove these issues, various interpolation-based techniques were introduced, namely shearlet-based iterative refinement, sparsity priors, and

grayscale level zooming [15–17]. These methods failed to get quality image. The researches were implemented on the basis of edge-directed interpolation for getting high-resolution image [18]. Thus, it is observed that the image still does not giving reliable information. Therefore, various interpolation methods were mixed to check the accuracy of the results with previous failures [19–25]. These provided the image with better results but were not up to the mark, so these would not be used in the long run for providing zoomed images. Hence, bicubic interpolation was combined with wavelet transform in which all the regions were divided into subbands and can further be reused [26]. This approach would come out to be beneficial in the area of image processing as it helped to a certain limit to get a particular area of the image. Various measures were done to check the performance and getting super-resolution images and comparison is made with other interpolation techniques of zooming for getting better results [27–29]. A modified approach over edge direction and interpolation with edge direction was provided to get better quality image than wavelet transform [30–32]. However, all these findings failed to provide better quality images.

From this literature survey, one can conclude that there is a need to design an image zooming technique in frequency domain which can provide better visual quality-zoomed images.

Proposed Algorithm

In this section the proposed technique is discussed.

- Step 1.** Transform the image using *DWT* process up to required level.
- Step 2.** Image is transformed into wavelet subbands.
- Step 3.** Apply interpolation technique on each of the four subbands to get the zoomed subbands.
- Step 4.** Apply inverse *DWT* on zoomed subbands to get the zoomed image.

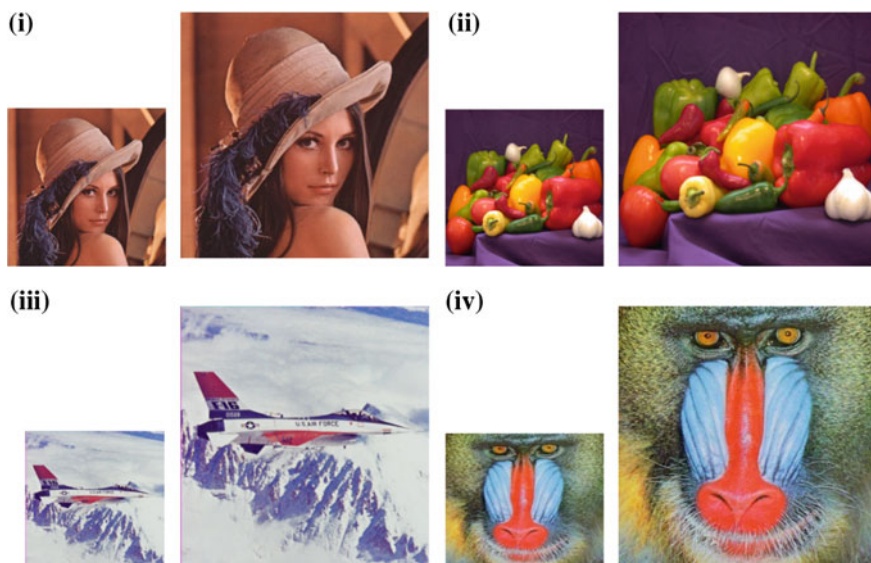
Experimental Results

The *PSNR*(dB) is calculated between the original and zoomed images. The various interpolation techniques with *DWT* are applied on various images and calculated *PSNR* values are shown in Table 1.

Thus from Table 1, it is observed that the *DWT* with spline interpolation is far better than other interpolation techniques for providing better quality images. The resultant images are shown in Fig. 1 and are zoomed using *DWT* with various interpolation techniques.

Table 1 Calculated *PSNR*(dB) using *DWT* with various interpolation techniques

Images	Methods					
	DWT with pixel replication	DWT with beeline interpolation	DWT with bilinear interpolation	DWT with bicubic interpolation	DWT with spline interpolation	DWT with nearest neighbor interpolation
Airplane	63.2432	65.5544	61.1754	68.2324	74.1646	71.4145
Baboon	60.0028	57.2344	59.3321	66.0032	67.7835	65.2972
Lena	62.3321	53.4565	67.5443	65.3023	74.5855	68.4338
Peppers	60.7421	56.9879	65.6654	66.5560	77.3646	66.1501

**Fig. 1** Original and surged images of **i** Lena **ii** Peppers **iii** Airplane **iv** Baboon [34]

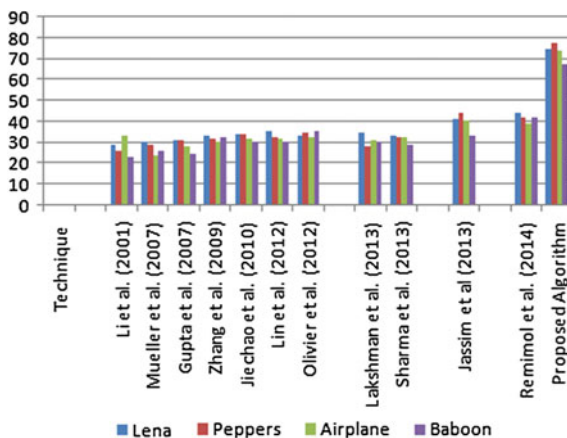
Comparison with Existing Algorithms

A model graph has been prepared in Table 2 in order to depict the difference in values of the image taken into consideration. This result is shown in a way to show that a better quality image can be formed using *DWT* technique.

The above tabular notation depicts the obtained values of images on which the various operations had been applied by different researches, where observational value is recorded parallel to proposed algorithm, stating the application of *DWT* applied before obtaining the resultant values. The marginal difference is more than 22 % when calculated as an average for all the values when compared.

Table 2 Graphical depiction of compared values of *PSNR*(dB)

Technique	Image			
	Lena	Peppers	Airplane	Baboon
Li et al. [18]	28.97	25.92	33.46	23.54
Mueller et al. [23]	30.29	29.39	24.06	25.85
Gupta et al. [7]	31.55	30.98	28.40	24.63
Zhang et al. [33]	33.62	31.74	30.49	32.46
Jiechao et al. [13]	33.98	34.37	32.25	30.38
Olivier et al. [19]	35.37	32.65	32.24	30.50
Olivier and Hanqiang [24]	33.16	34.50	32.92	35.47
Lakshman et al. [15, 16]	34.81	28.40	31.41	30.84
Sharma and Swami [28]	33.08	32.80	32.43	29.33
Jassim [10]	41.34	43.93	40.32	33.34
Remimol and Sekar [26]	44.12	41.94	39.48	42.22
Proposed algorithm	74.58	77.36	74.16	67.78

Fig. 2 Graphical notation of abstracted value-based tabulation

Hence it is observed from graphical notation of the comparison chart (Fig. 2) that the proposed algorithm gives higher values depicting the variation of change in comparison with other researches.

Conclusion

Thus, for enhancing the property aspect of the image, by performing various operations on the image, *DWT* is applied. The applicability of *DWT* processing using different wavelet sets that can be applied on an image and the transformations

are made which follow some given rules in a prescribed format. This can be executed as per the available values of the image, and then can further be divided into four different parts. Each part can be further evaluated individually, and independent values can be obtained applying a different set of rules on all the four different images. In other words, the wavelet transform helps to decompose the image into mutually adjoined sets of wavelet subbands.

Acknowledgments The research and findings are supported by Thapar University, Patiala, under Seed Grant Project Scheme. I thank Dr. Singara Singh Kasana and Dr. Sharad Saxena for sharing their pearls of wisdom with me during the course of this work.

References

1. Allebch, J., Wang, P.W.: Edge directed interpolation. *Int. J. Image Process.* **5**(4), 707–710 (1996)
2. Chadda, S., Kaur, N., Thakur, R.: Zooming techniques for digital images: a survey. *IJCST* **3** (1), 519–523 (2012)
3. Choi, K.-S., Ko, S.-J.: Fast content aware image resizing scheme in the compressed domain. *Trans. Consum. Electron.* **55**(3), 1514–1521 (2009)
4. Dengwen, Z.: An edge-directed bicubic interpolation algorithm. In: *Third International Conference on Image and Signal Processing*, vol. 3, pp 1186–1189 (2010)
5. Feng, W.X., Fei, L.H.: An edge-adaptive interpolation algorithm for super-resolution reconstruction. *ICMINS* **2**, 81–84 (2010)
6. Gao, R., Song, J.P., Tai, X.C.: Image zooming algorithm based on partial differential equations technique. *IJNAM* **6**(2), 284–292 (2009)
7. Gupta, B.R., Lee, G.B., Lei, J.J.: A new image interpolation technique using exponential B-spline. *Int. J. Emerg. Trends Technol. Comput. Sci.* Dongseo University, Busan, S. Korea, 169–176 (2007)
8. Hajzadeh, M., Helfrush, M.S., Tahk, A.: Improvement of image zooming using least directional differences based on linear and cubic interpolation. In: *Second International Conference (ICCCC)*, pp 1–6 (2009)
9. Hung, K.-W., Siu, W.C.: Fast image interpolation using the bilateral filter. *Image Process.—IET* **8**(5), 877–890, (2012)
10. Jassim, F.A.: Image inpainting by Kriging interpolation technique. *WCSIT J.* **3**(5), 91–96 (2013)
11. Jean, R.: Demosaicing with the Bayer pattern. In: *International Conference (ICASSP)*, pp 11–15. University of North Carolina (2013)
12. Jeong, B.G., Kim, H.S., Kim, S.C., Eom, I.K.: Edge adaptive demosaicking for reducing artifact along line edge. In: *Conference on Image and Signal Processing*, pp. 316–319 (2008)
13. Jiechao, W., Zhiwei, L., Min, Z.: Two new proposed image zooming methods. In: *6th International Conference (ICWCNMC)*, pp 1–4 (2010)
14. Kim, H., Cha, Y., Kim, S.: Curvature interpolation method for image zooming. *Int. Conf. Image Process.* **15**(5), 1895–1903 (2011)
15. Laksman, H., Limm, W.Q., Schwaz, H., Mape, D., Kutniok, G., Wigand, T.: Image interpolation using Shearlet based iterative refinement. In: *International Conference on Image Processing. IEEE*, Aug 2013a
16. Laksman, H., Limm, W.Q., Schwaz, H., Mape, D., Kutniok, G., Wigand, T.: Image interpolation using Shearlet based sparsity priors. In: *The International Conference on Image Processing*, pp 655–659. IEEE (2013b)

17. Li, J., Xin, M., Jin, J.: An evolutionary approach for gray-level image zooming. In: NASA/ESA Conference on Adaptive Hardware and Systems, pp 383–389 (2011)
18. Li, X., Orchard, M.T.: New edge-directed interpolation. *Trans. Image Process.* **10**(10), 1521–1527 (2001)
19. Lin, T.C., Truong, T.K., Hong, S.H., Wang, L.: Novel approaches to the parametric cubic spline interpolation. *Image Process. Comput. Vis.* **4**, 448–454 (2012)
20. Liu, H., Wei, Z.: An edge adaptive structure tensor kernel regression for image interpolation. *ICFCC* **2**, 681–685 (2010)
21. Lukin, A.: High-quality spatial interpolation of interlaced video. *Laboratory of Mathematical Methods of Image Processing, Computer Vision and Graphics*, pp 301–307 (2008)
22. Lukin, A., Krylov, A.S., Nasonov, A.: Image interpolation by super-resolution. *IATCIS*, 483–489 (2009)
23. Mueller, N., Lu, Y., Do, M.N.: Image interpolation using multiscale geometric representations. *Int. Soc. Opt. Photonics Electron. Imaging.* 11–16 (2007)
24. Olivier, R., Hanqiang, C.: Nearest neighbor value interpolation. *IJACSA J.* **3**(4), 318–321 (2012)
25. Patel, V., Mistree, K.: A review on different image interpolation techniques for image enhancement. *IJETAE J.* **3**(12), 129–133 (2013)
26. Remimol, A.M., Sekar, K.: A method of DWT with Bicubic interpolation for image scaling. *IJCSE J.* **3**(02), 131–135 (2014)
27. Roy, R., Pal, M., Gulati, T.: Zooming digital images using interpolation techniques. *IJAEM J.* **2**(4), 34–45 (2013)
28. Sharma, A., Swami, P.D.: Redundant wavelet transform based image super resolution. *IJERA J.* **3**(4), 2055–2062 (2013)
29. Sinha, A., Kumar, M., Jaiswal, A.K., Saxena, R.: Performance analysis of high resolution images using interpolation techniques in multimedia communication system. *Signal Image Process. Int. J.* **5**(2), 39–49 (2014)
30. Tam, W.S., et al.: A modified edge directed interpolation for images. In: 17th European Conference (ESPCGS), pp 283–287. Scotland (2009)
31. Wang, M., Blu, T.: Generalized YUV interpolation of CFA images. In: 17th International Conference (ICALIP), pp 1062–1065 (2010)
32. Wong, C. S, et al.: Adaptive directional window selection for edge-directed interpolation. In: 19th Conference (ICCCN), pp 1–6 (2010)
33. Zhang, J., Ma, S., Zhang, Y., Zhao, D.: Fast and effective interpolation using median filter. In: Pacific-Rim Conference on Multimedia, pp 1176–1186 (2009)
34. <http://in.mathworks.com/discovery/digital-image-processing.html>

Analysis of Operational Transformation Algorithms

Santosh Kumawat and Ajay Khunteta

Abstract In multiuser groupware systems, consistency maintenance and concurrency control are the most significant challenges. In groupware systems, user groups are permitted to update the shared data simultaneously. Operational transformation (OT) is a successful method for consistency maintenance in multiuser shared applications. OT, in general, supports two basic operations: insert/delete for character operations. We have done the literature review of the evolution of OT algorithms over the last 25 years since 1989. OT is discussed based on existing main OT algorithms such as dOPT, adOPT, GOT, GOTO, SDT, SOCT2, SOCT3/4, and ABT which are analyzed on the basis of the main properties as criteria of correctness, remote operation property, storage, etc. Then, categorization is done for all existing OT algorithms on the basis of major existing algorithms such as dOPT, adOPTed, GOT, GOTO, SDT, SOCT2, SOCT3/4, and ABT and then further classified on the basis of area of operation like undo, char, string, web, graph, etc. OT algorithms supporting string handling are also analyzed.

Keywords Groupware system · Distributed system · Operational transformation · Inclusion transformation · Concurrency · String handling · Consistency maintenance

Introduction

In real-time groupware systems which have multiple users, the actions of all users must be immediately propagated to all other users. Groupware systems are multiuser systems which have a shared environment and require sharing of data. The

Santosh Kumawat (✉)
Poornima University, Jaipur, Rajasthan, India
e-mail: santoshkumawat82@gmail.com

Ajay Khunteta
Poornima College of Engineering, Jaipur, Rajasthan, India
e-mail: khutetaajay@poornima.org

prime requirements of groupware systems are fast response times, fine granularity, and concurrency control. Transformation algorithms are needed for consistency control in multiuser shared systems.

Traditional concurrency control methods were not suitable for distributed shared applications because they may cause the loss of user interaction results and so fail to satisfy requirement of quick local response which fulfills user intentions. Also in this case local response satisfies consistency and convergence.

In the past 25 years, OT [1, 2] is used for concurrency control in multiuser shared collaborative systems. OT achieves better user intention preservation with convergence and causality preservation. It does not reduce responsiveness and concurrent work [3] but permits users to modify shared matter at the desired time [4], which helps in development of collaborative systems in the desired collaboration medium.

Operational Transformation

In the multiuser environment, OT does replication of the shared data at all user sites. At a site, first, local operations are executed and OT transformations remote operations repair differences and inconsistencies.

OT Framework

Consider the example in which data get replicated at two shared sites. At site A and site B we have a list of cities. If we perform insert and delete operations at sites A and B and then broadcast it to another site, then without OT we get the wrong output but with OT we get the right output. The process is explained in Figs. 1 and 2.

Algorithms

This paper studies the major OT algorithms of the past 25 years for consistency maintenance in group editors, which consist of the distributed operation transformation (dOPT) algorithm [5], the SCOT2 [6], SCOT 3/4 algorithm [7], the adopted (adOPTed) algorithm [8], admissibility-based transformation (ABT) algorithm [9], ABT-undo (ABTU) algorithm [10], the state difference transformation (SDT) algorithm [11], admissibility-based sequence transformation (ABST) [12], and admissibility-based transformation with strings (ABTS) algorithm [13], the GOT optimized (GOTO) algorithm [2], and the generic operational transformation (GOT) algorithm [14].

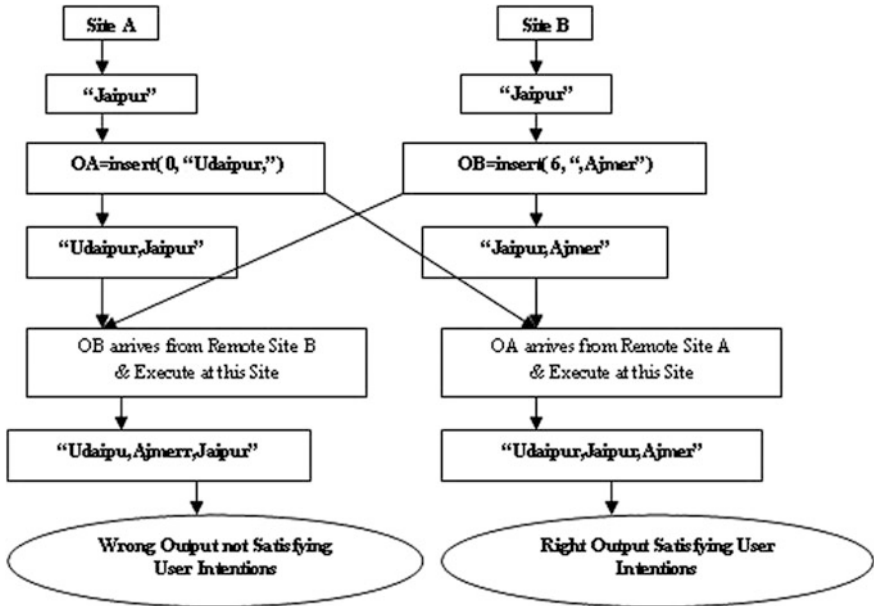


Fig. 1 Example of string operations without OT implementation

dOPT

GROVE adopted a replicated architecture of shared users to avoid a single point of failure and achieve good responsiveness in the system. GROVE has invented distributed operation transformation algorithm [5]. The dOPT-puzzle is the weakness of this algorithm. This algorithm has for local operations immediate feedback. It is distributed and does not have a central server. It fulfills the precedence property and enforces the transformation property. Properties of dOPT are explained in Fig. 3.

adOPTed

The adOPTed algorithm proposed by Ressel [8]. The adOPTed algorithm is right in general but has not proved intention preservation property. The algorithm has all the positive strengths of dOPT which have improved it. Various properties of adOPTed algorithm such as correctness criteria, etc., are explained in Fig. 4.

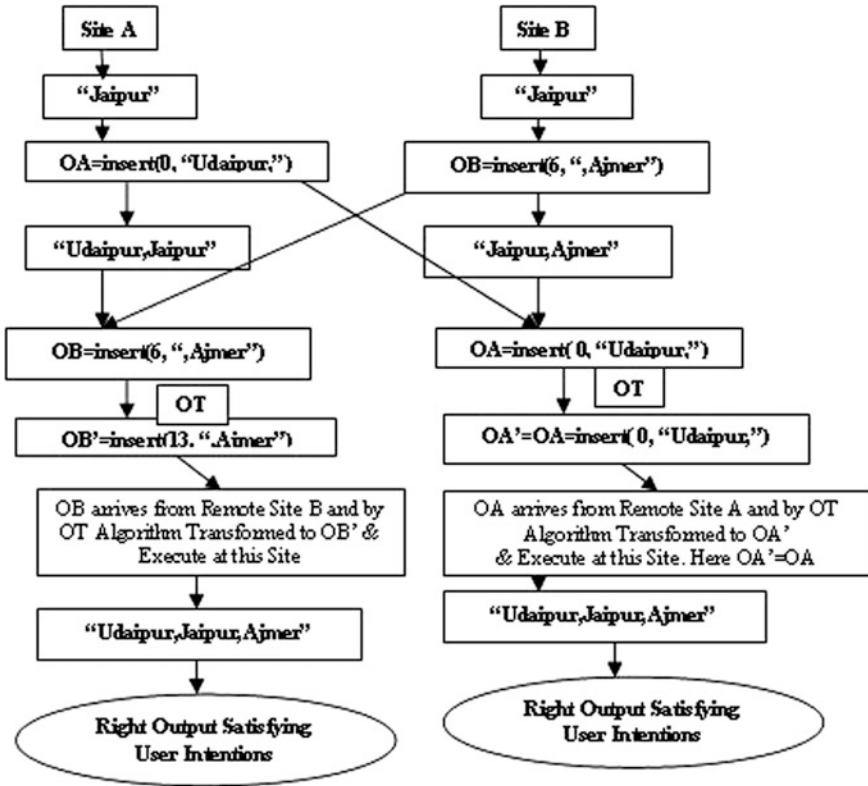


Fig. 2 Example of string operations with OT implementation

GOT

The GOT control algorithm is good for convergence. It is integrated with undo/do/redo scheme [14]. Correctness proof of algorithm is missing. It supports only basic string operations: Insert/Delete.

In this convergence TP2 is not a necessary condition. IT and ET algorithms pair has been devised for string-wise insert/delete. In a fully replicated system, convergence is achieved by GOT, which ensures at all sites cursor position maintenance and consistency maintenance. By adopting an undo/do/redo scheme GOT ensures total order. Properties of GOT can be seen in Fig. 5.

GOTO

Optimization of the GOT control algorithm is possible by two postconditions, TP1 and TP2 to reduce the number of IT/ET transformations. The optimized algorithm

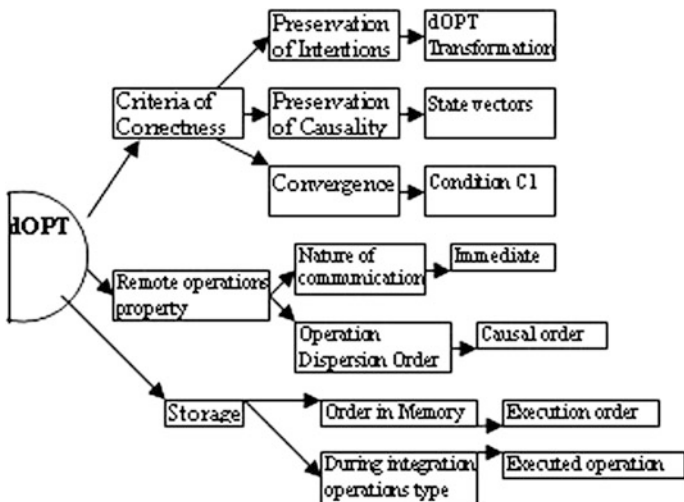


Fig. 3 Analysis of dOPT algorithm

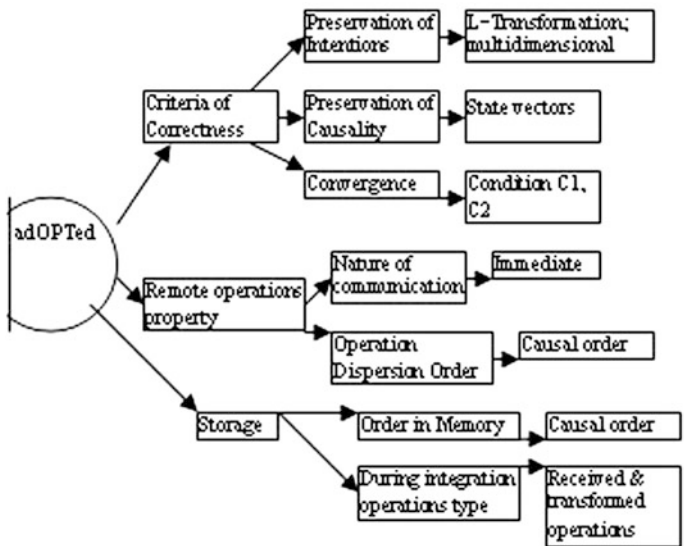


Fig. 4 Analysis of adOPTed algorithm

of the GOT control algorithm is called GOTO (GOT Optimized). To handle the so-called “lossy IT” problem GOTO [2] needs extra memory. Time complexity of the GOTO control algorithm is $O(n^2)$. It is required to extend the algorithm to support strings. It should have integration of sequences. It fulfills the convergence property, precedence property, transformation property 1, and transformation

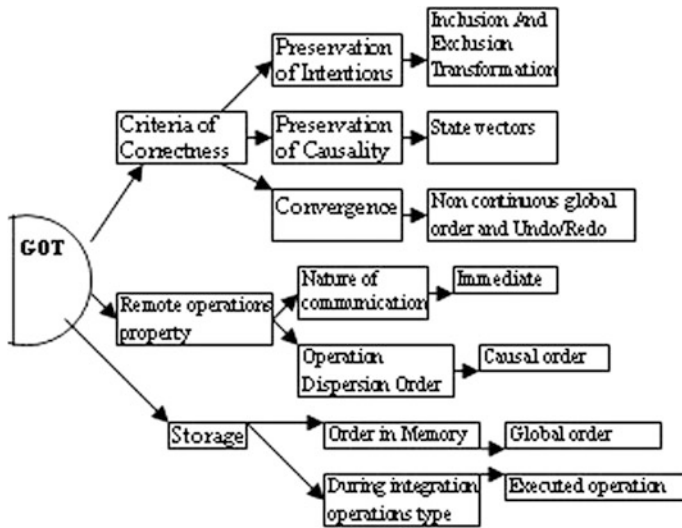


Fig. 5 Analysis of GOT algorithm

property 2 and has better undo-based operations. It is tested in editing programs such as CoMaya, CoWord, etc. Properties of GOTO control algorithm are explained in Fig. 6.

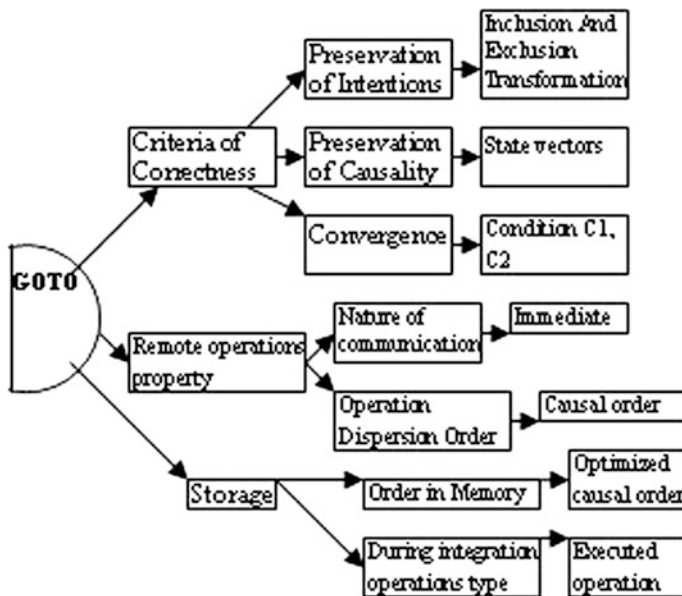


Fig. 6 Analysis of GOTO algorithm

SOCT3/SOCT4

SOCT3 has local execution, broadcast, and reception of operations. In SOCT4 and SOCT3, the operations are ordered globally by a timestamp which is given by a sequencer. In SOCT3/SOCT4 string handling are not supported. It desires implementation of algorithms in real-time applications. State vectors are not needed. Properties of SOCT3/4 are highlighted in Fig. 7.

SDT

SDT [11] has solved the TP2 puzzle. Properties of SDT can be seen in Fig. 8. Various mechanisms such as group undo, optional locking, and multi-version should be based on the concept of SDT.

ABT

ABT [9] depends on conditions like admissibility and preservation of causality and which under all conditions do not require transformation functions to work. Exclusive transformation (ET) is simple in ABT.

The string-wise ABTS algorithm by Li and Li [13] is extended from its character-wise ABT algorithm. ABTS is the first string-wise algorithm based on

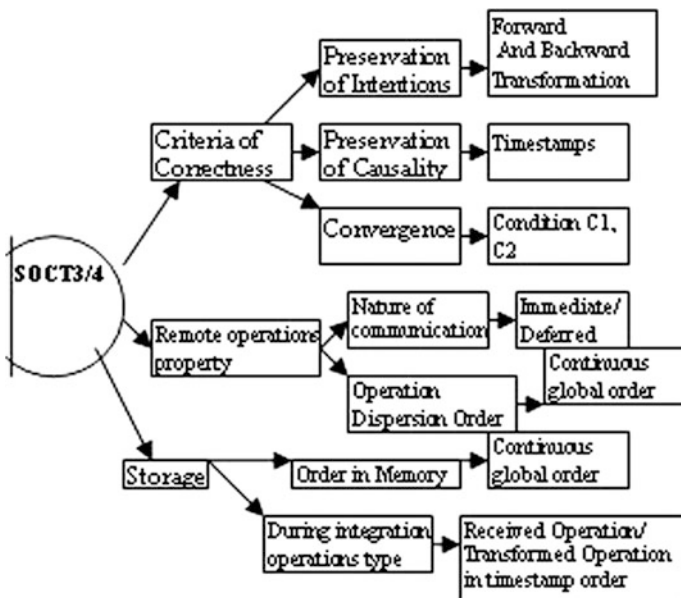


Fig. 7 Analysis of SOCT 3/4 algorithm

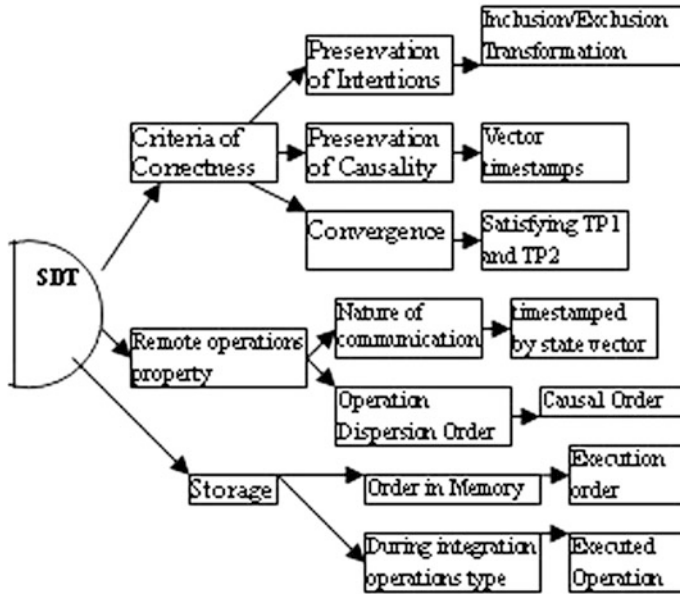


Fig. 8 Analysis of SDT algorithm

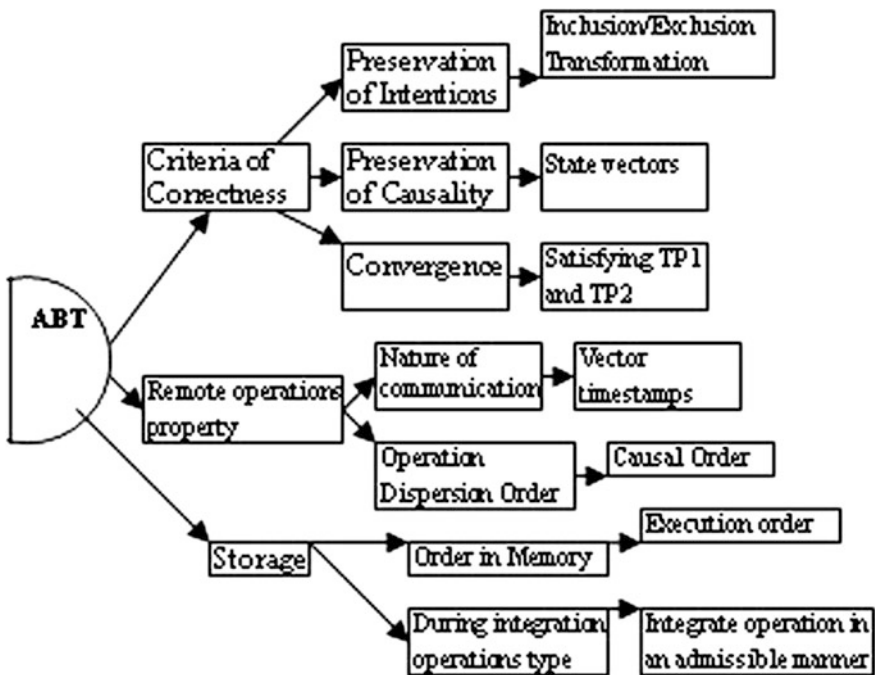


Fig. 9 Analysis of ABT algorithm

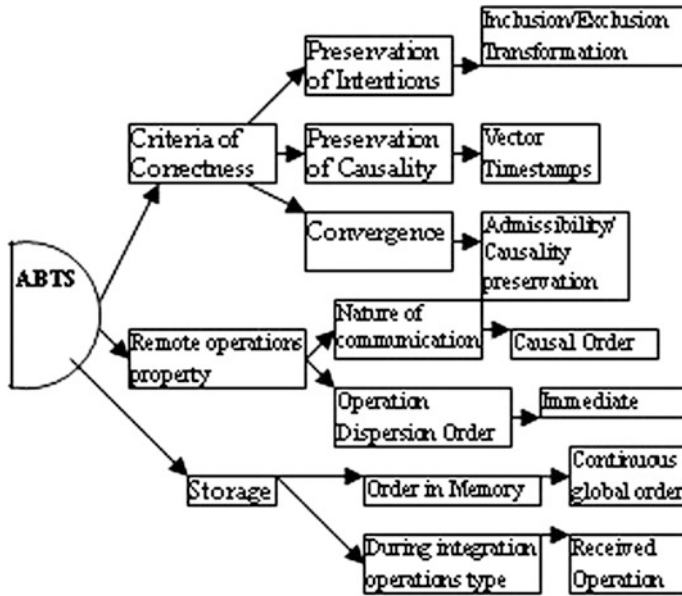


Fig. 10 Analysis of ABTS algorithm

ABT framework, which is formally proved without saving object relation. The time and space complexity of the presented ABTS algorithm is $O(IHI)$. ABTS does not need a total order of execution and reversibility of operations. In algorithms like ABT, ABTS, and ABTU, IHI grow indefinitely. ABTU provides integrated support of do and selective undo. ABST follows concepts like ABT and hence its correctness could be formally proved. Properties of ABT can be seen in Fig. 9 and properties of ABTS are explained in Fig. 10.

Categorization of OT Algorithms

On categorizing all existing algorithms on the basis of major existing algorithms such as dOPT, adOPTed, GOT, GOTO, SDT, SOCT2, SOCT3/4, ABT, and then further classified on the basis of area of operation like undo, char, string, web,

Table 1 Categorization of OT algorithms

Operations	Major algorithm							
	dOPT	adOPTed	GOT	GOTO	SOCT2	SOCT3/4	SDT	ABT
Character	6	5	5	13	3	4	3	7
Undo/Do	2	1	1	2	1		1	2
Graph/Web-based	6			8	2		2	2
String		1	1					1
Total papers	14	7	7	23	6	4	6	13

Table 2 Comparison of OT algorithms

Table	dOPT	adOPTed	GOT	GOTO	SOCT2	SOCT3	SOCT4	SDT	ABT	ABTS
Time complexity	Consume more time	Less than dOPT	A bit less than adOPTed	$O(H^2D)$	$O(H^2D)$	A bit more than SCOT4	A bit more than ABT	$O(H^2D)$ which is slower than	$O(H^2D)$	$O(H)$
Support string handling	No	No	<u>Yes</u>	<u>Yes</u>	No	No	No	No	No	<u>Yes</u>
Framework	CC Framework	CC Framework	CC Framework	CC Framework	CC Framework	CC Framework	CC Framework	CCI Framework	ABT Framework	ABT Framework
Space complexity	More space	A bit less than dOPT	$O(H^2D)$	$O(H^2D)$	$O(H^2D)$	A bit more than SCOT4	A bit more than ABT	A bit more than ABT	$O(H)$	$O(H)$

graph, etc., we get as in Table 1. In Table 1 is shown classification of 80 papers. In Table 1, a column is for a particular algorithm and a row is for a particular operation. The quantity in a cell shows the number of papers based on a particular algorithm supporting a particular operation. From Table 1 we find that only three algorithms support string handling—GOT, GOTO, and ABTS.

In Table 2 a comparison is done of GOT, GOTO and ABTS with respect to parameters like string handling, time, and space complexity. The second row indicates support for string handling and the values for GOT, GOTO, and ABTS are underlined. Only these three algorithms—GOT, GOTO, and ABTS support string handling which have value ‘yes’ and the rest all have value ‘No’. In the third row space complexity is shown and the values are encircled. In the first row time complexity is shown and the values are underlined. GOT and GOTO have time and space complexity of order $O(|H^2|)$ but ABTS have time and space complexity of order $O(|H|)$. So From Table 1 we conclude that only three OT algorithms support string handling called GOT, GOTO and ABTS. From Table 2 we conclude that ABTS have support for string handling and is better than GOT and GOTO because it has less time and space complexity. Also, ABTS is based on ABT framework which can be formally proved.

Conclusion

In distributed systems groupware systems are multiuser interactive computer-based systems where users have great interaction with each other. Traditional consistency methods do not apply in groupware systems because they only consider system limited issues, serial application, and may not satisfy interaction results and user intention consistency. It is analyzed that OT is the most desired standard solution to concurrency control and consistency maintenance which satisfies intentions. In this review a study of OT techniques, over the past 25 years is presented. A comparative study of 80 papers is done of various algorithms of OT based on different parameters and it has discussed major issues, algorithms, achievements, and remaining challenges.

All existing OT algorithms are classified on the basis of main properties like criteria of correctness, remote operation property, storage, etc., which can be observed from Fig. 3 to Fig. 10. Also, a relative comparison of a number of OT algorithms including dOPT, adOPTed, GOT, GOTO, SDT, SOCT2, SOCT3, SOCT4, ABT, ABTS has been done relative to various parameters and constraints that are intention preservation, causality preservation, convergence for correctness criteria, in case of remote operations nature of communication and order of operation dispersion and memory operations like order in memory or during integration operation type in memory and also other parameters like time complexity, space complexity, support for string handling, transformation functions, and framework. All 80 papers at first get classified on the basis of major algorithms like dOPT, adopted, GOT, GOTO, ABT, SDT, SOCT2, SOCT3/4. Also, they are further are subcategorized on the basis of area of operation like string, character, undo,

web-based, graphical, etc. In the literature, only the GOT, GOTO and ABTS algorithms support string-wise operations. ABTS is the best string handling algorithm as it has less time and space complexity.

User intentions preservation should be considered more in OT algorithms. More work is required to reduce time complexity and space complexity of OT algorithms. Very few OT algorithms support insert/delete string operations so it is required development of OT algorithms supporting new composite string operations like cut-paste, find-replace, which can be formally proved. Also, integration of string handling and undo operation is still pending in OT algorithms.

References

1. Davis, A.H., Sun C., Lu, J.: Generalizing operational transformation to the standard general markup language. In: ACM (2002)
2. Sun, C., Ellis, C.: Operational transformation in real-time group editors: issues, algorithms, and achievements. In: ACM CSCW'98 (1998)
3. Sun, C., Jia, X., Zhang, Y., Yang, Y., Chen, D.: Achieving convergence, causality-preservation, and intention preservation in real-time cooperative editing systems. *ACM Trans. Comput. Hum. Interact.* **5**(1), 63–108 (1998)
4. Bentley, R., Dourish, P.: Medium versus mechanism: supporting collaboration through customization. In: ECSCW'95 Proceedings (1995)
5. Ellis, C.A., Gibbs, S.J.: Concurrency control in groupware systems. *ACM Sigmod Rec.* **18** (2): 399–407 (1989). doi:[10.1145/66926](https://doi.org/10.1145/66926). Retrieved 2007-07-26
6. Suleiman, M., Cart, M., Ferrié, J.: Concurrent operations in a distributed and mobile collaborative environment. In: Proceedings of the Fourteenth International Conference on Data Engineering, pp. 23–27, Feb 1998
7. Vidot, N., Cart, M., Ferrié, J., Suleiman, M.: Copies convergence in a distributed real-time collaborative environment. In: Proceedings of the 2000 ACM conference on Computer supported cooperative work, pp. 171–180. ACM Press New York, NY, USA (2000)
8. Ressel, M., Nitsche-Ruhland, D., Gunzenhäuser, R.: An integrating, transformation-oriented approach to concurrency control and undo in group editors. In: CSCW '96 Proceedings of the 1996 ACM conference on Computer supported cooperative work. pp. 288–297 (1996). doi:[10.1145/240080.240305](https://doi.org/10.1145/240080.240305)
9. Li, D., Li, R.: An admissibility-based operational transformation framework for collaborative editing systems. *Comput. Support. Coop. Work J. Collab. Comput.*, Aug 2009. Accepted
10. Shao, B., Li, D. Gu, N.: An algorithm for selective undo of any operation in collaborative applications. In: ACM (2010)
11. Li, D., Li, R.: An approach to ensuring consistency in peer-to-peer real-time group editors, in Springer (2006)
12. Shao, B., Li, D. Gu, N.: A fast operational transformation algorithm for mobile and asynchronous collaboration, *IEEE Trans. Parallel Distrib. Syst.* **21**(12) (2010)
13. Shao, B., Li, D., Gu, N.: ABTS: a transformation-based consistency control algorithm for wide-area collaborative applications. In: 5th International Conference on Collaborative Computing: Networking, Applications and Worksharing. CollaborateCom 2009, pp. 1–10. 11–14 Nov. 2009. doi:[10.4108/ICST.COLLABORATECOM2009.8271](https://doi.org/10.4108/ICST.COLLABORATECOM2009.8271)
14. Sun, C., Jia, X., Zhang, Y., Yang, Y., Chen, D.: Achieving convergence, causality preservation, and intention preservation in real-time cooperative editing systems. *ACM Trans. Comput. Hum. Interact.* **5**(1): 63–108 (1998)

A Digital Image Watermarking Technique Using Cascading of DCT and Biorthogonal Wavelet Transform

Arvind Kumar, Pragya Agarwal and Ankur Choudhary

Abstract Modern communication technology facilitates easy transmission of multimedia content. But if copyright protection of multimedia data, prevention of illegal access, and rights of intellectual property are considered, so this field needs more attention of researchers. It is a very simple process to make a copy of the multimedia data, alter it, and then put it back for business profits. Digital watermarking techniques provide a solution for this issue, by embedding some information, which can be further used to claim the ownership of multimedia data. In this paper, a new algorithm for the watermarking of digital images is proposed by cascading of two frequency domain transform techniques, i.e., biorthogonal wavelet transforms (BWT) and discrete cosine transform (DCT). Proposed technique takes the approximation component of the biorthogonal transform of cover image and then applies DCT to embed watermark. Embedding of watermark data is done in middle frequency component by comparison-based correlation technique. Also, this technique has been analyzed and compared with the existing ones by applying various image attacks and subsequently measuring the results and proved to be fairly robust.

Keywords Image watermarking · Discrete wavelet transform (DWT) · Biorthogonal wavelet transform (BWT) · Discrete cosine transform (DCT) · Copyright protection.

Arvind Kumar (✉)
Pitney Bowes Software, Noida, India
e-mail: arvind.jki@gmail.com

Pragya Agarwal · Ankur Choudhary
ASET, Amity University Uttar Pradesh, Noida, India
e-mail: dpragya@gmail.com

Ankur Choudhary
e-mail: ankur.tomer@gmail.com

Introduction

Multimedia technologies are a boon for modern society. Representation of information in the form of image, audio, or video is much more informative compared to textual form. But it also facilitates easy duplication and claiming false ownership problem. Watermarking is emerged as a technological solution to these false ownership problems. Here owner can embed a message in source media. This message, which may be some text, image, or audio, is called watermark, and media is called cover object. Whenever any situation arises to prove ownership, the watermark message may be extracted from media, and ownership can be proved. If the cover object is an image, then this whole process is called image watermarking. This concept has already been used for a long time to print currency notes, where the watermark is embedded in different parts of notes, to check the originality. We can use the same concept for multimedia data for checking the authenticity and originality of the content [1].

Watermarking can be done in two domains, i.e., spatial domain also called time domain and frequency domain. There are a variety of techniques proposed by different researchers. Some of them include least significant bit (LSB), discrete wavelet transform (DWT), discrete cosine transform (DCT) [4], biorthogonal wavelet transform (BWT) [7, 9], singular value decomposition(SVD) [3], Schur decomposition [2], etc. Again, for gaining more robustness and imperceptibility two of them are combined by different researchers [6, 10].

In this paper, authors have proposed a new watermarking technique which uses the cascading of two well-known domains, DCT and BWT. Proposed technique has also been analyzed and compared with the current ones by applying various image attacks and subsequently measuring the results and proved to be better. This technique mainly uses the approximation coefficients of the BWT transformed image, calculates DCT, and then uses the comparison-based correlation method for embedding the watermark in middle frequency band coefficients. Section 2 discusses DCT domain watermarking. Section 3 discusses DWT domain watermarking. In Sect. 4, we discuss. Then in Sect. 5, we discuss the proposed algorithm followed by the results (Sect. 6), conclusion (Sect. 7), and references.

DCT Domain Watermarking

Frequency domain techniques are more suitable for watermarking compared to special domain techniques. Here, we can improve quality as well as robustness, if we understand and effectively use the information contained in a digital image.

DCT is the most popular transform domain-based technique. The DCT allows an image to be decomposed into three different frequency bands: low, middle, and high frequency bands [4]. So a suitable frequency band is decided to embed watermark. The literature survey deals mainly with middle frequency components for watermark embedding. The watermark embedding in a middle frequency band does not

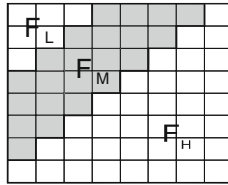


Fig. 1 DCT regions [6]

much impact the important visual components of the image, i.e., the low frequencies [5]. Figure 1 shows the middle frequency component FM, the low frequency component FL, and the high frequency components FH of the 8×8 DCT block. FM is chosen as the embedding region so that the visibility of the image is not impacted and the watermark cannot be easily removed by various attacks [6].

The DCT-based watermarking technique contains the following steps:

- i. Split the cover object image into 8×8 blocks.
- ii. Calculate DCT coefficients of each block.
- iii. Select the coefficients from these blocks for watermark embedding.
- iv. Modify the selected coefficients selected in Step 3, for watermark embedding.
- v. Take inverse DCT of each block.

Almost all the algorithms that are based on DCT differ on the basis of block selection criteria and coefficient selection criteria. Most of the techniques do the comparison of middle-DCT coefficients to embed a single bit into a DCT block.

DWT Domain Watermarking

Wavelet domain is a comparatively new and promising transform domain for watermarking. When DWT (discrete wavelet transform) is applied to an image, it separates the image into four different components: Approximation image component (LL), horizontal detail component (HL), vertical detail component (LH), and diagonal detail component (HH). This process of decomposition can be repeated to compute multilevel decomposition. Figure 2 shows the two-level wavelet decomposition of an image.

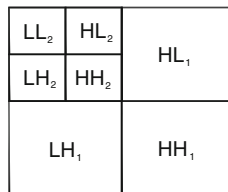


Fig. 2 Two-level wavelet decomposition [6]

One of the advantages of the wavelet transform is that it is believed to be a more accurate model aspect of the human visual system (HVS) compared to the fast Fourier transform (FFT) or DCT. In general, most of the signal energy is concentrated in the approximation subband and embedding watermarks in this subband may degrade the image quality, but provides higher robustness. On the other hand, the detailed subbands LH, HL, and HH include the edges and textures of the image and we can get higher imperceptibility, but at the expense of the robustness. So using these facts, we can easily select the subband for the embedding. DWT transform has recently gained popularity because it provides multi-level decomposition. Because DWT-based techniques are similar to the theoretical model of HVS, this is a preferred way to use image watermarking.

Biorthogonal Wavelet Transform

Biorthogonal wavelets are members of compactly supported symmetric wavelets family [7]. The filter coefficients symmetry is often desirable because it results in linear phase of the transfer function. In the biorthogonal wavelets case, there are two scaling and wavelets functions in place of having one scaling and wavelet function. This may generate different multiresolution analyses, and accordingly two different wavelet functions [8, 9]. The dual wavelet and scaling functions contain the following important properties:

- i. The calculation functions are easily constructed numerically.
- ii. Outside of a segment, they are zero.
- iii. The calculation algorithms are maintained and therefore are very simple.
- iv. The associated filters have symmetrical nature.

Performance improvements in BWT can be obtained by combining it with DCT. The idea is based on the fact that combining both transform techniques could compensate for the drawbacks of each other. This results in more effective watermarking. BWT decomposes original image into four frequency components: LL, HL, LH, and HH. We use LL subband to embed the watermark data by cascading with DCT. Complete detail is given in the following section.

Proposed Algorithm

This paper is about the conception and implementation of a new image watermarking technique which is based on the cascading of these two well-known transform domain techniques: DCT and biorthogonal wavelet transform. First, we decompose the cover image using the biorthogonal wavelet transform and then its approximation component is used for further processing. Then, we use the comparison-based correlation method in DCT domain for embedding. The main feature of this algorithm is

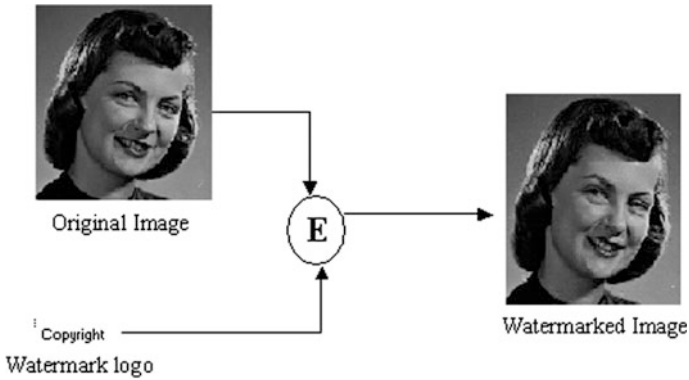


Fig. 3 Embedding the watermark [6]

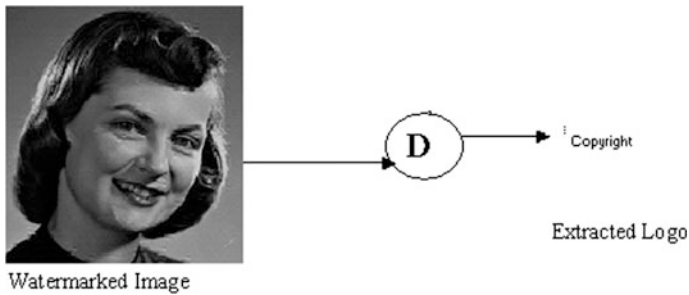


Fig. 4 Extracting the watermark [6]

that we are using the advantages of JPEG compression in approximation component of the image. Figures 3 and 4 give the overview of embedding and extraction of watermark into given cover image. In the figures, E represents embedding algorithm and D represents extraction algorithm (Figs. 5 and 6).

Fig. 5 Cover and watermarked image



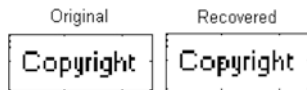


Fig. 6 Original and Recovered watermark

Proposed algorithm's embedding steps are as follows:

- i. Perform the biorthogonal wavelet transform of the given image, which decomposes the cover image into four components named as LL, HL, LH, and HH. Here approximation component (LL) is selected for embedding.
- ii. Segment the approximation (LL) component into blocks of size 8×8 .
- iii. Apply the discrete cosine transform (DCT) to all the 8×8 blocks.
- iv. Apply coefficient selection criteria using the quantization table of JPEG compression. Modify the selected coefficients to embed watermark data.
- v. Perform inverse DCT for each block.
- vi. Apply inverse biorthogonal wavelet transform.

Proposed algorithm extraction steps are as follows:

- i. Take the biorthogonal wavelet transform of the watermarked image to get the approximation component.
- ii. Segment the approximation (LL) component into 8×8 block size.
- iii. Apply forward DCT to all the 8×8 blocks.
- iv. Apply coefficient selection criteria using the quantization table of JPEG compression.
- v. Extract the watermark on the basis of coefficient values.

Results

We have implemented and executed this algorithm using MATLAB software. Cover image and the watermark image are both taken in .jpeg format. We embed watermark into the cover image and various attacks such as JPEG compression, scaling, and adding salt-and-pepper noise, have been performed on the watermarked image to measure the robustness of the technique. The robustness of the technique is compared with existing technique on the basis of parameters such as peak signal-to-noise ratio (PSNR) for embedding and extraction, bit error rate (BER) and correlation between the original watermark and the extracted watermark. In Table 1, we have compared image embedding result with the parameters of correlation BER ratio and PSNR of original image versus watermarked image. In Table 2, we compared results on the basis of correlation and PSNR of original watermark and extracted watermark image. This table also reflects the result of watermark extraction after applying different image attacks. In JPEG compression,

Table 1 Watermark embedding results

Embedding technique	Correlation	BER	PSNR
BWT	0.961865	0.381789	25.94993
Proposed (BWT-DCT)	0.997070	0.153697	36.17858

Table 2 Watermark extraction results

Watermark extracting technique	Attack applied	Correlation	PSNR
Biorthogonal wavelet transform	Without attack	0.984359	0.515784
	JPEG compression	0.984359	0.515784
	Resize	0.874514	0.514827
	Noise	0.568971	0.509740
Proposed technique (BWT-DCT)	Without attack	0.994716	0.515861
	JPEG compression	0.989503	0.515822
	Resize	0.855301	0.514750
	Noise	0.232501	0.505152

watermarked image’s quality is degraded to 75 % and then reverts back to original size. In resizing, we scaled image to 50 %, saved it, and resized it to the original size. In noise attach, we added salt-and-pepper noise and then tried to extract the watermark. Figures 7, 8, and 9 give a graphical representation of comparison data. On the basis of this comparison, we can conclude that the proposed technique has proved to be fairly robust against JPEG compression image processing attack.

Fig. 7 Quality of watermark embedding

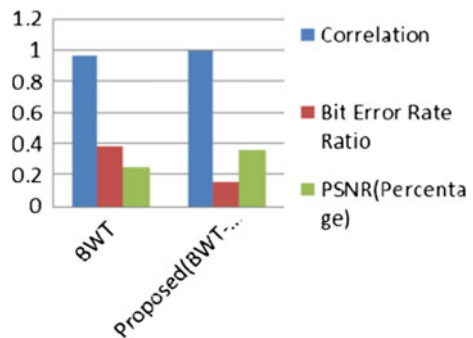


Fig. 8 Extracted watermark PSNR quality

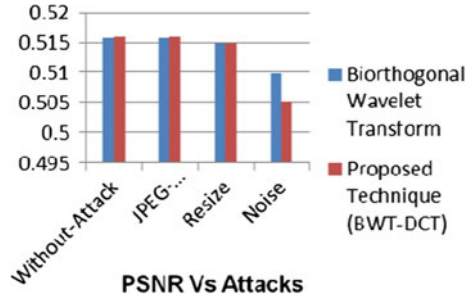
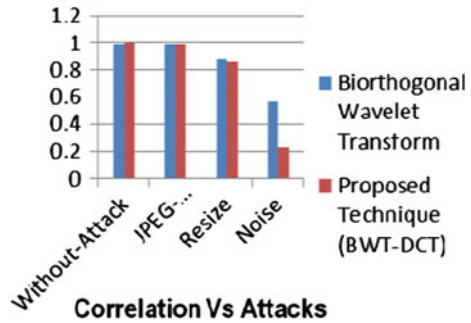


Fig. 9 Extracted watermark correlation



Conclusion

The proposed technique for digital image watermarking shows robustness and it also has a very little effect on the image quality. This can be seen in Figs. 5 and 6. We have used biorthogonal wavelet transform as it reduces the time for extraction and embedding. Proposed embedding and extraction watermarking quality are better than BWT technique.

The conclusion table shows result on the basis of comparison of the proposed technique with existing technique. On the basis of measuring parameters, we can conclude that proposed algorithm gives comparatively better result on some parameters compared to biorthogonal wavelet transform techniques.

References

1. Cox, I.J., Kilian, J., Leighton, F.T., Shamoon, T.: Secure spread spectrum watermarking for multimedia. *IEEE Trans. Image Process.* **6**(12), 1673–1687 (1997)
2. Mohammad, A.A.: A new digital image watermarking scheme based on Schur decomposition. *Multimed. Tools Appl.* **59**(3), 851–883 (2012)
3. Bao, P., Ma, X.: Image adaptive watermarking using wavelet domain singular value decomposition. *IEEE Trans. Circuits Syst. Video Technol.* **15**(1), 96–102 (2005)

4. Barni, M., Bartolini, F., Cappellini, V., Piva, A.: A DCT-domain system for robust image watermarking. *Signal Process.* **66**(3), 357–372 (1998)
5. Suhail, M.A., Obaidat, M.S.: Digital watermarking-based DCT and JPEG model. *IEEE Trans. Instrum. Meas.* **52**(5), 1640–1647 (2003)
6. Tomar, V., Kumar, A., Choudhary, A.: Conception & implementation of a novel Digital image watermarking algorithm using cascading of DCT and LWT. In: *International Conference on Optimization, Reliability, and Information Technology (ICROIT)*, pp. 501–505. IEEE, February 2014
7. Prasad, B.R., Kota, K.V., Reddy, B.M.: Biorthogonal Wavelet Transform Digital Image Watermarking. *Int. J. Adv. Comput. Res.* **2**(5) Number-3 (2012)
8. Sweldens, W.: The lifting scheme: a custom-design construction of biorthogonal wavelets. *Appl. Comput. Harmon. Anal.* **3**(2), 186–200 (1996)
9. Maity, S.P., Kundu, M.K., Mandal, M.K.: Capacity improvement in spread spectrum watermarking using biorthogonal wavelet. In: *48th Midwest Symposium on Circuits and Systems*, pp. 1426–1429. IEEE, Aug 2005
10. Majumder, S., Das, T.S., Sarkar, S., Sarkar, S.K.: SVD and lifting wavelet based fragile Image watermarking. *ACEEE Int. J. Signal Image Process.* **2**(1) (2011)

Multi-domain Image Enhancement of Foggy Images Using Contrast Limited Adaptive Histogram Equalization Method

Garima Yadav, Saurabh Maheshwari and Anjali Agarwal

Abstract Enhancement process is used in image processing for improving quality and contrast of noise images or video. In digital signal processing, enhancement process is applied in spatial domain and frequency domain. In these two domains, process is applied over a pixel value but in frequency domain enhancement process is applied over frequency. In image processing for improving the quality of image-used image filtering, morphological operation, deblurring, ROI-based processing, neighborhood, and block processing. Contrast adjustment, morphological operation, ROI-based processing and deblurring enhancement processes are used in spatial domain. Digital filter is used in frequency domain. In this article, the author used top-hat filter for enhancement process and CLAHE methods are used in spatial and frequency domains. Contrast limited adaptive histogram equalization method is used in spatial domain and finite impulse response filter is used in frequency domain. At the end of this paper is shown the comparative results which prove frequency domain enhancement method with spatial domain, which is better than the spatial domain enhancement method.

Keywords Enhancement methods · Top-hat filter · Contrast limited adaptive histogram equalization · Finite impulse response filter

Garima Yadav (✉) · Saurabh Maheshwari · Anjali Agarwal
Department of Computer Science and Engineering, Government Women Engineering
College, IIEEE, Rajasthan, India
e-mail: garimancet@gmail.com

Saurabh Maheshwari
e-mail: saurabh.maheshwari.in@ieeee.org

Anjali Agarwal
e-mail: anjalilagarwal@gmail.com

Introduction

Contrast and quality level of any image degrades due to noise. Noise is also called unwanted signal or unwanted partials. This research focuses on enhancement method comparison in spatial domain and frequency domain methods. Spatial domain is used when enhancement process is applied over pixel values while frequency domain is used when enhancement process is applied over frequency values. Fog is a type of noise which reduces the visible quality and contrast level of any images in bad weather condition. In the field of computer vision, two technologies are used for fog removal and fog correction. In this paper, the author compares two approaches: one is used in spatial domain and the other is used in frequency domain. Contrast limited adaptive histogram equalization is used in the spatial domain. Finite impulse response filter is used for enhancement in frequency domain. When working over noise frequency digital filters are used for noise removal [1], low bandpass filter is used in FIR filter for noise reduction [2]. Contrast adjustment, region of interest (ROI)-based processing, contrast limited histogram equalization [3], and morphological operation are used in spatial domain, and work over single pixel value or neighbor pixels.

Literature Review

Enhancement process is applied for fog removal. Enhancement process is applied over two domains: spatial and frequency [1]. In spatial domain, work over single pixel value or neighbor pixel values for improving contrast. In histogram equalization method, find the histogram $h(x)$ of noise image that represents the number of pixel that has specific intensity [3]. Contrast limited adaptive histogram equalization process is a modified part of histogram equalization [3]. In histogram equalization process, equalization process is applied over whole image but in contrast limited adaptive histogram equalization image is divided into segments. Enhancement process is applied over these segments. Limit is applied over dynamic range for equalization process [3, 4]. Among low-pass filter, high pass filter, homomorphism filter, and median filter, in computer vision processing, two main filters are used: finite impulse response filter (FIR) [4] and infinite impulse response filter (IIR). Frequency is normalized between 0 and 1 in FIR filter [5] which is designed by window design method.. Top-hat filter is a filter that works over pixel intensity values. In this process, filter window is applied over large size of pixels. Window size is not bounded in $4 * 4$ normal window sizes. Image is divided into segments and is applied with enhancement process for intensity adjustment. First, if any foggy image $I(x, y)$ is used for enhancement then convert color 3-D image into 2-D grayscale image $I(x, y)$. In the second step, morphological operation is applied over 2-D grayscale image or binary image. Operation for intensity adjustment is applied n time over an image. Value of n depends on level of noise in any image. Operation

is repeated until changes no longer occur. After applying filtering process over a noise image, intensity values are improved but contrast level and visibility level are decreased; for improving these factors contrast adjustment method is applied. In intensity adjustment, operation is applied over $12 * 12$ window size. If two neighbor zeros are present then it converts into 1.

Proposed Work

In this paper is proposed a new approach for image enhancement. Foggy image is a type of noise mixed image. In this approach, for noise removal we use top-hat filter with contrast limited adaptive histogram equalization process. Different types of filters are used for noise reduction, some filters for spatial domain and some for frequency domain. Finite impulse response filter is used in frequency domain, but top-hat filter performs better result than FIR or other spatial domain methods.

Proposed Algorithm Steps

- Step 1: Read true color image
- Step 2: Convert colored image into grayscale or binary image
- Step 3: Apply morphological operation over an image and find the center pixel
- Step 4: Apply tophat filter operation over window size image
- Step 5: Repeat morphological operation until change no longer occurs over intensity values
- Step 6: Contrast adjustment function is applied over filtered image
- Step 7: Apply contrast limiter adaptive histogram equalization method over digital filter image for histogram equalization
- Step 8: Restore better quality enhanced image

Comparison and Result Analysis

This paper used top-hat filtering method for filtering process of noise image. After filtering process, contrast limited adaptive histogram is applied for contrast and histogram equalization process. The author compares enhancement method of both spatial and frequency domains [6, 7]. Contrast limited adaptive histogram [7] method is used in spatial domain which works over pixel values [8]. In CLAHE, image is divided into subparts. When image divides into horizontal and vertical parts it reduces the time complexity of noise reduction process. When author used FIR filter level of noise is reduced and less number of noise pixels are present in noise image than the original image. After applying, FIR used CLAHE which gives



Fig. 1 Original noise images and images after used Top-hat filter

better quality result and peak signal-to-noise ratio (PSNR) is also increased when using both enhancement methods for the same image. Using top-hat morphological operation for filtering produces better quality results compared to others. In this article, both methods are used in spatial domain which works over pixel intensity values. The number of visible edges is increased because of morphological operation. This operation generates the structure of noise image and then segmentation is applied before the filtering process. When filter is applied over window size image number visible edges are increased compared to other approaches (Fig. 1).

Figures 2, 3, and 4 represent the number of visible edges in noise images. Fog is a type of noise or unwanted signal in such images; fog is mixed in atmosphere

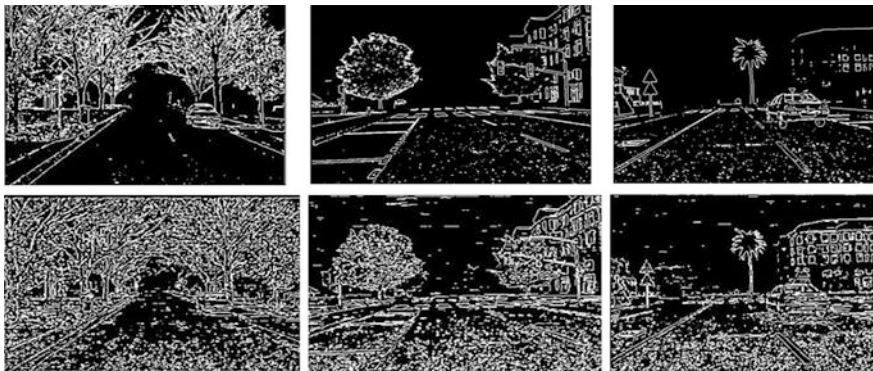


Fig. 2 Visible edges in original noise images and visible edges after enhancement in frequency and spatial domains

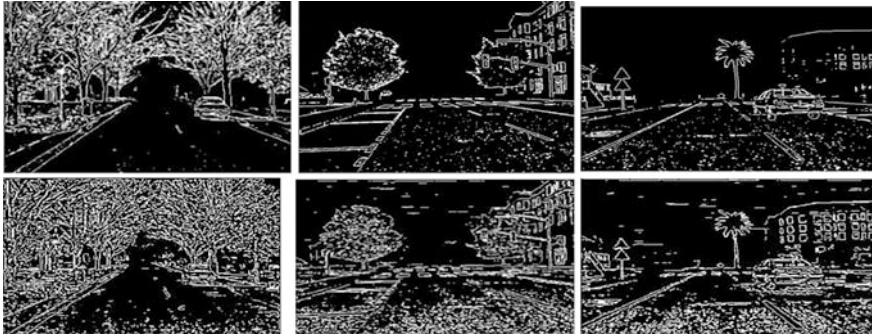


Fig. 3 Visible edges in original noise images and visible edges in visible edges after enhanced image using spatial domain CLAHE method

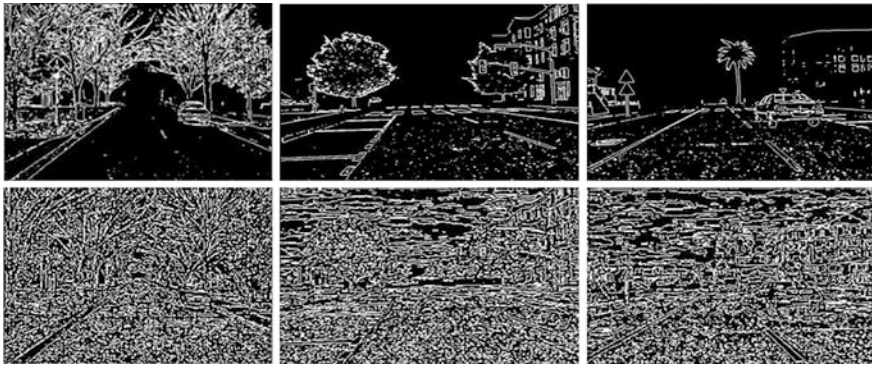


Fig. 4 Visible edges in original noise images and visible edges in visible edges after enhanced image using top-hat filter and spatial domain CLAHE method

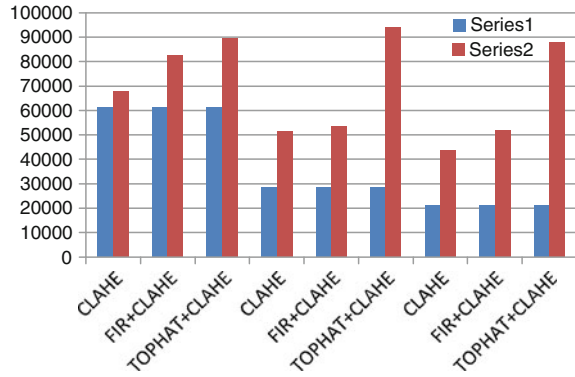
which creates a noise between viewer and real object. Figure 1 shows the visible edges in that foggy images, where the rate of new visible edges (e) in images [7], r represents quality of restoration after contrast enhancement process [7]; r calculates the geometric mean of visibility level of restored image which represents saturation factor [7]. Table 1 represents quantitative result of CLAHE enhanced image, FIR + CLAHE and TOP-HAT filtered image.

In Fig. 5 the blue line represents the number of visible edges in original image and the red line represents the number of visible edges in restored image after enhancement process.

Table 1 Comparisons of spatial domain and frequency domain with spatial domain methods

Enhancement methods	CLAHE	FIR + CLAHE	TOP-HAT FILTER + CLAHE	CLAHE	FIR + CLAHE	TOP-HAT FILTER + CLAHE	CLAHE	FIR + CLAHE	TOPHAT FILTER + CLAHE
	Image 1	Image 1	Image 1	Image 2	Image 2	Image 2	Image 3	Image 3	Image 3
Visible edges in original image	61071	61071	61071	28469	28469	28469	20917	20917	20917
Visible edges after restoration	67951	82431	89587	51646	53358	93824	43646	51799	87601
Saturation factor	0.001126 %	0 %	0 %	0 %	0 %	0 %	0 %	0 %	0 %
Rate of new visible edges (e)	0.11266	0.34976	0.46693	0.81411	1.2255	2.2957	1.4764	1.4787	3.1888
Quality of toration (t)	2.4515	3.0842	3.2935	6.5429	6.1659	6.2366	7.1357	7.0406	4.2921
Peak signal-to-noise ratio (PSNR)	12.8620	62.6147	57.3515	12.4356	63.4890	54.2160	13.2096	62.5271	52.7042

Fig. 5 Comparative representation of proposed algorithm and privies approaches



Future Work

In this article, the author compares image enhancement method between two domains; spatial and frequency. Experimental results show that a combination of both the enhancement methods produced better quality noise-free image. Many methods are used in spatial domain for image enhancement process, but compared with spatial domain less number of methods is presented in frequency domain. This paper used contrast limited adaptive histogram method in spatial domain and finite impulse response filter in frequency domain, but in the future work other spatial domain methods like histogram equalization, and FIR, and not black pixels contrast and FIR will be used. Infinite impulse response filter is used in place of FIR filter so, use of IIR [9, 10] with CLAHE is also useful for future direction.

References

1. Yadav, G., Maheshwari, S., Agarwal, A.: Fog removal techniques from images: A comparative review and future directions. In: International Conference on Signal Propagation and Computer Technology (ICSPCT), pp. 44–52, 12–13 July 2014
2. Yadav, G., Maheshwari, S., Agarwal, A.: Foggy image enhancement using contrast limited adaptive histogram equalization of digitally filtered image: Performance improvement. In: International Conference on Advances in Computing, Communications and Informatics (ICACCI), pp. 2225–2231, 24–27 Sept 2014
3. Yadav, G., Maheshwari, S., Agarwal, A.: Contrast limited adaptive histogram equalization based enhancement for real time video system. In: International Conference on Advances in Computing, Communications and Informatics (ICACCI), pp. 2392–2397, 24–27 Sept 2014
4. Kim, P.S., Kwon, W.-H.: Forgetting least squares estimation FIR filters without noise covariance information. In: SICE 2000. Proceedings of the 39th SICE Annual Conference. International Session Papers, pp. 1–6 (2000)
5. Safari, M.S., Aghagolzadeh, A.: FIR filter based fuzzy-genetic mixed noise removal. In: 9th International Symposium on Signal Processing and its Applications, 2007. ISSPA 2007, pp. 1–4, 12–15 Feb 2007

6. Stark, J.A.: Adaptive image contrast enhancement using generalizations of histogram equalization. *IEEE Trans. Image Process.* **9**(5), 889–896 (2000)
7. Hautière, N., Tarel, J.-P., Aubert, D., Dumont, E.: Blind contrast enhancement assessment by gradient ratioing at visible edges. *Image Anal. Stereol. J.* **27**(2), 87–95 (2008)
8. Xu, Z., Liu, X., Chen, X.: Fog removal from video sequences using contrast limited adaptive histogram equalization. In: *International Conference on Computational Intelligence and Software Engineering*, 2009. *CiSE 2009*, pp. 1–4, 11–13 Dec 2009
9. Yun, S.-H., Kim, J.H., Kim, S.: Image enhancement using a fusion framework of histogram equalization and laplacian pyramid. *IEEE Trans. Consum. Electron.* **56**(4), 2763–2771 (2010)
10. Shuai, Y., Liu, R., He, W.: Image haze removal of wiener filtering based on dark channel prior. In: *Eighth International Conference on Computational Intelligence and Security (CIS)*, pp. 318–322, 17–18 Nov 2012

Comparison of Various Reliability Measures of a Computer System with the Provision of Priority

Ashish Kumar and Monika Saini

Abstract In this study the comparative analysis of various reliability measures of a computer system is carried out under the concepts of maximum repair time, maximum operation time, and priority. An immediate repair facility is provided to the system. The system consists of two identical unit one in operative mode and other in cold standby mode. For the derivation of various reliability measures, two stochastic models are developed hereby using the concept of priority. Priority to preventive maintenance over h/w repair in Model II whereas no priority is given in Model I. The failure time distribution of the s/w and h/w follows exponential while other random variables are taken as arbitrary. Graphs are drawn with respect to preventive maintenance to analyze the mean time to system failure and profit function of both models comparatively.

Keywords Maximum operation and repair times • H/W and S/W failure • Computer system • Priority and H/W replacement

2000 Mathematics Subject Classification 90B25 • 60K10

Introduction

The necessity of integrated h/w and s/w systems has increased rapidly in our day-to-day life. Some major areas in which the use of computer systems is visualized are as follows: air traffic control, nuclear reactors, aircraft, automotive mechanical and safety control, telephone switching and hospital patient monitoring systems. And, the influence of failures of these systems varies from disruption to

Ashish Kumar (✉) · Monika Saini
Department of Mathematics & Statistics, Manipal University Jaipur,
Jaipur 303007, Rajasthan, India
e-mail: ashishbarak2020@gmail.com

Monika Saini
e-mail: drmnksaini4@gmail.com

loss of human life. Therefore, under such critical situations it becomes necessary to utilize such systems with proper protection and high reliability. Thus an overall evaluation of the reliability of such systems is necessary to provide better services to consumers. During last few years, some researchers such as Friedman and Tran [1] and Welke et al. [2] established a combined reliability model for the computer system in which hardware and software work together. Recently, some stochastic models of computer systems having redundancy and priority have been developed by Malik and Anand [3] and Malik and Kumar [4] subject to independent h/w and s/w failures.

It is also observed by many researchers that preventive maintenance of a system after a maximum operation time can slow the deterioration process of that system. Thus, reliability of computer systems can be improved by conducting preventive maintenance. Malik and Nandal [5] used the concept of preventive maintenance for analyzing a cold standby system with maximum operation time. It becomes necessary sometimes to give priority in repair to one unit over repair activities of other unit not only to reduce the down time but also to minimize the operating cost. Kumar et al. [6] and Kumar and Malik [7] suggested some stochastic models for computer systems by giving priority to preventive maintenance. Malik and Anand [8] analyzed the computer system with arbitrary distribution for h/w and s/w replacement times. Nandal et al. [9] discussed a stochastic model for a cold standby system by using the concept of priority for operation and preventive maintenance. Reliability modeling of computer system is discussed by Malik [10]. Kumar [11] carried out the comparison of an integrated h/w and s/w system by using the concept of preventive maintenance and priority to s/w replacement over h/w repair. By using the above facts, here two reliability models are developed by considering the concept of s/w upgradation, priority and preventive maintenance. In both models, system consists of one operative and one cold standby unit with an immediate single repair facility. Preventive maintenance of the system is carried out after a maximum operation time. The failed hardware is replaced with some replacement time, if its repair is not possible with in a maximum repair time, by a new unit. Upon the unsatisfactory performance of s/w, it is upgraded by new version. In Model I, no priority is given whereas; in Model II, priority is given to preventive maintenance over h/w repair. All random variables corresponding to failure activities follow exponential distribution while other random variables are arbitrary distributed. The following measures of reliability are obtained such as transition state probabilities, mean sojourn times, busy period of repairman, steady-state availability, expected maintenances and repairs by the server, expected number of visits, and profit function.

Notations

E	Collection of regenerative states
No	Operative unit
Cs	Cold standby unit
b/a	Probability that the system has software/hardware failure
λ_2/λ_1	Constant software/hardware failure rate
α_0	Constant maximum operation time
β_0	Constant maximum repair time
©/⊗	Symbol for Laplace/Laplace–Stieltjes convolution
H(t)/h(t)	Cdf/pdf of software upgradation time
G(t)/g(t)	Cdf/pdf of hardware repair time
M(t)/m(t)	Cdf/pdf of hardware replacement time
F(t)/f(t)	Cdf/pdf of the time for preventive maintenance
Cdf/pdf	Cumulative density function/probability density function
HFurp/HFURP	Failed h/w under replacement/continuously under replacement
HFwr/HFWRp	Failed hardware waiting for repair/continuously waiting for repair
Pm/PM	Unit is under preventive maintenance/continuously from previous under preventive maintenance
WPm/WPM	Unit is waiting for preventive maintenance/waiting continuously from previous state for preventive maintenance
HFur/HFUR	Unit suffer from hardware failure and under repair/suffer hardware failure and continuously under repair from preceding states
SFurp/SFURP	Unit suffers due to software failure and under upgradation/under upgradation continuously from preceding state
SFwrp/SFWRP	Unit suffers due to software failure and wait for upgradation/continuously wait for upgradation

The probability density function for the transition of the system from one regenerative state S_i to another regenerative state S_j or to a failed state S_j either directly or via visiting to states S_k, S_l once in time $(0, t]$ is denoted by respectively $q_{ij}(t)$ & $q_{ij,kl}(t)$. The cumulative density function for the same situations is denoted by $Q_{ij}(t)$ & $Q_{ij,kl}(t)$ respectively.

Considering these symbols, the system can be in any one of the following states.

For Model I

- $S_0 = (N_0, Cs), S_1 = (N_0, Pm), S_2 = (N_0, HFur), S_3 = (N_0, SFurp),$
 $S_4 = (N_0, HFurp), S_5 = (HFUR, Wpm), S_6 = (HFwr, PM), S_7 = (SFURP, HFwr),$
 $S_{13} = (WPm, PM), S_8 = (PM, SFwrp), S_9 = (SFURP, WPm), S_{10} = (SFURP, SFwrp),$
 $S_{11} = (HFUR, SFwrp), S_{12} = (HFUR, HFwr) S_{14} = (SFWRP, HFurp), S_{15} = (HFurp, HFWR),$
 $S_{16} = (HFurp, WPM), S_{17} = (HFURP, Wpm) S_{18} = (HFURP, SFwrp) S_{19} = (HFURP, HFwr)$

For Model II

$$\begin{aligned}
 S_0 &= (N_0, Cs), & S_1 &= (N_0, Pm), & S_2 &= (N_0, HFur), & S_3 &= (N_0, SFurp), \\
 S_4 &= (N_0, HFurp), & S_5 &= (HFwr, Pm), & S_6 &= (HFwr, PM), & S_7 &= (SFURP, HFwr), \\
 S_8 &= (PM, SFwrp), & S_9 &= (SFURP, WPm), & S_{10} &= (SFURP, SFwrp), & S_{11} &= (HFUR, SFwrp), \\
 S_{12} &= (HFUR, HFwr), & S_{13} &= (WPm, PM), & S_{14} &= (SFWRP, HFurp), & S_{15} &= (HFurp, HFWR), \\
 S_{16} &= (HFURP, WPm), & S_{17} &= (HFURP, SFwrp), & S_{18} &= (HFURP, HFwr)
 \end{aligned}$$

Transition Probabilities

By using the simple probabilistic arguments, we obtained the following transition probabilities

$$p_{ij} = Q_{ij}(\infty) = \int_0^{\infty} q_{ij}(t) dt \quad \text{as} \quad (1)$$

Common for Both Models

$$\begin{aligned}
 p_{01} &= \frac{\alpha_0}{a\lambda_1 + b\lambda_2 + \alpha_0}, & p_{02} &= \frac{a\lambda_1}{a\lambda_1 + b\lambda_2 + \alpha_0}, & p_{03} &= \frac{b\lambda_2}{a\lambda_1 + b\lambda_2 + \alpha_0}, \\
 p_{10} &= f^*(a\lambda_1 + a\lambda_2 + \alpha_0),
 \end{aligned}$$

$$p_{16} = \frac{a\lambda_1}{a\lambda_1 + b\lambda_2 + \alpha_0} [1 - f^*(a\lambda_1 + b\lambda_2 + \alpha_0)] = p_{12.6},$$

$$p_{18} = \frac{b\lambda_2}{a\lambda_1 + b\lambda_2 + \alpha_0} [1 - f^*(a\lambda_1 + b\lambda_2 + \alpha_0)] = p_{13.8},$$

$$p_{20} = g^*(a\lambda_1 + b\lambda_2 + \alpha_0), p_{30} = h^*(a\lambda_1 + b\lambda_2 + \alpha_0),$$

$$p_{1.13} = \frac{\alpha_0}{a\lambda_1 + b\lambda_2 + \alpha_0} [1 - f^*(a\lambda_1 + b\lambda_2 + \alpha_0)] = p_{11.13},$$

$$p_{24} = \frac{\beta_0}{a\lambda_1 + b\lambda_2 + \alpha_0 + \beta_0} [1 - g^*(a\lambda_1 + b\lambda_2 + \alpha_0 + \beta_0)]$$

$$p_{40} = m^*(a\lambda_1 + b\lambda_2 + \alpha_0), p_{16.1} = m^*(0),$$

$$p_{25} = \frac{\alpha_0}{a\lambda_1 + b\lambda_2 + \alpha_0 + \beta_0} [1 - g^*(a\lambda_1 + b\lambda_2 + \alpha_0 + \beta_0)],$$

$$p_{2.11} = \frac{b\lambda_2}{a\lambda_1 + b\lambda_2 + \alpha_0 + \beta_0} [1 - g^*(a\lambda_1 + b\lambda_2 + \alpha_0 + \beta_0)],$$

$$\begin{aligned}
 p_{62} &= f^*(0), \quad p_{72} = h^*(0), \quad p_{83} = f^*(0), \\
 p_{91} &= h^*(0), \quad p_{2.12} = \frac{a\lambda_1}{a\lambda_1 + b\lambda_2 + \alpha_0 + \beta_0} [1 - g^*(a\lambda_1 + b\lambda_2 + \alpha_0 + \beta_0)], \\
 p_{37} &= \frac{a\lambda_1}{a\lambda_1 + b\lambda_2 + \alpha_0} [1 - h^*(a\lambda_1 + b\lambda_2 + \alpha_0)] = p_{32.7}, \\
 p_{10.3} &= h^*(0), p_{11.3} = g^*(\beta_0), p_{11.14} = 1 - g^*(\beta_0), p_{12.2} = g^*(\beta_0), \\
 p_{39} &= \frac{\alpha_0}{a\lambda_1 + b\lambda_2 + \alpha_0} [1 - h^*(a\lambda_1 + b\lambda_2 + \alpha_0)] = p_{31.9}, \\
 p_{3.10} &= \frac{b\lambda_2}{a\lambda_1 + b\lambda_2 + \alpha_0} [1 - h^*(a\lambda_1 + b\lambda_2 + \alpha_0)] = p_{33.10}, \\
 p_{12.15} &= 1 - g^*(\beta_0), p_{13.1} = f^*(0), p_{14.3} = m^*(0), \quad p_{15.2} = m^*(0), \\
 p_{21.5} &= \frac{\alpha_0}{a\lambda_1 + b\lambda_2 + \alpha_0 + \beta_0} [1 - g^*(a\lambda_1 + b\lambda_2 + \alpha_0 + \beta_0)]g^*(\beta_0) \\
 p_{21.5,16} &= \frac{\alpha_0}{a\lambda_1 + b\lambda_2 + \alpha_0 + \beta_0} [1 - g^*(a\lambda_1 + b\lambda_2 + \alpha_0 + \beta_0)][1 - g^*(\beta_0)], \\
 p_{23.11} &= \frac{b\lambda_2}{a\lambda_1 + b\lambda_2 + \alpha_0 + \beta_0} [1 - g^*(a\lambda_1 + b\lambda_2 + \alpha_0 + \beta_0)]g^*(\beta_0) \\
 p_{23.11,14} &= \frac{b\lambda_2}{a\lambda_1 + b\lambda_2 + \alpha_0 + \beta_0} [1 - g^*(a\lambda_1 + b\lambda_2 + \alpha_0 + \eta_0)][1 - g^*(\eta_0)], \\
 p_{22.12} &= \frac{a\lambda_1}{a\lambda_1 + b\lambda_2 + \alpha_0 + \beta_0} [1 - g^*(a\lambda_1 + b\lambda_2 + \alpha_0 + \beta_0)]g^*(\beta_0) \\
 p_{22.12,15} &= \frac{a\lambda_1}{a\lambda_1 + b\lambda_2 + \alpha_0 + \beta_0} [1 - g^*(a\lambda_1 + b\lambda_2 + \alpha_0 + \beta_0)][1 - g^*(\beta_0)]
 \end{aligned}$$

For Model I

$$\begin{aligned}
 p_{4.17} &= \frac{\alpha_0}{a\lambda_1 + b\lambda_2 + \alpha_0} [1 - m^*(a\lambda_1 + b\lambda_2 + \alpha_0)] = p_{41.17}, \\
 p_{4.18} &= \frac{b\lambda_2}{a\lambda_1 + b\lambda_2 + \alpha_0} [1 - m^*(a\lambda_1 + b\lambda_2 + \alpha_0)] = p_{43.18}, \\
 p_{17.1} &= m^*(0), p_{18.3} = m^*(0), \quad p_{19.2} = m^*(0), p_{51} = g^*(\beta_0), \\
 p_{4.19} &= \frac{a\lambda_1}{a\lambda_1 + b\lambda_2 + \alpha_0} [1 - m^*(a\lambda_1 + b\lambda_2 + \alpha_0)] = p_{42.19},
 \end{aligned}$$

For Model II

$$\begin{aligned}
 p_{52} &= f^*(0), \quad p_{16.1} = m^*(0), p_{4.16} = \frac{\alpha_0}{a\lambda_1 + b\lambda_2 + \alpha_0} [1 - m^*(a\lambda_1 + b\lambda_2 + \alpha_0)] = p_{4.16}, \\
 p_{4.17} &= \frac{b\lambda_2}{a\lambda_1 + b\lambda_2 + \alpha_0} [1 - m^*(a\lambda_1 + b\lambda_2 + \alpha_0)] = p_{4.17}, \quad p_{17.3} = m^*(0), \quad p_{18.2} = m^*(0), \\
 p_{4.18} &= \frac{a\lambda_1}{a\lambda_1 + b\lambda_2 + \alpha_0} [1 - m^*(a\lambda_1 + b\lambda_2 + \alpha_0)] = p_{4.18},
 \end{aligned}$$

Mean Sojourn Times

The mean sojourn times (μ_i) for different states S_i are as follows:

Common for both Models

$$\begin{aligned}
 \mu_0 &= \frac{1}{a\lambda_1 + b\lambda_2 + \alpha_0}, \quad \mu_1 = \frac{1}{a\lambda_1 + b\lambda_2 + \alpha_0 + \alpha}, \quad \mu_2 = \frac{1}{a\lambda_1 + b\lambda_2 + \alpha_0 + \theta + \beta_0}, \\
 \mu_3 &= \frac{1}{a\lambda_1 + b\lambda_2 + \alpha_0 + \beta}, \quad \mu_4 = \frac{1}{a\lambda_1 + b\lambda_2 + \alpha_0 + \gamma}, \quad \mu'_1 = \frac{1}{\alpha}, \quad \mu'_3 = \frac{1}{\beta}, \quad \mu'_4 = \frac{1}{\gamma}
 \end{aligned}$$

For Model I

$$\begin{aligned}
 \mu'_2 &= \beta_0 + \frac{\gamma(\theta + \beta_0)}{(a\lambda_1 + b\lambda_2 + \theta + \alpha_0 + \beta_0)} \\
 &+ \frac{(a\lambda_1 + b\lambda_2 + \alpha_0)\{-\theta^2(\theta + \beta_0)^2 + \gamma\theta(a\lambda_1 + b\lambda_2 + \theta + \alpha_0 + \beta_0) + \beta_0(\theta + \beta_0)(a\lambda_1 + b\lambda_2 + \theta + \alpha_0 + \beta_0)(a\lambda_1 + b\lambda_2 + \alpha_0 + \beta_0) - \beta_0(\theta + \beta_0)\gamma\theta(a\lambda_1 + b\lambda_2 + \theta + \alpha_0 + \beta_0) + (\theta + \beta_0)\gamma(a\lambda_1 + b\lambda_2 + \alpha_0 + 2\beta_0)(a\lambda_1 + b\lambda_2 + \alpha_0 + \beta_0)\}}{(\theta + \beta_0)^2(a\lambda_1 + b\lambda_2 + \theta + \alpha_0 + \beta_0)(a\lambda_1 + b\lambda_2 + \alpha_0 + \beta_0)}
 \end{aligned}$$

For Model II

$$\begin{aligned}
 \mu_5 &= \frac{1}{\alpha}, \\
 \mu'_2 &= \frac{(a\lambda_1 + b\lambda_2 + \alpha_0 + \theta + \beta_0)^3(\theta + \beta_0)^3 + (a\lambda_1 + b\lambda_2)(a\lambda_1 + b\lambda_2 + \alpha_0 + \beta_0)^2\{\theta(a\lambda_1 + b\lambda_2 + \alpha_0 + \theta + \beta_0)(a\lambda_1 + b\lambda_2 + \alpha_0 + \beta_0) + \theta(a\lambda_1 + b\lambda_2 + \alpha_0 + \theta + \beta_0)(\theta + \beta_0) - \theta\beta_0(\theta + \beta_0)\} + (a\lambda_1 + b\lambda_2)(a\lambda_1 + b\lambda_2 + \alpha_0 + \theta + \beta_0)\{(a\lambda_1 + b\lambda_2 + \alpha_0 + \beta_0)^3(\theta + \beta_0)^3 + (a\lambda_1 + b\lambda_2 + \alpha_0 + \beta_0)^3(\theta + \beta_0)^3 + (\theta + \beta_0) - \theta(a\lambda_1 + b\lambda_2 + \alpha_0 + \theta + \beta_0)(\theta + \beta_0)\} - \alpha_0(a\lambda_1 + b\lambda_2 + \theta + \alpha_0 + \beta_0)^2}{\frac{(\theta + \beta_0)^3(a\lambda_1 + b\lambda_2 + \alpha_0 + \beta_0) + \theta_0(a\lambda_1 + b\lambda_2 + \alpha_0 + \beta_0)(a\lambda_1 + b\lambda_2 + \alpha_0 + \theta + \beta_0)(\theta + \beta_0) - \theta(a\lambda_1 + b\lambda_2 + \alpha_0 + \beta_0)^2(\theta + \beta_0)^2}{(a\lambda_1 + b\lambda_2 + \alpha_0 + \beta_0)^2(a\lambda_1 + b\lambda_2 + \theta + \alpha_0 + \beta_0)^2(\theta + \beta_0)^2}}
 \end{aligned}$$

It can be easily verified that sum of all the transition probabilities form one state to other state is equal to one.

Reliability and Mean Time to System Failure

In this section, we obtained the mean time to system failure (MTSF) and reliability of a computer system. The cumulative probability density function of the first passage time denoted by $\Delta_i(t)$ between $S_i, S_j \in E$. Here, on the basis of model

description, we obtain the following recurrence relation for $\Delta_i(t)$ by assuming the down state S_j as an absorbing state,

$$\Delta_i(t) = \sum_j Q_{i,j}(t) \textcircled{R} \Delta_j(t) + \sum_k Q_{i,k}(t) \tag{2}$$

where state $S_j \in E$ to which the given state $S_i \in E$ can transit and S_k is a down state to which the state S_i can transit directly. We solve the recurrence relation (2) by taking LST for $\tilde{\Delta}_0(s)$. We have

$$R^*(s) = \frac{1 - \tilde{\Delta}_0(s)}{s} \tag{3}$$

By taking the Laplace inverse transform of Eq. (3), we can obtain the reliability of the system. Now MTSF is given by $\text{MTSF} = \lim_{s \rightarrow 0} \frac{1 - \tilde{\Delta}_0(s)}{s} = \frac{N_1}{D_1}$, where $N_1 = \mu_0 + p_{01}\mu_1 + p_{02}\mu_2 + p_{03}\mu_3 + p_{24}p_{02}\mu_4$ and $D_1 = 1 - p_{01}p_{10} - p_{02}p_{20} - p_{03}p_{30} - p_{02}p_{24}p_{40}$.

Steady State Availability

By using probabilistic arguments, following recurrence relation are obtained for availability $X_i(t)$, where $X_i(t)$ is the system's up-state probability at time $t = 0$:

$$X_i(t) = O_i(t) + \sum_j q_{i,j}^{(n)}(t) \textcircled{C} X_j(t) \tag{4}$$

where S_j and S_i are regenerative states which transit from one to another in n steps. $O_i(t)$ is the up-state probability of the system at any regenerative state. Taking LT of above relations (4) and solving for $A_0^*(s)$, the steady state availability is obtained by the following relation for both the system models: $A_0(\infty) = \lim_{s \rightarrow 0} sA_0^*(s) = \frac{N_2}{D_2}$.

Busy Period Analysis for Server

By probabilistic arguments, $B_i^P(t)$, $B_i^R(t)$, $B_i^S(t)$ and $B_i^{HRP}(t)$ be the probability that repairman is busy in preventive maintenance, hardware repair, software upgradation, and hardware replacement of the unit at an instant 't' given that the system entered state S_i at $t = 0$. The recursive relations for these are as follows:

$$\begin{aligned}
B_i^P(t) &= W_i(t) + \sum_j q_{i,j}^{(n)}(t) \odot B_j^P(t), B_i^R(t) = W_i(t) + \sum_j q_{i,j}^{(n)}(t) \odot B_j^R(t), B_i^S(t) \\
&= W_i(t) + \sum_j q_{i,j}^{(n)}(t) \odot B_j^S(t) \text{ and } B_i^{HRP}(t) = W_i(t) + \sum_j q_{i,j}^{(n)}(t) \odot B_j^{HRP}(t)
\end{aligned} \tag{5}$$

where S_j & S_i are regenerative states which transit from one to another in n steps. The time up to which server remains busy at any state S_i due to preventive maintenance, hardware repair, software upgradation, and hardware replacement without transiting to any other state is obtained by probability $W_i(t)$. Taking LT of above relations (5) and solving for $B_i^{*P}(s)$, $B_i^{*R}(s)$, $B_i^{*S}(s)$ and $B_i^{*HRP}(s)$, we obtained the time during which server remains busy due to maintenance, repair and replacements respectively $B_0^H = \lim_{s \rightarrow 0} sB_0^{*H}(s) = \frac{N_3^H}{D_2}$, $B_0^S = \lim_{s \rightarrow 0} sB_0^{*S}(s) = \frac{N_3^S}{D_2}$, $B_0^R = \lim_{s \rightarrow 0} sB_0^{*R}(s) = \frac{N_3^R}{D_2}$ & $B_0^{HRP} = \lim_{s \rightarrow 0} sB_0^{*HRP}(s) = \frac{N_3^{HRP}}{D_2}$.

Expected Number of S/W Upgradations and H/W Replacement

By simple probabilistic arguments, we obtained the following recurrence relations for $R_i^H(t)$ and $R_i^S(t)$ made by server in $(0, t]$.

$$R_i^H(t) = \sum_j Q_{i,j}^{(n)}(t) \otimes [\delta_j + R_j^H(t)] \quad R_i^S(t) = \sum_j Q_{i,j}^{(n)}(t) \otimes [\delta_j + R_j^S(t)] \tag{6}$$

where $S_j, S_i \in E$ and state S_i can transit to state S_j while $\delta_j =$

$$\begin{cases} 1 & \text{if } S_j \in E \text{ where repairman starts a new job} \\ 0 & \text{otherwise} \end{cases} \quad \text{Taking LT of relations (6) and}$$

solving for $\tilde{R}_0^H(s)$ and $\tilde{R}_0^S(s)$ we obtain the expected numbers of replacements per unit time to the hardware and upgradation of software respectively by using the following relations:

$$R_0^H(\infty) = \lim_{s \rightarrow 0} s\tilde{R}_0^H(s) = \frac{N_4^H}{D_2} \quad \text{and} \quad R_0^S(\infty) = \lim_{s \rightarrow 0} s\tilde{R}_0^S(s) = \frac{N_4^S}{D_2}$$

Expected Number of Visits by the Server

By probabilistic arguments, on the basis of both models we obtained the following recurrence relations for expected number of visits $N_i(t)$:

$$N_i(t) = \sum_j Q_{ij}^{(n)}(t) \textcircled{R} [\delta_j + N_j(t)] \tag{7}$$

where $S_j, S_i \in E$ and state S_i can transit to state S_j while $\delta_j = \begin{cases} 1 & \text{if } S_j \in E \text{ where repairman starts a new job} \\ 0 & \text{otherwise} \end{cases}$ Taking LT of relation (7), we obtained the expected number of visits by the server by following formula $N_0(\infty) = \lim_{s \rightarrow 0} s\tilde{N}_0(s) = \frac{N_s}{D_s}$.

Profit Analysis

The profit earned by the system model in steady state can be obtained as

$$P = K_0A_0 - K_1B_0^p - K_2B_0^R - K_3B_0^S - K_4B_0^{HRp} - K_5R_0^H - K_6R_0^S - K_7N_0$$

K_0 = Income per unit uptime of the system.

K_i = Expenditure per unit time for which server is busy due to various repair activities.

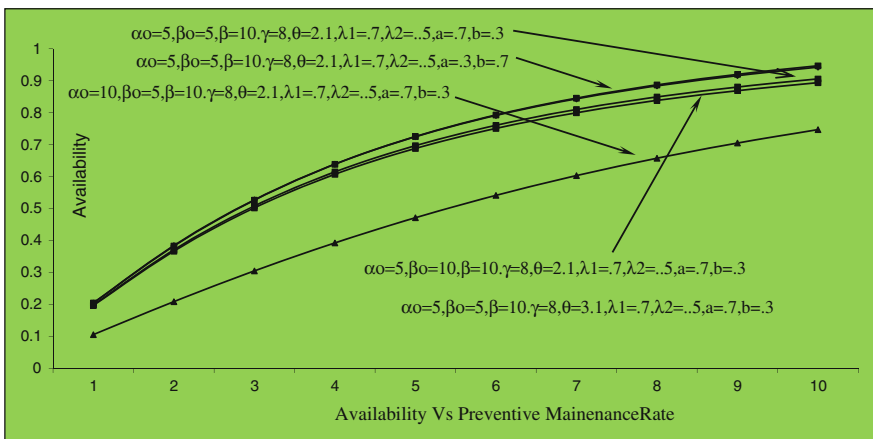


Fig. 1 Availability versus PM rate (Model I)

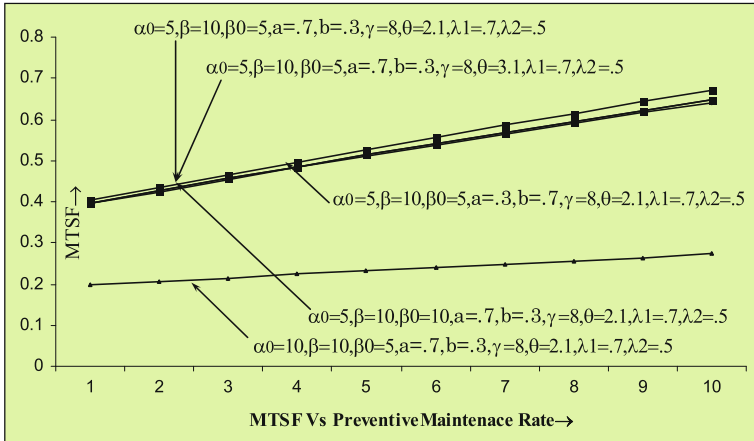


Fig. 2 MTSF versus preventive maintenance rate

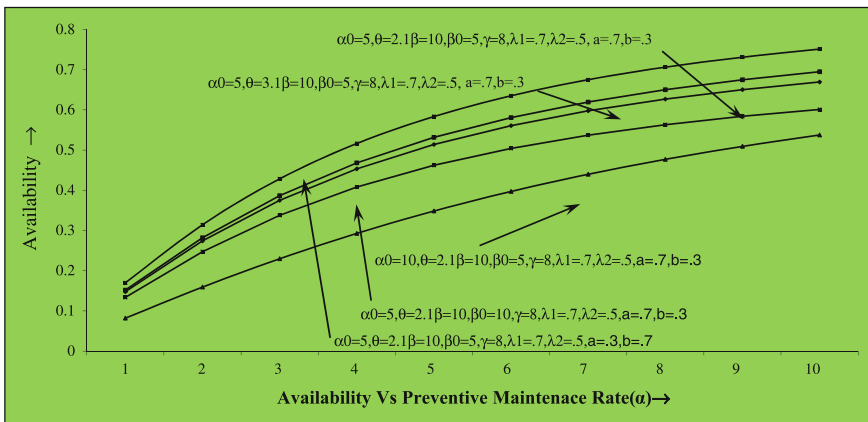


Fig. 3 Availability versus PM rate (Model II)

Comparative Studies

For a particular case, by considering all the random variables as exponential distributed various graphs are drawn respectively in Figs. 1, 2, 3, and 4. In both models, the results shows that with the increment of PM rate (α) and hardware repair rate (θ) the availability of the system models increase. But with respect to increase of maximum operation time (α_0), its values decrease. Again, if we increase maximum constant rate of repair time (β_0), then the value of availability will increase.

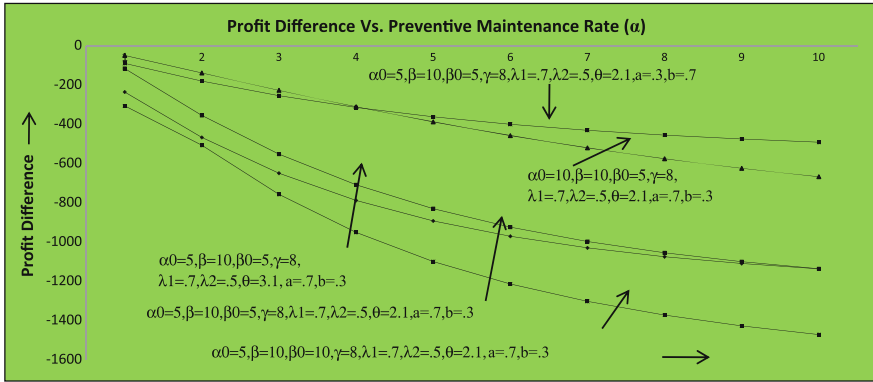


Fig. 4 Profit difference (P1-P2) versus PM rate (M1-M2)

Comparison of MTSF: The MTSF of Model I and Model II is same as shown in Fig. 2.

Comparison of Profit: Profit of the Model II is always more than that of the Model I as shown in Fig. 4. Hence we conclude that the concept of priority to preventive maintenance over h/w repair is beneficial over the system where no priority is given.

References

1. Friedman, M.A., Tran, P.: Reliability techniques for combined hardware/software systems. In: Proceedings of Annual Reliability and Maintainability Symposium, pp. 290–293 (1992)
2. Welke, S.R., Labib, S.W., Ahmed, A.M.: Reliability modeling of hardware/software system. *IEEE Trans. Reliab.* **44**(3), 413–418 (1995)
3. Malik, S.C., Anand, J.: Reliability and economic analysis of a computer system with independent hardware and software failures. *Bull. Pure Appl. Sci. (Math. Stat.)* **29 E** (1), 141–153 (2010)
4. Malik, S.C., Kumar, A.: Profit analysis of a computer system with priority to software replacement over hardware repair subject to maximum operation and repair times. *Int. J. Eng. Sci. Technol.* **3**(10), 7452–7468 (2011)
5. Malik, S.C., Nandal, P.: Cost-analysis of stochastic models with priority to repair over preventive maintenance subject to maximum operation time, Edited Book. In: *Learning Manual on Modeling, Optimization and Their Applications*, pp. 165–178. Excel India Publishers (2010)
6. Kumar, A., Malik, S.C., Barak, M.S.: Reliability modeling of a computer system with independent H/W and S/W failures subject to maximum operation and repair times. *Int. J. Math. Achieves* **3**(7), 2622–2630 (2012)
7. Kumar, A., Malik, S.C.: Stochastic modeling of a computer system with priority to PM over S/W replacement subject to maximum operation and repair times. *Int. J. Comput. Appl.* **43**(3), 27–34 (2012)

8. Malik, S.C., Anand, J.: Analysis of a computer system with arbitrary distribution for h/w and s/w replacement time and priority to repair activities of h/w over replacement of the s/w. *Int. J. Syst. Assur. Engg. Manage.* **3**(3), 230–236 (2012)
9. Nandal, J., Sureria, J.K., Malik, S.C.: Reliability measures of a cold standby system with priority for operation and preventive maintenance. *Int. J. Math. Archives.* **4**(3), 84–91 (2013)
10. Malik, S.C.: Reliability modeling of a computer system with preventive maintenance and priority subject to maximum operation and repair times. *Int. J. Syst. Assur. Engg. Manage.* **4**(1), 94–100 (2013)
11. Kumar, A.: Comparison of performance measures of an integrated H/w and S/w systems under priority and preventive maintenance. *Elixir Stat.* **80**, 31289–31300 (2015)

Dual-Band Filter Using DGS for X-Band Applications

Suman Kumari, Amit Singh Bhadouria and Mithilesh Kumar

Abstract A novel dual-band planar bandpass filter for X-band applications is proposed in this paper. The proposed filter operates at two bands where the first band is from 7.7 to 8.5 GHz and the second from 9.4 to 10.3 GHz with resonant frequencies 8.2 and 10.0 GHz, respectively. The filter is compact in size with dimension $24 \times 15 \times 1.34 \text{ mm}^3$ with ground plane. For designing this structure heraeus substrate of thickness 1.27 mm and with dielectric constant as 9 is used. The EMS software, CST microwave studio is used for simulation and optimization of the proposed filter structure. The results obtained after simulation of filter are too good and the return loss and insertion loss of bands are -23.5 and -1.2 dB, respectively for the first band and -19 and -2.3 dB, respectively for the second band. Also, group delay for both the bands is less than 0.5 ns. As both the bands are from X-band, the first band is used for satellite uplink and the second band is used for radiolocation applications and hence this filter is suitable for X-band applications.

Keywords Bandpass filter (BPF) · Defective ground structure (DGS) · Dual-band · Microstrip planar (MSP)

Introduction

Nowadays, in modern communication systems requirement for miniature planar filters with excellent performance has increased. So dual-band filters are the basic requirement for modern communication systems. One of the ways to design a

Suman Kumari (✉) · A.S. Bhadouria · Mithilesh Kumar
Electronics Engineering Department U.C.E, RTU Kota, Kota, India
e-mail: sumannehra15891@gmail.com

A.S. Bhadouria
e-mail: amit05singh@gmail.com

Mithilesh Kumar
e-mail: mith_kr@yahoo.com

dual-band filter is by combining two bandpassfilters which have their individual passbands [1], but then the implementation area will be increased. Various designs were proposed for dual-band filters from [2–5]. Dual-band filters are designed using both short or open-circuited stubs which we place in series or shunts for creating the transmission zeros in the middle passband of bandpass filter (BPF) [6–8]. Using these resonators the filter structure becomes compact and also economical but it increases in complexity. Hence SIR-based dual-band filters are famous because of their well-known design methods, versatile resonant frequencies, and simpler structure [9].

The proposed filter operates in X-band region of microwave range. X-band is defined by an IEEE standard for radio-waves and RADAR engineering with frequency that ranges from 8 to 12 GHz. X-band has wide applications like short range tracking, missile guidance, marine, RADAR, and airborne intercept [10].

The passband and stopband characteristics of the proposed filter design are improved using defective ground structure (DGS); we can introduce the DGS structure by etching any simple shape from ground plane. Using DGS the characteristics of a transmission line such as capacitance and inductance can be changed as DGS disturbs the current distribution in ground plane [11].

This paper proposes a compact planar dualband BPF for X-band applications. The filter is composed of two shunt stubs and two rectangular pads with DGS. Using DGS we improve the S-parameters of filter. Two bands in X-band are received by simulating the proposed filter. The first band achieved is from 7.7 to 8.5 GHz, which is used for fixed satellite communication systems and another band is from 9.4 to 10.3 GHz with resonant frequency 10 GHz used for radiolocation applications.

This paper includes four sections. In the second section the design of proposed dual-band filter is explained, a simple planar BPF with slot 1 is discussed and then the proposed filter with defected ground is explained. In the third section the simulated results of the designed filter are mentioned. In the results we discuss the return loss, insertion loss, and group delay of filter, and in the final section we draw the conclusions.

Filter Design

The filter is designed on the heraeus substrate of thickness 1.27 mm, dielectric constant 9 is used with dimension $24 \times 15 \text{ mm}^2$, and the designed filter operates on two bands of X-band. The input and output microstrip lines are of dimensions $L1 \times W1$. For designing this filter, first we designed a simple planar filter due to which we get two bands in X-band and then to improve its results we introduced the DGS in ground plane. The designing steps of the proposed filter are explained in detail in this section.

Simple Microstrip Planar Filter with Slot 1

A simple MSP filter is designed using two shunt stubs and two rectangular pads. The first rectangular pad has length L_2 and width W_2 and it is attached to the input and output microstrip lines with two shunt stubs. The shunt stubs have length L_5 and width W_5 . With this configuration the filter worked for X-band but the results were not good. So for increasing coupling between these two shunt stubs we inserted a rectangular pad between the two and the inserted rectangular stub has dimensions $L_3 \times W_3$. For improving results we cut a rectangular slot in the first rectangular pad where the dimensions of slot 1 are $L_4 \times W_4$; the filter is shown in Fig. 1. By simulating this structure two bands are achieved where return loss of the first band is good but return loss of second band is ≤ -15 dB; the results are shown in the following section. Dimensions of the proposed filter are tabulated in Table 1.

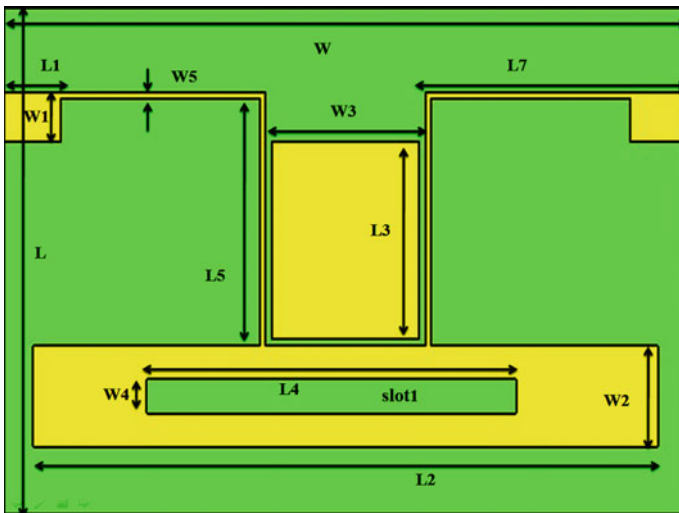


Fig. 1 Front view of proposed filter design for dual band

Table 1 Dimensions of proposed dual-band filter

Parameter	Value (mm)	Parameter	Value (mm)
L	15.0	W	24.0
L1	2.0	W1	1.50
L2	22.0	W2	3.0
L3	6.0	W3	5.20
L4	13.0	W4	1.0
L5	7.50	W5	0.20
L6	4.0	W6	3.0
L7	9.20		

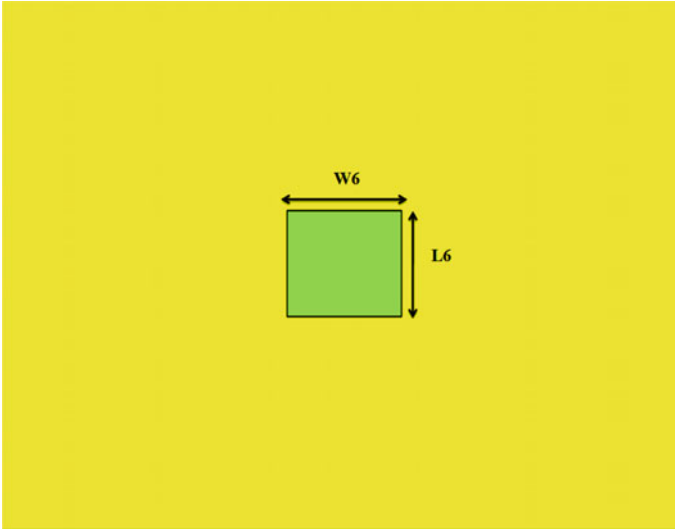


Fig. 2 Back view of proposed filter design for dual band

Proposed Filter with DGS

Using the above structured results was not good hence to improve the results of the proposed filter a rectangular slot is cut of length L_6 and width W_6 in ground plane as shown in Fig. 2. Using DGS the characteristics of a transmission line such as capacitance and inductance can be changed as DGS disturbs the current distribution in ground plane [11]. By simulating this structure two bands are achieved in X-band, one from 7.7 to 8.5 GHz and the second from 9.4 to 10.3 GHz with resonant frequencies 8.2 and 10.0 GHz, respectively. The return loss of the first band was good from the above structure but return loss of second has improved using DGS. The variations in results are explained in detail in the following section and are also clarified using comparative graphs of S-parameters.

Result and Discussion

This dual-band BPF is simulated using electromagnetic (EM) simulation software. In the results the return loss, insertion loss, and group delay of proposed filter are discussed. and we also discuss how our results have improved using DGS.

Initially, the filter we designed was without slot 1 and DGS. Then we cut a slot in rectangular pad and then we cut a rectangular patch in the ground for making filter a DGS-based structure. From the first design a single band was received from 7.7 to 9.25 GHz and from the second design two bands were received— first from

7.7 to 8.1 GHz and second from 9.7 to 10.15 GHz— but return loss of the second band was not good, hence for improving the second band a DGS was introduced. The S-parameter of three designs are compared and shown in Fig. 3a, b. The final filter with DGS has two operating bands, one from 7.7 to 8.5 GHz and the second from 9.4 to 10.3 GHz with resonant frequencies 8.2 and 10.0 GHz. The insertion loss and return loss of first band are -1.25 and -23.54 dB, respectively, and for the second band they are -19 and -2.3 dB, respectively, as shown in Fig. 4a. The group delay of the designed filter for both bands is less than 0.5 ns as shown in Fig. 4b.

Fig. 3 Variation in S-parameters of filter using DGS and slot1. **a** Return loss. **b** Insertion loss

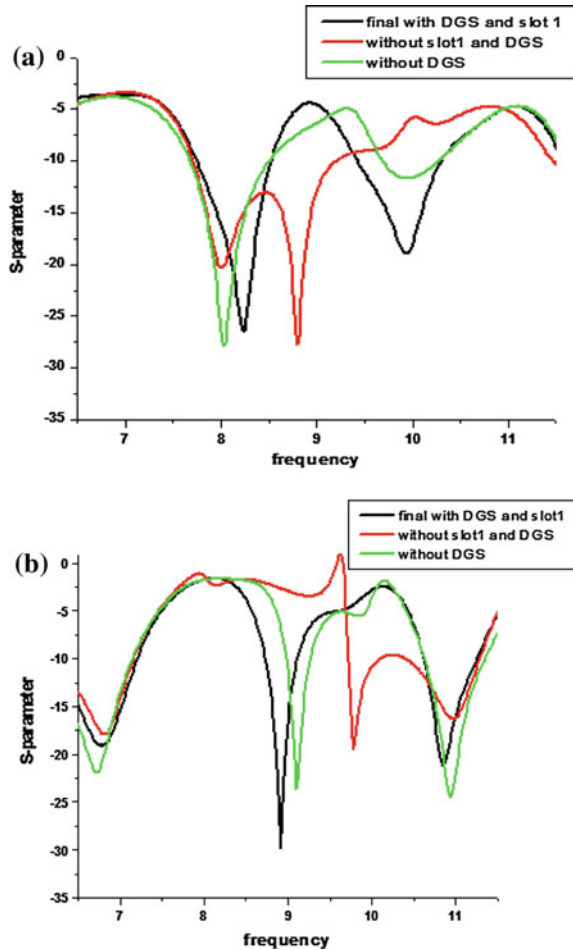
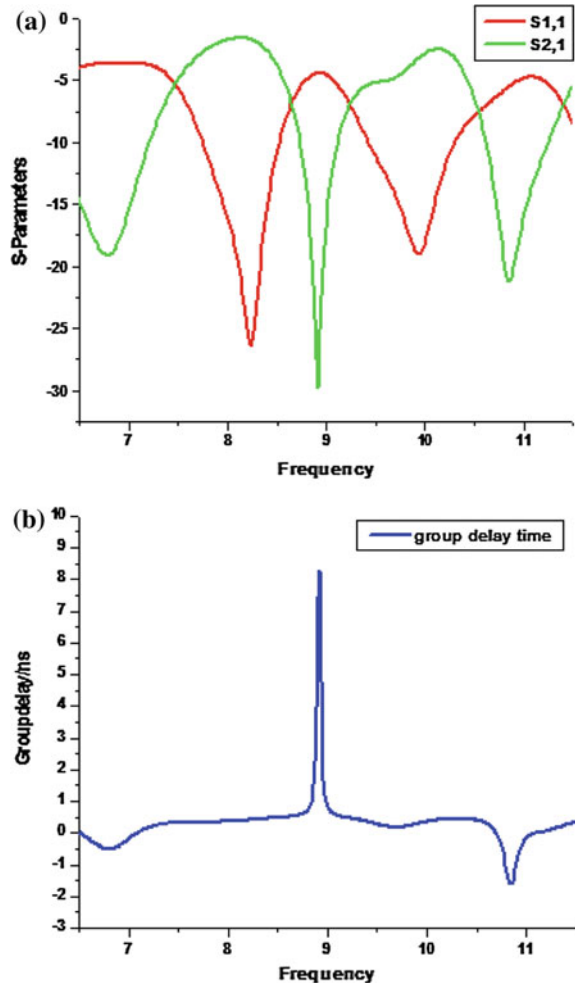


Fig. 4 Simulation results of final proposed filter. **a** S-parameters. **b** Group delay



Conclusions

In this paper a dual-band filter for X-band applications is proposed. The DGS is introduced in simple planar structure of filter to improve the characteristics of filter. The insertion loss of filter without DGS at first band (7.7–8.1 GHz) and second (9.7–10.15 GHz) are -2 and -4 dB, respectively, and return loss of first band is -27 dB and of second band is -13 dB. After introducing DGS in the main structure return loss at first band (7.7–8.5 GHz) is -26.5 dB and at second band (9.4–10.3 GHz) is -19 dB which is improved from above. The proposed filter works on two bands, the first for fixed satellite applications and the second for radiolocation applications. Both bands can be used for X-band applications such as

short range's tracking, missile guidance, marine, RADAR, and airborne intercept. The final simulated results of both filters, S-parameter and group delay, are good and this can be used in modern communication systems. The simulated results are good and its simple planar geometry makes it suitable for microwave integrated circuits. In the future we can convert this filter into the tunable bandpass filter using pin diode or RF/MEMS switches.

References

1. Miyake, H., Kitazawa, S., Ishizaki, T., Yamada, T., Nagatomi, Y.: A miniaturized monolithic dual band filter using ceramic lamination technique for dual mode portable telephones. In: IEEE MTT-S International Microwave
2. Tsai, L.-C., Huse, C.-W.: Dual-band bandpass filters using equal length coupled-serial-shunted lines and Z-transform techniques. *IEEE Trans. Microw. Theory Tech.* **52**(4), 1111–1117 (2004)
3. Sun, S., Zhu, L.: Compact dual-band microstrip bandpass filter without external feeds. *IEEE Microwave Wirel. Compon. Lett.* **15**(10), 644–646 (2005)
4. Kuo, J.-T., Yeh, T.-H., Yeh, C.-C.: Design of microstrip bandpass filter with a dual-passband response. *IEEE Trans. Microw. Theory Tech.* **53**(4), 1331–1337 (2005)
5. Huang, T.-H., Chen, H.-J., Chang, C.-S., Chena, L.-S., Wang, Y.-H., Houg, M.-P.: A novel compact ring dual-mode filter with adjustable second-passband for dual-band applications. *IEEE Microwave Wirel.*
6. Quendo, C., Rius, E., Person, C.: An original topology of dual-band filter with transmission zeros. *IEEE MTT-S Int. Microwave Symp. Dig.* **2**, 1093–1096 (2003)
7. Tsai, C.M., Lee, H.M., Tsai, C.C.: Planar filter design with fully controllable second passband. *IEEE Trans. Microw. Theory Tech.* **53**(11), 3429–3439 (2005)
8. Lee, H.M., Tsai, C.M.: Dual-band filter design with flexible passband frequency and bandwidth selections. *IEEE Trans. Microw. Theory Tech.* **55**(5), 1002–1009 (2007)
9. Chang, W.-S., Chang, C.-Y.: Member, IEEE “Analytical Design of Microstrip Short-Circuit Terminated Stepped-Impedance Resonator Dual-Band Filters”. *IEEE Trans. Microwave Theory Tech.* **59**(7) (2011)
10. Datta, B., Das, A., Kundu, A., Chatterji, S., Mukhrji, M., Choduray, S.K.: Twice-band irregular rectangular cut-in Microstrip Patch Antenna for Microwave Communication. In: International Conference on Information Communication and Embedded System (2013)
11. Weng, L.H., Guo, Y.C., Shi, X.W., Chen, X.Q.: An overview on defected ground structure. *Prog. Electromagn. Res. B* **7**, 173–189 (2008)

A Review on Performance Evaluation of Routing Protocols in MANET

Shruti Thapar and Anshuman Kalla

Abstract MANET is a networking paradigm that facilitates users to communicate with one another by establishing a temporary network without any form of centralized administrative infrastructure. In MANET, particularly, specialized routing protocols are needed in order to cope up with distinctive characteristic of MANET, which is time-varying topology due to anticipated frequent node mobility. The paper contributes by making a review of different authors who have worked to analyze the performance of various routing protocols in MANET.

Keywords MANET · AODV · DSDV · DSR · ZRP

Introduction

Advent of wireless communication and its recent advancements have fuelled the extensive use of mobile handheld devices like PDA, smart phones, palmtops, mini laptops, etc. [1]. The obvious need of such mobile devices would be to communicate and share data with each other with least physical and financial efforts. Infrastructureless networking approach that allows mobile nodes to communicate as and when required without preconfiguring them is termed as mobile ad hoc network (MANET) [2]. In order to setup a proper network some sort of routing protocol (control plane operation) is necessary to establish and maintain routing tables which forwards (data plane operation) data packets from a source to a destination. The basic requirement of ad hoc network routing protocol is to establish effective,

Shruti Thapar (✉) · Anshuman Kalla
Department of Electronics & Communication Engineering, Jaipur National University,
Jaipur, Rajasthan, India
e-mail: shrutithapar5@gmail.com

Anshuman Kalla
e-mail: kallajnu@gmail.com

correct, and efficient routes between two nodes such that the packet containing messages can be delivered in a timely manner without intolerable delays even with node mobility [3].

The remaining part of the paper is organized as follows: Sect. 2 describes the concept of routing protocol and its classification. Section 3 discusses in detail the related work carried out so far by other researches over MANET. Section 4 summarizes, concludes, and discusses the future scope of MANET and areas to research on.

Routing Protocols in Nutshell

Designing of routing protocol is more complex in MANET as routing protocol is often vulnerable to node's mobility and misbehavior (selfish and malicious). A node dropping off the packets is stated as selfish node and it does so, because it wants to save battery life for only those communications which are of its own interest [4]. A malicious node advertises attractive but fake routes so that it could get access and control over those message packets that were not supposed to traverse it or reach to it [5]. Routing protocols are divided into three subcategories: reactive, proactive, and hybrid routing protocol.

Reactive Routing Protocol

Reactive routing protocol performs a route discovery procedure, in on-demand basis only, i.e., when the route is required. It is source node that initiates a route discovery process in reactive routing protocols [6, 7]. Reactive group follows the flooding process and the examples are ad hoc on-demand distance vector (AODV), dynamic source routing protocol (DSR), cluster-based routing protocol (CBRP), etc. It is a bandwidth-efficient routing protocol and has a capability to support multi-casting routing also.

AODV: An ad hoc on-demand distance vector routing protocol uses different messages to discover and maintain links. It broadcasts a route REQuest (RREQ) messages to all its neighbors [8]. The RREQ propagates through the network for fresh routes until it reaches the destination node. The moment the fresh route is found at any intermediate node, it is being intimated to the source by unicasting a route reply (RREP) message back to the source node [9]. Each node broadcasts "HELLO" message to all its neighbors periodically to update them and continue with the existence of present node. Any kind of interruption in hello messages from a particular neighboring node beyond a certain time limit implies that the node has moved away from its position. Consequently, the associated network links are marked as broken and a link failure notification is sent to all the concerned set of

nodes [10]. The sequence numbers used in AODV represent freshness of a route. It is incremented by one when something happens in the surrounding area, i.e., relevant change in network.

Proactive Routing Protocol

Proactive routing protocols continuously evaluate the current network to find out the possible routes, so that, if user wants to forward a packet from source to destination node, the route is already known and can be immediately used. Examples of proactive routing protocol are destination sequence distance vector (DSDV), optimized link state routing protocol (OLSR), temporal ordered routing algorithm (TORA), etc.

DSDV: A proactive routing protocol uses hop-by-hop distance vector routing protocol. It maintains a routing table for all neighboring nodes. DSDV stores the next hop and the number of hops for a given destination in its routing table. It periodically broadcasts routing updates of each node [1]. DSDV uses a sequence number to tag each route [11].

Hybrid Routing Protocol

A hybrid routing protocol uses a mixture of both proactive and reactive approaches, as it has two states of functions viz., intrazone and interzone routing protocol. Intrazone routing protocol uses proactive routing protocol and interzone routing protocol uses reactive routing protocol to find optimal routes. The examples are zone routing protocol (ZRP), sharp hybrid adaptive routing protocol (SHARP), etc. [12].

Related Work

Works done by various researchers on performance evaluation of different routing protocols are in detail reported as follows.

In [13–15], researchers have tried to evaluate the MANET security issues, using AODV routing protocol. They worked on various network parameters like packet delivery ratio, throughput, delay, jitter, and packet drop rate. Researchers have used different techniques for detection and prevention of attacks in mobile ad hoc network. TDMA-based energy efficient technique is used to improve various performance metrics [15]. Here, TDMA is used to divide the simulation time into small slots of time for multi-hop routing methods with AODV protocol [15]. “Packet Leash” mechanism [14] is used for detection and prevention of attacks for enhancing security. Here all nodes in the MANET will obtain an authenticated

symmetric key of every other node in network. Using this technique, receiver becomes capable of authenticating received data packets and thereby the information contained in them. Another technique used for prevention of attacks invokes the concept of “Time of Flight” [14]. It calculates the round-trip journey time of a message. It evaluates the distance between nodes based on time and calculates the maximum possible communication range between them. If any attacker intercepts, then packets end up traveling further, and thus would not return within the estimated time [13]. Hence, man-in-the-middle attacks can be detected. Authors have concluded that there is no particular method for security which can allow detecting and preventing attack simultaneously. Further, author concluded that in AODV as the number of nodes increases, it will simultaneously increase the rate of packet delivery ratio and throughput. In addition, the delay also increases with increased number of nodes. The reason is that, if the number of nodes increases, it will increase the traffic, which in turn enhances the probability of collision between the working nodes for route discovery process resulting in increased delay.

In [3, 16–20], survey and comparison over various existing solutions for black hole attack on AODV, DSR, and DSDV routing protocol are carried out. Authors used various mobility models like random way point (RWP), reference point group mobility (RPGM), freeway (FW), and manhattan(MH) mobility models for their analysis using OPNET [20] and NS-2 simulator [17, 19]. In black hole attack a malicious node is being used which announces to all the other nodes within the network the possibility to reach any destination through it, i.e., flooding of fake attractive routes information [18]. On learning in the presence of such routes all nodes send/forward packets to this malicious node. In contrite to normal forwarding, malicious node drops all packets that it receives [21]. In [16], author evaluated the performance of reactive protocols and proactive protocols for MANET, for both constant bit ratio (CBR) and transmission control protocol (TCP) traffic patterns with different mobility models. Author uses various parameters such as average end-to-end delay, throughput, and packet delivery ratio to evaluate the performance of different routing protocols. Authors have concluded that there is no reliable procedure to detect and avoid black hole attack [3]. Protocols have to suffer with higher time delay and network overhead because of false route reply messages to route request. This increases the chances of fake routes for particular destination. Results showed that DSR will give average path density with increasing load as compared to high path density in AODV. Here, path density describes the portion of potential connection between nodes in a network that are actually able to connect with each other. The reason behind better performance of DSR in terms of path density is that DSR is having cached routes and it can also find routes by on-demand basis.

Papers [22–24] present detailed description about various routing protocols, i.e., reactive (AODV and DSR) and proactive (OLSR and TORA) routing protocols using OPNET 14.5 simulator [24] and NS-2 simulator [22, 23]. The simulations focus on the evaluation of routing protocols by varying (increasing) scalability and mobility with constant file transfer protocol (FTP) and video conferencing traffic [5]. It has been concluded that AODV gives best result for throughput with

increasing number of nodes followed by OLSR. This is due to on-demand routing nature of AODV which results in fresh routes with minimum number of hop counts. This in turn reduces the delay factor in AODV routing protocol. As DSR is showing better network performance like packet delivery ratio, throughput and delay factor with increasing node speed is followed by AODV and OLSR routing protocol [22]. This is due to the fact that DSR is having stored cached routes in its memory as discussed previously.

In [25–33], performance evaluation is carried out between reactive (AODV, DSR) and proactive (DSDV) routing protocols, with various network parameters like delay, throughput, and packet delivery ratio using different simulators like NS-2 simulator [25, 27, 33] and ViSim 1.0 [29]. Authors worked on two models, i.e., traffic and mobility models. Random waypoint model is used as mobility model [26, 32, 33] and traffic model used as continuous bit rate (CBR) [25, 30]. Network scenarios use different numbers of source—destination pair, which varies to change network load. Each packet starts traveling in a random way from source to destination with varying speed. After pause time, a packet reaches to another random destination [31]. Here, pause time is that time interval which defines the stay time at any particular node in the network; if any node is showing high pause time, then the node is dynamic in nature and if pause time is less then the node is static in nature. In [31] first scenario, the duration of pause time is varied and the value of maximum movement speed and sending data rate were kept fixed, whereas in another scenario, to calculate the impact of movement speed on routing protocols, researcher varied the maximum movement speed, while keeping pause time and sending rate unchanged. Authors concluded that DSR has best throughput and packet delivery ratio, followed by AODV with increasing load condition. DSR suffers from a higher delay when load, number of node, and mobility increase simultaneously, but this does not affect AODV, as it has less delay factor compared to DSR. The reason being DSR is based on source routing protocol having cached routes in its memory and can also find routes by on-demand basis. This leads to increase in the throughput. It is interesting to note that DSR provides less delay up to certain level with increasing number of nodes in the network. After that threshold overall performance degrades significantly. DSDV resulted in worst delay performance in this scenario, as it is proactive in nature.

In [34], performance of proactive (DSDV, CBRP) and reactive (AODV, DSR) routing protocols is evaluated with RWP model and varying number of nodes using NS-2 simulator. Authors considered a network in which nodes are placed randomly within an area and operated over fixed simulation time. In this experiment, different iterations with different node speeds and number of nodes were made for each scenario and collected data is arranged in order, to examine the performance of different routing protocols. Authors took into account the metrics like packet delivery ratio, throughput, delay, and network parameters to evaluate different routing protocols. The results advocate that DSR has better throughput and delay factor when the number of nodes increases, because DSR uses source routing protocol. AODV gives less throughput and higher delay factor as compared to DSR routing protocol. CBRP shows average packet delivery ratio and throughput.

DSDV shows the higher delay factor with increasing number of nodes as it is proactive in nature, which needs to be updated timely in order to improve its route cache table with frequent changes in the environment.

In [20, 35, 36], performance evaluation with two different network traffic, i.e., constant bit rate (CBR) and transmission control protocol (TCP), with varying pause time, offered load, transmission power, and average node speed for AODV, DSR, OLSR, and WRP routing protocols is presented. OPNET [20] and GloMoSim [35, 36] are used as simulation tools. Researcher has worked on static and dynamic scenarios. For each scenario, both UDP and TCP connections were used with various attributes [20]. In static scenario, nodes were motionless and routes were valid during the entire simulation time. In second scenario, some nodes were made to move with very low speed, that is, less dynamic scenario. The last scenario comprises nodes capable of moving with high speed. Author created large set of simulation scenarios and examined end-to-end delay, download response time, route discovery time, and routing traffic overhead for UDP and TCP connections. Researchers concluded that when low load and high transmission power condition prevails, AODV shows high packet delivery ratio and quick download response time, but when load also increases with high transmission power, it shows less packet delivery ratio and slow download response time. This is because when transmission power is increased, the AODV being reactive routing protocol will discover route faster, under fewer nodes condition. If the number of nodes also increases, then load will increase and performance will degrade accordingly, whereas OLSR shows good throughput, average download response time, and high packet delivery ratio with low load and low transmission power, due to proactive nature.

The paper [12] worked on three routing protocols, namely, reactive (AODV, DSR), proactive (DSDV), and hybrid (ZRP) routing protocols using varying number of nodes, mobility in speed, and pause time for various network parameters using NS-2 simulator. Both traffic model and mobility model were used by researcher to work on different routing protocols. For traffic model, cbgen (constant bit rate generation) utility was used and for mobility model, setdest (set destination) utility was used for node positions and their movements. In order to perform simulations, different scenario files were generated by varying some parameters and keeping other values constant at that particular time, for example, varying number of nodes and maximum speed while keeping pause value constant. Authors observed that AODV and DSR show higher throughput and packet delivery ratio as the number of nodes and pause time increases, because both routing protocols follow the concept of reactive routing protocol. ZRP shows average throughput, packet delivery ratio, and delay as it follows both reactive and proactive routing protocols. DSDV showed higher delay factor with increase in pause time, because increasing pause time will increase the stale route cached in routing tables and that is why the destination node will receive packet with delay.

Papers [37–40] deal with two reactive (AODV, DSR) routing protocols, to find the energy consumption between various nodes, delay, packet delivery ratio, throughput, and jitter control factor, by varying pause time using NS-2 simulator. When MAC layer fails to deliver a unicast packet to the next hop, then the signal

being sent through routing layer implies that link is broken. No additional network layer mechanisms were used. The result shows that DSR is better to deal with, as it follows the concept of source routing protocol. DSR stores some route in its cache memory. It can also discover new routes by on-demand basis, and if routes are already stored in its cache then it will consume less bandwidth for new route discovery, its maintenance, and reply [41].

Papers [42–44] deal with the study of various routing protocols like ad hoc on-demand multicast distance vector (AOMDV), source routing-based multicast protocol (SRMP), ad hoc on-demand distance vector (AODV), and dynamic source routing (DSR) protocols. Researchers tried to find which one is the best among them, when node has to search for multipath or unicast route, during discovery process [42, 43]. In this research, RWP (Random Way Point) and RPGM (Random Point Group Mobility) models were used to find out the best suitable path [44]. RPGM model defines a random motion for a group of mobile nodes and for individual mobile node too within a given group. The nodes belonging to a group are randomly distributed around the reference point. Both group's motion and motion of individual mobile nodes within a group follow the RWP model. Researcher simulated these two models for different routing protocols with varying pause time and network size. The results demonstrate that SRMP routing protocol shows highest throughput and least packet drop ratio, as it follows the source routing process. SRMP can cope up with varying load, nodes, and pause time because of routes being cached in the memory. AOMDV also provides good throughput with average load only because of the involved on-demand route discovery process.

The paper [45] deals with AODV, DSDV, ZRP, OLSR, and OSPF routing protocols. Researchers worked on packet delivery ratio, delay, throughput, overhead, and jitter control factors, using mobile nodes in QUALNET. Researchers divided this work into two equal parts. In the first part, performance is estimated within 4 h simulation with 19 mobile nodes and one base station. Dual counter rotating ring mobility pattern is being followed by nodes with inner and an outer loop. Five nodes move along the inner loop and 14 nodes move along the outer loop. Outer loop nodes rotate clockwise, whereas inner loop nodes rotate counter clockwise. Second scenario tries to perform comparison of routing protocols based on the identical network scenario. The analysis exhibits that AODV routing protocol has best performance in terms of throughput, packet delivery ratio, and delay with increasing number of nodes and load. Since it is reactive in nature, performance increases with increasing mobility. DSDV has higher delay factor because, due to increase in the mobility, cached routes equally become stale and this provides false route information, which further results in congestion. ZRP gives average throughput with increasing mobility as it follows both proactive and reactive routing protocols. OLSR results in worst performance with increasing mobility for delay and throughput factors because of stored route cache, which demands periodic updates for routing table.

Conclusion and Future Work

In this paper, an overview of routing protocols in MANET is presented which is followed with detailed review of crucial work done so far by various authors for performance evaluation of routing protocols in MANET. It has been observed that with constant speed and with less traffic scenarios, protocols react in a similar way. With increase in number of nodes, proactive routing protocol shows high throughput and high packet delivery ratio, but shows poor routing overhead and delay factor, whereas reactive routing protocol shows low overhead, low throughput as well as low packet delivery ratio but high delay factor. It could be concluded by studying the work of several authors that no single routing protocol in MANET could be declared as best routing protocol. The performance is governed by several critical factors like network environment, network scenario, traffic, mobility model, etc.

References

1. Larsson, T., Hedman, N.: Routing protocols in wireless Ad-Hoc network—A simulation study, ISSN: 1402-1617.ISRN: LTU-EX-98/362-SE (1998)
2. Sun, J.-Z.: Mobile Ad Hoc Networking: an essential technology for pervasive computing, media team. In: Machine Vision and Media Processing Unit. IEEE, Oulu, Finland (2001)
3. Madhusudhananagakumar, K.S., Aghila, G.: A survey on black hole attacks on AODV protocol in MANET. *IJCA* **34**(7), 0975–8887 (2011)
4. Zhang, Y., Low, C.P., Ng, J.M.: Performance evaluation of routing protocols on the reference region group mobility model for MANET. *Wirel. Sens. Netw. Sci. Res.* 92–105 (2011)
5. Sahadevaiah, K., Oruganti Bala, V.R.: An empirical examination of routing protocols in mobile Ad Hoc networks. *IJCNS*, **3**, 511–522 (2010)
6. Perkins, C.E., Royer, E.M., Das, S.R., Marina, M.K.: Performance comparison of two on-demand routing protocols for Ad Hoc networks. *IEEE Pers. Commun.*, 1070-9916/01 (2001)
7. Xu, H., Wu, X., Sadjadpourand, H.R., Garcia-Luna-Aceves, J.J.: A unified analysis of routing protocols in MANETs. *IEEE Trans. Commun.* **58**(3) (2010)
8. Akhtar, M.D., Sahoo, G.: Behavior based high performance protocol for MANET. *INDJST* **6**(10) (2013)
9. Mani, U., Chandrasekaran, R., Sarma Dhulipala, V.R.: Study and analysis of routing protocols in mobile Ad-Hoc network. *JCS* **9**(11), 1519–1525 (2013)
10. Khiavi, M.V., Jamali, S., Gudakahriz, S.J.: Performance comparison of AODV, DSDV, DSR and TORA routing protocols in MANETs. *IRJABS* **3**(7), 1429–1436 (2012)
11. Das, S.R., Castaneda, R., Yan, J.: Simulation based evaluation of mobile Ad-Hoc networks routing protocols. In: *ICCCN Conference, Lafayette, LA; Oct 1998*
12. Pandey, K., Swaroop, A.: A comprehensive performance analysis of proactive, reactive and hybrid MANETs routing protocols. *IJCSI J.* **8**(6), 3 (2011)
13. Zhou, Y., Xia, C., Wang, H., Qi, J.: Research on survivability of mobile ad-hoc network. *JSEA* **2**, 50–54 (2009)
14. Jhaveri, R.H., Patel, A.D., Parmar, J.D., Shah, B.I.: MANET routing protocols and wormhole attack against AODV. *IJCSNS J.* **10**(4) (2010)

15. Praveen Raj, P., Gowtham, S., Shetty, P.: Energy aware quality of service routing protocol. *IJCSITS J.* **3**(1) (2013)
16. Maan, F., Mazhar, N.: MANET Routing Protocols v/s Mobility Models: A Performance Evaluation. *IEEE* (2011). doi:978-1-4577-1177-0/11
17. Divecha, B., Abraham, A., Grosan, C., Sanyal, S.: Impact of node mobility on MANET routing protocols models. *JDIM*, **5**(1), 19–24.6 (2007)
18. Yang, H., Luo, H.Y., Ye, F., Lu, S.W., Zhang, L.: Security in mobile Ad-Hoc networks: challenges and solutions. *IEEE Wireless Commun.* **11**(1), 38–47 (2004)
19. Sadagopan, N., Bai, F., Krishnamachari, B., Helmy, A.: PATHS: Analysis of PATH Duration Statistics and their Impact on Reactive MANET Routing Protocols, *ACM 1-58113-684-6/03/0006, MobiHoc'03, USA* (2003)
20. Lally, S., Trajkovic, L.: Performance Analysis of Routing Protocols for Wireless Ad-Hoc Networks, *OPNET Technologies Inc., OPNETWORK 2011, Communication Networks laboratory, Canada* (2011)
21. Goyal, P., Parmar, V., Rishi, R.: MANET: vulnerabilities, challenges, attacks, application. *IJCEM*, **11** (2011)
22. Al-Maashri, A., Ould-Khaoua, M.: Performance analysis of MANET routing protocols in the presence of self-similar traffic., In: *Proceedings of the 31st IEEE Conference on Local Computer Networks*, pp. 14–16, Nov 2006
23. Vetrivelan, N., Reddy, A.V.: Performance analysis of three routing protocols for varying MANET size. In: *Proceedings of the I MECS*, vol. II, pp. 19–21, Mar 2008
24. Shrestha, A., Tekiner, F.: On MANET Routing protocols for mobility and scalability. *ICPDCAT* (2009)
25. Gupta, V., Lala, A., Dubey, S., Chaurasia, A.: Scenario based performance and comparative simulation analysis of routing protocols of MANET. *IJCSIT J.* **3**(4), 4751–4756 (2012)
26. Hassan, Y.K., Abd El-Aziz, M.H., Abd El-Radi, A.S.: Performance evaluation of mobility speed over manet routing protocols. *IJNS* **11**(3), 128–138 (2010)
27. Said El Kafhali, Y.S., Haqiq, A., Nassereddine, B.: Simulation analysis of routing protocols using manhattan grid mobility model in MANET. *IJCA* **45**(23) (2012)
28. Lal, A., Dubey, V., Pesswani, B.: Reliability of MANET through the performance evaluation of AODV, DSDV, DSR. *IJARCSSE* **2**(5) (2012)
29. Saquib, N., Rahman, S., Sakib, M., Pathan, A.-S.K.: Performance Analysis of MANET Routing Protocols Using an Elegant Visual Simulation Tool, *Cornell University Library, CORR abs/0911.2620; 11/2009*
30. Johansson, P., Larsson, T., Hedman, N., Mielczarek, B., Degermark, M.: Scenario-based performance analysis of routing protocols for mobile Ad-hoc networks. In: *Proceedings of. MOBICOM'99*, pp. 195–206 (1999)
31. Barakovic, S., Kasapovic, S., Barakovic, J.: Comparison of MANET routing protocols in different traffic and mobility model. *TELFOR J.* **2**(1) (2010)
32. Igbesoko, E.E., Eze, T.O., Ghassemian, M.: Performance analysis of MANET routing protocols over different mobility models. In: *Proceedings of the London Communications Symposium (LCS)*, University College London, Sept. 2010
33. Chen, H.G., Jou, J.-S., Dharmaraju, D., Papageorgiou, G., Baras, J.S.: Performance Evaluation and Traffic Analysis for Routing Protocols in a real MANET, *DARPA, SPAWAR, San Diego*, under project of Collaborative Technology Alliances (CTA) Conference, College Park, MD; April 2003
34. Kumar, A., Singh, P., Kumar, V., Tyagi, N.: Performance analysis of AODV, CBRP, DSDV and DSR MANET routing protocol using NS2 simulation. *IJCSIS J. MECS* **9**, 45–50 (2013)
35. Nilsson, A. Performance analysis of traffic load and node density in ad hoc networks. In: *Proceeding of European Wireless* (2004)
36. M.L. Sharma, Rizvi, N.F., Sharma, N., Malhan, A., Sharma, S.: Performance evaluation of MANET routing protocols under CBR and FTP traffic classes. *IJCTA* **2**(3), 392–400 (2011)
37. Dyer, T.D., Boppana, R.V.: A comparison of TCP performance over three routing protocols for mobile Ad Hoc networks. *ACM Mobihoc*, Oct 2001

38. Feeney, L.M.: An Energy Consumption Model for Performance Analysis of Routing Protocols for Mobile Ad Hoc Networks, *Mobile Networks and Applications* 6, pp. 239–249. Kluwer Academic Publishers (2001)
39. Das, S.R., Perkins, C.E., Royer, E.M., Marina, M.K.: Performance comparison of two on-demand routing protocols for ad hoc networks. *IEEE INFOCOM* (2000)
40. Gupta, S., Arora, S., Banga, G.: Simulation based performance comparison of AODV and DSR routing protocols in MANET. *IJAER J. ISSN 0973-4562*, 7(11), Research India Publications (2012)
41. Mohamed, H., Lee, M.H., Sanugi, B., Taguchi, M.S.: Approach for performance evaluation of routing protocols in mobile Ad Hoc networks. *J. Stat. Model. Analytics*, 1(2), 10–18 (2010)
42. Lee, S.-J., Su, W., Hsu, J., Gerla, M., Bagrodia, R.: A performance comparison study of Ad Hoc wireless multicast protocols. *IEEE INFOCOM* (2000)
43. Kute, V.B., Kharat, M.U.: Analysis of quality of service for the AOMDV routing protocol. *ETASR*, 3(1) 359–362 (2013)
44. Yongsheng, F., Xinyu, W., Shanping, L.: Performance comparison and analysis of routing strategies in Mobile ad hoc networks, 978-0-7695-3336-0/08, CSSE.2008.799, IEEE (2008)
45. Hsu, J., Bhatia, S., Takai, M., Bagrodia, R., Acriche, M.J.: Performance of Mobile Ad-Hoc Networking Routing Protocol in Realistic Scenario, Defense advance research project, DAAD 19-01-09-0005, DAAB 07-02-C-P603, MILCOM '03, IEEE, vol. 2; pp. 1268–1273 (2003)

Retinal Nerve Fiber Layer Analysis in Digital Fundus Images: Application to Early Glaucoma Diagnosis

Dharmanna Lamani, T.C. Manjunath, M. Mahesh
and Y.S. Nijagunarya

Abstract Glaucoma is a second biggest eye disease which leads to permanent vision loss. The present day glaucoma diagnosis includes analysis of cup-to-disk ratio and detection of retinal nerve fiber layer (RNFL) loss. Glaucoma detection using cup-to-disk ratio approach is possible only after 40 % of vision loss. Also, OCT instruments are not widely available in all hospitals due to the cost factor, thereby making them a costly approach. In this paper, fundus images are considered for texture property analysis. Texture properties of RNFL region are analyzed using image-based fractal dimension (FD) feature and gray level co-occurrence matrix method (GLCM). Positive correlation coefficient is achieved for FD and contrast property of GLCM. Such analysis of texture property involving RNFL on fundus images lead to low cost and early diagnosis of glaucoma.

Keywords Glaucoma · RNFL · GLCM · Fractal dimension · Contrast

Dharmanna Lamani (✉)
Department of CSE, SDMIT, Ujire, Mangalore, India
e-mail: dharmannasdmit@gmail.com

T.C. Manjunath
Department of E & C, H.K.B.K, Bangalore, India
e-mail: tcmanjunath@gmail.com

M. Mahesh
Department of E & C, SDMIT, Ujire, Mangalore, India
e-mail: mahesh.m12@gmail.com

Y.S. Nijagunarya
Department of CSE, SIT, Tumkur, India
e-mail: nijagunarya@yahoo.com

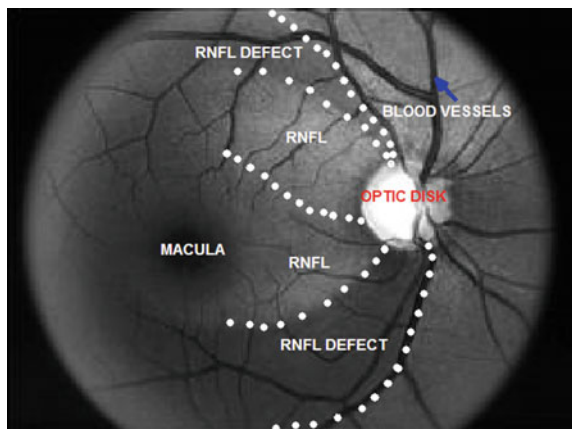
Introduction

Reports from world health organization (WHO) suggest that over 5.2 million people are blind due to glaucoma. This statistics show a noticeable share on the causes for blindness across the globe. Unlike OCT images, ophthalmoscopes' images are analyzed in a faster and cost-effective manner. Ocular fundus images are used as a tool for diagnosis of many retinal diseases such as primary and secondary glaucoma. Analysis of cup-to-disk ratio, intra ocular pressure, and neural rim area lead in to detection of glaucoma. But the retinal nerve fiber layer (RNFL) loss, if analyzed, may be very productive in the early detection of glaucoma so that clinicians may initiate the treatment to control the progression of glaucoma. Figure 1 shows one of the images from our database with RNFL loss. Major components of retina are also noted in this figure: prominently one healthy RNFL area and two areas with RNFL losses. Optic disk (OD) is a section where blood veins and retinal nerve fibers (RNF) are concentrated. Macula is another important region with the highest concentration of retinal ganglion cells (RGC). The RNFL is placed in between OD and macula. RNFL loss can be quantified by extracting features from fundus images. Many authors have worked in order to detect and quantify the changes in RNFL thickness.

Literature Review

The variations due to atrophy of RNFL were analyzed by Jan Odstrcilika et al. [1] through a method which used Gaussian random Markov fields and local binary patterns. Apart from these, a few regression models were also designed to quantify RNFL thickness. The results were correlated with those obtained through OCT. Cup-to-disk ratio was calculated with the aid of detecting edges and exploitation of

Fig. 1 Retina with healthy and damaged part of the retina



variational level set method by Chalinee Burana-Anusorn et al. [2]. The results obtained through the proposed method were compared with the readings of ophthalmologists achieving an accuracy of 89 %. A segmentation algorithm was proposed for frequency domain data of RNFL on OCT scans of healthy and glaucomatous retina [4]. The authors minimized the energy function which comprised of local smoothing terms and the gradient. This automated segmentation procedure was compared with those of three manual corrected segmentations. The authors considered 72 scans of glaucomatous and 132 scans of healthy retina in order to evaluate the segmentation procedure. The authors achieved 2.9 μm of mean absolute error per A scan over the set of glaucomatous retina, whereas 3.6 μm on the set of healthy retina. A dimension reduction technique based on appearances was considered to compress various features of fundus images [5]. A classifier comprising of double stages was designed using probability theory to extract the risk index which showed the performance of detection of unhealthy retina. The RNFL was quantified by Xiang-Run Huang et al. [6] using confocal laser scanning microscopy. Fluorescent stains were used to detect the nerve regions. The obtained results were not compared with those of clinicians' measurements. Such issues drive us to quantify RNFL in a novel manner and correlate them with the data obtained from clinicians. Stokes parameters were calculated by Park et al. [7] to quantify RNFL. The fast axis of the retina was also found. Finally, phase retardation of RNFL was estimated. A bilateral filter was used to extract non-vessel regions from the retinal blood vessels [8]. Hence the boundaries were detected and thus segmentation was achieved. A probabilistic model was designed to make sure that OCT scans on the vessel regions of retina [9]. Data acquisition was achieved for better reproducibility. An accuracy of over 91 % was achieved in the detection of glaucoma when the texture and higher order spectra features were used with random forest classifier [10].

The present article is organized in the following sections. Section “[Introduction](#)” presents RNFL loss leading to glaucoma along with review of previous works. Section “[Dataset](#)” describes retinal image database and preparation of class A and class B samples containing healthy and unhealthy (RNFL loss) RNFL regions. Section “[Methodology](#)” presents methodology of the present work. Section “[Result and Discussion](#)” demonstrates results and discussion, and section “[Conclusion](#)” includes conclusion of work.

Data Set

This section describes about preparation of database and retinal sample data in subsection A and B, respectively.

Database

The database is prepared using state-of-the-art technique. Our retinal database consist of 24 colored images of glaucoma affected retina with significant loss in RNFL and 10 colored images of healthy retina. The retinal images were of high resolution with joint photograph expert group (JPEG) format. Red, green, and blue channels were obtained from these retinal images taken by non-mydratiac fundus camera. For RNFL loss detection, green channel is considered since red channel component does not carry any useful information. Green wave length is excellent than gray, red, and blue components of retina as shown in Fig. 2.

Dimensions of retinal images were 1500×1200 pixels with a field of view 45° . The damaged RNFL is due to result of decrease in RNFL bundles. Due to this, there will be lowering of reflection of incident light by the image acquisition system. Hence such a region appears darker. The visual parameter is not a feasible factor for RNFL identification. Figure 3 depicts details of another retina, showing the areas of healthy and unhealthy RNFL regions.

In this paper, testing of features was done on two sets of samples. Each square sample of size 32×32 was selected from the images for texture analysis using imcrop image function. In Fig. 3, the dark squares represent healthy RNF regions which are shown as dark squares and RNF loss region are shown as white squares.

1. Class A (100) samples are the healthy RNF from region of non glaucoma retina.
2. Class B (105) samples are the RNF tissue damage from patients with glaucoma.

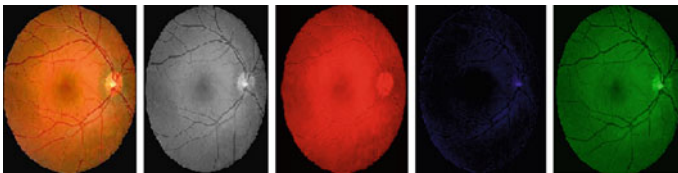


Fig. 2 Description of healthy and damaged RNFL area

Fig. 3 Description of healthy and damaged RNFL area



The dimensions of class A and class B samples were selected in order to cover a sufficiently large area of RNFL region. The maximum dimensions of samples were controlled because blood veins, other components of retina, and pathological structure in the image may disrupt the analysis. The samples were selected in areas between macula and optic disk and surrounding area of optic disk. Pixel values were normalized to the gray level range before further processing.

Methodology

This section describes fractal theory, fractal dimension, method used to analyze texture feature of selected region, and GLCM matrix.

Fractal Theory

In 1966, mathematician of T.B.M Corporation, Mr. Mandelbrot developed a theory called noninteger or fractal theory. The word fractal defined refers to a series in which the Hausdroff–Besicovitch dimension exceeds the topological dimension.

Fractal Dimension (FD)

Fractal dimension has been used to estimate roughness in object and is helpful in modeling natural objects such as sea waves, trees, clouds, and mountains. The concept of FD is exploited to describe the texture feature of image. Fractal dimension has diverse applications in areas such as antenna design, computer simulation, and in detection of various diseases. Investigators have found several fractal dimension techniques such as box counting technique, Hausdroff dimension, power spectral fractal dimension, semi variance technique, information dimension, and perimeter fractal dimension. In this paper, we present box counting method to demonstrate the retinal image texture feature description. In next section box counting method is been described.

Box Counting Technique

The box counting technique is one of the popularly applied methods for computing fractal dimension of a binary image.

Box counting principle is defined by the ratio of logarithmic scale of number of boxes which contain ones (1 s) to the logarithmic scale of box size in a binary image as depicted in below equation

$$FD = \frac{\log N(\lambda)}{\log\left(\frac{1}{\lambda}\right)}$$

The reciprocal of box size is also recorded as $\frac{1}{\lambda}$. This procedure is iterated for all binary retinal samples extracted by several threshold values from 0.2 to 0.5 with intervals of 0.05. The fractal dimension of retinal sample is calculated as slope of line obtained by plotting graph of logarithmic of $N(\lambda)$ and $\frac{1}{\lambda}$ as shown in the example below.

Assume dimension of image matrix as 4×4 . Let the matrix be divided into 2×2 ($\lambda = 2$) subsections. Hence we obtain four submatrices of dimension 2×2 each. Consider $N(\lambda) = 3$. That is, each submatrix having a nonzero element.

If box size (S) = 2, number of boxes which contains at least 1 ones, i.e., $N(\lambda) = 3$

$$FD = \frac{\log(3)}{\log\left(\frac{1}{2}\right)} = -1.58$$

Pseudocode of BCM

For each binary retinal sample

 Divide the sample into boxes of dimension $\lambda * \lambda$

 For each box of dimension λ

 Enumerate the occupied boxes: N

 Estimate the magnitude factor $\frac{1}{\lambda}$

 End for

End for

Gray Level Co-occurrence Matrix (GLCM)

Gray level co-occurrence matrix (GLCM) is a popular second-order statistics method to obtain texture feature from retinal images. According to GLCM method, Haralick identified 14 texture features estimated by probability matrix to obtain the characteristics of texture feature. In this paper, we describe few important features such as contrast, correlation, energy, homogeneity, entropy, etc. The contrast property is selected for implementation using MATLAB 7.10.

Contrast is a gray scale variation in the GLCM method. It estimates intensity contrast between a pixel and its neighbor over the selected region of image contrast mathematically defined in the following equation:

$$\text{GLCM contrast} = \sum_i \sum_j (x - y)^2 p(x - y)$$

In the above equation, x and y are the coordinates and p is the magnitude.

Algorithm of GLCM

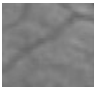





```
im1=imread('healthy.jpg');
disp(im1);
sample=imcrop(im1);
sample_resize=resize (sample [32 32]);
display(sample_resize);
disp properties glcm;
select contrast;
End.
```

Result and Discussion

MATLAB 7.10 code was written for a box counting fractal dimension & GLCM method to analyze healthy RNFL and RNFL loss. Region of interest (ROI) with different thresholds were considered ranging from 0.2 to 0.5 for BCM method to estimate fractal dimension. For damaged RNFL the FD range is 1.0772–1.840. For healthy region the FD range exceeds upper limit. Sample is analyzed for contrast property of gray level co-occurrence matrix method. The contrast value was found to be in the range of 0.0111–0.1002 for RNFL damaged region, whereas for healthy RNFL region the contrast range was above 0.100–0.3900. In the experiment, we analyzed for 100 RNF damaged samples and 105 RNF healthy samples. In Table 1, we show the result for three samples each for RNF damaged and RNF healthy. Figure 4a, b describe 1.8650 and 1.4685 FD obtained for RNFL healthy and RNFL damaged samples shown in Table 1 (Healthy 1 and Loss 1).

In Table 2, Fractal dimension and Contrast values for 32 (out of 205) samples each for healthy and unhealthy (RNFL damaged) RNFL areas are shown. We can observe in Fig. 5, contrast is ranging from 0.111 (x-axis) to 0.1222 and Fractal dimension (y-axis) is ranging from 1.079 to 1.839 for RNFL damaged area. For healthy RNFL area, contrast is ranging from 0.0972 to 0.3247 and FD is ranging from 1.844 to 1.983.

Table 1 Examples of RNFL healthy and damaged samples

	RNFL (Healthy 1)	RNFL (Healthy 2)	RNFL (Healthy 3)	RNFL (Loss 1)	RNFL (Loss 2)	RNFL (Loss 3)
Samples (RNFL healthy and damaged)						
FD	1.8650	1.8437	1.8450	1.4685	1.1965	1.0791
Con	0.2551	0.1136	0.1473	0.0667	0.0444	0.0222

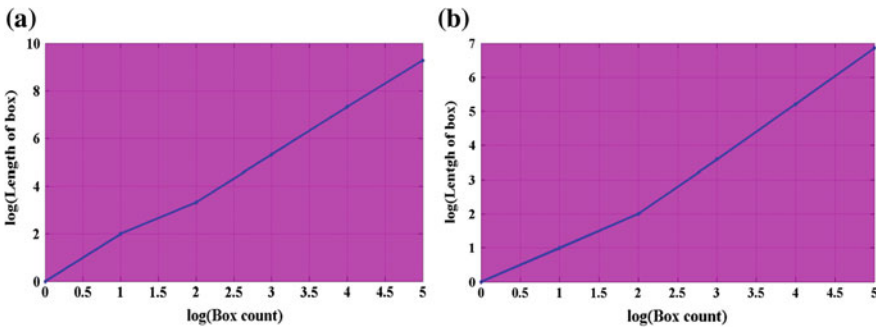


Fig. 4 Describes the estimation of fractal dimension for RNFL

Table 2 Result of 32 samples of each RNFL loss and RNFL healthy

SL. no	RNFL loss		RNFL healthy	
	Contrast	FD	Contrast	FD
1	0.0943	1.7315	0.1136	1.8437
2	0.0877	1.7777	0.1473	1.8450
3	0.0909	1.7649	0.2735	1.8444
4	0.0667	1.4685	0.2551	1.8650
5	0.0444	1.1965	0.1648	1.8744
6	0.0222	1.0791	0.2254	1.8437
7	0.0781	1.5663	0.2431	1.8437
8	0.0781	1.4728	0.2593	1.9050
9	0.0111	1.4997	0.1918	1.9150
10	0.1222	1.1773	0.2527	1.8950
11	0.0247	1.0996	0.1553	1.9350
12	0.0500	1.5233	0.1926	1.9210
13	0.1000	1.3652	0.1358	1.8999

(continued)

Table 2 (continued)

SL. no	RNFL loss		RNFL healthy	
	Contrast	FD	Contrast	FD
14	0.1074	1.7549	0.1806	1.8450
15	0.0617	1.2081	0.1616	1.8551
16	0.0972	1.6515	0.1141	1.8760
17	0.0591	1.3669	0.1233	1.8851
18	0.0751	1.7872	0.1313	1.9359
19	0.1000	1.3013	0.1477	1.8666
20	0.0606	1.3867	0.1534	1.9277
21	0.0590	1.3208	0.1600	1.8457
22	0.0598	1.2200	0.1571	1.8450
23	0.0438	1.5602	0.1583	1.9111
24	0.0300	1.2725	0.1626	1.9098
25	0.0433	1.4527	0.2692	1.8921
26	0.0614	1.3235	0.1818	1.9513
27	0.0950	1.3063	0.1174	1.9438
28	0.0646	1.3588	0.1317	1.9499
29	0.0573	1.3915	0.1761	1.9401
30	0.0751	1.3737	0.1667	1.9501
31	0.0904	1.2181	0.1639	1.8487
32	0.0598	1.3797	0.1786	1.8549

In Table 3, the values of first-order statistics such as min, max, mean, standard deviation, range, median, and mode are depicted. These values are estimated with respect to FD and contrast property of GLCM method.

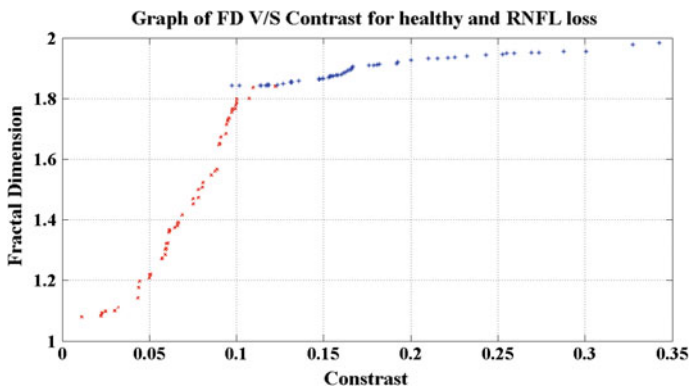


Fig. 5 Graphically shown result of RNFL healthy and unhealthy region

Table 3 Statistical data of healthy and RNFL loss texture region

SL. No	Attributes	RNFL Loss		RNFL(Healthy)	
		FD	Con	FD	Con
1	Min	1.079	0.0111	1.844	0.0972
2	Max	1.839	0.1222	1.983	0.3427
3	Mean	1.459	0.07125	1.894	0.1785
4	Median	1.434	0.672	1.887	0.1626
5	Mode	1.079	0.0598	1.844	0.0972
6	SD	0.239	0.0256	0.0404	0.0578
7	Range	0.760	0.111	0.139	0.245

Conclusion

Identifying RNFL damage through FDs and GLCM method is helpful for early glaucoma detection. GLCM method is used as second-order statistics analysis for texture property of fundus image. Positive correlation is observed for fractal dimension and GLCM property. Such experimentation can be set up in rural place also. This technique can be further enhanced by estimating RNFL and central corneal thickness (CCT). Also relationship between RNFL, CCT thickness, and image feature fractal dimension can be developed.

References

1. Odstreilik, J., Kolar, R., Tornow, R.P., Jan, J., Budai, A., Mayer, M., Vodakova, M., Laemmer, R., Lamos, M., Kuna, Z., Gazarek, Z., Kubena, T., Cernosek, P., Ronzhina, M.: Thickness related textural properties of retinal nerve fiber layer in color fundus images. *Comput. Med. Imaging Graph.* **38**, 508–516 (2014)
2. Burana-Anusorn, C., Kongprawechnon, W., Kondo, T., Sintuwong, S., Tungpimolrut, K.: Image processing techniques for glaucoma detection using the cup-to-disc ratio. *Thammasat Int. J. Sci. Technol.* **18**(1) (2013)
3. Annadhasan, A.: Methods of fractal dimension computation. In: *IRACST—International Journal of Computer Science and Information Technology & Security (IJCSITS)* vol. 2, No. 1 (2012). ISSN: 2249-9555
4. Mayer, M.A., Hornegger, J., Mardin, C.Y., Tornow, R.P.: Retinal nerve fiber layer segmentation on FD-OCT scans of normal subjects and glaucoma patients. *Biomed. Opt. Express* **1**(5), 1358 (2010)
5. Bock, Rüdiger, Meier, Jörg, Nyúl, László G., Hornegger, Joachim, Michelson, Georg: Glaucoma risk index: automated glaucoma detection from color fundus images. *Med. Image Anal.* **14**, 471–481 (2010)
6. Huang, X.-R., Knighton, R.W., Shestopalov, V.: Quantifying retinal nerve fiber layer thickness in whole-mounted retina. *Exp. Eye Res.* **83**, 1096e–1101 (2006)
7. Park, J., Kemp, N.J., Zaatari, H.N., Milner, T.E., Rylander, H. G.: Analysis of phase retardation in the primate retinal nerve fiber layer by polarization sensitive optical coherence tomography. In: *Proceedings of the 25* Annual International Conference of the IEEE EMBS, Cancun, Mexico, 17–21 Sept 2003*

8. Lu, S., Cheung, C.Y., Liu, J., Lim, J.H., Leung, C.K., Wong, T.Y.: Automated layer segmentation of optical coherence tomography images. *IEEE Trans. Biomed. Eng.* **57**(10) (2010)
9. Zhu, H., Crabb, D.P., Schlottmann, P.G., Wollstein, G., Garway-Heath, D.F.: Aligning scan acquisition circles in optical coherence tomography images of the retinal nerve fibre layer. *IEEE Trans. Med. Imaging* **30**(6) (2011)
10. Acharya, U.R., Dua, S., Du, X., Vinitha Sree, S., Chua, C.K.: Automated diagnosis of glaucoma using texture and higher order spectra features. *IEEE Trans. Inf. Technol. Biomed.* **15**(3) (2011)
11. Gazarek, J., Jan, J., Kolar, R., Odstrcilik, J.: Retinal nerve fibre layer detection in fundus camera images compared to results from optical coherence tomography. In: *International Conference on Image Information Processing (ICIIP 2011)* (2011)
12. Lamani, D., Manjunath, T.C., Ramegowda: Cup-disk segmentation and fractal dimension to detect glaucomatous eyes. In: *National Conference on Current Trends in Research and Technology (CRT-13)*, Sponsored by IET (The Institute of Engineering & Technology, UK), SDMIT, Ujire, South Kanara, Karnataka, India, 27–28 Sep 2013
13. Lamani, D., Manjunath, T.C., Ramegowda: Fractal dimension with object rotation: a case study with glaucoma eye. In: *5th IEEE International Conference on Signal and Image Processing (ICSIP-2014)*, BNMIT, Bangalore, Karnataka, India, 978-0-7695-5100-5/13 \$31.00 © 2013 IEEE DOI [10.1109/ICSIP.2014.22](https://doi.org/10.1109/ICSIP.2014.22), ISBN: 978-0-7695-5100-5, Paper No. ICSIP-31, Session-Medical Image Processing, pp. 111–116, 8–10 Jan 2014
14. Lamani, D., Manjunath, T.C.: Automatic detection of diabetes retinopathy through image feature power spectral fractal dimension. In: *8th Elsevier International Conference on Image and Signal Processing (ICISP-2014)*, UVCE, Bangalore, Karnataka, India, Paper ID : ICISP-357, Reference No.: 357I-S, 25–26 July 2014
15. Kersey, T., Clement, C.I., Bloom, P., Cordeiro, M.F.: New trends in glaucoma risk, diagnosis & management. *Indian J Med Res* **137**, 659–668 (2013)
16. Kolar, R., Tornow, R.P., Jan, Laemmer, R., Odstrcilik, J., Mayer, M.A.: Analysis of visual appearance of retinal nerve fibers in high resolution fundus images: a study on normal subjects. *Comput. Math. Methods Med.* **2013**, Article ID 134543, 1–10 (2013)
17. Kolar, Radim, Jan, Jiri: Detection of glaucomatous eye via color fundus images using fractal dimensions. *Radio Eng.* **17**(3), 109–114 (2008)
18. Kolar, R., Vacha, P.: Texture analysis of the retinal nerve fiber layer in fundus images via Markov random fields. In: *IFMBE Proceedings 25/XI*, pp. 247–250 (2009)
19. Cheung, C.Y.L., Leung, C.K.: A practical guide for interpretation of optical coherence tomography retinal nerve fiber layer measurement. *J. Current Glaucoma Pract.* **1**(3), 9–13 (2009)
20. Lamani, D., Manjunath, T.C., Kulkarni, U.P.: Automated detection of neovascular glaucoma through fractal dimension method. *Int. J. Comput. Sci. Inf. Technol.* **5**(4), 5252–5257 (2014). ISSN: 0975-9646

Design, Development of MC-CDMA, and Reduction of ISI for Different Modulation Techniques

Arun Kumar and Manisha Gupta

Abstract With the increasing demand of high data rate and increase in capacity, it becomes necessary to analyze the different modulating techniques. Using good modulation schemes, the growth in speed and capacity can be achieved. In this paper, we have designed a MC-CDMA for different modulation methods like BPSK, QPSK, 256-QAM, 512-QAM, and 1024-QAM. To reduce the Intersymbol Interference, MSE equalization technique is used. Result shows the plot of signal-to-noise ratio versus Eb/No and MMSE versus SNR which clearly shows the performance improvement in MC-CDMA as compared to any existed MC-CDMA system for proposed modulation techniques.

Keywords Modulation · Equalizer · Intersymbol Interference (ISI) · CDMA

Introduction

In a CDMA system, a distinctive binary spreading code is consigned for each call to the users. Users data are multiplying and spread into a spectrum much broader. The entire dynamic subscriber shares the identical frequency bandwidth at the similar time. The signal of each customer is alienated or “de-spread” from the different users at the receiver by using a correlator key with the associated code sequence [1]. The CDMA with existing modulation schemes has a disadvantage that the presence of a strong interferer can raise the noise significantly for other channels which can cause communication to halt under serious condition and also it needs huge amount of power which results in implementation of extra hardware to adjust the current and voltage requirement. Land-based wireless communications have been analyzed [2]. For instance, non-line of sight (NLOS) transmission is not a severe problem in

A. Kumar (✉)

Department of ECE, JECRC University, Jaipur 303905, India
e-mail: arun.kumar1986@live.com

M. Gupta

SMIEEE, Department of Physics, JECRC University, Jaipur 303905, India

© Springer India 2016

N. Afzalpulkar et al. (eds.), *Proceedings of the International Conference on Recent Cognizance in Wireless Communication & Image Processing*, DOI 10.1007/978-81-322-2638-3_9

wireless CDMA (code division multiple access), but it can become a big problem for wireless location. Research is going on in the field of multiple user detection in a given bandwidth and also on improving BER [3–9].

Review of Work

In nineteenth century, a period of CDMA application, there were three categories of new several access systems centered on amalgamation of CDMA and OFDM was suggested such as multicarrier CDMA [10]. In DSS technique, the transmission bandwidth is much wider than the bandwidth of the original signal [11]. QAM gives less error that makes CDMA more flexible and suitable for mobile communication next generation technology [12]. QPSK is a better modulation scheme for CDMA [13]. CDMA gives us safe and dependable-based calls [14]. An estimation designates that researchers have tried to find ways to outspread the user dimensions of CDMA using optimum maximum likelihood (ML) detection, noise revocation, or different techniques like the noncorrelating receiver [15]. This technique is alike where different users talking the same language can recognize one other, but cannot recognize other users. In wireless CDMA, all the users are given a unique code. Codes subjugate the common medium, however meticulous users related with a particular code can correspond [16]. The authors have designed a CDMA where different modulation techniques and BER were studied and realized. They concluded that BPSK is better and robust modulation scheme as compared to QPSK and QAM [17]. The authors have designed 16-QAM CDMA with a combination of Rayleigh and AWGN channel and concluded that the performance of CDMA is better in AWGN channel as compared to Rayleigh channel [18]. In this study, they have taken a task to increase the data rate up to 1tbps and they have considered a QAM-256 for this ISI is a severe problem while considering the high-order modulation [19]. The authors have realized several modules of DS-CDMA communication system and their research also showed that DS-CDMA may provide efficient area utilization on FPGA [20].

Methodology

In this paper, we have designed a MC-CDMA for different modulation techniques as discussed above. The suggested policy is presented in Fig. 1. We have considered a multiple user and four number of data subcarriers. The multiple user data are spread, summed, and passed to the Rayleigh channel which adds a noise in the signal. Channel calculation at the receiver is performed and MSE equalizer is used to reduce the Intersymbol interference. Finally the signals are despreading and demodulated.

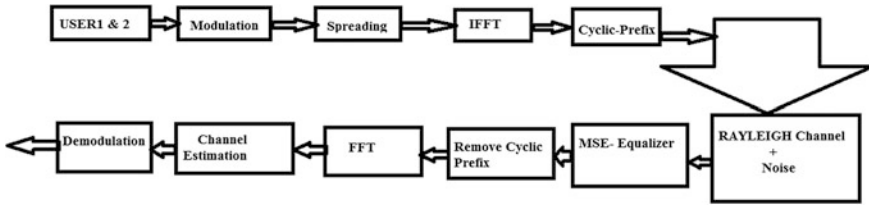


Fig. 1 Proposed block diagram

System Model

Let $a = a_1, a_2, a_3, \dots, a_n$ are random codes
 Let $b = b_1, b_2, b_3, b_4, \dots, b_n$ are Walsh codes
 Performing spreading of the signals by taking XOR

$$X = a(E - \text{XOR}) b \tag{1}$$

Taking IFFT of equation in Eq. 1

$$X(K) = \frac{1}{N} \sum_{k=0}^n x(n) e^{j2\pi K \frac{n}{N}} \tag{2}$$

Insertion of cyclic prefix (cp) in Eq. 2

$$X(K) = \frac{1}{N} \sum_{k=0}^n x(n + \text{cp}) e^{j2\pi K \frac{n + \text{cp}}{N}} \tag{3}$$

Addition of noise (Rn) in Eq. 3

$$X(K) = \frac{1}{N} \sum_{k=0}^n (x(n + \text{cp}) + \text{Rn}) e^{j2\pi K \frac{n}{N}} \tag{4}$$

where Rn is noise in Rayleigh channel
 Removal of CP at the receiver [21]

$$X(K) = \frac{1}{N} \sum_{k=0}^n (x(n1) + \text{Rn}) e^{j2\pi K \frac{3 \cdot 14}{N}} \tag{5}$$

Taking FFT of Eq. 5.

$$x(n1) = \sum_{k=0}^n X(k) e^{-j2\pi Kn} \tag{6}$$

Applying MMSE equalizer

$$\text{MSE} = \text{tr} [E(X(n1)^* - X(n1)) (X(n1) - X(n1)^*)] \quad (7)$$

where $M = \text{exception}$.

Simulation Result

In this section, the result of BER estimation and MMSE for multicarrier CDMA is analyzed and compared under a Rayleigh channel (with addition of noise) where the system is designed by MATLAB-Simulink as shown in Figs. 2, 3, 4, 5, 6, 7, 8, 9, 10, and 11. The constraint used in the simulation is given in Table 1. The BER is determined by taking the ratio of errors in received data to the ratio of transmitted data. The BER performance plot shows for high-order modulation technique, the BER is increased. For different values of Eb/No (dB), the BER is calculated and repeated for different modulation techniques. The proposed system gives least BER as compared to current technologies. MSE versus SNR shows reduction in error which means a vast improvement in Intersymbol interference for high-order modulation techniques.

Figure 2 describes the plot of BER versus Eb/No of two users. For user-1, at 10 dB, the BER is among 0.01–0.001, again at 20 dB, BER is 0.001, BER is less at the scale of 26–30 dB. For second user, at 10 dB, the BER is same as user-1, again at 20 dB, the BER is at 0.001, and finally BER amplified between 26 and 30 dB due to more fading for user-2 as compared to user-1. Overall, the BER of BPSK is least minimum which means it is one of the most robust technologies and it will give an excellent result in fading environment.

MSE is the measure of total error in communication link. It also shows that MSE is less for high value of SNR as compared to other modulation techniques which means Intersymbol Interference is greatly reduced as shown in Fig. 4.

As shown in Fig. 4, for user-1 at 10 dB, the BER is measured approximately at 0.001 and for 20 dB, the BER is measured between 0.0001 and 0.001 and finally from 25 to 30 dB, the BER is sharply reduced. For user-2 at 10 dB, BER is matching with user-1 at 20 dB, the BER is stuck between 0.001 and 0.0001 greater than user-2 and finally from 25 to 30 dB the BER is increased. The BER of QPSK

Table 1 Simulation parameter

Modulation: BPSK, QPSK, 64-QAM, 256-QAM, 512-QAM and 1024-QAM.
Active user: 2
Output code: Original codes XOR with Walsh Code.
IFFT bin: 1024
Rayleigh channel
Equalizer: MMSE

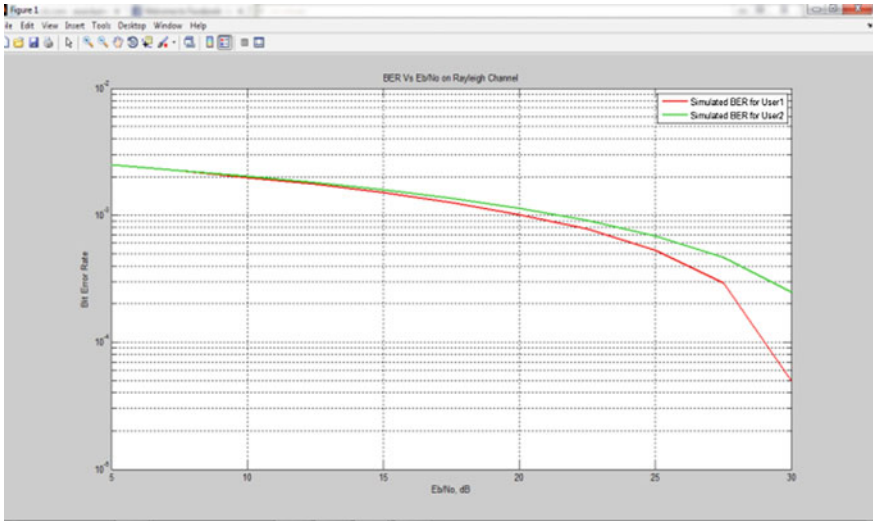


Fig. 2 BER versus Eb/No for BPSK

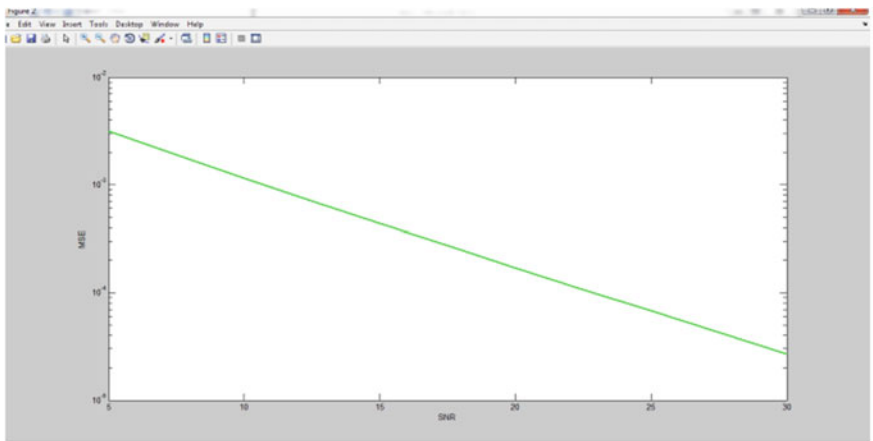


Fig. 3 Plot of MMSE versus SN for BPSK

is similar to BPSK but in the case of QPSK the capacity is doubled for the same BER.

Figure 5 shows the reduction in MSE for different SNR which means a reduction in ISI.

As shown in Fig. 6, for user-1, at 10 dB, the BER is measured between 0.01 and 0.001 again at 20 dB, the BER is between 0.01 and 0.001 and finally at the range of 25 to 30 dB BER is reduced. For second user, at 10 dB, BER lies in the range of 0.01–0.001, again at 20 dB, BER is between 0.001 and 0.0001 and finally from 25

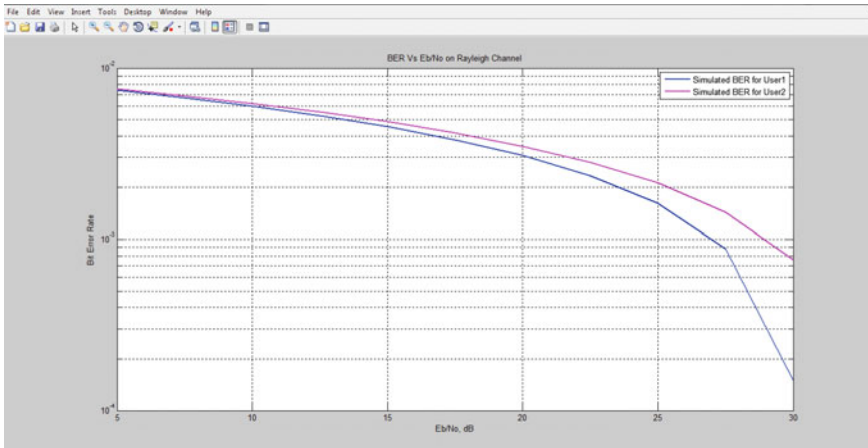


Fig. 4 Plot of BER versus Eb/No for QPSK

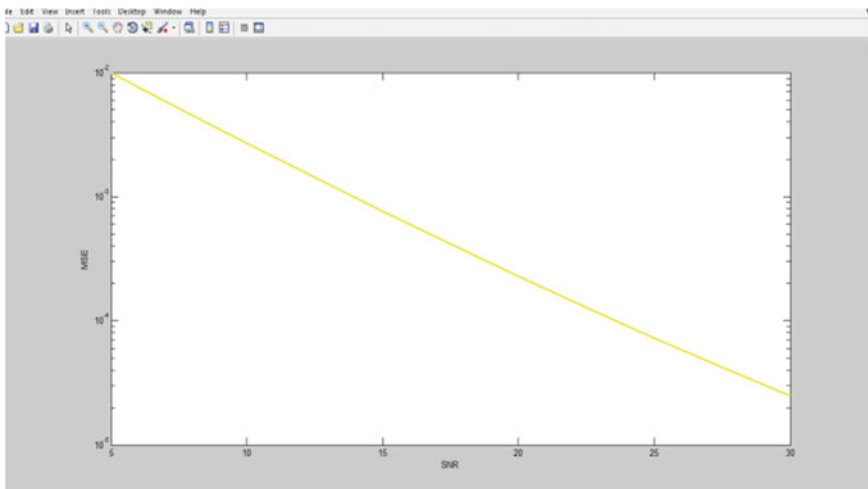


Fig. 5 Plot of MMSE versus SNR for QPSK

to 30 dB, BER still lies between 0.001 and 0.001. For user-2, at 10 dB, BER lies in the range of 0.01–0.001, again at 20 dB, BER is at 0.01 to 0.001 and finally from 25 to 30 dB there is a little decrease in BER for User-2. On the whole, the result shows that the BER of QAM-64 is more than PSK due to ISI but the data rate and capacity greatly increased in qam-64.

Figure 7 shows the reduction of MSE for different SNR which means reduction in ISI.

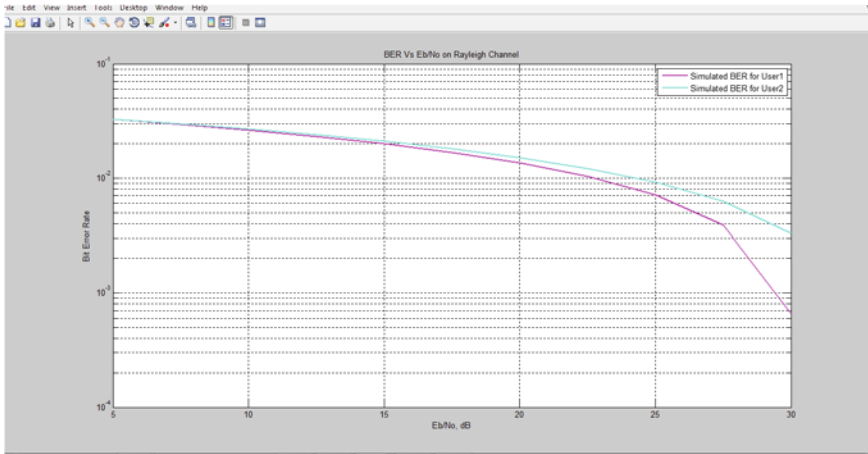


Fig. 6 Plot of BER versus Eb/No for QAM-64

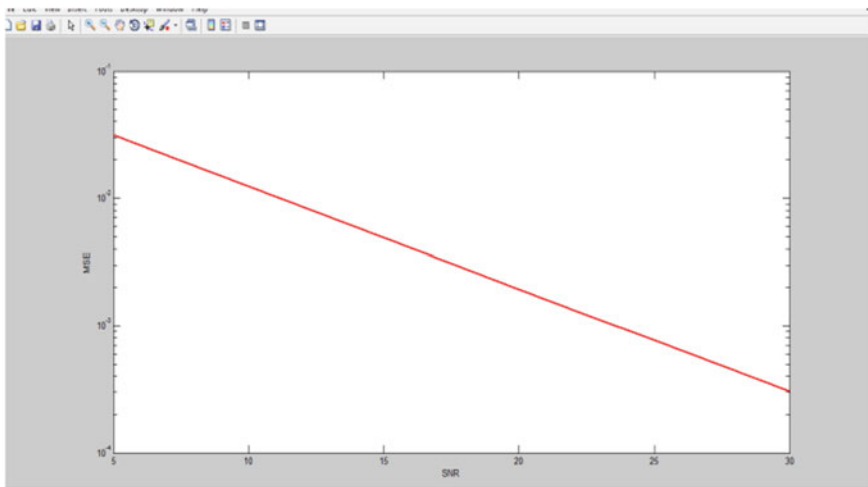


Fig. 7 Plot of MMSE versus SNR for QAM-64

In Fig. 8, for user-1, at 10 db, 20 db, the BER lies in the range of 0.01–0.001 and finally for 25–30 db, BER is reduced till 0.001. For user 2, from 10 to 20 db, the BER is identical to user 1 and finally at 25 to 30 db, BER is more or less equals to 0.0001. In general, BER of QAM-256 for different SNR is more as compared to QPSK, QAM, and BPSK. Reduction of BER in the SNR has to be increased which is technically not a good idea.

Figure 9 shows the reduction of MSE for different SNR but as compared to the above modulation schemes the ISI is more which is due to the fading and distortion

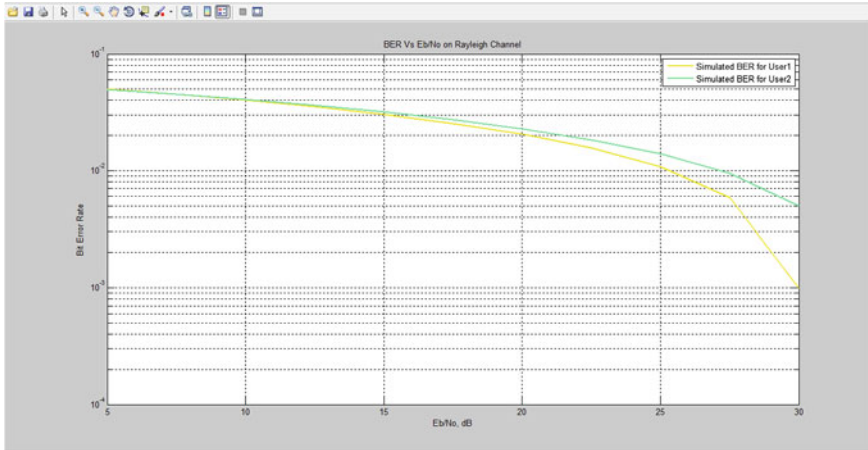


Fig. 8 Plot of BER versus Eb/No for QAM-256

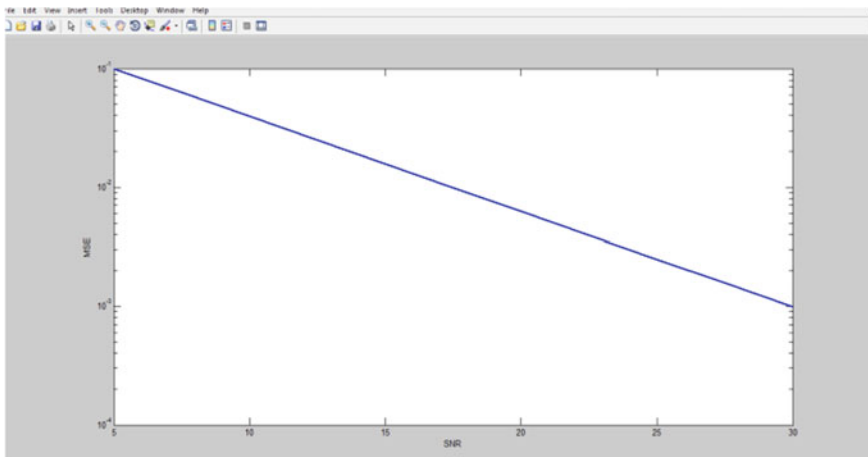


Fig. 9 Plot of MMSE versus SNR forqam-256

of the signal. Data rate and capacity can be additionally improved as compared to QAM-64.

Figure 10 shows that BER is reduced only when EB/NO is increased. Overall, we can say that the BER of qam-1024 and ISI effect is more as compared to the above modulation schemes. Till now this scheme is not introduced for CDMA, if it is introduced it is expected that data rate and capacity will greatly increase if we manage to reduce ISI effect.

Again in Fig. 11, it shows that MSE is more for different SNR as compared to the above modulation schemes.

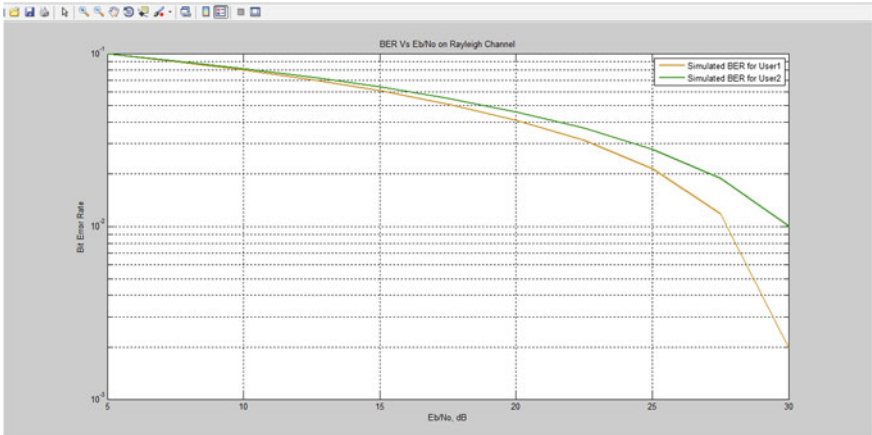


Fig. 10 Plot of BER versus Eb/No for QAM-1024

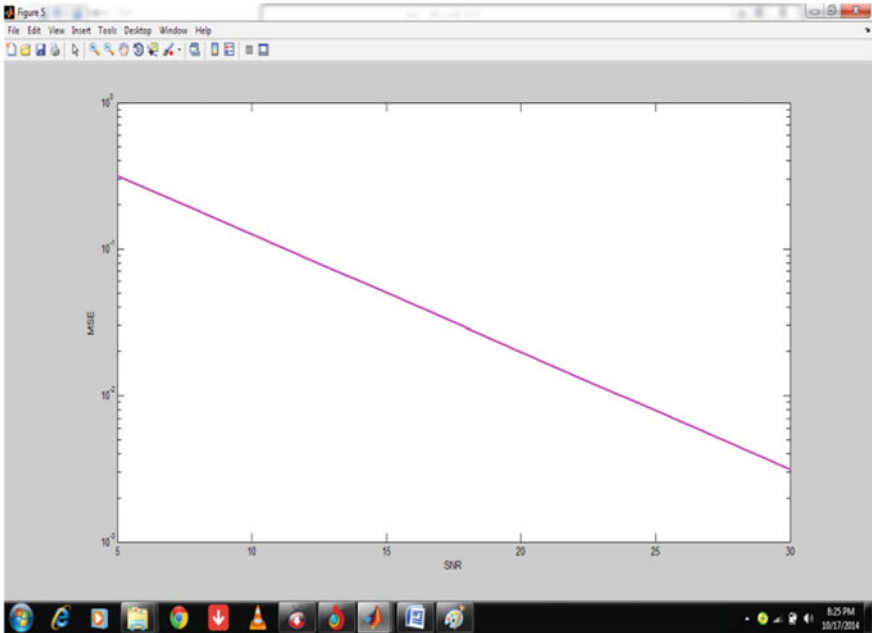


Fig. 11 Plot of MMSE versus SNR for QAM-1024

Table 2 Summary of bit rate

Modulation	Bits per symbol	Symbol rate
BPSK	1	1* bitrate
QPSK	2	½ bit rate
QAM-64	6	1/6 bit rate
QAM-256	8	1/8 bit rate
QAM-1024	10	1/10 bitrate

Discussion/Conclusion

The demand of mobile communication is growing. So it is necessary to raise the capacity at a limited bandwidth and provide a high data rate. High-order modulation technique is the possible solution to increase the capacity and data rate but with high-order transmission scheme, Intersymbol interference is an immense setback. In this work, reduction in ISI is achieved using a MMSE equalizer but with the use of equalizer, the hardware implementation of the system becomes very difficult. So one has to look at the technique which can reduce ISI without increasing the complication of structure. In this work, MC-CDMA is designed with a least BER for different modulation techniques and it is also shown that with the use of MSE equalizer and better design technique at receiver and transmitter, the intersymbol interference can be reduced and the performance of MC-CDMA system can be enhanced. The summary of bit rate is given in below Table 2.

References

1. Chih-lin, I., Sabnani, K.K.: Variable spreading gain CDMA with adaptive control for true packet switching wireless network. In: Proceedings IEEE International Conference on Communications ICC-95, vol. 10, pp. 725–730 (1995)
2. Ojima, M., Hattori, T.: PAPR reduction method using clipping and peak-windowing in CI/OFDM system. In: Vehicular Technology Conference, USA, pp. 1356–1361 (2007)
3. James, J., Caffery, Jr., Stuber, G.L.: Subscriber location CDMA cellular networks. IEEE Trans. Veh. Technol. **47**(2), 406–416 (1998)
4. Rappaport, T.: Wireless Communications: Principles and Practice, 2nd edn. Prentice–Hall publications, New Jersey (2002)
5. Netherton, C.R.: Data Randomizing with pseudo-Noise coding techniques. In: Spread Spectrum Scene, Part-1 (1995)
6. Chen, S., Samingan, A.K., Mulgrew, B., Hanzo, L.: Adaptive minimum-BER linear multiuser detection for DS-CDMA signals in multipath channels. IEEE Trans. Signal Process. **49**(6), 1240–1247 (2001)
7. Rupf, M., Tarkoy, F., Massey, J.: User-separating demodulation for code-division multiple access systems. IEEE J. Sel. Areas Commun **2**, 786–795 (1994)
8. Giallorenzi, T., Wilson, S.: Multiuser ML sequence estimator for convolutionary coded asynchronous DS-CDMA systems. IEEE Trans. Commun. **45**, 997–1008 (1996)
9. Ullah, M.A., Kyung, H.: BER performance comparison between FHP B/MCCDMA and MC-CDMA under Rayleigh fading channels. In: IEEE Asia-Pacific Conference on Communications 2006, pp. 1–5 (2006)

10. www.comsoc.org
11. Fazel, K., Papke, L.: On the performance of convolutionally coded CDMA/OFDM for mobile communication. In: Proceedings of IEEE PIMRC, Japan, pp. 468–472 (1996)
12. Ghanim, M., Abdullah, M.: Analysis of MC-CDMA system in mobile communications. *Int. J. Inf. Technol. Sci.* **12**(2), 87–94 (2012)
13. Kumar, A., Naznin, R.: Simulation of different modulation technique in CDMA System using AWGN channel. *Int. J. Comp. Technol.* **1**(3), 2346–2354 (2013)
14. Chouly, A., Brajal, A., Jopurdan, S.: Orthogonal multi carrier technique applied to DSSS. In: Proceedings of IEEE Globe Communication, USA, pp. 1728–1732 (1992)
15. Divsalar, D., Simon, M.K., Raphaeli, D.: Improved parallel interference cancellation for CDMA. *IEEE Trans. Commun.* **46**(2), 258–268 (1998)
16. Verdu, S.: Minimum probability of error for asynchronous gaussian multiple-access channels. *IEEE Trans. Inf. Theory* **IT-32**, 85–96 (1986)
17. Kumar, A., Gupta, M.: Comparative study and analysis of ber of cdma for different modulation scheme. *Int. J. Comput. Technol.* **12**(8), 3839–3843 (2014)
18. Kumar, A., Gupta, M.: Comparative study and analysis of BER of CDMA for different modulation scheme. *Int. J. Comput. Technol.* **12**(8), 3839–3843 (2014)
19. Kumar, A., Gupta, M.: Analysis and simulation of CDMA QAM-16 for AWGN and Rayleigh channel. *Int. J. Electron. Commun. Comput. Eng.* **5**(4), 958–962 (2014)
20. Naanaa, A., Belghith, S.: Performance enhancement of a time hopping—pulse position modulation ultra-wideband system using guided local search. *IET J. Commun.* **5**(15), 192–196 (2011)
21. Coroianu, L., Gal, S.G.: Approximation by nonlinear Lagrange interpolation operators of max-product kind on Chebyshev knots of second kind. *J. Comput. Anal. Appl.* **13**(2), 211–224 (2011)

A Compact Dual Wide Band Patch Antenna with Modified Ground Plane

Priyanka Jain, Shagun Maheshwari and Archana Agarwal

Abstract A compact rectangular patch UWB antenna design has been proposed in this paper which has been designed on a FR4 (lossy) sheet with relative permittivity of 4.4 and a compact size of 12 mm × 47 mm. To achieve ultra-wideband characteristics, two slots are cut in ground plane and fed by microstrip feed technique. The designed antenna resonates in two bands and shelters maximum of allocated ISM band and ultra-wideband (UWB) ranging from 2.2459 to 2.7207 GHz and 5.2698 to 10.863 GHz, respectively. The antenna has been simulated using CST and from observed outcomes it is interpreted that the proposed antenna has good performance with respect to bandwidth and radiation pattern. The proposed antenna is plain and hence easy to fabricate and also it is very compact, so it can be used in a mobile devices or a USB dongle. This antenna is applicable for Bluetooth, WiMAX, military, and medical applications.

Keywords Ultra-wideband (UWB) · Bandwidth · Microstrip patch antenna · ISM band

Introduction

Microstrip patch antennas have numerous benefits over other type of antennas such as reduced cost and size, low profile, simple structure, and ease to make and due to planar structure they can be easily integrated with other circuitries. Due to the above-mentioned features, patch antennas are commonly used for commercial communication applications. Recently, rapid advancement of ultra-wideband (UWB) technology has been found [1]. Hence, antenna design for UWB has been explored to a great extent and as a result provoked the researchers to start

Priyanka Jain (✉) · Shagun Maheshwari
Electronics & Communication Engineering, I.T.M. University, Gurgaon, India
e-mail: priyankajainitmec@gmail.com

Archana Agarwal
EC Department, Sangam University, Bhilwara, India

designing the antennas for ultra-wideband systems. According to FCC, UWB antenna must operate in UWB band which is from 3.1–10.6 GHz, and also maintain satisfactory characteristics including desirable return loss, VSWR below 2, minimum dispersion in the received waveform, etc. With these most of the ultra-wideband applications required an antenna with light weight, low cost, and low profile these entire requirements can be fulfilled by planar printed antennas. But microstrip antennas has major drawback of narrow impedance bandwidth. Hence in the past few years, various technologies were proposed to overcome the above-mentioned major drawbacks of patch antenna such as shorting pins, shorting wall, shorting plate, balanced network for proper impedance matching [2], low dielectric constant, thick substrate material and several resonators [3–5], stacked parasitic patch above the basic patch or stacked parasitic patch in the same plane as of basic patch. [6, 7], tapering, slotting, and modification in ground plane. Among the proposed UWB antenna, antennas with modified ground plane show wider impedance bandwidth.

Also in recent years, demands for laptop wireless communication systems and mobile phones, supporting multiple wireless services and also providing fast connectivity among devices have been increased rapidly [8]. These portable products demand antenna of small size and planar configuration in order to get fit into small space; usually, laptops, mobile phones, and computers are small in size. The best favorable way out for these communication devices is microstrip antennas. Then again, various wireless applications such as WiMAX operates in several band including 2.5 GHz band, 3.2–3.7 GHz band, 3.5 GHz band, etc. [9], requires multiband patch antenna hence, multiband antenna has been widely discussed.

The main goal of this paper is to present a new antenna configuration which is compact in size and operates in two bands; one is ISM band ranging from 2.2459 to 2.7207 GHz and other is portion of ultra-wideband from 5.2698 to 10.863 GHz. In this paper, a compact rectangular microstrip patch antenna of dimension $12\text{ mm} \times 47\text{ mm}$ is proposed which has been designed on the FR4 (lossy) substrate (permittivity = 4.4 and loss tangent = 0.02) of thickness of 1.6 mm, fed by 50- Ω microstrip feed line. The proposed antenna design, its optimized dimensions and simulated results are discussed in next sections.

Antenna Design

First, we designed a rectangular patch antenna of dimension $W1 = 9\text{ mm}$ and $L1 = 8\text{ mm}$ on FR4 lossy substrate of dimension $12\text{ mm} \times 47\text{ mm}$ with ground plane of dimension $L = 47\text{ mm}$ and $W = 12\text{ mm}$ and fed it by 50- Ω microstrip feed line of dimension $10\text{ mm} \times 2\text{ mm}$. Later on to achieve ultra-widebandwidth, we incorporated some bandwidth enhancement techniques such as slotting and modification in ground plane. These techniques and their effect on performance of designed antenna were discussed below.

Effect of Modification in Ground Plane

To minimize the antenna dimensions and to enhance, the bandwidth optimized the dimension of ground plane and feed line. The prototype of the antenna with altered ground plane is displayed in Fig. 1. The optimized parameters of modified ground plane are: $W = 12$ mm, $L' = 32$ mm, of feed line are $S = 2$ mm and $T = 10$ mm and of patch are $W1 = 9$ mm, $L1 = 8$ mm, and $H = 4$ mm.

The simulated return loss of the rectangular patch antenna at different length of ground plane is shown in Fig. 2. It is observed from Fig. 2 that as we reduced the length of ground plane, bandwidth enhanced. We obtained best result at length of 32 mm of ground plane. It is clear from Fig. 2. that by optimizing the ground plane dimension we obtained -10 dB impedance bandwidth from 2.4554 to 3.22 GHz and 5.4296 to 10.142 GHz.

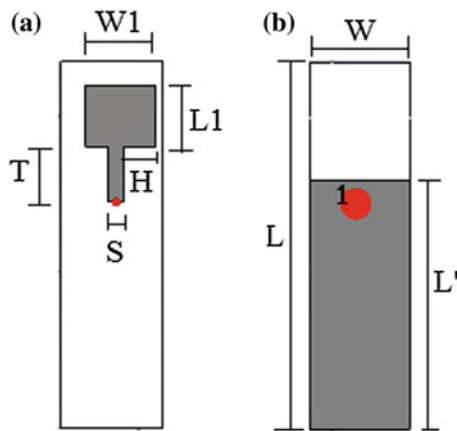


Fig. 1 Rectangular patch antenna with optimized ground plane. a Front view b Back view

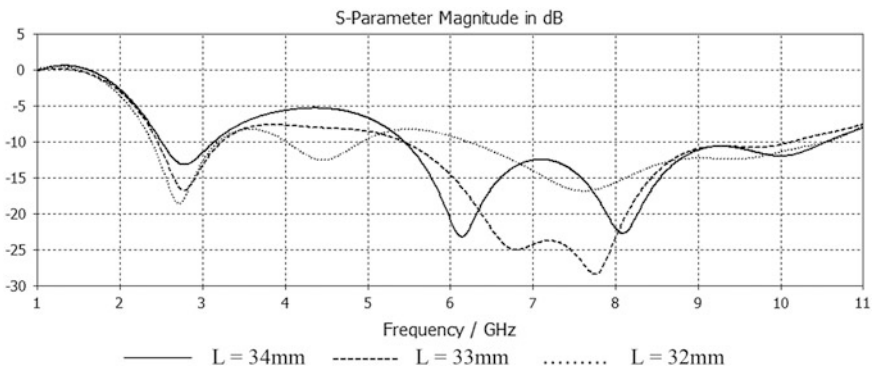


Fig. 2 Return loss curve for rectangular patch antenna at different lengths of ground plane

Effect of Slotting in Ground Plane

Further to enhance the impedance bandwidth, we cut two slots in ground plane and optimized their dimensions to get better results. The proposed antenna design is shown in Fig. 3.

The optimized dimensions of slots are $L2 = 11$ mm, $W2 = 3$ mm, $L3 = 10$ mm, and $W3 = 4$ mm. This antenna design is simulated using CST software and results are discussed in next sections.

Simulation Results

The simulated result of the presented antenna design is revealed in Fig. 4 and from figure it is verified that the above presented antenna operates in two bands one is from 2.2459 to 2.7207 GHz with resonance frequency of 2.4617 and other band

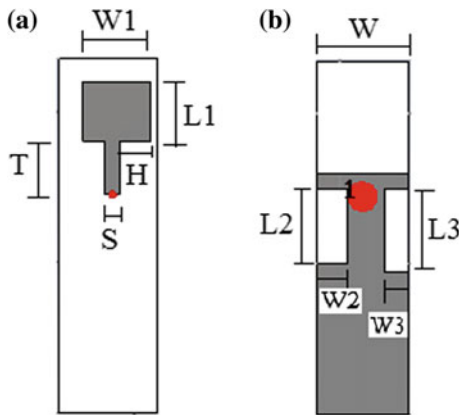


Fig. 3 Rectangular antenna design. a Front view b Back view

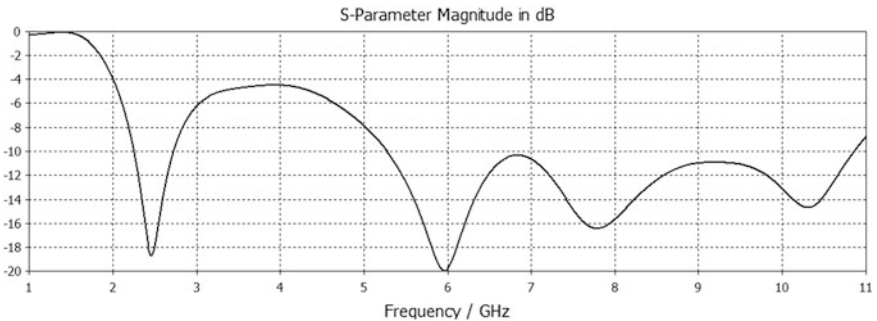


Fig. 4 Return loss curve for proposed antenna

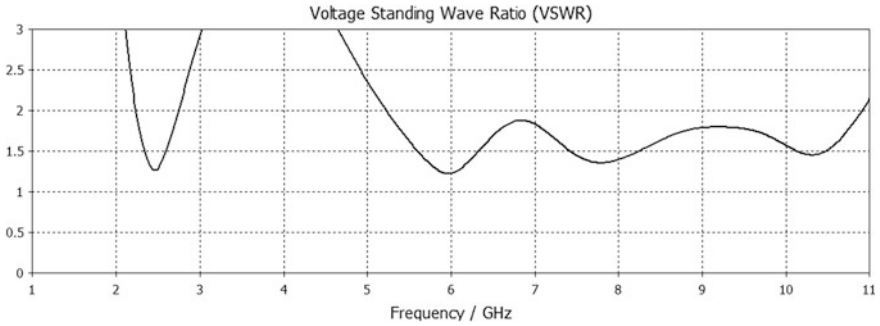


Fig. 5 VSWR of proposed antenna at all resonance frequencies

ranging from 5.2698 to 10.863 GHz having three peaks at resonance frequency 5.961, 7.8025, and 10.322 GHz with return loss of -20 , -16.434 , and -15 dB, respectively.

Figure 5 shows the VSWR curve for proposed antenna and figure indicates that proposed antenna has VSWR less than 2 for frequency 2.2459–2.7207 GHz and 5.2698–10.863 GHz.

Conclusion

A compact dual band rectangular patch antenna is introduced with modified ground plane. From simulated result, it is clear that proposed antenna have wide impedance bandwidth which covers ISM band ranging from 2.2459 to 2.7207 GHz and portion of ultra-wideband ranging from 5.2698 to 10.863 GHz. Small size, wide bandwidth, low profile, and low cost make this antenna suitable for Bluetooth, WiMAX, WLAN, and ultra-wideband applications.

References

1. FCC report and order on ultra wideband technology. Federal Communications Commission, Washington, DC, (2002)
2. Pues, H.F., Van de Capelle, A.R.: An impedance matching technique for increasing the bandwidth of microstrip antennas. *IEEE Trans. Antennas Propag.* **AP-37**(11), pp. 1345–1354 (1989)
3. Park, K.-S., Choi, S.-Y., Lee, H.-B., Ko, Y.-H.: The wide band antenna for both IMT2000 and PCS using U-slot. In: *Proceedings of IEEE Antennas Propagation Symposium Digest*, pp. 1895–1898 (2004)
4. Yang, F., Zhang, X.-X., Ye, X., Rahmat-Samii, Y.: Wide-band E-patched patch antenna for wireless communications. *IEEE Trans. Antennas Propag.* **49**(7), pp. 1094–1100 (2001)

5. Chang, E., Long, S.A., Richards, W.F.: Experimental investigation of electrically thick rectangular microstrip antennas. *IEEE Trans. Antennas Propag.* **AP-34**(6), pp. 767–772 (1986)
6. Rowe, W.S.T., Waterhouse, R.B.: Investigation of proximity coupled patch antennas suitable for MMIC integration. In: *Proceedings of IEEE Antennas Propagation Symposium Digest*, pp. 1591–1594 (2004)
7. Wu, C.K., Wong, K.L.: Broadband microstrip antenna with directly coupled and gap-coupled parasitic patches. *Microw. Opt. Technol. Lett.* **22**, pp. 348–349 (1999)
8. Wireless USB Promoter Group. <http://www.usb.org/developers/wusb/> (2013). Accessed Jan 2013
9. Intel WiMAX technology (2004). <http://www.intel.com/technology/wimax/index.htm>

Contention Sensitive Routing for Mobile Ad Hoc Networks

Richa Sharma, Neha Janu and Chhagan Doot

Abstract Wireless mobile ad hoc network (MANETs) has emerged as a key technology for next-generation wireless networking. Admission control as always works out to be the foundation for QoS. If an AC protocol discovered route for an application shakes hands with QoS Gateway, it is welcomed in the network, else denied. In this paper, CSRP (contention sensitive routing protocol) for MANETS is explained that provides routes with sufficient bandwidth to satisfy the QoS requirements of the requesting application already running sessions.

Keywords MANETs · Qos · Admission control

Introduction

Today, MANETs are more popular as they are highly adaptive, deployable, and dynamically reconfigurable wireless networks with no predefined layout. Hence inevitably, these networks can be easily proposed at any war fields, sales and residential layouts, therapies, etc.

Real-time applications development in recent times has obviously moved attention to wireless networks that support QoS. A full system for providing QoS assurances requires QoS-aware routing, admission control, resource reservation, and traffic guideline and scheduling, hence valuing the warranty requires a QoS-aware MAC protocol [1]. There are different protocols like [2–4] proposed for the QoS support having different purposes and considerations. The current protocols mentioned in the literature [5–7] focus on QoS in terms of bandwidth, excluding delay and jitter, the other factors liable for QoS.

Richa Sharma (✉) · Neha Janu · Chhagan Doot
Swami Keshwanand Institute of Technology, Jaipur, India
e-mail: richa324@gmail.com

Richa Sharma · Neha Janu · Chhagan Doot
Department of Computer Science, Rajasthan Technical University, Kota, India

In this paper, an approach called CSRP is proposed and evaluated which is responsible for admission control (AC), one of the major issues of QoS. In this proposal, the bandwidth of each of the nodes in the network is calculated and judged with the application's bandwidth trying and requesting entry in the network that will be admitted only if it has an adequate bandwidth without affecting any data session in progress.

Simulation is performed on Qualnet and results are generated, evaluated, and compared with AODV on various scenarios which show the efficiency of the proposed method. The rest of the paper is organized as follows: the literature review is covered in section "[Literature Review](#)". In section "[Contention Sensitive Routing Protocol](#)", algorithm of proposed protocol CSRP is introduced; simulation results are outlined in section "[Simulation Results and Analysis](#)"; section "[Conclusion](#)" concludes the paper.

Literature Review

In [6], the author proposed a protocol called (AQOR) ad hoc QoS ondemand network routing and signaling algorithm is based on reserving resources across the network. The main aim of this protocol is to support proper and accurate admission control by computing the available bandwidth and end-to-end delay in ad hoc networks.

The author of [7] proposed PAC which means perceptive admission control. In this protocol, each of the nodes take the AC decision itself. This protocol talks not only about the reach of originating node but also a complete range is accounted that might get affected by the admission of this new session. To avoid the congestion problem, this protocol checks how long the channel is busy, which in turn estimates the available bandwidth for a particular new session to be admitted.

In order to provide more priority to real-time traffic compared to best effort traffic, a new protocol SWAN-AC (admission control for stateless wireless Ad hoc Network) was introduced by the authors of [4]. The admission control is source-based and uses distributed control algorithm explicit congestion notification method. It dynamically regulates admitted real-time traffic in the face of the network dynamics brought in by mobile or traffic overload.

To set up bandwidth-aware QoS routes, author of [6] presented a timeslot allocation assignment algorithm, which is used together with the route discovery mechanism of AODV. In [5], a QoS conscious steady path routing is explained that is based on signal constancy-based adaptive routing which is targeted to choose stable QoS routes that can endure for a longer amount of time. In [7], the author investigated the QoS and bandwidth consumption in on demand multicast routing protocol under 2-hops interference model and proposed interference aware QoS support for ODMRP that computes the available bandwidth and creates the routes with enough bandwidth surety.

Contention Sensitive Routing Protocol

In this section, the implementation details of proposed protocol CSRP with theoretical proof of its effectiveness are explained. This makes sure that the route discovered for routing between a source–destination pair contains nodes having local bandwidth which is greater than the required bandwidth of the communication flow. It also makes sure that all the neighbors of the intermediate nodes also have available bandwidth that is greater than the required bandwidth of the requesting flow.

In this method, a source node gets a request from an application to send data to some destination node. The source asks the bandwidth requirements to the application and based on the given bandwidth requirements it starts the route discovery process. When an intermediate node receives RREQ, it determines how much bandwidth it has currently and matches it up with the bandwidth mentioned in that RREQ. If the requesting flow bandwidth is greater than the available bandwidth of this node, the node will discard RREQ without further re-broadcasting. On the other hand, when an intermediate node that receives a nonduplicate RREQ has an available bandwidth which is greater, then it queries its one-hop neighbors of whether they have enough bandwidth to support the data communication of the requesting session.

The neighbors reply with the RREP message about whether they have the available bandwidth to support the flow. When a timer is set by intermediate node for commencing a query and getting its reply back expires, the responses received from one-hop neighbors of the node are checked. The intermediate node will rebroadcast the RREQ if each of the neighbors of this middle node is capable to sustain the requesting communication process, otherwise it discards the RREQ. All the intermediate nodes that receive the nonduplicate RREQ messages do the same process mentioned above. When the RREQ is received by the destination node, it initiates the unicast RREP that goes through the same route over which the RREQ it received has traveled.

When intermediate nodes receive RREP, they will again check their available bandwidth before forwarding it toward the source node. This is done to make sure that the available bandwidth of this node is not fluctuating because if it is, then this time its bandwidth is different than it was when it forwarded the RREQ message. If the node has fluctuating decreased bandwidth then our second test of this available bandwidth checking will find and avoid such nodes to take part in the active routes.

Pseudo Code: Route Detection Procedure of CSRP

```

/* Originating Node = S; Target Node = D;
Midway Node = I; */

// Local Bandwidth of a node at time t =
L_BWDt;
// Required Bandwidth of application =
R_app;
// Requesting application = Req_app

IF1(S got an admission request from
Req_app)
  S asks for the R_app to Req_app
  S creates a new RREQ and adds the R_app
  in it
  S starts a ROUTE DISCOVER PROCESS
  by initiating a RREQ message

ENDIF1
IF2 (I receive a RREQ message)
  I checks whether it is duplicate or not
IF3 (RREQ is duplicate)
  I discard the RREQ
ELSE
  I calculates it L_BWDt and checks it with
  the R_app given in received RREQ message
IF4 ( I (L_BWDt) > I (R_app))
  I buffer the RREQ and set an expiration
  timer
  I start the query-reply process to ensure its
  neighbors has enough L_BWDt to support
  the flow
IF5 (All neighbors has(L_BWDt) >(R_app))
  I re-broadcast the RREQ

```

ELSE

I discard the RREQ message

ENDIF5

ENDIF4

ENDIF3

ENDIF2

IF6 (*D receives a non-duplicate RREQ*)

*D initiates the unicast RREP message and
copies the R_app from the received RREQ to
this RREP*

ENDIF6

IF7 (*I receive a RREP message*)

I estimate its L_BWDt

IF8 ($I(L_BWDt) > I(R_app)$)

I forward the RREP towards source

ELSE

I discard the RREP message

ENDIF8

ENDIF7

Simulation Results and Analysis

The proposed CSRP protocol is compared with AODV to show its effectiveness in terms of increased network load and mobility. The simulation results are generated by performing various experiments on a large set of scenarios that are conducted using a trail version of a network simulator called Qualnet.

All the source destination pairs used for data communications are selected randomly in distributed node placement area. The parameters used for simulation and scenario creation are shown with their respective values in Table 1.

From Fig. 1, it is clear that as the number of data sessions increases in the network, the proposed CSRP protocol gets unaffected as the admission control process of CSRP will only admit new data sessions in the network if their admission does not create congestion in the existing data communication routes.

It can be seen in Fig. 2 that the SAC of the proposed protocol is lower due to the number of stops or rejections by the CSRP protocol.

Table 1 Simulation parameters and values

Simulation parameters	Values
Simulator	Qualnet
Simulation time	700 s
Application layer protocol	Constant bit rate (CBR)
Number of CBR sessions	1–10
Transport layer protocol	UDP
Routing protocols	AODV, CSRP
MAC layer protocol	802.11
PHY layer protocol	802.11b
timer timeout	5 s
Data rate	2 Mbps
Mobility model	Random way point
Packet size	512 Bytes
Inter packet time	30 ms
Mobility speed	0–5 m/s
Path-loss model	Two ray ground wave
Node pause time	5–45 s
Number of nodes	50
Simulation area dimensions	800 m × 800 m

Fig. 1 Consequence of enlarged quantity of data sessions on delay

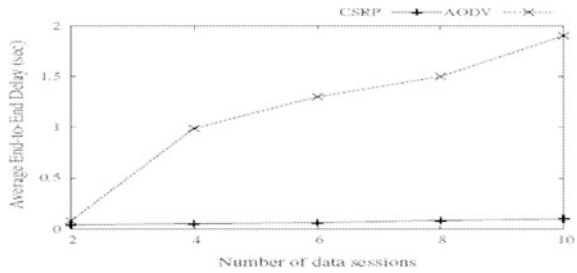


Fig. 2 Effect of increased number of data sessions on session admission ratio

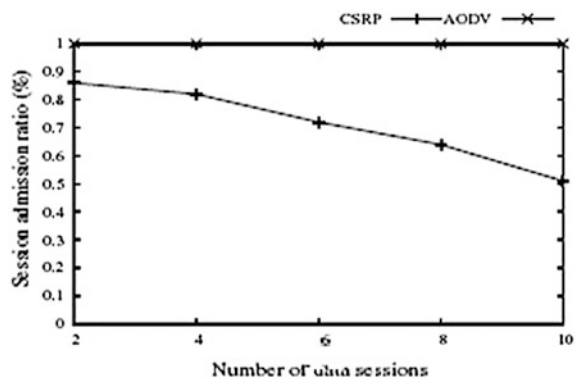


Fig. 3 Overhead with increased number of video sessions

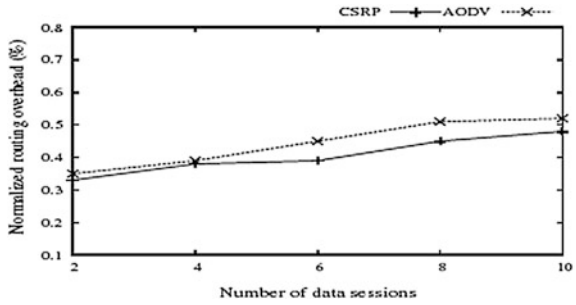
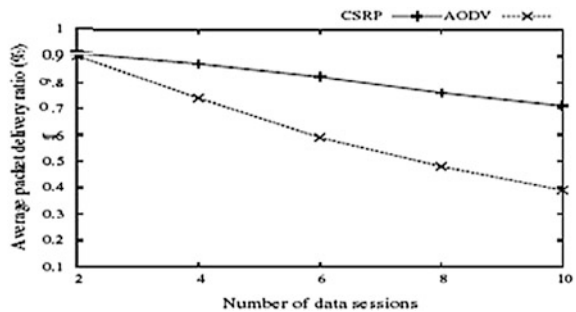


Fig. 4 Effect of increased number of data sessions on PDR



In Fig. 3, routing overhead increases due to increase in collisions and route breaks caused by the increased traffic in the network, which is a result of increases in the data sessions in the network, though it is lower than AODV.

In Fig. 4, the PDR of the CSRP drops is smoother compared to AODV. In CSRP, collisions are controlled by its admission control process.

Conclusion

In this paper, a protocol CSRP is proposed which finds such a route between a specified source and destination pair that has more than enough bandwidth necessary by the application to be introduced into the network and also takes concern of the inter-contention problem caused by the neighbor nodes during the communication process of a data session. Finally, we can say that in our proposed work an application is only admitted into the network if there is a route having each of the nodes with sufficient bandwidth to handle the data transmission of that application.

Simulations have been conducted using trial version of Qualnet network simulator for performance analysis and compared with AODV protocol.

References

1. Hanjos, L., Tafazoli, R.: Admission control scheme for 802.11-based multihop mobile networks: a survey. *IEEE Commun. Surv. Tuts.* **11**(4), 78–108 (2009)
2. Ahn, G.-S., Campbell, A.T., Veres, A., Sun, L.-H.: Supporting service differentiation for real-time and best-effort traffic in stateless wireless ad hoc networks (SWAN). *IEEE Trans. Mob. Comput.* **1**, 192–207 (2002)
3. Chakeres, I.D., Belding-Royer, E.M.: PAC: Perceptive admission control for mobile wireless networks. In: *Proceedings of 1st International Conference on Quality of Service in Heterogeneous Wired/Wireless Networks (QShine)*, (Dallas, TX, USA), pp. 18–16 (2004)
4. Xue, Q., Ganz, A.: Ad hoc QoS on-demand routing in MANETs. *J. Parallel Distrib. Comput.* **63**(2), 154–165 (2003)
5. Chauan, G., Nandi, S.: Qos Aware Stable path Routing (QASR) Protocol for MANETs. In: *First International Conference on Emerging Trends in Engineering and Technology*. 978-0-7695-3267-7/08\$25.00. IEEE (2008)
6. Zhen, X., Wenzhong, Y.: Bandwidth-aware routing for TDMA-based mobile ad hoc networks. 978-1-4673-5742-5/13/\$31.00. IEEE
7. Yu, Y., Zhou, Y., Du, S.: Providing interference aware quality of service support for ODMRP. In: *2009 Asia Pacific Conference on Information Processing*, 978-0-7695-3699-6/09 \$25.00. IEEE (2009)

An Analytical Approach for Accurate Design of MSPA Using Dielectric Constant Engineering (DCE)

Monika Mathur, Ghanshyam Singh and S.K. Bhatnagar

Abstract This paper introduces a novel technique for retuning the microstrip patch antenna (MSPA) during fabrication to meet the desired frequency. Designing the patch antenna is a rigorous process due to its very low manufacturing tolerances. To defeat such limitations of the microstrip patch antenna, a new technique named as dielectric constant engineering (DCE) is proposed. In this proposed method, a new formula is given to cut the dielectric material from the substrate part of the patch antenna during fabrication so that the targeted resonant frequency can be achieved without affecting patch dimensions. The process is suitable for multilayer substrates. This method is very useful for bulk fabrication of patch antennas. The results are simulated and verified using FDTD-based optimizing tool HFSS® version 11.

Keywords Patch antenna · Dielectric constant engineering · Substrate cutting · Cavity

Introduction

MSPA has significant role in communication systems due to its compact structure and low cost. But, it has the limitations of poor efficiency, low gain, and narrow bandwidth [1, 2]. To overcome these limitations, various multilayer structures are proposed in the literature [3]. New designs protect the antenna from rain, heat, and structural damage [4, 5]. But, still the designers have a big challenge for low manufacturing tolerance of patch antenna. Yazdandoost et al. (2001) have studied the consequences of errors during the fabrications on the radiation characteristics of

Monika Mathur (✉) · S.K. Bhatnagar
ECE Department, SKIT, Jaipur 302025, Rajasthan, India
e-mail: monikamathur16@gmail.com

Ghanshyam Singh
ECE Department, MNIT, Jaipur 302017, Rajasthan, India
e-mail: gschoudhary75@gmail.com

the patch antenna [6]. As per the designing formula, the effective dielectric constant of the MSPA has an inverse relation to the resonant frequency of patch antenna [7]. This paper proposes a new terminology “Dielectric constant engineering.” According to this, the resonant frequency of MSPA can be tuned by changing the effective dielectric constant of substrate material beneath the patch.

The proposed dielectric constant engineering (DCE) is emerging as a new tool for manipulating the characteristics of microstrip patch antenna (MSPA). This technique is useful for multilayered substrate structure such as the one used in low temperature co-fired ceramic (LTCC) technology. Multilayer substrate is preferred due to ease in modification in the physical structure of the material. The term “Dielectric Constant Engineering” means modifying the dielectric constant of the material to a new desired value. It is proposed that the DCE can be achieved by: (i) modifying the physical structure of the material and (ii) incorporating a second material in the original material. In the former case, a small cavity is cut from the dielectric substrate beneath the patch. During fabrication, air automatically fills the cavity. Therefore, it will be treated as an air-filled cavity with the dielectric constant as unity. In the latter case, another material of some other dielectric constant can be inserted into that cavity of the specified size. The proposed work is based on the former technique only.

In this paper, several substrate materials have been studied at three different resonant frequencies. A graph between the area ratio (AR) and the ratio of resonant frequency with and without cavity (f/f_0) has been plotted for broad basing the results. Ratio of cavity top area to patch area has been termed as AR.

This work has involved the well-known relation of dielectric constant (ϵ_0) and resonance frequency (f_0) [7]

$$f_0 = \frac{c}{2(L + 2\Delta L)} \sqrt{\frac{1}{\epsilon_0}} \quad (1)$$

Variation in one parameter can be offset by changing the other parameters. The resonant frequency may be changed by inserting a cavity of specific dimensions below the patch. To analyze the mathematical relation of variation in resonant frequency with the cavity dimensions, the equivalent capacitor model of patch antenna has been considered in this work. This relation has a significant role in the proposed concept of DCE.

Design

For an in-depth study of the technique, several antennas have been designed. These have been simulated with the help of HFSS software. Standard design formulae have been used [7].

Figure 1 shows the four-layered structure of the design and the basic design parameter is specified as per Table 1.

Fig. 1 Layered structure of the proposed MSPA

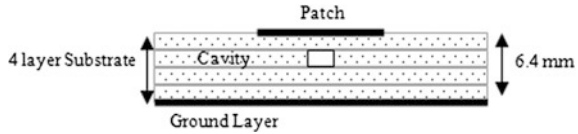


Table 1 Design parameter specifications

S. No.	Parameters	Specifications
1	Type of the antenna	Rectangular patch antenna
2	Feeding method	Microstrip line feed
2	Dielectric constant of the substrate (ϵ_0)	4.4 (basic structure) 3 and 2.2 (validation)
3	Operating frequency (f_0)	2.4 GHz (basic structure) 1.8 GHz, and 1.6 GHz (validation)
4	Total number of layers in the substrate	4
5	Height of the substrate (h)	6.4 mm (each layer is 1.6 mm thick)

The measurements are done on three resonant frequencies. For each frequency the structure consists of four layers of same dielectric substrate. Table 2 elaborates the change in frequency from the targeted frequency for FR4 epoxy composition and the effect of cavity on tuning the resonant frequency. This signifies that the resonant frequency is varying if the cavity size (or cavity area ratio AR or R) is changed.

Simulation Results

Three-dimensional electromagnetic simulating software HFSS®11 was used for the simulation of aforementioned structures. Simulation results are shown in Table 2. These provide a valid linear relation between change in frequency and area ratio. This means, the resonant frequency (f_0) of the structure changes with respect to the cavity dimensions. This cavity is made below the patch area in the second layer of antenna substrate. During antenna fabrication, dimensions of the patch may become different from the designed dimensions due to fabrication tolerances. This may result in shift in the resonant frequency. The investigations reported here suggest that the designed resonant frequency can still be achieved by dielectric constant engineering (DCE). For this, a cavity is cut in the second and/or third layer of the substrate. Effective dielectric constant of the substrate can be suitably changed by appropriately choosing the cavity dimensions.

Table 2 Desired cavity area ratio in tuning frequency

For dielectric constant (ϵ_0) 4.4			
Resonant frequency (without cavity) (f_0)	Measured resonant frequency (with cavity) (f)	Percentage change in frequency ($P(f) = \{((f - f_0)/f_0)*100\}$)	Desired cavity area ratio (R) = (AC/AP)
2.541 GHz	2.546	0.197	0.01
	2.544	0.118	0.04
	2.545	0.157	0.09
	2.547	0.236	0.16
	2.559	0.708	0.25
	2.575	1.338	0.36
	2.604	2.479	0.49
	2.656	4.526	0.64
	2.727	7.32	0.81
	2.843	11.89	1
	2.949	16.06	1.1
	3.004	18.22	1.2
	3.003	18.06	1.3
	3.004	18.22	1.4
3.003	18.06	1.5	

To define this, some empirical formulas were prepared [8]. Mathematical equation for the proposed design curve is

$$P(f) = \alpha R^2 + \beta R + \gamma$$

This model is valid upto $R = 1.27$ [8]. Beyond that, a straight line $P(f) = mR + \beta$ describes the changes. Here, $P(f)$ is defined as the percentage change in frequency, i.e., $\{((f - f_0)/f_0)*100\}$, R is defined as area ratio which is the ratio of area of cavity to area of patch, and α , β , γ , and m are constants.

Figure 2 indicates the relation between percentage change in frequency $P(f)$ and area ratio (R) for different dielectric constant (ϵ_r) and frequencies represented in the form of series 1–10. The equation associated with series 1–10 is also shown in Fig. 2.

The curve in Fig. 2 gives the dependency of resonant frequency of patch antenna on the area of the cavity. The proposed model can be verified as if $R = 0$ means $P(f)$ is constant. This means there is no change in frequency when there is no cavity therefore, f equals f_0 . The change in frequency occurs when R is increased from zero value. This means the cavity is now being created below the patch center. The relation is valid till the R value reaches 1.27, i.e., the area of cavity is 1.27 times area of patch. When this ratio exceeds 1.27, the relation becomes linear because now all the substrates below the patch have been used. The fitness function and the empirical constants α , β , γ , and m may vary with substrate dielectrics but the $P(f)$ and R relation will be the same.

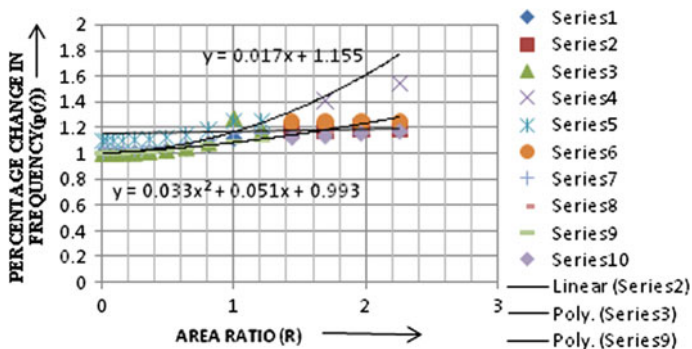


Fig. 2 Relation between percentage change in resonant frequency and area ratio

Analysis

Capacitor Analytical Model

The proposed structure is analyzed using capacitor analytical model as shown in Fig. 3. In MSPA layer structure, the capacitor can be hypothetically formed when the patch and the ground of MSPA work as two conducting plates of capacitor. Then, substrate between patch and conducting ground will act as an electric field storing dielectric layer.

The entire capacitance between patch and ground plate is denoted as C_{Patch} . The capacitance due to cavity can be denoted as C_{cav} . The value of this capacitance will vary with changing cavity dimensions. C_{sub} is the capacitance of the area under and above the cavity area. C_{ccav} is the capacitance of area rest of the ($C_{cav} + C_{sub}$) area. There will be no capacitance formed outside patch area as no upper conducting plate exists. Now, the effective capacitance can be formulated as below.

$$C_{eff} = \frac{\epsilon_{eff} \times A_{eff}}{4d} \tag{2}$$

This C_{eff} is the effective capacitance between the patch and the ground when air cavity is cut in the second layer of the four-layered substrate. From above Eq. (2),

$$\epsilon_{eff} = \frac{C_{eff} \times 4d}{A_{eff}} \tag{2a}$$

now, C_{eff} can also be expressed as,

$$C_{eff} = \underbrace{(C_{Patch} - C_{ccav})}_I + \underbrace{\left(\frac{1}{C_{cav}} + \frac{1}{C_{SUB}}\right)}_{II} \tag{3}$$

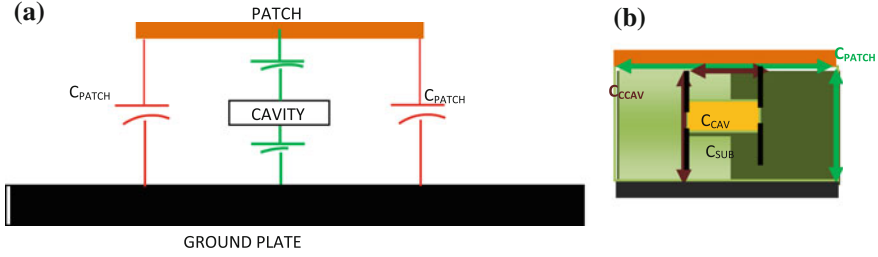


Fig. 3 Capacitor equivalent model of the proposed MSPA

Here, C_{ccav} is defined as the capacitance of cavity area. In the first part of the equation, C_{ccav} is removed from the patch. In the second part of the equation, this removed capacitance C_{ccav} is reinserted by modifying it as the series combination of C_{cav} and C_{sub} . Here, C_{sub} is the capacitance of substrate layer along the cavity dimensions. Thus, here

$$C_{Patch} = \frac{\epsilon_{sub} \times A_P}{4d} \quad (4)$$

$$C_{ccav} = \frac{\epsilon_{sub} \times A_C}{4d} \quad (5)$$

$$C_{cav} = \frac{\epsilon_{air} \times A_C}{d} \quad (6)$$

$$C_{sub} = \frac{\epsilon_{sub} \times A_C}{3d} \quad (7)$$

Here, the thickness of substrate along the cavity layer is $3D$, because it is considered that the cavity is cut from the second layer from the top of the patch. Now putting these values in Eq. (4)

$$C_{eff} = \underbrace{\left(\frac{\epsilon_{sub} \times A_P}{4d} - \frac{\epsilon_{sub} \times A_C}{4d} \right)}_I + \underbrace{\left(\frac{1}{\frac{\epsilon_{air} \times A_C}{d}} + \frac{1}{\frac{\epsilon_{sub} \times A_C}{3d}} \right)}_{II} \quad (8)$$

ϵ_{air} is the dielectric constant of air and is considered as unity. The second section of the equation is solved [8].

$$C_{eff} = \underbrace{\left(\frac{\epsilon_{sub} \times A_P}{4d} - \frac{\epsilon_{sub} \times A_C}{4d} \right)}_I + \underbrace{\left(\frac{A_C}{d} \left[\frac{\epsilon_{sub}}{(\epsilon_{sub} + 3)} \right] \right)}_{II} \quad (9)$$

Using Eqs. (2) and (9).

$$\frac{\epsilon_{eff} \times A_{eff}}{4d} = \underbrace{\left(\frac{\epsilon_{sub} \times A_P}{4d} - \frac{\epsilon_{sub} \times A_C}{4d} \right)}_I + \underbrace{\frac{(A_c)}{d} \left[\frac{\epsilon_{sub}}{(\epsilon_{sub} + 3)} \right]}_{II} \quad (10)$$

Here, A_{eff} is the effective patch area A_P because the effective dielectric constant is measured below the patch area only.

$$\epsilon_{eff} = 4\epsilon_{sub} \left[\frac{1}{4} - \frac{1}{4} \frac{Ac}{Ap} + \frac{1}{(\epsilon_{sub} + 3)} \frac{Ac}{Ap} \right] \quad (11)$$

Solving Eq. (11)

$$\epsilon_{eff} = \epsilon_{sub} \left[1 - \frac{Ac}{Ap} \left(\frac{\epsilon_{sub} - 1}{\epsilon_{sub} + 3} \right) \right] \quad (12)$$

Now from the resonant frequency and dielectric constant relation,

$$\frac{f}{f_o} = \sqrt{\frac{\epsilon_o}{\epsilon_{eff}}} \quad (13)$$

Here as explained before, f is resonant frequency of the patch antenna deviated from the theoretical resonant frequency. Now from the above relation in Eq. (12) ϵ_{eff} can be calculated for particular dielectric specification by putting the value of it in Eq. (13).

$$\frac{f}{f_o} = \frac{1}{\sqrt{1 - \frac{Ac}{Ap} \left(\frac{\epsilon_{sub} - 1}{\epsilon_{sub} + 3} \right)}} \quad (14)$$

Here, f is the frequency to be tuned to f_o . In the proposed work, the investigations are done for material FR4 epoxy (where $\epsilon_{sub} = 4.4$), thus,

$$\frac{f}{f_o} = \frac{1}{\sqrt{1 - \frac{Ac}{Ap} (0.46)}} \quad (15)$$

Equation (15) proposes the relation between the area ratio of cavity to patch and the frequency for retune.

Conclusion

In the present work, a new technique of dielectric constant engineering (DCE) is presented. It has been effectively used in accurate designing of microstrip patch antenna. For practical implementation, some fine-tuning formulae are also proposed to give functional relationship between designed resonant frequency of patch antenna and amount of material to be removed from the layer of dielectric substrate. The results are validated for three different dielectric materials with three different design frequencies. It is observed that the proposed idea is successfully working for all these substrate materials at any frequency band because the frequency to be tuned has direct relation with the area ratio of cavity to the patch. Increasing cavity size will result in an increase in resonant frequency and a decrease in cavity size will decrease the frequency. Another important conclusion is that, if we prefer multilayer substrate for patch antenna design then it is beneficial for fine-tuning. Single layer substrate cannot be fine-tuned using the proposed technique.

Acknowledgments The investigators express their gratitude to the management of SKIT and MNIT for constant encouragement.

References

1. Balanis, C.A.: *Antenna Theory: Analysis and Design*, 2nd edn. Wiley, Hoboken (1997)
2. Pozar, D.M., Schubert, D.H.: *Microstrip Antenna: The Analysis and Design of Microstrip Antenna and Arrays*, pp. 59–60. IEEE Press, New York (1995)
3. Bahl, I.J., Bhartia, P.: Design of microstrip antennas covered with a dielectric layer. *IEEE Trans. AP* **30**, 314–318 (1982)
4. Yang, H.Y., Alexopoulos, N.G.: Gain enhancement methods for printed circuit antenna through multiple superstrate. *IEEE Trans. AP*. **35**, 860–863 (1987)
5. Kumar, R., Malathi, P.: Effects of superstrates on the resonant frequency of rectangular microstrip antennas. *Microw. Opt. Technol. Lett.* **49**(12), 2946–2950 (2007)
6. Yazdandoost, K.Y., Sato, K.: Fabrication error in resonant frequency of microstrip antenna. In: *Proceedings of International Symposium on Micromechatronics and Human Science*, Kawasaki, Japan, pp. 41–44 (2001)
7. Garg, R., Bartia, P., Bahl, I., Ittipiboon, A.: *Microstrip Antenna Design Handbook*, pp. 1–68 and 253–316. Artech House Inc., Norwood (2001)
8. Mathur, M., Singh, G., Bhatnagar, S.K.: A novel approach for fine tuning of resonance frequency of patch antenna. In: *Proceedings of SPIE, International Conference in Communication and Electronic Sysyetm Design*, vol. 8760, pp. 8760-1T, Jan 2013

Design of CAN-Based Enhanced Event Data Recorder and Evidence Collecting System

Pankaj H. Chandankhede and M.M. Khanapurkar

Abstract An event data recorder (EDR), in general, is an on-board system or device installed in cars to record vehicle data during accidents or crashes [2]. The system proposed in this paper was made with the help of different sensors, navigation system (GPS), and GSM kit. This design provides information related to position and vehicle speed on real-time basis and also the status about the airbag deployment break status, seatbelt status, etc., just prior to accident. The design objective is to design an advanced microcontroller system to record and analyze the vehicular components. The ARM7 processors collect the information using modules or sensors which are connected to different ports of the processor. The collected data acts as information to the monitoring station [1]. These data recorded in real time can help people to analyze the fault protection at extreme conditions. This EDR displays the messages on LCD mounted on kit to alert as well as record it on storage device [2]. These data are useful to better understand the driving habits. This recorded data can be used to analyze the accident easily and also to settle many problems related to car accident such as vehicle maintenance, investigation, crash litigation, driver performance, and reconstruct the accident as well as insurance settlement.

Keywords Event data recorder • GSM module • GPS • ARM7 processor • CAN module

P.H. Chandankhede (✉)

Department of Electronics Engineering, G. H. Rasoni College of Engineering,
Nagpur 440016, India

e-mail: pankaj.chandankhede@raisoni.net

M.M. Khanapurkar

Department of Electronics & Telecommunication Engineering,
G. H. Rasoni College of Engineering, Nagpur 440016, India

e-mail: milind.khanapurkar@raisoni.net

© Springer India 2016

N. Afzalpulkar et al. (eds.), *Proceedings of the International Conference on Recent Cognizance in Wireless Communication & Image Processing*,
DOI 10.1007/978-81-322-2638-3_13

Introduction

According to the global status report 2013, more than 231 people are killed in crashes of road traffic in India. According to WHO, India recorded the highest number of road accidents in 2011; the death toll being 105,000 in 2008 and around 1.3 million people died. So, the concept of black box was first introduced by David Warren in 1953. The main use of this flight black box is to facilitate the investigation of an aircraft incident or accident. It records important parameters of the flight and its instruments with the cockpit voices during the flight. An event data recorder (EDR) is a device that stores or records information from various sensors of vehicles immediately before and/or during accident or during most serious crashes. The EDR module provides alerts on LCD as well as provides information about possible causes of the accident to the monitor station remotely. This data from EDR memory can help to understand the exact changes in various sensors that happened during accident. These changes can be extracted by the authorized person.

The police or crash investigators can download the data from the EDR's memory to help better understand what happened to the vehicle [2].

Real-time data recording can be achieved using this system. This real-time data can help people to analyze the fault protection at extreme conditions. The EDR saves the latest record in the SD card to avoid further accidents. This data can be sent to the main stations for monitoring and for finding the actual reasons behind the accident [2]. The black box receives real-time data about all the sensors including status, position, and speed. The EDR consists of A/D convert module, ARM processor, input–output interface, storage unit, UART, GPIO, and different sensing modules [2]. This process of gathering, processing, and recording the multiple signals at the same time requires a processor that works in real time with high speed read and write capability. Secondary device memory card is required for long-term data storage to maintain data.

System Model

Event Data Recorder

In EDR, two systems can be used; these are sensing and diagnostic module (SDM) and crash data retrieval (CDR) system. To download post- and pre-crash data from the vehicles, CDR systems are used [1]. SDM is used for the crash phase of a traffic collision. It records the actions and events of the driver before, after, and at the time of collision. This is useful in conditions where there is sudden increase or decrease in velocity, deployment of airbag, and it records changes in acceleration, speed, and direction of travel [3–5].

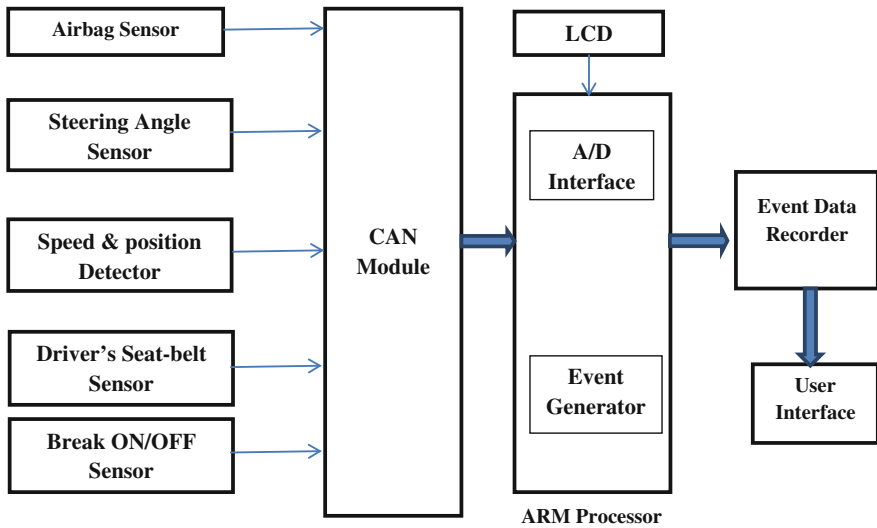


Fig. 1 Block diagram of event data recorder

An EDR is an on the board mechanism capable of displaying, recording, monitoring, storing, and transmitting post- and pre-crash data element parameters from a vehicle. Many crashes can be prevented by making proper use of EDR and make the driving crash free [3–8]. EDRs are cheap and small. EDR should be placed under the front seat or under the central console where the impact of collision is not severe. Figure 1 shows the basic block diagram of the complete system. In this paper, EDR was designed by making use of ARM7 microprocessor. The EDR consists of ARM-LPC2148-32 bit; ARM7 TDMI-based core supporting real-time simulation was used in this proposed design.

A GPS determines the car’s current location in the world. It provides information in terms of latitude and longitude. GPS antenna in the receiver is tuned to specific frequencies. There are two levels of navigation and positioning; standard positioning service (SPS) and precise positioning service (PPS). GSM modems are a specialized type of modem. GSM operation means controlling through simple AT command from microcontrollers and computers. This controlling command comes with a standard RS232 interface. Figure 2 shows various system components used in this design.

As shown in Fig. 2, the single-axis gyro is essentially a breakout board for the ST LISY300AL microelectromechanical system gyroscope. It produces outputs voltage as analog in proportion to the angular rate. Its breakout board has a 3.3 V regulator voltage. It uses a low-pass filter for reduction of noise. Gyro sensor consists of an IC interface and sensing element capable of providing the measured angular rate. An accelerometer is an electromechanical device which will measure acceleration forces. An accelerometer measures the acceleration or vibration of a

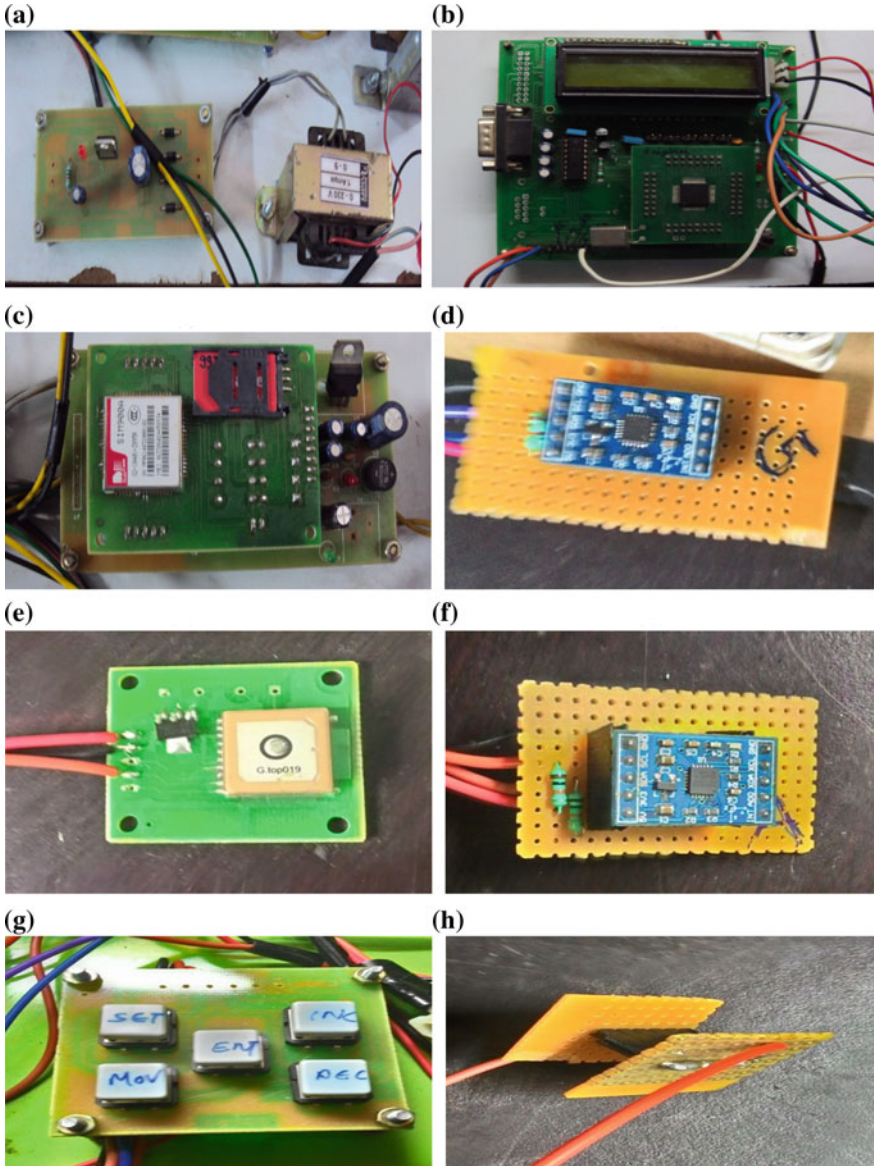


Fig. 2 a Power supply. b ARM7 kit. c GSM kit. d Gyro sensor. e GPS. f Accelerometer. g Keypad. h seat belt arrangement

structure. The force caused by the change in motion produces pressure on the piezoelectric material.

CAN was developed for the automotive market and it can significantly reduce the cost and weight of the wiring attached. It consists of only two wires (physical

layer), the highest priority message always gets through first (priority scheme), and some error detection and handling circuitry. CAN allows messages from 0 to 8 bytes to be passed on to the system as shown in Fig. 1.

Real-Time Monitoring

Real monitor is a configurable software module information and is taken from the ARM processor.

The flow of process of this project takes place in the following manner [1–13].

First, the system needs to be started. The system senses the sensor value that is located at various parts of the vehicle. This sensed value needs to be made compatible with ARM processor for further processing, so it is first given to the ADC unit. Then ARM processor processes the data with some predefined attributes. If the value of sensor exceeds above the predefined limits, the ARM LPC2148 sends appropriate commands to retrieve the status of all connected sensors to the system along with GPS and sends the parameters to the monitoring station via GSM. If the value of sensor does not exceed their predefined limit, then it will be continued.

Circuit Description

As shown in Figs. 3 and 4, the ARM processor LPC2148 is the main part of the system. It consists of two UART ports [1]. GPS module is connected to UART port 1. The LPC kit refreshes itself every 10 s [2]. Two sensors, GSM module and GPS modem, are connected to the LPC2148. Figure 3a, b shows transmitter and receiver side, respectively.

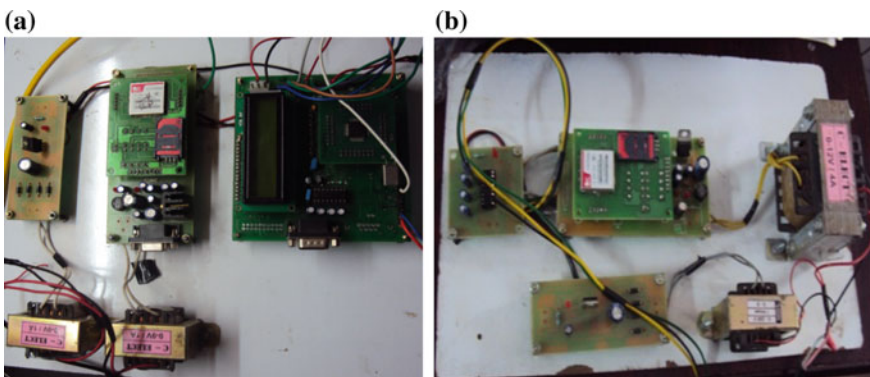


Fig. 3 Setup of transmitting and receiving end. **a** Transmitting end. **b** Receiving end

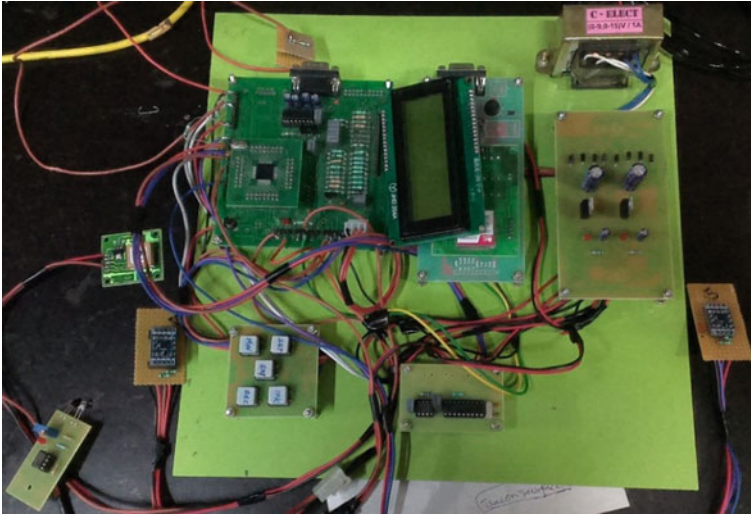


Fig. 4 Actual arrangement

For example, if accident occurs, then the accelerometer which is connected to the voltage regulator vibrates and logic 0 is produced, where logic 0 indicates that the car meets with an accident. Then it sends the car's location to the user's provider with the help of GSM technique. Thus, logic 0 is an indication of sending the signals. For communication between microcontroller unit and GSM module, AT commands are used. Figure 4 shows the actual arrangement of all the components in the system.

These steps are repeated a number of times till the values of different sensors do not cross the predefined limit. If any value of sensors exceeds the threshold value, then in such cases the current status of all sensors are recorded, saved in SD card, and transmitted through GSM kit to a particular predefined number. For continuous storing purpose, SD card with higher data storage capacity is required.

Result

This paper helps to find the exact causes behind the accident. For e.g., EDR helps us to find solutions for a few questions such as, whether the driver was drunk, whether the driver observes the obstacle and tries to avoid the collision, etc. The following results show various steps in design and implementation:

Here, as shown in Fig. 5 results in terms of GSM transmitter and receiver can be shown. GSM transmitter consists of keypad with which the mobile number of the end user can be changed. This end user is the authorized person who can view the data from various sensors and conclude about the causes of the accident. This



Fig. 5 Output on LCD screen

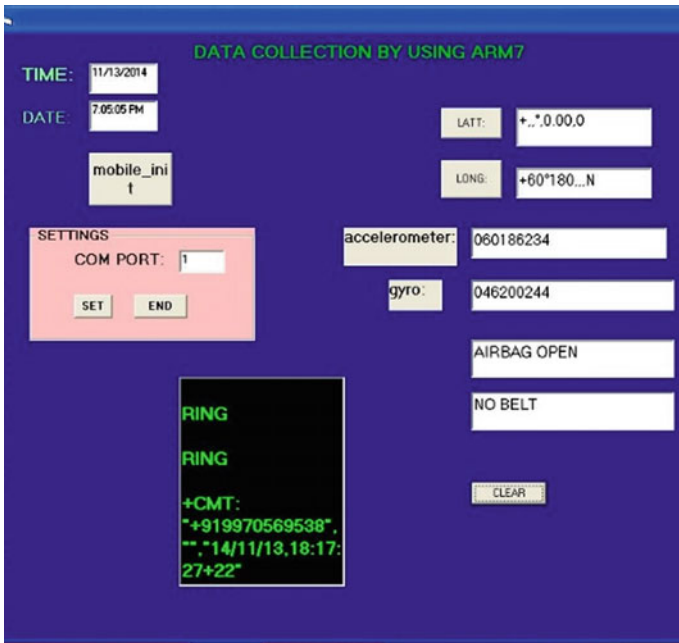


Fig. 6 Output on web page

message contains all data from various sensors separated by a comma. This data also gets filled in the web page as shown in Fig. 6. Data analysis is done at the receiver end to find the causes of the accident.

Conclusion

The proposed design aims to implement EDR data collection mechanism for the vehicle to record the data. In this paper, detection of extreme conditions, sensing data, and recording the extreme conditional data into the SD card were found. These data which can be saved in an SD card can also be displayed on the web page. EDR

system acts as one of the witnesses during an accident, so that it can be used in court cases. Thus, it can be used for (1) insurance purpose, (2) evidence, (3) crash investigation, (4) safety purpose, and (5) driver monitoring and training.

Future Scope

The future work will include connected parameters such as vibration unit, detecting number of passengers in car, side indicator movement, throttle movement, etc., so as to find out more precisely the reasons of accidents. Testing in real-time environment is also one of the major issues followed by prototyping.

References

1. Sirsikar, N.P., Chandankhede, P.H.: Design of ARM based enhanced event data recorder & evidence collecting system. *IOSR-JECE* 9(V), Sept–Oct 2014. e-ISSN: 2278-2234
2. Vaidya, S., Chandankhede, P.H.: Designing of event data recorder for vehicle monitoring based on ARM processor. *Image Process. Netw.* 8(IV), Feb 2014. ISSN:0973-299
3. Chim, T.W., Yiu, S.M., Yeung, C.Y., Li, V.O.K.: Securing, privacy-preserving, distributed motor vehicle event data recorder. In: *International Conference on Connected Vehicle & Expo in Las Vegas, NV*, 2–6 Dec. 2013, pp. 337–342
4. Le Nguyen, D., Lee, M.-E., Lensky, A.: The design and implementation of new vehicle black box using OBD information, 7th *International Conference on Computing and Convergence Technology (ICCT)*, 3–5 Dec. 2012, Seoul, pp. 1281–1284
5. Zhang, T., Huang, A., Wang, S.: Design and implementation of vehicle travelling data recorder based on the Newest Chinese standard. In: *International Conference on Computational and Information Sciences*, 21–23 June 2013, Shiyang, pp. 1190–1193
6. Wen, Z., Meng, J.: Design of vehicle positioning system based on ARM. In: *Business Management and Electronic Information (BMEI), International Conference 2011 IEEE*, 13–15 May 2011, Guangzhou, pp. 395–397
7. Kim, M.S., Jeong, C.Y.: An efficient data integrity scheme for preventing falsification of car black box. In: *ICT Convergence 2013, Jeju*, pp. 1020–1021
8. Mednis, A., Elsts, A., Selavo, L.: Embedded Solution for Road Condition Monitoring Using Vehicular Sensor Networks, 17–19 Oct 2012, pp. 1–5, Tbilisi. *IEEE*
9. Wu, B.-F., Chen, Y.-H., Yeh, C.-H.: Driving behaviour-based event data recorder. In *IET International Transport System Conference 2013*, vol. 8, no. 4, pp. 361–367. ISSN: 1751-956X
10. Chen, Y.-K., Tsai, T.-H.: Sky recognitions for driving-view images. In: *2013 IEEE International Conference on Vehicular Electronics and Safety (ICVES)*, 28–30 July 2013, Dongguan, pp. 119–124
11. Patil, C., Marathe, Y., Amoghmath, K., David, S.S.: Low cost black box for cars. In: *India Educators' Conference (TIIEC), 2013 Texas Instruments*, 4–6 Apr 2013, Bangalore, pp. 49–55
12. Tanaka, Y., Yamada, N., Tsuji, T., Suetomi, T.: Vehicle active steering control system based on human mechanical impedance properties of the arms. In: *IET International Transport System Conference 2014*, vol. 15, no. 4, pp. 1758–1769 (2014). ISSN: 1524-9050
13. Chakole, S.S., Kapur, V.R., Suryawanshi, Y.A.: ARM hardware platform for vehicular monitoring and tracking. In: *2013 International Conference on Communication Systems and Network Technologies*, Gwalior, India, pp.757–761. ISBN-978-1-4673-5603-9

Detection of Brain Tumor in MRI Images, Using Fuzzy C-Means Segmented Images and Artificial Neural Network

Parveen and Amritpal Singh

Abstract Brain tumors are the most serious concerns in the field of medicine. In this research paper, ANN and fuzzy c-means clustering are combined together and a model is developed to predict the preoperative prediction of brain tissues. The purpose of this study was to develop a method of the preoperative prediction and classification of brain tumors. A new hybrid model is developed for classification where image segmentation is done using fuzzy c-means clustering algorithm which pinpoints the cancerous area in a brain MRI image. Here, features are extracted from brain MRI images using GLRLM technique. Then artificial neural network is used to classify these images. This enables higher percentage detection and overall provides an excellent classification rate.

Keywords Artificial neural network (ANN) · Fuzzy c-means clustering · Gray level run length matrix (GLRLM) · Data mining

Introduction

The brain is the most important part of the body. A brain tumor is an abnormal growth of tissue in the brain. It can be malignant or benign and caused due to various reasons such as pollution, mobile, lack of awareness, and genetic disorder. So many imaging techniques are available for diagnosis of the disease, but MRI imaging technique is the best because of its higher resolution and most researchers have used MRI imaging for brain disease diagnoses [1]. MRI imaging technique is popularly used for diagnosing brain tumor but these images need some enhancement for accurate detection of brain tumor in early stage and further classification.

Parveen (✉) · Amritpal Singh
Department of CSE, Government Women Engineering College,
Ajmer, Rajasthan, India
e-mail: rjlabsparveen@gmail.com

Amritpal Singh
e-mail: palamrit83@gmail.com

Brain MRI images are processed in a step-by-step procedure to obtain better classification. To extract information from huge data sets computationally efficient tools are required which are both simple and robust.

Data mining is a process to convert the data into an understandable form and to classify them [2].

To extract information from huge data sets computationally efficient tools are required which are both simple and robust. A major goal post in medicine for a long time has been to cure tumors, both benign and malignant. Malignant tumors grow in an uncontrollable manner; though benign tumors do not spread to other parts of the body they nevertheless can harm delicate brain tissues. Development of new treatments takes time and money. It is essential to carry out accurate diagnosis of these tumors in order to provide a prognosis of tumor development.

Enhancement—this is done to improve and augment brain MRI images used. Normally, these medical images are dull, and hence this is essential. In this enhancement, contrast improvement and mid-range stretch are used to improve the quality of images. Skull striping, two-method double thresholding, and morphological operations are involved. Fuzzy c-means clustering is done by segmenting the image for delineating the potentially suspicious region from brain MRI image [3]. The procedure of distilling out relevant information from brain MRI image is called features extraction and is used for further easy classification [4]. In artificial neural network (ANN), the computing elements are so interconnected with each other that a huge network comes into being. This is an information handling model that has complex relationship between input and output [5]. A good method is backpropagation training algorithm that has many functions such as `trainlm`, `trainbfg`, `trainrp`, `trainscg`, etc. This is a systematic method of training multilayer artificial networks which is mathematically robust. The main objective of this research is to develop an easy and efficient novel hybrid system for brain tumor detection. Subsequently, this system is evaluated using different parameters.

Method and Material

The procedure used to classify brain MRI images is shown in Fig. 1. This uses the following steps: (a) enhancement (ii) skull striping, (b) fuzzy c-means algorithm, (c) feature extraction, (d) training and storing the MRI images database, and (e) testing. First, training database, that is, brain MRI images provided to ANN classifier for training purposes, then the new MRI images that is the testing image database given as an input to ANN classifier, which docket it accurately. Real database of patients brain MRI images are collected from different diagnosis centers. Since these images are RGB, they have to be first converted into new form (grayscale). These are ready for further processing according to the proposed system. Figure 2 shows (a) normal brain MRI (b) abnormal brain MRI.

Fig. 1 Proposed classification algorithm flow

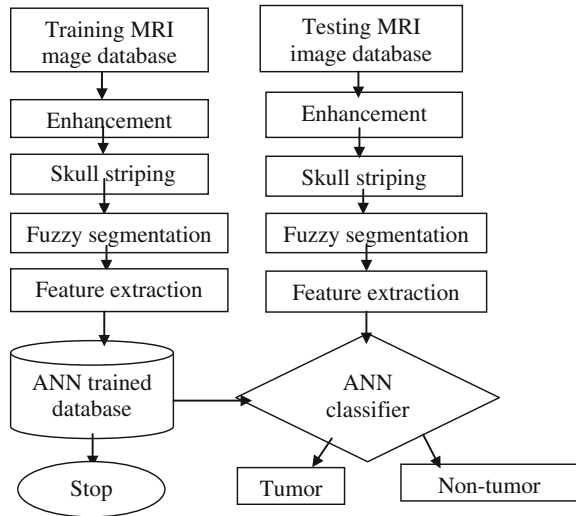
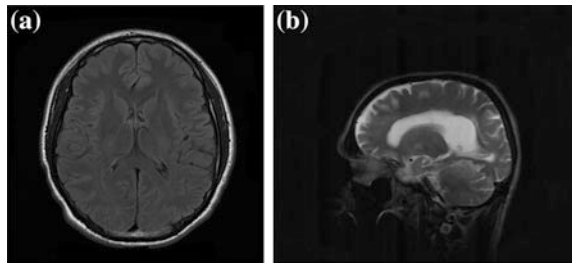


Fig. 2 **a** Normal brain MRI. **b** Abnormal brain MRI



Enhancement of MRI Images

Enhancement is essential to brighten the soft tissues of MRI images making it easier and more accurate for human viewers. These enhanced images fed into data mining techniques lead to better results. This is done using the following two methods: (1) contrast improvement and (2) mid-range stretch.

Contrast Improvement

This is done by implementing this formula.

$$\text{out} = \text{high_out} - \text{low_out} \tag{1}$$

$$\text{in} = \text{high_in} - \text{low_in} \tag{2}$$

$$J = \text{low_out} + \text{out} * ((I - \text{low_in})/\text{in})^y \quad (3)$$

This produces a new set of values such that higher contrast is obtained. Here, the grayscale images are used as input and these grayscale image intensity values are converted into new intensity values. This mapping increases the contrast of the output image.

Mid-range Stretch

Using this enhancement technique, the distinction between brain tissues and non-brain tissues are made clearer. As segmentation is necessary, this method of mid-range stretch produces a good result.

Using brain tissue intensity values between “0.1 and 0.88”.

$$X_{ij} = \text{Image}_{ij}/255 \quad (4)$$

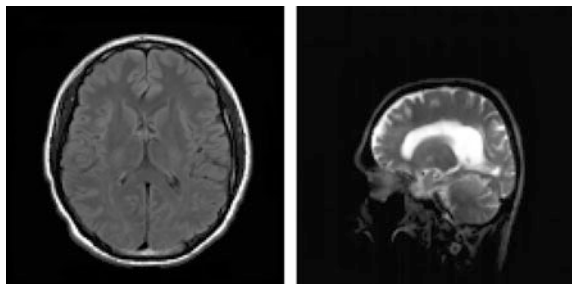
where i is row index and j is column index of the new mapped image matrix X_{ij} , respectively. This divided by 255 gives a specific intensity value for every single pixel which has to be between 0 and 1.

Further, a function $f(x_{ij})$ is computed such that

$$f(x_{ij}) = \begin{cases} 0.5 * x_{ij}, & x_{ij} < 0.1 \\ 0.1 + 1.5 * (x_{ij} - 2), & 0.1 \leq x_{ij} \text{ and } x_{ij} \leq 0.88 \\ 1 + 0.5 * (x_{ij} - 1) & x_{ij} > 0.88 \end{cases} \quad (5)$$

Thus an indexed image is generated which uses the smallest possible colormap. These improved images are used for further processing. Figure 3 shows the result of enhancement.

Fig. 3 Result after enhancement



Skull Stripping

Skull stripping means deleting all the irrelevant tissues such as neck, skull, eyes, etc., from brain MRI image. After clipping out the skull portion, it segments for fast further processing. The process of skull masking is given in detail below.

Double Thresholding

Double thresholding generates a mask for brain MRI images. In this step, grayscale images are converted into binary images; pixels ranging between 0.1 and 0.88 are converted into white and the remaining image intensity values are converted to black. Thus, the grayscale image gets transformed into a binary black-and-white image.

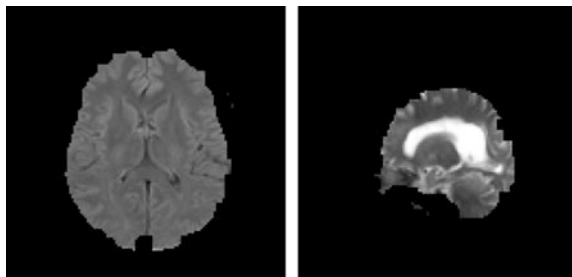
Erosion

Erosion is a method used to delete all the unnecessary pixels contributing to the skull portion in the mask generated by double thresholding given above.

Region Filling

The tumor present in MRI images will leave holes in the eroded images as defined above; these are filled using the region filling operation. Once this is done, a complete skull stripping image is obtained. Figure 4 shows the result of skull masking.

Fig. 4 Result after skull masking



Fuzzy C-Means

Fuzzy c-means clustering is also called soft clustering, as a single data point can belong to multiple clusters. This is a segmentation technique that divides the image obtained into more than one cluster. Here, there are three clusters based on three different intensity values. The fuzzy c-means clustering algorithm enables spotting of the potential tumor area. Figure 5 shows the effect of fuzzy c-means algorithm.

Feature Extraction

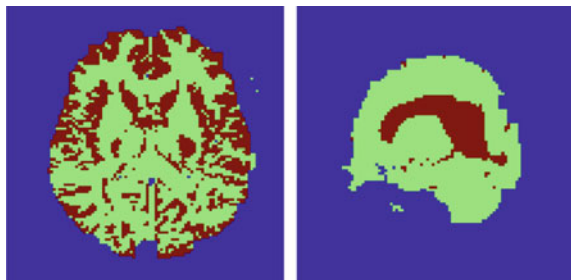
Calculation using the large matrix is cumbersome and some of the data may be redundant; using feature extraction this can be transformed to a smaller dimension matrix which retains all the relevant information. Feature extraction is used to draw out features from the MRI images, where the fuzzy c-means output is the input.

Yet, processing of large input image features are time- and space-consuming. This reduces further using the GLRLM. The compact form now obtained is called feature extraction; additionally, it requires smaller amount of space [6].

ANN Classifier

ANN is a computational model, which mimics the brain, specifically the central nervous system. So a network is constructed using information processing units analogous to the neurons in the brain. This system responds to stimuli and learns from given examples [7]. There are different types of ANN. Here, supervised learning feedforward backpropagation ANN is used to classify brain MRI images into tumor or nontumor. The simple structure of ANN is shown in Fig. 6.

Fig. 5 Result after fuzzy c-means algorithm



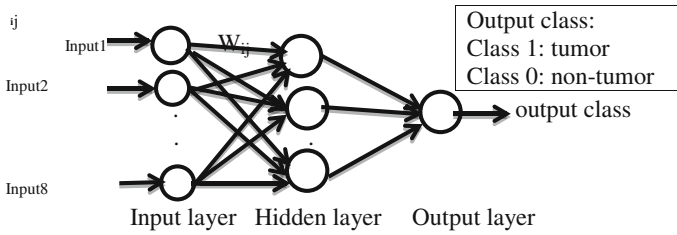


Fig. 6 Structure of simple ANN

Artificial Neural Network Design

When designing the ANN, a decision is to be made if supervised or unsupervised learning technique is to be used. The number of features is fixed by GLRLM, but the number of hidden layers to be included, kind and number of output are to be decided. Further, the data are divided into two parts, one for training and the other for testing.

Supervised learning ANN is implemented and the brain MRI images are classified as normal or abnormal. Here there are three basic layers; the first layer consists of input with weight, the second layer is the hidden layer and has 20 neurons, and the last layer is the output layer and has one neuron.

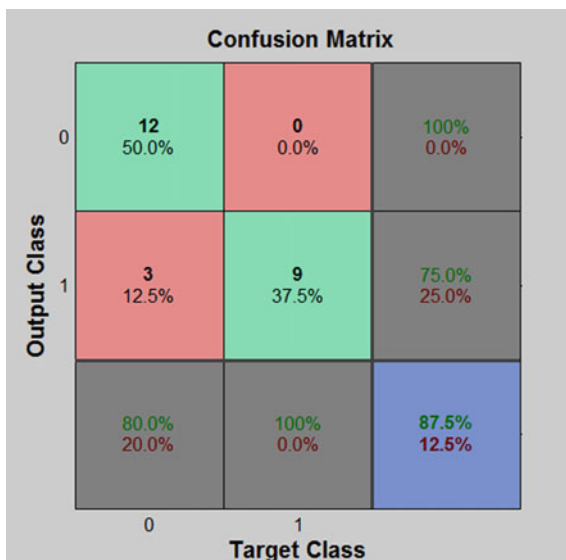
ANN Training

Multilayer feedforward neural network training is done by backpropagation learning algorithm, which has fast learning properties for network training. There are several backpropagation algorithms, but `trainlm` (levenberg-marquardt algorithm) is a default and fast training function. For maximizing the performance of the network, the values of weight and bias are tuned; this is done during training. Evaluating the network performance is done by mean square error (MSE) between network output and targets.

ANN Testing

Now, the testing performance provides the final result of the ANN classification efficiency. Here, all the steps used in training phase are also used in testing phase. The new 24 MRI images are taken and are tested in the trained network. The classification results of the test data sets are shown in Fig. 7.

Fig. 7 Confusion matrix from testing



Performance Measures

The large data sets are classified to measure the performance. The classification rates are calculated using the formulas given below: correct positive (CP): Abnormal brain MRI correctly identified as abnormal. Correct negative (CN): Normal brain MRI correctly identified as normal. Incorrect positive (IP): Normal brain MRI incorrectly identified as abnormal. Incorrect negative (IN): Abnormal brain MRI incorrectly identified as normal.

$$\text{Sensitivity} = \text{CP}/(\text{CP} + \text{IN}) * 100 \%$$

$$\text{Specificity} = \text{CN}/(\text{CN} + \text{IP}) * 100 \%$$

$$\text{Accuracy} = (\text{CP} + \text{CN})/(\text{CP} + \text{CN} + \text{IP} + \text{IN}) * 100 \%$$

Result and Discussion

This section describes the classification rate of the ANN classifier as shown in Table 1. An experiment was performed using 120 real brain MRI images, for training as well as testing phase. It was found that 60 were normal and the rest were abnormal images. Initially, the ANN classifier is trained using 96 brain MRI images. The remaining 24, 12 normal, and 12 abnormal brain MRI images were used for testing. Since a larger data set is used, a more accurate result was obtained. The network was able to classify 87.50 % of the cases in the testing set.

Table 1 Performances of the ANN classifier for 24 brain images

S. no.	FFBPNN	Classification parameters ANN classifier		
		Accuracy in %	Sensitivity in %	Specificity in %
1		87.50	75.00	100

Conclusion

This paper proposes a method for automatic and efficient detection of brain tumor. A system is developed for image classification; the image quality is improved using two enhancement techniques (a) contrast improvement and (b) mid-range stretch. Now these enhanced images will be successfully segmented. Skull striping is also an image segmentation method using double thresholding, erosion, and region filling operations. Fuzzy c-means algorithm divided the image into different clusters. Gray level run length matrix technique is used for relevant feature extraction; this in turn undergoes further processing. ANN classifier differentiates the testing images into tumor and nontumor. This new hybrid technique classifies the images accurately. So, the future work using real images, in combination with this new hybrid technique will increase the accuracy for tumor prognosis.

References

1. Chudler, E.H.: Brain facts and figures. <http://faculty.washington.edu/chudler/facts.html> (2011). Accessed 18 Mar 2011
2. Han, J., Kamber, M., Pei, J.: Data Mining: Concepts and Techniques. Morgan Kaufmann (2011). ISBN: 978-0123814791
3. Rahmi, S., Zargham, M., Thakre, A., Chhillar, D.: A Parallel Fuzzy C-Mean Algorithm for Image Segmentation, 0-7803-8376-1/04/\$20.00 Copyright 2004. IEEE (2004)
4. Kumar, G.V., Dr. Raju, G.V.: Biological early brain cancer detection using artificial neural network. *Int. J. Comput. Sci. Eng.* **02**(08), 2721–2725 (2010)
5. Rajasekaran, S., Vijayalakshmi Pai, G.A.: Neural Networks, Fuzzy Logic, and Genetic Algorithms. PHI Learning Private Limited, New Delhi (2010)
6. RajKumar, R.S., Niranjana, G.: Image segmentation and classification of MRI brain tumor based on cellular automata and neural networks. *IJREAT Int. J. Res. Eng. Adv. Technol.* **1**(1) (2013). ISSN: 2320–8791
7. Murat, C., Mehmet, E., Erkan, Z.B., Ziya, Y.A.: Early prostate cancer diagnosis by using Artificial Neural Networks and support vector machines. *Expert Syst. Appl.* **36**, 6357–6361 (2009)

Multiple Inputs Combinational Logic Minimization by Minterms Set

Sahadev Roy, Rajesh Saha and Chandan Tilak Bhunia

Abstract The paper presents an easy technique to simplify multiple inputs combinational digital logic circuits. By grouping of minterms in different sets, multiple inputs can be easily synthesized. The proposed technique is an exact method of minimization. The new approach reduces the minimization complexity of combinational circuits. The proposed method is fast, can be solved by paper–pen, and also by computer programming.

Keywords Multiple inputs · Simplification · Combinational logic · Algorithm · Minterms · Set · SOP · Minimization · Boolean function · Weighted sum

General

The studies on digital logic circuit minimization through minterms sets are analyzed here. An attempt is made to generate a SOP term with minimum number of literals. Details of the minimization technique using set of minterms are discussed in steps with few examples. The elements of minterms sets are chosen from minterms expression of the logic function. To determine SOP terms for a particular set of minterms, first represent minimum and maximum elements of the set as 0 for a complemented term and 1 for without complement of that variable and perform bitwise comparison. For those variables, if the values for minimum element and maximum elements of the set are complement just neglect and the matches are marked. If the marked terms are 0 valued take complements of those variables otherwise non complement for the variables for value of 1, which give product

Sahadev Roy (✉) · Rajesh Saha
Department of ECE, National Institute of Technology,
Yupia, Arunachal Pradesh 791112, India
e-mail: sdr.ece@nitap.in

C.T. Bhunia
National Institute of Technology,
Yupia, Arunachal Pradesh 791112, India

term, i.e., AND operation of the literals for the particular set of minterms. Logical sum of those product terms are minimized SOP expression of the given minterms. The proposed minimization method reduces the complexity to certain extents.

Review of the Literature

Boolean expressions can be simplified using algebraic method, but this method is not a systematic method. This method does not guarantee that the obtained minimal expression is the real minimal or not. So, to get a correct minimal form it should be required to apply Boolean algebraic rules laws and theorems very carefully, and sometimes it is very difficult to simplify some Boolean expressions by applying algebraic theorems. To simplify the expressions easily Veitch [1] made a diagram in 1952; later Maurice Karnaugh modified Veitch chart in 1953 [2] and introduced a graph/chart which is known as Karnaugh map. The Karnaugh map method is a systematic method of simplifying the Boolean expressions. It is a simple method and is used widely. This method can perform tough and big calculations rapidly, efficiently used for four inputs of variables, and may be used up to six variables. The results are expressed in a truth table in the sum of products (SOP) or product of sums (POS) form. In a truth table gray code is used to identify the cells. Two-variable K-map contains 2^2 cells, three-variable K-map contains 2^3 cells, ... n-variable K-map contains 2^n cells. K-map is a trial procedure, which depends on the ability of the user. Karnaugh map method is less appropriate for more than six variables, to overcome these difficulties Quine–McCluskey [3, 4] developed a method in 1956 which is known as Quine–McCluskey method of minimization of logic functions. This method is also known as *tabulation method*, because its tabular form is more capable to determine the minimal form of a large number of variables in Boolean expression and widely used in computer algorithms. Its function is similar to Karnaugh mapping. Many heuristic techniques are present for logic networks optimization [5, 6]. “Many of these heuristics have exponential time complexity and thus can only be applied to small components of a circuit being built” [7]. Break up technique for minimization for multi inputs logic circuit [8]. If the numbers of input variables increase the number of minterms increase two times which causes different problems like large number of minterms and large possible combination between minterms, irregular patterns of minterms circuit becomes complicated. Most of researchers [9, 10] have focused on developing low-power switching circuit using AND/OR or NAND and NOR-based circuits. In certain minimization techniques, XOR realizations require less gate count over the conventional AND/OR or NAND and NOR logic.

Formation of Minterm Sets

Number of Elements Determination in the Set

“For n input variables system un-minimized input variable are n , let after minimization input variable are m , so the numbers of minterms (r) required for minimization from n input variable to m input variable are 2^{n-m} because $(n-m)$ inputs must be take all possible combination of binary value” [11]. So in Eq. (1), r is the required number of the elements in the minterms set from n inputs to m number of minimized literals.

$$r \in 2^{n-m}. \quad (1)$$

Relation of Elements in the Minterm Set

$$m_{r-1} = m_0 + (r - 1)d. \quad (2)$$

where ‘ m_0 ’ and ‘ m_{r-1} ’ is minimum and maximum elements of minterms, ‘ d ’ is difference between two consecutive member of the minterms set. For different values of d , minimized SOP terms can be determined from Eq. (2).

For $m = 1$:

If ‘ d ’ is 1, then the minimized product term is the highest weighted literal.

If ‘ d ’ is 2^1 , then the minimized product term is the lowest weighted literals.

For $m = 2$:

If ‘ d ’ is 1, then minimized variables are consecutive two highest weighted literals. If ‘ d ’ is 2^2 , then minimized variables are two consecutive lowest weighted variables [12]. For $m = 3$:

If ‘ d ’ is 1, then minimized variables are consecutive three highest weighted literals. If ‘ d ’ is 2^3 , then minimized variables are consecutive three lowest weighted variables.

For m number of minimized literals:

In general, if ‘ d ’ is 1, then minimized variable consecutive ‘ m ’ highest weighted literals else if ‘ d ’ is 2^m , then minimized variables are consecutive ‘ m ’ number of consecutive lowest weighted variables.

Generalized Rule for Minimum Literals

Minterms are identified using Eqs. (1) and (2) present in the switching function. If a recursive set S from as (3) then minimum number of consecutive literal can be easily determined using Table 1.

Table 1 Example of identifications table of minimized literals

Set	Minterms	Input variables								Product
		A	B	C	...	P	Q	S	R	
S_1	m_0 of S_1	0	0	1	...	0	1	0	1	$\overline{Q}SR$
	m_r of S_1	1	1	0	...	1	1	0	1	
S_2	m_0 of S_2	1	0	0	...	0	0	0	0	$A\overline{B}$
	m_r of S_2	1	0	1	...	1	1	1	1	

$$S = \left\{ m_{r-1} \mid m_{r-1} = m_0 + (r-1)d, \forall r \in 2^{(n-m)} \right\}. \quad (3)$$

Identification of Minimized Literals

Identifications of minimized literals are easily possible using Table 1. First express the minimum and maximum elements of the set 'S' created which follows Eq. (3) in binary form. Here we assume the input variables nomenclature from A to S and it may be any number. Cancel all different bits of the same position and the only common bit of the same position is the minimum literals. If the common bit is 0, then complement of the literal has to be considered.

Examples

Minimization into One Literal

Let a five-variable switching function whose minterms are as A particular set of minterms as Eq. (4). These minterms form a recursive set as Eq. (5).

$$f_1(A, B, C, D, E) = \sum m(1, 3, 5, 7, 9, 11, 13, 15, 17, 19, 21, 23, 25, 27, 29, 31). \quad (4)$$

$$S_1 = \left\{ m_{r-1} \mid m_0 = 1, m_{r-1} = m_0 + (r-1)2, \forall r \in 2^{(5-1)} \right\}. \quad (5)$$

Table 2 Identifications table of minimized literals

Set	Minterms	Input variables					Product
		<i>A</i>	<i>B</i>	<i>C</i>	<i>D</i>	<i>E</i>	
S ₁	$m_0 = 1$	0	0	0	0	1	E
	$m_r = 31$	1	1	1	1	1	

From Table 2, only literal *E* is fixed and its value is 1 so the minimized SOP term is *E*, i.e.,

$$f_1(A, B, C, D, E) = E.$$

Minimization into Two Literals

Let a six-variable function and its minterms with don't-care terms be Eq. (6).

$$f_2(A, B, C, D, E, F) = \sum m(2, 6, 10, 14, 16, 17, 18, 19, 20, 22, 23, 24, 25, 26, 27, 28, 29, 31, 34, 38, 42, 46, 50, 54, 62) + d(21, 30, 58, 59, 64). \quad (6)$$

These minterms form two recursive sets as Eqs. (7) and (8).

$$S_2 = \{m_{r-1} | m_0 = 2, m_{r-1} = m_0 + (r-1)4, \forall r \in 2^{6-2}\} \\ = \{2, 6, 10, 14, 18, 22, 26, 30, 34, 38, 42, 46, 50, 54, 58, 62\}. \quad (7)$$

$$S_3 = \{m_{r-1} | m_0 = 16, m_{r-1} = m_0 + (r-1)1, \forall r \in 2^{6-2}\} \\ = \{16, 17, 18, 19, 20, 21, 22, 23, 24, 25, 26, 27, 28, 29, 30, 31\}. \quad (8)$$

So, the minimized Sum of Products (Table 3) form is,

$$f_2(A, B, C, D, E, F) = E\bar{F} + \bar{A}B$$

Minimization into Three Literals

Let a six-variable function and its minterms with don't-care terms be Eq. (9).

Table 3 Identifications table of minimized literals

Set	Minterms	Input variables						Product Terms
		A	B	C	D	E	F	
S_2	$m_0 = 2$	0	0	0	0	1	0	$E\bar{F}$
	$m_r = 62$	1	1	1	1	1	0	
S_3	$m_0 = 1$	0	1	0	0	0	0	$\bar{A}B$
	$m_r = 31$	0	1	1	1	1	1	

$$f_3(A, B, C, D, E, F) = \sum m(4, 8, 9, 11, 12, 13, 14, 20, 28, 36, 44, 52) + d(10, 15, 60). \quad (9)$$

These minterms form two recursive set as Eqs. (10) and (11) and can be easily minimized using Table 4.

$$S_4 = \{m_{r-1} | m_0 = 4, m_{r-1} = m_0 + (r-1)8, \forall r \in 2^{6-3}\} \\ = \{4, 12, 20, 28, 36, 44, 52, 60\}. \quad (10)$$

$$S_5 = \{m_{r-1} | m_0 = 8, m_{r-1} = m_0 + (r-1)1, \forall r \in 2^{6-3}\} \\ = \{8, 9, 10, 11, 12, 13, 14, 15\}. \quad (11)$$

Hence from Table 4, minimal SOP equation is

$$f_3(A, B, C, D, E, F) = \bar{A}\bar{B}C + D\bar{E}\bar{F}.$$

Table 4 Identifications table of minimized literals

Set	Minterms	Input variables						Product Term
		A	B	C	D	E	F	
S_4	$m_0 = 4$	0	0	1	0	0	0	$\bar{A}\bar{B}C$
	$m_r = 60$	0	0	1	1	1	1	
S_5	$m_0 = 8$	0	0	0	1	0	0	$D\bar{E}\bar{F}$
	$m_r = 15$	1	1	1	1	0	0	

Table 5 Identifications table of minimized literals

Set	Minterms	Input variables						Product Term
		A	B	C	D	E	F	
S_6	$m_0 = 13$	0	0	1	1	0	1	$C\overline{D}\overline{E}F$
	$m_r = 61$	1	1	1	1	0	1	
S_7	$m_0 = 44$	1	0	1	1	0	0	$\overline{A}\overline{B}CD$
	$m_r = 47$	1	0	1	1	1	1	

Minimization into Four Literals

Let a logic expression given by Eq. (12),

$$f_4(A, B, C, D, E, F) = \sum m(13, 29, 44, 46, 47) + d(45, 61). \quad (12)$$

Using minterms and don't-care terms two recursive set Eqs. (13) and (14) from.

$$S_6 = \{m_{r-1} | m_0 = 13, m_{r-1} = m_0 + (r-1)16, \forall r \in 2^{6-4}\} \\ = \{13, 29, 45, 61\}. \quad (13)$$

$$S_7 = \{m_{r-1} | m_0 = 44, m_{r-1} = m_0 + (r-1)1, \forall r \in 2^{6-4}\} \\ = \{44, 45, 46, 47\}. \quad (14)$$

Minimal SOP obtained from Table 5 is $f_4(A, B, C, D, E, F) = C\overline{D}\overline{E}F + \overline{A}\overline{B}CD$.

Conclusion

This paper presents a new methodology to simplify Boolean logic function for successive literals. By comparing maximum and minimum element of minterms set we easily realized the minimal SOP. The proposed minterms grouping method of minimization is able to minimize multiple input variables fast and can be easily implemented by computer programming.

Acknowledgments The authors gratefully acknowledge Dr. Mihir Kr. Shome, Associate Professor and HoD of Management and Humanities and Shri Anish Kr. Saha, Assistant Professor of CSE in NIT, Arunachal Pradesh for their kind support. Sahadev wants to give special thanks to Mahadev Roy, Sr. Teacher, Kanduria High School for his constant motivation to complete the research work and Momin for her all support.

References

1. Veitch, E.W.: A chart method for simplifying truth functions. In: Transactions of the 1952 ACM Annual Meeting, ACM Annual Conference/Annual Meeting "Pittsburgh", pp. 127–133. ACM, NY (1952)
2. Karnaugh, M.: The map method for synthesis of combinational logic circuits. AIEE Committee on Technical Operations for presentation at the AIEE summer General Meeting, Atlantic City, NJ, pp. 593–599 (1953)
3. Quine, W.V.: The problem of simplifying truth functions. *Am. Math. Mon.* **59**(8), 521–531 (1952). doi:[10.2307/2308219](https://doi.org/10.2307/2308219)
4. McCluskey, E.J.: Minimization of boolean functions. *Bell Syst. Tech. J.* **35**(6), 1417–1444 (1956)
5. Faber, W., Leone, N., Pfeifer, G., Ricca, F.: On look-ahead heuristics in disjunctive logic programming. *Ann. Math. Artif. Intell.* **51**(2–4), 229–266 (2007)
6. Kunz, W., Stoffel, D., Menon, P.R.: Logic optimization and equivalence checking by implication analysis. *IEEE Trans. Comput. Aided Des. Integr. Circuits Syst.* **16**(3), 266–281 (1997)
7. Choudhury, A.K., Das, S.R.: Some studies on connected cover term matrices of switching functions. *Int. J. Control* **2**(5), 441–501 (1965). doi:[10.1080/00207176508905564](https://doi.org/10.1080/00207176508905564)
8. Roy, S., Bhunia, C.T.: Constraints analysis for minimization of multiple inputs logic programming. In: Proceedings of International Conference on Signal and Speech Processing ICSSP-14, India, pp. 61–64 (2014). http://www.elsevierst.com/conference_book_download_chapter.php?id=4436&file=9789351072676_ICSSP_11.pdf
9. Shui, Y., Wei, X., Almaini, A.E.A.: Power minimization of FPRM functions based on polarity conversion. *J. Comput. Sci. Technol.* **18**(3), 325–331 (2003)
10. Panda, R., Najm, F.: Technology decomposition for low power synthesis. In: IEEE Custom Integrated Circuits Conference, Santa Clara, California, USA, pp.650–655 (1997)
11. Roy, S., Bhunia, C.T.: Minterms generations algorithm using weighted sum method. *Int. J. Curr. Sci. Technol.* **1**(2), 34–38 (2013). www.nitap.in/Documents/IJCST_V1N2_05_F1.pdf
12. Roy, S., Bhunia, C.T.: Minimization algorithm for multiple input to two input variables. In: Proceedings of the 2014 International Conference on Control, Instrumentation, Energy and Communication (CIEC), pp. 555–557 (2014). doi:[10.1109/CIEC.2014.6959150](https://doi.org/10.1109/CIEC.2014.6959150)

Design and Simulation of 16×8 Synchronous SRAM in 90 nm CMOS Technology

Vipul Bhatnagar, Pradeep Kumar and Sujata Pandey

Abstract We report the design of a 128-bit (16×8) synchronous static random-access memory in this paper. Standard 90 nm CMOS technology is being used for the design process. The approach is to design each single functional block by keeping in view the layout feasibility. The main functional blocks, i.e. bit cell, preconditioning circuits, clock tree, flip-flops row and column decoders are designed and implemented. The cell matrix of 16×8 has been designed, avoiding the usage of fully complementary CMOS gates, thus equalizing the voltage levels between bit lines using pass transistors for faster clocking, keeping the default pre-charge level of the word lines to one. Also, aspect ratio of each transistor is maintained so as to obtain the desired results.

Keywords SRAM · Clock tree · Leakage power reduction

Introduction

High-performance processors demand fast memory access. With the increased amount of computational requirements the size of memory is increasing day by day. Also, memory occupies a major portion of chip area. So, the designing of memory plays a vital role in designing of other circuits in the IC as it is desired that memory design should also utilize the same fabrication process steps. The other considerations include fast access time and reduced power consumption.

Static random-access memory (SRAM) is widely used as cache memories as they operate as fast as logic circuits. Also it should consume little power when in standby mode. Many SRAM topologies were proposed by researchers [1–10]. The bit cell is the main component of the SRAM array. The widely used topologies for

Vipul Bhatnagar · Pradeep Kumar · Sujata Pandey (✉)
Department of Electronics and Communication Engineering,
Amity University Uttar Pradesh, Noida, India
e-mail: spandey@amity.edu

bit cell are 6T, 7T, 9T and 10T. Recently some bit cells are designed with lower number of transistors and termed as 1T, 3T, etc.

In this paper, we have designed a 128-bit synchronous SRAM array. The main aspect in the approach is to design every single functional block keeping the layout feasibility in mind. The main functional blocks designed are bit cell, row and column decoders, preconditioning circuit, clock tree and flip-flops. The key design features include a cell matrix of 16×8 , avoiding usage of fully complementary CMOS gates, equalizing the voltage levels between bit lines using pass transistors for faster clocking, keeping the default pre-charge level of the word lines to one. In nanometer CMOS technologies, the SRAM cell read and write stability are major concerns due to continuous increase in intra-die variability and voltage scaling. Read stability N-curve metrics and write stability curves are also analyzed. Static noise margin (SNM) has also been calculated for the same. The aspect ratios of each transistor are appropriately chosen for 90 nm CMOS Technology in Cadence EDA to obtain the desired results. Also the other parameters in designing SRAM such as cell ratio, and pull up ratio have been taken into consideration.

Design Consideration

The block diagram of SRAM array is shown in Fig. 1. The main modules under consideration are SRAM bit cell, row and column decoder design, column (write) circuitry and sense amplifier (read circuitry). The designing and analysis of all the modules are being done separately and integrated to obtain the desired SRAM array. The design is then optimized for speed and layout area.

Figure 2 refers to the general topology of a 6T SRAM bit cell. Transistors M1, M2, M3 and M4 store each bit.

The cell is accessed by enabling the word line (WL). The two transistors M5 and M6 are controlled by WL, which in turn controls the connection of the cell either to BL or BLBar. Proper sizing of the transistors are being done for determining the read and write stability.

Fig. 1 Block diagram of SRAM array [2]

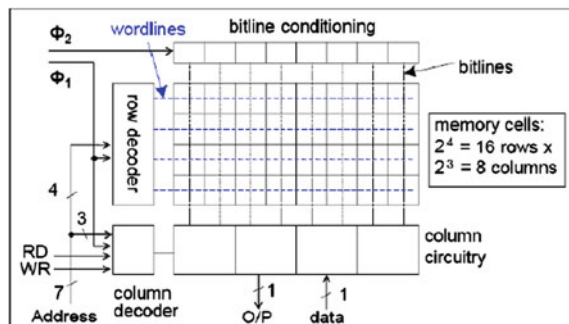
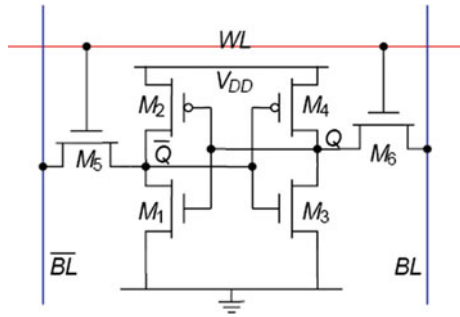


Fig. 2 General 6T SRAM cell



To ensure read stability, the voltage (V_Q bar) across M_1 should be less than its threshold voltage ($V_{th} = 0.4$ V) when the charge on BLB is discharged through transistors M_1 and M_5 . Similarly, read stability can be met by choosing the size of M_1 greater than M_5 . The exact size of M_1 can be obtained from the cell ratio (CR) as

$$CR = \frac{\frac{W_1}{L_1}}{\frac{W_5}{L_5}} = \frac{W_1}{W_5}, \tag{1}$$

In the above equation, L is fixed. The cell ratio is to be chosen greater than 1.2 to have reads stability. In the present case, cell ratio has been properly adjusted to ensure read stability.

Similarly for write stability, the exact size of M_6 can be obtained from pull up ratio (PR) given as

$$PR = \frac{\frac{W_4}{L_4}}{\frac{W_6}{L_6}} = \frac{W_4}{W_6}, \tag{2}$$

PR should be selected less than 1.8 to ensure read stability.

After sizing is done we have:

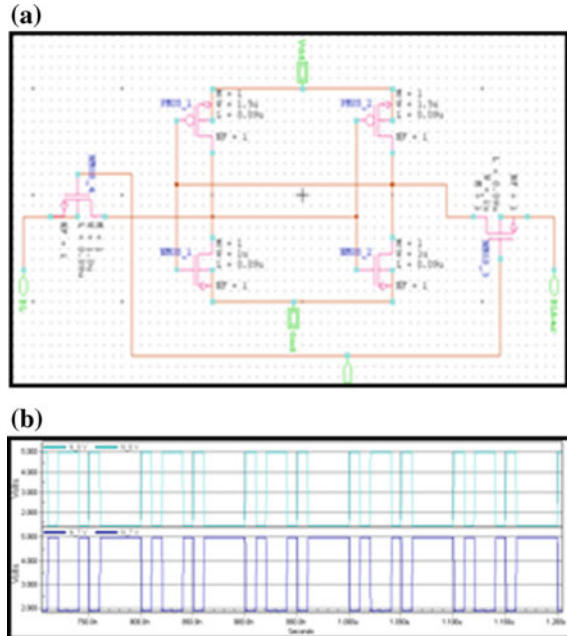
$$W_2 = W_4 = W_5 = W_6 = \text{Minimum layout width} = 1 \mu\text{m}$$

$$W_1 = W_3 = 1.5W_2 = 1.5 \mu\text{m}.$$

After the transistor sizing, the basic 6T CELL was designed.

Decoder is designed with basic NAND and NOR gates. To design a synchronous SRAM the decoder is controlled by a clock. During positive edge of the clock, the address to be read into the decoders is allowed and correct bit line and word line are enabled. The pre-charge input is asserted which turns on all the pMOS devices and all the outputs of the decoder are set high (to V_{DD}). After pre-charging, the pMOS devices are turned off. Since the charge will be stored in capacitors the outputs will be at logic high. Now the inputs are applied on address line, the corresponding nMOS devices will be turned on and the charge on the capacitance on that line will be discharged to ground. Thus all except one line will go to ground (logic 0).

Fig. 3 Design of 6T bit cell.
a Schematic of 6T SRAM cell. **b** Output of the cell



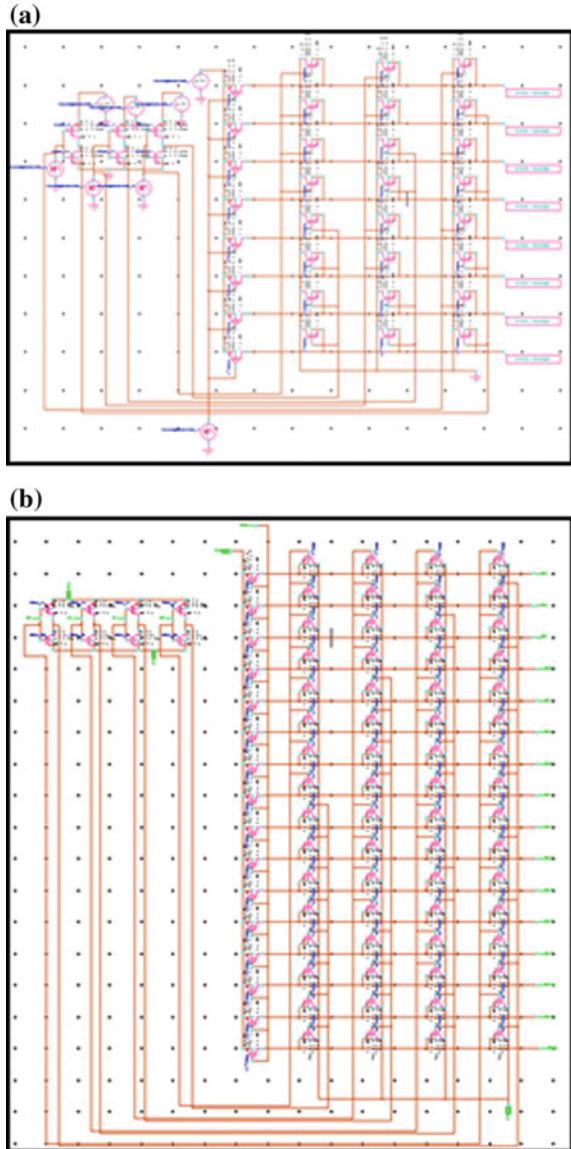
The line which remains high will be the decoded line. For 16×8 SRAM, a 3–8 column decoder and a 4–16 row decoder are designed.

For writing the data in cell, the corresponding cell is selected by a proper combination of row and column decoder address lines. The working of the complete cell is well-known and available in the literature [5].

A voltage mode sense amplifier circuit has been chosen for design purpose. Sense amplifier is basically used for reading the value stored in the cell. The two pMOS transistors form a current mirror and carry same reference current from the voltage source. The SE (sense enable) input is kept high for sensing operation which turns on M3 which provides conducting path to ground. Depending upon the bit stored in cell, the values of BL and BLB are determined which turn on/off M1 and M2. If the BLB voltage finds a conducting path to ground then the output is asserted as 1 via an inverter and in the other case if BLB remains pulled up then the output is determined as 0. Thus the value of BL which is actually the bit stored in cell is asserted at output.

Instances of different circuits were created on the tool so that they can be reused. All the instances were now arranged appropriately to form the required array and connections were established according to the functionality required. The 6T cells were arranged in a manner of 8 columns and 16 rows. The row input to these cells was the WL from the row decoder and column inputs were the column decoder outputs. Each and every cell has two I/O ports BL and BLB, which are connected to sense amplifier and write circuitry. Also these are connected to column decoder output. The final structure is tested and results were obtained as discussed in the next section.

Fig. 4 Design of row and column decoders.
a Schematic of column decoder. **b** Schematic of row decoder



Result and Discussions

All the modules were designed in Cadence EDA and simulations were performed. Figure 3a, b show the bit cell and corresponding output.

Fig. 5 Schematic of sense amplifier circuitry

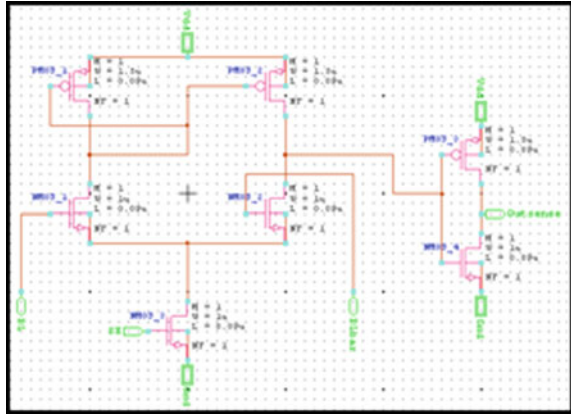
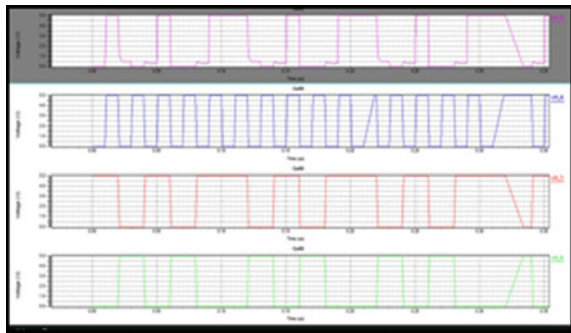


Fig. 6 Output waveform from sense amplifier circuitry



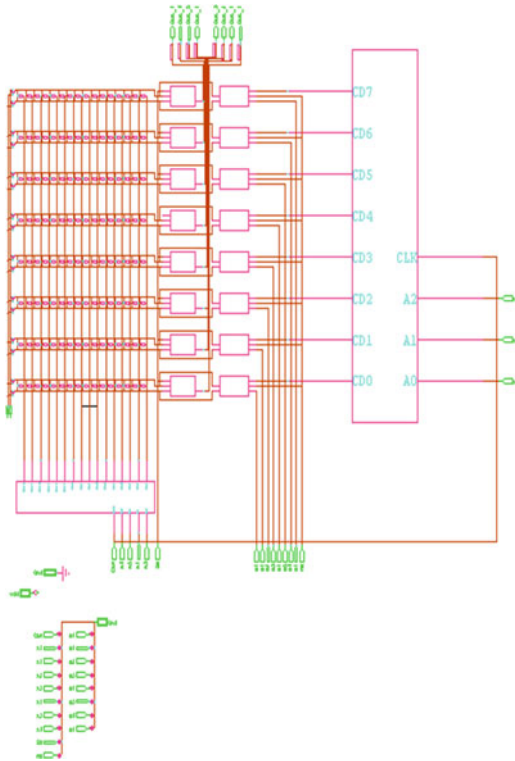
Similarly row and column decoders were designed and tested as shown in Fig. 4. A 3 input–8 output circuit is selected as a column decoder. A NOR-based circuit has been chosen for design purpose.

In the design process, pMOS transistors are used to act as pre-charge devices. The gates of these pMOS transistors are connected to a level triggered clock pulse. Clock pulse used is synchronous and all the operations are clock dependent. A set of 24 NMOS transistors are used to design the NOR-based circuit. A clock is connected to the gates of the pMOS transistors. This enables the pre-charging operation whenever the clock is high. Row decoder is designed with the similar approach as of column decoder.

The sense amplifier is one of the most important components of semiconductor memories used to sense stored data. It is a part of read circuitry which is used when data are read from the chip. In the present case, voltage sensing has been used. The designed circuit is shown in Fig. 5 and the corresponding output is shown in Fig. 6.

Starting from the bottom the waveforms are in order of BL, BLB, SE (sense enable) and output. The BL is taken as 0011001100 for 1 cycle in which analysis has to be done. As BLB is the complement of BL, thus, the input provided is

Fig. 7 128-bit SRAM array



1100110011. The SE input is used to initiate the sensing operation. Whenever the $SE = 1$ the NMOS₃ is ON and provides conducting path to ground. In this analysis, the $SE = 0101010101$, hence, the output is obtained for logic 1 signal at SE. For the first $SE = 1$, $BL = 0$ and $BLB = 1$, therefore the output is a high pulse giving the state as of BLB as discussed above.

And finally the write circuitry is being implemented.

The schematic and instances of all the components, i.e. 6T cell, row decoder, column decoder, sense amplifier and write circuitry are designed in a single schematic editor file and compiled into a single cell and required connections are made. The common terminals of the modules such as BL, BLB and word line (WL) are connected together and provided with appropriate voltage levels. The ground and the power supply V_{DD} and provide 0 and 1, respectively, to all the modules are made as global ports and not shown via wired connections which improve clarity of the schematic drawn.

The complete compiled SRAM array is shown in Fig. 7. The inputs to the array are taken out separately to facilitate clear understanding of the array as shown in the extreme left of the array. These are the row and column decoder inputs, clock, write

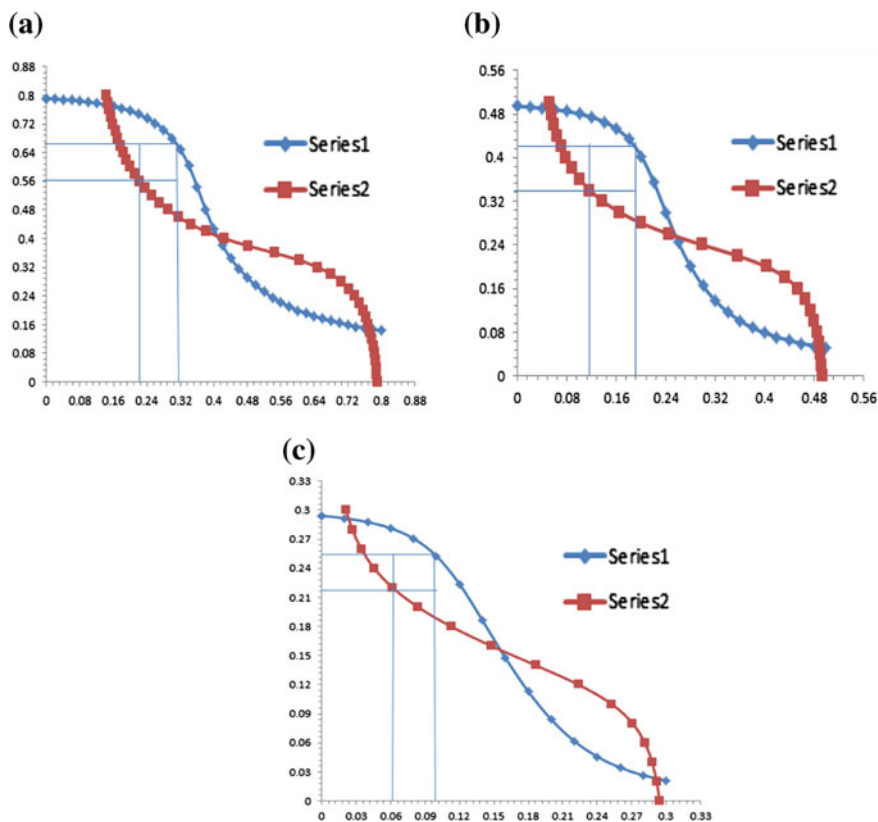


Fig. 8 a SNM = 96 mV at $V_{dd} = 0.8$ V. b SNM = 80 mV at $V_{dd} = 0.5$ V. c SNM = 36 mV at $V_{dd} = 0.3$ V

enable (WE), sense enable (SE) and various data inputs (D_0 – D_7). The user can change these inputs as desired to store his data or information.

Static noise margin (SNM) is the parameter through which one can measure the stability of the SRAM cell. SNM of SRAM is defined as minimum amount of noise voltage present on the storing nodes of SRAM required to flip the state of cell. SNM is being calculated for single-bit SRAM cell at different power supply voltages and shown in Fig. 8.

Thus it can be seen that at reduced voltages the static noise margin deteriorates. So the bit cell design becomes one of the main design parameters for improving the SNM at reduced voltages. With the advancement in technology, various upcoming devices such as FinFET, FlexFET, GAA (gate all around) MOS, etc., can be used for the memory design so as to improve the SNM of SRAM array.

Conclusions

The main aim of this work is to design a 16×8 SRAM array. The main aspect of the approach is to design every single functional block keeping the layout feasibility in mind. The main functional blocks designed are bit cell, row and column decoders, preconditioning circuit, clock tree and flip-flops. The key design features include a cell matrix of 16×8 , avoiding usage of fully complementary CMOS gates, equalizing the voltage levels between bit lines using pass transistors for faster clocking, keeping the default pre-charge level of the word lines to one. The access times obtained are within the desired limits.

References

1. Kang, S., Leblebici, Y.: CMOS Digital Integrated Circuits. McGraw-Hill, New York (1999)
2. Daya, B., Jiang, S., Nowak, P., Sharief, J.: Synchronous 16×8 SRAM design. Electrical Engineering Department, University of Florida
3. Khatwal, R., Jain, M.K.: An efficient synchronous static memory design for embedded system. *Int. J. Comput. Appl.* **66**(18), 975–8887 (2013)
4. Gadhe, A., Shirode, U.: Read stability and Write ability analysis of different SRAM cell structures. *Int. J. Eng. Res. Appl. (IJERA)* **3**(1), 1073–1078 (2013)
5. Dhanumjaya1, K., Sudha, M., Giri Prasad, M.N., Padmaraju, K.: Cell stability analysis of conventional 6t dynamic 8t SRAM Cell in 45 nm technology. *Int. J. VLSI Des. Commun. Syst. (VLSICS)* **3**(2), 41–51 (2012)
6. Wann, C., Wong, R., Frank, D.J.: SRAM cell Design for stability methodology. IBM Semiconductor Research and Development Center (SRDC)
7. Pavlov, A.S.: Design and Test of Embedded SRAMs. University of Waterloo
8. Rabaey, J., Chandrakasan, A., Nicoloc, B.: Digital Integrated Circuits: A Design Prospective. Prentice Hall, India (2003)
9. Sharma, A.: Advanced Semiconductor Memories: Architectures, Design and Applications. Wiley Inter Science, USA (2003)
10. Alorda, B., Torrens, G., Bota, S., Segura, J.: Static-Noise Margin Analysis during Read Operation of 6T SRAM Cells University de les Illes Balears, Departamento de Fisica, Cra. Valldemossa, 07071 Palma de Mallorca, Spain

A Voltage-Mode Nonlinear-Synapse Neural Circuit for Bi-partitioning of Graphs

Mohd Samar Ansari

Abstract An NP-complete problem that finds applications in various fields in engineering and sciences is the graph partitioning problem. This paper presents a novel recurrent neural network, which makes use of nonlinearities in the feedback interconnections, for bipartitioning a given planar graph of n vertices (nodes). The scheme comprises of n neurons and n^2 synaptic interconnection weights, as compared to the n^2 neurons and n^4 synapses required by conventional Hopfield network approaches. PSPICE simulation results serve as verification for the proposed theory.

Keywords ANN · Graphs · Neural network · Nonlinear feedback · Partitioning

Introduction

The graph partitioning problem is defined as a mathematical operation on a graphical representation of (any) data, having n nodes (or vertices) connected by e edges, i.e., $G = (n, e)$, thereby resulting in smaller individual components having some predefined characteristics. Graph partitioning problems are categorized as NP-hard ones [1], with solutions generally obtained using heuristics and approximation techniques. However, one particular class of graph partitioning problems, viz. the uniform partitioning has been shown to be NP-complete [1]. Pertinent engineering and scientific avenues where graph partitioning is typically employed include complex computing, VLSI design, and process scheduling in multiprocessor environments [2]. In the contemporary context, graph partitioning is used in clustering and clique identification in social [3], and biological [4] networks.

Since uniform graph partitioning is an NP-complete problem, even the best reported algorithms exhibit run times, which are exponential functions of $|n|$. Two well-known methods for partitioning are the Kernighan–Lin (KL) algorithm

M.S. Ansari (✉)

Department of Electronics Engineering, Aligarh Muslim University, Aligarh, India
e-mail: mdsamar@gmail.com

© Springer India 2016

N. Afzalpulkar et al. (eds.), *Proceedings of the International Conference on Recent Cognizance in Wireless Communication & Image Processing*,
DOI 10.1007/978-81-322-2638-3_17

151

(a $O(n^2 \log[n])$ heuristic), and Fiduccia–Mattheyses (FM) algorithm which employ local search methodologies [5, 6]. Other variants include global approaches, such as the spectral partitioning, and genetic algorithms [7].

Another approach to partition graphs, in solution times short enough for real-time applications, is to employ the massively parallel processing inherent in artificial neural networks (ANNs) [2, 8, 9]. The proposed work is one such attempt and presents a graph partitioning recurrent neural network with nonlinearity in the synapses. For a test graph having n nodes, Hopfield network-based solutions require n^2 neurons and require n^4 linear synaptic interconnections typically implemented with resistors. The present work accomplishes the same task using only n neurons and n^2 comparators.

The paper is organized as follows: A new nonlinear feedback neural circuit graph bipartitioning is presented in section “[Proposed Graph Partitioning ANN](#).” The associated Lyapunov (or ‘energy’) function is also discussed. Section “[Simulation Results and VLSI Implementation Issues](#)” contains results of PSPICE simulations for the proposed circuit for partitioning two sample graphs. Comparisons with other methods are drawn in section “[Comparison with Existing Works](#)”. Concluding remarks appear in section “[Conclusion](#)”.

Proposed Graph Partitioning ANN

The Hopfield neural network (HNN), working on the principle of dissipative dynamics of neurons, was employed with mixed results in a large number of combinatorial optimization problems [10]. However, the HNN when applied to solve graph-related problems such as vertex coloring and partitioning exhibited two major shortcomings—first, convergence to local minima (rather than the global minimum) and second, several parameters need to be set.

Figure 1a presents the i th neuron of the proposed voltage-mode neural circuit for graph coloring. The output of the i th neuron, V_i , corresponds to a voltage label (indicating that the node belongs to a particular group/cluster) assigned to the i th node. Each node of the graph is represented by a single neuron, which is the basic element of ANN. Thus the number of neurons is equal to the number of nodes (n). Each neuron in the proposed network is implemented by $(n-1)$ comparators and an amplifier (providing the ‘activation function’ of the neuron). Output of individual neurons is fed back to all other neurons through unipolar comparators thereby making the feedback nonlinear whereas linear recurrence is present in HNNs. The architecture having comparators as synapses has also been applied to other problems like graph coloring [11, 12], and ranking of numbers [12, 13]. However, only the feedback connections that caused repelling actions amongst the neuronal states are used for graph coloring, whereas for the present problem of graph partitioning, attractive connections have also been introduced. The switch over from repelling to

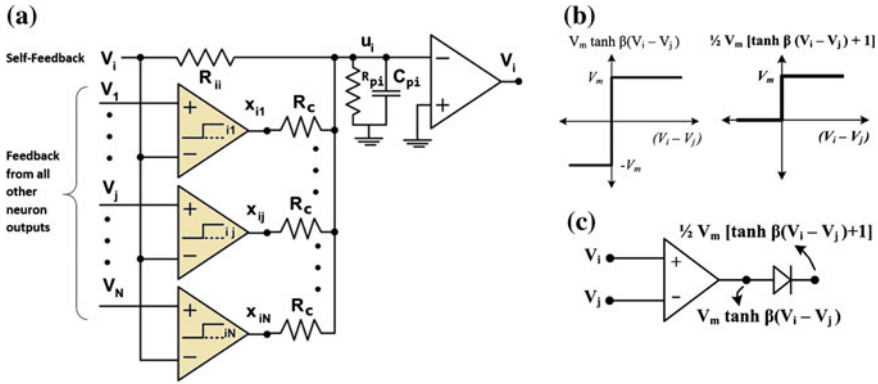


Fig. 1 i th neuron of the proposed circuit for bipartitioning a given graph. **a** i th neuron. **b** Transfer characteristics of bipolar and unipolar comparators. **c** Obtaining unipolar comparator characteristics using a bipolar comparator

attractive interconnection is achieved by interchanging the input terminals of the comparator through which feedback is being given. As will be evident later, this inverts the corresponding term in the energy function of the proposed network. In order to map to the graph partitioning problem, the neurons corresponding to those nodes of the graph which are connected through an edge are provided with an attractive feedback connection. Neurons corresponding to unconnected nodes in the graph are interconnected through a repelling feedback connection.

In Fig. 1a, C_{pi} and R_{pi} denote the parasitics offered by the i th neuron, u_i represents the neuron state, and R_{ii} denotes self-feedback for the i th neuron. Idealized characteristics of bipolar and unipolar comparators are shown in Fig. 1b. One possible circuit realization for obtaining the unipolar transfer characteristics of Fig. 1b is presented in Fig. 1c, which shows a diode used in conjunction with an opamp. The self-feedback resistance R_{ii} can be calculated as $R_{ii} = \frac{R_c}{n}$ where R_c is a constant resistance. Since the exact output voltages of the neurons are immaterial and only grouping/clustering of nodes is to be identified, there is no unique value of R_c and it can be taken as any convenient one. From Fig. 1a, x_{ij} , which is the comparator output, may be obtained as

$$X_{ij} = V_m/2 [\tanh \beta(V_j - V_i) + 1] \tag{1}$$

where β is the open-loop gain of the comparator (practically very high) and V_m is the saturation voltage level of the comparator output. Node equation at u_i gives the equation of motion of the i th neuron in the state space as

$$x_{ij} = \frac{V_m}{2} [\tanh \beta(V_j - V_i) + 1] \tag{2}$$

$$C_i \frac{du_i}{dt} = \sum_{\substack{j=1 \\ j \neq i}}^N \frac{x_{ij}}{kR_c} + \frac{V_i}{R_{ii}} - \frac{u_i}{R_i} \quad \text{where} \quad \frac{1}{R_i} = \sum_{\substack{j=1 \\ j \neq i}}^N \frac{1}{R_{ij}} + \frac{1}{R_{ii}} + \frac{1}{R_{pi}} \quad (3)$$

and $k = -1$ if nodes j and i are connected, else $k = +1$. Using (1) in (2), we have

$$C_i \frac{du_i}{dt} = \sum_{\substack{j=1 \\ j \neq i}}^N \frac{V_m}{2kR_c} [\tanh \beta (V_j - V_i) + 1] + \frac{V_i}{R_{ii}} - \frac{d_i}{R_i} \quad (4)$$

Also, for dynamical systems based on Hopfield approach, the following holds [12]

$$C_i = \frac{du_i}{dt} = - \frac{dE}{dV_i} \quad (5)$$

Therefore, the energy function E of the network in Fig. 1a can be given as

$$E = \frac{1}{2} \sum_{i=1}^N \frac{V_i^2}{2R_{ii}} - \frac{V_m}{4k\beta R_c} \sum_{i=1}^N \sum_{\substack{j=1 \\ j \neq i}}^N \ln \cosh(\beta(V_j - V_i)) - \frac{V_m}{2kR_c} \sum_{i=1}^N \sum_{\substack{j=1 \\ j \neq i}}^N V_i + \sum_{i=1}^N \frac{1}{R_i} \int_0^{V_i} u_i dV \quad (6)$$

If the opamps have a high value of β , then the last term in (6) is rendered negligible. The first term on the right hand side of (6) is quadratic which tries to minimize the number of labels assigned. The transcendental second term will have a negative or positive sign depending upon whether the j th node is connected to the i th node or not. For the case when the two nodes are joined by an edge, a positive term ensures that the two nodes attract (thereby belonging to the same partition). Therefore, E will be minimized if second term is maximized. This happens when the voltages corresponding to all unconnected nodes are far away from each other and voltages corresponding to all connected nodes are in proximity. The last (third) term eliminates all minima for which node voltages are negative.

Simulation Results and VLSI Implementation Issues

To ascertain the validity of the proposed approach, PSPICE simulations were performed for two 8-node graphs as shown in Fig. 2a, d. Digits on the nodes correspond to neuron numbers used for simulation. Result of PSPICE simulations

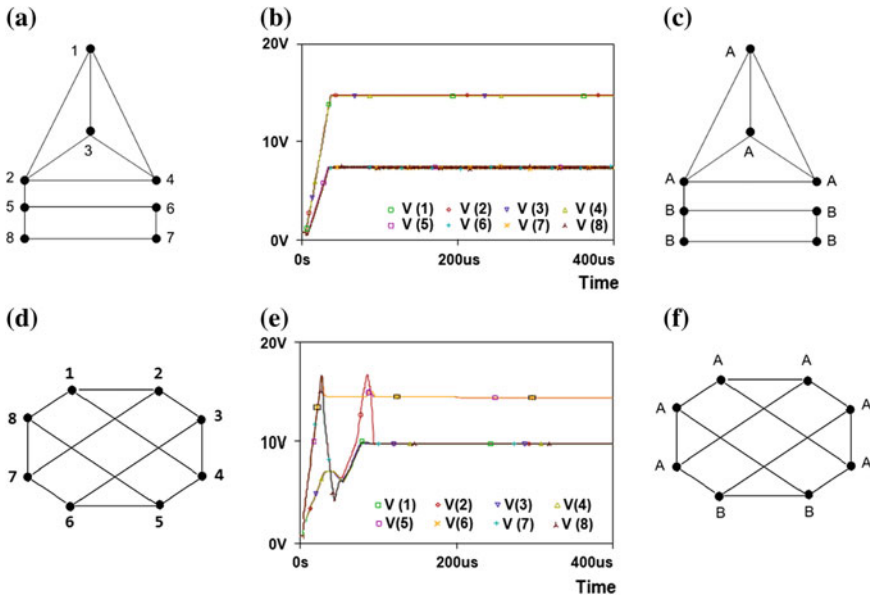


Fig. 2 a The first 8-node graph b SPICE simulation output after partitioning c Partitioned first 8-node graph d The second 8-node graph e SPICE simulation output after partitioning f Partitioned second 8-node graph

for the two graphs are presented in in Fig. 2b, e. It can be seen that the proposed network assigns voltage levels to all the 8 nodes, and the voltage assignment leads to two broad classes of nodes. Figure 2c, f show the assignment of labels with nodes ‘A’ and ‘B’ assigned to different partitions. PSPICE simulations were carried out using CMOS LMC-7101A opamp. The value of β for this opamp was estimated at 1.08×10^4 . The value of R_c was set at 10 K Ω .

The circuit is amenable for CMOS integration by virtue of the use of opamps and resistances only. However, floating resistors could be replaced by MOSFET-based resistances for fabrication compatibility [14]. A better alternative for reducing chip area is the use of transconductance elements, having voltage inputs and a current output, in the feedback paths [15]. Conveying of the synaptic signals as currents reduces the overall number of resistances drastically and makes the circuit favorable from the viewpoint of actual VLSI implementation.

Comparison with Existing Works

The techniques proposed for min-cut bipartitioning can broadly be divided into software and hardware ones. While the former utilizes algorithms and/or heuristics which are run on a digital processor, the latter generally are custom-made circuits.

Among the software methods, Soper, Wilshaw, and Cross gave an evolutionary search and multilevel optimization approach [16]. Applicability for real-time applications is in doubt since the algorithm needs to be run for at least 5000–10,000 trials. Ver-belen's et al. partitioning algorithm are suited specifically for the purpose of cloud computing applications, with runtimes of hundreds/thousands of milliseconds [17]. Hager, Phan, and Zhang presented an exact algorithm for graph partitioning which converted the problem into a quadratic programming problem. However, the runtimes for all test cases reported were in hundreds of milliseconds [18].

Among the hardware circuit-based approaches, Pain, Oliveira, and Goddard gave a technique to first construct a 'coarse' graph from the graph to be cut, which was partitioned. Extrapolation was then applied to obtain the final solution. However, the algorithm suffered from unpredictable run times with most test runs going into tens of seconds [8]. Merida-Casermeyro and Lopez-Rodriguez employed multivalued feedback neural networks for partitioning. Although the technique outperformed most known algorithms at the time in terms of speed, the run times were still in tens of milliseconds [19]. The proposed neural network has the following advantages over its predecessor partitioners. First, the circuit has lesser complexity than HNN-based variants. Second, the convergence time as estimated from PSPICE simulations, is in microseconds, as compared to the best reported millisecond results.

Conclusion

A nonlinear-synapse neural network for graph partitioning is presented. Test results of PSPICE simulation for two chosen 8-node graphs are presented. The proposed circuit was found to correctly partition the chosen graphs. The technique is suitable for VLSI implementation as the ubiquitous operational amplifier is employed to emulate the functionality of the neurons and the nonlinear synapses.

References

1. Arora, S., Rao, S., Vazirani, U.: Expander flows, geometric embeddings and graph partitioning. *J. ACM*, **56**(5), 1–5:37 (2009)
2. Du, K.L.: Clustering: a neural network approach. *Neural Networks* **23**(1), 89–107 (2010)
3. Mandala, S.R., Kumara, S.R.T., Rao, C.R., Albert, R.: Clustering social networks using ant colony optimization. *Oper. Res. Int. J.* **13**(1), 47–65 (2013)
4. Mitra, M., Carvunis, A.-R., Ramesh, S.K., Ideker, T.: Integrative approaches for finding modular structure in biological networks. *Nat. Rev. Genet.* **14**(10), 719–732 (2013)
5. Kernighan, B.W., Lin, S.: An efficient heuristic procedure for partitioning graphs. *Bell Sys. Tech. J.* **49**(2), 291–307 (1970)

6. Fiduccia, C.M., Mattheyses, R.M.: A linear-time heuristic for improving network partitions. *J. ACM* **175**–181 (1982)
7. Talbi, E.-G., Bessiere, P.: A parallel genetic algorithm for the graph partitioning problem. In: *Proceedings of 5th International Conference on Supercomputing, ICS'91*, pp. 312–320. ACM, USA (1991)
8. Pain, C.C., De Oliveira, C.R.E., Goddard, A.J.H.: A neural network graph partitioning procedure for grid-based domain decomposition. *Int. J. Num. Methods Eng.* **44**(5), 593–613 (1999)
9. Yih J.-S. and Mazumder P. A neural network design for circuit partitioning. *IEEE Trans. Comput.-Aided Des. Int. Cir. Sys.* **9**(12), 1265–1271 (1990)
10. Smith, K.A.: Neural networks for combinatorial optimization: a review of more than a decade of research. *INFORMS J. Comput.* **11**(1), 15–34 (1999)
11. Ansari, M.S.: The graph coloring problem—review of algorithms & neural networks and a new proposal. In: *International Conference on Multimedia, Signal Processing and Communication Technologies (IMPACT)*, pp. 310–314. India (2013)
12. Ansari, M.S., *Non-Linear Feedback Neural Networks*. *Studies in Computational Intelligence*, vol. 508. Springer (2013)
13. Jayadeva, Rahman S.A. A neural network with $O(N)$ neurons for ranking N numbers in $O(1/N)$ time. *IEEE Tran. Circ. Sys. I: Regul. Pap.* **51**(10):2044–2051 (2004)
14. Senani, R.: Realisation of linear voltage-controlled resistance in floating form. *Electron. Lett.* **30**(23), 1909–1911 (1994)
15. Ansari, M.S.: Employing differential voltage current conveyor in graph coloring applications. In: *International Conference on Power, Control and Embedded Systems (ICPCES)*, pp. 1–3 (2010)
16. Soper, A.J., Walshaw, C., Cross, M.: A combined evolutionary search and multilevel optimisation approach to graph-partitioning. *J. Global Optim.* **29**(2), 225–241 (2004)
17. Verbelen, T., Stevens, T., De Turck, F., Dhoedt, B.: Graph partitioning algorithms for optimizing software deployment in mobile cloud computing. *Future Gener. Comput. Syst.* **29**(2), 451–459 (2013)
18. Hager, W.W., Phan, D.T., Zhang, H.: An exact algorithm for graph partitioning. *Math. Prog.* **137**(1–2), 531–556 (2013)
19. Mérida-Casermeyro, E., López-Rodríguez, D.: Graph partitioning via recurrent multivalued neural networks. In: *Computational Intelligence and Bioinspired Systems*, pp. 1149–1156. Springer (2005)

CNFET-Based Resistive Sensor Interface with Voltage/Current-Mode Readouts

Mohd Samar Ansari and S.K. Tripathi

Abstract Integrated sensors, which are frequently electronic and occasionally electromechanical, can be placed in the broader set of mixed-signal systems where the interface circuitry is analog in nature and the processing is usually performed in a digital environment. Existing sensor interface analog circuitry is mostly based upon the ubiquitous MOSFET technology. Moreover, the lower transconductance gain of the MOSFET restricts the bandwidth of such CMOS sensor interface circuits. As the development over the present resistive sensor interfacing circuits, a substitute using CNFET has been presented in which a buffered-output current conveyor (CC-II) is employed to realize an electronic interface for resistive sensors. The circuit gives voltage-mode (VM) as well as current-mode (CM) outputs, and may be used in various resistive sensing applications like photocell sensor, strain gauge sensor, position sensor, temperature sensor, etc. SPICE simulations with CNFET 32 nm parameters are incorporated to authorize the design.

Keywords Carbon nanotube field-effect transistor • Current conveyor • CMOS • Sensor interface

Introduction

The benefit of integrated circuit-based sensing and signal conditioning is the calibration through on-chip techniques. The overall performance of a system can be improved effectively and cost can be reduced by inclusion of the functions of

M.S. Ansari (✉)

Department of Electronics Engineering, Aligarh Muslim University, Aligarh, India
e-mail: mdsamar@gmail.com; msansari.ece@mnit.ac.in

S.K. Tripathi

Department of Electronics and Communication Engineering,
Malaviya National Institute of Technology, Jaipur, India
e-mail: shailendra.amu@gmail.com

© Springer India 2016

N. Afzalpulkar et al. (eds.), *Proceedings of the International Conference on Recent Cognizance in Wireless Communication & Image Processing*, DOI 10.1007/978-81-322-2638-3_18

159

sensing block, actuators, and electronic interfacing circuits in single structure. Wherever technology allows, the overall system may be realized on a common integrated circuit or chip [11]. In smart systems, the functions combine sensing and signal conditioning for a dedicated application [15].

Boosting the performance and reliability, with reducing the cost of electronic circuits through better integration, are well-known procedures for semiconductor industry. The integration of electronics with sensors assures to transform next generation smart systems and force new applications. A sensor with interface circuit on same board has many benefits [16]. For example, the device based on integrated circuit takes advantage of temperature measurement to more accurately track the temperature of the sensing element and recovers other effects over the wide temperature range. Also, reducing the count of internal connections, the characteristics, and reliability of sensor systems with electronic interface is better than a discrete sensor and measuring circuit combination [4].

Over the past four decades number of current-mode building blocks, such as current conveyors (CCs), operational transconductance amplifiers (OTAs), and current feedback operational amplifier (CFOA) have been developed [1, 3, 12]. However, among these blocks the current conveyors have proved to be a functionally flexible and versatile CM active element. The current-mode blocks have attained major attention due to their benefits compared to voltage-mode circuits in account of wider bandwidth of signal, greater linearity, simpler circuitry, and lower power requirement. The current conveyor-II (CC-II) has initiated extensive exploit in range of realizations of active elements and CM circuits [2, 6, 10]. It is attempted here to explore CM solutions for the task of designing an analog interfacing circuit.

The paper is organized as follows. Section “[Carbon Nanotube Field Effect Transistor](#)” deals with a brief overview of the CNFET. The fundamental design aspects of current conveyor-based resistive sensor interface have been illustrated in Section “[Circuit Design](#)”. Performance and results of the proposed circuit have been elaborated in Section “[Simulation Results](#)”, and finally Section “[Conclusion](#)” concludes the paper.

Carbon Nanotube Field-Effect Transistor

Since the discovery of carbon nanotubes (CNTs) in 1991, various developments have been made in various engineering and scientific applications [7–9, 13]. The CNT, which essentially is a rolled sheet of graphene, which has carrier transport that is nearly ballistic across several hundred nanometers, and has been used to boost the channel conductivity in MOSFETs, causing the growth of carbon nanotube field-effect transistor (CNFET) [5]. Figure 1a shows the top view of CNFET with three nanotubes. However, the structure remains the same as in the case of a conventional MOSFET, albeit with the inclusion of nanotubes in the channel region below the gate polysilicon. Various techniques have been developed for improving the performance of CNT-based transistor such as scaling of the

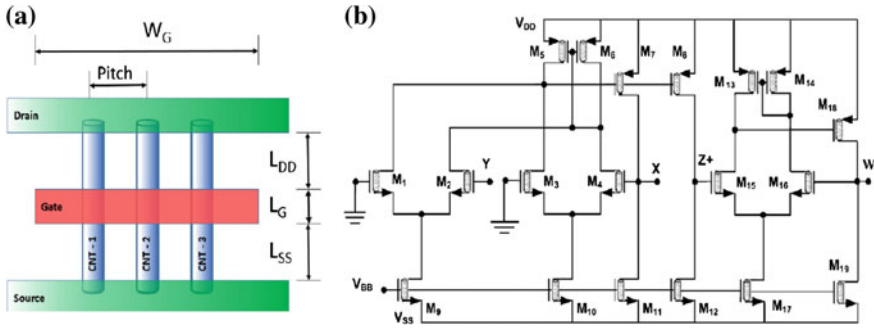


Fig. 1 **a** Top view of a CNFET with three carbon nanotubes **b** CNFET-based buffered output CC-II

nanotube channel, integration of high-gate dielectric materials, use of superior source/drain contacts, and implementation of the self-aligned techniques [9, 14]. These recent developments have paved the way for the CNFET to move from a theoretical concept to an actual reality.

Circuit Design

The second generation current conveyor (CC-II) is a very versatile analog building block and widely used for voltage and/or current-mode circuit design for various assorted applications [6, 10, 12, 16]. The symbol of CC-II is depicted in Fig. 2a with an additional voltage buffer output. Additionally, the port relations are illustrated in Fig. 2b. Figure 2c shows the current conveyor-based resistive sensor interface circuit. It uses two resistors R_1 and R_2 for setting the proper voltage reference at the high impedance Y-terminal. The resistive element of a sensor can be employed to the low impedance terminal X. The change in resistance of the sensor has an effect on the current I_{SENS} , which can be able to deliberate from Z+ node. The extra stage of

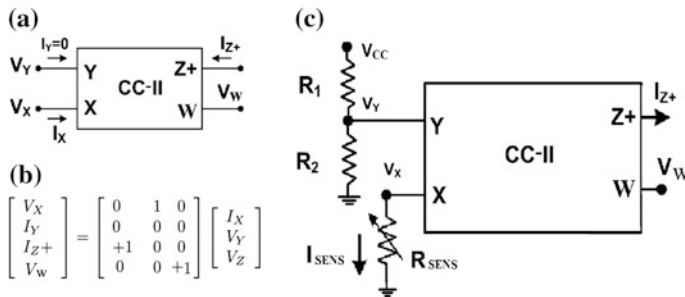


Fig. 2 **a** Symbol CC-II **b** Characteristic matrix **c** CC-II-based circuit for resistive sensor interface

buffer is used to obtain equivalent voltage output as illustrated in the transistor level implementation of CC-II in Fig. 1b. The Eqs. (1) through (5) give the various node voltages and branch currents of the proposed resistive sensor interface circuit using the properties of building block given in Fig. 2b. Moreover, the CNFET technology is expected to provide reduced power consumption, higher reliability, and space reduction for very low power applications [7].

$$V_Y = \frac{R_2 V_{CC}}{R_1 + R_2} \quad (1)$$

$$I_{SENS} = \frac{V_X}{R_{SENS}} \text{ where, } V_X = V_Y \quad (2)$$

$$I_{SENS} = \frac{R_2 V_{CC}}{(R_1 + R_2) R_{SENS}} \quad (3)$$

$$I_Z = \frac{R_2 V_{CC}}{(R_1 + R_2) R_{SENS}} A_s, I_Z + = I_X \quad (4)$$

$$V_W = \frac{R_2 V_{CC} R_Z}{(R_1 + R_2) R_{SENS}} A_s, V_W = V_Z \quad (5)$$

Simulation Results

The resistive sensor interface block presented in Fig. 2c has been analyzed and simulated to examine the relation between resistance (R_{SENS}) and electrical outputs of interface circuit, i.e., I_{SENS} and V_W as predicted from (3) and (5), I_{SENS} as well as V_W decreases with increase in R_{SENS} . Figure 3 depicts the simulation responses

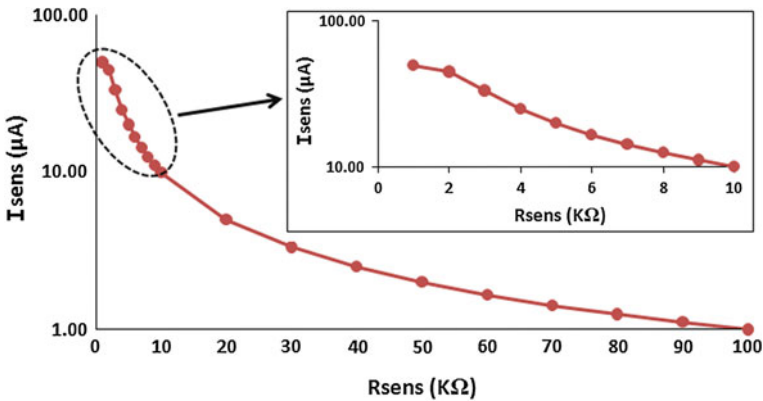


Fig. 3 Current-mode response of resistive sensor interface, I_{SENS} versus R_{SENS}

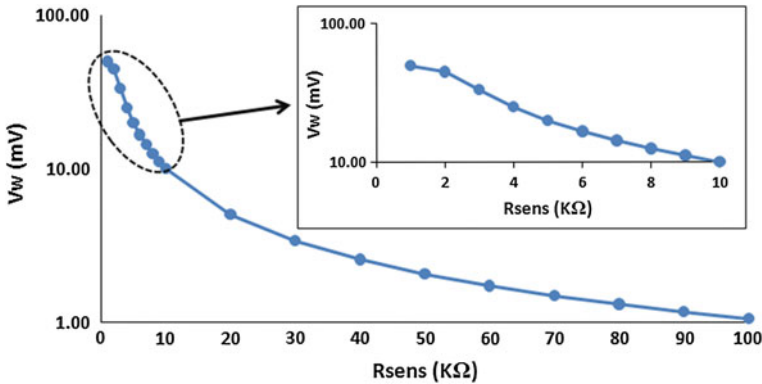


Fig. 4 Voltage-mode response of resistive sensor interface, V_W versus R_{SENS}

between R_{sens} and I_{SENS} for the range of R_{sens} from 1–100 K. The passive components of circuit are taken as $R_1 = 8$ K and $R_2 = 1$ K. An additional benefit of the proposed circuit is that, it also offers the voltage-mode output. Additionally, Fig. 4 presents the similar effect of R_{SENS} for output voltage (V_W). Some important parameters of CNFET which have been used in the design are given in Table 1a. Also, various specific applications of resistive sensors are taken into the consideration as shown in Table 1b.

Table 1 a Design parameters for CNFET-based CC-II b Some specific applications of resistive sensors

(a)		(b)		
Parameters	Value	Resistive device	Application	Resistance range
Oxide thickness (T_{ox})	4 nm	Stain gauge	Force sensor	2.1–3.5 KΩ
Dielectric constant (K_{ox})	16	Photo cell	Light sensor	30–60 KΩ
Power supply	±0.9 V	Potentiometer	Position sensor	Few KΩ–Few MΩ
Chirality of the tube (n_1, n_2)	19,0	Resistive bend pads	Collision sensor	10–35 KΩ
Physical channel length (L_{ch})	32 nm			
No. of tubes in the device	6			
Pitch (S)	20 nm			
Diameter of CNT (D_{CNT})	1.5 nm			

Conclusion

The present era of sensor technology requires interface circuits to have minuscule chip area, ultra low power consumption, and possibility of integration on a monolithic substrate. In this work, a CNFET-based design is presented for sensing applications to meet the challenges and specifications of current scenario. A current conveyor-based resistive sensor interface, based on the carbon nanotube FET, was proposed. The range of amend in corresponding resistance of the sensor block under observation (R_{SENS}) has been taken as 1–100 K Ω to target several specific applications. Moreover, the proposed circuit has the benefit of simultaneous voltage and current-mode outputs. The simulation results were present to confirm the validity of the proposal. These circuits can be utilized as an opening point to design futuristic low voltage, low power nano-electronic circuits capable of operating in voltage-, current-, and mixed-mode regimes.

References

1. Ansari, M.S., Khan, I.A.: A generic canonical OTA-C universal filter. *J. Act. Passive Electron. Devices* **9**, 1 (2014)
2. Bhaskar, D., Abdalla, K.K., Senani, R.: New SCRO with explicit current-mode output using two CCs and grounded capacitors. *Turkish J. Electr. Eng. Comput. Sci.* **19**(2), 235–242 (2011)
3. Bhaskar, D., Senani, R., Singh, A.: Linear sinusoidal VCOs: new configurations using current-feedback-op-amps. *Int. J. Electron.* **97**(3), 263–272 (2010)
4. De Marcellis, A., and Ferri, G.: *Analog Circuits and Systems for Voltage-Mode and Current-Mode Sensor Interfacing Applications*. Springer (2011)
5. Deng, J., Wong, H.-S.: A compact spice model for carbon-nanotube field-effect transistors including nonidealities and its application part I: model of the intrinsic channel region. *IEEE Trans. Electron. Devices* **54**(12), 3186–3194 (2007)
6. Ferri, G., Stornelli, V., Fragnoli, M.: An integrated improved CCII topology for resistive sensor application. *Analog Int. Circ. Sig. Process.* **48**(3), 247–250 (2006)
7. Javey, A., Guo, J., Wang, Q., Lundstrom, M., Dai, H.: Ballistic carbon nanotube field-effect transistors. *Nature* **424**(6949), 654–657 (2003)
8. Jin, C., Suenaga, K., Iijima, S.: Plumbing carbon nanotubes. *Nat. Nanotechnol.* **3**(1), 17–21 (2007)
9. Kang, S.J., Kocabas, C., Ozel, T., Shim, M., Pimparkar, N., Alam, M.A., Rotkin, S.V., Rogers, J.A.: High-performance electronics using dense, perfectly aligned arrays of single-walled CNTs. *Nat. Nanotechnol.* **2**(4), 230–236 (2007)
10. Khan, I.A., Samsim, M.T.: A novel impedance multiplier using low voltage digitally controlled CCII In GCC Conference and Exhibition (GCC), 2011 IEEE, pp. 331–334. IEEE (2011)
11. Kraver, K.L., Guthaus, M.R., Strong, T.D., Bird, P.L., Cha, G.S., Hold, W., Brown, R.B.: A mixed-signal sensor interface micro instrument. *Sens. Actuators A: Phys.* **91**(3), 266–277 (2001)
12. Maheshwari, S.: Analogue signal processing applications using a new circuit topology. *IET Circ. Devices Syst.* **3**(3), 106–115 (2009)
13. Marani, R., Gelao, G., Perri, A. G.: Modeling of CNFETs oriented to spice software for a/d ckt. design. *Microelectron. J.* **44**(1), 33–38 (2013)

14. Patil, N., Lin, A., Myers, E. R., Ryu, K., Badmaev, A., Zhou, C., Wong, H.-S., Mitra, S.: Wafer-scale growth and transfer of aligned single-walled carbon nanotubes. *Nanotechnology. IEEE Trans.* **8**(4), 498–504 (2009)
15. Sifuentes, E., Casas, O., Reverter, F., Pallas-Areny, R.: Direct interface circuit to linearize resistive sensor bridges. *Sens. Actuator A: Phys.* **147**(1), 210–215 (2008)
16. Singh, T., Saether, T., Ytterdal, T.: Current-mode capacitive sensor interface circuit with single-ended to differential output capability. *Instr. and Measurement. IEEE Trans.* **58**(11), 3914–3920 (2009)

Design of CMOS Ring Oscillators with Low Phase Noise and Power Dissipation for Data Transmission in RF Range

Dhruba Ghosh, Malay Ranjan Tripathy and Sujata Pandey

Abstract This paper presents designing and comparative analysis of noise and power for ring voltage-controlled oscillator (VCO) architectures. A two-stage complementary metal–oxide–semiconductor (CMOS) ring VCO and differential ring oscillator are designed with 180 nm technology and 3.3 V supply for high-resolution and low phase noise. The relative parameters that influence the VCO phase noise are discussed and analysed comprehensively. The tuning range of the designed VCO is from 1 to 5 GHz for a five-stage circuit and 1–2 GHz for a two-stage circuit. An improved VCO unit circuit is obtained by adding a wave shaping circuit at the output of VCO. We have taken the upper frequency range as 5 GHz because it will work properly for a data rate of up to 10 Gbps for an evenly phased signal passing with Nyquist data rate. Our simulation result proves that the designed two-stage CMOS differential VCO has low noise in comparison to other architectures. The circuit can also provide higher stability, better gain and dissipate low power. Our designed VCO is a relaxation oscillator and it will form triangular waveform in the high speed frequency range. The value obtained for phase noise for the two-stage differential CMOS ring oscillator is -292.52 dBc/Hz. Cadence Virtuoso has been used for simulation purpose.

Keywords CMOS · Differential ring oscillator · Inter-symbol interference · Phase-locked loop · Voltage-controlled oscillator · Voltage stabilizer

Introduction

The VCO lies in the heart of the high speed transmitter. The primary function of VCO is to control the frequency in a phase-locked loop of high speed transmitter. With due advancement of ultra-large scale integration, CMOS ring structure of

Dhruba Ghosh (✉) · M.R. Tripathy · Sujata Pandey
Department of Electronics and Communication Engineering, Amity University,
Noida 201301, India
e-mail: dhrubaghosh5@gmail.com

VCO comes in place of LC-tuned oscillator because of its higher level of integration [1]. The low swings in serial link create a significant noise. With increasing data rate in a high speed serial link, the effect of noise becomes much more effective. Many designs of VCOs are available in literature [2–6]. Most report on designing ring VCOs using differential CMOS and the power dissipation is also calculated. Until now no data is available that reports on the reduction in noise at circuit level in the RF frequency range using two-stage VCO architecture.

The two-stage differential CMOS VCO reported in this paper has the capability to suppress the noise extensively as compared to the simple CMOS ring oscillators. The CMOS differential ring VCOs do not have high Q factors, very small amount of phase noise and a broader frequency range as compared to other architectures. Although the designed VCO dissipates a less amount of power, it is higher than the value of dissipated power of simple CMOS ring oscillators.

This paper discusses various noise models that analyse different parameters affecting VCO noise. The VCO designed in this paper uses two-stage differential ring oscillator. In Section “Noise Models” noise modelling is discussed, Section “Circuit Design” gives a brief description of the designed differential ring oscillator, Section “Simulated Results” presents the simulated results and Section “Conclusion” concludes the paper.

Noise Models

The high Q low-pass filter can also be implemented using an injection-locked oscillator (ILO) but the behaviour of a first-order PLL circuit closely resembles the closed-loop circuit of ILO [2]. The working principle of ILO depends on the local oscillation frequency. If the frequency difference of the injection-locked oscillator and local oscillation is very small, then ILO will automatically lock the phase of the injected signal. The VCO acts as a voltage stabilizer by controlling the phase of the input signal. Leeson’s model describes phase noise by the following expression:

$$L(f) = 10 \log \left[0.5 \left(\frac{f_c}{f} + 1 \right) \left(\frac{FkT}{Ps} \right) \left(f_0 + 2Q_fm \right)^2 \right] + 1 \quad (1)$$

where f is the excess amount of noise responsible for degradation of quality factor, k is the Boltzmann’s constant, T is the absolute temperature at which noise is measured, Ps is the average oscillator output power, f_0 is the output frequency, Q_l is the loaded quality factor, f_c is the $1/f$ corner frequency, fm denotes the offset frequency and the noise factor of the amplifier is denoted by F .

$$f = 1/n (\text{delay for rise time} + \text{delay for fall time}) \quad (2)$$

Power is the second foremost parameter of trade-off designing in radio frequency integrated circuit

As oscillation frequency is $f = 1/\text{time period}$, therefore, average power [4] and peak-to-peak voltage is related to the maximum slew rate by the following equation:

$$P(\text{avg}) = \left[(\text{supply voltage})^2 * \text{Cload} \right] / \text{time period} \tag{3}$$

$$V_{pp} = 2|\delta v / \delta t|_{\text{max}} 2\pi f_0 \tag{4}$$

Therefore, switching current is also increased with increase of peak-to-peak voltage.

As a result, phase noise can be reduced with increase of peak-to-peak voltage.

It is suggested that the value of phase noise for a LC tank oscillator is -120 dBc/Hz for 600 kHz offset and 900 MHz centre frequency [5].

Circuit Design

In the present analysis, a two-stage differential ring VCO is used to generate frequency in four evenly spaced phases. With the increasing number of stages in a VCO, the noise is also effective. The VCO simply measures the phase shift of the input signal in a RF transmitter. The noise in a PLL is rejected using a low-pass filter. Figure 1 shows a simple two-stage CMOS ring oscillator and Fig. 2 shows a two-stage differential CMOS ring VCO.

The two differential outputs in Fig. 2 are taken from vout and vout1. Capacitors used are of 100 pF and aspect ratio of p-MOS is two times of n-MOS in our designed oscillators. The two-stage simple CMOS ring oscillator generally provides an easy structure in comparison to the five-stage CMOS ring oscillators. As the structural complexity decreases, the fabrication process is also easier. The power dissipated by two-stage CMOS ring oscillators will also be lower in comparison to five-stage CMOS ring oscillators. Consequently, the value of phase noise will also decrease.

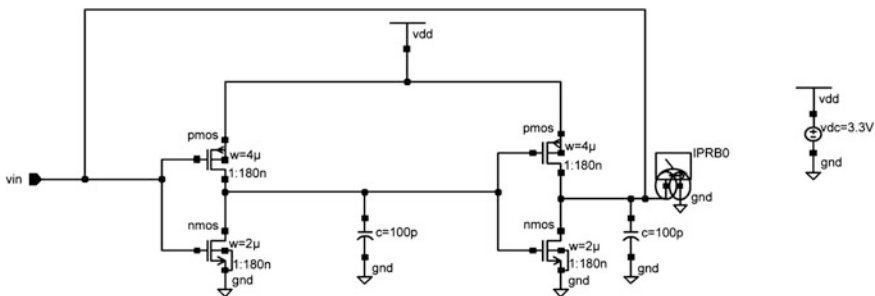


Fig. 1 Ring CMOS oscillator of two stages based on the model of Ali Hajimiri

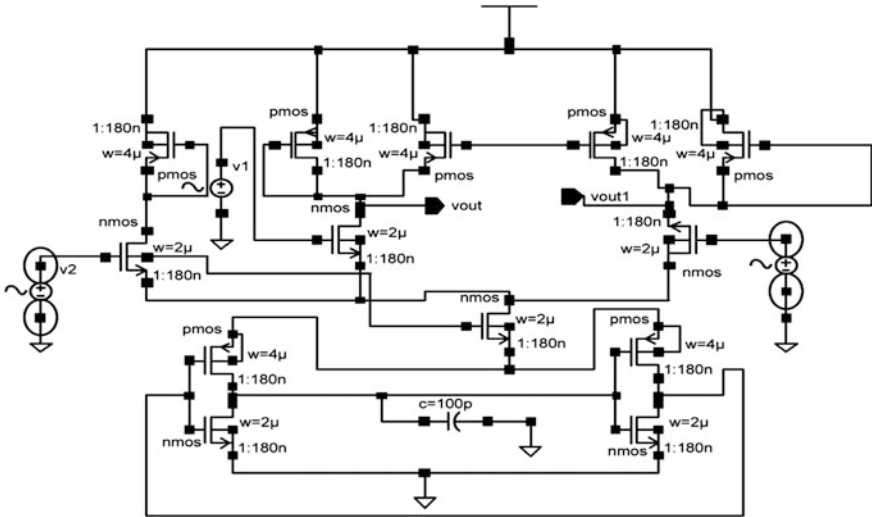


Fig. 2 Designed two-stage differential ring oscillator

The device noise is only considered as the phase noise. When an oscillator is connected with the same power supply, there is a significant amount of stray signals produced through the substrate. The supply and substrate noise generally increase at a rate of 20 dB/decade up to 500 MHz frequency range.

Due to common mode phase of differential architecture, the suppression of noise occurs. The wave shaping circuit at the output also acts to filter noise.

Simulated Results

According to Ali Hajimiri’s noise model, the noise spectral density is solely dependent on W/L. In order to reduce noise, it is expected that the ratio of W/L will be less. On the other hand, the ratio of W/L is also dependent on channel resistance. Thus it is advantageous to take the ratio in between 1 and 1.5.

With increase of load capacitance, average power dissipation increases. That is why the load capacitance for CMOS oscillator is chosen as 100 pF in the present design. Table 1 compares the power dissipation reported in various VCO architectures studied presently.

Table 1 Comparison of average power dissipation of 2 stage ring VCO and 2 stage differential ring VCO

Reference	Type	Technology (nm)	Frequency (GHz)	Average power (mW)
Figure 1	2 stage ring VCO	180	1–2	1.36×10^{-7}
Figure 2	2 stage differential ring VCO	180	1–2	37.73

In the previous work [5–9], though the supply voltage was reduced to 1.8 V, the power dissipation reported was higher (6.4–27 mW) except for Armstrong oscillator [6] that reported a power dissipation of 3.9 mW using a combination of inductor and capacitor at the output node. However, integrating an inductor in a RFIC is very difficult keeping in view of the fabrication process.

Table 1 clearly proves that the differential ring VCO dissipates greater power in comparison to the simple five-stage CMOS VCO but it has superior noise properties. Although the present work uses a higher supply voltage (3.3 V), a much reduced power dissipation is observed as compared to other existing circuits. If power supply voltage is reduced further, the proposed circuit is predicted to dissipate a much lower power for which work is being carried out.

The differential CMOS VCO though has disadvantage of increased power dissipation but it has good noise immunity as compared to others as shown in Table 2.

Table 2 clearly proves that our designed two-stage differential CMOS ring oscillator performs at lowest noise level in comparison to other architectures.

Differential ring VCO works in lower noise level in comparison to the simple CMOS ring VCO as it draws negligible amount of current from the power supply. Figure 3 depicts the figure of transient response for differential ring oscillator. Here, the transient response forms the triangular waveform because the designed differential ring oscillator is basically a relaxation oscillator.

Table 2 Comparison of phase noise of five stage ring VCO, two stage ring VCO and two stage differential ring VCO

	Five-stage ring VCO	Two-stage ring VCO	Two-stage differential ring VCO
Technology (nm)	180	180	180
Frequency range (GHz)	1–5	1–2	1–2
Phase noise (dBc/Hz)	-189.68	-219.34	-292.52

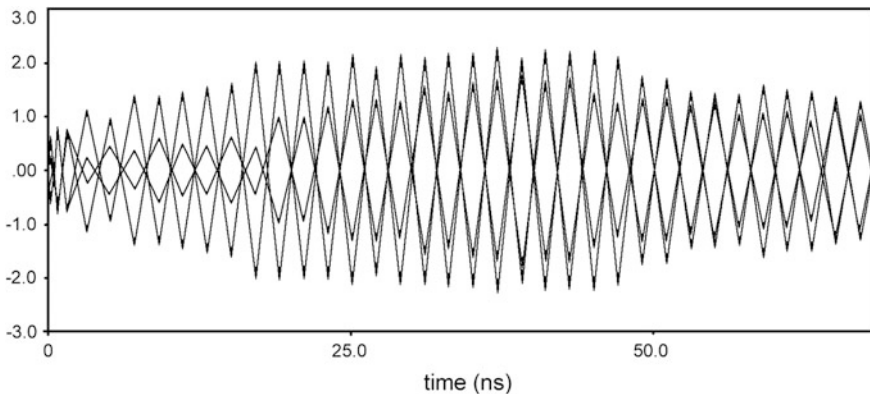


Fig. 3 Transient response of designed two-stage CMOS differential CMOS ring oscillator

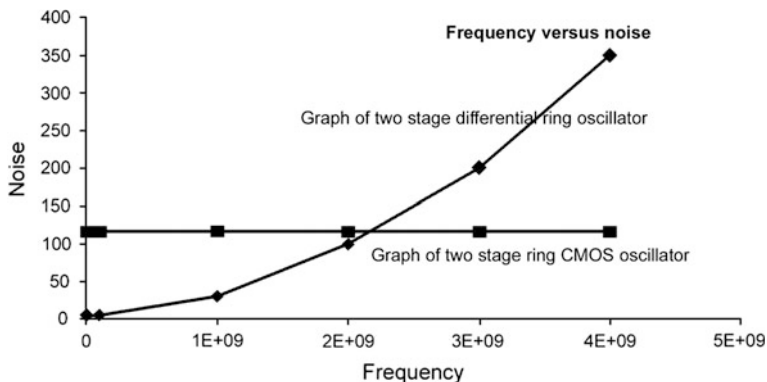


Fig. 4 Frequency versus noise amplitude graph for two-stage oscillators

Figure 3 shows that the two differentiated waveforms created from v_{out} and v_{out1} have an angle of 180° in between them.

The variation of noise versus frequency is shown in Fig. 4. As it can be seen from the graph that circuit follows primitive Leeson's equation and hence proved the validity of our proposed circuit, the frequency is increased from initial value and increased with logarithmic value. The frequency range is in the level of GHz and the simulated graph for two-stage simple CMOS ring oscillator follows a constant noise level in the RF range. The frequency is measured in Hz and noise amplitude is measured in "Volt Per Square root Hertz". The graph for two-stage differential ring oscillator will work at the noise level of above $350 \text{ V}\sqrt{\text{Hz}}$ and the noise level for two-stage ring oscillator will work at the noise level of above $100 \text{ V}\sqrt{\text{Hz}}$ in the RF range of frequency.

The noise for two-stage VCO is calculated as $10 \log_{10}[1.0761 * 10^{-19}] = -189.68 \text{ dBc/Hz}$ and the noise for two-stage VCO is calculated as $10 \log_{10}[1.164653905 * 10^{-22}] = -219.34 \text{ dBc/Hz}$ with offset frequency of 100 kHz.

The noise for designed two-stage differential ring VCO is calculated as $10 \log_{10}[5.5988 * 10^{-30}] = -292.52 \text{ dBc/Hz}$.

The noise for five-stage ring oscillator is increasing due to the increased number where differential CMOS oscillator is decreasing as compared to two-stage simple CMOS differential stage.

Conclusion

In the present paper, we have designed three types of oscillators. The simple ring oscillators dissipate lower power as compared to the differential topology but they have higher noise levels. Although the differential ring oscillator dissipates larger amount of power in comparison to simple two-stage ring oscillator, it works in the

range of lowest noise level. Here, it is clear that the dissipated power is dependent on the load capacitance. The phase noise is strictly affected by the amount of current. In this paper, a complete two-stage differential CMOS ring oscillator is designed using Cadence Virtuoso in 180 nm Technology. Our noise analysis is based on Leeson's primitive model and Ali Hazimiri's new model. The phase noise is -292.52 dBc/Hz. Our noise model gives the best result in the range of 1–2 GHz. A wave shaping circuit can also be added to the output of VCO to further reduce the effect of noise.

References

1. Horowitz, M., Yang, C.K.K., Sidiropoulos, S.: High speed electrical signaling: overview and limitations. *IEEE Micro* **18**(1), 12–24 (1998)
2. Rategh, H.R., Lee, T.H.: Super-harmonic injection locked frequency dividers. *IEEE J. Solid State Circuits* **34**(6), 813–821 (1997)
3. Razavi, B.: *RF Microelectronics, Communications Engineering and Emerging Technologies Series*. Prentice Hall, Englewood Cliffs (2011)
4. Docking, S.: A method to derive an equation for the oscillation frequency of a ring oscillator. Master of Applied Science thesis, Electrical and Computer Engineering, University of Waterloo, Waterloo, Ontario, Canada (2002)
5. Nguyen, T.N., Lee, J.W.: Low phase noise differential Vackar VCO in 0.18 μm CMOS technology. *IEEE Microwave Wirel. Compon. Lett.* **20**(2) (2010)
6. Chung, Y.-H., Jang, S.-L., Lee, S.-H., Yen, R.-H., Jhao, J.-J.: 5 GHz low power current reuse balanced CMOS differential Armstrong VCO. *IEEE Microwave Wirel. Compon. Lett.* **17**(2), 139–141 (2007)
7. Hou, J.-A., Wang, Y.-H.: A 5 GHz differential Colpitts CMOS VCO using the bottom PMOS cross couple current source. *IEEE Microwave Wirel. Compon. Lett.* **19**(6), 401–403 (2009)
8. Hou, J.-A., Wang, Y.-H.: A 5 GHz differential Colpitts CMOS VCO using the bottom PMOS cross couple current source. *IEEE Microwave Wirel. Compon. Lett.* **19**(6), 401–403 (2009)
9. Lee, S.-H., Chuang, Y.-H., Jang, S.-L., Chen, C.-C.: Low phase noise Hartley differential CMOS voltage controlled oscillator. *IEEE microwave Wirel. Compon. Lett.* **17**(2), 145–147 (2007)

A Novel Hybrid Method for Segmentation of Ultrasound Images

Yogendra Singh Poonia, Ramesh Kumar Sunkaria, Deepti Mittal
and Dipesh Kumar Patidar

Abstract Ultrasound (US) is a very convenient and safe diagnostic tool to distinguish benign from malignant masses of the body. As subjective interpretation is time consuming so a computer-aided segmentation approach is needed to assist doctors to estimate tumor margin, and it helps in providing real-time targeted image guidance during surgery. But due to higher noise in Ultrasound image segmentation is a challenging task. In this paper a novel and robust algorithm has been proposed for edge detection of diseased area for effective clinical use. The algorithm divides itself in four stages. Initially, thresholding using moving averages is done to overcome nonuniform illumination of US image which is followed by edge detection with different gradient masks. Morphological operations are used to carve out ROI. Results with several US images with various levels of noises are used to demonstrate the effectiveness of the proposed approach.

Keywords Ultrasound · Variable thresholding · Edge map · Mathematical morphology

Y.S. Poonia (✉) · R.K. Sunkaria
Department of ECE, NIT Jalandhar, Jalandhar, India
e-mail: yogendra2009@gmail.com

R.K. Sunkaria
e-mail: sunkariark@gmail.com

Deepti Mittal
Thapar University Patiala, Patiala, Punjab, India
e-mail: deeptimit@gmail.com

D.K. Patidar
Poornima Institute of Engineering and Technology Jaipur, Jaipur, India

Introduction

Liver diseases have been a great threat for people's health all over the world. The most common cause is advancing years and poor diet and lifestyle. In clinical diagnosis and medication, liver diseases are treated seriously because it is important for healthy human body [2]. The commonly used imaging techniques for the detection and diagnosis of liver diseases include B-scan Ultrasound, Computer Tomography (CT) Magnetic Resonance imaging (MRI) [3]. MRI images are more inclusive than US images which are having high levels of noise such as speckles, shadowing, and having low contrast. However, MRI screening is costly, often unavailable in many community hospitals, time consuming, and requires more patient preparation time. Therefore, US is more popular for screening and biopsy guidance for liver diseases [3].

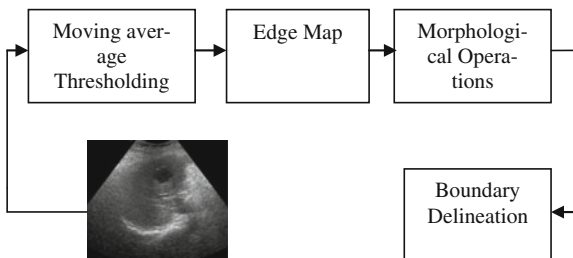
Image segmentation is a necessary step in diagnosis and treatment procedures and surgical planning for various diseases such as tumors, malignant cysts, and Prostate cancer because it partitions the image into meaningful anatomic or pathological structures [8]. There are characteristic artifacts which make the segmentation process complicated such as attenuation (Low intensity), high level of speckle noise, shadows and signal dropout; due to orientation dependency of acquisition that may lead in incorrect boundaries. Common image segmentation techniques, based on edge detection, neural network and threshold-based segmentation method, are difficult to present accurate results. But due to the above-discussed artifacts segmenting Ultrasound image on basis of intensity or spatial information does not provide accurate results so a hybrid method that incorporates both spatial and intensity information is required [7].

In this paper an algorithm is presented for ultrasound image delineation which consists of a hybrid model of variable thresholding and gradient-based approach for feature extraction. First thresholding of image is done using moving averages which segments image by thresholding its intensities based on moving averages of intensities along individual rows of an image. After that, gradient masks are used to find out the edge-map of test images followed by multiple morphological operations to smoothen image and to fill out unnecessary regions and finally boundary is delineated by setting the pixels on border to one and rest to zeros.

Method

In the present work, a hybrid methodology for boundary delineation of region of interest in Ultrasound images has been proposed. The composite block diagram of this technique is shown in Fig. 1.

Fig. 1 Composite block diagram for ROI delineation



Thresholding

To segment image moving average along scan lines of image is computed. The scanning is typically carried out line by line in a zigzag pattern to reduce illumination bias presented in US image. It reduces

If, z_{k+1} is intensity of point at $k + 1$, then the mean intensity at $k + 1$ is represented by:

$$\begin{aligned}
 m(k + 1) &= \frac{1}{n} \sum_{i=k+2-n}^{k+1} z_i \text{ where } k \geq n - 1 \\
 &= m(k) + \frac{1}{n} (z_{k+1} - z_{k-n}) \text{ where } k \geq n + 1
 \end{aligned}
 \tag{1}$$

where, n —number of points used in computing the average. Algorithms need not to be initialized every time, it computes moving average for every point in the image, and this segmentation is implemented as:

$$I1(x, y) = \begin{cases} 1 & \text{if } I(x, y) > Km_{xy} \\ 0 & \text{otherwise} \end{cases}
 \tag{2}$$

where, K —constant in the range $[0, 1]$ and m_{xy} —moving average at point (x, y) of the input image [7]. A Binary Image has been computed from step A as shown in Fig. 3b.

Edge Map

After segmenting image using step described in an edge map of an image is processed using enhanced Sobel edge detection technique [12]. Applying this have two advantages (1) Due to average factor incorporated, it has some smoothening effect on nonuniform illumination. (2) Because it is differential of two rows and two columns so the pixel of the edge on both sides has been enhanced, so the edge looks thick and bright. So a brief overview of edge detection is following Image $I1(x, y)$ is

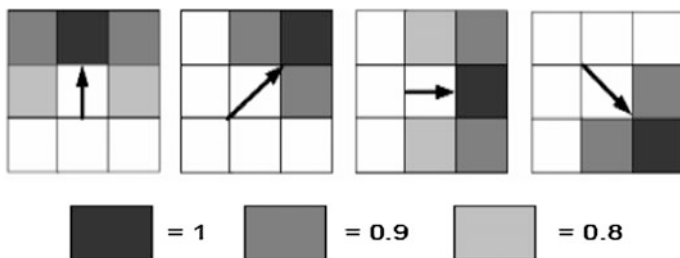


Fig. 2 Different edge masks used to detect edges

a continuous function in the position (x, y) , its gradient is expressed as a vector (the two components are two first derivatives which are along the X and Y directions, respectively):

$$\nabla I(x, y) = [G_x G_y]^T = \left[\frac{\partial I}{\partial x} \frac{\partial I}{\partial y} \right] \tag{3}$$

The magnitude and direction angle of the vector are:

$$mag(\nabla I) = |\nabla I| = [G_x^2 G_y^2]^{1/2}$$

$$\theta(x, y) = \arctan\left(\frac{G_x}{G_y}\right) \tag{4}$$

Four 3×3 Edge Masks that are used in this edge detection technique are shown in Fig. 2. These masks will help in finding out every possible edge in binary segmented image from previous operation. Every point in the image should use these two kernels to do convolution.

Edge point of an image $I(x, y)$ is judged when it satisfies one of the following two conditions.

1. Condition (1)

(a)
$$h(x, y) > 4 \times \sum_{i=1}^{row} \sum_{j=1}^{list} h^2(i, j) / row \times list$$

(b)
$$h_1(x, y) > h(x, y)$$

(c)
$$h(x, y - 1) \leq h(x, y)$$

(d)
$$h(x, y) \geq h(x, y + 1)$$

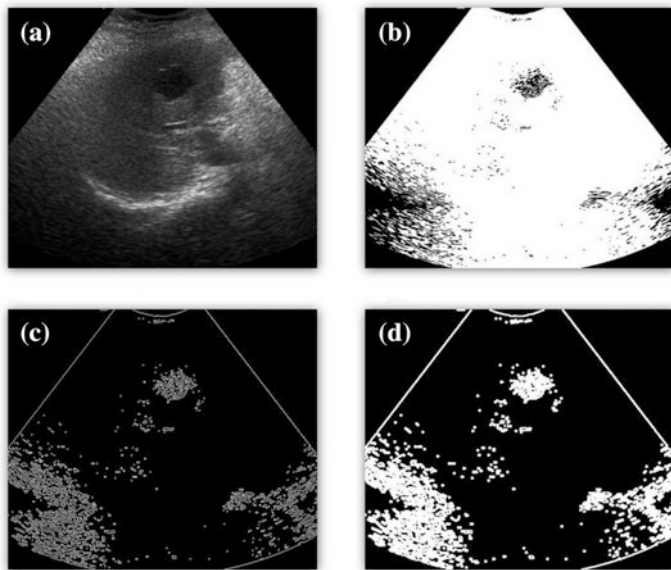


Fig. 3 a Ultrasound image and results from b Variable Thresholding c Edge Map d Dilation

2. Condition (2)

$$(a) \quad h(x, y) > 4 \times \sum_{i=1}^{row} \sum_{j=1}^{list} h2(i, j) / row \times list 2$$

$$(b) \quad h_1(x, y) > h_2(x, y)$$

$$(c) \quad h(x - 1, y) \leq h(x, y)$$

$$(d) \quad h(x, y) \geq h(x + 1, y)$$

Binary gradient mask (BGI) of US image is computed by applying edge map on binary image generated from step A, here, as shown in Fig. 3c

Morphological Operations

The binary gradient mask shows high contrast lines (as observed in Fig. 3c) in the test image. It does not delineate accurately the outline of ROI and undesired edges are also highlighted. The proposed algorithm has the advantage of dilation to fill these linear gaps.

Binary gradient mask is dilated two times initially by horizontal structuring element (S1) followed by vertical structuring element. Result from dilation is shown in Fig. 3d but still the objects that are on borders need to be removed.

$$DILI = BGI \oplus S1 = \{z|(S)_z \cap BGI \neq \emptyset\}$$

Another morphological operation is applied to resultant image which shows the ROI boundaries very clearly but still there are holes inside as depicted from Fig. 3d. To remove these holes, the following operation is executed:

$$F(x, y) = \begin{cases} I(x, y) & \text{if } (x, y) \text{ is on the border of } DILI \\ 0 & \text{otherwise} \end{cases}$$

Then,

$$H1 = [R_{I^c}(F)]^c \quad (5)$$

$H1$ is a binary image equal to I with all holes filled that are inside malignant part. The object that need to be delineate lies within image not on borders so these objects are removed from image so objects detected on border need to be removed by following operation.

$$F(x, y) = \begin{cases} I(x, y) & \text{if } (x, y) \text{ is on the border of } H \\ 0 & \text{otherwise} \end{cases}$$

$$H2 = R_I(F) \quad (6)$$

$H2$ contains only the objects touching the borders. So the difference, $H3 = 1 - H2$ contains only the objects from the binary image that do not touch the border as shown in Fig. 5b. To look the segmented image natural erosion operation is applied. Smoothing of resulting image is done by erosion with help of diamond structuring element. Binary segmented image gives ROI as object rest as a background is obtained from last step and further processing is done to carve out exact boundaries.

Extraction of Final Boundaries

Last step is to delineate boundaries from image achieved after applying multiple morphological operations. To remove the interior pixels are pixels are set to 0 in between ROI and 1 on the points where intensity is changing from low to high or vice versa. Alternatively, to achieve ROI boundaries by setting pixel values to zero if all its four connected neighbors as one. That resulted in only boundary pixels as shown in Fig. 4c and contour is traced along the cyst which is superimposed on original image to get final result as shown in Fig. 4d.

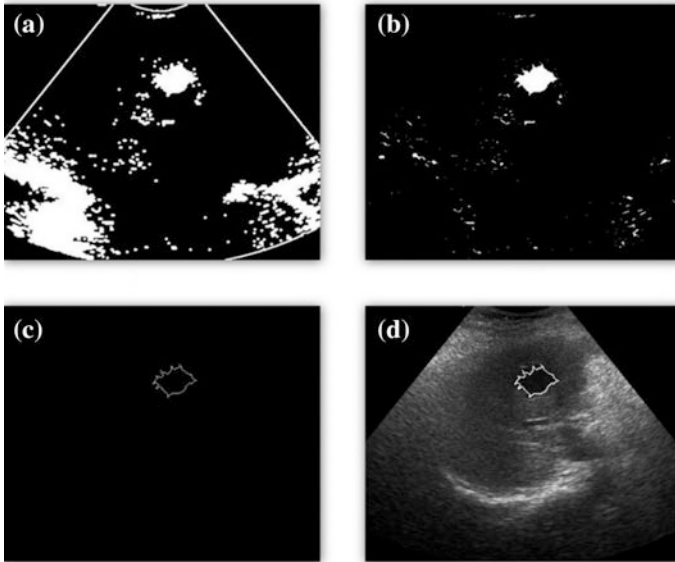


Fig. 4 a–b Results from multiple Morphological Operations c Segmented Image d Boundary Superimposed on original image

Results and Discussions

The Ultrasound Cyst images have been used as the test images shown in Fig. 5. Cysts are thin-walled structures that contain fluid due to that hypoechoic regions are observed in US images. It is observed from test images are having cyst and tumors having different shape and size so a segmentation algorithm needed that will encounter ideal edges in all test images. Figures 6 and 7 show segmentation results of various cyst images and Figs. 8 and 9 compares the results with doctor's delineation. It is a semiautomatic approach so a manual input is needed to adjust values of K and n (window size to compute average) to delineate images with acceptable accuracy. Values of these variable for which ideal edges is encountered is shown in Table 1.

To evaluate the accuracy of our segmentation scheme, we quantitatively compared the results of this work with the manual delineations produced by experts/Doctors that has been considered as reference for yields the contours that are very close to the expert's opinions. Numerically, it can be evaluated with the help probability of error.

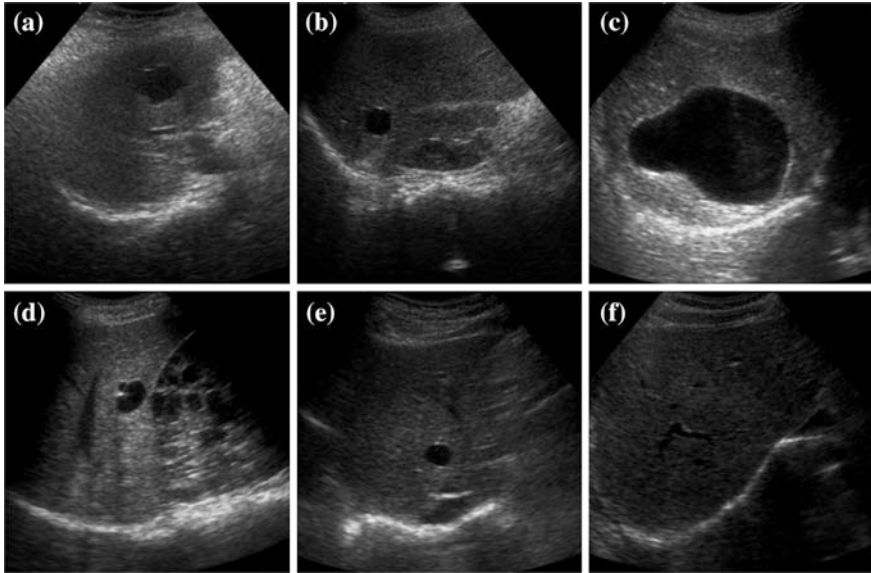


Fig. 5 Test images used in performing the experiment

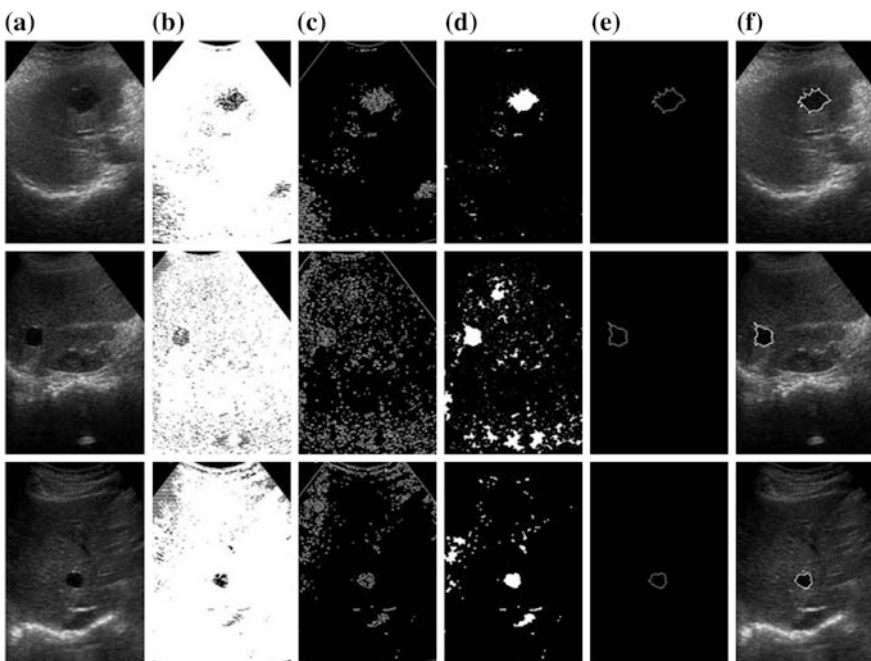


Fig. 6 **a** Ultrasound images of Cyst in liver, **b** Result from variable thresholding **c** After Edge map **d** Applying various morphological operation **e** Extracting final ROI **f** Overlapping it on original image

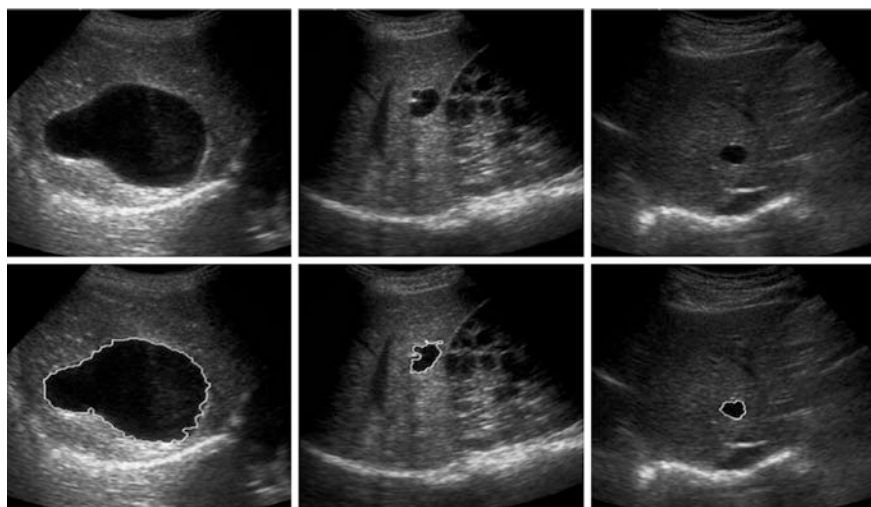


Fig. 7 Boundary delineated by proposed method

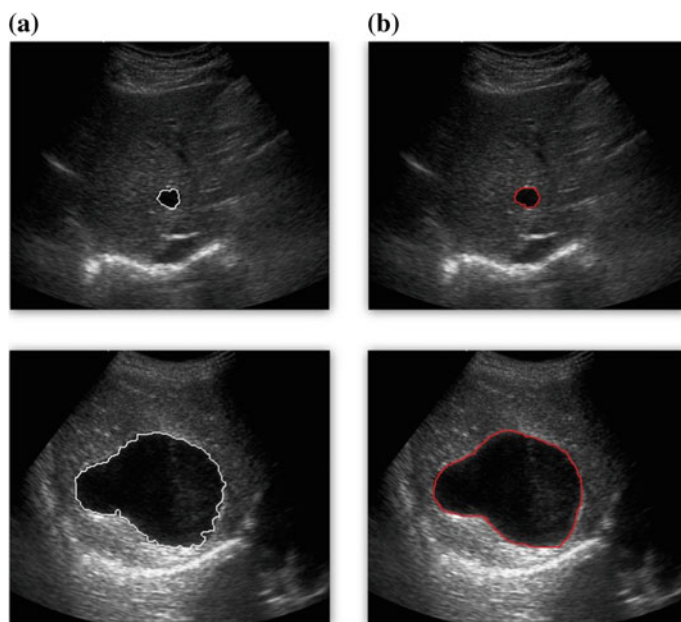


Fig. 8 a Proposed method b Doctor's Delineation

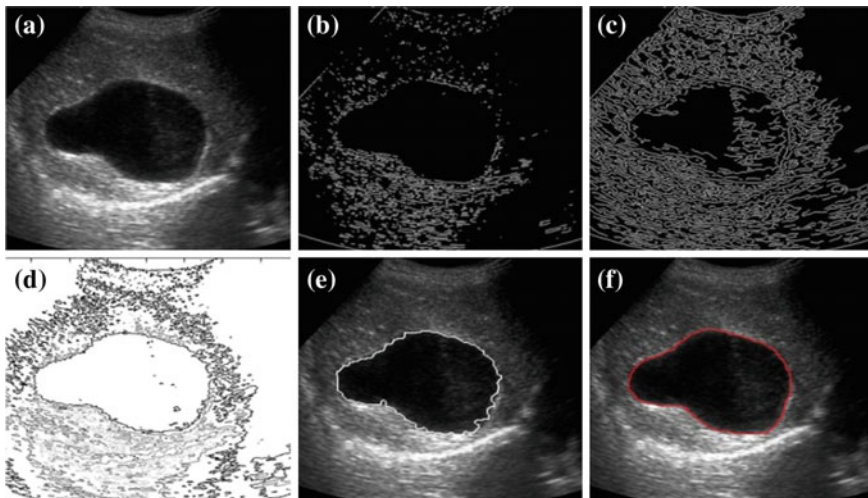


Fig. 9 Cyst in liver ultrasound. **a** Original image. Results of **b** Sobel edge, **c** Canny Edge, **d** Contour Method, **e** Proposed technique, **f** Doctor's delineation

Table 1 Value of K and window size (N) for us images

Image no.	K	Window size(n)
1	0.5	60
2	0.5	20
3	0.45	40
4	0.4	45
5	0.6	40
6	0.5	45

$$\text{Prob of error} = P(\text{Object})P(B.G/\text{Object}) + P(B.G)P(\text{Object}/B)$$

Hausdorff is another method to evaluate the accuracy of image segmentation, it is a distance-based metric which calculates distances between the two contours or in other words it is the farthest point of a contour that you can be to the closest point of another contour. Proposed method is also compared with two conventional methods for detecting ill-defined edges, i.e., the active contour model and the gradient vector flow. The results show that the proposed method produces has a very effective edge detection performances and is better than its competitive counterparts on this particular problem as shown in Tables 2 and 3.

Table 2 Probability of error in various edge detection techniques (%)

Image	Canny edge	Contour method	Proposed
1	20.12	9.44	4.33
2	18.34	8.32	5.22
3	12.11	7.05	3.33
4	13.45	10.21	7.55
5	16.32	12.30	6.09
6	11.21	6.76	5.01
Average	15.25	9.01	5.25

Table 3 Results evaluation on US images by hausdorff distance (Pixel)

Image	Canny edge	Contour tracing	Proposed
1	6.23	5.32	3.90
2	5.90	5.45	3.60
3	5.33	5.44	3.33
4	5.47	4.87	3.21
5	5.44	5.05	3.56
6	6.01	4.98	3.98
Average	5.73	5.18	3.57

Conclusion

In the present work, an improved hybrid algorithm has been proposed that keeps track of both intensity and spatial information of Ultrasound Image. Special measures have been taken to detect ill defined edges, complex shapes, and various sizes of tumors to achieve acceptable accuracy. Morphological operators proved to be effective in removing unwanted regions that has been detected falsely.

References

1. Kermani, A., Ayatollahi, A., Talebi, M.: Segmentation of medical ultrasound image based on local histogram range image. In: 2010 3rd International Conference on Biomedical Engineering and Informatics (BMEI), vol. 2, pp. 546–549, 16–18 Oct 2010
2. Somkantha, K., Theera-Umpon, N., Auephanwiriyaikul, S.: boundary detection in medical images using edge following algorithm based on intensity gradient and texture gradient features. *IEEE Trans. Biomed. Eng.* **58**(3), 567–573 (2011)
3. Lee, S., Jo, A., Kim, K.W., Lee, J.Y., Ro, Y.M.: Enhanced classification of focal hepatic lesions in ultrasound images using novel texture features. In: 2011 18th IEEE International Conference on Image Processing (ICIP), pp. 2025–2028, 11–14, Sept 2011
4. Chen, S., Haralick, R.M.: Recursive erosion, dilation, opening, and closing transforms. In: *IEEE Transactions on Image Processing*, vol. 4, no. 3, pp. 335–345, Mar 1995. doi:[10.1109/83.366481](https://doi.org/10.1109/83.366481)

5. Wang, X.: Laplacian operator-based edge detectors. In: IEEE Transactions on Pattern Analysis and Machine Intelligence, vol. 29, no. 5, pp. 886–890, May 2007
6. Setarehdan, A.M., Bahrami, N., Rezaatofighi, S.H., Adeli, S.K.: Boundary delineation for hepatic hemangioma in ultrasound images. In: Annual International Conference of the IEEE on Engineering in Medicine and Biology Society, EMBC (2011)
7. Boukerroui, D., Noble, J.A.: Ultrasound image segmentation: a survey. IEEE Trans. Med. Imaging (2006)
8. Maragos, P.: Morphology-based symbolic image modeling, multi-scale nonlinear smoothing, and pattern spectrum. In: Proceedings of Computer Society Conference on Computer Vision and Pattern Recognition CVPR '88, pp. 766–773, 5–9 June 1988
9. Vasavada, Tiwari, J.: A hybrid method for detection of edges in grayscale images. Int. J. Image, Graph. Signal Process. (IJIGSP) (2013)

Temperature Sensor Using a SMF-PCF-SMF Heterostructure

Rekha Mehra and Heena Shahani

Abstract In this paper, a temperature sensor is designed and simulated using an interferometric configuration formed by inserting a photonic crystal fiber (PCF) between two single-mode fibers (SMFs). In this device, phase delay at the output is achieved by the index difference between core mode and cladding mode of PCF. In this type of interferometer, greater index difference is possible because of air-hole structure of PCF. It indicates that a small length of PCF can introduce large delay, i.e., large phase shift while keeping optical loss of the cladding mode at a relatively low level. With increase in temperature, effective refractive index difference between core and cladding of PCF decreases which results in decrease in peak output power of the interferometer. Variation of output power with temperature is observed to be linear; it is thus applicable as a temperature sensor.

Keywords Temperature sensor · Photonic crystal fiber (PCF) · Finite domain time domain (FDTD) · Single-mode fiber (SMF)

Introduction

Photonic crystal fibers (PCFs) were introduced in the mid-1990s [1] and are also called microstructured optical fibers or holey fibers. They have been under a lot of research and have considerably changed the traditional fiber optics. They have a periodic arrangement of small holes that run along its entire length. The PCFs have two kinds of cross sections: in one cross section, a conventional solid core is surrounded by cladding consisting of air-holes while in the other, a hollow core (or a material with refractive index less than that of the cladding) is surrounded by cladding with air-hole structure. In former type, light gets propagated through a

Rekha Mehra (✉) · Heena Shahani
Department of Electronics and Communication, GEC Ajmer, Ajmer, Rajasthan, India
e-mail: mehra_rekha@rediffmail.com

Heena Shahani
e-mail: heenashahani@gmail.com

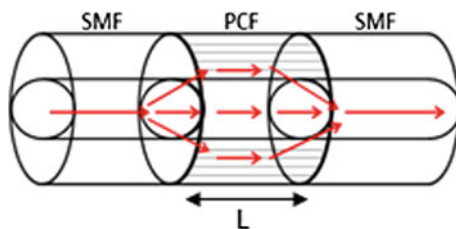
phenomena called modified total internal reflection (also called index guiding), while in the latter light is guided through the photonic band gap effect (called PBG guiding). The unique guiding mechanism and modal properties of PCF vary according to the shape, size, number, and arrangement of air-holes in PCF [2]. Due to its unique wave-guiding properties and freedom in design, they have been used for a large number of sensing applications which are not easy to realize with the use of conventional optical fibers, even if realized will not have performance as good as with PCF. The PCFs have undergone a lot of research in recent years in the measurement of strain [3], refractive index [4], pressure [5], temperature [6], and so on.

Optical interferometers are widely used in sensing applications as they give high resolution in the output; fiber optic interferometers are constructed with additional advantages such as stability and compactness. The commonly used approaches to build fiber optic interferometer are modal interferometer and two-arm interferometer.

Two-arm interferometer requires a sufficient length of optical fiber and two couplers, one at the input and the other at the output. Input light split by the first coupler travels through two different arms of fiber and gets recombined at the output by the second coupler. Modal interferometer makes use of the relative phase difference between two modes of the same fiber. The susceptibility to environmental effects is less in modal interferometers in comparison to their two-arm counterparts because mode propagates through in the same fiber. Due to unique properties of PCF, they are widely used in sensing applications. Design of PCF-based interferometric sensors, in particular, is interesting because of their proved high sensitivity and wide range of applications. Modal interferometers using PCFs are as follows: PCFs in a fiber loop mirror [7], interferometer constructed using long periodic gratings [8], interferometers using tapered PCFs [9], and interferometers fabricated through collapsing of micro-holes [10]. Other configurations reported so far are as follows: a PCF having two collapsed regions separated by a length of few centimeters [11], a small section of a PCF placed longitudinally between two SMFs by fusion splicing [10] and a stub of PCF with its cleaved end spliced to the distal end of an SMF (reflection type) [12]. The last two configurations have an advantage that they are cost-effective as interrogation is done with traditional optical fibers while using the modal properties of the PCF.

The interferometer using a PCF between two SMFs shown in Fig. 1 is demonstrated in this paper as a temperature sensor. In this device, phase delay at the output is achieved by the index difference between core mode and cladding mode of

Fig. 1 SMF-PCF-SMF structure [10]



PCF. Large index difference (higher than 0.01) is achieved in this type of MZI (Mach Zehnder interferometer) structure due to the presence of air-holes in the cladding of PCF. It indicates that a small length of PCF can be used to introduce large delay or large phase shift. The sensor discussed here has an advantage that it can measure temperature without the requirement of some special coating. To realize the full potential of PCFs, it is necessary to efficiently couple light from SMFs to PCFs. However, because PCFs have air-hole structure which is totally different from conventional fibers splicing PCFs to conventional fibers is a significant challenge.

The transfer function of the in-line MZI structure can be expressed as [13]

$$I = I_1 + I_2 + 2\sqrt{I_1 I_2} \cos\phi$$

where I is the intensity of the interference signal, I_1 and I_2 are the intensities of the light propagating in the fiber core and cladding, respectively, ϕ is the phase difference between the core and cladding modes which is approximately equal to

$$\phi = \frac{2\pi(\Delta n_{\text{eff}})L}{\lambda}$$

where

$\Delta n_{\text{eff}} = n_c - n_{\text{cl}}$ = effective refractive index difference of the core and cladding.

L = Interferometric region length

λ = the input wavelength.

In this paper, L is taken as $1 \mu\text{m}$ and $\lambda = 1.5 \mu\text{m}$.

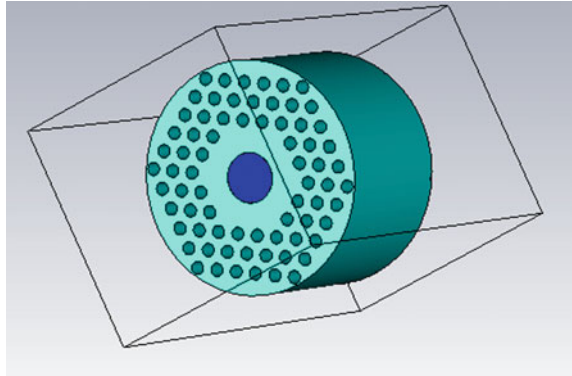
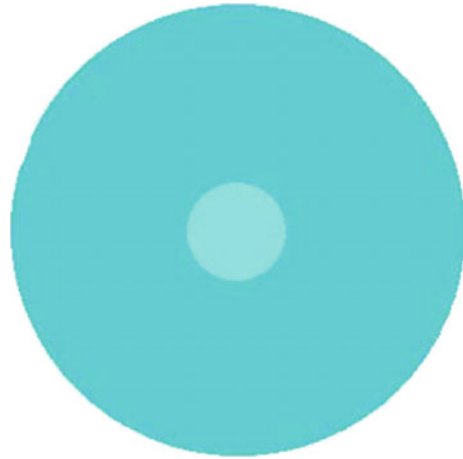
Design of the in-line MZI is discussed in detail in the next section.

Design

We have used OptiFDTD to observe the propagation of light through PCF-MZI structure [14]. Design specifications of the proposed sensor are given in Table 1. The PCF is composed of a hexagonal array of silica holes passing along the length of PCF and has refractive index of 1.444. Figures 2 and 3 show the cross section of PCF and SMF, respectively.

Table 1 Design specifications

Input wavelength	1.5 μm
Lattice constant	0.13 μm
Radius of holes in PCF	0.04 μm
Refractive index of silica holes	1.444
Core refractive index	3.46
Core radius	0.15 μm
Cladding radius	0.7 μm
Length of SMF and PCF	1 μm

Fig. 2 Cross section of PCF**Fig. 3** Cross section of SMF

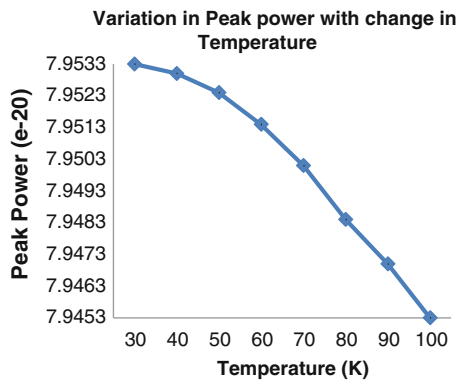
Simulation and Analysis

Change in refractive index of silicon with temperature (30–100 K) is given in Table 2 [15]. With increase in temperature, electron polarizability increases which leads to increase in refractive index of the material. As refractive index of cladding in an optical fiber increases keeping refractive index of core constant, index difference between core and cladding decreases and hence, effective index of the fiber decreases. Due to this, attenuation in the fiber increases and the peak output power decreases as shown in Fig. 4. By calculating the slope of the linear region of the graph shown in Fig. 4, sensitivity of the sensor can be obtained. Sensitivity is found to be $1 \times e^{-20}$ mW/K.

Table 2 Variation in refractive index of silicon with change in temperature [15]

Temperature (K)	Refractive index of silicon	Effective refractive index
30	3.45309	0.00691
40	3.45319	0.00681
50	3.45340	0.0066
60	3.45373	0.00627
70	3.45417	0.00583
80	3.45471	0.00529
90	3.45535	0.00465
100	3.45609	0.00391

Fig. 4 Change in peak output power with temperature



Conclusion

We demonstrated the use of PCF-MZI interferometer formed by using a PCF between two SMFs as a temperature sensor using FDTD method. It can be observed that the SMF-PCF-SMF heterostructure can be used as a good sensing device because of the perfect linear variation of refractive index with temperature. Sensitivity of the device is obtained as $1 \times e^{-20}$ mW/K.

References

1. Knight, J.C., Birks, T.A., Russell, P.S.J., Atkin, D.M.: All-silica single-mode optical fiber with photonic crystal cladding. *Opt. Lett.* **21**(19), 1547–1549 (1996)
2. Russell, P.: Photonic-crystal fibers. *J. Lightwave Technol.* **24**(12), 4729–4749 (2006)
3. Frazao, O., Baptista, J.M., Santos, J.L.: Temperature-independent strain sensor based on a Hi-Bi photonic crystal fiber loop mirror. *IEEE Sens. J.* **7**(10), 1453–1455 (2007)
4. Li, Y., Chen, L., Harris, E., Bao, X.Y.: Double-pass in-line fiber taper Mach-Zehnder interferometer sensor. *IEEE Photon. Technol. Lett.* **22**(23), 1750–1752 (2010)

5. Fu, H.Y., Tam, H.Y., Shao, L.-Y., Dong, X.Y., Wai, P.K.A., Lu, C., Khijwania, S.K.: Pressure sensor realized with polarization-maintaining photonic crystal fiber-based Sagnac interferometer. *Appl. Opt.* **47**(15), 2835–2839 (2008)
6. Qian, W.W., Zhao, C.L., He, S.L., Dong, X.Y., Zhang, S.Q., Zhang, Z.X., Jin, S.Z., Guo, J.T., Wei, H.F.: High- sensitivity temperature sensor based on an alcohol-filled photonic crystal fiber loop mirror. *Opt. Lett.* **36**(9), 1548–1550 (2011)
7. Zhao, C.L., Yang, X., Lu, C., Jin, W., Demokan, M.S.: Temperature-insensitive interferometer using a highly birefringent photonic crystal fiber loop mirror. *IEEE Photon. Technol. Lett.* **16**(11), 2535–2537 (2004)
8. Lim, J.H., Jang, H.S., Lee, K.S., Kim, J.C., Lee, B.H.: Mach–Zehnder interferometer formed in a photonic crystal fiber based on a pair of long-period fiber gratings. *Opt. Lett.* **29**(4), 346–348 (2004)
9. Monzón-Hernández, D., Minkovich, V.P., Villatoro, J., Kreuzer, M.P., Badenes, G.: Photonic crystal fiber microtaper supporting two selective higher-order modes with high sensitivity to gas molecules. *Appl. Phys. Lett.* **93**(8), 081106 (2008)
10. Villatoro, J., Minkovich, V.P., Pruneri, V., Badenes, G.: Simple all-microstructured optical-fiber interferometer built via fusion splicing. *Opt. Express* **15**(4), 1491–1496 (2007)
11. Choi, H.Y., Kim, M.J., Lee, B.H.: All-fiber Mach-Zehnder type interferometers formed in photonic crystal fiber. *Opt. Express* **15**(9), 5711–5720 (2007)
12. Jha, R., Villatoro, J., Badenes, G.: Ultrastable in reflection photonic crystal fiber modal interferometer for accurate refractive index sensing. *Appl. Phys. Lett.* **93**(19), 191106 (2008)
13. Jasim, A.A., Harun, S.W., Arof, H., Ahmad, H.: Inline Microfiber Mach–Zehnder interferometer for high temperature sensing. *IEEE Sens. J.* **13**(2) (2013)
14. Verma, J.K., Dash, S.P., Tripathy, S.K.: Design of a concentration sensor based on photonic crystal fibre placed between two single mode fibres. *Soft Nanosci. Lett.* **3**, 36–38 (2013)
15. http://www.google.co.in/imgres?imgurl=http://www.radiantzemax.com/content_images/glass/thermal/Fig1_IndexDataSi.jpg&imgrefurl=http://kben.radiantzemax.com/Knowledgebase/How-to-Fit-Temperature-Dependent-Index-Data-to-the-Zemax-Thermal-Model-&h=203&w=500&tbnid=4RWNqx_t7bFtM:&zooom=1&docid=KyEOh4AFISkkM&ei=rOF4U5CJNM28uASqtoLoDg&tbn=isch

Investigation of Channel Drop Filter Based on Two Dimensional Photonic Crystal Structure

Ritu Sharma, Mayur Kumar Chhipa and Lalit Kumar Dusad

Abstract In this paper, the design and performance of two dimensional (2-D) photonic crystal (PhC) channel drop filter is investigated using finite difference time domain (FDTD) method. Plane wave expansion (PWE) method has been utilized to calculate the photonic band gap (PBG). The channel drop filter has been optimized for telecommunication wavelengths $\lambda_1 = 1.531 \mu\text{m}$ and $\lambda_2 = 1.551 \mu\text{m}$ for two designs with refractive indices 3.11 and 3.325, respectively. The number of rods in Z direction is 21 and in X direction is 20 with lattice constant 0.540 nm. By varying the radius of scatter rods of PCRR, it is observed that this filter may be used for filtering several other channels also. The designed structure is useful for CWDM systems. This device may serve as a key component in photonic integrated circuits. The device is ultra compact with the overall size around $123 \mu\text{m}^2$.

Keywords CWDM • PWE method • FDTD • Photonic crystal • PCRR

Introduction

Photonic crystals (PhC) are analogous to semiconductors because they allow the control of photons as semiconductors allow for electrons. They are composed of periodic dielectric nanostructures that affect the propagation of electromagnetic (EM) waves. Yablonovitch [1] and John [2] proposed the idea that periodic dielectric structures are able to provide photonic band gap (PBG) for distinct regions in the frequency spectrum, just like the electronic band gap (EBG) in solid

Ritu Sharma (✉) · L.K. Dusad
Department of ECE, MNIT, Jaipur, India
e-mail: ritusharma.mnit@gmail.com

L.K. Dusad
e-mail: 2013rec9572@mnit.ac.in

M.K. Chhipa
Department of ECE, GEC, Ajmer, India
e-mail: mayurchhipa1@gmail.com

state crystal behavior by Mohammad Ali Mansouri-Birjandi et al. [3]. Based upon the variation of refractive index in one, two and three dimensions, photonic crystals are classified into one, two and three dimensional crystals, respectively. The photonic band gap (PBG) is the region where the propagation of light is completely prohibited in certain frequency ranges as shown by Yablonovitch [1]. The periodicity of this band gap can be broken if a point defect or line defect or both are introduced in the photonic crystal structure and then the propagation of light can be localized at these defect regions.

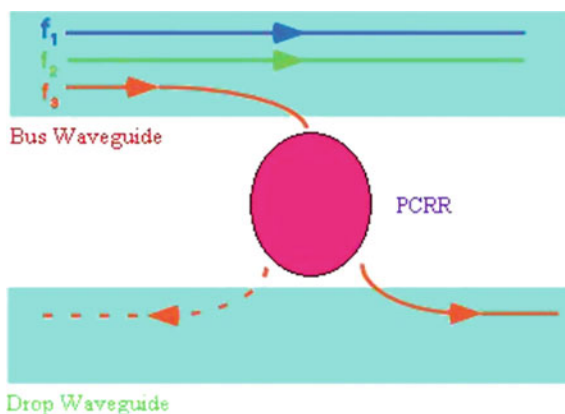
Researchers all around the world have reported about many photonic crystal-based devices such as Multiplexer by Manzacca et al. [4], De-multiplexer by Hadi Ghorbanpour et al. [5] and Hui Liu et al. [6], Mach-Zehnder interferometer by Geng et al. [7], Optical logic gates by Susan Christina et al. [8], Photonic crystal power splitters by Ghaffari et al. [9] etc. This 2-D photonic crystal structure is designed, simulated and analyzed by using OptiFDTD simulation software of Optiwave System Inc. (Using official license).

Design Parameters

Channel drop filter is an important constituent of optical communication system. Coarse wavelength division multiplexing (CWDM) and dense wavelength division multiplexing (DWDM) are the two WDM technologies where CWDM is characterized by wider channel spacing. There are 18 central wavelengths as per the ITU-T G.694.2 CWDM grid which ranges from 1271 nm to 1611 nm with 20 nm channel spacing. By varying the radius of scatter rods of PCRR, it is observed that this filter may be used for filtering different optical channels.

A schematic diagram of a generic resonant cavity channel drop filter is shown in Fig. 1. There are two optical waveguides and an optical resonator system.

Fig. 1 A schematic diagram of a generic resonant cavity channel drop filter



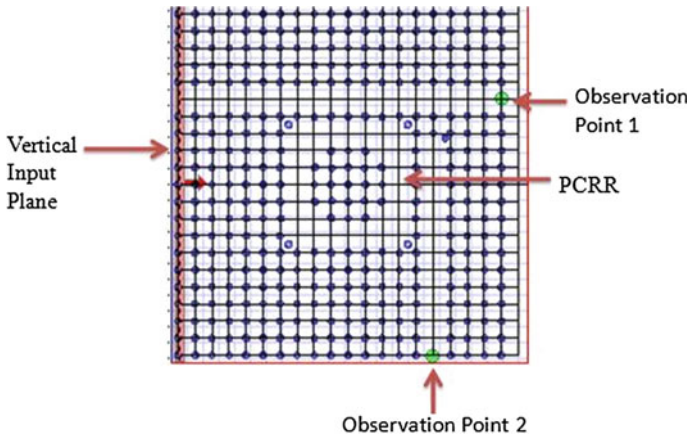


Fig. 2 The channel drop filter based on 2-D photonic crystal structure

The performance of a channel drop filter is determined by the transfer efficiency between the bus and drop waveguides. In this paper, we have utilized the characteristics of a photonic crystal ring resonator. The designed structure is shown in Fig. 2.

Many researchers all around the world have utilized the characteristics of PCRRs in designing optical devices. Different designs based on PCRR are reported like Channel drop filter by Djavid et al. [10] and Robinson et al. [11], Add-drop filter by Robinson et al. [12] and Weidong Zhou et al. [13] and triplexer by Yaw-Dong Wu et al. [14], etc. In this paper, these designs are further investigated by varying the various parameters. Here, in this design the number of dielectric rods in z direction and in x directions are 21 and 20, respectively. These rods are surrounded by air (refractive index = 1). The refractive indices of rods are 3.11 and 3.325 for the first and second designs, respectively, and radius of dielectric rods is $r = 0.1 \mu\text{m}$. The lattice constant 'a' is kept equal to $0.540 \mu\text{m}$.

The Photonic band gap (PBG) is calculated by PWE method as given by Leung et al. [15]. The PBG is calculated for TE mode. Figure 3 shows photonic band gap of photonic crystal structure without introducing any defects. The PBG for first design extends from $0.601992 \text{ 1}/\lambda$ to $0.834912 \text{ 1}/\lambda$ and PBG for second design extends from $0.566366 \text{ 1}/\lambda$ to $0.817832 \text{ 1}/\lambda$.

Both point and line defects are utilized to design this channel drop filter. Analysis of gap map diagram gives the idea about the radii of point defects. There is one input port and two output ports. In between them is photonic crystal ring resonator. Four scatter rods are placed at all the four corners of PCRR. Two observation points are placed at the two output ports.

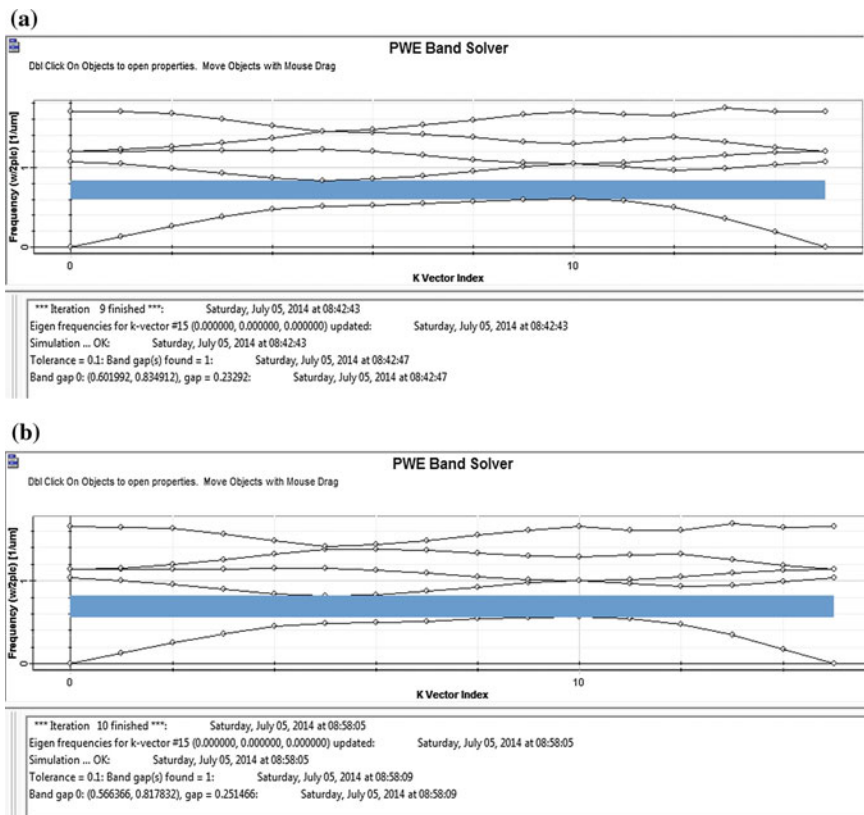


Fig. 3 Photonic band gap diagram of PhC structure with rods of refractive index: **a** 3.11, **b** 3.325, surrounded by air (without introducing any defect)

Analysis

As shown in the Fig. 3, there is a vertical input plane and it injects a Gaussian modulated continuous wave signal into the device. The output is observed at the observation points at output ports. A 2-D 32 bit simulation is performed to obtain the response of this channel drop filter. The simulation runs for 10,000 time steps. The output is obtained using frequency discrete Fourier transforms (DFT) calculations of the field by finite difference time domain (FDTD) method. Analysis is done by varying the radius of scatter rods. The DFT of E_y field is analyzed.

The transmission spectra obtained for the two designs is shown in Fig. 4. Figure 4a shows the transmission spectra when the refractive index of the whole structure is 3.11 and radius of the dielectric rods is $0.1 \mu\text{m}$ and Fig. 4b shows the transmission spectra when the refractive index of the whole structure is 3.325 and radius of the dielectric rods is kept same, i.e., $0.1 \mu\text{m}$. Further, the analysis is done

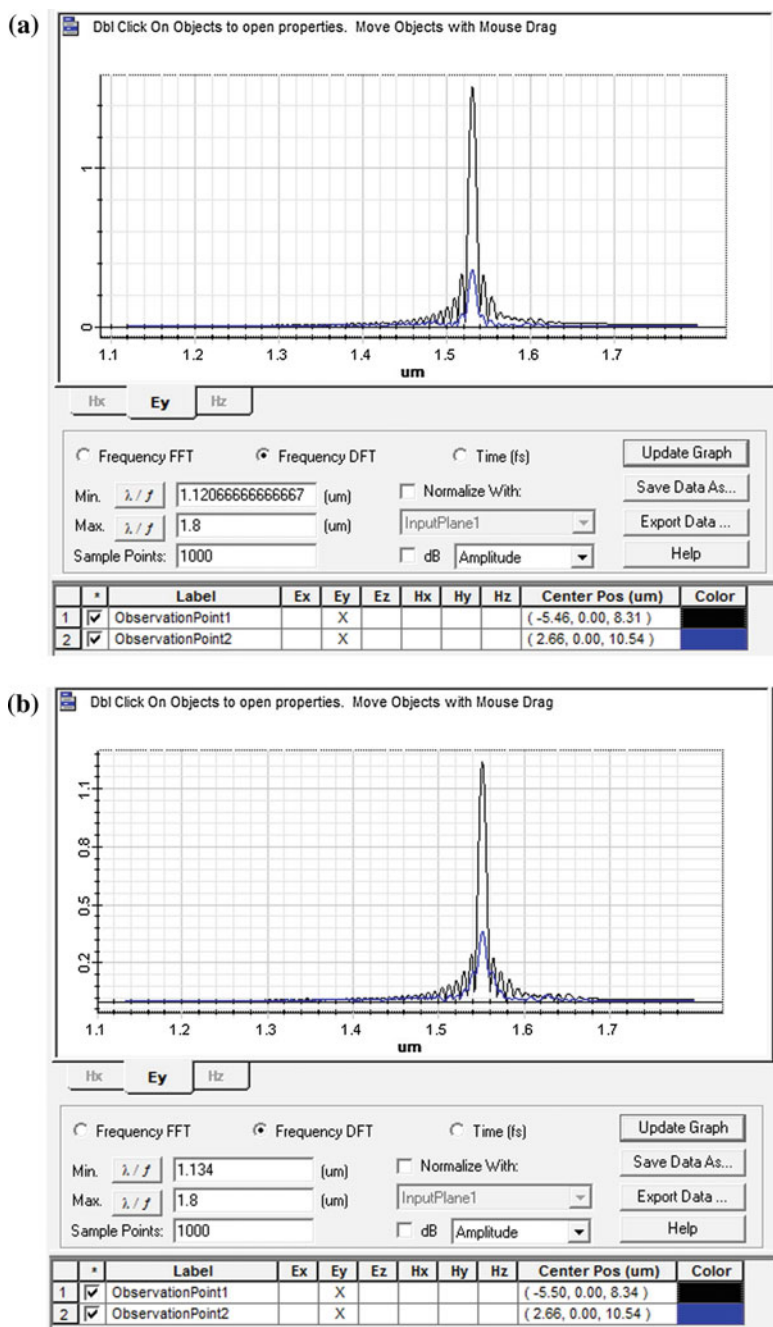


Fig. 4 Transmission spectra of PCRR based CDF for a 1531 nm and b 1551 nm wavelength

Table 1 Output response when refractive index is 3.11

S. no.	Scatter rod radius (μm)	Dropped wavelength (μm)
1.	0.12	1.5351
2.	0.1	1531
3.	0.09	1.5289

Table 2 Output response when refractive index is 3.325

S. no.	Scatter rod radius (μm)	Dropped wavelength (μm)
1.	0.12	1.5540
2.	0.1	1551
3.	0.09	1.5496

by varying the radius of scatter rods for the two designs. The output response has been summarized as shown in Tables 1 and 2.

It is clear from Tables 1 and 2 that the output response of the channel drop filter is function of the radius of the scatter rods.

Conclusion

In this paper, the response of PCRR-based channel drop filter is investigated using finite difference time domain (FDTD) method. The designed structures are based on 2-D photonic crystal in square lattice with two different refractive indices 3.110 and 3.325, respectively. Plane wave expansion (PWE) method is utilized to calculate the photonic band gap (PBG). It is observed that the output response of this channel drop filter is function of the radius of the scatter rods. The design parameters may be further optimized to get the better response. The designed structure may be useful for CWDM systems. This CDF is ultra compact in size and the overall size of the chip is around $11.4 \mu\text{m} \times 10.8 \mu\text{m}$. Hence, such kind of devices may be useful in photonic integrated circuits (PICs) for CWDM systems, optical networking communication and applications, etc.

References

1. Yablonovitch, E.: Inhibited spontaneous emission on solid-state physics and electronics. *Phys. Rev. Lett.* **58** (20): 2059–2062 (1987)
2. John, S.: Strong localization of phonics in certain disordered dielectric Super-lattices. *Phys. Rev. Lett.* **58**, 2486–2489 (1987)
3. Mansouri-Birjandi, M.A., Rakhshani, M.R.: A new design of tunable four-port wavelength demultiplexer by photonic crystal ring resonators. *Optik* **124**, 5923–5926 (2013)

4. Manzacca, G., Paciotti, D., Marchese, A., Moreolo, M.S., Cincotti, G.: 2D photonic crystal cavity-based WDM multiplexer. *Photonics Nanostruct. Fundam. Appl.* **5**, 164–170 (2007)
5. Ghorbanpour, H., Makouei, S.: 2-channel all optical demultiplexer based on photonic crystal ring resonator. *Front. Optoelectron.* **6**(2), 224–227 (2013)
6. Liu, H., Cai, X.-B.: Study of wavelength demultiplexer based on two-dimensional photonic crystals. *Optoelectron. Lett.* **4**(5), 339–341 (2008)
7. Geng, Y., Li, X., Tan, X., Deng, Y., Yu, Y.: A cascaded photonic crystal fiber Mach-Zehnder interferometer formed by extra electric arc discharges. *Appl. Phys. B* **102**(3), 595–599 (2011)
8. Susan Christina, X., Kabilan, A.P.: Design of optical logic gates using self-collimated beams in 2D photonic crystals. *Photonic Sens.* **2**(2), 173–179 (2012)
9. Ghaffari, A., Monifi, F., Djavid, M., Abrishamian, M.S.: Analysis of photonic crystal power splitters with different configurations. *J. Appl. Sci.* **8**, 1416–1425 (2008)
10. Djavid, M., Ghaffari, A., Monifi, F., Abrishamian, M.S.: T-shaped channel-drop filters using photonic crystal ring resonators. *Physica E* **40**, 3151–3154 (2008)
11. Robinson S., Nakkeeran, R.: Channel drop filter based on 2D square-lattice photonic crystal ring resonator. In: *IEEE International Conference on Wireless Optical. Communication. Networks (WOCN)*. Colombo, Sri Lanka (2010)
12. Robinson, S., Nakkeeran, R.: Hetero structure based add drop filter for ITU-T G.694.2 CWDM systems using PCRR. In: *IEEE International Conference on ICCCNT*. Coimbatore, India (2012)
13. Zhou, W., Qiang, Z., Soref, R.A.: Optical add-drop filter design based on photonic crystal ring resonators. In: *Conference on Lasers and Electro-Optics Baltimore, Maryland US* (2007)
14. Wu, Y.-D., Shih, T.-T., Lee, J.-J.: New design of a triplexer using ring resonator integrated with directional coupler based on photonic crystals. In: *Communications and Photonics Conference and Exhibition (ACP)*, Shanghai, China. (2009)
15. Leung, K.M., Liu, Y.F.: Photon band structures: the plane-wave method. *Phys. Rev. B* **41**, 10188–10190 (1990)

Design and Analysis of a Nano-Fiber with All-Normal and Flat Dispersion for Supercontinuum Generation

Than Singh Saini, Ajeet Kumar and Ravindra Kumar Sinha

Abstract A new design of nano-fiber having all-normal and flat-top dispersion in As_2Se_3 chalcogenide glass has been reported for broadband supercontinuum spectra ranging from 1580 to 7090 nm. Such broadband spectra in mid-infrared region has been obtained using only 2 mm long nano-fiber with 50 fs laser pulses of 500 W peak power. Proposed nano-fiber has been optimized to obtain zero dispersion wavelength at 3800 nm.

Keywords Nanofiber · Supercontinuum generation · All-normal dispersion

Introduction

Mid-infrared supercontinuum generation is one of the most exciting research topics for past few years. Supercontinuum is a broad spectrum of coherent white light that finds numerous novel applications in the field of telecommunication, optical metrology, optical coherent tomography (OCT), microscopy, cosmological studies, ultra-short pulse generation [1–5]. Supercontinuum generation (SCG) is the phenomenon of broadening of the optical pulses due to the combined response of various nonlinear effects along with group velocity dispersion and higher-order dispersions [6]. The first demonstration of the SCG is made in the year 1970 when glass sample was encountered by the highly focused picosecond pulses [7]. Thereafter SCG was obtained in a step-index single-mode optical fiber in the year of 1987 [8, 9]. Ranka et al. [10] was first to demonstrated SCG in the PCF. A flat-top dispersion profile with small slop dispersion curve crossing the near/at the pump wavelength is preferred for SCG [11]. By selecting the pump wavelength near to the zero dispersion wavelength (ZDW) reduces its power requirement and also smoothes the generated spectrum [12]. If the pumping is in the region of

T.S. Saini (✉) · Ajeet Kumar · R.K. Sinha
TIFAC-Center of Relevance and Excellence in Fiber Optics and Optical Communication,
Department of Applied Physics, Delhi Technological University, Delhi 110 042, India
e-mail: tsinghdph@gmail.com

anomalous group velocity dispersion the spectral broadening of SC spectrum is mainly depends on soliton dynamics [13, 14].

To generate highly coherent and stable SC, the noise-sensitive soliton dynamics must be suppressed and soliton fission should be completely removed. This can be done by generating the SC exclusively in the normal GVD [15]. Pumping the conventional fiber far below the ZDW is another technique to generate the SC in normal dispersion region. A more efficient method, and the one used in this work, is to generate SC in PCF which has an all-normal dispersion profile, with zero dispersion at the pump wavelength. Recently, our group has reported a new design of triangular-core photonic crystal fiber with all-normal dispersion profile for SCG [16].

In this work, a new As_2Se_3 -based chalcogenide nano-fiber design has been proposed with ZDW at 3800 nm. We have reported broadband SC spectra ranging from 1580 to 7090 nm using only 2 mm long nano-fiber with 50 fs laser pulses of 500 W peak power.

Proposed Design of Nano-Fiber

The design of proposed nano-fiber has been illustrated in Fig. 1a. Proposed design of nano-fiber consists of the air-holes arranged in triangular lattice in the As_2Se_3 -based chalcogenide glass. Central air-holes along with left three holes of the first ring have been removed to construct the core of the nano-fiber. The separation between two nearby air-holes (i.e., pitch, A) is kept same in the proposed design of nano-fiber. The diameter of the holes in cladding region is considered as 'd'. The electric field distribution of propagating mode in proposed nano-fiber has been shown in Fig. 1b.

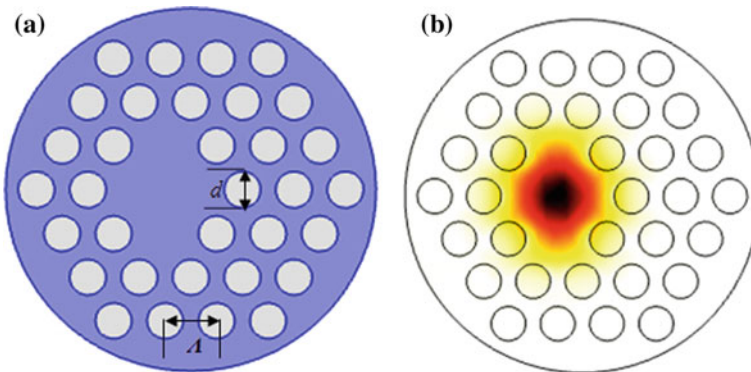


Fig. 1 Transverse cross-sectional view of the proposed nano-fiber (a); the electric field distribution of propagating mode at 3800 nm pump wavelength with $d = 545$ nm and $A = 1$ μm (b)

Optical Characterization: Dispersion and Non Linearity

Broadening of the SC spectra primarily depends upon two major optical parameters, nonlinearity and dispersion profile of the structure. A careful study on these parameters is needed to get accurate and required results. We have defined the nonlinearity coefficient; γ by the following equation [17]

$$\gamma = \frac{2\pi n_2}{\lambda A_{\text{eff}}}$$

where n_2 is the nonlinear refractive index of material, λ is the pump wavelength and A_{eff} is the effective-mode-area of the fundamental mode. The A_{eff} is given as [6]

$$A_{\text{eff}} = \frac{\left(\iint |E|^2 dx dy\right)^2}{\left(\iint |E|^4 dx dy\right)}$$

where, E —is the transverse electric field of the fundamental mode.

In tellurite glass, the long-wavelength side of the transmission window cuts off around at 3 μm [18], which is significantly low SC generation in the range of 4 to 10 μm . However, in As_2Se_3 glass the long-wavelength side of the transmission window cuts off is more than 10 μm . The total or chromatic dispersion is an important factor concerned in spectral broadening of SC is calculated using the equation [6]

$$D(\lambda) = -\frac{\lambda}{c} \frac{\partial^2 \text{Re}(n_{\text{eff}})}{\partial \lambda^2}$$

where, c —is the speed of the light in vacuum, and $\text{Re}(n_{\text{eff}})$ is the real part of the effective index of fundamental mode. At optimized parameters (i.e., $d = 545 \text{ nm}$ and $A = 1000 \text{ nm}$.) the dispersion profile of proposed nano-fiber has been shown in Fig. 2. The zero value of dispersion has been obtained at 3800 nm wavelength. Therefore, this wavelength (i.e., 3800 nm) can be used as a pump wavelength.

Fig. 2 The dispersion profile of proposed asymmetric PCF with optimized parameters: $d = 545 \text{ nm}$, and $A = 1 \mu\text{m}$

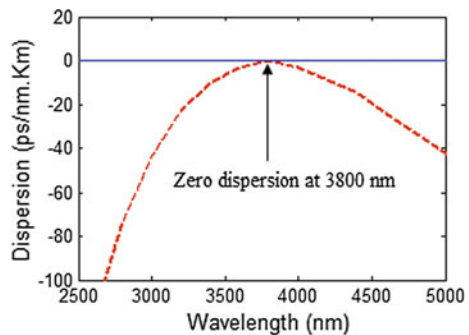
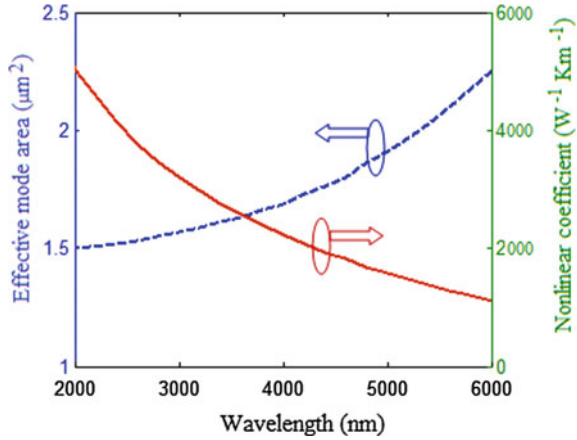


Fig. 3 The dispersion profile of proposed asymmetric PCF with optimized parameters: $d = 545 \text{ nm}$, and $A = 1 \text{ }\mu\text{m}$



The effective-mode-area of the propagating mode plays an important role to enhance the nonlinearity of fiber designs. For proposed nano-fiber, the variations of effective-mode-area and nonlinear coefficient with wavelength have been shown in Fig. 3. At the 3800 nm pump wavelength the nonlinear coefficient is as high as $23960 \text{ W}^{-1} \text{ km}^{-1}$ with effective-mode-area (A_{eff}) of $1.66 \text{ }\mu\text{m}^2$.

Results and Discussion

We have used split-step Fourier method to solve the nonlinear-Schrodinger equation (GNLSE). The following GNLSE has been solved to achieve the SC spectrum [6].

$$\frac{\partial A}{\partial z} = -\frac{\alpha}{2}A - \left(\sum_{k \geq 2} \beta_k \frac{i^{k-1}}{k!} \frac{\partial^k A}{\partial t^k} \right) + i\gamma \left(1 + \frac{i}{\omega_o} \frac{\partial}{\partial t} \right) \left[A(z, t) \int_{-\infty}^{\infty} R(t') |A(z, t-t')|^2 dt' \right]$$

where, α —is the attenuation constant of the nano-fiber, $A(z, t)$ —is the envelope of the output optical field, β_n —is the n th derivatives of the propagation constant, β , and γ —is the nonlinear coefficient. The nonlinear response function. $R(t)$ includes both instantaneous electronic as well as delayed is given by the relation

$$R(T) = (1 - f_r)\delta(T) + f_r h_r(T)$$

with $f_r = 0.115$ [19]. Raman response function, h_r , can be calculated by equation

$$h_r(t) = \frac{\tau_1^2 + \tau_2^2}{\tau_1 \tau_2} \exp\left(-\frac{t}{\tau_2}\right) \sin\left(\frac{t}{\tau_1}\right)$$

where Raman period $\tau_1 = 23.1$ fs and life time $\tau_2 = 195$ fs for As_2Se_3 -based glass [19].

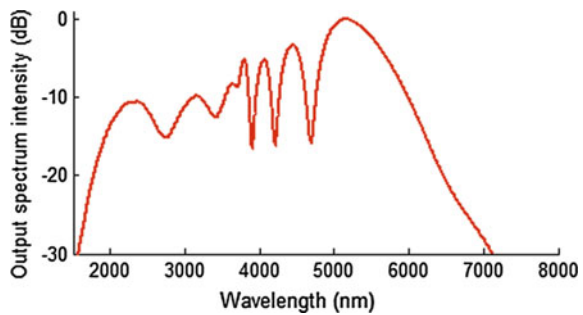
The hyperbolic-secant pulses can be expressed by the relation

$$A(z = 0, t) = \sqrt{P_o} \operatorname{sech}\left(\frac{t}{t_o}\right) \exp\left(-i \frac{C t^2}{2 t_o^2}\right)$$

where $t_0 = T_{FWHM}/1.7627$ and P_o is peak power and C is the chirp coefficient. The value of transmission loss, α taken in our simulation is 4.8 dB/m [20]. In the calculations, we have set the pump wavelength to 3800 nm at zero dispersion in order to have smooth and broad spectra. Unchirped optical pulses of $T_{FWHM} = 50$ fs and peak power = 500 W are considered in the simulations of SC spectrum from the proposed nano-fiber.

Figure 4 illustrate the SC spectrum as the optical pulses propagate through the nano-fiber. During the initial phase of its propagation, self-phase-modulation causes the symmetrical spectral broadening. Beyond 2 mm of fiber length, the Raman effect comes into play for extending the spectrum of SC. It is clear that within the 2 mm length of the nano-fiber a broadband, flat, and smooth SC is generated spanning 1580–7090 nm.

Fig. 4 Spectral broadening of SC spectrum at the output of proposed PCF with optimized parameters: $d = 545$ nm, and $\Lambda = 1 \mu\text{m}$ at 3800 nm pump wavelength



Conclusions

A structure of nano-fiber has been designed to achieve all-normal flat dispersion profile along with zero dispersion at mid-infrared domain at 3800 nm. Using 2 mm long nano-fiber SC spectra has been generated covering a broad range of 1580 nm to 7090 nm with 50 fs laser pulses of 500 W peak power. The reported design of nano-fiber can be used in various applications such as metrology, optical coherence tomography, spectroscopy, sensing, and short pulse generation.

Acknowledgement The authors gratefully acknowledge the (i) TUN-IND bilateral research project, Department of Science and Technology, Govt. of India, and (ii) initiatives and support toward establishment of the TIFAC-Center of Relevance and Excellence in Fiber Optics and Optical Communication at Delhi Technological University (Formerly Delhi College of Engineering) Delhi, through the “Mission REACH” program of Technology Vision-2020 of the Government of India.

References

1. Morioka, T., Takara, H., Kawanishi, S., Kamatani, O., Takiguchi, K., Uchiyama, K., Saruwatari, M., Takahashi, H., Yamada, M., Kanamori, T., Ono, H.: 1 Tbit/s (100 Gbit/s x 10 channel) OTDM/WDM transmission using a single supercontinuum WDM source. *Electron. Lett.* **32**, 906–907 (1996)
2. Cundiff, S.T., Ye, J., Hall, J.L.: Optical frequency synthesis based on mode-locked lasers. *Rev. Sci. Instrum.* **72**(10), 3749–3771 (2001)
3. Povazay, B., Bizheva, K., Unterhuber, A., Hermann, B., Sattmann, H., Fercher, A.F., Drexler, W., Apolonski, A., Wadsworth, W.J., Knight, J.C., Russell, P.S., Vetterlein, M., Scherzer, E.: Submicrometer axial resolution optical coherence tomography. *Opt. Lett.* **27**(20), 1800–1802 (2002)
4. Paulsen, H.N., Hilligse, K.M., Thogersen, J., Keiding, S.R., Larsen, J.J.: Coherent anti-Stokes Raman scattering microscopy with a photonic crystal fiber based light source. *Opt. Lett.* **28** (13), 1123–1125 (2003)
5. Dudley, J.M., Coen, S.: Fundamental limits to few-cycle pulse generation from compression of supercontinuum spectra generated in photonic crystal fiber. *Opt. Exp.* **12**(11), 2423–2428 (2004)
6. Agarwal, G.P.: *Nonlinear Fiber Optics-4e*. Academic, New York (2007)
7. Alfano, R.R., Shapiro, S.L.: Emission in the region 4000 to 7000 Å via four-photon coupling in glass. *Phys. Rev. Lett.* **24**(11), 584–587 (1970)
8. Baldeck, P.L., Alfano, R.R.: Intensity effects on the stimulated four photon spectra generated by picosecond pulses in optical fibers. *J. Lightwave Technol.* **5**, 1712–1715 (1987)
9. Nelson, B.P., Cotter, D., Blow, K.J., Doran, N.J.: Large nonlinear pulse broadening in long lengths of monomode fiber, *Opt. Commun.* **48**(4): 292–294 (1983)
10. Ranka, J.K., Windeler, R.S., Stentz, A.J.: Visible continuum generation in air silica microstructure optical fibers with anomalous dispersion at 800 nm. *Opt. Lett.* **25**(1), 25–27 (2000)
11. Dudley, J.M., Genty, G., Coen, S.: Supercontinuum generation in photonic crystal fiber. *Rev. Mod. Phys.* **78**(4), 1135–1184 (2006)

12. Kudlinski, A., Bouwmans, G., Douay, M., Taki, M., Mussot, A.: Dispersion-engineered photonic crystal fibers for CW-pumped supercontinuum sources. *J. Lightwave Technol.* **27** (11), 1556–1564 (2009)
13. Herrmann, J., Griebner, U., Zhavoronkov, N., Husakou, A., Nickel, D., Knight, J.C., Wadsworth, W.J., St, P., Russell, J., Korn, G.: Experimental evidence for supercontinuum generation by fission of higher-order solitons in photonic fibers. *Phys. Rev. Lett.* **88**(17), 173901 (2002)
14. Islam, M.N., Sucha, G., Bar-Joseph, I., Wegener, M., Gordon, J.P., Chemla, D.S.: Femtosecond distributed soliton spectrum in fibers. *J. Opt. Soc. Am. B* **6**(6), 1149–1158 (1989)
15. Dudley, J.M., Coen, S.: Coherence properties of supercontinuum spectra generated in photonic crystal and tapered optical fibers. *Opt. Lett.* **27**(13), 1180–1182 (2002)
16. Saini, T.S., Kumar, A., Sinha, R.K.: Highly nonlinear triangular core photonic crystal fiber with all normal dispersion for supercontinuum generation, *Frontier in Optics (FiO)*, FW1D-4 (2014)
17. Sanghera, J.S., Shaw, L.B., Pureza, P., Nguyen, V.Q., Gibson, D., Busse, L., Aggarwal, I.D.: Nonlinear properties of chalcogenide glass fibers. *Int. J. Appl. Glass Sci.* **1**, 296–308 (2010)
18. Feng, X., Mairaj, A.K., Hewak, D.W., Monro, T.M.: Nonsilica glass for holey fibers. *J. Lightwave Technol.* **23**, 2046–2054 (2005)
19. Ung, B., Skorobogatiy, M.: Chalcogenide microporous fibers for linear and nonlinear applications in the mid-infrared. *Opt. Exp.* **18**(8), 8647–8659 (2010)
20. Shaw, L.B., Nguyen, V.Q., Sanghera, J.S., Aggarwal, I.D., Thielen, P.A., Kung, F.H.: IR supercontinuum generation in As-Se photonic crystal fiber. In: *Proceeding Advanced Solid State Photonics, TuC5, Vienna, Austria* (2005)

Investigation of Semiconductor Optical Amplifier for DWDM System with 50 GHz Channel Spacing

Aruna Rani and Sanjeev Dewra

Abstract In this paper, the performance of a 32 channel SOA-based dense wavelength division multiplexing system at 10 GB/s data rate with channel spacing of 50 GHz in terms of quality factor, BER, output optical power, and eye closure is investigated. Transmission over fiber optical link of different lengths at low signal input powers is demonstrated. The communication over fiber optical link is evaluated up to 215 km transmission distance at -35 dBm input signal power. It is also found that the signal can be transmitted effectively up to 241 and 260 km for -30 dBm and -25 dBm signal input power, respectively.

Keywords Dense wavelength division multiplexing (DWDM) · Semiconductor optical amplifier (SOA) · Quality factor · Bit error rate · Channel spacing

Introduction

DWDM technology is well recognized for its flexibility and remarkable increase in transmission capacity for optical communication system. For the next generation of optical communication systems, semiconductor optical amplifier is interesting and key device for dense wavelength division multiplexing technology [1, 2] because of their wide gain spectrum, compact size, low cost, low power dissipation, large optical gain, and possible integration with other semiconductor optical devices that allows the communication of several channels under the same fiber and the utilization of SOAs to carry out both linear and nonlinear functionalities necessary in high-speed optical communications systems [3–5]. Semiconductor optical amplifier performs a significant role in modern optical networks, enabling the

Aruna Rani (✉) · Sanjeev Dewra
Department of Electronics & Communication Engineering,
SBSSTC, Ferozpur 152004, Punjab, India
e-mail: arunarani70@gmail.com

Sanjeev Dewra
e-mail: sanjeev_dewra@yahoo.com

broadcast of several terabits of information over thousands of kilometers [6, 7]. Semiconductor optical- amplifier technology offers high-speed switching capacity in addition to gain, high integration potential and high extinction ratio. Moreover, it is a key technology for numerous other purposes, as well as all-optical wavelength regeneration, conversion, selection, booster, and in-line optical amplification [8]. The SOA is operated in slightly saturated gain regions that did not have significant inter channel crosstalks and therefore, the output power is incredibly limited [9]. Kim et al. [10] effectively transmitted 10 GB/s optical signals using SOA as a booster amplifier over 80 km transmission distance through standard single mode fiber. They had also found the parameters like extinction ratio, chirp parameter, rising, and falling time of input signals for SOAs to increase the output dynamic range and output power. Singh et al. [11] investigated 10 GB/s NRZ format in dispersion compensated and single mode fiber link by using semiconductor optical amplifier. In this work, post, pre, and symmetrical compensation methods for different locations of the SOA in fiber link had been observed. These post, pre and symmetrical power compensation methods were compared in terms of eye closure penalty, bit error rate, output received power, and eye diagram. It was found that when SOA was used, the post power compensation method was better to symmetrical and pre power compensation methods. Paola Parolari et al. [12] demonstrated the WDM networks at 10 GB/s data rate. Transmission up to 72 km of single mode fiber had been calculated confirming the absence of chromatic dispersion penalties. Here, the performance of DWDM system using optimized SOA is evaluated by enhancing the transmission distance, number of channels, and reducing the channel spacing.

This paper is structured as follows. Section “[Introduction](#)” describes introduction. Section “[System Setup](#)” discusses the schematic setup of DWDM system using SOA. In Section “[Results and Discussion](#)”, results using different input signal powers are presented and Section “[Conclusion](#)” gives a brief outlook for the conclusion.

System Setup

In the simulation model as illustrated in Fig. 1, 32 channels are communicated at 10 GB/s bit rate with 50 GHz channel interval. The system model composed of three stages, i.e., transmitter, semiconductor optical amplifier and receiver. The transmitter block consists of 32 channels, each of them operating at center frequencies, i.e., 193.1–196.2 THz. Each transmitter consists of NRZ rectangular driver, data source, laser source and optical amplitude modulator. A pseudo-random binary sequence of bits at a data rate of 10 GBps is produced by the data source. Each of the input signals first modulates in NRZ format and then pre-amplified with semiconductor optical amplifier. The amplified signals are transmitted over the DS-Normal fiber. The output of data source is given to modulator driver which generates a non return to zero rectangular pulse train.

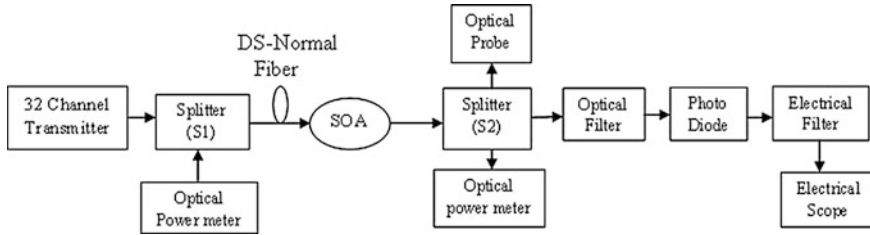


Fig. 1 System model

This data is converted into optical carrier by using continuous wave lorentzian laser source. The laser source and driver output is passed to the optical modulator. The pulses are then modulated using Sin^2 Mach-Zehnder modulator. The output of the transmitter is boosted up by using the semiconductor optical amplifier. The optimized parameters of SOA used in the simulation are as follows: bias current is 400 mA, the length is 650 μm , the width of the active layer is 2 μm , its thickness is 0.2 μm and the confinement factor is 0.4. The transparency carrier density in the SOA is taken to be $1.5 \times 10^{24} \text{ cm}^{-3}$, spontaneous carrier lifetime is 0.3 ns and the differential gain is $2 \times 10^{-16} \text{ cm}^2$. The input and output coupling losses of SOA are taken as 3 dB. The SOA provides a gain of 26 dB. The optical signal power and spectrum at different levels are observed from optical Power meter and optical probe by splitting the signal from transmission link with the use of optical splitters. Optical and electrical raised cosine filter, PIN photodiode are the part of a single receiver. Optical filter has 0.5 raised cosine roll off, 193.15 THz center frequency, 60 GHz bandwidth. PIN photodiode converts the optical signal into electrical signal having responsivity of 0.87 A/W; zero dark current and quantum efficiency is 0.7. Electrical filter in the receiver side is raised cosine filter and has bandwidth 10 GHz. To observe the changes in the performance, Electrical scope is used to obtain the eye diagram. The values of Q factor, BER and Eye closure can be analyzed from the eye diagram.

Results and Discussion

In this study, we report transmission results obtained with optimized semiconductor optical amplifier in optical communication system. The performance of 320 GB/s dense wavelength multiplexed system is investigated by varying the signal input power with 50 GHz channel spacing. In Fig. 2, bit error rate versus transmission distance for different input signal power is plotted. It is observed that minimum BER is obtained which is 1×10^{-40} at 100 km transmission distance at -20 dBm input signal power. The acceptable bit error rate (1.02×10^{-9}) is achieved up to 294 km. It is also observed that the bit error rate increases with the reduction in the

Fig. 2 Bit error rate versus transmission distance at different signal input powers

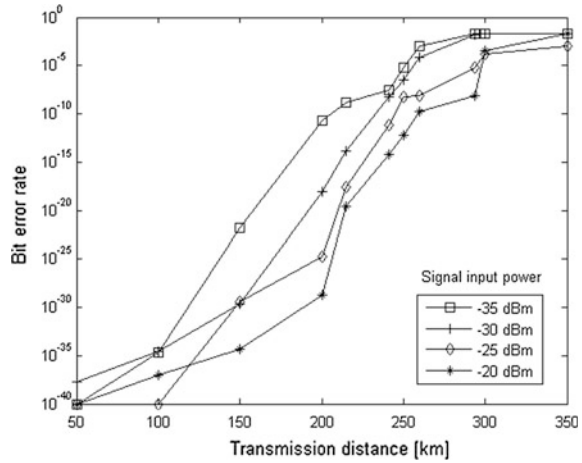
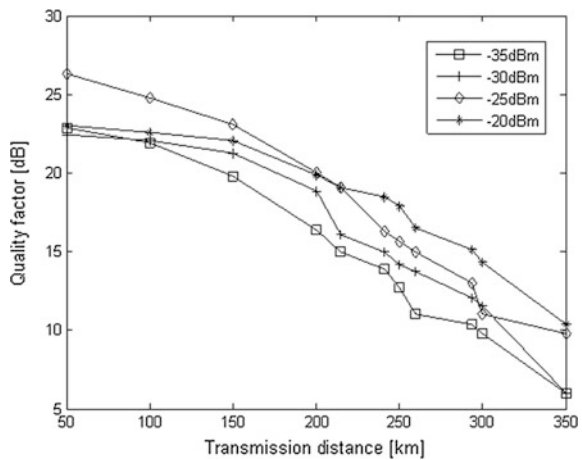


Fig. 3 Quality factor versus transmission distance at different input signal powers

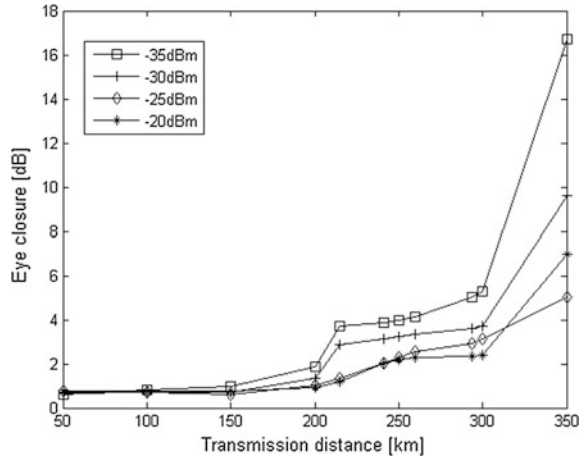


input signal power at the optical fiber link. At -35 dBm input signal power, bit error rate reduces and successfully transmission up to 215 km is achieved.

For different input signal power, the Q factor versus transmission distance is as shown in Fig. 3. It is evident that the quality of the output signal decreases with increasing the length of the fiber due to the fiber non-linearities and fiber attenuation. The acceptable Q factor (15.02 dB) is obtained at -35 dBm signal input power up to 215 km transmission distance. This shows improvement over the results reported in [10], where they analyzed the transmission distance of 204 km with only one channel at 100 GHz channel spacing.

The plot of eye closure vs. transmission distance for different input signal powers is shown in Fig. 4. For high input signal power of -20 dBm, eye closure of

Fig. 4 Eye closure versus transmission distance at different signal input powers



2.32 dB is achieved at 294 km and at low input signal power of -35 dBm it becomes 3.95 dB for 215 km transmission distance.

Figure 5 depicts the transmission distance versus optical output power for different input signal powers. For -20 dBm input signal power up to 294 km transmission distance, -35.59 dBm output power is obtained. The output optical power of -34.00 dBm is achieved for 215 km transmission distance at low input signal power of -35 dBm.

Figure 6 shows optical power spectrum from simulation results. The optical output power of -34.00 dBm is observed at -35 dBm signal input power up to 215 km transmission distance. At high value of input signal power (-25 dBm), -32.98 dBm output optical power is received for 260 km transmission distance.

Fig. 5 Output optical power versus transmission distance at different signal input powers

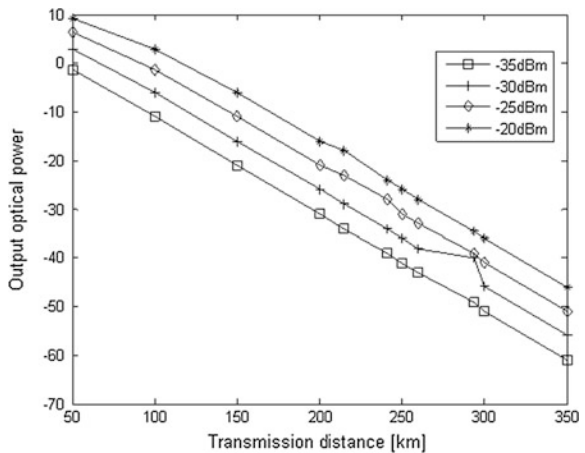
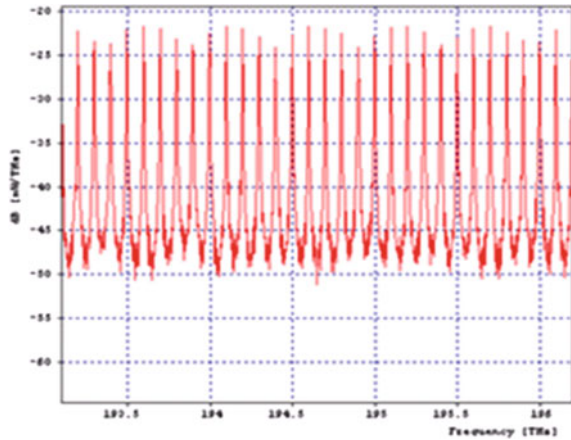


Fig. 6 Optical output power spectrum



Conclusion

The 32 channel DWDM system at 10 GB/s have been reported in this paper. The results are compared on the basis of eye closure, output optical power, bit error rate, and quality factor for different input signal powers and transmission distances by using optimized SOA. The quality of the transmitted signal is greatly degraded when the signal input power decreases. We investigate the maximum single span distance up to 215 km at -35 dBm signal input power using optimized semiconductor optical amplifier. It is also observed that the signal can be effectively transmitted with acceptable performance up to 294 km transmission distance for -20 dBm signal input power.

References

1. Wei, J.L., Hamie, A., Giddings, R.P., Tang, J.M.: Semiconductor optical amplifier-enabled intensity modulation of adaptively modulated optical OFDM signals in SMF-based IMDD systems. *J. Lightwave Technol.* **27**(16), 3678–3688 (2009)
2. Marazzi, L., Parolari, P., Brunero, M., Martinelli, M., Chanclou, P.: O-Band 10-Gb/s operation of a reflective semiconductor optical amplifier based self-seeded transmitter for optical access applications. *Fiber Integr. Opt.* **33**(3), 173–183 (2014)
3. Khaleghi, H., Morel, P., Sharaiha, A., Rampone, T.: Experimental validation of numerical simulation and performance analysis of a coherent optical-OFDM transmission system employing a semiconductor optical amplifier. *J. Lightwave Technol.* **31**(1), 161–170 (2013)
4. Dewra, S., Kaler, R.S.: Performance evaluation of optical add drop multiplexers with Mach-Zehnder interferometer techniques for dense wavelength division multiplexed system. *OSA: J. Opt. Technol.* **80**(9), 526–531 (2013)
5. Zoiros, K.E., O’Riordan, C., Connelly, M.J.: Semiconductor optical amplifier pattern effect suppression using Lyot filter. *Electron. Lett.* **45**(23), 1187–1189 (2009)

6. Webb, R.P., Dailey, J.M., Manning, R.J.: Applications of semiconductor optical amplifiers. In: 17th Opto-Electronics and Communications Conference (OECC 2012) Technical Digest, Busan, Korea, pp. 825–826 (2012)
7. Li, Z., Yi, D., Mo, J., Wang, Y., Lu, C.: 1050-km WDM transmission of 8×10.709 Gb/s DPSK signal using cascaded in-line semiconductor optical amplifier. *IEEE Photonics Technol. Lett.* **16**(7), 1685–1687 (2004)
8. Rani, A., Dewra, S.: Performance evaluation of DWDM system using semiconductor optical amplifier in the presence of fiber non-linearities. *Int. J. Enhanced Res. Sci. Technol. Eng.* **3**(2), 301–305 (2014)
9. Jennen, J., de Waardt, H., Acket, G.: Modeling and performance analysis of WDM transmission links employing semiconductor optical amplifiers. *J. Lightwave Technol.* **19**(8), 1116–1124 (2001)
10. Kim, Y., Jang, H., Kim, Y., Lee, J., Jang, D., Jeong, J.: Transmission performance of 10-Gb/s 1550-nm transmitters using semiconductor optical amplifiers as booster amplifiers. *IEEE J. Lightwave Technol.* **21**(2), 476–478 (2003)
11. Singh, S., Kaler, R.S.: Placement of optimized semiconductor optical amplifier in Fiber optical communication systems. *Optik—Inter. J. Light Electron Opt.* **119**(6), 296–302 (2008)
12. Parolari, P., Marazzi, L., Brunero, M., Martinelli, M., Brenot, R., Maho, A., Barbet, S., Gavioli, G., Simon, G., Saliou, F., Chanclou, P.: 10-Gb/s Operation of a colorless self-seeded transmitter over more than 70 km of SSMF. *IEEE Photonics Technol. Lett.* **26**(6) 599–602 (2014)

Automatic License Plate Recognition System Using Raspberry Pi

Vijayaraghavan Sundararaman, T.G. Vijayalakshmi, G.V. Swathi and Sambit Mohapatra

Abstract In the last few decades, Automatic License Plate Recognition (ALPR) has been employed in many developed countries for Traffic management, Automatic speed control, tracking the stolen cars and also in automatic Toll systems for improving the Traffic Control. Due to the increase in the number of cars and other transportations it has become very difficult to control the traffic by the Humans. Automatic License Plate Recognition (ALPR) is a surveillance system that extracts the information from the vehicle license plate by capturing the images. The objective of this paper is to introduce a Completely Automated license Plate Recognition system using the Optical Character Recognition (OCR) to read the information on the images of license plate of vehicles captured by the camera on real time basis. The image of the Vehicles License plate is captured and is processed by the segmentation of the characters and is verified by the Raspberry Pi Processor for the authentication purpose.

Keywords ALPR · OCR · Character segmentation · Character recognition · Raspberry Pi

Vijayaraghavan Sundararaman (✉) · T.G. Vijayalakshmi · G.V. Swathi
Nagarjuna College of Engineering and Technology, Bangalore, India
e-mail: vijaygenius123@gmail.com

T.G. Vijayalakshmi
e-mail: vijayalakshmi.tg3@gmail.com

G.V. Swathi
e-mail: swathi.venkatadri@gmail.com

Sambit Mohapatra
National Institute of Electronics and IT, Calicut, India
e-mail: mohapatra.sambit8467@gmail.com

Introduction

Automatic license plate recognition (ALPR) [1] is a large-scale vigilance system that is based on mainly two important factors they are acquisition of the image through the camera and the character recognition system. As there is tremendous growth in the number of vehicles in the developed as well the developing countries, it is important to have a strict traffic regulation that needs to be implied. This method can be employed in Automatic Toll payment systems and also by the Police forces for tracking the stolen vehicles easily [2]. Since the license plate of the vehicle is unique to each vehicle and it is very easy for the identification and also the location of the vehicle. The image of the vehicle is captured and is processed by Raspberry Pi [3, 4] processor to identify the license plate of the vehicle and is given to the optical character recognition (OCR) system for the robust character recognition from the vehicle license plate. The OCR reduces the noises in the picture and recognizes the character. Further Raspberry Pi processes the information for the authentication of the vehicle's number plate and collects the information regarding the authenticity of the registered vehicle. It further stores this information for future use.

Proposed Methodology

ALPR is a region specific system, due to the variation of the license plate patterns that differ from place to place. The image is captured using a camera shown in Fig. 1. The captured image is processed by the single-board credit card sized computer called Raspberry Pi. It detects the rectangular license plate and figures it out with a rectangle as shown in Fig. 2. Later the Processed image is subjected to the Optical Character Recognition where the characters are segmented. The segmentation is continued by matching it with the templates for the recognition of the characters of the license plate.

Fig. 1 Captured image



Fig. 2 Processed image



Fig. 3 Raspberry Pi processor



Raspberry Pi is a single-board single chip computer that employs python platform for the detection of the captured from the captured images [6]. Later the recognized characters are used for the vehicle identification. The Raspberry pi processor is shown in Fig. 3. The processor stores the information regarding the license plate and the registered vehicle driver for further interactions. A high quality camera is used for acquiring the image of the license plate on real time basis from a toll system or from the traffic signal polls.

The image acquisition is being done by interfacing a camera to the processor. The Raspberry Pi extracts only the vital dimensions of the license plate from the image for the recognition of the characters as depicted in Figs. 4 and 5.

The processed image is given to the OCR for recognition of the characters. The OCR involves two major stages those are character segmentation and character recognition. The character segmentation [5] can be employed by various methods. The method used in this proposed system is by increasing the contrast of the image



Fig. 4 Python program for image acquisition



Fig. 5 Extracted image



Fig. 6 Character segmentation

initially and each character on the image is segregated by drawing rectangles around each character as shown in Fig. 6.

The characters are then matched with the templates and are recognized. The character recognition becomes difficult if the segmentation is not done properly which may result in misidentification of the characters [7, 8]. Therefore, the picture's contrast should be increased in such a way that it reduces the noise in the images. The OCR matches the characters along with the template characters and the corresponding template character is the recognized character in the license plate.

The flowchart of the operations of this system is illustrated in Fig. 7.

The output of the system is as shown in Fig. 8.

Fig. 7 Flowchart of the system

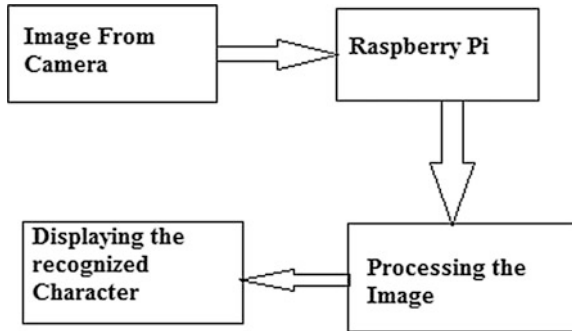
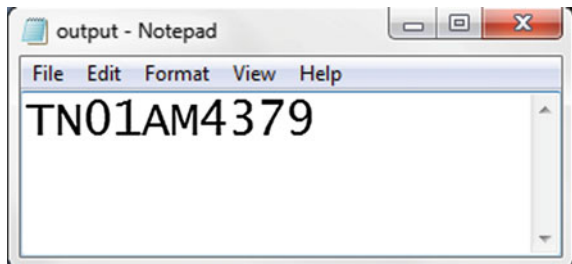


Fig. 8 Recognized character output



Experimental Results

The Automated License Plate Recognition system is programmed in Python on Raspberry Pi Processor has been tested. The pictures of around 100 vehicles have been taken and are tested for its reliability. The results were quite satisfactory with 96 % accuracy in the recognition of the characters of the License plate of the vehicles.

References

1. Hsieh, C.T., Juan, Y.S., Hung, K.M.: Multiple license plate detection for complex background. Proc. Int. Conf. AINA 2, 389–392 (2005)
2. <http://www.ct.aegean.gr/people/anagnostopoulos/cv/T-ITS-05-08-0095.pdf>
3. VallapReddy, K., Sunkari, S.: A new method of license plate recognition system using raspberry Pi processor. IJCSJET–Int. J. Comput. Sci. Inf. Eng. Technol. ISSN: 2277-4408
4. http://en.wikipedia.org/wiki/Raspberry_Pi
5. <http://inf.ucv.ro/~ami/index.php/ami/article/viewFile/388/351>
6. Anagnostopoulos, C.-N.E., Anagnostopoulos, I.E., Psoroulas, I.D., Loumos, V., Kayafas, E.: License plate recognition from still images and video sequences: a survey. IEEE Trans. Intell. Transp. Syst. 9(3), 377–391 (2008)

7. Kumar, T.S., Sivanandam, S.N.: Object detection and tracking in video using particle filter. In: 2012 Third International Conference on Computing Communication and Networking Technologies (ICCCNT), pp. 1–10 (2012). [Abstract](#) | [Full Text: PDF \(1900 KB\)](#)
8. Coetzee, C.C, Botha, C. Weber, D.: PC based number plate recognition system. In: Proceedings of IEEE International Symposium on Industrial Electronics, vol. 2, pp. 605–610, July 1998

Multiple Sink Data Aggregation

Krishna Joshi, T.P. Sharma, Shadab Siddiqui and Shahin Fatima

Abstract In-network aggregation is a technique in which queries are propagated in the network and in response phase information is processed at aggregator node only. In wireless sensor network, nodes are deployed in a particular area for sensing certain parameters like sound vibration, humidity, temperature etc. Information sensed by nodes may be highly correlated and redundant. It is not energy efficient to send correlated, redundant data to the sink. In wireless sensor network, correlation (spatial or temporal or spatiotemporal) among sensor readings may be exploited to reduce battery consumption and increase network lifetime. In this paper we propose an approach that handles multiplicity of sinks and shares information among sinks.

Keywords Multiple sink · Data aggregation · Aggregation protocol · Query aggregation

Krishna Joshi (✉) · Shadab Siddiqui · Shahin Fatima
Department of Computer Science and Engineering, BBDNITM, Lucknow, India
e-mail: kr.rocks08@gmail.com

Shadab Siddiqui
e-mail: cshadabsiddiqui@gmail.com

Shahin Fatima
e-mail: shahinfatima@hotmail.com

T.P. Sharma
Department of Computer Science and Engineering, National Institute of Technology,
Hamirpur, Himachal Pradesh, India
e-mail: teekparval@gmail.com

General

Wireless sensor node is a network of sensor nodes. Each sensor node in a network has sensing and communication abilities. In sensor network, sensor nodes have generally resource and battery limitations. Basic purpose is to increase network lifetime and reduce the energy consumption in processing and communication among nodes. Wireless sensor network exhibits some correlation among nodes reading. Spatial correlation is one such relation among node readings in which neighbor nodes have similar type of readings. Network energy can be saved by identifying those nodes and only one node from cluster is sufficient to represent the whole cluster reading without need to send data reading from every node. Only cluster head sends the reading towards sink node after processing. In data aggregation there are some problems. Optimization function used for data aggregation is spatial or temporal or spatiotemporal. Schemes proposed by various researchers [1–3] use spatiotemporal approach for data aggregation. Multiple sinks handling is a research area in the field of data aggregation. In this paper, we focus on two problems handling of multiple sink and sink results utilization for another sinks. CAG [1] uses tree based aggregation approach. For single sink, query request is propagated in the network and aggregator nodes are decided. whereas in our work tree is again used for another sinks. Purpose of this paper is to utilize tree again for another sink if request is same and time difference between requests is below threshold value.

Critical Review of Literature

Villas et al. [2] states that temporal correlation is used in sensor network when sensors consecutive reading difference is below specified threshold, in that case no need to send repeated data towards sink node. Data aggregation perform remove data redundancy at intermediate nodes [4]. In many existing approaches aggregator nodes are decided either statically or dynamically. Aggregator nodes fuse data from multiple sensors at intermediate level and finally the fused data are sent towards base station or sink. Query operator may be max, min, avg, sum etc.

Yoon et al. [1] proposes CAG technique for data aggregation in wireless sensor network. CAG works for query operator *max for maximum, min for minimum, avg, for average, sum for summation, std for standard deviation*. CAG exploits both spatial and temporal correlation in data aggregation. CAG works in two modes: streaming and interactive. In interactive mode sink node sends query $Q = \langle \text{Queryid}, O_i, \tau, \text{Parentid}, \text{Myid}, \text{level}, \text{CR} \rangle$, where O_i is the attribute and τ is the user-provided error threshold, *Parentid* is the ID of the parent node in the forwarding tree, *Myid* is

the node ID of the node that transmit data, *level* represents depth of the current node in the tree. After receiving the query, each node compares Clusterhead reading *CR* with sensor's own reading *MR*. If $\text{mod}(\text{MR}-\text{CR}) \leq \text{range} \times \tau$ where $\text{Range} = \text{MaxValue} - \text{MinValue}$ of the entire dataset, then sensor node joins cluster and broadcast message. In query phase cluster head decides.

In response phase, timer is triggered at each level from bottom level to top level. It is assured that child nodes trigger should be fired before parent node trigger. At each trigger cluster heads at corresponding level aggregate their readings with received readings and send aggregate results upwards in the tree. Finally base station or sink receives the aggregate query result from the network. In Streaming mode CAG uses both spatial and temporal correlation in data aggregation. In query phase streaming mode works same as in interactive mode but in response phase periodic responses are generated. In streaming mode tree is not changed when reading changes below specified threshold but only cluster heads are changed. *Cluster Adjustment* function adjusts node when the sensor readings change. Disadvantage of this approach is that multiple sink problem is not resolved in it.

LEACH [5] is cluster based hierarchical protocol and distributes battery power consumption among sensor nodes. Clusters are decided in setup phase and data transfers in steady state phase. Depend on the strength of message node joins cluster head.

HEED [6] is a tree based data aggregation protocol. HEED make assumption about multiple power level at each node but do not make assumption about location awareness.

Lindsey et al. [7] proposes an approach in which data aggregation is chain based. Chain formation start from the farthest node.

Sharma et al. [8] states that when no grid is present then grid formation is started by sink node. All the nodes in the grid forms cluster and accordingly communication range also. Multiplicity of link is handled and ensures continuous delivery.

Goel et al. [9] proposed an algorithm prediction based monitoring in data model is predicted based upon correlation like spatial, temporal, spatio temporal.

Deshpande et al. [10] proposes a model BBQ for data aggregation in sensor network through database queries. In BBQ time varying Gaussian function is used for data prediction.

Gupta et al. [11] proposed spatial correlation approach called *connected correlation dominating set*. Exploits only spatial correlation.

Villas et al. [2] proposed an algorithm that exploits both spatial and temporal correlation. In this scheme author divides sensor area into cells. In every cell there is a *coordinator node* that ensures spatial correlation, *representative node* ensures temporal correlation, *relay node*, *sink node*.

Energy Efficient Data Collection approach exploits both temporal correlation. In this approach cluster formation is converted into a *clique covering problem* (an NP complete problem). The proposed algorithm is solvable in $O(n^2 \log n)$ time.

In EEDC, the Sensor Network is represented as a graph considering Sensor nodes as vertices and connects them by an edge if difference between sensor readings of two vertices is below threshold value. Now the problem is to find all the cliques in a graph. Remaining of this paper is structured as follows.

Section “[Critical Review of Literature](#)” describes protocol and structure including system model, algorithm and flow charts. Section “[Protocol and Structure](#)” is concluded with conclusion included research issues in data aggregation.

Protocol and Structure

System Model

The main components of a sensor node are a microcontroller, transceiver, external memory, power source and one or more sensors. In our proposed scheme all nodes are homogeneous. Nodes are randomly and densely distributed. Inter node distance is decided as greater than 10 m and less than 35 m. Two types of topologies are used (1) Lossless Topologies (2) Topologies constructed using empirical data loss. WSNs use license-free communication frequencies: 173, 433, 868, and 915 MHz; and 2.4 GHz. Wireless sensor nodes are typically equipped with a limited power source of less than 0.5–2 A h and 1.2–3.7 V. Data Based Correlation Scheme

Multiple Sink Aggregation Algorithm

Function *Query Received at node n*

```

If (query entry corresponding to  $j \neq i$  present
  &&Operator $j=Operatori$ &&Timestamp $i-Timestampj$ )
  While(  $node \neq Sinkj$ )
    Send query  $Q$  for sink  $i$  to Parentid of node  $n$ .
    .  $node=node.Parentid$ .
  Get result from Sink  $j$ .
Else
  Sink $i$ .clusterhead=FALSE.
  Broadcast query  $q$ .
Else
  Sink $i$ .clusterhead=TRUE.
  Broadcast query  $Q$ .
end If
end If

```

Function *Temporal Adjustment Timer.fired* at node *n* for sink *i*

```

If (node.reading (clusterheadreading+ ,
clusterheadreading- ))
    If(node.reading neighbours clustering range)
        Set parent id corresponding to Neighbour's node.
        Notify old and new clusterhead.
    Else
        Declare itself clusterhead.
        Notify change membership to old
        clusterhead.
    end If
end If
If(clusterdeclare,clusterjoin,clusteradjustment msg received)
    Propagate temporaladjustment msg.
endif
Function Temporaladjustment message received at node n for sink i
If(clusterheadid==clusteradjustmentmsg.previous clusterheadid)
    Process temporal adjustment.
Else
    Discard message.

```

Function *Message.Fired* at node *n* for sink *i*

```

If clusterhead then
    Forward aggregate(buff,Myreading,sinkid)
Else
    If (size(buff)>0)
        Forward aggregate(buff,sinkid). end If
end If

```

Flowchart

In Fig. 1. Flowchart for query received function is explained, in which sensor node receives query from other nodes. In Fig. 2. Temporal adjustment function is explained. Temporal adjustment function implement temporal correlation. In Fig. 3 flowchart for temporal adjustment timer function is explained. Multiple sink data aggregation approach is an extension of CAG. CAG exploits both temporal and spatial correlation among data. Disadvantage of CAG is that it works for single sink or base station. In this paper some optimization are performed for data aggregation if multiple sinks are present in the network. Sink location is static but sink may enter dynamically in the network. In military applications sink may enter from anywhere in the network. Aim of this approach is to use sink results by another sinks that may

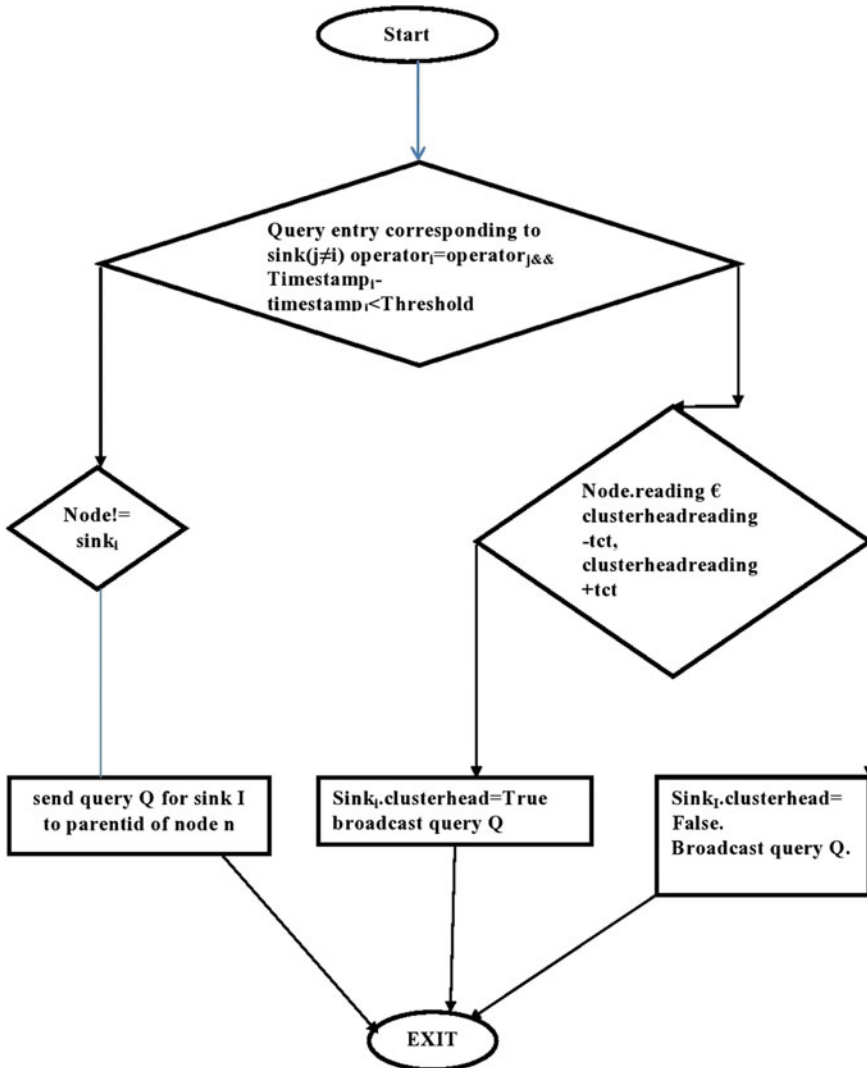
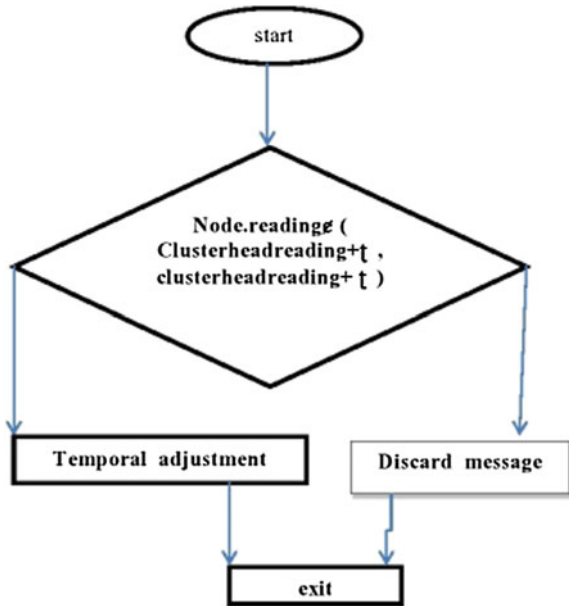


Fig. 1 Flowchart for query received function

enter dynamically in the network. Sink node send query $Q = \langle Sinkid, Queryid, Tct, Operator \rangle$ to the root node. *Sinkid* is the id of sink, *Queryid* is the id of query, *Operator* is query operator like *max*, *min*, *sum*. *Tct* is user defined threshold. Root node receives query from base station and appends some parameters $Q = \langle UQ, Parentid, Clusterheadreading, Timestamp, Myid \rangle$ *Parentid* is the node id of parent in forwarding tree *Timestamp* is time of query request to the network. After receiving query node checks that if there is request present in the network for another sink for

Fig. 2 Flowchart function temporal adjustment message



same operator and difference between requests is within threshold. If request is present in the network then query receiving node searches the path towards sink that has made request for same operator and find that sink. After finding sink result is sent back and reply path is same as the path used in forwarding data. If no such query exists at the node or time between query requests is greater than threshold than node that received request from root node broadcasts request to neighbor nodes that are in communication range with node. *Clusterheadreading* parameter is included in the query to be compared with each MR when it is received by a node. Initially root node copies its own value in the *Clusterheadreading* field. Node checks its value lies between $[Clusterheadreading - Tct, Clusterheadreading + Tct]$ or not, if lies then node joins cluster otherwise node makes itself as cluster head and copies its own value in the *Clusterheadreading* parameter and broadcasts packet forward. In query propagation phase routing tree is formed and cluster heads are decided. Temporal adjustment timer is fired in top to bottom order of tree. If some nodes readings change in a tree than tree adjust itself. When temporal adjustment timer fires for that tree Node checks its value with its cluster range, if the reading does not lie in range $[Clusterheadreading - Tct, Clusterheadreading + Tct]$ than node checks its neighbors readings. If node's reading lies within range of neighbor's cluster head than node joins its neighbor and informs to old and new cluster head and propagate message to its children, else node declares itself as cluster head, inform to old cluster head from which node belongs and propagates message to child node. Upon receiving message child nodes whose cluster head is same as message sending node, process temporal



Fig. 3 Flowchart temporal adjustment timer function

adjustment function again according to their reading. At message fired event cluster heads aggregates data receive from children nodes and forward aggregate data towards sink in upward direction. Message fired event is performed in bottom to top order for every tree. Multiple tree may exist at a time when different sinks request for different operators at a time.

Conclusion

Our scheme extends multiple sinks handling in data aggregation technique and also sharing of information among sinks. CAG exploits spatial and temporal correlation but not handles multiple sink whereas our scheme extends the functionality provided in CAG. Our scheme exploits spatial and temporal correlation and also sinks can share information among them. Results of one sink may be used by other sinks if request is for same operator and time between requests is below specified threshold. Faulty sinks detection is a research issue in this area. In case of dynamic or movable sink, sharing information among sink is an another research issue. Unlike CAG our scheme need not to form tree again if request for same operator is present in the network.

References

1. Yoon, S., Shahabi, C.: The clustered aggregation (CAG) technique leveraging spatial and temporal correlations in wireless sensor networks. *ACM Trans. Sens. Netw.* **3**(1) (2007) (Article 3, Publication date March)
2. Villas, L.A., Boukerche, A., Guidoni, D.L., de Oliveira, H.A.B.F., de Araujo, R.B., Loureiro, A.A.F.: An energy-aware spatio-temporal correlation mechanism to perform efficient data collection in wireless sensor networks. *Comput. Commun.* **36**(9), 1054–1066
3. Liu, C., Wu, K., Pei, J.: An energy-efficient data collection framework for wireless sensor networks by exploiting spatiotemporal correlation. *Parallel Distrib. Syst.* **18**(7) (2007)
4. Rajagopalan, R., Varshney, P.K.: Data aggregation techniques in sensor networks: a survey. Department of Electrical Engineering & Computer Science Syracuse University Syracuse, NY
5. Heinzelman, W.B., Chandrakasan, A.P., Balakrishnan, H.: An application-specific protocol architecture for wireless microsensor networks. *IEEE Trans. Wireless Commun.* **1**(4), 660–670 (2002)
6. Younis, O., Fahmy, S.: HEED: a hybrid, energy-efficient, distributed clustering approach for ad hoc sensor networks. *IEEE Trans. Mob. Comput.* **3**(4), 366–379 (2004)
7. Lindsey, S., Raghavendra, C., Sivalingam, K.M.: Data gathering algorithms in sensor networks using energy metrics. *IEEE Trans. Parallel Distrib. Syst.* **13**(9), 924–935 (2002)
8. Sharma, T.P., Joshi, R.C., Mishra, M.: GBDD: grid based data dissemination in wireless sensor networks. In: 16th International Conference on Advanced Computing and Communications, 2008. ADCOM 2008. 14–17 Dec 2008, pp. 234–240, Chennai
9. Goel, S., Imielinski, T.: Prediction-based monitoring in sensor networks: taking lessons from MPEG. *ACM Comput. Commun. Rev.* **31**(5) (2001)
10. Deshpande, A., Guestrin, C., Hellerstein, J.M., Madden, S.R., Hong, W.: Model-driven data acquisition in sensor networks. In: 30th VLDB Conference, Toronto, Canada (2004)
11. Gupta, H, Navda, V., Das, S.R., Chowdhary, V.: Efficient gathering of correlated data in sensor networks. In: *MobiHoc'05*, May 25–27, 2005, Urbana- Champaign, Illinois, USA

Handwritten Devnagari Script Database Development for Off-Line Hindi Character with Matra (Modifiers)

Maninder Singh Nehra, Neeta Nain and Mushtaq Ahmed

Abstract Due to advancement in digital technology, handwritten Character recognition plays a significant role for interaction between human and computer. For recognition of handwritten character a standard database is required. There is no benchmark data base of Devnagari script in Hindi with matra's (modifiers). A database for off-line Hindi handwritten character with modifier is developed. The database consist more than 23000 images of their original size with programmatically segmented consonant and vowels. The Data set is collected from persons of different gender, age, profession and educational qualification. Data are also collected from person of different geographical location of India.

Keywords Handwritten text · Database · Modifiers

Introduction

Recognition of handwritten character is challenging area in pattern recognition because of different writing style of writers. Handwritten character is change according to human age, sex, qualification, working culture and frame of mind. For research in this area required proper escalation in technology. Digitization of handwritten document increase and it is an integral part of optical character recognition. Research in the handwritten character recognition plays a significant role in historical document recognition and their proper arrangement. There are many application of handwritten character recognition like in banking, offices, postal services, form processing, exam evaluation etc.

M.S. Nehra (✉) · Neeta Nain · Mushtaq Ahmed
Malaviya National Institute of Technology, Jaipur, India
e-mail: maninder4nehra@yahoo.com

Neeta Nain
e-mail: neetanain@yahoo.com

Mushtaq Ahmed
e-mail: mahmed.cse@mnit.ac.in

क	ख	ग	घ	ङ	च	छ	ज	झ	ञ
ट	ठ	ड	ढ	ण	त	थ	द	ध	न
प	फ	ब	भ	म	य	र	ल	व	श
ष	स	ह	क्ष	त्र	ळ				

Fig. 1 Hindi handwritten consonants

Devnagari script is anonomatopoeic of ancient Brahmi script which is the mother of almost all Indian scripts. Devnagari is script in which many languages are written, like the most popular language Hindi, Sanskrit, Konkani, Nepali, Marathi and Sindhi due to Chaudhary [1]. Hindi is the national language of India and the third most frequently used language in the world. So the research in Devnagari script (Hindi) is very useful. The alphabet set of Devnagariscript has 36 consonants and 12 vowels as shown in Figs. 1 and 2. Besides the consonants and vowels it has modifiers also called matra's which when combined with vowels form compound characters. The modifiers can be placed at the left or right and above or bottom of a vowel. Handwritten character recognition for Devnagari script (Hindi) is of two types, off-line and on-line character recognition. Off-line handwritten characters are those in which handwritten character of writer is converted into digital form by scanning the handwritten paper. On-line handwritten characters are those in which, character are written on electronic surface such as digitizer with special pen. In on-line handwritten, two-dimensional coordinates of successive points of the characters take as function of time are stored which is spatial temporal demonstration of the input character. Whereas in off-line handwritten, the completed character is existing as an image [2]. A standard data base of hand-written Devnagari (Hindi) character is required to train a classifier for recognition. There are many handwritten text databases for languages like English database by Marti and Bunke [3], Urdu database by Sagheer and He [4], Chinese database by Wang

Fig. 2 Hindi handwritten vowels and modifiers

अ	आ	इ	ई	उ	ऊ
ए	ऐ	ओ	औ	अं	अः
व	वि	वी	उ	र	वै
वै	वै	वै	वाँ	वं	वः

and Cheng-Lin [5], Spanish database by Llorens et al. [6], Japanese database by Nakagawal and Matsumotol [7] etc. There are some datasets for Devnagari handwritten character recognition also but no standard Devnagari benchmarked data set with modifiers is available till date.

Bhattacharya and Chaudhuri [8, 9] developed handwritten numeral database for Devnagari and BanglaIndic script, in which they scanned digitized data at 300 dpi. Suen and Nadal [10] developed database for numerals at CENPARMI (Centre for Pattern Recognition and Machine Intelligence) at Canada. Hull [11] developed database for handwritten text at CEDAR (Center of Excellence for Document Analysis and Recognition) in state university of New York, Marti and Bunke [1] developed IAM-DB database for English etc. are not available freely and are specific. Ram Sarkar and Basu [12] developed a database for handwritten Bangla and Bangla-English (CMATERdb). In which they collected data from 40 different writers and scanned the documented data at 300 dpi.

Aggarwal and Rani [13] recognized handwritten Devnagari characters by gradient techniques. No standard data set was used; only a sample of 20 writers handwriting is taken. Al-Ma'adeed et al. [14] designed a data set for offline Arabic handwritten text with the help of around 100 different writers. Hull [15] prepared database for hand-written text of city names, states names and ZIP codes for post office. Dongre and Mankar [16] designed a data set for Devnagari handwritten character without matras (modifiers) with the help of 750 different writers. They scanned the handwritten sheet at 300 dpi. Ramdan et al. [17] designed a data set for Arabic handwriting with help of five writers of different ages and educational qualification. Marti and Bunke [3] describes database for English sentences offline handwriting (IAM- database) recognition with the help of around 400 different writers. Liwicki and Bunke [18] described a database for on-line English sentences of handwritten text. Bhattacharya and Chaudhuri [8] discussed a dataset that have 22,556 handwritten data. Sharma et al. [11] discussed quadratic classifier technique for recognition off-line handwritten Devnagari characters. In this technique the character data set used is around 11000 images, digitized at 300 dpi.

Hindi Handwritten Database Creation

Data Collection

For database creation of Hindi handwritten characters with matra, a blank paper of A4 size on which 60 rectangle blocks was designed. Consonants with modifiers and vowels are printed as the first line. A sample form is shown in the Fig. 3a. A total of 37 forms are designed (36 for consonant and one for vowels). The form also has boxes for writers to write their name, profession and tick on rectangles for gender, age-group, region and qualification. To cater to maximum syntactic variations the writers are chosen from different age groups, profession, region and educational

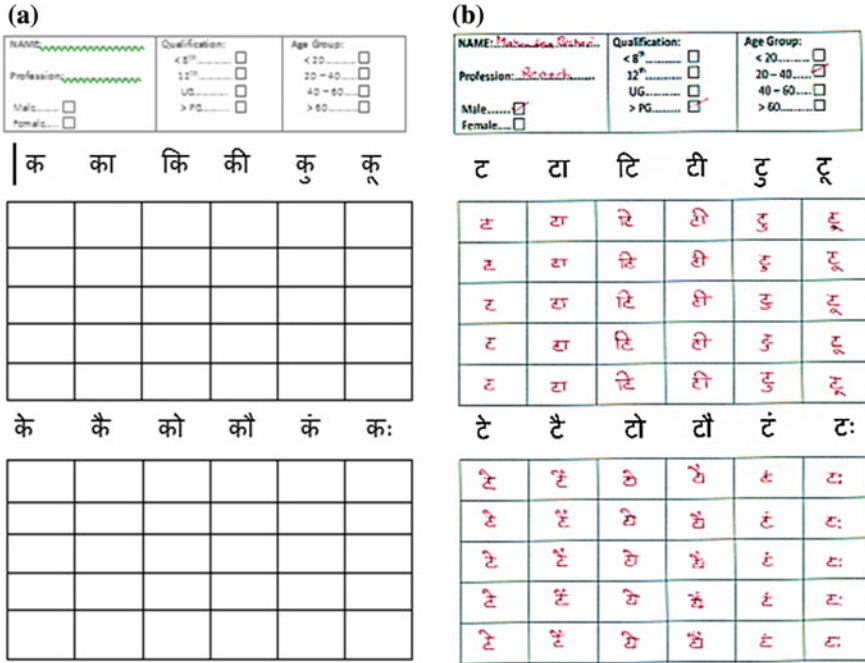


Fig. 3 a A sample blank form. b A sample filled form

qualifications. The forms filling sessions were carried out at geographically distant locations like shopping malls, railway stations, bus stand and hospitals etc., as the handwriting of a person sometimes gets affected by the mood, situation and surroundings. Multicolored ink (red, blue, green and black) and different styles like gel and ink pens are used for form filling. A sample of the filled sheet is shown in Fig. 3b. Besides this the persons from different graphical location of India are also involved in data collection; those who are comfortable with Hindi and those whose mother tongue is not Hindi. Approximately 1500 hundred of persons have filled the forms.

Segmentation and Digitization of Data

For digitization of collected data written by different writers, filled papers were scanned with the help of HP scanner at 600 dpi and scanned images were save in PNG image format. Total 48 folders are created for storage. A sample segmented characters output from is shown in Fig. 4. We have done a manual check on the



Fig. 4 Sample segmented characters extracted from a form filled by a writer

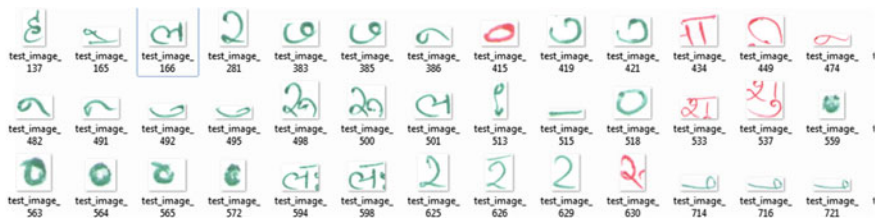


Fig. 5 Discarded characters and invalid strokes of modifiers

segmented characters and discarded the erroneous images. A sample of some discarded characters is shown in Fig. 5.

The segmentation of different characters from the scanned image is a puzzling work. The algorithm for segmentation of characters is explained in the following steps:

Algorithm: Handwritten character recognition.

Input: {Scanned form of handwritten characters}.

Output: {Isolated segmented characters}.

BEGIN

- Step1:** Read the scanned PNG image.
- Step2:** Convert the scanned image into binary image with appropriate threshold value.
- Step3:** Noise removal.
- Step4:** Calculate eight connected components for segmentation.
- Step5:** Check the segmented characters manually for proper shape.
- Step6:** Discard the erroneous characters.
- Step7:** Store the useful characters in separate folders (per character) in PNG format.

END

Information About Data Base

Devnagari script characters are written in cursive style and character are associated with lines and written on lined paper. The characters are sling from a horizontal line called the header stroke and there is no lower and upper cases like English characters. In Devnagari script about two third of space between line is used by the characters. In general the first stroke, or strokes, in a character are written from the left to the right and are then followed by any down strokes and eventually the head stroke is added. In handwritten documents due to improper writing of persons, character is not associated with lines. By this during the segmentation characters and their modifiers are segmented in improper format. Because of some writers may merge the characters which could not be recognized and sometimes the modifiers are also not properly placed. Such characters are not included in the data base and are discarded. Some of the Devnagari character(Hindi) are not used often like ञ, ड, ढ, etc. Some of the characters are written in more than one way like झ. The configuration of the properly segmented character with their modifiers is shown in the Table 1. The frequency of all characters is not equal as we have discarded the characters written in error and which encountered segmentation errors. The database is developed, so that it useful for the research in the handwritten character recognition.

Table 1 Hindi Handwritten character data set with frequency

S. No.	Hindi char.	Freq.	S. No.	Hindi char.	Freq.
1.	क	390	25.	म	390
2.	ख	304	26.	य	290
3.	ग	250	27.	र	260
4.	घ	290	28.	ल	280
5.	ङ	230	29.	व	270
6.	च	310	30.	श	300
7.	छ	280	31.	ष	280
8.	ज	300	32.	स	250
9.	झ	320	33.	ह	290
10.	ञ	280	34.	क्ष	230
11.	ट	350	35.	त्र	200
12.	ठ	230	36.	त्त	190
13.	ड	150	37.	अ	300
14.	ढ	230	38.	आ	290
15.	ण	200	39.	इ	250
16.	त	360	40.	ई	230
17.	थ	300	41.	उ	180
18.	द	380	42.	ऊ	200
19.	ध	320	43.	ए	190
20.	न	390	44.	ऐ	160
21.	प	340	45.	औ	170
22.	फ	360	46.	ओ	150
23.	ब	390	47.	अं	190
24.	भ	370	48.	अः	160

Conclusion and Future Work

We have developed database for off-line Hindi hand written characters with matras (modifiers) written by around 1500 writers from diverse places and from different backgrounds. During the development procedure, in output, some of the character images are not visibly identifiable, because they are not written properly by the writer and they not recognized by the system. Such characters are discarded. In this database more than 23000 handwritten (alphabets) characters images of consonants and vowels scanned at 600 dpi are created and the character images are stored as images in PNG image format for efficient use. To the best of our knowledge there is no such type of data set available for handwritten characters of Devnagari script in Hindi with modifiers. Such a dataset is very useful for validation of handwritten text recognition algorithms. It could be used for cross validation by dividing it suitably as training and testing data set. The database will be made available publically for researchers.

In future the data set will be extended to develop a complete corpus of hand-written Hindi words and lines which is very useful for benchmarking of handwritten segmentation algorithms.

References

1. Pal, U., Chaudhuri, B.B.: Automatic separation of machine-printed and hand-written text lines. In: Proceedings of ICDAR IEEE, pp. 645–648 (1999)
2. Plamondon, R., Srihari, S.N.: On-line and off-line handwriting recognition: a comprehensive survey. IEEE Trans. Pattern Anal. Mach. Intell., 63–84 (2000)
3. Marti, U.V., Bunke, H.: The IAM-database: and English sentence database for offline handwriting recognition. In: Int. J. Document Anal. Recognit., 39–46 (2002)
4. Sagheer, M.W., He, C.L., Nobile, N., Suen, C.Y.: A new large Urdu database for off-line handwriting recognition. In: Proceedings of ICIAP Springer, pp. 538–546 (2009)
5. Wang, D.H., Zhou, X.D.: CASIA-OLHWDB1: a database of online handwritten chinese characters. In: Proceedings of ICDAC IEEE, pp. 1206–1210 (2009)
6. Llorens, D., Prat, F., Marzal, A., Vilar, J.M.: The UJIPenchars Database: A Pen-Based Database of Isolated Handwritten Characters, pp. 2647–2651
7. Nakagawal, M., Matsumotol, K.: Collection of on-line handwritten Japanese character patterndatabases and their analyses. IJDAR, 69–81 (2004)
8. Bhattacharya, U., Chaudhuri, B.B.: HN databases of Indian scripts and multistage recognition of mixed numerals. IEEE Trans. Pattern Anal. Mach. Intell. 444–457 (2009)
9. Chaudhuri, B.B.: A Complete Handwritten Numeral Database of Bangla—A Major Indic Script. CVPR Unit, Indian Statistical Institute, Kolkata-108, India
10. Suen, C.Y., Nadal, C.: Computer recognition of unconstrained handwritten numerals. Proc. IEEE 80(7), 1–6 (1992)
11. Sharma, N., Pal, U., Kimura, F., Pal, S.: Recognition of off-line handwritten devnagari characters using quadratic classifier. In: Proceedings of the ICVGIP, pp. 805–816 (2006)
12. Sarkar, R., Basu, K.: MATERdb1: a database of unconstrained handwritten Bangla and Bangla–English mixed document image. IJDAR (Springer), 1–5 (2012)

13. Aggarwal, A., Rani, R.: Handwritten Devanagari character recognition using gradient features. *Int. J. Adv. Res. CSE*, 85–90 (2012)
14. Al-Ma'adeed, S., Elliman, D., Higgins, C.: A data base for arabic handwritten text recognition research. *Int. Arab J. Inf. Technol.* 117–121 (2004)
15. Hull, J.J.: A database for handwritten text recognition research. *IEEE Trans. Pattern Anal. Mach. Intell.* **16**, 550–554 (1994)
16. Dongre, V.J., Mankar, V.H.: Development of comprehensive Devnagari numeral and character database for offline HCR. *Proc. ACI Soft Comput.*, 1–5 (2012)
17. Ramdan, J., Omar, K., Faidzul, M., Mady, A.: Arabic handwriting database for text recognition. In: *Proceedings of the 4th International Conference on Electrical Engineering and Informatics*, pp. 580–584 (2013)
18. Liwicki, M., Bunke, H.: IAM-OnDB—An on-line English sentence database acquired from handwritten text on a whiteboard. <http://www.iam.unibe.ch/~fki/iamondb/>
19. Aryan, P.R., Supriana, I., Purwarianti, A.: Development of Indonesian Handwritten Text Databaseoffline Character Recognition. In: *International Conference on Electrical Engineering and Informatics*, pp. 1–5 (2011)
20. Bhattacharya, U., Chaudhuri, B.B.: Databases for research on recognition of handwritten characters of Indian scripts. In: *Proceedings of the 8th ICDAR*, pp.789–793 (2005)

Part-of-Speech Tagging of Hindi Corpus Using Rule-Based Method

Deepa Modi and Neeta Nain

Abstract The main goal of analysis of NLP (natural language processing) is to understand natural languages by parsing them. In the practice of analyzing natural languages there exist various sub-tasks. These sub-tasks depend on inbuilt structure of language and do not require complete knowledge and understanding of language. Part-of-speech tagging is one of them. Part-of-speech tagging is basically a practice of assigning language-specific grammatical tags to each word of language-specific input text, according to word's appearance in the text. These tags can be like noun, adverb, number, negative, etc. There exist a variety of taggers for most popular language in the world, i.e., English. But such taggers cannot be used for morphologically rich Hindi language as difference exists between structures of both languages. A "Rule-based system" is presented in this paper. 29 standard part-of-speech tags are used, including two special tags for date and time also in multiple formats. The special tags like punctuation, time, and date are based on regular expressions. Main aim of the proposed system is to increase automaticity and maintain high precision, while limiting the size of human made corpus. Proposed system uses human made corpus of around 9,000 words to increase tagging and rule-based (lexical features based) approach to decrease the size of already trained corpus. The system yields 91.84 % of average precision and 85.45 % of average accuracy.

Keywords Hindi · Probabilistic method · Rule-based method · Part-of-speech tagging

Deepa Modi (✉) · Neeta Nain
Department of Computer Science and Engineering, MNIT, Jaipur 302017, India
e-mail: deepa.modi22@gmail.com

Neeta Nain
e-mail: neetanain@yahoo.com

Introduction

Corpus annotation is a basic technique for processing natural languages. In the process of language annotation, input/output always appears in the pattern of a natural language like English, Hindi, etc. There exists more than one level of corpus annotation. For example, morphological analysis, POS tagging, chunk tagging, etc. POS tagging is basic step for language processing and can work as starting phase in other language processing tasks. It is a technique of assigning a token in a sentence as a particular POS tag or lexical belonging to a particular class (noun, number, adverb, time, date, etc.) based on its definition, contextual information, and morphological information. Formally it can be stated as, “While at the input a meaningful sequence of words $w_1 \dots w_n$ is given, at the output the system have to assign respective POS tags $t_1 \dots t_n$ to the provided sequence.” These tags are useful in assigning some additional information about a word. They state about relevance of word in the given context, they tell what the word’s role is in a given sentence; they give grammatical category to the word and assign grammatical features like person, number to the word. POS tagging is an intermediate step in processing of various NLP tasks, such as shallow and full parsing, word-sense disambiguation, machine learning, etc.

Hindi language is a feature rich language. So the most challenging objective in the area of POS tagging for Hindi language is identifying the ambiguities in tags.

Related Work

There exist a number of part-of-speech taggers for many languages using a number of approaches, especially for English language. Brill [1] defined a system based on transformation rules. Accuracy of this system is around 95 %. Zin and Thein [2] developed an algorithm for efficient POS tagging for Myanmar language based on pre-tagged corpus and probabilities calculated using HMM. The highest accuracy achieved by them is 97.56 % with training data of 1,000,000 words. For Hindi Language also there exists a number of implementation of POS taggers. AnnCorra, shortened for “Annotated Corpora,” is a project of Lexical Resources for Indian Languages (LERIL), is a collaborative effort of several groups. They developed a system using statistical approach, which provides syntactic and semantic information [3]. Mishra and Mishra [4] designed a POS system based on manually developed database of tagged Hindi words and an approach using rule-based method. Garg et al. [5] also implemented a POS system in their research for Hindi language based on rule-based approach and achieved average precision of 85.47 % on different data sets. Singh et al. [6] defined a system based on morphological analysis and CN2 algorithm (decision tree based learning algorithm). They got 93.45 % of accuracy for part-of-speech tagging for Hindi language which is further

increased by Dalal et al. [7] to 94.38 % using maximum entropy Markov model based on different features.

There are two types of approaches for POS tagging, stochastic based and rule based. Generally, stochastic methods are used to develop POS taggers as these methods require small knowledge of language and are very easy to implement. We propose a POST system which is based on rule-based technique. Rule-based approach generally requires vast knowledge of the language and is difficult to develop.

System Description

The proposed designed POS tagging system is useful for Hindi language processing. This system is developed using rule-based approach, which includes grammatical rules (based on prefixes and suffixes) and regular expression-based rules. 29 part-of-speech tags are used in standard format. 27 POS tags are taken from IIT—Hyderabad tagset [8] and two new special tags are included for time and date. Around 9,000 Hindi words database is prepared, which is stored in an .XML file. The proposed system is developed in Java language.

Approach Followed by the System

The proposed part-of-speech tagger (POST) system accepts data in Devanagari Hindi. The system verifies the input text, as text must be in Devanagari Hindi. After verification of input data, the system works in three sequential steps. In the very first step, it finds similarity of every word of the input data with the already trained language dependent corpus and tries to find a match. If a match is available then corresponding tag is assigned to input word. If there is no match available for a word then system goes to second step for further tagging.

In second step, the system searches various regular expressions (based on various finite state machines) in input text for numbers, punctuation marks, special symbols, time, and date like 987, *, &, 23:59, etc., and allot specific POS tag to input text. This kind of matching of regular expressions is very good as it increases the precision and accuracy of the system with significant percentage. Various string matching algorithms are applied here for matching a particular pattern.

In the final and third steps, the POST system applies various lexical rules (works on assumption that the tag for a word depends only on current word and not dependent on previous and next words and their tags) based on suffixes and prefixes of Hindi language to assign tags to the remaining unknown words. These rules are very powerful in part-of-speech tagging as there are many words in Hindi language, which start from prefixes or end with suffixes. Some of the examples of these rules are shown in Table 1.

Table 1 Some example rules based on prefixes and suffixes

S.No.	Prefix/ Suffix	Tag	Example
1	अति	Adjective	अतिशय,
2	अधि	Noun	अधिकरण, अधिकार
3	अनु	Noun	अनुकरण, अनुचर
4	अक /आक	Noun	लेखक, तैराक, लडाक
5	अक्कड	Adjective	भुलक्कड, घुमक्कड
6	आलू	Adjective	झगडालू

System Modules Description

A system can be very large to manage means as size and functionality of a system increases, it is very difficult to handle the system. So to manage the system, generally system is divided in subsystems or modules. Modularity defines the degree to which system components can be separated or recombined. As the value of the modularity increases, the system becomes more manageable and easy to handle. The presented system has following modules.

Read and Verify Hindi Text

The very first module of system reads and verifies Hindi data. It contains a text area in GUI. Here user has to enter his Hindi text. Module reads and verifies this text. Data must be Devanagari Hindi.

Split in Sentences

This module breaks input Hindi data in individual sentences according to delimiter, which can be “Puranviram” or “prashanvachak chinha.” In this module input will be Hindi (Devanagari) data and output will be individual Hindi sentence.

Tokenize in Words

This module breaks input Hindi data in individual words according to delimiter “space.” In this module input will be Hindi (Devanagari) data and output will be individual Hindi words. Output will be displayed in GUI.

Tag Hindi Data

This module tags each word of input Hindi (Devanagari) data with tags like pronoun, adverb, date, number, verb, time, etc. Words which are not tagged using corpus matcher or various rules are tagged as “SYM” tag. In this module input will be Devanagari Hindi data and output will be POS tagged Devanagari Hindi data. Output will be displayed in GUI.

Experiments and Results

A POS tagger system generally gives three main functionalities as breaking of input text in individual sentences and words and POS tagging for input text. Our system too provides these functionalities with 100 % correctness of split and tokenizes functionalities and 91.84 % precise POS tagging functionality. Various experiments have been performed to check validity of the system. In the following section, some experiments are stated with their respective results. Hindi text for experiments is taken from various domains like news, online data, Stories.

Experiment 1: Splitting

This experiment states system functionality of “split input Hindi text in individual sentences according to delimiter full stop or question mark.” Consider the following example,

Input text to the system:

“नई दिल्ली। सिविल सेवा देने वाले अभ्यर्थियों को इस साल से आयु में दो साल का फायदा मिलेगा। उन्हें दो अतिरिक्त मौके परीक्षा देने के लिए मिलेंगे।

Output of the system:

1. नई दिल्ली।
2. सिविल सेवा देने वाले अभ्यर्थियों को इस साल से आयु में दो साल का फायदा मिलेगा।
3. उन्हें दो अतिरिक्त मौके परीक्षा देने के लिए मिलेंगे।

Experiment 2: Tokenization

This experiment states system functionality of “Tokenize input Hindi text in individual words according to space delimiter.” Consider the following example, Input Text to the system:

“दो साल का फायदा मिलेगा”

Output of the system:

दो, साल, का, फायदा, मिलेगा

Experiment 3: POS Tagging

This experiment shows system functionality of “Part-of-speech tagging of input Hindi sequence.” Consider the following example,

Input Text to the system:

“सिविल सेवा देने वाले अभ्यर्थियों को इस साल से आयु में दो साल का फायदा मिलेगा।

Output of the system:

सिविल_NNC सेवा_NN देने_VNN वाले_PREP अभ्यर्थियों_NN को_PREP इस_PRP
साल_NN से_PREP आयु_NN में_PREP दो_QFNUM साल_NN का_PREP फायदा_NN
मिलेगा_VFM ।_PUNC

Evaluation

The system has validated on various data sets. We performed validation through holdout method. Evaluation measures of a system as Precision and Accuracy can be defined as [9],

$$Precision = \frac{\text{Number of correctly tagged words}}{\text{Total number of tagged words}} \quad (1)$$

$$Accuracy = \frac{\text{Number of correctly tagged words}}{\text{Total number of words}} \quad (2)$$

The system yields 91.84 % of average precision and 85.45 % of average accuracy. To the best of our knowledge, achieved precisions through this system are highest with good accuracies while having smallest database of already tagged corpus. In past Garg et al. [5] reported 85.47 % of precision with training data of around 18,000 words. Dalal et al. [7] and Singh et al. [6] achieved 94.38 % and 93.45 % respective accuracies with around training data of 15,500.

Conclusion and Future Work

The presented POST system is designed with the help of rule-based approach. Corpus matching is applied while tagging known words. For unknown words tagging various Hindi grammar rules are applied. These rules increase precision as well as accuracy of the system. The system can split and tokenize input Hindi text successfully. Input Hindi text can be tagged by presented system with average precision of 91.84 %. In future we would increase the precision and accuracy of the implemented POS system by focusing on increasing the number of effective grammatical rules or by applying more hybrid techniques, instead of increasing the size of already tagged corpus. We would also provide some additional functionality with POS tagging.

Reference

1. Brill, E.: A simple rule-based part of speech tagger. In: Proceedings of the Third Conference on Applied Natural Language Processing ANLC '92, Stroudsburg, PA, USA, pp. 152–155 (1992)
2. Zin, K.K., Thein, N.L.: Part of speech tagging for Myanmar using hidden markov model. In: Proceedings of International Conference on the Current Trends in Information Technology (CTIT), Dubai, Dec 2009, pp. 1–6 (2009)
3. Bharati, A., Sharma, D.M., and Sangal, R.: AnnCorra: An Introduction (Vol. 14), Technical Report no: TR-LTRC (2001)
4. Mishra, N., Mishra, A.: Part of speech tagging for Hindi corpus. In: Proceedings of the International Conference on Communication Systems and Network Technologies (CSNT), Katra, Jammu, India, June 2011, pp. 554–558 (2011)
5. Garg, N., Goyal, V., Preet, S.: Rule based Hindi part of speech tagger. In: Proceedings of Coling, Mumbai, India (2012)
6. Singh, S., Gupta, K., Shrivastava, M., Bhattacharyya, P.: Morphological richness offsets resource poverty—an experience in building a POS tagger for Hindi. In: Proceedings of Coling, Sydney, Australia (2006)
7. Dalal, A., Nagaraj, K., Sawant, U., Shelke, S., Bhattacharyya, P.: Building feature rich POS tagger for morphologically rich languages: experiences in Hindi. In: Proceedings of ICON (2007)
8. A part of speech tagger for Indian languages (pos tagger) (2007)
9. Fayyad, U.M., Shapiro, G., Smyth, P., Uthurusamy, R.: Advances in Knowledge Discovery and Data Mining, American Association for Artificial Intelligence, Menlo Park, CA, USA (1996)

A Survey on Security Analysis in Cloud Computing

Suryambika, Abhishek Bajpai and Shruti Singh

Abstract In the era of mobile computing, the number of mobile users has increased day by day. The computing capability, storage capability, processing speed of mobile, etc., required by a mobile user is higher, which may not be affordable by a mobile device. The advanced customers of e-Science require high performance, flexibility, and scalability (according to their demand, they can increase and decrease their use of resources), reduced cost, mobility, easy upgrades, etc. The cloud computing paradigm can fulfill the requirements of customers. The cloud computing is becoming the most profitable technology for service industries and can provide a new paradigm for business computation. Cloud provides the paradigm by which the users can access the resources from any geographical location at any time like using Google Doc, Microsoft SharePoint, GoGrid, etc. The different geographical locations and large number of users lead to different security issues for cloud. The main focus of this paper is to pinpoint the security threads for cloud computing. In this paper, we discuss design objectives, different models, challenges, and security of cloud with intrusion detection techniques.

Keywords Cloud · Design objectives · Model · Security

Introduction

The mobile users increased day by day, meanwhile the small data storage capacity, lower computation speed, etc, of mobile devices can be considered as a barrier in high performance. Cloud computing can help to overcome the small footprints of

Suryambika (✉) · Shruti Singh
Department of Computer Science and Engineering, SRMU, Barabanki 225003, India
e-mail: suryambikasingh12@gmail.com

Shruti Singh
e-mail: srt0701@gmail.com

Abhishek Bajpai
Faculty of Computer Science and Engineering, SRMU, Barabanki 225003, India
e-mail: abhishek_vajpayee@hotmail.com

mobile devices. Cloud computing empowers the storage, performance, flexibility, scalability, etc, and gives a high computation on mobile device.

Cloud computing-based business is predicted to rise from \$2.6 billion to \$ 39 billion between 2011 and 2016 [1]. Cloud system enables the users to access cloud according to their requirement of resources, services, network, data storage, etc, from the shared pool. The cloud computing is leveraged from utility computing and provides computing resources as a service with the advantage of pay-per-use.

Other than the storage and downloading of services, mobile application marketing has larger use of cloud computing [2]. Some of the commercial cloud providers are Amazon [3], Oracle [4], and Google [5], whereas Nimbus [6] and OpenNebula [7] provide academic accomplishment to build a Cloud.

In mobile computing, the virtual cloud plays an important role in computation. Generally, people would like to communicate and collaborate with the people having similar goal and task [8]. The virtual cloud computing provides benefits as the task distribution can reduce processing time of the device, increases performance of device, and reduces the energy consumption of the device.

A scenario of mobile computing where users have similar task to perform can be understood as follows:

John visited to Delhi. He loves to read different authors book. He visited to Book Fair in Delhi. He starts reading a Hindi novel but he has not sufficient knowledge of Hindi to understand it. So, he wants to translate Hindi into English from the book. He uses his mobile device for translating Hindi into English but the mobile device is not able to translate the text completely. Then he checks for the other interested users in nearby. The people can create cloud to translate Hindi into English. The users realized the common task is computing that is useful for them, then they can also create an Ad hoc network with John. All users can broadcast the translated data in the network, so all the others can save translated data. This can help everyone in the network to translate Hindi into English [9]

The cloud computing users can perform their tasks more efficiently and fast through the task sharing [9]. The sharing of task with other users reduces computation time as well as increases the computation speed. Cloud computing behaves as both centralized and distributed systems [10]. The five elements of cloud computing are as follows:

On-Demand Self-service

The customer needs the resources at anytime. The resources are automatically available to the customer as per their demand without any human interaction [11].

Broad Network Access

The resources in the cloud are delivered over internet so that the clients of a cloud can access these resources from any geographical location through different devices.

Resource Pooling

The cloud service provider pools the resources of the cloud so that the multiple users of the cloud can access as per their requirement [11]. The customer is unaware to the physical location of the resource. Generally, they have no information about the origin of the resource.

Rapid Elasticity

If the client of a cloud demands any resource, then the resource should be immediately available to the client. Scale up of the resource is done if client requires and scale down is done after the client releases the resource [11].

Measured Service

The resources in a cloud are used by multiple users of cloud; there is always a mechanism through which the usage of resource is calculated for each user [11].

Cloud Design Objective

The cloud design objectives mainly emphasize on the cloud model development which is universally acceptable [10], and these design objectives are as follows:

Switching Computation from Desktop to Data Centers

As the technology grows, the customers require fast and anytime access to their data, while the small footprints of mobile devices resist the user to access their data. As the users access the cloud from remote locations, the whole computation is not possible on devices. These data centers can be accessed by any geographical location so the user of the cloud does not need to carry large storage device with them. As per ad hoc demand of customer, it accesses the data center. The computation, data memory, and software delivery switched from desktop to data center over internet [10].

Service Provisioning and Cloud Economics

The service level agreement (SLAs) is signed between client and vendor, which is used for service efficiency and pay-per-used scheme [10].

Scalability in Performance

The services provided by cloud such as cloud platforms, software, and infrastructure services should vary in performance as per the number of users [10]. The scalability of performance provides the efficient use of cloud.

Data Privacy Protection

The data in data centers may be the private data of user, confidential data of an organization, etc, [10]. The random access to cloud creates vulnerabilities to the privacy of data.

High Quality of Cloud Services

The quality of service (QoS) of cloud must be universally accepted for making cloud interoperable amid number of providers [10].

New Standards and Interfaces

This provides a solution to data lock-in problem related to data centers or cloud provider. Standardized protocols are required to give high portability and flexibility of virtualization application [10].

Basic Concepts

There are various services and models that work behind to make cloud computing feasible and approachable to the end users.

The working models for cloud system are as follows:

Deployment Models

The deployment model provides the logical structure of a cloud. The deployment model indicates the type of access to the cloud. They are as follows:

- (1) *Private cloud*: The private cloud provides the solely operated infrastructure within an organization’s intranet [10]. The private cloud is mainly used for the security of intranet of organization, optimization of resources and cost, and full control over the activities that reside inside the organization’s firewall [11]. There is limited access for the cloud clients which can be defined by the rules of organization. It is fully controlled by the organization or the provider of cloud.
- (2) *Public cloud*: It is created on Internet and accessible by any random use as per the pay-per-use scheme. The cloud provider has its full ownership by which they decide the policies, cost, values, and charging models as per the profit [11]. GoogleApp and AmazonEC2 are the public clouds.
- (3) *Community cloud*: Multiple organizations jointly create cloud for the similar requirements with similar policies. The community cloud provides the access to the services and system to the group of organizations [11].
- (4) *Hybrid cloud*: The hybrid cloud inherits the characters from private and public cloud [12]. The expected situations are performed as a private cloud and unexpected situations are performed as a public cloud. Organizations use the hybrid cloud for the optimization of resources (Fig. 1).

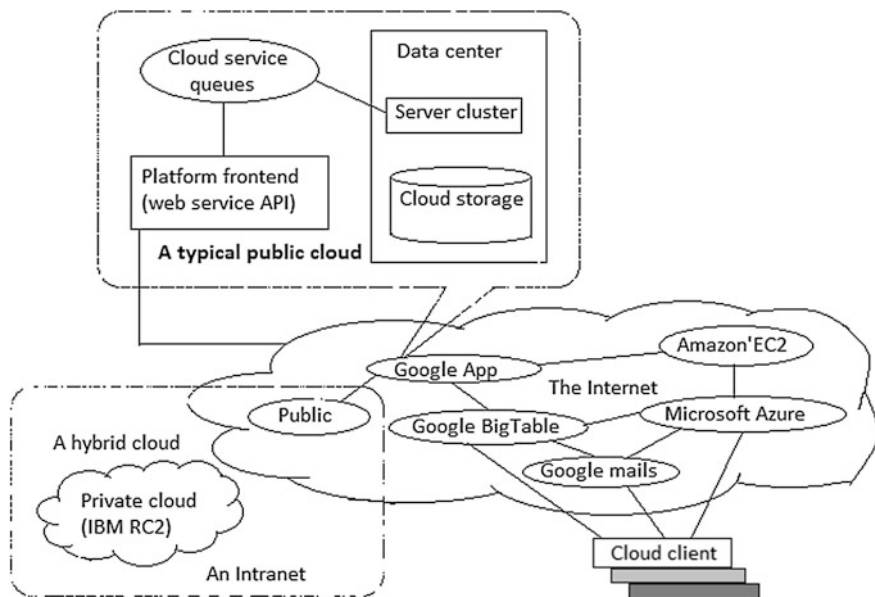


Fig. 1 Deployment model of cloud computing: public, private, and hybrid cloud (Source Ref. [10])

Service Model

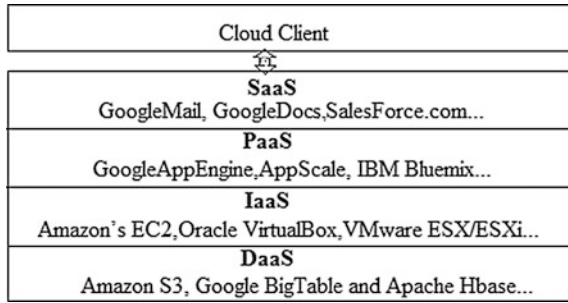
Cloud computing provides different services to its user, for which there are various service models. The different service models used in the cloud computing are as follows:

- (1) *Infrastructure as a service (IaaS)*: Cloud users can use IT resources for processing, data storage, and networking. The user can perform their tasks by renting cloud infrastructure. The users utilize the service with their OS environment [10]. Virtualization is largely used in IaaS cloud for integrating physical resources according to the requirement of user [11]. Examples of IaaS are Amazon Web Service (AWS), Windows Azure, Amazon'EC2, GoGrid, and Joyent Cloud.
- (2) *Platform as a service (PaaS)*: Cloud provides its users to build, deploy, and manage the processing of applications. It provides full "Software Lifecycle" so that a user can create cloud services and applications on PaaS [11]. The PaaS provides service to a developer through which they can purchase a fully functioned development and production environment [13]. Examples of PaaS are GoogleApp Engine, Microsoft Azure, and Amazon Elastic.
Types of PaaS: 19 k,
 - (a) Add on development facilities
 - (b) Stand-alone development environment
 - (c) Application delivery only environment
 - (d) Open platform as a service
- (3) *Software as a service (SaaS)*: Cloud provides its customers to create and release their applications, which can be approached by multiple users. At customer's end, they are not liable to make any advance investment in servers and software [10]. At the provider's end, the charges of application tried to be at the lowest, in comparison with the traditional hosting of applications [10]. Examples of SaaS are Google Gmail, Google Doc, Microsoft SharePoint, Microsoft 365, Citrix GoToMeeting, and Cisco WebEx.
- (4) *Data storage as a service (DaaS)*: DaaS can be considered as a special type of IaaS. The consumers pay for what they use. This scheme is similar to utility computing [14]. Normally, data centers are constructed at minimal developed locations [15]. Examples of DaaS are Amazon S3, Google BigTable, and Apache Hbase (Fig. 2).

Challenges in Cloud Computing

The distributed environments of cloud computing lead to different challenges for cloud computing. They are as follows:

Fig. 2 Service models of cloud computing (*Source Ref. [15]*)



Service Availability and Data Lock-in Problem

The data centers are located at different geographical locations with the replicas of data. For huge availability, we can take various cloud providers. This approach can optimize the data center protection from failure [10]. Another issue for data center is denial of service (DoS) [16]. The attacker puts the heavy load on cloud, so the cloud provider cannot be able to serve their service to its customers (attack on SaaS). The switching of customer with its data and services from one cloud to another is difficult. To overcome this issue, the standardized API can be adopted which will enable the SaaS developers to utilize services and data among the various cloud providers [10].

Data Privacy and Confidentiality

The increased number of users leads to increase in number of access points, which increases the risk of data compromise. The multitenancy, which is a cloud characteristic of resource sharing, creates serious vulnerability to the data center [12]. The data stored at one data center may not be secured as another data center due to the different security rules [14]. Confidentiality refers to that only valid clients can access data. Unauthorized access can be done through the applications. So the trust on the applications is a compulsory requirement. Privacy of information depends upon the willing of user to disclosure. The user's personal data is stored at the organizations server, so the privacy and confidentiality for the data is important concern [14].

Integrity

The integrity refers to the modification of data/information by any valid or invalid user. The entity admittance is required to control the unauthorized access. The

number of threads related to integrity can be created by the sophisticated insiders of the cloud [12]. Software integrity deals with the protection of software from unauthorized access and modification [12].

Cloud Scalability, Interoperability, and Standardization

The cloud provider charges client on the basis of bytes used. The pay-per-use scheme is used for the use of data and network bandwidth. The scalability provides user to access and use the resource as per their requirement, i.e., they can scale up or scale down according to their requirements [10]. There are different vendors of cloud, who provide optimized resources. The integration of cloud services with an organization's own existing legacy system becomes difficult due to the proprietary API. The main goal of interoperability is to provide seamless data across cloud and local servers [10].

Software Licensing and Reputation Sharing

The license paradigm for the profitable software does not fit on the utility computing. The cloud systems can be considered as open-source software. The cloud providers can use both pay-for-use and bulk-use license scheme to increase the business [17].

Mobile Elements Rely on Finite Energy Source

The power consumption in the member devices of cloud computing is not reduced [18]. The energy problem in mobile devices in today's scenario is due to limited battery capacity in devices and the increasing requirement of users for energy-hungry applications [19]. In [20], the offloading can be used to reduce the energy consumption in devices. The offloading can save energy only if the transmission energy is less than the local execution energy cost. The offloading can achieve by offloading the task of a device to their nearby richer resource device [20].

Security in Cloud

Security Issues

The security issues in cloud computing are increased due to the dynamic nature of attacks, the complication of software, and the increased vulnerable nature of platforms [21]. The identity, integrity, and security of a platform are important due to the distributed system environment [22]. The security can be considered as the combined responsibility of the user and the provider of services in IaaS [23]. The trust between the client and the vendor is important. The service level agreement is exchanged among the client and vendor [11]. In service level agreement (SLA) the valid rights of user and provider are specified; if anyone violates the policies, then they have to give penalty as mentioned in SLA. The security issues are large in cloud computing because there may be an involvement of third-party vendor which may not always safeguard data [14].

Another violation is the “tracking” of members of cloud from their physical location [14]. The different users of the cloud security tools such as antivirus, host-based intrusion detection for preventing intruders [19]. As the intruder/attackers are watching the security tools, they may change the logs and configure the security tools [19].

- (1) *Trust*: The trust is the faith between multiple stakeholders of cloud. In cloud environment, there are three types of stakeholders: the customer of services, the provider of service, and the provider of cloud infrastructure [24]. It is considered that the one entity acts similar as the other entity expected [25]. If a service provider or the user of cloud is not behaving as expected, then it directly affects security of cloud. The trust is a way of persuading the observer that the system is safe and accurate [26]. The absence of trust between cloud provider and cloud user leads to the situation of unfaithfulness. The trust in cloud depends upon the deployment model of the cloud [12]. As in private cloud and community cloud, the security architecture is defined and managed by the concerting organization [12], while in public cloud, the infrastructure owner is the concerting authority for defining and managing security [12].
- (2) *Securing data in cloud*:
 - (a) *Integrity*: Integrity is the modification of data by unauthorized or authorized users without sufficient privileges [12]. The data modification by an unauthorized user may lead to several vulnerabilities for the cloud. The unauthorized user can disturb data according to them which can misguide the authorized user.
 - (b) *Authentication*: Cloud provider provides access to its valid users [27]. The access control is important because there may be the unauthorized access to the cloud through the software; this may lead to the data

leakage and data loss [28]. The server and client authentication can be ensured by public key infrastructure certificates [12].

- (c) *Digital rights management*: The unstructured content, like video, image, etc, should be distributed with the legal permission. The piracy of this type of content is very important, so it is important to protect these contents from illegal access [15].
- (d) *Confidentiality*: Confidentiality refers to the access privilege to the valid user [29]. In cloud, the data centers are at multiple geographical locations. The cloud customers use Internet or other sources for entering into storage of cloud [29]. The distributed environment of a cloud increases the vulnerabilities to the data and resources. Deficiency in strong authentication process leads to invalid access through the unauthorized users.
- (e) *Availability*: Availability refers to the accessibility of data or resources at the time of demand from the authorized user [29]. Availability ensures that the cloud resource/content should be accessible by the cloud authorized user from anywhere at any time [29].
- (f) *Privacy*: The privacy refers to the need of a user to protect their information from the discloser [29]. The user's personal information should be confidential until he/she does not want to disclose in front of others. In the cloud computing environment, the user has no command on data. The cloud provider and the third party rule over the data centers, so the personal information of user can be easily disclosure. The privacy is important in the scenario of confidential data like a country's information, military operations, etc.

Intruder to the Cloud System

There are various types of security threads to the cloud computing. There are a few common intrusions which affect the availability, confidentiality, and integrity of cloud resources and its services.

- (1) *Insider attack*: An insider attack is a malevolent attack which is carried out by the member of logical network. Insiders are valid users and are well known with network architecture [30]. This is also called an insider threat. Insider threat or attack can affect all computer security elements and scale from stealing subtle data to injecting Trojan viruses in a system or network. Insiders also may affect the system availability by overloading network or processing capacity and directing to system crashes.
- (2) *Flooding attack*: Flooding is a denial of service (DoS) attack that is intended to bring a network or service down by flooding it with huge amount of packets from innocent host [30]. Flooding attacks arise due to the large number of bogus packets in the network. It stops the processing of valid connection

requests. The host’s memory buffer is filled due to these bogus packets. Once the memory buffer is full, no further connection request is processed, and the result is a denial of service. It may raise the usage bills intensely as the cloud could not distinguish between the normal and fake usage.

- (3) *User to root attacks*: User to root (U2R) attack is an attack where an intruder gets entry to the valid user’s account. The access may be taken through the valid user’s system (physically), credentials, dictionary attacks, etc. The intruder uses the holes to get root access into the system [30].
- (4) *Port scanning*: Port scanning refers to the inspection of computer ports by hackers for malicious purposes. Through this attack, all network-related details such as IP address, MAC address, router, gateway filtering, firewall rules, etc., can be known. Some port scanning techniques are TCP scanning, UDP scanning, ACK scanning, etc.
- (5) *Attacks on virtual machine (VM) or hypervisor*: Attacks on virtual machine happen due to the ease in which users can create many VMs, which is very difficult to secure, monitor, and maintain. VMs are built in very short time and they cannot be guaranteed that every VM are updated and free of vulnerabilities. In every VM, the client operating system uses the network, so conventional security approaches are used on every VM. VM is the most likely accessing point for intruders to the virtual machine monitor (VMM) and host [30] (Table 1).

Table 1 Security requirements of user

Level	Service level	Security requirements	Threads
Application level	Software as a Service (SaaS)	<ul style="list-style-type: none"> • Privacy in multitenant Environment • Data protection from exposure (remnants) • Access control • Communication protection • Software security • Service availability 	<ul style="list-style-type: none"> • Interception • Modification of data at rest and in transit • Data interruption (deletion) • Privacy breach • Impersonation • Session hijacking • Exposure in network
Virtual level	Platform as a Service (PaaS)	<ul style="list-style-type: none"> • Access control • Application security 	<ul style="list-style-type: none"> • Programming flaws • Software modification • Software interruption • Impersonation • Session hijacking • Traffic flow analysis • Exposure in network • DDOS
	Infrastructure as a Service (IaaS)	<ul style="list-style-type: none"> • Data security, • Cloud management control security • Secure images • Virtual cloud Protection • Communication security 	
Physical level	Physical data center	<ul style="list-style-type: none"> • Legal not abusive use of cloud computing • Hardware security • Hardware reliability • Network protection • Network resources protection 	<ul style="list-style-type: none"> • Network attacks • Connection flooding • DDOS • Hardware interruption • Hardware theft • Hardware modification • Natural disasters

- (6) *Backdoor channel attacks*: Backdoor channel attack is a method to access a computer or its data by bypassing into the system security mechanism without being detected. The backdoor, also known as trapdoor, is written by the programmer who develops a program. Sometimes, a network administrator creates or installs a backdoor program for troubleshooting or other official use, while the hackers use backdoors to install malicious files or programs, modify code, and gain system and/or data access. Backdoors installed by network administrators pose high security risks as they provide a mechanism by which the system can be exploited if discovered by any hacker.

IDS/IPS Used in Cloud Computing

The IDS can be a device or software, which is used for identifying malicious behavior. There are mainly four types of IDS/IPS:

- (1) *Host-Based Intrusion Detection System*: It detects malicious behavior by watching the log files, accessing information, etc. The host-based IDS (HIDS) determines the intruders from the individual host machines. HIDS monitors the incoming and outgoing packets. If it detects any malicious behavior, then it alarms to the system user and administrator [30].
- (2) *Network-Based Intrusion Detection System*: In network-based intrusion detection system (NIDS) the malicious behavior is identified by monitoring the network. It continuously watches the network traffic. The NIDS provides efficient detection of malicious behavior in real time.
- (3) *Hypervisor-Based Intrusion Detection System*: The hypervisor-based IDS monitors the malicious activities through the hypervisor/ virtual machine [30]. It deals with the communication between the host machine and hypervisor, VMs, etc.

Table 2 Different IDS/IPS types

IDS/IPS type	Positioning in cloud	Deployment and monitoring authority
Host based intrusion detection systems (HIDSs)	In every virtual machine, Hypervisor/Host system	On VMs: Cloud users On hypervisor: Cloud provider
Network intrusion detection systems	In external network or in virtual network	Cloud provider
Hypervisor-based IDS	In hypervisor	Cloud provider
Distributed intrusion detection system	In external network, on Host, on Hypervisor or on VM	On VMs: Cloud users Otherwise: Cloud provider

- (4) *Distributed Intrusion Detection System (DIDS)*: It deals with the communication between different IDSs. The information from different IDSs is collected at a central server [30]. At the central server, the malicious activities are identified through the anomaly and signature-based detection approaches (Table 2).

Conclusion

The cloud computing is the fastest growing IT industry. This paper introduced and discussed the concept of cloud computing in our daily life along with providing the resources and services from the shared pool. The objective of the cloud design is to bring users to the pool known as cloud, where they can store their data securely at convenient cost and access them from anywhere. We discussed various services and deployment models in cloud computing. The distinct methods to implement cloud and to make it feasible for various users are discussed. The distributed environment of cloud leads to different issues to the cloud provider and cloud users, so the challenges faced in cloud computing have increased rapidly in last few years and the ways to counter them are to be improved to overcome these challenges. Some intrusion detection techniques such as use of IDS/IPS have been discussed here to help in overcoming the difficulties faced by cloud computing. There are multiple challenges and threads in the cloud system, which are not completely resolved.

References

1. Juniper Research. Mobile Cloud: Smart Device Strategies for Enterprise & Consumer Markets 2011–2016 (2011). <http://juniperresearch.com/>
2. Hariprasath, L., et al.: The content distribution strategy enhancing cloud into mobile cloud. Int. J. Res. Eng. Adv. Technol. (2013)
3. Amazon Elastic Computing Cloud: www.aws.amazon.com/ec2
4. Oracle Cloud: www.cloud.oracle.com. Access Nov 2014
5. Google Cloud: www.googlecloud.com. Access Nov 2014
6. Nimbus: www.workspace.globus.org. Access Nov 2014
7. OpenNebula Project: <http://www.opennebula.org>. Access Nov 2014
8. Kangasharju, J., Ott, J., Karkulahti, O.: Floating content: information availability in urban environments. In: Proceedings of the 8th Annual IEEE International Conference on Pervasive Computing and Communications (PerCom) (WiP), Mannheim, Germany (2010)
9. Huerta-Canepa, G., Lee, D.: A virtual cloud computing provider for mobile devices. In: Proceedings of the 1st ACM Workshop on Mobile Cloud Computing & Services: Social Networks and Beyond. ACM (2010)
10. Hwang, K., et al.: Cloud platform architecture over virtualized data centers. In: Distributed and Cloud Computing: From Parallel Processing to the Internet of Things, 225 Wyman Street, Waltham, MA 02451, USA: Elsevier Inc., Chap. 4, pp. 193–205 (2012)

11. Dillon, T., Wu, C., Chang, E.: Cloud computing: issues and challenges. In: 2010 24th IEEE International Conference on Advanced Information Networking and Applications (AINA). IEEE (2010)
12. Zissis, D., Lekkas, D.: Addressing cloud computing security issues. *Future Gener. Comput. Syst.* **28**(3), 583–592 (2012)
13. Durkee, D.: Why cloud computing will never be free. *Queue* **8**(4), 20 (2010)
14. Kumar, K., Lu, Y.-H.: Cloud computing for mobile users: can offloading computation save energy? *Computer* **43**(4), 51–56 (2010)
15. Dinh, H.T., et al.: A survey of mobile cloud computing: architecture, applications, and approaches. *Wirel. Commun. Mob. Comput.* **13**(18), 1587–1611 (2011)
16. Armbrust, M., et al.: A view of cloud computing. *Commun. ACM* **53**(4), 50–58 (2010)
17. Marinelli, E.E.: Hyrax: cloud computing on mobile devices using MapReduce (No. CMU-CS-09-164). Carnegie-Mellon Univ Pittsburgh Pa School of Computer Science
18. Satyanarayanan, M.: Fundamental challenges in mobile computing. In: Proceedings of the fifteenth annual ACM symposium on Principles of Distributed Computing. ACM (1996)
19. Cuervo, E., et al. MAUI: making smartphones last longer with code offload. In: Proceedings of the 8th International Conference on Mobile Systems, Applications, and Services. ACM (2010)
20. Ma, X., et al. Energy optimizations for mobile terminals via computation offloading. In: 2012 2nd IEEE International Conference on Parallel Distributed and Grid Computing (PDGC). IEEE, New York (2012)
21. Varadharajan, V., Tupakula, U.: Counter acting security attacks in virtual machines in the cloud using property based attestation. *J. Netw. Comput. Appl.* **40**, 31–45 (2014)
22. Subashini, S., Kavitha, V.: A survey on security issues in service delivery models of cloud computing. *J. Netw. Comput. Appl.* **34**(1), 1–11 (2011)
23. Takabi, H., Joshi, J.B.D., Ahn, G.-J.: Security and privacy challenges in cloud computing environments. *IEEE Secur. Priv.* **6**, 24–31 (2010)
24. Cloud Computing Security: http://en.wikipedia.org/wiki/Cloud_computing_security. Access Nov 2014
25. International Telecommunication Union: X-509 | ISO/IEC 9594-8, The directory: Public-key and attribute certificate frameworks, ITU, X-Series (2001)
26. Nagarajan, A., Varadharajan, V.: Dynamic trust enhanced security model for trusted platform based. *Future Gener. Comput. Syst.* (2010). doi:10.1016/j.future.2010.10.008
27. Chaurasia, R.: Security in cloud computing. *Int. J. Sci. Res. Educ.* **2**(06), 896–902 (2014)
28. Top Threats to Cloud Computing Security: <http://www.infoworld.com/article/2613560/cloud-security/9-top-threats-to-cloud-computing-security.html>
29. Tianeld, H. Security issues in cloud computing. In: 2012 IEEE International Conference on Systems, Man, and Cybernetics (SMC). IEEE (2012)
30. Modi, C., et al.: A survey of intrusion detection techniques in cloud. *J. Netw. Comput. Appl.* **36**(1), 42–57 (2013)

Copper Nanofilm Antenna Design and Development: For X-Band Wireless Sensor Applications

Rajendra R. Patil, R.M. Vani and P.V. Hunagund

Abstract In this paper we present design, fabrication, and experimental characterization of microstrip antenna with copper nanofilm of 43 nm thicknesses as radiating element. The copper nanofilm patch is 15 times smaller than the skin-depth of copper at 10 GHz. The proposed antenna is non-contact feeding type proximity coupled microstrip patch antenna designed for 'X' band applications. The antenna design is validated with IE3D simulation software. The simulated antennas are fabricated for both 17 μm thickfilm and 43 nm nanofilm patches on low-cost 1.6 mm height FR4 substrate. The thickfilm antenna is fabricated using common photolithography, whereas copper nanofilm is fabricated using RF-sputtering deposition system at room temperature. The thickness and uniform distribution of copper nanofilm is confirmed by scanning electron microscope. The radiation result shows nanofilm antenna exhibits outstanding performance over thickfilm antenna in terms of bandwidth. The nanofilm antenna presents wide bandwidth of 47.29 % over thickfilm antenna.

Keywords Nanofilm · Proximity coupled microstrip patch antenna · Wide bandwidth · RF-sputter · Skin-depth · Surface resistivity

Introduction

Recently, there has been a growing interest in exploiting nanotechnology and tools [1] for developing microstrip patch antennas for improving radiation properties such as bandwidth, gain, return loss, size reduction (antenna miniaturization), and so on. Over year's antenna size reduction is achieved by traditional techniques like

R.R. Patil (✉) · P.V. Hunagund
Department of Applied Electronics, Gulbarga University, Gulbarga 585106, India
e-mail: rajendra.nano@gmail.com

R.M. Vani
USIC, Gulbarga University, Gulbarga, India
e-mail: vanirm12@rediffmail.com

introducing slits, slots, parasitic stubs, meandering lines, or converting patch into fractals or use of high dielectric constant substrates. However, these techniques result in high-quality factor ‘Q’ and reducing the bandwidth. Nanotechnology can be applied to either substrate part or metallic parts in particular radiating patch of the microstrip antenna. In substrate part of antenna, varying relative permittivity ϵ_r and relative permeability μ_r of the material, antenna can be miniaturized in addition to improved bandwidth and gain. Whereas, at metallic level, particularly radiating element, controlling the thickness of the patch, bandwidth can be varied without reduction in antenna size. At substrate level, lot of work is being carried out using magneto-dielectrics (MD) [2–5]. However, at patch thickness level, only a few literatures are available [6–9]. In this paper, we demonstrate the use of copper nanofilm as a radiating patch to enhance the bandwidth for ‘X’ band applications.

In [8, 9], aperture-coupled microstrip patch (ACMPA) antenna utilizing nanofilm as radiating patch is fabricated on thin silicon wafer. In our work, we investigate the effect of copper nanofilm as a radiating element on thick FR4 substrate for antenna properties like resonant frequency, return loss, gain, and bandwidth. Out of many antenna-feeding techniques, we have selected microstrip line fed proximity-coupled microstrip patch antenna (PCMPA), as it offers excitation of nanofilm patch through electromagnetic waves from microstrip feed line [10]. The interesting features of PCMPA are easy to model and its wider bandwidth. However, after fabrication it is little difficult to align the center of radiating patch over the other end of micro strip feed line for proper electromagnetic coupling between patch and feed line.

In this paper, we realize two identical PCMPAs, one is with thickfilm and another is with nanofilm, which differs only in the radiating patch thickness. The thick and nanofilm antennas are designed to resonate at 10 GHz, with a circular patch of 3.2 mm radius. IE3D software is used to simulate basic antenna design for optimized radiating patch and microstrip feed line dimensions [11]. For antenna to resonate at 10 GHz, FR4 substrate ($\epsilon_r = 4.4$) with a thickness of 1.6 mm and loss tangent about 0.0245 is used. The data for thick copper film are: copper patch thickness t is 17 μm , conductivity σ is 5.8×10^7 S/m, and $\epsilon_r = \mu_r = 1$.

Design, Modeling and Simulation of Antenna

The structure of the circular PCMPA is illustrated in Fig. 1. The circular patch is fed by proximity coupled microstrip feed line placed between two FR4 substrates. The antenna is designed to resonate at 10 GHz with input impedance of 50 Ω . The IE3D simulator version 14.65 is used to optimize the patch and microstrip feed line for antenna to resonate at 10 GHz. The simulated PCMPA antenna operates at 10.08 GHz with a return loss of -21.1 dB and bandwidth of 1.71 GHz.

The dimensions of antenna structure are listed in Table 1.

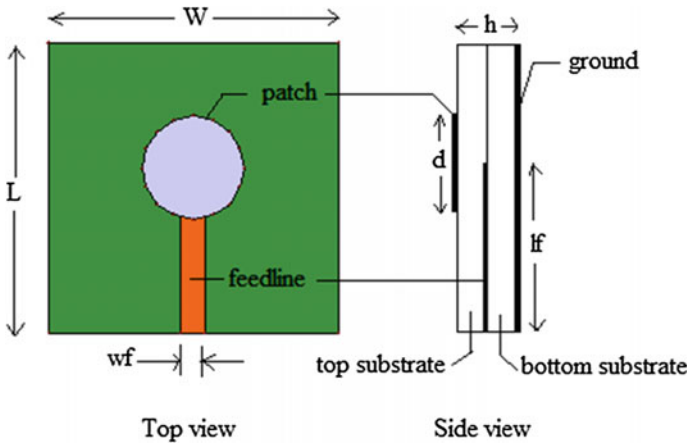


Fig. 1 Geometry of PCMPA antenna

Table 1 Dimension data for thick and nanofilm antenna

Antenna structure	Parameter	Dimension
Patch diameter	D	6.4 mm
Thickfilm	t_{thick}	17 μm
Nanofilm	t_{nano}	43 nm
Microstrip feedline	$w_f \times l_f \times t_{\text{thick}}$	3 mm ³ \times 20 mm ³ \times 0.017 mm ³
FR4 substrate	$W \times L \times h$	35 mm ³ \times 35 mm ³ \times 3.2 mm ³

Fabrication of Antennas

Thickfilm Copper Patch PCMPA

A circular thick copper disk of 6.4 mm diameter was fabricated using photolithographic process on the top side of upper FR4 substrate. On the grounded lower substrate, a microstrip feed line made of 17 μm thick copper was etched. The fabricated antenna is shown in Fig. 2a.

Copper Nanofilm PCMPA

In this top FR4 substrate is metallized with copper nanofilm using RF-Sputter system at room temperature. The sputtered copper nanofilm thickness on FR4 substrate is measured by field emission scanning electron microscopy (FESEM-SUPRASS) is found to be 43 nm. The fabricated copper nanofilm antenna is shown in Fig. 2b.

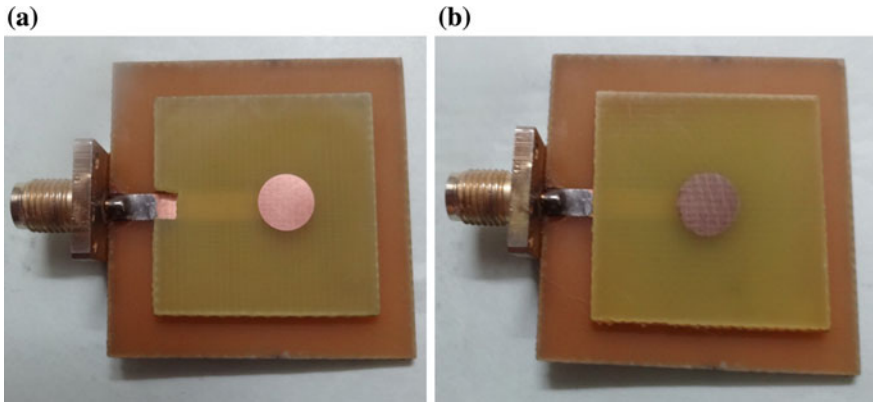
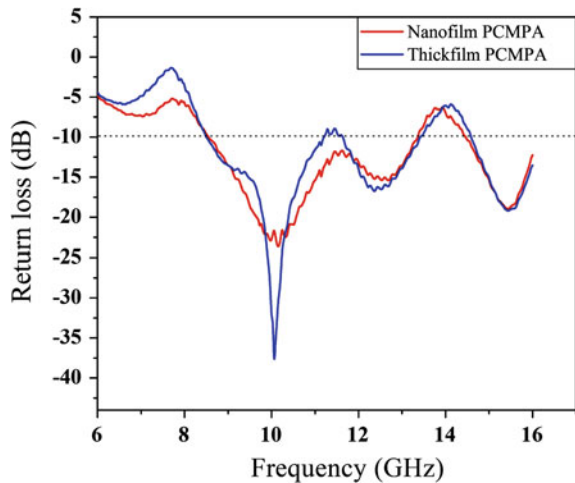


Fig. 2 Fabricated PCMPA. a Thickfilm, b Nanofilm

The Antenna Experimental Characterization

The fabricated thickfilm and nanofilm PCMPA antennas are experimentally characterized for resonance frequency (f_r), return loss (RL), bandwidth (BW), and gain (G) using Rhode–Schwarz vector network analyzer with model no. ZVK 1127.8651.60. For radiation pattern and gain measurements, the pyramidal horn antenna and the antenna under test (AUT) were connected to the Rhode–Schwarz VNA. The return loss characteristics and radiation patterns of PCMPA antennas are shown in Figs. 3 and 4. The gain of thickfilm and nanofilm PCMPA is calculated using the absolute gain method. The experimental results are listed in Table 2 for analysis.

Fig. 3 Return loss versus frequency characteristics of thick and nanofilm PCMPA



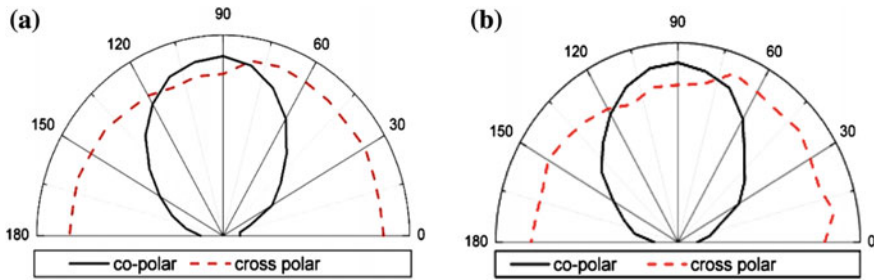


Fig. 4 Radiation pattern measurement. **a** Thickfilm antenna, **b** Nanofilm antenna

Table 2 Experimental results

Antenna type	Antenna radiation parameters				
	f_r (GHz)	RL (-dB)	BW (GHz)	BW (%)	G (dB)
Thickfilm	10.00	39.3	2.70	27.00	15.34
Nanofilm	10.15	23.7	4.80	47.29	13.87

Comparison of Results

The antennas are fabricated from copper thickfilm and nanofilm on FR4 substrate at 10 GHz. It is known that higher electrical resistance of thin film arises due to electron scattering, point defects, impurities, film surfaces and interfaces, grain boundaries, etc. [12]. As the film thickness t decreases and approaches electron mean-free-path, the patch resistivity increases due to increase in surface resistance [13, 14]. There are two parameters which affect antenna radiation properties. The first one is the surface current that affect resonant frequency of antenna, and the second one is surface resistivity R_s that affect input impedance, bandwidth, quality factor 'Q', and gain of the antenna. In our work, surface current have little effect on resonant frequency since there is no significant change in resonant frequency between nanofilm and thickfilm antennas. However, surface resistivity plays major role in decreasing the RL, Q, G, and increasing the BW of an antenna. Due to higher surface resistance, the following comparison and discussion are made.

Decrease in return loss from -39.3 dB in thickfilm antenna to -23.7 dB in nanofilm antenna does not change the property of a nanofilm antenna as a resonator. The radiating patch less than many skin depths in thickness exhibit higher surface resistance. The higher surface resistance decreases Q-factor of an antenna, thereby increase in BW of an antenna. The Q-factor of nanofilm antenna decreases to 2 from 3.7 of thickfilm antenna at -10 dB points [15]. The nanofilm antenna produces wide BW of 4.80 GHz (47.29 %) over 2.70 GHz (27 %) of thickfilm antenna. This amounts to 43.75 % higher BW over thickfilm antenna. In frequency response graph (Fig. 3), it is observed that the sharp resonant frequency peak of nanofilm antenna is disappeared. As the surface resistance increases, the sharp resonant peaks

gradually decrease and spread out. Also, we observe decrease in gain from 15.34 dB of thickfilm antenna to 13.87 dB in nanofilm antenna (Table 2). The slight decrease in gain is primarily due to the role of lesser surface current (higher surface resistivity) on the patch that decreases the antenna efficiency, since gain of an antenna is depend upon efficiency. As for as radiation patterns are concerned, we observe that there is a similarity in measured radiation patterns of thickfilm and nanofilm antennas. This confirms radiating patch thickness difference (from micron to nano thickness) do not affect radiation patterns.

Conclusion

This paper presented experimental characterization of copper nanofilm for 10 GHz frequency. Since nanofilm antenna presents wide bandwidth, it can be used in applications where high data rate transmission is required. The reduction in antenna gain makes nanofilm antenna suitable for short distance wireless applications such as wireless sensor system for example in remote patient monitoring, aircraft monitoring, or collision warning in cars.

Acknowledgments Authors acknowledge DST and UGC, Govt. of India for granting VNA and IE3D software under major research project to Gulbarga University. Author RRP gratefully acknowledges constant support from APPA IET Gulbarga, to carry out this work.

References

1. Ashutosh, S., Jayesh, B., Archana, S.: *Advances in Nanoscience and Nanotechnology*. National Institute of Science Communication and Information Resources, Council of Scientific and Industrial Research, New Delhi (2004)
2. Raj, P.M., Muthana, P., Xiao, T.D., Wan, L., Balaraman, D., Abothu, I.R., Bhattacharya, S., Swaminathan, M., Tummala, R.: Magnetic nanocomposites for organic compatible miniaturized antennas and inductors. In: *Proceedings of the 10th International Symposium on Advanced Packaging Materials: Processes, Properties and Interfaces, APM 2005, USA, 16–18 Mar 2005*
3. Guo-Min, Y., Xing, X., Daigle, A., Liu, M., Obi, O., Stoute, S., Naishadham, K., Sun, N.X.: Tunable miniaturized patch antennas with self-biased multilayer magnetic films. *IEEE Trans. Antennas Propag.* **57**(7), 2190–2193 (2009)
4. Hansen, C., Burke: Antenna with magneto-dielectrics. *Microwave Opt. Technol. Lett.* **26**(2), 75–78 (2000)
5. Jungyub, L., Jeongkyu, H., Joonghee, L., Youngho, H.: Design of small antennas for mobile handsets using magneto-dielectric material. *IEEE Trans. Antennas Propag.* **60**(4), 2080–2084 (2012)
6. Verma, A., Fumeaux, C., Truong, V.T., Bates, B.D.: Effect of film thickness on the radiation efficiency of a 4.5 GHz polypyrrole conducting polymer patch antenna. In: *Proceedings on the Asia-Pacific Microwave Conference, APMC 2010, Japan, 7–10 Dec 2010*

7. Guan, N., Furuya, H., Himeno, K., Goto, K., Ito, K.: Basic study on an antenna made of transparent conductive film. In: Proceedings of the 11th International Symposium on Antennas and Propagation, ISAP 2006, Singapore, 1–4 Nov 2006
8. Urbani, F., Stollberg, D.W., Verma, A.: Outstanding performance of a nanofilm microstrip antenna. In: Proceedings of the 4th IEEE Nanotechnology Materials and Devices Conference, NMDC 2010, USA, 12–15 Oct 2010
9. Urbani, F., Stollberg, D.W., Verma, A.: Experimental characterization of nanofilm microstrip antennas. *IEEE Trans. Nanotechnol.* **11**(2), 406–411 (2012)
10. Garg, R., Bhartia, P., Bahl, I., Ittipiboon, A.: *Microstrip Antenna Design Handbook*. Artech House (2001)
11. IE3D ver. 14.67, 2010. Mentor Graphics, USA
12. Liu, H.D., Zhao, Y.P., Ramanath, G., Murarka, S.P., Wang, G.C.: Thickness Dependent Electrical Resistivity of Ultrathin (<40 nm) Cu Films, *Thin Solid Films*, vol. 384, pp. 151–156. Springer (2001)
13. Saberini, J.R.: *Optically transparent antennas for small satellites*. Doctoral dissertation, The University of Utah (2010)
14. Liao, S.Y.: *Microwave Devices and Circuits*. Pearson Education, Inc., New Delhi (2003)
15. Robbins, W.B., Skogland, T.S.: *Microstrip patch antennas using very thin conductors*. US Patent Number 5,767,808 (1998)

Vein Biometric Template Security Using Overlapped Shares Accounting for Minimum Storage

Ruchika Solanki, Saurabh Maheshwari, Vineet Khanna
and Kalpana Sharma

Abstract A human vasculature-based algorithm has been proposed for template security. The complete biometric template is binarized and divided into specific number of shares. These shares are overlapped so that all the binary bits are overlapped. This leads to formation of entirely new pattern. The vein biometric information is kept secured in the overlapped shares but in an encrypted way. These overlapped shares are stored as coefficients of the vein curves instead of image for individuals. This exponentially reduces space to store the templates. If anyone steals this secured template then also no useful information regarding the vein biometric can be obtained. The proposed method has been implemented and proved for very small false acceptance and false rejections on standard datasets.

Keywords Vein biometric · Template security · Shares · Cryptography

Introduction

Along with the progress in science, human beings life has also become threatened by crime which can occur at anytime, anywhere with an intensifying risk. Currently, the biometrics is being used as a protection method where a person is recognized by his physical or behavioural features, securing the identity from being stolen. Various parts of the human body are used as biometrics such as finger, iris,

Ruchika Solanki · Vineet Khanna · Kalpana Sharma
RCEW, Jaipur, India
e-mail: rsolanki31286@gmail.com

Vineet Khanna
e-mail: vineet.khanna81@gmail.com

Kalpana Sharma
e-mail: kalpanasharma23july@gmail.com

Saurabh Maheshwari (✉)
GWEC, Ajmer, Rajasthan, India
e-mail: saurabh.maheshwari.in@ieee.org

hand, voice, face, odour, DNA, etc., because of their uniqueness, permanence, universality, acceptability, measurability, performance and circumvention [1]. The major components of the biometric systems are acquisition sensors, signal processing algorithms, data storage, matching algorithm and decision process. Nowadays, vein pattern biometrics applications are rapidly increasing in research and industries. The vein biometric trait which is mostly utilized is dorsal hand vein. Also there is a need for contactless biometric because of some problems with touch-based systems. There are also some risks associated with the biometric systems such as spoofing and mimicry risk where an artificial fingerprint may be used. Fake reference templates may be stored in the data base, Transmission risk is there during enrolment or at the time of acquisition data may be intercepted, etc. [2]. Finger vein system requires small size device so can be used in home, office, car, automobile, etc., for security purpose. Since veins are hidden they are not directly visible to forgers. Both finger vein and finger texture images are acquired using webcam and an IR camera [3].

Literature Survey

Raw acquisition of image is succeeded by noise removal using filters like Match, Weiner and Smoothing [2]. Specific noises such as Salt and pepper noise are removed by Gaussian Blurring method. Other methods like local dynamic threshold segment method [3], anisotropic fusion [4] brings a clear segmented vein image. Contrast Limited adaptive histogram equalization (CLAHE) [1] is a method to restrict the intensities in a specific range and to convert the intensity varying histogram into an equalized histogram with frequency of all bins being almost same. This has an impact on both light and dark pixels as both of them get intensified in the respective range to appear lighter and darker, respectively [5, 6]. Thinning is used for obtaining the skeleton which represents the shape much better and helps in removing all the curved points from the image leaving only the points that relates to the skeleton. Smoothing is done to smooth the contours, fuse narrow breaks and long thin gulfs and remove small holes to obtain the exact structure of the veins [2]. ROI (region of interest) is selected from the acquired images and as it contains lot of information it needs to be preprocessed and features are extracted from it. Features have been extracted using SIFT (scale-invariant feature transform) [1] which are invariant against image size and orientation transformations and noise. Gabor filters [4] have been historically used to identify the image texture [4], pattern recognition such as character recognition [6], fingerprint recognition [7], iris recognition [1] and face recognition [3]. The maximum curvature points method proposed by [8, 9] is used for extracting the finger veins. The minutiae features extracted from the vein patterns are used for recognition. The minutiae points include bifurcation points and ending points [6]. Matching of the templates can be done through phase only correlation [4], Hausdorff distance (HD) is used for matching the two feature sets by computing the distance between every point in

both the sets [2], Euclidean distance classifier which is used to check whether it is a genuine vein or imposter vein, Matching using hamming distance where minimum hamming distance from all database templates is find out.

Proposed Method

The hand vein images are normalized to 100×100 window size using bi-cubic interpolation as given in Fig. 1a. The region of interest (ROI) image (Fig. 1c) extracted from binary dorsal hand image by getting the pixels only inside the largest square possible to inscribe as shown in Fig. 1b. Contrast enhancement of only the ROI image is done so that the veins appear distinct to other skin area as shown in Fig. 1d. The image size is reduced to one-fourth of the original size. The smaller image is restored it back to its original size and then resizing it to one-third of its size. The visual quality of the image is thus improved. The vessels are delineated for vessels areas and non-vessel areas of the image. Using Cleaning and subsequent thinning reduces the number of pixels to a single fine vein lines. Remaining non-vein pixels are discarded during pruning, deducing a cleaned skeletonized (single pixel thickness) vein patterns. From the thinned image, we can extract thermal minutia points. Polynomial curve fitting method based on least squares is used to identify each vein segment curves. 5 longest curves in terms of pixels are selected as candidate features and stored in database due to their high probability of occurrence even in noisy templates.

We are proposing a new method which makes the template secure. The steps of the proposed algorithm are:

1. The division of thinned patterns template takes place generating four non-overlapping blocks.
2. These binary templates have 0 for non-vessel area and 1 for the vessels.
3. All of them are subjected to ORing pixel by pixel, to generate the overlapped pattern.
4. This creates an entirely new pattern for the template.

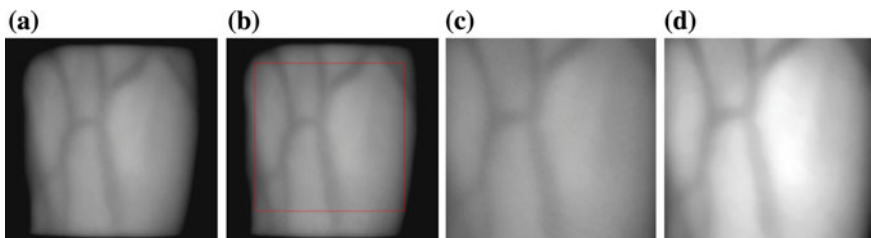


Fig. 1 ROI extraction and contrast enhancement. **a** Input image. **b** ROI marked. **c** ROI. **d** Contrast adjustment

5. This template has complete vein information but it has lost its spatial information about the veins location.
6. This leads to a secure template for the person.
7. If this template is lost then also the attacker cannot get any detail from it since this does not have any spatial information of the actual biometric template.
8. The shares are overlapped so the number of curves and geometry of the curves is now changed.
9. The coefficients of the five longest curves are stored for the identification and regeneration of the curves during matching.

Matching Algorithm:

1. The raw template is taken as input. Which is processed same as it was done during registration.
2. The five longest curves identified by coefficients are compared with the data stored for remaining registered templates.
3. The matching is done using Hausdorff distance [10] which computes similarity between two images A and B by computing distance from A to B and vice versa and then considering among 2.

$$\max\{dhd(A, B), dhd(B, A)\}$$

Only five longest curves are matched among each other for similarity. Coefficients of these curves are the only data that we are storing which is very less in comparison to literature [2, 4, 8, 11–13] where the storage requirement per template is very high. The curves having at least 30 pixels over 100×100 windows have been observed to be longest experimentally. Curves below that length are considered to be noise. If the distance between two template data is greater than matching threshold, then the query may be termed as a match [10, 13].

Testing Results

Currently, test was carried out on 50 samples from NCUT and FV dataset. The matching threshold is kept to be 6. The false acceptance and rejection rates are both 0 %. Hausdorff distance is calculated between the query image and the stored information regarding each template in database. On the basis of this distance, best match is identified and is termed as matched template. At least one of the stored templates should match with distance less than minimum threshold of 6 otherwise the query is discarded. In Fig. 2a, the input template is shown which is raw input. The thinned binary vein curves are shown in Fig. 2b. Figure 3 shows the shares of the thinned binary vein curves where all the curves have been shared in different blocks. Figure 3 shows the share pattern generated by overlapping the shares in Fig. 3. This is our secured overlapped share.

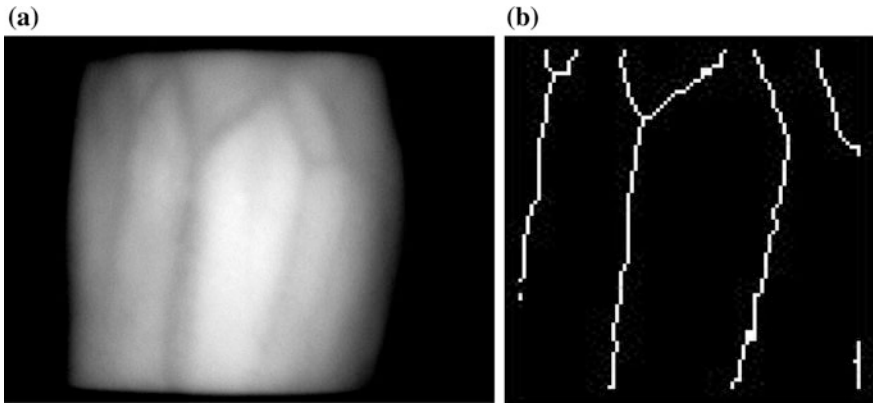


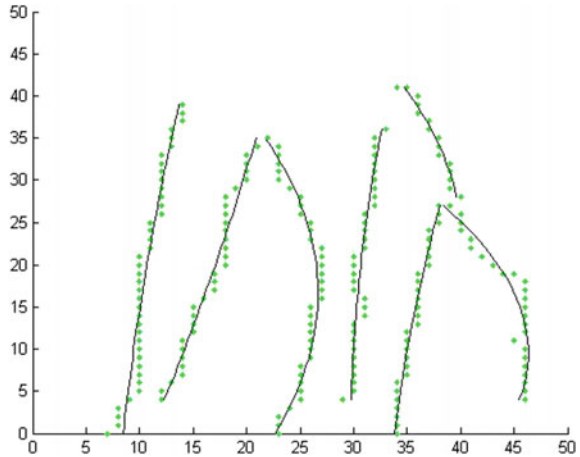
Fig. 2 a Vein biometric template input. b Thinned binary vein curves



Fig. 3 Shares of vein curves which will be overlapped and overlapped share

The vein curves are extracted from the overlapped share. There are many curves from them the best curves selected are shown in Fig. 4. The coefficients of these curves will only be stored and matched with the query template. The matched part is shown through overlapping dots.

Fig. 4 Best curves extracted from the overlapped curves to show the match



Conclusion and Future Work

This paper has described a vein biometric identification system which we targeted for hand-held devices. The amount of space needed for each template has been reduced. The templates have been secured against template copy attack by proposed share overlapping method utilizing a very less complex polynomial curve fitting process. Actual curves' spatial locations are hidden since the storage of curve information is done after the share overlapping. The matching process has been speeded up since the data to be matched is now very less in comparison of previous approaches. Verification of more images is in process. Very few approaches have targeted storage reduction and security of the template both. The problem for final benchmark is lack of availability of proper benchmark dataset for the vein biometric modality with good template quality. The results were tested over 50 instances and are satisfactory.

References

1. Agarwal, A., Maheshwari, S., Yadav, G.: A review on vein biometric recognition using geometric pattern matching techniques. In: 2014 Conference on IT in Business, Industry and Government (CSIBIG), pp. 1–7, 8–9 Mar 2014
2. Wang, Y., Fan, Y., Liao, W., Li, K., Shark, L., Varley, M.R.: Hand vein recognition based on multiple keypoints sets. In: 2012 5th IAPR International Conference on Biometrics (ICB), pp. 367–371, 29 Mar–1 Apr 2012
3. Font Aragonés, X., Faúndez Zanuy, M., Mekyska, J.: Thermal hand image segmentation for biometric recognition. *IEEE Aero. Electron Sys. Mag.* **28**(6), pp. 4–14 (2013)
4. Lingyu, W., Leedham, G., Cho, D.S.: Minutiae feature analysis for infrared hand vein pattern biometrics. *Pattern Recogn.* **41**(3), 920–929 (2008)

5. Wang, Y., Li, K., Shark, L., Varley, M.R.: Hand-dorsa vein recognition based on coded and weighted partition local binary patterns. In: IEEE International Conference on Hand-Based Biometrics (ICHB), pp. 1–5 (2011)
6. Liu, Z., Song, S.: An embedded real-time finger-vein recognition system for mobile devices. *IEEE Trans. Consum. Electron.* **58**(2), 522–527 (2012)
7. Zhao, S., Wang, Y., Wang, Y.: Extracting hand vein patterns from low-quality images: a new biometric technique using low-cost devices. In: Fourth International Conference on Image and Graphics, 2007, ICIIG 2007, pp. 667–671 (2007)
8. Miura, N., Nagasaka, A., Miyatake, T.: Feature extraction of finger-vein patterns based on repeated line tracking and its application to personal identification. *Mach. Vis. Appl.* **15**(4), 194–203 (2004)
9. Zhang, Z.B., Wu, D.Y., Ma, S.L., Ma, J.: Multiscale feature extraction of finger-vein patterns based on wavelet and local interconnection structure neural network. In: International Conference on Neural Networks and Brain, 2005, ICNN&B'05, vol. 2, pp. 1081–1084
10. Agarwal, A., Maheshwari, S., Yadav, G.: Vein biometric security using irreversible curve fitting accounting for minimum storage. In: 2014 International Conference on Signal Propagation and Computer Technology (ICSPCT), pp. 179–183, 12–13 July 2014
11. Im, S., Park, H., Kim, Y., Han, S., Kim, S., Kang, C.: A biometric identification system by extracting hand vein patterns. *J. Korcan Phys. Soc.* **38**(3), 268–272 (2001)
12. Pal, M.M., Jasutkar, R.W.: Implementation of hand vein structure authentication based system. In: International Conference on Communication Systems and Network Technologies (CSNT), 2012, pp. 114–118, May 2012
13. Chun, L.J.: A novel biometric system based on palm vein image. *Pattern Recogn. Lett.* **33**(12), 1520–1528 (2012)

Miniaturization of MEMs-Based Smart Patch Antennas for Biomedical Applications

Shankar Bhattacharjee and Santanu Maity

Abstract In this paper, MEMs-based smart patch antennas which can be used for biomedical applications were investigated. An attention over the main constraints in designing efficient antennas for biomedical devices was made and the analysis is presented, in addition with some of the main issues in their categorization. The foremost constraint which was encountered during simulation was the miniaturization problem. As the size of the antenna is reduced different parameters of the antenna such as directivity, gain, antenna efficiency show degradation in values. The patch antenna is a trendy antenna which can be used in various sophisticated applications due to its small size, robust nature, and low power handling capacity which is the prerequisite in our study. The antenna which has been developed basically consists of a patch antenna along with a meta-material-based rectangular slot over the patch. Bulk micromachining technique is used to etch out certain portions of the silicon substrate and Rogers RT-duroid substrate is intentionally been added within the micro-machined portion. MEMs-based switches have been added in our design in order to make the antenna reconfigurable in nature. The results obtained after simulation is astonishing with considerable increase in bandwidth, directivity, and gain which make the antenna viable for the required purpose despite of considerable reduction in size of the antenna.

Keywords MEMs · Micromachining · HFSS · Miniaturization · Meta-material · RF · Biomedical

Shankar Bhattacharjee
Computer Science and Engineering, National Institute of Technology,
Yupia, Arunachal Pradesh 791112, India
e-mail: shankarsam68@gmail.com

Santanu Maity (✉)
Electronics and Communication Engineering, National Institute of Technology,
Yupia, Arunachal Pradesh 791112, India
e-mail: santanu.ece@nitap.in

Introduction

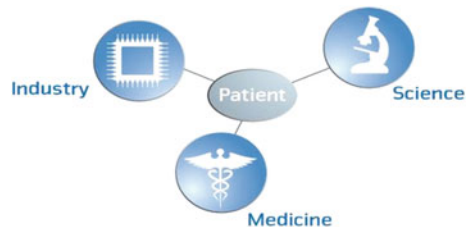
The history of implantable biomedical devices started with pace makers in the early 1960s [1]. Since then implantable medical devices have become extra appealing for health care services. Recently, the devices designed to monitor and diagnosis physiological statistics inside the human body have under gone enormous changes to provide major relief to disease prevention, diagnosis, and medication. In addition, minimally invasive devices permit reducing patient's ailments which could be a great step in health monitoring systems. Major factors concerning the design of the implantable antennas can be the effect of RF radiation within the body, miniaturization of the antenna and finally biocompatibility issue leading to packaging problem of the antenna. Taking into consideration of the above factors the industry, medicine, and science must be combined in such a way so as to give maximum benefit to the patient and drive future innovations in medical fields as seen from the Fig. 1.

The study of electrically small antennas and its effect on radiation properties started in mid-1940s where the analysis was made on radiation power factor that gives an idea about the antenna's radiated power, and indeed the product of efficiency and bandwidth is directly related with the volume of the antenna [3]. Decreasing the electrical size of an antenna will direct to the alteration in electromagnetic performances like gain, bandwidth, efficiency the antenna, and many studies spotlight on how to obtain a good negotiation between size and various performance parameters.

Miniaturization Techniques for Biomedical Implantable Antennas

Different techniques have been proposed earlier in order to design efficient miniaturized antennas. One efficient way to design miniaturized antenna is to bend their contour, so as to constrict the current to move long path which will make the antenna seem longer than its actual shape such as in planar inverted f-antenna (PIFA) [4]. Variety of miniaturization techniques are loading the antenna with lumped elements, using high dielectric substrate material, using of ground planes as

Fig. 1 United action of three fields for improving existing technologies [2]



in PIFA configuration, optimizing the geometry [3]. Only miniaturizing cannot be used to obtain highly efficient antennas in addition further improvement of the structure should be made that would result into multiband radiating antenna along with high gain and efficiency. Miniaturized simple patch antenna yields only single radiating band with low gain. In order to obtain higher efficiency we have used meta-material-based patch antenna and a combination of two types of substrate in a single design in our antenna by micromachining technique. These have a negative permittivity and a negative magnetic permeability and in such a left-handed (LH) material the electric field, the magnetic field, and the wave vector of an electromagnetic wave propagating makes a left-handed triplet and follow the left-hand rule [5]. To make the antenna reconfigurable in nature that is to obtain multiple dieting bands and to make shifts in frequency we have used MEMs-based switches. The development of new integrated antennas using MEMs solution has the ability to make the devices miniaturized and more consistent, which will make them cheaper and plenty for batch production, resulting in a key benefit for competitors in the RF market. Use of wafer-level chip-scale packaging (WLCSP) techniques like adhesive wafer bonding and through-wafer electrical via formation, united with the radio frequency (RF) structures allow a novel level of antenna integration [6].

Antenna Design and Specification

The important parameters required for designing the patch antenna are frequency of operation, substrate height, and dielectric constant of the substrate. In the following design, silicon substrate having dielectric constant (ϵ) of 11.9 is used along with substrate height of 275 μm and operative frequency of 12–14 GHz has been used. The designed parametric analysis has been carried out using the following equations [7]:

$$W = \frac{c}{2f_0 \sqrt{\frac{\epsilon_r + 1}{2}}} \tag{1}$$

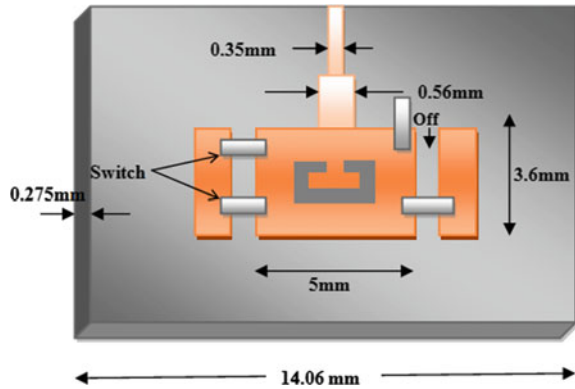
$$\epsilon_{\text{reff}} = \frac{\epsilon_r + 1}{2} + \frac{\epsilon_r - 1}{2\sqrt{1 + 12\frac{h}{w}}} \tag{2}$$

$$\Delta L = 0.412h \frac{(\epsilon_{\text{reff}} + 0.3)\left(\frac{w}{h} + 0.264\right)}{(\epsilon_{\text{reff}} - 0.258)\left(\frac{w}{h} + 0.8\right)} \tag{3}$$

$$L = \frac{c}{2f_r \sqrt{\epsilon_{\text{reff}}}} - 2\Delta L \tag{4}$$

Thus from the above Eqs. (1–4), width and length of the patch is computed for the design to be considered. The width and length of the patch is found as

Fig. 2 Improved patch antenna design using MEMS-based switches



$(4.9219 \times 3.5954) \text{ mm}^2$. Further the transition line thickness and width are found out to be 0.5582 and 2.141 mm.

$$\text{Length of the ground plane} \geq (\lambda/4) \times 2 + L = 14.64 \text{ mm}$$

$$\text{Width of the ground plane} \geq (\lambda/4) \times 2 + W = 13.06 \text{ mm}$$

Insert feed technique has been used in the design of the patch antenna.

The evaluated design of the antenna is shown below.

In the given analysis, micro-electrical mechanical system (MEMS) switches were projected to design a reconfigurable/multiband antenna to replaced PIN diode switches or semiconductor switches due to lower insertion losses, good isolation, low reinter-modulation distortion, and less power consumption [8]. A configurable antenna that is capable to radiate at more than one frequency is proposed by adding two adjacent wing patches along with main radiating patch and four MEMS switches as shown in Fig. 2. The MEMS switch is helpful in reducing the size of the antenna along with providing higher efficiency.

Antenna Simulation and Results

The designed antenna is simulated in ANSOFT HFSS (high-frequency simulation software) solver using the given parameters. Gain comparison of two types of antenna for simple patch and different configurations in MEMS-based patch antenna is shown below:

From Fig. 3, it can be observed that gain of the newly designed antenna has increased substantially from the previously simple rectangular patch where the initial value of the gain obtained is only 0.2 dB but the improved version has conceived to obtain a gain of 3.1 dB when alternate switches are in ON state and a gain around 4.07 dB has been obtained when all the switches are kept in OFF mode which is a good result.

Fig. 3 Gain comparison of two patch antennas

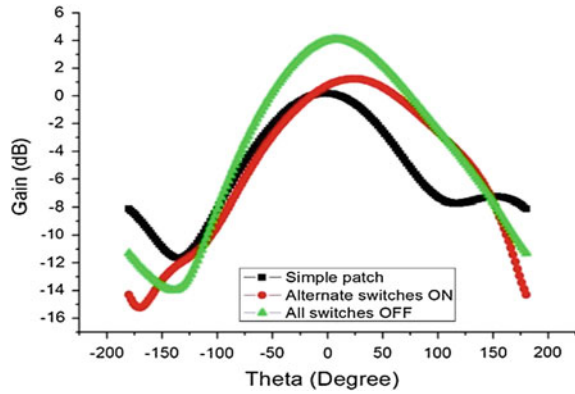
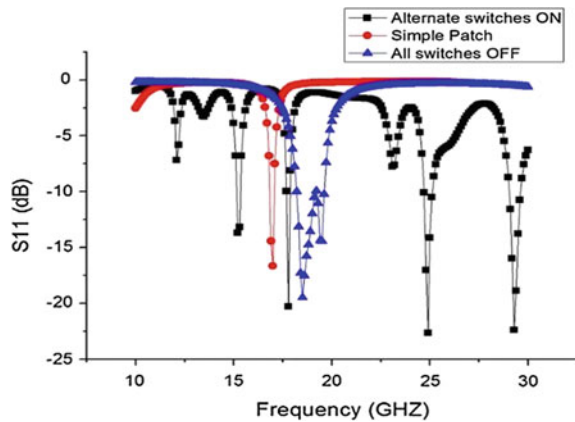


Fig. 4 S11 parameter of the two antennas for different configurations



The S11 parameter obtained for the two types of antenna is shown below along with different configuration in the position of the switches.

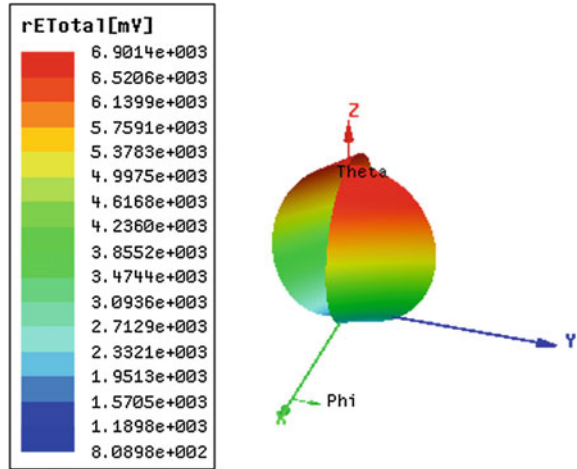
The S11 parameter graph obtained in the two cases given in Fig. 4 gives an idea that in the latter case due to the introduction of MEMs-based switches where the bridging material that has been used is gold to connect them in patch with the wing patches. The switch may be closed or open and it changes the antenna resonant frequency. When the switch closes, the wing patch is coupled with main patch due to inductance which is in the first state. When the switch opens, the wing patch is coupled with main patch via capacitance [9] for the second case.

Micromachining is done in the substrate to etch out certain portion of silicon and Rogers RT-duroid substrate has been added in the etched out portion.

With this technique the various parameters of the improved version of the antenna has increased considerably than the previous case.

From Fig. 5, it can be concluded that the antenna has a stable radiation pattern around the axis. The resonant frequency alter can be understood by studying the electric currents on the patch antennas. When the switch is in the OFF mode, the

Fig. 5 3D polar plot of the electric field of the antenna



electric currents on the patch have to flow around the entire patch, resulting in a relatively long length of the electric path. As frequency is inversely proportional with current path length so the antenna resonates at a low frequency. In contrast, when the switch 2 and 3 or 3 and 4 is in the ON mode, some of the electric currents can go directly through the switch in the wing patch. In this case, the average length of the current path is shorter, so that the antenna has a higher resonant frequency [10].

Results and Discussions

The design of miniature antenna as results into poor radiation performances such as narrow bandwidth and low efficiency so the ability of dual and performances might be of enormous use, to shrink power consumption and extend lifetime [1]. The bandwidth of the improved antenna is 384 MHz where that of the initial antenna was mere 57.5 MHz resulting in 85.03 % enhancement of overall bandwidth, which is indeed a good result. Further there is an enhancement of gain from 0.2 to 3.1 dB in the improved antenna and when all the switches were kept in OFF mode there is a gain around 4.07 dB. With the increase in bandwidth, there is a possibility to increase the communication speed between the implants and base station, but an increase of the bandwidth will result in enhancement in the noise level at the input. An up surge of bandwidth by 10 times will result into increase the noise level by 10 dB, so negotiation between gain and bandwidth has to be maintained for best results [11]. Bodily fluids greatly influence the performance of the antenna as normally these are lossy liquids which could affect the radiation properties such as gain, bandwidth in addition SAR (specific absorption rate) plays a major role here. In order to obtain an efficient design of such an antenna, the influence of the lossy medium adjacent the antenna on both near and far field terms have to be considered properly [12].

Conclusion

The antenna which is designed provides a much better choice for implantable biomedical devices in terms of size, gain, and bandwidth. The conventional patch antennas are not reconfigurable in nature, with the use MEMs technology it has been achieved in the design proposed. Further with the inclusion of meta-material and introduction of two types of substrates in the same plane, the antenna became quite efficient in nature.

Acknowledgments We would like to thank our parents because without their support and blessings, we would have never reached this position. After that we also want to say thanks to all of our friends who helped Eduson writing this paper and Jadavpur University for supporting with this software.

References

1. Implantable antennas for biomedical applications thè seno 5110 (2011) écolepoly technique federal edelausanne present éele 2 septembre 2011 àla faculté sciences et techniques de l'ingénieur laboratoired' electromagnetism eet acoustique programme doctoral engnieélectrique
2. Article-Science, Industry and Medicine—to benefit the Patient. 2nd Announcement Medical Physics and Biomedical Engineering World Congress, Munich/Germany, 7–12 Sept 2009. <http://www.wc2009.org>
3. Skrivervik, A.K., Zurcher, J.-F., Staub, O., Mosig, J.R.: PCS antenna design: the challenge of miniaturization. *IEEE Antennas Propag. Mag.* **43**(4) (2001)
4. Fujimoto, K., Henderson, A., Hirasawa, K., James, J.R.: *Small Antennas*. Wiley, Research Studies Press (1987)
5. Singhal, P.K., Bimal Garg, Department of Electronics Engineering, Madhav Institute of Technology and Science, Gwalior-474005, India: A high gain & wide band rectangular micro strip patch antenna loaded with interconnected SRR metamaterial structure. *Int. J. Eng. Technol.* **1**(4) (2012)
6. Mendes, P.M., Correia, J.H.: *Wireless Communications Research Trends*, Lee, T.S. (ed.) Chapter 7. pp. 223–260. Nova Science Publishers, Inc. ISSN: 978-1-60021-674-9
7. Fatthi Alsager, A.: *Design and Analysis of Microstrip Patch Antenna Arrays*, Thesis No. 1/2011
8. Zahirul Alam, A.H.M., Rafiqul Islam, Sheroz Khan, Md., Muhammad Mahbubur Rashid: Micro electrical mechanical systems switch for designing multi-band antenna. *J. Comput. Sci.* **5**(7), 479–486. ISSN 1549-3636 ©2009 Science Publications
9. Prasad, P.C., Chattoraj, N.: Design and development of reconfigurable micro strip patch antenna using MEMs switch for Ku-band application. In: *Progress in Electromagnetics Research Symposium Proceedings*, Stockholm, Sweden, 12–15 Aug 2013, p. 1039
10. Ramola1, E., Pearson, T.: Reconfigurable micro strip patch antenna using MEMs technology. *IOSR J. Electron. Commun. Eng. (IOSR-JECE)* **4**(4), 44–51 (2013). ISSN: 2278–2834, ISBN: 2278-8735
11. Johansson, A.J.: *Wireless communication with medical implants: antennas and propagation*. Ph.D. thesis, June 2004
12. Skrivervik, A.K.: Implantable antennas: the challenge of efficiency. In: *7th European Conference on Antennas and Propagation (EUCAP 2013)—Convended Sessions*

Authentication of Primary User at Physical Layer Through Approximation in Cognitive Radio

Muzzammil Hussain and Suditi Choudhary

Abstract Cognitive Radio (CR) is a mechanism that adjusts its radio parameters dynamically to use the unoccupied spectrum holes so as to overcome the problem of spectrum shortage arose due to enormously increasing wireless devices. It is done by assigning free spectrum to the unlicensed users without compromising the licensed users. Hence, distinguishing Primary Users (PUs) from Secondary Users (SUs) is a major concern in CRN and it becomes more challenging when it has to be done at the physical layer, without understanding the data in the signals. Here, we propose a mechanism to authenticate a PU based upon approximation of distance and angle of arrival of the signal received from it. We also propose a mechanism where a SU can be hopped to Dedicated Control Channel (DCCH) for seamless communication, when it has to vacate the spectrum for PU and there are no traffic channels (TCH) to continue its ongoing communication.

Keywords Cognitive Radio · Primary user · Secondary user · Frequency hopping

Introduction

The number of users of wireless devices is enormously increasing, to access services through Internet and also there are different technologies, hence it is the need of the hour to integrate them. Cabric et al. [1] said that this integration will not only simplify the usage and also will save spectrum which otherwise would create scarcity in spectrum especially over few bands. Mitola [2] pioneered Cognitive Radio (CR) as a radio mechanism that has been derived from term Software Defined Radio (SDR), which can change its parameters dynamically and is

Muzzammil Hussain (✉) · Suditi Choudhary
Department of Computer Science and Engineering, Central University of Rajasthan,
Kishangarh 305817, India
e-mail: mhussain@curaj.ac.in

Suditi Choudhary
e-mail: suditichoudhary@gmail.com

intelligently controlled by software. The primary objective of CR is to dynamically improve spectrum utility but they are neither field programmable nor have any software. CR is a radio, in which a node can change its transmission/reception parameters with time to efficiently communicate with environment and that too not at the expense of interference. In CR, the users are classified as Licensed (Primary) and Unlicensed (Secondary). The Secondary Users are allocated the available bandwidth and have to be vacated whenever a Primary User requests for such occupied band. The CRN has been developed to efficiently utilize the available spectrum and incorporate reliability in communication. As predicted by Akan et al. [3] CRN finds its application in areas like emergency management or disaster relief, search and rescue, mining industry, road traffic control, medicine, weather forecasting, military, etc.

Cognitive Radio Network Working Process

Akyildiz et al. [4] showed the cyclic process of CR which starts with sensing the environment, followed by analyzing and understanding, making decisions and adapting to the environment as shown in Fig. 1.

(a) *Sense*

Sensing the environment shows the cognitive capability of a CRN where the spectrum is sensed and detected for the spectrum holes.

(b) *Understand*

Further the sensed information is analyzed, this shows the self-organization capability of the CRN which is similar to that of Wireless Sensor Network (WSN), where due to limited energy of nodes, they self-organize, cooperate and turn them off when not used.

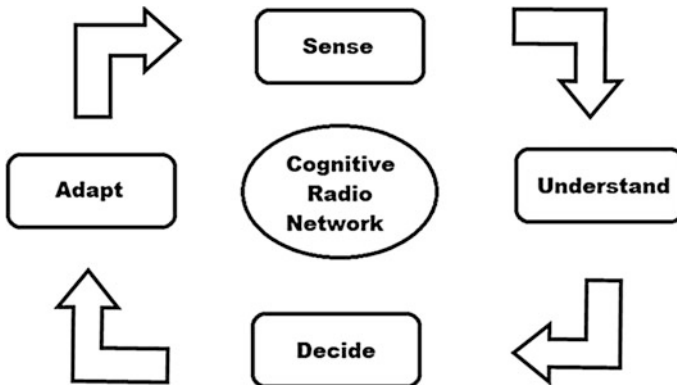


Fig. 1 Working process of CRN

(c) *Decide*

After analyzing the information, decision is to be made by selecting reasonable spectrum for SUs from licensed band. This shows the decision capability of CRNs.

(d) *Adapt*

As CRs can learn and change their transmission characteristics according to the requirements of the environment, this is how they show reconfiguration capability.

Frequency Hopping and CRN

It is a technique for modulation in the spread spectrum transmission in which the total available bandwidth is divided into many small channels of smaller bandwidth with guard spaces between them. Transceiver stays on in any of these channels for a certain time then hop to the other or we can say that transceiver hops between these channels to avoid interception or jamming of communications. According to some hopping pattern if the transmitter changes its carrier frequency, it is known as frequency hopping as shown in Fig. 2a. The main purpose of this is that the signal will see a different channel and interfering signals in every hop. Hence, the problem of failure in communication at each frequency is avoided.

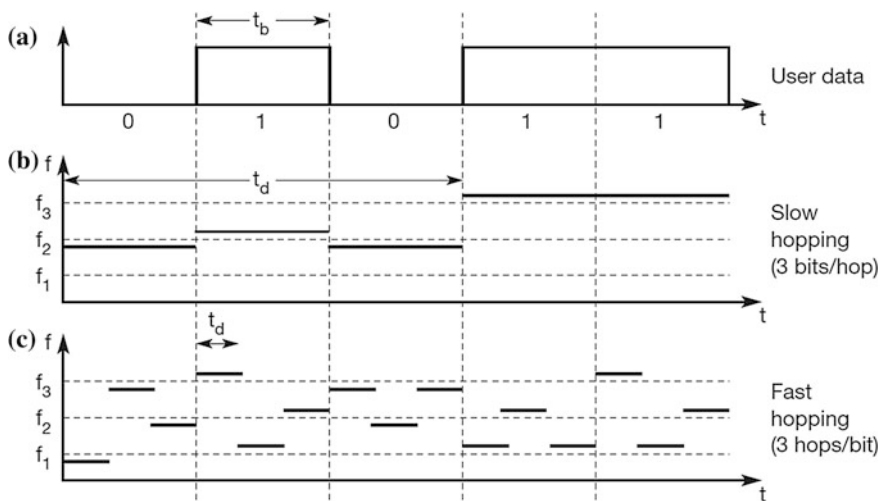


Fig. 2 a Frequency Hopping, b SFH and c FFH

Hopping between frequencies is either slow (SFH) or fast (FFH). In SFH as in Fig. 2b every transceiver changes its frequency periodically; one or more data bits are transmitted in one hop. Generally, loss of bits can be restored in one hop by employing error control coding. This is followed to avoid link breakage between stationary terminal located in fade and the Base Station. It is shown in Fig. 2, where three bits are transmitted in one hop. In FFH a transmitter may change its frequency multiple times to transfer a single bit as in Fig. 2c, they are very hard to implement as transceiver should be synchronized within smaller intervals to perform hopping on almost similar points of time. Transmitter is hopping three times during transmission of a single bit in Fig. 2. The transmitter stays on a frequency for a very short time; hence they can effectively overcome interference due to narrow bands and fading of selective frequencies.

CRN is a concept designed based on frequency hopping. Whenever a Primary User enters into the radio area of the Base Station then the spectrum bands are vacated for it by hopping the Secondary User's spectrum bands and the vacated channels are allocated to the incoming Primary User. The slow frequency hopping technique is followed and an effective frequency hopping mechanism would increase the performance of CRN by a large factor. Later by following the same technique secondary users are allocated the available spectrum; they keep on doing frequency hopping as they move.

Security Threats in CR/CRN

Zhang et al. [5] observed that security threats in CRN are quite different than that of WSN as they arise here due to integration of different networks with properties of each of them and due to spectrum mechanisms. The major threat in CRN is threat to spectrum. There are three types of security threats in CRN.

(a) *Artificial intelligence behaviour threats*

(i) *Policy threats*: Reacting to different environments is based upon the policies of CR. They may lead to two security threats: Lack of policy and failure while using policy. In both the cases CR cannot make appropriate operations due to threat in policy.

(ii) *Learning threats*: Many CRs have the capability to learn from the surroundings and adapt to it. An attacker may modify the past statistics or spoofs the present conditions to alter the behaviour of CR.

(iii) *Parameters threats*: CR is controlled by many radio parameters and its performance depends on them. An attacker may alter their parameters for manipulating a CR to make it behave maliciously.

(b) *Dynamic spectrum access threats*

(i) *Spectrum sensing threats*: In CR allocation of TCH to PUs and hopping of users takes place through Common Control Channel (CCH). An attacker can spoof the identity of a PU by intercepting on CCH and an attacker can jam or take over the control of CCH easily.

(ii) *Spectrum management threats*: The efficiency of a CR depends on the efficiency of spectrum management. Spectrum management involves spectrum analysis and spectrum decision. An attacker can modify the spectrum characteristic parameters that affect the spectrum analysis and thereby affecting spectrum decision and a CR may end up choosing a wrong band and hence degrading its performance.

(iii) *Spectrum mobility threats*: Spectrum handoff is a common phenomenon in CR where a SU is hopped to some other band in order to vacate its occupied band for an incoming PU. An attacker may try to control CCH and modify parameters affecting smooth and seamless communication in spectrum mobility.

(c) *Threats in CRN*

A CRN may be of centralized or distributed architecture and connected via cooperation or non-cooperation. In centralized architecture with cooperation, it is easy for an attacker to jam the central node and bring down the whole network. Hence, DoS attack is very easy to implement. In distributed architecture with non-cooperation, jamming attack on single user will not affect the whole network. In overlay environment an attacker may spoof a PU and prevent SU from detecting holes in spectrum thereby creating DoS attack.

Significance of Authentication in CRN

The prime objective of CR is not to let the unlicensed users use the spectrum when licensed users are waiting for it, also the unauthorized users should not get access to the protected systems. Hence, authentication of the user turns out to be an inherent requirement to identify whether the detected signal is from PU or SU. Therefore, in CRNs authentication is significant. Going by Tan et al., a PU can only be authenticated at physical layer in CRN. If authentication is based on understanding the data correctly, CR receiver cannot authenticate PU. Also, as in CR licensed users should not be compromised; an attacker may try to mimic a PU's signal to evict other SUs. So, it becomes important to distinguish an original PU's signal from attacker's signal. Authenticating PUs through cryptographic link signatures was proposed by Tan et al. and through trusted Certificate Authority (CA) was by Zhu and Mao [6].

(a) *Authentication in Cognitive Radio Networks through Certification Authority*

Zhu and Mao [6] proposed a mechanism for authentication of PU in CRNs using third party CA by combining EAP-TTLS and EAP-SIM, where SIM authentication is used to authenticate the terminal users and TTLS + certificates to authenticate servers.

(i) *EAP-SIM*: It is an Extensible Authentication Protocol based on security environment of SIM used to authenticate the terminal users. It uses A3/A8 encryption mechanism algorithms and offers dynamic key distribution mechanism.

(ii) *EAP-TTLS*: It is an Extensible Authentication Protocol which extends the TLS handshaking protocol which includes handshaking between the client and the server to perform key agreement, mutual authentication, and encryption algorithms. Client does one-sided authentication to the server using TLS handshaking, and then the server authenticates the terminal user. It turns out to be strongest in security performance. Though EAP-SIM is weaker than EAP-TTLS in security aspect, but its complexity is low and configuration is easy.

CA ensures the legacy and legitimacy of MS and BS, random number is extended twice in handshake to ensure freshness of message, ECC can be adopted to reduce computational cost and secure tunnel and certificate ensures authentication between MS and BS. Performing configuration is complicated and this mechanism will slow down when large number of SUs are spread across a large geographical area.

(b) *Authentication of Primary Users' Signals by integrating Cryptographic and Wireless Link Signatures*

Identifying a PU can be done using Energy and feature detection. In energy detection a threshold is fixed and if the received signal's energy is more than it, then the transceiver is a PU. Similarly, in feature detection method PU is identified if it has some specific feature, SUs try to adopt the features of the PU such as a synchronization word, a pilot, and a cyclostationarity, in such cases SU can identify an attacker as a PU and do not use the empty spectrum. This attack is known as Primary User Emulation Attack (PUEA). Therefore, identifying a PU's signal in the presence of attackers is much essential.

Cryptographic signatures alone cannot be used as; Federal Communications Commission (FCC) has restricted any modifications to the system for accommodating spectrum usage by SU's opportunistically. To make the distinction of location more robust and secure, channel impulse responses, complex amplitude and time delay are used as link signatures. In order to authenticate a PU, its historical link signature should be known in order to make comparison later on. A SU may not learn the link signatures of the PU until it knows that it is from a PU or not. Liu et al. [7] combined both the approaches of cryptographic and link signatures to enable PU detection when attackers are present. Also there will be no change to the PU signal due to this approach and hence satisfies the FCC requirement.

Helper nodes are deployed close to each PU (physically bound) which can be modified on its cryptographic signatures. The helper node is kept very near to PU hence its link signature will almost match to the PU present nearby; SU can learn the link signature of helper node by verifying and can be further used to compare it with that of PU's link signature [8]. In this approach, a SU need not to keep history of link signatures of PU as they will get it from the helper node and this mechanism adheres to FCC standard. But an attacker can impersonate a PU by using channel of PU or by emulating signal of PU.

Our Propositions

(a) *Ad hoc allocation of DCCH to SU for seamless communication*

Cognitive Radio Network is the network in which the licensed band will be shared with secondary users if the spectrum seems to be vacant without compromising the functionality of the PU. In this case whenever a SU signal is observed as a new entry in the network, it will be allocated a spectrum from the available bands. If a PU entry is observed and it wants to occupy a particular band which is not free or already occupied by the SU, then the SU is supposed to hop to some other available band without creating any delay for the PU.

There are fixed channels reserved for licensed users, if all these channels in some case are occupied, the unlicensed users have to be vacated from these fixed channels to accommodate the licensed users, in order to avoid the disconnection of their ongoing communication of such unlicensed users, they can be temporarily allocated Dedicated Control Channel (DCCH). This allocation of DCCH is done when there are no free TCHs available and the SU is in middle of some communication. This allocation is ad hoc and once the SU completes its communication, the allocated DCCH will be pre-empted and the SU may be allocated suitable TCH when found to be free. The DCCH are allocated to the SU only if it is in middle of an ongoing communication and it has to be hopped to vacate TCH for an incoming PU. In this a SU is hopped from TCH to a DCCH and back to TCH if available.

(b) *Authentication at Physical layer*

Parvin et al. [2] found that authentication has inherent requirement in CRs to distinguish between PU and SU, CR should not serve SUs by compromising PU's services, and also no outsider (intruder) should be able to access the protected system. Identifying the source (PU or SU) of a signal at a particular spectrum is a major challenge for any receiver in CRN. A PU can only be authenticated at physical layer as told by Tan et al. because it is nearly impossible for a receiver to authenticate the PU if authentication depends on understanding the data correctly.

Here, we propose an algorithm to authenticate a PU by calculating its distance and angle.

(c) *Algorithm*

The proposed algorithm to authenticate a PU at physical layer is in three phases as:

(i) Register (ii) Update (iii) Authenticate.

Variables:

- t1 Time of projection of signal
- t2 Time of Arrival (ToA) of signal
- θ Angle of Arrival of the signal (AoA)
- Δt Time Difference of Arrival (TDoA)

(i) *Register:*

- If the bandwidth of the Mobile Station (MS) matches with that of the Base Station (BS) then it is a PU.
- Calculate the distance of MS by Doppler effect, project a signal to MS and wait for its arrival. Let $t1$ be the time of projection and $t2$ is ToA of signal.
- Calculate TDoA as follows:

$$\Delta t = t2 - t1$$

- Calculate distance:

$$D = (\Delta t * c)/2$$

where, c = speed of light/radio signal and D = distance of the MS from the BS

- Calculate the Angle of Arrival (AOA) of the signal.
- Store in the table of BS for PU:

(ii) *Update:*

- Whenever a new node arrives in the radio cell, apply register phase.
- When a node moves away from the BS, remove its entity from the table.
- Whenever MS moves from its current location calculate its new distance through difference in ToA of two successive signals from it and calculate the AoA of new signals. Update the table with new ordered pair <new distance, new AoA>.

(iii) *Authenticate:*

When there are fewer empty channels for communication and there is a sudden increase in the number of PUs, then for a signal received from a MS over a TCH:

- Calculate the distance ‘D’ and angle ‘ θ ’, compare them in Table 1, if found the MS is a PU else SU.

Table 1 Location table for PU

ID	Distance (D)	Angle (θ)

Register phase is applied when a new user enters into the vicinity of the BS, MS will send a signal to the BS, which checks the characteristics of the received signal to identify the PU and this way MS will register itself with the BS. A new entry is logged in the table with MS's ID, distance of that MS and the BS and its angle. If the MS is not a PU or we say that if its entry is not in the table it will be considered as a SU.

Update phase will be done in two cases; whenever a new MS enters into the vicinity of the BS it should go through the registration phase and hence a new entry is made into the table, similarly if MS having its entry in the PU table move out off the vicinity of the BS, its entry from this table is removed.

Authenticate phase is to identify PUs when there will be a shortage of spectrum due of enormous requests from the PUs. To distinguish between a PU and SU, the distance of the node is calculated by determining the Time of Arrival (ToA) and speed of radio signal. The Angle of Arrival (AoA) of the signal is determined and the calculated distance and angle are searched in the table, if a match is found then the node is identified as PU else will be SU.

Conclusion

Authentication is significant in CRN and it is very essential to distinguish PU and SU in CRN. Whenever, there is scarcity of spectrum, the SU should be hopped to other bands. The authentication of PU should be done at physical layer in CRN without understanding the data in the signal. We have proposed a mechanism that is simple and authenticates a PU by its signal properties at physical layer. Here, we find the approximate distance and Angle of Arrival (AoA) of signals from a node and compares it with the known location of PUs. An attacker cannot emulate the PU because the location is calculated as an ordered pair <Distance, AoA> and it is highly impossible to emulate both distance and AoA of PU by an attacker node. The only overhead of the proposed mechanism is that the BS should have the table of locations (<Distance, AoA>) of each known PU. This table is updated dynamically whenever a PU enters into the vicinity or leaves the area of the BS. Hence, BS has the updated location table.

Acknowledgments Authors gratefully acknowledge the support offered by Dr. Garimella Rama Murthy, IIITH and also the resources provided by the Department of Computer Science and Engineering at Central University of Rajasthan, Kishangarh to complete this work.

References

1. Cabric, D., Mishra, S., Willkomm, D., Brodersen, R., Wolisz, A.: A cognitive radio approach for usage of virtual unlicensed spectrum. In: Proceedings IST Mobile and Wireless Communications Summit, Dresden, Germany (2009)
2. Parvin, S., Hussain, F.K., Hussain, O.K., Han, S., Tian, B., Chang, E.: Cognitive radio network security: a survey. *J. Netw. Comput. Appl.* **35**, 1691–1708 (2012)
3. Akan, O.B., Karli, O.B., Ergul, O.: Cognitive radio sensor networks. *IEEE J. New.* **23**(4), 34–40 (2009)
4. Akyildiz, I.F., et al.: A survey on spectrum management in cognitive radio networks. *IEEE Commun. Mag.* **46**(4), 40–48 (2008)
5. Zhang, Y., Xu, G., Geng, X.: Security threats in cognitive radio networks. *IEEE Int. Conf. High Perform. Comput. Commun.* **10**, 1036–1041 (2008)
6. Zhu, L., Mao, H.: Research on authentication mechanism of cognitive radio networks based on certification authority. In: Computational Intelligence and Software Engineering (CiSE 1–5) (2010)
7. Liu, Y., Ning, P., Dai, H.: Authenticating primary users signals in cognitive radio networks via integrated cryptographic and wireless link signatures. In: Proceedings of IEEE Symposium on Security and Privacy (2010)
8. Kim, H.S.: Location-based authentication protocol for first cognitive radio networking standard. *J. Netw. Comput. Appl.* **34**(4), 1160–1167 (2011)

Data-Based Correlation Scheme

Krishna Joshi, Shadab Siddiqui and Shahin Fatima

Abstract In wireless sensor network the work of spatial correlation is to find those nodes having common readings and to form a group of them called clusters. A node from the cluster is selected to represent the whole cluster and is called cluster head. The idea of using spatial correlation is to increase lifetime of network and to increase the energy of sensor nodes.

Keywords Correlation · Spatial correlation · Temporal correlation · Data collection

General

Wireless sensor network consist of sensors that are deployed randomly over a particular area. In wireless sensor network the nodes work by observing any physical phenomenon over a particular area such as temperature. The main issue in WSN is the energy of sensor nodes. To protect this energy of nodes in wireless sensor network various protocols such as in network aggregation has been applied. Spatial correlation in wireless sensor network is achieved by covering the whole area with higher density of nodes having similar reading. In wireless sensor network the sensors are deployed densely to cover the area. As a result of this many sensors record the details of a single event in the field. Due to this the data which is recorded is highly correlated in spatial domain.

Krishna Joshi · Shadab Siddiqui (✉) · Shahin Fatima
Department of Computer Science & Engineering, BBDNITM, Lucknow, India
e-mail: cseshadabsiddiqui@gmail.com

Krishna Joshi
e-mail: kr.rocks08@gmail.com

Shahin Fatima
e-mail: shahinfatima@hotmail.com

Critical Review of Literature

In [1] villas et al. propose an algorithm that exploits both the temporal and spatial correlation of data. For the implementation of spatial correlation author divides the sensor area into cells. Each sensor node in the network is associated with a cell. In every cell there is a coordinator node, representative node, relay node, sink node. A representative node in each cell sends the similar reading towards the coordinator node. Temporal correlation is performed at periodic interval of time to observe and sense the data. In this paper the author performed temporal correlation at representative node and if the previous and current readings differ then the data is transmitted otherwise there is no need to send data.

In [2] Liu et al. had proposed an approach to use spatial and temporal correlation of data in wireless sensor network. This approach is an algorithm called EEDC in which cluster formation is done to achieve spatial correlation. In this paper author converts cluster formation problem into a clique covering problem, an NP-complete problem. Author proposes an algorithm that is solvable in $O(n^2 \log n)$ time. In this problem sensor nodes are drawn as vertices and an edge is drawn between them if sensor reading is below a threshold value. Then a graph is formed and problem is to search all the cliques in a graph.

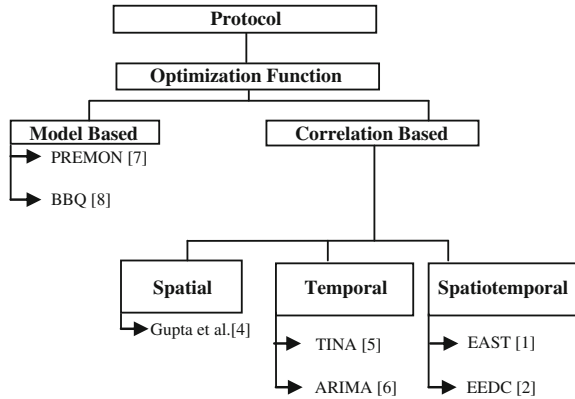
In [3] Yoon et al. propose an approach in which data aggregation is performed and spatial and temporal correlation functions are performed simultaneously. In CAG hierarchical data aggregation is performed. CAG works in two modes, interactive and streaming modes. In interactive mode the cluster head is decided on the basis of propagation of query. In response phase aggregation is performed on cluster head node and only cluster head sends its value, in this way spatial characteristic is preserved.

In [4] Gupta et al. propose an approach to exploit the data correlation in wireless sensor network enabling nodes to minimize the communication cost. In this approach author proposes an algorithm that is sufficient to represent the whole sensor network. Thus only selected nodes are involved in communication.

In [5] a scheme is proposed by author, which exploits temporal correlation and is used in network aggregation called TINA. The author states that in network aggregation the aggregation is done at internal nodes and the information is routed up in the routing tree. Figure 1 Diagram of Classification of Aggregation Protocol on the basis of Optimization Technique.

In [6] the author has proposed a scheme for performing data aggregation through database queries in wireless sensor network called as BBQ model. In BBQ model Gaussian function is used to prepare the model.

Fig. 1 Diagram of classification of aggregation protocol on the basis of optimization technique



Protocol and Structure

System Model

In our proposed scheme all nodes are homogeneous. Nodes are randomly and densely distributed. Inter-node distance is decided as greater than 10 m and less than 35 m. WSNs use license-free communication frequencies: 173, 433, 868, and 915 MHz; and 2.4 GHz. Wireless sensor nodes have less battery capacity.

Data-Based Correlation Scheme

Function for choosing coordinator node having highest energy in network

The Fig. 2 shown below shows the flowchart of choosing the coordinator node having highest energy in network

```

    D[n] ← Sensor Data
    L[n] ← Sensor location
    For each N ∈ Nodes
    N.Role ← Coordinator
    N.incidence ← event occurred //INPUT to corresponding Node
    First ← N.incidence
    Rem < N-N.incidence
    if(First.Role = Coordinator)
    send message to other nodes
    for each Rem ∈ Nodes
  
```

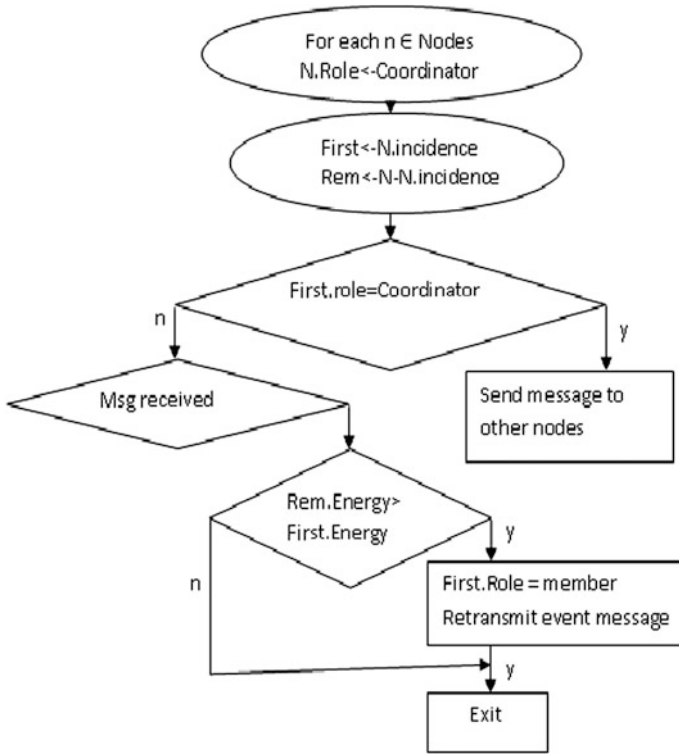


Fig. 2 The figure shows the flowchart of choosing the coordinator node having highest energy in network

```
(Rem) ← msg received.  
For each N ∈ Nodes -First  
if (Rem.Energy) > First.Energy  
First.Role = member  
Retransmit event message
```

Function for cluster formation and scheduling of active nodes

The sensor will sense the value, energy and location and send it to the coordinator node. The coordinator node stores the value in array form as D[n], L[n], E[n].

```

while(j<n)
{
    k=1
    Make_Set(L[k])
    for j=k+1 to n
    {
        if ( mod(D[k]-D[j])<predefined Threshold))
        {
            add(L[j])
            j+1
        }
        else
        {
            k=j;
            Make_Set(L[k]);
            increment j;
        }
    }
}

```

Coordinator node on/off or active/passive sensor depends upon the energy left, stored in array $E[n]$ from each cluster.

Explanation

In above-mentioned algorithm first coordinator node is selected on the basis of energy of the sensor nodes. Node having highest energy is selected as coordinator node. All the sensor nodes send their values and locations to the coordinator node. Coordinator node divides sensors into clusters based upon its data. The difference between the value of sensors will decide their place in group. If the difference is within the limit then the nodes are placed in group by coordinator node, otherwise it

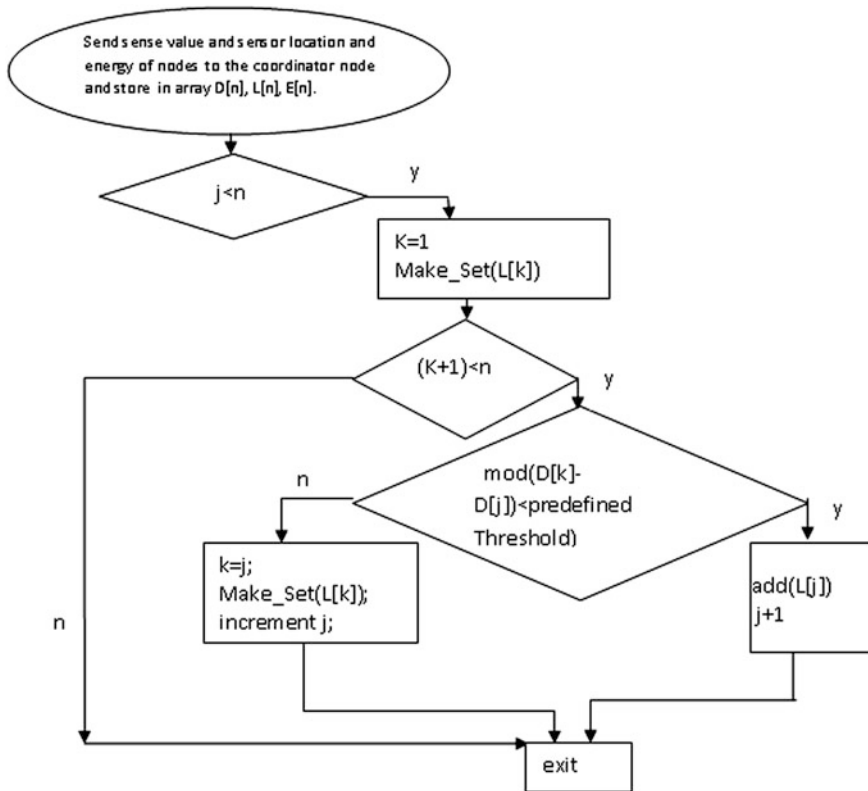


Fig. 3 The figure shows the function for cluster formation and scheduling of active nodes

is placed in different groups. The sensor nodes which are selected by coordinator node will send their values to the sink nodes. By using this algorithm we are exploiting the spatial as well as temporal correlation also Fig. 3. The Fig. 3 shows the function for cluster formation and scheduling of active nodes.

Conclusion

Spatial and temporal correlations reduce redundant data transfer. In this paper author proposed an approach in which spatial correlation technique is used. Author proposed an algorithm in which sensor nodes having nearby readings are identified and then only single node reading is send towards sink node that represents the reading of group of sensors. Redundant data need not to send towards sink node, it reduces sensor’s communication energy and network lifespan. Faulty node detection and fault tolerance are another research area. Encryption and decryption of data with correlation is another research area.

Future Work

The schemes described above for in-network aggregation is for single sink only. The in-network aggregation for multiple sinks is still an area of research. According to Ozdemi et al. [7] data aggregation protocols in which cluster heads change significantly is another research area. Ozdemir et al. [8] state that heterogeneity of sensor nodes is another research area. Another research area is compromised aggregator that sends false data [9]. Node monitoring mechanism is proposed but it consumes more energy and computational effort, so the security of Data Aggregation has a lot of future scope. Development of light weight monitoring node is another research problem [10]. “Many existing public key cryptography based privacy homomorphic functions are not suitable for resource limited sensor nodes”. In some secure data aggregation schemes elliptic curve cryptography is employed [11] but if elliptic curve cryptography is used then only some queries like sum and average can be used. So a method must be applied which is able to work with all types of data aggregation functions needs to be explored. The protocols that use powerful sensor nodes as data aggregators give promising results [9]. “However, determining locations of these nodes for the best data aggregation results needs further research” [12].

References

1. Villas, L.A., Boukerche, A., Guidoni, D.L., de Oliveir, H.A.B.F., de Araujo, R.B., Loureiro, A.A.F.: An energy-aware spatio-temporal correlation mechanism to perform efficient data collection in wireless sensor networks. *Comput. Commun.* **36**, 1056–1066 (2013)
2. Liu, C., Kui, W., Pei, J.: An energy-efficient data collection framework for wireless sensor networks by exploiting spatiotemporal correlation. *IEEE Trans. Parallel Distrib. Syst.* **18**(7), 21 (2007)
3. Yoon, S., Shahabi, C.: The Clustered AGgregation (CAG) technique leveraging spatial and temporal correlations in wireless sensor networks. *ACM Trans. Sensor Netw.* **3**(1), Article 3, Publication date: March 2007
4. Gupta, H., Navda, V., Das, S.R., Chowdhary, V.: Efficient gathering of correlated data in sensor networks. In: *MobiHoc’05*, 25–27 May. Urbana-Champaign, Illinois, USA (2005)
5. Sharaf, M.A., Beaver, J., Labrinidis, A., Chrysanthis, P.K.: TiNA: a scheme for temporal coherency-aware in-network aggregation. In: *MobiDE’03*, 19 Sept 2003, San Diego, California, USA
6. Deshpande, A., Guestrin, C., Hellerstein, J.M., Madden, S.R., Hong, W.: Model-driven data acquisition in sensor networks. In: *30th VLDB Conference*, Toronto, Canada (2004)
7. Ozdemir, S., Xiao, Y.: Secure data aggregation in wireless sensor networks: a comprehensive overview. *Comput. Netw. USA* **53**, 2022–2037 (2009)
8. Ozdemir, S.: Concealed data aggregation in heterogeneous sensor networks using privacy homomorphism. In: *Proceedings of the ICPS’0’*: IEEE International Conference on Pervasive Services, Istanbul, Turkey, pp. 165–168 (2000)
9. Miriyala Markandeyulu, Guttikonda Prashanti: Secure reference based data aggregation protocol for wireless sensor networks. *Int. J. Adv. Res. Comput. Sci. Softw. Eng.*
10. Akyildiz, I.F.: *Wireless Sensor Networks: A Survey*. Elsevier

11. Westhoff, D., Girao, J., Acharya, M.: Concealed data aggregation for reverse multicast traffic in sensor networks: encryption key distribution and routing adaptation. *IEEE Trans. Mobile Comput.* **5**(10), 1417–1431 (2006)
12. Miriyala Markandeyulu, Guttikonda Prashanti: Secure reference based data aggregation protocol for wireless sensor networks. *Int. J. Adv. Res. Comput. Sci. Softw. Eng.* **3**(7) (2013)

A Comparative Analysis of Different LFSR-Based Ciphers and Parallel Computing Platforms for Development of Generic Cipher Compatible on both Hardware and Software Platforms

Trishla Shah, Darshana Upadhyay and Priyanka Sharma

Abstract Pseudorandom numbers are at the core of any network security application. Pseudorandom numbers find its application in the network security domain in key generation, re-keying, authentication, smart-phone security, etc. These random numbers are produced through PRNG (Pseudorandom Number Generator). Hence, if there is a flaw or the PRNG produces predictable sets of random numbers, then the entire application would be prone to attacks. Therefore, development of a generic framework for generating strong sets of pseudorandom numbers is proposed. Hardware implementation for GSM stream cipher has already been implemented, under a particular segment of mobile communication. The project advanced into many dimensions like vulnerability testing, protocol designing, implementation in both software and hardware and evaluating. The proposal aims to build an in-general framework and a unified model for enhanced security specifically for LFSR (Linear-feedback shift register)-based stream ciphers. Hence, a thorough study on already existing LFSR-based ciphers is done. This study aims to extract out the behaviour of different ciphers under different application domains. As pseudorandom numbers are used in both software (stream ciphers, protocol design) as well as hardware (wireless devices, smart phones) areas of security, the generic model proposed is aimed at using a co-simulation of both hardware and software. For software development of the cipher, a parallel computing environment has been chosen because in today's computing trends, multi-core processors are superseding the sequential ones; hence, the basic force for growth of processor is to increase parallelism rather than increasing the clock rate. The paper thus

Trishla Shah (✉)

Department of Computer Science and Engineering, Institute of Technology,
Nirma University, Ahmedabad 382481, India
e-mail: 13mcei15@nirmauni.ac.in

Darshana Upadhyay · Priyanka Sharma
Institute of Technology, Nirma University, Ahmedabad 382481, India
e-mail: darshana.upadhyay@nirmauni.ac.in

Priyanka Sharma
e-mail: priyanka.sharma@nirmauni.ac.in

presents the CSPRNG (Cryptographically secure pseudo-random number generator) model based on hardware and software co-simulations, using a generic approach.

Keywords CSPRNG · GSM · Attacks · Keys · Generic · Co-simulation · LFSR

Introduction

In today's era, the use of networks and its applications are growing at a rapid rate. Users often reveal critical information like account numbers, bank passwords, personal and financial details, important transaction details, etc., over the internet. Apart from its legitimate use, vulnerabilities like password theft, virus attacks, spoofing, message confidentiality threats, message integrity threats, etc. have been found, causing potential loss of the users' private information. Hence, it is important to build a secure system providing a perfect balance of confidentiality, integrity and availability of user's private data. These security parameters are provided by a mechanism of key generation (public and private keys), random password generation, one-time password (OTP) generation, strong authentication, etc. Implementation of these mechanisms is done through generation of unpredictable sets of random numbers having high uncertainty, called pseudorandom numbers. Hence, pseudorandom numbers are at the core in providing security to network applications. These random numbers are produced through a pseudorandom number generator. Hence, if there is a flaw or the PRNG (Pseudorandom number generator) produces predictable sets of random numbers, then the entire application would be prone to attacks. Therefore, development of a generic framework for generating strong sets of pseudorandom numbers, using a co-simulation of hardware and software, is proposed. The proposal aims to build an in-general framework and a unified model for enhanced security specifically for LFSR (Linear-feedback shift register). Here, the design of the model has been constrained specifically for enhanced security of LFSR-based stream ciphers, because it has got good statistical property, high period, well suited to low-power or high-speed necessities. For the software implementation a parallel computing platform, i.e. GPU programming, is chosen, for increasing throughput. Therefore, the entire model aims to develop a CSPRNG (Cryptographically secure PRNG), using hardware and software co-simulations, for its use in various security applications. The research is thus constrained to network security domain.

Basic Concept

LFSR-based stream ciphers are currently used in almost all network security applications like military cryptography, conversion of plaintext to cipher text, etc.

Recent research shows that these are prone to various threats like eavesdropping, snooping and masquerading, and in the specific wireless network domain poor security mechanisms are explored [1]. Stream ciphers currently are implemented on both hardware (A5/1, A5/2, KASUMA, E0, MICKEY, GRAIN, SNOW, FISH) and software (HC-256, Rabbit, Salsa20, SOSEMANUK) [2] platforms. These ciphers have been detected to be prone to various network attacks like dynamic cube attack, basic correlation attack, refinement attack, guess-and-determine attack, linear approximation attack, algebraic attack, Berlekamp-Massey attack and fast time memory trade-off attack which requires some precomputation [3]. Hence, designing of a strong LFSR-based PRNG, resistant to above-mentioned stream cipher attack, is needed.

Challenges

Many stream ciphers have been designed, for the generation of a strong set of pseudorandom numbers, but certain limitations have been examined as follows: (i) In designing of hardware ciphers, the computational complexity over software performance decreases; (ii) Very few ciphers have been designed, working for network security applications in both hardware and software domains; (iii) The software implementation is mostly done on sequential basis, i.e. CPU, thus increasing complexities of overhead and time; (iv) Ciphers compatible for generating good pseudorandom series on a generic platform for diverse applications has not yet been designed.

Literature Survey

The design features of this CSPRNG are done, keeping in mind its compatibility with both hardware and software. Hence, the entire literature survey is branched up into analysis of network applications requiring PRNs, analysing hardware and software ciphers and analysing parallel computing platforms.

Analysis of Network Applications Requiring Pseudorandom Numbers

- i. Application in generation of keys and in re-keying:
As per Tara Chand Singhal [4], key-distribution and re-keying are major problems in any research, and in wireless infrastructure, these problems increase due to lesser sources of infrastructure, power and memory cost. The

stream ciphers are used in confidential communication in WEP (Wired equivalent privacy) and military applications. Hence, in all these applications, generation of pseudorandom numbers is important for maintaining privacy and security. Hence, a strong cipher needs to be designed, which provide a highly random and attack-resistant encrypted text. Here the cipher needs to be designed at SSL (Secure Sockets Layer). Here re-keying is used, if in the same communication band (which may be long enough), different keys are used for security purpose.

ii. Mobile Devices for Mobileagent Communication:

With mobile agents, like mobile devices, major attacks occur during the process of communication and migration from one cell to another. Agent state, which is achieved at previous executions, needs to be encrypted, so that an intruder cannot change or take advantage of it. This requires the generation of secret key, which is a strong pseudorandom number [5].

iii. Application on Smart Phones:

In any security applications, ubiquitous computing devices, not having necessary computing capacities, are hard to operate. Smart cards have PRN (Pseudorandom numbers) for security. Usually, PRN are produced by physical random number generator, but these are vulnerable to environmental changes. Hence, for securing against attacks, generation of the PRN is required [6].

iv. Authentication to counter DOS (Denial of Service) Attack on 802.11:

WLANs (Wireless LAN) which are based on 802.11 standards are vulnerable to DOS attacks because of unprotected and authenticated management and control frames. DOS attacks based on management and control frames can be filtered by pseudorandom number generator authentication. Here a mechanism for authentication is provided, for security against unwanted access. A strong and highly unpredictable random sequence is required. Hence, a PRNG based on software mechanism is required [7].

Analysis of Hardware Ciphers

For understanding the design specification of hardware, many hardware ciphers have been studied. It includes the following: (i) GRAIN-128 [8], (ii) GRAIN-128a [9], (iii) SNOW 2.0 (both h/w and s/w) [10], (iv) SNOW 2.0 modified [11] and (v) RFID (AES) [12]. The following table [13] presents a detailed study of all hardware ciphers, useful in cipher designing (Table 1).

The hardware, hence to be used in cipher, is concentrated on its clock cycles, feasibility in applications, its orientation in bits or words, etc.

Table 1 Analysis of hardware ciphers

Parameters	RFID	GRAIN-128	GRAIN-128a
Purpose	Providing security using strong symmetric authentication, using low-power and low die-size	Providing security in all hardware applications needing low memory and low power, using smaller no of components	Enhanced from GRAIN-128, it supports strong authentication and better hardware performance
Security issues to be overcome by the ciphers	Consumer tracking, tag forgery and the unauthorized access to the tag’s memory content	Correlation attack, Chosen IV attack, Time Memory trade-off attack	All Attacks observed by Grain-128
Input to Ciphers	Blocks (128 bits)	Bit-oriented	Bit-oriented
Reason for input	AES provides better security	Bit-oriented, because it is easy to implement it in hardware	Bit-oriented, because it is easy to implement it in hardware
Functions applied to input text (bytes)	Functions applied to input text (bytes)	LFSR, NFSR, filter function	LFSR, NFSR, pre-output function
Key size	128 bits	80 bits	128 bits
Reason for key-size selection	–	To prevent all attacks with computational complexity lower than 2^{80}	–
S-box or NFSR use(if yes), then reason for selection	The more the S-boxes are used, the less the clock cycles are needed for encryption	Generation of nonlinearity	Both shift registers are regularly clocked so the cipher will output one bit every second clock. This regular clocking is an advantage, both in terms of performance and resistance to side-channel attacks, compared to using irregular clocking or Decimation

(continued)

Table 1 (continued)

Parameters	RFID	GRAIN-128	GRAIN-128a
Reason for selection of algorithms on hardware implementation	AES -Main aim of using AES in RFID is using min hardware (constraint is size) and min power consumption. Hence, an 8-bit architecture instead of 32-bit, reduces number of S-boxes and reduce in power consumption	GRAIN -Main aim is to avoid attacks with computational complexity not more than 2^{80} and min hardware. Hence a memory of 160 bits is chosen and functions are chosen appropriately minimize hardware	GRAIN-128a -Main aim is to provide in-built support for authentication and improve hardware performance against older version of GRAIN. The authentication depends on the security of pre-output stream (to provide more randomness)
Throughput	Gate equivalent -3595	Gate equivalent -2243	Gate equivalent -2133
	Clock rate -992	Clock rate -256	Clock rate -160
Improvements from previous ciphers	Previous AES implementations never focused on AES module low die-size and low-powerconsumption requirements. This implementation focused only on low hardware complexity and low-power consumption, providing authentication	The AES implementation on RFID used more number of gates, thus increasing hardware complexity. GRAIN 128 is specifically tailored for using low hardware complexity and security against attacks	GRAIN 128 didn't have authentication so, GRAIN 128a provided authentication support, and high security by its highly random pre-output generator

Analysis of Software Ciphers

The software ciphers implemented till date were designed specifically for CPU computation, i.e. sequential generation. Hence, it was intended to study these ciphers for the purpose of understanding its sequential computation and replacing it with parallel computing, and also to check the feasibility of these ciphers for parallel computation. The following analysis was made, refer Table 2 [14].

The analysis of software ciphers concludes the need to use parallel computing rather than sequential in their implemented approach. The advantages of using CUDA are done in latter part of paper.

Table 2 Analysis of software cipher

Cipher	Usage	Implemented approach
SNOW 1.0	Development of a more secure and fast cipher	1. Outputs from two components LFSR and FSM are independent of each other yet it is sequential 2. A technique called hard coding is used, to increase the speed of computation but memory used is high 3. XORing of outputs of LFSR and FSM is done sequentially
SNOW 2.0	Improvements over previous version	(1) Mathematical equations derived for SNOW 2.0 are as follows: $(x) = x^{16} + x^{14} + 1x^5 + 1 F232$ $[x],4 = 233 + 2452 + 48 + 239$ $MUL[c] = (c23, c245, c48, c239)$ $MUL1[c] = (c16, c39, c6, c64)$ All above equations are solved sequentially using gcc or Microsoft C++ Compiler
RC4 Cipher	(1) Used for checking out effect of adversaries on embedded devices	(1) The implementation of RC4 is on CPU with the verification process being sequential, leading to overheads

Experimental Basis

For implementation on software, it is necessary to choose a robust platform equalizing the trade-off between time and speed. This demand is satisfied by computing on a GPU rather than CPU. Hence, a parallel computation is beneficial rather than sequential one. While surveying on parallel platforms, two most prominent one’s are (i) Nvidia’s GPU and (ii) Intel’s GPU. The API used for Nvidia is CUDA and for Intel is OpenCl. A thorough analysis of these programming languages has been done at thread level. The analysis branches up in the following segments.

Analysis of Parallel Computing Platform

The software implementation is to be done on parallel computing platforms. Here parallel platform, i.e. computing, is chosen rather than normal sequential CPU computing, to increase efficiency and decrease time. A parallel computing environment has been chosen because in today’s computer trends, multi-core processors are superseding the sequential ones; hence, the primary purpose for processor performance growth is to increase parallelism in spite of increasing the clock rate. Hence, increased parallelism would increase the efficiency of random number generation. Many parallel programming platforms are available like CUDA

(Compute Unified Device Architecture), OpenCL, etc. The survey analysis to find a better platform is done. The following graph shows the performance metrics of CUDA over OpenCL in terms of throughput, timings, overhead, etc.

Survey of Default Pseudorandom Generating Libraries

Both the platforms have in-built pseudorandom number generating libraries. The CUDA library for pseudorandom number generation is CURAND [15] and OpenCL has PRNGCL [16] for pseudorandom number generation. The common basic algorithm which is used in pseudorandom number generation is MTGP (Mersenne Twister). A thorough analysis of MTGP algorithm is done and is based on LFSR. This made the direction of survey much clear and precise.

Analysis of Randomness of Generated Algorithms Through NIST Statistical Toolkit

The random numbers generated from the two platforms were tested on NIST statistical toolkit. Randomness was checked based on 14 parameters [17]. The below graph indicates a comparison between CUDA and OpenCL based on various tests. The tests were carried out for various bit streams including 10,100,1000,10,000. The X-axis indicates various tests and Y-axis indicates its comparison results. The results showed CUDA's MTGP to have a better randomness rather than OpenCL. Hence, it was concluded that CUDA's pseudorandom platform is more effective in PRNG generation rather than OpenCL. The following figure gives its analysis [18]. The brief analysis is shown in Table 3 [19] (Fig. 1).

Observations

On the basis of above literature survey, the following conclusions have been made for the proposed cipher. (i) A hybrid of word-oriented and bit-oriented cipher is to be implemented for designing of LFSR. This would best optimize the initial cycles as well as increase efficiency in software-based ciphers. (ii) A cipher is to be designed keeping in mind its basic utility, i.e. security over communication with multiple messages using a single common key, and in telecommunication scenario for recovery from frame loss of sync messages. To design the above features, MODES can be designed in the cipher. (iii) To increase efficiency, the component structure needs to work independently, i.e. their o/p must be independent of each other and only the final output must be XORed. This can be best fitted in CUDA.

Table 3 Effectiveness of CUDA for designing existing ciphers

Implemented approach using sequential computing	Suggested approach using CUDA	How is CUDA better
(1) In many ciphers, Output from two components, LFSR and FSM is independent of each other, yet it is done sequential	(1) Using CUDA, generation of outputs from LFSR and FSM can be done in parallel	Generation of parallel outputs would save time and increase efficiency
(2) A technique called hard coding is used, to increase the speed of computation, but memory used is high	(2) Hard coding LFSR is done sequentially; this can be done in parallel	
(3) XORing of outputs of LFSR and FSM, is done sequentially	(3) XORing of outputs of LFSR and FSM can be done in parallel	
Mathematical equations derived for SNOW 2.0 are as follows: $(x) = x_{16} + x_{14} + x_5 + 1 F_{232}$ $[x]_4 = 233 + 2452 + 48 + 239$ $MUL[c] = (c_{23}, c_{245}, c_{48}, c_{239})$ $MUL1[c] = (c_{16}, c_{39}, c_6, c_{64})$ All above equations are solved sequentially using gcc or Microsoft C ++ Compiler	These equations can be solved in parallel like splitting entire equation as $x_{16}, x_{14}, 233$, etc., with one thread solving one term. All these can then be added in parallel	Computational complexity of Matrix multiplication for these equations would decrease exponentially to the base 2
The implementation of RC4 is on CPU with the verification process being sequential, leading to overheads	The same approach can be done in parallel, leading to low overheads of cycles	With CUDA the entire algorithm can be optimized

P1	P2	P3	P4	P5	P6
App Entropy Test	Block Frequency Test	Cumulative Test Forward	Cumulative Test Reverse	FFT	Fq

Fig. 1 NIST analysis of CUDA and OpenCl

Discussion

A primary objective of this paper is to design, implement and evaluate the cryptographically secure PRNG on parallel computing platforms. Towards the realization of this objective, the short-term goals of this proposal are to:

- (i) Investigate vulnerabilities and security mechanisms in LFSR-based stream ciphers.
- (ii) Design wireless interface and techniques for stream ciphers vulnerability modelling, and evaluate security requirements for each component network;

(iii) Design the proposed algorithm for PRNG using a hybrid of various methods (shrinking generator, nonlinear filter, generator and alternating step generator) to break the predictability of LFSRs. (iv) Comparative analysis of different parallel computing environments, namely OPENCL and CUDA. (v) Analyse and design proposed algorithm using VHDL (very high speed integrated circuit hardware description language) on hardware platform FPGA–SPARTAN 6 and using CUDA on software parallel platform. (vi) Identifying the hardware utilization using Spartan-6, FPGA, measurement of execution speed using parallel computing software CUDA, evaluate randomness of key stream using the NIST statistical test package.

Technical Requirements and Feasibility

As the project is focused on both hardware and software implementations, it confines its technical requirements in both these domains. **Hardware Requirements:** VHDL—Very high speed integrated circuit hardware description language analysis and designing of the proposed algorithm is done using VHDL language. FPGA–SPARTAN 6—The simulation of the proposed algorithm is to be done, using FPGA–Spartan 6 toolkit. **Software Requirements:** CUDA—Compute Unified Device Architecture—is a parallel computing platform to parallelize the given algorithm, developed by NVIDIA. The GPU used is Geforce 480.

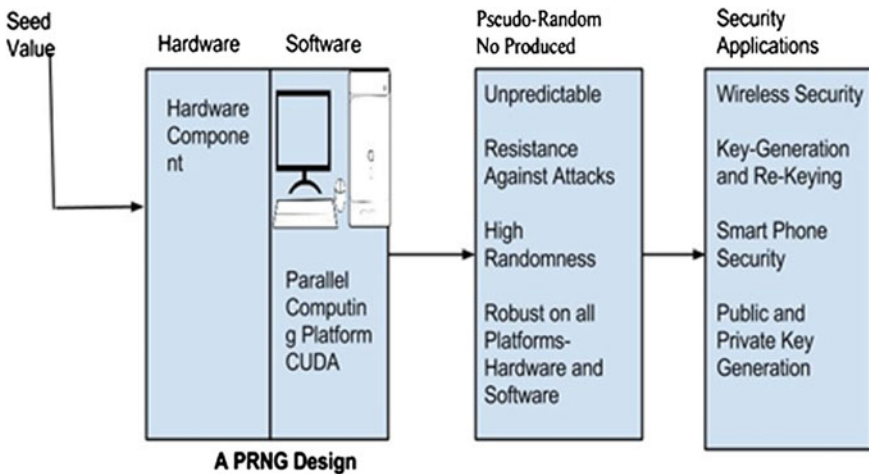


Fig. 2 Block diagram of PRNG generation

Conclusion and Future Work

Through this paper, a precise review on different network applications, hardware and software ciphers, and parallel computing platforms have been done. This study thus enforces the need to build a generic cipher which works efficiently both on hardware and software platforms. From the literature and the experimental basis, designing of the strong cipher is quite clear and easy. An n -bit LFSR cipher, customized for different applications and different requirements of computation capacities, is proposed. Figure 2 [20] shows the block diagram of proposed cipher.

Acknowledgement Towards the progress of the project, I would first like my organization Institute of Technology, Nirma University for granting of ample resources and a strong platform. I would like to thank all the associated professors and dignitaries.

References

1. Garland, M., Le Grand, S., Nickolls, J., Anderson, J., Hardwick, J., Morton, S., Phillips, E., Zhang, Y., Volkov, V.: Parallel computing experiences with CUDA. *IEEE Micro* **28**, 13–27 (2008)
2. Al-Hamdani, W.A., Griskell, I.J.: A proposed curriculum of cryptography courses. In: *Proceedings of the 2nd Annual Conference on Information Security Curriculum Development*, pp. 4–11. ACM (2005)
3. Preneel, B., Paar, C., Pelzl, J.: *Understanding Cryptography: A Textbook for Students And Practitioners*. Springer (2009)
4. Singhal, T.C.: Systems and methods for complex encryption keys. US Patent 8,363,834, Jan 29 2013
5. Topaloglu, U., Bayrak, C., Iqbal, K.: A pseudo random number generator in mobile agent interactions. In: *IEEE International Conference on Engineering of Intelligent Systems*, pp. 1–5 (2006)
6. Fan, J.-W., Chan, C.-W., Chang, Y.-F.: A random increasing sequence hash chain and smart card-based remote user authentication scheme. In: *9th International Conference on Information, Communications and Signal Processing (ICICS)*, pp. 1–5. IEEE (2013)
7. Khan, M.A., Hasan, A.: Pseudo random number based authentication to counter denial of service attacks on 802.11. In: *5th IFIP International Conference on Wireless and Optical Communications Networks, WOCN'08*, pp. 1–5. IEEE (2008)
8. Hell, Martin, Johansson, Thomas, Meier, Willi: Grain: a stream cipher for constrained environments. *Int. J. Wirel. Mob. Comput.* **2**(1), 86–93 (2007)
9. Agren, M., Hell, M., Johansson, T., Meier, W.: A new version of grain-128 with authentication. In: *Symmetric Key Encryption Workshop* (2011)
10. Ekdahl, P., Johansson, T.: Snow-a new stream cipher. In: *Proceedings of First Open NESSIE Workshop, KU-Leuven*, pp. 167–168 (2000)
11. Ekdahl, P., Johansson, T.: A new version of the stream cipher snow. In: *Selected Areas in Cryptography*, pp. 47–61. Springer (2003)
12. Feldhofer, M., Dominikus, S., Wolkerstorfer, J.: Strong authentication for rfid systems using the aes algorithm. In: *Cryptographic Hardware and Embedded Systems-CHES 2004*, pp. 357–370. Springer (2004)
13. Analysis of different hardware ciphers
14. Analysis of software ciphers

15. Cuda toolkit documentation—Developer Zone
16. Passerat-Palmbach, J., Mazel, C., Hill, D.R.C.: Pseudo-random number generation on gp-gpu. In: IEEE Workshop on Principles of Advanced and Distributed Simulation (PADS), pp. 1–8. IEEE (2011)
17. A Statistical Test Suite for Random and Pseudorandom Number Generators for Cryptographic Applications
18. NIST Analysis of Cuda and OpenCl
19. Effectiveness of Cuda for existing ciphers
20. Block Diagram of PRNG generation

Generation of Automatic Variable Key to Make Secure Communication

**Bishal Kumar Singh, Subhasish Banerjee, Manash P. Dutta
and C.T. Bhunia**

Abstract By the modernization of computer technology, the possibility of various cryptanalytic attacks increases rapidly, due to which maintaining the confidentiality on insecure channel becomes the burning problem and makes a large arena for the researchers. To tackle such problems and provide suitable solution, many methods have been introduced out of which automatic variable key (AVK) is the most dominated mechanisms as found in theoretical survey. In this paper, we have proposed a new scheme in AVK to generate the sequence of keys on the basis of divisibility factor of previous key. To prove the fruitfulness of our proposed scheme, we have compared our scheme with the existing related schemes based on randomness and standard deviation among the successive keys.

Keywords AVK · Randomness · Standard deviation · Security

Introduction

As such computer networks act like an essential part in our daily life, assuring the security of shared information becomes unavoidable requirements in insecure channel. From the last few decades, many mechanisms have been introduced to prevent the various well-known attacks of shared information. However, attaining the confidentiality with the help of a single key cannot sustain [1, 2] over time.

B.K. Singh (✉) · Subhasish Banerjee · M.P. Dutta · C.T. Bhunia
Department of Computer Science & Engineering, National Institute of Technology,
Yupia, Arunachal Pradesh 791112, India
e-mail: bishalsingh1991@gmail.com

Subhasish Banerjee
e-mail: subhasish.cse@nitap.in

M.P. Dutta
e-mail: manash.cse@nitap.in

C.T. Bhunia
e-mail: ctbhunia@vsnl.com

In 2005, Bhunia [3–5] brought an idea and invented AVK to achieve the security of shared information. As the name suggests, key generator generates keys variable in nature. Due to random variation among the auto-generated successive keys in AVK, chances of cipher text-only attack such as frequency attack or brute force attack can be reduced considerably as per theoretical survey. Afterwards, many researchers like Chakraborty et al. [6], Konar et al. [7], Goswami et al. [8–10], Banerjee et al. [11, 12] and Dutta et al. [13] have proposed many schemes and developed some new ideas in this context to preserve the security over insecure communication channel. In this paper, we have proposed a new and efficient mechanism to generate the keys based on divisibility factor of previous key. The rest of this paper is organized as follows. Proposed scheme with key generation examples and experimental results has been introduced in sections “Proposed Scheme” and Experimental Results, respectively. In section “Analysis and Comparison”, we have compared our scheme with other related schemes to prove the efficiency. Finally, we have concluded our paper with conclusion in section “Conclusion”.

Proposed Scheme

In this section, we have proposed a new key generation technique (Divisible Automatic Variable Key, DAVK) to enhance the unpredictability among the consecutive auto-generated keys based on divisible by 2. In this technique, the key generator generates the keys depending on even or odd of decimal equivalent of previous key. The complete description of our proposed scheme is given below:

```

Key_Generation (Initial key, Data set)
{
    K0=Initial key
    i=1
    repeat
    {
        if (Ki-1%2==0) then
            Ki=CLS (Ki-1)⊕CLS (Di-1)
        else
            Ki=CRS (Ki-1)⊕CRS (Di-1)
        i++;
    } while (Dataset != φ)
}

```

where

CLS(x) = Circular Left Shift of x by 1 bit position,

CRS(x) = Circular Right Shift of x by 1 bit position.

Examples:

Let us assume 8 bits of initial key as “11010110” and “formatted” as a data set. Then, subsequent keys will be generated for individual data block (8 bits), and automatic keys will be produced by the key generator as per defined scheme:

Initial key (K_0) = 11010110 (even number in decimal form)

Binary form of first block of data (D_0), ‘f’ = 01100110

To encrypt next block of data ‘o’, the key K_1 will be generated by performing XOR operation of circular left shifted K_0 and circular left shifted of D_0 , as K_0 was even.

$K_1 = 10101101 \oplus 11001100 = 01100001$ (odd number in decimal form)

Binary form of next data (D_1), ‘o’ = 01101111

To encrypt next block of data ‘r’, the key K_2 will be generated by performing XOR operation of circular right shifted K_0 and circular right shifted of D_0 , as K_1 was odd.

$K_2 = 10110000 \oplus 10110111 = 00000111$ and so on.

Experimental Results

Here, we have illustrated some of the experimental results to measure the randomness among the successive keys. As key generator generates the keys depending on initial key and data set pairs, we have measured the randomness in various such sets. For simplicity, we have used the block size of 8 bits only with same size of initial key.

Experiment 1:

In this experiment, we have taken “11010110” as an initial key and “A network packet is a formatted unit of data (a list of bits or bytes) carried by a packet-switched network.” as data set. The randomness among the auto-generated successive keys is depicted in Fig. 1.

Experiment 2:

Here, we have taken “10101110” as an initial key and “A packet consists of two kinds of data: control information and user data (also known as payload).” as dataset to calculate randomness and plot the graph shown in Fig. 2.

Experiment 3:

In this last experiment, the initial key and data set are taken as “11111001” and “The control information provides data the network needs to deliver the user data,

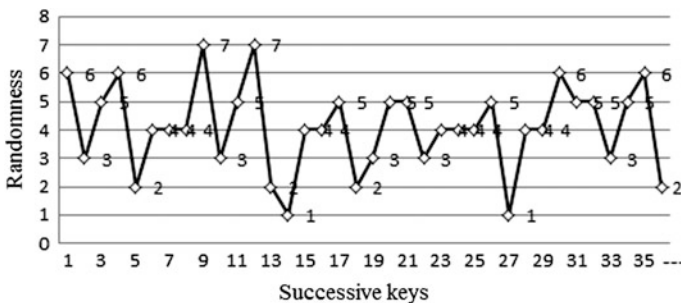


Fig. 1 Randomness variation of Experiment 1

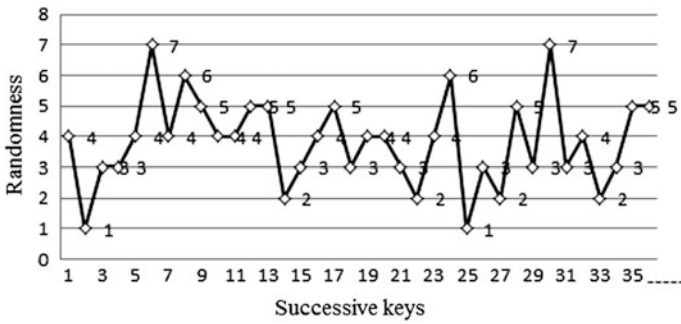


Fig. 2 Randomness variation of Experiment 2

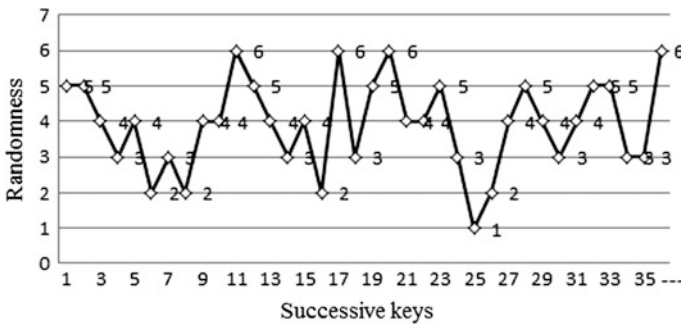


Fig. 3 Randomness variation of Experiment 3

source and destination network addresses.”, respectively, to calculate randomness of the auto-generated successive keys which is shown in Fig. 3.

Analysis and Comparison

For analysis and comparison of DAVK with the other related schemes, we have considered the average randomness and standard deviation in our account, where the randomness is calculated among the keys in the same way as defined in the existing schemes.

Due to average randomness of the successive keys is highly dependent on initial key and data set pairs, we have taken all the above Experiments 1–3 for comparison purpose. The average randomness comparison has been depicted in Fig. 4.

However, to define the degree of heterogeneity among the successive keys, average randomness may not work always as two series of observation may have the same average, but with unequal dispersion, and thus standard deviations for all the above three Experiments 1–3 are shown in Figs. 5, 6 and 7.

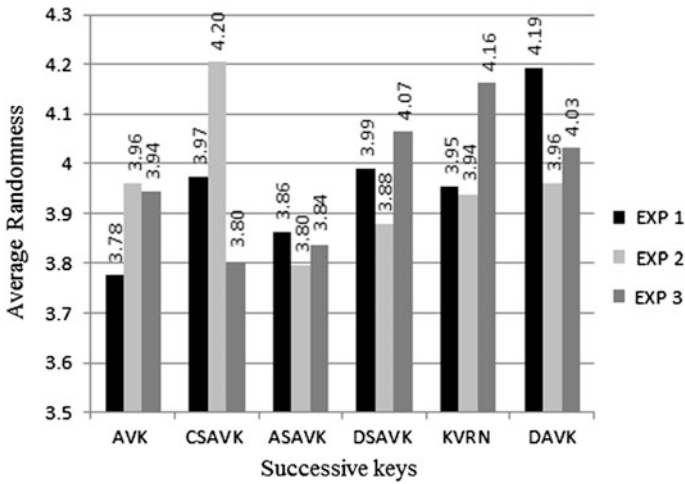


Fig. 4 Comparisons of average randomness

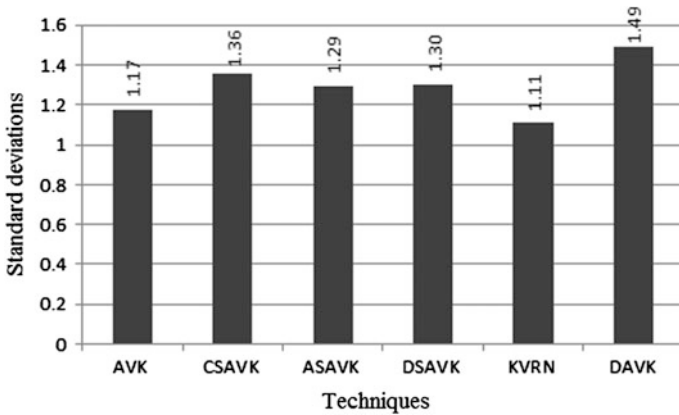


Fig. 5 Standard deviation variation of Experiment 1

Performance Analysis

While trying to find out the excellency among the techniques, the following observations are made:

1. For similar set of data and initial keys, the average randomness graph is shown in Fig. 4.
2. For similar set of data and initial keys, the standard deviation graph is also plotted and that is depicted in Figs. 5, 6 and 7.

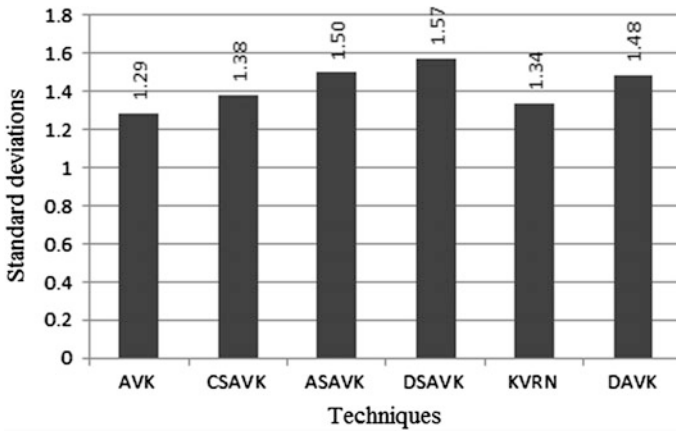


Fig. 6 Standard deviation variation of Experiment 2

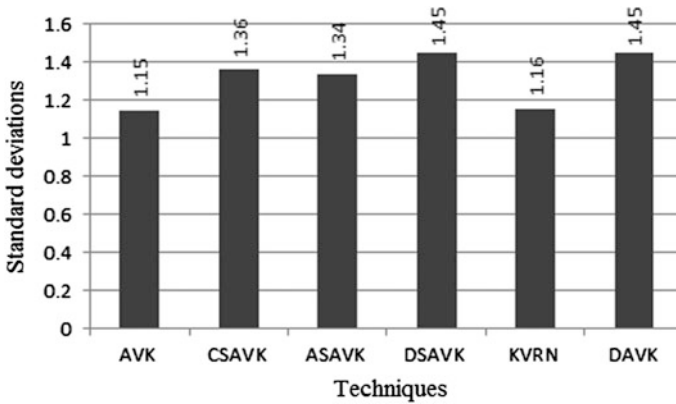


Fig. 7 Standard deviation variation of Experiment 3

3. Randomness and standard deviation are measured under the same experiment and it is found that for some set of keys the randomness are varying in different session.
4. In some existing cases, the standard deviation of our proposed scheme is found superior than that of other techniques and likewise randomness too, but for some set of keys it gives the reverse.
5. From Fig. 4, we can summarize that the average randomness of CSAVK is superior to other techniques, but at the same time, it is observed that the standard deviation of DAVK is superior to other techniques shown in Figs. 5, 6 and 7.
6. Therefore, from the above analysis we can state that the randomness and standard deviation depend on set of initial keys and set of data and they will vary accordingly.

Conclusion

Based on performance analysis, it has been observed that the DAVK is found to be better scheme to generate the keys based on standard deviation as compared to other techniques, but average randomness of DAVK is slightly weaker as compared to CSAVK for the same set of experiments. However, as we defined earlier the truthfulness of randomness among the successive keys, average randomness cannot withstand alone. Therefore, our proposed scheme can provide higher security than existing ones. Hence, DAVK is well suitable for practical implementation to reduce the chances of brute force attack, frequency attack and differential frequency attack.

References

1. Shannon, C.E.: Mathematical theory of communication. *Bell Syst. Tech. J.* **27**(379–423), 623–656 (1984)
2. Shannon, C.E.: Communication theory of secrecy system. *Bell Syst. Tech. J.* **28**, 656–715 (1949)
3. Bhunia, C.T.: New approaches for selective AES towards tackling error propagation effect of AES. *Asian J. Inf. Technol.* **5990**, 1017–1022 (2006)
4. Bhunia, C.T.: *Information Technology, Network and Internet*. New Age publication
5. Bhunia, C.T., Mondal, G., Samaddar, S.: Theories and application of time variant key in RSA and that with selective encryption in AES. In: *Proceedings of the EAIT*, pp. 219–221. Elsevier, Calcutta (2006)
6. Chakraborti, P., Bhuyan, B., Chowdhuri, A., Bhunia, C.T.: A novel approach towards realizing optimum data transfer and automatic variable key (AVK). *Int. J. Comp. Sci. Netw. Secur.* **8**(5), 241 (2008)
7. Konar, C., Bhunia, C.T.: A novel approach towards realizing optimum data transfer and AVK in cryptography. *Int. J. Comp. Sci. Netw. Secur.* **8**(5), 241–250 (2008)
8. Goswami, R.S., Chakraborty, S.K., Bhunia, A., Bhunia, C.T.: Generation of automatic variable key under various approaches in cryptography system. *J. Inst. Eng. India Ser. B* **94**(4), 215–220 (2014)
9. Goswami, R.S., Chakraborty, S.K., Bhunia, A., Bhunia, C.T.: Approach towards optimum data transfer with various automatic variable key techniques to achieve perfect security with analysis and comparison. *Int. J. Comput. Appl.* **82**(1), 28–32 (2013)
10. Goswami, R.S., Chakraborty, S.K., Bhunia, A., Bhunia, C.T.: Various new methods of implementing AVK. In: *2nd International Conference on Advances in Computer Science and Engineering*, pp. 149–152 (2013)
11. Banerjee, S., Dutta, M.P., Bhunia, C.T.: A New three dimensional based key generation technique in AVK. *Commun. J. Inst. Eng. India Ser. B*
12. Banerjee, S., Dutta, M.P., Bhunia, C.T.: A novel approach to achieve the perfect security through AVK over insecure communication channel. *Commun. J. Inst. Eng. India Ser. B*
13. Dutta, M.P., Banerjee, S., Bhunia, C.T.: An approach to generate 2-Dimensional AVK to enhance security of shared information. *Int. J. Sec. Appl.* **9**(10), 147–154 (2015)

Vector Evaluated Genetic Algorithm-Based Distributed Query Plan Generation in Distributed Database

Vikash Mishra and Vikram Singh

Abstract Distributed query processing (DQP) determines an optimal query plan, which generates user query results in efficient manner by selecting optimal set of database sites. Multi-objective DQP problems become more complex because a query optimizer has to select optimal, non-dominated QEP's, query equivalent plans, based on conflicting objective values. In past few years, evolutionary techniques are employed on such problems, although they are unable to get a good balance between efficacy and efficiency in all attempts. A meta-heuristic-based algorithm is presented which determines the combinations of database sites, in response to a query or group of queries. In this paper a technique is proposed for the optimal query plan generation, based on the meta-heuristics, modelled for distributed query processing, through an improved vector evaluated genetic algorithm for generation and selection of optimal query plans on distributed database. The algorithm's optimization performance is evaluated with other approaches and optimization reliability along with efficiency is benchmarked using performance graphs; comparisons indicate that the vector evaluated genetic algorithm (VEGA) converges better than aggregation-based method (weighted-sum approach). Top-K query plans, average query cost and number of generations are the parameters used for the comparative analysis.

Keywords Aggregation-based genetic algorithm · Bi-objective genetic algorithm · Distributed database · Distributed query processing · Top-K · Query vector evaluated genetic algorithm

Vikash Mishra (✉) · Vikram Singh
National Institute of Technology, Kurukshetra, Haryana, India
e-mail: mishravikash03@gmail.com

Vikram Singh
e-mail: viks@nitkkr.ac.in

Introduction

In modern history, the Internet in its all probability is the most desired and used distributed processing and computing environment and on the other hand, a user in this environment with limited capabilities for retrieving the desired result are at best. In such distributed processing environment, queries posed by user or applications routinely require gathering data from multiple sites or data sources [1]. Advanced database systems are embedded with the capability of various transparency mechanisms due to which as user never face or feel the effect of distribution of data and in such systems the data pertinent to a query move to a single server for final compilation. In traditional way, query on distributed processing environment is optimized centrally and executed synchronously [2]. Improving the performance of a database system is one of the key research issues from over the decades. Distributed database system (DDBS) is effectual means to improve reliability and availability of data to improve the overall performance of a processing system [3]. The users at local sites can work independently as well as communicate with other sites to retrieve data for answering global queries. Such a setup is referred to as a distributed database system (DDS) [4]. Query posed on a DDS is generally decomposed into secondary queries, which are executed at respective local sites with local data store, before communicated to central control sites for final result generation and finally at the user end, an integrated result is displayed.

A distributed query processing (DQP) strategy aims to minimize the overall cost of query processing in such systems [5, 6]. The cost of query processing in a DDS comprises two costs: the local processing cost and the site-to-site communication or the transmission cost of relation fragments. The total cost incurred in processing a distributed query can thus be taken as the sum of the local processing cost, cost of local operations on local data and cost of transferring locally processed data from participating sites to a central control sites. DQP iteratively evaluates all QEPs of a user query and determines the most optimal query plan that minimizes the total cost that is local processing (CPU, I/O) cost and communication cost [7]. In DDBS, the number of query equivalent plans (QEPs) grows at least exponentially through the increase in amount of relations accessed by the query, as relations are either replicated fully or replicated with partitioned sub-relations. Performing an exhaustive search for optimal QEPs over the all possible combinations of query plans is not viable due to a huge solution space. Therefore, in large DDB, devising a query processing strategy that optimizes the total query processing cost is shown to be a combinatorial optimization problem with NP-complete in complexity nature [8].

Over the last two decades, evolutionary algorithms have gained immense popularity due to their applicability in solving engineering optimization problems and complex scientific problems. These algorithms are inspired by the Darwinian evolution that accentuates the concept of “Survival of the Fittest”. It is, thus, metaphorical to the natural social behaviour and biological evolution of species. The evolutionary strategies are now proved to be the most proficient method of choice for solving such problems. Genetic algorithm-based techniques which belong to the

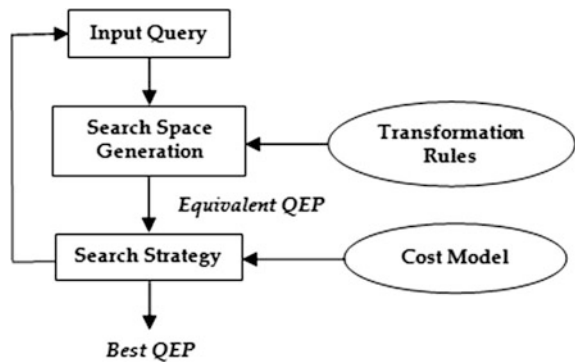
class of evolutionary algorithms have also been widely used in solving complex real-life science and engineering problems. The strength of GA as a meta-heuristic comes from its ability to combine the good features from several solutions to create new and better solutions over generations. Most real-world scientific and engineering problems have often conflicting and competing objectives that need to be optimized. In subsequent years, several different evolutionary algorithms (VEGA [9], NPGA [10], NSGA [11], NSGA-II [4], SPEA [11], SPEA-II [11], PAES [11], PESA [12, 11]) have effectively employed to solve the classic optimization problems.

This paper is organized as follows. Next section describes DQP and its motivation and proposed heuristic. Fundamentals of MOEA are discussed in subsequent section, also its suitability for DQP problem. Vector evaluated genetic algorithm (VEGA) is described in next section and an example illustrate the use of VEGA-based DQPG algorithm for generating optimal query plans. In graph section performance over other techniques in same section, in which comparison. In the last section conclusive discussion is presented with summary of approach.

Distributed Query Processing

In today’s scenario, with a multifold increase in the size operational data leads to growth of size of DDBS, the communication cost asserts a major impact on the overall cost of query processing. The cost incurred in communicating data through a congested network path or the communication of large data units between sites with higher communication costs can highly influence the cost of query processing. It thus also plays a key role in determining the overall performance of a DDBS [4, 6]. There can be a number of possible ways to process and communicate sub-relations relevant to the user query. In difference to the centralized query processing, distributed query processing cannot statically generate result at one single site. In DQP the user query is executed at node and its neighbours [6, 13, 14]. The optimal query plan generation and selection greatly depend on the cost function, as shown in Fig. 1.

Fig. 1 Distributed query optimization



In distributed relational database, logical data is replicated either fully or partitioned way to achieve higher degree of reliability in environment and serve higher availability data for efficient processing closer to the user sites or locations. This leads query processing to complex optimizations scenario, as a number of QEPs are exponentially increased. An approach is proposed in this paper using genetic algorithm (GA) to generate the query plans keeping optimality among solutions at highest priority. Primarily, a query optimization focuses on to diminish cost or amount of data a query requiring from multiple logical sites for processing queries. As a result, computing optimal distributed query plans becomes a multifaceted problem. In [14] a distributed query plan generation (DQPG) approach for single-objective, query proximity cost (QPC) is proposed, where optimization among QEPs is according to the heterogeneity within a QEP on the order of sites used. We proposed a solution for DQPG problem, and analysed optimization performance by including additional design objective. In the following objectives are briefly discussed.

Motivation: DQP is a model to determine the optimal policy for processing any given user query. The model is based on operating cost (cost of local processing and communication), which is a function of processing sites for query operators and sequence of these database operators. In DQP quality of QEP is evaluated according to the processing time required by the QEP [15]. In DQP, cost of data transmission between sites is the dominating cost. The objective of distributed query processing is to minimize the data transmission among sites thereby reducing the data transmission cost. Semi-joins have been used [16, 17] to reduce the communication cost. Semi-join reduces the communication cost and exploits the parallelism for query plan execution. Semi-joins carry out this by reducing the amount of attributes or tuples/attributes transfers among sites for generating results, thereby reducing the communication cost. DQP is phenomenon driven by the heuristics [18].

Heuristic-1: Query proximity cost (QPC) quantifies the heterogeneity in a QEP; a QEP with least number of distinct sites is better as it leads to less data transfer among sites. In this case, more than one QEPs with higher number of same relation is considered better [13, 14]. The fitness function, i.e. the QPC, based on these two heuristics is given below:

$$\text{QPC} = \sum_{i=1}^M \frac{K_i}{N} \left(1 - \frac{K_i}{N} \right)$$

where M indicates the total number of sites required in a QEP, K_i refer times the i th site in the QEP and finally N is the total number of relations required in QEP. GA uses the above fitness function to select the query plans having minimum QPC for the next generation. The selected query plans undergo genetic operator (crossover, mutation) for the generation of new pool.

Heuristic-2: Communication cost (CC), first of all algorithm forms the all possible trees assuming sites as nodes of tree, then evaluate minimum cost tree

among all. The communication path between two node is defined on the basis of data stored into the sites, such as the communication cost between node A and B is different in the case when we want move from B to A or A to B. The data from sites is transferred such a way that caused minimum cost to overall plan. So we are trying to minimize this heuristic. For the generation of the communication cost for query plan set, we need a communication cost table consisting communication cost of all site-to-site path.

Multi-objective Evolutionary Algorithm (MOEA)

These algorithms are inspired by the Darwinian evolution that accentuates the concept of “Survival of the Fittest” [19, 20]. It is, thus, metaphorical to the natural social behaviour and biological evolution of species. The evolutionary techniques are now proved to be the most proficient method of choice for solving such problems. Genetic algorithm-based techniques which belong to the class of evolutionary algorithms have also been widely used in solving complex real-life science and engineering and scientific problems [21]. The strength of GA as a meta-heuristic comes from its ability to combine the good features from several solutions to create new and better solutions over generations. Most real-world scientific and engineering problems have often conflicting and competing objectives that need to be optimized [22]. The evolutionary tactics are established as a best possible tool for many engineering and science related problems to optimize the different objectives and find efficient trade-offs unlike the classic techniques. The strength of GA as a meta-heuristic comes from its ability to combine the good features from several solutions to create new and better solutions over generations. Design objectives in most engineering and science scenario are disparate and contradictory for which optimized solution is required [20, 22]. A technique based on evolution is best fit for these kinds of problem, each evolution or iteration generated new improved solution and continues until certain degree of optimality is achieved over set of solutions. Evolutionary techniques are being used and suited for such problems on which concurrent optimization can be achieved over multiple objectives. The best part of GA emerges for multi-heuristic problems on its ability to combine the good features from several solutions to create new and better solutions over generations [20]. Most real-world scientific and engineering problems have often conflicting and competing objectives that need to be optimized. The evolutionary strategies are proved to be best suited for this class of problems as they can simultaneously optimize the different objectives and find efficient trade-offs unlike the classic techniques.

Many engineering and scientific problems cannot realistically modelled using single design objective, and thus multiple and often conflicting objectives are designed. Single genetic algorithm (SGA) is potentially unable to solve optimization problems with multiple conflicting objective functions, and this leads to a set of evolution of customized genetic algorithms; these are demonstrated and observed

effective on determining the excellent solutions. The solution set consists of a pareto front of optimal solutions for problem, and a solution in pareto front is considered best with respect to other solution for each of the objectives.

Schaffer (1985) considers the capability of single-objective GA (SGA) for multi-objective-based optimization problems and adapted a new variant of GA, named vector evaluated genetic algorithm (VEGA). In this new development, basic methodology of GA is same except the selection process of chromosomes, as selection is based performed on entire population by applying fitness values from each of the objectives, simultaneously and this generates set of population equal to the number of objectives considered. A problem having m design objectives and total population size of N , m subpopulations of N/m size is created. The selection step was modified to perform proportional selection at each generation for each of the objectives [15], and next for algorithm to proceed with the application of crossover and mutation in the standard mode.

VEGA is implemented over bi-objective query optimization, and performance of aggregation-based genetic algorithm (weighted-sum approach) with VEGA is analysed. The outcome of VEGA-based optimizations is better, as a aggregation-based GA has main demerits in complexity to decide the weights that can be appropriate to scale the objective, to accomplish this prior information which is required about problem, particularly if we consider that optimal point obtained will be purpose of these weights [23].

Vector Evaluated Genetic Algorithm (VEGA)

VEGA is first practical algorithm, implemented for the population with multiple properties or objectives. In [24] Schaffer adapted fundamental GA for multi-objectives by modifying the selection genetic operator of GA. In VEGA vector term represents the objective value for the multi-objective problem. This variant of genetic algorithm is a simplest and an uncomplicated adaption of single-objective genetic algorithm (SGA) for multi-objective optimization with modified selection genetic operator [25]. This algorithm divides total population into set of subpopulations equal to number of design objectives. Each subpopulation is created based on the fitness values of specific objectives, and for each generation, fitness assignment for first subpopulation is done according to the values of first objective function, and so on [24]. Selection techniques are applied on each of the subpopulations and based on the objectives, fitness value due to mating pool is created. In order to minimize positional partiality among the solutions by randomly shuffling before they are partitioned according to the objectives into set of subpopulations, this is useful in managing problems on which objective takes values of different domains and orders of magnitudes. As all QEPs of each of subpopulations is allotted fitness and restricted selection within each of subpopulations, this emphasizes better solution equivalent to respective objective function. Moreover, since neither two QEPs are compared on different objective functions

nor generate any complexity. In VEGA, any fundamental operator of selection can be used, and we used for a proportionate (Roulette wheel method) as selection operator. Selected QEPs are inserted into the mating pool for the further reproduction using genetic operators, like crossover using crossover probability (P_c) and mutation using mutation probability (P_m). VEGA iteratively evolves solutions until as stopping criteria met or fulfilled these criteria values are provided by decision maker or user [26].

(a) *Algorithm*

Input: Query plans {query₁ [], query₂ []...}

Output: New set of Query Plans

Step 1: Initialized set of query plans, P₀

Step 2: Evaluate Objective 1 (Proximity cost) and Objective 2 (communication cost) for each Query plan.

Obj1: $(PC) = \sum_{i=1}^{Ki} \frac{Ki}{CL} (1 - \frac{Ki}{CL})$; // Ki is count of i_{th} server used in query plan, CL is length of query plan//

Obj2: (CC)= Spanning Tree (query plan[]); //to evaluate minimum communication cost among all possible combination of sites for specific query//

Step3: Set a objective function counter i=1;
 Define q =N/M; // N is size of population & M no. of objective//
 For (J = 1 + (i - 1) * q to J= i * q) //Assign fitness for each query plan within subpopulation//
 {
 F(x_i^(j))=f(x_i^(j)); //f(x_i^(j)) is objective value & F(x_i^(j)) is fitness value of i_{th} chromosome in j_{th} subpopulation// }

Step 4: Perform Selection through Tournament selection method on each sub-populations (q), mating pool p_i

Step 5: #if (i=M) then Go to step (6)
 #else i =i+1; and Go to step (2)

Step 6: Combine all mating pools from sub-populations :**Mating Pool** = $\bigcup_{i=1}^M P_i$ //P_i is mating pool for i_{th} subpopulation//

Step 7: Apply genetic operator on mating pool of query plans,
 Apply Crossover with Crossover probability (Pc)
 Mutate chromosome with Mutation probability (Pm)

Step 8 : #if (stopping criteria meet), then
 Final set of chromosome copy to output (Optimal solutions);
 #else Go to Step (2); // to next iteration//

(b) *Example*

In GA, first chromosomes for a population are initialized. In proposed solution, two important aspects are the values used for encoding a chromosome and the sizes of the chromosome. The size of a QEP(chromosome) is equal to the number of relation required in FROM clause of the query and values in a QEP are name of sites of relations. Tables 1 and 2 show relation site matrix and some valid query plans. VEGA initially divides entire population into subpopulations, as 20 chromosomes are in Table 3, initial population (P₀). The number of objective decides the size of subpopulation (q) = N/M, where N is the total number of query plans and M is the number of objectives. Initial population (P₀) consists of 20 query plans, and is now equally divided into subpopulation of 10 query plans in each.

Table 1 Relation site matrix

Relation	Site								
	1	2	3	4	5	6	7	8	9
R ₁	1	0	0	1	0	1	0	0	1
R ₂	1	0	0	1	1	0	1	0	0
R ₃	1	0	1	0	1	0	0	1	0
R ₄	1	1	0	1	0	0	1	0	0

Table 2 Valid query plans (chromosomes)

Query plan	Description
[1,1,1,1]	All relations are in site 1
[4,4,3,7]	R ₁ and R ₂ from site 4, R ₃ from site 3 and R ₄ from site 7
[6,7,8,2]	R ₁ , R ₂ , R ₃ , R ₄ from site no. 6, 7, 8, 2 respectively
[4,4,8,4]	R ₁ , R ₂ , R ₄ from site 4 and R ₃ from site 8

Table 3 Partitioned population, subpopulation 1 (objective 1) and subpopulation 2 (objective 2)

S. no.	Query plans	Fitness value	Comm. cost
1	[4,4,3,4]	6/16	32
2	[1,1,1,1]	0	0
3	[4,4,1,2]	10/16	21
4	[9,4,8,4]	10/16	46
5	[6,1,1,1]	6/16	20
6	[9,4,3,4]	10/16	74
7	[4,5,5,4]	8/16	16
8	[6,5,5,1]	10/16	36
9	[1,7,8,4]	12/16	61
10	[4,4,8,4]	6/16	61
11	[6,4,8,4]	10/16	70
12	[1,4,4,1]	8/16	20
13	[4,5,5,9]	12/16	63
14	[9,5,5,9]	8/16	47
15	[6,5,5,9]	10/16	51
16	[1,7,5,9]	12/16	38
17	[9,7,8,9]	12/16	30
18	[6,4,5,4]	10/16	56
19	[9,1,8,4]	12/16	44
20	[1,1,1,9]	6/16	14

Table 4 Mating pool sub

Mating pool 1			
S No	Query plans	Fitness value	Comm. cost
1	[4,4,3,4]	6/16	32
2	[1,1,1,1]	0	0
10	[4,4,8,4]	6/16	61
5	[6,1,1,1]	6/16	20
6	[9,4,3,4]	10/16	74
7	[4,5,5,4]	8/16	16
4	[9,4,8,4]	10/16	46
Mating pool 2			
18	[6,4,5,4]	10/16	56
12	[1,4,4,1]	8/16	20
17	[9,7,8,9]	12/16	30
19	[9,1,8,4]	12/16	44
14	[9,5,5,9]	8/16	47
20	[1,1,1,9]	6/16	14
15	[6,5,5,9]	10/16	51

Query: *Select a, b*
From R_1, R_2, R_3, R_4
Where $R_{1.a} = R_{4.t}$
and $R_{4.p} = R_{2.x}$
and $R_{2.x} = R_{3.n}$;

In this query R_1, R_2, R_3, R_4 are required for result retrieval. Relation R_1 is replicated on sites (1, 4, 6, 9), R_2 at sites (1, 4, 5, 7), R_3 at sites (1, 3, 5, 8) and similarly relation R_4 at sites (1, 2, 4, 7) as shown in Table 1 relation site matrix (RSM). Total number of relation required by the query is 4, and the QEP size would be 4. The values into QEP are names of sites for the relation and ordering will be from R_1 to R_4 , from left to right.

Selection of the fitter and better chromosomes is achieved parallel in VEGA, as both subpopulation are treated differently with different heuristics, as first subpopulation is based on the heuristic 1 and second on the heuristic 2. In Table 3, query plans with lower fitness value are inserted into the mating pool from subpopulation 1, similarly from the subpopulation 2, query plans with lower communication cost are inserted into mating pool.

Now for implementing the crossover and mutation, combine all mating pool of different subpopulations. Table 4 mating pool consists of fitter and better QEPs, combine mating pool 1 and pool 2. Next, apply crossover with P_c in [0.5, 0.9]. In graph section, the effect of different crossover probability (P_c) values on generation

Table 5 New population

S No	Query plans	Fitness value	Comm. cost
4	[9,4,8,4]	10/16	46
7	[4,5,5,4]	8/16	16
2	[1,1,1,1]	0	0
1	[4,4,3,4]	6/16	32
5	[6,1,1,1]	6/16	20
12	[1,4,4,1]	8/16	20
14	[9,5,5,9]	8/16	47
20	[1,1,1,9]	6/16	14
N1	[4,4,5,4]	6/16	14
N2	[6,5,5,4]	8/16	25
N3	[6,4,5,9]	10/16	41
N4	[6,5,8,4]	10/16	42
N5	[4,4,5,9]	8/16	16
N6	[9,4,5,9]	8/16	16
N7	[6,5,3,4]	10/16	40
N8	[9,4,3,4]	8/16	18
N9	[9,1,5,4]	10/16	41
N10	[9,4,5,4]	8/16	23
N11	[4,5,8,4]	8/16	20
N12	[9,1,3,4]	10/16	42

of new population is shown. Mutation required in the QEP (chromosomes) according to P_m value, for VEGA P_m is [0.0, 0.2]. In Table 5, new population consists of new set of QEPs for initial population given in Table 4.

(c) Graphs

The comparative analysis of optimization performance is according to parameters, e.g. Number of generations, Average query cost and Top-K query of VEGA; aggregation-based genetic algorithm is shown in the following graphs. The experimental setup includes simulation on genetic algorithm toolkit in MATLAB with modelled cost functions and pool of QEP given relation site matrix. For the comparative experimentation, different crossover schemes are implemented: single point crossover (SPC), double point crossover (DBC) and uniform point crossover (UPC). UPC converged more consistently as compared to other schemes for all set of parameters. In Figs. 2 and 3, the comparative results are shown. The experimental analysis states that VEGA's convergence is better than any multi-objective aggregation-based genetic algorithm for different values of crossover and mutation probability, P_c and P_m .

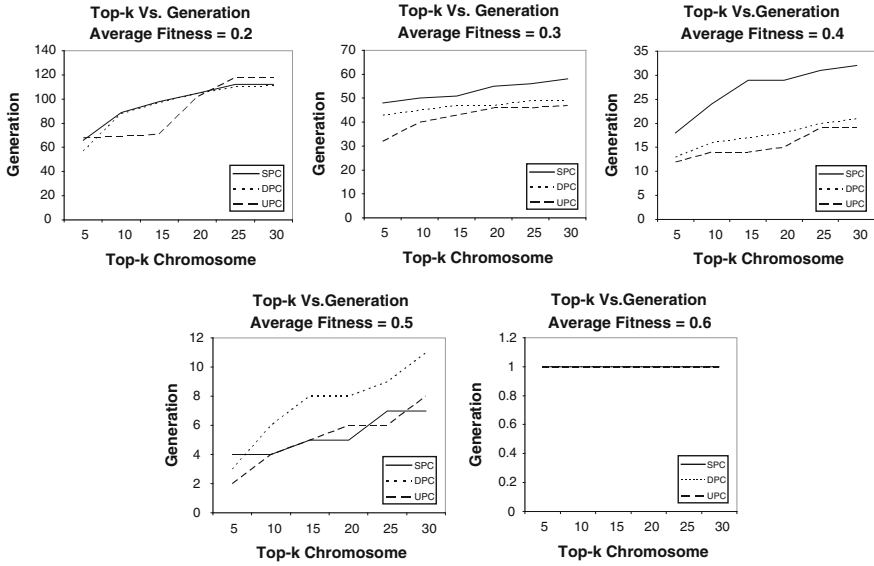


Fig. 2 Top-K versus generation for fixed average fitness

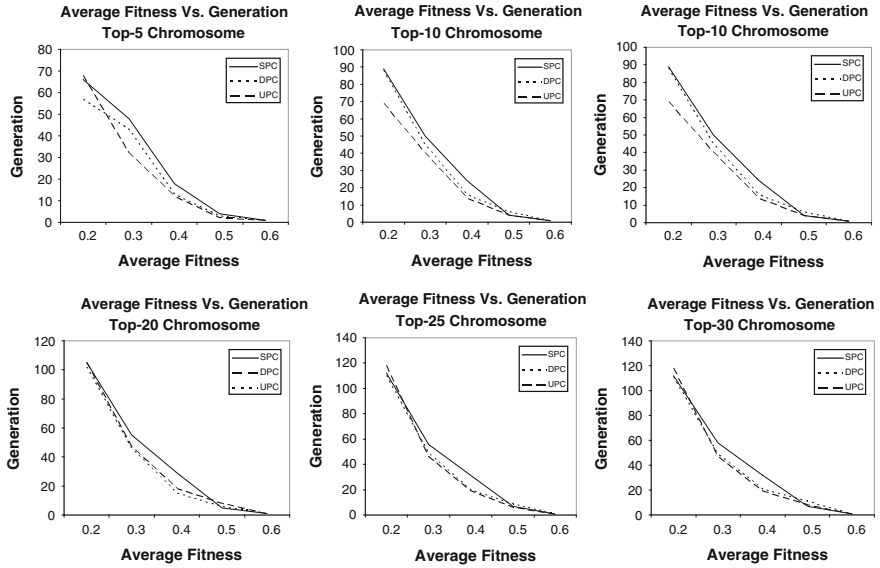


Fig. 3 Average fitness versus generation for fixed Top-K

Conclusion

Distributed database system is one of the most reliable processing environments; logical data is kept in multiple sites. The users at local sites can work independently as well as communicate with other sites to retrieve data for answering global queries; setup is defined as distributed query processing (DQP). A distributed query processing strategy aims to reduce the overall cost of query processing. The query optimizer primarily minimizes the time required for result retrieval for a user query. Genetic algorithm is nature-based optimization technique which has also been widely used in solving complex real-life optimization problems. The strength of GA as a meta-heuristic comes from its ability to combine the good features from several solutions to create new and better solutions over generations. Schaffer proposed a multi-objective genetic algorithm to accommodate the different types of fitness function, vector valued fitness values, called vector evaluated genetic algorithm. Initial steps are similar to single-objective GA, while selection is modified, so that at proportional selection according to each of the objectives is achieved. This selection approach justifies the importance of each of the design objectives of optimization problem, and in query optimization query plans are selected for evolution in proportional contribution of each of the objective populations. The performance trade-offs are discussed result section, and the comparative graphs are drawn between various parameters, e.g. number of generation (evolution) and average query cost.

References

1. Bernstein, P.A., Goodman, N., Reeve, C.L, Rothnie, J.B., Wong, E.: Query processing in a system for distributed database. *ACM Trans. Database Syst.* **4**(602–625) (1981)
2. Chu, W., Hurley, P.: Optimal query processing for distributed database systems. *IEEE TC C-31*(835–850) (1982)
3. Chang, C.C., Yu, C.T.: Distributed query processing. *ACM Comput. Surv.* **16**(4), 399–433 (1984)
4. Ceri, S., Pelagati, G.: *Distributed Database: Principles and Systems*. McGraw Hill (1984)
5. Gregory, M.: Performance issues in distributed query processing. *IEEE Trans. Parallel Distrib. Syst.* **4**(8) (1993)
6. Kossmann, D.: The State of the art in distributed query processing. *ACM Comput. Surv.* (2000)
7. Chang, J.M.: A heuristic approach to distributed query processing. In: *Proceedings of VLDB* (1982)
8. Jarke, M., Koch, J.: Query optimization in database systems. *ACM Comput. Surv.* (1984)
9. Fonseca, C.M., Fleming, P.J.: An overview of evolutionary algorithms in multiobjective optimization. *Evol. Comput.* **3**(1), 1–16 (1995)
10. Coello, C.A.: A comprehensive survey of evolutionary-based multiobjective optimization techniques. *Knowl. Inf. Syst.* (1999)
11. Ishibuchi, H., Narukawa, K.: Comparison of evolutionary multi-objective optimization with reference solution-based single-objective approach. In: *Proceedings of GECCO-2005, USA*, pp. 787–794 (2005)

12. Fleming, P., Wang, R., Purshouse, R., Fleming, P.: Local preference-inspired co-evolutionary algorithms, In: Proceedings of the 14th Annual Conference on Genetic and Evolutionary Computation, vol. 3, no. 1, pp. 513–520 (2012)
13. Vijay Kumar, T.V., Singh, V., Verma, A.K.: *Int. J. Comput. Theory Eng.* **3**(1) (1793–8201) (2011)
14. Panicker, S., Vijay Kumar, T.V.: Distributed query plan generation using multiobjective genetic algorithm. In: ICICA (2011)
15. Goldberg, D., Deb, K.: A comparative analysis of selection schemes used in genetic algorithms. *Found. Genet. Algorithms* (69–93) (1991)
16. Epstein, S.R., Wang, M.E.: Distributed query processing in relational databases system. In: Proceedings of ACM SIGMOD (1978)
17. Kambayashi, Y.S., Yoshikawa, M.: Query processing for distributed databases using generalized semi-joins. In: International Conference of Management of Data in ACM SIGMOD, pp. 151–160 (1982)
18. Bodorik, P., Riordon, J.S.: Distributed query processing optimization objectives. In: Proceedings of the IEEE Fourth ICDE, LA CA, pp. 320–329 (1988)
19. Holland, J.H.: *Adaptation in Natural and Artificial Systems*. University of Michigan Press (1975)
20. Mitchell, M.: *An Introduction to Genetic Algorithms*. MIT Press (1998)
21. Deb, K.: *Multi-objective Optimization Using Evolutionary Algorithms*. Wiley (2001)
22. Deb, K., Goldberg, D.E.: An investigation of niche and species formation in genetic function optimization. In: Proceedings of the Third ICGA, pp. 1–10 (1990)
23. Deb, K.: Multi-objective genetic algorithms: Problem difficulties and construction of test problems. *Evol. Comput.* **7**(3), 205–230 (1999)
24. Schaffer, J.D.: Multiple objective optimization with vector evaluated genetic algorithms. In: Proceedings of ICGA, Hillsdale, pp. 93–100 (1987)
25. Zitzler, E., Deb, K., Thiele, L.: Comparison of multi-objective evolutionary algorithms: empirical results. *Evol. Comput.* **8**(2), 173–195 (2000)
26. Deb, K., Agrawal, S.: Understanding interactions among genetic algorithm parameters. *Found. Genet. Algorithms* **V**, 265–286 (1998)
27. Yu, C.T., Guh, K.C., Chen, A.L.P.: An integrated algorithm for distributed query processing. In: IFIP Conference on Distributed Processing, Amsterdam (1987)

A Novel MEMS-Based Frequency Tunable Rectangular Patch Antenna

Rajesh Saha, Santanu Maity and Lipi Sarkar

Abstract This paper comprises of a frequency tunable patch antenna on which a U-shaped metamaterial structure is designed. The antenna is loaded with coplanar waveguide (CPW) stub on which two MEMS shunt switch with capacitive gap of $1.5 \mu\text{m}$ were placed at 0.2 mm distant from each other. The tunability in frequency is achieved by changing the gap between the bridge and the insulating layer, at up state of the switches. The antenna resonant frequency shifted from 10.54 GHz down to 10.52 GHz by changing the capacitive height from 1.5 to $1 \mu\text{m}$. The simulation of designed model has been carried out in Ansoft HFSS and different antenna parameters like gain, radiation pattern, efficiency, and scattering parameter have been adopted in this paper.

Keywords Frequency tunable · MEMS · Micromachining · Metamaterial

Introduction

Due to exponential development of wireless communication in many fields like commercial, telecommunication, military, microwave, etc., there is growing need for single antenna that can operate at different frequencies. In MEMS (Microelectromechanical System) technology, the mechanical components like

Rajesh Saha (✉)

Computer Science and Engineering, National Institute of Technology,
Yupia, Arunachal Pradesh 791112, India
e-mail: rajeshsaha93@gmail.com

Santanu Maity · Lipi Sarkar

Electronics and Communication Engineering, National Institute of Technology,
Yupia, Arunachal Pradesh 791112, India
e-mail: santanu.ece@nitap.in

Lipi Sarkar

e-mail: lipi.ece.2011@gmail.com

© Springer India 2016

N. Afzalpulkar et al. (eds.), *Proceedings of the International Conference on Recent Cognizance in Wireless Communication & Image Processing*,
DOI 10.1007/978-81-322-2638-3_38

actuators, sensors, glass, etc., is integrated with electrical circuit on the same chip using micro fabrication process [1, 2]. MEMS-based RF component such as switches, variable capacitors, phase shifters, antennas, filters, tuners, etc. impose better performance because of their less power consumption, lower signal attenuation, low insertion loss, excellent isolation, small size, reliability, and their performance can further be increased by reducing signal time and noise effect through the use of on-chips component [3, 4].

Frequency tunable antennas can be realized by changing the frequency band and maintaining the radiation characteristic [5]. Such kinds of frequency tunable antennas can be designed by MEMS-based switch technology. MEMS switch can be series or shunt type depending on signal path [6]. In our design, we have concentrated on shunt switch as it required minimum parasitic element and also handle more RF power compared to series switch. In this paper, we present U-slot metamaterial structure patch antenna loaded with CPW stub on which MEMS shunt switches are designed to achieve tunability in frequency. Substrate micro-machining has been done for the designed patch antenna which is discussed in next section.

Concept of Metamaterial and Micromachining

Metamaterial is one of the hot research topics and it exhibits properties that are not found in traditional materials. In 1968, Dr. Veselago [7] examined the existence of material which has negative value of permeability (μ) and permittivity (ϵ). After almost 30 years later, in the year 2000 Dr. Smith [8] practically showed the presence of such material by periodically arranging the Split Ring Resonator (SRRs) and metallic thin wires. The SRRs provides the negative permeability (μ) and thin wires give the negative value of permittivity (ϵ). Because of having simultaneously negative value of permeability (μ) and permittivity (ϵ), metamaterial is also named as Negative Refraction Index (NRI) [9] material. Due to having negative refraction index, the phase and group velocity moves in opposite direction and hence the power density (S) is reversed with respect to the direction of propagation. As the power density (S) which is equal to curl of electric field (E) and magnetic field (H) moves in backward direction to wave vector (k), metamaterial is also known as Left Handed Metamaterial (LHM) [10]. In our design, metamaterial structure is used to improve the antenna performance parameters like gain, directivity, efficiency, etc.

A patch antenna designed on high dielectric constant substrate will exhibit narrow bandwidth and poor in performance [11]. This problem can be overcome by producing low index material in the substrate of the patch antenna. To designed patch antenna on high dielectric substrate without losing the advantage of low index material, a portion of substrate between the patch and ground is removed by etching process. This elimination technique of the substrate between radiating patch and ground is called as micromachining technique [12].

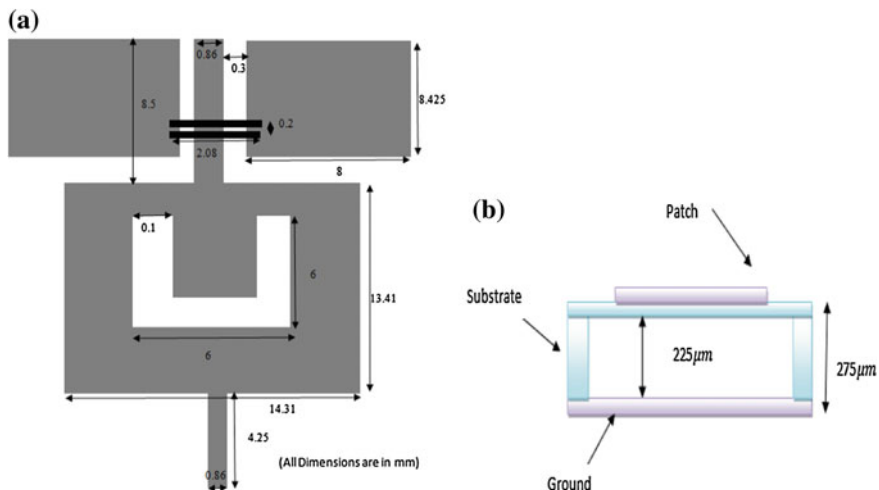


Fig. 1 **a** Schematic top view of frequency tunable antenna and **b** Micromachining part of the antenna

Device Structure

Figure 1a depicts the schematic view of the frequency tunable patch antenna. At first, rectangular patch antenna resonating at 10 GHz frequency on silicon substrate having relative permittivity (ϵ_r) = 11.9 is designed. Because of having very high permittivity value, the size of the device decreases, but simultaneously because of excitation of surface waves, performance become poor. To overcome these problems, micromachining has done between radiating patch and ground. To improve the performance further, structure is loaded with a U-slot metamaterial structure and CPW stub on which MEMS shunt switch are placed periodically. The patch, CPW, and ground are made of same material (gold). A layer of silicon nitride as isolating layer is placed above the center line of CPW where switches are placed. Figure 1b shows the view of micromachining part of the antenna. The height of the cavity is 225 μm and total substrate thickness is 275 μm. The value of permittivity (ϵ_{cavity}) within cavity between the patch and ground can be calculated from Eq. (1) [13].

$$\epsilon_{cavity} = \frac{\epsilon_{air}\epsilon_{Si}}{\epsilon_{air} + (\epsilon_{Si} - \epsilon_{air})x_{air}} \tag{1}$$

where x_{air} is the ratio of air to full substrate thickness. In our design, the calculated value of permittivity within the cavity (ϵ_{cavity}) is 1.197.

Simulation Result

Simulation has been carried out by using HFSS v. 13 software and simulated results are depicted in this section.

Results and Discussion

Figure 2 shows the plot of S11 parameter at both up and down positions of the switch. The frequency is tuned from 10.54 to 10.52 GHz when the capacitive gap changes from 1.5 to 1 μm , but the radiation pattern is same at both capacitive gaps shown in Fig. 3. The maximum gain obtained in both the cases approximately equal

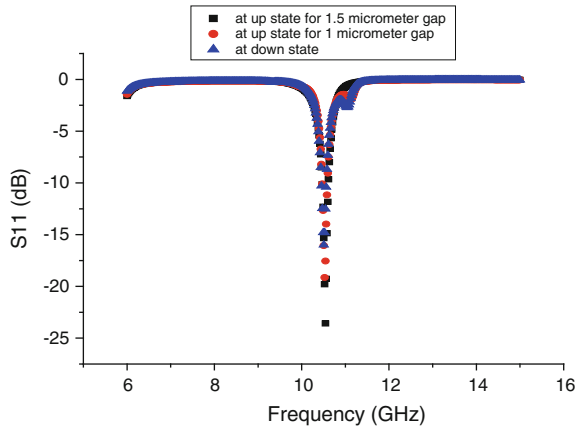


Fig. 2 S11 parameter both at up and down state of the switch

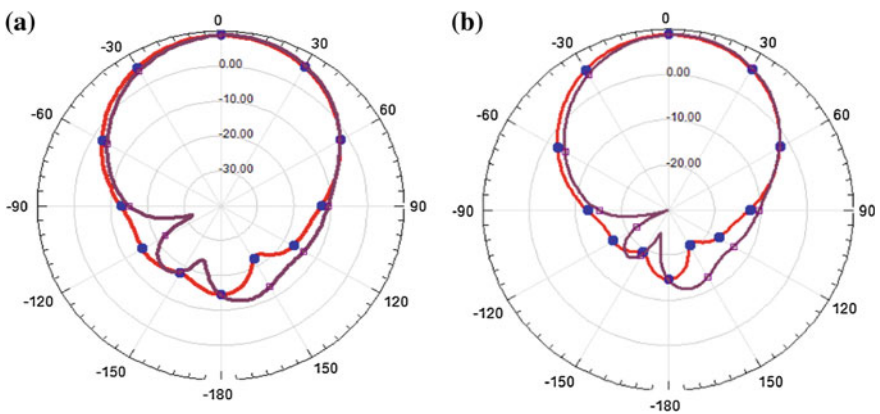


Fig. 3 Radiation pattern at up state with capacitive **a** gap 1.5 μm **b** gap 1 μm

Fig. 4 Realized gain at up and down state of the switch

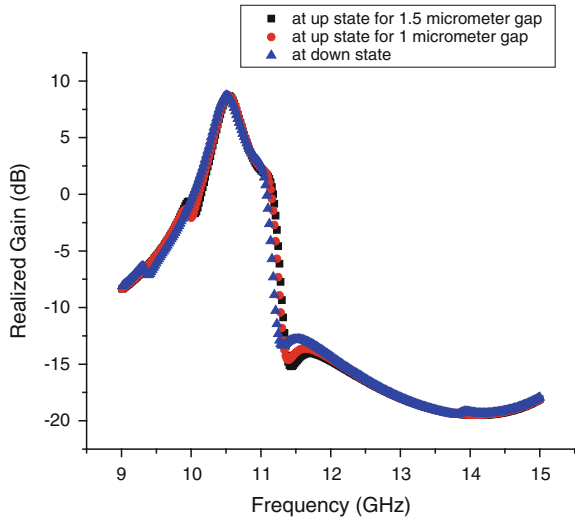
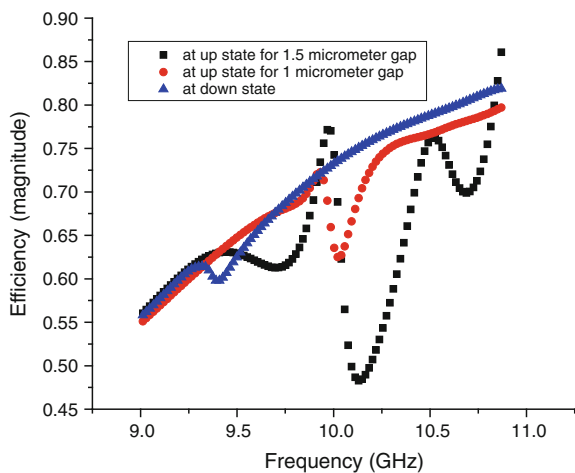


Fig. 5 Radiation efficiency of the antenna at up and down position of the switch



to 9 dB. Figure 4 depicts the realized gain versus frequency plots of designed antenna. The simulation shows that value of maximum gain and realized gain are same near resonance frequency. No losses occurs in our designed antennas, hence perfect impedance matching takes place. Figure 5 illustrates the efficiency of antennas for down state and up state of the capacitance switch. The efficiencies are 79, 77, and 76 % for down state, up state with gap 1 μm and 1.5 μm , respectively. The loss is slightly less for down state in comparison to up state of capacitive switches. The performance parameters of the antenna at their up and down state of the switches in tabular form is described in Table 1. From Table 1, it can be concluded that the value of gain at up and down state of the switches are equal.

Table 1 Antenna parameters at up state and down state of MEMS switch

Antenna switch at different state	Resonance frequency (GHz)	S11 (dB)	Gain (dB)	Realized gain (dB)	Efficiency (in %)
Up state with capacitive gap = 1.5 μm	10.54	-23.59	8.83	8.68	76
Up state with capacitive gap = 1 μm	10.52	-19.13	8.7	8.71	77
Down state	10.51	-16	8.76	8.72	79

Conclusion

Therefore, tunability in resonance frequency has been achieved by changing the capacitive gap at up state of the switch, without affecting the radiation pattern of the antenna. The tunability in resonance frequency can further be increased by increasing the number of switches. Therefore, RF-MEMS switch shows excellent switching properties among microwave devices. The other simulated antenna parameters such as gain, efficiency, etc., are shows better performance.

Acknowledgement The authors would like to thank Jadavpur University for providing software and all the colleges at NIT Arunachal Pradesh on writing this technical paper.

References

1. Simons, R.N., Chun, D., Katehi, L.P.B.: Microelectromechanical systems (MEMS) actuator for antenna reconfigurability. *IEEE MTT-S International Microwave Symposium Digest*, pp. 215–218, May 2001
2. Christodoulou, C.G., Tawk, Y., Lane, S.A., Erwin, S.R.: Reconfigurable antennas for wireless and space applications. In: *Proceedings of the IEEE*, vol. 100, no. 7, pp. 2250–2261, July 2012
3. Rebeiz, G.M.: *RF MEMS Theory, Design and Technology*. Wiley, Hoboken (2003)
4. Civi, O.A., Demir, S., Akin, T.: Reconfigurable Antennas Using RF-MEMS Research in Turkey, 978-1-61284-757-3/11/\$ 26.00 C IEEE (2011)
5. Erdil, E., Topalli, K., Unlu, M., Civi, O.A., Akin, T.: Frequency tunable microstrip patch antenna using RF MEMS technology. *IEEE Trans. Antennas Propag.* **55**(4) (2007)
6. Verma, P., Singh, S.: Design and simulation of RF MEMS capacitive type shunt switch & its major applications. *IOSR J. Electron. Commun. Eng. (IOSR-JECE)* **4**(5), 60–68 (2013). e-ISSN: 2278-2834, p-ISSN: 2278-8735
7. Veselago, V.G.: *Usp. Fiz. Nauk* **92**, 517 (1967). *Sov. Phys. Usp.* **10**, 509 (1968)
8. Smith, D.R., Padilla, W.J., Vier, D.C., Nemat-Nasser, S.C., Schultz, S.: *Phys. Rev. Lett.* **84**, 4184 (2000)
9. Wang, J., Qu, S., Xu, Z., Ma, H., Yang, Y., Gu, C., Wu, X.: A polarization-dependent wide-angle three-dimensional metamaterial absorber. *J. Magn. Magn. Mater.* 2805–2809 (2009)
10. Saha, R., Bhattacharjee, S., Bhunia, C.T., Maity, S.: Dual band operation using metamaterial structure for Radio Frequency Identification (RFID) system. In: 2014 International Conference

- on Signal Propagation and Computer Technology (ICSPCT), pp. 16–19 (2014). 978-1-4799-3140-8/14/\$31.00IEEE
11. Katehi, L.P.B., Harvey, J.F., Brown, E.: MEMS and Si micromachined circuits for high frequency applications. *IEEE Trans. Microw. Theory Tech.* **50**(3), 858–866 (2002)
 12. Öjefors, E.: *Micromachined Antennas for Integration with Silicon Based Active Devices*. Uppsala University (2004)
 13. Papapolymerou, I., Drayton, R.F.: Micromachined patch antennas. *IEEE Trans. Antennas Propag.* **46**(2) (1998)

Design and Optimization of Band-Stop Filter Using Metamaterial Structures for K-Band Applications

Ngasepam Monica Devi and Santanu Maity

Abstract This work describes the design, simulation and fabrication of a metamaterial-based band-stop filter operating at K-band with a resonant frequency of 24.5 GHz and a notch level of -33.15 dB. The device specifically implements metamaterial structures which are of practical interest in microwave applications to obtain wide bandwidth, high performance and small electrical lengths. The device consists of four unit cells with two cells placed in each ground plane on a coplanar waveguide (CPW) structure. Achieving a good suppression level has been made possible by the four unit cells which are nothing but the metamaterial structures. The band-stop performances for various widths and the gaps of the rectangular-shaped resonators (complementary split ring resonators) have been shown proving that the response characteristics of the metamaterial-based filter can be dynamically tuned. The device shows the capability of CSRR/CPW structures for microwave applications such as filters.

Keywords Coplanar waveguide (CPW) · Metamaterial structures · Band-stop filter · Complementary split ring resonators (CSRRs)

Introduction

With the advancements in communication technologies, communication services are growing side-by-side. This necessitates the efficient utilization of the electromagnetic radio spectrum available to us. Filters are one of those devices that help in

N.M. Devi (✉)

Department of Computer Science & Engineering, National Institute of Technology,
Yupia, Arunachal Pradesh 791112, India
e-mail: ngcanimo@gmail.com

Santanu Maity

Department of Electronics & Communication Engineering,
National Institute of Technology, Yupia, Arunachal Pradesh 791112, India
e-mail: santanu.ece@nitap.in

© Springer India 2016

N. Afzalpulkar et al. (eds.), *Proceedings of the International Conference on Recent Cognizance in Wireless Communication & Image Processing*,
DOI 10.1007/978-81-322-2638-3_39

achieving it, and not only suppressing harmonics and parasitics. These days, materials with unique electrical and magnetic properties are now emphasized in designing passive microwave elements, such as filters, which plays an inevitable role in modern wireless communications. These materials are known as metamaterials. Metamaterials are a special kind of artificial structures which are not found in nature. Their properties are determined by their structure rather than their composition. The uniqueness about metamaterials is the ability to exhibit either negative permittivity or permeability or simultaneous negative values of permittivity and permeability in the resonance region [1]. Metamaterials are of high interest in microwave and millimetre wave applications due to its properties such as exhibition of anti-parallel group and phase velocities, reversal of Snell's law (negative refractive index) [2], and the possibility to achieve miniaturization of devices. The implementation of metamaterial started with the proposal of SRRs by Pendry to form an effective medium with a negative magnetic permeability when arranged periodically [3]. Eventually, in 2004, complementary split ring resonators (CSRRs) were obtained by applying the Babinet principle to the conventional SRRs [4]. Unlike electromagnetic bandgap structures (EBG), which were proposed to mitigate the limitations of conventional filters [5–7], microwave circuits are conventionally realized in microstrip technology. However, CPWs are ideally suited for microwave applications because of the benefits it provides such as easy integration with lumped or active components, low dispersion and reduction of the radiation losses [8, 9]. Thus, most of the implementations of SRRs and CSRRs have been carried out in CPW. However, the CSRR/CPW structure has shown superior performance [10]. In CPW structures incorporated with CSRRs, CSRRs can be etched either into the ground plane or central conductor to achieve stop-band behaviour in the transmission response. Theoretically, CSRRs are electrically excited by the lines on the top of the substrate [4]. Several works related to the design of band-stop filters on CPW have been illustrated [11–14]. In this paper, a compact band-stop filter is designed on silicon substrate by etching CSRRs on the ground planes. The resonant frequency depends on the dimensions of CSRRs, thus the rejected bandwidth can be tailored as per requirements. It has been shown that many cells are added to achieve a good level of rejection [15]. Here, in this design, two identical unit cells are placed on each ground plane and a good band-stop performance is observed, owing to the depth of the notch and the low value obtained in reflection coefficient at the same frequency.

Device Structure, Design and Fabrication

Figure 1 shows the side view of the proposed device with CSRRs loaded CPW transmission lines and the layout of a unit cell of the proposed band-stop filter. Basically, a CSRR consists of two concentric structures etched out of metallization. Miniaturization is supported by using two concentric structures. The proposed device consists of a $50\ \Omega$ CPW structure loaded with rectangular shaped CSRRs in

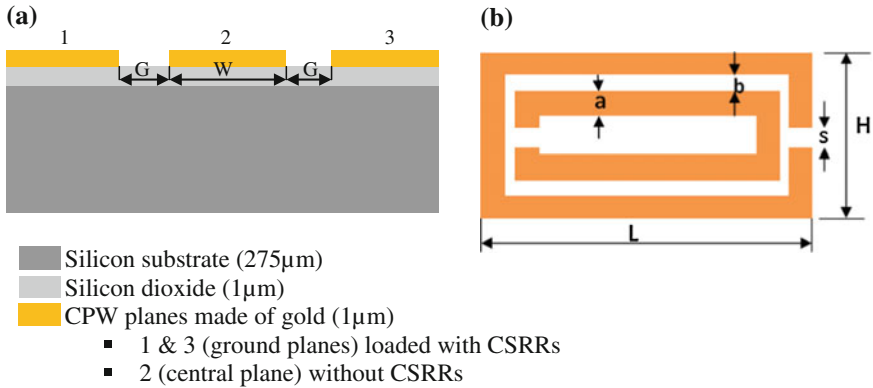


Fig. 1 a Side view of the proposed band-stop filter. b A unit cell of CSRRs along with its parameters

the ground planes. The CPW structure made of gold with a configuration of 30/150/30 µm is put on an oxidized high resistivity silicon substrate with a dielectric constant $\epsilon_r = 11.9$. CSRRs behave as a resonant tank electrically coupled to the host line that can be driven by a time varying electric field. By etching these elements in the ground planes of the CPW lines, the resonators can be excited. For a particular unit cell, the length of the CSRR, the width of the CSRR, the width of the rings, the spacing between the rings and the split of the rings have been denoted as L , H , a , b , and s , respectively. The length of CSRR (L) depends on the unit cell length (p) for a particular centre frequency and is given by

$$p = \lambda_g / 4 \tag{1}$$

where λ_g is the guided wavelength and is given by

$$\lambda_g = \lambda_0 / \sqrt{\epsilon_{eff}} \tag{2}$$

and ϵ_{eff} is the effective permittivity [16].

The dimensions of a unit cell of CSRRs have been defined as follows: $L = 490 \mu\text{m}$, $H = 330 \mu\text{m}$, $a = b = s = 30 \mu\text{m}$.

The fabrication is done on high resistive (5–10 kΩ-cm) silicon substrate of 275 µm thickness. Initially, using pyrogenic oxidation process, 1 µ thick oxidized layer is prepared on silicon wafer which is to be used as mask layer. To give better adhesion with silicon substrate, gold-chrome stag is used just above the silicon layer. The CSRRs have been performed by etching the ground planes of the gold layer. The required pattern is generated using the prepared mask of CPW with SRR structure through photo lithography process. Then the remaining portion is developed and etched out using gold-chrome etchant and finally, the PPR (positive photoresist) layer is removed using acetone. Figure 2 shows the fabricated device with CSRRs on the ground planes.

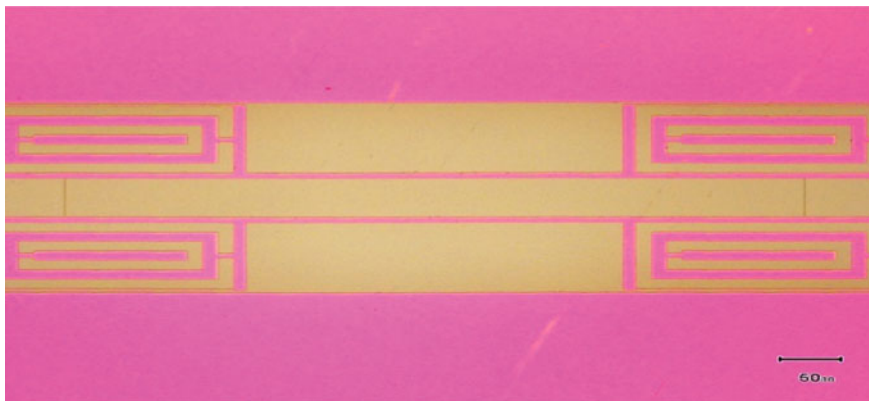


Fig. 2 Fabricated image of the band-stop filter with four identical unit cells with dimensions $a = b = s = 30 \mu\text{m}$, $L = 490 \mu\text{m}$ and $H = 330 \mu\text{m}$

Simulation Results and Discussions

The simulation of the proposed band-stop filter design is carried out using ANSOFT HFSS [17]. The filter gives a band rejection performance at a resonant frequency of 24.5 GHz with an insertion loss of -33.15 dB and a bandwidth of 11.14 GHz. The simulated S-parameters for different values of ‘ a ’ are shown in Figs. 3 and 4. The high suppression level can be accounted due to the use of four unit cells in the ground planes. The transmission depicts band-stop behaviour near the electric resonance frequency. The stop-band is wide because the negative permittivity occurs in a wide bandwidth. The return loss level at the resonant frequency is -1.05 dB . Figure 5 shows the shift in resonant frequencies and the rejection levels

Fig. 3 Simulated S_{11} for three different values of width of the rings a with $L = 490 \mu\text{m}$

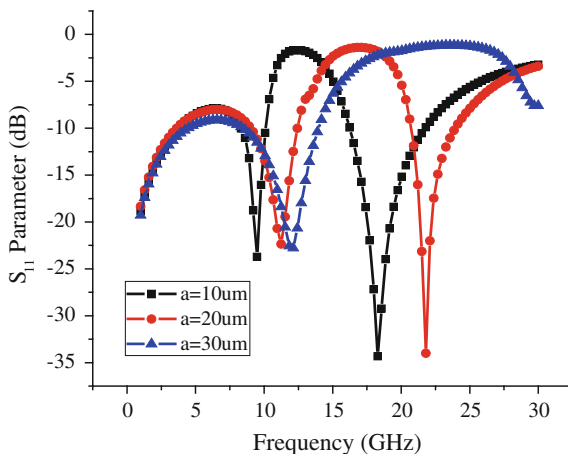


Fig. 4 Simulated S_{21} for three different values of width of the rings a with $L = 490 \mu\text{m}$

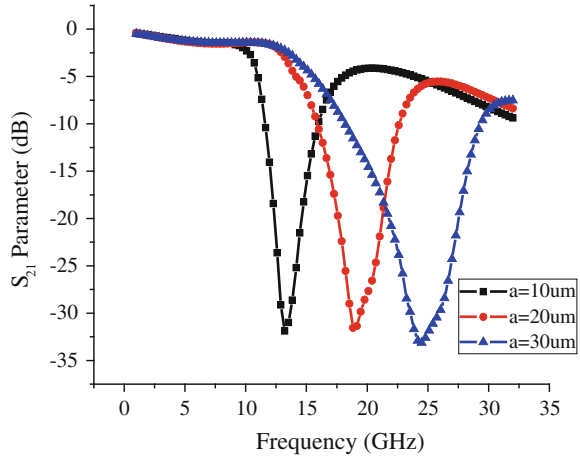
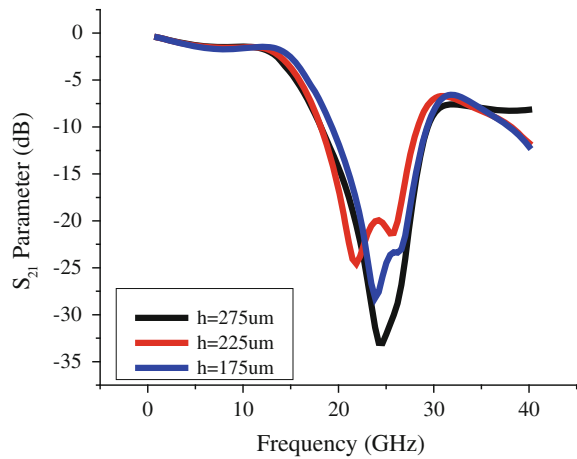


Fig. 5 Simulated S_{21} for three different heights (h) of silicon substrate



when the height (h) of the silicon substrate is varied. Accordingly, $275 \mu\text{m}$ shows the best performance, hence it has been chosen for design and fabrication.

Conclusion

We have successfully reported the design, simulation and fabrication of a metamaterial-based band-stop filter operating in K-band with a resonant frequency of 24.5 GHz with a rejection level of -33.15 dB . It is seen that the band-stop filter designed can be mechanically tuned by altering the dimensions of CSRRs coupled to the CPW and required resonant frequency can be obtained. Work is in progress to carry out the characterization of the device.

Acknowledgements We would like to thank the Almighty God for His blessings and our parents for their unconditional support and motivating us in all our endeavours. We would also like to acknowledge Jadavpur University for supporting us with the HFSS software.

References

1. Veselago, V.G.: The electrodynamics substances with simultaneously negative values of ϵ and μ . *Sov. Phys.Usp* **10**, 509–514 (1968)
2. Caloz, C., Itoh, T.: *Electromagnetic Metamaterials*. Wiley, Hoboken
3. Pendry, J.B., Holden, A.J., Robbins, D.J., Stewart, W.J.: Magnetism from conductors and enhanced nonlinear phenomena. *IEEE Trans. Microwave Theory Tech.* **47**, 2075 (1999)
4. Falcone, F., Lopetegi, T., Baena, J.D., Marqués, R., Martín, F., Sorolla, M.: Effective negative ϵ stopband microstrip line based on complementary split ring resonators. *IEEE Microwave Wirel. Compon. Lett.* **14**, 280–282 (2004)
5. Joannopoulos, J.D., Meade, R.D., Winn, J.N.: *Photonic Crystals: Modeling the Flow of Light*. Princeton University Press, Princeton (1995)
6. Radistic, V., Qian, Y., Coccioli, R., Itoh, T.: Novel 2-D photonic bandgap structure for microstrip lines. *IEEE Microwave Guided Wave Lett.* **6**, 69–71 (1998)
7. Laso, M.A.G., Lopetegi, T., Erro, M.J., Benito, D., Garde, M.J., Sorolla, M.: Multiple-frequency tuned photonic bandgap microstrip structure. *IEEE Microwave Guided Wave Lett.* **10**, 220–222 (2000)
8. Simons, R.N.: *Coplanar Waveguide Circuits, Components and Systems*. Wiley-IEEE Press, Hoboken (2001)
9. Martín, F., Falcone, F., Bonache, J., Marqués, R., Sorolla, M.: Miniaturized coplanar waveguide stop band filters based on multiple tuned split ring resonator. *IEEE Microwave Wirel. Compon. Lett.* **13**(12), 511–514
10. Al-Naib, I.A.I., Koch, M.: Coplanar waveguides incorporating SRRs or CSRRs. *Prog. Electromagn. Res. B* **23**, 343–355 (2010)
11. Tseng, C.-H., Itoh, T.: Dual-band Bandpass and Band-Stop Filters Using Composite Right/Left-Handed Metamaterial Transmission Lines, 0-7803-9542-5/06. IEEE (2006)
12. Lee, C.-J., Kevin, M.K., Leong, H., Itoh, T.: Metamaterials Transmission Line Based Band Stop and Bandpass Filter Designs Using Broadband Phase Cancellation, 0-7803-9542-5/06. IEEE (2006)
13. Tong, W., Hu, Z.R.: Compact Left-Handed Dual Mode Notch Band Stop Filter, 0-7803-9542-5/06. IEEE (2006)
14. Das, S., Kundu, A., Maity, S., Dhar, S., Gupta, B.: Novel Compact Filter for MICs Using Metamaterial Structures. IEEE
15. García-García, J., Martín, F., Falcone, F., Bonache, J., Baena, J.D., Amat, I., Lopetegi, T., Laso, M.A.G., Iturmedi, J.A.M., Sorolla, M., Marqués, R.: Microwave filters with improved stop band based on sub-wavelength resonators. *IEEE Trans. Microwave Theory Technol.* **53**, 1997–2004 (2005)
16. Erdemli, Y.E., Sondas, A.: Dual-polarized frequency-tunable composite left-handed slab. *J. Electromagn. Waves Appl.* **19**, 1907–1918 (2005)
17. <http://www.ansoft.com/products/hfss/>

Low-Cost Crash Protection System for Heavy Motor Vehicles

Vishwajit Nandi, Rijita Poddar, Rajesh Saha and Sahadev Roy

Abstract This paper proposes the use of an ultrasonic sensor module which is used to calculate the ground clearance of a Heavy Motor Vehicle (HMV). The sensor calculates distance based on the estimation of the travelling time of an ultrasonic pulse, transmitted by an ultrasonic sensor, which gets reflected back from the ground. This low cost sensors seems ideal to be housed underneath HMVs running in hilly areas with narrow roads, which has the risk of falling off the cliffs in sharp turns; the sensors will be placed such that whenever the vehicle's rear wheel senses a height more than that of the wheel by a considerable amount, the vehicle will move away from the cliff and the automatic braking system will be activated. The system may be used similarly in Dumper HMVs that needs to fill large shallow holes with mud, sand etc.; the sensor will be place differently in such condition.

Keywords Ultrasonic sensor · Crash protection · Heavy motor vehicles · Micro-controllers · Speed of sound · Time of flight

Vishwajit Nandi (✉) · Rajesh Saha
Electronic Design & Manufacturing, National Institute of Technology,
Yupia, Arunachal Pradesh 791112, India
e-mail: vishwajitnandi@live.in

Rajesh Saha
e-mail: rajeshsaha29@gmail.com

Rijita Poddar
Mobile Communication & Computing, National Institute of Technology,
Yupia, Arunachal Pradesh 791112, India
e-mail: rijitapoddar@live.com

Sahadev Roy
Department of ECE, National Institute of Technology,
Yupia, Arunachal Pradesh 791112, India
e-mail: sdr.ece@nitap.in

Introduction

The design of smart vehicles requires new sensors technology which are able to measure ground clearance in the range of 0.2 cm to 2 m approximately. Parking aids, headlight levelling, intelligent suspensions etc. are some applications that require distance measurement which is done using isolated sensors attached to the HMV body. Several techniques can be employed to measure the ground clearance [1, 2], but cost restricts the choice of an appropriate sensor.

There have been numerous records of accidents associated to HMTVs driven in narrow hilly roads, involving personal injury and damage to property. Even a co-pilot cannot guide the driver so as to guide the driver to eliminate the blind spot. Thus, various gadgets has been developed to improve vision to the blind spots by short range target detection and distance measurement. These devices may be categorized as follows:

- i. Optical systems (image, IR, video or laser devices)
- ii. Conductivity measurement systems, and
- iii. Ultrasound systems.

In the ISO Technical Report 150/TR 12155 published by the International Organization for Standardization [3], ultrasonic sensors has been mentioned as the preferred technology for the purpose. Several ultrasonic systems has been developed with the basic underlying technology of ultrasonic signal trans-receiver. This technology has been proven to be suitable for any weather or visibility condition. Several research work has been undergone and numerous obstacle detection and avoidance systems has already been developed using ultrasonic trans-receiver systems [4–10].

Operating Principle

The distance of selected point on the vehicle body from the ground is computed using the ultrasonic sensor module as per the formula mentioned below:

$$D = k \times T_f \times V_s \quad (1)$$

where

k a constant close to 0.5 (depends on the geometry of the sensor);

T_f travelling time of the pulse;

V_s speed of sound in air (approx. 346 m s^{-1} at $25 \text{ }^\circ\text{C}$).

The pulse stream from ultrasonic sensor, which is generated by a piezoelectric transducer (the transmitter), is reflected back from the surface which is also received by a different piezoelectric transducer (the receiver). Both the transmitter and receiver transducer are placed close to each other to compensate the measuring head [11, 12].

The uncertainty $u(D)$ in the calculated distance is given from Eq. (1) as follows [3, 13]:

$$u(D) = \sqrt{(k \cdot T_f)^2 \cdot u^2(V_s) + (k \cdot V_s)^2 \cdot u^2(T_f)} \tag{2}$$

where $u(V_s)$ and $u(T_f)$ are considered as uncertainties of the speed and travelling time of the ultrasonic wave.

But the speed of the ultrasound wave in air also varies with absolute temperature, T , which is also dependent on humidity, h , and hence we can rewrite Eq. (2) as

$$u(D) = \sqrt{(k \times T_f)^2 \times \left\{ \left(\frac{\partial f}{\partial T} \right)^2 \times u^2(T) + \left(\frac{\partial f}{\partial h} \right)^2 \times u^2(h) \right\} + (k \times V_s)^2 \times u^2(T_f)} \tag{3}$$

Many techniques have been put to trial to solve this sub-wavelength uncertainties [4–9], but most of the proposed solutions are based on some sort of digital signal processing, and consequently raising the cost.

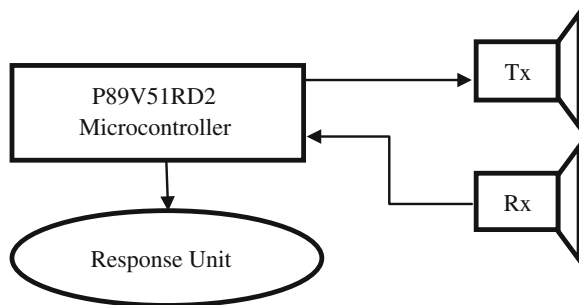
After the proper measurement of the distance of appropriately selected point of the vehicle from the ground, it is compared with a pre-defined threshold beyond which the distance from the ground may be considered to be unsafe; and when such a distance is computed, a fail-safe mechanism is triggered in order to prevent the HMV from a possible accident.

System Design

Figure 1 shows the proposed representation of the system. The proposed design consist of 2 units:

- (a) Height Measurement Unit
- (b) Response Unit

Fig. 1 A simple block diagram of the system



(a) *Height Measurement Unit*

The Ultrasonic Sensor module is connected to a NXP’s P89V51RD2 family microcontroller. The microcontroller controls the transmission of the ultrasonic wave and measures its time of flight. The “sensor transmitter” transmits a 40 kHz frequency ultrasonic sound wave which reflects from the obstacle. The “sensor receiver” keep listening until it receives the reflected ultrasound. The duration for which the receiver is listening is interpreted by the microcontroller unit. Subsequently, the microcontroller converts the time taken to receive the ultrasound and measures the height from the ground as per Eq. (1). If this unit detects a shallow hole or may be a cliff in front of the rear wheel, it alerts the Response unit immediately, so that the possible crash/accident may be avoided.

(b) *Response Unit*

Anti-lock Braking System (ABS) of the vehicle as well as the Power Steering System (PSS). Whenever the Height Measurement Unit sends an alert to the Response Unit, the ABS is activated and makes the vehicle stop without drifting; and the PSS make the vehicle move away from the hole or the cliff. Figures 2 and 3 shows the arrangement of the sensor in different HMVs.

Fig. 2 Sensor arrangement on a public carrier truck

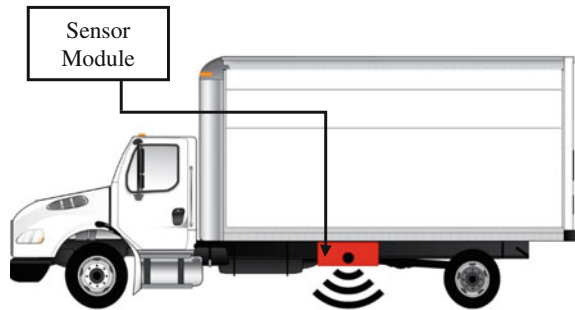
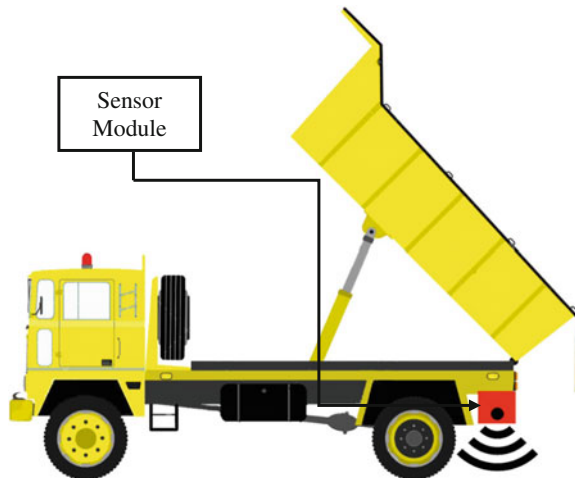


Fig. 3 Sensor arrangement on a dumper truck



Algorithm

Figure 4 shows the flowchart of the proposed design. The complete procedure of edge detection and protection can be described in the following steps.

- Step 1: Start
- Step 2: Initialize the controller
- Step 3: Trigger ultrasonic transmitter
- Step 4: Transmit ultrasonic signal pulses
- Step 5: Listen for echo
- Step 6: Calculate the travelling time of the pulse
- Step 7: Calculate distance of obstacle
- Step 8: Turn ON/OFF the Response Unit accordingly
- Step 9: Repeat Step 3

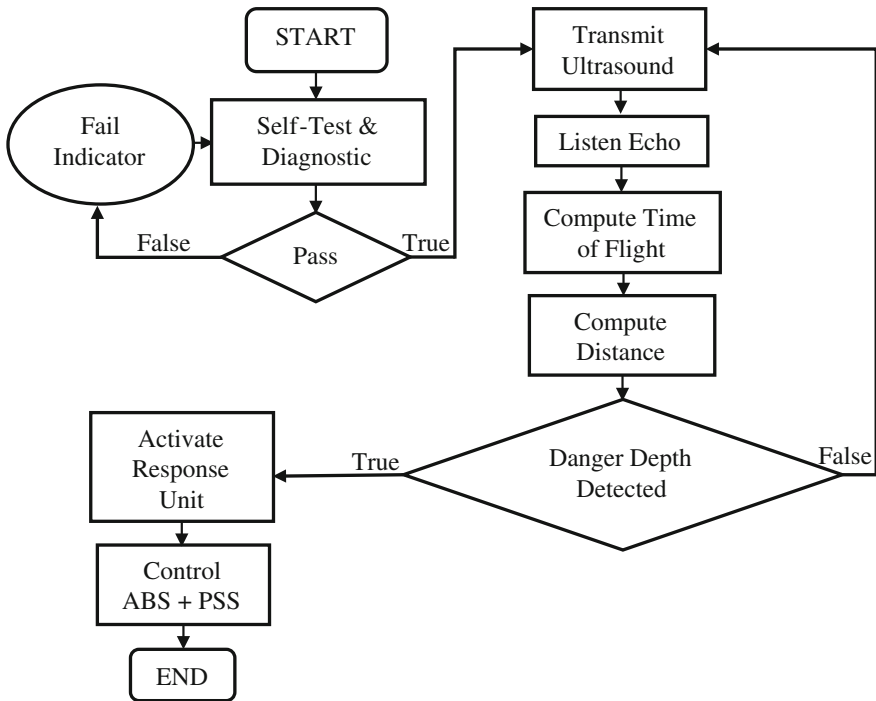


Fig. 4 Flow chart of the crash protection system

Conclusion

A simple, cheap crash protection system is proposed to provide protection against accidents due to limitations of a HMV driver to keep an eye on all the wheels of the vehicle.

The algorithm of the system depends heavily on the performance of the ultrasonic sensors under different weather condition. Future works may be focused on the effect of the limitation of the sensor on the Crash Protection Algorithm.

Acknowledgments This work has been carried out under the Research and Development Cell of National Institute of Technology, Arunachal Pradesh and the authors would like to express their utmost gratitude for the same.

References

1. Sensors for Displacement, Distance and Position: Micro-Epsilon Measurement. <http://www.micro-epsilon.com/displacement-position-sensors/index.html>. Accessed 10 Sept 2014
2. Distance Measuring Sensors: Sharp Devices Europe. <http://www.sharpsde.com/optoelectronics/sensors/distance-measuring-sensors>. Accessed 14 Oct 2014
3. ENV 13 005: Guide to the expression of uncertainty in measurement (1999)
4. Parrilla, M., Anaya, J.J., Fritsch, C.: Digital signal processing techniques for high accuracy ultrasonic range measurements. *IEEE Trans. Instrum. Meas.* **40**, 759–763 (1991)
5. Marioli, D., Narduzzi, C., Offelli, C., Petri, D., Sardini, E., Taroni, A.: Digital time-of-flight measurement for ultrasonic sensors. *IEEE Trans. Instrum. Meas.* **41**, 93–97 (1992)
6. Cai, C., Regtien, P.L.: Accurate digital time-of-flight measurement using self-interference. *IEEE Trans. Instrum. Meas.* **42**, 990–994 (1993)
7. Gueuning, F., Varlan, M., Eugène, C., Dupuis, P.: Accurate distance measurement by an autonomous ultrasonic system combining time-of-flight and phase-shift methods. In: *Proceedings of IMTC, Brussels, Belgium*, vol. 1, pp. 399–404 (1996)
8. Andria, G., Attivissimo, F., Lanzolla, A.: Digital measuring techniques for high accuracy ultrasonic sensor application. In: *Proceedings of IMTC, St. Paul, MN*, vol. 2, pp. 1056–1061 (1998)
9. Carullo, A., Ferraris, F., Graziani, S., Grimaldi, U., Parvis, M.: Ultrasonic distance sensor improvement using a two-level neural network. *IEEE Trans. Instrum. Meas.* **45**, 677–682 (1996)
10. Hanumante, Vivek, Roy, Sahadev, Maity, Santanu: Low cost obstacle avoidance robot. *Int. J. Soft Comput. Eng. (IJSCE)* **3**(4), 52–55 (2013)
11. Borenstein, J., Koren, Y.: Obstacle avoidance with ultrasonic sensors. *IEEE J. Robot. Autom.* **4**(2) 1988
12. Shrivastava, A.K., Verma, A., Singh, S.P.: Distance measurement of an object or obstacle by ultrasound sensors using P89C51RD2. *Int. J. Comput. Theory Eng.* **2**(1) (2010)
13. Carullo, A., Parvis, M.: An ultrasonic sensor for distance measurement in automotive applications. *IEEE Sensors J.* **1**(2) (2001)

Effect of Parasitic Elements on Non-inverting Buck-Boost Converter Used in PV System

Subramanya Bhat and H.N. Nagaraja

Abstract In the proposed study, MOSFET device used in non-inverting buck-boost converter for photovoltaic (PV) system is analyzed. The parameters $R_{ds(on)}$ are varied and the output of buck-boost converter is observed. The inductor and capacitor are used as filter elements in the converter. The parasitic resistance of these filter elements are varied and the performance of the converter is analyzed. From the study, the variation of parasitic element of capacitor will not much disturb the output voltage, whereas the variation of parasitic element of inductor will disturb the output voltage and has significant contribution on the output voltage of converter. Also, the proposed study gives better insight into parasitic effect of printed circuit board and losses incurred due to the same. In PV systems buck-boost converter is used to convert solar energy to electrical energy which is then stored in battery to drive the loads. These parasitic elements will have considerable effect on the performance of converter used in solar power system.

Keywords Reliable • Parasitic element • Antiparallel diode • Deep cycle discharge

Introduction

The conventional energy sources are decreasing at an exponential rate and therefore power generation from nonconventional energy sources is gaining importance. The solar energy is one of the promising nonconventional energy sources. For efficient conversion of solar energy to electrical energy, a reliable buck-boost converter is required. In the proposed study, a non-inverting buck-boost converter is used.

Subramanya Bhat (✉)

Department of Electronics and Communication Engineering,
Canara Engineering College, Mangalore 574 219, India
e-mail: sbhat22@yahoo.com

H.N. Nagaraja

Indus Institute of Technology and Engineering, Gujarat, India
e-mail: nagraj_hp@yahoo.com

© Springer India 2016

N. Afzalpulkar et al. (eds.), *Proceedings of the International Conference on Recent Cognizance in Wireless Communication & Image Processing*,
DOI 10.1007/978-81-322-2638-3_41

359

In non-inverting converter, two switches, two diodes, and filter elements are used. In switches and filter elements, there will be parasitic elements which have significant contribution on the output voltage. In the proposed study, the variation of parasitic elements on the performance of the converter is analyzed. The filter elements will have significant contribution on the output voltage and have been discussed in [1]. Bhat and Nagaraja [1] discussed the variation of filter elements on the output voltage of converter. However, the variation of parasitic elements on the performance of converter is not discussed. Mohan et al. [2] discussed the variation of parasitic elements on the performance of DC-DC converters in general. The parasitic element of inductor is considered but the parasitic element of MOSFET such as on state resistance $R_{ds(on)}$ is not considered. The parasitic element of capacitor is also not taken into account. Mohammad et al. [3] discussed on parasitic effects on the performance of DC-DC single ended primary inductor converter (SEPIC) for PV systems. The PV system's performance is decreased due to parasitic elements. In this study [3], the switch parasitic elements are not considered. Ramanarayan [4] discussed the variation of parasitic elements on the performance of DC-DC converters and while analyzing the performance, in addition to parasitic elements, the source resistance is also considered. Erickson and Maksimovic [5] analyzed the converter behavior at low frequencies. The effect of parasitic element in MOSFET is described in section "Effect of Parasitic Element in MOSFET." The effect of printed circuit board parasitic is discussed in section "Effect of Printed Circuit Board (PCB) Parasitics." The effect of parasitic element in inductor is given in section "Effect of Parasitic Element of Inductor." The effect of parasitic element in capacitor is presented in section "Effect of Parasitic Element of Capacitor."

Effect of Parasitic Element in MOSFET

In the proposed study, the MOSFET model from MATLAB SIMULINK has been considered. The MOSFET switching symbol and its circuit representation is given in Fig. 1. The antiparallel internal diode in MOSFET will give protection against overvoltage. The model is made using an ideal switch and it is turned ON or OFF using a gate signal g . The diode is connected in antiparallel with the switch.

The ON state voltage of MOSFET V_{ds} will vary according to following aspects [6, 7]:

- When MOSFET is turned ON $V_{ds} = R_{ds(on)} * I$, where I is the current flowing through the device.
- When the device is turned OFF, antiparallel diode starts conducting then,

$V_{ds} = R_d * I - V_f + L_{on} * di/dt$, where V_f is the internal diode's forward voltage drop.

The L_{on} is the antiparallel diode inductance and R_d is the diode resistance. The R_{on} is MOSFET on state resistance. The design specification of buck-boost converter is taken as follows:

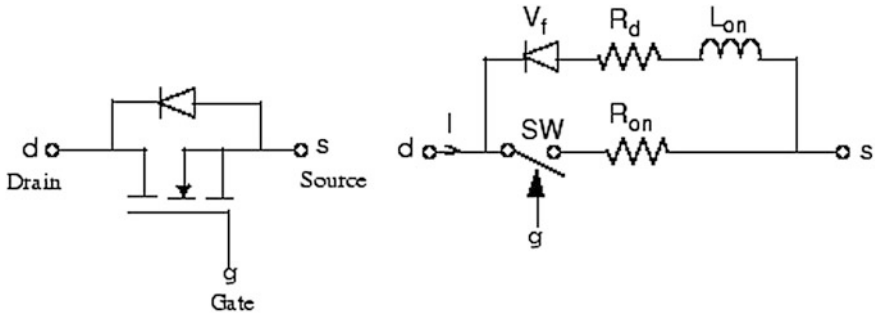


Fig. 1 MOSFET switch and internal circuit diagram

- Input voltage = 5–20 V
- Output voltage = 12 V
- Switching frequency = 50 kHz
- Wattage rating = 25 W
- Inductor ripple current (ΔI_L) = 3 % of I_L output.

Voltage Ripple (ΔV_{out}) = $0.01 * V_{out} = 0.12$ V. The buck-boost converter is designed and the values obtained are inductor $L = 1.5$ mH and capacitor $C = 220$ μ F.

The non-inverting buck-boost converter is simulated with these values and the expected results are achieved. The simulation diagram of non-inverting buck-boost converter is shown in Fig. 2. The parasitic resistance $R_{ds(on)}$ plays a role when the switch is closed. The effect MOSFET parasitic resistance $R_{ds(on)}$ on output voltage is observed and it is shown in Fig. 3. $R_{ds(on)}$ computes power loss and efficiency in a circuit containing a MOSFET switch. The power dissipated in the MOSFET is given by the product of $R_{ds(on)}$ and drain current. In Fig. 3, different series represent different $R_{ds(on)}$ values. The different series and the corresponding $R_{ds(on)}$ values are given in Table 1. The variation of $R_{ds(on)}$ on buck-boost converter output voltage is given in Table 1.

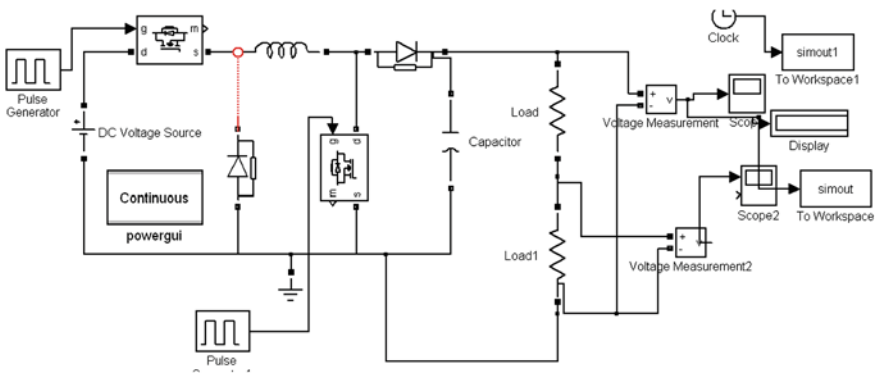


Fig. 2 Non-inverting buck-boost converter simulation diagram

Fig. 3 Effect of $R_{ds}(On)$ on output voltage

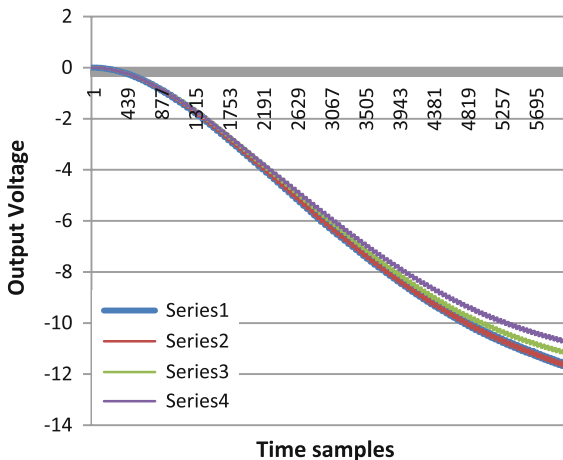


Table 1 Effect of $R_{ds}(On)$ on output voltage

$R_{ds}(on)$	Output voltage (V)
$R_{ds} = 0 \Omega$ (series 1)	11.95
$R_{ds} = 0.001 \Omega$ (series 2)	11.85
$R_{ds} = 0.05 \Omega$ (series 3)	11.27
$R_{ds} = 0.08 \Omega$ (series 4)	10.92

Effect of Printed Circuit Board (PCB) Parasitics

The inductances and capacitances of printed circuit board on which the converter circuit is rigged up will affect the performance of non-inverting buck-boost converter. The effect of these parasitics therefore must be considered to improve efficiency and regulation of the converter. The power loss due to trace,

P_{trace} is given by

$$P_{trace} = I_{trace}^2 R_{trace} \tag{1}$$

Power loss due to inductance of PCB is called as $P_{L_{stray}}$ and is given by [8]

$$P_{L_{stray}} = I_{trace} L_{stray} \left(\frac{di}{dt} \right) \tag{2}$$

where L_{stray} is calculated from

$$L_{stray} = 2 \times 10^{-4} Le \left[\ln \left(\frac{2Le}{W+H} \right) + 0.2 \left(\frac{w+H}{Le} \right) + 0.5 \right] \tag{3}$$

The capacitance of PCB is calculated as $C_{stray} = 0.085 \epsilon r A / d$ (4)

The power loss due to capacitance of PCB, P_{cstray} is given by

$$P_{cstray} = \frac{V_d^2 C_{stray} f_{sw}}{2} \tag{5}$$

$$\text{The total loss in PCB is given by } P_{PCB} = P_{trace} + P_{Lstray} + P_{cstray} \tag{6}$$

where L_e is length of PCB trace, H is height of PCB trace, W is width of PCB trace; ϵ_r is dielectric constant of air, A is the area of plates, and d is separation between the plates.

Effect of Parasitic Element of Inductor

The effect of variation in inductor parasitic resistance on output voltage is shown in Fig. 4. The results are tabulated in Table 2.

From Fig. 4, we can conclude that the voltage gain of the converter is inversely proportional to the inductor parasitic. In order to achieve good gain, the inductor parasitic should be less. The efficiency of an ideal buck-boost converter is one. When the parasitics are taken into account there will be degradation of efficiency [9, 10] and is given by

Fig. 4 Effect of parasitic resistance variation of inductor

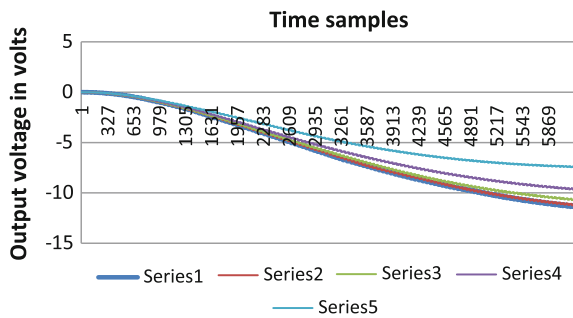


Table 2 Effect of parasitic resistance variation of inductor

Parasitic resistance of inductor value	Output voltage (V)
Ideal inductor $R_L = 0$ (series 1)	12.03
$R/R_L = 100$ ($R_L = 0.03215 \Omega$, series 2)	11.68
$R/R_L = 80$ ($R_L = 0.047 \Omega$, series 3)	11.29
$R/R_L = 40$ ($R_L = 0.093 \Omega$, series 4)	10.7
$R/R_L = 8$ ($R_L = 0.467 \Omega$, series 5)	7.2

$$\eta = \left[1 - \frac{V_{sn}}{V_g} - \frac{V_{sf}(1-d)}{dV_g} \right] \left[\frac{1}{1 + \frac{\alpha + \beta d}{(1-d)^2}} \right] \tag{7}$$

where V_{sn} is the ON state switch voltage drop and V_{sf} OFF state switch voltage drop, d is the duty ratio and V_g is the source voltage $\alpha = R_L/R$ $\beta = R_g/R$.

Effect of Parasitic Element of Capacitor

The parasitic resistance in a capacitor used in buck-boost converter is varied and its effect on the performance of buck-boost converter is seen and this is as shown in Fig. 5. The output voltage values are tabulated in Table 3. It has been found that the parasitic resistance in capacitor has no significant effect on the output voltage. Higher the value of parasitic resistance, lesser will be the output voltage.

Fig. 5 Effect of parasitic resistance variation of capacitor

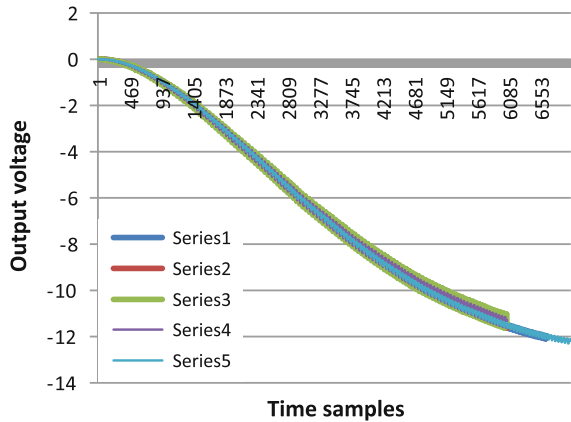


Table 3 Effect of parasitic resistance variation of capacitor

Parasitic resistance value	Output voltage (V)
$R = 0$ (series 1)	12
$R = 0.001 \Omega$ (series 2)	11.95
$R = 0.01 \Omega$ (series 3)	12.13
$R = 0.05 \Omega$ (series 4)	11.79
$R = 0.07 \Omega$ (series 5)	11.5

Conclusion

From the proposed study, it has been found that the effect of capacitor parasitic is less as compared to other parasitic and hence the significance of this parasitic is less and can be neglected. In the proposed study, the effect of parasitic elements in MOSFET gate to drain capacitance, C_{gs} and gate to source capacitance, C_{gd} are not considered. These capacitances effect on the performance of converter can be considered as a future study. The proposed method also highlighted the significance of PCB parasitic losses. In the proposed study, the parasitics of solar panel are not considered and can be considered as a future work. The parasitic elements studied in the proposed study even affect the deep cycle discharge batteries used in PV systems.

References

1. Bhat, S., Nagaraja, H.N.: Effect of filter elements on the performance of buck converter. In: IEEE International Conference on Advances in Energy Conversion Technologies (ICAECT), pp. 169–173, Manipal, India, Jan 2014
2. Mohan, N., Undeland, T.M., Robbins, W.P.: Power Electronics: Converters, Applications, and Design. Wiley, New York (1995)
3. Mohammad, N., et al.: Parasitic effects on the performance of DC-DC SEPIC in photovoltaic maximum power point tracking applications. *Int. J. Smart Grid Renew. Energy* 113–121 (2013)
4. Ramanarayan, V.: Lecture notes on switched mode power conversion. IISC, Dec 2007
5. Erickson, R.W., Maksimovic, D.: Fundamentals of Power Electronics. Kluwer Academic Publishers (2000)
6. AN11158: Understanding Power MOSFET Data Sheet Parameters NXP Semiconductors. REV, 4 Feb 2014
7. Rashid, M.H.: Power Electronics: Circuits, Devices and Applications, 3rd edn. Prentice Hall (2003)
8. Spiazzi, et al.: Analysis of MPPT algorithms for photovoltaic panels based on ripple correlation techniques in presence of parasitic components. In: IEEE Power Electronics Conference, Brazil (2009)
9. Maniktala, S.: Switching Power Supplies A to Z. Elsevier, London (2003)
10. Gupta, A., et al.: Increasing efficiency of the photovoltaic system of mobile robotic platforms for military application and exploration. In: IEEE International conference on Power Electronics (2011)

Effective Medium Approximation for Defining the Unavoidable Resistance of Solar Cell Front Contact

S. Maity, P. Chakraborty, R. Raushan, C.T. Bhunia and P.P. Sahu

Abstract Contact resistance and series resistance are the most crucial problem to collect carrier from the both electrodes. In general, contacts are made by screen printing process which is industrially established. After the screen printing process some factors arises like change of width and thickness of finger and pores are created on the top side due to solvent. For the unavoidable pores series resistance is decreased. In this paper, the mathematical modeling has done considering resistance and distribution of pores.

Keywords Front contact · Series resistance · Generalized effective medium approximation · Screen printing technology · Void fraction of finger · Light induced plating

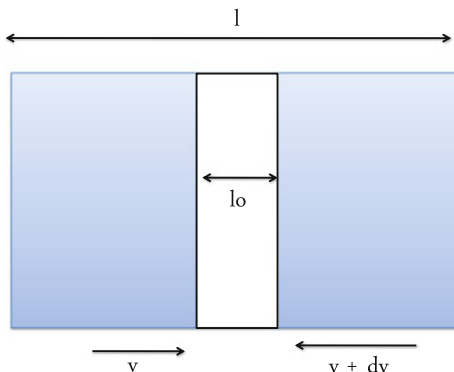
Introduction

Screen printing is one of the most industrial processes for making front contact. At the time of screen printing process two steps are crucial printing one is paste use (height and width depending on this), and other firing (electrical performance depends on firing step). Solar cells internal series resistance and which is related to different phenomena affects on external quantum efficiency as well as power conversion efficiency (PCE). Several methods are considered to define the effective series resistance and related device parameters of solar cells [1–13] which reduces the solar cell efficiency. One of the effective series resistance is arises due to contact elements like fingers and bus bars. From the several decades Silver (Ag) screen printing has been the dominant technology for front-side metallization of silicon

S. Maity (✉) · P. Chakraborty · R. Raushan · C.T. Bhunia
Electronics and Communication Engineering, National Institute of Technology, Yupia,
Arunachal Pradesh 791112, India
e-mail: santanu.ece@nitap.in

P.P. Sahu
Electronics and Communication Engineering, Tezpur University, Assam 784028, India

Fig. 1 Finger with single void



(Si) solar cells. Also different technology arises for the contacts like next generation selective-emitter technologies for laser-doping and self-aligning technology for laser-doping [14–17]. Self-aligning technology for laser-doping reduces the wafer to cell manufacturing. Light-induced electroplating of silver (Ag) metal on top of the front contact grid has shown promise in reducing line resistance and increasing cell power output [18–20].

In this paper, first mathematical modeling of front-side contact (like finger and bus bar) is done and by using generalized effective medium approximation (GEMA) and the model is drawn for distributed voids present over the fingers and busbar. And for the reduction of voids light-induced plating (LIP) experiment is done by using different experimental condition.

Modeling of Finger Parameter

Considering l is the length finger and l_o is the length of void, present in the finger (shown Fig. 1).

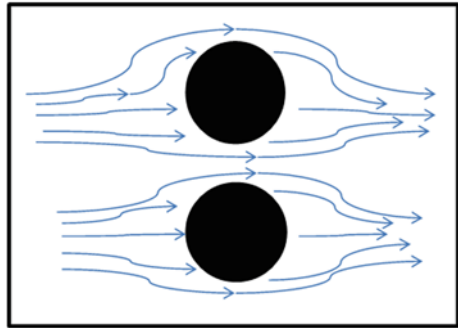
Electric field $E = \frac{v}{l}$ here v is total potential. When l_o is introduced the electric field expression can be define as $E = \frac{v_o}{l-l_o}$, as we know that $J = \sigma E$ and, $I = \sigma A \cdot E = \sigma A \cdot \frac{v_o}{l-l_o}$ from this it is obtained that $dv_o = \frac{l-l_o}{A} * \frac{I}{\sigma}$.

Again by considering the voids are spherical or any arbitrary shape and they are distributed haphazardly (shown Fig. 2) on the contact then it can be modeled by GEMA approach where field lines are going toward the curvature and from the Eq. 4 which derived from GEMA theorem is following the basics of Ohm’s law.

$$V_{\text{air}} \frac{\sigma_{\text{air}} - \sigma_e}{\sigma_{\text{air}} - 2\sigma_e} + (1 - V_{\text{air}}) \frac{\sigma_{\text{metal}} - \sigma_e}{\sigma_{\text{metal}} - 2\sigma_e} = 0 \tag{1}$$

σ_{air} = Conductivity due to the air portion, σ_e = Effective conductivity, σ_{metal} = Conductivity due to the metal portion.

Fig. 2 Spherical voids are distributed in the finger



If $V_{\text{air}} = 0$ then $\sigma_e = \sigma_{\text{metal}}$.
 And also if $V_{\text{air}} = 1$ then $\sigma_e = \sigma_{\text{air}}$.
 If $\sigma_{\text{air}} \rightarrow 0$

$$-V_{\text{air}} \left(\frac{1}{2} \right) + (1 - V_{\text{air}}) \frac{\sigma_{\text{metal}} - \sigma_e}{\sigma_{\text{metal}} - 2\sigma_e} = 0 \tag{2}$$

$$\frac{\sigma_{\text{metal}} - \sigma_e}{\sigma_{\text{metal}} - 2\sigma_e} + \frac{1}{2} = V_{\text{air}} \left[\frac{\sigma_{\text{metal}} - \sigma_e}{\sigma_{\text{metal}} - 2\sigma_e} + \frac{1}{2} \right] \tag{3}$$

$$\sigma_{\text{metal}} - \sigma_e = V_{\text{air}} (3\sigma_{\text{metal}})$$

$$\sigma_e = \sigma_{\text{metal}} (1 - 3V_{\text{air}})$$

$$R = \rho \frac{l}{A} = \frac{1}{\sigma_{\text{metal}} (1 - 3V_{\text{air}})} \cdot \frac{l}{A} \tag{4}$$

$$R = \rho \frac{l}{A} = \frac{1}{\sigma_{\text{metal}} (1 - 3V_{\text{air}})} \cdot \frac{l}{A}$$

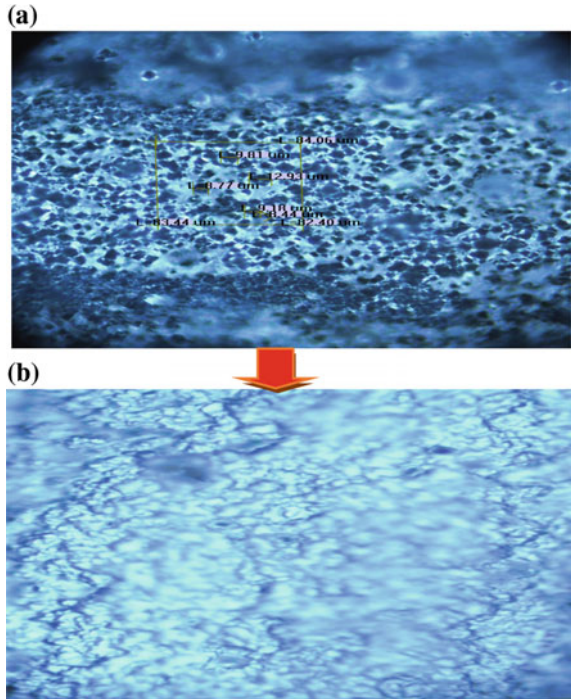
Experimental Verification

Solvent of silver paste used in screen printing process (SPP) evaporate making unwanted pores on the front-side contacts. Due to the increased pores series resistance increases therefore, the efficiency of the solar cell decreases (as shown in Fig. 3a). But after LIP process the pores get filled with silver particles as shown in Fig. 3b reducing the series resistance and increasing the solar cell efficiency.

Fig. 3 Microscopic view of solar cell contact.

a Microphotograph of finger before LIP (100X).

b Microphotograph of finger after LIP (100X)



LIP experiment is carried out using different light intensities and different concentration of electrolyte solutions. It is shows that the series resistance of front-side contact is decreasing with respect to time but it decreases rapidly for higher light intensity and higher concentration of solution as the optical shading occurs due higher deposition rate.

Conclusion

From mathematical modeling, it is seen that all models are follow Ohm's law. After that for experimental verification LIP experiment is done and it is seen that the series resistance is significantly reduced, which can rise of the fill factor of solar cells. In the LIP process, silver paste penetrates the deposited nitride layer to make contact with the n layer. Though solar cells with high fill factors benefit little from LIP, LIP is helpful in reducing the increasing contact resistance when narrowing the grids.

References

1. Wolf, M., Rauschenbach, H.: Series resistance effects on solar cells measurements. *Adv. Energy Convers.* **3**, 455–479 (1963)
2. Easwarakhanthan, T., Bottin, J., Bouhouch, I., Boutrif, C.: Nonlinear minimization algorithm for determining the solar cell parameters with microcomputers. *Int. J. Sol. Energy* **4**, 1–12 (1986)
3. Araujo, G.L., Sanchez, E.: A new method for experimental determination of the series resistance of a solar cell. *IEEE Trans. Electron. Dev.* **29**, 1511–1513 (1982)
4. Handy, R.J.: Theoretical analysis of the series resistance of a solar cell. *Solid-State Electron.* **10**, 765–775 (1967)
5. Rajakanan, K., Shewchun, J.: A better approach to the evaluation of the series resistance of solar cells. *Solid-State Electron.* **22**, 193–197 (1979)
6. Chegaar, M., Ouennouchi, Z., Hoffmann, A.: A new method for evaluating illuminated solar cell parameters. *Solid-State Electron.* **45**, 293–296 (2001)
7. Kaminski, A., Marchand, J.J., Laugier, A.: I-V methods to extract junction parameters with special emphasis on low series resistance. *Solid-State Electron.* **43**, 741–745 (1999)
8. Radziemska, E.: Dark I-U-T measurements of single crystalline silicon solar cells. *Energy Convers. Manage.* **46**, 1485–1494 (2005)
9. Jain, A., Kapoor, A.: A new approach to study organic solar cell using Lambert W-function. *Sol. Energy Mater. Sol. Cells* **86**, 197–205 (2005)
10. Murayama, M., Mori, T.: Equivalent circuit analysis of dye-sensitized solar cell by using one-diode model: effect of carboxylic acid treatment of TiO₂ electrode. *Jpn. J. Appl. Phys. Part 1* **45**, 542–545 (2006)
11. Ortiz-Conde, A., Garcia, F.J.: Sanchez, J. Muci, New methods to extract model parameters of solar cells from the explicit analytic solutions of their illuminated I-V characteristics. *Sol. Energy Mater. Sol. Cells* **90**, 352–361 (2006)
12. Ishibashi, K.I., Kimura, Y., Niwano, M.: An extensively valid and stable method for derivation of all parameters of a solar cell from a single current–voltage characteristics. *J. Appl. Phys.* **103**, 094507 (2008)
13. Chegaar, M., Nehaoua, N., Bouhemadou, A.: Organic and inorganic solar cells parameters evaluation from single I-V plot. *Energy Convers. Manage.* **49**, 1376–1379 (2008)
14. B.S. Tjahjono, et al., High efficiency solar cell structure through the use of laser doping. In: *Proceedings of the 22nd European Photovoltaic Solar Energy Conference*, 3–7 Sept 2007, Milan, Italy, pp. 966–969 (2007)
15. Mai, L., et al.: Rear junction laser doped solar cells on CZ n-type silicon. In: *Proceedings of the 34th IEEE Photovoltaic Specialists Conference*, 7–12 June 2009, Philadelphia, PA, pp. 1811–1815 (2009)
16. Sugianto, A., et al.: 18.5 % laser-doped solar cell on CZ p-type Silicon. In: *Proceedings of the 35th IEEE Photovoltaic Specialists Conference*, 20–25 June 2010, Honolulu, HI, pp. 689–694 (2010)
17. Kray, D., et al.: Industrial LCP selective emitter solar cells with plated contacts. In: *Proceedings of the 35th IEEE Photovoltaic Specialists Conference*, 20–25 June 2010, Honolulu, HI, pp. 667–671 (2010)
18. Mette, A., Schetter, C., Wissen, D., Lust, S., Glunz, S.W., Willeke, G.: Increasing the efficiency of screenprinted silicon solar cells by lightinduced silver plating. In: *Proceedings of IEEE 4th World Conference on Photovoltaic Energy Conversion*, Hawaii, USA (2006)
19. Glunz, S.W.: High-efficiency crystalline silicon solar cells. *Adv. OptoElectron.* (2007)
20. Jensen, J.D., Moller, P., Bruton, T., Mason, N., Russell, R., et al.: Electrochemical deposition of buried contacts in high-efficiency crystalline silicon photovoltaic cells. *J. Electrochem. Soc.* **150**, G49–G57 (2003)

A Novel Low-Power Design Approach to Exploit the Power Usage of AMBA APB Bridge

Kiran Rawat, Kanika Sahni, Sujata Pandey and Ziauddin Ahmad

Abstract In this paper, AMBA advanced peripheral bus bridge (APB Bridge) is implemented with a new design approach. The approach consists of a gated clock and reset controller circuits with APB Bridge for efficient optimization of power and for synchronizing the sequential circuits. Though clock net does not have any significant role in digital computation, it only provides synchronization to the sequential circuits, but unnecessary switching activities of clocks may cause a huge amount of power dissipation around 15–50 %. A proposed approach is to implement the effective gated clock circuit with negative latch to produce a gated clock as an output. This gated clock provides a selective control over clock net that means when a target's device clock functioning is required at that time controlling device's clock had been switched off. When the proposed approach is implemented in Verilog as APB Bridge with reset controller, clock power has been reduced to some level and provides power utilization in circuit. Simulation results are verified in ModelSim version 10.3c and then power report is extracted from Xilinx ISE suite 13.4 version. Result of the proposed approach: Total clock domain power of 0.39 mW, total hierarchy power of 0.49 mW, and total on chip power of 0.109 W are consumed by the proposed design. Hence total clock domain power consumption is 27.78 %, total hierarchy power consumption is 47.31 %, and total on chip power consumption is 6.84 % less than the bridge without clock gating and reset controller conditions. Simulation results and power summary reports are also included with the proposed design.

Kiran Rawat · Kanika Sahni · Sujata Pandey
Amity University, Noida, Uttar Pradesh, India
e-mail: kiran.5gemini@gmail.com

Kanika Sahni
e-mail: kanikasahni27@gmail.com

Sujata Pandey
e-mail: spandey@amity.edu

Ziauddin Ahmad (✉)
3ST Technologies Pvt. Ltd., Noida, Uttar Pradesh, India
e-mail: er.ziauddinahmad@gmail.com

Keywords VLSI · AMBA · SoC · APB · Clock gating · Low-power VLSI · FSM · Verilog

Introduction

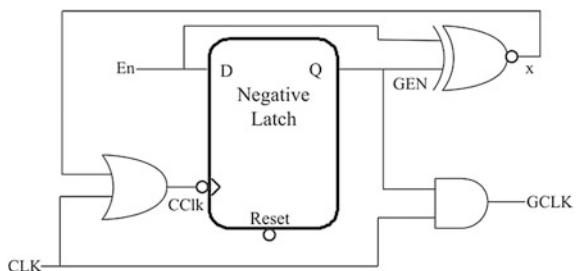
Nowadays, system on chips (SoCs) are shifting toward the nanometer ranges and the smaller feature sizes. These may cause for the introduction of higher design complexities in the new design approaches. The complexities also tend to power consumption of the implemented designs. So the main task of the design engineer is to achieve the correct utilization of the power of the SoC parts. Several low-power design techniques have been proposed for managing and optimizing the power of a device or SoC. One of the simplest method is to shut off the clock for some duration until sequential block functioning is again required by the device. Thus, clock gating is a technique in which dissipated power is being controlled and unwanted switching, which leads to sufficient part of power dissipation, reduces by just disabling the clock when it is not required. Gated clock is an efficient technique to optimize power and can be used at system, gate, or RTL levels. Clock consumes power because it toggles the registers. Clock gating shuts off the clock when there is no toggle in its state. One of the new approaches proposed for clock gating is to generate the gated clock when negative latch is used.

Effective Clock Gating Approach Using Negative Latch

One of the latest methods which generate the gated clock is using negative latch as a clock gated circuit. This approach has been proposed in the paper for designing of AMBA APB (advanced peripheral bridge). The proposed approach could have provided for minimal power consumption.

Firstly, proposed clock gating technique has been explained and then its implementation in AMBA APB Bridge has been explained. Figure 1 shows an effective clock gating approach using negative latch. A gated clock (GCLK) is

Fig. 1 GCLK generation using negative latch [3]



generated at the output. This proposed design can provide an efficient control over the clock by avoiding unnecessary switching at the clock net. When a target's device clock functioning is required at that time the controlling device's clock had been switched off. Hence, the purpose of clock gating is achieved for utilizing the clock only when it is required in the circuits.

To understand the working of proposed clock gating circuit (Fig. 1), consider an input 'En' which is given to the latch. When the condition for input is 'En = 1', at that same time 'GEN = 0' is obtained and EXNOR gate will produce an output 'x = 0' and provides first clock generation logic that generates clock for controlling device or latch [3]. As the next clock pulse is arrived and as GEN becomes to '1', second clock generation logic is achieved as an AND gate which is an operation of GEN and global clock—CLK signals. Hence it generates clock signal that goes to target device. Also 'GEN = 1' produces 'x = 1' due to EXNOR operation. After that OR gate produces its output as CCLK high until 'EN' becomes to '0'. Hence GCLK will be operating. 'CCLK = 1' state represents that without any switching activities latch will only hold its state. This GCLK generation using negative latch has been implemented and its waveforms are shown in Fig. 3.

Implementation of AMBA APB Bridge Using Gated Clock Circuit

The clock signals are the major source of power dissipation, though clock signals do not play any role in digital computation and do not carry any relevant information. These signals are only used for synchronization of sequential circuits. Hence, by appropriate control over clock signal, one can save power by avoiding unnecessary switching activities inside any gate module. This approach is proposed in Fig. 1 and it has been implemented with AMBA APB Bridge. In VLSI system design applications, AMBA buses are used frequently. Some examples of AMBA buses have been seen in modern portable mobile devices like smart phones, digital cameras, hard disks, etc. In the paper, APB Bridge design with gated clock and reset controller circuits is proposed for optimizing the power. APB Bridge provides a reduced complexity interface between AHB/ASB and APB buses [1]. The implementation of bridge consists of various blocks as stated below.

State Machine for AMBA APB Bridge

State machine for APB Bridge which is considered to be independent is used for device memory mapping [4]. The defined signals in the state machine are referred by ARM technical reference manual [2]. Five states used in state machine are: ST_IDLE, ST_WAIT, ST_WRITE, ST_ENABLE, and ST_READ. The input

signals used are: BnRES is used for current reset status of the system; DELperi is used to indicate that peripheral bus controller has been selected, BWRITE is used to indicate a write transfer, and PrevDESL is used to indicate a registered DSELPeri.

AMBA Reset Controller

AMBA reset controller is generally used to indicate a system for bus reset condition. As an output of reset controller, BnRES signal is generated which indicates current status of the system. BnRES signal also provides the removal of glitches and metastable states and design can provide an efficient utilization of power [5]. Three states ST_POR, ST_INI, and ST_RUN are used in a state machine. An input signal POReset indicates an asynchronous input to system clock. Hence, to eliminate glitches and metastable conditions synchronization is required which is achieved by output signal BnRES only asserted during power on reset conditions [2].

Gated Clock AMBA APB Bridge

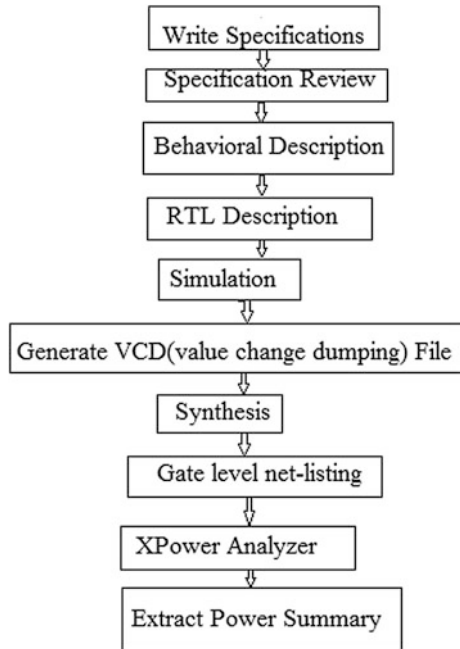
The system clock as an input is connected to clock pin of negative latch as shown in Fig. 1 and as an output gated clock, GCLK is generated. The major components which contribute to power consumption are combinational logic, flip-flops, and clock buffer tree in design [3]. Various clock reduction techniques have been planned earlier which can be used at different levels as system, gate, and RTL levels. One of the latest approaches is a gated clock which can be easily applied at the three levels mentioned above. It saves the power and optimizes the power dissipation with a simple approach where clock gets shut off when no toggle is required. Switching activities of clocks cause a major degradation in power consumption between the SoC parts. In synchronous digital circuits the clock net plays an important role as sources of power dissipation. Hence, clock gating techniques reduce the unwanted switching activities of clock and provide effective control over clock activities which lead to maximal power utilization.

Design Flowchart

The design specifications are referred from Ref. [5]. A flowchart for the proposed design, which is shown in Fig. 2, develops a clear understanding for the designers.

Figure 2 represents the process flow of the new approach proposed in the paper.

Fig. 2 Flowchart of proposed design



Simulation Results

ModelSim version 10.3c is used for designing of AMBA APB Bridge with gated clock approach. Xilinx ISE Design suite 13.4 XPower analyzer is used to extract the power summary.

Figure 3 represents the simulation result of the clock gating circuit. System clock is considered as an input and GCLK of the gated clock circuit is considered as an output.

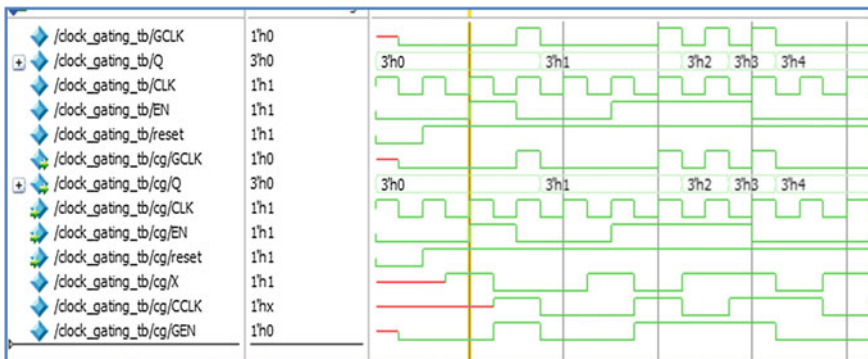


Fig. 3 Gated clock circuit simulation result

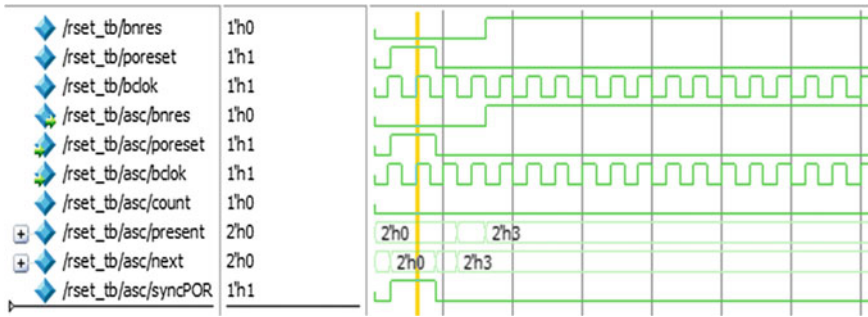


Fig. 4 Reset controller simulation result

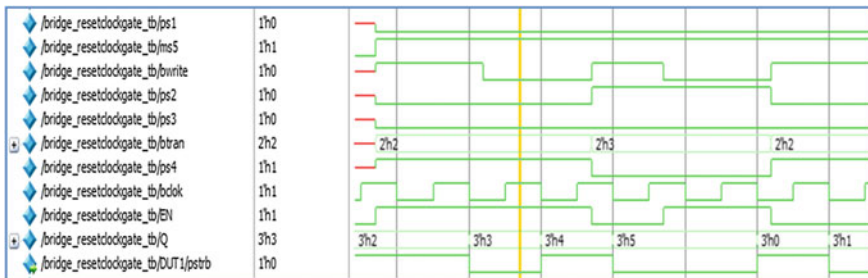


Fig. 5 Simulation of APB Bridge with gated clock circuit

Figure 4 represents the simulation result of the reset controller used for BnRES signal generation. Figures 5, 6, and 7 show the simulation results of the new approach: AMBA APB Bridge with gated clock and reset controller circuit for power optimization.

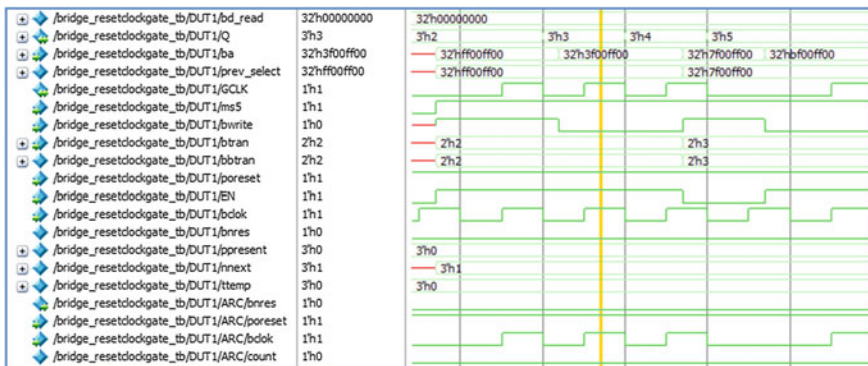


Fig. 6 Simulation of APB Bridge with gated clock circuit (continued)

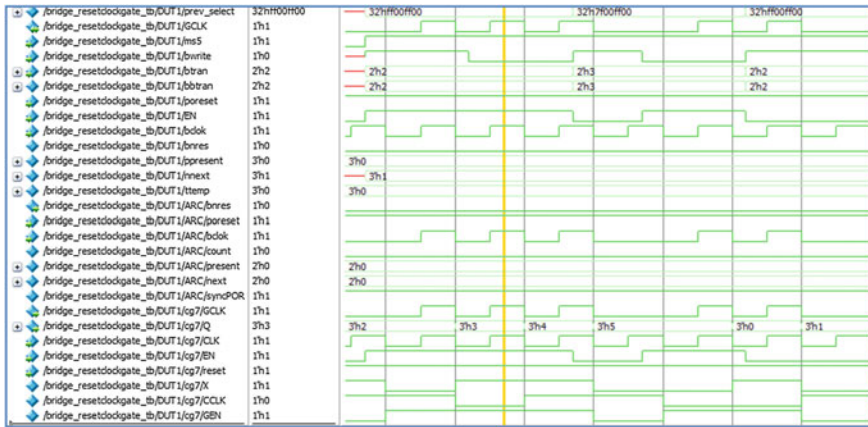


Fig. 7 Simulation of APB Bridge with gated clock circuit (continued)

Conclusion

Clock nets are the major sources of power dissipation. Clock nets themselves are responsible for 15–50 % power dissipation in a SoC. Hence, a new approach has been proposed in this paper which provides efficient control over the clock nets. Verilog language with finite state machines is used for the implementation of the new proposed approach. The proposed approach says that, a latest gated clock circuit should be implemented with the AMBA APB Bridge. For more power utilization reset controller is introduced with the implementation [5]. The results can be shown in a tabular form as following.

Power summary is extracted from Xilinx ISE suite 13.4 version. As a result, Table 1 represents that only total clock domain power of 0.39 mW, total hierarchy power of 0.49 mW, and total on chip power of 0.109 W are consumed by the proposed design. The difference between the power factors has been observed when clock gating and reset controller approach is implemented over the AMBA APB Bridge. The differences can be observed as:

Table 1 Power report of the proposed design approach for AMBA APB at 50 MHz system clock

Frequency (MHz)	Power report with proposed clock gating and reset controller approach (W)	Power reports without clock gating and reset controller approach (W)
50	Total clock domain = 0.00039	Total clock domain = 0.00054
	Total hierarchy power = 0.00049	Total hierarchy power = 0.00093
	Total on chip power = 0.109	Total on chip power = 0.117

- Total clock domain power under proposed design approach consumes 27.78 % which is less than bridge without clock gating and reset controller conditions.
- Total hierarchy power under proposed design approach consumes 47.31 % which is less than bridge without clock gating and reset controller conditions.
- Total on chip power under proposed design approach consumes 6.84 % which is less than bridge without clock gating and reset controller conditions.

References

1. AMBA Specification 2.0, copyright ARM Limited 1999
2. ASB Example AMBA System, Technical Reference Manual
3. Jagrit Kathuria, Ayoubkhan, M., Arti Noor: A review of clock gating technique MIT. Int. J. Electron. Commun. Eng. **1**(2) (2011). MIT Publications, ISSN 2230-7672
4. Manu, B.N., Prabhavathi, P.: Design and implementation of AMBA ASB APB Bridge. In: IEEE, Proceeding of 2013 International Conference on Fuzzy Theory and its Application. National Taiwan University of Science and Technology, Taipei, 6–8 Dec 2013
5. Rawat, K., Sahni, K., Pandey, S.: Design of AMBA APB bridge with reset controller for efficient power consumption. Paper presented at 9th IEEE International Conference on Industrial and Information System (ICIIS2014). Indian Institute of Information Technology and Management, Gwalior, 15–17 Dec 2014

Solar Wind and Diesel Hybrid Energy System: A Review

R.A. Gupta, Bhim Singh and Bharat Bhushan Jain

Abstract Access to electricity is now a basic requirement of mankind. There are still many places in the world which have no access to electrical energy. Even though many of these places might have substantial potential for energy generation the resources are not utilized or identified properly. So, in remote places generation of electricity from renewable energy sources, like solar and wind, could be a good option. For stand-alone, isolated, or off-grid system the energy needs to be stored whenever it is available from these sources and supplied if required. In hilly and remote regions where renewable energy potential is high, large-scale generating systems could also be an option but due to the complex geography and difficult infrastructure, small-scale systems might seem more feasible. The energy from these renewable/natural sources tends to vary throughout the day and hence optimizing the energy capture is necessary. The major objective of this paper is to identify and suggest a simple and flexible system that optimizes the power generation from all of these renewable sources. In this paper, a brief overview of various hybrid systems' connection topologies having wind, solar, and diesel genset has been discussed.

Keywords Renewable energy · Solar PV · Wind · Wind turbine · Wind generator · Hybrid system

R.A. Gupta · B.B. Jain (✉)
Department of Electrical Engineering, MNIT, Jaipur, India
e-mail: bharat.pce@gmail.com

R.A. Gupta
e-mail: ragmnit@gmail.com

Bhim Singh
Department of Electrical Engineering, IIT, Delhi, India
e-mail: bhimsinghiitd@gmail.com

Introduction

Energy is the most common measure of work by human beings and nature. Everything that happens in the world is expressed by the flow of energy in one of its form. Energy crisis is due to the rapid increment of population and standard living of human beings has increased.

Nowadays, the future of the earth and energy requirement is much concerned by most of the people. Conventional energy technologies based on thermal, gas, diesel, etc., are widely recognized as a major cause of environmental destruction—both in terms of pollution and depletion of natural resources. Solar PV, wind, and other renewable energy technologies are most popular in maintaining and improving living standards without harming the environment. More and more energy utilities are using wind and solar/PV in their supply mix [1].

However in a short term, in developing countries, renewable energy sources like wind and solar are not capable to generate a considerable amount of electrical power. They have some advantages:

- Renewable energy source is an original resource accessible in significant amount to all developing countries and competent in principle of having a considerable confined, regional, or national economic impact.
- Several renewable options such as micro hydro, bio gas, etc., are economically and cost-effectively competitive for remote or isolated locations' applications.

Hybrid Energy Systems

In hybrid system two or more resources of renewable energy such as solar, wind, micro/mini-hydropower, and biomass are combined together with power electronic equipments, batteries, diesel generator, etc. Above all, the solar hybrid system consists of a combination of solar with battery or diesel generator. As compared to stand-alone energy generation, the hybrid system provides robust and efficient energy, which is also cost-effective than sole diesel systems. Thus, for stand-alone or off-grid power generation uses of renewable energy options are preferred solutions.

Connection Topologies of Hybrid Power Systems

For understanding the various connection topologies, a hybrid system of renewable sources as wind and solar with diesel genset and battery bank is taken. In these topologies, AC and DC power generating units are connected at some point in the system and somewhere before the loads are supplied. Some common topologies in practice are:

(A) AC/DC-coupled Hybrid Power Systems

For the hybrid power system whose demand is to be supplied from PV-system, wind turbine, a battery, and a diesel generator various configurations are explained in [2–5]. In general, there are three accepted categories of hybrid system technological configurations; according to the voltage they are coupled with each other and to load. They are:

- (I) AC-coupled hybrid power systems
- (II) DC-coupled hybrid power systems
- (III) Mixed-coupled hybrid power systems

(I) AC-coupled Hybrid Power Systems

With this type of configuration, the different HPSs are connected at the AC-bus with the load. The AC-coupled HPSs are further divided into two sub-topologies.

- i. Centralized AC-coupled HPSs
- ii. Distributed AC-coupled HPSs

These two sub-topologies are explained below in detail with schematic block diagrams which may help to give us the insight of the overall system.

(i) Centralized AC-coupled Hybrid Power Systems

In centralized AC-coupled HPS, a main AC-bus comprises of all the energy generating systems before being supplied to the load. This configuration can be depicted in Fig. 1.

The wind turbine and diesel generator produces AC powers, thus they can be directly coupled onto the main AC-bus or with AC/AC converters. While DC power is produced by the PV-array, thus an inverter must be used before it is coupled onto the main AC-bus [6–8]. The charging or discharging of the battery bank with a DC current seeks for a bidirectional inverter which must be used (Fig. 1).

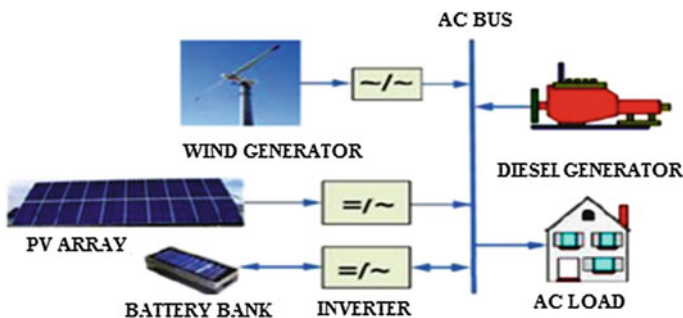


Fig. 1 Centralized AC-coupled HPSs

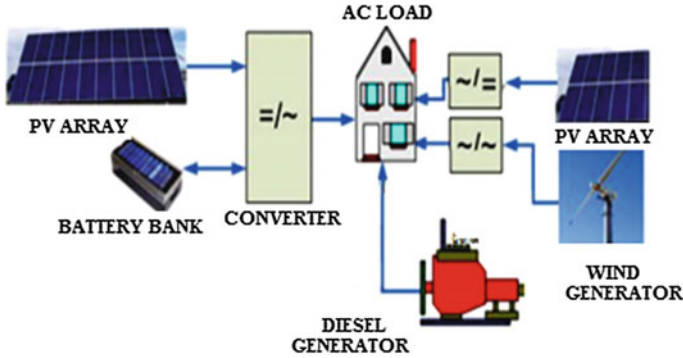


Fig. 2 Decentralized AC-coupled HPSs

(ii) Distributed AC-coupled Hybrid Power Systems

AC-coupled HPSs are said to be distributed or decentralized when the all energy conversion systems are not supplied to a main AC-bus; whereas the load is supplied by the individual or all of these units. Fig. 2 depicts the configuration.

In this topology, the power sources need not be supplied in one common bus as in the previous cases. These sources may not also be installed close to each other, i.e., the generation sources are scattered in different appropriate locations and each source is supplying load separately. The DC powers obtained from the PV-system and the battery need to be converted to AC before feeding the AC load, thus appropriate inverters are required. This type of topology is advantageous in a sense that the different sources are appropriately located and installed geographically in such a way that the PV-systems are installed in places where there is more solar irradiation and the wind turbines in locations where the wind availability is more. However, this topology has disadvantage of difficulty in controlling the system [9]. On comparing the centralized and decentralized ones, centralized HPSs have advantages over decentralized HPSs in that they are robust and have easy control.

(II) DC-coupled Hybrid Power Systems

In DC-coupled HPSs configuration all the ECSs, unlike AC-coupled HPSs, are supplied to a DC main bus, than supplying the load. AC loads are connected through a main inverter. This configuration is also termed as centralized DC-bus topology. Figure 3 shows the configuration scheme for DC-coupled HPSs [8, 10, 11].

Since the energy sources are connected at the DC-bus the diesel genset and wind turbine need AC–DC converters before they are connected to the main bus. The AC load is connected to the main bus via the main inverter.

(III) Mixed-coupled Hybrid Power Systems

It is also possible to combine AC-coupled and DC-coupled HPS systems and form mixed HPSs [9, 12, 13]. With this type of configuration some of the RESs (PV-array, in this case) are connected with the battery bank at the DC-bus and other RESs (wind turbine as in this case) are connected with the genset at the AC-bus. Figure 4 shows the mixed type of HPSs configuration.

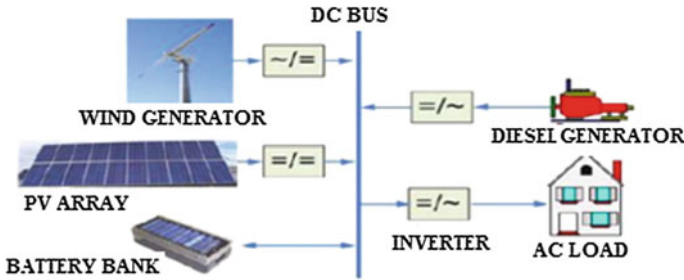


Fig. 3 (Centralized) DC-coupled HPSs

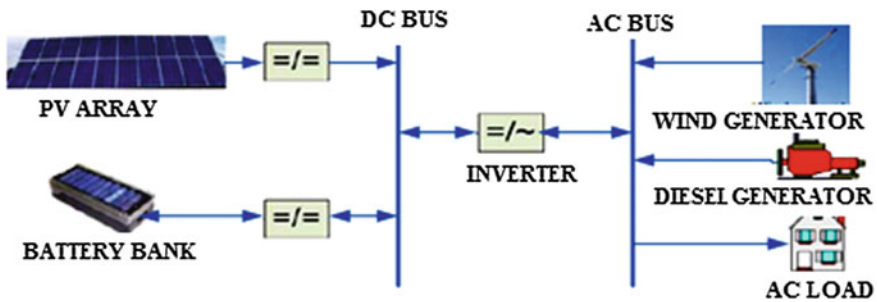


Fig. 4 AC-coupled sources connected with DC-coupled sources or mixed HPSs

A comparison of mixed, AC-coupled, and DC-coupled hybrid systems shows that AC-coupled hybrid systems have many advantages [14] such as simplified design, standardized coupling of various components, common available grid components can be used, operation of island grids, compatibility with existing grids, reduced system cost, good reliability, and expandability of electrical power supply. Special hardware, repair and maintenance requirements, high costs, and more importantly power system expandability for covering the need of upward energy and power demand is also difficult with DC integration [15].

(B) Series-Parallel Hybrid Power Systems

As the load is supplied from the RESs and the genset, a hybrid energy system whose power is to be captured from wind energy system, PV-system, diesel generator, and battery bank, two broad classes of configurations can be explained in [9, 16, 17]. These are

- (I) Series hybrid systems
- (II) Parallel hybrid systems

From this point of view, the AC/DC-coupled or mixed HPS schemes, which have been explained earlier, can be included within these classes.

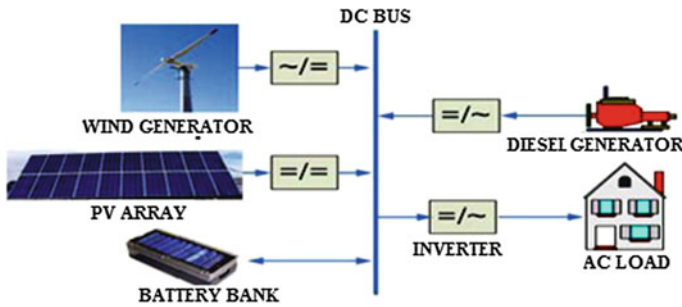


Fig. 5 Series hybrid power system

(I) Series Hybrid Power Systems

In the series HPSs scheme, all the DC power is fed into the battery. Thus, a battery bank is charged by the energy supplied by diesel generator, wind energy system, and solar PV-system before being supplied to the load. Therefore, an individual charge controller for each component has to be set up in the case of diesel generator with a AC to DC conversion. Then, energy stored in the battery bank is converted to AC at a desired level of voltage and frequency by an inverter and then fed to the AC load. The charge regulators help the system by not allowing the flow of the energy from RE generators to battery bank when the batteries are fully charged and the renewable power exceeds the load demand. In a similar fashion, they will protect the battery bank from deep discharge when demand exceeds the supply, if it happens. Figure 5 shows a typical series configuration of HPSs [6, 7, 9, 17].

This type of configuration is also termed as centralized DC-bus topology in the sense that all the energy generating sources and the battery are connected at the DC-bus and the AC load is supplied via a single point. Here, it has to be noted that the AC power from the wind turbine and the diesel generator must be converted into DC by utilizing AC/DC converters or rectifiers before the power is delivered to the DC-bus where the BB is connected. This configuration type, results in relatively simple operation. However, there are some disadvantages of this configuration as listed below

- System efficiency is reduced due to the increase in cycling of the battery bank which passes off most of the energy through the battery [9, 16, 18].
- The depth of discharge is limited by increasing the size of battery bank and since site load does not play an important role to the system as it is based on level of charge in the battery, there is a limited control of the diesel generator [9, 16].
- Most of the current available systems operate at battery voltages having ranges 24–120 V. So the cost of the system increases because standard components or parts are not used and every possible solution needs to be designed separately [2–5, 9, 12–16, 18, 19].

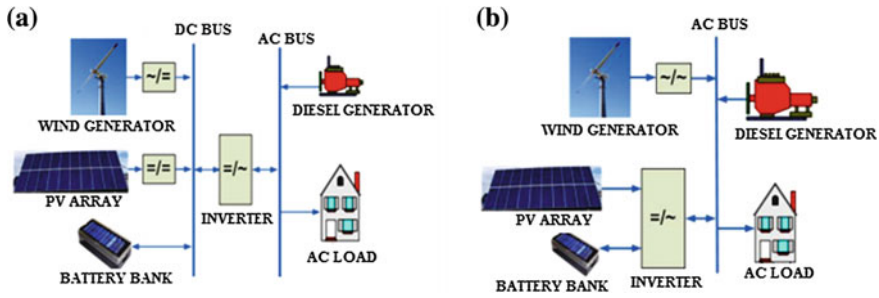


Fig. 6 Parallel hybrid power system. **a** DC-coupling configuration. **b** AC-coupling configuration

(II) *Parallel Hybrid Power Systems*

Figure 6 shows a parallel hybrid system configuration in which a portion of the load demand is supplied directly by renewable energy generators and diesel generator. There are two types of sub-configurations of this hybrid system. These are the DC-coupled and AC-coupled configurations.

A bidirectional inverter is used in the DC-coupling configuration system which works as an inverter and rectifier or battery charger connected in parallel with the diesel generator as shown in Fig. 6a. It is a DC-coupled configuration hybrid system, in a sense that the renewable energy sources are connected together at the DC-bus to the battery and fed to the AC load via the bidirectional inverter. Here, the AC power received from the wind turbine must be converted into DC by utilizing AC/DC converters or rectifiers before the power is delivered to the DC-bus.

AC-coupling configuration is formed by connecting renewable generators to the AC-bus as shown in Fig. 6b and hybrid power system can be improved further. The load can be supplied from the renewable energy supplies in parallel with the diesel genset. A bidirectional inverter is utilized here such that the battery can either supply the load or be charged depending upon the load requirement and the status of other energy sources. Above all, the DC power obtained from the PV-array system and battery must be converted to AC using an inverter before it is fed into the AC-bus. This type of configuration is also referred as centralized AC-bus topology in a sense that all the energy generators are connected at the AC-bus and the load is supplied at a single point [6–11, 17].

Conclusion

Required energy demand for any day is not met by only a stand-alone or off-grid solar/PV, or wind system ideally and it requires a battery bank. A hybrid energy system, with solar/PV and wind can reduce the battery bank requirement, but for the supply of peak load, diesel system cannot be violated. Viability and efficiency of renewable hybrid energy system strongly depends on quality and quantity of solar

radiation and wind energy potential at the site. Battery storage capacity, PVs array area, and number and size of wind machines also have a significant contribution in operation of hybrid solar-wind-diesel system while supplying load as per the demand.

In view of system costs contribution of wind is big as compared to the share of solar. It is observed that wind to solar power ratio in hybrid solar wind energy system in order to have least cost is 30 %.

Brief overview of various topologies for solar, wind, battery, and diesel genset hybrid energy system are discussed here.

References

1. Khatib, H.: Renewable energy in developing countries. In: Renewable Energy Conference, Publication no. 385, IEE, pp. 1–6, Nov 1993
2. Valera, P., Esteban, A.: Solar energy: Comparative analysis of solar technologies for electricity production. In: 3rd World Conference on Photovoltaic Energy Conversion, TP-CP-24, pp. 2482–2485, May 2003
3. Yang, H.X., Lu, L., Burnett, J.: Weather data and probability analysis of hybrid photovoltaic–wind power generation systems in Hong Kong. *Sci. Direct J. Renew. Energy* **28**(11), 1813–1824 (2003)
4. Bhuiyan, M.M.H., Asgar, M.A.: Sizing of a stand-alone photovoltaic power system at Dhaka. *Sci. Direct J. Renew. Energy* **28**(6), 929–938 (2003)
5. Barker, P.P., Bing, J.M.: Advances in solar photovoltaic technology: an applications perspective. IEEE Power Engineering Society Summer Meeting, pp. 1–6, June 2004
6. Deshmukh, M.K., Deshmukh, S.S.: Modeling of hybrid renewable energy systems. *Sci. Direct J. Renew. Energy* **12**, 235–249 (2008)
7. Karaki, S.H., Chedid, R.B., Ramadan, R.: Probabilistic production costing of diesel–wind energy conversion systems. *IEEE Trans. Energy Convers.* **15**(3), 284–289 (2000)
8. El-Hefnawi, S.H.: Photovoltaic diesel–generator hybrid power system sizing. *Sci. Direct J. Renew. Energy* **13**(1), 33–40 (1998)
9. Nelson, D.B., Nehrir, M.H., Wang, C.: Unit sizing and cost analysis of stand-alone hybrid wind/PV/fuel cell power generation systems. *Sci. Direct J. Renew. Energy* **31**(10), 1641–1656 (2006)
10. Chedid, R., Akiki, H., Rahman, S.: A decision support technique for the design of hybrid solar–wind power systems. *IEEE Trans. Energy Convers.* **13**(1), 76–83 (1998)
11. Wichert, B.: PV–diesel hybrid energy systems for remote area power generation—a review of current practices and future developments. *Renew. Sustain. Energy Rev.* **1**(3), 209–228 (1997)
12. Lund, H., Munster, E.: Modeling of energy systems with a high percentage of CHP and wind power. *Sci. Direct J. Renew. Energy* **28**(14), 2179–2193 (2003)
13. Celik, A.N.: Techno-economic analysis of autonomous PV-Wind hybrid energy systems using different sizing methods. *Energy Convers. Manag.* **44**(12), 1951–1968 (2003)
14. Murphy, J.D., McKeogh, E.: Technical, economic and environmental analysis of energy production from municipal solid waste. *Sci. Direct J. Renew. Energy* **29**(7), 1043–1057 (2004)
15. Kolhe, M., Kolhe, S., Joshi, J.C.: Economic viability of stand-alone solar photovoltaic system in comparison with diesel-powered system for India. *Energy Econ. Incorporating J. Energy Fin. Dev.* **24**(2), 155–165 (2002)
16. Hegde, G., Pullammanappallil, P., Nayar, C.: Modular AC coupled hybrid power systems for the emerging GHG mitigation products market. *IEEE-Centre Renew. Energy Sustain. Technol.* **3**(15–17), 971–975 (2003)

17. Jain, S., Agarwal, V.: An integrated hybrid power supply for distributed generation applications fed by nonconventional energy sources. *IEEE Trans. Energy Convers.* **23**(2) (2008)
18. Ro, K., Rahman, S.: Control of grid-connected fuel cell plants for enhancement of power system stability. *Sci. Direct J. Renew. Energy* **28**(3), 397–407 (2003)
19. Gow, J.A., Manning, C.D.: Photovoltaic converter system suitable for use in small scale stand-alone or grid connected applications. *IEE Proc. Electr. Power Appl.* **147**(6), 535–543 (2000)

Analysis and Optimization of Stability for 6T SRAM Cell Using 180 nm Technology

Nidhi Tiwari, Srishti Gusain, Surabhi Chakravorty, Ankita Nirankari and Apoorva Khandelwal

Abstract This paper presents a simple circuit design of 6Transistor SRAM. This work is focused on an important parameter of any memory device known as stability. The 6T SRAM cell is simulated to improve stability. This paper focuses on two techniques for analysis of stability: trial and error technique and graphical technique for SNM calculation. SNM is the measure of stability. The analysis of stability is done on different ratios of W_{access} and W_{driver} transistor and on different supply voltages. Simulation is done using a 180 nm technology and different power supplies. Simulated results have important implications in the design of low-power SRAM.

Keywords SRAM · SNM · Stability · VLSI

Introduction

Memories are the fundamental units of the digital devices and thereby cutting the energy requirement of memories as well as reducing the area is an essential aspect for raising system performance, effectiveness, accuracy, and constancy [1]. The SRAM cells are used because of its simplicity as well as low leakage currents. SRAM caches are mostly used in modern high-performance microprocessor design.

A type of semiconductor memory, 6T static random access memory uses bistable latching circuitry for storing each bit. The term static differentiates it from dynamic RAM which is refreshed periodically. SRAM is one of the memories which exhibits data remembrance, but is still volatile in conventional sense, i.e., when memory is

Nidhi Tiwari (✉) · Srishti Gusain · Surabhi Chakravorty · Ankita Nirankari
Apoorva Khandelwal
Department of Electronics & Communication, Medi-Caps Group of Institutions,
Indore, India
e-mail: nidhitiwari.vlsi@gmail.com

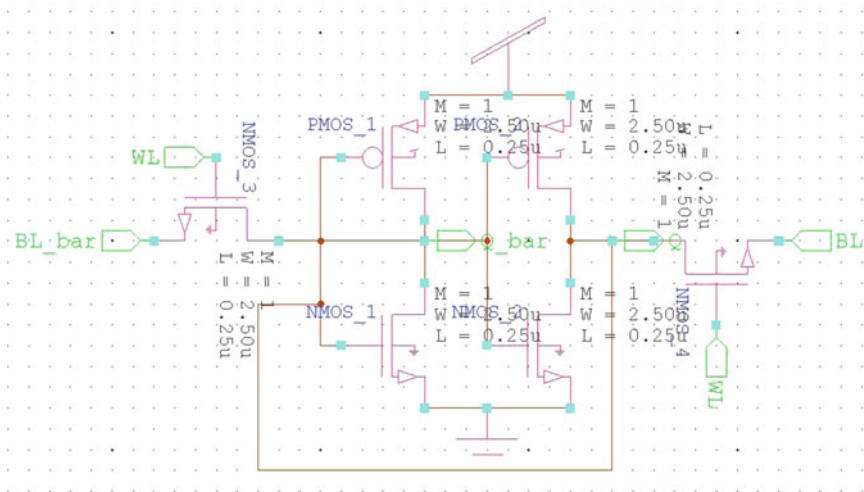


Fig. 1 6Transistor SRAM cell circuit diagram

not powered data are lost. The 6T SRAM Cell is commonly used in chips to store data in cross-coupled inverters. A number of 6T SRAM cell models have been proposed for a differential signaling operation that consists of read and write circuits for variability tangible SRAM design.

However, using a differential signaling, the write operation causes notable access delay that deteriorates system performance [2]. Static noise margin (SNM) was proposed by an asymmetric 6T SRAM by a weak pull-down transistor. In SRAM, the 6T cell is most widely used for practical implementation. The 6T SRAM cell exhibits the finest electrical characteristics with respect to others. The process variation shows its inability to acquire a desirable write margin keeping a high read margin for newer technology nodes, therefore to overcome this new concept this SRAM cell is being designed.

A six-transistor SRAM cell (6T SRAM cell) is traditionally used as a memory shown in Fig. 1. But, when compared to DRAM cell it occupies large area thereby lowering the memory density. This results in low capacity for cell phones-related applications. This paper shows techniques to approximate the read and write stability of 6T cells by outlining computation of the SRAM cells without reshaping its composition.

The paper is organized as follows: Circuit of 6Transistor SRAM cell is described in section “[Circuit Description.](#)” In section “[Stability Techniques](#)” simulations results based on stability technique are presented. Conclusion is shown in section “[Conclusion.](#)”

Circuit Description

The 6T SRAM cell as in Fig. 1 consists of two access transistors (NMOS_3 and NMOS_4) connected with complementary bit lines and two cross-coupled CMOS inverters. The PMOS transistors are called the pull-up transistors (PMOS_1 and PMOS_2) and the NMOS are called driver transistors (NMOS_1 and NMOS_2). The two inverters are connected in feedback loop so as to stabilize it into respective states. Due to this feedback loop, a high value on the second transistor is generated when first is fed with a low thereby storing the current logic value. The access transistors, bit lines (BL and BL_bar), and word lines (WL) are used to perform read and write operations of the cell, respectively. To write information, the data are imposed over the bit line (BL) and inverse bit line (BL_bar) and the word line (WL) is kept high for turning on the access transistor. For the data to be stored in the cell the word line (WL) is kept low thereby making the transistors off. The data stored in the cell can be read by triggering the access transistors, i.e., by making it high. Since a single bit line (BL) is used for read operation, read stability can therefore be improved by strengthening the driver transistor [3].

Stability Techniques

Basic Trial and Error Technique

It is a basic technique, in which we find minimum noise voltage to upturn the state of the cell. In this technique, we introduced two voltage sources between one inverter input to second inverter output as depicted in Fig. 2. Initially, noise source voltage is set to zero to check states; observed states are the same which were

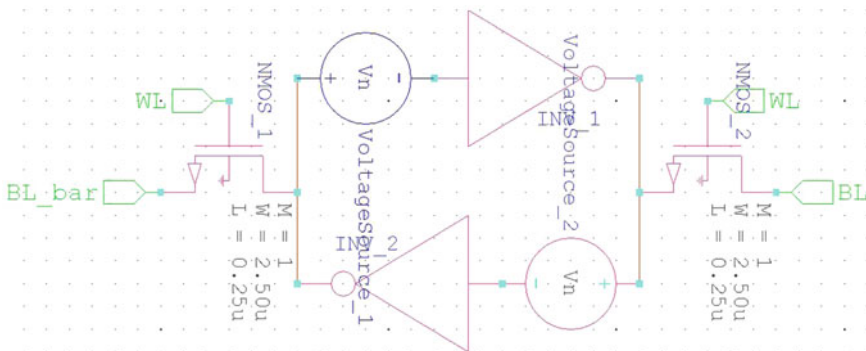
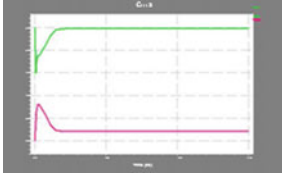
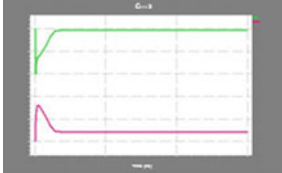
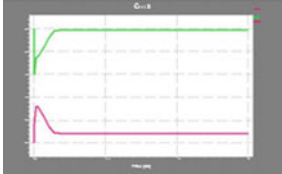



Fig. 2 Noise voltage source inserted for trial and error technique

Table 1 Output states on different noise voltage sources

S. no.	Vnoise (V)	Simulation results (initially: $Q = V_{dd}$ and $Q_bar = 0$)
1.	0	
2.	0.40	
3.	0.41	
4.	0.42	

defined previously. Then, increase the noise voltage source for checking the states. The circuit remains stable until the states are same and the least noise voltage at which it upturns the state of the cell.

From this approach, the voltage which shows the deviation in the states of the cell is observed.

Table 1 represents the initial states of the cell at zero voltage. At 420 mv noise voltage source, states are flipped. Hence 6T SRAM cell is stable below 420 mv.

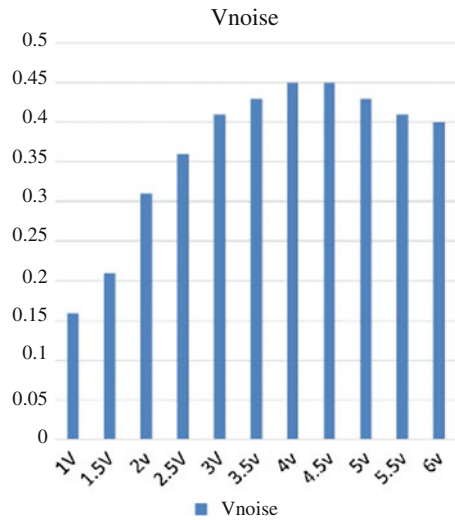
From Table 2, we observed flip point at various voltages. Circuit is simulated on different power supply. Table shows that as we increased power supply, the point at which states are flipped also increased.

Figure 3 shows the graphical representation of variation of noise voltage with respect to supply voltage.

Table 2 States flipped point on different power supplies

Voltage (V)	Vnoise value
1	0.16
1.5	0.21
2	0.31
2.5	0.36
3	0.41
3.5	0.43
4	0.45
4.5	0.45
5	0.43
5	0.43

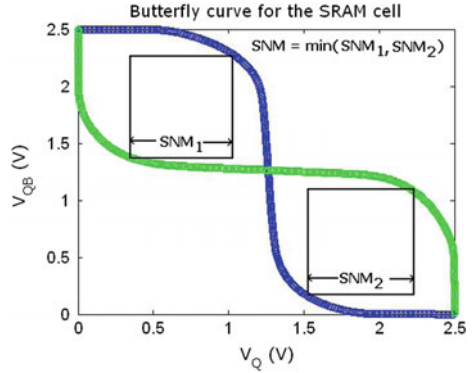
Fig. 3 Flipped states versus power supply



Method 2: Graphical Technique

CMOS has many parameters which affect the operation. We used CMOS and pass transistor for constructing SRAM cell. The important parameter is stability which affects the states of the cell. This stability factor is directly related to the SNM [5]. The SNM states for signal noise margin. SNM is defined as the noise voltage which flipped the state of cell. At first, we used trial and error technique to find out this noise voltage. By using this technique, we can directly calculate noise voltage. In the SRAM cell structure, we are using two CMOS inverters; both are having DC transfer characteristics. The butterfly curve can be constructed by rotating a transfer characteristic of one inverter with another. From Fig. 4, we can calculate the maximum square which fitted between transfer characteristics. This SNM should be as large as possible [4].

Fig. 4 Butterfly curve for SRAM cell [4]



We simulated our 6T SRAM cell on 180 nm technology. On different power supplies, we calculated different SNMs.

Simulated Results:

Figure 5 shows transfer characteristics of inverters and the simulated butterfly curve. The butterfly curve is plotted for different power supply voltages and observed SNM for stability.

Table 3 shows SNM on different voltages. We observed from Table 3 and Fig. 6 that SNM is increased with respect to increase in voltage.

We also simulated our circuit for different width ratios of driver transistor and access transistor. This variation of SNM is shown in Fig. 7 as well as in Table 4. Pass transistor is used in the SRAM cell for read and write operation. These pass transistors are used just for passing the values. So, there is no need to take care of width of these transistors. Here, pass transistor is called access transistor and NMOS in CMOS inverters is known as driver transistor. As driver transistor reinforces the states, so care has to be taken on its width. Below equations show the ratios which we used in our simulations.

$$\text{Cell Ratio} = \frac{W_{\text{driver transistor}}}{W_{\text{access transistor}}} = 1.1$$

Fig. 5 Butterfly curve for read stability

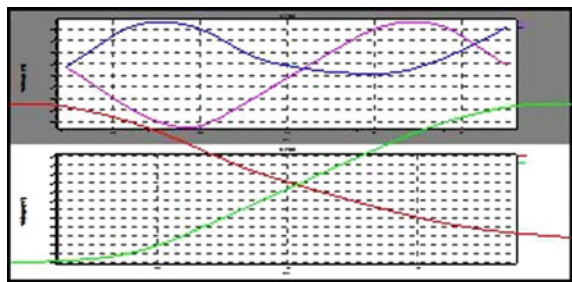


Table 3 SNM on different power supplies

S. no	Voltage source (V_{dd}) (V)	SNM
1.	1.2	4.9521e-001
2.	1.4	5.4501e-001
3.	1.6	5.9067e-001
4.	1.8	6.3704e-001

Fig. 6 SNM on different power supplies

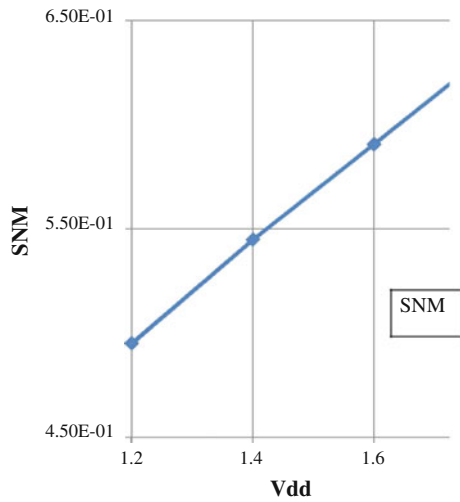


Fig. 7 Width versus SNM

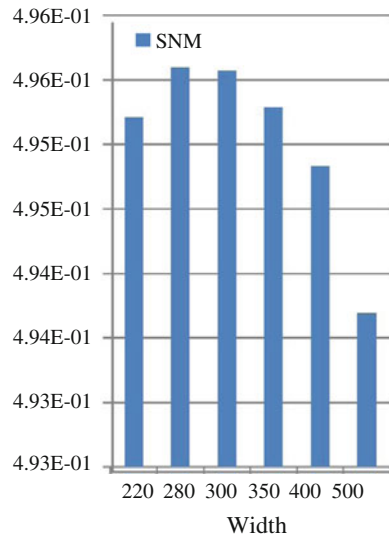


Table 4 SNM on different driver transistor widths

Width (driver in nm)	SNM
220	4.9521e-001
280	4.9560e-001
300	4.9557e-001
350	4.9529e-001
400	4.9483e-001
500	4.9369e-001

$$\text{Pull – up Ratio} = \frac{W_{\text{PMOS}}}{W_{\text{access transistor}}} = 3$$

Simulated Results:

Length = 180 nm

Conclusion

In this paper, 6T SRAM cell is presented in 180 nm CMOS technology. Circuit is simulated for two techniques to analyze stability of the cell. In the first technique, we inserted noise voltage again and again to analyze the states. This technique is so time-consuming, but the graphical technique is quite easy for calculating SNM, also it is fast and reliable. The results derived from the simulation of circuit: as power supply increases, SNM will be increased, as width of driver transistor increases SNM will be stable.

References

1. Liu, D., Svenson, C.: Power consumption estimation in CMOS VLSI chips. *IEEE J. Solid State Circuits* 29(6), 663–670 (1994)
2. Singh, J., Pradhan, D.K., et al.: A single ended 6T SRAM cell design for ultra low voltage applications. *IEICE Electron. Express* 750–755 (2008)
3. Azam, T.: Robust asymmetric 6T-SRAM cell for low-power operation in nano-CMOS technologies. *Electron. Lett.* 46(4), 273–274 (2010)
4. Seevinck, E., List, F.J., Lohstroh, J.: Statis-Noise Margin analysis of MOS SRAM Cells. *IEEE J. Solid-State Circuits* SC-22(5), (1987)
5. Oniciuc, L., Andrei, P.: Random doping fluctuation effects on static noise margins of 6-TSRAM cells. *Solid-State Integr.-Circuit Technol.* 488–491, (2008)

Harvesting Electric Field Energy for Powering Wireless Sensors of Smart Grid

Anil Boyal, Akanksha Deo, Amit Kr. Pandey and Amit Limba

Abstract In this paper, a new energy together with technology using stray electric field of an electric power line is presented. It is discovered that energy can be gathered and stored in the place for storing capacitor 1 that is connected to a body of roller form of aluminium foil covered up around an advertisement-insulated 220 V power line. The average current flowing into 47 μF storage capacitor-2 is about 4.53 A with 60 cm^3 long body of roller form of aluminium foil, and it is possible to do medical operation on radio sensor network point to send RF facts every 42 s. The gathered mean power is about 47 W 4 in this example. Since the energy can be gathered without removing insulating cover, it is a belief that this made an offer on getting together with technology which can be sent in name to power the sensor network points in radio everywhere sensor network 5 and well-dressed network system.

Keywords Stray electric field · Energy harvesting · Wireless sensor node · Smart grid · Self-sustaining sensor

Introduction

As ubiquitous wireless sensor network (USN) has evolved recently, numerous sensor nodes are being installed in the streets, houses, buildings, automobiles, etc., to realize a “Smart Environment” [1]. This smart environment is based on wireless

Anil Boyal (✉) · Akanksha Deo · A.Kr. Pandey · Amit Limba
Electrical Engineering, Poornima Institute of Engineering and Technology, Jaipur, India
e-mail: anilboyal@poornima.org; anilboyaliit@gmail.com

Akanksha Deo
e-mail: akanksha.deo@poornima.org

A.Kr.Pandey
e-mail: amitkr.pandey@poornima.org

Amit Limba
e-mail: amitlimba@poornima.org

sensor network and various systems are employing tens or hundreds of wireless sensor nodes to collect and transmit information. However, in this sensor-rich world, powering the numerous wireless sensor nodes is a serious problem. Currently, battery is used as a power source in most wireless sensor nodes, but, periodical replacement of batteries of numerous wireless sensor nodes is impractical. To solve this problem, research on self-sustainable wireless sensor node using environmental energy such as solar or vibration energy has been performed actively [2]. However, a serious problem in using environmental energy is that the power extracted from environmental energy is not constant over time and its magnitude varies significantly [3]. Energy can be harvested using magnetic field around power line, but, the problem in this case is that current must flow through the power line [4]. To solve this problem, harvesting energy using electric field around commercial insulated 220 V power line is introduced in this paper. According to Maxwell's equation, the displacement current (dI) from a power line can be

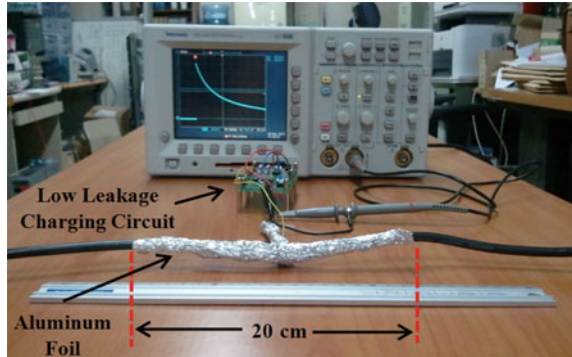
$$I_d = \int_s^e \frac{d\epsilon}{dt} \cdot ds \quad (1)$$

where ϵ is dielectric constant, E is electric field intensity. This displacement current can be used to charge the capacitor that is placed near the power line. Since the energy would be harvested from the stray electric field of the current carrying (voltage applied) conductor, this method can be termed as electric field energy harvesting [4]. Unlike magnetic field energy harvesting, electric field energy harvesting can collect energy from a no-load AC power line in which conduction current does not flow. Rohit Moghe et al. in Georgia Institute of Technology harvested electric field energy by connecting a metal plate through an electric wire to an uninsulated bare wire [4]. This method cannot be applied to insulated power line as the insulating sheath must be removed. In this paper, aluminium foil is wrapped cylindrically around an insulated AC power line to harvest electric field energy without removing the insulating sheath. The method is experimentally confirmed to successfully operate low-power wireless sensor nodes.

Proposed Stray Electric Field Energy Harvesting

Figure 1 shows an experimental setup measuring the energy collected with cylindrical 20 cm aluminium foil wrapped around an insulated no-load AC power line connected to 220 V power. Diameter of the power line is 0.7 cm, thickness of the insulating sheath is about 0.2 cm, and diameter of the inner conducting wire is 0.15 cm, respectively. Equivalent circuit for the experimental setup is shown in Fig. 2. When an aluminium foil is wrapped around the insulated 220 V power line, in a cylinder shape as shown in the Fig. 2a, stray capacitance is generated between the inner conducting wire and the foil as shown in the Fig. 2b. When a 20 cm long foil is used, C1 is measured as about 80 pF and the parallel capacitance of C2 and

Fig. 1 Experimental setup for stray electric field energy harvesting



C3 is measured as about 92 pF. When voltage is applied to the AC power line, it is divided by the stray capacitors, and charge is stored in the storage capacitor. Since charges are transferred by capacitance, electric energy can be harvested even though current is zero, i.e., in open-circuit case.

Experimental Results

Results for Electric Field Energy Harvesting

Figure 3 shows the experimental result when the length of the aluminium foil is 20 cm and the capacitance of the storage capacitor is varied. About 1600 nA of current flows into the storage capacitor regardless of its capacitance, when the power line and the harvesting circuit are directly grounded together during energy harvest (DG), and about 70–80 nA of current flows when the harvesting circuit is not grounded (No Ground, NG). The average current of NG harvesting circuit is very small since there is no loop for current flow. However, it is impractical to peel off the insulating sheath in order to connect with the ground. To solve this problem, the following ground method is devised and tested.

It is well known that the ground line of the AC power line is grounded to the earth. Since concrete of buildings is connected to the earth by metal structures such as metal reinforcements, the earth and the concrete floor of the laboratory are assumed to be at the same zero electric potential. In this work, a $3 \times 4 \text{ cm}^2$ conductor plate is contacted with concrete floor of building as shown in Fig. 4. In this case, oscilloscope probes are not connected to the storage capacitor during energy accumulation stage to prevent discharging to the ground. When 20 cm long aluminium foil and $2 \text{ }\mu\text{F}$ storage capacitor are used, the average current flowing into storage capacitor for concrete plate ground circuit in which metal plate is used, therefore contact resistance is reduced, is 1570 nA. This average current is close to the average current of DG circuit and this result confirms that the concrete floor of

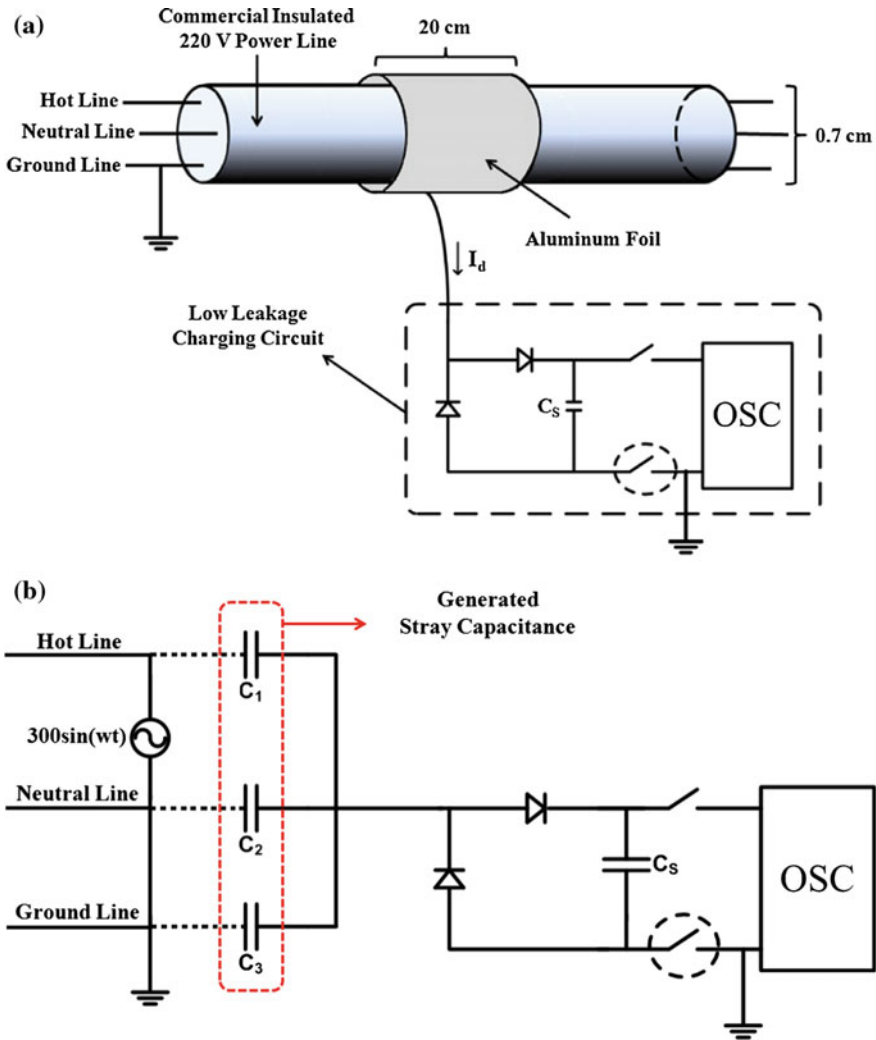


Fig. 2 a Diagram of stray electric field energy harvesting experiment. b Equivalent circuit

the building is at ground potential. The results imply that stray electric field energy can be collected using a harvesting circuit grounded to building floor or wall without removing the insulating sheath of the power line. Figure 5 shows the average current flowing into 6.8 μF storage capacitor versus foil. It can be seen that average current is almost proportional to the foil length. Theoretical explanation is as follows. The stray capacitance increases are proportional to the length of the foil wrapped around the power line.

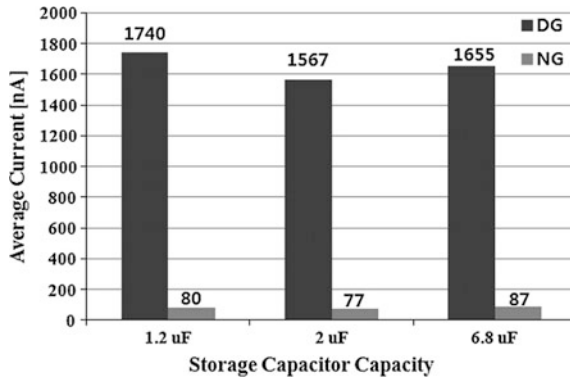


Fig. 3 Average current with respect to storage capacitor capacitance

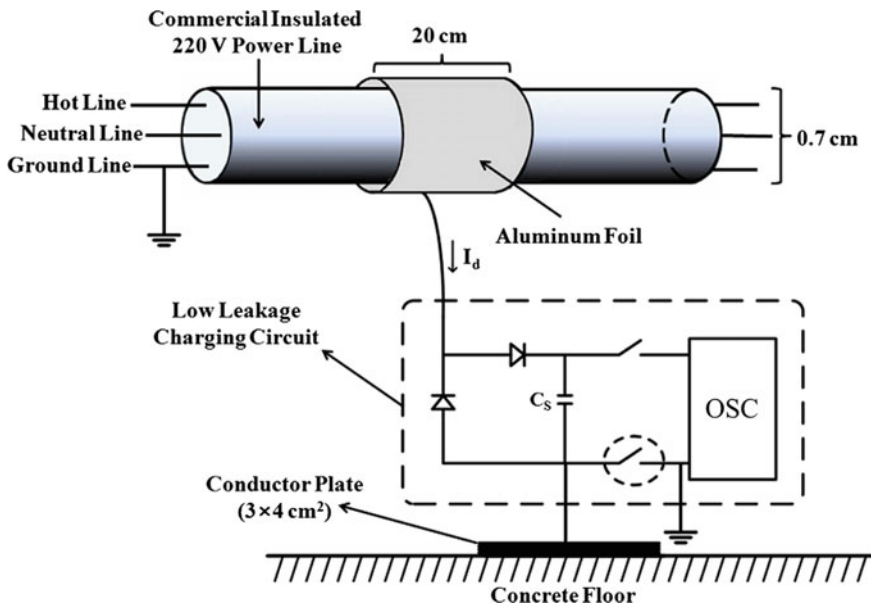


Fig. 4 Diagram of conductor plate ground harvesting circuit

Because impedance is inversely proportional to the stray capacity in AC, average current flowing into the storage capacitor is proportional to the foil length. Accordingly, the amount of energy that can be collected in a given time increases proportionately to the square of the foil length. Figure 6 shows the voltage of 6.8 μF storage capacitor for 1 min when voltage of the power line is changed. The foil length used is 60 cm. As shown in Fig. 7, the voltage of the storage capacitor for a given time increases almost proportionately to the power line voltage. The result

Fig. 5 Average current with respect to foil length

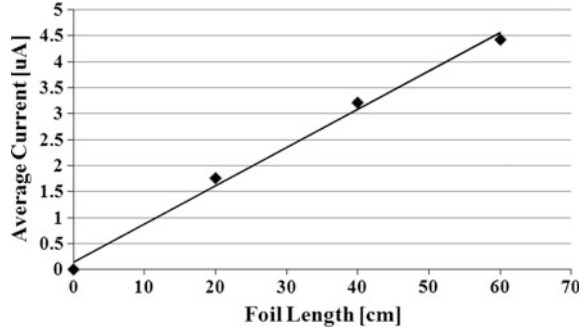


Fig. 6 Voltage charged in the storage capacitor for 1 min versus power line voltage

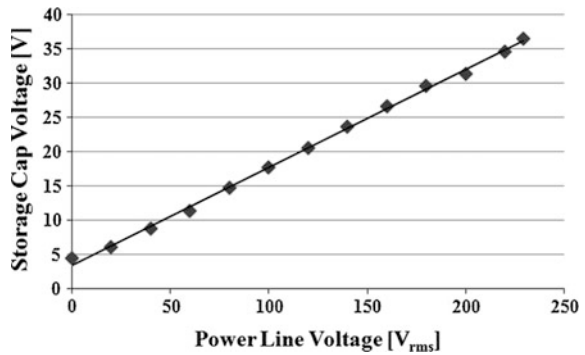
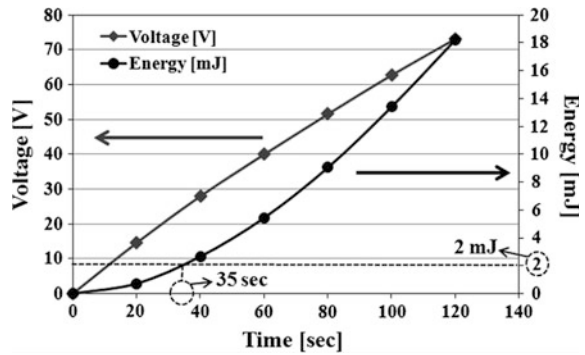
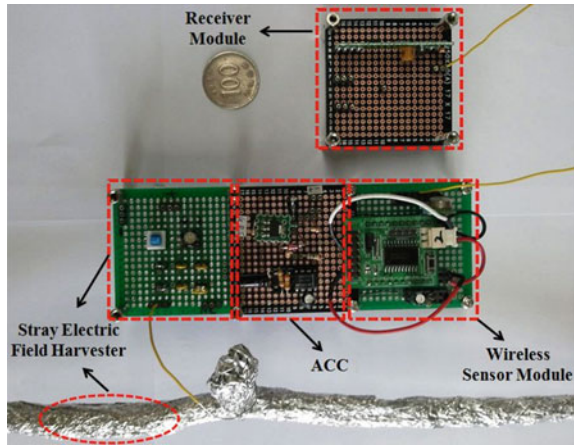


Fig. 7 Voltage and energy charged in storage capacitor over time



implies that average current stored in the storage capacitor is increased and more energy can be collected. If this property is used to collect energy from high-voltage transmission line, the collected energy may be used to power the smart grid sensor for monitoring of power line.

Fig. 8 Manufactured self-sustaining sensor module



Result for Energy Harvesting Wireless Sensor Node

According to the previous research by the authors, 3300 μF capacitor charged to 10.5 V by a solar cell can be used to operate low-power wireless temperature sensor and transmit 100 sessions of RF data to the receiver module in the complete dark [5]. This means that it is required about 2 mJ of energy to transmit a single wireless datum. Figure 7 shows the voltage and energy of 6.8 μF storage capacitor over time when 60 cm long aluminium foil is used. It is found that about 2 mJ of energy is collected in 35 s. The result implies that temperature measurement, A/D conversion, digital signal processing, and RF data transmission can be performed every 35 s, using the energy collected by wrapping 60 cm aluminium foil around the AC power line without peeling off the insulating sheath.

Figure 8 shows the actual circuit used to operate wireless sensor using the collected stray electric field energy. The circuit is composed of energy harvester, power management circuit, RF wireless sensor node, and RF data receiver circuit.

Generally, the energy that can be collected by the energy harvesting is very small. Therefore, energy for wireless sensor operation must be collected until the stored energy is enough to drive the wireless sensor node and used at once. For this operation, an autonomous connection circuit (ACC) is required which can autonomously connect the sensor node when the harvested energy is high enough to operate the sensor node, and autonomously disconnect the sensor node for the next harvesting stage [6]. Figure 9 shows the circuit diagram for wireless node and receiver module. Because Q2 is off at first, energy is stored in C1 by the stray electric field energy harvester. When the charged voltage exceeds the breakdown voltage of Zener diode (D1), Q1 is turned on to make the current flow. As a result, voltage is applied to Q2 gate and Q2 is turned on. At this moment, previously disconnected ground path of the circuit is connected, which makes the storage capacitor to discharge and the following circuit to perform wireless data

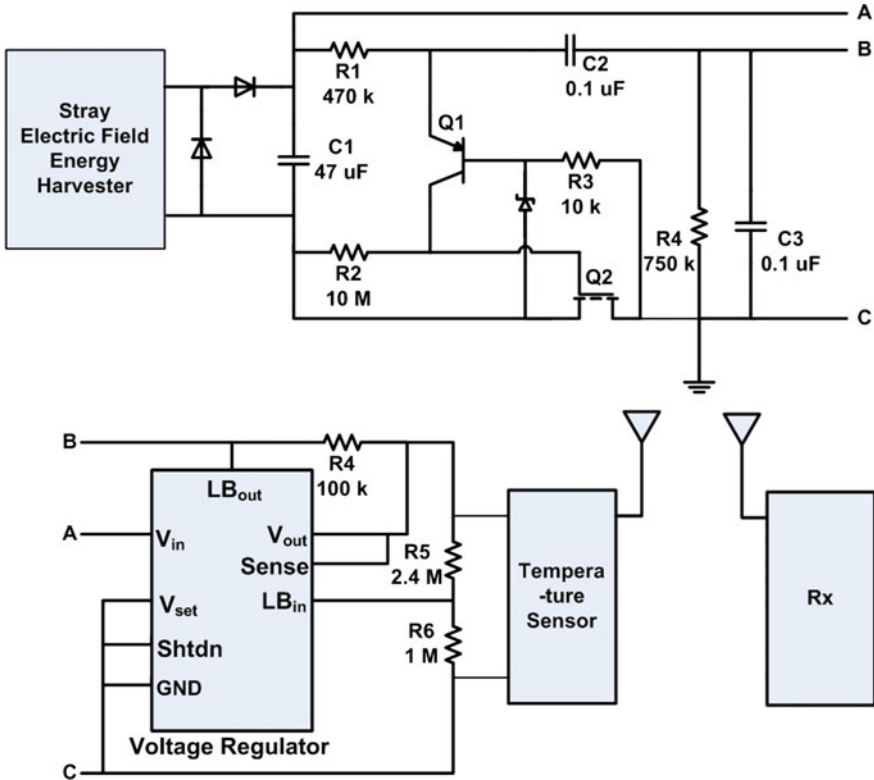


Fig. 9 Circuit diagram for wireless node and receiver Module

transmission. When voltage of the storage capacitor drops below 5.9 V due to the power consumption, low battery out (LB_{out}) terminal of voltage regulator is grounded, then Q1 and Q2 are turned off automatically, and storage capacitor is again charged. This prevents unnecessary discharge of the storage capacitor to 0 V. Figure 10a shows storage capacitor voltage waveform and received digital data waveform when 60 cm long aluminium foil and 47 uF storage capacitor are used. Completely discharged storage capacitor is charged in 130 s to reach 10.9 V, wireless data transmission then occurs. Subsequently, the capacitor starts charging again from 5.9 V and data is transmitted every 42 s. Figure 10b shows the detailed digital data waveform of wireless data. It can be seen that voltage of the storage capacitor decreases during RF data transmission. The experimental results confirm that temperature measurement, A/D conversion, digital signal processing, and RF data transmission can be performed every 42 s, using the energy collected by wrapping 60 cm aluminium foil around the AC power line without peeling off the insulating sheath.

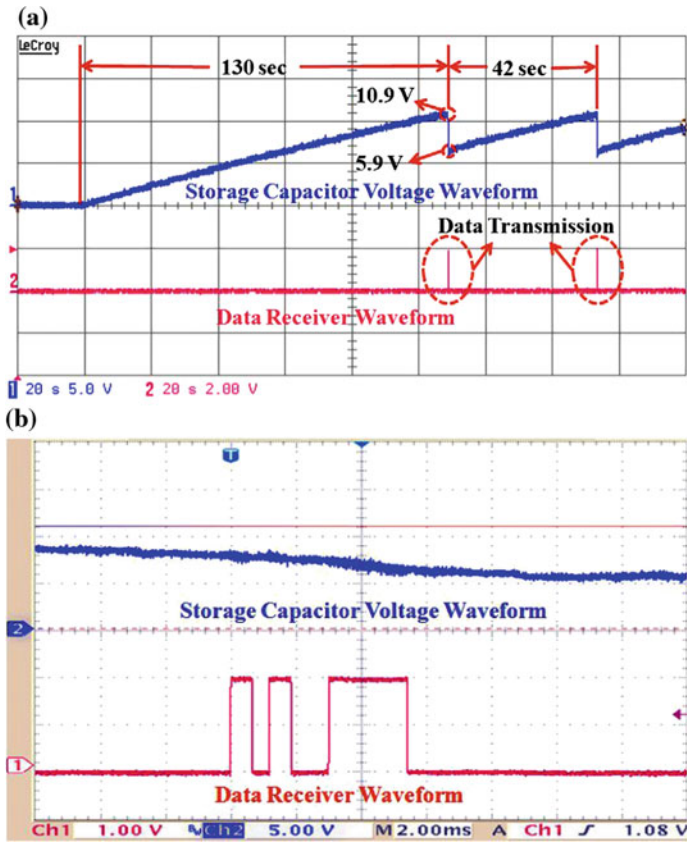


Fig. 10 a Storage capacitor voltage waveform and received digital data waveform. b Detailed digital data waveform

Conclusion

In this paper, a stray electric field energy harvesting technology of electric power line is presented as a novel concept for energy harvesting. This technology can be used to harvest energy from the power line using very simple energy harvesting circuit and metallic foil wrapped around the power line without peeling off the insulating sheath. It is experimentally confirmed that RF data transmission in every 42 s is possible when 60 cm long aluminium foil is wrapped around a 220 V insulated power line. Because of easy installation, the proposed electric field energy harvesting technology can be employed widely in wireless ubiquitous sensor nodes. Furthermore, greater amount of energy can be harvested near the high-voltage power transmission lines; it is believed that the proposed technology can be used to supply electric power to the wireless sensors in smart grid.

References

1. Mathuna, C.Ó., O'Donnell, T., Martinez-Catala, R.V., Rohan, J., O'Flynn, B.: Energy scavenging for long-term deployable wireless sensor networks. *Talanta* **75**(3), 613–623 (2008)
2. Paradiso, J.A., Starner, T.: Energy scavenging for things not fixed and radio electronics. In: *IEEE Coming into Existence Everywhere Computing 3*, vol. 4, issue 1, pp. 18–27, Jan/Mar 2005
3. Roth, K., Brodrick, J.: Energy getting together for radio sensors. *ASHRAE J.* **50**(5), 84–90 (2008)
4. Moghe, R., Yang, Y., Lambert, F., Divan, D.: A Scoping work-room of electric and magnetic field 4 energy getting together for radio sensor networks 2 in power system requests. In: *IEEE Energy Make into Different Sort Congress and Account in Detail*, pp. 3550–3557, 20–24 Sept 2009
5. Kim, H.S., Kang, S.-M., Park, K.-J., Baek, C.-W., Park, J.-S.: Power management circuit for wireless ubiquitous sensor nodes powered by scavenged energy. *Electron. Lett.* **45**(7), 373–374 (2009)
6. Shenck, N.S., Paradiso, J.A.: Energy scavenging with shoe-mounted piezoelectrics. *IEEE Micro* **21**(3), 30–42 (2001)

Chalcogenide (LiGaSe₂, LiGISE, LiGaS₂): A Perfect Material to Design Highly Nonlinear PCFs for Supercontinuum Generation

Sandeep Vyas, Manish Tiwari, Takasumi Tanabe
and Ghanshyam Singh

Abstract In this paper, we have investigated photonic-crystal fibers based on lithium ternary compounds, namely LiGaSe₂, LiGaS₂, and LiGISE (LiGa_{0.5}In_{0.5}Se₂) and characterized them for supercontinuum generation. These highly nonlinear chalcogenide photonic crystal fibers are suitable for supercontinuum generation for pump wavelength at 2.2 μm . We have designed the fibers and optimized them to have a flat dispersion which yields ultra flat supercontinuum spectrum over a wide range of frequencies.

Keywords Photonic Crystal Fiber (PCF) structures · Nonlinear PCFs · Effective area (A_{eff}) · Flat spectrum · Supercontinuum generation

Introduction

In this neoteric age, photonic crystal fiber has shown its importance in the field of communication, medical, and sensors. PCFs are also called microstructured fibers (MFs) or holey fibers. They have a microscopic array of air holes throughout the

Sandeep Vyas (✉) · Ghanshyam Singh
Department of ECE, Malaviya National Institute of Technology, Jaipur, India
e-mail: vyas.sandeep@vitej.ac.in

Ghanshyam Singh
e-mail: gschoudhary75@gmail.com

Sandeep Vyas
Department of ECE, Vivekanand Institute of Technology (East), Jaipur, India

Manish Tiwari
Department of ECE, Rajdhani Engineering College, Jaipur, India
e-mail: manishtiwari@ieee.org

Takasumi Tanabe
Department of EEE, Keio University, Keio, Japan
e-mail: takasumi@elec.keio.ac.jp

core that runs parallel to the entire length of the fiber. This type of structure produces design flexibility in nonlinearity and tailoring dispersion slope.

Supercontinuum generation (SC) has drawn more attention in recent years and PCFs have been inferred to itself as a medium for efficient SC generation. Many applications in optical coherence tomography, frequency metrology, spectroscopy, and wavelength conversion can be achieved by SC generation. Wavelength-division multiplexing is also a useful application of SC.

The fact about optical fiber is that, nonlinear effects emersion is mainly affected by either intensity dependence of refractive index of the medium or inelastic scattering phenomenon. Due to the intensity dependence of refractive index and stimulated inelastic scattering, mixed nonlinear effects, e.g., self-phase modulation, cross-phase modulation, four-wave mixing, stimulated Raman scattering, self-steepening, and stimulated Brillouin scattering can be reconnoitered because the light propagates across the nonlinear medium. SC generation is a phenomenon in which an ultrashort laser pulse passes through highly nonlinear spectral broadening to give spectrally continuous broadband due to the interaction between different nonlinear processes and higher order dispersion. Nowadays, PCFs play an important role in SC generation on account of reduced input power necessity that can be achieved by minimizing effective area (A_{eff}) and enhancing nonlinear properties of PCFs.

In comparison to silica as a background material for PCF, nonsilica materials can be used to obtain interesting optical properties due to their unique material properties. One such important property is nonlinearity, $\gamma = 2\pi n_2/\lambda A_{\text{eff}}$, which governs the optical pulses; spectral broadening can be controlled and maximized by the tailoring of effective area (A_{eff}) of PCFs [1], and choosing a suitable material for high Kerr nonlinear coefficient (n_2), e.g., lead silicate glass [1–3], bismuth oxide glass [3], tellurite glass [4, 5], and chalcogenide glass [6]. With PCF structures, it is possible to work in anomalous dispersion regime even though the material dispersion is very high [7].

The research work presented in this paper is directed toward exploring chalcogenide materials for PCF to take advantage of their extended transmission range and intrinsic nonlinearity. In this work, we have designed and characterized highly nonlinear PCFs that have zero dispersion wavelength (ZDW) around 2.2 μm and very flat dispersion profile in anomalous dispersion region.

Nonlinear Chalcogenide Crystals

In the mid-IR spectrum, LiGaSe_2 , LiGISE ($\text{LiGa}_{0.5}\text{In}_{0.5}\text{Se}_2$), and LiGaS_2 are promising nonlinear chalcogenide crystals. The new mixed crystal, $\text{LiGa}_{0.5}\text{In}_{0.5}\text{Se}_2$ is a solid solution of LiGaSe_2 and LiInSe_2 . It has the same orthorhombic structure as the base compounds (LiGaSe_2 and LiInSe_2). The nonlinear refractive index of all

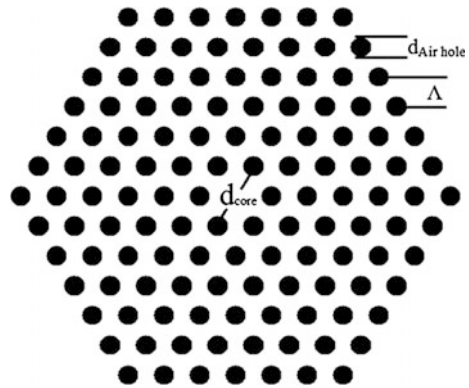
Table 1 Transparency window and bandgap energy

Chalcogenide crystals	Transparency window (μm)	Bandgap energy (eV)
LiGaSe ₂	0.37–13.2	3.34
LiGaS ₂	0.32–11.6	4.15
LiGISE (LiGa _{0.5} In _{0.5} Se ₂)	0.47–13	2.94

the materials is approximately $3 \times 10^{-15} \text{ m}^2/\text{W}$, which is 10^5 times higher in comparison to silica. The transparency window and bandgap energy of all the materials is shown in Table 1 [8, 9].

Fiber Design

We have designed LiGaSe₂, LiGaS₂, and LiGISE (LiGa_{0.5}In_{0.5}Se₂) based on PCF that are compatible for SC generation at 2.2 μm (2200 nm) pumping. Tailoring of dispersion has been done advertently to achieve the required dispersion characteristics, because dispersion and the zero dispersion wavelength(s) play a determinative role in achieving the favored characteristics of SC, e.g., spectral shape, flatness, and width. Due to obtained wide and flat spectrum, we have proposed hexagonal PCFs whose basic XY plane layout is depicted in Fig. 1 and the designing parameters are shown in Table 2.

Fig. 1 The structure of hexagonal PCF**Table 2** Designing parameters of PCF

Chalcogenide crystals	Number of rings	Fiber core diameter (d_{core}) (μm)	Pitch (Λ) (μm)	d/Λ
LiGaSe ₂	6	0.96	3.2	0.7
LiGaS ₂	6	1.6	4.0	0.6
LiGISE (LiGa _{0.5} In _{0.5} Se ₂)	6	0.64	3.2	0.8

Results

The chromatic dispersion of the PCFs has been computed using multipole method which is an efficient and fast method of computing dispersion for symmetric and nonsymmetric fiber structure. The refractive index and material dispersion of chalcogenide glass is calculated by Sellmeier’s Eq. (1) [8, 9]. The Sellmeier coefficients for each crystal are in Table 3.

$$n^2 = A + \frac{B}{\lambda^2 - C} - D\lambda^2 \tag{1}$$

The chromatic dispersion characteristics of the proposed PCF are shown in Fig. 2. The ZDW is $\sim 2.2 \mu\text{m}$ for all the three fibers.

Dispersion curve of the fiber is flat in the anomalous dispersion region which is a suitable characteristic for a flat SC spectrum and due to high intrinsic nonlinearity of LiGaSe_2 , LiGaS_2 , LiGISE ($\text{LiGa}_{0.5}\text{In}_{0.5}\text{Se}_2$) and small effective area, the non-linearity of the γ is very high due to which the width of SC is also expected to be very high.

Table 3 Sellmeier coefficients of material

Chalcogenide crystals	A	B	C	D
LiGaSe_2	5.22442	0.18365	0.07493	0.00232
LiGaS_2	4.493881	0.1177452	0.0337004	0.0037767
LiGISE ($\text{LiGa}_{0.5}\text{In}_{0.5}\text{Se}_2$)	5.26219	0.21331	0.0755	0.00209

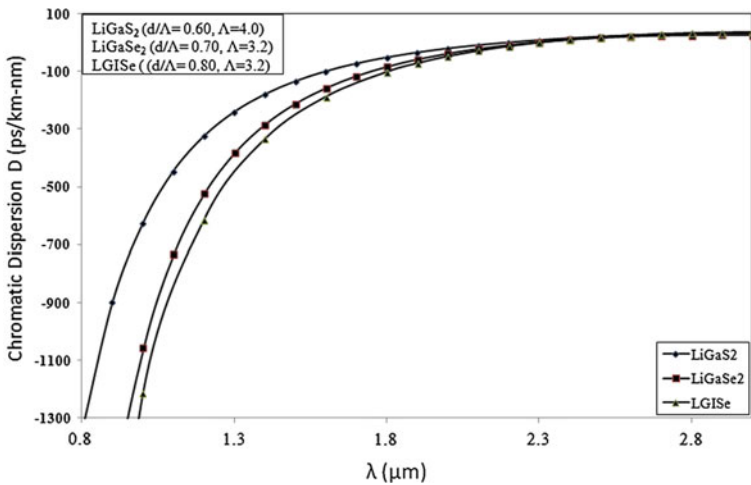


Fig. 2 Dispersion properties of the PCFs, ZDW at $2.2 \mu\text{m}$

Conclusion

We have designed highly nonlinear chalcogenide PCFs compatible for SC generation at pump wavelength at 2200 nm (2.2 μm). In anomalous region, the fibers have very flat dispersion which is a desirable characteristic for a flat SC spectrum. Due to high intrinsic nonlinearity of LiGaSe₂, LiGaS₂, LiGISE (LiGa_{0.5}In_{0.5}Se₂), and small effective area, the nonlinearity (γ) of the fibers is very high.

References

1. Kumar, V.V.R.K., et al.: Extruded soft glass photonic crystal fiber for ultrabroad supercontinuum generation. *Opt. Express* **10**, 1520–1525 (2002)
2. Tiwari, M., Janyani, V.: Two-octave spanning supercontinuum in a soft glass photonic crystal fiber suitable for 1.55 μm pumping. *J. Lightwave Technol.* **29**(23), 3560–3565 (2011)
3. Ebendorff-Heidepriem, H., et al.: Bismuth glass holey fibers with high nonlinearity. *Opt. Express* **12**(21), 5082–5087 (2004)
4. Kumar, V., George, A.K., Knight, J.C., Russell, P.S.: Tellurite photonic crystal fiber. *Opt. Express* **11**, 2641–2645 (2003)
5. Agrawal, A., Tiwari, M., Azabi, Y.O., Janyani, V., Rahman, B.M.A., Grattan, K.T.V.: Ultrabroad supercontinuum generation in tellurite equiangular spiral photonic crystal fiber. *J. Mod. Opt.* **60**(12), 956–962 (2013)
6. Monro, T.M., Hewak, D.W., West, Y.D., Broderick, N.G.R., Richardson, D.J.: Chalcogenide holey fibers. *Electron. Lett.* **36**(24), 1998–2000 (2000)
7. Kiang, K.M., et al.: Extruded single mode nonsilica glass holey optical fibres. *Electron. Lett.* **38**, 546–547 (2002)
8. Isaenko, L., Yelisseyev, A., Lobanov, S., Titov, A., Petrov, V., Zondy, J.-J., Krinitsin, P., Merkulov, A., Vedenyapin, V., Smirnova, J.: Growth and properties of LiGaX₂ (X = S, Se, Te) single crystals for nonlinear optical applications in the mid-IR. *Cryst. Res. Technol.* **38**(3–5), 379–387 (2003)
9. Vedenyapin, V., Yelisseyev, A., Isaenko, L., Lobanov, S., Tyazhev, A., Marchev, G., Petrov, V.: New mixed LiGa_{0.5}In_{0.5}Se₂ nonlinear crystal for the mid-IR. In: Vodopyanov, K.L. (ed.) *Nonlinear Frequency Generation and Conversion: Materials, Devices, and Applications X*, Proceedings of SPIE, vol. 7917, 79171L 2011 SPIE

Mach–Zehnder Interferometer: A Review of a Perfect All-Optical Switching Structure

A.I. Stanley, Ghanshyam Singh, James Eke and Hiroyuki Tsuda

Abstract This article reviews Mach–Zehnder interferometer waveguiding structure-based optical switches in terms of their working principle, design, fabrication, and related performance issues. The effect of the material chosen and the use of tapered interferometric arms on the performance of such switching structures are also explained in brief. In the later part, discussion on the popular applications of the structure is given in brief.

Keywords All-optical switching · Mach–Zehnder interferometer waveguiding structure · Design and performance issues · Applications

Introduction

The days of ultra-high-speed communication and immense Internet network demand the most efficient system to be engaged for this purpose. The telecom and broadband sectors are shedding their old technologies very fast and switching to the era of optical communication. However, the ultrafast switching characteristics of photonics are still untapped. The research in this domain is recently the most happening topic and has been adopted by all the large players from pioneer institutes around the globe. All-optical switches [1, 2] in principle are capable of per-

A.I. Stanley (✉) · Ghanshyam Singh
Department of ECE, MNIT, Jaipur, India
e-mail: stanleyanyigor@gmail.com

Ghanshyam Singh
e-mail: gsingh.ece@mnit.ac.in

A.I. Stanley · James Eke
Department of EEE, Ebonyi State University, Abakaliki, Nigeria
e-mail: drjimmyeke@yahoo.com

Hiroyuki Tsuda
Department of EEE, KEIO University, Yokohama, Kanagawa, Japan
e-mail: tsuda@elec.keio.ac.jp

forming the same functions as electronic switches, e.g., guide the signal flow in an optical network as desired and constitute the basic component of the optical computational systems.

The capability of transmitting large amounts of information over long distances at nearly the speed of light and without any significant loss of data or interference has made optical fibers the perfect choice to be used with modern communication systems. Electro-optic (EO) properties such as refractive index of certain materials can be changed by modulating the electric field [2]. The light, when transmitted through such material undergoes a bending effect and thus, it can be utilized for switching. For example, the coupling ratio of a directional coupler-based switch is modified by changing the composition of the material in the coupling region and thus modifying its refractive index.

Due to this change in the refractive index, the light is guided to the desired port through the appropriate waveguide path. Some of the EO-effect-based popular optical switches have been realized with Mach–Zehnder interferometer (MZI), multimode interferometer (MMI), and Y-junction waveguiding structures. In most of them, the switching response time typically less than 1 ns has been reported, which makes them suitable for optical packet switching [3–5]. Structures such as MZI, MMI [6], directional couplers, etc., have been employed to fabricate optical switches with improvement in switching speed, excess loss (EL), extinction ratio (ER), and device size, etc. However, problems with these switches such as high insertion loss (IL) and high crosstalk (CT) need to be taken care of for their efficient operation [7]. Among the various available topologies, conversion of phase modulation into intensity modulation can be carried out using MZI structures most efficiently. These structures are commonly used to build a variety of applications such as optical modulators, splitters, switches, etc., using EO- or TO(thermo-optic)-effects [4, 8–16].

Various materials and their constituents such as silica [17], polymers [4, 18], III–V semiconductors, and their composites such as InP [3], GaAs–GaAlAs [19, 5], InGaAsP–InP [20], InGaAs–AlGaInAs [10], and also with LN [11, 16, 21, 22] have been used as constituents to design and fabricate optical switches using conventional symmetric MZI structure. Recently, photonic crystal structures have also been used to fabricate MZI structures to achieve the required optical characteristics as per demand of integrated photonics [21, 23]. Monolithically integrated SOA–MZI structures facilitate better control on switching characteristics due to their small size, thermal stability, and low-power requirements [23, 24]. Utilizing the EO-effects, the symmetric MZI structure has been preferred to design adaptable and high-performance switches with low power requirements for smaller bandwidth operation [1–4]. Lithium niobate (LN) is a suitable material for MZI structure-based switches due to large EO-coefficients. These devices exhibit stability in performance parameters, even for inputs having a wide range of optical power levels [25]. These switches use metal electrodes over the interferometric arms that generate a refractive index gradient of an optical medium under the influence of an electric field. Due to this, the light transmitted through the medium undergoes a bending effect, which is called as phase modulation. In this paper, the working principle with design and fabrication aspect

relating to the performance analyses has been discussed. It also enlightens the impact of material chosen and the tapering of interferometric arms on the performance of such switching structure. In the end, we have discussed MZI switching applications in optical integrated circuits and realization of large switching matrix.

Mach–Zehnder Interferometer Optical Switch: Structure and Working Principle

The MZI structure-based optical switch can operate in the bar state, where most of the light is guided to the output side same as the input, and the cross state, where most of the light is guided to the output side opposite to the input side. The switching in a conventional MZI structure can be achieved by introducing a path delay among the propagating beams either by inserting a delay element as shown in Fig. 1a or with TO/EO-effects-induced index change in the interferometric arms as shown in Fig. 2.

Fig. 1 Layout of **a** MZI structure and **b** Path delay with unequal interferometric arms

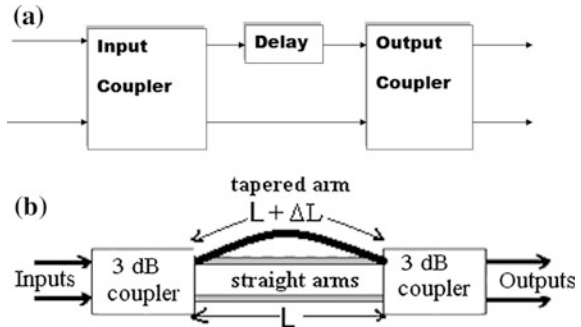
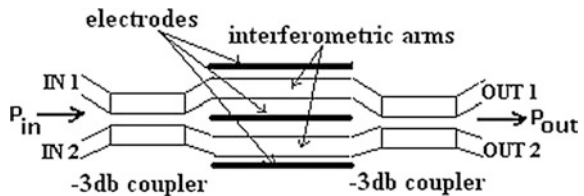


Fig. 2 Generic layout of an EO-MZI switch, Refs. [1, 8]



MZI Switch with Path Delay Element

Wavelength-dependent switches [8] can be made using either active or passive MZI structures. In passive MZI structures, phase modulation is achieved by inserting a delay element or changing the optical path length directly. In active MZI case, the electro-optic or thermo-optic effects are used for change in the phase or the intensity. Figure 1 a, b illustrate the structure of a 2×2 passive MZI structure. This consists of three stages: first, a 3-dB directional coupler in which the input signals are split, then second, a central section which has two different length waveguides, where the longer one (by ΔL) gives a wavelength-dependent phase shift (delay) between the two arms, and the final stage has another 3-dB coupler in which the signals at the output are recombined. The recombined signals undergo constructive interference at one output and destructive interference at the other output if the delay is chosen properly to deliver the optical power only at one output port [1–8]. In the end of interferometric region, the outputs from its two arms have a phase difference of $\Delta\phi = k \cdot \Delta L$, where $k = \frac{2\pi n_{\text{eff}}}{\lambda}$. Therefore, by producing a delay in the propagating path, signal can be switched from one port to another port.

Electro-optic MZI Switch

A conventional EO-effect-based 2×2 MZI switch (passive MZI structure) comprises of two equal interferometric arms connected between two 3-dB couplers as shown in Fig. 2. To avoid any evanescent coupling between the arms, they are widely spaced.

The constituent first 3-dB coupler split the light equally in two parts, which undergoes a net phase change of $2\Delta\phi$ as it travels through the interferometric arms. This phase difference is due to a push–pull effect which comes into picture when waveguides under the electrodes create fields in opposite directions [26]. As it has been observed with this structure, the output intensity is periodic. The minima and maxima of the output intensity occur at odd and even integer multiples of applied voltage. Therefore, the light can be received at output ports by constructive or destructive interference phenomena [8]. Accumulation of a phase difference between the two arms causes the recombined light to interfere according to the following equation [27].

$$\frac{P_{\text{out}}}{P_{\text{in}}} = \frac{[1 + \cos(\Delta\phi)]}{2} \quad (1)$$

Various materials have been used with their EO properties to design and implement MZI structure-based optical switches for the two most popular optical windows, i.e., 1.3 and 1.55 μm . A comparison of some EO-switches based on MZI is given in Table 1 reported in last more than one decade.

Table 1 Overview of few realized EO–MZI switches

Ref. no.	Material	Switch voltage (V)	Performance parameters
[18]	Polymer	15	CT: –22 to –27 dB, IL: 9–10 dB, Propagation loss: 1–1.25 db/cm
[3]	InP	7.5–9	CT: –20 to –30 dB, IL ≤ 2 dB, Total on-chip losses: 3–9 dB
[19]	GaAs–GaAlAs	1.35–1.48	IL: 2 dB, Prop. loss: 0.5 dB/cm, E.R. ≥ 20 dB, Power consumption ≤66mW
[4]	Polymer	±0.925	CT: –30 dB, IL: ≤5.91 dB
[22]	LN	±40	waveguide loss: 1 dB/cm at 632.8 nm
[13]	IPC-E/polysulfone	–	CT ≥ –25 dB, IL ≤ –1.8 dB
[14]	Si	–	CT: ± 28 dB, E.R.: 40 dB
[16]	Ti–LN	8	IL: 0.06–0.70 dB, E.R.: 11.9–22.94

Design Issues and Performance Parameters

As explained earlier, the MZI structure requires various types of waveguides interconnected with each other such as waveguide bends, straight waveguides, tapered waveguides, etc. Therefore, suppression of additive losses due to the sectional waveguides can be achieved by precise designing of all component waveguides [28]. For example, in a waveguiding structure, absorption losses increases if the wavelength difference between the signal wavelength (λ_s) and the bandgap wavelength (λ_{bg}) decreases ($\lambda_s > \lambda_{bg}$) [3]. Therefore, such losses within such guiding layer will be more for wavelengths, which are closer to or shorter than the constituent material bandgap wavelength. On the other side, transition losses also vary as per the shape and size of the channel waveguides.

Therefore, one has to investigate the linear and curved sections of the structure for suitable dimensions to achieve the optimal size parameters. This task can be done by observing closely the effect of different types of channel waveguides (straight and curved), on their respective transition losses by varying dimensions for applied wavelengths. (Usually 1.3 and 1.55 μm). These loss calculations can be equivalent to the sum of all the optical losses like propagation loss, absorption loss, bending loss, etc. The most significant source of optical loss in straight waveguides is scattering, which is caused by the surface roughness and improper channel design. This further depends upon the quality of the wafer and the fabrication process parameters. While fabricating such waveguides (e.g., in case of channel waveguides based on Ti-indiffused lithium niobate), the roughness of the interfaces of the different layers in the stack and etched ridge surface also need to be taken care of as they may cause more optical losses. To change the propagation direction of the light, bent waveguides are required in various optical structures. Waveguide with bends has been proven as better option as compared to mirrors due to low transition losses. In waveguide bends, most of the optical power concentrates near

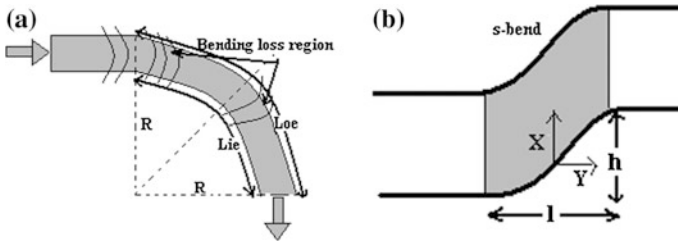


Fig. 3 Layout of **a** Generic bend and **b** S-type bending structure

the edges of the waveguide that result in an increase of the loss due to surface roughness which is in addition to the radiation loss caused by coupling between waveguide modes and radiation modes [29, 30]. Due to these losses, the overall performance is affected and the component density of an integrated optical device, i.e., the number of components that can be fabricated on a single substrate is also affected. Among all known bend structures, s-bends are most commonly used in integrated optical circuits [31].

The basic MZI layout consists of a portion of channel waveguide, which requires bending in the propagation direction. In these kinds of curved structures, total optical loss in general is termed as bending loss, which is due to translational invariance in the guiding structure and the transition loss caused by the discontinuities in the curvature [31]. When the radius of the curvature is varied along the transitional path, the structure is said to have discontinuity that result in transitional loss, which can be calculated using conformal mapping technique as explained at [31]. As shown in Fig. 3a, across a generic curved waveguide, the length of the optical path along the outer edge (L_{oe}) is greater than that along the inner edge (L_{ie}) [31].

More optical losses are contributed by such bending structure and therefore can be replaced by a proper bend waveguide; s-type bends shown in Fig. 3b suppress the losses. The losses in s-bends waveguides for propagating modes (Transverse electric: TE, Transverse magnetic: TM) can be reduced by taking small transition length (l) and large Ti indiffusion thickness (t_s), within the essential sensitivity limit of the structure [31, 32]. Titanium (Ti) indiffusion with LN (Ti-LN) achieves optical switching due to the perfect EO behavior. Adequate doping enhances the sensitivity of the device and state switching time is reduced to appropriate values (in the range of picoseconds). In the indiffusion process, a titanium strip of fixed thickness and width is placed onto LN substrate and then heated within a definite process environment. After the process, a graded index waveguide of defined pattern is formed due to the penetration of the Ti-ions into the host substrate [33].

The bell-shaped refractive index distribution of the graded waveguide in the sideways and in-depth directions is due to the diffusion lengths [33]. In case of Ti-indiffused s-bend waveguiding channel, with fixed valued transition length and lateral offset of 3 mm and 10.75 μm , respectively, the transition losses are negligible (≤ 0.003 dB, Ref. [34]), by choosing strip thickness (t_s) more than 0.050 μm 1.3 μm as test wavelength and 0.065 μm corresponding to 1.55 μm as test

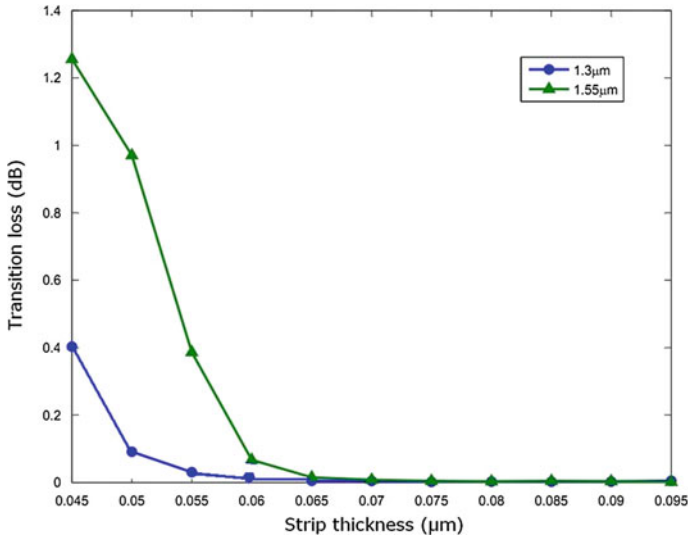


Fig. 4 Loss variation (dB/mm) with respect to the strip thickness (t_s in μm) for curved (s-bend) waveguides, Ref. [34]

wavelength as shown in Fig. 4. There are many important parameters which can be used to characterize the suitability of a switch for optical networks. The switching time of the switch is the most important parameter. Other important performance parameters can be summarized as crosstalk (CT), excess loss (EL), insertion loss (IL), polarization, and wavelength-dependent loss, etc.

There are other types of losses that are incurred during switching and may influence switch performance, like reflectance or return loss, directivity, isolation factor, etc. Other parameters that can also be considered are scalability, energy usage, temperature resistance, and reliability [8]. Commercial fused couplers can be used to obtain an MZI structure by splicing. These structures suffer less isolation factor, which is a difference between optical losses of the two arms caused during splicing [12]. Due to this reduced isolation ratio, the optical signal-to-noise ratio is also reduced, which increases power levels of destructive interferences at the MZI outputs. This will further reduce the power level difference of constructive and destructive interferences of MZI leading to an increased bit error rate at the reception. The quality of the interferometer is also affected by a defect in coupler coupling ratio (ideally 50/50, 3 dB) [12]. Similarly, mismatching of couplers due to variations in the coupling region (narrowing the waveguides at coupling region) results in degradations of switch performance.

Also, to turn the switch completely OFF, the input optical field amplitude must be split equally between the two arms, so that the minimum power out will be zero. In such cases, the MZI structure said to possess power imbalance. Also the extinction ratio is then not infinite, but can be made greater than 10 to 20 dB easily [26]. It has been reported at [34, 35] that CT levels as depicted in Fig. 5 tend to

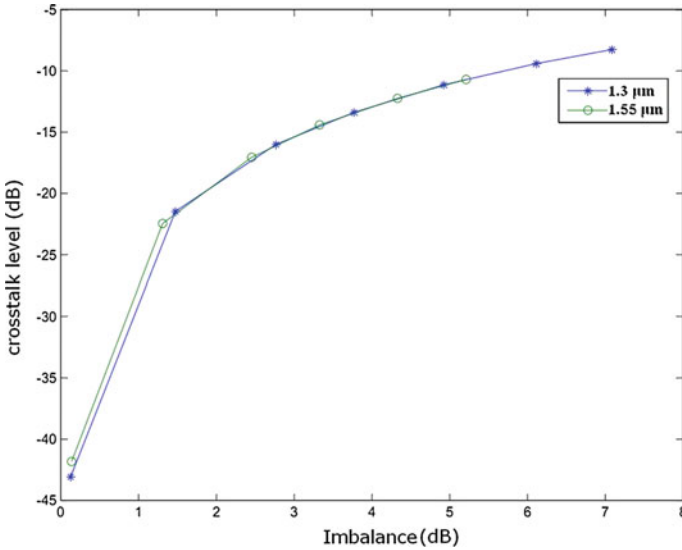


Fig. 5 Calculated CT levels due to variation in generated power imbalance

become worse in case of increased power imbalance levels at the first coupler, which varies almost equally for both test wavelengths (1.3 and 1.55 μm). It is also concluded by [35] that the effect of power imbalance on CT levels strongly depends on waveguide shaping, process parameters, and polarization as well.

MZI Switch Applications in Optical Fiber Networks

Integrated all-optical switching architecture finds many applications in optical communication networks such as demultiplexing, add-drop multiplexing, sampling, etc. The geometry of the switch and the switching scheme are the two factors that must be chosen carefully in order to achieve optimal performance of the structure. The nonlinear interferometric structures with inbuilt semiconductor optical amplifier (SOA) are suitable for integrated optical switching [36]. Due to the high-optical nonlinearity of SOA, it is very appropriate for all-optical switching applications. For this purpose, the optical properties of a nonlinear medium can be changed by using an optical control signal. These changed transmission properties are experienced by the data signal when switched by the device [24]. Compact SOA–MZI structure may be used to design ultrafast optical switches [37], optical gates, all-optical wavelength converters [38, 39], flip-flops, and arithmetic operation [15, 40–43].

The SOAs are found in many applications like with optical switching and wavelength converters [44], signal processing systems, as in-line amplifiers, and as functional devices in growing optical networks and thus, are significant components for optical communication systems. SOAs have been proved as a suitable device to show nonlinear characteristics with fast transient time while incorporating them within MZI switching structures to achieve moderate polarization dependence, lower gain, and less area coverage.

Conclusion

The EO-MZI switches can be effectively used with the proper control signals to facilitate connectivity and switching. However, in MZI structures, interferometer arms are kept far apart to avoid the optical coupling between them, even then electrode positioning shall also adjust in a way to, when these covers arm fully to further avoid these losses, which may arise due to fabrication error in arms spacing. The scope of further work for designing such switches maybe to enhance the flexibility of the structure and minimization of loss with proper signal channeling. This review article is dedicated to the basic MZI switching element modification and improvement of its characteristics.

Acknowledgment The author (A.I. Stanley) gratefully acknowledges the excellent design and simulation facilities available at the Department of Electronics and Communication Engineering for optics research at MNIT Jaipur and the tertiary education trust fund (TETFUND) awarded by Ebonyi State University, Abakaliki (Nigeria) to visit and work at MNIT Jaipur (India).

References

1. Singh, G., Yadav, R.P., Janyani, V.: High performance Machzehnder optical switch. *Optica Applicata* **XLII**(3), (2012). ISSN: 1899-7015, doi:[10.5277/oa1203](https://doi.org/10.5277/oa1203)
2. Singh, G., Yadav, R.P., Janyani, V., Ray, A.: Design of 2×2 optoelectronic switch based on MZI and study of the effect of electrode switching voltages. In: *Proceedings of World Academy of Science, Engineering and Technology*, Bangkok, vol. 29, pp. 401–407, May 2008. ISSN: 1307-6884
3. Maat, D.H.P.: InP-based integrated MZI switches for optical communication. A Ph.D. thesis, Department of Applied Physics, Delft University of Technology, The Netherlands, 9 Apr 2001
4. Zheng, C.T., Ma, C.S., Yan, X., Zhang, D.M.: Design of a spectrum-expanded polymer MZI electro-optic switch using two-phase generating couplers. *Appl. Phys. B, Laser Opt.* 1–10, (2010)
5. Cao, S.C., Noad, J., Sun, L., et al.: Small AC driving voltage for MZI-based GaAs-GaAlAs electrooptic modulators/switches with coplanar electrodes. *IEEE Photon. Technol. Lett.* **21**(9), 584–586 (2009)
6. Singh, G., Sirohi, A., Varma, S.: Performance enhancement of a 2×2 multimode interference photonic switch using size modulated index regions. *IETE J. Res.* **59**(5), 1–6 (2013)

7. Potasek, M.J., Yang, Y.: Multi terabit-per-second all-optical switching in a nonlinear directional coupler. *IEEE J. Sel. Top. Quantum Elect.* **8**(3), 714–21 (2002)
8. Papadimitriou, G.I., Papazoglou, C., Pomportsis, A.S.: *Optical switching*. In: Wiley series in Microwave & Optical Engineering. Wiley Inter science (2007). ISBN: 0-471-68596-8
9. Singh, G., Yadav, R.P., Janyani, V.: Ti: LiNbO₃ based Machzehnder interferometric all optical switches: a review. In: A chapter with New Advanced Technologies, pp. 311–322. INTECH Publication, Austria (2010). ISBN: 978-953-307-067-4
10. Wong, H.Y., Sorel, M., Bryce, A.C., Marsh, J.H., Arnold, J.M.: Monolithically integrated InGaAs–AlGaInAs MZI optical switch using quantum-well intermixing. *IEEE Photon. Technol. Lett.* **17**(4), 783–785 (2005)
11. Suzuki, K., Yamada, T., Moriwaki, O., et al.: Polarization-insensitive operation of Lithium Niobate with silica based PLC-based polarization diversity circuit. *IEEE Photon. Technol. Lett.* **20**(10), 773–775 (2008)
12. Ducourmau, G., Latry, O., Kétata, M.: Fiber based MZI structures: principles and required characteristics for efficient modulation format conversion. In: *Passive Components and Fiber-based Devices II*, Proceedings of SPIE, vol. 6019, 60190A (2005)
13. Li, H.P., Liao, J.K., Tank, X.G., et al.: 2×2 Polymeric electro-optic MZI-switch using MMI-couplers. In: *SPIE Proceedings*, vol. 7509, Nov 24 2009
14. Jun, X.X., Wu, C.S. et al., High-speed 2×2 Silicon-based EO-switch with nanosecond switch time. *Chinese Physics B* **18**(9), (2009). IOP Science
15. Yahya, E.H.M.: Mach–Zehnder interferometer, An M. Tech thesis, Faculty of Electrical Engineering, University of Technology Malaysia, Apr 2007
16. Rahman, M.S.A., Shaktur, K.M., Mohammad, R.: Analytical and simulation of new electro-optic 3×3 switch using a Ti: LiNbO₃ waveguide medium. In: *International Conference on Photonics, IEEEExplorer*, pp. 1–5, Oct 14, 2010. ISBN: 978-1-4244-7186-7
17. Kenya, S., Yamada, T., Moriwaki, O., Takahashi, H., Okuno, M.: Polarization—insensitive MZI switch composed of an in phase shifter array and silica-based plc—integrated polarization beam splitter. *OFC/NFOEC, IEEEExplorer* (2008)
18. Hwang, W.Y., Oh, M.C., Lee, H.M., Park, H., Kim, J.J.: Polymeric 2×2 EO-switch consisting of asymmetric Y junctions and MZI. *IEEE Photonics Tech. Lett.* **9**(6), 761–763 (1997)
19. Cao, S., Sun, L., Savoie, M.: 2×2 MMI–MZI GaAs–GaAlAs Carrier-Injection Optical Switch, pp. 207–208. *IEEEExplorer* (2010). 978-1-4244-3731-3/10
20. Agrawal, N., Weinert, C.M., Ehrke, H.4, Mekonnen, G.G., Franke, D., Bornholdt, C., Langenhorst, R.: Fast 2×2 Mach–Zehnder optical space switches using InGaAsP–InP multiquantum—well structures. *IEEE Photon. Technol. Lett.* **7**(6), 644–645, June 1995
21. Yong, H.T., Lee, H.S., Lee, El.H.: Design of Compact Silicon Optical Modulator Using Photonic Crystal MZI Structure, pp. 308–310. *IEEEExplorer*, 978-1-4244-1768-1/2008
22. Bentinia, G.G., Bianconia, M., Ceruttia, A., et al.: Integrated Mach–Zehnder micro-interferometer on LiNbO₃. *Opt. Lasers Eng.* **45**, 368–372 (2007)
23. Jiang, W., Gu, L., Chen, X., Chen, R.T.: Photonic crystal waveguide modulators for silicon photonics: device physics and some recent progress. *Solid-State Electronics* **51**(10), 1278–1286 (2007)
24. Tekin, T.: Monolithically integrated gain shifted Mach–Zehnder Interferometer for all—optical demultiplexing. A Ph.D. thesis, Faculty of Electrical Engineering and Computer Science, Technical University of Berlin, Germany, 20 July 2004
25. Beaumont, A.R., Atkins, C.G., Booth, R.C.: Optically induced drift effects in Lithium Niobate electro-optic waveguide devices operating at a wavelength of 1.51 μm . *Electron. Lett.* **22**(23), 1260–1261 (1986)
26. Barnes, Charles E., Greenwell, Roger A.: Radiation effects in photonic modulator structures. *Proc. SPIE* **2482**(48), 1–51 (1995)
27. Analui, B., Guckenberger, D., Kucharski, D., Narasimha, A.: A fully integrated 20-Gb/s optoelectronic transceiver implemented in a standard 0.13 μm CMOS–SOI technology. *IEEE J. Solid-State Circuits* **41**(12), 2945–2955 (2006)

28. Singh, G., Yadav, R.P., Janyani, V.: Design of symmetric & asymmetric 2×2 all optical Ti:LiNbO₃ MZI switches. *Int. J. Comput. Appl.* **33**(1), 36–40 (2011). ISSN: 1925-7074, doi:10.2316/Journal.202.2011.1.202-2977
29. Unger, H.G.: *Planar Optical Waveguides and Fibres*. Clarendon Press, Oxford (1977)
30. Snyder, A.W., Love, J.D.: *Optical Waveguide Theory*. Chapman and Hall, London (1983)
31. Ganguly, P., Biswas, J.C., Lahiri, S.K.: Modelling of Ti—indiffused Lithium Niobate channel waveguide bends: a matrix approach. *Opt. Commun.* **155**, 125–134 (1998)
32. Minford, W.J., Korotky, S.K., Alferness, R.C.: Low-loss Ti:LiNbO₃ waveguide ends at $\lambda = 1.3 \mu\text{m}$. *IEEE J. Quant. Electron.* **QE-18**(10), 1802–1806 (1982)
33. OptiBPM: Technical background and tutorials. Waveguide optics modeling software system, Version 8.0, 2nd edn. Optiwave Inc. (2006)
34. Singh, G., Yadav, R.P., Janyani, V.: Modeling of a 2×2 electro-optic Machzehnder interferometer optical switch with s-bend arms. *Photonic Lett. Poland* **3**(3), 119–121 (2011). ISSN: 094
35. Singh, G., Bothra, S., Gupta, S., Yadav, R.P., Janyani, V.: Process optimization to design Ti-indiffused Lithium Niobate channel waveguide for MZI switching element. In: *Micro-Technology, Proceedings of SPIE 8069, 80690 W*, Prague, C.R (2011)
36. Singh, G., Bhattacharjee, T.P., Mundra, R., Yadav, R.P., Janyani, V.: Design and analysis of the performance of MZI based all-optical switch exploiting the band gap shifting character of SOA's. *J. Opt.* **38**(1), 29–37, (2009). ISSN: 0972-8821
37. Wang, J.P., Robinson, B.S., et al.: Efficient performance optimization of SOA–MZI devices. *Opt. Soc. Am.* 1–5 (2007)
38. Jamro, M.Y., Senior, J.M., Leeson, M.S., Murtaza, G.: Chirp in a wavelength converter based on a symmetrical-MZI employing SOAs. *Opt. Commun.* **209**(4–6), 321–328 (2002)
39. Singh, S., Kaler, R.S.: All optical wavelength converters based on cross phase modulation in SOA–MZI configuration. *optik—Int. J. Light Electron Opt.* **118**(8), 390–394 (2007)
40. Singh, G., Yadav, R.P., Janyani, V., Sharma, R.: Performance analysis for all optical switch based on MZI switching element with SOA's. In: *Optical Metro Networks and Short-Haul Systems, Proceedings of SPIE, vol. 7235, 723509*, San Jose, CA, USA, Jan 26 2009
41. Houbavlis, T., Zoiros, K.E., Kanellos, G., Tsekrekos, C.: Performance analysis of ultrafast all-optical Boolean XOR gate using semiconductor optical amplifier-based MZI. *Opt. Commun.* **232**(1–6), 179–199, March 1 2004
42. Ye, X., Ye, P., Zhang, M.: All-optical NAND gate using integrated SOA-based Mach–Zehnder interferometer. *Opt. Fiber Technol.* **12**(4), 312–316 (2006)
43. Raffaelli, C., Vlachos, K., Andriolli, N., et al.: Photonics in switching: architectures, systems and enabling technologies. *Comput. Netw.* **52**(10), 1873–1890, July 16 2008
44. Connelly, M.: Semiconductor optical amplifiers and their applications. *OPTOEL* (2003)

Design and Analysis of Different Decoders for SAC-OCDMA Systems

Soma Kumawat and M. Ravi Kumar

Abstract Spectral amplitude coding for OCDMA (SAC-OCDMA) reduces MAI as compared to other types of OCDMA coding techniques. Different decoder designs are presented for spectral amplitude coding which are simulated on OptiSystem-13. Enhanced double weight code is used in wavelength selection of users for simulation. Variations in decoder configuration are attempted using fiber Bragg gratings and other components such as photodiode and power splitter to improve system performance. The effect of the different configurations of SAC-OCDMA decoder on system BER performance is analyzed.

Keywords SAC-OCDMA · EDW code · FBG filter · BER

Introduction

There has been taken much effort on the research of optical code division multiple access (OCDMA) technique because of its various advantages compared to the other multiple access techniques. The advantages of OCDMA over these multiple access techniques are asynchronous access in high system capacity, good network security, low-cost, decentralized, and simple high-speed multiple-access environment [1]. In addition to these advantages, it suffers from multiple access interference (MAI), phase-induced intensity noise (PIIN), and beat noise [2]. Reduction of these factors to enhance OCDMA network performance is still an open problem.

Spectral amplitude coding (SAC) is one of the OCDMA coding techniques which reduces the multiple access interference (MAI) [3] and provides a low-cost solution as it uses LEDs as light sources.

Soma Kumawat (✉) · M.R. Kumar
Department of ECE, MNIT, Jaipur, India
e-mail: Somakumawat25@gmail.com

M.R. Kumar
e-mail: rkmaddila.ece@mnit.ac.in.com

In 1D SAC-OCDMA code, wavelength domain is used for coding. For 2D and 3D, time domain or space domain is used [4, 5]. The technique of SAC-OCDMA has the capability to entirely remove MAI using code sequences having fixed in-phase cross-correlation [4]. Different detection techniques are used to eliminate MAI such as complementary subtraction technique, AND subtraction detection Technique, and so on [6].

This paper attempts to design and analyze different decoder configurations for an SAC-OCDMA system. The paper is organized as follows. Section “[System Description](#)” describes the SAC-OCDMA system; section “[Improved Decoder Designs](#)” explains the design of different decoder configurations. Results are discussed in section “[Results and Discussion](#)” and the paper is concluded with highlights of this article in section “[Conclusion](#)”.

System Description

As shown in Fig. 1, a transmitter has a single LED source having a linewidth of 30 nm and driven at 622 Mbps. LED output is sliced into three wavelengths using wavelength division demultiplexing and multiplexing to generate the OCDMA codes using enhanced double weight (EDW) code [7]. A spectral width of 0.8 nm is used by each chip. Pseudorandom bit sequence generator along with the non-return-to zero line coding is used to generate information which is embedded into optical signal using a Mach–Zehnder modulator. Ideal multiplexer is used to add the signal from different users before transmission in the single-mode fiber at 1550 nm. Each decoder divides the signal into two parts to reduce MAI. First part of the decoder goes to filter structure which is identical to the encoder. Second part of the decoder has an AND filter structure. Multiple fiber Bragg gratings (FBGs) are used in the filter structure with different Bragg wavelengths according to the filter signal. After filtering the desired signal, avalanche photo diode (APD) is used to convert the optical signal to the electrical domain. Both output signals from the respective APDs are subtracted using electrical subtractor and resultant signal is filtered by fourth-order Bessel low pass filter. A subtractor removes the overlapping data. For simulation, enhanced double weight (EDW) code as given in Table 1 [7] is used. The code has unity cross-correlation property [7] and the system is simulated on OptiSystem-13 with parameters shown in Table 2.

Improved Decoder Designs

Decoder design is changed on selecting the Bragg wavelength. Upper branch of the decoder is identical to the encoder filter structure. The reflected wavelength (zero position) or transmitted wavelengths (one position) of FBG changed the upper branch decoder filter structure as shown in Fig. 1.

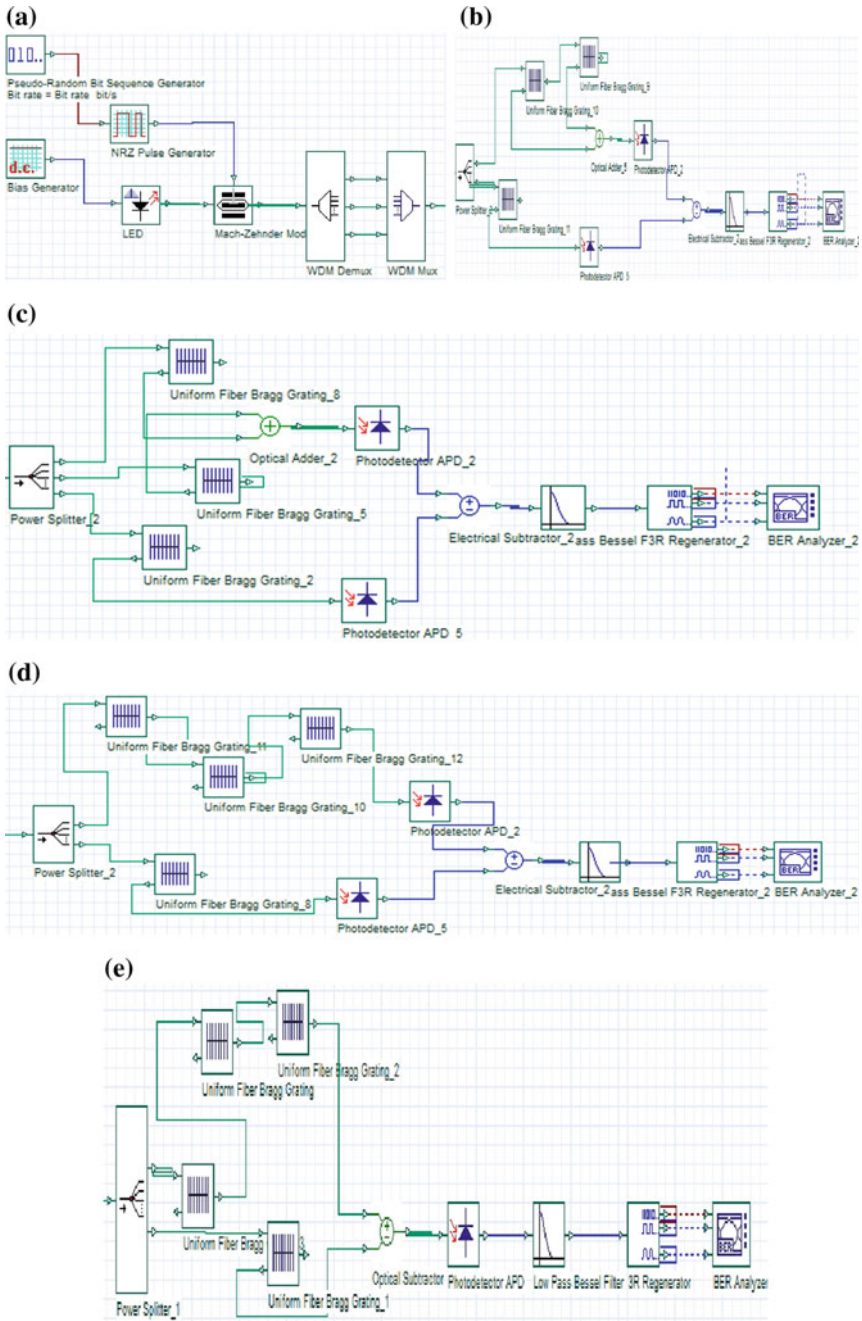


Fig. 1 SAC-OCDMA system for three-users design in optisystem-13. **a** Encoder structure using EDW code for single user. **b** Design 1 of decoder. **c** Design 2 of decoder. **d** Design 3 of decoder. **e** Design 4 of decoder

Table 1 Code design for EDW [7, 8]

L (code length)		1	2	3	4	5	6
Code sequences	User1	1	1	0	1	0	0
	User2	0	1	0	0	1	1
	User3	0	0	1	1	0	1

Table 2 Simulation parameters [7]

Parameter	Value
LED bandwidth	30 nm
LED input power	9.085 dBm
Signal data	128 PN sequence
Chip spectral width	0.8 nm
Signal format	NRZ
External modulator extinction	30 dB
Data rate	0.622 Gbps
FBGs reflectivity	0.99
Fiber dispersion, D	16.75 ps/nm/km
Fiber dispersion slope, S	0.075 ps/n/km
APD gain	10
Dark current	5 nA
Thermal noise coefficient	$100 * 10^{-24}$
Receiver filter bandwidth	$0.75 \times \text{Bit Rate}$
Number of users	3
Attenuation	0.2 dB/km

Signal is split using power splitter of two outputs. The wavelength of FBGs used in upper branch of decoder depends on transmitted wavelengths (one's in code). All the reflected outputs from FBG are added by optical adder and detected by the photo diode (PD) and called as design 1 which is shown in Fig. 1b. Splitting the signal using power splitter of three outputs configuration is called as design 2 as shown in Fig. 1c. When the reflected wavelength (zero position) is selected for FBG, the upper branch filter structure is similar to the complementary decoder filter structure but the difference is that the transmitted signal is given to next FBG as shown in Fig. 1d, e. The transmitted output of the last FBG of upper branch is given to PD. The output of PDs are subtracted using electrical subtractor as shown in Fig. 1d and are called as design 3. Both output signals from the respective branches are subtracted using the optical subtractor and the resultant signal is converted using one PD as shown in Fig. 1e and is called as design 4.

Results and Discussion

Figure 2 displays the log of BER as a function of received power (dBm). Design 4 requires only one PD compared to the other designs because it uses the optical subtractor instead of electrical subtractor. Design 4 gives less probability of error and more receive power compared to others up to length of 100 km. Design 2 receives less power along with smaller values of BER (Table 3).

Figure 3 displays the log of BER as a function of fiber length (km). Design 1 and 4 give less probability of error on comparing with design 2 and 3 up to length of 150 km as shown in Table 4 and for larger length, design 2 and 3 are receiving higher value of BER compared to others.

Figure 4 displays the relation between the fiber length (km) and Q factor for design 3 and 4. Design 4 has higher value Q than design 3 for a length of 150 km. For higher length compared to 150 km, Q factor is degrades more for design 4 and it becomes 0. Design 3 has less degradation and its value is 5.133 for the same length. Design 3 performs better for length greater than 150 km.

Fig. 2 Graph between log of BER and received power (dBm)

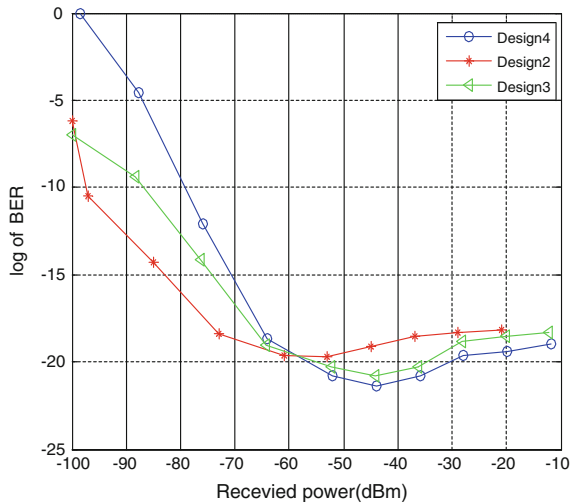


Table 3 Received power for designs at different length is shown

Parameter/design	Received power (dBm) 20 km	Received power (dBm) 100 km	Received power (dBm) 180 km
Design 1	-11.7559	-43.8018	-75.9379
Design 2	-20.9145	-52.9323	-85.0368
Design 3	-12.0989	-44.1431	-76.2735
Design 4	-11.8478	-43.8893	-75.9391

Fig. 3 Graph between log of BER and fiber length (km)

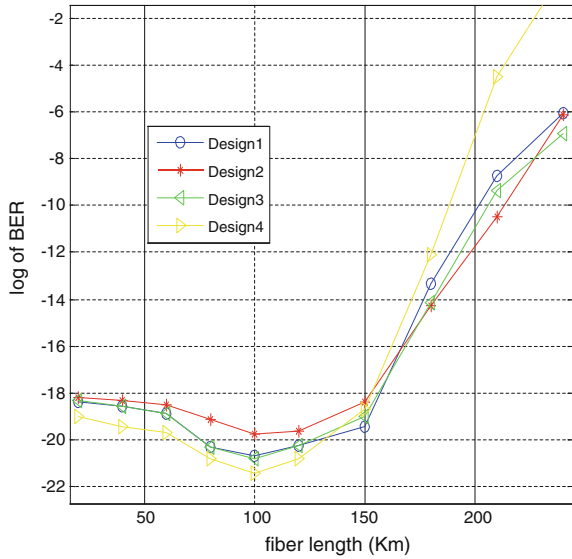


Table 4 BER for designs at different length is presented

Parameter/design	Log of BER 20 km	Log of BER 100 km	Log of BER 180 km
Design 1	-18.3957	-20.6557	-13.3212
Design 2	-18.1919	-19.7218	-14.2971
Design 3	-18.3014	-20.7858	-14.1481
Design 4	-19.0026	-21.4093	-12.1048

Fig. 4 Graph between Q factor and fiber length (km)

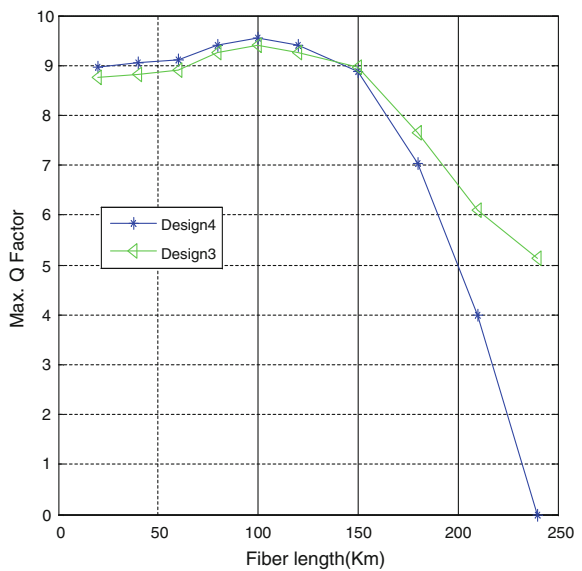


Fig. 5 Graph between log of BER and received power (dBm) for one's wavelength

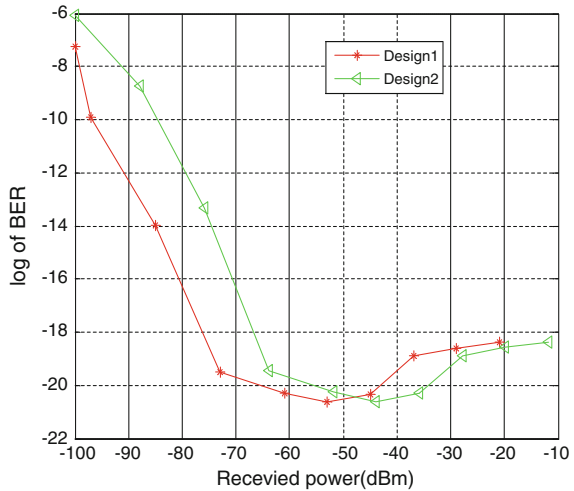


Figure 5 displays the relation between the received power (dBm) and the log of BER. Design 2 receives more power than design 3. Design 2 uses the power splitter of three outputs and design 3 uses the power splitter of two outputs.

Conclusion

Different improvised decoder designs for SAC-OCDMA are proposed and simulated on OptiSystem-13. Design 4 receives more power along with higher BER for lengths up to 150 km. Design 4 achieves Q factor of value 7 up to length 180 km. Design 4 gives better result and it requires one photodiode and not any optical adder for adding frequency compared to other. For length greater than 180 km, design 3 and design 1 are preferred.

References

1. Zhuo, C., Chongxiu, Y., Qi, Z., Zhihui, Y., Daxiong, X.: Spectral efficiency of incoherent OCDMA systems. In: SPIE, vol. 5636 (2005)
2. Arief, A.R., Aljunid, S.A., Anuar, M.S., Junita, M.N., Ahmad, R.B., Ghani, F.: Enhanced performance of new family modified double weight codes spectral amplitude coding optical CDMA system network. In: IEEE International Conference on Control System, Computing and Engineering (ICCSCE), pp. 488, 494, 25–27, Nov 2011
3. Farhat, A., Menif, M., Rezig, H.: Performances of spectral-amplitude-coding optical cdma systems. In: 13th International Conference on Transparent Optical Networks (ICTON), pp. 1–4, 26–30 June 2011

4. Arief, A.R., Aljunid, S.A., Anuar, M.S., Junita, M.N., Ahmad, R.B.: Cardinality enhancement of spectral/spatial modified double weight code optical code division multi-access system by PIIN suppression. *Optik* **124**(19), 3786–3793 (2013)
5. Wei, Z., Ghafouri-Shiraz, H.: Codes for spectral-amplitude-coding optical CDMA systems. *J. Lightwave Technol.* **20**(8), (2002)
6. Norazimah, M.Z., Aljunid, S.A., Fadhil, H.A., Md Zain, A.S.: Analytical comparison of various SAC-OCDMA detection techniques. *IEEE 2nd International Conference on Photonics (ICP)*, pp. 1, 5, 17–19 Oct 2011
7. Abd El Mottaleb, S.A., Fayed, H.A., Abd El Aziz, A., Aly, M.H.: SAC-OCDMA system using different detection techniques. *IOSR-JECE* **9**(2), 55–60 (2014) Ver. III
8. Zahid, A.Z.G., Hasoon, F.N., Shaari, S.: New code structure for enhanced double weight (EDW) code for spectral amplitude coding OCDMA system. In: *ICFCC*, Kuala Lumpur, Malaysia, pp. 658–661 (2009)

An Efficient Trust-Based Routing Scheme by Max-Min Composition of Fuzzy Logic for MANET

Joydeep Kundu, Koushik Majumder and Debashis De

Abstract Mobile ad hoc network is an infrastructure-less network of distributed nodes. It is spontaneous, self-organized, and also dynamic. In ad hoc environment, due to frequent communication among nodes and lack of enough information about nodes, it is complicated to measure trust. It has been observed that the nature of trust is dynamic that means its value varies with respect to time. Therefore, fuzzy logic is the more suitable technique for expressing and computing the node's trust value than other existing probabilistic approach. In this paper, node's trust values are converted into membership function of the fuzzy logic with the help of Gaussian membership function for clustered ad hoc network. Then cluster head is able to obtain the highly trusted nodes by the fuzzy logic-based max-min composition technique for the purpose of successful communication between sources and destination, so that it can be able to identify and save the nodes against non-cooperative nodes efficiently. It saves the energy consumption by avoiding packet delivery to the non-cooperative nodes by selecting the trusted neighbors for the purpose of communication. Therefore, we have been able to design a reliable and better throughput trust routing method for clustered ad hoc network using max-min composition technique of the membership function of fuzzy logic.

Keywords Cluster · Fuzzy logic · Fuzzy membership function · Max-min composition · Trust

Introduction

A mobile ad hoc network is made up of autonomous nodes which are communicated with others in a self-organizing manner. Thus it is a dynamic and infrastructure-less network [1]. The performance of such network depends on the

Joydeep Kundu · Koushik Majumder (✉) · Debashis De
Department of Computer Science and Engineering, West Bengal
University of Technology, Kolkata, West Bengal, India
e-mail: koushik@ieee.org

cooperative and trust nature of the neighborhood nodes. Each node in the network acts as a router and forwards data packets for other nodes. Several trust-based routings have been established but still it demands for newer methods for the purpose of more reliable, robust, simple, and secure routing in MANET. The routing protocols play an important role for transferring data packets. With respect to security, mainly two basic routings such as cryptographic and trust-based mechanism are used in the field of ad hoc environment. Cryptographic techniques are used to protect the data packets which are transmitted in the clustered ad hoc network. The primary goal of the cryptography-based mechanism is to address confidentiality, node's authentication, and integrity of the data for the purpose of information security. But the major problem with the cryptographic techniques is that this technique is computationally intensive and also fails to detect the malicious nodes. Therefore, these techniques are not suitable to be incorporated in the field of ad hoc network which is prone to different types of security vulnerabilities and where constraint of the resources is an important issue. Here, an alternative trust-based mechanism can also be chosen. These schemes are used to provide the trust values of the nodes in order to detect the nodes with malicious intention and thus it secures the data packet transmission from source and destination through trustworthy nodes. The most challenging routing issue in MANET is its dynamic topology due to nodes limited energy, nodes mobility, and the presence of the misbehaving nodes. Therefore, this topology disturbs the presence of current routes among the source and destination. Security mechanisms for wired network cannot be use in MANET due to its infrastructure-less dynamic topology and constraint battery power. Therefore, identifying the malicious nodes in MANET is the most challenging issue. So security solution for MANET routing scheme should satisfy both essential factors in terms of integrity and stability.

This paper contains five sections which are listed below: section "[Related Work](#)" of this paper describes a brief about the related work. Methodologies are discussed in section "[Methodology](#)". Section "[Implementation of Newly Proposed Trust Scheme](#)" explains the detailed description about the fuzzy-based proposed protocol. Finally, section "[Conclusion](#)" concludes the paper.

Related Work

Various types of trust-based methods have been developed that focus on different types of performance metrics of the nodes. It has been seen that the nodes in ad hoc network act as a router, so nodes may have complete processing capabilities, e.g., laptops, cell phones, etc. In most of the cases, in terms of secure routing protocols [2] or secure key management protocols [3], the security solutions can be described. Secure key management protocols require high computational overhead on the nodes. But in practice, nodes have limited power in the ad hoc network. Secure routing protocols depend on the trust model for avoiding the congestion within the network and influence them to perform in a self-organizing manner. Thus the total

trust measurement within a cluster is obtained by fuzzified the factors like packet delivery ratio and energy factor into our scheme. Some of the existing secure routing protocols are described below. Weighted cluster algorithm (WCA) is proposed for MANET in [4]. WCA chooses the cluster head based on the factors like ability to handle nodes, mobility, communication range, etc. It computes the average weight of every node using these factors. Then the node with minimum weight is elected as a cluster head (CH). K-hop connectivity ID clustering algorithm (KCONID) is described in [5]. According to mechanism, the node whose connectivity is large is selected as a cluster head. If the connectivity values of two cluster members within the same cluster same then KCONID protocol selects the node having lower ID as a CH.

Methodology

(a) *Fundamental concept about fuzzy logic implementation with fuzzy membership function*

In fuzzy logic, the truth value is the essential factor for any type of statements. The truth values of the statements and membership values of the functions are represented by a value within the range [0.0, 1.0] in fuzzy logic and fuzzy sets, respectively, where 0.0 and 1.0 indicate the absolute false and absolute true decision in fuzzy system. The other values within the range can be computed with the help of fuzzy membership function (Gaussian membership function, Triangular membership function). For implementing fuzzy logic into a trust-based model, it must have the characteristics [6]: (a) it takes the trust knowledge from different nodes into its trust score matrix; (b) each node should be able to compute its own trust score; and (c) it should be dependable and robust against a node with malicious intention. There are several fuzzy membership functions [7] used in fuzzy systems. One of the functions has listed below:

Gaussian Membership Function

A Gaussian membership function is represented by (1), where the parameters c and σ are used to compute the center and width of the curve of the membership function:

$$\text{Gaussian}(x : c, \sigma) = e^{-\frac{1}{2}(\frac{TR-c}{\sigma})^2} \quad (1)$$

The Gaussian membership function has two-sided membership function, where the first and second functions describe the left and right side curve of the membership function. The left side function represents the left side curve and right side function determines the right side curve. Normally, center of the left side curve is less than the center of the right side curve.

(b) Fuzzy logic-based Max-min composition rule

The basic rules for obtaining the trust scores (high (H), medium (M), low (L)) based on the max-min composition technique are listed below [8], where TR is the set of

universe of discourse of the trust values between the ranges 0–50 and N is the set of universe of discourse of node ratings between the ranges 1–10 ((1–3, Malicious node), (4–6, Medium trusted node), (7–10, High trusted node)).

Scenario 1

- (i) IF trust value is HIGH THEN node is TRUSTED:

$$R_1(TR, N) = (HXT) \cup (\bar{H}XN) \quad (2)$$

- (ii) The condition for highly trusted node is

$$R_H = H \circ R_1(TR, N); \quad (3)$$

where ‘ \circ ’ denotes max-min composition.

Scenario 2

- (i) IF trust value is MEDIUM THEN node is MEDIUM TRUSTED:

$$R_2(TR, N) = (MXMT) \cup (\bar{M}XN) \quad (4)$$

- (ii) The condition for medium trusted node is

$$R_M = H \circ R_2(TR, N); \quad (5)$$

Scenario 3

- (i) IF trust value is LOW THEN node is MALICIOUS:

$$R_3(TR, N) = (LXM) \cup (\bar{L}XN) \quad (6)$$

- (ii) The condition for Malicious/low trusted node is

$$R_L = H \circ R_3(TR, N); \quad (7)$$

So the general rule of fuzzy logic-based max-min composition for highly trusted nodes is represented below:

$$R_1(TR, N)_{50 \times 10} = HXT_{50 \times 10} \cup \bar{H}XN_{50 \times 10}$$

$$R_H = H \circ R_1(TR, N) = H_{1 \times 50} \circ R_{50 \times 11} = R_{1 \times 11}$$

$$\begin{aligned} R_H &= H \circ R_1(TR, N) = H_{1 \times 50} \circ R_{50 \times 11} = R_{1 \times 11} \\ &= [\text{Max}\{\min(H_{1,1}, R_{1,1,1}), \min(H_{1,2}, R_{1,2,1}), \dots, \min(H_{1,50}, R_{1,50,1})\}, \dots, \\ &\quad \text{Max}\{\min(H_{1,1}, R_{1,1,50}), \min(H_{1,2}, R_{1,2,50}), \dots, \min(H_{1,50}, R_{1,50,50})\}] \end{aligned} \quad (8)$$

Implementation of Newly Proposed Trust Scheme

The main objective of the proposed trust-based routing scheme is to send packets successfully through a trusted and energy-efficient route in clustered ad hoc network. Therefore, it is able to discard the non-cooperative node during the time of active route selection. In this protocol, CH calculates the trust score about its all cluster members (CMs) based on the max-min composition of fuzzy logic within its trust score matrix [8, 9]. At first, the source node forwards the 'Hello' message to the cluster head (CH) for discovering the multiple routes to destination. The CH examines if the destination node belongs to its cluster or not. If it is found into the same cluster, then a positive feedback should be sent to the source and source obtains the multiple destination routes through intra-cluster routing. Otherwise, it sends a negative acknowledgement that means the destination does not belong to that cluster. At that time CH of that cluster communicates with its neighbor CH via the gateway nodes for discovering the destination. Whenever the neighbor CH finds the destination within its cluster, it immediately sends the route discovery message to that CH through the gateway nodes either by direct or via neighbor CHs (inter-cluster routing). After finding the multiple routes, source forwards the route-request message to its neighbor cluster members for obtaining the instant values of packet forwarding ratio. Every cluster member computes the packet transmission ratio at its neighbor cluster member [9]. Then these numerical values are converted into the fuzzy membership value by fuzzy membership function (Triangular and Gaussian membership function). Source sends both the values of its neighbor CMs to the CH, and CH then calculates the total trust values of all individual CM within its trust score matrix. It (CH) converts the numerical value of trust scores into fuzzy membership value using max-min composition of fuzzy logic. The membership values of the cluster members are preserved by the CH in the form of matrix dynamically. Finally, CH finds the highly trusted CMs based on the fuzzy logic-based trust computation unit and send a most trusted route discovery message to the source. Thus source establishes a highly trusted route to the destination and transfers the data packets successfully until the better route is obtained.

Conclusion

In this paper we have designed a trust-based routing protocol for clustered-based MANET. The main objective of this routing scheme is to obtain the most reliable path during the time of packet transmission from source to destination. This mechanism is able to avoid the choosing of a malicious node which acts as a genuine node in the field of ad hoc network. This paper explains that how the cluster head computes its trust score matrix according to the fuzzy logic-based max-min composition for the highly trusted nodes. The CH is able to obtain the set of maximum trusted CMs (cluster members) from the participated member nodes

using the fuzzy logic-based max-min composition technique. In this trust routing scheme, we consider the max-min composition because it performs better than the other projection of fuzzy relation such as min-max composition, Cartesian product, etc. Thus our enhanced and simple trust evaluation scheme can efficiently detect and protect against malicious nodes.

References

1. Kumar, M., Mishra, R.: An overview of MANET: history, challenges and applications. *Indian J. Comput. Sci. Eng. (IJCSE)* **3**(1) 2012
2. Zapata, M.G., Asokan, N.: Securing ad hoc routing protocols. In: *Proceedings of ACM Workshop on Wireless Security (WiSe '02)*, pp. 1–10. ACM Press, Atlanta, USA. Sept 2002. <http://doi.acm.org/10.1145/570681.570682>
3. Capkun, S., Buttyan, L., Hubaux, J.-P.: Self-organized public-key management for mobile ad hoc networks. In: *Proceedings of ACM Workshop on Wireless Security (WiSe '02)*, Atlanta, USA, Sept 2002. <http://citeseer.nj.nec.com/capkun02selforganized.html>
4. Li, X., Yihui, Z.: A new reputation-based trust management strategy for clustered ad hoc networks. In: *An International Conference on Networks Security, Wireless Communications and Trusted Computing* (2009)
5. Chatterjee, P.: Trust based clustering and secure routing scheme for mobile ad hoc networks. *Int. J. Comput. Netw. Commun. (IJCNC)*, **1**(2) (2009)
6. Luo, j., Liu, X., Zhang, Y., Ye, D., Xu, Z.: Fuzzy trust recommendation based on collaborative filtering for mobile Ad-hoc networks. This work was supported in part by the National Study abroad Scholarship of China under the Grant No. 27U38009 and the NSERC Discovery Fund under the Grant No. 341823-07
7. Banerjee, P.S., Paulchoudhury, J., Bhadra Chaudhuri, S.R.: Fuzzy membership function in a trust based AODV for MANET. *Int. J. Comput. Netw. Inf. Secur.* **12**, 27–34 (2013). Published Online October 2013 in MECS (<http://www.mecs-press.org/>). doi:10.5815/jjenis.2013.12.04
8. Siddique, M.: Fuzzy decision making using max-min method and minimization of regret method (MMR) (720301-P254). June 2009
9. Kundu, J., Majumder, K.: Design of an efficient trust management mechanism for cluster based MANET using beta reputation rating. In: *Elsevier Science and Technology Publication Under the Book Series Computer Communication Networks*, pp 105–113. ISBN: 9789351072539

Modified D-Latch Enabled BEC1 Carry-Select Adder with Low Power-Delay Product and Area Efficiency

Sakshi Bhatnagar, Harsh Gupta and Swapnil Jain

Abstract In electronic applications, better performance of the digital systems can be achieved using a faster adder circuit. This paper shows a modified carry-select adder (CSA) architecture which has low power and reduced area compared to the regular CSA. This high speed CSA is achieved by replacing the existing binary to excess-1 converter (BEC-1) with D-latch enabled CSA. Regular square-root CSA (SQRT CSA) architectures have also been developed and compared with the proposed BEC-1 D-latch enabled CSA. This work evaluates the performance of delay, area, power, and their products for existing and proposed CSA designs. This shows that proposed D-latch CSA structure is better than the regular and modified SQRT CSA and existing Ripple CSA. The proposed CSA architecture requires approximately 86 % fewer gates and 77 % shorter delay than the original CSA designs.

Keywords Low power • Area efficient • Carry-Select Adder (CSA) • D-latch • Binary to excess-1 converter (BEC-1) • Ripple Carry Adder (RCA) • SQRT CSA

General: The primary focus of this work is to use binary to excess-1 converter (BEC) instead of RCA. This circuit has carry input = 1 in the regular CSA which gives reduced area and less consumption of power [1, 2]. The proposed D-latch CSA has been compared with SQRT CSA as it has lower power and reduced area [3, 4]. The delay and area evaluation methodology of the regular SQRT CSA and modified BEC-1 CSA is presented, and ASIC implementation details with results are analyzed.

Sakshi Bhatnagar (✉)

Apex Institute of Engineering & Technology, RTU, Kota, India
e-mail: sakshi.b22@gmail.com

Harsh Gupta

Department of ECE, SEEC, Manipal University Jaipur (MUJ), Jaipur, India
e-mail: harsh.gupta123@gmail.com

Swapnil Jain

Kautilya Institute of Technology & Engineering, RTU, Kota, India
e-mail: jain.ronik32@gmail.com

© Springer India 2016

N. Afzalpulkar et al. (eds.), *Proceedings of the International Conference on Recent Cognizance in Wireless Communication & Image Processing*,
DOI 10.1007/978-81-322-2638-3_51

Regular 16-Bit CSA

Regular CSA has a circuitry with two ripple carry adders and a MUX. Regular 16-bit CSA having larger area is shown in Fig. 1. It is split into five groups with different bit sized RCA.

In group 2 there are two RCAs, one with $C_{in} = 0$ and the other with $C_{in} = 1$. The output carry of each RCA full adder is directed to a MUX unit for calculating the partial sums and carry as shown in Fig. 2a.

The carry output of group 1 is $c1$ which is the input to MUX as the select logic. $c1$ arrives earlier than $s3$ but later than $s2$. $sum3$ is the result of summation of MUX output and partial sum $s3$; $sum2$ is the summation of MUX result and $c1$. Final carry, $c3$ is the summation of MUX outcome and internal carry. Arrival time of select lines of MUX in group 3, 4, and 5 is always greater than the output arrival time [5]. Group 2 having RCA with $C_{in} = 1$ has two full adders while another having $C_{in} = 0$ has one full adder and one half adder (as $C_{in} = 0$ requires only two inputs) [5]. One full adder has 13 logic gates, one half adder has six logic gates, and a 6:3 MUX comprising of three 2:1 MUXes, each containing four logic gates.

Gate count of CSA = total gates of (FA + HA + MUX)
 FA = $13 * 3 = 39$, HA = $6 * 1 = 6$, MUX = $4 * 3 = 12$
 Total gate count = $39 + 6 + 12 = 57$

Similarly, gate count of other groups can also be calculated. Table 1 shows the Gate Count and Delay of various groups.

So as to reduce the number of increasing logic gates, and make the CSA circuit area efficient, binary to excess-1 converter (BEC) in place of the second RCA block with $C_{in} = 1$.

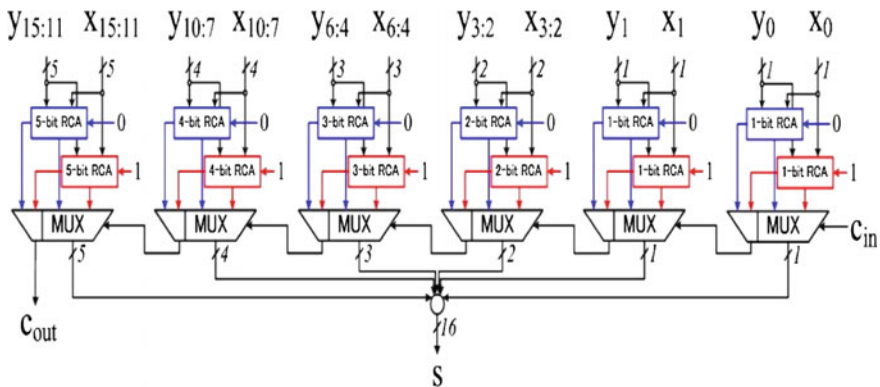


Fig. 1 Regular 16-bit carry-select adder

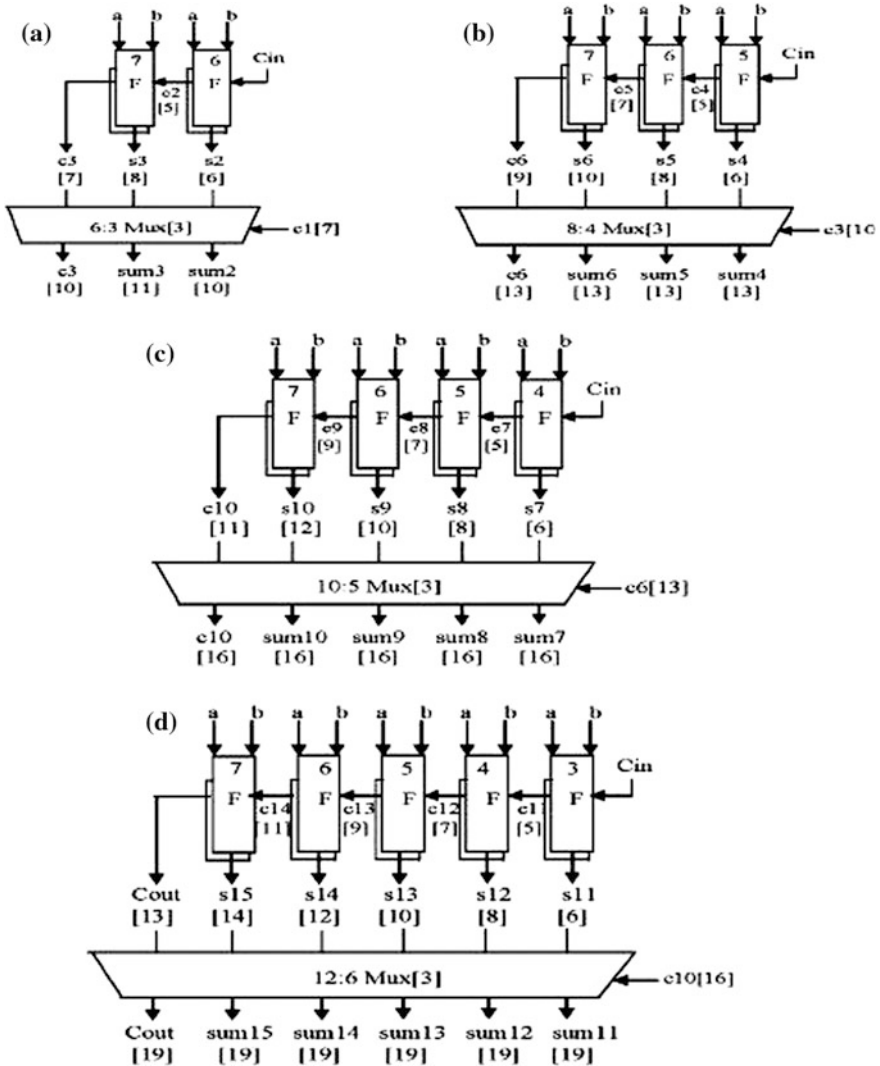


Fig. 2 a group 2, b group 3, c group 4, and d group 5. *F* denotes a full adder unit [5]

Table 1 Area count and delay of regular CSA

Groups	Gate count	Delay
Group 1	26	6
Group 2	57	11
Group 3	87	13
Group 4	117	16
Group 5	147	19

Modified 16-Bit SQRT CSA

The main motive to modify the existing 16-bit regular CSA is to reduce the area and power consumption of the circuit. For this, the n -bit RCA is replaced by an $n + 1$ bit BEC for $C_{in} = 1$.

The 8:4 MUX selects either one of the direct inputs (B0, B1, B2, and B3, each 4-bit) or the output of BEC (4-bit) as its output (S3, S2, S1, and S0) depending upon the value of C_{in} [4]. The 4-bit BEC contains XOR, AND, and NOT gates having inputs B0, B1, B2, B3, and outputs X0, X1, X2, X3. Figure 3 shows the modified 16-bit SQRT CSA. The output using Boolean expression is shown below:

$X3 = B3 \text{ XOR } (B0 \text{ AND } B1 \text{ AND } B2)$
$X2 = B2 \text{ XOR } (B0 \text{ AND } B1)$
$X1 = B0 \text{ XOR } B1$
$X0 = \text{NOT } B0$

16-bit modified CSA using BEC-1: Group 2 has one 2-bit RCA which contains one half adder and one full adder (for $C_{in} = 0$) and has one 3-bit BEC (thereby adding one to the output of 2-bit RCA) for $C_{in} = 1$. The arrival time of select line c1 of MUX is earlier than s3 and c3 but later than s2. Hence, fractional sum s3 and output of MUX gives sum3. Output c3 is dependent on partial input, i.e., c3 and output of MUX. Intermediate sum2 depends on input c1 and MUX output [5]. For the remaining groups, i.e., groups 3, 4, 5, the input select line c1 has greater arrival time than the input data of MUX from BECs (Fig. 4).

The working of modified 16-bit SQRT CSA is similar to regular 16-bit SQRT CSA with reduced area and less power consumption due to fewer number of logic gates used. The area is estimated by the gate count which is calculated below.

Gate count using BECs = total number of (full adder + half adder + MUX + BEC) [5]. Group 2 has one FA, one HA, three MUX, one BEC which contains one XOR gate, one NOT gate, and one AND gate.

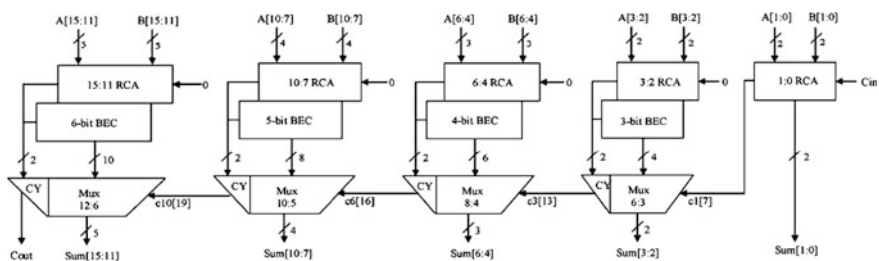


Fig. 3 Modified 16-bit SQRT CSA. The BEC replaces the existing parallel RCA for $C_{in} = 1$ [5]

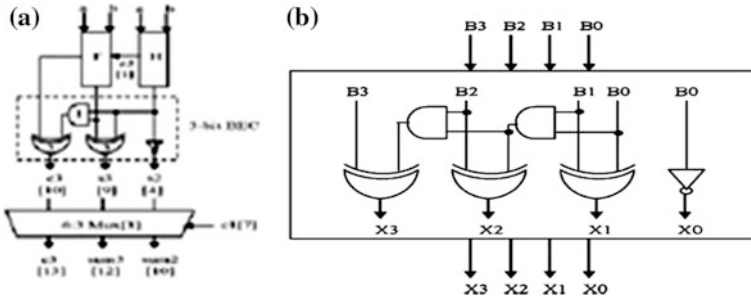


Fig. 4 a group 2 of 16 bit modified CSA. b Internal structure of 4-bit BEC [2]

FA = 1 * 13 = 13, HA = 1 * 6 = 6, MUX = 3 * 4 = 12, AND = 1, NOT = 1, XOR = 2 * 5 = 10

Total logic gates of modified RCA = 13 + 6 + 12 + 10 + 1 + 1 = 43

Total logic gates of modified CSA for group 2 is 43 which is less than the 57 logic gates of regular CSA. Gate counts of other groups can be calculated similarly. Thus, modified CSA saves a gate area of 113 than the existing RCA. Figure 5 shows the layout of a 1-bit modified CSA using BEC. Figure 6 shows 16-bit schematic of modified CSA using BEC and RCA. Here the total delay is calculated as follows:

Time delay = time to compute the first section + time to select sum from subsequent sections.

A CSA scheme using an add-one circuit to replace one carry-ripple adder requires 29.2 % fewer transistors with a speed penalty of 5.9 % for bit length $n = 64$ (Table 2).

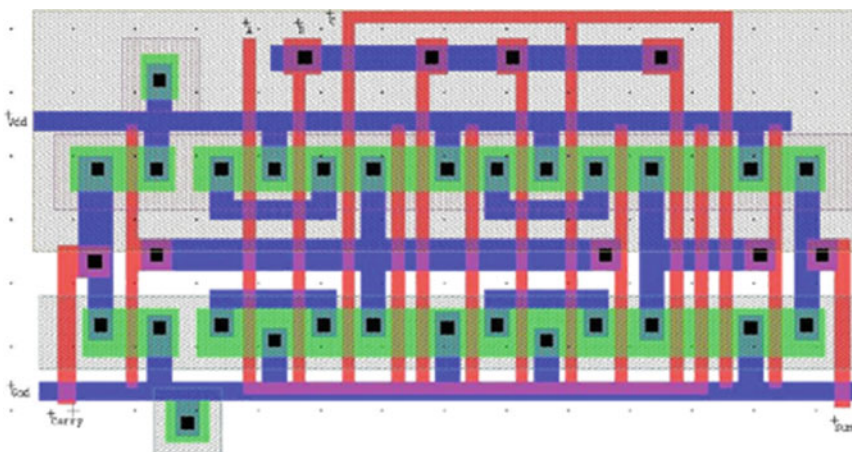


Fig. 5 Layout of 1-bit modified CSA using BEC's

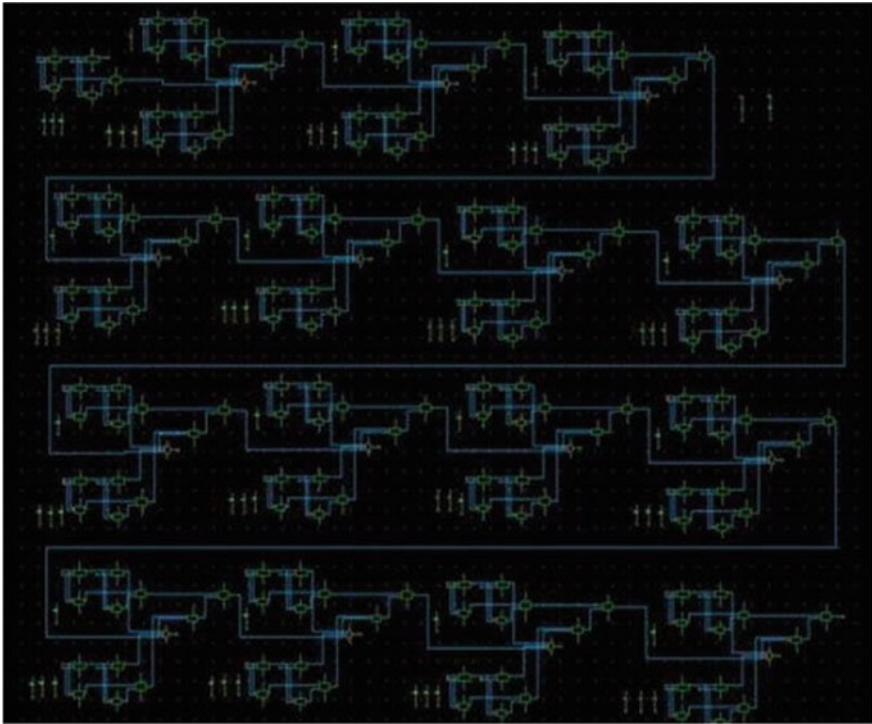


Fig. 6 16-bit schematic of modified CSA using binary to excess-1 convertor

Table 2 Area count and delay of modified CSA

Groups	Gate count	Delay
Group 2	43	13
Group 3	61	16
Group 4	84	19
Group 5	107	22

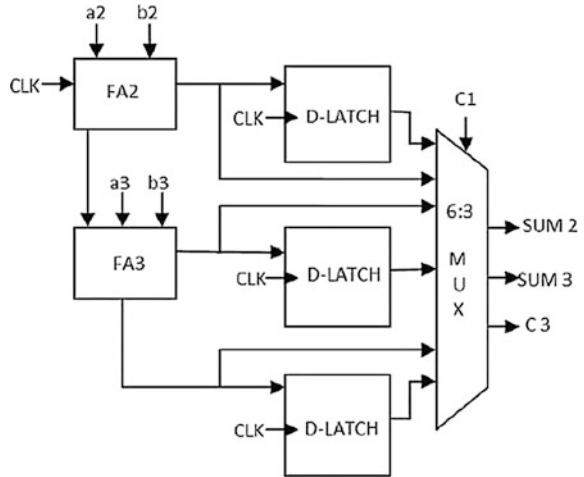
Delay Reduction Using D-Latch Enabled CSA

To reduce the delay, BEC is replaced by D-latch with an enable signal. D-latch is a 1-bit storage device in which when enable signal is HIGH, input data is copied to the output. When enable signal is LOW, then output remains unchanged until enable goes HIGH.

This modified D-latch structure has only one adder which is used to reduce area, delay, and power consumption. One clock cycle performs each of the two additions.

Here, FA2 has the third input as clock pulse. Output sum of FA2 is fed to D-latch and output carry as the third input to FA3. When CLK = 1, addition for

Fig. 7 Internal structure of group 2 [4]



$C_{in} = 1$ is performed, while $CLK = 0$, $C_{in} = 0$ and sum is stored in adder itself [4] (Fig. 7).

Two of the three D-latches are used to store SUM 2 and SUM 3 from FA2 and FA3, respectively, and the third latch is used to store carry. When the clock pulse is LOW, addition is performed with carry = 0, i.e., sum of a2 and b2 is produced assuming carry as zero. When clock pulse is LOW or zero, then all the latches are disabled. When clock pulse is HIGH or on, the latches are enabled. So in this case, addition is performed with carry = 1. Latches are used to store sum and carry. 6:3 multiplexer, which is a combination of three 2:1 MUX, is used to select the actual sum and carry depending on the value of C1, which is either 0 or 1 [4].

Result Analysis

Simulation results are given in Table 3 and Figs. 8 and 9 for different 16-bit CSA structures depicting the variation of power consumed and propagation delay.

Table 3 Simulation results of different CSAs

Primitive adder (16-bit)	Delay (ns)	Power (mW)	Gate count
Regular CSA	63	760	846
SQRT CSA	18	320	435
BEC enabled CSA	26	265	386
D-latched CSA	14	160	112

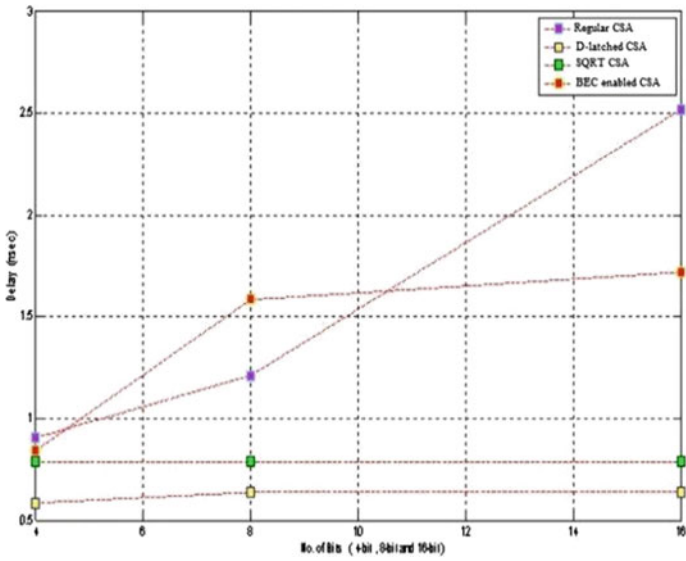


Fig. 8 Delay versus number of bits (4, 8, and 16)

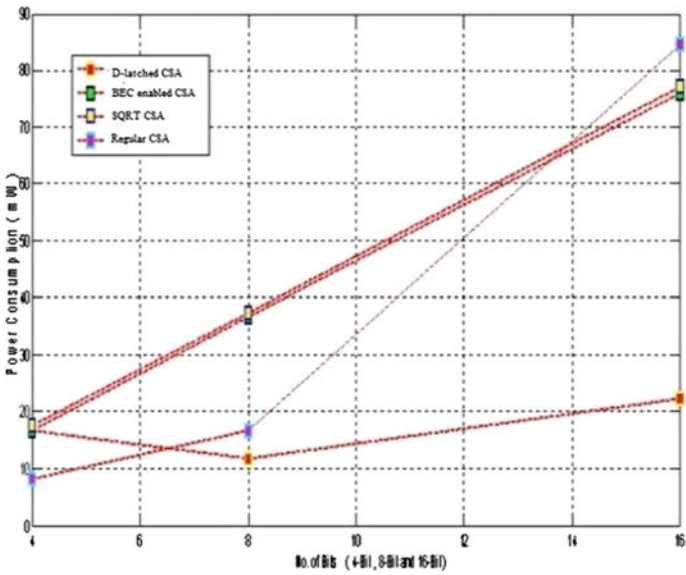


Fig. 9 Power versus number of bits (4, 8, and 16)

Conclusion

This paper presents a novel technique for area optimization by replacing the existing regular 16-bit SQRT CSA by modified CSA using BEC blocks by minimizing the gate count from 57 to 43 at the cost of increased delay. In order to further reduce area and power consumption, BEC adder blocks are replaced by D-latch enabled CSA, and used with existing RCA blocks. The reduced delay of D-latch CSA significantly has large improvements in power-delay product of the overall circuit. Figure 8 shows a 16-bit modified CSA using binary to excess-1 convertor, simulated using Tanner Tools v13. The simulation results are given in Table 3 for all the different CSA structures depicting the variation of power consumed and propagation delay with area count.

References

1. Mugilvannan, L., Ramasamy, S.: Low-power and area-efficient Carry Select Adder using modified BEC-1 converter. In: IEEE 4th ICCCNT 2013, 4–6 July 2013, Tiruchengode, India
2. Yasmeen, W., Sandhya Rani, M.: Area efficient Carry Select Adder using binary excess code. In: International Conference on Advances in Computer Theory and Engineering, 04 Aug 2013, Bengaluru. ISBN: 978-93-83060-08-5
3. Hemima, R., Chrisjin Gnana Suji, C.: Design of 4 bit low power Carry Select Adder. In: Proceedings of 2011 International Conference on Signal Processing, Communication Computing and Network Technologies (ICSCCN 2011)
4. Edison, A.J., Manikandababu, C.S.: An efficient CSLA architecture for VLSI hardware implementation. In: International Conference of Management, IT and Engineering, vol. 2, issue 5, May 2012
5. Ramkumar, B., Kittur, H.M.: IEEE Trans. Very Large Scale Integr. (VLSI) Syst. **20**(2) (2012)
6. Rama Krishna Reddy, J., Rakesh Chowdary, G., Venkata Rama Krishna, T.: High speed Carry Select Adder for ALU blocks. Int. J. Eng. Technol. **5**(3) (2013)
7. Paradhasaradhi, D., Anusudha, K.: An area efficient enhanced SQRT Carry Select Adder. Int. J. Eng. Res. Appl. **3**(6), 876–880 (2013). ISSN: 2248-9622
8. Saxena, P., Purohit, U., Joshi, P.: Analysis of low power, area efficient and high speed fast adder. Int. J. Adv. Res. Comput. Commun. Eng. **2**(9) (2013)
9. Devi, P., Girdher, A., Singh, B.: Improved Carry Select Adder with reduced area and low power consumption. Int. J. Comput. Appl. **3**(4) (2010)

Identification of Devanagari Script from Bilingual Printed Text Documents

Ranjana S. Zinjore and R.J. Ramteke

Abstract Bilingual script identification is one of the challenging steps in the development of optical character recognition (OCR). As India is a multilingual multiscrypt country, in its constitution for each state, the respective state language and the script is used for state official work. In Maharashtra, Marathi is the state official language with Devanagari script and English as the communication language. We need to develop the OCR that can identify and differentiate both scripts. This paper presents a research work for identification of Devanagari (Marathi) script from printed bilingual text document. In our work, we have developed a methodology that applies projection profile in line segmentation which is followed by twofold word segmentation. We examined the use of structural features (header-line pixel count and intercharacter gap) as a tool for determining the Devanagari words. The heuristic rule approach is used for classification. The proposed method is implemented on ten printed bilingual text images. These images consist of 77 lines and 474 words of varying font sizes. The result of our experimentation shows accuracy of 87.25 % in identification of Marathi words.

Keywords Bilingual optical character recognition • Script identification • Twofold word segmentation • Structural feature • Heuristic rule

Introduction

Automatic language/script identification and processing of an identified language from text document is useful and important in bilingual and multilingual environments like India, where a single document may contain words in two language

R.S. Zinjore (✉)

KCES's Institute of Management & Research, Jalgaon, India

e-mail: ranjanazinjore_14@rediffmail.com

R.J. Ramteke

School of Computer Sciences, North Maharashtra University, Jalgaon, India

e-mail: rakeshramteke@yahoo.co.in

© Springer India 2016

N. Afzalpulkar et al. (eds.), *Proceedings of the International Conference on Recent Cognizance in Wireless Communication & Image Processing*, DOI 10.1007/978-81-322-2638-3_52

scripts like bank forms and examination papers [1]. One language is the state official language and English is treated as a binding language. To develop bilingual optical character recognition (OCR) system, it is necessary to identify and separate both types of scripts before passing on to specific OCR. We have developed a system that can identify Devanagari (Marathi) script from ten different bilingual documents. In India, for official work, more than 22 languages are used which are derived from 12 different scripts [2]. Marathi is the official language of Maharashtra, where more than 73 million people use this language for communication purposes. Moreover, English is taught and used largely almost all over India. The script form of Marathi, called Devanagari, consists of 13 vowels, 36 consonants, and 10 numbers [3]. Marathi has one important distinct feature compared to English, which is known as header line/Shirorekha [4]. Also, Marathi does not consist of different characters formations such as upper and lower case. English is derived from Roman script that consists of 5 vowels, 21 consonants, and 10 numerals. It has a total of 26 upper case and lower case letters [5].

Motivation and Literature Review

In the recent research, there is a demand to develop printed and handwritten bilingual OCR which is useful in many areas such as in the post office, banks, railways, schools, income tax, and as reading aids for blind people. Society needs benefits from information technology to revolutionize the way visually impaired people read and write, and to make them totally independent for their education. The bilingual OCR system can work for visually impaired people if voice synthesizer is attached.

Chaudhuri proposed an OCR system for Bangla and Devanagari languages, where these two scripts have many features in common. For character recognition they considered a few stroke features [1, 6]. Sarkar et al. [2] discussed horizontalness, number of matra pixel and segmentation point pixel, and foreground-background transition as features for identification of handwritten Bangla/Devanagari text mixed with Roma script. Dhandra et al. [7] suggested horizontal and vertical projection profile method for line and word level segmentation. Aspect ratio, eccentricity, and strokes are the discriminating features used for implementation; in addition to this, k-nearest neighbor is used for classification. A system has been proposed for tri-lingual identification (Hindi, English, and Kannada) using morphological dilation and modular neural network for classification [8]. Zhou et al. [9] proposed a system for Bangla/English script identification using connected component profile with application to destination address block of Bangladesh envelop images. Hassan et al. [10] discussed bilingual script identification at page/block and word level using texture- and shape- based features. To differentiate between character and word aspect ratio it has been used and nine structural features for

identification of Gurumukhi and Roman characters [11]. Aithal et al. [12] discussed horizontal projection profile-based feature for finding peak and valley points. In addition to this, rule-based approach is used to classify Hindi, English, and Kannada languages. Padma et al. [13] suggested top and bottom profile as a feature for separating Hindi, English, and Kannada text lines from a sample document. Peak and moments of horizontal projection profile and runlength histogram are used for Arabic–English language identification from document images [14]. Godara et al. [15] proposed a word-level method for separating Latin words from Devanagari script based on horizontal and vertical projection profile.

Proposed Work

Automatic script identification for printed document can be classified into four categories: (a) The scheme based on analysis of connected component [9]. (b) Text-lines, words, and character-level analysis [10]. (c) Text blocks analysis (d) Hybrid information of connected component, text lines, etc. We have used word-level analysis for script identification; whereas script identification consists of stages like noise removal (preprocessing), line and word segmentation, feature extraction, and classification which are represented in Fig. 1. In this section, we have discussed some algorithms for separating Marathi words from bilingual documents.

Preprocessing and Segmentation

The experimental bilingual data have been collected from different sources such as newspapers, textbooks, book covers, and manually generated text. Some sample datasets are shown in Fig. 2.

The generated documents are scanned using scanner at 300 DPI. Color images are first converted into grayscale images and then into binary images using Otsu’s

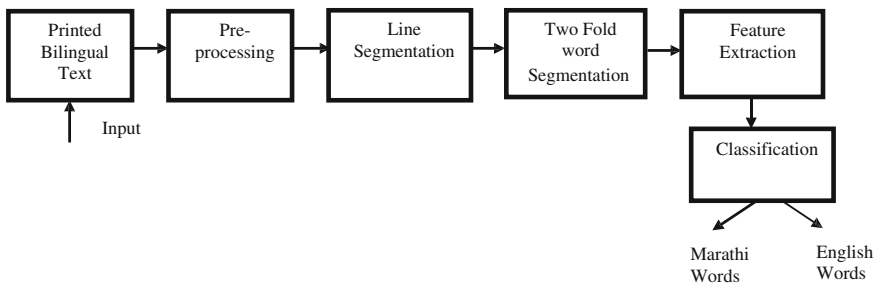


Fig. 1 Architecture of bilingual script identification

thresholding. Morphological opening operation is used for removing noise from the documents.

For line segmentation, horizontal projection profile is used. This approach has been experimented on ten different bilingual documents and we found satisfactory results of line segmentation except the problem of merge line shown in newspaper dataset of Fig. 2b. Merge line problem occurs in Devanagari script because, the gap between two consecutive lines are less due to some first line characters that appear in lower zone and the next line characters that appear in upper zone as shown in Fig. 3. Following line segmentation, algorithm is developed to solve this problem.

Algorithm Line_Segment(Image, LineImage)

1. Plot a histogram (H) based on row-wise sum of black pixels.
2. H consists of peak and valley of white pixels. With the use of H find white pixel vallies width (ws) as:

```

For i = 1: length(H)
Compute: ws1[i] = starting pixel of valley i
        ws2[i] = end pixel of valley i
End

```

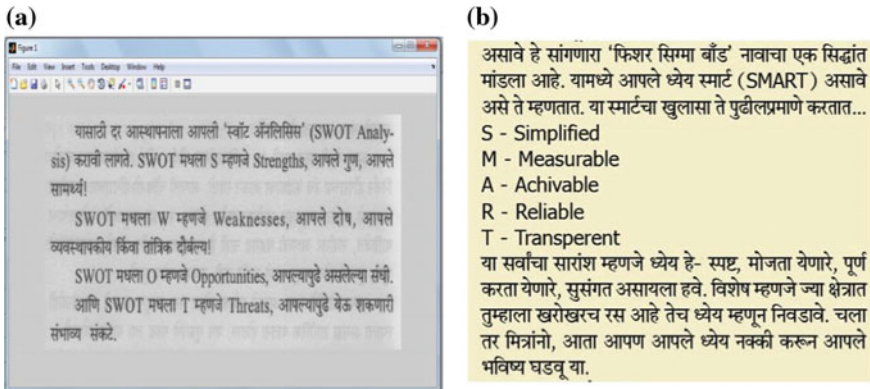


Fig. 2 Bilingual document datasets (a) and (b). a Book dataset. b Newspaper dataset

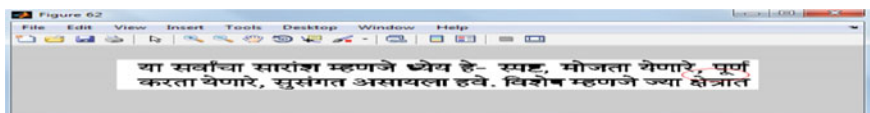


Fig. 3 Line segmentation problem

3. Calculate mean of ws1 using Eqs. 1 and 2, where n is length of ws1.

Let fcnt1 = 0

$$\text{fcnt1} = \text{fcnt1} + \sum_{i=1}^n \text{ws1}(i+1) \quad (1)$$

$$\text{mean} = \text{fcnt1}/n \quad (2)$$

4. Find maximum difference (max_diff) from ws1 using Eq. 3.

$$\text{max_diff} = \max \left(\sum_{i=1}^n \text{ws1}(i+1) - \text{ws1}(i) \right) \quad (3)$$

5. Calculate ceil of the ratio (max_diff/mean) to identify how many lines are merged into a single line.
6. For segmenting the merged line into separate lines, threshold (Th-value) is calculated using Eq. 4.

$$\text{Th-value} = \text{Ratio} * \text{mean} \quad (4)$$

7. For line segmentation we perform the following steps:

Let k = 1, endp = size(ws1), v1 = 1, and v2 = size of image

While ws2(k) < ws1(endp)

diff = ws1(k+1) - ws1(k)

If (diff > Th-value)

Segment the merge lines using Eq. 5

$$\text{New-Cutoff-ht} = \text{max_Diff}/\text{Ratio} \quad (5)$$

kk1 = ws2(k)



Fig. 4 a Segmented line of dataset shown in Fig. 2b. b Segmented line of dataset shown in Fig. 2a

Crop-line-parameters = [v1 kk1 v2 New-Cutoff-ht]

For next line add the new-cutoff-ht to kk1; do until not reach (max_diff). Result [Fig. 4a].

Else

Separate the line easily using imcrop function by passing parameters as

kk1 = ws2(k)

kk2 = ws1(k+1) - ws2(k)

Crop-line-parameters = [v1 kk1 v2 kk2]; Result [Fig. 4b].

8. k = k+1

The segmented lines are divided into words for word-level script identification. The algorithm for word segmentation is as follows:

Twofold Word Segmentation Algorithm

Input: Invert segmented line

Output: Segmented words

First fold Segmentation

1. Plot a histogram (VH) based on column-wise sum of white pixels.
2. VH consists of peak and valley of black pixels. With the use of VH find black pixel vallies range (vs) as

For j = 1: length(VH)

 Compute: vs1[j] = starting pixel of valley j

 vs2[j] = end pixel of valley j

 vs3[j] = end pixel of valley j - starting pixel of valley j

End

3. It is easy to extract Marathi words from bilingual document due to Shirorkha, whereas English words have intercharacter gap (Fig. 5). To extract English words threshold value is set.
4. Threshold value is calculated as follows:
 - 4.1. Let h1 = height of a line
 - 4.2. If height of a line is in between 20 and 29 then threshold value is th = h1/7;

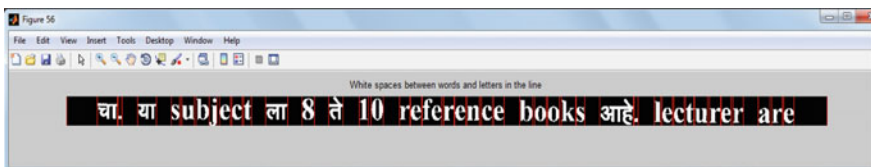


Fig. 5 Spacing between the words and characters

4.2.1. Whereas for small font size document line, if height of the line is in between 10 and 20 then threshold value is

$$th = \text{floor}(h1/3);$$

4.3. For other lines threshold is considered as

4.4.1 Let $cntz = 0$, $finalth = 0$, $newcnt = 0$ and $p = \text{length}(VS3)$

```

For z = 1: length(VS3)
  if ( z <= p-1)
    cntz = cntz + p(z)
  else
    If the line having more white space in compared to words then:
    newcnt = 3*cntz;
    if (VS3(p) <= newcnt)
      finalth = cntz+VS3(p);
    else
      finalth= cntz;
    end
  end

```

5. Apply morphological operation as thinning on segmented words.
6. Finally, extract the boundary of a word by finding left, right, top, and bottom first pixels from thin word image.

Infold Segmentation

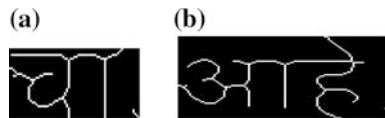
According to firstfold word segmentation algorithm, the words are segmented with a full stop as shown in Fig. 6. For feature extraction, it is necessary to remove full stop from the word image. It is observed that full stop is present at the right bottom corner of the word and the size of full stop after thinning is not more than 6 pixels.

Algorithm

Input: Bilingual words considered as $img1$

Output: Bilingual words without full stop

Fig. 6 Segmented word of Fig. 4 according to firstfold word segmentation



1.1 Calculate column-wise summation of white pixel as

Let col_pixel = [column_no; column-wise summation of white pixel of a input word image]

```
colsum = col_pixel(:,2)
Len1 = Length (colsum)
Len2 = 93% of Len1
dot = 1, cnt = 0 and cutimage =0
```

1.2 Find the presence of the dot in the rightmost corner of the word image as follows: For a = Len1:-1:Len2

```
For a = Len1 : -1 : Len2
if colsum(a) == 1 || 2 and dot is in between 1-6 then increment the dot by 1.
else
if colsum(a) == 0 && dot<=6 && colsum(a+1) == 1||2
cutimage = a
```

1.3 Remove the dot from the image as (result is shown in Fig. 7):

```
If cutimage > 0
[r11 c11] = size(img1)
maxno = max(r11,c11)
Imagecrop-parameters = imcrop(img1,[ 0 0 cutimage maxno])
```

Feature Extraction

Feature extraction is an integral part of recognition system that aims to identify patterns by means of minimum numbers of features that are effective in discriminating pattern classes. Feature extraction is considered under structural, statistical, and global transformation. For word-level Devanagari script identification we used two different word-level structural features that involve header-line pixel count and intercharacter gap.

1. Header-line Pixel Count (F1): Header-line is defined as horizontal row in upper 40 % part of a word with the maximum number of white pixels (maxpixel), if image is inverted as shown in Fig. 7. [11]. Header line is a very important

Fig. 7 Images of removed full stop from Fig. 5



feature for Marathi words compared to English words. The maxpixel is useful to separate Marathi words from English words by considered threshold value (th). In our work, we considered 53 % of word length as the threshold value.

2. Intercharacter gap (F2): Another distinct feature of Marathi words is the absence or approximately 2 % of intercharacter gap as the words are connected with header-line/Shirorekha, whereas maximum English words has intercharacter gap (approximately more than 98 %). For extracting this feature, we calculated column-wise summation of white pixels (vcnt) and from vcnt we have counted only those pixels whose value is equal to zero and stored in totnoofvzero.

Classification

For classification of Marathi words from bilingual documents we used heuristic rule-based approach as follows:

Algorithm()

Input: Marathi and English words

Output : Marathi words

1. Compute Feature F1
2. Compute Feature F2
3. Identification of Marathi words as follows:
 - If $\text{maxpixel} > \text{th}$ OR $\text{totnoofvzero} < (2 * \text{vcnt})$
 - Words = "Marathi"
 - Else
 - Words = "English"
 - End
4. Return words

Result and Discussion

We evaluated the performance of the proposed system for identification of Devanagari (Marathi) script from bilingual document. For experimentation, ten documents with varying font size are used with 77 lines and 474 words. Horizontal projection profile is used for line segmentation. In addition to this, merge line segmentation problem is solved in our system. In firstfold segmentation, words are segmented by varying threshold value based on different line heights followed by morphological thinning operation. According to secondfold segmentation full stop is removed from thin word image for feature extraction. Header-line pixel count and intercharacter gap is used as a feature for script identification. For the total accuracy of Marathi words correct classification from bilingual document is 87.25 % as shown in Table 1. Proposed algorithm misclassified some single English characters like (T, F, R, E, I) as Marathi words.

Table 1 Accuracy (%) of Marathi words identification

No. of Bilingual documents	Total no. of lines	Total no. of words	Total no. of Marathi and English words		Total no. of Marathi words identified	Marathi words		
			Marathi words	English words		Correct classified (%)	Misclassified (%)	Rejection (%)
Document1 (manually created dataset)	08	78	45	33	45 + 03 (English)	93.75	6.25	0.00
Document2 (manually created dataset)	04	29	18	11	18	100	0.00	0.00
Document3 (scanned book chapter)	08	51	36	15	34 + 03 (English)	87.18	7.69	5.13
Document4 (scanned book chapter)	08	90	49	41	41	83.67	0.00	16.33
Document5 (scanned book chapter)	11	67	52	15	48 + 03 (English)	87.27	5.46	7.27
Document6 (newspaper advertisement)	05	38	28	10	27	96.43	0.00	3.57
Document7 (newspaper text)	13	76	65	11	65 + 04 (English)	94.20	5.80	0.00
Document8 (book cover text)	06	16	03	13	03 + 01 (English)	75	25	0.00
Document9 (book cover text)	08	13	05	08	04	80	0.00	20
Document10 (book cover text)	06	16	03	13	03 + 01 (English)	75	25	0.00

Conclusion

In this paper, a simple and efficient algorithm is used for identification of Devanagari (Marathi) script from printed bilingual document with accuracy of 87.25 %. Marathi and English language are considered for experimentation due to the requirement of bilingual optical character recognition (OCR) in various areas like at the post office, bank, school, railways. In the future, we propose to separate English numerals and words from sampled bilingual documents used officially in bank and government operations.

References

1. Chaudhuri, B.B., Pal, U.: Automatic separation of words in Multi-lingual Multi-script India Documents. In: Proceedings of the Fourth International Conference on Document Analysis and Recognition, IEEE, 18–20 Aug 1997
2. Sarkar, R., Das, N., Basu, S., Kundu, M., Nasipuri, M., Kumar Basu, D.: Word level script identification from Bangla and Devanagari handwritten texts mixed with Roman Script. *J. Comput.* **2**(2) (2010). ISSN: 2151-9617
3. Ajmire, P.E., Dharaskar, P.V., Thakare, V.M.: A Comparative study of handwritten Marathi character recognition. In: National Conference on Innovative Paradigms in Engineering and Technology (NCIPET-2012), Proceedings published by International Journal of Computer Application, pp. 26–28 (2012)
4. Shelke, S., Apte, S.: A multistage handwritten Marathi compound character recognition scheme using neural networks and wavelet features. *Int. J. Signal Process. Image Process. Pattern Recogn.* **4** (2011)
5. Ambekar, A.G., Hinge, C.S., Kulkarni, S.S.: Bilingual OCR for printed English and Devnagari Text. *Int. J. Res.* **2**(1) (2013). ISSN: 2250-1991
6. Chaudhuri, B.B., Pal, U.: An OCR system to read two Indian language scripts: Bangla and Devnagari (Hindi). In: Proceedings of the Fourth International Conference on Document Analysis and Recognition, IEEE, 18–20 Aug 1997
7. Dhandra, B.V., Mallikarjun, H., Hegadil, R., Malemathl, V.S.: Word level script identification in Bilingual documents through discriminating features. In: International Conference on Signal Processing, Communications and Networking (ICSCN), IEEE, pp. 630–635 (2007)
8. Patil, S.B., Subbareddy, N.V.: Neural network based system for script identification in Indian documents. *Sadhana Special Issue Indian Lang. Doc. Process.* **27**, Part-1, 83–97 (2002)
9. Zhou, L., Lu, Y., Tan, C.L.: Bangla/English script identification based on analysis of connected component profiles. In: Proceedings of 7th IAPR Workshop on Document Analysis System, New land, pp. 234–254 (2006)
10. Hassan, E., Garg, R., Chaudhury, S., Gopal, M.: Script based text identification: a multi-level architecture. In: Proceedings of the 2011 Joint Workshop on Multilingual OCR and Analytics for Noisy Unstructured Text Data, ACM (2011)
11. Dhir, R., Singh, C., Lehal, G.S.: A Structural Feature based approach for script identification of Gurumukhi and Roman characters and words. In: Proceedings of 39th Annual National Convention of Computer Society of India, Dec 2004 (2004)
12. Aithal, P.K., Rajesh, G., Acharya, D.U., Krishnamoorthi, M., Subbareddy, N.V.: Text line script identification for a tri-lingual document. In: IEEE Second International conference on Computing, Communication and Networking Technologies, pp. 1–3 (2010). ISBN: 978-4244-6589-7

13. Vijaya, P.A., Padma, M.C.: Text line identification from a multilingual document. In: IEEE International Conference on Digital Image Processing, pp. 302–305 (2009). ISBN: 978-0-7695-3565-4
14. Elgammal, A.M., Ismail, A.M.: Techniques for language identification for hybrid Arabic-English document images. In: Proceedings Sixth International Conference on Document Analysis and Recognition, IEEE (2001)
15. Godara, S.P., Patwal, P.S.: Latin script detection and removal from Devanagari document image for OCR. *Int. J. Comput. Organ. Trends* **6**, 33–36 (2014). ISSN: 2249-2593

Ultra-Wideband Equal Power Divider Using Stepped-Impedance Technology

Atul Kumar Agrawal and Deepak Bhatia

Abstract A novel approach to design ultra-wideband (UWB) equal power divider which uses stepped-impedance technology on microstrip line has been proposed in this paper. This divider uses the method of multi-section impedance transformer of microstrip lines. The designed power divider demonstrates that power from one input port is divided equally into two output ports. It also exhibits matched impedance termination at all the three ports and very good isolation between two output ports over the specified 3.1–10. Also, the simulated return loss is better than 10 dB over the UWB. In addition, the group delay and average insertion loss are around 0.20 ns around 3 dB across the UWB. The output ports are isolated by an amount greater than 10 dB over the UWB.

Keywords Microstrip · Power divider · Impedance matching · Ultra-wideband (UWB) · Vector Network Analyzer (VNA) · Power-dividing ports · Wilkinson power divider

Introduction

A power divider is a basic passive component for RF power division and combination, and is used in many millimeter-wave systems and in many microwave applications such as power amplifiers, phased antenna arrays, antenna feeders, etc. Because of the great characteristics shown by ultra-wideband (UWB) technology such as low power consumption, low cost, high data transmission rate, it is useful in a lot of industrial electronic systems [1]. The major disadvantage of waveguide-based power divider results in increasing the radius of the radial waveguide in [2], when there is an increase in the number of power-dividing ports, but in the case of

A.K. Agrawal (✉) · Deepak Bhatia
Department of Electronics, UCE, RTU, Kota, India
e-mail: agrawalatul.1988@gmail.com

Deepak Bhatia
e-mail: shreenathji26@gmail.com

microstrip-based power divider, it does not have this type of problem. A very good isolation performance is observed in proposed UWB power divider in [3]. Constituting principle of divider are of two types: (1) a branch-line type divider having two or more output lines which are parallel to an input line [1, 4] and (2) a planar circuit type one which is designed using the two-dimensional current distribution (electromagnetic field) on a strip conductor pattern [3].

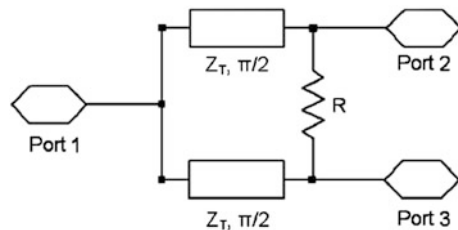
A novel approach has been presented in this paper, to design an UWB power divider. The divider has been established by introducing stepped-impedance structure to achieve UWB performance. Satisfactory return/insertion losses are achieved as demonstrated in simulation. Obviously, the performance of this type of microstrip planar UWB power divider is better than the waveguide-based power dividers [1].

Structure and Design

A traditional two-section Wilkinson power divider with matched port is shown in Fig. 1. According to the odd–even mode theory, the impedances of the input and output ports are both 50Ω and the characteristic impedance of transmission lines $Z_1 = 70.7 \Omega$.

Stepped-impedance lines are used for better coupling and impedance matching, as seen in Fig. 2. The stepped-impedance lines can not only increase the coupling degree, but also make up the wide passband. Commercial software CSTv11 is used to simulate the proposed UWB power divider. The dimensions of a power divider for good performance were determined. The isolating resistor $R = 100 \Omega$. Here, basically multi-section impedance transformer of microstrip lines are used in which the connection is established using multi-section of microstrip line of different length and width, which is shown in the layout diagram in Fig. 2. Improving the large bandwidth using stepped-impedance technology is shown in Fig. 2, with the width and length of substrate. The UWB power divider is simulated on the substrate of Rogers 5880 which is characterized by dielectric constant of 3.2. The thickness is 0.8 mm. and the isolator resistor $R = 100 \Omega$ has been used. Figure 3 shows CST structure of proposed UWB power divider and Table 1 shows dimensions of the power divider (Figs. 4 and 5).

Fig. 1 Traditional two-way Wilkinson power divider



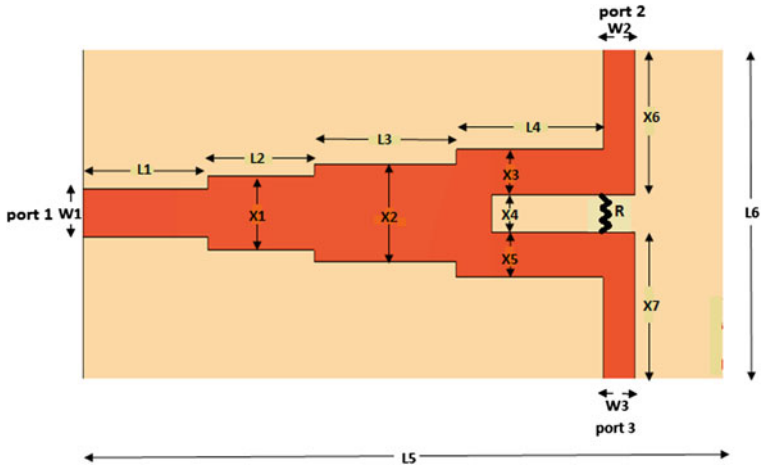


Fig. 2 Layout of proposed UWB power divider (simulated structure) (dimension 36 mm × 11.2 mm)

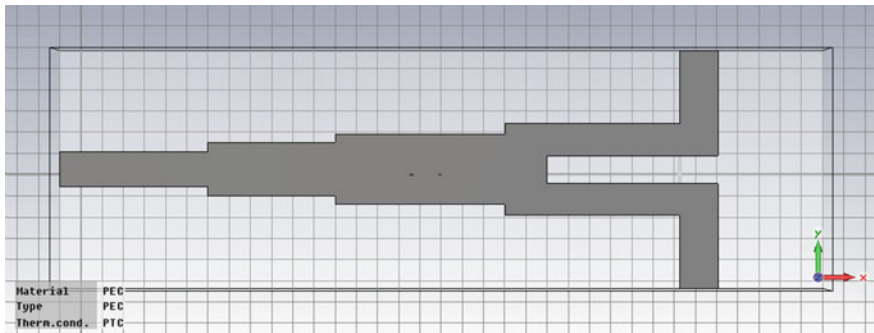


Fig. 3 CST structure of proposed UWB power divider

Table 1 Dimensions of the power divider (Unit Millimeters)

Dimension	L1	L2	L3	L4	L5
Calculated value	7.0	6.0	8.0	8.25	36.0
Dimension	L6	X1	X2	X3	X4
Calculated value	11.2	2.5	3.3	1.515	1.27
Dimension	X5	X6	X7	W1	W2
Calculated value	1.515	4.95	4.95	1.6	1.6
Dimension	W3				
Calculated value	1.6				

Fig. 4 Return loss of proposed power divider

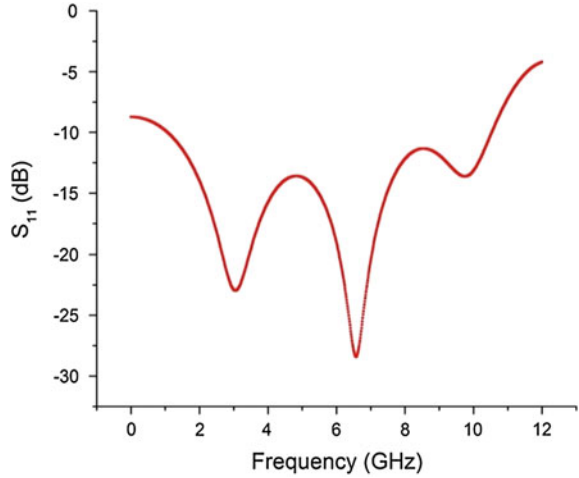
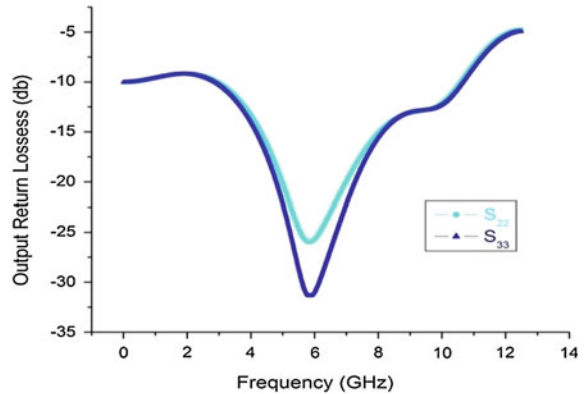


Fig. 5 Return loss at output ports



Simulation and Results

Figure 6 shows the simulated results of the designed UWB power divider. As shown in Fig. 6, the input power is split equally into the two output ports. S_{11} is below 28 dB at the design frequency (6.84 GHz) as shown in Fig. 6 and synchronization between both full-wave simulators is clearly observed. In Fig. 7a, the transmission parameters (S_{21} and S_{31}) are in very close variation to their theoretical values of 3 dB at the design UWB range, which exhibits the equal-split behavior of this divider. Some losses and discontinuities cause small discrepancies. As earlier mentioned, the output ports are well isolated at the design frequency (6.84 GHz). From Fig. 8, it can be observed that the value of parameter S_{23} is equal to 27 dB at design frequency 6.84 GHz, while the best isolation is between ports 2 and 3, which is around 32 dB at the UWB. Output ports matching is shown in Fig. 5 as

Fig. 6 Simulated result of the proposed power divider

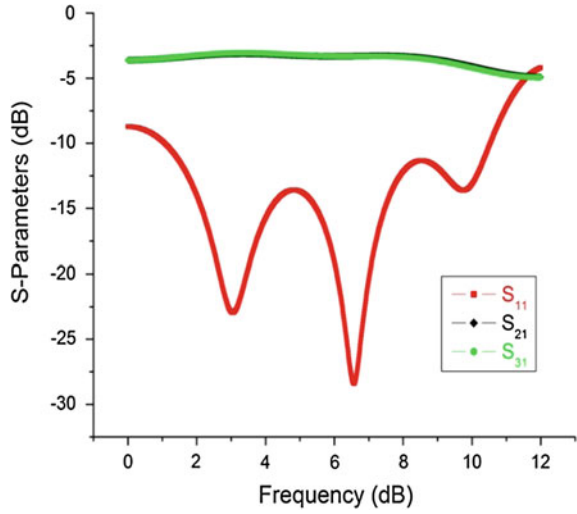


Fig. 7 Simulated transmission coefficients of UWB power divider ($n = 2, 3$). **a** Amplitude. **b** Insertion phase

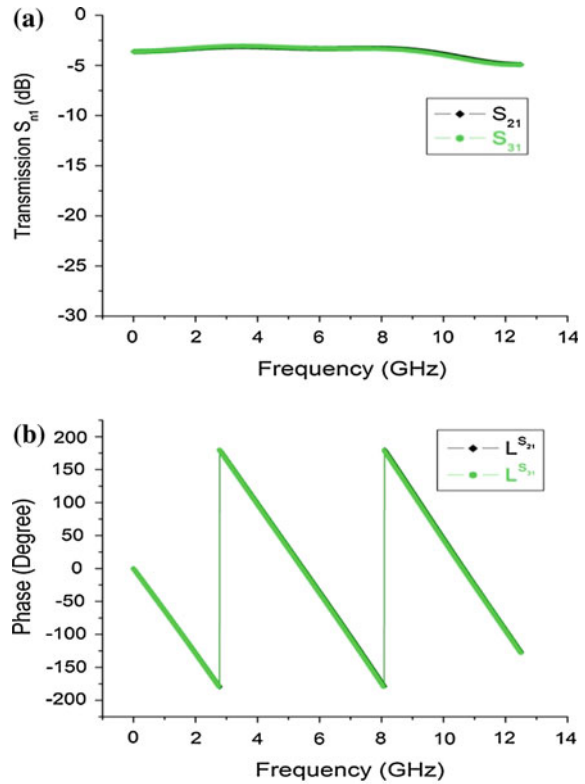
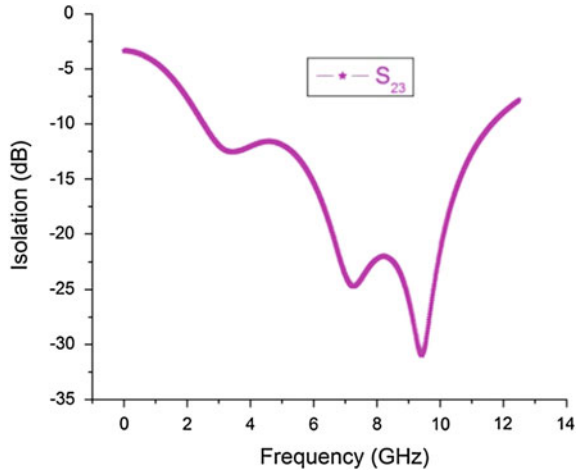


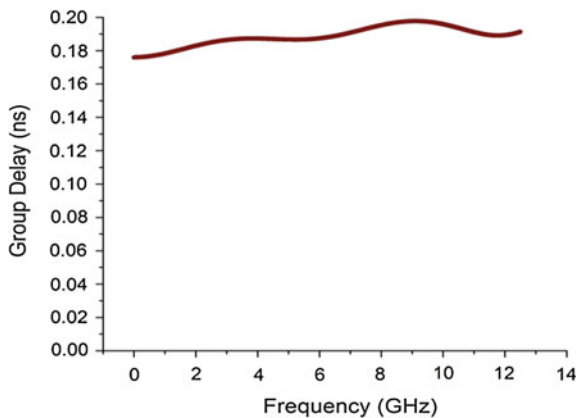
Fig. 8 Isolation between output ports



parameters S_{22} and S_{33} of *UWB* power divider. From Fig. 5, return losses for the output ports are all less than -10 dB at the design frequency (6.84 GHz).

While using power divider as component in different applications such as antenna arrays or applications demanding antenna diversity, another advantage is that the number of output ports can be easily extended in contrast to other dividers, which results in the increment in the number of fed antennas. Thus, there is a need for increasing the number of splitters, when there is an increment in the number of output ports, which results in more complex and larger circuit area. Also, it should be brought to notice that if the matched loading at the output ports is necessary, some simple matching networks that help to match the output ports at a certain design frequency can be easily designed and used in the circuit. In addition, good linearity is shown by the simulated group delays within *UWB*, as shown in Fig. 9. Here the total group delay is 0.02 ns. The simulated group delays are around 0.19 ns at 6.84 GHz within very little variation of only about 0.02 ns over the *UWB* (3.1–10.6 GHz) frequency range, so we can say that the group delay is flat.

Fig. 9 Simulated group delays of the proposed power divider



Fabricated Design

We have fabricated the above UWB power divider on the substrate of Rogers 5880, characterized with a dielectric constant of 3.2 and a thickness of 0.8 mm. A photograph of fabricated design is shown in Fig. 10. It was further tested using VNA. The comparison of simulated and fabricated results is shown in Fig. 11 and both are nearly the same.

Fig. 10 Photograph of the fabricated design

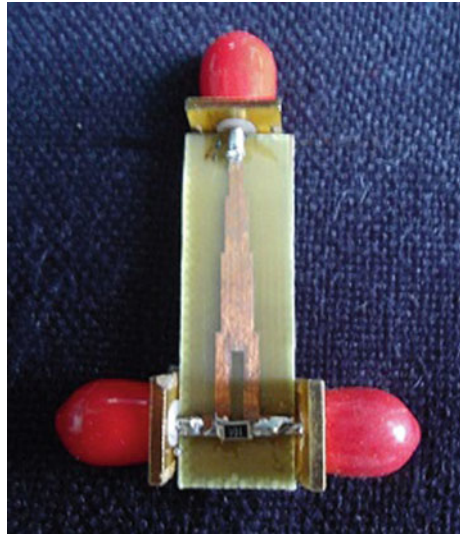
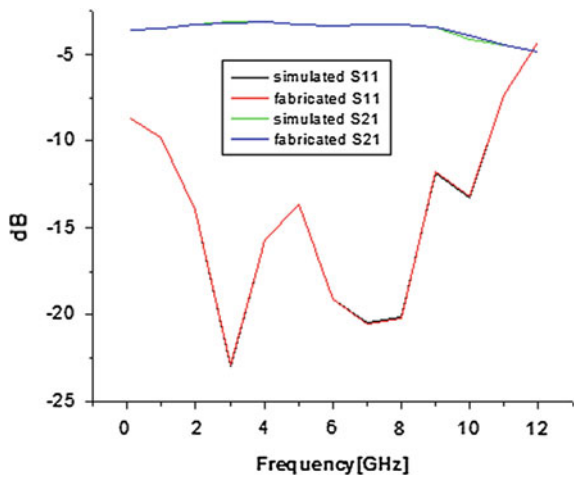


Fig. 11 Comparison of simulated and fabricated results



Conclusion

In this paper, a unique method of designing an ultra-wideband (UWB) equal power divider on microstrip lines, (using stepped-impedance technology) is proposed. Using the simulations tool, good power splitting, matched loading, and isolation can be obtained. The structure occupies an area of $36 \text{ mm} \times 11.2 \text{ mm}$.

References

1. Park, M.-J., Lee, B.: Design of ring couplers for arbitrary power division with 50Ω lines. *Electron. Lett.* **21**(4), 892–893 (2011)
2. Tarui, J.Y., Nakahm, K., Itoh, Y., Maisunaga, M.: A method for dividing ratio equalization of power divided combiner used in a power amplifier. *IEICE Trans. (GI)* **J81-C-I**(9), 553–558 (1998)
3. Hong, Y.-P., Kimball, D.F., Asbeck, P.M., Yook, J.-G., Larson, L.E.: Single-ended and differential radial power combiners implemented with a compact broadband probe. *IEEE Trans. Microw. Theory Tech.* **58**(6), 1565–1572 (2010)
4. Zhou, J., Morris, K.A., Lancaster, M.J.: General design of multiway multi section power dividers by interconnecting two-way dividers. *IEEE Trans. Microw. Theory Tech.* **55**(10) (2007)

Implementation and Performance Analysis of Enhanced SHA-192

Harshita and Sarvesh Tanwar

Abstract Hash functions used to provide integrity and authentication on messages sent over unsecure network. There are two most commonly used hash and MD algorithms: SHA-1 and MD5, which are vulnerable to collision attack. The weakness of these hash algorithms is that sometimes two different inputs will produce the same hash as output. To reduce this collision attack there is need to have a better hash algorithm so that the output in each round will be different and not to be equal with the same output in the next coming stages. In this paper, modified SHA-192 is implemented having a message digests of length 192 and we have also compared the security analysis of famous secure hash algorithm with enhanced SHA-192.

Keywords SHA-192 · Collision attack · Bit and time calculation · SHA-1

Introduction

The main working of hash function is to provide integrity and authenticity on the messages. We can define hash function as it accepts a variable length of data M as input and produces a fixed length of output, that is, $h = H(M)$. One important characteristic of hash is that it cannot be decrypted back so we can use it to sign a file or data. There are three main properties of hash functions: (i) collision resistance, (ii) pre-image, and (iii) second pre-image resistance [1].

National institute of Standards and Technology (NIST) developed various series of message digest (MD) and SHA algorithms. There are four secure hash algorithms: SHA-1, SHA-256, SHA-384, and SHA-512 found in SHA series [2]. SHA-1 (produce digest of 160 bits) is the most popular hash algorithm used by

Harshita (✉) · Sarvesh Tanwar
Department of Computer Science, MUST, Lakshmanagarh, India
e-mail: harshu.singh1992@gmail.com

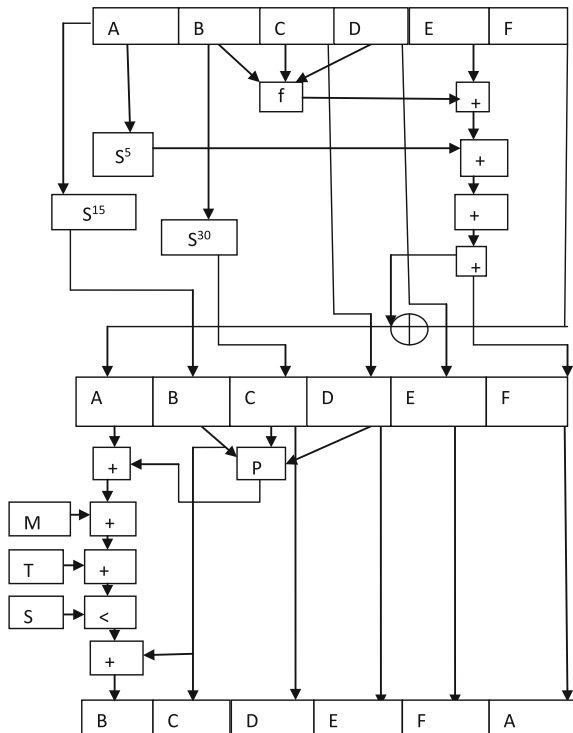
Sarvesh Tanwar
e-mail: s.tanwar1521@gmail.com

many applications such as digital signature and MAC. The collision attack is found on SHA1, in which two inputs produce the same hash values, so we need to use more secured hash algorithm in place of SHA-1. In previous research, the SHA-192 was proposed which contains the output length of 192 bits. We implemented enhanced SHA-192 which uses the concept of both SHA-192 and MD5 proposed by [3]. Later, we are comparing it with SHA-1 and SHA-256 in terms of time and bit difference.

Structure of Enhanced SHA-192 Algorithm

The algorithm structure contains both properties of SHA-192 and MD5 which is described in Fig. 1. The output of each round will be different and not be equal to the same output coming in next rounds for good diffusion so that not two inputs produce the same output [3]. The algorithm contains total of 64 steps, and in each step the message is calculated and sent to the next step by some mathematical calculation. There are three main steps of algorithm which are described below.

Fig. 1 Enhanced SHA192 block diagram



Preprocessing

In this step, the message is padded and parsed for forwarding to the processing step. This contains the following steps:

- (a) *Padding the message*
In this step, the message is padded so that its length becomes multiple of 512 bits such that 1 bit is append to the end of message followed by k zero bits and L is the actual length of message (64 bits); the equation formed by it is $L + 1 + k = 448 \pmod{512}$.
- (b) *Parsing the padded message*
For parsing the padded message, divide the input message into N 512 bits of blocks such that M1, M2, ..., MN.
- (c) *Initialize Hash values*
In this step we are going to initialize six hash chaining variables from A to F and each variable consists of 32 bits each.

Enhanced SHA 192 Processing

After preprocessing, the next step contains 4 rounds and each round consists of 16 steps; hence, the total steps of this algorithm are 64. It contains the following steps:

- (a) Copy the hash variables A through F into hash array.
int [] H = {0x67452301, 0xEFCDAB8, 0x98BADCF, 0x10325476, 0xC3D2E1F0, 0x40385172}
- (b) Initialize the T [] constant variable array which contains the 64 values and each of 32 bits and the values are same as defined by NIST in MD5 algorithm.
- (c) Initialize the K [] constant array which contains four constants for values:
K [1] = 0x5A927999 for round 1 and step 1–16.
K [2] = 0x6ED9EBA1 for round 2 and steps 17–32.
K [3] = 0x9F1BBCDC for round 3 and steps 33–48.
K [4] = 0xCA62C1D6 for round 4 and steps 49–64.
- (d) Initialize the S [] array values. S array values will be same as in MD5 algorithm.
- (e) The algorithm contains the 64 steps and 4 rounds, and hence initialize the word array of W and M, W parse of the 512 bit padded message into 16 subblock of 32 bits W[1], ..., W[16] and M parse of the each 32 bit W block into 32 16 bits words M[1], ..., M[32].

Table 1 Function value

Round	Steps	Function value F(x, y,z)	Function value P(x,y, z)
1	0–15	(band c) or ((not b) and d)	(b and c) or ((not b) and d)
2	16–31	b xor c xor d	(d and b) ((not d) and c)
3	32–47	(b and c) or (b and d) or (c and d)	(b and c) and d
4	48–63	b xor c xor d	C and (b (not d))

```

1. int[] W = new int[64];
2. int[] M = new int[32];
3. for (int outer = 0; outer < 16; outer++) {int temp = 0;
4. for (int inner = 0; inner < 4; inner++) {
5. temp = (work[outer * 4 + inner] & 0x000000FF) << (24 - inner * 8);
6. W[outer] = W[outer] | temp;}}
7. for(int outer = 0; outer < 32; outer++){int temp = 0;
8. for(int inner = 0; inner <2; inner++){
9. temp = (work[outer*2 + inner]&0x000000FF) << (24 - inner * 8);
10. M[outer] = M[outer] | temp;}}

```

In this algorithm first 16 words are copied to first 16 blocks of W.

The remaining words are calculated by the given equation:

```

for (int j = 16; j < 64; j++)
{W [j] = (W [j - 3] ^ W [j - 8] ^ W [j - 14] ^ W [j - 16]);}

```

- (f) Initialize the value of functions used in four rounds of each of 16 steps which is given in Table 1.
- (g) The main structure of algorithm is as follows:

Before proceeding to main structure of algorithm, first initialize the six hash variables with initial hash values given in step (a):

```

1. for (int j = 0; j < 63; j++) {
2. temp = rotateLeft(A, 5) + f(B,C,D) + E + K[j] + W[j];
3. temp1 = rotateLeft(A, 5) + f(B,C,D) + E + F + K[j] + W[j];
4. E = D;
5. D = C;
6. C = rotateLeft(B, 30);
7. B = rotateLeft(A, 15);
8. F = temp;
9. A = temp1;
10. F = E;
11. E = D;
12. D = C;
13. C = B;
14. B = rotateLeft((A + P(B,C,D) + M[j/2] + T[j]), S[j]) + B;
15. A = F;}

```


(h) Compute the final hash values:

$$\begin{aligned} H [0] += A; H [1] += B; H [2] += C; H [3] += D; H [4] \\ += E; H [5] += F; \end{aligned}$$

Output

We have implemented this algorithm in java and it produces the hash of length 192 bits, whereas SHA-160 produces hash of length 160 bits. The output of hash on various strings is described in Table 2. Using SHA-160, it gives 40-byte-length hash and using SHA-192 it gives 48-byte-length hash.

Performance

We have compared the algorithm with other hash algorithms in terms of bit and time difference. The larger bit difference means that if a single input bit changes then there will be more bit changes in output. The algorithm performance is measured in the two given analyses.

Time Complexity and Hash Collision Analyses

In this we have compared enhanced 192 with SHA-1 and SHA-256 in terms of time (nanoseconds). We have calculated the time to generate the hash of message with various algorithms which are given in Fig. 2 and the graph of calculation of time on various strings given in Fig. 3. For getting accurate time, we run one message for 100 times due to context switching then calculate the average time for generating the hash by algorithms. After calculating the time, the result shows that the algorithm takes less time to generate the hash than SHA-256 but more than SHA-160.

The birthday attack is very popular for the collision attack. For output m , there are $2^{m/2}$ possibilities to find out the two messages which produce the same hash which is faster than brute force attack which takes 2^m possibilities for pre-image and second pre-image attack. In SHA-160 the rate of collision is 2^{61} whereas in enhanced SHA-192 it takes 2^{96} operations, which is difficult for cryptanalyst to break the security of hash algorithm. Hence, the enhanced SHA-192 is more secured than the SHA-1 in terms of collision attack.

Table 2 Output of SHA-160 and enhanced SHA-192

String	SHA-160	Enhanced SHA-192
"abc"	a9993e364706816aba3e25717850c26c9cd0d89d	da0a46d4c2081a0fade77a8fe960a1519ca8c07bb2fd7545
"hello"	aaf4c61ddcc5e8a2dabede0f3b482cd9aea9434d	889ed55fad1f88d64b6b449d8bec229b24f5e6d1619203d0
"harshita"	bb38d84ec2e960d64caf3560e34248c328ac1ecf	4fa30c6ecb7b0a38f4d49ebf16bf8b8ea0a4504728963adf

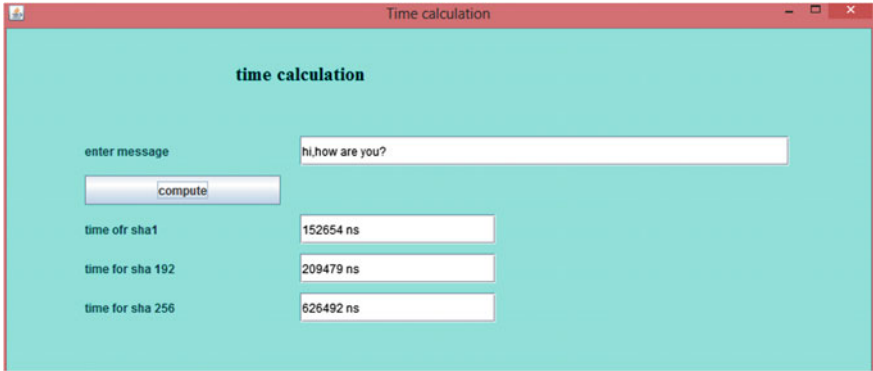
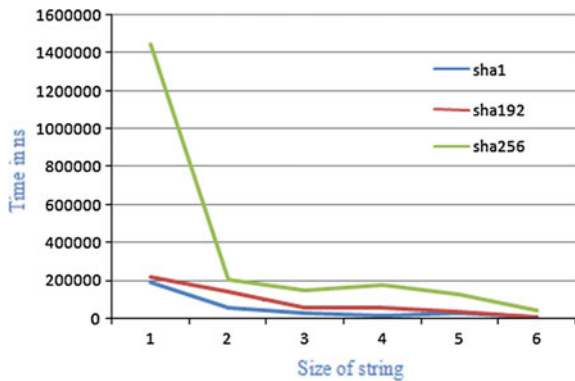


Fig. 2 Time calculation output

Fig. 3 Graph comparison of time



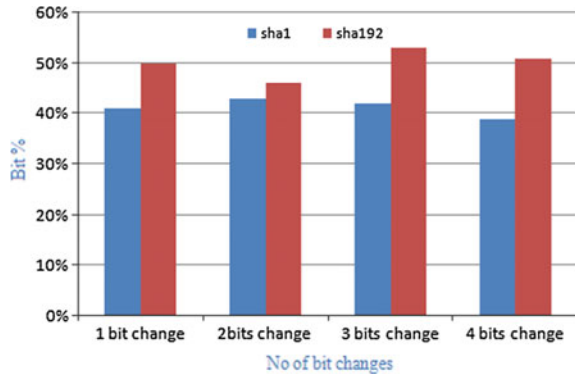
Bit Difference Analysis

The bit difference is calculated for algorithm between the changes of single or more bits in messages and compared it with SHA-160 algorithm. Table 2 describes a message “my name is harshita” and calculates its hash value, when we change message one bit by ‘m’ to ‘b’ then the difference between bit is calculated by taking hash of two messages than XOR them; after XOR ing calculate the changes in bit and bit percentage by formula $((\text{no of bits changes}/\text{total no of bits}) * 100)$. After calculating we conclude that bit percentage in our implemented algorithm is more than SHA-160. Hence, we can say that the algorithm is more secured than SHA-160 in terms of time difference. In Table 3, it shows bit percentage using SHA-160 and SHA-192 on single bit change in message, whereas in Fig. 4 we calculate the bit percentage graph at various changes of bit.

Table 3 Bit percentage

Message	SHA-160	Enhanced SHA-192	Hash Enhanced SHA-192 output
“my name is harshita”	41 %	50 %	“a6ff6ddacb7650d4e0a634f58422f5bde64f29dd7ff29c4b”
“by name is harshita”			“1764f7de4497b9e4017fb42f20b9565671e41ba6f058264f”

Fig. 4 Graph of bit difference



Conclusion

We have compared the enhanced SHA-192 algorithm with other hash algorithms. The algorithm is time efficient when it compared with SHA-256 and it is more secured than SHA-160 in terms of bit difference. If a small bit changes in input, it will result to larger bit changes in output, so it make more difficult to break. In our future work, we can try to reduce the time delay comparison of algorithm with SHA-160.

References

1. Tiwari, H., Asawa, Dr.: A secure hash function MD-192 with modified message expansion. *Int. J. Comput. Sci. Inf. Secur.* 7(2) (2010)
2. Turner, S., Chen, L.: Updated security considerations for the MD5 message-digest and the HMAC-MD5 algorithms. *IETF* (2011)
3. Gupta, G., Sharma, S.: Enhanced SHA192 algorithm with larger bit difference. In: *International Conference on Communication Systems and Network Technologies.* IEEE (2013)
4. Srinivas, S., Yeligati, S.: FPGA implementation of Proposed SHA-192 algorithm for digital signature application. *Int. J. Emerg. Eng. Res. Technol.* 2(4) (2014)

5. Lakshmanan, T., Muthusamy, M.: A novel secure hash algorithm for public key digital signature schemes. *Arab J. Inf. Technol.* **9**(3) (2012)
6. Garg, P., Tiwari, N.: Performance analysis of SHA algorithms (SHA-1 and SHA-192): a review. *IJCTEE* **2**(3) (2012)
7. Xiao-hui, C., Jian-zhi, D.: Design of SHA-1 algorithm based on FPGA. In: *IEEE Second International Conference on Networks Security, Wireless Communications and Trusted Computing, (NSWCTC)*, vol. 1, pp. 532–534 (2010)
8. Thulasmani, L., Madheswaran, M.: Security and robustness enhancement of existing Hash algorithm. In: *International Conference on Signal Processing Systems. IEEE* (2009)
9. Ming, H., Wang, Y.: The collision rate tests of two known message digest algorithms. In: *International Conference on Computational Intelligence and Security*, vol. 2. *IEEE* (2009)
10. Stallings, W.: *Cryptography and Network Security*, 4th edn. (2006)
11. Biham, E., Chen, R., Joux, A., Jalby, W.: Collisions of SHA-0 and reduced SHA-1. In: *Advances in Cryptology. Springer, Berlin* (2005)

Human Object Detection in Images Using Shift-Invariant Stationary Wavelet Transform

Om Prakash, Manish Khare, Nguyen Thanh Binh and Ashish Khare

Abstract Surveillance system has proven as a key step in providing public security in many crowded places like railway stations, bus stops, cinemas, malls, etc. Several advancements in computer vision have been found but very less is applied in actual implementation of surveillance system. There is a need to add some intelligence in the surveillance system which can accurately detect human objects. This paper presents a method for human object detection using stationary wavelet transform (SWT) coefficients. Stationary wavelet transform coefficients are independent to the other parameters like color, shape, size, etc., of the object. The proposed method detects the human object from the complex images. The use of shift-invariance property of stationary wavelet transform handles object translations well. The detection of human object has been performed using Adaboost classifier. The quantitative assessments of the proposed method have shown improved performance over other state-of-the-art methods.

Keywords Stationary wavelet transform · Shift-invariance · Human object detection · Machine vision

Om Prakash (✉) · Manish Khare · Ashish Khare
Department of Electronics and Communication, University of Allahabad,
Allahabad, India
e-mail: au.omprakash@gmail.com

Manish Khare
e-mail: mkharejk@gmail.com

Ashish Khare
e-mail: ashishkhare@hotmail.com

Om Prakash
Centre for Computer Education, Institute of Professional Studies,
University of Allahabad, Allahabad, India

N.T. Binh
Ho Chi Minh City University of Technology, Ho Chi Minh City, Vietnam
e-mail: ntbinh@hcmut.edu.vn

Introduction

Human object detection is one of the challenging problems in machine learning and has applications in surveillance application. Human detection in public places is one of the key problems in the implementation of the surveillance system [1]. Detection of human object in any scene is mainly concerned with distinguishing humans from other objects in a visual scene on the basis of suitable discriminative feature. Another challenge of the intelligent surveillance system is that it should work on real constraints. Object detection in images has been performed based on the pixels and features as well [2]. The pixel-based methods have shown poorer performance because finite quantity of data is difficult to train using pixels. Many researchers have used different features to perform the human detection in real scenes [3–7]. The detection accuracy depends on the feature to be used. For selection of suitable feature, some heuristics has been needed. Thus, for better object detection accuracy, we need suitable features. Selected features of an object must meet following three important criteria.

- (a) All features of a specific class are represented by the same population in a set of trained features.
- (b) Different population sets are used to represent each individual object class.
- (c) Class of features must be optimized in the sense that there should be no redundant features.

Most of the human detection algorithms proposed in the literature are based on the spatial domain feature. Some of the feature based methods are: Haar feature-based method proposed in [3]. For accomplishing object detection using modified reminiscent of Haar basis function has been proposed in [4]. Weighted linear combination of feature [5] has been used for classification with Adaboost classifier. Scale-invariant feature transform (SIFT) is used as a feature descriptor for object recognition [6]. Dalal and Triggs [7] proposed histogram of oriented gradient (HoG) as a feature descriptor for object detection, but HoG feature suffered from the problem of high dimensionality. To overcome high dimensionality problem, Cao et al. [8] proposed a method by introducing an extension of the HoG features, known as boosting HoG feature. They used Adaboost scheme for boosting the HoG feature and the SVM classifier has been used for final object classification. Lu et al. [9] proposed a visual feature for object classification based on binary pattern. These visual features are rotation invariant and exploit the property of pixel patterns.

In this work, we have proposed a novel human detection algorithm based on stationary wavelet transform. Shift-invariance property of the stationary wavelet transform is well recognized and used for handling the translation of object. Also, the use of single feature for human detection adds an advantage of low computational cost. The selected feature is independent of the other parameters of the object like size, color, shape, etc. For detection of human object, we have used Adaboost

as classifier. The coefficients up to decomposition level-7 have been used for human detection. The proposed method has been compared with the other state-of-the-art methods viz. Renno et al. [5] and Lu et al. [9] in terms of predicted positive rate (precision) and average classification accuracy.

The Stationary Wavelet Transform

Stationary wavelet transform (SWT) provides efficient numerical solutions in the image processing and machine vision applications. Unlike the classical discrete wavelet transform (DWT), stationary wavelet transform gives a better approximation because of its linear, redundant, and shift-invariance nature [11].

The Adaboost Classifier

Boosting is a method to improve the performance of any learning algorithm. Adaboost itself trains an ensemble to weak learners to form a strong classifier which performs at least as well as an individual weak learner [5]. Viola and Jones [4] described first the Adaboost algorithm in their face detection system. In our proposed work, we have used Adaboost algorithm for human object detection.

Adaboost algorithm for classifier

1. Given example images $(I_1, J_1), (I_2, J_2), \dots (I_n, J_n)$ where $J_i = 0, 1$ for negative and positive example, respectively.
2. Initialize weights $W_{1,i} = \frac{1}{2n} \cdot \frac{1}{2^p}$ for $j_i = 0, 1$, respectively, where p and n are the number of positive and negative examples, respectively.
3. For $t = 1, 2, \dots T$ (Number of iterations)
 - (a) Normalize the weights

$$W_{t,i} \leftarrow \frac{W_{t,i}}{\sum_{j=1}^m W_{t,j}}$$

W_t is the probability distribution

- (b) For each feature, j , train is a classifier h_j , which is restricted to using a single feature. The error (E_j) is evaluated with respect to W_t

$$E_j = \sum_i W_i |h_j(I_i) - J_i|$$

- (c) Choose the classifier, h_t with the lowest error E_t .
- (d) Update the weights

$$W_{t+1,i} = W_{t,i} \beta_t^{1-\epsilon_i}$$

where $\epsilon_i = 0$, if example x_i is classified correctly
 $\epsilon_i = 1$, otherwise

$$\beta_t = \frac{E_t}{1 - E_t}$$

4. The final strong classifier is

$$h(I) = \begin{cases} 1, & \text{if } \sum_{t=1}^T \alpha_t h_t(I) \geq \frac{1}{2} \sum_{t=1}^T \alpha_t \\ 0, & \text{otherwise} \end{cases}$$

where, $\alpha_t = \log \frac{1}{\beta_t}$.

The Proposed Method

In this paper, a human object detection method has been proposed that uses stationary wavelet transform (SWT) coefficients as feature. The use of only SWT as single feature makes the method simple in implementation. The method consists of the following steps:

(a) *Sample collection*

First, sample images have been collected for training the Adaboost classifier. In the proposed method, we have used a standard INRIA dataset [12] of images for training the classifier. In this image dataset, each image is of the size 96×160 .

(b) *Preprocessing of images*

The collected sample images are normalized to 256×256 pixel dimensions and converted to gray level images to reduce the complexity and hence processing time.

(c) *Feature vector generation*

This is the most important step in the classification problem. SWT coefficients of each image are computed by decomposing the image using SWT. Use of SWT yields different components of the image namely LL, LH, HL, and HH. Each component resembles the size of the original image size. The wavelet coefficients of the components LH, HL, and HH have been used as image feature.

(d) *Human object detection*

The computed SWT coefficients in the previous step have been provided to the Adaboost classifier which classifies images with human object. The test images have been categorized by the Adaboost classifier.

The training and testing of images with computed feature and Adaboost classifier are shown in Fig. 1 a, b.

Experiments and Results

In this section, we have presented experimental results. The results with DWT coefficients as feature and with the proposed method using SWT coefficients as feature have been computed separately and compared with methods given by Renno et al. [5] and Lu et al. [9]. The performance of each method is tested in terms of precision and average classification accuracy. The proposed method for human object detection has been tested on standard INRIA dataset [12] and the classification results have been reported. Few sample images of INRIA dataset with human and nonhuman objects are presented in Fig. 2.

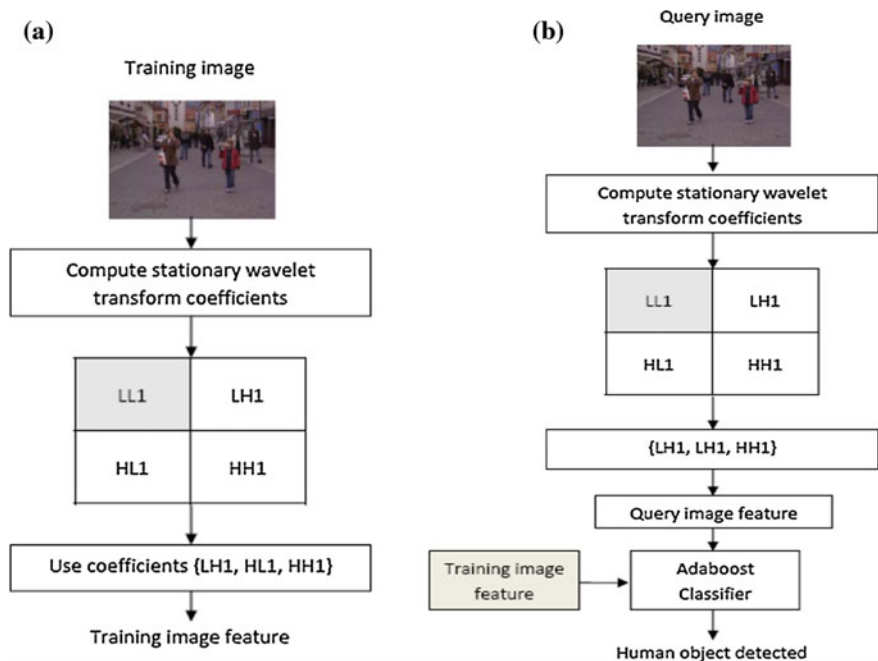


Fig. 1 a Computation of stationary wavelet transform coefficients as feature for training image dataset, b detection of human object using the computed feature and Adaboost classifier



Fig. 2 Sample images with human and nonhuman objects of INRIA dataset. **a** images with human object, **b** images without human object

In the proposed method, we have performed the classification on the basis of selected features and found that the proposed method has performed better. The performance has been evaluated in terms of precision and average classification accuracy. These metrics are defined as follows.

$$\text{PPR (Precision)} = \frac{\text{TP}}{\text{TP} + \text{FP}}$$

$$\text{Average Classification Accuracy} = \frac{\text{TP} + \text{TN}}{\text{TP} + \text{FN} + \text{TN} + \text{FP}}$$

where TP (True Positive) represents the number of images which are positive and detected as positive, TN (True Negative) are the number of images which are negative and detected as negative, FP (False Positive) are the number of negative images but detected as positive, and FN (False Negative) are the number of originally positive but detected as negative object.

Conclusions

In this work, we have developed and demonstrated a new method for human object detection in images having complex background, color, texture, etc. In the proposed method, we train the Adaboost classifier using stationary wavelet coefficients as

Table 1 Performance measure values using Adaboost classifier

Method	PPR (Precision) (%)	Average classification accuracy (%)
The method proposed by Renno et al. [5]	74.17	79
The method proposed by Lu et al. [9]	75.00	80
DWT coefficients as feature	66.5	66.02
The proposed method	81.27	82.5

feature for human detection and then detection of human objects in two classes: human object and nonhuman objects have been performed. Shift-invariance property is well recognized to maintain the object boundaries and hence suitable for object detection. The comparison of the proposed method in terms of precision and average classification accuracy is shown in Table 1; the improved performance over the other state-of-the-art methods proposed by Renno et al. [5] and Lu et al. [9].

References

1. Hu, W., Tan, T.: A survey on visual surveillance of object motion and behaviors. *IEEE Trans. Syst. Man Cybern. Part C Appl. Rev.* **34**(3), 334–352 (2006)
2. Brooks, R.R., Grewe, L., Iyengar, S.S.: Recognition in wavelet domain: a survey. *J. Electron. Imaging* **10**(3), 757–784 (2001)
3. Sialat, M., Khlifat, N., Bremond, F., Hamrouni, K.: People detection in complex scene using a cascade of boosted classifiers based on Haar-like features. In: *Proceeding of IEEE International Symposium on Intelligent Vehicles*, pp. 83–87 (2009)
4. Viola, P., Jones, M.: Rapid object detection using a boosted cascade of simple features. In: *Proceeding of IEEE International Conference on Computer vision and Pattern Recognition*, vol. 1, pp. 83–87 (2001)
5. Renno, J.P., Makris, D., Jones, G.A.: Object classification in visual surveillance using Adaboost. In: *Proceeding of IEEE International conference on Computer Vision and Pattern Recognition (CVPR)*, pp. 1–8 (2007)
6. Lowe, D.: Object recognition from local scale invariant features. In: *Proceeding of 7th IEEE International Conference on Computer Vision*, pp. 1150–1157 (1999)
7. Dalal, N., Triggs, B.: Histograms of oriented gradients for human detection. In: *Proceeding of IEEE International Conference on Computer vision and Pattern Recognition*, pp. 886–893 (2005)
8. Cao, X., Wu, C., Yan, P., Li, X.: Linear SVM classification using boosting HoG Features for vehicle detection in low-altitude airborne videos. In: *Proceeding of IEEE International Conference on Image Processing*, pp. 2421–2424 (2011)
9. Lu, H., Zheng, Z.: Two novel real-time local visual features for omni directional vision. *Pattern Recogn.* **43**(12), 3938–3949 (2010)
10. Chen, L., Feris, R., Zhai, Y., Brown, L., Hampapur, A.: An integrated system for moving object classification in surveillance videos. In: *Proceeding of IEEE International conference on Advanced Video and Signal based Surveillance*, pp. 52–59 (2008)
11. Nason, G.P., Silver, B.W.: The stationary wavelet transform and some statistical applications. Technical report BS8 ITw, University of Bristol (1995)
12. INRIA Person dataset. <http://pascal.inrialpes.fr/data/human> (2014). Accessed 23 Aug 2014

A Novel Framework for Extracting GeoSpatial Information Using SPARQL Query and Multiple Header Extraction Sources

Poonam Malpani, Paras Bassi, Mehul Mahrishi and Vipin Jain

Abstract In the current digital world, where all the data is available digitally, data extraction has become quite a massive field of research. Web mining uses the data mining techniques to discover knowledge from the Web. Such sort of technique can be very useful in some applications which require massive and updated data. One of such applications that can deploy such an expertise automated query engine having a user-friendly graphical interface that can provide data regarding competitive exams. This paper proposes such a system that is more appropriate and advanced as it fetches data directly from one of the largest regularly updated database, i.e. Wikipedia.

Keywords SPARQL · RDF · Wikipedia · Dbpedia · Infoboxes · YAGO · General knowledge base

Introduction

The most frequently updated and authentic information that can be available on Internet is Wikipedia. The humongous data [1] that Wikipedia provide can also be used to harness some specific useful information. The concept of Infoboxes in

Poonam Malpani (✉) · Paras Bassi
Department of Information Technology,
Poornima Institute of Engineering and Technology, Jaipur, India
e-mail: poonam.dengg@gmail.com

Paras Bassi
e-mail: paras.bassi@poornima.org

Mehul Mahrishi · Vipin Jain
Department of Computer Science,
Swami Keshvanand Institute of Technology, Jaipur, India
e-mail: mehul.aqua@gmail.com

Vipin Jain
e-mail: vipin@skit.ac.in

Wikipedia provides a very easy access to such data. The information stored in Infoboxes is provided in RDF (Resource Descriptive Framework) format [2]. The concept is to develop a query engine [3] that can fetch the desired information from Wikipedia and provide the same in a structured manner [4]. The precise information needed for developing such interface can be found in Wikipedia Infoboxes. An Infobox is a table having fixed format that is available in every Wikipedia page that provides summary of the article of that page; this improves navigation between various interrelated articles. Using this feature of Wikipedia one can extract any data in any specific format. The query engine for extracting data from Infoboxes is SPARQL [5], which is further discussed in this paper. The data sets that can provide access to this Wikipedia data are Dbpedia [6]. The DBpedia works around harnessing the Wikipedia information into a structured knowledge, so that Wikipedia data can be used to query some semantic information [4], that are interlinked with other articles, which helps to acquire better data mining.

Figure 1 above shows idea of process of information extraction [7] in DBpedia and gives an overview of how to publish extracted data on the Web. Currently, the most popular DBpedia interfaces are Virtuoso and MySQL as storage points [8] at back end.

The paper is divided into four sections. The first section gives overview about YAGO [9] ontology and discrete development tools. The second section discusses the Infoboxes structure and its templates [10]. The third section includes the proposed idea for extraction of data and development of application through Infoboxes. The fourth section shows various test sets and output scenarios. The last section concludes the paper.

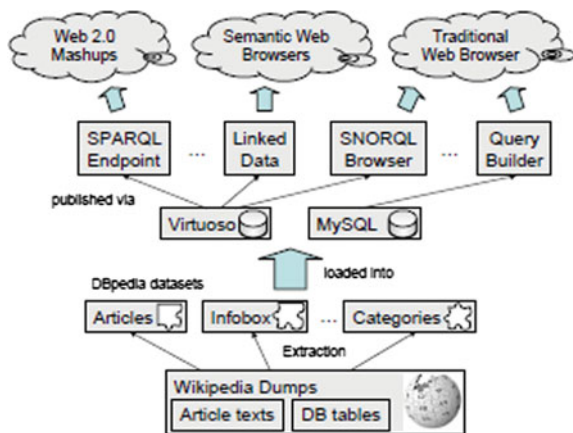


Fig. 1 Overview of the DBpedia components

Ontology Framework and Development Tools

YAGO ONTOLOGY: CORE OF SEMANTIC KNOWLEDGE is a very lightweight ontology which can be easily extended. As per paper [9]: “YAGO has been created on objects and relations and comprises of more than 1 million entities and 5 million facts.” YAGO has been derived from Wikipedia and Word Net (Fig. 2) [9].

The base paper for YAGO class shows that it contains the following (axiomatic) rules (Fig. 3).

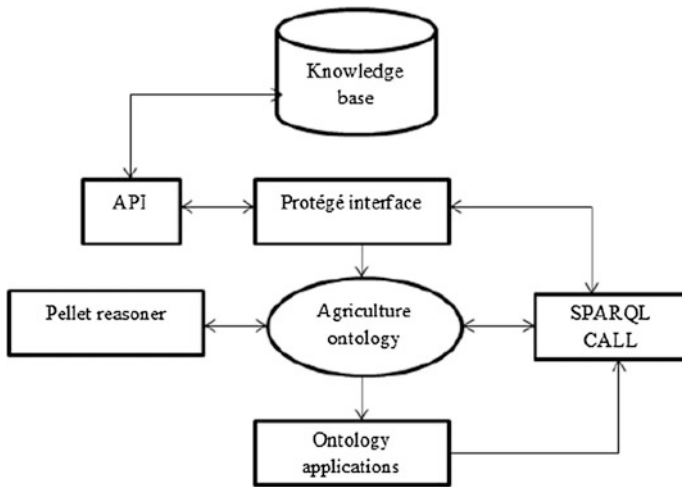


Fig. 2 Architecture of YAGO technology

- | | |
|---|--|
| <ul style="list-style-type: none"> ∅ → (domain, domain, relation) ∅ → (domain, range, class) ∅ → (range, domain, relation) ∅ → (range, range, class) ∅ → (subClassOf, type, acyclicTransitiveRelation) ∅ → (subClassOf, domain, class) ∅ → (subClassOf, range, class) ∅ → (type, range, class) ∅ → (subRelationOf, type, acyclicTransitiveRelation) ∅ → (subRelationOf, domain, relation) ∅ → (subRelationOf, range, relation) ∅ → (boolean, subClassOf, literal) | <ul style="list-style-type: none"> ∅ → (number, subClassOf, literal) ∅ → (rationalNumber, subClassOf, number) ∅ → (integer, subClassOf, rationalNumber) ∅ → (timeInterval, subClassOf, literal) ∅ → (dateTime, subClassOf, timeInterval) ∅ → (date, subClassOf, timeInterval) ∅ → (string, subClassOf, literal) ∅ → (character, subClassOf, string) ∅ → (word, subClassOf, string) ∅ → (URL, subClassOf, string) |
|---|--|

Fig. 3 YAGO axiomatic rules (Source Ref. [9])

Extracting Structured Information from Wikipedia

Wikipedia articles comprise variety of information and distinguish structured information, likely Infoboxes, Categorized data, Images, Links to related articles, and also provide multilingual support. There are two methods currently deployed to extract semantic relationships:

- a. Map the relationships which are previously stored in RDF [11], and
- b. Extract further information directly from the free text and the infobox template that is present within the article

Here an example of Template for Infobox for district.

We see the example of information extraction of semantics from free texts with a Wikipedia infobox template (Fig. 4). In Fig. 5 we see a Wikitext fragment that specifies the infobox data for the “**Solapur District**” Wikipage. The name of this

```

{{Infobox India district
| Name           =
| Local          =
| State          =
| Division       =
| HQ             =
| Map            =
| Coordinates    =
| Area           =
| Population     =
| Year           =
| Urban          =
| Literacy       =
| SexRatio       =
| Collector      =
| Tehsils        =
| LokSabha       =
| Assembly       =
| Highways       =
| Vehicle        =
| Rain           =
| Website        =
}}

```

Fig. 4 Template of Infobox

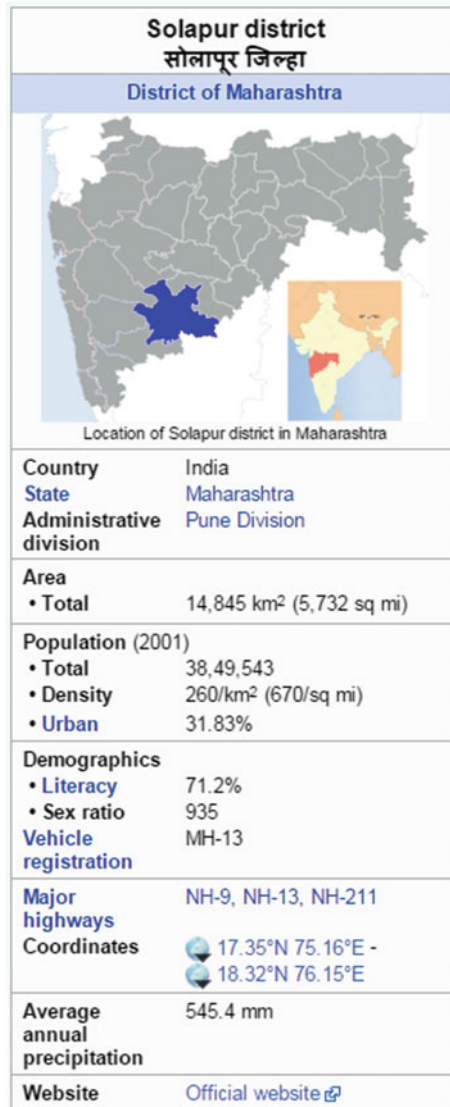


Fig. 5 Infobox of Solapur District

infobox is Solapur and consists of various parameters, e.g. Country, State, Area, Sex Ratio, etc. These fields are defined in the Solapur infobox template and shared by all infoboxes about District. Each field specifies an attribute of the object or concept described by the Wikipeage. For example, the district name is “**Solapur District**” (Fig. 6).

```

{{Infobox India district
| Name           = Solapur
| Local          = सोलापूर जिल्हा
| State         = Maharashtra
| Division      = [[Pune Division]]
| HQ            = Solapur
| Map           = MaharashtraSholapur.png
| Coordinates   = {{coord|17.35|75.16}} - {{coord|18.32|76.15}}
| Area         = 14845
| Population    = 38,49,543
| Year         = 2001
| Urban        = 31.83%
| Literacy     = 71.2%
| SexRatio     = 935
| Tehsils     = 1. [[Akkalkot]], 2. [[Barshi]], 3. [[Karmala]], 4. [[Madha, Maharashtra|Madha]]
| LokSabha    = 1. [[Solapur (Lok Sabha constituency)|Solapur(SC)]], 2. [[Madha (Lok Sabha con
| Assembly    = 10
| Highways    = [[National Highway 9 (India)|NH-9]], [[National Highway 13 (India)|NH-13]], [[N
| Vehicle     = MH-13
| Rain        = 545.4
| Website     = http://solapur.gov.in/
}}

```

Fig. 6 The infobox data for the “Solapur District” Wikipedia

Proposed Scheme

We explained about discrete technologies above like, Dbpedia, SPARQL, and Infoboxes. Using these technologies and methods we are proposing an application that will provide details of general knowledge-related facts and figures that can be simultaneously used by multiple organizations. The system will be providing the user with the list of options from which one can formulate customized information. For example, if one wants to find out the capitals of countries, GDPs, Area, etc., one can select the multiple sets of data and will get the desired and correct list of data (Fig. 7).

1. User is given a choice and asked to find data regarding that choice. For instance—Find the Asian countries among all the countries? (Figs. 8 and 9)
2. The user is given some data of an sample and asked to fetch data of another sample that is linked to the previous sample. For instance—What is the capital and currency of Asian countries? (Fig. 10)
3. Querying for number of samples of a distinct class. For instance—How many countries are Asian countries? (Fig. 11)
4. Retrieve class samples with specific value. For instance—What are the numbers of Asian countries in which largest city are present in infobox? (Fig. 12)

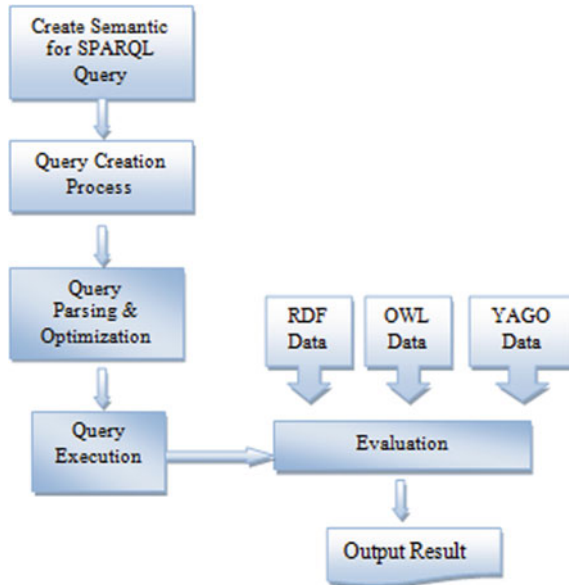


Fig. 7 Framework for the proposed system

countrylabel	Virtuoso SPARQL Query Editor
"Georgia"@en	Default Data Set Name (Graph IRI)
"De facto"@en	http://dbpedia.org
"Uzbekistan"@en	Query Text
"Afghanistan"@en	SELECT ?countrylabel WHERE {
"Azerbaijan"@en	?capital rdf:type <http://dbpedia.org/class/yago/CapitalsInAsia>.
"Bangladesh"@en	?capital dbpedia-owl:country ?country .
"Brunei"@en	?country rdfs:label ?countrylabel .
"Burma"@en	FILTER (lang(?countrylabel) = 'en') .
"China"@en	}
"Cyprus"@en	LIMIT 10

Fig. 8 Query 1 demonstration

Framework Implementation on Test Sets

The queries discussed above were implemented in the system using interfacing of PHP, MySQL and SPARQL. The figures below show the procedure of the system discussing how to fetch some information from Wikipedia Infoboxes. The system processes in the manner:

1. The end-user needs to choose one of the topics of which he/she wants to mine the information. For example, In Fig. 13 the user selects Currency as topic.
2. The user then selects the continent from which it needs to fetch data from (Fig. 14).

Virtuoso SPARQL Query Editor

Default Data Set Name (Graph IRI)
<http://dbpedia.org>

Query Text

```

SELECT ?countrylabel ?capitallabel ?currencylabel WHERE {
?capital rdf:type <http://dbpedia.org/class/yago/CapitalsInAsia>.
?capital rdfs:label ?capitallabel.
?capital dbpedia-owl:country ?country .
?country dbpprop:currency ?currency.
?currency rdfs:label ?currencylabel.
?country rdfs:label ?countrylabel.
FILTER (lang(?countrylabel) = 'en') .
FILTER (lang(?capitallabel) = 'en') .
FILTER (lang(?currencylabel) = 'en') .
}
LIMIT 10
        
```

Fig. 9 Query 2 demonstration

countrylabel	capitallabel	currencylabel
"Cyprus"@en	"Nicosia"@en	"Euro"@en
"Thailand"@en	"Bangkok"@en	"Thai baht"@en
"Armenia"@en	"Yerevan"@en	"Armenian dram"@en
"Iran"@en	"Tehran"@en	"Iranian rial"@en
"Oman"@en	"Muscat, Oman"@en	"Omani rial"@en
"Yemen"@en	"Sana'a"@en	"Yemeni rial"@en
"Azerbaijan"@en	"Baku"@en	"Azerbaijani manat"@en
"Turkmenistan"@en	"Ashgabat"@en	"Turkmenistan manat"@en
"North Korea"@en	"Pyongyang"@en	"North Korean won"@en
"Afghanistan"@en	"Kabul"@en	"Afghan afghani"@en

Fig. 10 Output for Query in Fig. 9

Virtuoso SPARQL Query Editor

Default Data Set Name (Graph IRI)
<http://dbpedia.org>

Query Text

```

SELECT count(?countrylabel) as ?NumberOfAsianCountries WHERE {
?capital rdf:type <http://dbpedia.org/class/yago/CapitalsInAsia>.
?capital dbpedia-owl:country ?country .
?country rdfs:label ?countrylabel .
FILTER (lang(?countrylabel) = 'en') .
}
        
```

NumberOfAsianCountries

41

Fig. 11 Query 3 demonstration

Virtuoso SPARQL Query Editor

Default Data Set Name (Graph IRI)
 http://dbpedia.org

Query Text

```
SELECT count(?larcity) as ?countLarCity|WHERE {
?capital rdf:type <http://dbpedia.org/class/yago/CapitalsInAsia>.
?capital dbpedia-owl:country ?country .
?country dbpedia-owl:currency ?currency .
?country dbpedia-owl:largestCity ?larcity .
}
```

countLarCity
 18

Fig. 12 Query 4 demonstration

**GENERAL KNOWLEDGE BASE
USING SPARQL**

Select Topic
Currency ▼
Select
Currency
GDP
Population
Area

Fig. 13 Primary identifier selection

**GENERAL KNOWLEDGE BASE
USING SPARQL**

Select Topic
Currency ▼
Select Continent
Select ▼
Select
Asian Countries
European Countries

Fig. 14 Secondary identifier selection

3. After user selects the countries the system fetches the list of countries of the selected Continent from DBpedia base using YAGO class Ontology. In the figure below as we select the country name as “India”, we will get the currency in the next step (Fig. 15).
4. The final output screen will be like as shown below for desired query made by user (Fig. 16).

GENERAL KNOWLEDGE BASE
USING SPARQL

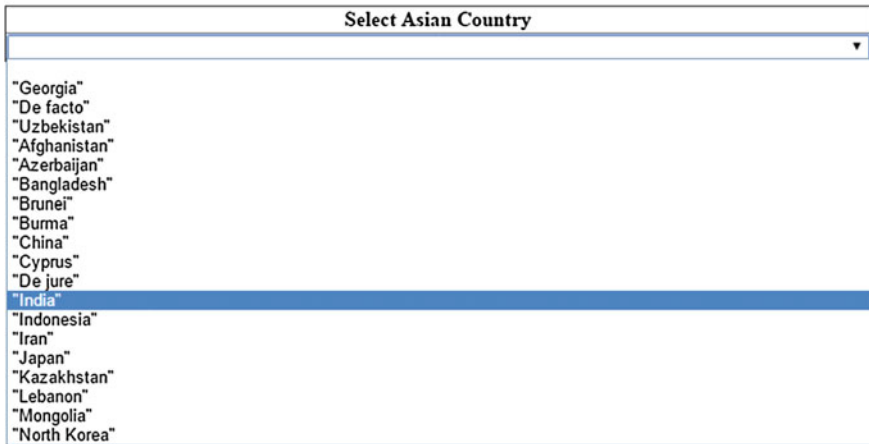
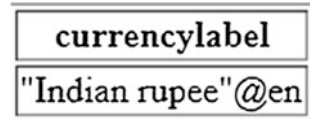


Fig. 15 Final output selection

Fig. 16 Output window



Conclusion

This paper proposes a GUI-based solution for students, organizations and other statuarities which need to access and analyse data. The system fetches the data from the open source Wikipedia Database. This property of the proposed framework makes it a cost-efficient solution of Data Extraction mechanism. The system exploits the Infoboxes of Wikipedia, and the experimental set-up above shows that any Semantic query for extraction can be created at runtime and the inputs and outputs can be produced in user-friendly Graphical User Interface for even Naïve users.

References

1. Shu, Y., Pin, W.X., Gang, W.: Analysis of semantic query performance for jena-based storage model. In: IEEE International Conference on Software Engineering and Service Sciences (ICSESS) (2010)
2. Kumar, N., Kumar, S.: Querying RDF and OWL data source using SPARQL. In: ICCCNT (2013)
3. Farouk, M., Ishizuka, M.: An inference based query engine for RDF data. In: International Conference on Information Retrieval & Knowledge Management (CAMP) (2012)
4. P'erez, J., Arenas, M., Gutierrez, C.: Foundations of RDF databases. In: Reasoning Web. Semantic Technologies for Information Systems, vol. 5689/2009, pp. 158–204 Springer, Berlin (2009)
5. Prud'hommeaux, E., Seaborne, A.: SPARQL Query Language for RDF. <http://www.w3.org/TR/2008/REC-rdf-sparql-query-20080115/> (2008)
6. P'erez, J., Arenas, M., Gutierrez, C.: nSPARQL: a navigational language for RDF, In: Proceedings of the 7th International Conference on The Semantic Web, pp. 66–81 (2008)
7. Kim, J.-D., Shin, H., Jeong, D., Baik, D.-K.: Jena storage plug-in providing an improved query processing performance for semantic grid computing. In: 11th IEEE International Conference on Environment Computational Science and Engineering Workshops, CSE WORKSHOPS '08 (2008)
8. Hayashi, M., Horii, H., Kweon, I., Yoshida, T: A medical information management system. In: IEEE (2008)
9. Suchanek, F.M., Kasneci, G., Weikum, G.: YAGO: a core of semantic knowledge unifying WordNet and Wikipedia. In: ACM (2007)
10. Chen, L., Gupta, A., Kurul, M.E.: A semantic-aware RDF query algebra. In: COMAD 2005, Hyderabad, India (2005)
11. Han, H., Li, Y.: The Research and application of custom rules constructed in jena intelligent reasoning query. In: International Conference on Computer Sciences and Applications (CSA) (2013)

Secure Data Sharing with Data Integrity in Public Clouds Using Mediated Certificate-Less Encryption

Atesh Kumar, Saurabh Mishra, Priyank Dubey and Niraj Kumar

Abstract The popularity and widespread use of cloud have brought great convenience for data sharing and collection. Data sharing with a large number of participants must take into account several issues, including data integrity, efficiency, and privacy of data owners. The shared data must be strongly secured from unauthorized accesses. Many encryption mechanisms support fine-grained encryption. The existing mediated Certificate-less Public Key Encryption scheme reduces the management of key, but the method was found to be insecure against partial decryption attack. Although their scheme relies on pairing operations that incur considerably high computational costs. The proposed mediated Certificate-less Public Key Encryption (mCL-PKE) scheme provides its formal security without pairing operations on based access control.

Keywords Algorithm · Public key encryption · Data sharing · Cloud computing

Introduction

Cloud computing is the approach of delivering IT services over the Internet and emerging as a promising technology to offer services pay-as-you-go basis. The elastic property of cloud enables customer to scale up or down the resources based

Atesh Kumar (✉) · Saurabh Mishra · Priyank Dubey · Niraj Kumar
Department of Computer Science & Engineering, People's College of Research and
Technology, Bhopal 462037, India
e-mail: ateshsingh@yahoo.com

Saurabh Mishra
e-mail: saurabh.mish3@gmail.com

Priyank Dubey
e-mail: priyankdubey01@gmail.com

Niraj Kumar
e-mail: nirajkumar.cse09@gmail.com

upon the requirements dynamically and reduces up-front IT investment significantly [1]. Cloud computing promises to cut the operational cost and capital costs and more importantly let IT departments focus on strategic projects instead of keeping the data center running.

In essence, cloud computing is a construct that allows the user to access applications that actually reside at a location other than the user's system or other Internet connected devices; more often this will be a distant data center. The data center is a collection of servers where the user subscribed application is housed. The widespread adoption of cloud storage services, the public cloud storage model should solve the critical issue of data confidentiality [2, 3]. That is, shared sensitive data must be strongly secured from unauthorized accesses. In order to assure confidentiality of sensitive data stored in public clouds, the encryption of the data before uploading it to the cloud is used. Since the cloud does not have the keys used to encrypt the data, the data confidentiality from the cloud is guaranteed. However, as many organizations are required to enforce fine-grained access control to the data, the encryption method must be able to support fine-grained encryption-based access control.

Problem Statement

The key management problem was solved by Identity-Based Public Key Cryptosystem (IB-PKC), but it suffers from the key escrow problem as the key generation server learns the private keys of all users. Recently, Attribute-Based Encryption (ABE) has been proposed that allows one to encrypt each data item based on the access control policy applicable to the data [4]. However, in addition to the key escrow problem, ABE has the revocation problem as the private keys given to existing users should be updated whenever a user is revoked. To solve these issues and for secure data sharing, Certificate-less Proxy Re-Encryption (CL-PRE) is used. It relies on pairing operations. The recent advances in running techniques, the computational costs required for pairing are still considerably high compared to the costs of standard operations. The existing security model is often not sufficient to guarantee security in general protocol setting. Thus a secure mediated scheme without pairings is needed [5].

Existing System

The existing mediated Certificate-less Public Key Encryption scheme reduces the key management. In this scheme, user's private key consists of a secret value chosen by the user and a partial private key generated by the Key Generation Center (KGC) [6]. If any user compromised the cloud, using its private key attempts to

access the data in the cloud. The scheme was found to be insecure against partial decryption attack, since their security model did not consider the capabilities of the adversary in requesting partial decryptions.

Drawbacks

- Users are required to manage a number of keys equal to at least the logarithm of the number of users.
- It is based on bilinear pairings, they are computationally expensive

Their security model did not consider the capabilities of the adversary in requesting partial decryptions [7]

Proposed Method

The proposed mCL-PKE scheme consists of five entities, namely the data owner, users, the Security Mediator (SEM), the Key Generation Center (KGC), and the storage service. The SEM, KGC, and the storage service are semi-trusted and reside in a public cloud. They are trusted for executing the protocols correctly. The KGC in the cloud generates master key which is a set-up operation. Each user generates public and private keys using mCL-PKE scheme and sends their public key and Identity (ID) to the KGC. The KGC in turn generates two partial keys and a public key for the user. The public key, referred to as KGC-key, is used to encrypt data. The two partial keys and user's private key are used together to decrypt encrypted data.

The data owner obtains the KGC-keys of users from the KGC in the cloud and encrypts each data using a random session key K . The data owner encrypts K using the KGC-keys of users. The encrypted data along with the access control list is uploaded to the cloud. The encrypted content is stored in the storage service in the cloud and the access control list, signed by the data owner, is stored in the SEM in the cloud. When a user wants to read some data, it sends a request to the SEM to obtain the partially decrypted data. If the verification is successful, the SEM retrieves the encrypted content from the cloud and partially decrypts the content using the SEM-key for the user. The user uses its private key and partial key given by KGC to fully decrypt the data.

Once the initial partial decryption for each user is performed, the SEM stores back the partially decrypted data in the cloud storage. If a user is revoked, the data owner updates the access control list at the SEM so that future access requests by the user are denied.

Advantages

- It simplifies the task of key management.
- It reduces the computational overhead by using pairing free approach.
- The computation costs for decryption at the users are reduced as a semi-trusted security mediator partially decrypts the encrypted data before the users decrypt.
- It supports immediate revocation of compromised users.
- The scheme does not suffer from the key escrow problem.
- Secure against the partial decryption attack.

Architectural Diagram

See Fig. 1.

Algorithm Used

Step 1 Input: U, U_d

Output: ID (U_{id}), key (U_k) from Key Generation Center (KGC)

for (Each U_d ($i, i = 1,2...m$))**{**

1. $KGC \leftarrow$ user details (U_d); // **KGC receives User details**
2. Generate (U_{id}) \rightarrow user (U); // **KGC generates Id to U**
3. Stores the details in KGC Database;
 generateKey();}generateKey ()**{for** (each U_{id})**{**

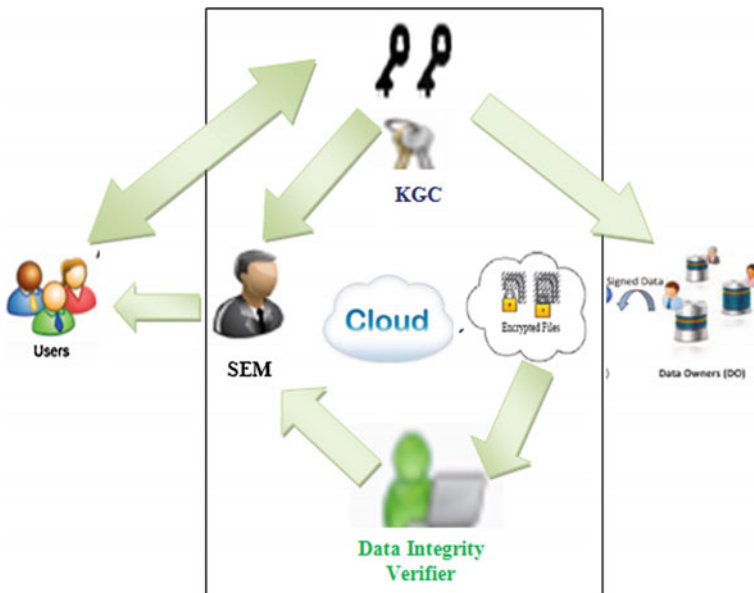


Fig. 1 Architectural view

1. Generate Public (Pu), Partial (Pa₁, Pa₂) Key Pairs;


```
int prime; // Bit length of each prime number
BigInteger p, q; // Two distinct large prime numbers p and q
BigInteger N; // Modulus N
BigInteger r; // Public exponent E and Partial exponent D;
BigInteger E, D, N = p * q; r = (p - 1) * (q - 1);
Choose E, coprime to and less than r;
D = E.modInverse(r); // Compute D, the inverse of E mod r;
Pu = E; Pa = D;
```
2. (Pa₁, Pa₂) → U, M; // **Send the Partial keys to User and Mediator** }

where:- U → User, U_d → User details, U_{id} → Unique Id for U,
 U_k → Keys for U; Pu → Public key, Pa₁, Pa₂ → Partial Keys,
 M → Mediator

Step 2 Input: S_k, Pu, D

Output: E_D

User U, Log in:

If U's action to perform is "Data out Source" means U act as an Owner

1. Select the data (D) to encrypt
2. Encrypt D using AES Symmetric Encryption // **generate the secretkey using keygenerator**
 - (i) S_k = KeyGenerator.getInstance("AES").generateKey(); // **initialize**
 - (ii) Cipherc = Cipher.getInstance("AES/CBC/PKCS5Padding");
 - (iii) c.init(Cipher.ENCRYPT_MODE, S_k, alg);
 - (iv) Use E_D ← CipherOutputStream;
3. Set the Access Control for the encrypted data. for (each E_D) {


```
Ulist ← Registered Users in the cloud;
Ul = Select {Ulist}; // Select the user from the list;
ACU ← Put Ul; PuUl = KGC {ACUl, Pu}; ESk ← Encrypt(Sk, PuUl);
Where:- Ua → User Access; Uo → Data Owner; D → Data;
Sk → Secret Key; ED → Encrypted Data; ESk → Encrypted Secret Key;
ACU → Access Control List; PuUl → Public key of selected user
```

Block Diagram

See Fig. 2.

Modules Description

I. User authentication and key generation

Input: New User

Output: Private and public Keys

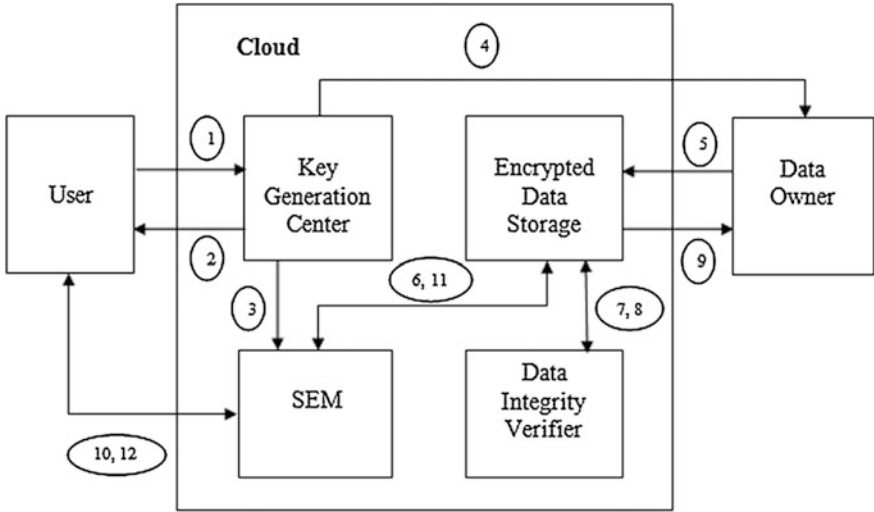


Fig. 2 Block view

New user obtains the token from Identity Provider by submitting their details. Whenever a new user accesses CSP (Cloud Service Provider), it asks for token to authenticate the user. Hence user should obtain the token from the Identity Provider before starting access of the data in CSP. Identity provider forwards the details of the user to the CSP. CSP stores the token and user details in database. Users provide the token obtained from Identity provider while login for the access in CSP. CSP validates the token using the details stored in database. If the token is valid, users are allowed for the access in cloud. Otherwise access is denied for the user. Each user first generates its own private and public key pair, called SK and PK, using the Set-Private Key and Set-Public Key operations respectively (Fig. 3).

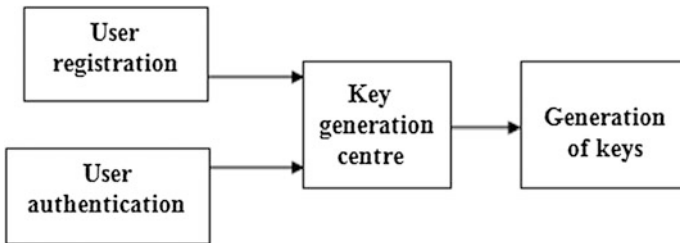


Fig. 3 User authentication

II. Encryption of data

Input: Private and public keys

Output: Encrypted data

The user sends its public keys and its identity (ID) to the KGC in the cloud. The KGC in turn generates two partial keys and a public key for the user. One partial key, referred to as SEM-key, is stored at the SEM in the cloud. The other partial key, referred to as U-key, is given to the user. The public key, referred to as KGC-key, consists of the user generated public key as well as the KGC generated public key. The KGC-key is used to encrypt data. The SEM-key, U-key, and SK are used together to decrypt encrypted data. The data owner obtains the KGC-keys of users from the KGC in the cloud. The data owner then symmetrically encrypts each data item for which the same access control policy applies using a random session key K and then the data owner encrypts K using the KGC-keys of users (Fig. 4).

III. Data uploading

Input: Encrypted data

Output: Intermediate key with access control list

The encrypted data along with the access control list is uploaded to the cloud. Data owner generates intermediate key with hash value for each data. The encrypted content is stored in the storage service in the cloud and the access control list, signed by the data owner, is stored in the SEM in the cloud. Intermediate key is send to SEM and hash value is send to data integrity verifier (Fig. 5).

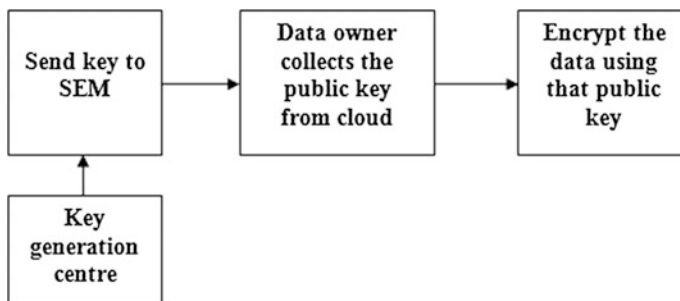


Fig. 4 Encryption of data

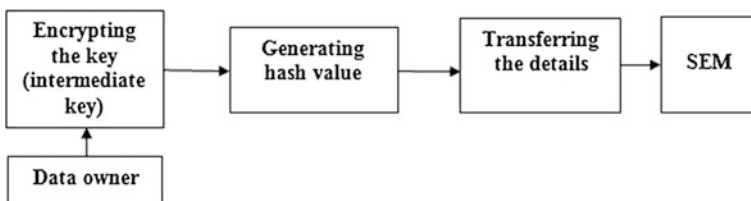


Fig. 5 Encryption of data

IV. Data integrity verification

Input: Encrypted data and its hash value

Output: Hash Value for received Encrypted data + Verification

Data integrity verifier generates the hash value for received encrypted data for security. It verifies the encrypted data hash value with data owner encrypted data hash value. Data integrity verifier stores the encrypted data in storage module, if hash value verification is true otherwise; it sends the data to data owner for re-encryption (Fig. 6).

V. Decryption of SEM and user

Input: User request for retrieval

Output: Original data

A user wants to read some data; it sends a request to the SEM to obtain the partially decrypted data. The SEM first checks if the user is in the access control list and if the user's KGC-key encrypted content is available in the cloud storage. If the verification is successful, the SEM retrieves the encrypted content from the cloud and partially decrypts the content using the SEM-key for the user. The partial decryption at the SEM reduces the load on users. The user uses its SK and U-key to fully decrypt the data. In order to improve the efficiency of the system, once the initial partial decryption for each user is performed, the SEM stores back the partially decrypted data in the cloud storage. If a user is revoked, the data owner updates the access control list at the SEM so that future access requests by the user are denied. If a new user is added to the system, the data owner encrypts the data using the public key of the user and uploads the encrypted data along with the updated access control list to the cloud (Fig. 7).

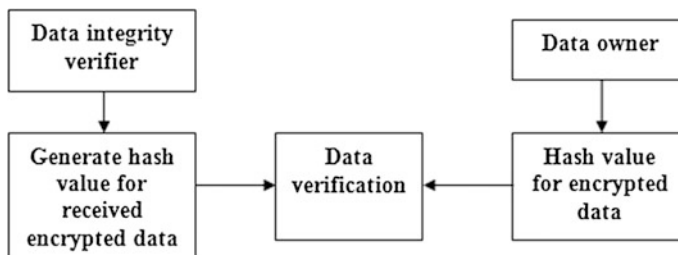
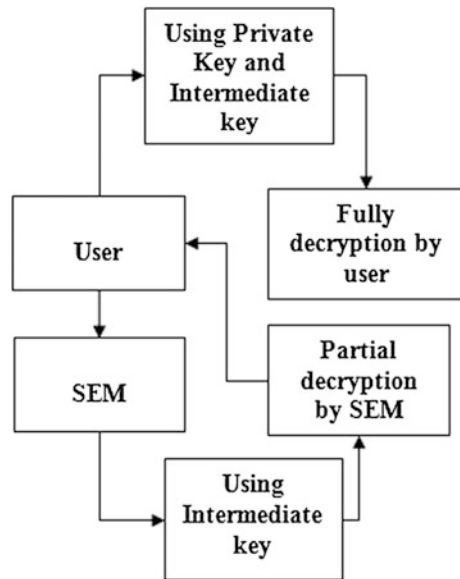


Fig. 6 Data integrity

Fig. 7 Encryption of data



Result and Conclusion

In this paper we have proposed the first mCL-PKE scheme without pairing operations and provided its formal security. Our mCL-PKE solves the key escrow problem and revocation problem. Using the mCL-PKE scheme as a key building block, we proposed an improved approach to securely share sensitive data in public clouds. Our approach supports immediate revocation and assures the confidentiality of the data stored in an untrusted public cloud while enforcing the access control policies of the data owner. Furthermore, it provides the data with high security using data integrity verifier that verifies the encrypted data using hash value generation.

References

1. Baek, J., Safavi-Naini, R., Susilo, W.: Certificate less public key encryption without pairing (2005)
2. Al-Riyami, S., Paterson, K.: Certificate less public key cryptography. In: Springer transaction on Advances in Cryptology—ASIACRYPT, vol. 2894, pp. 452–473 (2003)
3. Bethencourt, J., Sahai, A., Waters, B.: Cipher text-policy attribute-based encryption (2007)
4. Boneh, D., Ding, X., Tsudik, G.: Fine-grained control of security capabilities. *ACM Trans. Internet Technol.* **4**(1), 60–82 (2004)
5. Chow, S.S.M., Boyd, C., Nieto, J.M.G.: Security mediated certificate less cryptography. In: Proceedings of the 9th International Conference on Theory and Practice of Public-Key Cryptography, PKC'06, pp. 508–524 (2006)

6. Yu, S., Wang, C., Ren, K., Lou, W.: Attribute based data sharing with attribute revocation. In: Proceedings of the 5th ACM Symposium on Information, Computer and Communications Security, ASIACCS'10, pp. 261–270 (2010)
7. Wu, X., Xu, L., Zhang, X.: CL-PKE: a certificate less proxy re-encryption scheme for secure data sharing with public cloud. In: ACM Symposium on Information, Computer and Communications Security (2012)

K-N Secrete Sharing Scheme of Visual Cryptography for Hiding Image Using 2×2 Blocks Replacement

Ashish Sharma and Devesh Kumar Srivastava

Abstract Visual cryptography is a method offering a plan which uses pictures circulated as shares in such a way that when the shares are stacked, a sensitive or secrete image is uncovered. According to extended visual cryptography, the offer pictures are built to hold the scattered images together, simultaneously opening a way to assist biometric security and visual cryptography methods. In this paper, we entail a proposal for halftone pictures that beautify the nature of the shares to come about from secrete image and to regain the secret picture in an extended visual cryptography plan for which the figure size of the secret pictures and the reconstructed picture by stacking shares is similar with respect to the first halftone secret picture. The ensuing plan upholds the ideal security of the first developed visual cryptography approach. This process includes 2×2 block replacement for generating shares from secrete image.

Keywords Image processing · Visual cryptography · Extended visual cryptography · Simple block replacement · Balanced block replacement · Secret sharing

Introduction

Visual cryptography (VC), was first presented by Naor and Shamir in 1994. VC is a method of secret sharing; this technique is precisely bank upon white and black or binary pictures [1]. Sensitive information in the form of an image is set apart into shares; by stacking these shares a secrete image can be recovered. This stacked share does not reveal any kind of information of the original secret. Shares generated from the secrete image may be circulated to different parties so that only by superimposing an appropriate number of shares, we can reveal the secrete image.

Ashish Sharma (✉) · D.K. Srivastava
Department of CSE, Manipal University Jaipur, Jaipur, India
e-mail: ashish.sharmasy2k@gmail.com

D.K. Srivastava
e-mail: devesh988@yahoo.com

Recuperation of the secret image is possibly done by stacking or superimposing the share pictures and thus, the interpreting procedure obliges no extraordinary equipment or programming and could basically be completed by the normal human eye. VC is of specific enthusiasm for security provisions depending on biometrics [2]. For illustration, biometric data such as facial and finger impressions, which are more signature pictures might be kept secret by apportioning into shares, which could be appropriated for security to various parties. This paper includes a short review on various visual cryptography schemes like $(2, 2)$, $(2, n)$, (k, n) ; in addition, two techniques of block replacement are also described in depth which are based on the replacement process of 2×2 pixels blocks of an image. Then, the main work is presented in detail with the help of the proposed algorithms and figures developed in a MATLAB environment.

The secret picture can then reveal when the shares containing parties give their share pictures which are then superimposed.

Related Work

Visual cryptography contains various schemes like:

(A) *2 out-of-2 visual cryptography scheme:*

A normal scheme of $(2, 2)$ VCS generates two share pictures on the basis of an original image from the sharer's to the user's end and must superimpose both the shares to generate the original image; its layout is shown in Fig. 1. To secure the ratio of the obtained secret image from shares in $(2, 2)$ scheme, every pixel in the secret image (original image) can be replaced in the share image by a 2×2 block of subpixels. According to Table 1, for white original pixel, one of six combinations is created. Same process is applicable for black pixel. After superimposing the shares, the original image will be obtained [3, 4].

(B) *2 out-of- n visual cryptography scheme:*

In this scheme, n shares will be generated from a secret image and any two of them are required for stacking to obtain the original image [5–16] as shown in Fig. 2.

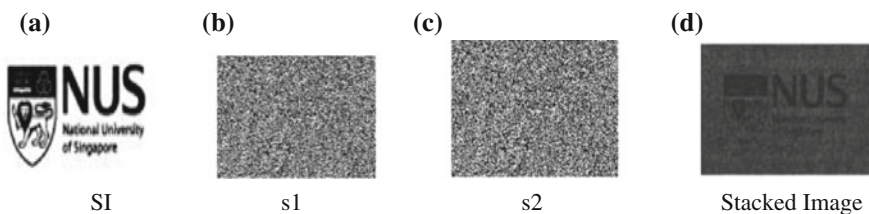


Fig. 1 The 2-out-of-2 VCS with 4-subpixel layout **a** Secret image, **b** S1, **c** S2, and **d** S1 + S2 [3]

Table 1. (2;2) VC scheme with four subPixels

Pixel	Probability	Share 1	Share 2	After Stacking
<div style="display: inline-block; width: 15px; height: 15px; border: 1px solid black; background-color: white;"></div> White	1/6			
	1/6			
	1/6			
	1/6			
	1/6			
	1/6			
<div style="display: inline-block; width: 15px; height: 15px; background-color: black;"></div> Black	1/6			
	1/6			
	1/6			
	1/6			
	1/6			
	1/6			

(C) K out-of N visual cryptography scheme:

In the previous scheme of (2, 2) VC, both the shares are needed to obtain the secrete image. If one of them gets hacked by someone or lost, the secrete image cannot be obtained. So there is a confinement of keeping all the partitions secure to unleash the sensitive information in the form of image and parties cannot afford to let go of a solid share. To resolve this hazard and provide some laxity in this systematic plan, the initial model of VC brought to us by Naor and Shamir could be juxtaposed into a visual variant of k out-of n visual cryptography scheme [17]. In (k, n) VC scheme, n shares generated from the secrete image are circulated. The secrete image is obtained only if k shares are superimposed together, where the value of k lies from 2 to n. If less than k shares are superimposed together, the secrete image cannot be obtained as the example shows in Fig. 3. It gives some feasibility to the user. Even if a party lost one or two of the shares, the secrete image can still be obtained, if the minimum k number of shares are obtained [16].

The (2, 2) extended VC scheme introduced [18] in this scheme with the help of expansion of one pixel in the secrete image to four subpixels, which can then be chosen to generate the required cover images for each share. It is absolutely secure and no share image leaks any secrete information of the original image. Figure 4 illustrates a (2; 2) scheme containing the original binary secrete image, “Engineering,” with two cover images, “Memorial” and “University,” embedded into the shares.

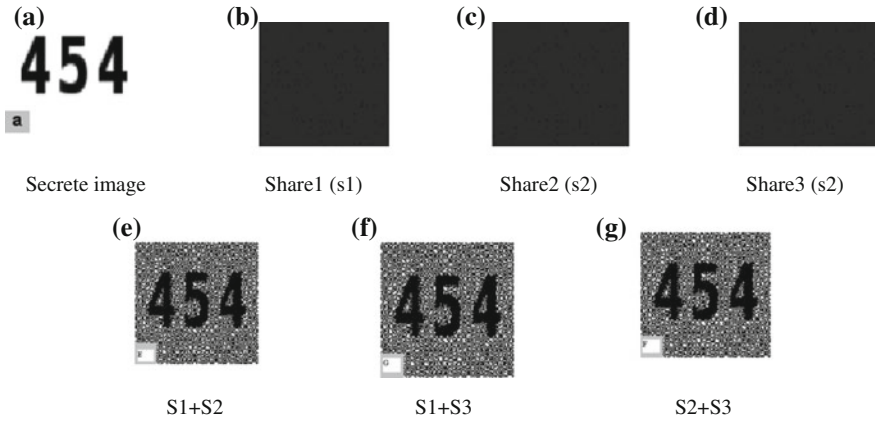


Fig. 2 The 2-out-of-n VCS using the image secret image (SI) **a** SI **b** S1, **c** S2, **d** S3, **e** S1 + S2, **f** S1 + S3, and **g** S2 + S3 [6]

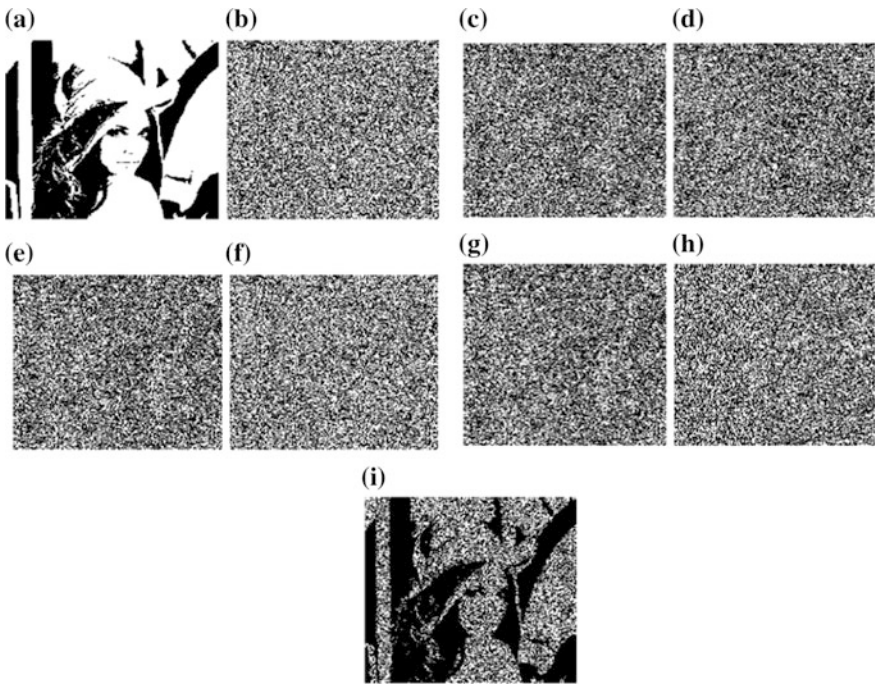


Fig. 3 The 3-out-of-6 VCS with ABM of secret image (SI): **a** SI **b** S1, **c** S2, **d** S3, **e** S4, **f** S5, **g** S6, **h** S3 + S4, **i** S1 + S2 + S3, **j** S1 + S2 + S4, **k** S2 + S3 + S4 [18]

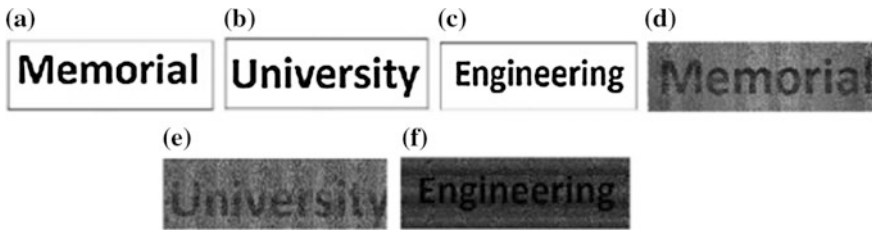


Fig. 4 Example of (2; 2) EVC Scheme: **a** first cover image **b** second cover image **c** secret image; **d** share 1 **e** share 2 **f** recovered secret image [20]

Generally, VC performs on binary images; it can also be applicable on grayscale images by converting them to binary images using halftoning. So, halftoning is the process of converting grayscale image into binary image; this process is referred as the preprocessing step for VC. Past schemes integrating halftoning and visual cryptography have experienced issues, for example, picture extension (that is, obliging essentially more pixels for the shares and/or revealed secret picture) [19] and compromise of the security of the visual cryptographic scheme [20]. The target of the research portrayed in this paper is to bring about a safe (k, n) visual cryptography scheme, which essentially does not need additional amount of pixels in the shares and revealed picture than the first secret picture but contains a great quality picture for both the shares and the revealed picture. Our proposed plan keeps up the ideal security of the fundamental EVC plan.

Block Replacement Process on Halftone Image (Preprocessing)

In this area, we think about the requisition of VC to grayscale pictures by first changing over the pictures to a binary picture by applying a halftoning scheme. In the wake of making a halftone picture, to protect the size of secret picture when applying VC and EVC, straightforward scheme might be applied. For instance, a fundamental secure scheme that is not difficult to execute is based on a block-wise methodology to preprocess the binary halftone picture prior to applying VC [19]. In this paper, we include some normal approach of block replacement. They are:

(A) Simple block replacement:

According to this scheme, it is considered that the SBR plan recognizes a group of four pixels from the halftone secret picture in one 2×2 blocks, alluded as a secret block that peddles to form the shares block by block (in place of pixel by pixel) shown in Fig. 5. As each block of 2×2 with four pixels are converted into n secret shares, each one getting four pixels, the size of the revealed picture is the same as the first secret picture after stacking the any k shares among n shares together. In this method, all the secret blocks in a picture need to be transformed before visual



Fig. 5 Black block replacement using SBR

cryptography encoding and every secrete block is swapped by the comparing foreordained applicant, which is a block containing four white pixels (a white block) or a block containing four black pixels (a dark piece).

If the number of black pixels in 2×2 block is less than or equal to 1, then the block is converted into a complete white block. An example of block replacement using SBR is shown in Fig. 6.

The SBR preprocessing method is particularly based on various dark and white pixels in every secrete block, as shown in Fig. 7. On the off chance, the amount of black pixels in a secrete block is bigger than or equivalent to 2, the secrete block is replaced by a black block. On the off chance, if the amount of black pixels in a secrete block is short of what are equivalent to 1, it will transform into a white block. A trouble is related with the procedure if it contains two black pixels and two white pixels. To terminate this hazard, a resplendent procedure was introduced called as the balanced block replacement (BBR) method.

(B) *Balanced Block Replacement (BBR):*

The novel viewpoint in this methodology is to perform the replacement of a block such that there is a superior equalization of white and dark in the processed secrete image. The example of this method is shown in Fig. 8. The previous SBR method brings about darker pictures, since the block which holds two white and two black pixels are changed over to a black pixel. The BBR approach balances white and black in the processed picture by providing some candidate blocks to black and



Fig. 6 An example of block replacement using SBR



Fig. 7 White block replacement using SBR

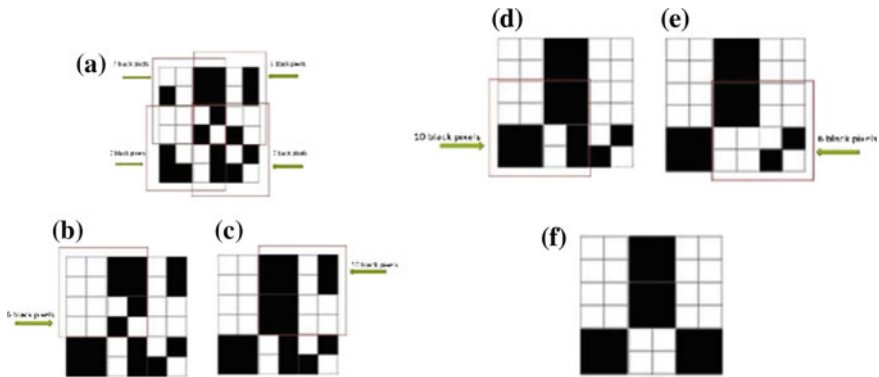


Fig. 8 Example of the BBR Method [3]

others to white. The assignment of these candidate blocks is performed randomly; this improves the quality of the visually processed secrete image [19].

Proposed Scheme—An Improved Block Replacement Algorithm

This scheme includes few steps for use in VC. These are as follows:

- Step1.* First, convert the secret grayscale image into a halftone image. If there is a color secrete image, then first convert it into grayscale image and then perform halftoning. Prior to halftoning of a grayscale picture, the magnitude of a picture should be adhered to escape pixel expansion. For halftoning, Jarvis halftoning algorithm is used.
- Step2.* Similarly, a different image is taken for covering the secrete image by this image. Again, the first step is applied for this image also. This image is referred as “stego image”
Note—here 1 stands for white and 0 stands for black; for applying algorithm we have to convert the images to negative
- Step3.* is to hide the secrete image by covering it from a stego image. For this, bit ending operation is done between stego images and secrete image. This refreshed picture is known as “processed image”
- Step4.* Formation of share is done on “processed image”. So for this, the entire image is divided into 2×2 blocks and also divide the stego image and the secrete image in 2×2 blocks. Count operation is performed to identify the number of ones in each block. After this, four conditions arise for block replacement

4.1 if count ≥ 2 , type1 algorithm is used for shares generation. This includes three subconditions. They are

4.1.1 If counts == 4, then type14 algorithm is used for share generation.

4.1.2 If counts == 3, then type13 algorithm is used for share generation.

4.1.3 If counts == 2, then type12 algorithm is used for share generation.

4.2 If counts == 1, then type2 algorithm is used for share generation.

4.3 If counts == 0, then type3 algorithm is used for share generation.

Step5. by performing the bit or operation on shares, the final output secrete image is revealed

General Algorithm Description

In this scheme of VC, it includes the various algorithms for halftoning shares generation. This section describes some general information related to the algorithm. They are

(1) *Type 14-*:

This algorithm is applicable to the number of 1 in 2×2 blocks is 4. Here base matrix is used for block replacement.

$B1 = [1,1;0,0]$, $B2 = [0,1;1,0]$, $B3 = [0,0;1,1]$, $B4 = [1,0;1,0]$, $B5 = [0,1;0,1]$, $B6 = [1,0;0,1]$

Here, 1 stands for black and 0 stands for white. A random value is generated from 1 to 6 and base matrix is marked in accordance to the arbitrarily aroused figure. For instance, if arbitrarily aroused figure is 3 then $B3 = [0,0;1,1]$ is chosen. The implementation of this procedure lies on the number of shares; if there exists 6 shares then, 6 time execution of process takes place. In (k, n) scheme, n number of zero matrix of certain size equating to the dimension of processed image is needed for share generation. At every execution, 2×2 block of a single zero matrix is imposed by the chosen base matrix.

(2) *Type 13-*:

This algorithm is applicable to the number of 1 in 2×2 blocks is 3. Here, base matrix is used for block replacement. Here, the number of 1's is 3 and in base matrix the number of 1's is 2; for a block replacement first convert the 2×2 blocks containing 3 ones in processed image into a 1×4 matrix. For example,

$$\begin{array}{ccc} [1, 1, 1, 0] & \rightarrow & [1, 1, 1, 0] \\ 2 \times 2 & & 1 \times 4 \end{array}$$

Now calculate the position m of min value n in 1×4 matrixes. Suppose, here it is 4. Random value r is generated from 1 to 4

If $r == m$, then again generate random value from 1 to 4

St = ones (2, 2)

Replace the position m in S_t with value n
 If $r == 1$ or $m == 1$ then replace $st(1, 1) = 0$ end
 If $r == 2$ or $m == 2$ then replace $st(1, 2) = 0$ end
 If $r == 3$ or $m == 3$ then replace $st(2, 1) = 0$ end
 If $r == 4$ or $m == 4$ then replace $st(2, 2) = 0$ end

At each execution, 2×2 block of a single zero matrix is replaced by S_t Matrix.

(3) *Type 12*-:

This algorithm is applicable is the number of 1 in 2×2 blocks is 2, then value of 2×2 block of zero matrix is replaced by the same value of 2×2 block of processed image.

For example,

1	0
0	1

2x2 block of processed image

0	0
0	0

2x2 block of single share

1	0
0	1

After replacement 2x2 block of single shares

(3) *Type 2*-:

This algorithm is applicable and the number of 1 in 2×2 blocks is 1. Here, base matrix is used for block replacement. For generating the base matrix, input is taken from the bit-ended matrix (processed image) and input from the secrete image (original image). Replacing zero matrix (2×2) on the base matrix of S and Sec (S is a 2×2 block of processed image and Sec is 2×2 block of original secrete image).

(3) *Type 3*-:

This algorithm is applicable and the no of 1 in 2×2 blocks is 0. Here, base matrix is used for block replacement. For generating the base matrix, input is taken from stego image denoted by “ St_e ” (cover image used for hiding secrete image) and input from secrete image denoted by “ Sec ” (original image). Replacing zero matrix (2×2) on the base matrix of S and Sec (St_e is a 2×2 block of cover image and Sec is 2×2 block of original secrete image).

Results

See Fig 9.

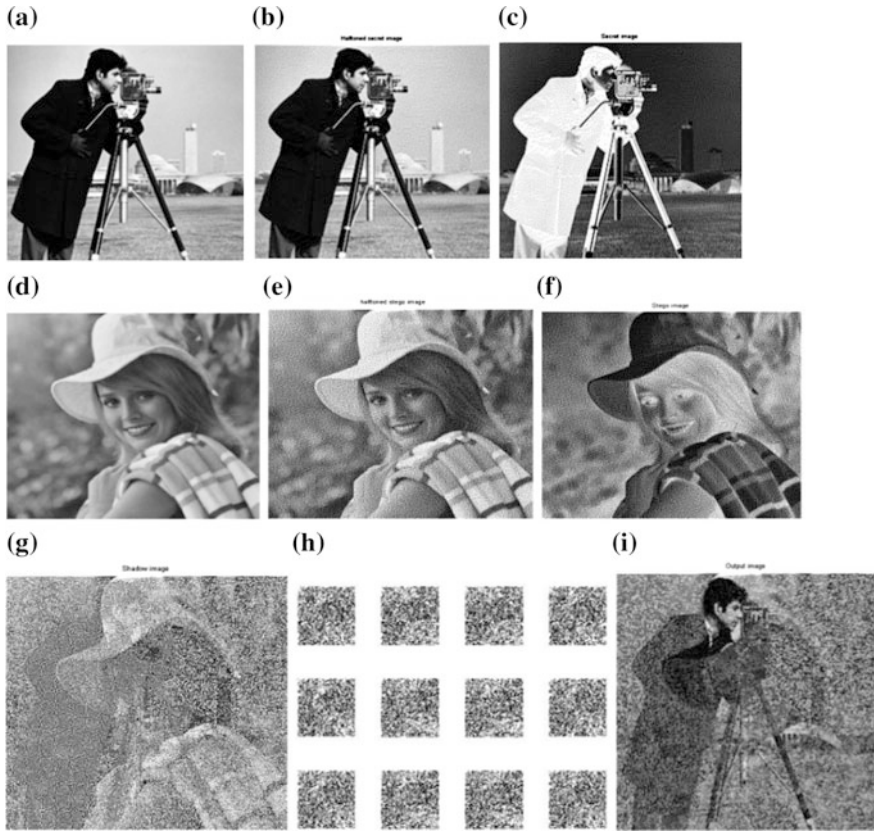


Fig. 9 Process of (k, n) visual cryptography scheme. **a** Secrete image (Sec). **b** halftone secrete image. **c** Negative of halftone secrete image. **d** Cover image (Ste). **e** Halftone cover image. **f** Negative of halftone cover image. **g** Bit ending between generation. **h** (7,12) share using stacking. **i** Reconstructed Image Sec and Ste (Processed image S)

Conclusion

In this paper, we developed visual cryptography (VC) without pixel expansion. We have demonstrated through Fig. 9 that by utilizing best preprocessing of halftone pictures based on the aspects of the first secrete picture, we can handle great quality pictures in the shares and the obtained picture. Note that different provisions can likewise profit from the preprocessing methodology, for example, different picture VC which conceals different pictures in shares.

References

1. Naor, M., Shamir, A.: Visual cryptography. In: EUROCRYPT'94 Proceedings, Lecture Notes in Computer Science, vol. 950, pp. 1–12. Springer (1995)
2. Ross, A., Othman, A.A.: Visual Cryptography for Biometric Privacy. *IEEE Trans. Inf. Forensics Secur.* **6**(1), 70–81 (2011)
3. Askari, N., Moloney, C., Heys, H.M.: A Novel Visual Secret Sharing Scheme Without Image Size Expansion. In: IEEE Canadian Conference on Electrical and Computer Engineering (CCECE), Montreal, pp. 1–4 (2012)
4. Hwang, K.F., Chang, C.C.: Recent Development of Visual Cryptography, Intelligent Watermarking Techniques, pp. 459–480. World Scientific Publishing Company (2004)
5. Stinson, D.: Visual cryptography and threshold schemes. *Dr. Dobb's J.* 36–43 (1998)
6. BorkoFurht, EdinMuharemagic, Socek, Daniel: Visual and Audio Secret Sharing, pp. 163–192. *Multimedia Encryption and Watermarking*, Springer (2005)
7. Zhou, Z., Arce, G.R., Crescenzo, G.Di.: Halftone visual cryptography. *IEEE Trans. Image Process.* **15**, 8 (2006)
8. Hsu, C.-Y., Lu, C.-S., Pei, S.-C.: Joint Screening Halftoning and Visual Cryptography for Image Protection. *LNCS 4283*, pp. 212–225. Springer, Berlin (2006)
9. Walden, D.E.: A Benchmarking Assessment of Known Visual Cryptography algorithms. B.S. M.E. Thesis, Chester F. Carlson Center for Imaging Science Rochester Institute of Technology, Valparaiso University, New York, 16 May 2012
10. Horng, G., Chen, T., Tasi, D.S.: Cheating in Visual Cryptography, Designs, Codes and Cryptography, pp. 219–236 (2006)
11. Shih, F.Y.: *Digital Watermarking and Steganography Fundamentals and Techniques*, CRC Press, Taylor & Francis Group (2008)
12. Yang, C.-N., Yang, Y.-Y., Chen, T.-S., Ye, G.-C.: New steganography scheme in halftone images. In: Proceedings of the IEEE International Conference on Intelligent Information Hiding and Multimedia Signal Processing, pp. 1520–1523 (2008)
13. S., Cimato, De Santis, A., Ferrara, A.L., Masucci, B.: Ideal contrast visual cryptography schemes with reversing. *Information Processing Letters* **93**(4), 199–206 (2005)
14. Naor, N., Shamir, A.: Visual cryptography. In: *Advances in Cryptology: Eurocrypt'94*, pp. 1–12. Springer, Berlin, Germany (1995)
15. Lin, C.-C., Tsai, W.-H.: Visual Cryptography for Gray-Level Images the 13th IPPR Conference on Computer Vision, Graphic and Image processing, pp. 221–226 (2000)
16. Ateniese, Giuseppe, Blundo, Carlo, De Santis, Alfredo, Stinson, Douglas R.: Extended capabilities for visual cryptography. *Theoret. Comput. Sci.* **250**, 143–161 (2001)
17. Naor, M., Shamir, A.: Visual cryptography. In: Proceedings of Advances in Cryptology, EUROCRYPT 94, Lecture Notes in Computer Science, vol. 950, p. 112 (1995)
18. Ateniese, G., Blundo, C., De Santis, A., Stinson, D.R.: Extended capabilities for visual cryptography. *Theoret. Comput. Sci.* **250**, 143–161 (2001)
19. Zhou, Z., Arce, G.R., Di Crescenzo, G.: Halftone visual cryptography. *IEEE Trans. Image Process.* **15**(8), 2441–2451 (2006)
20. Nakajima, M., Yamaguchi, Y.: Extended visual cryptography for natural images. In: Proceedings of WSCG, pp. 303–310 (2002)

Stepping Stone Detection Techniques: Classification and State-of-the-Art

Rahul Kumar and B.B. Gupta

Abstract Today, the most common way to perform various attacks is to use stepping stone hosts in the attacking path. In stepping stone attacks, attacker creates a long chain of connections via intermediary previously compromised nodes, to execute attack. The only way to break this chain is to detect stepping stones and applying some security constraints on the traffic flowing through them, not to allow malicious traffic through them. In this paper, we present classification and state-of-the-art of existing schemes proposed for stepping stone detection in recent past. Moreover, we compare these techniques based on their merits and demerits, and discuss open issues and challenges that can be used for further research in this domain.

Keywords Stepping stone host · Stepping stone connection chain · Stepping stone connection pair · Stepping stone intrusion path

Introduction

Internet plays a vital role in today's daily life and business. Online availability of various services like banking, shopping, software and hardware services, social networking etc., has number of benefits such as time saving, better customer services and experience, storing and sharing information, etc. Due to these benefits, a mammoth part of population on earth is now getting connected to it. But Internet also has some security holes which creates serious security issue to its user. Lack of security in any of the services can cause a loss of lots of money and most importantly it may cause loss of secret information of any organization, country, or of an individual. Therefore, proper security of these services is required to protect

Rahul Kumar · B.B. Gupta (✉)
National Institute of Technology Kurukshetra, Kurukshetra, India
e-mail: gupta.brij@gmail.com

Rahul Kumar
e-mail: Rahulkumarbit72@gmail.com

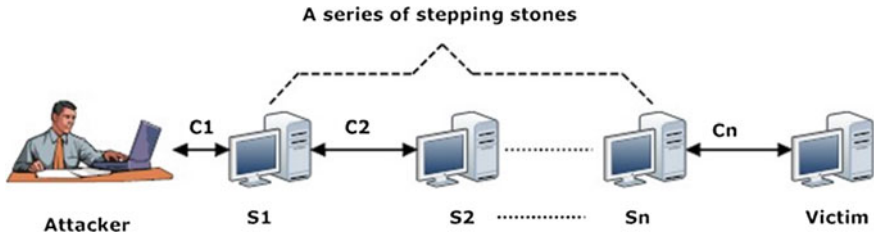


Fig. 1 Stepping stone attacks model

these services from attackers. But attackers are more dominating and they never give up; every time researcher come up with new solution, attackers find new evasion techniques [1, 2].

In most of the cases, attacker uses stepping stone hosts to execute attacking commands instead of attacking from his/her personal computer machine, due to which attacker remains unidentified [3]. Attacker uses various scanners to find out vulnerable computer machines over Internet and then exploit the vulnerabilities found over these machines to compromise it. Moreover, attacker can use these compromised machines to find some more vulnerable machines over Internet to compromise and so on. In this way attacker is able to create chain of connections through compromised hosts/machines, which also known as stepping stone hosts, and use these compromised hosts to execute attacking command [4]. Due to the property of TCP/IP protocol, packets arriving at victim host will contain IP address of last stepping stone host in the chain, therefore last stepping stone host in connection chain appears as an attacker [5].

Stepping stone attacking model is shown in Fig. 1. In this attacking model, there are n stepping stone hosts namely S_1, S_2, \dots, S_n . The series of connections $\langle C_1, C_2, \dots, C_n \rangle$ is called stepping stone connection chain and any pair of these connections is called stepping stone connection pair. For example, (C_1, C_2) is a stepping stone connection pair [3].

There is flexibility in the way stepping stones can be used to execute attacks due to which different kinds of attacks can be executed such as denial-of-service attacks [6], creating backdoors, dictionary attacks, spreading virus and worms, etc. [4]. Stepping stone attacks are not limited to national boundaries, as in stepping stone attacks, some stepping stone hosts may present in different countries. Presence of stepping stone hosts in different countries can make tracing of attacker more difficult as different countries can have its own cyber laws [4]. In 1995, Stanford-Chen and Heberlein [7] first proposed a stepping stone detection approach based on the content of attacking packets which is also called "thumbprint approach." However, this approach is unable to detect stepping stone hosts when the attack traffic is encrypted.

Different types of techniques have been proposed by various researchers time to time for stepping stone detection. However, every time researchers come up with new solution, attackers try to find some evasion techniques to escape the detection system. Chaff and Timing perturbation, reshuffling, encryption, etc., are commonly used techniques by the attacker to escape detection system. There are certain characteristic of TCP/IP traffic such as packet size, packet timestamp, etc. which can help to detect stepping stone host [2]. In this paper, we present classification and state-of-the-art of existing schemes proposed for stepping stone detection in recent past and compare these techniques based on their merits and demerits. In addition, we discuss current issues and challenges in detection of stepping stone hosts that can be used for further research in this domain.

The rest of this paper is organized as follows. Section “[Problem of Stepping Stones](#)” discusses about stepping stone problem. In section “[Stepping Stone detection Techniques](#),” we discuss some excellent stepping stone detection techniques, section “[Open Issues and Challenges](#)” discusses issues and challenges in the detection of stepping stones. Finally, section “[Conclusion and Future Work](#)” concludes the paper and discusses scope for future work.

Problem of Stepping Stones

One major application of computer machines is to store useful and secret information so that they can be accessed at later time. Development of Internet technology allows people to share information easily, access services online, remotely login to other computer, and so on. Attackers generally use Telnet, Open SSH, etc., to remotely login to other computer systems. To remain unidentified attackers execute attacking command through intermediate compromised rather from their personal computer. To make it possible attacker uses remote login tools such rlogin and open SSH to remotely login into vulnerable computers and take over the control and use these systems to remotely login into other and take control of them and so on. In this way attacker creates a long connection chain through intermediate compromised hosts, and launch attacking command from last host in the chain. The intermediate compromised hosts are called stepping stone hosts. Once attack is able to take control over a machine as stepping stone host, he/she can use it to compromise and control other remote computer machines and so on. In stepping stone attacks, origin of attack cannot be detected without detecting stepping stone hosts. The difference between cyber laws of different countries also helps attackers to escape detection processor making detection more difficult, because a country may consider an activity as an offensive while other may not. Due to which attacker may create and use stepping stone in different countries, in that case detecting origin of attack is more difficult.

Stepping Stone Detection Techniques

Various stepping stone detection techniques have been proposed by the researchers. Some of them find out intrusion path created by the attacker while other detects stepping stone by comparing incoming and outgoing connections of host. The efficiency and quality of stepping stone detection techniques can be evaluated by calculating both false negative rate and false positive rate. False positive means a normal host is detected as stepping stone by the algorithm, while false negative means a stepping stone host is left undetected by the algorithm. A high false negative rate is more serious and unacceptable than a high false positive rate. The amount of chaff that an algorithm can handle also measures the effectiveness of the algorithm. Chaff packets are the dummy packets that attackers can insert into connection to escape detection process. Chaff packets need not to be arrived at victim. It may be dropped at an intermediate host. If an algorithm can detect stepping stone host even when attacker has inserted lots of chaff, which is more effective than other approaches that cannot do the same.

Correlation Techniques

Zhang and Paxson [3] proposed an ON/OFF correlation approach. ON/OFF approach correlates incoming and outgoing connections of a host by correlating ON and OFF periods of the connections. A connection is in OFF period if there is no data in connection for more than a specified period of time say T_{ideal} . ON period of a connection begins, when a packet with new payload enters into connection. Suppose C_{in} is an incoming and C_{out} is an outgoing connection on computer host H . C_{in} and C_{out} will be correlated if their OFF periods end at similar time. This will indicate that host H is a stepping stone host and C_{in} , C_{out} is called stepping stone connection pair. This is also true that if two connections form stepping stone pair, they will leave their OFF period at similar times. Using these two definitions, following mathematical expression can be derived:

Suppose $T1$ and $T2$ are the time when two OFF periods OFF1 and OFF2 end, respectively. OFF_{n1} and OFF_{n2} are OFF periods that occur in C_{in} and C_{out} , respectively, and OFF_{12} is the number of correlated OFF period. Here δ and γ are two control parameters.

- OFF1 and OFF2 are said to be correlated if $T2 - T1 \leq \delta$.
- C_{in} and C_{out} is a pair stepping stone connection, if $\frac{OFF_{12}}{\min(OFF_{n1}, OFF_{n2})} \geq \gamma$.

Refinement of this approach is done using the concept of *casuality*, if two connections C_{in} and C_{out} are part of connection chain and OFF period of C_{in} end before C_{out} , then OFF period of C_{in} will always end first among the OFF periods of C_{in} and C_{out} . This observation helps to remove unwanted connection pair. Another

improvement in this approach can be done by considering consecutive coincidences, because consecutive coincidence occur more for stepping stone connection pair as compared to normal connection pair. Using this definition, C_{in} and C_{out} form a stepping stone pair if $OFF_{1,2}^* \geq \min_{CSC}$ and $\frac{OFF_{1,2}^*}{\min(OFF_{n1}, OFF_{n2})} \geq \gamma'$. $OFF_{1,2}^*$ is the number of consecutive coincidence. \min_{CSC} is the minimum number of consecutive coincidence and γ' is new control parameter.

Stepping Stone Detection with Encrypted Attacking Traffic

Ting He et al. [8] proposed a stepping stone detection technique which can detect stepping stones in the presence of encrypted attacking traffic. While performing stepping stone attacks, attacker has to face two constraints. First is the *Bounded memory constraints*, which state that there is limit on the amount of memory that attacker can use on stepping stone host. Second is *Bounded delay constraints*, which state that attacker cannot delay a packet more than specified amount of time.

To detect stepping stone with bounded memory, consider that attacker is allowed to use memory for only M packet. Suppose S_{in} and S_{out} are incoming and outgoing streams of host H , if maximum variation between these streams is less than or equal to M then S_{in} and S_{out} is called stepping stone connection pair with bounded memory M otherwise (S_{in}, S_{out}) is called normal pair.

Suppose $N_{in}(w)$ and $N_{out}(w)$ represent the number of packets observed in S_{in} and S_{out} , respectively, where w is the total number of packets observed. Suppose $diff(w)$ represents the packet difference between S_{in} and S_{out} , then $diff(w)$ can be calculated as given below: $diff(w) = N_{in}(w) - N_{out}(w)$. Similarly, maximum variation can be defined as $var(w) = \max_{1 \leq i \leq w} diff(i) - \min_{1 \leq i \leq w} diff(i)$. Using definition of maximum variation stepping stone detector with bounded memory is given by

$$\delta_{DMV}(S_{in}, S_{out}, M, n) = \begin{cases} 1 & \text{if } var(n) \leq M \\ 0 & \text{otherwise} \end{cases} \quad (1)$$

Here 1 (one) indicates that S_{in}, S_{out} is a stepping stone pair, and 0 (zero) indicates that S_{in}, S_{out} is a normal pair.

Delay constraints approach assumes a value Δ which represents the maximum value of delay in the delivery of a packet. A pair of stream (S_{in}, S_{out}) is a stepping stone pair with bounded delay Δ , if for each packet in S_{in} there exist a corresponding packet in S_{out} subjected to maximum bounded delay Δ .

To detect stepping stone pair with bounded delay a *detect match (DM)* algorithm was given by in [8]. *DM* algorithm searches valid pair for each packet p in S_{in} . Pair (p, q) is valid pair where $p \in S_{in}$ and $q \in S_{out}$. Time stamp difference between p and q is $t(q) - t(p) \leq \Delta$, where $t(q)$ and $t(p)$ are the timestamps of q and p , respectively. If *DM* algorithm found a valid pair for each incoming packet then *DM* indicates that host is

stepping stone otherwise it is a normal host, *DM* performs same operation for all incoming connection. *detect match* has exponential time complexity but it searches for order preserving mapping, an order preserving mapping reduces miss detection.

To detect stepping stone with bounded memory in the presence of chaff, they proposed *detect bounded memory chaff (DBMC)* algorithm. *DBMC* algorithm uses a counter *C*, to count number of times the memory goes *underflow* and *overflow*. If $C/n < (1/(M + 1))$ then *DBMC* returns attack otherwise normal. Here *n* is the number of packet observed. *DBMC* can handle $1/(M + 1)$ amount of *chaff*, over which detection quality will decrease. *DBDC* algorithm counts the number of *chaff* packet using counter *C*, and if $C/n < (1/(1 + \lambda\Delta))$ algorithm returns attack otherwise returns normal. *DBDC* can handle $1/(1 + \lambda\Delta)$ amount of *chaff*. λ is decision parameter and Δ is the maximum tolerable delay.

Detecting Intrusion Path Using Data Mining Techniques

Data mining approach was proposed by Yang et al. [9], which focuses on detection of origin of attack. They gave a *clustering-partitioning (C-P) algorithm*, which uses *maximum-minimum distance clustering algorithm*. clustering-partitioning algorithm matches *send* and *echo* packet globally which results in correct value of RTT and estimates the length of intrusion path correctly. C-P algorithm captures all send and echo packets for certain period of time. C-P algorithm one by one computes timestamp difference among a send packet *p* and all echo packets that arrive after *p*. This ensures that the correct RTT for *P* is one of these differences. RTT of TCP/IP send packet is given by $RTT(t) = RTT_0 + \Delta RTT(t)$, where RTT_0 represents fixed delay and $\Delta RTT(t)$ represents variable delay. The idea behind this approach is that RTT's of connection chain with same length will form a single cluster.

To prepare RTT dataset, C-P algorithm captures send and eco packet in certain period of time, and computes timestamp difference between each send packet *P* and all echo packets after *P*. In first step, C-P algorithm applies *maximum-minimum distance clustering algorithm* on RTT data set. In second step, C-P algorithm removes all duplicate elements from each cluster. Third step of C-P algorithm is to measure the likelihood of each cluster to check whether it can represent a RTT level or not. In Steps 4 and 5 *C-P* algorithm searches for set of clusters where each cluster represents an RTT level, for that algorithm searches for clusters having higher ratio than other. Ratio of cluster *R* is considered to be higher if $2\sigma > \mu$, where μ and σ are mean and standard deviation of *R*, respectively. If all send packets can be partitioned into a set of clusters with no send packet command between them, such set of clusters is called true cluster set. A set of cluster satisfying these two properties represent the true RTT levels, number of cluster is equal to the number of connection in the chain.

Packet Context Approach for Stepping Stone Detection

Yang et al. [10] proposed a packet context approach to detect stepping stones. In this approach they correlate packet context of TCP/IP packets using *Pearson product moment correlation coefficient* to find which incoming connection is correlated to which outgoing connection. Packet context based approaches compute context distance between packet context of each packet P in incoming connection and packet context of all packets in outgoing connection. A host is a stepping stone if any two connections of it are relayed. Packet context approach computes context distance between packet context of each packet P in incoming connection and packet context of all packets in outgoing connection. This computation results into a context distance set $D = \{d_1, d_2, d_3, \dots, d_m\}$. Packet corresponding to outlier d_i ($|d_i - \mu| < 2\delta$) represents matched packet for packet P , where δ and μ are the standard deviation and mean of D , respectively. Context distance between two contexts X and Y is given by $d_i = 1 - P_{X,Y}$, where $P_{X,Y}$ is Pearson product moment correlation coefficient between packet context X and Y and is given by

$$P_{X,Y} = \frac{n \sum_{i=1}^n x_i y_i - \sum_{i=1}^n x_i \sum_{i=1}^n y_i}{\sqrt{n \sum_{i=1}^n x_i^2 - (\sum_{i=1}^n x_i)^2} \sqrt{n \sum_{i=1}^n y_i^2 - (\sum_{i=1}^n y_i)^2}} \quad (2)$$

To find relayed connections, authors have used packet context approach to compute a relay degree set $R = \{r_1, r_2, r_3, \dots, r_l\}$ for each incoming connection C_{in} , where r_i is relay degree between an incoming and an outgoing connection, C_{in} and C_i , respectively. The connection corresponding to outlier r_i ($|r_i - \mu| > 2\delta$) of set R represents the relayed connection of incoming connection C_{in} . The same process can be applied for each incoming connection to find its relay.

Neural Network Approach for Stepping Stone Detection

A neural network approach was given by Wu et al. [11] to detect length of intrusion path, which is based on RTT's of TCP/IP send packet. This approach is called *RTT group approach* because RTT dataset is divided into groups and each group is applied as input to the input layer of neural network. A monitoring and capturing system is placed on the host next to the attacker. Packets are captured from the time when there is one connection in the chain to the time when complete stepping stone chain is established. RTT of each send packet is computed by timestamp difference between send and echo packets. Training of neural network is needed before they engaged for function, same is here and then incoming packet can be used as testing data, due to which we do not require to observe connection chain continuously. This RTT group scheme consists of three preprocessing steps, first step is to capture

send and echo packet only, second step is to run a matching algorithm to compute RTT of send packets, third step is to build neural network using RTT dataset created in previous step. To detect number of host in the connection, one can simply plot output of neural networks, where X-coordinate represents RTT group number and Y-coordinate represents number of host. The number of steps in the graph represents the number of connection in the chain.

Applying Stepping Stone Approach for Network Threat Detection

Omar et al. [12] use stepping stone perspective to detect various network threats like spam, proxy attacks, DoS attacks, backdoor attack. Stepping stone approach for spam detection is based on monitoring of incoming and outgoing email ports. There are three main ports *SMTP port 25*, *IMAP port 143*, and *POP3 port 110* required to monitor for spam detection. In spam attacks a host is used as medium to send email to multiple receiving host, thus an email is sent to host which in turn forwarded to multiple receivers. Therefore, number of emails that a host receives is always lesser than it sends to other, thus this can be mathematically formulated as follows:

$$\text{SPAM}_{\text{SSD}} = \begin{cases} 1, & \text{if } n_{\text{in}} < n_{\text{out}} \\ 0 & \text{if } n_{\text{in}} \neq n_{\text{out}} \end{cases} \quad (3)$$

Stepping stone approach to detect proxy server compares incoming connection with outgoing connections of a host, if any incoming connection is equal to any outgoing connection and vice versa, this indicates that host is acting as a proxy server. Mathematical expression of proxy detector is given by

$$\text{PROXY}_{\text{SSD}} = \begin{cases} 1 & \text{if } n_{\text{in}} = n_{\text{out}} \\ 0 & \text{if } n_{\text{in}} \neq n_{\text{out}} \end{cases} \quad (4)$$

Backdoor creates an unauthenticated user access to any normal computer machine. Backdoor programs work in background without the knowledge of actual user of computer system. They may be an installed program or may be associated with some virus or worms. This approach detects backdoor without using their signatures. This approach find out whether a host is sending data to outside world using same port for same period of time again and again or not, if yes means backdoor exists in system otherwise not.

Stepping stone approach for DoS detection involves comparing the number of incoming and outgoing connections. If the number of incoming connections is less than number of outgoing connections in a host, then it indicates that the host is a victim of DoS attacks. Using this definition DoS detector can be define as

$$\text{DoS}_{\text{SSD}} = \begin{cases} 1 & \text{if } n_{\text{in}} < n_{\text{out}} \text{ for all } n \\ 0 & \text{if } n_{\text{in}} \neq n_{\text{out}} \text{ for all } n \end{cases} \quad (5)$$

Hybrid Stepping Stone Detection

Omar et al. [13] proposed a hybrid approach for stepping stone detection. Hybrid approach is a combination of two different types of approaches, the host-based approach and network-based approach. Intrusion detection system is an integral part of architecture of hybrid stepping stone detection system, which detects intrusion whenever occurs and raises alarm. Network-based stepping stone detection system starts working and captures network traffic within its boundary. After that it identifies a unique feature from packets captured. The unique feature is then used to detect stepping stone hosts. Network-based stepping stone detection results in a list of stepping stone hosts.

After that host-based stepping stone detection system comes into picture and uses list produced by network-based stepping stone detection system. Each host in list runs its own host-based stepping stone detection. Moreover, each successful host-based detection is listed in a host-based detection list. Host-based detection list is then compared with the list produced by network-based stepping stone detection, if both lists contain same hosts then this indicates that stepping stone host exists in the network.

Open Issues and Challenges

Researcher has proposed many stepping stone detection techniques, but still there are some open issues which researchers can exploit for further development of efficient stepping stone detection techniques. Hybrid approaches are the combination of network-based and host-based stepping stone detection approaches. It combines the advantages of both types of approaches and removes their problem which makes it more efficient but it is more complex in nature. As shown in Table 1, most of the host-based stepping stone detection approaches have some limitations. Scheme proposed in [10] is packet context approach and works correctly only with large number of incoming and outgoing connections. Researcher has used stepping stone perspective for detecting network threats but not supporting it by implementation. As hybrid approach have high detection rate and there are very few hybrid approaches, thus there is need and scope for the development of hybrid approaches. The stepping stone detection approaches which find out the length of intrusion path assumes sensor to be placed on next host to attacker. However, it is difficult to detect a host which is placed next to the attacker.

Table 1 Comparison between various stepping stone detection techniques

Approach	Strength	Weaknesses
ON/OFF (Y. Zhang et al. 2000) [3]	<ul style="list-style-type: none"> –Detect stepping stones with encrypted attacking traffic –Resistance to evasion 	<ul style="list-style-type: none"> –Chaff packet, Timing perturbation, high false positive rate –Failed to anticipate legitimate stepping stones
Encrypted stepping stone detection (T. He et al. 2007) [8]	<ul style="list-style-type: none"> –Low false alarm probability –No miss detection using detect match algorithm 	<ul style="list-style-type: none"> –Can handle limited amount of chaff only
Data mining (J. Yang et al. 2007) [9]	<ul style="list-style-type: none"> –Higher matching rate results in correct RTT dataset. –High quality matching due to global matching 	<ul style="list-style-type: none"> –Higher time complexity –Require continuous monitoring of connection chain
Neural network (H. Wu et al. 2008) [11]	<ul style="list-style-type: none"> –Do not require continuous monitoring of the connections –Fast regeneration of neural network 	<ul style="list-style-type: none"> –Neural network has to be regenerated for different datasets
Correlating TC/IP packet context (J. Yang et al. 2011) [10]	<ul style="list-style-type: none"> –No false detection in case of chaff perturbation 	<ul style="list-style-type: none"> –High false negative rate –Require large number of connection
Threat detection using stepping stone perspective (Omar et al. 2013) [12]	<ul style="list-style-type: none"> –Spam and proxy detection is faster and do not require any signature of backdoor to detect it 	<ul style="list-style-type: none"> –Incomplete and nonreal-time approach
Hybrid approach (Omar et al. 2008) [13]	<ul style="list-style-type: none"> –Low false negative, low false positive rate, high accuracy 	<ul style="list-style-type: none"> –Undefined behavior when both network- and host-based list are totally different

Therefore, there is a need to design and develop an efficient scheme which can find host next to attacker which can make the talk easier to detect origin of attack.

There are various factors which are required to be considered while evaluating a stepping stone detection approach. These factors include *false negative rate*, *false positive rate of algorithm*, and amount of *time delay*, *chaff packets* that algorithm can handle. A high false negative rate is undesirable because it lowers the detection rate while false positive rate is tolerable to some extent. Stepping stone detection algorithm must be capable of handling high amount of chaff. It must also be capable of handling time delays.

Conclusion and Future Work

In this paper, we discussed various stepping stone detection techniques proposed in recent past. Some of these approaches compare incoming and outgoing connections on a host to test whether that host is stepping stone host or not. Some techniques

estimate the length of intrusion path created by attacker by which they can detect all stepping stone hosts in single attempt. Most of the comparison-based schemes are vulnerable to time delays, chaff perturbation, and have high false positive rate. Stepping stone detection schemes estimate that length of intrusion path, mostly estimate downstream length from sensor to victim and do not consider distance between attackers to sensor due to which they find incorrect length of stepping stone path. In addition, we have also discussed a proposed hybrid approach which has high accuracy but there is some undefined behavior in this approach. Therefore, there is need of a real-time stepping stone detection approach. In future, we will work to design and develop a stepping stone intrusion path detection algorithm which can detect correct length of intrusion path.

References

1. Srivastava, A., Gupta, B.B., Tyagi, A., Sharma, A., Mishra, A.: A recent survey on DDoS attacks and defense mechanisms. In: Book on Advances in Parallel Distributed Computing, pp. 570-580. Springer (2011)
2. He, T., et al.: Packet scheduling against stepping-stone attacks with chaff. In: the proceeding of 25th IEEE Military Communications Conference (MILCOM), pp. 1-7 (2006)
3. Zhang, Y., Paxson, V.: Detecting stepping-stones. In: Proceedings of the 9th USENIX Security Symposium, pp. 67-81. Denver, CO, Aug 2000
4. Hsiao, H., Fan, W.-C.: Detecting step stone with network traffic mining approach. In: the proceeding of 4th IEEE Conference on Innovative Computing, Information and Control (ICICIC), pp. 1176-1179 (2009)
5. He, T., Tong, L.: Signal processing perspective to stepping stone detection. In: proceeding of 40th IEEE Annual Conference on Information Sciences and Systems, (CISS), pp. 687-692 (2006)
6. Gupta, B.B., Joshi, R.C., Misra, M.: Defending against distributed denial of service attacks: issues and challenges. *Inf. Secur. J. Global Perspect.* **18**(5), 224-247 (2009)
7. Staniford-Chen, S., Heberlein, L.T.: Holding intruders accountable on the internet. In: Proceedings of IEEE Symposium on Security and Privacy, pp. 39-49. Oakland, CA (1995)
8. He, T., Tong, L.: Detecting encrypted stepping-stone connections. *IEEE Trans. signal process.* **55**(5), 1612-1623 (2007)
9. Yang, J., Huang, S.-H.S.: Mining TCP/IP packets to detect stepping stone intrusion. *Comput. Secur.* **26**(7-8), 479-484 (2007)
10. yang, J., Woolbright, D.: Correlating TCP/IP packet context to detect stepping stone intrusion. *Comput. Secur.* **30**(4), 538-546 (2011)
11. Wu, H., Stephen Huang, S.-H.: Stepping stone intrusion detection using neural networks approach. *J. Expert Syst. Appl.* **37**(2), 431-437, Mar 2010
12. Omar, M.N., et al.: A stepping stone perspective to detection of network threats. *Int. J. Appl. Math. Inf.* **7**(3), 97-106 (2013)
13. Omar, M.N. et al.: Hybrid stepping stone detection method. In: the Proceeding of 1st IEEE Conference on Distributed Framework and Applications (DFmA-2008), pp. 134-138 (2008)

CBIR Feature Extraction Using Neuro-Fuzzy Approach

Ajay Kumar Bansal and Swati Mathur

Abstract This paper proposes a neuro-fuzzy based CBIR framework for image retrieval. Here, in the first phase, the fuzzy clustering algorithm is used for the classification of the images on the basis of their texture feature. In second phase, result of first phase serves as an input to the back propagation algorithm which helps to find images most semantically related to the query images. Our experiment shows that the proposed method results in better performance in terms of precision and recall as compared to the traditional CBIR techniques.

Keywords Tamura features · Fuzzy clustering · Backpropagation neural network

Introduction

In ancient times, images are retrieved from the hard drive by its subject. However, it is very difficult to memorize the name of an image, thus it is not an efficient way.

But in past few years, there is an exponential increase in the collection of digital images. As the size of the digital image database increases, it becomes so difficult to memorize the name of the image. There are many fields where digitized images are required like multimedia, pattern recognition, education and many more. On the basis of its need it culminate the development of another way of accessing the image on the basis of their content or feature.

Thus content-based image retrieval (CBIR) is defined as a process of searching a digital image from the large database on the basis of their visual features like shape,

A.K. Bansal

Department of Electrical Engineering, Poornima Institute of Engineering & Technology,
Jaipur, India

e-mail: ajaykumarbansal@poornima.org

Swati Mathur (✉)

Department of Information Technology, Poornima Institute of Engineering & Technology,
Jaipur, India

e-mail: swatimathur@poornima.org

© Springer India 2016

N. Afzalpulkar et al. (eds.), *Proceedings of the International Conference on Recent Cognizance in Wireless Communication & Image Processing*,
DOI 10.1007/978-81-322-2638-3_60

535

color and texture. According to the user query image, images are classified with the help of various classification techniques to identify the most similar images.

About CBIR

Content-based image retrieval is an application of computer vision where digitally similar images are retrieved from the large database on the basis of their content. Content in this context refer to the Information that describes the image like color, texture, and shapes. The detailed survey on CBIR can be referred [1, 2]. Much research has been already proposed in content-based retrieval system whose goal is to minimize the semantic gap between low-level features and high-level semantics.

- a. Color-based retrieval: Color has been used for CBIR. The basic technique used for color-based retrieval is color [3]. There are various types of histograms: normal, weighted, dominant, and fuzzy, various color spaces: HSV, grayscale, HSL, Lab, Luv, HMMD, and YCbCr.
- b. Texture-based retrieval: Texture is a very important for the analysis of an image. Images having same color and shape differ in their texture. Thus, many techniques were proposed [4, 5]. Tamura et al. [5] proposed a texture representation on six statistical features which were considered to be the most visually meaningful.
- c. Shape-based retrieval: Another parameter used for image retrieval is shape [6]. Generally, each image differs in their shape and to distinguish them shape feature is used. There are two main features of the shape: global feature (like aspect ratio) and local feature (like boundary segments).

There is much commercially used software available in market like: QBIC: IBM QBIC (Query by Image Content) System, Virag, and Blobworld.

Fuzzy logic [7–10, 5] and neural network [6, 11] are the powerful tools used for image retrieval. Still there are some drawbacks of fuzzy logic and neural network exist. To overcome those problems, this paper proposed a new framework based on neuro-fuzzy approach.

Proposed Architecture

The proposed architecture is to search an image on the basis of its texture is illustrated schematically in Fig. 1. Texture feature of the images are extracted and are stored in the Feature database. The query image is given to the system. The proposed architecture uses the advantages of membership function of fuzzy logic to identifying the similar images. Tamura features [3] used to measure six different properties of the images—coarseness, contrast, directionality, line-likeness, regularity, and roughness. Based on the texture content of the query image the grouping

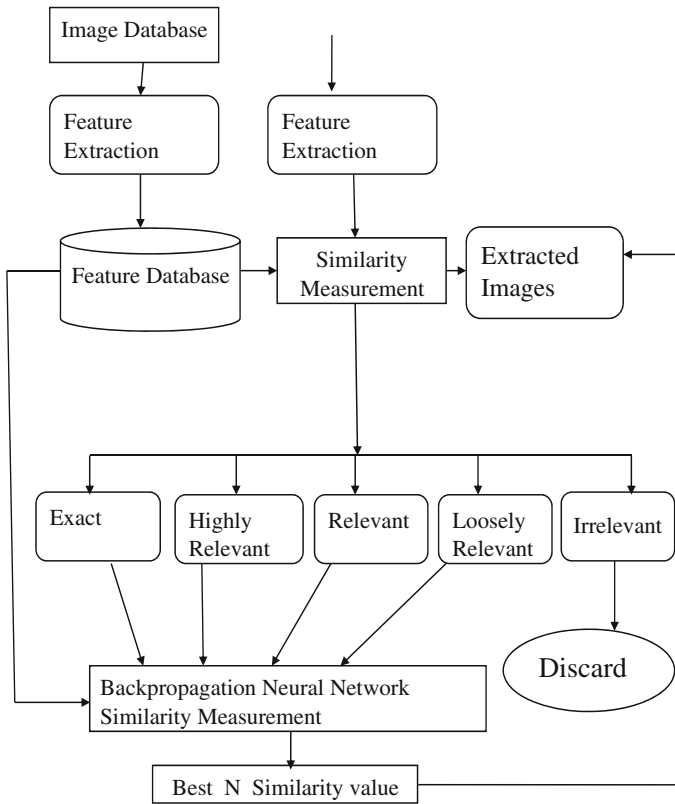


Fig. 1 Proposed architecture

is done with the help of fuzzy clustering This clustering classify the data according to its texture properties such as very low, low, medium, high, and very high. The output given from the fuzzy clustering is given as input to the Back propagation neural network algorithm. Basic aim of the neural network is to identify the most relevant images from the database.

Fuzzy Logic Approach

Image analysis is performed based on texture feature. Classification of images is performed according the concept proposed by tamura. The term set on each tamura feature is interpreted by five natural languages terms such as very low, low, medium, high, and very high. To implement this concept images are clustering according to the fuzzy clustered algorithm.

The algorithm used for fuzzy clustering is as follows:

Fuzzy Clustering (Algorithm)

Input: Data sequence x_1, x_2, \dots, x_n , where x_i denotes a tamura feature of the i th texture image and n is the number of texture images.

Output: Five membership functions of the tamura feature, i.e., a term set on the tamura feature

Step 1. Let $c_0 = \min(x_1, x_2, \dots, x_n)$ and $c_6 = \max(x_1, x_2, \dots, x_n)$. Compute c_1, c_2, \dots, c_5 as follows

$$c_j = c_0 + \frac{j}{6} * (c_6 - c_0)$$

Initialize membership functions in which c_1, c_2, \dots, c_5 denote class centers of the membership functions

Step 2. Set $U = 0$. For each datum x_j , update each element u_{ij} using one of the following rules, where $u_{ij}, 1 \leq i \leq 5$ and $1 \leq j \leq n$, is the membership value of x_j in the i th linguistic term

Rule 1. If $x_i \leq c_1, u_i = 1$ and $u_{i,k \neq 1} = 0$

Rule 2. If $c_j < x_i \leq c_{j+1}$, compute $u_{ij} = (c_{j+1} - x_i) / (c_{j+1} - c_j)$

Rule 3. If $x_i > c_5, u_{i,k \neq 5} = 0$ and $u_{i,5} = 1$

Step 3. Compute c_1, c_2, \dots, c_5 using the following equation:

$$C_i = \frac{\sum_{j=1}^n u_{ij} x_j}{\sum_{j=1}^n u_{ij}}$$

If c_1, c_2, \dots, c_5 are unchanged, the algorithm stops; otherwise go to Step 2.

Neural Network Approach

The ANN model contains the three layers: input layer, hidden layer, and output layer. ANN model will learn the network with the help of backpropagation neural network where input layer contains the output of the fuzzy logic. Activation function used is $\frac{1}{1 + \exp^{-T}}$. Query image feature is supplied as input to the trained neural network system. System will calculate the output on the basis of training. Now with the help of output value we calculate the similarity between the result and the images in the databases. The image with more similarity will be extracted from the database and it will be displayed as output.

Results and Discussion

To evaluate the performance of proposed architecture, a database of 1000 images was assembled. Images are collection of different categories like flowers, animals, etc. Proposed framework will accept a query image as given in the Fig. 2 from the user and then query image will form the cluster and identify the similar images from the database. The simulation of the result is given in Fig. 3.



Fig. 2 Query image



Fig. 3 Result of neuro-fuzzy system

Table 1 Detailed comparison of precision

	K = 1	K = 5	K = 10	K = 15	K = 20
	N = 1	N = 5	N = 9	N = 14	N = 15
Fuzzy	0	0.4	0.3	0.4	0.3
Neuro-fuzzy	1	1	0.9	0.9933	0.99

Table 2 Detailed comparison of recall

	K = 1	K = 5	K = 10	K = 15	K = 20
	N = 1	N = 5	N = 9	N = 14	N = 15
Fuzzy	0	0.02	0.3	0.4	0.3
Neuro-Fuzzy	0.01	0.01	0.09	0.14	0.15

Parameters used for the evaluation of the proposed framework are: precision and recall.

Precision is the fraction of retrieved instances that are relevant. **Recall** can be calculated as the fraction of relevant instances that are retrieved. Here N—number of relevant images retrieved. K—Total number of images retrieved. As precision increases, algorithm will return substantially more relevant results, whereas high recall means that an algorithm returns most of the relevant results. This results that as you increase the value of K as well as of N, the performance of neuro-fuzzy increases to that of fuzzy approach. The following table compares the precision of fuzzy and neuro-fuzzy approach (Table 1).

Similarly, the following table compares the recall factor of fuzzy and neuro-fuzzy in parallel. After analysis, in the proposed architecture recall factor of neuro-fuzzy is more appropriate than of fuzzy approach (Table 2).

Conclusion

The proposed neuro-fuzzy framework proves that performance of neuro-fuzzy is better than fuzzy technique. Performance of the system is evaluated on the basis of two parameters: precision and recall. The experiment is conducted with 10 different query images and the performance of the system has improved significantly.

References

1. Saad, M.: Content-Based Image Retrieval, A Literature Survey (2008)
2. Datta, R., Li, J., Wang, J.: Content-based image retrieval—a survey on the approaches and trends of the new age, ACM multimedia. In: Proceedings of International Retrieval 2005
3. Tamura, H., et.al., Textural Features Corresponding to Visual Perception, Transactions on Systems, man, and cybernetics (IEEE), vol. SMC—8, No. 6 (1978)
4. Thompson, W.B.: Textural Boundary Analysis, Transactions on computers (IEEE) (1997)

5. Kulkarni, S.: Natural language based fuzzy queries and fuzzy mapping of feature database for image retrieval. *J. Inf. Technol. Appl.* 4(1), 11–20 (2010)
6. Rama Krishna Rao, T.K., Usha Rani, R.: Content based image retrieval through feed forward neural networks. In: *IEEE 8th International Colloquium on Signal Processing and its Applications* (2012)
7. Verma, B., Kulkarni, S.: Fuzzy logic based Texture Queries for CBIR. In: *IEEE proceedings of the fifth International Conference on Computational Intelligence and Multimedia Applications (ICCIMA'03)* (2003)
8. Lin, H.-C., Chiu, C.-Y., Yang, S.-N.: Finding textures by textual descriptions, visual examples and relevance feedbacks. *Pattern Recogn. Lett.* (2003)
9. Ahmed, H.A., Onsi, H., Gayar, N.E.: A New Approach in Content- Based Image Retrieval using Fuzzy Logic, *INFOS2008, Cairo-Egypt* (2008)
10. Medasani, S., Krishnapuram, R.: A fuzzy approach to content-based image retrieval. In: *IEEE International Fuzzy Systems Conference Proceedings, Seoul, Korea, 22–25 Aug 1999*
11. Borse, R., et.al. Efficient implementation of CBIR system and framework of fuzzy semantics. In: *Proceedings of IEEE International Conference on Advances in Mobile Network Communication and its Applications* (2012)
12. Fazal-e-Malik, Baharudin, B.: Efficient Image Retrieval Based on Texture Features (*IEEE*) (2011)

Multiband and Wideband Antenna for Wi-Fi, WLAN, X-Band and Space Research Applications

Goswami Siddhant Arun, Deepak C. Karia and Bhushan Dhengale

Abstract With the rapid growth of high speed wireless communication, there is a need for a single antenna operating at different frequencies. Multiband antenna has provided the much needed solution for single antenna with wide bandwidth that will support multiple standards at the same time. Here, we have proposed a compact annular ring-shaped monopole antenna. The antenna has an L-shaped slot etched along with an additional slot near the feed point. The additional slot contributes in minimizing the return loss S_{11} . Further for bandwidth enhancement to cover the wide range upper bevel cut with defected ground plane is proposed, two C-shaped slots are etched in the ground plane were made for obtaining new band at 7.5 GHz. The stepwise design procedure is thoroughly discussed along with parametric analysis and can be independently controlled for most applications. The proposed monopole antenna has dimensions of $50.9 \times 33 \times 0.8 \text{ mm}^3$ with FR4 as its substrate. The FR4 substrate has a dielectric constant value $\epsilon_r = 4.4$. This paper analyses the impedance bandwidth, return loss along with radiation plots. We have also verified the housing effect by placing the antenna in the vicinity of copper plate. Efficiency is improved up to 90 % with better return loss of -40 db is obtained.

Keywords Planar monopole antenna • C-shaped cut • Ultra wideband (UWB) antenna • Defected ground plane with upper Bevel cut • Wideband antenna

G.S. Arun (✉) · Bhushan Dhengale
Department of Electronics and Telecommunication Engineering,
S.P.I.T, Mumbai 400058, India
e-mail: siddhantgoswami23@gmail.com

Bhushan Dhengale
e-mail: bhushandhengale123@gmail.com

D.C. Karia
Department of Electronics Engineering, S.P.I.T, Mumbai 400058, India
e-mail: deepak_karia@spit.ac.in

Introduction

It has been a good research area to design compact antennas which support multiple standards simultaneously. To support different standards, multiband antennas are largely demanded due to recent growth in wireless communication. Planar monopole antenna has characteristics of good impedance bandwidth, low profile and low cost. Because of these features, they are considered for wide research in the area of multiband. Numerous monopole designs such as circular, annular ring, rectangle and square were seen in the literature along with variation in ground plane [1].

Achieving both multiband and wideband antenna is a real challenge in designing antenna. Numerous techniques such as hook-shaped arm [2], shorting walls and V-shaped groove [3], Fractal geometry in the ground plane [4], multi-layered designing [5] were suggested for multiband approach.

In this paper, miniature circular monopole antenna is presented for multiband operation. An L-shaped slot has been etched with defected ground in design with an additional slot near the feed point for improving return loss. Length of each slot is optimized using the technique of guiding wavelength ($\lambda_g/2$) [6]. The performance of the antenna with respect to parameters such as gain, magnitude impedance curve, radiation plots, impedance bandwidth along with radiation efficiency and Smith chart are addressed in this paper. Moreover, housing effect is observed by keeping antenna in the vicinity of metal plate, the amount of degradation in return loss is analysed [7]. The antenna used in the paper have used two C-shaped slots along with upper bevel-shaped in ground plane, which has created a notch at 7.5 GHz causing an addition of band-notch characteristics [8]. Use of upper bevel-shaped structure in the ground plane improves the impedance bandwidth and covers a wider range.

For years, designing a multiband antenna is a great research topic. The most challenging work in designing an antenna is to minimize antenna cost along with mutual coupling between parasitic strips and slots due to reduction in size. The design of each notch needs to have an independent control over each frequency band [9, 8].

The proposed antenna covers the following bands: UNII band (5.15–5.92 GHz), Wi-Fi operates in 5 GHz band frequency ranges (5.150–5.350 GHz, 5.47–5.725 GHz and 5.725–5.875 GHz), vehicle Communication band (5.9 GHz), public safety band (4.9 GHz), have covered a wide C-band (4–8 GHz), WIMAX (5.8 GHz) in Australia, India and China, X-Band Satellite Communication (7.1–7.7 GHz), 5 GHz WLAN (5.15–5.35/5.725–5.825 GHz specified by IEEE 802.11a), ITS (5.795–6.4 GHz), RFID semi active tags in ultra wideband (UWB) also can be used in space research and radio navigation.

Design of Multiband Antenna with Wideband Characteristics

Antenna Geometry

Figures 1 and 2 shows the schematic of the proposed antenna. The antenna uses FR4 (fire retardant material) substrate with dielectric constant $\epsilon_r = 4.4$ and $\tan \alpha = 0.002$ which is easily available in the market. Overall area of antenna is $50.9 \times 33 \text{ mm}^2$ and of thickness 0.8 mm with an SMA coaxial connector of 50Ω to fully show the characteristics of the antenna. An annular ring monopole antenna with an L-shaped slot, additional slot near feed line and upper bevel-shaped defected ground with C-shaped slot is used in the design to get optimum results.

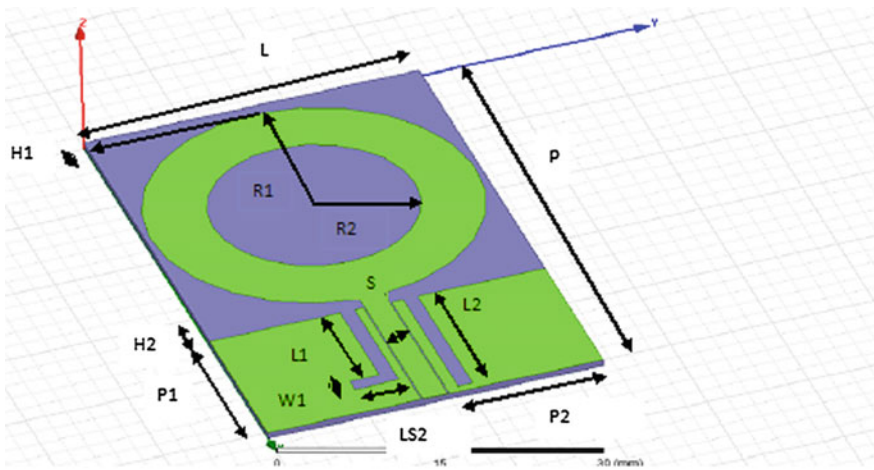


Fig. 1 Top view

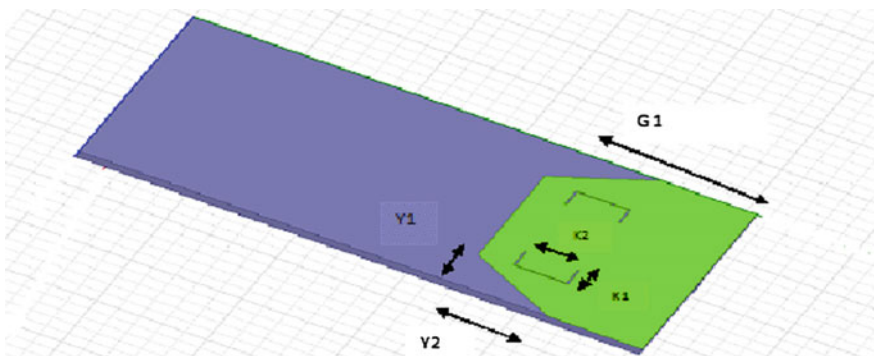


Fig. 2 Bottom view

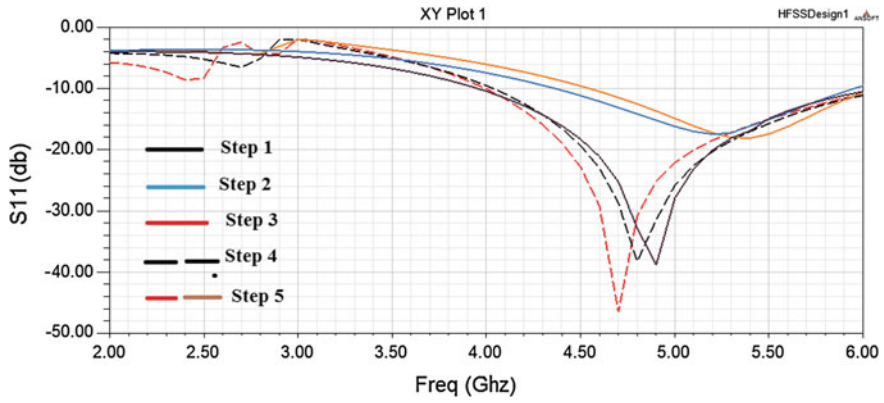


Fig. 3 First five steps for designing the proposed antenna

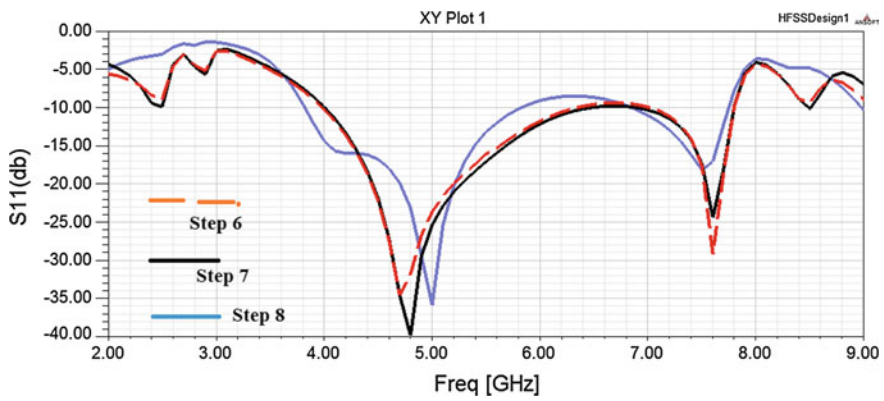


Fig. 4 Final steps for designing the proposed antenna

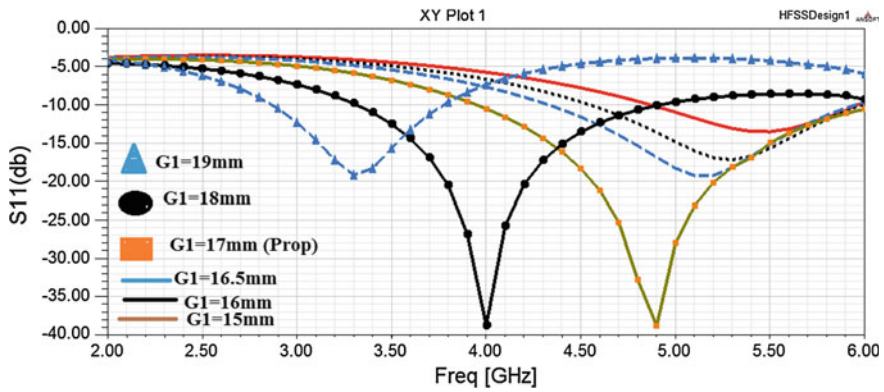


Fig. 5 Step 1–Ground plane variations for optimised results

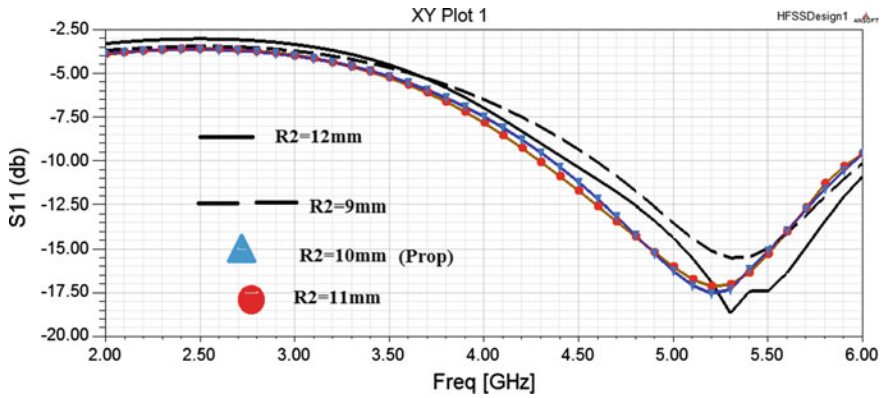


Fig. 6 Step 2- R_2 circle variations for optimised results

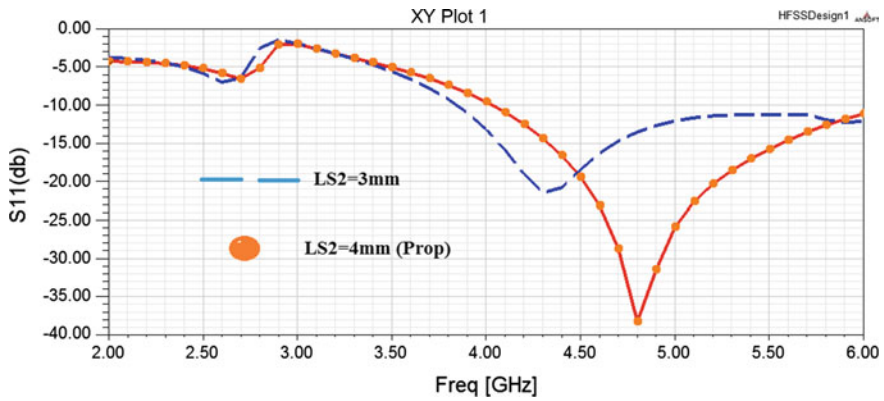


Fig. 7 Step 3- LS_2 variations

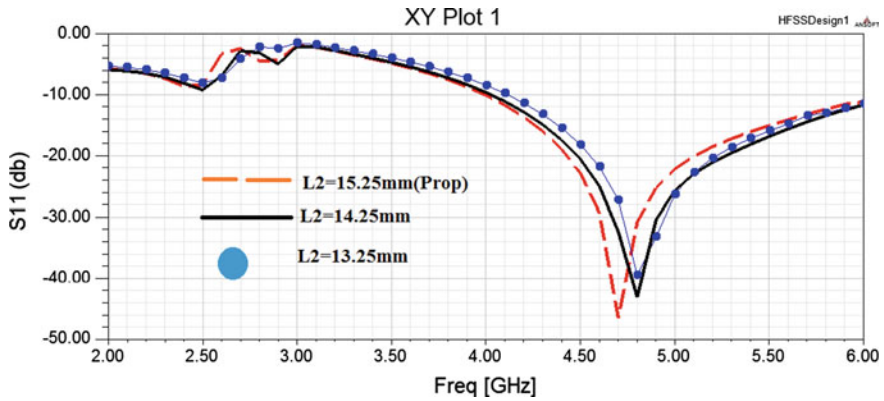


Fig. 8 Step 4-Variations in second slot better S_{11} (db)

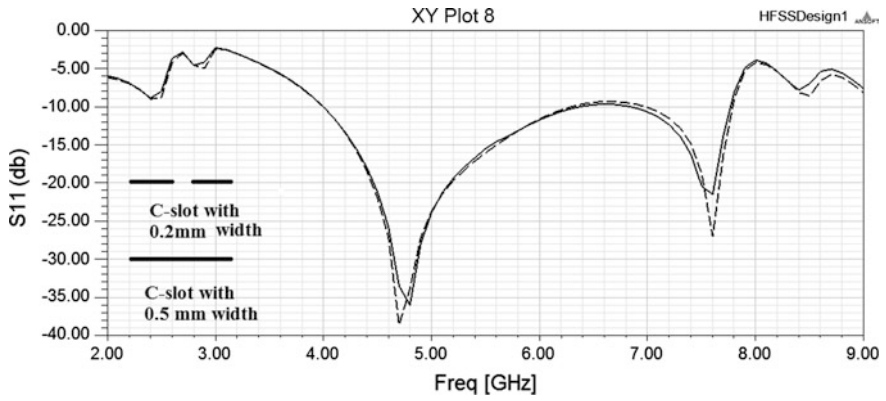


Fig. 9 Step 5–C-shaped Variations led to notch at 7.5 GHz

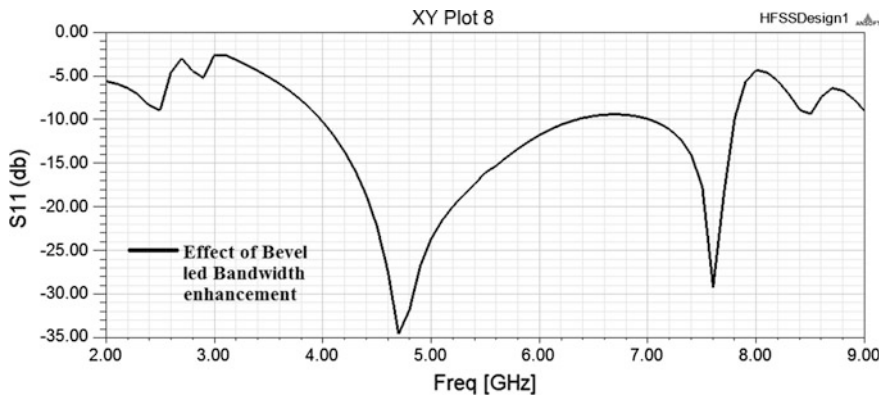


Fig. 10 Step 6–Bevel-shaped ground was used for enhancing bandwidth

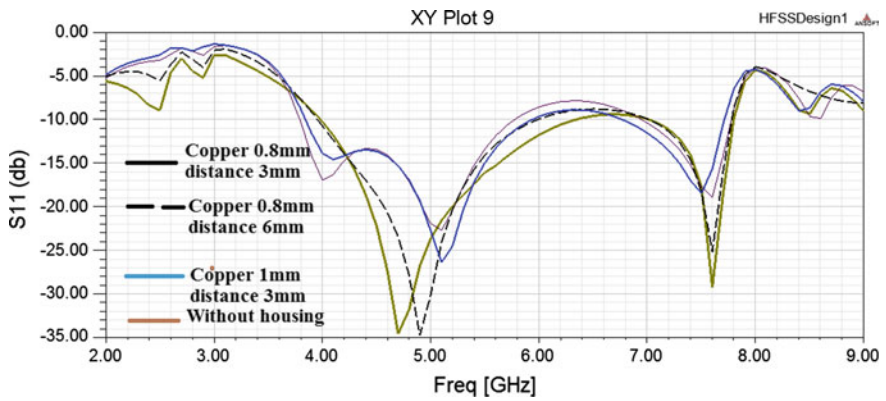


Fig. 11 Step 7–Variations in the return loss by housing effect

Fig. 12 Radiation Pattern of E_{θ} and E_{ϕ} at freq 4.5 GHz in **a** $x-z$ plane, **b** $y-z$ plane **c** $x-y$ plane

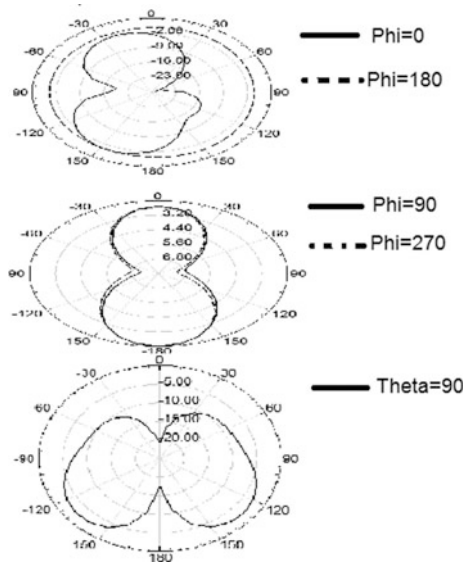
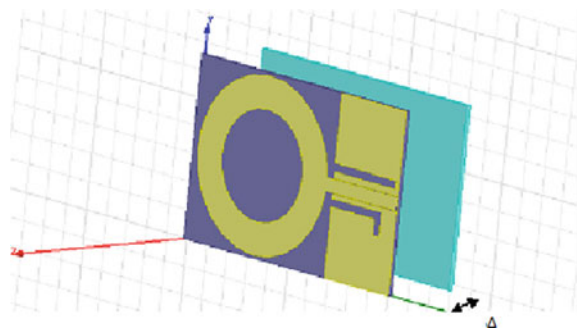


Fig. 13 Antenna in the vicinity of copper plate



The design is optimized in terms of minimizing reflection coefficient S_{11} and obtaining a wide range of applications. The applications supported by the proposed antenna are shown in Fig. 17. The design is carried out using ansoft high frequency simulation software (HFSS) for solving electromagnetic structures. The optimized results obtained with the key dimensions are stated in Table 1.

Table 1 Key dimensions of the proposed antenna in millimetres

L	P	R1	R2	P1	P2	H1	H2	S
33	50.9	16	10	16	15.1	1	1.9	2.4
L1	LS2	W1	L2	K1	K2	G1	Y1	Y2
12.25	3	1.5	15.25	3	5	17	7	8.5

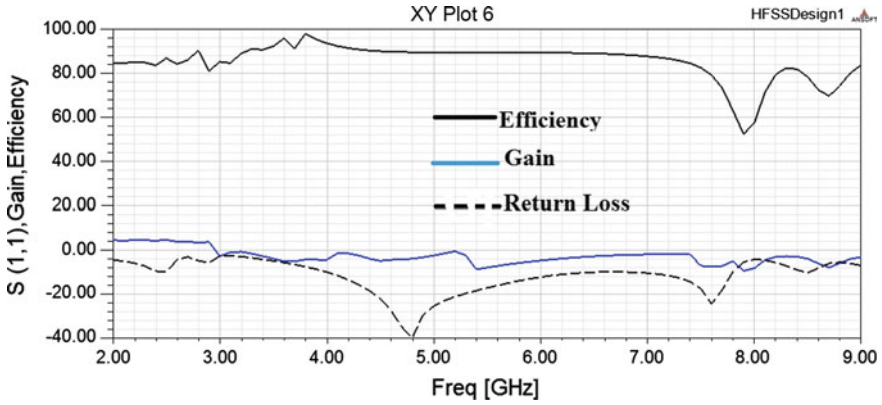
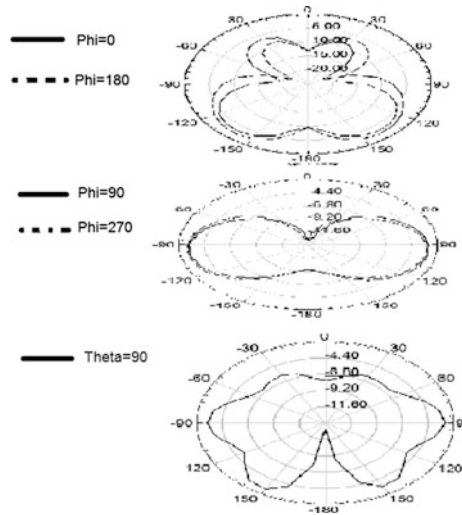


Fig. 14 Measured efficiency, gain and return loss of the proposed antenna

Fig. 15 Radiation pattern of E_{θ} and E_{ϕ} at Freq 7.5 GHz in **a** x-z plane, **b** y-z plane **c** x-y plane



Stepwise Simulation for Analytical Results

The stepwise design evaluation is stated in the simulations shown below in Figs. 3 and 4.

Step 1: A printed circular monopole antenna is designed to operate at a frequency of 4.5 GHz [10]. The length of ground plane is varied for minimizing return loss and maximizing impedance bandwidth. It is observed that as the length of ground plane decreases, the frequency of operation shifts towards the right, as shown in Fig. 5. For certain desired applications in desired range the ground plane dimension can be adjusted. With the increase in the frequency the impedance moves in the clockwise direction

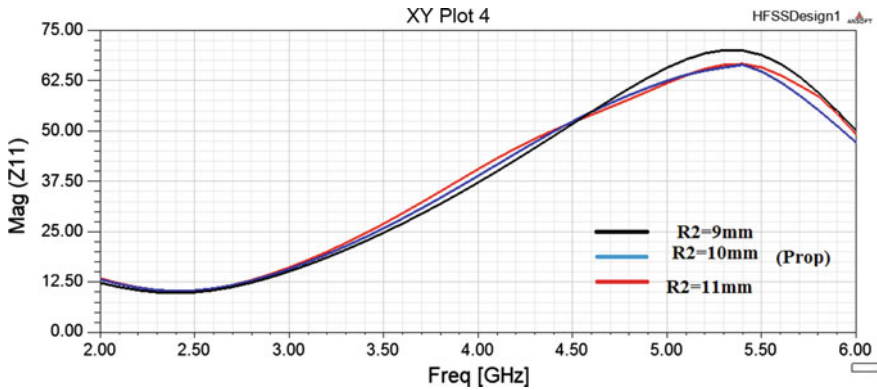


Fig. 16 Effect of annular ring variations on impedance curve

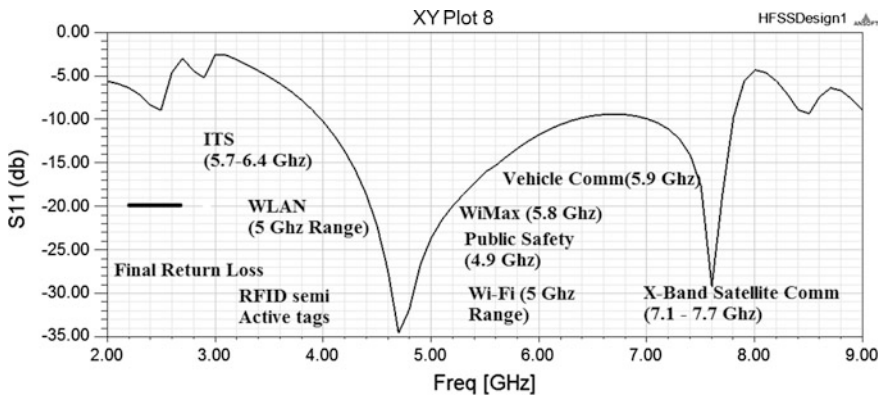


Fig. 17 Applications supported by the antenna

in the Smith chart as shown in Fig. 19. As the length of ground plane decreases the impedance loci shifts that the impedance is increasing. This is also verified with the magnitude impedance curve as shown in Fig. 18. From Smith chart, it can be seen that the curve shifts in the clockwise direction due to increase in the length of ground plane. This leads to soaring in capacitive part which in turn increases the capacitive shift (Fig. 20)

Step 2: Circular slot of radius R_2 is etched out from the design that leads to annular ring shape. Increasing the radius of the circular slot results in an increase in bandwidth. The amount of patch area is reduced by the annular ring shape. This also leads to an improvement in return loss. Hence an annular ring has been chosen in the design. The effect of the increase in radius R_2 of the circle on S_{11} is shown in Fig. 6. As the

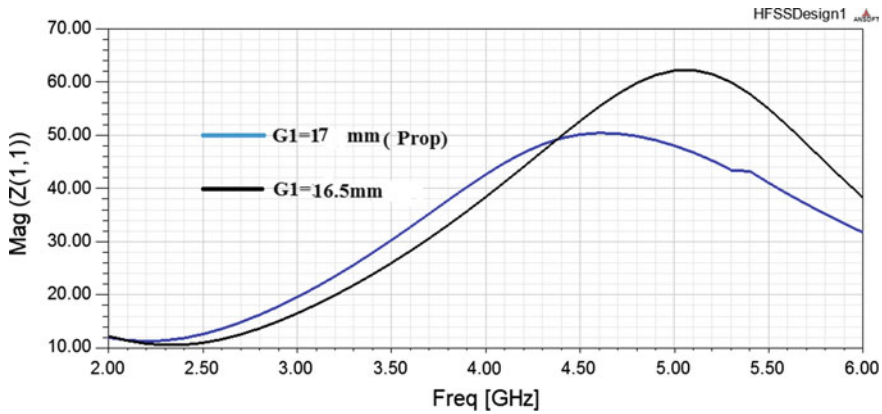


Fig. 18 Effect of variations in ground plane on impedance curve

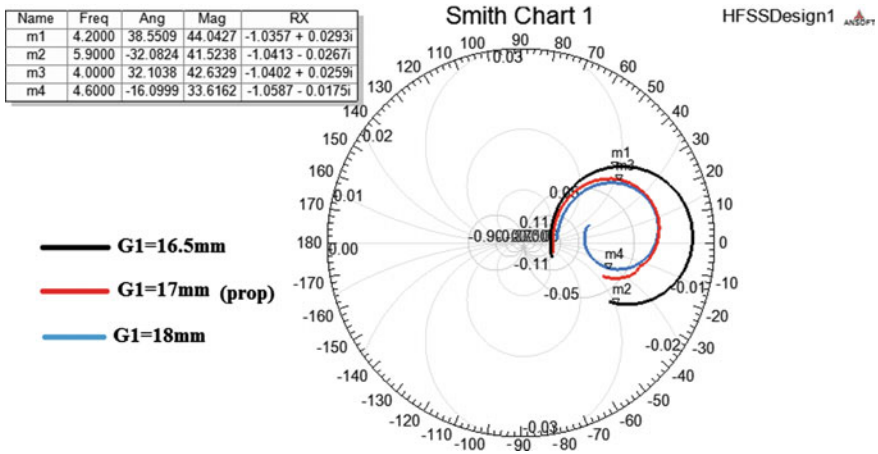


Fig. 19 Smith chart analysis of ground plane variations

frequency of operation increases the impedance moves in the clockwise direction in the Smith chart as shown in Fig. 21. The impedance loci shift towards left with the increase in radius R_2 in Smith chart, implying that the impedance is decreasing. This is vindicated by the magnitude impedance curve shown in Fig. 16

Step 3: An inverted L-shaped slot is introduced near the feed line [11]. The length of each slot [12] is taken about half the guided wavelength [6, 8], as shown in Fig. 7. The inverted L-shaped [11] slot creates an alternate current path and improves return loss from -6 db to -9 db at 2.4 GHz. The LS_2 variations are made and analysed on Smith chart. As the slot

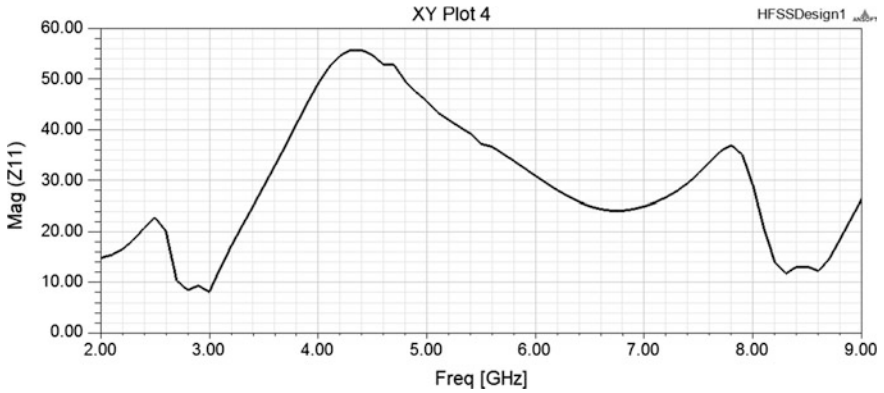


Fig. 20 Effect of C-shaped on impedance curve

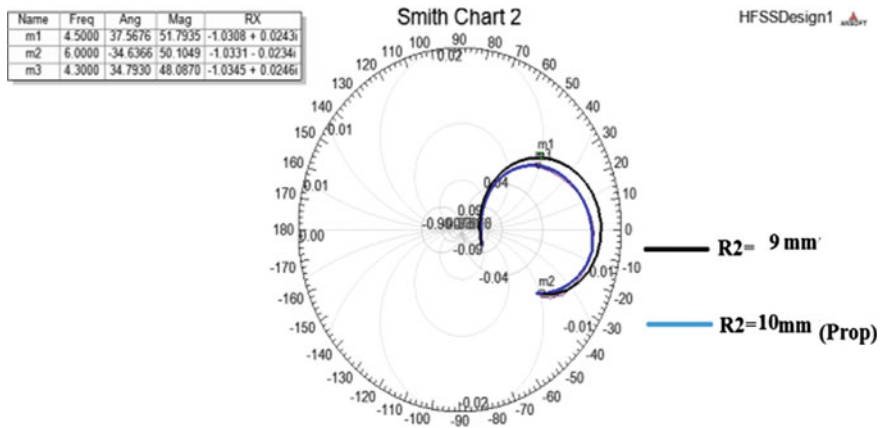


Fig. 21 Smith chart analysis of annular ring

length is increased from 3 mm to 4 mm the impedance loci shift left which shows decrease in impedance as shows in Smith chart as illustrated in Figs. 22, 23 and 24

$$L = (\lambda_g/2) \tag{1}$$

$$\lambda_g = \lambda_o / \sqrt{\epsilon_{reff}} \tag{2}$$

$$\epsilon_{reff} = (\epsilon_r + 1)/2 \tag{3}$$

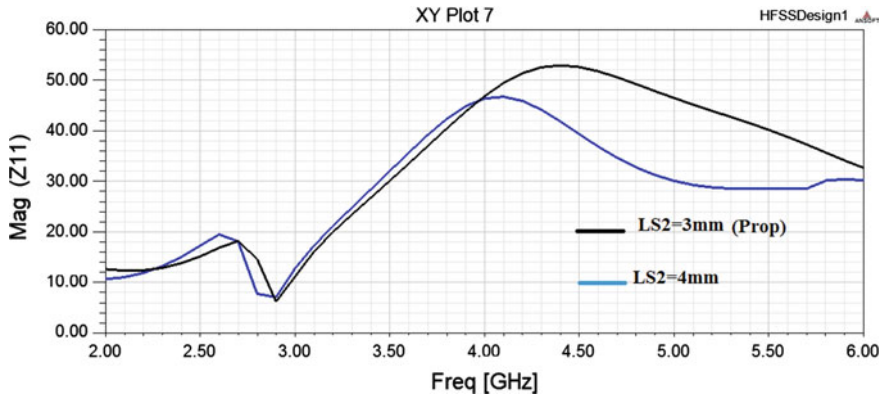


Fig. 22 Effect of change in LS_2 on impedance curve

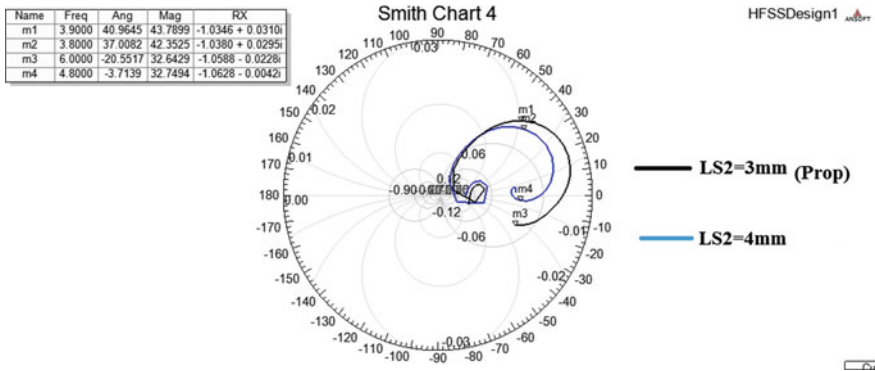


Fig. 23 Smith chart analysis of LS_2 variations

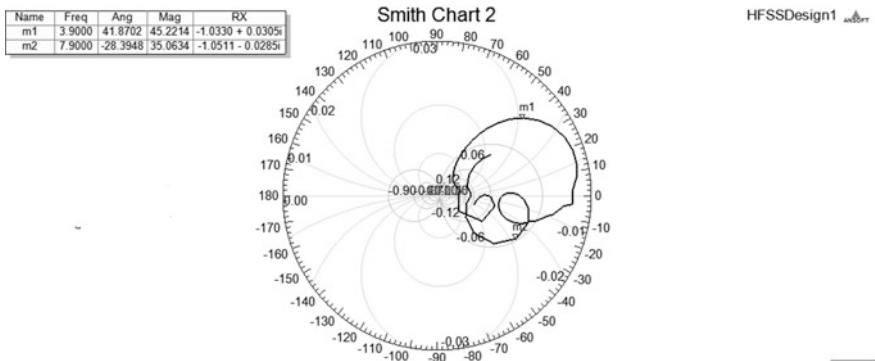


Fig. 24 Smith chart analysis of C-shaped curve

- Step 4: A new slot near the feed line is introduced whose length is as stated in (1) that shows a return loss of about -45 db with an improvement in the bandwidth as shown in Fig. 8
- Step 5: For creating a Notch at 7.5 GHz, a C-shaped slot is introduced in the ground plane. The dimensions of C-shaped slot are chosen to be nearly half of guided wavelength [8]. A notch is observed with good Bandwidth at 7.5 GHz as shown in Fig. 9. The results are checked with impedance curve as shown in Fig. 20. A loop in Smith chart shows multiband operation which can be verified with the return loss curve (S_{11}). Due to C-shaped slot, a sharp rise in impedance curve up to 40Ω at 7.5 GHz is observed that shows an improvement in impedance matching at 7.5 GHz

$$2 \times K_1 + K_2 = 0.53 \times \lambda_g = L \quad (4)$$

- Step 6: Further the operating frequency range is improved using upper bevel-shaped ground, as shown in Fig. 10
- Step 7: The antenna design has been checked for housing effect [7]. The results show an adverse effect on lower frequency band up to 4 GHz as shown in Fig. 11

A parametric study has been carried out and the effects on resonant frequencies, bandwidth and change in return loss is thoroughly observed.

Results

Reflection Coefficient and Bandwidth

The designing of the antenna was carried out using Ansoft high frequency simulation software (HFSS). The proposed antenna has good return loss up to -40 db as shown in Fig. 10. There may be some discrepancies between measured and obtained results due to practical considerations and manufacturing tolerances. As can be perceived from the results, the antenna can be widely operated in two bands 4–6.3 and 7–7.8 GHz, with good impedance bandwidth ($S_{11} < -10$ db) by considering FCC standards. This can cover a wide range of applications as stated above by changing the ground plane which in turn changes frequency of operation.

Radiation Patterns, Gain and Efficiency

The radiation pattern, gain and efficiency are measured using software simulations. The radiation plots at 4.5 and 7.5 GHz are observed, it is nearly omnidirectional and stable in pattern are shown in Figs. 12 and 15. The measured peak gain at 4.5 GHz

is about -5 dBi, at 7.5 GHz is about -7 dBi and at 2.4 GHz is about 4 dBi. The measured efficiency at 4.5 GHz is 90 % and at 7.5 GHz is about 88 % as shown in Fig. 14. A good return loss about -40 dB at 4.5 GHz and -26 dB at 7.5 GHz are obtained. Simulation results have shown that the efficiency has improved by 5 % and the reflection coefficient S_{11} is obtained up to -40 dB as compared to normal circular patch [8] and hooked shaped arm [2], as shown in Fig. 10

Housing Effect

Housing effect is a critical factor in determining the antenna performance in environment of metal object [7]. This effect is important in mobile phones and laptops. A copper plate of 50.9×33 mm² was kept in the vicinity of the antenna. During the simulation process, the width of the copper plate was varied from 0.8 mm to 1 mm. The performance of the antenna as observed from the results is inversely proportional to its thickness. As the thickness increased, the performance of the antenna impaired. Along with variation in width, the distance of antenna from copper plate was varied from 3 mm to 6 mm. As this distance decreases, the performance of the antenna degraded as shown in Figs. 11 and 13.

Conclusion

This paper has covered a wide range of frequency, with good range of applications. Further wide band is obtained by using upper bevel-shaped ground. The radiation pattern obtained is bidirectional. The antenna proposed herein does not use lumped elements makes the design simple and reduction in cost and so can be used in MIMO systems. The antenna is tested for housing effect which has an adverse effect on lower frequencies which can be discerned from the simulations. Simulation has shown enhanced efficiency, improved return loss and analysed effect of other components on it. A notch at 2.4 GHz can be further improved for covering more applications.

References

1. Balanis, C.A.: *Antenna Theory: Analysis and Design*, Wiley (2012)
2. Naser-Moghadasi, M., Sadeghzadeh, R.A., Fakheri, M., Aribi, T., Sedghi, T., Virdee, B.S.: Miniature hook-shaped multiband antenna for mobile applications. *Antennas Wirel. Propag. Lett.* **11**, 1096–1099 (2012)
3. Hala, E., Nashaat, Dalia M.B.S.: Multiband and UWB V-shaped antenna configuration for wireless communications applications, *Antennas Wirel. Propag. Lett.* (7):89–91 (2008)
4. Gemio, J., Granados, J., Castany, J.: Dual-band antenna with fractal-based ground plane for WLAN applications. *IEEE Antennas Wirel. Propag. Lett.* **8**, 748–751 (2009)

5. Hala, E., Nashaat, Dalia, M.B.S.: Multifrequency microstrip patch antenna using multiple stacked elements. *IEEE Microwave Wirel. Compon. Lett.* **3**(13), 123–124 (2003)
6. Antoniadis, M.A., Eleftheriades, G.V.: A Compact Multiband Monopole Antenna With a Defected Ground Plane. *IEEE Antennas Wirel. Propag. Lett.* (7), 652–655 (2008)
7. Lai, X.-Z., Xie, Z.-M., Xie, Q., Cen, X.-L.: Compact multiband planar antenna for 2.4/3.5/5.2/5.8-GHZ wireless applications. *IEEE Antennas Wirel. Propag. Lett.* (11), 144–147 (2012)
8. Bakariya, P.S., Dwari, S., Sarkar, M.: Triple band notch UWB printed monopole antenna with enhanced bandwidth. *Int. J. Electron. Commun.* (2014)
9. Abutarboush, Hattan F., Nilavalan, Nasif, R.: Multiband and wideband antenna for GSM900 and other wireless applications. *IEEE Antennas Wirel. Propag. Lett.* **11**, 539–542 (2012)
10. Kurniawan, A., Mukhlisin, S.: Wideband antenna design and fabrication for modern wireless communications systems. *Procedia Technol.* **11**, 348–353 (2013)
11. Pazin, L., Telzhensky, N., Leviatan, Y.: Multiband flat-plate inverted-F antenna for Wi-Fi/WiMAX operation. *IEEE Antennas Wirel. Propag. Lett.* **7**, 197–200 (2008)
12. Khalilzadeh, A., Tan, A.E.-C., Rambabu, K.: Design of an integrated UWB antenna with dual band notch characteristics. *AEU-Int. J. Electron. Commun.* **5**, 433–437 (2013)

Triple Band Slotted Antenna for Wireless Applications

Ankur Dalmiya and Om Prakash Sharma

Abstract In this paper, a compact triple frequency band antenna has been proposed using combinations of S-shaped and two comb-shaped slots. The FR-4 substrate has been used for the proposed design. This work aims to meet the requirements of weather radar system, Wi-Fi, WLAN, and Wi-MAX. The obtained simulated results show that the antenna has triple band in the frequencies ranging from 5 to 7.5 GHz for C band. The antenna resonates at 5.4, 5.8, and 6.8 GHz. The proposed design is simulated using CST software.

Keywords CST · Wi-Fi · Wi-MAX · WLAN · Weather radar system · Triple band

Introduction

Antennas are basic components of any electronic appliances and are connecting links between the transmitter and free space or free space and the receiver [1]. Wireless LANs (WLANs) are being utilized by the masses these days due to their low cost. They are exercised as free roaming network elements in various industries and commercial sectors. Wired LANs can be replaced by WLANs any wired infrastructure can be restored with it [2].

Worldwide Interoperability for microwave access (WiMAX) technology contains the base transceiver station and a central antenna. The central antenna communicates with subscriber using point to multipoint link [3–5].

Ankur Dalmiya (✉)

Digital Communication, Poonima College of Engineering, Jaipur, India
e-mail: ankurdalmiya@yahoo.co.in

O.P. Sharma

Department of Electronics & Communication,
Poonima College of Engineering, Jaipur, India
e-mail: opsmnit@gmail.com

© Springer India 2016

N. Afzalpulkar et al. (eds.), *Proceedings of the International Conference on Recent Cognizance in Wireless Communication & Image Processing*, DOI 10.1007/978-81-322-2638-3_62

559

The geometry of proposed antenna is so designed that it may be employed for WiMAX and IEEE 802.11a wireless local area network commonly used in USA (5.15–5.35, 5.7–5.825 GHz) and HIPERLAN/2 in Europe (5.15–5.35, 5.47–5.725 GHz). It is also suitable for wireless application of STM link 1 (Synchronous Transport Module level 1) [6–8]. The simulated output justifies as the proposed antenna resonates at 5.4, 5.8, and 6.8 GHz.

This paper comprises of four sections. Brief introduction of antenna and its application is described in section “Introduction”. The proposed antenna geometry is discussed in section “Antenna Design and Geometry”. Section “Result Analysis” analyzes the results obtained. Section “Conclusion” represents the conclusion of the research work.

Antenna Design and Geometry

The design of proposed antenna is shown in Fig. 1. In this design of S-shaped planar patch antenna, two comb-shaped slots are interpolated. Further, in between each leg of the slotted comb structure, another rectangular slot has been introduced. The proposed antenna has a simple geometry which is printed on FR4 substrate

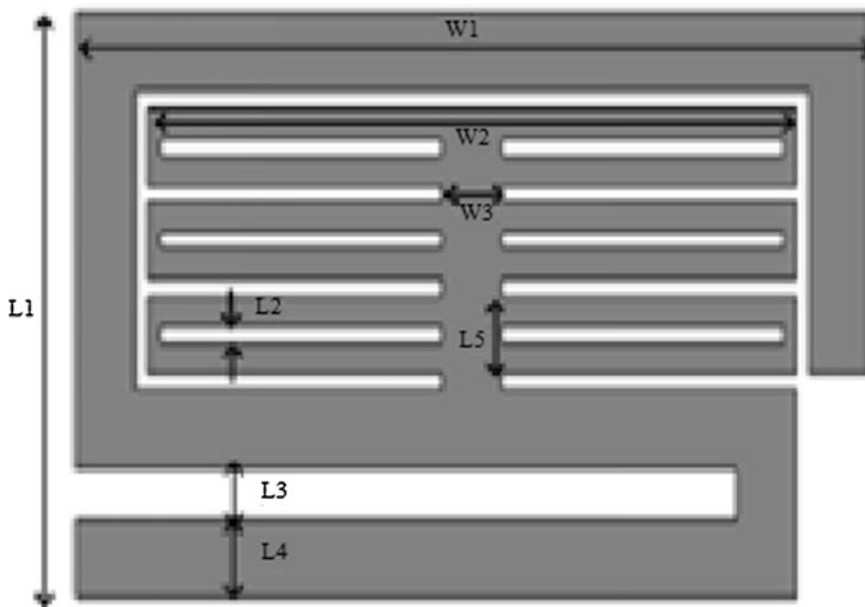


Fig. 1 Design of proposed antenna; $L1 = 9$ mm, $L2 = 0.25$ mm, $L3 = 0.8$ mm, $L4 = 1.2$ mm, $L5 = 1.2$ mm, $W1 = 16$ mm, $W2 = 13.1$ mm, $W3 = 1.2$ mm

having thickness 1.6 mm and relative permittivity 4.4. A triple band slotted antenna is fed by 50Ω probe feeding with point $x = 13.95$ mm and $y = 0.6$ mm with respect to the dimensions of patch.

The proposed antenna has patch dimensions length 9 mm, width 16 mm, and height 0.05 mm having resonant frequency 6.8 GHz. The various parameters, such as return loss, VSWR, polar plot, smith chart, and radiation pattern has been simulated and discussed. The dimension of each leg of the comb-shaped slot is $5.95 \text{ mm} \times 1.2 \text{ mm}$.

Result Analysis

After simulating the proposed antenna geometry, following resulting parameters were derived.

Return Loss of Proposed Antenna

Return Loss is a measure of how well antenna matching is done. The proposed antenna is resonating at three different resonant frequencies 5.4, 5.8, and 6.8 GHz which has been shown in Fig. 2, representing its triple frequency band operation.

It shows a multiband behavior of antenna with resonant frequencies at 5.4 GHz, 5.8 GHz and 6.8 GHz having return losses -15.37 dB, -18.45 dB, and -18.27 dB, respectively.

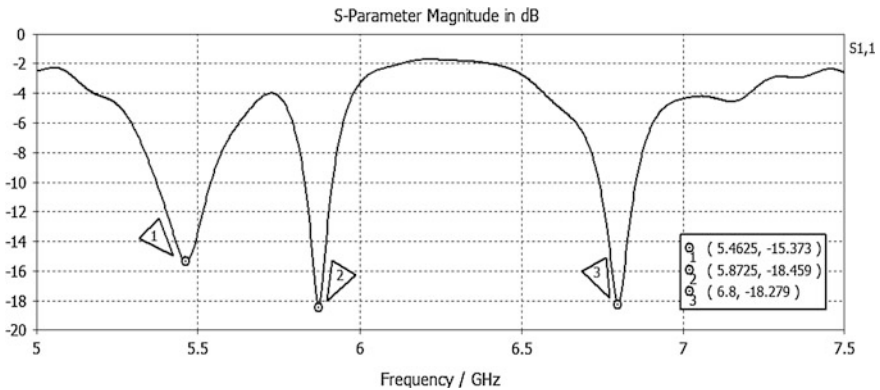


Fig. 2 Return loss of proposed antenna

VSWR of Proposed Antenna

VSWR defines the amount of reflected power from the antenna and is a function of return loss. Figure 3 represents the VSWR of the proposed antenna which lies in the range from 1 to 2.

It shows that VSWR is 1.41, 1.27, and 1.27 at 5.4 GHz, 5.8 GHz, and 6.8 GHz respectively.

Smith Chart and Polar Plot of Proposed Antenna

Smith Charts are very helpful for impedance matching of an antenna. For proposed design the smith chart and polar plot are presented in Figs. 4 and 5, respectively in which 50 Ω impedance matching is represented.

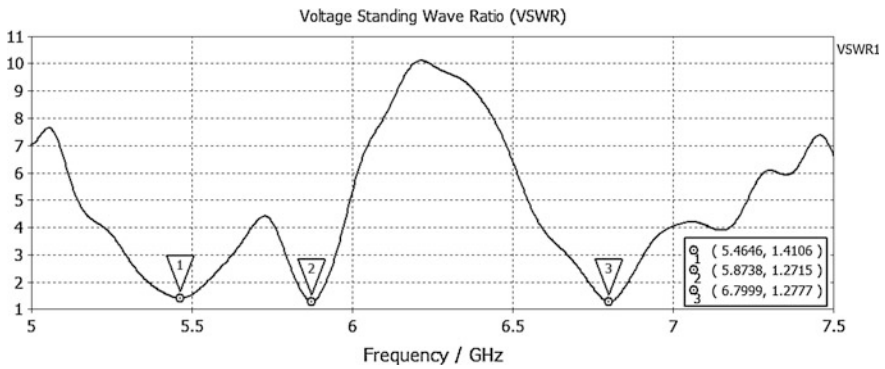


Fig. 3 VSWR of proposed antenna

Fig. 4 Smith Chart of proposed antenna

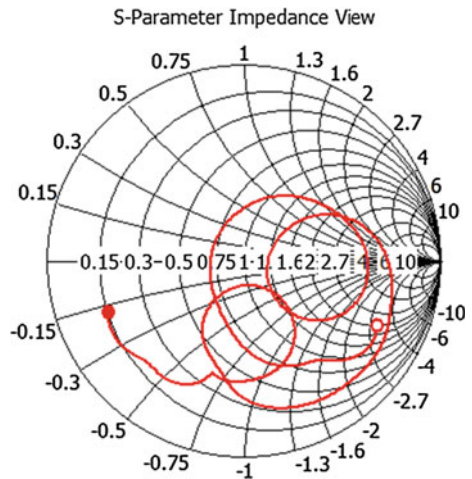
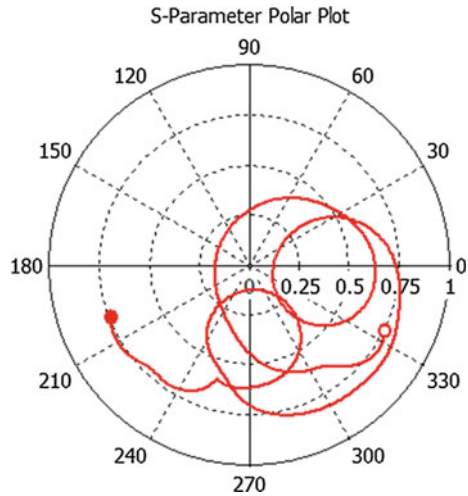


Fig. 5 Polar Plot of proposed antenna



It shows that the antenna performance has been exactly matched with 50Ω impedance (at feeding points $x = 13.95$ mm and $y = 0.6$ mm with respect to the dimensions of patch of the antenna).

Radiation Pattern of Proposed Antenna

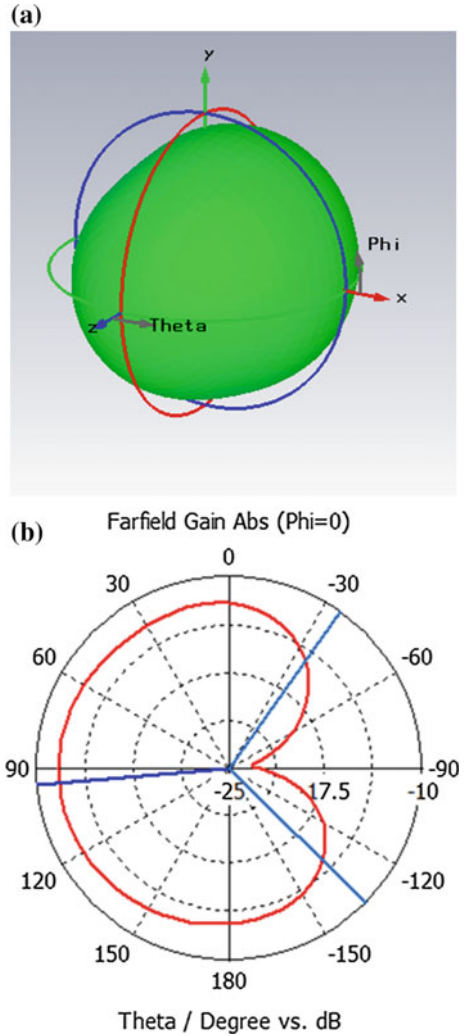
In general, radiation pattern of an antenna is defined as the variation of radiated power by that antenna as a correlation of the direction which is away from it. This variation in power is observed in the far-field properties of the antenna. The radiation pattern for 5.87 GHz is shown in Fig. 6.

Figures 6a, b reveals that antenna is very close to omnidirectional pattern and further justifies its suitability for multiple applications.

Conclusion

A new triple-band antenna design has been presented in this paper. The design consists of joining two comb-shaped slots with S-shaped structure resonating at three frequencies 5.46 GHz (at lower level), 5.87 GHz (in between), and 6.8 GHz

Fig. 6 Radiation pattern of proposed antenna for $f_r = 5.87$ GHz. **a** 3D View. **b** Polar View



(at higher level). Analysis of the proposed design justifies its suitability in form of multiband operation to be useful for applications HIPERLAN/2, IEEE 802.11a, and STM link 1.

References

1. Dhande, P.: Antennas and its applications. DRDO Sci. Spectr. 66–78 (2009)
2. Chauhan, B., Prachi: Triple band high gain slotted antenna. IEEE Indian Antenna Week (2014)
3. Sutzman, W.L., Thiele, G.A.: Antenna Theory and Design. Wiley (1998)

4. Kumar, G., Ray, K.P.: *Broadband Microstrip Antennas*. Artech House, pp. 3–5 (2003)
5. Maidurrahman, S.M., Das, S., Yadaw, V.K., Ramkanu, A.P., Karmkar, A.: New compact tri-band microstrip patch antenna using dual T-shaped slit for Wi-Max and microwave C band application. *Int. J. Eng. Sci. Res.-IJESR* **3**(5) (2012). ISSN: 2230-8504, e-ISSN: 2230-8512
6. Maci, S., Gentili, G.B.: Dual-frequency patch antennas. *IEEE Mag. Antennas Propag.* **39**, 13–20 (1997)
7. Chowdhury, M.R., Zuboraj, M.R.A., Ovi, A.A.N., Matin, M.A.: Novel design of triple band rectangular patch antenna loaded with metamaterial. *Electromagnet. Res. Lett.* **21**, 99–107 (2011)
8. Khairul, M., Ismail, H., Esa, M.: Low profile printed antenna with a pair of step loading for dual-frequency operation. In: *Proceedings of Asia Pacific Conference on Applied Electromagnetics (APACE 2003)*, Shah Alam, Malaysia (2003)

A Compact Design of Modified E-shaped Ground Plane Patch Antenna for Broadband Applications

Sanjay Sharma and Sanyog Rawat

Abstract A compact design of modified E-shaped antenna with wideband characteristics has been designed for high-speed WLAN and other wireless communication systems covering the operating frequency ranging from 3.295 to 5.655 GHz. Two parallel slots are incorporated into the patch of a microstrip antenna to expand its bandwidth. The length of the intermediary wing can be clipped and the length of the lower arm can be modified to tune the frequency of the resonant mode. Extensive study of E-shaped antenna has been carried out to improve the radiation performance of the proposed geometry. Low dielectric constant substrate is chosen to achieve a small-size radiating structure that meets higher bandwidth. Simulation is performed on CST software.

Keywords Microstrip antenna · E-shaped · Wideband · Radiating patch

Introduction

The antenna is a key building block in a mobile telecommunication system. Antennas which are low profile are mostly used in the operation of many modern mobile telecommunication systems. Microstrip patch antennas represent one family of low-profile antennas that are conformable to planar and nonplanar surfaces, very simple and not expensive to construct by printed circuit technology [1]. Microstrip antennas can be designed in variety of shapes and there are various feeding methods for exciting the antennas. Basically, a conventional antenna consists of a top layer of conducting material treated as patch followed by a relatively thick layer of dielectric material which is used as a substrate and finally a bottom layer of conducting material as ground [2]. The microstrip antennas have been in wide use due

Sanjay Sharma (✉) · Sanyog Rawat
Amity University, Jaipur, India
e-mail: sanjay.sharma.amity@gmail.com

Sanyog Rawat
e-mail: sanyog.rawat@gmail.com

to light weight, conformability with host surface, and good radiation parameters. It also has a disadvantage of narrow bandwidth; researchers have done many efforts to defeat this problem and get extended bandwidth [3].

There are several methods to increase the bandwidth of microstrip antenna such as using air substrate [4–7]. However, if compact antenna size is required then dielectric substrate must be used. To improve the microstrip patch antenna bandwidth, few techniques are applied like adding parasitic structures over the same plane. It is a very effective technique to enhance the bandwidth on a compact size [8]. The examples are U-slot patch antennas, E-H shaped patch antennas, and E-shaped patch antennas [9–15].

Antenna Geometry

The conventional antenna consists of a three-layer structure. The material used for substrate is FR-4 lossy with dimension as 30 mm × 30 mm × 1.59 mm; low dielectric constant is selected to achieve a small-size radiating structure that provides the required bandwidth. The finite ground plane has dimensions of 30 mm × 30 mm × 0.035 mm. The microstrip patch antenna is basically a low bandwidth antenna; so for enhancing the bandwidth, we cut two parallel slots in the ground plane which looks like alphabet E shape.

The dimensions of the ground structure are $L_1 = 22$ mm, $L_2 = 20$ mm, $L_3 = 20$ mm, $L_4 = 22$ mm, and $W_1 = 20$ mm, $W_2 = 3$ mm, and $W_3 = 4$ mm which have been depicted in Fig. 1 where L shows the length of the parallel slots and W shows the width of slots. Here for enhancing the bandwidth, the patch is also modified by inserting slots as shown in Fig. 2.

The variations in the ground plane and patch are done to enhance the bandwidth. The optimized design is shown in Fig. 2.

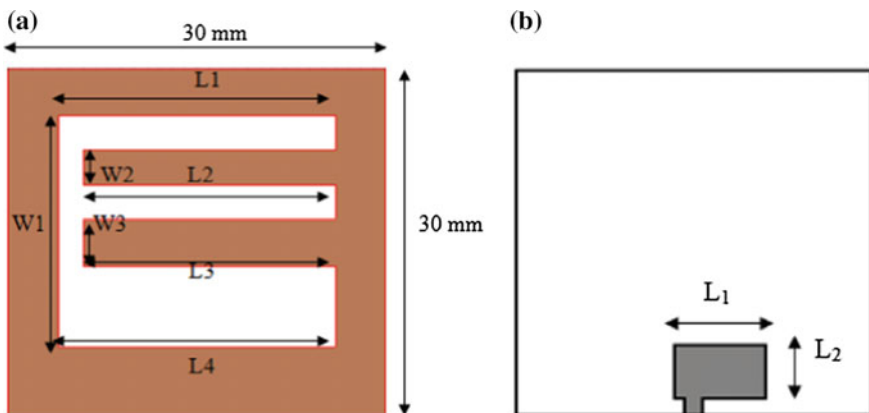


Fig. 1 a Initial ground structure. b Initial patch structure

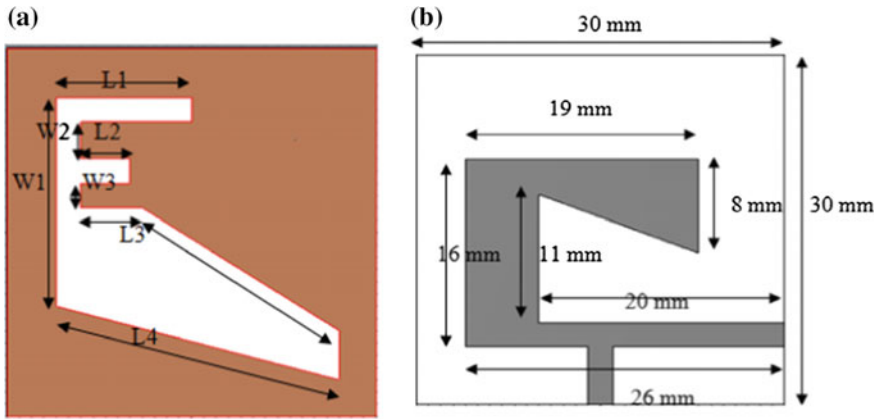


Fig. 2 a Initial ground structure. b Initial patch structure

Simulation and Result Analysis

The simulated variation of return loss as a function of frequency is shown in Fig. 3 for the initial geometry considered. The impedance bandwidth of about 51 % is achieved at -10 dB and the return loss level is obtained for the proposed antenna (Fig. 4).

The proposed antenna is operating at frequencies of 3.81 GHz and 5.365 GHz and corresponding reflection coefficient (S_{11}) are -14.80 and -13.20 dB for the dual resonant frequencies and has a bandwidth of nearly 51 % ranging from 3.295 to 5.655 GHz. The VSWR of the proposed antenna is less than 2 in frequency band range which is shown in Fig. 5.

The proposed antenna has a stable gain of nearly 3 dBi over the entire frequency range which is shown in Fig. 6.

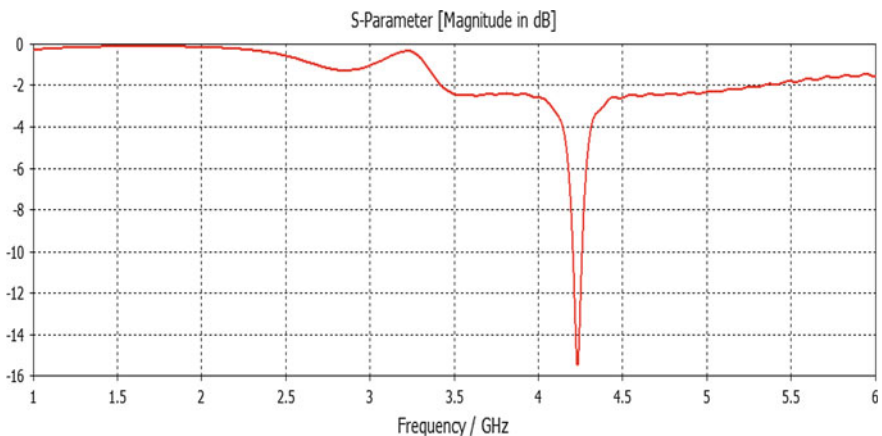


Fig. 3 Simulated return loss as function of frequency for initial design

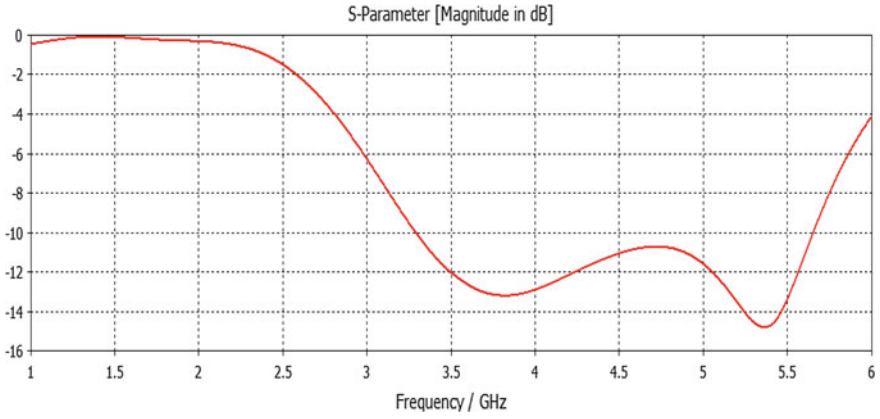


Fig. 4 Simulated variation of return loss with frequency for proposed antenna

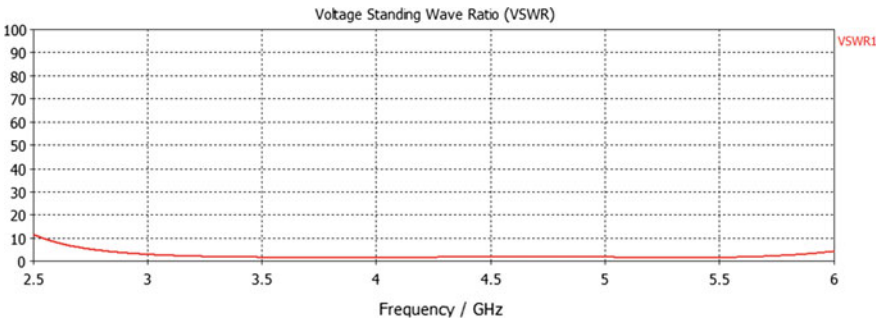


Fig. 5 Simulated VSWR of proposed antenna

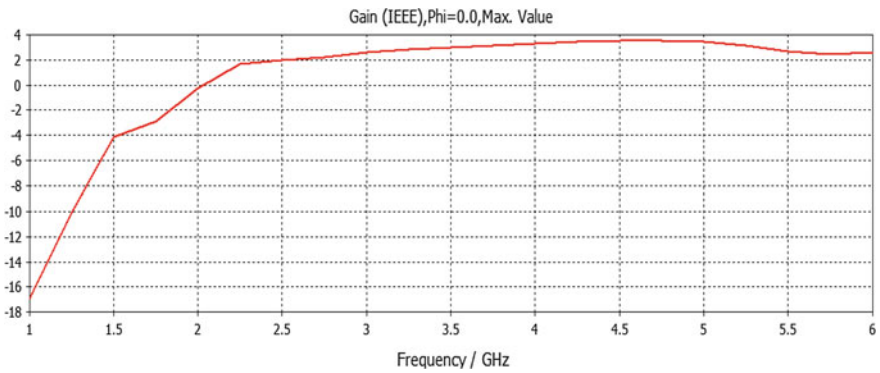


Fig. 6 Gain of proposed antenna

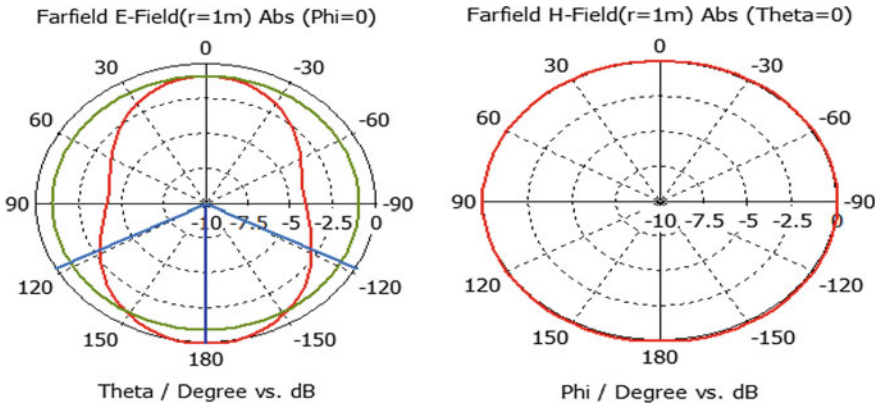


Fig. 7 E-field and H-field radiation pattern at resonant frequency 3.81 GHz

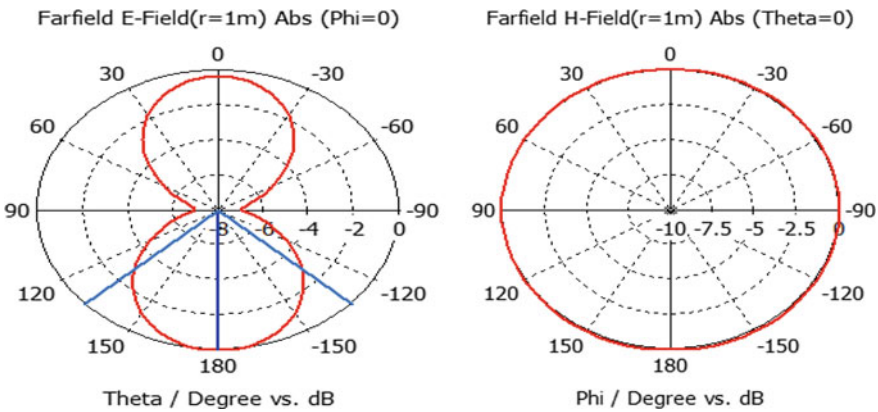


Fig. 8 E-field and H-field radiation pattern at resonant frequency 5.365 GHz

The E-Field and H-field of the proposed antenna at both the operating frequencies which are 3.81 and 5.365 GHz are shown in Figs. 7 and 8.

Conclusion

The above proposed antenna is a broadband microstrip patch antenna with modified E-shaped ground structure. The microstrip patch antenna inherently is narrow band in nature, so for enhancement of the bandwidth various changes in the shape of patch and ground were performed. The proposed antenna has stable gain with a value of 2.9 dBi over the whole frequency band. The bandwidth of designed

antenna is 51 % at frequency range of 3.295–5.655 GHz. The designed microstrip patch antenna supports the S-band, (microwave frequency band range) so it is applicable for wireless communication applications.

References

1. David, M.P.: Microstrip antennas. Proc. IEEE, pp. 79–91 (1992)
2. Huang, J.: Microstrip Antennas for Commercial Applications. Jet Propulsion Laboratory, California Institute of Technology Pasadena, CA, pp. 91–109 (1994)
3. Rafferty, W., Dessouky, K., Sue, M.: NASA's mobile development program. In: Proceedings of the Mobile Conference, pp. 11–22 (1988)
4. Carver, K.R., Mink, J.W.: Microstrip antenna technology. IEEE Trans. Antennas Propag. AP **29**, 2–24 (1981)
5. Bahl, J., Bhartia, P.: Microstrip antennas. Artech House, Dedham (1980)
6. James, J.R., Hall, P.S., Wood, C.: Microstrip Antenna Theory and Design. Peter Peregrinus, London (1981)
7. James, J.R., Hall, P.S.: Handbook of Microstrip Antennas. Peter Peregrinus, London (1989)
8. Richards, W.F., Lo, Y.T., Harrison, D.: An improved theory for microstrip antennas and applications. IEEE Trans. Antennas Propag. AP **29**, 38–46 (1981)
9. Ang, B.-K., Chung, B.-K.: A wideband E-shaped microstrip patch antenna for 5–6 GHz wireless communications. Prog. Electromagnet. Res. PIER **75**, 397–407 (2007)
10. Yang, Fan, Zhang, Xue-Xia, Ye, Xiaoning, Rahmat-Samii, Yahya: Wide-band E-shaped patch antennas for wireless communications. IEEE Trans. Antennas Propag. **49**(7), 1094–1100 (2001)
11. Islam, M.T.: Broadband E-H shaped microstrip patch antenna for wireless systems. Prog. Electromagnet. Res. PIER **98**, 163–173 (2009)
12. Wi, Sang-Hyuk, Lee, Yong-Shik, Yook, Jong-Gwan: Wideband microstrip patch antenna with U-shaped parasitic elements. IEEE Trans. Antennas Propag. **55**(4), 1196–1199 (2007)
13. Yang, S.L.S., Lee, K.F., Kishk, A.A.: Design and study of wideband single feed circularly polarized microstrip antennas. Prog. Electromagnet. Res. PIER **80**, 45–61 (2008)
14. Khodaei, G.F., Nourinia, J., Ghobadi, C.: A practical miniaturized U-slot patch antenna with enhanced bandwidth. Prog. Electromagnet. Res. B **3**, 47–62 (2008)
15. Weigand, Steven, Huff, Greg H., Pan, Kankan H., Bernhard, Jennifer T.: Analysis and design of broad-band single-layer rectangular U-slot microstrip patch antennas. IEEE Trans. Antennas Propag. **51**(3), 457–468 (2003)

Frequency Switching in Coupled Microstrip Line Loaded with Split-Ring Resonator

Gurwinder Singh, Rajni and Anupma Marwaha

Abstract This paper presents investigation of frequency switching of split-ring resonator-loaded microstrip line. We loaded the microstrip line with planar square split-ring resonator structure of a copper on Rogers RO3010, a substrate. The electric and magnetic interaction of split-ring resonator (SRR) with microstrip line is presented by simulating microstrip line-loaded split-ring resonator inside a waveguide with “High Frequency Structure Simulator” software. In this paper, the change in magnetic resonance is observed at varying loading distance between microstrip line and split-ring resonator.

Keywords Metamaterials (MTM) · Split-ring resonator (SRR) · Microstrip line · Double-negative metamaterials (DNG)

Introduction

Metamaterials are engineered by metallic inclusions in the host media like substrate. The interaction between the metamaterial and an electromagnetic field can be tailored by shape, dimensions, and the position of the medium. These materials get their effective properties from its structures rather than inheriting them directly from its constituents. The group and phase velocity in these materials are antiparallel to

Gurwinder Singh (✉)

Department of ECE, Government Polytechnic College, Ferozepur 152002, Punjab, India
e-mail: gurwinder08singh@gmail.com

Rajni

Department of ECE, Shaheed Bhagat Singh State Technical Campus,
Ferozepur 152004, Punjab, India
e-mail: rajni_c123@yahoo.co.in

Anupma Marwaha

Department of ECE, SLIET, Sangrur 148106, Punjab, India
e-mail: marwaha_anupma@yahoo.com

© Springer India 2016

N. Afzalpulkar et al. (eds.), *Proceedings of the International Conference on Recent Cognizance in Wireless Communication & Image Processing*,
DOI 10.1007/978-81-322-2638-3_64

573

each other. Metamaterials created an indelible sign in microwave engineering applications like waveguides, antennas, filters, phase shifters, delay lines, etc.

The novel idea of metamaterials was given by Victor Veselago in 1968, when he analyzed an incident uniform propagation of plane wave in a media possessing negative permittivity, ϵ and negative permeability, μ [1] also named as left-handed metamaterials (LHM) or double-negative metamaterials (DNG). If only permeability (μ) is negative or permittivity (ϵ) is negative is termed as mu negative (MNG) and epsilon (ENG) metamaterials, respectively, and termed as single-negative (SNG) metamaterials. Pendry proposed split-ring resonator (SRR) to achieve negative permeability [2] and thin wire to achieve negative permittivity [3] and a combined structure of SRR and thin wire to realize LHM [4]. Later, Smith and his colleagues demonstrated metamaterials to show negative ϵ and negative μ simultaneously and tested its unusual properties by carrying out microwave experiments in 2000.

In 2001, Smith et al. showed negative refraction experimentally using metamaterials with continuous unit cells of SRR and copper strips [5–7]. Marques et al. investigated bianisotropic behavior of the SRR unit cell structure in 2002. A modified version of SRR, i.e., broadside coupled (BC-SRR) is suggested in the same paper to avoid bianisotropy. A comparative analysis of the conventional (or edge-coupled) SRR and BC-SRR is shown with printed metallic rings of the BC-SRR on both sides of the dielectric substrate and aligned in such a way that their splits were displaced by 180 degrees [8]. Bilotti et al. in 2007 suggested and analyzed SRR unit cells with multiple rings. Bilotti et al. proposed a model with multiple split-ring resonators and spiral resonators to increase the miniaturized rate [9]. In 2010, Joshi et al. proposed SRR-loaded microstrip patch antenna and proved that loading the patch antenna with SRR can shift resonant frequency to lower frequency side [10]. In 2011, Pattnaik et al. also obtained that by changing the distance between SRR and microstrip patch antenna, the resonant frequency shifts and decreases as the distance increases [11]. In 2012, Joshi et al. partially loaded the rectangular, slotted microstrip patch antenna with multiple split-ring resonators at ground plane and showed that the resonant frequency of the rectangular patch antenna decreases after loading with MSRR [12]. In 2014, Bojanic et al. presented an equivalent circuit approach for the magnetic/electric interaction of single split-ring resonators (SRRs) with printed lines and extracted the different parameters of microstrip line with parallel and perpendicular gap to line [13].

The aim of the present work is to design a microstrip line loaded with metamaterials and examine the shifting of resonant frequency with variable loading distance. The outline of paper is as follows: section two gives proposed design of microstrip line loaded with planner square SRR, its equivalent circuit, and the methodology of SRR; Section three presents results and discussions; Section four gives the conclusion of the paper.

Proposed Design of Microstrip Line Loaded with Split-Ring Resonator

In the proposed model, a conventional microstrip line is loaded with planar square SRR in the same plane. The SRR is coupled to microstrip line by placing it at distance ‘s’ with gap parallel to the microstrip line as depicted in Fig. 1. This coupled line is modeled on RO3010 substrate of Rogers with thickness (h) 1.27 mm, dielectric permittivity $\epsilon_r = 10.2$, and loss tangent 0.035.

The dimensions of SRR coupled to rectangular microstrip line are given in Table 1:

The switching of resonating frequency is observed by changing this distance coupled line. The switchable configuration of coupled line is obtained by varying the loading distance s, to 0.1, 0.5, and 0.9 mm, respectively. To extract the parameters L and C of the transmission line in Fig. 2, taking into account the

Fig. 1 Layout of microstrip line loaded with SRR (*Top view*)

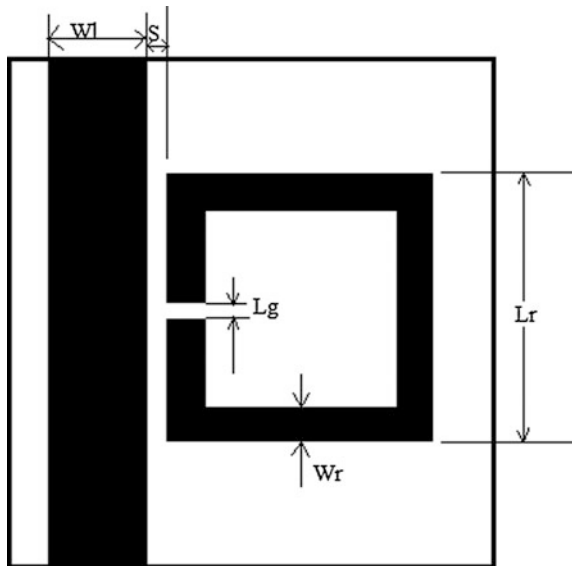


Table 1 Dimensions of microstrip line loaded with SRR

S. no	Parameters		
	Name of parameter	Representation	Dimensions (in mm)
1	Width of microstrip line	Wl	1.2
2	Length of SRR	Lr	3.0
3	Width of SRR	Wr	0.2
4	Gap of split	Lg	0.5

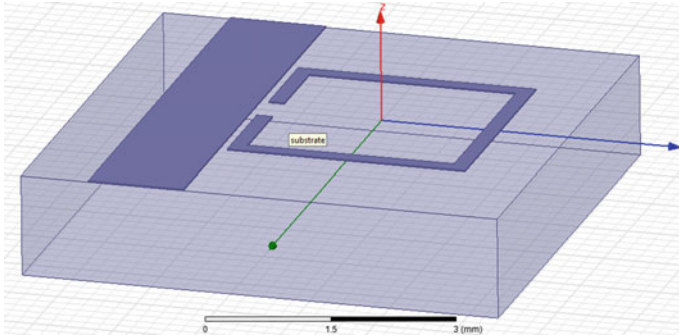


Fig. 2 3-D view of microstrip line loaded with SRR in HFSS platform

coupling between the line and the nearest SRR arm, the system is modeled as a section of the multiconductor transmission line. Inductance consists of two parts:

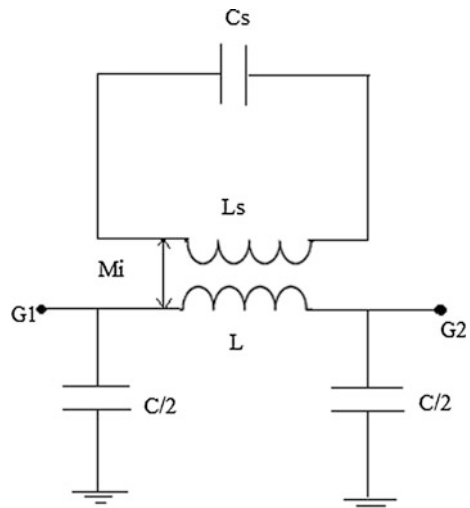
- From the section that is coupled with the transmission line, which is calculated using the corresponding diagonal element of the inductance matrix.
- From an isolated transmission line with length equal to the remaining uncoupled part of the SRR length.

Figure 3 shows the equivalent circuit of microstrip line coupled to split-ring resonator (SRR) where L_s and C_s is inductance and capacitance of SRR, respectively, and L_C is inductance and capacitance of microstrip line, respectively.

G_1 and G_2 are two ports and M_i is mutual inductance. The capacitance C_s is obtained from the SRR resonance frequency as follows:

$$f_r = \frac{1}{2\pi\sqrt{L_s C_s}} \tag{1}$$

Fig. 3 Equivalent circuit of SRR-loaded microstrip line



where resonance frequency is also calculated as:

$$f_r = \frac{w_r}{2\pi} \tag{2}$$

The coupling coefficient M_i is then obtained as a function of f_{min} , the resonance frequency f_r , and the line parameters L and C as follows:

$$M_i^2 = \left(1 - \frac{w_r^2}{w_{min}^2}\right) (1 - a_1) \tag{3}$$

The term mutual inductance M_i is also varied by variation of the distance ‘S’ between the microstrip line and split-ring resonator (SRR). Where a_1 corresponds to the circuit with one cell and $f_{min} = \frac{w_{min}}{2\pi}$. These coefficients are given by

$$a_1 = \left[\frac{L}{C} Y_0^2 + 2b \right] \tag{4}$$

where Y_0 is the characteristic admittance of the microstrip line and

$$b = \left(\frac{w_{min}}{w_0} \right); w_0^2 = \frac{8}{LC} \tag{5}$$

SRR gets excited due to field induced by magnetic coupling of SRR with microstrip line and it exhibits metamaterials characteristics. In loading situation, the resonant frequency of SRR-coupled microstrip line shifts to higher frequency region with increase in the loading distance.

Results and Discussion

SRR-loaded microstrip line is simulated inside a waveguide to attain the resonating frequency region. The perfect electric conductor (PEC) boundary conditions are used on the z-faces of the unit cell. The perfect magnetic conductor (PMC) boundary conditions are used on y-faces of the unit cell. The two wave ports 1 and 2 are assigned to both the sides of microstrip line on the x-faces of waveguide. The proposed structure is simulated with Ansoft software “High Frequency Structure Simulator (HFSS)”.

Initially, we placed SRR at 0.1 mm, the reflection coefficient characteristics (S_{11}) of SRR-coupled microstrip line is shown in Fig. 4 which indicates a dip at 4.8 GHz. Then the distance of SRR from strip line is varied from 0.1, 0.3 0.5, 0.7, and 0.9 mm. The resonating frequency of 4.8, 5.3, 5.4, 5.6, and 5.9 GHz is achieved at the respective loading distance 0.1, 0.3, 0.5, 0.7, and 0.9 mm. It is clear that the

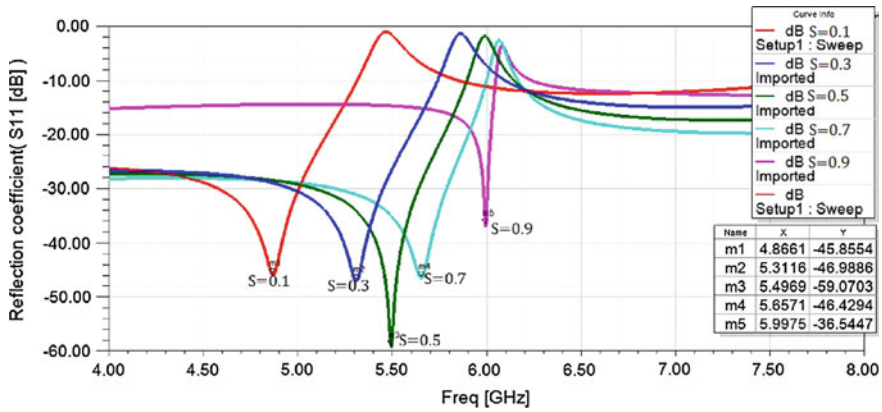


Fig. 4 Reflection coefficient S_{11} of proposed microstrip line

resonating frequency increases with increase of distance ‘s’ between microstrip line and SRR.

This is due to the fact that mutual inductance gets decreased with variation in spacing between SRR and microstrip.

Figure 5 presents transmission coefficient, S_{21} of proposed design at respective loading distance and it is seen that the dip of transmission coefficient S_{21} shifts to right side of the graph as distance increases.

Figure 6 confirms the metamaterial behavior of SRR as phase reversal of S_{21} and S_{11} is seen. From the simulated results of loaded strip line, it is concluded that according to the application requirements, the frequency can be varied by changing the distance ‘s’ between microstrip line and split-ring resonator.

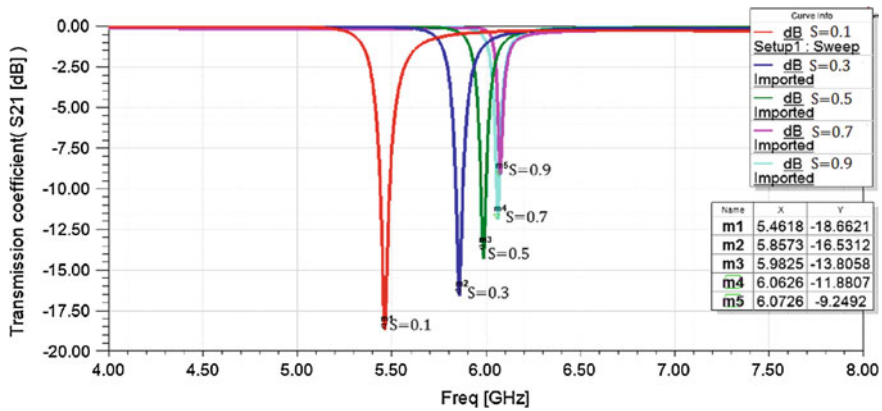


Fig. 5 Transmission coefficient S_{21} of proposed microstrip line

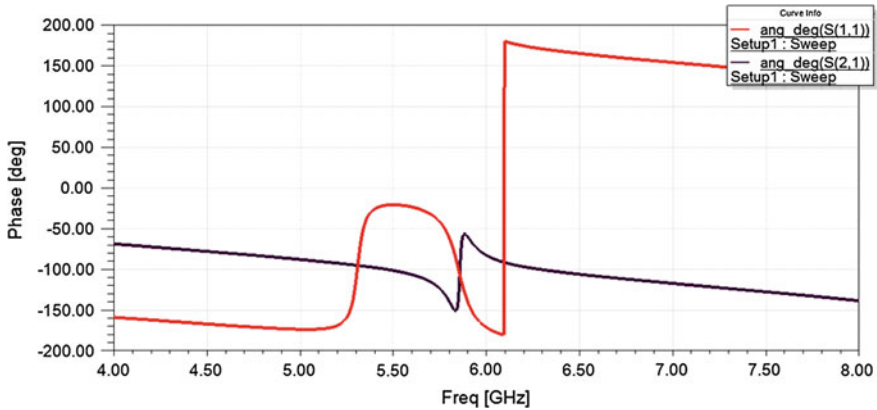


Fig. 6 Phase of reflection coefficient S_{11} and transmission coefficient S_{21} parameters

Conclusions

In this paper, varied frequency of rectangular microstrip line loaded with SRR is examined. The loading distance between rectangular microstrip line and the SRR unit cell is positioned at 0.1, 0.3, 0.5, 0.7, and 0.9 mm, respectively. The microstrip line resonates at 4.8, 5.3, 5.5, 5.7, and 6 GHz, respectively, with loading distances. This is due to the decrease of mutual inductance with increase in distance. Thus, the frequency switching is possible by changing the loading distance (s). Thus, the proposed circuit can be used for design of filters.

References

1. Veselago, V.G.: The electrodynamics of substances with simultaneously negative values of “ ϵ ,” and “ μ ”. *Sov. Phys.—Usp.* **47**, 509–514 (1968)
2. Pendry, J.B., Holden, A.J., Stewart, W.J., Youngs, I.: *Phys. Rev. Lett.* **76**, 4773 (1996)
3. Pendry, J.B., Holden, A.J., Robbins, D.J., Stewart, W.J.: Low frequency plasmons for thin wire structure. *J. Phys.: Condens. Matter* **10**, 20 (1998)
4. Pendry, J.B., Holden, A.J., Robins, D.J., Stewart, W.J.: Magnetism from conductors and enhanced non-linear phenomena. *IEEE Trans. Microwave Theor. Technol.* **47**(11), 2075–2084 (1999)
5. Shelby, R.A., Smith, D.R., Schultz, S.: Experimental verification of negative index of Refraction. *Sci. Mag.* **292**(5514), 77–79 (2001)
6. Smith, D.R., Padilla, W.J., Vier, D.C., Nemat-Nasser, S.C., Schultz, S.: Composite medium with simultaneously negative permeability and permittivity. *Phys. Rev. Lett.* **84**, 4184–4187 (2000)
7. Smith, D.R.: What are electromagnetic metamaterials? *Novel electromagnetic materials* (2006). The research group of D.R. Smith, 2009-08-19

8. Marqués, R., Mesa, F., Martel, J., Medina, F.: Comparative analysis of edge- and broadside-coupled split ring resonators for metamaterial design—theory and experiments. *IEEE Trans. Antennas Propag.* **51**(10), 2572–2581 (2003)
9. Bilotti, F., Toscano, A., Vegni, L.: Design of spiral and multiple split-ring resonators for the realization of miniaturized metamaterial samples. *IEEE Trans. Antennas Propag.* **55**(8), 2258–2267 (2007)
10. Joshi, J.G., Pattnaik, S.S., Devi, S., Lohokare, M.R.: Electrically small patch antenna loaded with metamaterial. *IETE J. Res.* **56**(6), 373–379 (2010)
11. Joshi, J.G., Pattnaik, S.S., Devi, S., Lohokare, M.R.: Frequency switching of electrically small patch antenna using metamaterial loading. *Int. J. Radio Space Phys.* **40**(3), 159–165 (2011)
12. Joshi, J.G., Pattnaik, S.S., Devi, S.: Rectangular slotted microstrip patch antenna with partially loaded metamaterial ground plane. *Int. J. Microwave Opt. Technol.* **7**(1), 1–10 (2012)
13. Bojanic, R., Milosevic, V., Jokanovic, B., Medina-Mena, F., Mesa, F.: Enhanced modelling of split-ring resonators couplings in printed circuits. *IEEE Trans. Microwave Theor. Tech.* **62**(8), 1605–1615 (2014)

A New Compact Dual Band Microstrip BPF for GSM (1.8GHz) and WiMAX Using Asymmetric Stepped Impedance Resonators

Tasher Ali Sheikh, Janmoni Borah, Sahadev Roy
and Abhishek Kumar Pandey

Abstract We propose a design of a compact dual-bandpass microstrip filter (DBPF) for the GSM (1.8 GHz) and WiMAX (3.4 GHz) application using asymmetric SIRs. The presented filter has very low insertion loss (S_{21}) and high selectivity for the desired band. Appearance of transmission zeroes near the edges of passband in the proposed design guarantees sharp cut off frequency and improves the selectivity of proposed band pass filter with fractional bandwidth (FBW) of 10 and 7.08 %. The proposed filter has low insertion losses, (S_{21}) -0.24 and 0.14 dB and the return losses, (S_{11}) -14.71 dB and -25.01 dB for the center frequencies 1.8 GHz and 3.4 GHz, respectively.

Keywords BPF · GSM · WiMax · Asymmetric sirs · FBW

Introduction

Tasher et al. [1, 2] it is shown that in modern communication system especially in mobile communication, compact size and high performance filters are always an obligation to encouragement, to emerge growing end users and to increase the

T.A. Sheikh (✉) · Janmoni Borah · Sahadev Roy · A.K. Pandey
Department of Electronics & Communication Engineering, National Institute of Technology,
Itanagar, Arunachal Pradesh 791112, India
e-mail: tasher372@gmail.com

Janmoni Borah
e-mail: borah1989@gmail.com

Sahadev Roy
e-mail: sdr.ece@nitap.in

A.K. Pandey
e-mail: abhis2808@gmail.com

coverage range for the multimedia services. Hong and Lancaster [3] make it visible that in radio frequency communication, a bandpass filter acts as a key role for obtaining the desired passband spectrum and attenuated signals in another frequency range. The performance at the receiver end in communication systems increases because of the use of high quality filters, which is provided by the reported filter. Chen et al. [4] it is found that bandpass filters are significant components which are used in the transceiver of the communication systems. Li et al. [5] it is shown that, designing a wide passband filter which supports multiple services is becoming a vital issue nowadays. In recent years, particularly, in radio frequency applications multifunctional bandpass filter is widely and abrasively designed and developed. Chen et al. [6] showed that in microstrip filter design procedure with stepped impedance, resonators are generally used to design bandpass filters because of their freedom for selecting the electric length and impedance ratio, small size, and lower insertion loss, which provide exact coupling flexibility for desired specific bands. Thanet [7] presented the conventional bandpass filters that are generally used in our daily life, cell phone-based station to reduce the cost and has low selectivity. Zhang and Mei [8] and Sagawa et al. [9] showed that stepped impedance resonators (SIRs) are widely used for dual-band filter. Qing and Chen [10] found that SIRs is a new coupling scheme in the filter design technology. Wu et al. [11] and Chang et al. [12] studied some new methods of using defected SIR to improve the response in BPF. This paper reported a novel miniaturized dual-band bandpass filter which was designed using the asymmetric SIRs and DGS which sustain effort for GSM (1.8 GHz) and WiMAX (3.4 GHz). The major achievement of the proposed filter is that by controlling the resonators modes of the filter, it can tune the two desired passbands of the proposed filter. This can be achieved by interestingly selecting the electric length of the strip and impedance ratio of the asymmetric SIRs to satisfy required responses for GSM-1.8 GHz and WiMAX (3.4 GHz).

Design Methodology and Analysis of Result

The designed layout of the bandpass filter is presented in Fig. 1. The black circles in the proposed layout 1, 2, 3 and 4 represent four resonator modes of the filter. The reported filter having two asymmetric SIRs, which are used to obtain the desired passband resonance frequency, are GSM-1800 and WiMAX (3.4 GHz). The structure is compact in size and has good return loss and also insertion loss. The design specifications of the GSM-1.8 GHz and WiMAX passband filter at center frequencies 1.8 and 3.4 GHz are presented in Fig. 2.

The magnitude of S_{21} for GSM (1.8 GHz) and WiMAX (3.4 GHz) versus frequency response and also their phase difference of transmissions are shown in Fig. 3. The appearance of the three transmission zeros as shown in Fig. 3 which are denoted as f_{Z1} , f_{Z2} , and f_{Z3} in each of the passband edge evidence that the proposed filter increases the sharpness of the S-parameters and selectivity (Fig. 4). The group

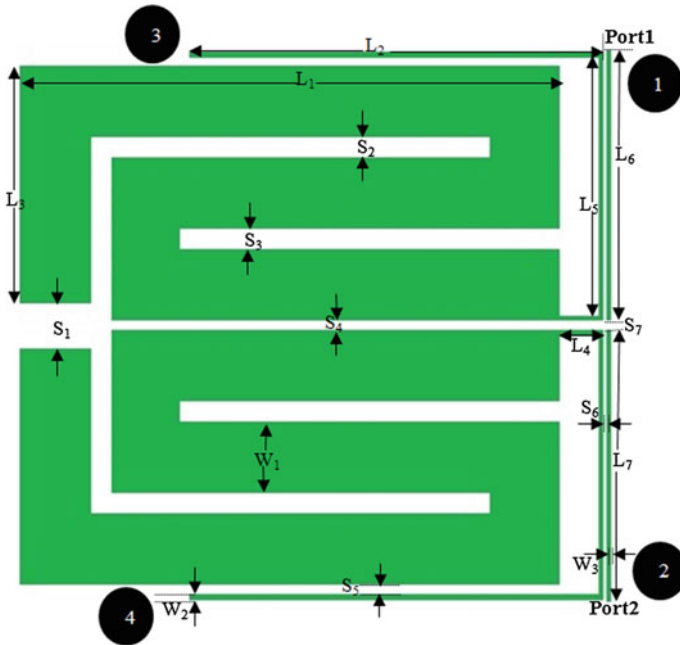
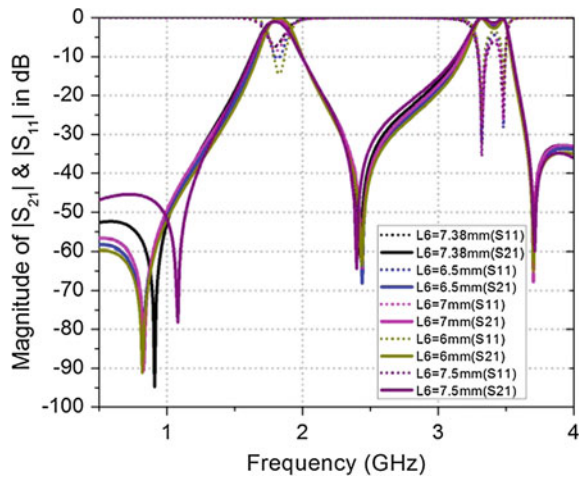


Fig. 1 Design layout of proposed filter

Fig. 2 S_{21} and S_{11} versus frequency plot for different S_7, L_6 and L_7 values



delay which is inversely proportional to bandwidth is obtained by deriving the phase as shown in Fig. 5 allocated within 2.5–2.3 ns at 1.8 GHz frequency and 2.3–5 ns at 3.4 GHz frequency is very low. In this design, the group delay for GSM-1.8 GHz and WiMAX are good and satisfactory.

Fig. 3 S_{21} versus frequency plot of the different L_6 and L_7 , and S_7 values

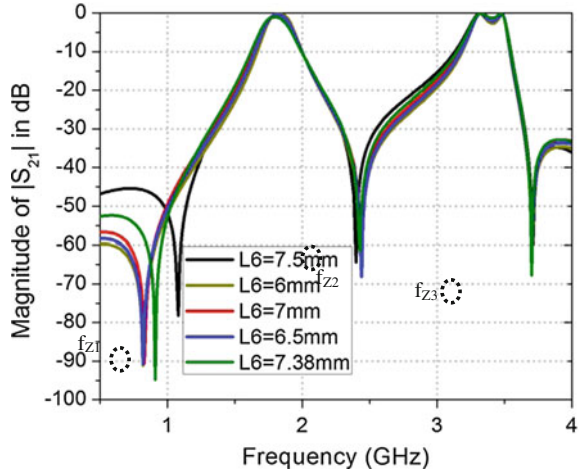
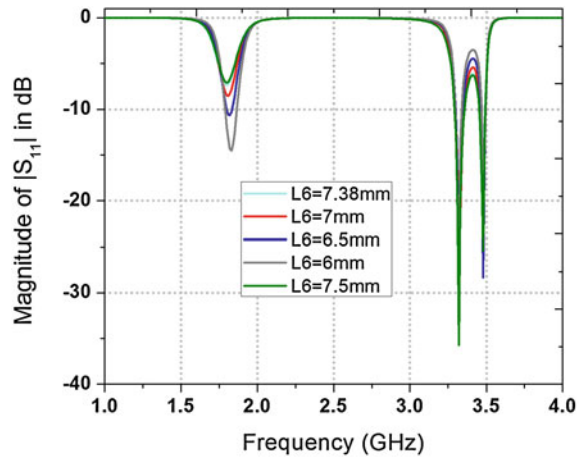


Fig. 4 S_{11} versus frequency plot different S_7 values



The fractional bandwidths (FBW) are calculated using Ansoft HFSS Simulator for different values of L_6 , L_7 , and S_7 . The FBW is 10 and 7.08 %, with a very low insertion loss, (S_{21}) -0.24 and -0.14 dB and return losses, -14.71 and -25.01 dB for the center frequencies, 1.8 and 3.4 GHz for the $L_6 = L_7 = 6$ mm and $S_7 = 3.08$ mm which are given in Table 1. The magnitude response of return loss (S_{11}) of GSM (1.8 GHz) and also WiMAX (3.4 GHz) responses and phase difference of transmission are depicted in Fig. 4. The returns losses are -14.71 and -25.01 dB with center frequency 1.8 and 3.4 GHz for $L_6 = L_7 = 6$ mm and $S_7 = 3.08$ mm are also shown in Table 1.

Fig. 5 Simulated group delay versus frequency plot for different S7 values

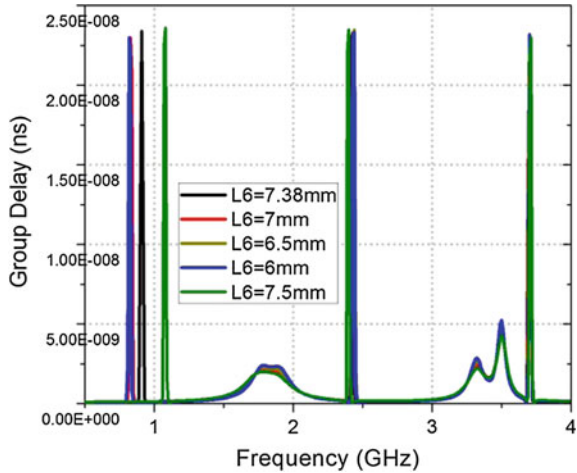


Table 1 Different S7 and L6 and L7 values and result

$L_6 = L_7$ (mm)	S_7 (mm)	Insertion loss $ S_{21} $ (dB)		Transmission loss $ S_{11} $ (dB)		FBW (%)	
		1.8 GHz	3.4 GHz	1.8 GHz	3.4 GHz	1.8 GHz	3.4 GHz
6.00	3.08	0.24	0.14	14.71	25.01	10	7.08
6.50	2.08	0.48	0.12	10.43	31.30	9.94	7.4
7.00	1.08	0.75	0.12	8.47	27.26	10	7.08
7.38	0.28	0.53	0.10	7.49	32.28	9.49	7.7
7.50	0.08	1.79	0.09	6.84	35.69	10	8.01

Dimension Calculation and Comparison of Result

The proposed filter was simulated using the Ansoft HFSS Simulator design on a Rogers RT/Duriod 5880 substrate with a thickness of 0787 mm, whose tangent loss (δ) is 0.0009 and the dielectric constant (ϵ_r) is 2.2. High impedance (96.2Ω) of the filter is obtained when strip width is 0.2 mm and low impedance is ($Z_2 = 45.17 \Omega$) with strip width 3.85 mm. The dimensions of the proposed filter are $L_1 = 15.05$ mm, $L_2 = 11.35$ mm, $L_3 = 6.5$ mm, $L_4 = 1$ mm, $L_5 = 7$ mm, $L_6 = 7.38$ mm, $L_7 = 7.38$ mm, $S_1 = 1.2$ mm, $S_2 = S_3 = 0.5$ mm, $S_4 = S_5 = 0.2$ mm, $S_6 = 0.02$ mm, $S_7 = 0.28$, $W_1 = 2$ mm, and $W_2 = W_3 = 0.2$ mm, with microstrip width of 0.2 mm. The complete size of the proposed filter is $19 \times 15.28 \text{ mm}^2$ which is very compact in size compared to other traditional design filters. It is found that the filter provides a very low insertion loss, even when the strip width is high (3.87 mm). The performance improvement comparisons with previous work are shown in Table 2.

Table 2 Comparison with other proposed dual-band BPF

Comparison of model	Filter Size (mm)	S ₂₁ (dB)	S ₁₁ (dB)	FBW (%)	Passband (GHz)	Application
Wu et al. [13]	30.14 × 21.16	1.1 1.1	30 20	6 4	1.575 2.4	GPSWLAN
Pankaj et al. [14]	30 × 10	0.5 0.3	25 27	1.8 3.4	2.46 3.51	WiMAX WiMAX
Ali et al. [15]	22.6 × 22.6	0.62 0.78	17.2 17.9	4.7 3.3	1.8 2.75	GSM WiMAX
Proposed design	19 × 15.28	0.24 0.14	14.71 25.01	10 7.08	1.8 3.40	GSM WiMAX

Conclusion

The size of the proposed filter is reduced greatly to about 50 % as compared to other dual-band BPF based on conventional SIRs methods. The proposed filter is very compact in size, with very low insertion loss -0.24 and 0.12 dB and return losses (S_{11}) 14.71 and -25.01 dB, and has a good passband selectivity. The fractional bandwidths obtained for GSM (1.8 GHz) and WiMAX (3.4 GHz) are 10 % and 7.08 %, respectively. The proposed miniaturized filter is suitable for any smart communication devices such as wireless communication, satellite communication, and radar communication systems.

Acknowledgements The authors like to acknowledge the IC design centre of Jadavpur University for giving software support to complete this research.

References

1. Tasher, A.S., Borah, J., Roy, S.: Bandwidth improvement in BPF using microstrip couple lines. *Int. Conf. Signal Speech Process. ICSSP-14*. Elsevier publisher, Kerala, India, 21–23rd Aug **2014**, 105–109 (2014)
2. Tasher, A.S., Borah, J., Roy, S.: Miniaturized Tri-band BPF using Asymmetric SIRs and DGS. *Int. J. Signal Process. Image Process. Pattern Recogn. (IJSIP)* **8**(2), 337–346 (2015)
3. Hong, J.S., Lancaster, M.J.: *Microstrip Filters For RF/Microwave Applications*, pp. 153–158. Wiley, New York (2001)
4. Chen, X.P., Wu, K., Li, Z.L.: Dual-band and triple-band substrate integrated waveguide filters with Chebyshev and quasi-elliptic responses. *IEEE Trans. Microw. Theory Tech.* **55**, 2569–2578 (2007)
5. Li, J., Huang, S.S., Zhao, J.Z.: Design of a compact and high selectivity tri-band bandpass filter using asymmetric stepped-impedance resonators (SIRs). *Prog. Electromagn. Res. Lett.* **44**, 81–86 (2014)
6. Chen, W.Y., Weng, M.H., Chang, S.J., Kuan, H., Su, Y.H.: A new tri-band bandpass filter for GSM, WiMAX and UWB response by using asymmetric SIRs and DGS. *Prog. Electromagn. Res.* **124**, 365–381 (2012)

7. Thanet, T.: Dual-band microstrip bandpass filter for GSM. *KKU Eng. J.* **34**(3), 355–360 (2007)
8. Zhang, Y.P., Sun, M.: Dual-band microstrip bandpass filter using SIRs with new coupling scheme. *IEEE Trans. Microw. Theory Tech.* **54**(10), 3779–3785 (2006)
9. Sagawa, M., Makimoto, M., Yamashita, S.: Geometrical structure and fundamental characteristics of microwave stepped impedance resonators. *IEEE Trans. Microw. Theory Tech.* **45**(7), 1078–1085 (1997)
10. Qing, X.C., Chen, F.C.: A compact dual-band bandpass filter using meandering stepped impedance resonators. *IEEE Microwave Wirel. Compon. Lett.* **18**(5), 320–322 (2008)
11. Wu, B., Liang, C.H., Qi, L., Pei, Y.: Novel dual-band filter incorporating defected SIR and microstrip SIR. *IEEE Microwave Wirel. Compon. Lett.* **18**(6), 392–394 (2008)
12. Chang, Y.C., Kao, C.H., Weng, M.H., Yang, R.Y.: Design of the compact dual-band bandpass filter with high isolation for GPS/WLAN applications. *IEEE Microwave Wirel. Compon. Lett.* **19**(12), 780–782 (2009)
13. Wu, B., Liang, C.H., Yuan, P., Li, Q.: Compact dual-band filter using defected stepped impedance resonators. *IEEE Microwave Wirel. Compon. Lett.* **18**(10), 674–676 (2008)
14. Pankaj, S., Ghatak, R., Poddar, D.R.: A dual-band bandpass filter using SIR suitable for WIMAX band. In: *International Conference on Information and Electronics IPCSIT 2011*, vol. 6, pp. 70–74. IACSIT Press, Singapore (2011)
15. Ali, K.G., Basmaci, A.N., Karpuz, C.: Design of a dual-mode dual-band band pass filter with a novel feed scheme. In: *ELECO 2011 7th International Conference on Electrical and Electronics Engineering*, pp. 176–179. Bursa Turkey (2011)

Performance Analysis of ZigBee Mesh Networks Under Nodes Failure

Jashan Preet Kaur, Rajdeep Kaur and Gurpreet Singh Mann

Abstract ZigBee is an IEEE 802.15.4 standard which is created by ZigBee alliance. ZigBee uses three topologies star, mesh, and tree. In this research, the performance of mesh is analyzed with the failure of ZigBee end devices, ZigBee coordinator, and ZigBee routers. The effect of node failure, router failure, and coordinator failure is analyzed by changing the channel sensing duration from 1 to 3 s. The result is compared in terms of data traffic received, load, and throughput. The simulation is carried out by using Opnet 14.5 modeler.

Keywords ZigBee · WSN · Topology · IEEE 802.15.4 · OPNET

Introduction

In sensor network, all the devices are distributed randomly in wide area. Wireless sensor networks (WSN) consists of light-weight, low-power and small size sensor nodes (SNs). They have ability to monitor, calculate and communicate wirelessly [1]. WSN can be described as a collection of nodes linked together to form a network to control the interaction between persons or embedded computers and the surrounding environment [2, 3]. In a WSN, information is transmitted by first

J.P. Kaur (✉) · Rajdeep Kaur
Department of C.S.E, B.F.C.E.T, Bathinda, India
e-mail: jashan.sidhu303@gmail.com

Rajdeep Kaur
e-mail: er.rajdeepvirk@gmail.com

Rajdeep Kaur · G.S. Mann
Department of Information Technology, B.F.C.E.T, Bathinda, India
e-mail: waytomann@gmail.com

collecting the data and then computing it and lastly communication of data is done in a wireless network [4]. ZigBee devices transmit data in the range of 10–75 m. Its defined data rates are 20 kbps at 868 MHz, 40 kbps at 915 MHz, and 250 kbps at 2.4 GHz [5].

The name ZigBee has been derived from the honeybee's dance to communicate information from one bee to another in a zig-zag pattern [6]. WSN are used in many fields such as landslide detection, water tower level monitoring, greenhouse monitoring, natural disaster prevention, and smart home monitoring [7].

Related Work

In 2013, Hussnain [8] evaluated WSNs applications in agriculture and compared different IEEE802.15.4/ZigBee topologies. Multiple network scenarios were simulated to study the performance of WSNs topologies in terms of throughput, network load, and end-to-end delay. So the results concluded that WSNs have better throughput and network usage when tree topology is used.

Implementation

In carrying out the performance of ZigBee mesh topology in the presence of node failure.

We have performed the following experiments.

Experiment no. 1: In this experiment, ZigBee mesh network is deployed with ZigBee end device (ZED) failure, ZigBee router (ZR) failure, and ZigBee coordinator (ZC) failure. The performance is analyzed with ACK and beacon ON and then ACK and beacon OFF by changing the channel sensing duration from 1 to 3 s. The performance is measured using various parameters such as data traffic received, load, and throughput.

Experiment no. 2: In this experiment, ZigBee mesh network is deployed with ZigBee end device failure, ZigBee router failure, and ZigBee coordinator failure. In this experiment, the numbers of ZigBee end device failures are increased from 1 to 50 and ZigBee router failures are also increased from 1 to 4 by creating different scenarios. The result for this experiment has been shown in Figs. 1, 2, 3, 4, 5, and 6.

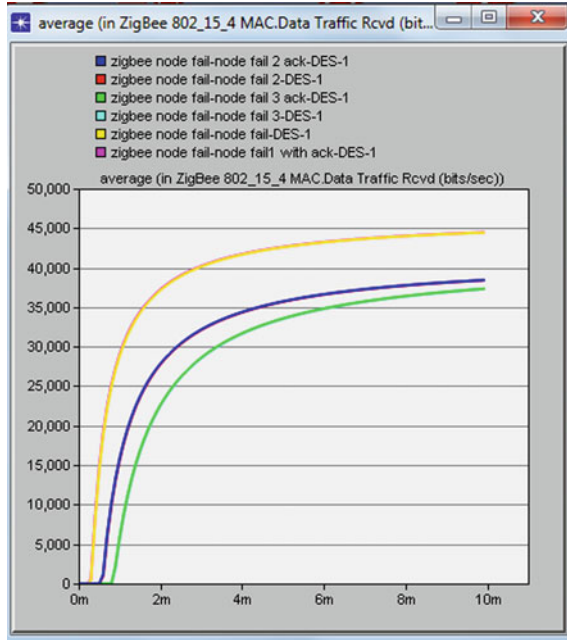


Fig. 1 Data traffic received for ZED fail

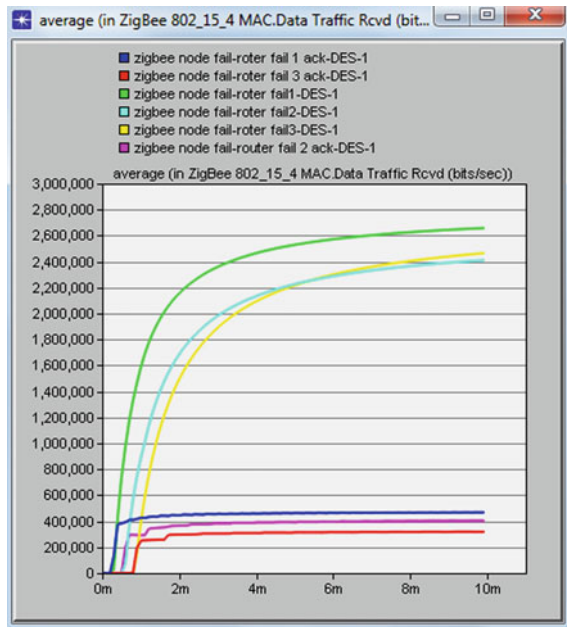


Fig. 2 Data traffic received for ZR fail

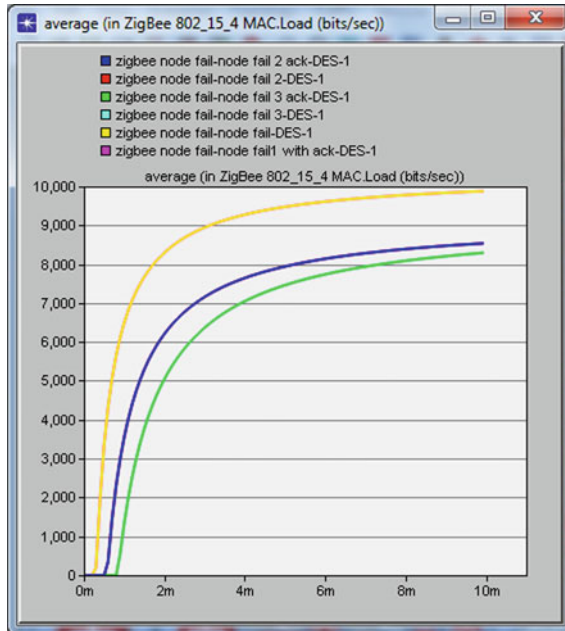


Fig. 3 Load for ZED fail

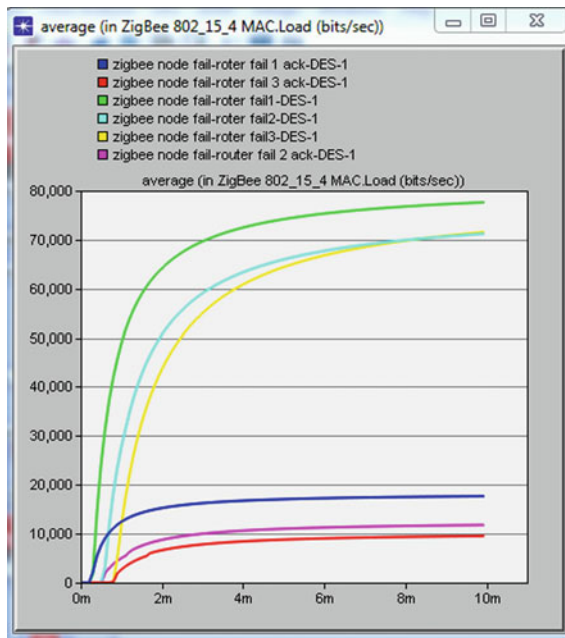


Fig. 4 Load for ZR fail

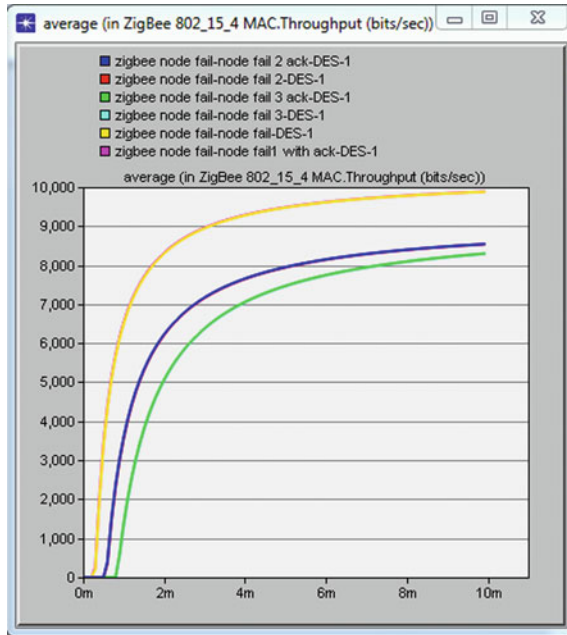


Fig. 5 Throughput for ZED fail

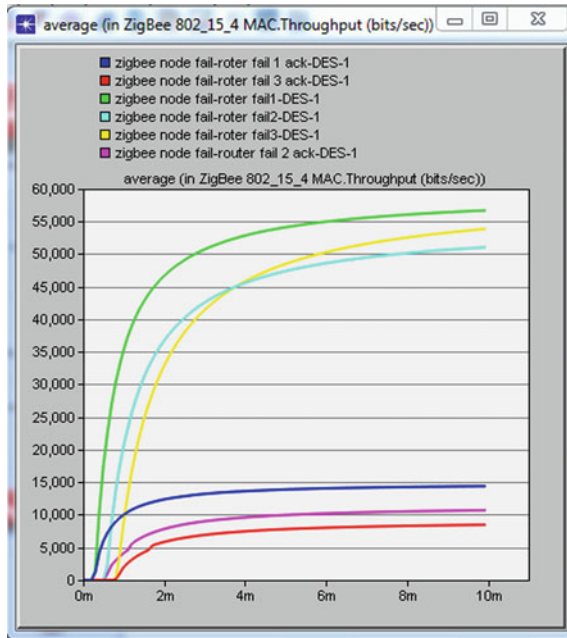


Fig. 6 Throughput for ZR failure

Results

(1) *Experiment No 1:*

- A. *Data traffic received*
- B. *Load*
- C. *Throughput*

(2) *Experiment No 2:*

- A. *Data traffic received for ZED failure:* In this ZEDs are failed by creating different scenarios, i.e., failing zero ZED, 1 ZED, 2 ZED, 3 ZED, 4 ZED, 5 ZED, 10 ZED, 15 ZED, 20 ZED, 25 ZED, 30 ZED, 35 ZED, 40 ZED, 45 ZED, 50 ZED. The result for this experiment has been shown in Figs. 7, 8, 9, 10, 11 and 12.

Fig. 7 Data traffic received for ZED fail

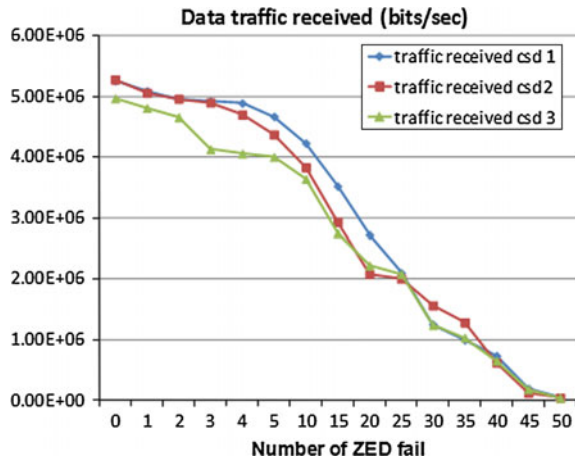


Fig. 8 Load for ZED fail

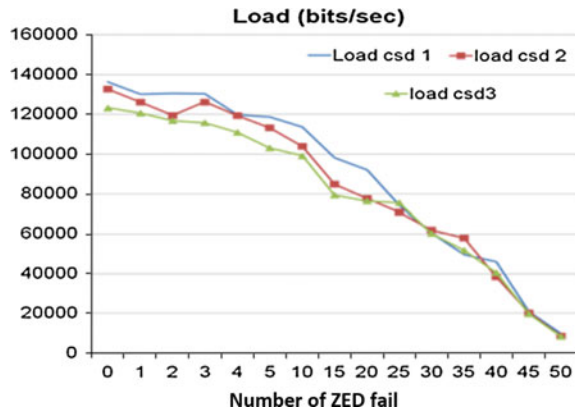


Fig. 9 Throughput for ZED fail

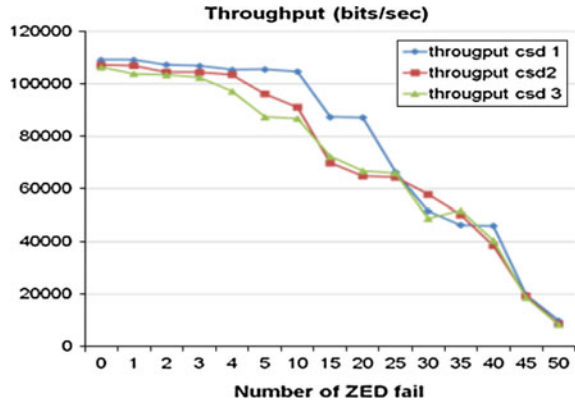


Fig. 10 Data traffic received for ZR failure



Fig. 11 Load for ZR failure

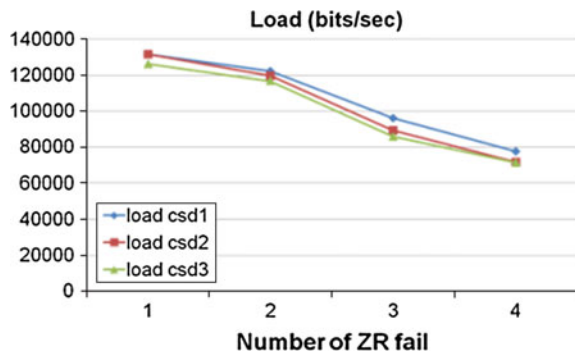
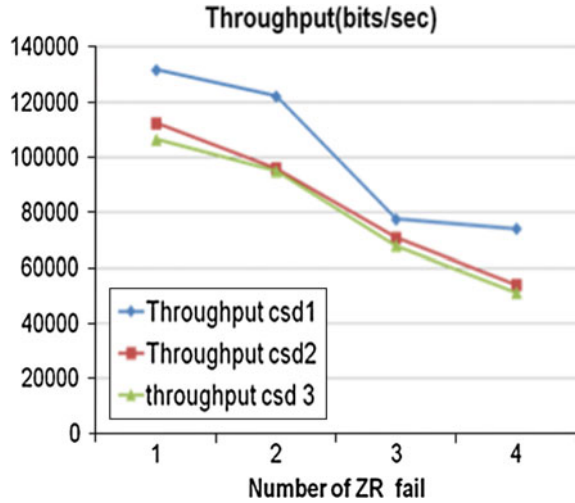


Fig. 12 Throughput for ZR failure



- B. Load for ZED failure
- C. Throughput for ZED failure
- D. Data traffic received for ZR failure
- E. Load for ZR failure
- F. Throughput for ZR failure.

Table 1 Comparative table of data traffic received in ZigBee end device failure

Scenarios (ZED fail)	Channel sensing duration 1 Traffic received	Channel sensing duration 2 Traffic received	Channel sensing duration 3 Traffic received
Zero	5,260,000	5,250,000	4,970,000
one	5,090,000	5,060,000	4,830,000
Two	4,960,000	4,960,000	4,660,000
Three	4,920,000	4,900,000	4,130,000
Four	4,890,000	4,700,000	4,060,000
Five	4,670,000	4,370,000	4,000,000
10	4,230,000	3,830,000	3,640,000
15	3,520,000	2,930,000	2,750,000
20	2,720,000	2,090,000	2,220,000
25	2,100,000	2,000,000	2,080,000
30	1,250,000	1,560,000	1,240,000
35	9,93,503	1.28 E + 06	1.03 E + 06
40	7,32,435	6,14,574	6,48,983
45	1,91,569	1,18,370	1,81,046
50	44,442.5	38,401.8df	37,302.7

Table 2 Comparative table of load in ZigBee end device failure

Scenarios (ZED fail)	Channel sensing duration 1 Load	Channel sensing duration 2 Load	Channel sensing duration 3 Load
Zero	1,36,241	1,32,725	1,23,282
1	1,30,235	1,26,203	1,20,558
2	1,30,514	1,19,953	1,16,746
3	1,30,270	1,26,227	1,15,784
4	1,19,688	1,19,266	1,10,795
5	1,18,744	1,13,250	1,02,973
10	1,13,553	1,03,963	99,105.2
15	98,150.8	84,768.3	79,245.1
20	91,947	77,581	76,366
25	74,130	70,853.2	75,498
30	60,401	61,960.7	60,195.1
35	49,587	57,881.2	51,817.4
40	45,982.5	38,493.2	40483.7
45	20,873.9	20311.4	19,731.8
50	9878.93	8536.64	8292.59

Table 3 Comparative table of throughput in ZigBee end device failure

Scenarios (ZED fail)	Channel sensing duration 1 Throughput	Channel sensing duration 2 Throughput	Channel sensing duration 3 Throughput
Zero	1,09,188	1,07,219	1,06,374
1	1,09,186	1,06,940	1,03,881
2	1,07,263	1,04,560.8	1,03,416.9
3	1,06,263	1,04,425	1,02,475
4	1,06,861	1,03,534	97,211.5
5	1,05,547	96,151.1	87,364.9
10	1,04,681	91,078	86,826.1
15	87,420.2	69,812	72,284.7
20	87,128.7	64,853	66,789.9
25	66,402.4	64,423.2	65,970.7
30	51,609.4	57,873.2	48,778
35	46,339.8	50,208	51,794.6
40	45,974.9	38,476	40,453.2
45	19,773.7	19,243.7	18,694.5
50	9878.93	8536.64	8292.59

Conclusion

ZigBee mesh network is deployed with ZigBee end device (ZED) failure, ZigBee router (ZR) failure, and ZigBee coordinator (ZC) failure. The comparative table of data traffic received, load, and throughput in ZigBee end device failure has been shown in Tables 1, 2, and 3. The performance is analyzed with ACK and beacon ON and then ACK and beacon OFF by varying the channel sensing duration. The performance is measured using various parameters like data traffic received, load, and throughput. The result specifies that data traffic received, load, and throughput decreases with increase in channel sensing duration. The result also specifies that when ACK and beacon is enabled the performance decreases. Simulation is carried out for 10 min using OPNET 14.5. The result shows that when number of ZED's and ZR's failure increases then data traffic received, load, and throughput decreases. The result also shows that data traffic received, load, and throughput is higher in case of channel sensing duration 1 and lower in case of channel sensing duration 3.

References

1. Mihajlov, B., Bogdanoski, M.: Overview and analysis of the performances of ZigBee based wireless sensor networks. *Int. J. Comput. Appl.* **29**(12), 28–35 (2011)
2. Huang, Y.-K. et al.: A comprehensive analysis of low power operation for beacon-enabled IEEE 802.15.4 wireless networks. *IEEE Trans Wireless Commun.* **8**(11), (2009)
3. Muthu Ramya, C. et al.: Study on ZigBee technology, IEEE 2011
4. Bharti, D., Behniwal, M., Sharma, A.K.: Performance analysis and mobility management in wireless sensor network. *Int. J. Adv. Res. Comput. Sci. Softw. Eng.* **3**(7), 1333–1342 (2013)
5. Aziz, A., Qureshi, M.A., Soorage, M.U., Kashif, M.N., Hafeez, M.A.: Evaluation of ZigBee based wireless sensor network with static sink and random sink mobility. *Int. J. Comput. Electric. Eng.* **4**(4), 562–566 (2012)
6. Singh, G., Bhardwaj, R., Singh, K., Mehla, S.: ZigBee: a review. *IJCST* **3**(1), 328–331 (2012)
7. Lohier, S. et al.: Multichannel access for bandwidth improvement in IEEE 802.15.4 wireless Sensor networks. *IFIP/IEEE Wireless Days 2011 (IEEE WD'2011)*
8. Hussnain, M., Sharjeel, M., Chaudhry, S.R., Hussain, S.A., Raza, I. Mirza, J.S.: Investigating multi-Topological ZigBee based wireless sensor network in precision agriculture. *J. Basic Appl. Sci. Res.* 195–201 (2013)

Probabilistic-Based Energy Efficient Dynamic Route Discovery in MANET's

Madan Mohan Agarwal, M.C. Govil and Anuj Kumar Jhankal

Abstract The routing is able to send request message from source to destination hop through intermediate hops. The intermediate hops forward the received messages to its neighbours. The replicated copies of the request message will received at each hop. Each hop transmits the copy of message to its neighbours. In receiving and transmitting the messages, it consumes much of energy of hop, which can be saved by using selective hop forwarding approach. This paper proposed a model name as dynamic probabilistic broadcast for route discovery (DPBRD), which tries to reduce the replicated copies of control messages to save energy. This method determines the forward probability by consider extended area and hop density to forwards request messages to its neighbours. The performance of the proposed protocol has been evaluated and compared with AODV (Flooding), THPRD and DPBSC protocols across different performance metrics—Average received duplicate messages, saved percentage of forward messages, and energy consumption. The results demonstrate that the proposed DPBRD protocol outperforms other. NS-2 environment was used to simulate and analyse the proposed protocol.

Keywords Forward probability · Energy efficient · Extended coverage area · Hops density · Coverage area

M.M. Agarwal (✉)

Department of Computer Engineering, BIT Mesra, Jaipur 302017, India
e-mail: mmagarwal@bitmesra.ac.in

M.C. Govil

Department of Computer Engineering, MNIT, Jaipur 302017, India
e-mail: gvilmc@gmail.com

A.K. Jhankal

Department of Mathematics, BIT Mesra, Jaipur 302017, India
e-mail: anujkumarjhankal@yahoo.com

© Springer India 2016

N. Afzalpulkar et al. (eds.), *Proceedings of the International Conference on Recent Cognizance in Wireless Communication & Image Processing*, DOI 10.1007/978-81-322-2638-3_67

Introduction

Mobile ad hoc network (MANET) has established its credibility due to hassle free deployment and wide spread applications in the field of networking. However, dynamic topology, communication channel characteristics and limited battery life of hops makes the design of these networks difficult and present a number of challenges to research community. The energy consumption is a predominant phenomenon in MANET due to the factors mentioned above. It can be attributed to hop energy consumption due to as repetitive overheads, high message loss, frequent path breakdown, more transmission range, congestion and collisions of messages. The existing limitations of these networks motivate research community to hunt for energy efficient routing protocol.

Jae-soo [1] state that the routing mechanism, route maintenance and routing are effectively manages by flooding. Some reactive routing protocols like AODV, AOMDV, DSR and OLSR using broadcast mechanism to discover the routes according to Perkins and Bhagwat [2], Johnson et al. [3], Perkins et al. [4] in ad hoc networks. These protocols are using on naive form of flooding. Each hop forwards the every received message just once and received these messages by all adjacent hops that are in the communication range.

The fixed forwarding probability is reduces the repetition of control messages in static environment but in case of mobile environment such static mechanism is less efficient. Authors Agarwal et al. [5] had designed a THPRD model addition in simple forwarding approach that enhances the properties of flooding forwarding to reduce repetition of messages. Each hop determine the forwarding probability of hop, based on own parameters of hop such as remaining battery power, expanse to sender hop, communication range number of adjacent hops, etc.

The routing process cause spread of control messages (overheads) in the network and resulting in drains of energy at the hop. Node receiving the request first has the responsibility to forward it. Lipman et al. [6] analysed that dynamic probabilistic-based flooding has some other associated drawbacks such as repetitive forwarding, contention and collision but optimize the routing by achieve the goal of energy conservation.

DPBSC is designed by Wang et al. [7]. It determines the forwarding probability of each hop to cover the extended area by flooding the request message. The determined forward probability of hop is high, if the extended coverage area (i.e. total coverage area of hop minus covered area of previous hop). The DPBSC consider only extended coverage area to determine the forward probability but did not consider the presence of hops in extended coverage area (i.e. hop density). Consider, a scenario, where the extended coverage area is large but hops density is very less or no hop exists; the DPBSC will determine the higher forward probability hence hop transmits more replicated copies of messages which promotes wastage of hop energy. This type of situations are occurred in networks when transmitted hops located nearby boundaries and sparse to each others.

The aim of this research is to develop more energy efficient routing protocol for MANETs. This can be achieved by controlling the replicated messages through dynamically adjusted forward probability. Designed routing protocol determines forward probability dynamically to discover the route based on extended coverage area and number of hop in coverage area is named as DPBRD protocol. Further sections will discuss the design of model, how to determine the forwarding probability, simulation and performance analysis of the proposed protocol.

Design and Implementation

DPBRD Architecture

A source hop sends a request message to find the routes from source hop to target hop. Intermediate hops forward request messages to its adjacent hops till the request messages reach their target hop. The better results can be obtained by designing a protocol depending on the different layers of the protocol as given in Fig. 1. The designed protocol determines the forward probability to forward the messages, which will combine the power strength of the incoming signal of the upper layer. The extended coverage area depends on the distance of the physical layer and the available number of hops in the extended coverage area of the network layer.

Forward Probability Determination

Based on Optimal Distance

Figure 2 shows a scenario in which hop-A broadcasts a request message to its adjacent hops which come in its coverage area. Hop-B receives the request message

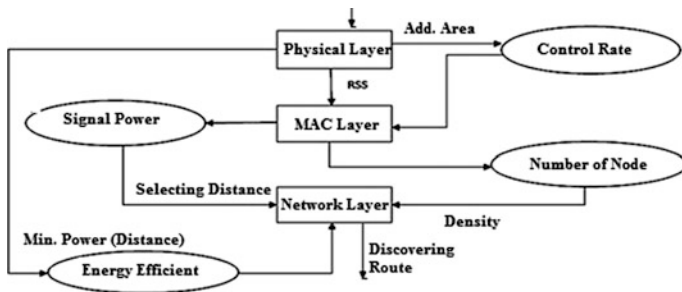


Fig. 1 DPBRD structural design

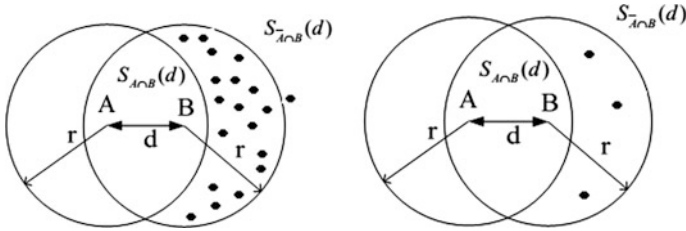


Fig. 2 Extended area with and without hops

and decides to forward the message. When Hop-B rebroadcast the request message to its adjacent hops comes in its transmission range. Hop comes in common range of both the hops are receives repetitive request messages. The other hops are adjacent to hop-B are also receives the request message first time in the extended area. The forwarding probability is of hop-B depending on the extended area in which hops are shown in dotted form in the figure.

The extended area is depends on distance between hop-A and Hop-B as states by Ni et al. [8]. If distance between hops is equal to zero then the extended coverage area is zero. If distance between hops is equal to transmission range then the extended coverage area to be largest approximate equal 61 % of the total coverage area of hop-B. This shows that hops exist in 61 % area, are ready to receive the request message broadcasted by hop-B. If distance between hops is less then transmission range than the extended coverage area is 41 % area in average. Determination of forwarding probability shows that hop with the larger extended coverage are forward the request message with high probability which reduce the contention and collision which helps to optimize the energy consumption.

Based on Hops Density

The forwarding probability is determined on the basis of the number of hops in the extended coverage area. If hops are not available in the extended coverage area then forwarding probability set to zero as shown in Fig. 2 because there are hops are not available. Hops density (db) can compute by using three components: transmission range, distance between hops, and total number of hops in the extended area. Adjacent hops are identified directly by broadcast a simple hello process. The hello process broadcast a ping message on definite time interval. It returns the number hops exist in the communication range. This process calls by both like hop-A and Hop-B. The number of neighbours hop N_t of current hop-B and number of hop N_o in the overlap area are identified by receiving the message transmitted by previous hop-A. The $(N_t - N_o)$ divided by the extended broadcast area is called density of

hop (db) in extended area. The probability due to non uniform distribution of hops can compute by given equation.

$$P_{\text{density}} = \begin{cases} N_t - N_o / S\bar{A} \cap B(d), & \text{for } 0 < d \leq r \\ 0, & \text{for } d = 0 \end{cases}$$

Resultant Forward Probability

Now protocol is calculating the resultant forward probability P_{trans} by comparing both the probabilities P_{distance} and P_{density} by method given below:

```

Ptrans = MinProb (Pdistance, Pdensity)
{
  If (Pdistance <= Pdensity) then
    Ptrans = Pdistance;
  else
    Ptrans = Pdensity;
}
    
```

The DPBRD dynamically receives the forwarding probability P_{trans} at each hop according to its extended area and hops density. Mobile agent set determined forward probability for current hop for forwards the request messages.

Algorithm to Provide Dynamic Forward Probability for DPBRD Protocol Model

The procedure DynamicForward() of DPBRD model is shown in Fig. 3, gives the whole procedure to implement the model to discover the route, request message initiated by source hop and repeats this till control message reached on the destination hop.

Simulation Results and Analysis

The simulation model in this study consists of a network area of 1000 m × 1000 m in which hops are free to move at defined speed. The mobility model used in proposed model discovered by Christian et al. [9] is random way point mobility model. The energy consumed/losses in transmission, receiving and idle mode is modelled according to bansal energy overhead model given by GowriShankar et al. [10].


```

Procedure DynamicForward (Message p, BroadcastRange r)
{
  If message receives first time then{
    Determine distance from the current hope to sender hope;
    If distance is greater than the transmission rage then
      Drop the message;
    else {
      Get forward probability  $P_{\text{distance}}$ ;
      If distance is equal to zero then
        Drop the message;
      Get forward probability  $P_{\text{density}}$ ;
      Find  $P_{\text{tarns}} = \text{MinProb}(P_{\text{distance}}, P_{\text{density}})$ ;
       $P_r = \text{Random Probability generated by Toss at current hope}$ 
      If  $P_r \leq P_{\text{tarns}}$  then
        Forwards the message p to neighbours in up direction
      else
        Drop the message;
    }
  }
  else
    Drop the message;
}
} //end of process

```

Fig. 3 DPBRD algorithm

Network Simulator (NS-2) manual by Fall and Varadhan [11] is used to implement AODV, THPRD, DPBRD and DPBSC protocols. The NS-2 makes use of above parameters for simulation and comparison of different protocols with proposed DPBRD protocol under different scenarios. A scenario of hops in area of $1000 \text{ m} \times 1000 \text{ m}$ is shown in Fig. 4, moving randomly with maximum speed 5 m/sec and 10 connections. The number of hops varying from 20 to 200. In this scenario, the source hop and destination hop may be nearby or may be far and may sparse.

The source hop broadcasts only single message to discover the route. According to algorithm the first time received messages are forward by received hop to its neighbour if forward probability is less than the random generated probability by toss. Average forward messages for given transmission range ($r = 100 \text{ m}$) is much more in numbers in case of flooding ($p = 1$) in comparison to other protocols as shown in Fig. 5. Implementation of THPRD by authors in paper Agarwal et al. [5] reduced the average received message by more than 50 % at each hop in comparison to flooding protocol. The threshold forward probability determined once when number of hop changes in network system. About 10 % reduction in average received message by implementing DPBSC protocol. and further reduction about 5 % average received messages when hops are 140 to 200 and about 10 %

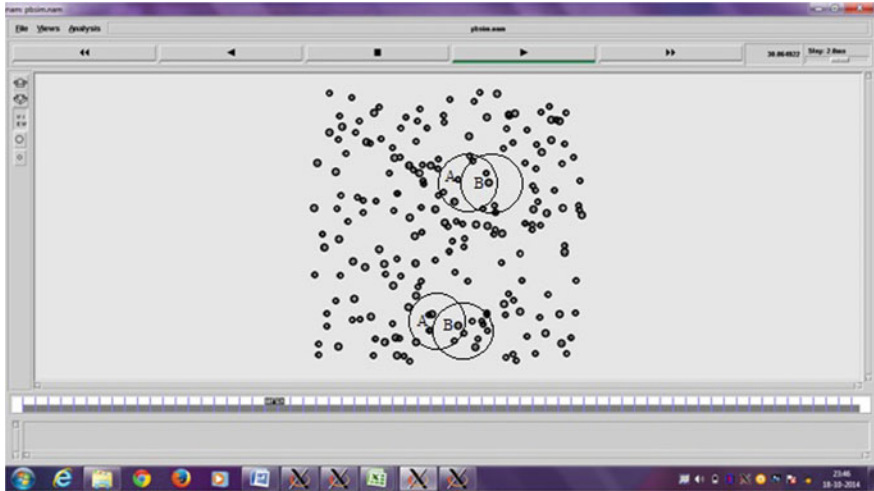
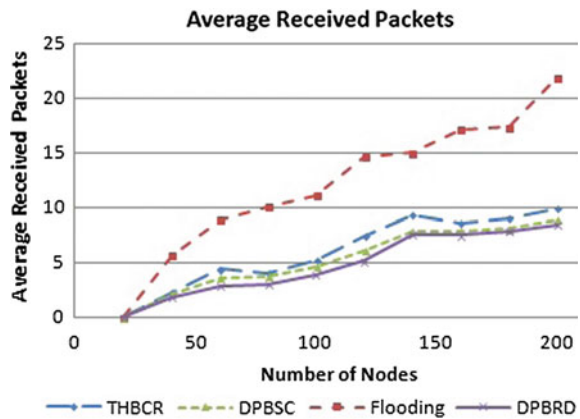


Fig. 4 Hops in 1000 m × 1000 m area with 200 hops

Fig. 5 Average received messages at each hop



when hops are less than 140 by proposed protocol DPBRD in comparison to previous.

Saved-Forward messages percentage in case of flooding is very less due to each hop transmitting the message at least once. In case of others protocols less number of hops forward the messages to cover the hops in the networks as shown in Fig. 6.

Figure 7 shows the comparison of energy consumption in the network. We can see that the energy consumption increases with increasing number of hops. The energy consumption is less for proposed DPBRD in comparisons to DPBSC and other protocols. The Flooding method consumes more energy in comparison to THPRD method. DPBRD protocol saves about 50 % energy than flooding.

Fig. 6 Saved forward messages (%)

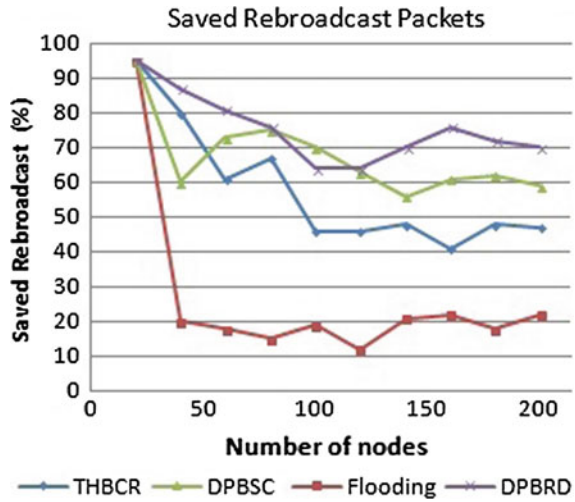
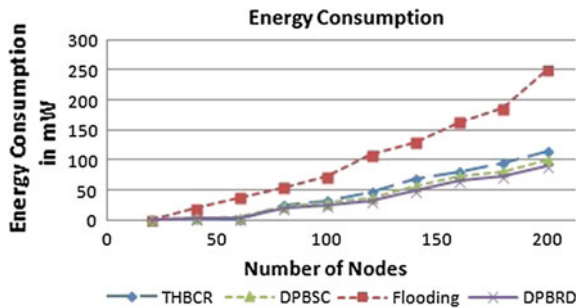


Fig. 7 Energy consumption by system



Conclusions

Proposed DPBRD routing protocol reduces overhead and repetitive request messages without compromising the attainability in the network within the specified time limit. The present analysis verifies that energy consumption for proposed routing protocol is less in comparison to other standard routing methods like AOMDV and AODV. After including hops density to determine the forward probability, it gives better result than the DPBSC routing protocol. DPBSC routing protocol determines the forward probability which is based on extended coverage area of sender hop. On the other hand, DPBRD routing protocol determines forward probability by considering both the parameters: hops density and extended coverage area. It also ensures that, improved technique will overcome the replicated request messages problem at some extent in boundaries and sparse hops in the network and makes better energy efficient routing protocol.

References

1. Jae-soo, K.: Probabilistic broadcasting based on coverage area and neighbour confirmation in mobile ad hoc networks. In: Global Telecommunications Conference Workshops, 2004, GlobeCom Workshops 2004, pp. 96–101. IEEE (2004)
2. Perkins, C., Bhagwat, P.: Highly Dynamic Destination-Sequenced Distance-Vector Routing (DSDV) for Mobile Computers, vol. 24, Issue-4, pp. 234–244. ACM, UK (1994)
3. Johnson, D.B., Maltz, D.A., Hu, Y.C.: The dynamic source routing protocol for mobile Ad Hoc networks (DSR). In: Internet Draft, IETF Mobile Ad hoc Networks (MANET) Working Group, pp. 1–108 (2003)
4. Perkins, C.E., Belding-Royer, E.M., Das, S.R.: Adhoc On-Demand Distance Vector (AODV) Routing, pp. 125–150. IETF, Internet Draft (2003)
5. Agarwal, M.M., Govil, M.C., Jhankal, A.K.: A Probabilistic method to optimize energy consumption in mobile Ad-hoc networks. In: Proceedings of the ICRAIE-2014, India, IEEE Xplore, pp. 1–5, May 2014
6. Lipman, J., Liu, H., Stojmenovic, I.: Broadcast in Ad Hoc Networks, pp. 121–150. Springer-Verlag London Limited (2009). doi:[10.1007/978-1-84800-328-6_6](https://doi.org/10.1007/978-1-84800-328-6_6)
7. Wang, Q., Shi, H., Qi, Q.: A dynamic probabilistic broadcasting scheme based on cross-layer design for MANET. IJMECS, pp. 40–47 (2010)
8. Ni, S., Tseng, Y., Chen, Y., Sheu, J.: The broadcast storm problem in a mobile ad-hoc network. In: Proceedings of the ACM/IEEE International Conference on Mobile Computing and Networking, Seattle, pp. 151–162. Washington, United States (1999)
9. Christian, B., Giovanni, R., Paolo, S.: The hop distribution of the random waypoint mobility model for wireless ad hoc networks. IEEE Trans. Mob. Comput. **2**(3), pp. 257–269, July 2003
10. Gowrishankar, S., Basavaraju, T.G., Sarkar, S.K.: Simulation based overhead analysis of AOMDV, TORA and OLSR in MANET using various energy models. In: Proceedings of the World Congress on Engineering and Computer Science, WCECS 2010, vol. I, pp. 1–15. San Francisco, USA (2010)
11. Fall, K., Varadhan, K.: The ns Manual (formerly ns Notes and Documentation), The VINT Project, UC Berkeley, LBL, USC/ISI, and Xerox PARC, 11 Feb 2007

A Survey Paper on Computational Intelligence Approaches

S. Taruna and Nidhi Bhartiya

Abstract Wireless sensor networks (WSN) is the collection of thousands sensor nodes. WSN faces many problems related to communication failures, data storage, and limited power supply. This paper includes the existing paradigms, such as fuzzy logic, neural network, evolutionary computing with some hybrid paradigms of computational intelligence, including some major challenges which help to reduce the gap between researchers and developers of WSN.

Keywords Fuzzy logic · Wireless sensor network · Neural network · Evolutionary computing · ACO

Introduction

A wireless sensor network is a collection of numbers of nodes which are measured according to various environment parameters such as light, heat, temperature. Sensor nodes are generally shown in a clustered form and each cluster act as a cluster head. Then all the nodes send their information to the cluster head and it would come back through a special node which is known as sink node. In WSN several technical issues like routing and controlling of network, network discover, information processing, querying and many more are faced. In addition to paradigms like neural network, evolutionary algorithm, and fuzzy approach, CI involves various techniques such as swarm intelligence, ACO and hybrids of two or more of the above for better results.

S. Taruna
Department of Computer Science, Banasthali University, Jaipur, India
e-mail: staruna71@yahoo.com

Nidhi Bhartiya (✉)
Department of Information Technology, Banasthali University, Jaipur, India
e-mail: nidhibhartiya.smile@gmail.com

Major Challenges

There are many challenges which are addressed by computational techniques in WSN are defined below [1].

(a) *Design and Deployment*

Sensor nodes have to be placed at their proper positions in some applications for designing a sensor network. Placing sensor nodes at their accurate locations is also very important to determining its functioning conditions.

(b) *Data Aggregation and Sensor Fusion*

Sensor fusion is a collection of data from various places such that either the data which are retrieved from multiple sources is provides better information than other sources, or load of sensor node related to base station is minimized. After deploy sensors nodes, data is originated in a huge volume, so collecting data in an efficient manner is a critical issue.

(c) *Energy Aware Routing*

Energy consumption is very serious issue in WSN because frequently replacing batteries is not an easy task it may be very dangerous and definitely it will increased the cost. Routing is used for determining route through which we can send our data to its desired destination.

Paradigm of CI

CI is defined as the computational tool of intelligence through which we would input the sensory data directly and after processing generate timely responses. CI encompasses paradigms, such as NN, swarm intelligence, evolutionary computation. These paradigms are defined below:

Neural Networks

Human brain is an excellent ability to discover and find out any new thing very easily and in a faster manner. Human brain is a collection of neurons and every neuron connected with more than 10,000 other neurons structure of neural networks shown in Fig. 1. The three basic components are:

- (1) W_{ji} weight is provided by a link, to the n inputs of j th neuron x_i , $i = 1, \dots, n$;
- (2) Sum of the weighted inputs for computing the input to the activation function $u_j = \Theta_j + \sum_{i=1}^n x_i W_{ji}$, is shown by aggregate function where Θ_j is the bias.
- (3) An activation function Ψ is used like $u_j - v_j = \Psi(u_j)$, which represent the output of neuron.

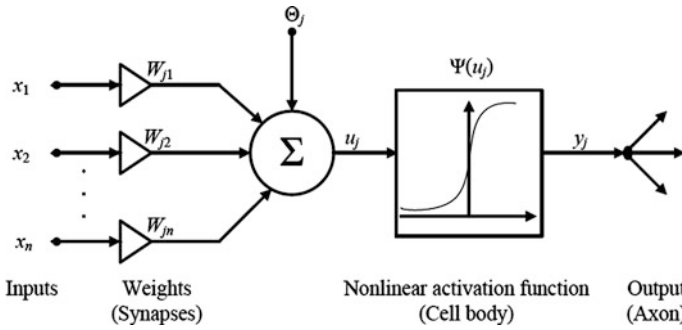


Fig. 1 Structure of neural network

Fuzzy Logic

Fuzzy approach is deal with human reasoning, which deals with uncertainty [2]. Fuzzy approach is a type of logic that recognizes more than simple true, partial true and false values. In Fig. 2, fuzzy model is defined. In this input will be taken from fuzzy inputs and sets, then after completing the process output will be generated with the help of defuzzification. Fuzzy approach is work on if-then rules.

Evolutionary Computing

Evolutionary computing is the process of adaptation with the target of enhancing survival capabilities by various processes like mutation, fitness and crossover. Evolutionary computing use a candidate’s option which called chromosomes. Chromosome is a combination of number of genes, at each level fitness calculated and remaining process will be done according to that fitness. This procedure is

Fig. 2 Fuzzy inference engine

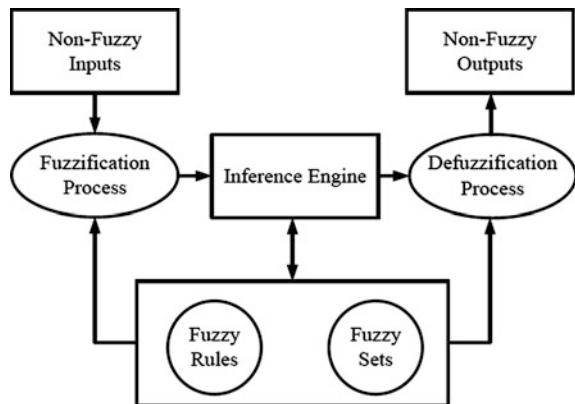
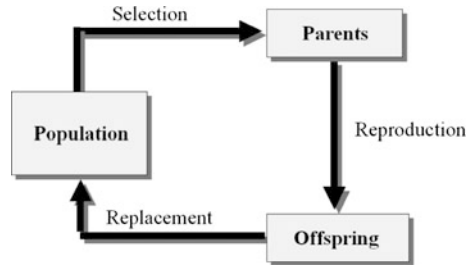


Fig. 3 Flowchart of an evolutionary algorithm



repeated until we get fit-enough solution. The flowchart of evolutionary algorithm is shown in Fig. 3.

Swarm Intelligence

Swarm Intelligence (SI) is one of the most important paradigms of computational intelligence. By studying the nature of biological species such as colonies of ants Swarm Intelligence (SI) generated.

(1) Particle Swarm Optimization

PSO is a collection of population of s particles. The particles discover an n -dimensional space in search of the global solution. Each particle i occupy two parameters, position x_{id} and velocity v_{id} . Position and velocity of particles are initially assigned within particular limit, i.e.

$$x_{\min} \leq x_{id} \leq x_{\max} \text{ and } v_{\min} \leq v_{id} \leq v_{\max}$$

Fitness is calculated with the help of particle position. Fitness value is increased when particle come close to solution. Updating the position and velocity at each level is also necessary to reach best fitness. Updating parameters and its values, this loop will continue until we reach our desired and best solution.

Ant Colony Optimization

ACO is composed of algorithms for optimization and is inspired on observations of how some ant species forage for food. Therefore, the ACO metaheuristic concerns about developing algorithmic models of the foraging behavior of real ants. Besides of the complex behavior for foraging, other collective behaviors of real ants that have been proposed and applied include the division of labor, cemetery organization, and construction of nests [3]. The ACO involves two basic procedures:

- (a) Procedure for building a solution, in which N_a (number of ants) ants build in parallel way N_a solutions to the problem.
- (b) Procedure for updating the pheromone concentration.
- (c) Cuckoo Search

Cuckoo Search is a new metaheuristic optimization algorithm that is inspired from the behavior of some cuckoo species. The cuckoo lays an egg in a host's nest with risk of surviving. If the egg is discovered by the host, it can either destroy the nest or reconstruct a new one [4, 5].

Algorithm 3: Cuckoo Search steps:

```

1 begin Cuckoo Search
2 Objective function  $f(x)$ ;  $x = (x_1; x_2; \dots; x_d)^T$ 
3 Originate initial population of  $n$  host nests  $x_i (i = 1; 2; \dots; n)$ 
4 either ( $t < \text{Max Generation}$ ) or (stop process)
5 Get a cuckoo randomly by random walk,  $x(t + 1) = x(t) + sE_t$ 
6 Calculate its Fitness  $F_i$ .
7 Select a nest among  $n$  randomly
8 If ( $F_i > F_j$ ), exchange  $j$  by any other solution
9 A fraction ( $P_a$ ) of the worse nests are blocked and new ones are construct
10 Rank the nests and find the current best and pass it to next generation
11 end

```

Hybrid Paradigms

Hybrid Model of PSO and DE

The most important factor in WSNs is to minimize the energy use of the sensors and the coverage problem. So in this paper, a new hybrid model using the PSO and DE algorithms is shown in Fig. 4 for distribution of the sensors for area coverage is proposed [6].

ACO Algorithm for Adjusting the Rule Base of the Fuzzy Inference System

In this approach, an ant colony optimization algorithm has been used for adjusting the rule base of the FIS. This way, the tour of an artificial ant is regarded as a combination of primary terms to the output linguistic variable from every rule of the rule base [7]. During its tour, the ant has to choose one primary term for each rule from a total of N_{pt} options. As the rule base relates the mapping of input values to the output value, an optimal adjustment of the rule base enhances the results produced by the FIS. For our purpose, the result produced by the fuzzy inference system is the quality degree of the routes acc to Fig. 5.

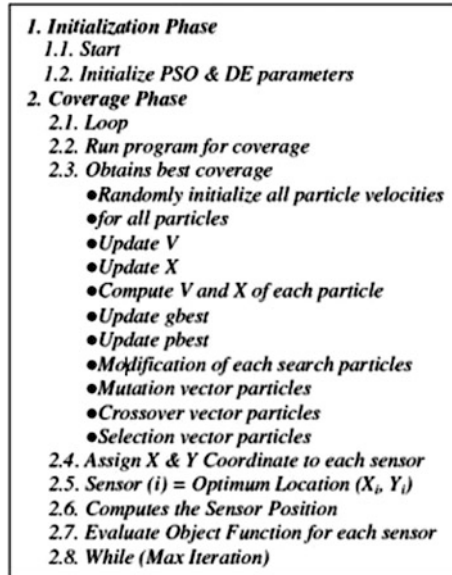


Fig. 4 Pseudocode of hybrid combination

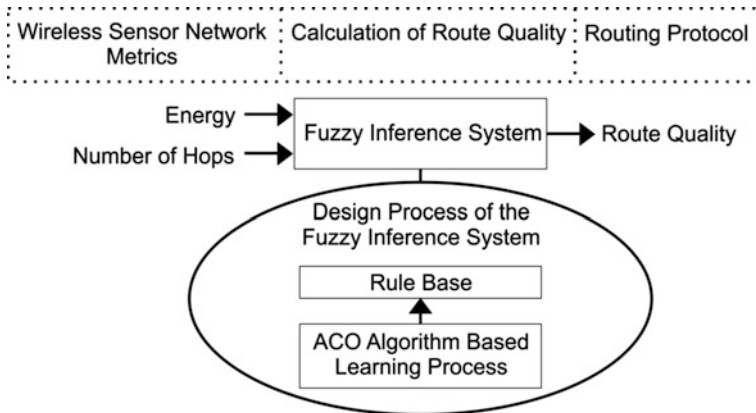


Fig. 5 Design process of FIS

The main aspects involved with the optimization of the fuzzy rule base are:

- Initialization of the parameters: In this, number of ants, the evaporation rate parameters, control the relative importance of pheromone information versus heuristic information.
- Selection of the primary term for each rule: the ants execute a probabilistic decision-making concerning what node should be visited. The decision-making process is based on the pheromone information and heuristic function.

The primary term represented through the selected node by the ant is inserted in the linguistic value of the associated rule.

- Evaluation of the built solutions: For this, the rule base obtained is inserted in the fuzzy inference system and a simulation of the WSN is realized. The lifetime of the WSN is used as the value for measuring the quality of the FIS because this value represents the energy level of the sensor nodes.
- Updating of the pheromone concentration: in the last stage, the ants deposit their own pheromone and it is proportional to the lifetime of WSN. Therefore, the highest value of pheromone deposited is obtained by the FIS that classified better routes and this way extends the lifetime of the WSN.

FAPSO (Fuzzy Adaptive Particle Swarm Optimization)

This optimization is a combination of original PSO and Fuzzy Approach [8].

In this framework as shown in Fig. 6 when fitness value is finding at the end then high leaning factors are preferred and when fitness value is stable at one point then the number of generations is not change and value of fitness is high.

Defuzzification method is used for get a final result a shown in Fig. 7.

Fig. 6 FAPSO framework

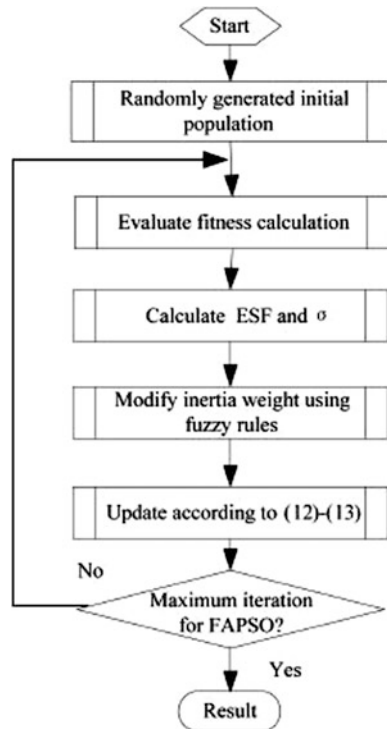
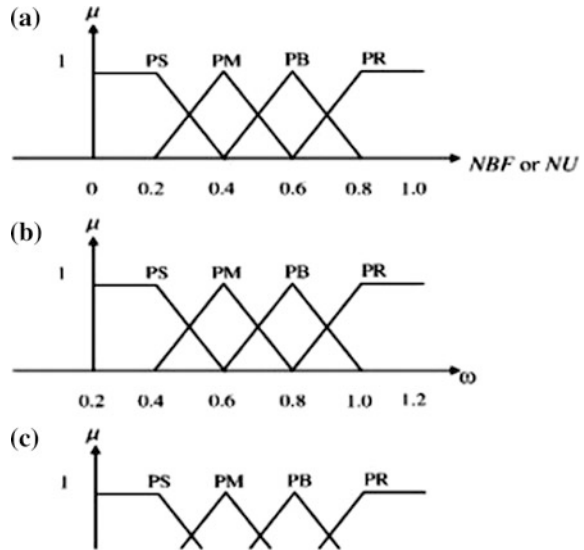


Fig. 7 Membership function of **a** NBF **b** ϕ **c** c_1 and c_2



Conclusion

In this paper, the computational intelligence paradigms had been discussed. In this paper, major challenges such as design, energy consumption are also define. Recently used CI methods to reduce the issues of WSN are also presented here. In this, hybrid combinations of different computational paradigms are also discussed. All the defined existing and hybrid paradigms are used to reduce the gap between researchers and developers and increased the lifetime of network and reduce the energy consumption.

References

1. Kulkarni, R.V., Forster, A., Venayagamoorthy, G.K.: Computational intelligence in wireless sensor networks: a survey. *IEEE Commun. Surv. Tut.* **13**(1) (2011)
2. Zadeh, L.: Fuzzy Sets. *Inf. Control* **8**(3) (1965)
3. Dorigo, M., Stutzle, T.: The ant colony optimization metaheuristic: algorithms, applications, and advances. In: *Handbook of Metaheuristics* (2003)
4. Kamat, S., Karegowda, A.G.: A brief survey on cuckoo search applications. *Int. J. Innovative Res. Comput. Commun. Eng.* **2**(2) (2014)
5. Solaiman, B., Sheta, A.: Computational intelligence for wireless sensor networks: applications and clustering algorithms. *IJCA* **73**(15) (2013)
6. Maleki, I., Khaze, S., Tabrizi, M.M., Bagherinia, A.: A new approach for area coverage problem in wireless sensor networks with hybrid particle swarm optimization and differential evolution algorithms. In: *International Journal of Mobile Network Communications & Telematics (IJMNCT)*, vol. 3 (2013)

7. Sobral, J.V.V., Sousa, A.S., Araujo, H.S., Baluzy, R.A., Lemosz, M.V.S.: A fuzzy inference system for increasing of survivability and efficiency in wireless sensor networks. In: The Twelfth International Conference on Networks(ICN) (2013)
8. Niknam, T., Amiri, B.: An efficient hybrid approach based on PSO, ACO and k-means for cluster analysis. Elsevier (2009)
9. Dorigo, M., Bonabeau, E., Theraulaz, G.: Ant algorithms and stigmergy. *Future Gener. Comput. Syst.* **16**(8) (2000)

Simulation of p-GaN/i-In_αGa_(1-α)N/n-GaN Solar Cell for Maximum Efficiency

Manoj Thosar, R.K. Khanna and Ashwini Joshi Thosar

Abstract The external efficiency of nonpolar p-GaN/i-In_αGa_(1-α)N/n-GaN solar cells was simulated using limited constituent approach. Reduction of the poor effect of conduction band peak is done which is seen at the n-GaN/i-In_αGa_(1-α)N interface. This particular effect is trimmed down by sinking the peak thickness. The optimization is done of p-doping in i-In_αGa_(1-α)N layer on different indium composition (α) which reduces the thickness of conduction band peak and assists the carriers to flow through the peak. Our optimizations are presented here which predict 53.53 % efficiency for p-GaN/i-In_{0.37}Ga_(1-0.37)N/n-GaN device at $1 \times 10^{16} \text{ cm}^{-3}$ p-doping and 480 nm thickness of i-In_αGa_(1-α)N layer using realistic material parameters.

Keywords Nonpolar In_αGa_(1-α)N material · Pin structured solar cell · Conduction band peak

Introduction

Al_αGa_(1-α)N and In_αGa_(1-α)N are the two ternary alloys of III nitride material system. Al_αGa_(1-α)N provides the band gap ranging from 3.42 to 6.2 eV whereas In_αGa_(1-α)N provides the band gap values from 0.7 to 3.42 eV [1–4]. Both these alloys have direct energy gap property which makes this material suitable for generating and

Manoj Thosar
Department of Physics, Vivekananda Institute of Technology-East, VIT Campus,
Jaipur, India
e-mail: labhesh9@gmail.com

R.K. Khanna
Department of Physics, Vivekananda Global University, VIT-Campus, Jaipur 303905,
Rajasthan, India
e-mail: rkkhanna.iitm@gmail.com

A.J. Thosar (✉)
Department of Electrical Engineering, Poornima University, Jaipur, India
e-mail: joshiashwini111@gmail.com

absorbing light. $\text{In}_\alpha\text{Ga}_{(1-\alpha)}\text{N}$ is able to capture sun radiations from 0.3 to 1.7 μm wavelength by changing indium composition from 0 to 1 [3, 4]. Thus, $\text{In}_\alpha\text{Ga}_{(1-\alpha)}\text{N}$ alloy is capable to absorb terrestrial spectrum (AM1.5D) radiations, more than 80 %. The $\text{In}_\alpha\text{Ga}_{(1-\alpha)}\text{N}$ material-based devices faces the problem due to polarization effect [5–8]. The polarization in $\text{In}_\alpha\text{Ga}_{(1-\alpha)}\text{N}$ material can be categorized in two ways. The spontaneous polarization is the inbuilt property while piezoelectric polarization is dominant in the heterojunction devices owing to different lattice values and different thermal expansion coefficient values [9, 10]. Both polarization effects are effective in the c-plane [11]. Overcoming the polarization effect, by growing the device in a perpendicular direction to the c-plane (Nonpolar a-plane) is a secured way [12–14]. $\text{In}_\alpha\text{Ga}_{(1-\alpha)}\text{N}$ devices grow in a-plane, do not bear the polarization effect, and therefore, higher efficiency is achievable.

In p-i-n solar cell, we insert a layer of intrinsic semiconductor which increases the width of active region but decreases the exciting field developed in the photo carrier generation region [15]. The width of intrinsic layer optimization is necessary to maintain the balance in both the rates of photocarrier generation and the photocarriers draining out from the cell. It is practical that the p-i-n solar cell with intrinsic layer of low energy band gap has higher external efficiency than that with intrinsic layer of high energy band gap [16]. But the creation of conduction band peak at the n-GaN/ $\text{In}_\alpha\text{Ga}_{(1-\alpha)}\text{N}$ interface plays an imperative role in degrading the performance of p-GaN/ $\text{i-In}_\alpha\text{Ga}_{(1-\alpha)}\text{N}$ /n-GaN solar cell [2]. This conduction band peak restricts the photoelectrons to flow from n-GaN region. The height of this conduction band peak depends on difference of forbidden gap between n-GaN and $\text{i-In}_\alpha\text{Ga}_{(1-\alpha)}\text{N}$ layer and its width varies with variations in conductivity of $\text{i-In}_\alpha\text{Ga}_{(1-\alpha)}\text{N}$ layer. Reduction in height of conduction band peak is possible by inserting graded layers of $\text{In}_\alpha\text{Ga}_{(1-\alpha)}\text{N}$ at different indium composition (α) between n-GaN and $\text{i-In}_\alpha\text{Ga}_{(1-\alpha)}\text{N}$ layer [2, 16]. In this method, the photoelectrons cannot pass through the conduction band peak if it is too wide so they bypass the peak from above. To increase penetration through conduction band peak we have done p-doping in $\text{i-In}_\alpha\text{Ga}_{(1-\alpha)}\text{N}$ layer, which minimizes the width of the peak. It assists the photocarriers to tunnel through the peak which results in higher efficiency. Therefore, a p-GaN/ $\text{i-In}_\alpha\text{Ga}_{(1-\alpha)}\text{N}$ /n-GaN solar cell with p-doped intrinsic layer at optimized energy band gap grown on a nonpolar epitaxial layer is simulated.

Method

By changing the indium composition (α) from 0 to 1 and doping concentration in $\text{i-In}_\alpha\text{Ga}_{(1-\alpha)}\text{N}$ layer, the energy band gap and conductivity of nonpolar $\text{In}_\alpha\text{Ga}_{(1-\alpha)}\text{N}$ material has been controlled. Here we have divided 1.4 μm wavelength absorption range of $\text{In}_\alpha\text{Ga}_{(1-\alpha)}\text{N}$ into 14 parts and determined all optical and electrical properties at desired indium composition [17–21]. The value of energy band gap (ΔE_g), cutoff wavelength (highest absorption wavelength— λ_c), refractive index (n) and lattice constant (a) at different value of indium composition (α) in $\text{In}_\alpha\text{Ga}_{(1-\alpha)}\text{N}$

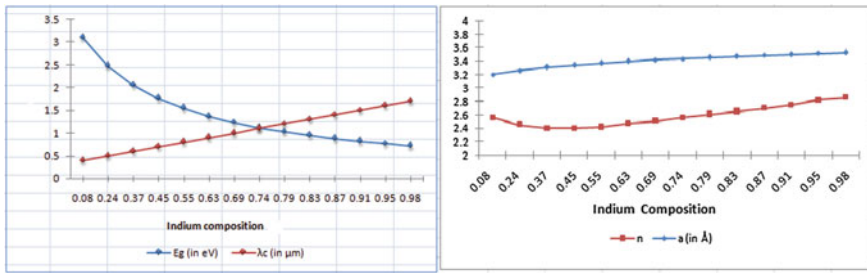


Fig. 1 The (ΔE_g), λc , n and a for optimized values of indium composition (α)

is revealed in Fig. 1. Figure 2 reveals the values of electron affinity (χ), average absorption coefficient and relative permittivity (ϵ) for i-In_αGa_(1-α)N layer at different values of indium composition (α). The p-GaN/n-GaN solar cell structure is simulated by using PC1D (Version-5.9). The optimized width of p-GaN layer was 400 nm and n-GaN layer was 100 nm. Here, we have considered that solar radiations of AM1.5D spectrum are entered from n-GaN region. Figure 3 reveals the I-V curve and the electric field generated inside the active region and transportation behavior of charge carriers inside the p-GaN/n-GaN solar cell.

In next step of simulation, we have inserted an i-In_αGa_(1-α)N layer between p-GaN and n-GaN region. After that we have changed the value of indium composition in i-In_αGa_(1-α)N layer, and optimized the thickness and doping of i-In_αGa_(1-α)N layer for maximum external efficiency of p-GaN/i-In_αGa_(1-α)N/n-GaN solar cell.

Results and Discussion

Initially, as we increase the indium composition in i-In_αGa_(1-α)N layer, the required thickness of i-In_αGa_(1-α)N layer to absorb the solar radiations is increasing linearly up to 0.37 indium composition. After that thickness of i-In_αGa_(1-α)N layer starts saturating and at 0.63 indium composition it saturates at 800 nm thickness. The

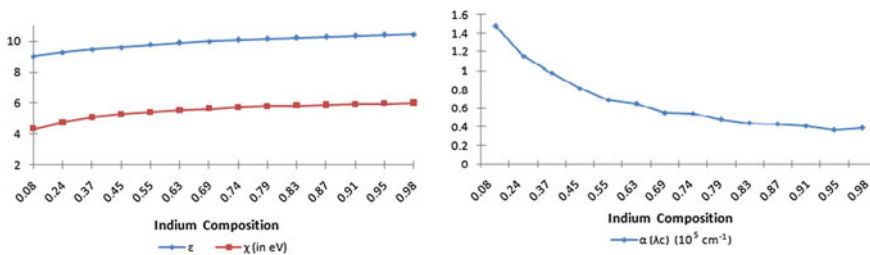


Fig. 2 The values of ϵ , χ and The average absorption coefficient for i-In_αGa_(1-α)N layer at different indium composition (α)

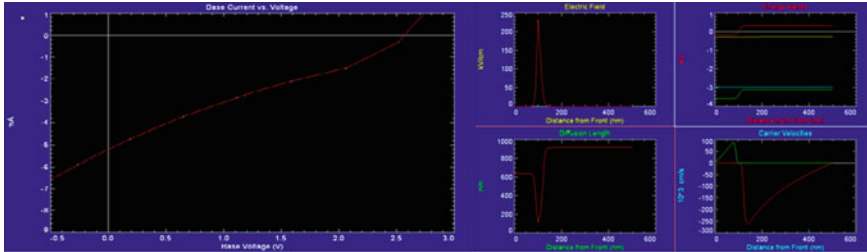


Fig. 3 I-V curve and Electrical and transport behavior of p-GaN/n-GaN solar cell

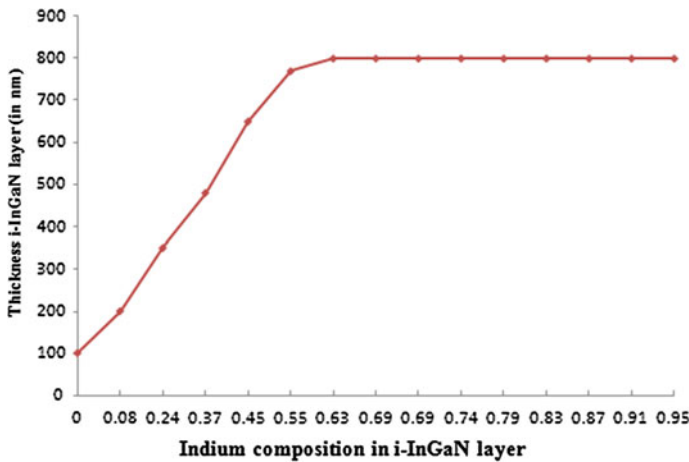


Fig. 4 Optimum thickness of $i\text{-In}_\alpha\text{Ga}_{(1-\alpha)}\text{N}$ layer with different indium composition for max. external efficiency

variation in thickness of $i\text{-In}_\alpha\text{Ga}_{(1-\alpha)}\text{N}$ layer with different indium composition is revealed in Fig. 4.

The saturation in thickness of $i\text{-In}_\alpha\text{Ga}_{(1-\alpha)}\text{N}$ layer at higher indium composition is due to the saturation in absorption coefficient of $i\text{-In}_\alpha\text{Ga}_{(1-\alpha)}\text{N}$ layer at higher indium composition which is revealed in Fig. 2. Figure 5 indicates the highest efficiency of p-GaN/ $i\text{-In}_\alpha\text{Ga}_{(1-\alpha)}\text{N}$ /n-GaN solar cells at optimized thickness for different values of indium composition with and without p-doping in $i\text{-In}_\alpha\text{Ga}_{(1-\alpha)}\text{N}$ layer. The highest efficiency of p-GaN/ $i\text{-In}_\alpha\text{Ga}_{(1-\alpha)}\text{N}$ /n-GaN solar cells were achieved at zero indium composition and 100 nm thickness of $i\text{-In}_\alpha\text{Ga}_{(1-\alpha)}\text{N}$ layer. After that as we increase the indium percentage, the efficiency of the solar cell is decreasing because of the following reasons. Higher is the indium percentage in $i\text{-In}_\alpha\text{Ga}_{(1-\alpha)}\text{N}$ layer, higher will be lattice values difference and conduction band peak. The different lattice values generate the trapping centers and dislocation density near the interface of two layers. These trapping centers reduce the penetration length of the photocarriers near the interface of two layers [22]. The

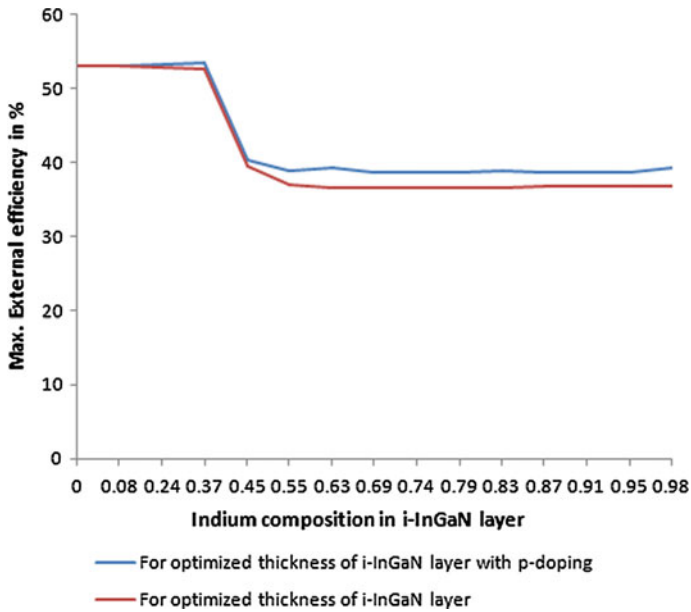


Fig. 5 Max. external efficiency on optimized i-In_αGa_(1-α)N layer

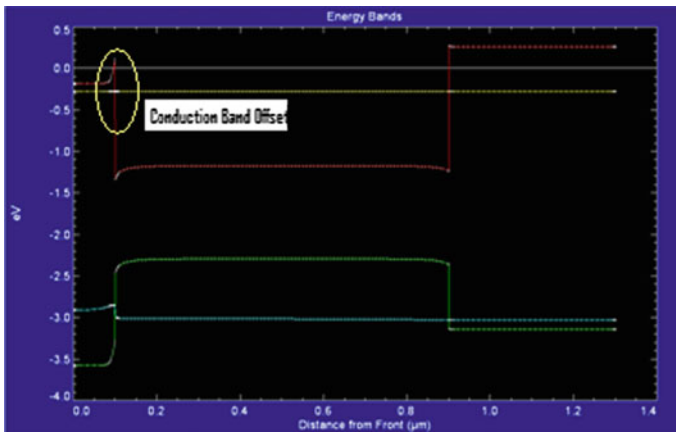


Fig. 6 Energy band diagram of p-GaN/i-In_αGa_(1-α)N/n-GaN solar cell with $\alpha = 0.74$ i-In_αGa_(1-α)N layer

conduction band difference develops an electric field at n-GaN/i-In_αGa_(1-α)N interface, which restrict the photoelectrons to flow outside from the interface. The value of conduction band peak at n-GaN/i-In_αGa_(1-α)N interface at 0.74 indium composition in i-In_αGa_(1-α)N layer is revealed in Fig. 6.

The combined effect of different lattice values and conduction band peak is responsible for reducing the efficiency of p-GaN/i-In_αGa_(1-α)N/n-GaN solar cells at higher values of indium composition. The highest efficiency of p-GaN/i-In_αGa_(1-α)N/n-GaN solar cells were 52.99 % with 10.7 mA short circuit current and 2.60 volt open-circuit voltage at 100 nm intrinsic layer thickness and zero indium composition in i-In_αGa_(1-α)N layer. The additional improvement in p-GaN/i-In_αGa_(1-α)N/n-GaN solar cells were possible by p-doping in i-In_αGa_(1-α)N layer, which improves the conductivity of intrinsic layer and hence reduces the thickness of conduction band peak. The reduction in conduction band peak provides opportunity for photoelectrons to tunnel from the peak. This tunneling process increases the number of photoelectrons which contributes in the solar cells efficiency. Results of our simulations indicate that the highest efficiency of n-GaN/i-In_αGa_(1-α)N/p-GaN solar cells were achieved 53.53 % at $1 \times 10^{16} \text{ cm}^{-3}$ p-doping and 0.37 indium composition in i-In_αGa_(1-α)N layer with 480 nm width. The maximum efficiency of n-GaN/i-In_αGa_(1-α)N/p-GaN solar cells at different indium composition for optimized p-doping and thickness of i-In_αGa_(1-α)N layer is revealed in Fig. 5.

Conclusion

Here, we have gone through nonpolar n-GaN/i-In_αGa_(1-α)N/p-GaN solar cell. We have done the simulation for maximum efficiency with three parameters; one was thickness of i-In_αGa_(1-α)N layer, second was p-doping in i-In_αGa_(1-α)N layer and third was indium percentage in i-In_αGa_(1-α)N layer. For zero indium percentage and 100 nm width of i-In_αGa_(1-α)N layer, we achieved 52.99 % efficiency. This efficiency of p-GaN/i-In_αGa_(1-α)N/n-GaN solar cell was improved by 0.53 % in comparison to simple p-GaN/n-GaN solar cell. But for the 480 nm thickness and 0.37 indium composition, we got the efficiency improved further by 1.02 % at $1 \times 10^{16} \text{ per cm}^3$ p-doping in i-In_αGa_(1-α)N layer.

References

1. Zhang, X., Wang, X., Xiao, H., et al.: Simulation of In_{0.65}Ga_{0.35}N single junction solar cell. *J. Phys. D* **40**(23), 7335–7338 (2007)
2. Jeng, M.-J.: Simulation of nonpolar p-GaN/i-InGaN/n-GaN solar cell. *Int. J. Photoenergy*, Article id: 910256, 1–8 (2012). doi:[10.1155/2012/910256](https://doi.org/10.1155/2012/910256) (2012)
3. Wu, J., Walukiewicz, W., Yu, K.M., Ager III, J.W., Haller, E.E., Lu, H., Schaff, W.J.: Small band gap bowing in In_(1-x)Ga_xN alloys. *Appl. Phys. Lett.* **80**, 4741–4743 (2002)
4. Wu, J.: When group III-nitrides go infrared: new properties and perspectives. *J. Appl. Phys.* **106** (2009)

5. Yu, E.T., Dang, X.Z., Asbeck, P.M., Lau, S.S., Sullivan, G.J.: Spontaneous and piezoelectric polarization effects in III-V nitride heterostructure. *J. Vac. Sci. Technol. B* **17**, 1742–1749 (1999)
6. Li, Z.Q., Lestradet, M., Xiao, Y.G., Li, S.: Effects of polarization charge on the photovoltaic properties of InGaN solar cells. *Phys. Status Solidi A* **208**, 928–931 (2011)
7. Chang, J.Y., Liou, B.T., Lin, H.W., Shih, Y.H., Chang, S.H., Kuo, Y.K.: Numerical investigation on the enhanced carrier collection efficiency of Ga face GaN/InGaN pin solar cell with polarization compensation interlayer. *Opt. Lett.* **36**(17), 3500–3502 (2011)
8. Bernardini, F., Fiorentini, V., Vanderbilt, D.: Spontaneous polarization and piezoelectric constants of III-V nitrides. *Phys. Rev. B* **56**(16), R10024–R10027 (1997)
9. Kuo, Y.K., Chang, J.Y., Shih, Y.H.: Numerical study of the effects of the hetero-interfaces, polarization charges and step graded interlayers on the photovoltaic properties of (0001) face GaN/InGaN pin solar cell. *IEEE J. Quantum Electron.* **48**(3), 367–374 (2012)
10. Bernardini, F., Fiorentini, V., Vanderbilt, D.: Accurate calculation of polarization related quantities in semiconductors. *Phys. Rev. B: Condens. Matter* **63**, 193201–193204 (2001)
11. Fiorentini, V., Bernardini, F., Sala, F.D., Carlo, A.D., Lugli, P.: Effects of macroscopic polarization in III-V nitride multiple quantum well. *Phys. Rev. B: Condens. Matter* **60**, 8849–8858 (1999)
12. Sanchez-Rojas, J.L., Garrido, J.A., Munoz, E.: Tailoring of internal fields in AlGaIn/GaN an InGaIn/ GaN hetero structure devices. *Phys. Rev. B: Condens. Matter* **61**, 2773–2778 (2000)
13. Ng, H.M.: Molecular beam epitaxy of GaN/AlGaIn multiple quantum wells on R-plane (1012) sapphire substrates. *Appl. Phys. Lett.* **80**(23), 4369–4371 (2002)
14. Chitnis, A., Chen, C., Adivarahan, V., et al.: Visible light emitting diodes using a-plane GaN/InGaIn multiple quantum wells over r-plane sapphire. *Appl. Phys. Lett.* **84**(18), 3663–3665 (2004)
15. Solanki, C.S.: *Solar Photovoltaics: Fundamentals, Technologies and Applications*, 2nd edn., 202 pp. PHI Learning Private Limited (2013)
16. Kushwaha, A.S., Mahala, P., Dhanavanti, C.: Optimization of p-GaN/InGaIn/n-GaN double heterojunction p-i-n solar cell for high efficiency: simulation approach. *Int. J. Photoenergy*, **2014**, Article ID 819637, pp. 1–6 (2014)
17. Chloe, A., Fabien, M.: Simulations, limitations and novel growth technology for InGaIn-based solar cell. *IEEE J Photovoltaics* 2156–3381 (2013). doi:[10.1109/JPHOTOV.2013.2292748](https://doi.org/10.1109/JPHOTOV.2013.2292748)
18. Levinshtein, M.E., Rumyantsev, S.L., Shu, M.S.: *Properties of advanced semiconductor materials*. Wiley, New York (2001)
19. Aziz, W.J., Ibrahim, K.: Simulation model for multi-junction InGaIn solar cell. *Int. J. Nanoelectron. Mater.* **3**, 43–52 (2010)
20. Brown, B.F., Ager, J.W.: Finite element simulations of compositionally graded InGaIn solar cells. *Sol. Energy Mater. Sol. Cells* **94**, 478–483 (2010)
21. Wu, J., Walukiewicz, W., Yu, K.M.: Small band gap bowing in InGaIn alloys. *Appl. Phys. Lett.* **80**(25), 4741 (2002)
22. Rajeghi, M.: *Fundamental of Solid State Engineering*, 3rd edn., pp. 326–330. Springer, New York (2009)

Assessing the Severity of Attacks in Wireless Networks

Jeril Kuriakose, V. Amruth, R. Jaya Krishna
and Devesh Kumar Srivastava

Abstract Sensor networks is an evolving technology and a hot exploration subject among scientists due to their tractability and individuality of network substructures, such as base stations, wireless access points, and moveable nodes. Sensor networks are widely used for solicitations, such as construction, traffic observation, and territory monitoring and several other scenarios. Wireless sensor network (WSN) makes a network malleable enough to go over concrete structures and it also evades lot of cabling. The primary encounters faced in WSN are security, and the hiatus in security leads to other constrains in energy efficiency, network life, and communication overhead. The hiatus in safekeeping the network is mostly because deficiency of the overriding of wave propagation, and computing constraints. In this paper, we have deliberated about numerous diversities of attacks in WSN, and their aftermath to the network.

Keywords WSN · Security · WSN attacks

Introduction

Generally, wireless sensor network denotes to a collection of spaciouly dispersed and devoted sensors for surveillance, recording and observing the physical surroundings of the location and collecting the information at regular intervals at a

J. Kuriakose

Department of Information Technology, St. John College of Engineering and Technology, Palghar, India

V. Amruth (✉)

Department of Information Science and Engineering, Maharaja Institute of Technology, Mysore, India
e-mail: amruth.v@isim.net.in

R. Jaya Krishna · D.K. Srivastava

School of Computing and Information Technology, Manipal University, Jaipur, India

© Springer India 2016

N. Afzalpulkar et al. (eds.), *Proceedings of the International Conference on Recent Cognizance in Wireless Communication & Image Processing*, DOI 10.1007/978-81-322-2638-3_70

principal locality. A WSN is mostly a dense network consisting hundreds to several thousands of sensing/sensor devices and the formation of WSN is due to large number of networked sensing nodes. The sensor nodes sense the change in the environment and reports it.

There are several scenarios where the sensor node size can vary from the grain of dust to the size of an apparel box. Meanwhile their cost can also diverge from a scarce pennies to hundreds of dollars liable on the computational limitations of a sensor device like disk size, processing speed, networking capacity, and energy efficiency. WSNs encompasses a bushfire response, military command, industrial eminence governor, communication intellect, perceivable dangerous structures, smart buildings, overseeing traffic, examining human heart rates.

WSNs regularly observers a perilous groundwork or hold powerful material. It also disseminate unembellished supply constrictions due to the shortage of information storing and energy conservation. As the wireless networks are ordinarily installed in isolated dwellings and left unattended, there is a need for security contrivances to preserve beside different sorts of attacks such as node arresting, physical interfering, and denial of service (DOS). Appallingly, old-fashioned safekeeping contrivances with excessive overhead are not at all reasonable for the resource self-conscious sensor nodes. So these sensor nodes match to the foremost difficulties in the operation of old-fashioned computer security procedures in a WSN.

Attacks can be unconfined by: Isolated and unexecuted operation, wireless communications, and meagreness of progressive security topographies.

Wireless sensors regularly involves in the handling individualities of technologies that are years old (or longer), and the engineering trend is to lesser the price of wireless sensors while sustaining comparable calculating power. Grounded on this influences, many scientists have started to report the encounters of exploiting the handling competences and power/energy monies of wireless sensor nodes as well as safeguarding them against invaders.

Outbursts in Wireless Sensor Networks

WSNs are defenceless in most of the scenarios to security attacks. It encompasses numerous procedures, such as node seizures, outbreaks on a node's bodily security and outbreaks on the routing protocols. The WSNs also face an added weakness because nodes are often sited in an unreceptive or unsafe location where they are not actually sheltered, so that the authorisations are uncovered to the invader. Chiefly outbreaks are categorized into mobile attacks and static attacks.

A. *Mobile Attacks*

Outbreaks on moveable networks are fairly expected in the existing decade. Figure 1 displays the common overview of localization outbreaks on mobile nodes and the outbreaks are generally categorized into two kinds:

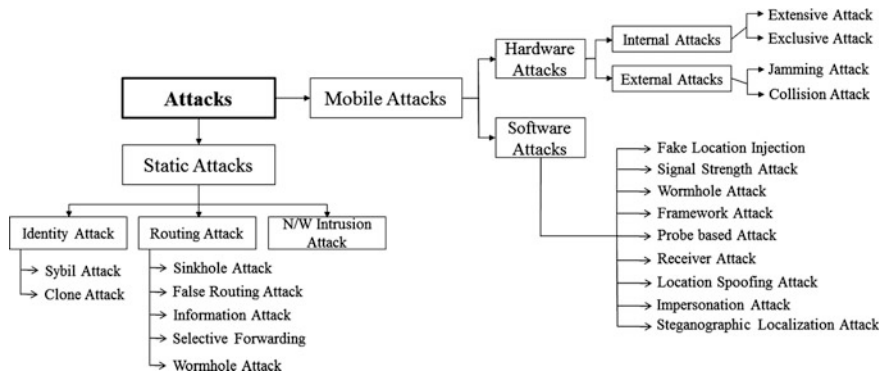


Fig. 1 Different types of attacks in wireless network

i. *Hardware Attacks*

a. *Internal Attacks*

The interior hardware attack is mostly because of the hardware producers, and is generally used as entrance to snip vital data. Interference of predictable performance, fabricating artefact properties, and hardware replicating are the motive behindhand the interior hardware outbreak.

(1) *Extensive Attack*

The outbreaks that can be lengthened or banished to the adjoining nodes are called as extensive attacks. A great level of intricacy and distrustful observing is essential to accomplish this kind of outbreak. Extensive attacks are extensively supported out by impounding the node and avoiding it becomes inaccessible in a thick network. Inhibiting the blowout of the extensive attack is an unsolved investigation problem and can be reflected for upcoming work.

(2) *Exclusive Attack*

Exclusive is supported out, aiming a solitary or explicit node. The vulnerable node comes to a useless genre and will deliver no essential functions. It is generally carried out through engineering by conquering the JTAG port, and is generally recommended to deactivate JTAG port after positioning. In [1] the authors effectively achieved an outbreak on a Harvard architecture mote. Distant software update for sensor nodes is currently being accepted out by consuming over-the-air programming, which fascinates the hackers to complete an outbreak.

b. *External Attacks*

Disruption or destruction of the hardware devices is an archetypal sample of external outbreak and is constantly through once capturing the

mobile node. Disruption instigated as of the low frequency signals with the greater frequency signals is also a typical external outbreak.

(1) *Jamming Attacks*

The weak or the beleaguered nodes are confronted by means of signals having greater strength. When the exposed or the directed node attempts to join the communication, its signals come to be mobbed.

(2) *Collision Attacks*

This outbreak is battered to spoil the packets referred by the nodes in the network.

ii. Software Attacks

The extensively performed outbreaks on moveable nodes are the software outbreaks and are as trails:

a. *Fake Location Injection*

In verdict to fetch down networks consistency moveable nodes are introduced with bogus position coordinates, making the localization of the unidentified nodes with incorrect position coordinates. The key intention after bogus position inoculation is to instigate anarchy in mobile nodes path. In [2] bogus traffic flow has been added into the network to fleece the factual commuter traffic from the trespassers.

b. *Signal Strength Attack*

The outbreaks on signal strength [3] are entirely intended to rise the localization inaccuracy ensued through RSSI built localization. As the localization inaccuracy surges accurate position identification is not conceivable. By classifying the occurrence of communication and reception, the trespasser achieves the outbreak.

c. *Wormhole Attack*

The dependability and suppleness of a moveable ad hoc network are truncated by the wormhole outbreak [4]. It is an emblematic instance of scheming outbreaks where two malevolent nodes link organized to achieve an involvement. A great level classy procedures and tunnelling instruments are essential to accomplish this outbreak.

d. *Framework Attack*

This method of outbreak is prolonged out, aiming the moveable networks structure [5]. The crucial peripherals, such as beacon nodes, routing procedures, and representatives are beset thus making an ignominy in the network.

e. *Probe based Attack*

Probe/Investigation is generally used in a wireless network to learn the state and nature of the network [6]. Enemy node exploits this technique to achieve its outbreaks by recognizing the choices to increase entree.

f. *Receiver Attack*

The disobedient receivers twitch flattering envious by disturbing the regular movement of procedure, this form of outbreak is identified as Receiver assaults [7]. If a position conscious node ensures noncooperation with the demanding node, then the localization might not be an achievement.

g. *Location Spoofing Attack*

Location bluffing attacks [8] can be smoothly instigated on a moveable network. Owing to the topological overhead, key management procedures is not constantly conceivable in a moveable network.

h. *Impersonation Attack*

A malevolent node executes an imitation outbreak [9] by giving the untruthful position coordinates. The imitation outbreak is like to man-in-the-middle attack; but the latter ensures no complete accountabilities.

i. *Steganographic Localization Attack*

This procedure of outbreak is consummated by inserting malevolent node in the movement. In [10] the authors effectively resolute the localization information by introducing malevolent pseudo-noise code into the network movement.

B. *Static Attack*

Stationary attack can be categorized into three main classes [11], and are as follows:

i. *Identity Attack*

Individuality outbreaks aims to steal the personalities of genuine nodes that is functioning in the wireless network. An individuality outbreak has one or more nodes unlawfully appealing an individuality of genuine node and imitation in entire WSN. The individuality outbreaks are characterized two types and are follows:

a. *Sybil attack*

In a Sybil attack, the WSN is overthrown by a malevolent node consequently counterfeiting a huge quantity of counterfeit individualities in direction to take the network's procedures. It was formerly designated as an outbreak that is talented to conquest the severance machineries of dispersed facts storing structures in peer-to-peer networks [12].

b. *Cloning Attack*

A Duplicating outbreak or an imitation outbreak is an endeavour by the enemy node to add one or supplementary nodes to the network and imitates as another genuine node using the ID of the genuine node. An assailant attempts to enhance a node to a prevailing sensor network by doubling the node ID of a contemporary node.

ii. *Routing Attack*

Routing outbreak purposes to domicile the malevolent nodes on a routing pathway from a foundation to the base station and will start to deploy it or abandon genuine information packets. It tries to modify the routing evidence to function and to acquire benefit since such a variation in numerous habits such as spreading or limiting provision directions, producing incorrect mistake information, producing routing hoops, and growing end-to-end interruption.

a. *Sinkhole Attack*

The sinkhole outbreak is a predominantly stark outbreak that avoids the base substation from gaining thorough and precise detecting information. Thus, it customs a thoughtful risk to higher-layer solicitations. The challenger forms a great range of inspiration which will appeal all traffic flow designed for the base substation from the mobile nodes those are several hops away from the conceded node is known as sinkhole outbreak.

b. *False routing attack*

False routing outbreak means that introducing bogus routing controller packets into the network. For instance: separate sensor nodes can issue to concede safety as they may be positioned in unfriendly surroundings and every sensor node connects wirelessly. A challenger can introduce incorrect intelligences into the networks via approved nodes.

c. *Selective forwarding attack*

Selective forwarding outbreak happens once conceded node may decline to advance choosy packets. Deliberate an instance: for army purposes the quick discovery and recording of every applicable incident in the ground are significant, but these procedures can be effortlessly tarnished by discriminating forwarding outbreaks. In such outbreaks, malevolent nodes may decline to advance definite packets and merely ruin them; to mark certain that is ensures not circulate.

d. *Wormhole Attack*

The wormhole outbreak can make a severe hazard in sensor networks, particularly in contradiction of numerous ad hoc network, routing procedures, and location-based wireless safety structures. In a wormhole outbreak, an assailant accepts packets/information at a single point, and “channels” them to an alternative location in the network, and then once more communicates them into the wireless network from the former point, thus creating the information or message has not reached its destination.

iii. *Network Intrusion*

Network interruption is an illegal admittance to a network or system by whichever a peripheral wrongdoer, or by on insider with minor treats [13].

Discussion and Future Events

Nearby several safety goals that need to be achieved while deploying a wireless sensor network. Information Concealment is the utmost significant matter in network safekeeping. Concealment is the capability to keep the evidence intimate from the illegal operators. Attentiveness must be taken that a vulnerable node should not betray its data to the attacking node. Data authentication thwarts third parties from contributing in the network, by letting genuine nodes to perceive messages or information from illegal nodes. Symmetric contraption data authentication is vital to avoid two party communication [14].

Data integrity guarantees the destination node that the data received is not been altered during transmission by an assailant. With the execution of secrecy, an attacker may be unable to steal evidence. Data freshness implies the freshness of data that suggests the data is recent and ensures that a challenger has not repeated ancient messages.

Many security algorithms consume more energy, which shrinks the lifespan of the sensor network. Designing an energy efficient security algorithm can be considered for the future event. Ensuring the data integrity would overcome unstable conditions occurred due to the loss of data, failure to do so may induce data loss or damage to the node. Most sensor network applications depend on some form of time synchronization. An individual sensor's radio may be switched off for some periods of time in order to conserve power.

Conclusion

WSNs are progressively being carried out in Territorial Army, conservation, medical purposes (such as body area networks) and merchantable purposes. Owing to its prominence, protecting the data/information in those scenarios are an imperative piece during the installation of WSNs. This paper studies the objectives, outbreaks, and their taxonomies in WSNs, and also concludes that the existing and forthcoming effort in confidentiality and trust would make WSNs an additional striking option in a diversity of innovative areas.

References

1. Francillon, Castelluccia, C.: Code injection attacks on harvard-architecture devices. In: Proceedings of the 15th ACM Conference on Computer and communications security, Alexandria, Virginia, USA (2008)
2. Reza, S., et al.: Quantifying location privacy: the case of sporadic location exposure. Privacy Enhancing Technologies. Springer, Berlin (2011)

3. Yingying, C., et al.: The robustness of localization algorithms to signal strength attacks: a comparative study. *Distributed Computing in Sensor Systems*, pp. 546–563. Springer, Berlin (2006)
4. Hu, Yih-Chun, Perrig, Adrian, Johnson, David B.: Wormhole attacks in wireless networks. *IEEE J. Sel. Areas Commun.* **24**(2), 370–380 (2006)
5. Dimitris, G., et al.: Preventing impersonation attacks in MANET with multi-factor authentication. In: *Modeling and Optimization in Mobile, Ad Hoc, and Wireless Networks*, 2005. Third International Symposium on IEEE WIOPT (2005)
6. Giovanni, V., et al.: NetSTAT: A network-based intrusion detection approach. In: *Computer Security Applications Conference*, 1998. Proceedings of 14th Annual. IEEE (1998)
7. Savage, Stefan, et al.: TCP congestion control with a misbehaving receiver. *ACM SIGCOMM Comput. Commun. Rev.* **29**(5), 71–78 (1999)
8. Kuriakose, Jeril, et al.: Secure Multipoint Relay Node Selection in Mobile Ad Hoc Networks. *Security in Computing and Communications*. Springer Intl. Publishing, pp. 402–411 (2015)
9. Bing, W., et al.: A survey of attacks and countermeasures in mobile ad hoc networks. *Wireless Network Security*, pp. 103–135. Springer, US (2007)
10. Wang, X., et al.: iloc: An invisible localization attack to internet threat monitoring systems. In: *Proceedings of the 27th IEEE International Conference on Computer Communications (INFOCOM) (Mini-conference)*, April 2008
11. Liang, W., Jussi, K.: Real-world sybil attack in Bit torrent mainlinedht. *IEEE GLOBECOM* (2012)
12. Yingying, C., et al.: The robustness of localization algorithms to signal strength attacks: a comparative study. *Distributed Computing in Sensor Systems*, pp. 546–563. Springer Berlin
13. Kuriakose, J., et al.: A review on localization in wireless sensor networks. *Advances in signal processing and intelligent recognition systems*, pp. 599–610. Springer Intl. Publishing (2014)
14. Jeril, K., et al.: A review on mobile sensor localization. *Security in Computing and Communications*, pp. 30–44. Springer, Berlin (2014)

SD and TCH Blocking KPI Improvement Without Adding TRX Unit in BTS in GSM Network

Jitendra Vaswani and Gaurav Sharma

Abstract Key performance indicators (KPIs) are used by all mobile service providers and their vendor as a benchmark to evaluate their performance and quality of service (QoS), and also to make comparative analysis with other service providers' QoS and network performance. The Telecom Regulatory Authority of India (TRAI) also has its own sets of KPIs and its benchmarks to monitor the QoS provided by service providers. There are hundreds of KPIs used monitor network quality, of which network blocking KPIs, SD Blocking, and TCH blocking are tackled in this paper. ACLC, half rate (HR) tuning, and cell load sharing (CLS) are the advocated methods for SD and TCH blocking KPI improvement without adding TRX unit in BTS in GSM network on-air sites. These methods were implemented in live GSM network to improve TCH and SD blocking KPIs without increasing number of transceiver (TRX) units in the base transceiver station (BTS) and are mentioned accompanied with the results obtained by parameter changes on live GSM sites of Bharti Airtel.

Keywords TRAI · GSM · BTS · TCH · FR · HR · SDCCH · KPI

Introduction

In 1982, a European group named CEPT started to develop GSM and it was first deployed by Germany in 1992 [1]. GSM architecture constitutes of mobile station (MS) handset with the user, base station subsystem (BSS) of different vendor companies, network and switching subsystem (NSS) and operation subsystem (OSS) for operation, and maintenance of the operator's GSM network and services [2]. BSS consists of base transceiver station (BTS) at the antenna site connected to base station

Jitendra Vaswani (✉) · Gaurav Sharma
Department of Electronics and Communication Engineering,
Mewar University, Gangrar, Chittorgarh, India
e-mail: jitendra2104@gmail.com

Gaurav Sharma
e-mail: gaurav@mewaruniversity.co

controller (BSC) that may control several BTSs [2]. The capacity of a BTS is decided by the maximum transceivers (TRXs) per base station [3]. Each TRX is subdivided into eight timeslots (TS) on the basis of time division multiple access (TDMA) as 1TDMA frame = 8 timeslots [4]. So, one TRX is supposed to possess eight channels for carrying network traffic. GSM sites are planned with several justified, viable, and practicable TRX configuration depending on the clutter and subscribers density of the discrete area under consideration. Suppose a sector of a particular site has four TRX (transceivers), which means $4 \times 8 = 32$ TS, i.e., 32 channels in that one cell or sector of the GSM site. Each sector of the GSM site must have a broadcast control channel (BCCH), n number of standalone dedicated control channels (SDCCH) depending upon traffic on that sector and remaining $\{32 - (n + 1)\}$ traffic channels (TCH). Traffic channels (TCH) are source of earning revenue for all telecom operators as they are used for voice calls and SDCCH may or may not be revenue source depending upon how the SDCCH is used. If SDCCH is used for short message service (SMS), it will generate revenues and if used in call setup procedure, no revenue is gained by the operators.

SD Blocking

Blocking is the term used if the request for the service is denied due to exhaustion of the allocated service rendering resources. SD blocking happens in GSM network when a subscriber wants to make a call or want to exploit SMS service but cannot do so as all defined SDCCH are already occupied or reserved. SD blocking is measured in terms of SD blocking rate and is defined as:

SD blocking rate (%) = (Total number (count) of blocked SDCCH request by the subscriber/Total number (count) of SDCCH requests by the subscriber) * 100

(a) Probable Reasons for SD Blocking

There can be many possible reasons for SD blocking in the GSM network as shown in Fig. 1.

High Volume of SMS

All SMS exploits SDCCH [4], except during an ongoing voice, therefore large volume of SMS in the network can cause SD congestion and SD blocking in the network.

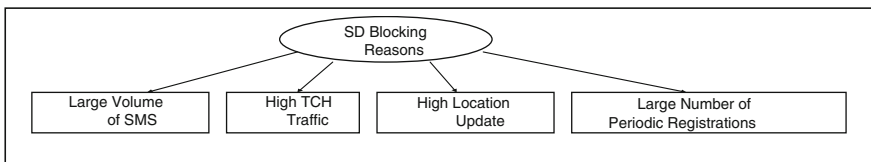


Fig. 1 Possible reasons for SD blocking

High TCH Traffic

All voice calls use SDCCH in the call setup procedure [4]. It implies a cell having high TCH traffic will also result in high SD traffic and it may result in SD blocking.

High Location Update

Location update (LU) occurs whenever a mobile station changes its location and moves from site of one BSC to other distinct BSC or from one LAC to other distinct LAC and registers itself. LU strategy also exploits SDCCH [4]. So, location updates, i.e., LU count will be much more due to inter BSC/LAC handovers at BSC/LAC boundary sites resulting in high location update and may become a cause of SD blocking.

Large Number of Periodic Registrations

Every MS registers itself after a time prespecified in the network parameters using SDCCH and is known as periodic registration. Perennial periodic registrations will increase the load on SDCCH and may result in SD blocking.

(b) Measures for SD Blocking KPI Improvement

Increasing number of SDCCH on permanent basis on the site will counter SD blocking but will simultaneously decrease the number of TCH on the cell/site. Methods are suggested for SD blocking removal from the network without causing much of a revenue loss to the operator.

Adaptive Configuration of Logical Channels (ACLC)

ACLC is used to dynamically reconfigure the TCH to SDCCH and vice versa depending on the traffic load conditions on SDCCH and TCH. If there is high traffic on SDCCH and there are vacant TCHs satisfying the conditions specified in the ACLC influencing algorithm, then a TCH is converted to SDCCH and if the load on SDCCH reduces, then the converted SDCCH may work as TCH again.

SLEVEL and STIME are the parameters controlling ACLC feature in GSM [5]. SLEVEL is defined as the number of vacant SDCCH/eight sub-channels when an attempt is made to configure an idle TCH to a SDCCH.

STIME is defined as the time in seconds for which the TCH converted into SDCCH by ACLC feature is not having any SDCCH traffic load. SLEVEL optimization statistics are shown in Table 1.

Table 1 Pre –post statistics for SLEVEL change implementation

Cells	SLEVEL change implementation statistics				Remarks
	Pre SLEVEL	Post SLEVEL	Pre SD blocking	Post SD blocking	
BRP0103	1	2	1.90	0.00	SLEVEL changed
CHAI013	1	2	1.76	0.00	SLEVEL changed
CHRP011	1	2	1.57	0.00	SLEVEL changed

Table 2 Pre –post statistics for cell reselection hysteresis (CRH) alteration

Cells	Cell Reselection Hysteresis (CRH) alteration statistics						Remarks
	Pre CRH	Post CRH	Pre blocked calls	Pre SD blocking %	Post blocked calls	Post SD blocking %	
JOB0011	6	8	66	2.60	0	0.00	BSC/LAC boundary cell
PTSU013	6	8	36	0.67	0	0.00	BSC/LAC boundary cell
SHAR013	6	8	59	0.87	0	0.00	BSC/LAC boundary cell
NIMS112	8	10	107	0.72	0	0.00	BSC/LAC boundary cell

Altering (CRH) Cell Reselection Hysteresis for BSC/LAC boundary sites

Cell reselection hysteresis (CRH) defines difference in the received signal level from the two sites of different location area code for specified time interval [5]. This would avoid ping pong in the cell reselection by mobile stations for the BSC/LAC boundary sites and would reduce the location updates. LAC boundary can be redesigned so as to include the sites with low traffic. This would also revamp SD blocking KPI. Cell reselection hysteresis (CRH) change implementation statistics are shown in Table 2.

Changing Periodic Registration Counter

Low value of periodic registration counter would make frequent registration of MS, and the outcome is heavy load on SDCCH due to perennial MS registrations. Periodic registration counter should be optimized so as to reduce the load on SDCCH and not affecting paging channel KPI.

(c) *Points to remember while maneuvering above suggested measures:*

- Adaptive configuration of logical channels (ACLC) will not be much efficacious for the cell with very heavy TCH traffic load conditions.
- High value of SLEVEL can be very aggressive in converting traffic channel to SDCCH. Advocated value is one (1) for the cells with low/occasional SD blocking and 2 for cells with high/frequent SD blocking.
- CRH value must not be very high as high values may upshot in call drops and handover failures.

TCH Blocking

TCH blocking materializes when subscriber wants to make a voice call is not dispensed a TCH even after completing all the signaling procedure. TCH blocking rate is defined as

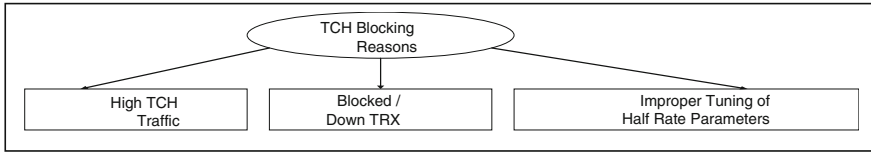


Fig. 2 Possible reasons for TCH blocking

TCH blocking rate (%) = (Number of blocked TCH request by the subscribers/Number of TCH requests by the subscribers) * 100

(a) *Possible Reasons for TCH Blocking*

There can be many possible reasons for TCH blocking in the GSM network as shown in Fig. 2.

High TCH Traffic

This is the foremost and most important reason for TCH blocking in the GSM network. Due to heavy TCH traffic on the cell, all traffic channels (TCH) are utilized and now no more calls can be accepted by the cell, and as a result TCH blocking occurs in the network.

Blocked/Down TRX

Every site/cell TRXs are planned according to the subscriber database so as to keep the cell utilization under control. A transceiver (TRX) can become blocked or can go down due to some hardware faults, and might initiate warning alarms on the site/cell, diminishing the net capacity and TCH utilization of cell become high causing TCH blocking in the network.

Improper Tuning of Half Rate Parameters

TCH can be classified as full rate (FR) TCH at 13 kbps and half rate (HR) TCH at 6.5 kbps, i.e., at FR, one transceiver (TRX) can support 8 calls while at HR, that same transceiver (TRX) can support 16 calls doubling the capacity of the cell/site [4]. So a TRX can work with FR as well as with HR. A HR voice call will suffer from inferior received signal quality and poorer speech quality index than a FR voice call. This inferior voice call quality has to be digested for the HR calls by the user. Whether a TRX will work at FR or at HR depends on the HR parameters tuning for the particular cell.

(b) *Measures for TCH Blocking KPI Improvement*

The best measure for TCH blocking KPI improvement is TRX addition on the cell/site which is a long process. There are some measures which can be implemented in the meantime to reduce TCH blocking without adding TRX unit in BTS.

Cell Load Sharing

Cell load sharing is the feature in GSM network through which a cell with high traffic and high TCH utilization shares its load (handover calls from MSs located at cell boundary) with the neighbor cells which are having low utilization based on specific parameters to offload its TCH traffic. Highly utilized cell (source cell) needs parametric optimization along with its neighboring cells (target cells having low

utilization). The parameters are cell load sharing state (CLSSTATE), cell load sharing acceptance (CLSACC), and cell load sharing level (CLSLEVEL) [5].

CLSSTATE decides whether cell load sharing is active or not. For cell load sharing this parameter should be set in active state for source cell as well as target cell [5].

CLSACC can be defined as minimum percentage of FR TCH channels vacant in the target cell so as to accept a handover due to cell load sharing (CLS), i.e., no load sharing will come off if percentage of vacant FR traffic channels in the target cell is below CLSACC [5].

CLSLEVEL is defined as the percentage of FR TCH channels vacant in the source cell, at or below which CLS procedure is started by the highly utilized source cell [5]. Cell load sharing will not come into picture whenever the percentage (%) of FR TCH channels vacant in the source cell is more than CLSLEVEL. Cell load sharing implementation statistics are given in Table 3.

Points to Remember

- For particular cell, the advocated value of parameter CLSACC must be greater than the value CLSLEVEL, otherwise cell will keep accepting the handovers from other cells simultaneously while trying to handover its own calls to target cells.
- CLS will be more effective for the call originating from cell border region as MS in the cell border region would be receiving abundant signal level from the target cell to initiate and carry on with the call.
- If in case, the TCH drop rate elevates or handover success rate (HSR) declines, the CLS parameters change should be retrogressed.

Table 3 Pre–post statistics for CLS (cell load sharing) change implementation

Cells	CLS (Cell Load Sharing) change implementation statistics							
	Pre CLS LEVEL	Pre CLSACC	Post CLS LEVEL	Post CLSACC	Cell type	Pre blocked calls	Post blocked calls	Difference blocked calls
HARIO11	20	40	40	60	Source cell	691	398	293
NANL011	20	30	40	60	Source cell	192	109	83
ARUD012	20	40	40	60	Source cell	285	173	112
AMWS112	20	30	15	20	Target cell	0	0	0
PNCL013	20	40	20	30	Target cell	0	0	0
HEL0012	20	30	15	20	Target cell	0	0	0

Table 4 Pre-post statistics for half rate parameters tuning

Cells	Half rate parameters tuning statistics									
	Pre DTHAMR	Pre DTHNAMR	Pre DMTHAMR	Pre DMTHNAMR	Post DTHAMR	Post DTHNAMR	Post DMTHAMR	Post DMTHNAMR	Pre blocking (avg)	Post blocking (avg)
BWSI013	20	0	40	0	90	90	90	90	6.94	0.00
HWR0913	20	10	10	0	90	90	90	90	2.93	0.00
RNWA012	40	30	10	0	90	90	90	90	8.37	0.00
CHU0132	20	10	10	10	90	90	90	90	0.4	0.00

Half Rate Parameters Tuning:

As improper tuning of HR parameters can cause TCH blocking in the live GSM network, so proper tuning and optimization of the same can reduce the TCH blocking in the GSM network. Parameters for HR tuning are DTHAMR, DTHNAMR, DMTHAMR, and DMTHNAMR [5].

DTHAMR is defined as the percentage of idle TCH to the total available TCH for a particular cell below which FR TCH will be used as HR TCH when allocated to AMR MSs [5]. This feature will not convert or affect ongoing calls to HR but will only convert new calls to HR calls.

DTHNAMR is defined as the percentage of idle TCH to the total available TCH for a particular cell below which FR TCH will be used as HR TCH when allocated to non-AMR MSs [5]. This feature will not affect ongoing calls to HR but will only convert new calls to HR calls.

DMTHAMR is defined as the percentage (%) of idle TCH to the total available TCH for a particular cell under consideration below which FR TCH will be utilized as HR TCH when allocated to AMR MSs. This feature will be converting ongoing calls to HR along with new calls [5].

DMTHNAMR is defined as the percentage of idle TCH to the total available TCH for a particular cell below which FR TCH will be used as HR TCH when allocated to non-AMR MSs. This feature will be converting ongoing calls to HR along with new originating calls [5]. Value of all these HR parameters has to be increased to counteract TCH blocking. Results of HR changes are given in Table 4.

Note

HR tuning for cells with very high TCH utilization will not give the desired results as on high utilized cells most of the calls will already be running on HR.

Conclusion

This paper describes the various methods that can be implemented in GSM network to counteract TCH and SD blocking in the GSM network. Methods suggested and results documented corresponding to the methods in this paper, prove that these methods can be very effective in improving the blocking KPIs of the network. Augmentation to the SD and TCH KPIs improvement results are the points to remember and the notes mentioned in the paper are not just theoretical points but suggested after heedful and prudent observations and after analyzing the outcomes of the parameter optimizations in the live network.

As the final solution to the SD and TCH blocking problem is TRX addition and the other suggested solutions to the blocking problems may affect network quality parameters like SQI and sometimes can cause loss of revenue to the operator. These KPIs are monitored very closely by the TRAI and it even imposes penalty on the operators if the benchmark set by TRAI is not met.

A few years back, more emphasis was given to sites count by operators and its vendors. As of now, GSM sites count is approaching saturation, WCDMA sites count is increasing, and more prominence is given to KPI improvement by the operators.

KPI improvement is ceaseless, relentless process; RF and DT engineers are working continuously in offices and field, day and night which improves network KPIs, and customers satisfaction is the target for every GSM operator.

Acknowledgments I would like to express my sincere thanks to Mr. Gaurav Sharma for his kind support and guidance that inspired me to complete my research work on time. I would also like to thank D&P team of Ericsson India Pvt. Ltd. Jaipur, Mr. M. Somani (Circle Head, EIL, Jaipur), Mr. R. Tripathi (D&P Head, EIL, Jaipur), and Ms. Ruchika Singh (Senior Engineer) for their encouragement and belief in me to execute and implement this work in Ericsson, Jaipur. I would inevitably like to thank Mr. S. Arif Ali and Mr. K. Srinivasrao who helped me all the way through paper writing.

References

1. Lee, W.C.Y.: Wireless & Cellular Telecommunications, 3rd edn., International Edition, pp. 110–111. McGraw-Hill Education (Asia), New York (2006)
2. Rappaport, T.S.: Wireless Communications Principles and Practice, pp. 553–556. Dorling Kindersley (India) Pvt. Ltd. (2010)
3. Mishra, A.R., Nokia Networks: Advanced Cellular Network Planning And Optimisation 2G/2.5G/3G. Evolution TO 4G, p. 20. Wiley (2007). ISBN: 13 978-0-470-01471-4 (HB)
4. Ericsson Radio Systems AB: GSM System Survey, Student Text, EN/LZT 123 3321, R4A. Copyright © 1998 by Ericsson Radio Systems AB, pp. 65–197. https://www.academia.edu/6140754/Ericsson_GSM_System_Survey
5. User Description, Radio Network Parameters and Cell Design Data for Ericsson's GSM Systems, USER GUIDE. © Copyright Ericsson AB 2011, pp. 53–285. https://www.academia.edu/5467282/Winfol_Parameter

Design and Analysis of Right-Angled EBG Structure

Ajay Yadav, Dinesh Sethi, Priyanka Rahi and R.K. Khanna

Abstract A compact ultra-wideband microstrip antenna with double band-notched characteristics is presented in this paper. A *circular split ring resonator* (CSRR) and a *Right Angled electromagnetic band gap* (RA-EBG) design has been used to create double band-notched characteristics for WiMAX (3.3–3.6 GHz) and WLAN (5.1–5.8 GHz), respectively. Analysis of CSRR and RA-EBG shows EBG structure has advantages over CSRR to design notched band, such as tuneable notched frequency and notch-bandwidth controllable capacity. The proposed antenna has broad bandwidth and includes UWB band with VSWR <2.

Keywords RA-EBG antenna · Band stop antenna · UWB antenna · CSRR antenna

Introduction

Ultra-wideband has been widely accepted by researchers from academia and organizations, after declaration of unlicensed radio frequency band of 3.1–10.6 GHz for commercial use by federal communication commission (FCC) [1]. Microstrip antennas have been widely used to design UWB antennas due

Ajay Yadav (✉) · Priyanka Rahi
Department of ECE, GIT, Jaipur, Rajasthan 302022, India
e-mail: ajay.yadav.1981@ieee.org

Priyanka Rahi
e-mail: rahipriyanka1993@gmail.com

Dinesh Sethi
Department of ECE, SGVU, Jaipur, Rajasthan 302022, India
e-mail: dinesh.sethi@rediffmail.com

R.K. Khanna
Department of R&D and Dean, Vivekananda Global University,
VIT-Campus, Jaipur, Rajasthan 303905, India
e-mail: rkkhann.iitm@gmail.com

Table 1 EBG structure type and covered band

Ref. no.	Size (mm ²)	Band covered (GHz)	EBG type
[19]	38 × 40	3.1–10.6	M- EBG
[20]	35 × 39	3.1–10.6	Mushroom
[21]	30 × 35	3.1–10.2	Square
[22]	42 × 48.7	2–10.6	L-shape
[23]	30 × 32	3–11	Mushroom
[24]	40 × 40	2–12	Mushroom
[25]	40 × 40	2–12	Mushroom
[26]	38 × 40	3–12	Mushroom
Proposed	30 × 30	3–12.24	Right angled-shape

to the attractive merits like compact size, low cost, ease of fabrication, and good omnidirectional radiation [2]. UWB system suffers from electromagnetic interferences due to the existing narrowband wireless applications such as WiMAX operating in 3.3–3.6 GHz band (IEEE 802.16), WLAN operating in 5.1–5.8 GHz band (IEEE 802.11a).

In the last decade, various techniques have been suggested and presented to design UWB antennas with band-notched characteristics to solve the earlier discussed problems. Usually, people used various conventional methods to design UWB antenna with band-notching characteristics. These methods have included distinct slots on patch or on the ground plane-like, SRR, tuning stubs, bended strips, and resonated shapes on CPW, stepped impedance resonators (SIRs) or capacitively loaded grummet, open-end resonators and diffracted ground structures (DGS) [3–17].

Recently, distinct types of EBG designs have been presented and implemented in different applications such as reduction of the mutual coupling between two planes and to eliminate spurious responses of filtering characteristics [18]. In the literature some EBG structures have been presented to create band-notched characteristics like modified-EBG structure [19], mushroom-shape EBG structure on patch plane [20], rectangular EBG cell [21], SRR resonator [22], use of artificial magnetic conductor (AMC) EBG [23], EBG in feed line [24, 25] and mushroom-type EBG [26].

In this paper, we have proposed a RA-EBG single cell near radiating patch which creates band-notched characteristics for WLAN. The complete antenna size is 30 mm³ × 30 mm³ × 1.6 mm³. This paper also shows that approach of EBG structure to create tunable notch is better over CSRR. Here authors substantiate their own work presented in [27] with measured radiation patterns and group delay. Following Table 1 provides some useful information about the EBG structures.

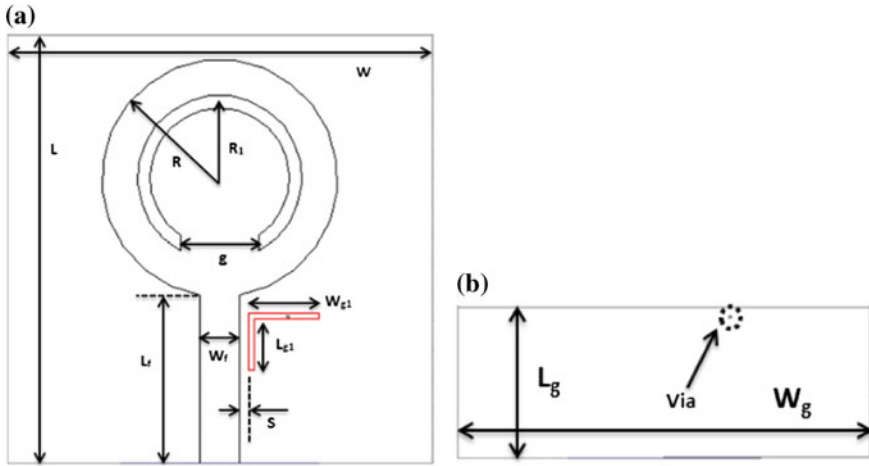


Fig. 1 a Proposed antenna top view. b Proposed antenna back view

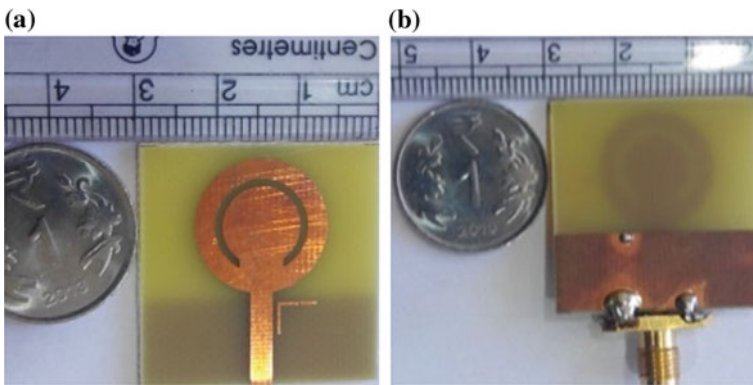


Fig. 2 Fabricated prototype antenna. a Top view. b Back view [27]

Antenna Building and Study

All the simulation and optimization of the proposed antenna has been done with the Ansoft HFSS 13. Configuration and geometry of suggested antenna is presented in Fig. 1. Fabricated prototype antenna is presented in Fig. 2. This antenna is designed on the FR-4 dielectric material, which has thickness of 1.6 mm, dielectric constant $\epsilon_r = 4.4$ and loss tangent of 0.02.

Table 2 Optimized dimensions of proposed antenna (mm)

Variable	W	L	R	$R1$	$R2$	g
Size (mm)	30	30	8.3	5.8	5	5.5
S	L_f	W_f	W_g	L_g	W_{g1}	L_{g1}
0.6	11.8	2.8	30	11	5	4

(a) *CSRR Antenna Design (WiMAX Notched Band)*

A CSRR provides filtering characteristic so, we have used a CSRR slot on radiating patch to create notch in WiMAX band. Figure 1a shows the antenna with CSRR slot, and its length is approximately $\lambda_g/2$. Proposed length of circular split ring resonator can be intended from the Eqs. (1) and (2).

$$L_{eq} = 2\pi * R_1 - g \tag{1}$$

$$f_c = \frac{C}{2 * L_{eq} * \sqrt{\frac{\epsilon_r + 1}{2}}} \tag{2}$$

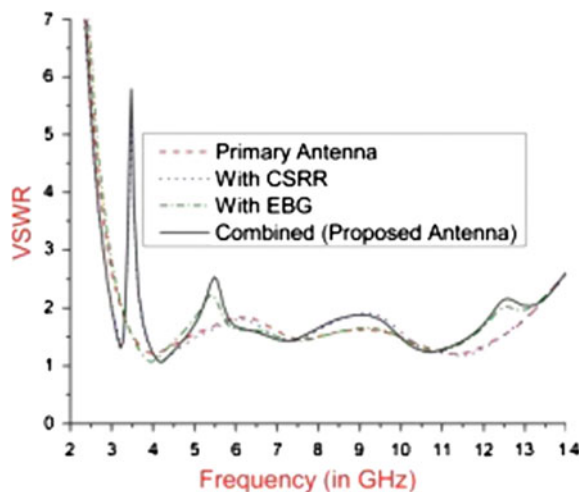
where g is 5.5 mm, R_1 is 5 mm and C is speed of light.

The value of equivalent length L_{eq} varied according to variation in gap “g” which is 5.5 mm. It is optimized to create notch at WiMAX band. All optimized dimensions of the proposed antenna are listed in Table 2.

(b) *RA-EBG Antenna (WLAN Notched Band)*

To create notch at WLAN (5.1–5.8 GHz) band we have proposed a RA-EBG cell grounded through via. The total length of RA-EBG resonator is 8.2 mm, which is approximately equal to the $\lambda_g/4$ calculated at 5.5 GHz for WLAN applications and can be calculated from Eq. (3) as given below.

Fig. 3 VSWR of proposed antenna



$$L = \frac{C}{4f\sqrt{\frac{\epsilon_r + 1}{2}}} \tag{3}$$

Dualband notch characteristic of proposed antenna have been achieved through the below described operation.

We have first designed a primary antenna (a circular patch antenna) which provides the UWB band as VSWR result shown in Fig. 3. To create notched characteristics for WiMAX applications a CSRR slot cut on circular patch and VSWR result is shown in Fig. 3. WLAN applications have been achieved by drawing an RA-EBG via near the right side of feed line and VSWR result is presented in Fig. 3. Suggested antenna is a combination of both the methods to create band-notching characteristics and the VSWR of proposed antenna (combined both CSRR and EBG) is presented in Fig. 3 by solid line.

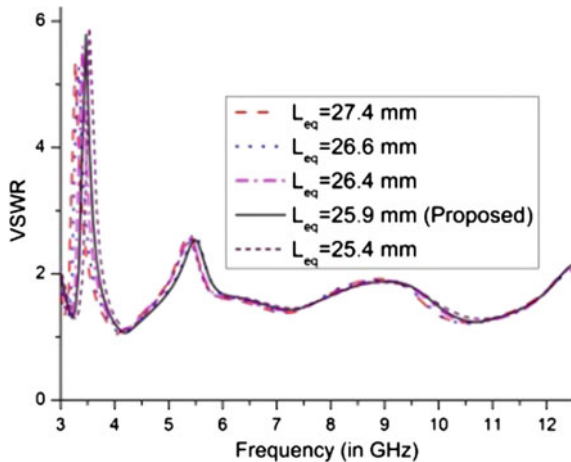


Fig. 4 VSWR variation due to CSRR length

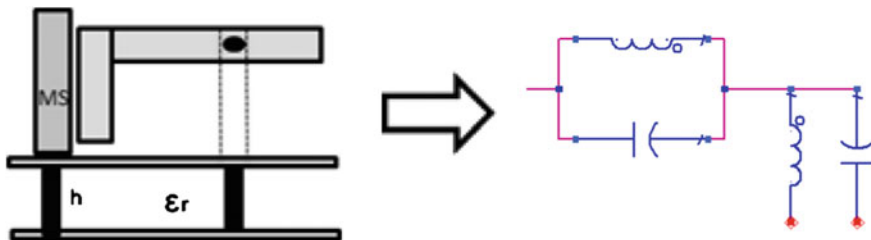


Fig. 5 Right-angled EBG structure and equivalent circuit

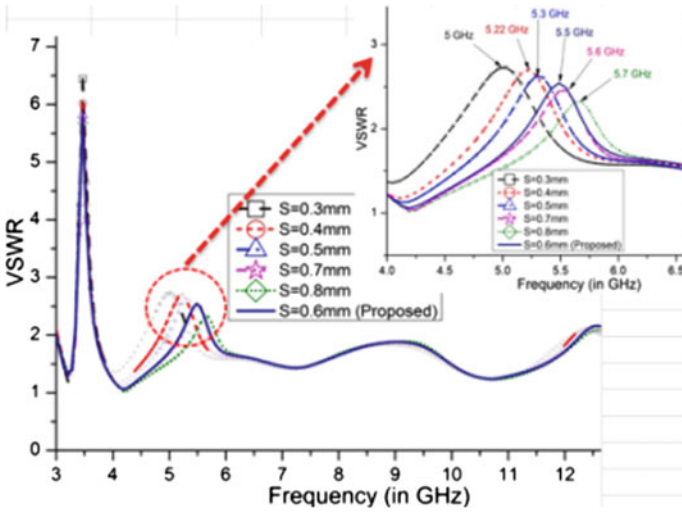


Fig. 6 VSWR variation with gap distance

We have varied gap size g over a range to optimize the equivalent length and VSWR result is shown in Fig. 4.

(c) *Equivalent Circuit of RA-EBG Structure*

Equivalent circuit of proposed EBG can be present as in Fig. 5. Resonance frequency of the circuit is given by

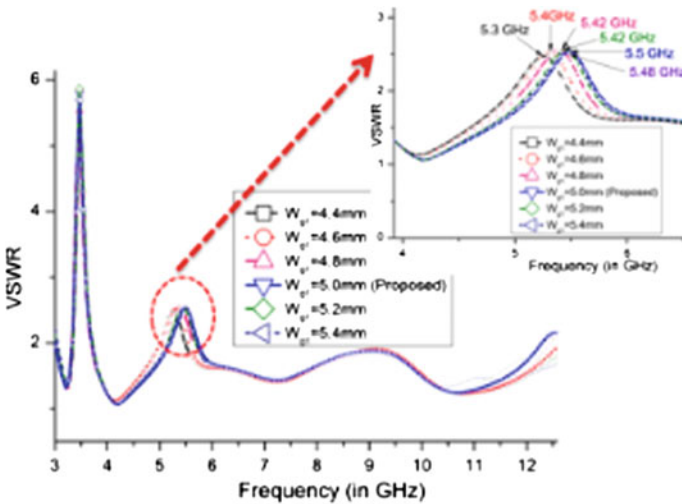


Fig. 7 VSWR variation for L_{g1} with $W_{g1} = 5$ mm

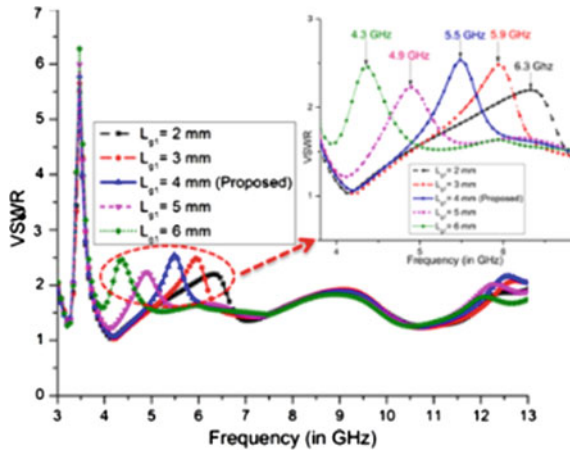


Fig. 8 VSWR variation for W_{g1} with $L_{g1} = 4$ mm

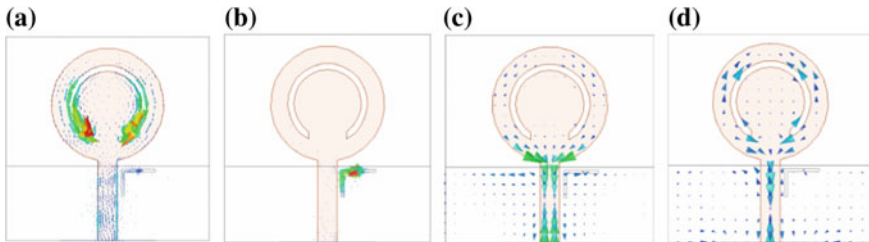


Fig. 9 Current distribution. a 3.5 GHz. b 5.5 GHz. c 6.5 GHz. d 7.5 GHz

$$\omega o = \frac{1}{\sqrt{L_{eq} C_{eq}}} \tag{4}$$

Near ωo , the surface impedance is much higher than free space impedance.

Dimensions of RA-EBG like L_{g1} , W_{g1} , and gap S between feed line and EBG can be varied over a range of optimization values. Gap between feed line and RA-EBG structure has played a great role to tune the band-notched characteristics that also show the variation in capacitance. Figure 6 shows the effect of gap variation on the band-notching characteristics. Effects of variation in W_{g1} of EBG during optimization are presented in Fig. 7.

Effects on VSWR due to variation in L_{g1} of EBG during optimization are presented in Fig. 8. Length optimization shows that we can tune and control the notched band according to our application requirements as it varies from C-Band to WLAN (including Hyper LAN).

From above optimization processes of EBG structure, we can say that to create tunable band notched, EBG structure approach is better over conventional slots and CSRR methods. Vector current effects on the suggested antenna at four distinct

frequencies are presented in Fig. 9. At a passband frequency of 6.5 and 7.5 GHz, i.e., passband for suggested antenna, shown in Fig. 9c, d whereas in Fig. 9a, b, for first notched band 3.5 GHz, and the second notched band 5.5 GHz, respectively.

Result and Discussion

The measurement of the suggested antenna was performed with Anritsu vector network analyser for return loss, VSWR, group delay and anechoic chamber for radiation pattern (E- and H-field co- and cross-polarization). A simulated and

Fig. 10 Return loss S_{11} versus frequency

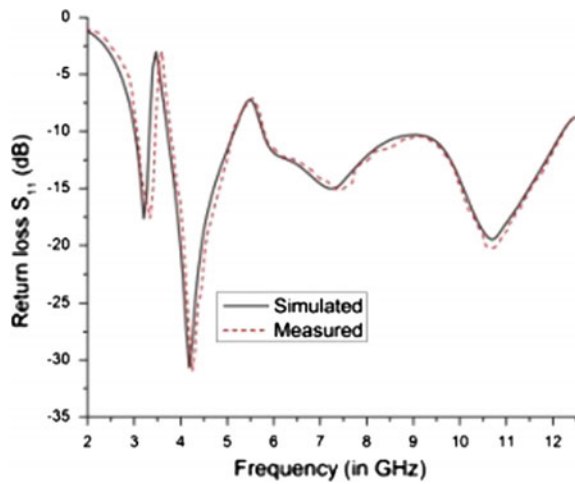
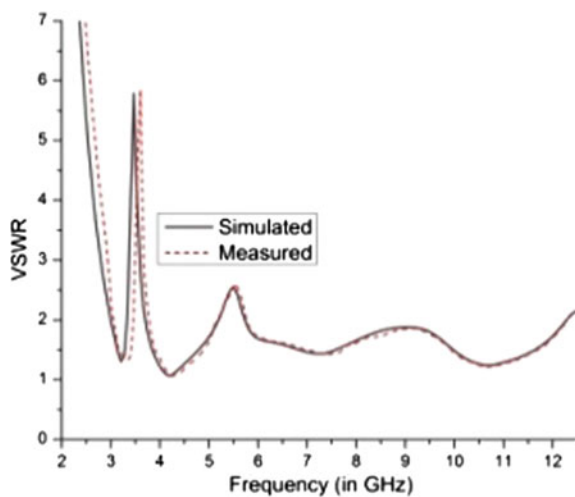


Fig. 11 VSWR versus frequency



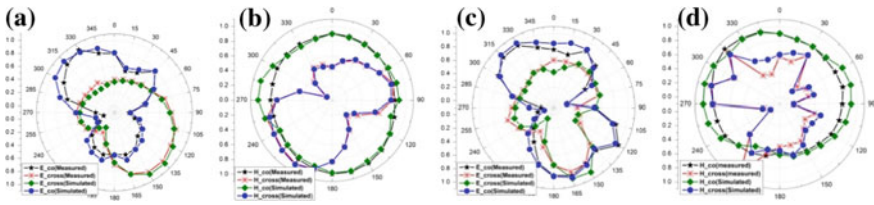


Fig. 12 Measured and simulated, normalized E- and H-field patterns. **a** E-field at 3.1 GHz. **b** H-field at 3.1 GHz. **c** E-field at 4.5 GHz. **d** H-field at 4.5 GHz

Fig. 13 Simulated radiation efficiency

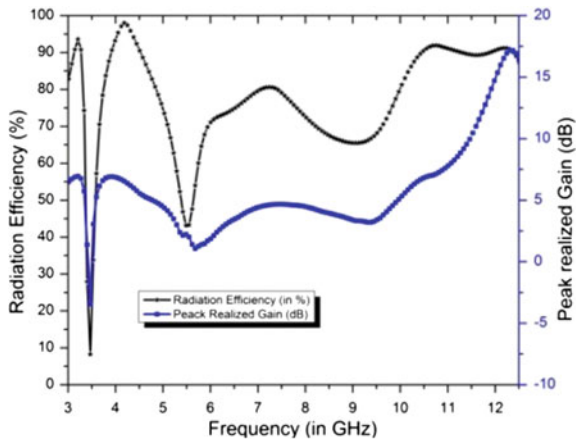
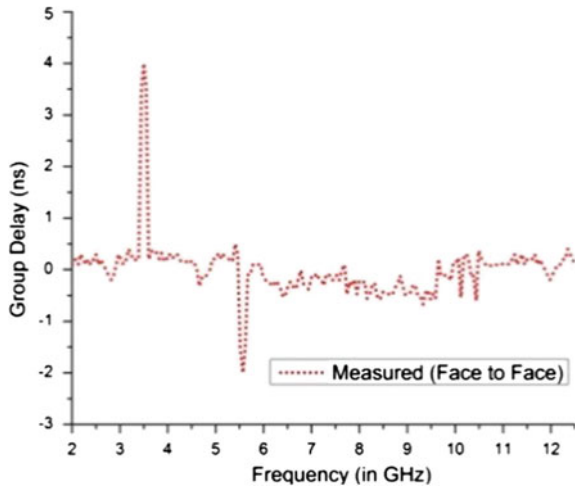


Fig. 14 Measured group delay and peak realized gain



measured result of suggested antenna for return loss and VSWR is presented in Figs. 10 and 11 respectively. The simulated and measured normalized E-field and H-field co- and cross-polarization patterns at 3.1 and 4.5 GHz are presented by Fig. 12a–d. The antenna shows omnidirectional radiation patterns in the H-plane and dipole-like radiation patterns in E-plane. Measured radiation pattern shows the good agreement with simulated results. The intended realized peak gain and radiation efficiency of the suggested antenna is shown in Fig. 13. Radiation efficiency and realized peak gain both are approximately zero for the WLAN band, while for WiMAX band peak realized gain is -5 dB.

Measured group delay of suggested antenna is presented in Fig. 14. Group delay measurement has been performed on two identical antennas face to face.

Conclusion

Proposed antenna covers UWB band and band stop filtering characteristics of CSRR and EBG have been used to minimize the interference problems from WLAN and WiMAX applications. This antenna has simple design and compact size of $30 \text{ mm}^2 \times 30 \text{ mm}^2$. Results and investigation of this antenna indicates that EBG approach is better than slot method to produce band notch.

Acknowledgments Authors are thankful to Profs. Ananjan Basu and S.K. Koul, (CARE), IIT Delhi, New Delhi, INDIA for providing the measuring facilities and useful discussions.

References

1. First report and order, Revision of part 15 of the commission's rule regarding ultra-wideband transmission system FCC 02-48, Federal Communications Commission (2002)
2. Chen, Z.N.: UWB antennas: from hype, promise to reality. In: IEEE Antennas and Propagation Conference, pp. 19–22 (2007)
3. Lee, W.S., Kim, K.J., Kim, D.Z., Yu, J.W.: Compact frequency notched wideband planar monopole antenna with an L-shaped ground plane. *Microw. Opt. Technol. Lett.* **46**(4), 340–343 (2005)
4. Fan, F., Yan, Z., Zhang, T., Song, Y.: Ultra-wideband planar monopole antenna with dual stopbands. *Microw. Opt. Technol. Lett.* **52**(1), 138–141 (2010)
5. Kim, Y., Kwon, D.H.: CPW-fed planar ultrawideband antenna having a frequency band notch functions. *Electron. Lett.* **40**(7), 403–404 (2004)
6. Chu, Q.X., Yang, Y.Y.: A compact ultrawideband antenna with 3.4/5.5 GHz dual band-notched characteristics. *IEEE Trans. Antennas Propag.* **56**(12), 3637–3644 (2008)
7. Qu, S.W., Li, J.L., Xue, Q.: A band-notched ultrawideband printed monopole antenna. *IEEE Antennas Wirel. Propag. Lett.* **5**, 495–498 (2006)
8. Li, W.T., Shi, X.W., Hei, Y.Q.: Novel planar UWB monopole antenna with triple band-notched characteristics. *IEEE Antennas Wirel. Propag. Lett.* **8**, 1094–1098 (2009)
9. Tang, J.C., Chen, M., Li, Y.J.: A novel planar UWB antenna with triple band-notched characteristics. In: IEEE Proceedings, pp. 340–343, June 2012. ISBN: 978-1-4673-1800

10. Sung, Y.: UWB monopole antenna with two notched bands based on the folded stepped impedance resonator. *IEEE Antennas Wirel. Propag. Lett.* **11**, 500–502 (2012)
11. Lin, C.C., Jin, P., Ziolkowski, R.W.: Single, dual and tri-band-notched ultra-wideband (UWB) antennas using Capacitively Loaded Loop (CLL) resonators. *IEEE Trans. Antennas Propag.* **60**(1), 102–109 (2012)
12. Chu, Q.X., Yang, Y.Y.: A compact ultrawideband antenna with 3.4/5.5 GHz dual band-notched characteristics. *IEEE Trans. Antennas Propag.* **56**(12), 3637–44 (2008)
13. Peng Gao, L.X., Dai, J., He, S., Zheng, Y.: Compact printed wide slot UWB antenna with 3.4/5.5 GHz dual band-notched characteristics. *IEEE Antennas Wirel. Propag. Lett.* **12**, 983–986 (2013)
14. Nguyen, D.T., Lee, D.H., Park, H.C.: Design and analysis of printed triple band-notched UWB antenna. *IEEE Antennas Wirel. Propag. Lett.* **10**, 403–406 (2011)
15. Lai, H.Y., Lei, Z.Y., Xie, Y.J., Ning, G.L., Yang, K.: UWB antenna with dual band rejection for WLAN/WiMAX bands using CSRRs. *PIER Lett.* **26**, 69–78 (2011)
16. Wang, Z.Q., Hong, W., Kuai, Z.Q., Yu, C., Zhang, Y., Dong, Y.D.: Compact ultra-wideband antennas with multiple notches. In: *IEEE, ICMMT2008 Proceedings*. ISSN: 978-1-4244-1880-0/2008
17. Yadav, A., Malav, A.: Microstrip UWB antenna with WiMax notched band characteristics. *Int. J. Recent Res. Rev.* **VII**(2) (2014). ISSN: 2277-8322
18. Yang, F., Samii, Y.R.: Microstrip antennas integrated with electromagnetic band-gap (EBG) structures: a low mutual coupling design for array applications. *IEEE Trans. Antennas Propag.* **51**(10), 2936–2946 (2003)
19. Liu, H., Xu, Z.: Design of UWB Monopole Antenna with Dual Notched Bands Using One Modified Electromagnetic Bandgap Structure. Hindwi Publishing Corporation, vol. 2013, articl.id 917965
20. Yazdi, M., Komjani, N.: Design of a band-notched UWB monopole antenna by means of an EBG structure. *IEEE Antennas Wirel. Propag. Lett.* **10** (2011)
21. Raghavan, S., Anandkumar, Ch., Subbarao, A., Ramaraj, M., Pandeewari, R.: A compact ultra wideband EBG antenna with band notched characteristics. In: *PIERS Proceedings, Moscow, Russia, 19–23 Aug 2012*
22. Yin, X.C., Ruan, C.L., Mo, S.G., Ding, C.Y., Chu, J.-H.: A compact ultra-wideband microstrip antenna with multiple notches. *PIER* **84**, 321–332 (2008)
23. Kumar, P., Alex, Z.C.: Realization of band-notch UWB monopole antenna using AMC structure. *IJET* **5**(3), 3020–3028 (2013). ISSN: 0975-4024
24. Yang, T.Y., Song, C.Y., Lin, W.W., Yang, X.L.: A new band-notched UWB antenna based on EBG structure. In: *IEEE, IWMMWCST Proceedings*. 978-1-4673-5504-9/2013
25. Song, C.Y., Yang, T.Y., Lin, W.W., Yang, X.L.: Design of a band-notched UWB antenna based on EBG structure. In: *Proceedings of 2013 IEEE International Conference on Applied Superconductivity and Electromagnetic, ID3106 Devices, Beijing, China, 25–27 Oct 2013*. 978-1-4799-0070-1/13
26. Peng, L., Ruan, C.L.: UWB band-notched monopole antenna design using electromagnetic-bandgap structures. *IEEE Trans.MTTs.* **59**(4) (2011)
27. Sethi, D., Yadav, A., Khanna, R.K.: Dual band notched ultra wideband microstrip antenna with CSRR slot and EBG structure. *IJERT* **3**(9), 791–795 (2014)

High-Speed Packet Encoded Error Correction Technique for Wireless HD Video Streaming

C.P. Latha, M.B. Manjunatha and A. Mohsin Khan

Abstract The commercial images videos presently need to be modified with high definition (HD) because of its high quality and resolution. But in real-time environment flickering is a major problem associated in HD because of packet loss during transmission. To overcome this problem, in this paper we have proposed a high-speed packet encoded error correction technique and comparative analysis of various error correction methods with reference to speed and capacity to correct errors. The time required for the computation for proposed work is 0.017 s/frame in HD video streaming.

Keywords Flickering · PSNR · Packet encoding · High definition

Introduction

The HD video standard has been developed as the successor to standard definition (SD). HD refers to streaming of high-quality video with multichannel audio signal. In most traditional method of store-and-forward HD streaming includes elaborate buffering techniques are used in turn that introduces significant latencies because of massive amount of data. Already HD video has delay problems due to buffering. Flickering is a major problem experienced because of packet loss due to buffered data. Through retransmission flickering effect can be reduced. But the end-to-end

C.P. Latha (✉)
Jain University, Bangalore, Karnataka, India
e-mail: cplathahms.12@gmail.com

M.B. Manjunatha
AIT, Tumkur, Karnataka, India
e-mail: manju.kari29@gmail.com

A.M. Khan
HMSIT, Tumkur, Karnataka, India
e-mail: mk_jak@rediffmail.com

latency will be further increase in retransmission [1–3]. In this paper an attempt has been made to optimize packet losses and improvement in latency.

In this proposed method, the frames of HD video are divided into packets of 216 bytes. Here packets are encoded for error correction such that the MSB bits of previous packets will be saved in LSB bits of next packet during transmission. The proposed method has given better performance in various error correction techniques.

Communication System

A simple communication system is shown in Fig. 1. HD video streaming connected has a source where the stream is subjected to proposed encoding block from where the first MSB bits of previous packet will be saved in first LSB bits of next packet and be fed to Reed Solomon (RS) encoder. After encoding, modulated signal passes through AWGN channel.

The error-free signals reached at the receiver after decoded through RS decoder and proposed decoding block. Hence avoids the problem of flickering of video stream without retransmission.

Error Correction Method

In our proposed scheme we divide the video frame into block of 216 bytes and 8 bytes are added as a parity to form a RS code word (224, 216) which has the error correction capability up to 4 bytes. For every video frame if the error is more than 5 bytes RS decoder fails to correct the errors [4, 5]. When the number of errors is more than 5 bytes in the frame our proposed error correction method capabilities of optimizing the errors by giving better performance, as compared to RS encoder. After encoding the each frame in the proposed method PSNR calculated is 51/frame. In our proposed work priority is given to MSB bits of each pixel of the frame.

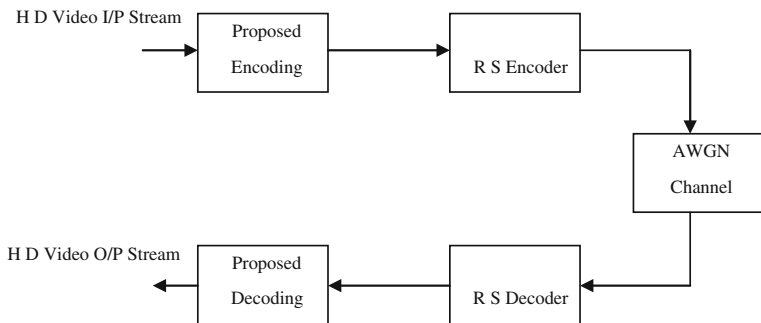


Fig. 1 Communication block

Table 1 PSNR encoding with MSB errors

Number of pixels having MSBs Error/Frame (%)	PSNR after encoding without MSB Error/Frame	PSNR after encoding with MSB Error/Frame
100	51	5.98
75	51	7.23
50	51	8.99
25	51	12.00

Suppose the MSB bits of all the pixel of a frame are in error then it results in PSNR of 5.98/frame. This implies that the maximum value of PSNR depends on MSB bits of the pixel in frame. Table 1 below indicates the importance of MSB bits in relation with PSNR.

(a) *Encoding procedure for proposed method.*

- Step1: We consider 1080p25 HD videos with frame size of 1920×1080 pixels encoded as RGB444 with 8 bits per pixel
- Step2: Here each frame is divided into the packets of size 216 bytes
- Step3: The packets of each frame are encoded such that the MSB bit of each pixels of previous packet will be saved in the LSB bit of next packet pixels
- Step4: The Step3 will be progressively repeated till the encoding is complete for full frame. The successive frames encoded accordingly for the complete video stream

(b) *Decoding procedure for proposed method.*

- Step1: At the decoder the frames are similarly divided into packets of size 216 bytes
- Step2: The packets are decoded in such a way that the LSB bit of each PIXELS of forth coming packet is saved in the MSB bit of each pixels of already received packet
- Step3: The Step2 is repeated progressively for successive frames

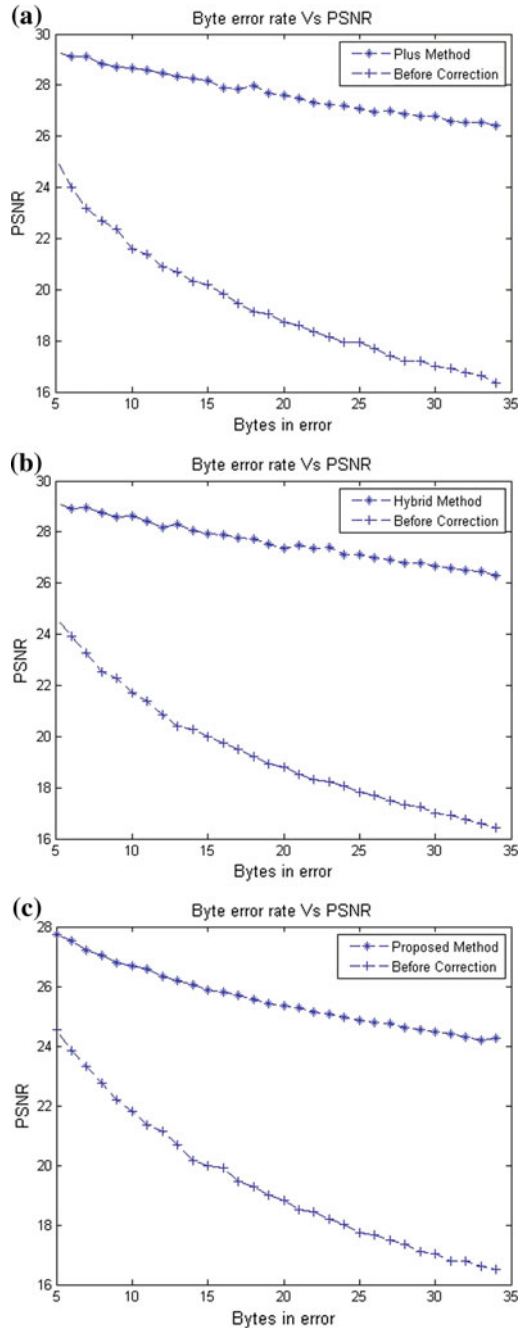
Analysis and Results

The error correction methods based on synonymous pixel information matching using 4 MSB bits of each neighboring pixels are proposed and discussed in [4, 5], out of which the plus method and the hybrid method have given better performance.

Table 2 Computation speed with PSNR

Error correction method	Computation speed in s/frame	Improvement in PSNR approximately (db)
Proposed	0.017	7
Plus	0.021	7
Hybrid	0.023	7.5

Fig. 2 a PSNR versus bytes in error for plus method. **b** PSNR versus bytes in error for hybrid method. **c** PSNR versus bytes in error for proposed method



Since HD video streaming requires fast computation at the receiver side to maintain high quality keeping this in view we proposed a new scheme of error correction technique. The proposed scheme gives better performance in computation speed and similar in error correction. Table 2 below shows the comparative analysis of [4, 5] said methods with respect to computation speed and PSNR.

Simulation results of above-discussed method are shown before error correction with RS encoder and after error correction with RS encoder including proposed scheme with reference to PSNR versus bytes in errors as shown in Fig. 2a–c.

Conclusion

In this work we proposed a new error correction scheme which has given better performance in computation speed with similar efficiency in error correction compared with other schemes. The simulation results for the proposed method reveal the computation speed of 0.017 s/frame.

References

1. High Definition Live Streaming. Society of Motion Picture Television Engineers
2. Apostolopoulos, J.G., Tan, W., Wee, S.J.: Video Streaming: Concepts, Algorithms and Systems. Streaming Media Systems Group, 18 Sept 2002
3. Ryan lawler: Next-Gen Video Format H.265 is Approved, Paving the Way for High-Quality Video on Low-Bandwidth Networks. Friday, 25 Jan 2009, IDC
4. Latha, C.P., Manjunatha, M.B., Khan, A.M.: Novel error correction schemes for enhanced wireless high definition video streaming. *Int. J. Eng. Sci. Innov. Technol.* 3(3) (2014). ISSN: 2319-5967. ISO 9001:2008 certified
5. Manohara, M., Mudumbai, R., Gibson, J.: Error correction scheme for uncompressed HD video over wireless. University of California Santa Barbara CA, ICME (2009)

Review of Circular Polarization Techniques for Design of Microstrip Patch Antenna

Madhuri Sahal and V.N. Tiwari

Abstract This paper is a review of the techniques used to generate circular polarized radiation with reference to the feeding techniques. Circular polarized antennas are increasingly gaining importance in wireless communication. The usable bandwidth is the overlap of axial ratio bandwidth and impedance bandwidth. Cross-polarization is a measure of the polarization purity of circular polarized antenna. Dual circular polarization techniques involve the generation of both right-handed circular polarized radiation (RHCP) and left-handed circular polarization (LHCP) using the same antenna. Dual circular polarized antennas may be used for either frequency reuse or diversity applications.

Keywords Circular polarization · Axial ratio · Impedance bandwidth · Single-feed · Dual-feed · Orthogonal

Introduction

Microstrip patch antennas are gaining attention of researchers for wireless communication, as they offer the benefits of low profile, light weight, compact, conformal to surfaces, and easy fabrication. However, major limitations of microstrip antennas are low gain and narrow bandwidth. Several techniques to increase the impedance bandwidth of patch antennas, such as aperture-coupled feed [1], L-shaped probe feed [2], U-slotted patch [3], have been proposed.

Communication using linear polarized antennas require the transmit and receive antenna to be of the same polarization and accurately aligned. Circular polarized antennas (referred to as CP antennas hereafter) allow signal reception irrespective of

Madhuri Sahal (✉) · V.N. Tiwari
Department of Electronics & Communication Engineering,
Manipal University, Jaipur, India
e-mail: madhuri.sahal@jaipur.manipal.edu

V.N. Tiwari
e-mail: vivekanand.tiwari@jaipur.manipal.edu

the orientation of transmit and receive antenna, and thus are seeking attention of the research fraternity. Circular polarized antennas possess the inherent ability to suppress multipath interference. Circular polarized microstrip patch antennas are widely used in portable/hand held devices, for example, RFID reader antenna, WLAN, GPS, rectenna for energy harvesting, mobile phone antenna, etc.

Generating circular polarized radiation involves exciting two equal-amplitude orthogonal modes. Feed position and feed technique decides the impedance bandwidth of the antenna. The overlap region of SWR bandwidth ($VSWR < 2$ or $S_{11} < -10$ dB) and axial ratio bandwidth ($AR < 3$ dB) decides the usable bandwidth of a CP microstrip patch antenna.

A number of techniques to generate circular polarized radiation are available in the literature. Circular polarization techniques may be classified as single feed and dual feed.

Single-Feed Configuration

Generating circular polarized radiation using single-feed configuration requires slight perturbation of the antenna structure, and optimizing the position of the perturbation with respect to the feed to excite orthogonal modes. Perturbation approaches for single-feed CP configuration involve the insertion of cross- or Y-shaped slots, slits [2], truncating corners [3], spur lines, stub loading [4] in the boundary of the patch. The single-feed circularly polarized antennas are fed at 45° with respect to the perturbation.

Different types of feeding techniques may be used for the circular polarized microstrip patch antenna. Coaxial probe feed [3–7] though simple, provides only narrow bandwidth. The authors have demonstrated a directional, wideband antenna having SWR bandwidth of 54.2 % fed using a nonplanar Γ -shaped feeding structure and two meandering strips [2]. The antenna shows a high gain of 9 dBi and good cross-polarization characteristics, polarization less than -27 dB over the entire operating frequency range.

In [3], truncated corner square patch is used to generate circular polarization characteristics. The antenna incorporates the use of U-slot to increase bandwidth, offers low gain (4.5 dBi), and AR bandwidth is 3.2 % at L band frequencies. By introducing asymmetrical triangular shaped slits in diagonal direction of square microstrip patches [5], the single coaxial-feed microstrip patch antenna is realized for CP radiation with compact antenna size. The impedance and axial ratio bandwidths are small around 2.5 and 0.5 %.

In [4] a reduction of size in the CP patch antenna is obtained by loading parasitic shorting strips, which provide a capacitive and inductive loading to the patch, hence concentrating the current from the patch along the shorting strip. The CP antenna has low impedance bandwidth and axial ratio bandwidth of 3.25 and 0.682 %, respectively. Also the gain is also relatively low, only 3.8 dBi. Single-feed techniques for CP generation offer the advantages of compactness and simplicity, but provide only

narrow axial ratio bandwidth. The impedance bandwidth can be enhanced, but the designs either cause low antenna gain (<6 dBi) or low axial ratio bandwidth.

An annular-ring slot antenna (ARSA) with inverted L-shaped modified stripline feed [8] to obtain high AR bandwidth of the order of 46 and 56 %, respectively in L and S bands is proposed. The two hat-shaped patches produce two equal-amplitude orthogonal resonant modes by perturbing the current distribution in the ring slot.

Antenna arrays may be used to improve the antenna gain. SRRs are integrated with a 2×2 E-shaped microstrip patch antenna array [9] in order to reduce cross-polarization and achieves a bandwidth of 8.5 % and achieve a gain of 12.60 dBi.

Some structures like defected ground structure, different meta-structures or resonators integrated with microstrip antenna, that perturb or suppress some property of the antenna are also employed to generate CP radiation in conjunction with patch antenna [6, 10]. A low-profile metamaterial-loaded patch antenna [6] is proposed to generate circularly polarized radiation. It uses single feed and is loaded with CRLH transmission line (mushroom-like) structures and inductive reactive impedance surface (RIS) for miniaturization and bandwidth enhancement. Two orthogonally polarized modes that are located in the left-handed (LH) region are simultaneously excited to achieve CP radiation. The CRLH mushroom-like structure resonates at a lower frequency compared to the microstrip patch. Circular polarization is obtained by either of the two techniques: by changing width-to-length ratio of the patch or the dimensions of the mushroom-like structure. Use of coaxial feed implies low impedance and axial ratio bandwidths. The antenna has an impedance bandwidth of 4.6 % and axial ratio bandwidth of 1.46 %. The bandwidth may be improved by means of stacking, but it causes undesired coupling that causes surface wave effects and hence reduces the efficiency. Gain of the antenna is low, only 2.98 dBi.

The arc-shaped DGS is shown to suppress the cross-polarization radiation by 10–12 dB in [10]. Feed positions affect only the E-plane cross-polar radiation levels.

In [11], the etched hole in truncated square patch allows the positive mode to have decreased resonance frequency; the negative mode is achieved using the 2×2 triangle mushroom antenna. The antenna exhibits peak gain of 6.26 and 6.97 dB, respectively, with CP bandwidth around 1 %.

A single-feed aperture-coupled fed patch antenna loaded with an S-shaped slot is designed for dual-band CP radiation for GPS applications in [12]. Asymmetrical S-shaped slot acts as perturbing structure to excite two orthogonal modes for CP operation at the lower band. The S-shaped is responsible for resonance in upper band and causes CP radiation in the upper band.

Dual-Feed/Multiple-Feed Configuration

Dual-feed/Multiple-feed configuration is based on the sequential phase-rotation technique to generate CP radiation with low cross-polarization and higher axial ratio bandwidth. Dual-feed configuration results in the sacrifice of compactness of

the antenna in order to accommodate the feed network, simultaneously improving axial ratio bandwidth.

A circular hook shaped microstrip line feed is used to feed the square patch by aperture-coupled technique through four Γ -shaped slots that generate four sequentially phased sources to excite the single layer patch antenna in [1]. The antenna exhibits peak gain of 7.4 dBi at 2.55 GHz and cross-polarization radiation is below 15 dB. Though the design enhances impedance bandwidth and axial ratio bandwidth, the achieved front-to-back ratio is only 5 dB. The front-to-back ratio may be increased using a reflector, which would increase the antenna size.

In [13], single-feed patch antenna consisting of low-profile stacked radiators is used to obtain dual-frequency circular polarization. Stub and slit loaded patch along the diagonal are used to obtain CP radiation. The design has poor CP bandwidths less than 1 % and low antenna gains 2.3 dBi, 2.4 dBi in GPS, and SDMB bands. A circular patch antenna having dual capacitively coupled feeds are used for broadband operation in [7]. A Wilkinson power divider network is used to excite orthogonal modes. A 7.0 dBi gain and axial ratio bandwidth 35 % (relative to center frequency 1843 MHz) is obtained. In [14], sequential phase-rotation technique is used to achieve dual circular polarized radiation from a 2×2 array of dual-frequency ACPAs; the dimensions of the patch correspond to the two frequency bands. The array is fed using stripline feed and Wilkinson power dividers. The antenna exhibits AR < 1.2 dB and isolation between the two modes is larger than 26 dB. The sequential rotation technique is used to achieve dual circular polarization properties of a 2×2 array of dual-frequency ACMAs. The proposed design [13] uses stripline feed and Wilkinson power dividers to achieve AR < 1.2 dB and isolation between the two modes exceeds 26 dB.

A circular patch antenna with dual capacitively coupled feeds connected to a Wilkinson power divider with a 90° phase shift between its two output feed lines are used for broadband operation [7]. Isolation between the two feeds is achieved using a $100\text{-}\Omega$ chip resistor in the power divider network. A 7.0 dBi gain and axial ratio bandwidth 35 % (relative to center frequency 1843 MHz) is obtained.

For applications that demand polarization diversity or enhance the spectrum efficiency by means of frequency reuse, it is desirable to design dual circular polarized antennas. In [15], a compact dual-feed, dual-polarized patch antenna for GPS applications (at center frequency of 1575.42 MHz) is proposed. The orthogonal feed excites two linearly polarized waves with a phase shift of 90° . A high permittivity substrate and four L-shaped slots at the center of the square patch that cause meandering of current path to obtain a reduction in antenna size at the cost of antenna gain and impedance bandwidth.

In [16], a compact CP square microstrip antenna employing an RF–dc power conversion circuit is proposed for RF energy harvesting for WSN at 2.45 GHz. The antenna is aperture-coupled fed by means of a cross-shaped slot etched in the ground plane and uses a band pass filter for harmonic rejections. Two linear polarized signals with a 90° phase shift are used to obtain CP characteristics, and the antenna generates LHCP. The cross-polar radiation level is below the copolar radiation by 0.7 dB at broadside. A pair of L-shaped stubs is loaded on adjacent

edges of a truncated corner patch [17] to excite an outer mode and inner mode for achieving unidirectional CP characteristics over dual bands. The antenna achieves low CP bandwidth, and is fed by a meandering probe. The frequency ratio is dependent on stub length.

A branch-line coupler [18] is used to feed a dual CP microstrip patch antenna with wideband isolation for RFID application between transmit and receive ports. The BLC provides dual CP radiation by coupling to the patch through H-shaped slots. BLC is located below the ground and maintains the CP purity because of its separation from the ground plane. A stacked patch antenna with a perpendicular feed substrate [19] is designed to generate CP characteristics. Coupling from the stacked patch to the perpendicular microstrip feed is through a slot in the ground plane of both the stacked patch and perpendicular substrate. The limitations of the design are the nonplanar structure, the sensitivity to the gap between the orthogonal substrates. The feed network uses Wilkinson power dividers to increase isolation between the outputs. An eight-element array is used to increase the gain and obtain wide angle scanning capability, but only a low CP bandwidth (2.8 %) is achieved.

Circular polarization in dual bands having a small frequency ratio of 1.18 is achieved by employing a circular patch below the rotated rectangular patch in [20]. The circular patch provides resonance a higher frequency band, and gives capacitive loading and hence tunes the operating frequency of the lower band. The rectangular patch and circular patch can be arranged on opposite sides of a thin substrate and fed by a single slot. A serial aperture-coupled feed is used to feed the two patches in [21]. The antenna comprises of a square patch enclosed in a square-shaped ring patch. Energy is coupled to the patch by means of cross-shaped slot, whereas the energy is coupled to the ring through diamond slot. The resulting dual-band CP antenna operates at 0.915 and 2.45 GHz bands.

In [22], use of quad feed network along with semi fan annular patches has been presented. The authors demonstrated a wide CP bandwidth equal to 72 %. QSFA patches improve the CP BW and reduce the antenna size effectively. In [23], CP DRA loaded with a modified circular patch is proposed for dual-band applications. The antenna is centrally fed by a coaxial probe, giving omnidirectional patterns with different senses of CP in two bands. Circular patch has four identical arc-shaped curved branches (oriented in a counterclockwise direction) to generate RHCP for patch and LHCP for DRA band. The patch not only functions as a polarizer that converts the omnidirectional LP fields of DRA mode into CP fields, but it also provides another resonance mode to realize a dual-band operation. In [24], an omnidirectional dual-band dual CP antenna uses TM_{01} and TM_{02} modes to generate wide beam radiation patterns. The antenna comprises of a circular patch having eight curved slots and a disk-loaded coaxial probe, which are employed for generating horizontal and vertical polarizations. An annular-ring slot is used to obtain good impedance matching at both resonant modes. Due to symmetrical structure, the phase difference between the vertical and horizontal polarizations is 90° . Hence, good omnidirectional CP properties in the azimuth plane at the cost of gain are obtained. The gains at lower and upper frequency are 0.1 and 1.1 dBic, respectively.

Conclusion

The use of dual-polarized antennas to achieve frequency diversity or frequency reuse brings about the need for design of dual circularly polarized antennas for wireless communication, where the orientation of the receiver being random with respect to that of receiver limits the use of linearly polarized antennas. Extensive research is being carried out on allied designs for obtaining dual circularly polarized radiation using microstrip patch antennas with special emphasis on enhancement of circular polarized bandwidth, gain, unidirectional radiation pattern, and cross-polarization reduction.

References

1. Hau, W.L., Ka, M.M., Ka, F.C.: Novel aperture-coupled microstrip-line feed for circularly polarized patch antenna. *Prog. Electromagnet. Res.* **144**, 1–9 (2014)
2. Jia-Yue, Z., Zhi-Ya, Z., Yang, L., Guang, F., Shu-Xi, G.: Wideband patch antenna with stable high gain and low cross-polarization characteristics. *Prog. Electromagnet. Res. Lett.* **45**, 35–38 (2014)
3. Ka, Y.L., Kwai-Man, L., Kai, F.L., Hang, W., Kung, B.N.: Small circularly polarized U-slot wideband patch antenna. *IEEE Antennas Wirel. Propag. Lett.* **10**, 87–90 (2011)
4. Hang, W., Kwok, K.S., Kung, B.N., Kwai, M.L., Chi, H.C., Quan, X.: Virtually shorted patch antenna for circular polarization. *IEEE Antennas Wirel. Propag. Lett.* **9**, 1213–1216 (2010)
5. Nasimuddin, Z.X.Q., Zhi, N.C.: Compact asymmetric-slit microstrip antennas for circular polarization. *IEEE Trans. Antennas Propag.* **59**(1), 285–288 (2011)
6. Yuandan, D., Hiroshi, T., Tatsuo, I.: Compact circularly-polarized patch antenna loaded with metamaterial structures. *IEEE Trans. Antennas Propag.* **59**(11), 4329–4334 (2011)
7. Kin-Lu, W., Tzung-Wern, C.: Broad-band single-patch circularly polarized microstrip antenna with dual capacitively coupled feeds. *IEEE Trans. Antennas Propag.* **49**(1), 41–44 (2001)
8. Jia-Yi, S., Wei-Hung, C.: Axial-ratio-bandwidth enhancement of a microstrip-line-fed circularly polarized annular-ring slot antenna. *IEEE Trans. Antennas Propag.* **59**(7), 2450–2456 (2011)
9. Chandan, K.G., Susanta, K.P.: Cross-polarization reduction of E- shaped microstrip array using spiral-ring resonator. *Prog. Electromagnet. Res. C* **38**, 217–227 (2013)
10. Chandrakanta, K., Debatosh, G.: Nature of cross-polarized radiations from probe-fed circular microstrip antennas and their suppression using different geometries of Defected Ground Structure (DGS). *IEEE Trans. Antennas Propag.* **60**(1), 92–101 (2012)
11. Seung-Tae, K., Byung-Chul, P., Jeong-Hae, L.: Dual-band circularly polarized patch antenna with first positive and negative modes. *IEEE Antennas Wirel. Propag. Lett.* **12**, 1165–1168 (2013)
12. Nasimuddin, Z.N.C., Xianming, Q.: Dual-band circularly polarized s-shaped slotted patch antenna with a small frequency-ratio, *IEEE Trans. Antennas Propag.* **58**(6), 2112–2115 (2010)
13. Jun-Hwa, O., Young-Pyo, H., Jong-Gwan, Y.: Dual circularly-polarized stacked patch antenna for GPS/SDMB. In: *IEEE International Symposium AP-S*, 5–11 July 2008
14. Smolders, A.B., Mestrom, R.M.C., Reniers, A.C.F., Geurts, M.: A shared aperture dual-frequency circularly polarized microstrip array antenna. *IEEE Antennas Wirel. Propag. Lett.* **12**, 120–123 (2013)
15. Ahmed, H., Fatma, E., Atef, Z.E., Moataza, H., Salwa, E.: Compact dual circularly-polarized microstrip antennas. In: *Proceedings of IEEE AP-S/URSI, Canada*, 11–17 July 2010

16. Zied, H., Laurent, C., Lotfi, O., Ali, G., Odile, P.: A dual circularly polarized 2.45-GHz rectenna for wireless power transmission. *IEEE Antennas Wirel. Propag. Lett.* **10**, 306–309 (2011)
17. Can-Hui, C., Yung, E.K.N.: A novel unidirectional dual-band circularly-polarized patch antenna. *IEEE Trans. Antennas Propag.* **59**(8), 3052–3057 (2011)
18. Xiao-Zheng, L., Ze-Ming, X., Qi-Qiu, X., Xuan-Liang, C.: A dual circularly polarized RFID reader antenna with wideband isolation. *IEEE Antennas Wirel. Propag. Lett.* **12**, 1630–1633 (2013)
19. Andrew, R.W., Nasiha, N.: Circularly polarized stacked patch antenna with perpendicular feed substrate. *IEEE Trans. Antennas Propag.* **61**(10), 5274–5278 (2013)
20. Changjiang, D., Yue, L., Zhijun, Z., Guoping, P., Zhenghe, F.: Dual-band circularly polarized rotated patch antenna with a parasitic circular patch loading. *IEEE Antennas Wirel. Propag. Lett.* **12**, 492–495 (2013)
21. The-Nan, C., Jyun-Ming, L.: Serial aperture-coupled dual band circularly polarized antenna. *IEEE Trans. Antennas Propag.* **59**(6), 2419–2423 (2011)
22. Qiang, L., Yuanan, L., Yongle, W., Ming, S., Junyu, S.: Compact wideband circularly polarized patch antenna for CNSS applications. *IEEE Antennas Wirel. Propag. Lett.* **12**, 1280–1283 (2013)
23. Yong, M.P., Shao, Y.Z., Weiwei, L.: Dual-band and dual-sense omnidirectional circularly polarized antenna. *IEEE Antennas Wirel. Propag. Lett.* **13**, 706–709 (2014)
24. Dan, Y., Shu-Xi, G., Yang-Tao, W., Wen-Feng, C.: Omnidirectional dual-band dual circularly polarized microstrip antenna using TM_{01} and TM_{02} modes. *IEEE Antennas Wirel. Propag. Lett.* **13**, 1104–1107 (2014)

A Proposed Modification Over Learning Vector Quantization and K-Means Algorithms for Performance Enhancement

Shirish Nagar and Ajay Khunteta

Abstract Neural networks are extensively used nowadays to carry out tasks like prediction, pattern matching, and detections primarily carried out by medical practitioners acquiring expertise and knowledge of a very high level in the area of medical science. The artificial neural networks (ANNs) are applied to conduct tasks like image analysis and interpretation, signal analysis, development of drugs, etc. The proposed work focuses on performing effectual prediction and diagnosis of diseases like diabetes using data classification techniques, thereby modifying these algorithms to enhance their performance. This proposed work contains simulated learning vector quantization algorithm, and replaced the conventional Euclidean distance function with the Canberra distance function. The simulation results revealed significant performance enhancement in the output produced by this modification. The modification is also applied to K-means algorithm and its outcome is recorded.

Keywords Artificial Neural Networks · Fault tolerance · Clinical diagnosis · Diabetes · Human experts · Classification techniques · Prediction · Patterns · Image analysis

Introduction

Learning vector quantization (LVQ) net's algorithm deals with finding the output unit which has a similar pattern in comparison to that of the input vector. After the process completes, if x and w correspond to the same class, weights are shifted towards the current input vector, otherwise, if they represent a dissimilar class then

Shirish Nagar (✉)

Department of IT, Poornima College of Engineering, Jaipur, India

e-mail: shirishnagar@poornima.org

Ajay Khunteta

Department of CSE, Poornima College of Engineering, Jaipur, India

e-mail: khuntetaajay@poornima.org

© Springer India 2016

N. Afzalpulkar et al. (eds.), *Proceedings of the International Conference on Recent Cognizance in Wireless Communication & Image Processing*, DOI 10.1007/978-81-322-2638-3_75

671

they are shifted away from the input vector [1]. This research work aims at conducting a comparative analysis between the executions and incorporation of LVQ algorithm implemented using *Euclidean distance function* and *Canberra distance function*, which shall be used in the place of Euclidean function as a proposed modification to the existing algorithm.

Learning Vector Quantization

An LVQ network contains a competitive layer at the first place followed by a second linear layer. The competitive layer is required to learn how to classify the input vectors similar to that of the competitive layers present in “self-organizing nets” [2]. The function of the linear layer modifies the classes of the competitive layer into respective target classifications which are given by the user. The classes which are learned and grasped by the competitive layer are defined as subclasses whereas the classes which correspond to the linear layer are referred to as target classes.

Working of the Algorithm

Both the competitive as well as the linear layers contain single neuron for every (sub or target) class. Therefore, the competitive layer is observed to learn up to S^1 subclasses, which, as a result, are united by the linear layer to structure S^2 target classes. (S^2 is always less than S^1 .) A_i occurring in the i th row of \mathbf{a}^1 (the remaining elements for \mathbf{a}^1 will be equal to 0) effectively selects the i th column of layer $\mathbf{LW}^{2,1}$ as the output of network [3]. Every such column contains a single value 1, with respect to a specific class. Hence, subclass 1s belonging to layer 1 gets into several classes by the $\mathbf{LW}^{2,1} \mathbf{a}^1$ multiplication in layer 2.

Notations used:

1. Input vector $X = (x_1, x_2, x_3, \dots, x_n)$
2. Weight vector for the j th output neuron: $W = (w_1, w_2, w_3, \dots, w_n)$
3. C_j = Preassigned category represented by j th neuron.
4. T = Target category for input X .

Overall objective of LVQ is dimensionality reduction or data compression [4]. The error of the approximation of vector quantization is expressed by Euclidean distance function value: $D = \sum_x \|X - W_{I(x)}\|^2$, which is the total squared distance between the input vectors $\{x\}$ and their representatives $\{W_{I(x)}\}$, which are aimed to be minimized.

Dataset for Prediction

The dataset used for the research work are obtained from “Pima Indians Diabetes Database” stored in UC Irvine (UCI) machine learning repository. **Number of instances:** 768, **number of attributes:** 9 (8 + 1 class attribute) as shown in Table 1 [5].

Importance of Distance Function

Any clustering or classification of genes and/or samples incorporates identification or combination of *similar* or *closer* objects. These similarities or distances are expressed as mathematical representations.

The selection of distance is extremely vital. In certain cases, a Euclidean metric may prove a sensible option, while in other cases a different distance function like a Manhattan metric can be effectively better option. On one hand, where some variables are continuous in nature, on the other hand other variables are categorical, there are more options and the respective implications of these various options should be analyzed carefully.

Pairwise distances can also be considered; that are functions which are required to satisfy only the non-negativity, symmetry, and identification mark properties. *Distances* shall be referred, which consist of *metrics* and only metrics shall be stated as per their specific interest [6]. In case of LVQ, concept of Centroid distance is utilized, as Euclidean distance is measured between the two clusters of the input vector and the weight vector.

Table 1 Attribute information of Pima Indians diabetes

S. no.	Parameter name	Parameter value
1	Number of times pregnant	Numeric
2	Plasma–glucose concentration after 2 h in an oral glucose tolerance test	Numeric
3	Diastolic blood pressure (mm Hg)	Numeric
4	Triceps skin fold thickness (mm)	Numeric
5	2-h serum insulin ($\mu\text{U}/\text{ml}$)	Numeric
6	Body mass index (weight in kg)/(height in m) ²	Numeric
7	Diabetes pedigree function	Numeric
8	Age (years)	Numeric
9	Class (Tested positive or negative)	0 or 1 (1-positive) (0-negative)

Proposed Modification in LVQ Algorithm

In this research work, it is proposed to modify the LVQ algorithm on the basis of a different distance function, called *Canberra Distance*. This is aimed to increase the sensitivity and accuracy of the prediction of diabetes using LVQ [7]. Existing LVQ algorithm makes use of Euclidean distance function to obtain the distance between the two vectors namely, the input vector and the weight vector.

Canberra Distance

The **Canberra distance** is expressed as a numerical parameter to represent the distance in between pairs of points present in a vector space. This distance function was proposed in 1966 and upgraded by G.N. Lance and W.T. Williams in 1967. It is signified as a weighted adaptation of L_1 (Manhattan) distance. The Canberra distance is described as a metric function often implemented for data which is scattered around an origin [8]. The generalized equation used to express the Canberra distance d between vectors \mathbf{x} and \mathbf{y} present in a real vector space of n -dimensions is given as follows:

$$\mathbf{d}(\mathbf{x}, \mathbf{y}) = \sum_{k=0}^{n-1} \frac{|\mathbf{x}_{i,k} - \mathbf{y}_{j,k}|}{|\mathbf{x}_{i,k}| + |\mathbf{y}_{j,k}|}$$

Here $x = (x_1, x_2, \dots, x_n)$ and $y = (y_1, y_2, \dots, y_n)$, are specified vectors.

The algorithm using this function must guarantee whether the input data matrix is a rectangular one or not. If the matrix is not rectangular, then the function returns FALSE value, along with a defined but an empty output matrix. When the matrix is a rectangular one, then Canberra distance ought to be calculated. Consequently, the dimensions of the relevant arrays corresponding to the output matrix and the titles for the rows and columns get finalized [9]. Since the result obtained is a square matrix, which are diagonally mirrored and only values for the diagonal and one triangular part are computed. When computational errors occur, the output of the Canberra function is returned as FALSE [10].

Utilization of Canberra Distance Method

Data should not be in signed form, in the original form for the Canberra metric. The modification of the metric proposed by Adkins bears the property that the result is found to be 1 unity where the variables are opposite signed. It is practically applicable in the special case where the signs of the variables represent differences instead of degree (as proposed by Lance and Williams 1967) [9]. Nevertheless, it is

generically used for values greater than 0. This metric has the property for being easily biased for those measures which are around the origin and it is also very sensitive for values which are close to 0, at the same time it is highly sensitive to proportional differences rather than to absolute differences [10]. This attribute becomes more noticeable in case of space of higher dimensions, respectively, with an increasing amount of variables. It is applicable as a highly sensitive measurement to categorize deviations from ordinary readings.

Experimental Results

The results are obtained in terms of *receiver operating characteristic (ROC)* graph and confusion matrix, which are used as analysis mechanisms for the performance of the neural network algorithms. These results shall be compared against each other, and the conclusion shall be derived. The algorithm for LVQ and its proposed modification trains the neural network over the dataset with 100 iterations, with learning rate 0.01 and the data is split as **90 % (691 cases) utilized for training and 10 % (77 cases) for testing**.

Application of LVQ with Euclidean Distance

According to the confusion matrix plot obtained by employing (Table 2) for Euclidean Distance function, the following parameter values are observed:

1. **Negative Cases: 157 (157 + 0) out of 691 (22.7 %)**

- (a) **True negative rate (TNR) or Specificity:** It is defined as the ratio of correctly classified negatives cases, as computed by the given equation: $TNR = \frac{TN}{TN+FP} = 157/157$ which is **100 %**.

Table 2 Confusion matrix plot for Euclidean distance

Actual class	Predicted class		Rates
	Negative	Positive	
Negative	True Negative 157 (22.7 %)	False Positive 0 (0.0 %)	100 % (TNR) 0.0 % (FPR)
Positive	False Negative 80 (11.6 %)	True Positive 454 (65.7 %)	85.0 % (TPR) 15.0 % (FNR)
Rates	Negative predictive value 66.2 %, 33.8 %	Precision 100 %, 0.0 %	Accuracy 88.4 %, 11.6 %

- (b) **False positive rate (FPR):** It is defined as the ratio of incorrectly classified negatives cases as positive ones, as computed by the given equation: $FPR = \frac{FP}{TN+FP} = 0/157$ which is **0.0 %**.

2. Positive Cases: 534 (80 + 454) cases of 691 (77.2 %)

- (a) **False negative rate (FNR):** It is defined as the ratio of incorrectly classified positive cases as negative ones, as computed by the given equation: $FNR = \frac{FN}{FN+TP} = 80/549 = 11.6 \%$
- (b) **Recall or True positive rate (TPR) or Sensitivity:** It is defined as the ratio of correctly classified positive cases, as computed by the given equation: $TPR = \frac{TP}{FN+TP} = 454/534 = 65.7 \%$

Precision (P) or Positive Predictive Value: It is defined as the ratio of the predicted correct positive cases, as computed by the given equation: $P = \frac{TP}{FP+TP} = 454/(0 + 454) = 100 \%$.

Finally, the **accuracy (AC):** It is defined as the ratio of the total number of correct predictions. This is the parameter of performance used in case of confusion matrix, calculated using the equation: $AC = \frac{TN+TP}{TN+FP+TN+TP} = (157 + 454)/(157 + 0 + 80 + 454) = 611/691 = 88.422 - 88.4 \%$.

The ROC graph in the case for using Euclidean Distance function is mentioned below (Fig. 1).

Fig. 1 ROC curve for Euclidean distance

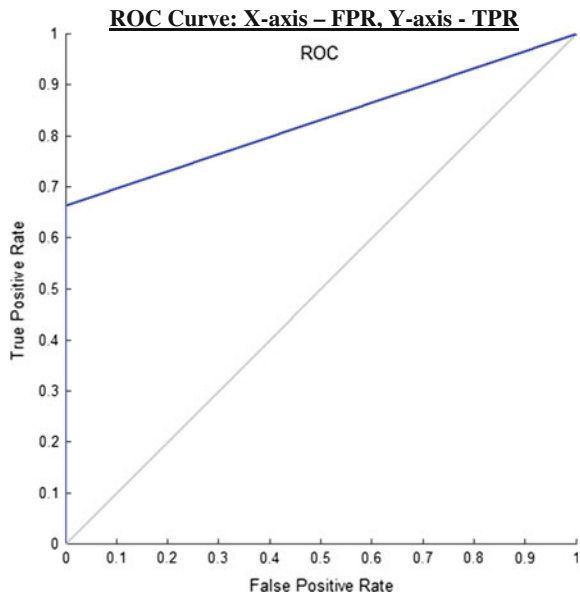


Table 3 Confusion matrix plot for Canberra distance

Actual class	Predicted class		Rates
	Negative	Positive	
Negative	True Negative 172 (24.9 %)	False Positive 0 (0.0 %)	100 % (TNR) 0.0 % (FPR)
Positive	False Negative 65 (9.4 %)	True Positive 454 (65.7 %)	87.5 % (TPR) 12.5 % (FNR)
Rates	Negative predictive value 72.6 %, 27.4 %	Precision 100 %, 0.0 %	Accuracy 90.6 %, 9.4 %

Application of LVQ with Canberra Distance

According to the confusion matrix plot obtained by employing (Table 3) for Canberra distance function, the following parameter values are observed:

1. **Negative Cases: 172 (172 + 0) out of 691 (24.9 %)**

- (a) **True negative rate (TNR) or Specificity:** $\frac{TN}{TN+FP} = 172/172$ which is **100 %**.
- (b) **False positive rate (FPR) =** $\frac{FP}{TN+FP} = 0/172 = 0 \%$.

2. **Positive Cases: 519 (65 + 454) cases of 691 (75.10 %)**

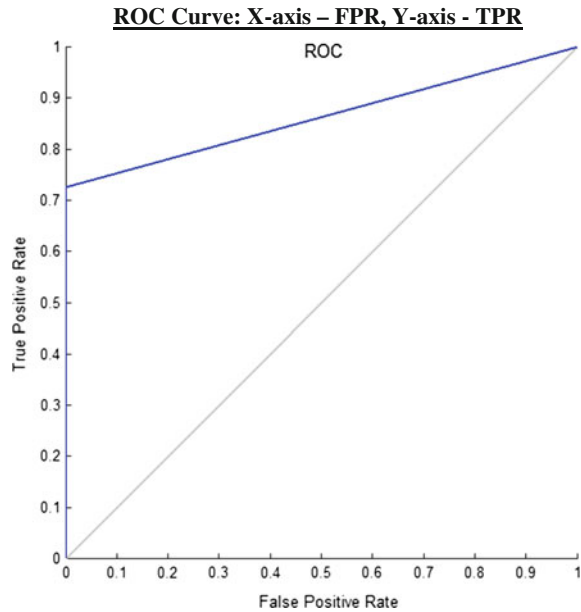
- (a) **False negative rate (FNR) =** $\frac{FN}{FN+TP} = 65/519 = 9.4\%$
- (b) **Recall or true positive rate (TPR) or Sensitivity:**
 $TPR = \frac{TP}{FN+TP} = 454/519 = 87.46 - 87.5 \%$

$$\text{Precision (P)} = \frac{TP}{FP + TP} = 454/(0 + 454) = 100 \%$$

$$\text{Accuracy (AC)} = \frac{TN + TP}{TN + FP + FN + TP} = (172 + 454)/(172 + 0 + 65 + 454) = 626/691 = 90.59 - 90.6 \%$$

The ROC graph in the case for using Canberra distance function is mentioned below (Fig. 2).

Fig. 2 ROC curve for Canberra distance



Modification of K-Means Algorithm

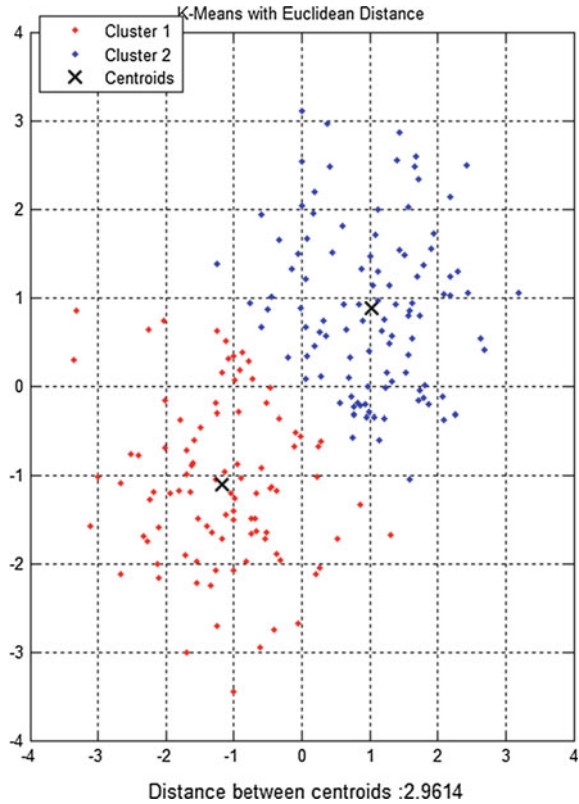
In this section, the experimental results obtained by applying K-means algorithm to the given dataset are referred. The Euclidean algorithm in the K-means algorithm is replaced with the Canberra distance to obtain the centroid between the two clusters during the cluster analysis [8]. Cluster analysis, which is also termed as taxonomy or segmentation analysis generates clusters or groups of data. Clusters are produced in a manner in which the objects existing in the same cluster closely resemble and are similar, and objects which are present in different clusters are very distinctive. Measures of similarity depend on the application [9].

Euclidean Version

As mentioned, the clustered outcome of the K-means algorithm is obtained using the Euclidean distance function, and in order to obtain the minimum distance between the two clusters, the distance between the two centroids from the corresponding clusters is recorded. Points from cluster 1 are denoted in red dots, and those of the cluster 2 are in blue dots, the centroids are marked with "X" symbol.

The resulting distance between the centroids is 2.9614 (as shown in Fig. 3).

Fig. 3 Cluster distribution for K-means with Euclidean distance function



Canberra Version

Now, the Euclidean distance function is replaced with the Canberra distance, and obtains the inter-centroid distance.

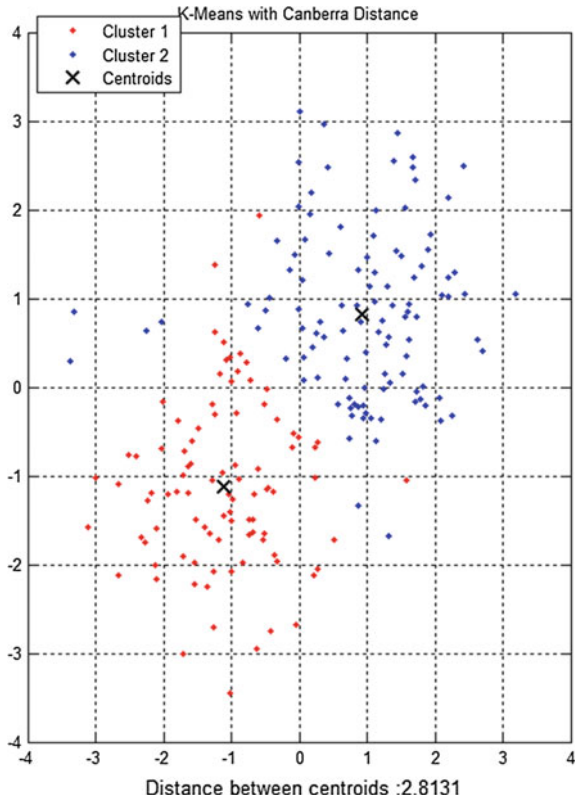
The resulting distance between the centroids using Canberra distance method is 2.8131 which is less than the distance obtained by using Euclidean algorithm (as shown in Fig. 4).

Result Analysis

Modification of LVQ Algorithm

After comparing the experimental results in the sections “[Application of LVQ with Euclidean Distance](#)” and “[Application of LVQ with Canberra Distance](#)”, **an increase by 2.2 % in the overall accuracy** of the algorithm was observed by providing the same dataset as the basis for algorithmic execution, as shown in Table 4.

Fig. 4 Cluster distribution for K-means with Canberra distance function



Modification of K-Means Algorithm

The experiment of K-means modification was carried out as an application of the proposed LVQ Algorithm to observe the deviations between the two versions. Following results were observed: distance between the centroid obtained by the application of Euclidean distance was **2.9614**. Distance between the centroid obtained by applying Canberra distance was **2.8131**

Table 4 Comparison of results obtained from application of Euclidean and Canberra distance functions

Parameter	Euclidean distance (%)	Canberra distance (%)
Negative cases	22.7	24.9
Positive cases	77.2	78.43
False Negative Rate (FN)	15	12.5
True Positive Rate (TP)	85.01	87.5
Accuracy	88.4	90.6

$$\frac{2.9614 - 2.8131}{2.9614} \times 100\% =$$

The distance between the centroids reduced by the use of Canberra distance algorithm, thereby indicating an **improvement of 5 %**.

Conclusion

This research paper aims to present the simulation of an artificial neural network (ANN) is carried out to incorporate LVQ algorithm and to implement the required modification in the distance function, thereby replacing the conventional Euclidean function with Canberra distance function. Following observations were reported as a result of the study:

- (a) Canberra distance method proves as an effective distance calculation method over the conventional Euclidean distance function applied in case of LVQ thereby *enhancing its performance from 88.4 to 90.6 %*. Hence there is an *increase in performance by 2.2 %*, as shown in respective confusion matrices.
- (b) The analyses of the experimental result shows that using Canberra distance function proves to be a fine and realistic option for the classification of a diabetes dataset by implementing algorithms like LVQ. The Canberra distance function is used to modify the existing K-means algorithm as an application of the concept. *This has enhanced its performance by 5 %*.

Limitations and Future Scope

The Canberra distance function is observed to perform better in conditions where the values of the parameters for a dataset are closer to zero. So its usage is limited to only the datasets bearing the aforementioned characteristic. Another limitation is that it only employs categorical data. For some diagnostic scenarios, continuous data may be essential. Also, only single data mining technique was used in the proposed work. Additional techniques for data mining can be implemented to obtain better diagnostic outcomes.

More usefulness and better performance is expected by such modifications based on Canberra distance function, where the values of the parameters are closer to 0. Future applications will reveal that to what extent the modifications in the distance functions and other parameters of classifications and clustering shall be beneficial over the standard distance calculation methods. In the future work of this research, the hybridization of different distance calculation functions shall be done,

implemented in certain data clustering and pattern classification algorithms like K-means, self-organized maps, and learning vector quantization. Later, expansion of the research shall focus on increasing the size of the datasets for the maximization of the result and also attempts to discover a novel and optimal algorithm.

References

1. Haykin, S.: *Neural Networks: A Comprehensive Foundation*. Prentice-Hall, NJ (1999)
2. Galushkin, A.: *Neural Networks Theory*. Springer, Berlin, Heidelberg, New York (2007)
3. Hagan, M.T., Demuth, H.B., Beale, M.: *Neural Network Design*. PWS Publishing Company, Boston (1996)
4. Anderson, J.: *An Introduction to Neural Networks*. MIT Press (1995)
5. Fausett, L.: *Fundamental of Neural Networks: Architectures, Algorithms, and Applications*. Prentice-Hall (1994)
6. Lee, H.G., Noh, K.Y., Ryu, K.H.: Mining biosignal data: coronary artery disease diagnosis using linear and nonlinear features of HRV. In: Washio, T., et al. (eds.) *PAKDD 2007 Workshops*, LNAI 4819, pp. 218–228. Springer, Berlin, Heidelberg (2007)
7. Parthiban, L., Subramanian, R.: Intelligent heart disease prediction system using CANFIS and genetic algorithm. *Int. J. Biol. Biomed. Med. Sci.* **3**(3) (2008)
8. Rumelhart, D.E., Hinton, G.E., Williams, R.J.: Learning representations by back-propagating errors. *Nature* **323**(6088), 533–536 (1986). doi:[10.1038/323533a0](https://doi.org/10.1038/323533a0)
9. Raúl Rojas: *The Back Propagation Algorithm of Neural Networks—A Systematic Introduction*, Chapter 7
10. Fahlman, S.E.: An empirical study of learning speed in back propagation networks. Carnegie Mellon Report, No CMU-Cs, pp. 88–162 (1988)

Taxonomy of Recent DDoS Attack Prevention, Detection, and Response Schemes in Cloud Environment

Omkar P. Badve and B.B. Gupta

Abstract In recent years the need for using cloud environment has increased abundantly. Threats to cloud computing are also rising with its usage. Among various threats to cloud, distributed denial-of-service (DDoS) attack is a main threat today. DDoS attack compromises the availability of the services and risks everything including financial loss, losing reputation, and loss of confidence of cloud users over the organization. To avoid this we need more profound and elegant way to secure cloud structure from DDoS attack. In this paper, we discuss recent development and protection mechanisms (i.e., prevention, detection, and response) against DDoS attack in cloud environment. These methods include preventive measures that are applied before the attack, detection method that can be applied while the attack is live, and responsive methods that are applied after the attack. This paper discusses about DDoS attack problem, currently proposed solutions, and research scope possible in future to deal with such attacks efficiently.

Keywords Cloud computing · DDoS attack · DDoS attack detection and filtering of DDoS attack

Introduction

People in business are more focused on business growth and product enhancements, only because of using cloud computing in business operations, rather than worrying about storage or maintaining 24-h server to ensure maximum throughput. Therefore, the use of cloud computing by commercial organizations is inevitable in near future. Cloud providers like Amazon [1], IBM [2], and Windows [3] took this

O.P. Badve · B.B. Gupta (✉)
National Institute of Technology, Kurukshetra, India
e-mail: gupta.brij@gmail.com

O.P. Badve
e-mail: omkarbadve89@gmail.com

responsibility to provide service on customer's demand with high scalability on pay-as-you-go basis.

But, despite all of these advantages of the cloud computing, there are still hiccups in the path of its encroachment. Securing the cloud environment has become critical issue in using and deploying cloud concepts in business. Cloud provides online memory storage for business, but what if attacker breaches the cloud defense mechanism and steals all the data or what if cloud service became unavailable for critical hour of business. Therefore, there are still many issues like this that need to be addressed before cloud providers reach to the customers. Customers will not get attracted to the cloud services if they hear news stories like cloud account has been hacked or web site went down due to DDoS attack [4] or any other news that downfalls the image of cloud computing. One of the major security concerns is denial-of-service (DoS) attack against the cloud providers. This attack is more dangerous than other possible attacks because of following reasons:

- DoS exploits new vulnerabilities to perform attack. Few modifications in the existing security systems may not work.
- To preserve the privacy of the data one knows that the possible target is the critical data, but in case of DoS, it is very hard to perform prediction about target.
- In case of DoS, attack packets are very much similar to normal, legitimate attacks.
- Since, the detection of the packets is difficult task, most of the time attack is detected after the system goes down.

Cloud computing also has the danger from distributed denial-of-service (DDoS) attack, which has similar effects but different strategy. In DDoS, attacker creates army (network of computers, botnet) of its own by infecting other computers (zombies or bots) with malware. Attacker then can instruct these bots to attack on some server machine and that server experiences a heavy traffic due to heavy load of traffic from numerous numbers of machines. DDoS attack can target on application web server by sending large number of requests in very less time or it can target on some router by flooding the interface by packets, or it can target on DNS server by sending queries that take too much time to resolve or DDoS attack can be made by utilizing all the memory available for particular data structure like it does in SYN flooding attack [5]. There are lots of types of DDoS attacks and it is very difficult for any defense mechanism for providing any general solution for all of these attacks. In this paper, we discuss recent development and various defensive mechanisms against DDoS attack in cloud environment. This paper discusses about DDoS attack problem, currently proposed solutions, and research scope possible in future to deal with such attacks efficiently.

Rest of the report is organized as follows. The second section contains “Need of Defense Mechanisms Against DDoS Attack in cloud Environment.” “Security Issues and Challenges in cloud Computing” are presented in the third section. “DDoS Attacks, Types, and Tools” are given in the fourth section. “Taxonomy of DDoS Defense Mechanisms in cloud Environment” is described in the fifth section in detail. Finally, last section concludes our paper and discusses “Scope for Future Research.”

Need of the Defensive Mechanisms Against DDoS Attack in Cloud

There is a stringent need of security measures that is to be employed against DDoS attack in the cloud environment. According to CSA report [6], number of incidents of attack on cloud environment has risen over the years. Size of the DDoS attack is also increasing every year. Attack carried out on spamhaus.org was around 75 Gbps [4]. The largest attack in 2013 was of 309 Gbps. Figure 1 shows the size of maximum recorded attack in the respective years. Attackers alter their way of attack with larger extent [7]. Duration of the attack is also important factor, because attack can be made in 30 min or even takes more than a month. This duration tells the defense systems that the mitigation techniques should be faster enough to detect and filter these attacks in time before loss is incurred. Arbor reports that [7] the largest reported attack is performed with the duration of below 6 h.

Security Issues and Challenges in Cloud Computing

There are various possible threats to the cloud computing environment that can cause every other user using the service and cloud providers since attackers target financial gain or business benefits. Some of the issues related to the security are security of the data that is stored onto the cloud storage system, geographical location of the data centers, proper segregation of the data from other cloud users, data confidentiality, data integrity, availability of the various resources, user access control of various privilege level, backup and data recovery in case of data loss and many other security issues that are there because of use of Internet as way of

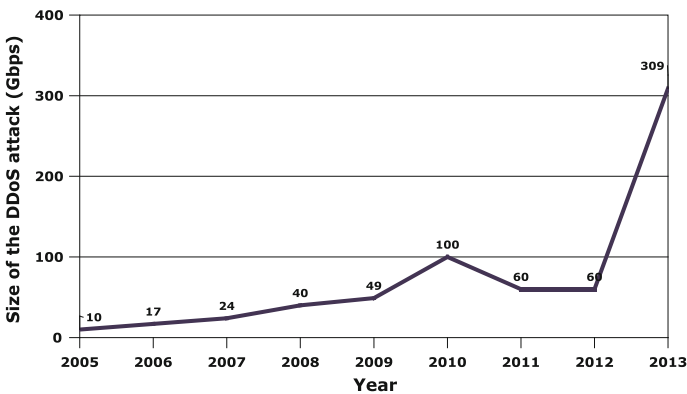


Fig. 1 Size of the maximum recorded attack (Source Arbor Networks, Inc.)

providing service like network security or web application security. Typical architecture of cloud computing makes it vulnerable to various attacks. For example, vulnerability in virtualization leads to an attack on critical data.

DDoS Attacks, Types, and Tools

Broadly, based on type of attack methods, DDoS attacks are classified as volume-based, protocol, and application layer attack. In volume-based attack, attacker targets the network bandwidth and chokes up the entire network. In protocol attack, attack is targeted at the resources of the victim machine. And in application layer attack, motive of the attacker is to crash the victim web server. Description of various types of DDoS attacks and corresponding category of attack is depicted in Table 1. Various softwares and tools are available freely online for attackers to carry out DoS attack to flood the server and bring down their network. Some of the tools are given in Table 2.

Taxonomy of DDoS Defense Mechanisms in Cloud Environment

A wide range of work has been performed in the area of cloud computing to defend the cloud network against DDoS attack. Most of the defense systems fall into three categories: One that secures the system by employing the methods before any attack takes place. These are called preventive systems. Another category is the security system that provides security by detecting attack and then filtering the attack traffic. This detection is done when attack is live. Third category is to take responsive measures after the attack takes place and victim is down due to attack. Responsive measures include tracing back the source of the attack and filter the future traffic that has come from same source.

Preventive Mechanisms

Best solution to defend the denial-of-service attack is to stop it before it happens. This is called prevention mechanism. For preventing malicious traffic *anomaly-based* or *signature-based* detection methods can be applied. These methods try to find out some pattern that is not usually visible while normal traffic is entering the network. Pattern of incoming traffic is made and is compared with normal traffic and results are obtained to find out malicious packet. Prevention can also be done with the help of ISPs (Internet service providers) that may provide techniques to

Table 1 Description of various types of DDoS attacks and corresponding methods of attack

Type of attack	Description	Attack category
Apache2 DDoS	Apache web server is crashed by sending requests with large number of http headers	Application Layer Attack
Back	Apache web server is crashed by sending requests containing large number of front slashes	Application Layer Attack
CrashIIS	IIS server is crashed by sending malformed GET requests	Application Layer Attack
DoSNuke	Out-of-band data is sent to server to crash NT-based servers	Application Layer Attack
RUDY	Consumes all sessions with POST command and large header value	Application Layer Attack
Slowloris	Keeps the connection alive until system breaks down	Application Layer Attack
Slow Read	Keeps the connection alive by reading the response of server very slowly	Application Layer Attack
ARPPoison	It changes the MAC address of packet to make the system unavailable	Protocol Attack
Land	Malformed SYN packets are sent to slow down server	Protocol Attack
MailBomb	Large number of mails are sent to server to slow down its processing	Protocol Attack
Neptune (SYN Flood)	TCP server gets large number of half-open connection to make server to reject new connections	Protocol Attack
Ping of Death (POD)	Ping request is sent with large size so buffer overflow happens in destination	Protocol Attack
SelfPing	It makes system reboot with one ping command	Protocol Attack
TCPReset	Attacker sends spoofed TCP reset signal to server, which terminates the connection	Protocol Attack
Teardrop	Forged fragment offset of IP fragment will crash down reassembly procedure	Protocol Attack
Smurf (ICMP Flood)	ICMP packets are sent with forged source address, that results in huge traffic flow toward victim with ICMP reply	Volume-Based Attack
UDPStorm	UDP connection between two machines is brought down by making them to send UDP packets to each other in loop	Volume-Based Attack
Peer-to-peer	All peer-to-peer data are redirected to victim's computer	Volume-Based Attack
Permanent DoS	Changes the firmware to corrupt whole system	Physical destruction or alteration of components

Table 2 Tools to perform DDoS attacks

Tools	Description
Trinoo	Trinoo works like a master/slave program. It creates the network that consists of attacker, masters, daemons, and victims
mstream	<i>mstream</i> enables the intruders to use computer systems which are connected to each other via Internet for commencing DDoS attack by flooding the target systems with large number of packets
Low Orbit Ion Cannon (LOIC)	This is the most simple, famous, and easy-to-use tool to perform denial-of-service attack on small server. It can be used to attack DDoS and DoS
XOIC	It is similar to LOIC tool in functionality but it is more powerful in performance and it performs DoS attack on user-specified IP address, port number, and type of protocol of packets to be sent
HTTP Unbearable Load King (HULK)	HULK generates large, unique, and difficult to understand traffic at web server. It bypasses caching engines and therefore, it is able to hit the victim's pool of resources
DDoSSIM (Layer 7 DDoS Simulator)	This is application layer DDoS attack. It simulates several zombie (infected with malware) hosts having random IP address. These zombies create full TCP connection with the server to be attacked
Tor's Hammer	It is slow POST denial-of-service tool, which is programmed in Python. This tool can work in TOR network to be anonymous while performing attack
PyLoris	PyLoris is a stress testing and DoS attacking tool for services provided by web servers. PyLoris perform DoS attack using SOCKS proxies and SSL connections
OWASP DoS HTTP POST	Using this tool one can check if particular host defends against DoS attack or not. And also, it can perform DoS attack against web site
DAVOSET	This tool uses executions on other sites to perform DDoS attack. Latest version has added some features like support for cookies and many other features
GoldenEye HTTP Denial-of-Service Tool	GoldenEye is an easy-to-use and efficient DoS attacking tool. It is programmed in Python for testing purpose, but it also can be used to attack DoS tool

prevent malicious traffic. For example, ISP can employ *Clean pipe* technique which allows traffic of only particular size through gateway. Other methods to prevent the traffic is to place the filtering devices at the network border and filter out the traffic before it can do any harm to systems that reside in internal part of the network.

As given in [8], for preventing the DDoS attack dynamic resource allocation can be applied by mathematically calculating approximate need of the resources by leveraging the dynamic allocation of resources—the important characteristic of

cloud computing. Also, in [9] another method to detect and filter the DDoS flooding attack is given. A simple distance-based estimation technique is given to protect the cloud environment. In [10] new form of DDoS attack is suggested, which exploits the limited bandwidth links between the routers and hosts in cloud environment. Prevention system is suggested by estimating the bandwidth of the vulnerable links and then migrating virtual machines (VMs) to other hosts.

Detection Mechanisms

A lot of techniques are available to detect denial-of-service attacks. One class of the detection of attack is to find out rate of flow of the packets and whether it is reaching some threshold value or not. Another class of detection is to find out some anomaly inside the packets by checking them with normal behavior of the packets. There are many intelligent detection and prevention systems, which use machine learning techniques to take decisions about whether particular packet is anomalous or not. These decisions are based on various parameters that generate certain pattern or behavior. As we have seen previously attack detection should be closer to source but it is not accurate enough because traffic is not so dense to find out any anomaly. Detection of DDoS attack should be done closer to source of attack to enhance safety, but it should also be closer to destination to improve accuracy.

One of the anomaly-based decision technique, confidence-based filtering (CBF), is used in [11], which creates nominal profile (pattern for normal traffic) determined in nonattack period. Later in attack period, i.e., actual network traffic period, nominal profile is checked against pattern recognized using traffic received in that period and anomaly is found out. Some DDoS attack targets on open ports and floods these ports by large number of packets. In paper [12], defensive technique is proposed which scans the port and uses adaptive port hopping with synchronization using clock drifts instead of the standard port hopping technique. For protecting cloud environment from the attacks XML-DoS and HTTP-DoS attacks, Vissers et al. [13] proposed a method which determines normal distribution of key attributes of the packet present in dataset and uses it to find out any anomaly in the incoming packets. Also, proposed method successfully detects spoofing done in source address of attack packets. By deploying this method cloud broker and cloud providers get secured in cloud environment. Another anomaly-based detection technique is proposed in [14], which first finds out correlation pattern between real-world packets and then with the help of multivariate correlation analysis it correctly modularizes features of network traffic. It is able to detect not only the attacks that are previously found but also the one which are new. Also, they have proposed triangle-area-based technique that enhances and speedup the process of MCA.

Responsive Defense Mechanisms

Since the DDoS attack is very difficult to detect, it often happens that attack is detected after victim suffers the downtime. Therefore, to develop a technique for handling the situation after system is being attacked is very important to ensure that the attacks will not happen again. One of the ways of dealing with this is the *identification* of source of the attack. It includes traceback strategies which reveals the source address of attack packets. It finds out the root of the packet by tracing back the route of the message. Software tools installed in routers are upgraded to support to such traceback techniques. Another way is to defend the system by giving proper response after attack is being detected. Response includes filtering the attack packets based on various criteria. For example, it can compare the behavior of the packet with normal behavior and discard the packets that mismatch with normal behavior. In addition to this, collaboration of various law enforcement agencies is essential to ease the prosecution of the attacker.

Chonka et al. [15] has given the traceback technique that can be deployed in cloud environment. It is basically packet marking technique based on service oriented architecture (SOA). It marks the packet as it enters the network (adds the tag in its SOAP header). So, when attack is detected, these marks are used to *traceback* the packet. It also provides filtering of the malicious packets using artificial neural network. More simplified and efficient method is proposed in [16] which traces back the attack packet and is also based on SOA. Table 3 summarizes various schemes.

Conclusion and Scope for Future Research Work

As the need of the cloud computing by the various organizations is increasing, necessity of more secure and reliable system is also growing. Since, distributed denial-of-service attack is more dangerous and not so difficult to carry out; there is an urgent need to design and develop efficient and global solution for protecting against these attacks. In this paper, we have discussed various security issues and challenges related to cloud computing. In addition to this, we discussed various DDoS attack types and tools to carry out DDoS attack. Finally, we have presented taxonomy of defensive solutions against DDoS attack and discussed its merits and demerits. This taxonomy will help researcher to have better understanding of the DDoS attack problem in cloud environment, current solution space, and scope for future research to deal such attacks efficiently.

Table 3 Summary of various defensive schemes against DDoS attack

Author	Approach	Type of DDoS attack	Advantages	Limitations
Liu [10]	Bandwidth estimation and migration to other host	New type of DoS attack that exploits underprovisioned link	Bandwidth estimation is much closer to average bandwidth Relative error is also better than other method like Spruce, Path load	Migration may be economically difficult to carry out
Yu et al. [8]	Prevention method by dynamic resource allocation	DDoS flooding	Use of real-world datasets Ensures DDoS filtering at cloud host Affordable cost	Used model can be improved No provision if cloud goes out of resources Real cloud environment implementation is needed
Chen et al. [11]	Anomaly-based detection and filtering	Flooding by botnet	Less size for storage is required Acceptable filtering accuracy Scoring speed is high	Consumption of memory at victim side is more Computation time at server is more
Varalakshmi et al. [12]	Port Hopping	DDoS attack on open ports	Proposed method has greater variance Execution interval is adaptive and it reduces the overhead	No provision for multiple client
Visser et al. [13]	Defense by generating pattern for each of the feature and inspecting one-by-one features of the packets that are related to HTTP and XML requests	XML-DoS and HTTP-DoS	Response time is better than S-MAS and cloud protector	Provides defense only for application layer; need to be used with current security system

(continued)

Table 3 (continued)

Author	Approach	Type of DDoS attack	Advantages	Limitations
Tan et. al. [14]	Detection system using correlation pattern with the help of MCA and the behavior-based detection technique	DoS attacks present in KDD CUP 1999 Dataset	95.2 % detection accuracy After applying statistical normalization, accuracy 99.95 % Almost 100 % detection rate for unknown type of DDoS attacks	It cannot identify Land, Neptune, Teardrop Not worked with real-world data
Chonka et al [15]	Traceback technique SOA-based solution (CTB) and filtering using ANN	HTTP-DoS, XML-DoS	Detection and filtering rate between 88 and 91 %	Use of SOAP messages increases the overhead for network as size is larger than payload
Yang et. al. [16]	SOA-based traceback and cloud filter for filtering	General DDoS flooding	Simpler and effective Routers help in tracing back the attacker	Needs heavy packet flow for detecting packet flow Result response is slow Frequent change in path leads to wrong results

References

1. Amazon Elastic Compute cloud (Amazon EC2), Amazon. <http://aws.amazon.com/ec2/>. Accessed Sept 2014
2. IBM cloud Computing, IBM. <http://www.ibm.com/cloud-computing/in/en/>. Accessed Sept 2014
3. Azure: Microsoft's cloud Platform, Microsoft Corporation. <http://azure.microsoft.com/en-us/>. Accessed Sept 2014
4. Prince, M.: The DDoS That Knocked Spamhaus Offline (And How We Mitigated It). cloudFlare Blog (2013). <http://blog.cloudflare.com/the-ddos-that-knocked-spamhaus-offline-and-ho/>. Accessed Sept 2014
5. Srivastava, A., Gupta, B.B., Tyagi, A., Sharma, A., Mishra, A.: A recent survey on DDoS attacks and defense mechanisms. In: Book on Advances in Parallel Distributed Computing, pp. 570–580. Springer (2011)
6. Ko, R., Lee, S.S.G.: cloud Computing Vulnerability Incidents: A Statistical Overview (2013). https://downloads.cloudsecurityalliance.org/initiatives/cvswg/CSA_Whitepaper_cloud_Computing_Vulnerability_Incidents.zip. Accessed Sept 2014
7. Arbor Networks, Inc.: Worldwide Infrastructure Security Report Volume IX (2014). <http://pages.arbornetworks.com/rs/arbor/images/WISR2014.pdf>. Accessed Sept 2014
8. Yu, S., Tian, Y., Guo, S., Wu, D.O.: Can we beat DDoS attacks in clouds? IEEE Trans. Parallel Distrib. Syst. **25**(9), 2245–2254 (2014)
9. Chapade, S.S., Pandey, K.U., Bhade, D.S.: Securing cloud servers against flooding based DDoS attacks. In: 2013 International Conference on Communication Systems and Network Technologies (CSNT), 6–8 Apr 2013, pp. 524, 528
10. Liu, H.: A new form of DOS attack in a cloud and its avoidance mechanism. In: Proceedings of the 2010 ACM Workshop on cloud Computing Security Workshop. ACM (2010)
11. Chen, Q., Lin, W., Dou, W., Yu, S.: CBF: a packet filtering method for DDoS attack defense in cloud environment. In: 2011 IEEE Ninth International Conference on Dependable, Autonomic and Secure Computing (DASC), pp. 427–434 (2011)
12. Varalakshmi, P., Murali, M.: Simplified clock drift management to avoid Denial of Service attacks in cloud. In: 2013 Fifth International Conference on Advanced Computing (ICoAC), pp. 331–336 (2013)
13. Vissers, T., Somasundaram, T.S., Pieters, L., Govindarajan, K., Hellinckx, P.: DDoS defense system for web services in a cloud environment. Future Gener. Comput. Syst. **37**, 37–45 (2014)
14. Tan, Z., Jamdagni, A., He, X., Nanda, P., Liu, R.P.: A system for denial-of-service attack detection based on multivariate correlation analysis. IEEE Trans. Parallel Distrib. Syst. **25**(2), 447–456 (2014)
15. Chonka, A., et al.: cloud security defence to protect cloud computing against HTTP-DoS and XML-DoS attacks. J. Netw. Comput. Appl. **34**(4), 1097–1107 (2011)
16. Yang, L., Zhang, T., Song, J., Wang, J.S., Chen, P.: Defense of DDoS attack for cloud computing. In: 2012 IEEE International Conference on Computer Science and Automation Engineering (CSAE), vol. 2, pp. 626–629. IEEE (2012)

Design of Compact Concentric Circular Ring Patch Antenna with Defected Ground Plane

Neelam Choudhary, Ajay Tiwari, Brajraj Sharma, J.S. Saini
and D. Bhatnagar

Abstract The design and radiation performance of a modified planar arrangement of concentric circular rings on defected ground plane (DGP) is reported for wireless communication and satellite applications. The etching of a defect in the ground plane is applied for antenna size reduction. The proposed compact antenna is simulated by applying CST Microwave Studio software and fed through strip line feeding. The overall size of the antenna is 39 mm × 46 mm × 1.59 mm. The antenna resonates at three frequencies and the obtained frequency bandwidth is close to 2.2 GHz (2.330–4.530 GHz). The gain of antenna is simulated in the desired frequency range and is found close to 3 dBi. The proposed arrangement of antenna provides maximum radiations normal to patch geometry and shape of realized radiation patterns is somewhat similar to a dumbbell shape in the upper hemisphere. This antenna is specifically designed considering the wireless communication systems applicable in India.

Keywords DGS · Compact · Concentric ring · CST microwave studio

Introduction

Microstrip antennas have some inherent features that make them suitable for modern day wireless and satellite communication systems. Extensive work on conventional regular shaped microstrip antennas may be found in the literature but these conventional shaped antennas fail to serve their purpose in modern communication systems. These antennas have narrow bandwidth, low gain, and provide optimum performance at a frequency corresponding to their dominant mode [1, 2]. For recent fast rate data communication systems, need for compact broadband patch antenna having wide bandwidth is realized. Microstrip antennas play an important role in improving the overall performance and reducing the overall size of wireless

Neelam Choudhary · Ajay Tiwari · Brajraj Sharma · J.S. Saini · D. Bhatnagar (✉)
Department of Physics, University of Rajasthan, Jaipur 302004, India
e-mail: dbhatnagar_2000@rediffmail.com

devices. Looking at inherent properties of patch antennas, antenna designers are modifying the conventional regular geometries, so that these may be applied in modern communication systems. It is realized that application of slot/slits in patch geometry or modifications in substrate parameters improves the performance of antenna to a great extent but after reaching an optimum value, no further improvement in the performance may be achieved. Further, these techniques have their own limitations, hence in recent years modifications in ground plane have been adopted [3–5] by researchers. It has been realized that with application of defected ground plane in antenna design, the desired compactness with broadband performance can be easily achieved.

In recent times, several single-layer ring patch geometries fed by microstrip line have been reported [6, 7], which mainly resonate at higher frequency and provide narrow impedance bandwidth. In this paper; a compact size wideband frequency antenna fed by strip line is designed. Starting with a conventional circular patch structure, the geometry is modified in several steps and radiation performances in each step of modification are simulated using CST microwave studio simulator.

Antenna Design and Analysis

The work started with consideration of a conventional circular patch antenna having patch radius 16 mm on Glass Epoxy FR-4 substrate. This dielectric substrate has substrate relative permittivity 4.4, substrate height (h) 1.59 mm and substrate loss tangent 0.025. A strip line of length 6.5 mm and width 3 mm is attached to this patch to feed this antenna and is connected with a 50 Ω cable through SMA connector. The size of ground plane is taken equal to 39 mm \times 46 mm, i.e., the ground plane is finite in nature. The front and rear views of considered antenna are shown in Fig. 1a, b respectively. CST Microwave Studio simulator [8] is used for analysis of this antenna. Figure 2 shows that the proposed conventional circular

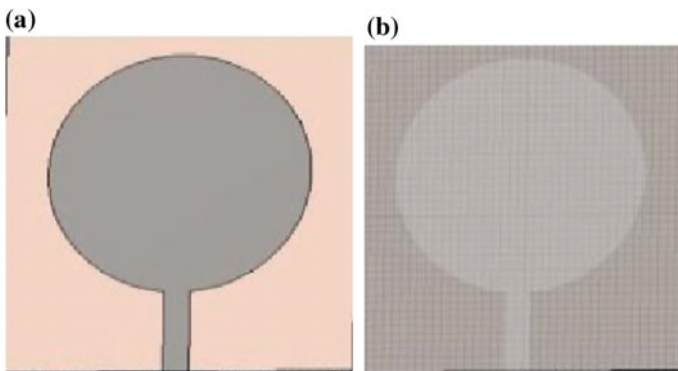


Fig. 1 a Front view of designed. b Rear view of designed

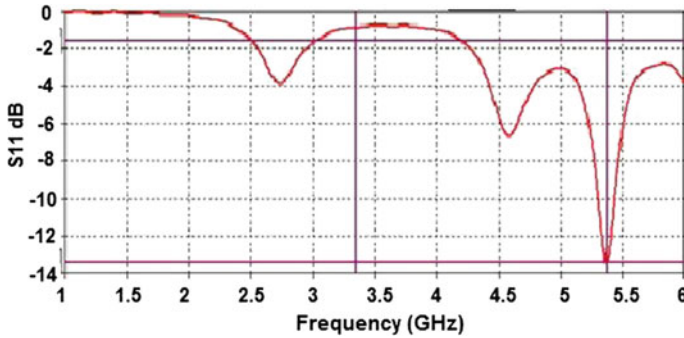


Fig. 2 Simulated variation of reflection coefficient with frequency for CCMP

patch antenna effectively resonates at frequency 5.37 GHz. The impedance bandwidth presented at this frequency is narrow ($\sim 3\%$), obtained gain of antenna is close to 2 dBi, and antenna mainly radiates normal to patch geometry. Under these conditions, considered strip line feed circular patch antenna is not suitable for modern day communication systems.

This patch geometry is modified in several steps by cutting concentric rings one by one in the circular patch without modification in finite ground plane ($39\text{ mm} \times 46\text{ mm}$). The innermost part of this geometry is a circle of radius 1 mm and thereafter four partial concentric rings are applied as shown as in Fig. 3. The separation between each ring is 2 mm. In each stage of modification in patch geometry, simulation of antenna performance is carried out. The design parameters of finally optimized geometry are provided in Table 1. The top and back views of this antenna are shown in Fig. 3a, b respectively. It is realized from simulation analysis of the considered antenna that the proposed modifications in patch geometry result in marginal improvement in the overall performance of antenna. In the present condition, antenna resonance is at three frequencies, namely 1.7, 3.2, and 4.79 GHz, as shown in Fig. 4, but it still provides narrow bandwidth at these

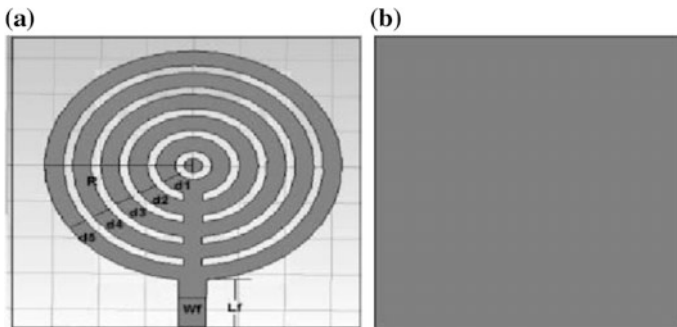


Fig. 3 a Front view of concentric ring antenna. b Rear view of designed antenna

Table 1 Dimensions of the proposed geometry

Outer radius of patch (R)	16 mm
Radius of inner most circle (r)	1 mm
Thickness of rings ($d1 = d2 = d3 = d4 = d5$)	2 mm
Spacing between rings	2 mm
Length of feed line (L_f)	6.5 mm
Width of feed line (L_f)	3 mm

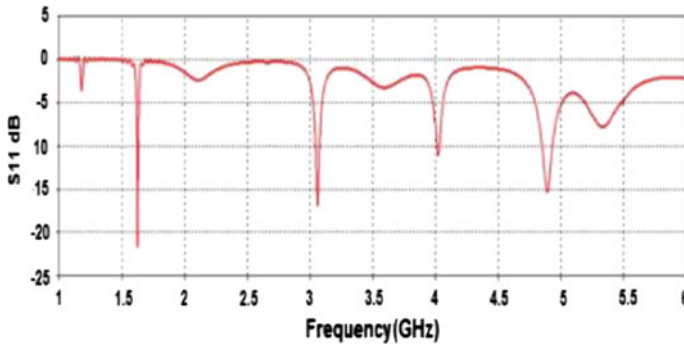


Fig. 4 Simulated reflection coefficient with frequency for circular concentric ring antenna

frequencies. Marginal improvement in gain of antenna (2.6 dBi) is also realized. The analysis reveals that even after proposed modifications in patch geometry, the antenna is not much suited for application in modern communication systems. Therefore in the next stage of modification, the ground plane of antenna is modified.

Defected ground structure (DGS) is an easy way to realize the slow wave effect. This technique is finding extensive application in obtaining miniaturized antennas [9, 10]. In the next step, the considered annular ringed circular microstrip patch antenna is further modified by converting finite ground plane into defected ground plane. The radiating patch as shown in Fig. 5a is retained unchanged and the size of ground plane is reduced from the previously considered 39 mm × 46 mm to 33 mm × 20 mm. Several narrow slits are introduced in the ground plane one by one. The top and bottom edges of ground plane are also modified in steps to finally obtain the structure of ground plane as shown in Fig. 5b. The design parameters of the finally considered geometry are listed in Table 2. After considering the modifications in ground plane, modified antenna resonates at three frequencies, namely 2.45, 3.0, and 4.53 GHz as shown in Fig. 6. The presented impedance bandwidth in the second band lying between 2.33 and 4.53 GHz is close to 2.20 GHz or 64.53 % with respect to central frequency 3.42 GHz. One can realize that obtained impedance bandwidth is significantly higher than that achieved for the earlier two geometries. The first resonance frequency 1.79 GHz is useful for mobile communication systems. The gain variation of antenna with frequency in the operating

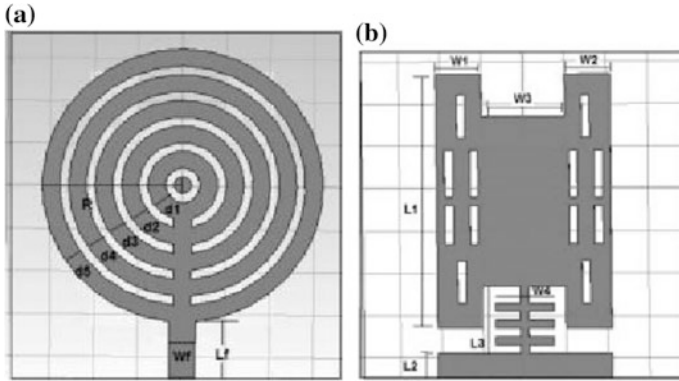


Fig. 5 a Front view of concentric ring antenna. b Rear view of modified ground

Table 2 Dimensions of the proposed geometry

L1	30 mm
L2	3 mm
L3	8 mm
W1 = W2	5 mm
W3	10 mm
W4	7 mm

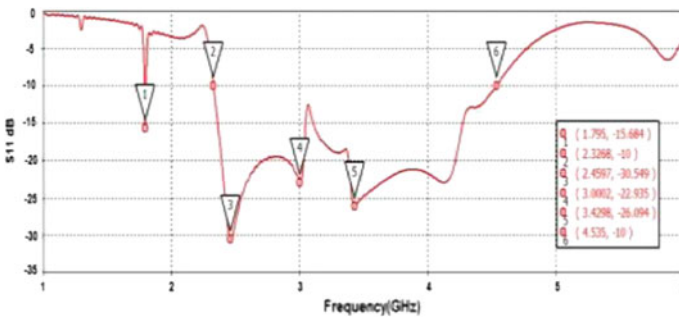


Fig. 6 Simulated reflection coefficient of circular patch having concentric rings and defected ground plane

frequency range is shown in Fig. 7, which indicates that gain of antenna is almost uniform in the considered frequency range. Maximum gain of antenna is 3.05 dBi at frequency 4.42 GHz, which is also improved considerably in comparison to those of the earlier reported two antenna geometries. The E plane simulated far-field radiation patterns obtained at frequencies 2.45 and 3.42 GHz are shown in Fig. 8. Antenna in its present form radiates maximum radiations normal to its patch and

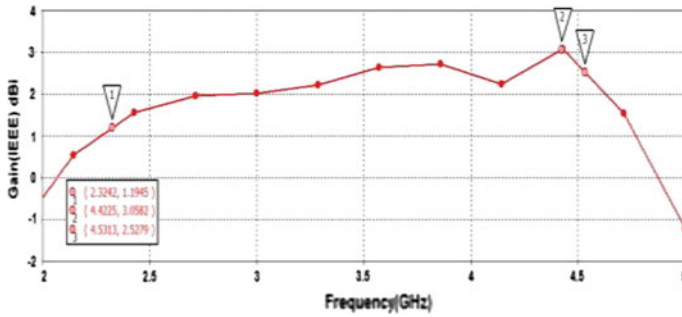


Fig. 7 Simulated gain of circular patch having concentric rings and defected ground plane

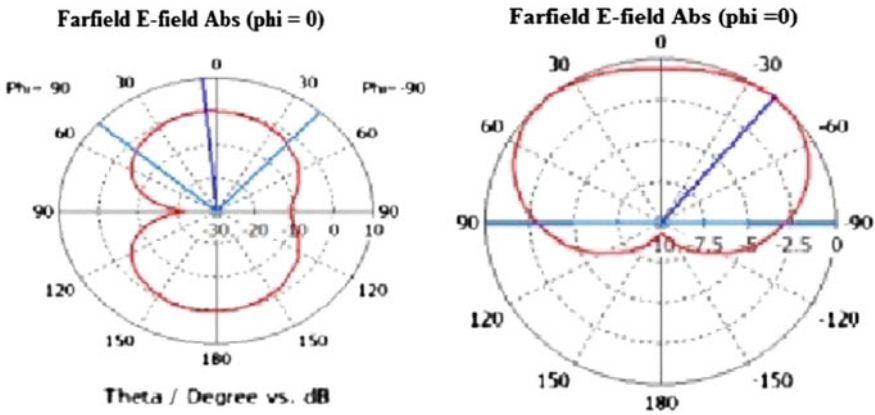


Fig. 8 E plane simulated far-field radiation patterns obtained at frequencies 2.45 and 3.42 GHz

shapes of patterns at two frequencies, somewhat similar to a dumbell and semi-hemispherical shape respectively. At first resonance frequency, the 3 dB beam width is close to 90° while at second resonance frequency the 3 dB beam width is close to 180°.

Conclusions

In this paper, the design and performance of a compact circular patch antenna having concentric rings and defected ground plane is obtained and compared with that of a conventional circular patch antenna with finite ground plane under similar test conditions. With the considered arrangement of patch and ground plane, the impedance bandwidth of antenna has attained a value close to 64 % while the gain has attained a value close to 3 dBi. These values are significantly higher than those

observed for a conventional circular patch antenna having finite ground plane. In E plane; simulated far-field radiation patterns obtained at frequencies 2.45 and 3.42 GHz indicate that antenna radiates maximum radiations normal to patch geometry and shape of patterns at two frequencies is more or less similar to a dumbbell and semihemispherical shape respectively. This antenna is specifically designed looking at Indian requirements for wireless communication systems.

Acknowledgments Authors are thankful to DEIT, New Delhi for the financial support provided to work on this project.

References

1. Garg, R., Bhartia, P., Behl, I., Ittipiboon, A.: *Microstrip Antenna Design Handbook*. Artech House Inc (2001)
2. Guha, D., Antar, Y.M.M.: *Microstrip and Printed Antennas New Trends, Techniques and Applications*. Wiley Int. Sc., U.K. (2011)
3. Guo, Y.X., Luk, K.M., Lee, K.F.: L-Probe fed thick-substrate patch antenna mounted on a finite ground plane. *IEEE Trans. Antennas Propag.* **51**(8) (2003)
4. Lien, H.C., Lee, Y.C., Lee, W.F., Tsai, H.C.: Microstrip slot antenna with a finite ground plane for 3.1 to 10.6 GHz ultra wideband communication. In: *PIERS Proceedings, Beijing, China, 23–27 Mar 2009*
5. Liu, H., Li, Z., Sun, X.: Compact defected ground structure in microstrip technology. *Electron. Lett.* **41**(3), 132–134 (2005)
6. Guo, Y.X., Bian, L., Shi, X.Q.: Broadband circularly polarized annular-ring microstrip antenna. *IEEE Antennas Propag.* (2009)
7. Bao, X., Ammann, M.: Compact concentric annular-ring patch antenna for triple frequency operation. *Electron. Lett.* **42**(10), 1129–1130 (2006)
8. <http://www.cst.com>
9. Liu, J.X., Yin, W.Y., He, S.L.: A new defected ground structure and its application for miniaturized switchable antenna. *Prog. Electromagnet. Res. PIER* **107**, 115–128 (2010)
10. Pan, C.Y., Duan, J.H., Jan, J.Y.: Co-planer printed monopole antenna using coaxial feed line for DTV application. *Prog. Electromagnet. Res. Lett.* **34**, 21–29 (2012)

On the Bandwidth Enhancement of Modified Star-Triangular Fractal Antenna

Simarpreet Kaur, Rajni and Gurwinder Singh

Abstract This paper presents a star-triangular fractal (STF) antenna operating between 1 and 30 GHz, which is modified by incorporating additional Sierpinski gasket fractal structure. The STF antenna is designed and simulated using adaptive mesh generation in Ansys software High Frequency Structure Simulator, based on finite element method (FEM) technique. The simulated outcome of amended fractal antenna has been evaluated in comparison to reference antenna. It is observed that the proposed antenna is applicable over super high frequency range.

Keywords Antenna · Fractal · Star-triangular fractal · Wideband

Introduction

Rapid growth in wireless communication demands wider band antennas with extremely compact sizes. A good approach toward this is implementation of fractal structures into antenna design field. The name FRACTAL, originated by B.B. Mandelbrot (French Mathematician) from a Latin word called “Fractus”, is linked to the verb “fangere”, which means “fractured” or “broken.” He defined certain geometries as fractal after exploring nature’s random and fragmented geometries, which were complicated to describe with the help of Euclidean geometry like trees, lightning phenomena, coastlines, mountains, clouds, etc. Fractal geometries are electrically long and have the unique capability of filling compact areas. In 1982, Mandelbrot introduced the concept of fractional structures in his book [1].

Simarpreet Kaur (✉) · Rajni · Gurwinder Singh
Department of ECE, SBSSTC, Ferozepur 152004, India
e-mail: ksimarpr@gmail.com

Rajni
e-mail: rajni_c123@yahoo.co.in

Gurwinder Singh
e-mail: gurwinder08singh@gmail.com

A number of fractal designs have previously been considered and examined as antennas such as Koch curve, Minkowski curve, Cantor patch, Sierpinski Carpet, etc [2]. The self-similar fractal linear and planar array, the first implementation of fractal structures into antenna design was investigated in 1986. Later, Werner continued with the same work and investigated the behavior of fractal antennas [3]. In 1995, Cohen bent the wire in a particular manner and designed the Koch fractal antenna. Later, the behavior of Koch fractal was investigated and compared with conventional antennas [4]. Puente studied the outcome of Sierpinski fractal antenna in 1998 and proposed that the multiband behavior of fractals is because of self-similar structure after comparing it with a simple bow-tie antenna [5]. In 2000, Romeu studied the behavior of Koch monopole by changing the number of recursions [6]. In 2001, mod-p Sierpinski gasket fractal antenna was designed using Pascal triangle [7]. In 2002, Steven considered the Koch and Sierpinski fractals and concluded that the resonant frequency of fractal antennas depend upon the geometry of antenna and wire length. In 2003, the resonant characteristics of fractal antennas were studied, like radiation resistance, quality factor, and efficiency of various fractal antennas [8, 9]. Kimoto and Kikkawa compared various characteristics of Sierpinski dipole fabricated on silicon in 2005 [10]. In 2007, Sinha proved the self-affinity property of fractal geometries [11]. In 2009, Chen used Microstrip feed line for bandwidth enhancement of slotted fractal antenna [12]. In 2011, A new E-shaped (probe feed) fractal was introduced by Bayatmaku as antenna [13, 14]. In 2013, Waladi and Mohammadi modified the monopole STF antenna so as to make it work in super wideband [15].

In this paper, a star-triangular fractal antenna is modified by changing the radius of metallic ring around it and another Sierpinski gasket fractal structure design is incorporated in the outer ring of STF and results have been evaluated with the help of HFSS. In this work, section “[Description of Fractal Structure](#)” describes the proposed fractal structure and its dimensions. Section “[Results and Discussion](#)” presents simulated results achieved and discusses them. Section “[Conclusion](#)” draws conclusions of the work done.

Description of Fractal Structure

The proposed fractal antenna is considered and simulated on FR4 substrate having dimensions $20 \times 20 \times 1 \text{ mm}^3$ with dielectric constant taken to be 4.4, having tangent loss of 0.02. The shape of ground plane taken is semi-elliptical, having length 3.5 mm and width 20 mm, with a notch of $2.4 \times 1.16 \text{ mm}^2$, at feeding position, for better impedance matching. The feed line is designed for 50Ω characteristic impedance, with length and width as $4.8 \times 1.9 \text{ mm}^2$. The STF antenna is simulated using finite element method-based Ansoft EM numerical solver High Frequency Structure Simulator (HFSS). FEM divides the problem domain into a group of sub-domains and each sub-domain is characterized by a set of mathematical

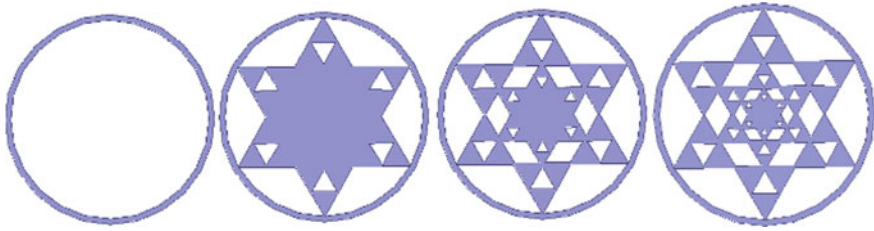


Fig. 1 Three iterations of STF design

Table 1 Parametric values of STF geometry

Parameter	Description	Value (mm)
R	Radius of external circle	7.2
r	Radius of inner circle	6.8
h_t	Height of elemental triangle	10.3
w_t	Width of elemental triangle	12
L_s	One face of primary slot	1.7

equations. All the equations are systematically recombined for the final computation of electromagnetic field and other performance parameters.

The recursive procedure of the proposed STF design is shown in Fig. 1, which consists of three iterations having iteration scaling factor of 0.5.

Table 1 shows the various parametric values of fractal geometry.

STF Antenna

Figure 2 with STF antenna is designed using the parametric values shown in Tables 1 and 2.

Table 2 shows the various parametric values of STF antenna.

In this proposed design, antenna parameters are adjusted and Sierpinski gasket is incorporated into the design to increase the bandwidth coverage and gain enhancement.

Proposed Modified Design

Model 1

In this design, a ring has been generated by taking outer circle radius of 7.8 mm, inner circle radius of 6.8 mm, and other parameters are kept the same, as shown in Fig. 3. The new antenna is simulated and its behavior is compared with the previous antenna.

Fig. 2 Geometry of STF antenna

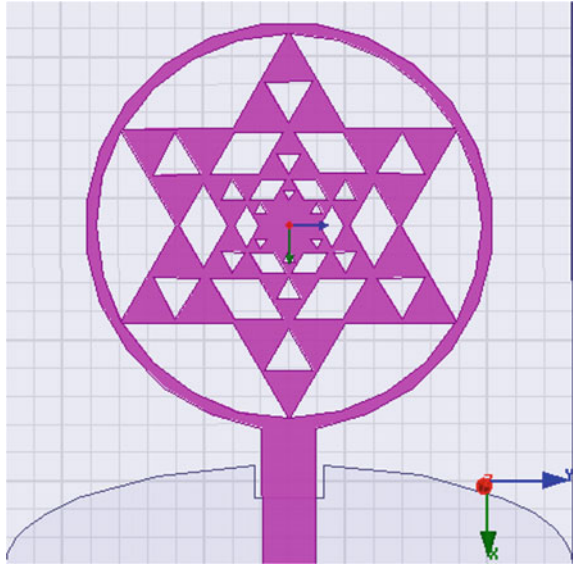


Table 2 Parametric values of STF antenna

Parameter	Description	Value (mm)
L_a	Length of antenna	20
W_a	Width of antenna	20
L_{fl}	Length of feed line	4.8
W_f	Width of feed line	1.9
L_{gp}	Length of ground plane	3.5

Fig. 3 Geometry of proposed modified STF antenna with higher outer ring radius

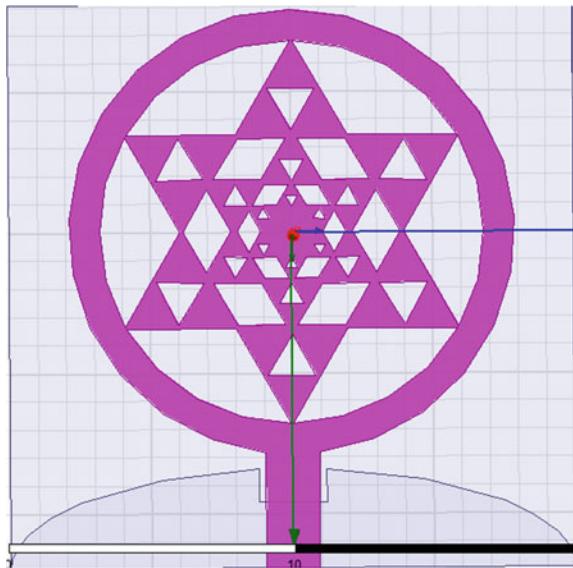
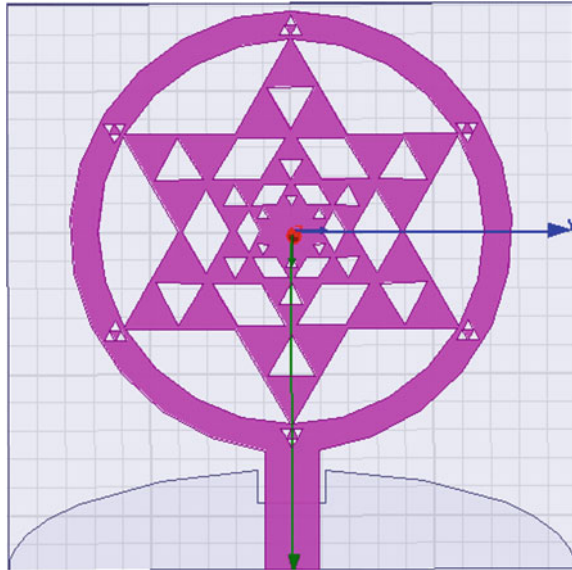


Fig. 4 Incorporation of Sierpinski Gasket into Model 1



Model 2

Model 2 has been generated from Model 1 by inserting the Sierpinski Gasket design into it so as to improve the performance of STF Antenna, as shown in Fig. 4. Each side of the equilateral triangle reduced from the outer ring is taken to be 0.8 mm. The inner triangle is rotated and scaled down by a factor of 0.5 approximately.

Results and Discussion

Return Loss Parameter of Reference Model, Model 1 and Model 2

Model 1 is designed by increasing the area of outer ring, as we can see in Fig. 5 the return loss and bandwidth of Model 1 is much better than the reference model. It is clear that the bandwidth of Models 1 and 2 is almost the same and is much more compared to reference model.

Gain of Reference Model, Model 1 and Model 2

Figure 6 shows the gain of reference model, Models 1 and 2. It can be seen that incorporating the Sierpinski Gasket into STF antenna results in much higher gain compared to reference model and Model 1.

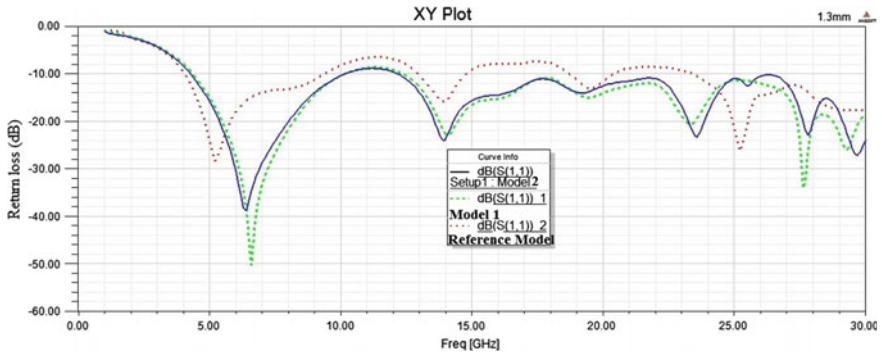


Fig. 5 Return Loss parameter of reference model, Model 1 and Model 2

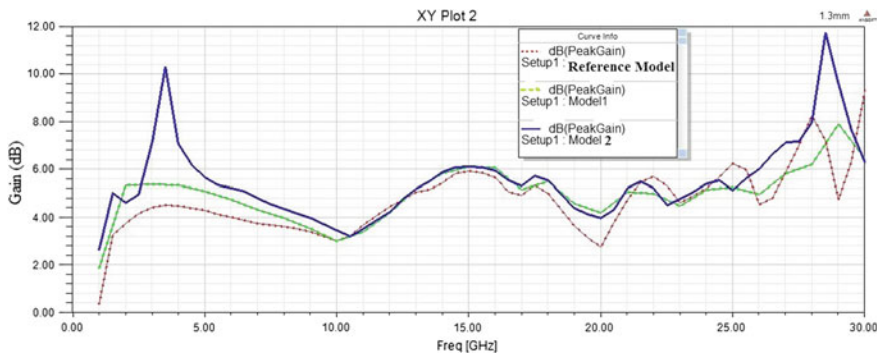


Fig. 6 Gain of reference model, Model 1 and Model 2

VSWR of Reference Model, Model 1 and Model 2

Figure 7 shows the VSWR parameter of reference model, Models 1 and 2 STF antenna. The value of VSWR varies between 1 and 2 over operating bands (4.3–10.1) GHz & (12.2–30) GHz for model 2 antenna. VSWR of model 2 is better compared to Model 1 and reference model.

The frequency bands over which the STF antenna can work efficiently are shown in Table 3.

The STF antenna can operate over super high frequency range. As the wavelength is in centimeter range, this frequency range is also known as centimeter band.

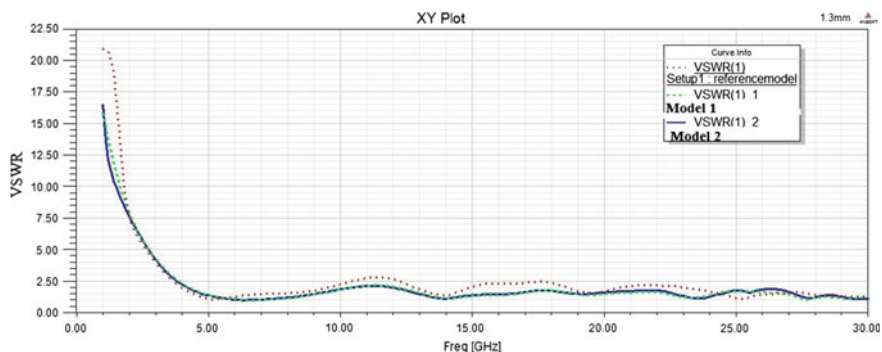


Fig. 7 VSWR of reference model, Model 1 and Model 2

Table 3 Comparison between reference model, Model 1 and Model 2

Model	Bandwidth (GHz)	Gain (dB)
Reference model	(4.05–9.36)	(4.47–3.27)
	(12.9–14.76)	(5–5.87)
	(18.7–20.3)	(4.053–3.36)
	(23.4–30)	(4.84–9.35)
Model 1	(4.35–10.13)	(5.27–3.00)
	(12.35–30)	(4.6–6.43)
Model 2	(4.3–10.1)	(6.53–3.4)
	(12.2–30)	(4.44–6.3)

Conclusion

The STF antenna is presented and simulated over wide bandwidth (1–30) GHz using HFSS. It is clear that optimization of the design parameters of antenna results in improvement of performance parameters, such as return loss, impedance matching, gain, bandwidth, and VSWR. Incorporation of additional fractal geometry, Sierpinski Gasket, into STF results in high gain and large bandwidth. Bandwidth depends on the gap among the patch and ground. As the gap among the patch and elliptical ground decreases, discontinuities in the current distribution decreases and impedance matching gets enhanced. The proposed STF antenna is applicable over super high frequency (SHF) range and is suitable for use in wireless USB, Wi-Fi, terrestrial data links, WLAN, satellite communication, etc. This work can be carried out in the future to achieve more bandwidth or shifting the resonant frequency to higher or lower frequencies, by modification of geometry, by changing the shape and dimensions of slot cut from ground, using different feeding methods, etc.

References

1. Mandelbrot, B.B.: The fractal geometry of nature. W.H. Freeman Company, NY (1983)
2. Kim, Y., Jaggard, D.L.: The fractal random array. Proc. IEEE 1278–1280 (1986)
3. Werner, D.H., Werner, P.L.: Frequency independent features of self similar fractal antennas. Radio Sci. **31**(6), 1331–1343 (1996)
4. Cohen, N.: Fractal antennas: Part I. Commun. Q. 7–22 (1995)
5. Puente, C., Romeu, J., Pous, R., Cardama, A.: On the behavior of the Sierpinski multiband fractal antenna. IEEE Trans. Antennas Propag. **46**(4) (1998)
6. Puente, C., Romeu, J., Cardama, A.: The Koch monopole: a small fractal antenna. IEEE Trans. Antennas Propag. **48**(11) (2000)
7. Romeu, J., Soler, J.: Generalized Sierpinski fractal multiband antenna. IEEE Trans. Antennas Propag. **49**(8) (2001)
8. Best, S.R.: On the resonant properties of the Koch fractal and other wire monopole antennas. IEEE Antennas Wirel. Propag. Lett. **1**, 74–76 (2002)
9. Best, S.R.: On the significance of self-similar fractal geometry in determining the multiband behavior of the Sierpinski Gasket antenna. IEEE Antennas Wirel. Propag. Lett. **1**, 22–25 (2002)
10. Kikkawa, T., Kimoto, K., Watanabe, S.: Ultra wideband characteristics of fractal dipole antennas integrated on Si for ULSI wireless interconnects. IEEE Electron Device Lett. **26**(10), 767–769 (2005)
11. Sinha, S.N., Jain, M.: A self-affine fractal multiband antenna. IEEE Antennas Wirel. Propag. Lett. **6**, 110–112 (2007)
12. Chen, W., Wang, G., Zhang, C.: Bandwidth enhancement of a microstrip-line-fed printed wide-slot antenna with a fractal-shaped slot. IEEE Trans. Antennas Propag. **57**(7), 2176–2179 (2009)
13. Casanova, J.J., Taylor, J.A., Lin, J.: Design of a 3-D fractal heat sink antenna. IEEE Antennas Wirel. Propag. Lett. **9**, 1061–1064 (2010)
14. Kaur, S., Rajni, Marwaha, A.: Fractal Antennas: a novel miniaturization technique for next generation networks. Int. J. Eng. Trends Technol. (IJETT) **9**(15) (2014)
15. Waladi, V., Mohammadi, N., Zehforoosh, Y., Habashi, A., Nourinia, J.: A novel modified star-triangular fractal (MSTF) monopole antenna for super-wideband applications. IEEE Antennas Wirel. Propag. Lett. **12** (2013)

A Simple Miniaturized Dual Band Antenna for WiMAX/WLAN Applications

Nirma Kumawat and Krishna Rathore

Abstract A simple miniaturized antenna for dual band operation is presented in this paper. A Microstrip line feed is used for achieving 50Ω impedance matching and the antenna consist of a square patch of a small size $18(W) \times 18(L)$ mM. By introducing two parasitic elements, two bands are created with resonating frequencies at 3.2 and 5.63 GHz. These two frequency bands range from 2.86 to 4.03 GHz (WiMAX) and 5.28–6.04 GHz (WLAN). It is a multiband antenna that could be easily integrated with portable mobile devices. The VSWR, gain, and radiation pattern of the proposed antenna are simulated using computer simulation technology software and shows good acceptance with the theoretical concepts.

Keywords Dual band • Parasitic element • Semicircle slot

Introduction

Recently, there has been a great demand of antennas capable of providing multiple services. These antennas should be compact so that they could be easily integrated with mobile portable devices. WiMAX (3.1–3.8 GHz) and WLAN (5–5.8 GHz) are two popular wireless standards. These wireless standards operate in the range of UWB (3.1–10.6 GHz), hence, such UWB antennas experience interference from these wireless standards [1]. Thus, filters are required to reduce these interferences. Antennas that cover only these wireless standards frequency band and neglecting remaining UWB band are a hot topic of research. Compact multiband antennas are need of hour. Multiband antennas are cost effective by suppressing the superfluous

Nirma Kumawat (✉)
Ajmer Institute of Technology, Ajmer, India
e-mail: kumawatnirma@gmail.com

Krishna Rathore
Government Engineering College Ajmer, Ajmer, India
e-mail: rathore65@gmail.com

bands. The portability of a modern personal wireless terminal device can be improved by using multiband communication system in a single system.

A Dual band antenna covering WiMax and WLAN in a single compact device is the need of hour. Several multiband antennas have been reported in the literature [2–10]. These technique involves use of DGS (defected ground structure) [2, 3] and use of meandered-shaped structures [4]. The planar monopole antennas have been designed for multiband operations [5, 6]. Some techniques include the use of inverted FL shapes [7], use of L shaped elements [8] and use of double T-shaped element [9]. CPW feeding has also been encountered [10]. But all these design are complex and inadequate with respect to one or more criteria. In this paper, a very simple antenna structure with parasitic elements has been introduced in order to create different bands covering WiMAX and WLAN applications. In this letter, we proposed a simple miniaturized antenna. This antenna simply employs two parasitic elements on both sides of the square patch to control flexible variation of frequency bands and a semicircle slot is cut in the ground plane to introduce a band. This is a quite simple antenna structure to achieve stable radiation performance as compared to other multiband antenna designs. The whole antenna designing is described in section “[Antenna Design](#)”. Section “[Results and Discussion](#)” gives the simulation results of the proposed antenna. Computer simulation technology (CST) is used as an electromagnetic solver to compute the results. Finally, the paper is concluded in section “[Conclusion](#)”.

Antenna Design

We have chosen a primitive antenna structure having square patch and a semicircular notch of radius R in the partial ground plane. In this antenna structure two parasitic elements are created at both vertical sides of the square patch as shown in Fig. 1. Figure 2 shows final optimized geometry of the proposed antenna design. The substrate used is FR4 having dielectric constant $\epsilon_r = 4.4$ and loss tangent $\tan\delta = 0.02$. The dimension of substrate is $38 (L) \times 28 (W) \times 1.6 \text{ mm}^3$. The antenna was fed using a microstrip line of thickness 4.2 mm. A square patch is of size $18 (L) \times 18 (W) \text{ mm}^2$ and ground plane has length 11.5 mm and width 28 mm. Two I-shaped slot were cut from both vertical sides of the patch to form the parasitic elements. These parasitic elements introduce a band from 5.28 to 6.045 GHz for WLAN and a semi circular slot introduce a band from 2.865 to 4.029 GHz for WiMAX application.

The cut portion acts as parasitic elements for the remaining portion of the patch. These parasitic elements are responsible for generating desirable resonance for the dual band operation. Computer simulation technology (CST) is used as an electromagnetic solver to simulate and analyze the radiation performance of the proposed antenna. The optimal dimensions of the antenna are as follows: $L1 = 38 \text{ mm}$, $W1 = 28 \text{ mm}$, $L2 = 18 \text{ mm}$, $W2 = 18 \text{ mm}$, $W3 = 14 \text{ mm}$, $W4 = 4.2 \text{ mm}$, $L3 = 11.5 \text{ mm}$, $L4 = 13 \text{ mm}$, $R = 4 \text{ mm}$, and $G = 0.5 \text{ mm}$.

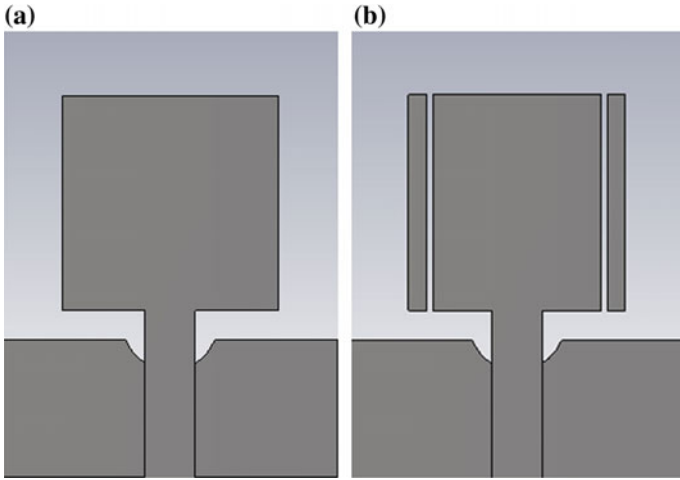
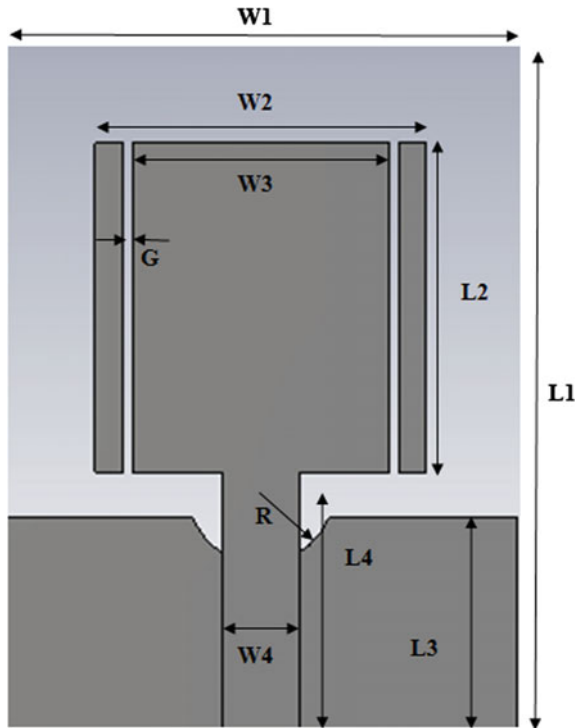


Fig. 1 Evolution of the antenna design a Primitive antenna b Dual band notched antenna

Fig. 2 Geometry of the proposed antenna



Results and Discussion

The antenna is simulated using CST electromagnetic solver. Figure 3 shows the return loss curve for varying values of the gap ‘G’ between the central patch and the parasitic elements. By varying the gap G, operating bands experience a shift toward left for WiMAX (3.13–3.8 GHz) region and right shift for WLAN (5–5.8 GHz) region. A third band can also be seen for the frequency band 9.54–10 GHz by varying the slot width as shown in Fig. 3. This characteristic could be used to handle the frequency shifting problem, which arises while implementing the antenna practically.

Figure 4 shows the simulated return loss curve for the proposed optimized antenna. The figure shows that this antenna covers two bands ranging from 2.87 to 4.03 GHz with bandwidth 1164 MHz and 5.28–6.04 GHz with bandwidth 758 MHz. The first band covers the operational range of WiMAX (3.1–3.8 GHz) and the second band covers the operational range of WLAN (5.1–5.8 GHz). Hence,

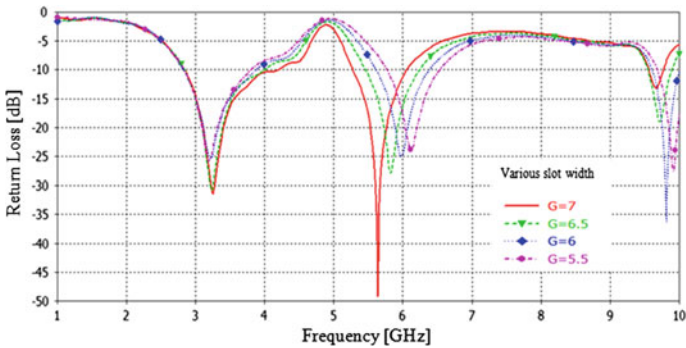


Fig. 3 Simulated return loss for different values of gap G

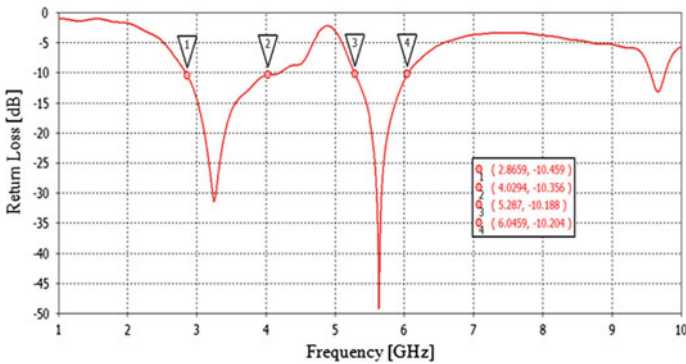


Fig. 4 Return loss of the proposed antenna

the proposed antenna is a dual band antenna capable of working for both the wireless standards. Surface current distribution is an important characteristic of the antenna and for the proposed antenna it is shown in Fig. 5 and at the resonant frequencies of 3.2 and 5.63 GHz. As shown in Fig. 5a a stronger resonance occurs across the semicircle slot in ground plane and at the bottom side surrounding the parasitic element for 3.2 GHz frequency. Figure 5b shows that for 5.63 GHz frequency surface current is maximum at upper side of parasitic elements as compared to bottom portion of the parasitic elements.

Figure 6a, b shows the far field radiation pattern at the frequencies of 3.2 and 5.63 GHz. The antenna shows bidirectional radiation patterns at both the

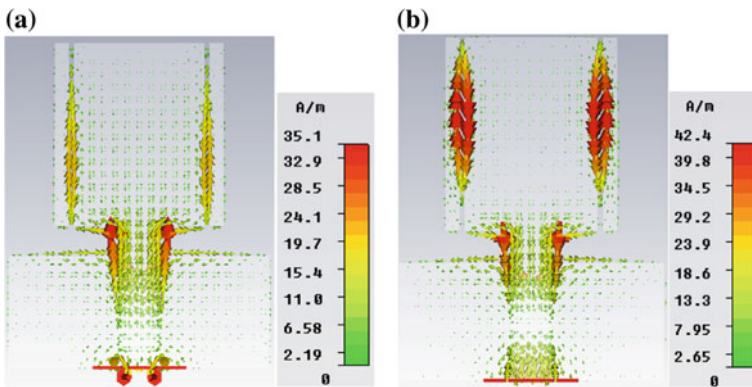


Fig. 5 Simulated surface current distribution for the resonant frequency a at 3.2 GHz and b at 5.63 GHz

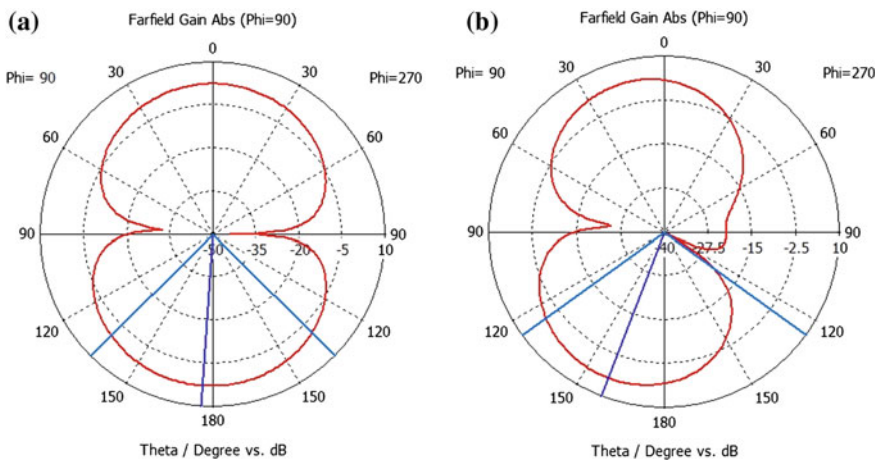


Fig. 6 Simulated radiation patterns for the proposed dual band antenna at a 3.2 GHz b 5.63 GHz

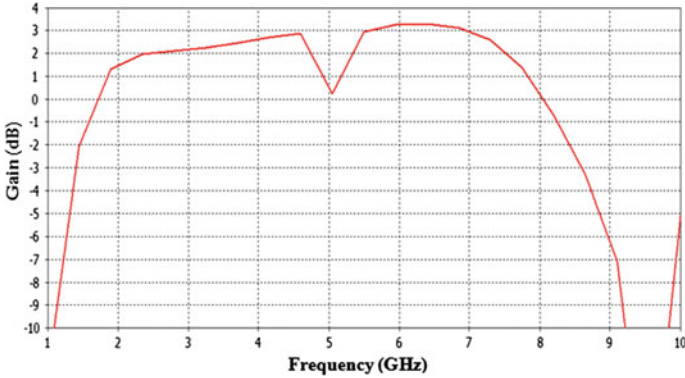
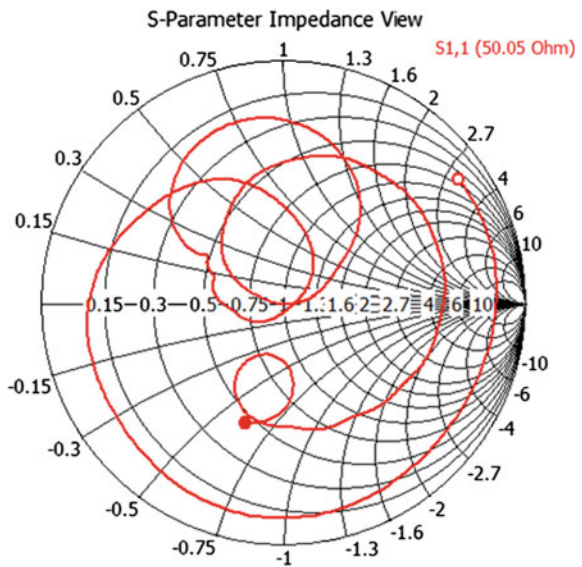


Fig. 7 Simulated gain of the proposed antenna

frequencies. This indicates that a large and uniform coverage can be obtained for both the frequency bands corresponding to WiMAX and WLAN.

Figure 7 represents the simulated antenna gain for the entire operating band. It is seen that the maximum gain is 3.1 dB for WiMAX and WLAN band. After that gain decreases to negative. Figure 8 shows the smith chart for the proposed antenna. It is seen that the impedance of the feed line is perfectly matched to that of antenna. The 50 Ω impedance is achieved by varying the width $W/4$ of the microstrip line.

Fig. 8 Smith chart of the proposed antenna showing impedance matching



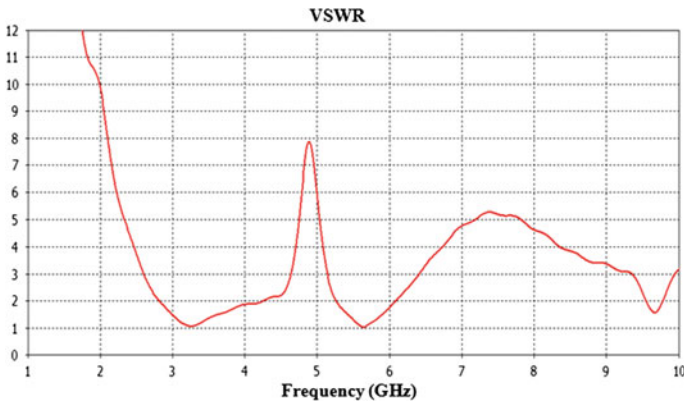


Fig. 9 Simulated VSWR of the proposed antenna

Figure 9 shows the VSWR result for the proposed antenna. It is seen that the value is less than 2 for the two operating bands corresponding to WiMAX and WLAN. For the rest of the frequencies it is greater than 2. It is desirable to have VSWR values below 2 for the operating frequencies.

Conclusion

A simple miniaturized monopole antenna with dual band characteristics has been presented. We illustrated that by inserting two parasitic elements in the patch, a multiband antenna could be designed. The surface current results at the two resonating frequencies well explained corresponding to WiMAX and WLAN regions. The radiation pattern shows good bidirectional behavior over the entire operating bands and the gain curve shows a drastic decrement outside the operating bands. The antenna feed line impedance is well matched to 50Ω . It is a simple compact dual band antenna for WiMax and WLAN wireless standards. This study has huge future scope and serves as a step for designing compact multiband antennas.

References

1. Abdollahvand, M., Dadashzadeh, G., Mostafa, D.: Compact dual band-notched printed monopole antenna for UWB application. *IEEE Antenna Wirel. Propag. Lett.* **9** (2010)
2. Hsieh, C.P., Chiu, T.C., Lai, C.H.: Compact dual band slot antenna at the corner of the ground plane. *IEEE Trans. Antennas Propag.* **57**(10), 3423, 3426 (2009)
3. Liu, W.-C., Wu, C.-M., Dai, Y.: Design of triple-frequency microstrip fed monopole antenna using defected ground structure. *IEEE Trans. Antenna Propag.* **59**(7) (2011)

4. Chang, T.N., Jiang, J.H.: Meandered T shaped monopole antenna. *IEEE Trans. Antenna Propag.* **57**(12), 3976, 3978 (2009)
5. Kim, S.C., Lee, S.H., Kim, Y.S.: Multiband monopole antenna using meander structure for handheld terminals. *Electron. Lett.* **44**(5), 331–332 (2008)
6. Zhu, J., Antoniadis, M.A., Eleftheriades, G.V.: A compact tri band monopole antenna with single cell metamaterial loading. *IEEE Trans. Antenna Propag.* **58**(4), 1031, 1038 (2010)
7. Nakano, H., Sato, Y., Mimaki, H., Yamauchi, J.: An inverted FL antenna for dual frequency operation. *IEEE Trans. Antenna Propag.* **53**(8), 2417, 2421 (2005)
8. Chen, J.S.: Studied of CPW fed equilateral triangular ring slot antennas and triangular ring slot coupled patch antennas. *IEEE Trans. Antenna Propag.* **53**(7), 2208, 2211 (2005)
9. Kuo, Y.L., Wong, K.L.: Printed double T monopole antenna for 2.4/5.2 GHz dual band WLAN operations. *IEEE Trans. Antenna Propag.* **51**(9), 2187, 2192 (2003)
10. Zhai, H., Ma, Z., Han, Y., Liang, C.: A compact printed antenna for triple band WLAN/WiMAX applications. *IEEE Antenna Wirel. Propag. Lett.* **12**, 65, 68 (2013)

Fault Detection for the Cluster-Based System in Wireless Sensor Networks

Rimpi Goyal and Sukhwinder Singh Sran

Abstract A wireless sensor network is a self-configuring network of sensor nodes. One of the major areas to be concerned in wireless sensor networks is fault management. Due to some undesirable circumstances like crash and energy enervation faults become obvious to occur. In order to avoid performance degradation of deployed system due to these faults, it is essential to detect faults at an early stage. Therefore, an energy efficient cluster-based fault detection system has been designed. This system uses neighbour's coordination approach to perform failure detection process. In addition to this failure detection, it is also mandatory to detect failure detection of cluster heads. So concept of detector is introduced for it. Failure detection for cluster heads is performed by this detector; a node having maximum residual energy among all cluster heads.

Keywords Wireless sensor networks · Fault detection · Clustering · Residual energy

Introduction

Micro-electromechanical technology burst out in technology world through development of multifunctional sensor nodes. These nodes have configured with unique features tiny size, wireless communication, low cost of development, low power and enable to communicate efficiently in short distances [1]. This new technology, wireless sensor network have gained extremely attention all over the world since it becomes a pertinent solution for applications located in hostile environment, such as monitoring of pressure, temperature, etc. [2, 3]. Clustering is a

Rimpi Goyal (✉) · S.S. Sran
Department of CE, YCoE, Punjabi University Guru Kashi Campus,
Talwandi Sabo - Bathinda, Punjab, India
e-mail: rimsgoyal@gmail.com

S.S. Sran
e-mail: sukhwinder.sran@gmail.com

technique in which nodes have segmented into a number of small groups known as clusters. Each cluster has a controller termed as CH and some nodes which become member of that cluster [4]. A large number of protocols have been used in WSNs for routing purposes such as: LEACH, LEACH C, PEGASIS, TEEN [5–8]. Sensor nodes are generally deployed in harsh environments and in unattended location leads to higher probabilities of occurrence of faults and failures. Faults are categorized as permanent faults, intermittent faults, transient faults. Sources of failures in sensor networks classified as: node level faults, sink level faults, network level faults, faults caused by adversaries [10]. Fault management is very essential to hold the network in working condition at gainful level. Fault management is to detect faults, isolate and recover the faults.

Fault detection is the leading and important step of the fault management process. The several existing approaches for fault detection have been categorized as: centralized approach, distributed approach. [11–19]. Fault detection in a clustered network has three types: Intra-cluster fault detection, Intra-cluster error detection, Inter-cluster fault detection [22]. Several fault detection techniques have been already proposed having its own strength and limitations, a couple of them suffers from high energy consumption problem because they requires a lot of communication between cluster head and member nodes [24]. Here, we have designed a more efficient fault detector for clustered-based systems.

Related Work

Wireless sensor networks have gained attention in recent years due to its unique features like small size, smart device, and less cost. Akyildiz et al. [1] explained the various features of wireless sensor networks, such as self-organizing capabilities, cooperative effort of sensor nodes. Potdar et al. [2] described various factors that should restrain in mind during the design of sensor networks like fault tolerance, battery power. Various clustering algorithms have been explained in [5–8]. Fault occurrence is frequent in sensor networks due to sensor device's constraints. Khan et al. [10] divided fault management process into three main phases: fault detection, fault diagnosis, fault recovery. Chen et al. [11] classified fault detection approaches as distributed approaches and centralized approaches. Warriach et al. [12] presented two major categories of faults, responsible for degradation of performance of network. Lee et al. [13] designed a fault detection algorithm for wireless sensor networks in which each sensor node identifies its own status based on local comparisons of sensed data with some thresholds. Ramanathan et al. [15] presented, Sympathy, a tool for detecting and debugging failures in sensor networks. Ssu et al. [17] proposed a data centric approach where a source sensor node forwards two copies of the data by way of different disjointed paths to the sink node. This approach considers crash and incorrect computation faults. Ding et al. [18] developed algorithm in which reading at a sensor is compared with median reading of its neighbours. If the difference is large, the sensing element is very probable to be

defective. Hsin et al. [19] recommended a two-phase neighbour coordination plan. In the first phase, a sensor node waits for its neighbours to inform regarding the faulty nodes. In the second stage, it discusses with its neighbours to take accurate decision. Afsar et al. [22] proposed a cluster-based fault tolerant technique which uses an energy efficient protocol for cluster formation. Failure detection process in it got executed using neighbour’s coordination technique. This method reduces the communication messages between the cluster heads and sinks. Azharuddin et al. [24] offered a novel algorithm Distributed Fault Tolerant Clustering Algorithm (DFCA) to trade with failure problem.

Proposed Algorithm

There are several techniques, implemented for failure detection in clustered systems but most of them extend communication overhead of system. This may lead to a great problem in success of deployed network. This research has focused on providing solution for said problem by optimizing the performance of present techniques through maximizing network lifetime when performing failure detection of nodes and cluster heads in the network. Basic steps of process have shown in Fig. 1. Proposed algorithm shown in Fig. 2 has main two phases:

First Phase: This phase covers the basic initial setup and clustering process. Clustering process includes cluster head selection and then clusters formation.

Cluster Head Selection: Here, we are using a clustering algorithm proposed by Afsar et al. [22] which also considers the energy level of node for CH selection. After becoming candidate CH it checks its energy level. Residual energy of any node got calculated on the basis of energy consumption rate of that node, if energy level is greater than threshold, CH candidate become able to play role of CH.

Cluster Formation: Each node have to join at least one CH. Distance within nearby member nodes and CH has been calculated, if the calculated distance is

Fig. 1 Steps of fault detection process

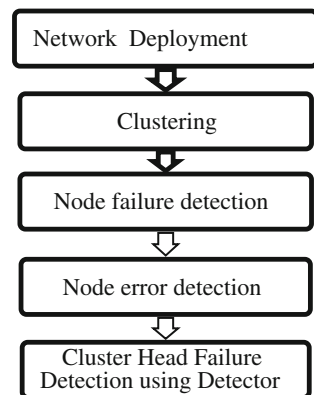
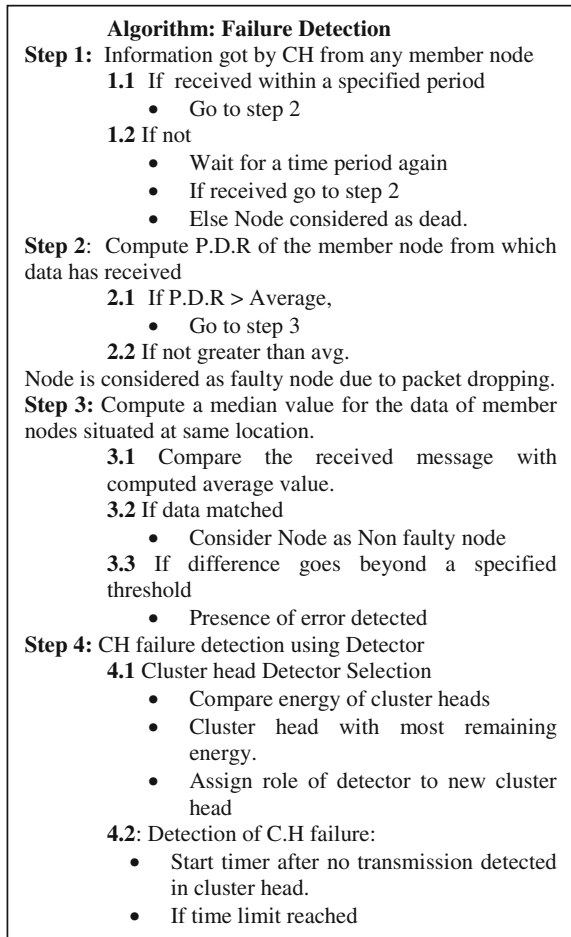


Fig. 2 Algorithm of fault detection



within communication range of member node, node will select the nearby CH as its cluster Head.

Second Phase: Last two steps of work have completed in second phase. This stage contains:

Intra-cluster fault detection: All member nodes send data to its group head, if CH does not get information from any of its member node in a predefined time period, it waits for a period again because data may misfortune due to some noise or interference problems, but if it does not receive data even after waiting then CH considers that node as faulty node. This detection is performed for two types:

- Nodes that became dead
- Nodes have Packet Delivery Ratio (P.D.R) less than average

Intra-cluster error detection: Nodes have densely deployed in the experiment area so it is assumed that nodes situated at same location may represent same values. So CH computes a median value for the data received from the nearby member nodes. On receiving data from any member node CH compares that acquired value with the computed median value [9]. If the difference is greater than a specified threshold, CH detects an error in the data and considers that node as faulty node.

Inter-Cluster Fault Detection by Detector: In our work, CH failure detection will be performed by ht sensor node (detector) which is at present playing role of CH and have highest amount of residual energy from all the cluster heads in that round.

We have performed experiments for proposed work using MATLAB 2010 with basic setup as shown in Table 1.

Discussion of simulation results: Experimental results have shown that the designed algorithm is more efficient than the fault detection clustering algorithm proposed by Azharuddin et al. [24] in terms of number of faulty sensor nodes in the network, remaining energy in the network.

Level 1: Total nodes deployed in experiment area at level 1 are 20.

1.1 **Packets Sent to Base station versus total number of rounds:** Figure 3 shows that how many packets have received by the base station from the different nodes or we can say that from different cluster heads.

1.2 **Faulty and Dead nodes Detection**

1.2.1 **Faulty Nodes:** The faulty nodes whose detection is represented by Fig. 4 are of 1st type faulty nodes imply nodes from where packets have received by the group head but when this CH compare the received message, it shows some error in it.

1.2.2 **Dead Nodes:** Nodes whose energy value becomes zero are examined as dead nodes and also as second category of faulty nodes. In the Fig. 5 there is comparison between DFCA and enhanced distributed fault tolerant clustering algorithm (EDFCA), it is shown that DFCA is showing more number of faulty nodes because in this method detection is not performed accurately and nodes which have still energy greater than zero but not possible to take part in communication due to failure

Table 1 Experimental setup

Experimental area	100 × 100 m ²
Node type	Static and homogenous
Deployment strategy	Random and densely deployment
No. of nodes	Level 1: 20 nodes; Level 2: 50 nodes; Level 3: 100 nodes
Parameters	Network lifetime, No. of faulty nodes, Residual energy, Communication range of cluster head, Distance between head and node,

of relay nodes also considered as faulty but in EDFCA this detection is performed accurately.

1.3 Energy of Network

Figure 6 demonstrates the aggregate energy staying in the system with progressing number of rounds. Total energy is figured on the basis of energy consumption of the sensing unit known as sensor.

Fig. 3 Graph for packets sent for 20 nodes

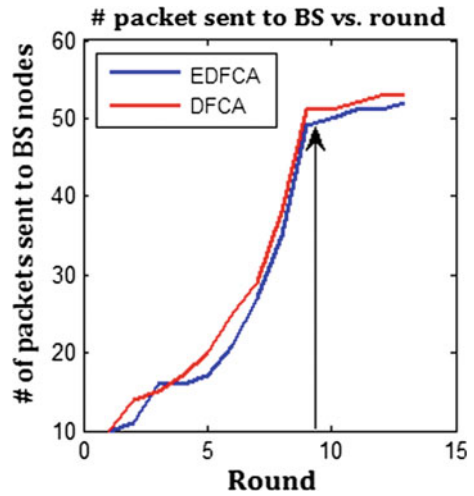


Fig. 4 Faulty nodes versus rounds

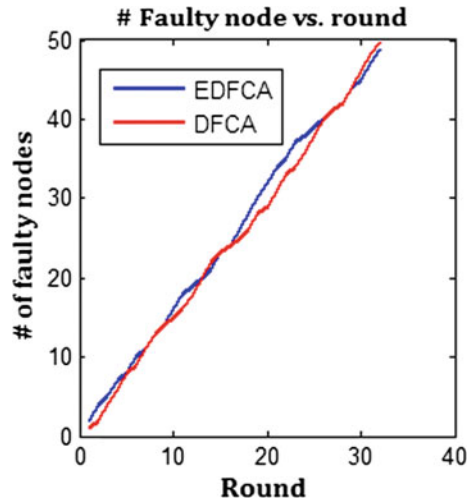


Fig. 5 Dead nodes versus rounds

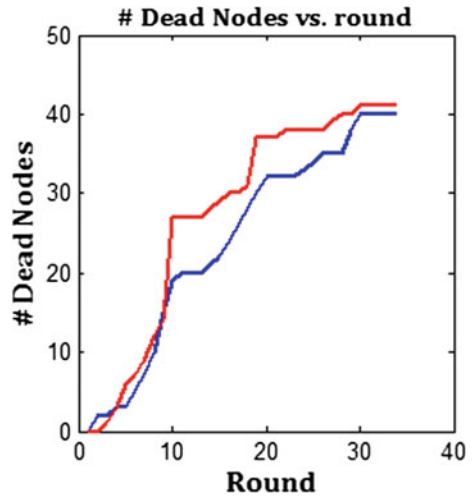
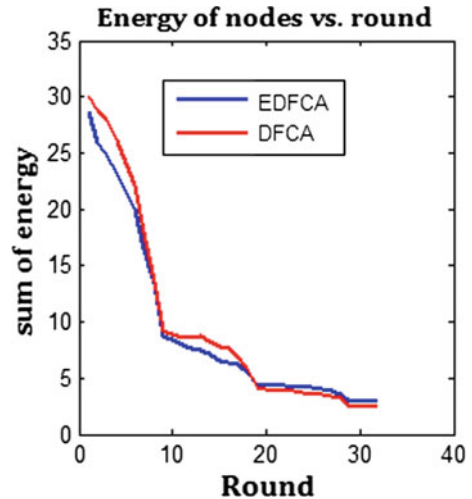


Fig. 6 Energy of network versus rounds



Conclusion and Future Scope

Fault management has been considered as a key factor for success of wireless sensor networks. We have designed a framework which performs fault detection in an energy efficient way. It is a decentralized fault detection method designed for cluster-based systems. Fault detection has performed for both intra- cluster and inter-cluster levels. Cluster head detects the failure of its member node by implementing comparison mechanism on the sensed data of that member node and its neighbour nodes while diagnosis process for cluster head's failure is implemented by the detector.

We have designed an energy efficient fault detection method but work can be extended with the second phase of fault management means fault recovery using same clustering and fault detection approaches.

References

1. Akyildiz, F., Su, W., Sankarasubramaniam, Y.: A survey on sensor networks. *IEEE Commun. Mag.* **40**, 102–114 (2002)
2. Potdar, V., Sharif, A., Chang, E.: Wireless sensor networks: a survey. In: Waina, International Conference on Advanced Information Networking and Applications Workshops, pp. 636–641, UK (2009)
3. Zheng, J., Jamalipour, A.: *Wireless Sensor Networks A Networking Perspective*, pp. 2–7. Wiley (2009)
4. Abbasi, A.A., Younis, M.: A survey on clustering algorithms for wireless sensor networks. *ACM Comput. Commun.* **30**, 2826–2841 (2007)
5. Anastasi, G., Conti, M., Di Francesco, M., Passarella, A.: Energy conservation in wireless sensor networks: a survey. *Ad Hoc Netw.* **7**, 537–568 (2009)
6. Ibrahim, A., Sis, M.K., Cakir, S.: Integrated comparison of energy efficient routing protocols in wireless sensor network: a survey. *IEEE Symposium on Business, Engineering and Industrial Application*, Langkawi, Malaysia, pp. 237–242 (2010)
7. Pantazis, N.A., Nikolidakis, S.A., Vergados, Ds D.: Energy efficient routing protocols in wireless sensor networks: a survey. *IEEE Commun. Surv. Tutorials* **15**, 551–591 (2013)
8. Manjeshwar, A., Agrawal, D.P.: TEEN: a routing protocol for enhanced efficiency in wireless sensor networks. In: *Proceedings of the 15th International Workshop on Parallel and Distributed Computing Issues in Wireless Networks and Mobile Computing*, pp. 2009–2015 (2002)
9. Aslam, S., Farooq, F., Sarwar, S.: Power consumption in wireless sensor networks. In: *Proceedings of the 7th International Conference on Frontiers of Information Technology* (2009)
10. Khan, M.Z., Merabti, M., Askwith, B.: Design considerations for fault management in wireless sensor networks. Presented at the 10th Annual Conference on the Convergence of Telecommunications, Networking and Broadcasting, Liverpool, UK (2009)
11. Chen, J., Kher, S., Somani, A.: Distributed fault detection of wireless sensor networks. In: *Proceedings of Workshop on Dependability Issues in Wireless Ad hoc Networks and Sensor Networks*, pp. 65–72 (2006)
12. Warriach, E., Nguyen, T.A., Tei, K.: Fault detection in wireless sensor networks: a hybrid approach. In: *IEEE Proceedings of the 15th International Conference on Computer Science and Engineering*, pp. 618–625, Apr 2012
13. Lee, M.H., Choi, Y.H.: Fault detection of wireless sensor networks. *Comput. Commun.* **31** (14), 3469–3475 (2008)
14. Yu, M., Mokhtar, H., Merabti, M.: Fault management in wireless sensor networks. *IEEE Wirel. Commun.* 13–19 (2007)
15. Ramanathan, N., Chang, K., Kapur, R., Girod, L., Kohler, E., Estrin, D.: Sympathy for the sensor network debugger. In: *ACM SenSys*, pp. 255–267 (2005)
16. Asim, M., Mokhtar, H., Merabti, M.: A fault management architecture for wireless sensor network. *Int. Wirel. Commun. Mobile Comput. Conf.* **8**(6), 779–785 (2008)
17. Ssu, K.F., Chou, C.H., Jiau, H.C., Hu, W.T.: Detection and diagnosis of data inconsistency failures in wireless sensor networks. *IEEE Comput. Netw.* **50**(9), 1247–1260 (2006)

18. Ding, M., Chen, D., Xing, K., Cheng, X.: Localized fault-tolerant event boundary detection in sensor networks. In: 24th Annual Joint Conference of the IEEE Computer and Communications Societies, vol. 2, pp. 902–913 (2005)
19. Hsin, C., Liu, M.: Self-monitoring of wireless sensor networks. *Comput. Commun.* **29**(4), 462–476 (2006)
20. Karim, L., Nasser, N., Sheltami, T.: A fault tolerant dynamic clustering protocol of wireless sensor networks. In: Global Telecommunications Conference, GLOBECOM, pp. 1–6 (2009)
21. Zahid Khan, M., Merabti, M., Askwith, B., Bouhaf, F.: A fault-tolerant network management architecture for wireless sensor networks. *PGNet* (2010)
22. Afsar, M.M., Yaghmaee, M.H., Zeinali, E.: A fault tolerant protocol for wireless sensor networks. In: IEEE International conference on Mobile Ad-hoc and Sensor Networks, pp. 475–478 (2011)
23. Bagheri, T.: DFMC: decentralized fault management mechanism for cluster based wireless sensor networks. In: International Conference on Digital Information and Communication Technology and It's Applications (DICTAP), pp. 67–71 (2012)
24. Azharuddin, Md., Kuila, P., Jana, P.K.: A distributed fault-tolerant clustering algorithm for wireless sensor networks. In: IEEE International Conference on Advances in Computing, Communications and Informatics, pp. 997–1002, Aug 2013
25. Choikani, T.A., Aroudaki, B.A., Ashouri, H., Artail, H.A.: A dynamic faulty node detection scheme using adaptive sleep scheduling for wireless sensor networks that employ data aggregation. In: Third International Conference on Communications and Information Technology (ICCIT), pp. 185–189 (2013)
26. Lent, C.S.: *Learning to Program with MATLAB Building GUI Tools*. Wiley (2001)
27. Jaikao, C., Srisathapornphat, C., Shen, C.-C.: Diagnosis of sensor networks. *Int. Conf. Commun.* **5**, 1627–1632 (2001)
28. Schurgers, C., Srivastava, M.B.: Energy efficient routing in wireless sensor networks. In: *The MILCOM Proceedings on Communications for Network-Centric Operations Creating the Information Force*, McLean, VA (2001)
29. Ruiz, L.B., Nogueira, J.M., Loureiro, A.A.F.: MANNA: a management architecture for wireless sensor networks. *Commun. Mag. IEEE* **41**, 116–125 (2003)

Gain and Bandwidth Enhancement of Single-Layered Slotted Triangular-Shaped Microstrip Patch Antenna with Stub for WLAN Applications

Dheeraj Bhardwaj, Gitansh Gulati, Lakshit Bhardwaj and Komal Sharma

Abstract The paper presents a triangle-shaped patch antenna designed for WLAN systems operating in the range of 5150–5350 MHz (IEEE 802.11 a,n) and 5725–5825 MHz (IEEE 802.11 a,n). This paper presents a single-layered equilateral triangle-shaped microstrip patch antenna having rectangular slots and one stub. The simulated antenna is resonating at two resonance frequencies 5.20 and 5.76 GHz with 18.01 % impedance bandwidth and, 7.94 and 6.24 dBi directivity, respectively. The performance along with the design of the patch antenna is optimized considering different slot variance to obtain an antenna with high gain and efficient bandwidth. The E-plane and H-plane radiation pattern have also been synthesized in accordance with the other parameters. The substrate material of FR4 Lossy with relative permittivity 4.4 and loss tangent of 0.025 is used in this proposed antenna. All the simulation work is carried using IE3D software.

Keywords Microstrip antenna · Slots · Dual frequency · Stub

Dheeraj Bhardwaj (✉)

Department of Applied Physics, BIT-Mesra (Jaipur Campus),

Jaipur 302017, India

e-mail: dbhardwaj.bit@gmail.com

Gitansh Gulati

ECE, BIT Mesra, Jaipur, India

e-mail: gitanshgulati@gmail.com

Lakshit Bhardwaj

ECE, LNMIIT, Jaipur, India

e-mail: lakshit.lnmiit@gmail.com

Komal Sharma

Department of Physics, SKIT, Jaipur, India

e-mail: kbhardwaj18@gmail.com

© Springer India 2016

N. Afzalpulkar et al. (eds.), *Proceedings of the International Conference on Recent Cognizance in Wireless Communication & Image Processing*, DOI 10.1007/978-81-322-2638-3_81

Introduction

Patch antennas have superseded many other antennas because of it is planar structure, thin profile, low cost, ease of design, multi-frequency operation, compactness, light weight and it is in accordance with the circuit elements for modeling. Apart from various other application-based parameters, bandwidth of patch antenna (limited to 2–4 %) is the prime concern for the research community. Therefore, it becomes necessary to introduce various broadband techniques to compensate the low bandwidth [1–3].

Various types of slots such as U-slot [4], spiral-shaped, Y-slot, stepped-impedance slot, H-slot, L-slot, etc., have been experimented and studied, but the patch has been restricted to rectangular and circular geometry because of their ease of design. There are other geometries which play an important role in the field of miniaturization, leading to concise and planar structure. In many wide-band communication applications, such as WLAN, WiMAX, GSM, Radar, Satellite, Zigbee, etc.; the use of multi-frequency patch antennas may refrain from the use of two or three different antennas [3, 5–7]. Multi-frequency patch antennas can be obtained by introducing slot loading on a single patch or stacking the two resonant patches in shunt or series configuration. Current distribution plays a vital role while introducing slots in any patch. Microstrip patch antenna fed by electromagnetic coupling is advantageous for improving bandwidth [8–10].

Techniques

Method of Moments (MoM)

IE3D software analysis is based on MoM. In the MoM, microstrip patch is modeled with the help of surface currents, and the fields in the dielectric slab are consistently being modeled by the volume polarization currents. Unknown currents are determined by the integral equation on the microstrip patches and the feed lines and their images in the ground plane. The solution to these integral equations can be computed after transforming them into algebraic equations. Finging fields are also taken into account for an accurate solution.

Coaxial Probe Feed

The probe of desired radius is inserted at the feed location, connected to the radiating patch, and soldered to the ground plane.

Antenna Design

Antenna design for wireless communication application is the most crucial part and various design constraints such as compactness and planar structure need to be fulfilled. Hence, apart from rectangular and circular geometry, equilateral triangle-shaped patch was chosen as shown in Fig. 1.

This antenna is resonating at 4.26, 4.79 and 6.56 GHz. Also termed as conventional triangle-shaped microstrip patch antenna (CTMPA) (as shown in Fig. 1), is having low bandwidth (4.7 % at 6.56 GHz). So to improve the performance of this antenna we modified it by inserting one slot on the left side of CTMPA (as shown in Fig. 2). As we energized it at feed location $X = 7$ mm and $Y = 3$ mm, the antenna will resonate at 5.68 GHz having gained 1.86 dBi and bandwidth 3.9 %. This is still not sufficient. It means the antenna required further modifications. Now, we insert another rectangular slot on the base of the triangle-shaped microstrip patch antenna. This modified triangle-shaped patch with two slots (ETPMATRS) is presented in Fig. 3. The design parameters for this patch are listed in Table 1. By

Fig. 1 Triangular patch [CTMPA] ($s = 38$ mm)

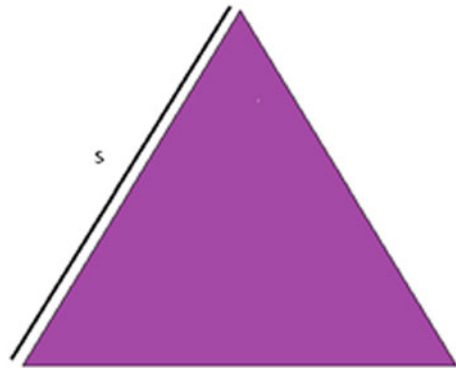


Fig. 2 Triangular patch with one slit

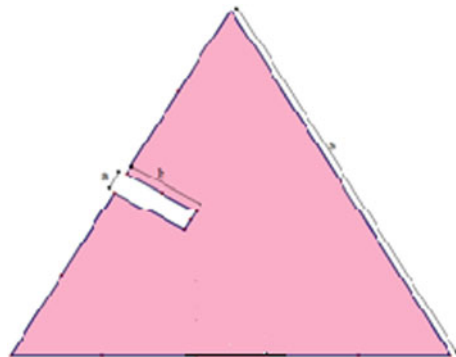


Fig. 3 Triangle-shaped patch microstrip antenna with two rectangular slots (ETPMATRS)

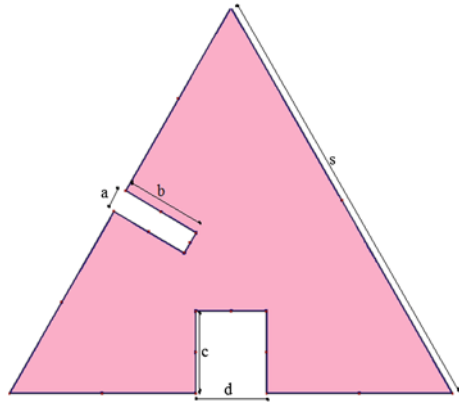
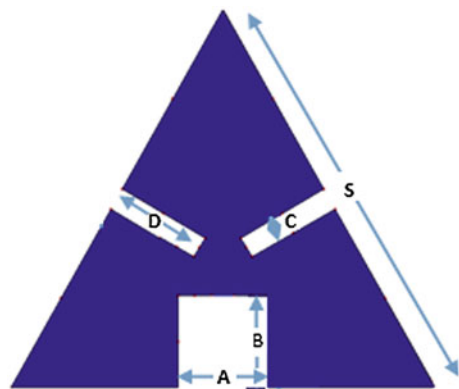


Table 1 Design constraints of triangle-shaped patch antenna with two slots

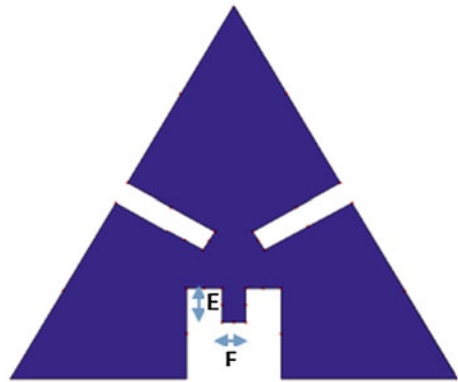
Constraints	Design considerations
Patch configuration (side length S)	38 mm
Substrate (FR4 Lossy)	$\epsilon = 4.4$ with $\tan\delta = 0.025$
Substrate thickness	1.59 mm
Feed radius	0.62 mm
a, b	2 mm, 7 mm
c, d	7 mm, 3 mm

Fig. 4 Triangle-shaped patch microstrip antenna with three rectangular slots (ETPMA3RS)



inserting slots into the triangle-shaped patch (acting as the inductive loading), we increased the electrical current path length of the excited patch surface which in turn increases the bandwidth. Now, the current is restricted somewhat more in the center of the patch as compared to patch with single slot (as shown in Fig. 2).

Fig. 5 Triangle-shaped patch microstrip antenna with three rectangular slots and one stub (ETPMA3RS with Stub)



Further modifications were made in the geometry by introducing third slot (as shown in Fig. 4) in an attempt to improve the ETPMATRS. The dimensions of the third slot are identical to the first slot which was introduced previously, but on the opposite side of the equilateral triangle patch with sides.

This modification of inserting another rectangular slot of same dimensions to maintain symmetry led to an increase in bandwidth up to 11.63 % but unfortunately the gain of this antenna [ETPMA3RS] (as shown in Fig. 4) was negative. Therefore, to counter the tradeoff, this antenna geometry was further modified by introducing a single stub as shown in Fig. 5.

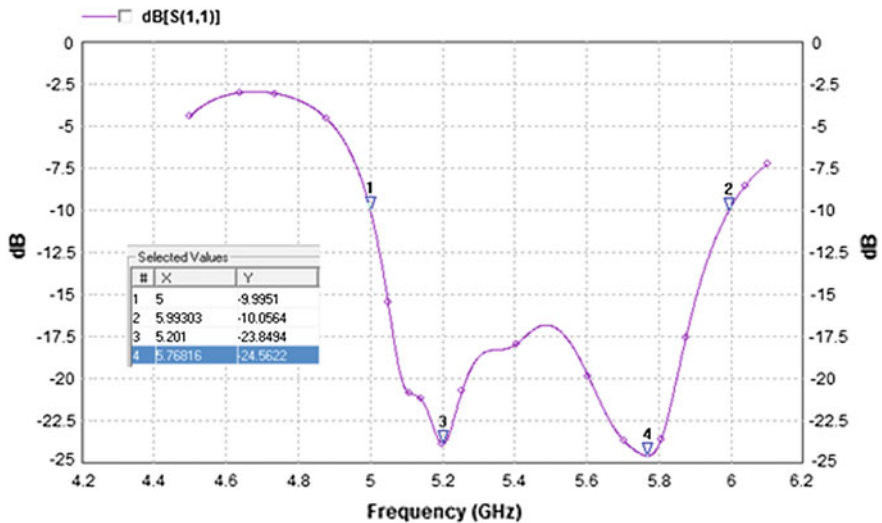


Fig. 6 Stimulated return loss of ETPMA3RS with stub

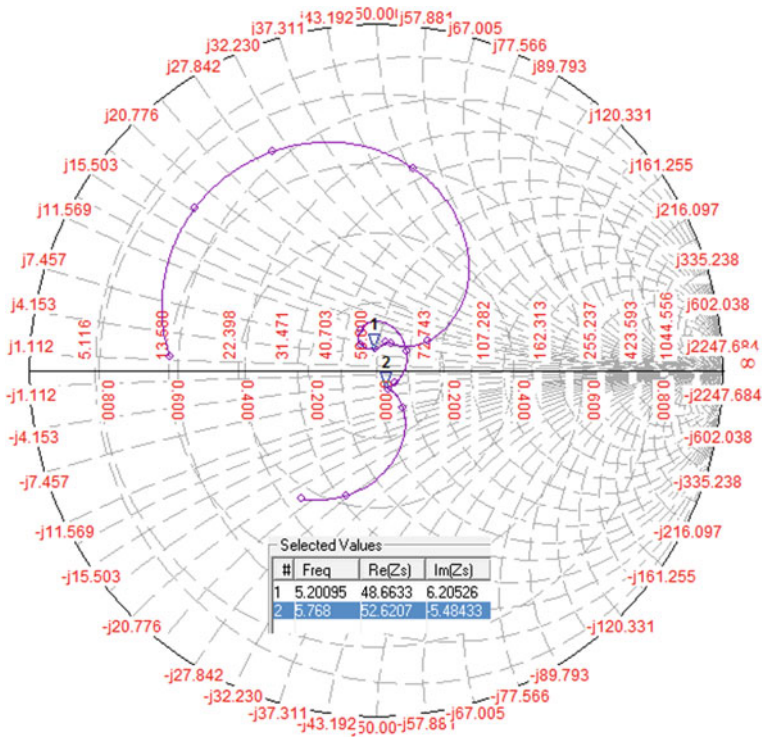


Fig. 7 Smith chart for ETPMA3RS with stub

Results and Discussions

ETPMATRS (Fig. 3) is resonating at two resonance frequencies 5.27 and 5.60 GHz wherein we achieve the bandwidth of the antenna 10.38 %, corresponding to the central frequency 5.45 GHz. The simulated VSWR for the two considered resonating frequencies 5.27 and 5.60 GHz was 1.148 and 1.071, respectively, which is close to unity. It shows proper impedance matching between the antenna and feed network. The variation of simulated gain with frequency at these two resonating frequencies is 2.31 and 3.70 dBi, respectively. The simulated results show that maximum radiation efficiency 34.64 and 25.39 % can be achieved for resonating frequency 5.60 and 5.27 GHz, respectively. Introducing three rectangular slots in the equilateral patch (TPMA3RS), there is a slight improvement in bandwidth up to 11.63 % with a trade off in the gain values. Hence stub matching technique was taken into account as shown in Fig. 5. Triangular patched microstrip antenna with

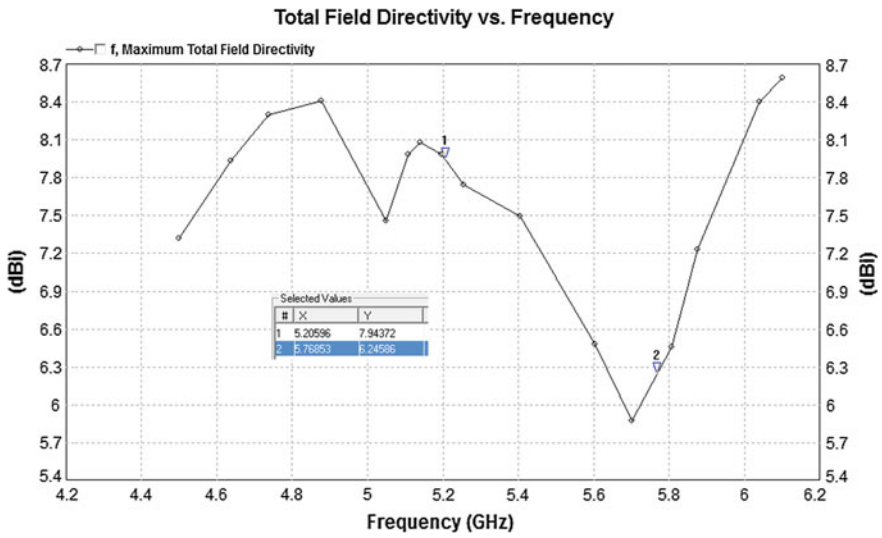


Fig. 8 Directivity of modified antenna ETPMA3RS with stub

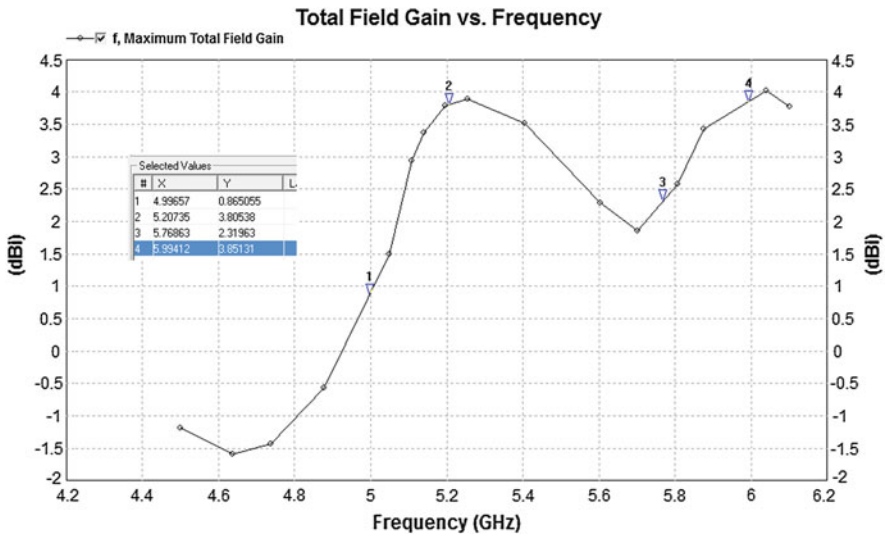


Fig. 9 Gain of ETPMA3RS with stub

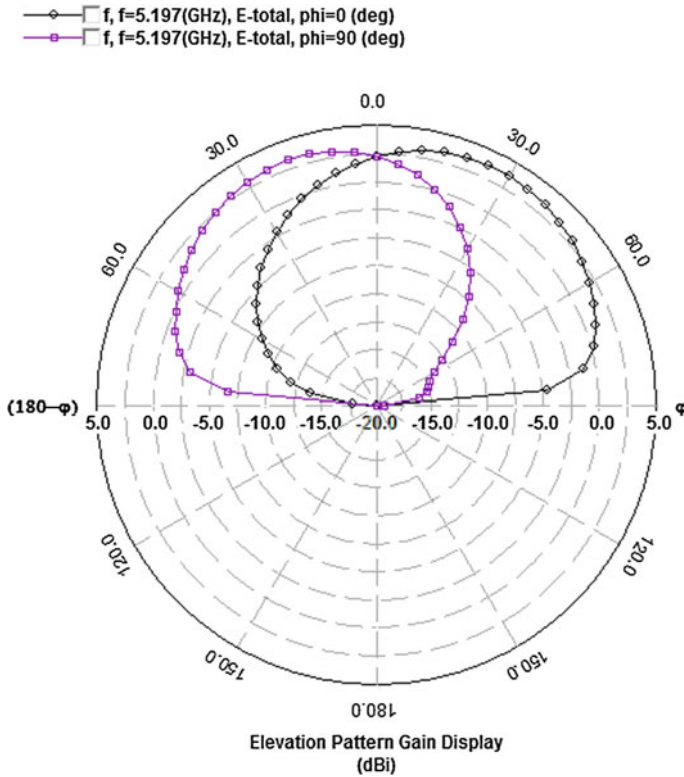


Fig. 10 2D radiation pattern at 5.195 GHz

two rectangular slots and one stub (ETPMA3RS) (Fig. 5) gave the bandwidth of 17.97 %, thus, resonating at 5.20 and 5.76 GHz (Fig. 6). Variation of gain and directivity with resonant frequencies is shown in Figs. 8 and 9.

For proper impedance matching, the real part of the impedance should be close to 50 Ω and the imaginary part should be close to 0 Ω to avoid radiation losses. The smith chart for the final modified antenna, thus validating the principle of impedance matching is depicted in Fig. 7.

The 2-D polar E-plane and H-plane radiation pattern at the respective resonant frequencies of the final modified antenna is shown in Figs. 10 and 11 which clearly presents the improvement in the radiation performance orthogonal to patch.

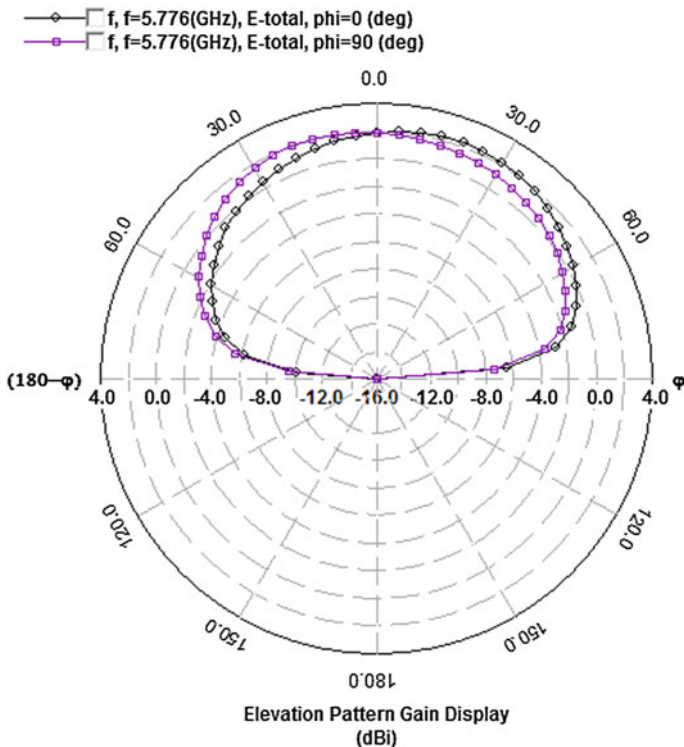







Fig. 11 2D radiation pattern at 5.776 GHz

Conclusions

This new slotted triangle-shaped patch antenna with stub at the central slot (Fig. 5) demonstrates the improved bandwidth and gain of the antenna as compared to the conventional antenna. The modified antenna resonates at two nearby frequencies for the communication systems for WLAN Application (IEEE 802.11 a,n standard). The effects of introducing varying slot dimensions in the triangular patch of the antenna have been successfully investigated. Analysis carried out on FR-4 Lossy substrate with a high loss tangent value still reported results that are very encouraging. With this antenna, we get much improved bandwidth 18.01 % at center frequency 5.3 GHz in comparison with a triangle-shaped patch antenna (having bandwidth 2.62, 2.47 and 4.70 % corresponding to the resonance 4.26, 4.79 and 6.56 GHz, respectively). This is approximately four times greater than the conventional antenna. These values may be increased further with the application of low loss materials. Table 2 shows the comparison between various intermediate geometries based on different antenna parameters for a detailed outlook.

Table 2 Comparison between antenna parameters of various modified antennas

Antenna no.	Antenna geometry	Patch	Dimensions (mm)	Resonance frequency (GHz)	Gain (dBi)	Bandwidth (%)
1.	Conventional equilateral triangle-shaped microstrip patch antenna		S = 38	6.56	-0.17	4.7
2.	Equilateral triangle-shaped patch with (ETP) one rectangular slot		S = 38 A = 5 B = 5	5.68	1.86	3.9
3.	ETP with two rectangular slots (ETPMATRS)		S = 38 A = 3 B = 7 C = 2 D = 7	5.27 5.60	2.31 3.70	10.38
4.	ETP with three rectangular slots (ETPMA3RS)		S = 39 A = 5 B = 5 C = 2 D = 5	5.02 5.56 5.65	-0.69 -5.69 -4.42	11.63
5.	ETP with three rectangular slots and one stub in the central slot (ETPMA3RS with Stub)		S = 36.6 A = 8 B = 8 C = 2 D = 7 E = 3 F = 2	5.20 5.76	3.80 2.31	18.01

Acknowledgments The authors express their sincere thanks to Professor Deepak Bhatnagar for providing the simulation facilities at their research laboratory.

References

1. Chai, W., et al.: Wideband microstrip antenna using U slot. *PIERS Online* **3**(7) (2007)
2. Mallikarjun, S.L., et al.: Development of microstrip array antenna for wide band and multi band application. *Indian J. Radio Space Phys.* **38** (2009)
3. Maci, S., Gentili, G.B.: Dual frequency patch antennas. *IEEE Antennas Propag. Mag.* **39**(6) (1997)
4. Pozar, D.M.: Microstrip antennas. *Proc. IEEE* **40**(1) (1992)

5. Surjati, I.: Dual frequency operation triangular microstrip antenna using a pair of slit. In: 11th Asia Pacific Conference on Communications, Perth, Western Australia, Oct 2005
6. Anguera, J., et al.: Dual frequency broadband microstrip antenna with a reactive loading and stacked elements. *Prog. Electromagnet. Res. Lett.* **10**, 1–10 (2009)
7. Surjati, I., et al.: Dual band triangular microstrip antenna using slot feed by electromagnetic coupling. In: *Proceeding Quality in Research*, Faculty of Engineering, University of Indonesia (2009)
8. Rahardjo, E.T.: Studies on the MSA fed by electromagnetic coupling. Doctoral thesis, Saitama University, Mar 1996
9. Sagne, D.S.: Broadband equilateral triangular microstrip antenna for Wi-Max application. In: *International Conference on Communication Systems and Network Technologies* (2012)
10. Bhardwaj, D., Bhatnagar, D., Sancheti, S., Soni, B.: Design of square patch antenna with a notch on FR4 substrate. *IET Microwaves Antennas Propag.* **2**(8), 880–885 (2008)

Design of Dual Resonator Broadband Multilayer Electromagnetically Coupled Microstrip Antenna for X-Band Applications

Dheeraj Bhardwaj, Aayush Dwivedi, Nidhi Jain and Komal Sharma

Abstract This paper demonstrates the Dual resonator Broadband microstrip patch antenna for X-band applications with high bandwidth and gain. The antenna has wide bandwidth of 3880 MHz (7.12–11.0 GHz) or 42.76 % and covers wide band of X-band. 10.0 and 10.5 GHz are two resonant frequencies for the designed antenna. The antenna presented in this paper is microstrip patch antenna with rectangular geometry which has multilayer arrangement with two biangular uniform slots, which has been fed by Electromagnetic coupling with air-gap. This antenna designed and simulated has been carried out by IE3D simulation software.

Keywords Microstrip antenna · Broadband · X-band

Introduction

In recent times, the interest among communication and microwave engineers in research work has increased on compact design of microstrip antenna due to requirement for miniature antennas in wireless communication [1–6]. Microstrip antennas find wide use in the microwave frequency range because of their simplicity and also as they are compatible with printed-circuit technology. They are very useful in applications related to antenna for many reasons. A few advantages

Dheeraj Bhardwaj (✉)

Department of Applied Physics, BIT-Mesra (Jaipur Campus), Jaipur 302017, India

e-mail: dbhardwaj.bit@gmail.com

Aayush Dwivedi · Nidhi Jain

Department of Electronics and Communication, BIT-Mesra, Jaipur, India

e-mail: ayu.dwivedi.92@gmail.com

Nidhi Jain

e-mail: jain.nidhie21@gmail.com

Komal Sharma

Department of Physics, SKIT, Jaipur, India

e-mail: drkomal18@gmail.com

© Springer India 2016

N. Afzalpulkar et al. (eds.), *Proceedings of the International Conference on Recent Cognizance in Wireless Communication & Image Processing*, DOI 10.1007/978-81-322-2638-3_82

are that they are cheap and easy to manufacture and planar. But these advantages are somewhat compromised by poor efficiency and bandwidth. Recently a lot of research work and testing has been performed to enhance the bandwidth as well as efficiency of patch antennas [7, 8]. It provides us with a broadband antenna of a low profile [9–15]. We try to reduce the size and increase the operating bandwidth of the antenna along with it. The designed antenna has a gain of 2.64 dBi. The simulation work for this design has been carried out using IE3D EMSS software. Due to the characteristics such as a less size, low cost as well as weight; this antenna is well suited for the application such as Ku-Band satellite and RADAR communication apart from IEEE X-Band applications. The X-band which is defined by an IEEE standard covers frequencies from 8.0 to 12.0 GHz. The X-band covers applications such as short range tracking, marine applications, missile guidance radar and air bone intercept. It is most commonly used for radar communication purposes with frequency ranging from 8.29 to 11.5 GHz. The proposed antenna is designed to operate in X-band at two frequencies of 10.0 and 10.5 GHz. The obtained results provide a design applicable in a satellite TV.

Methods

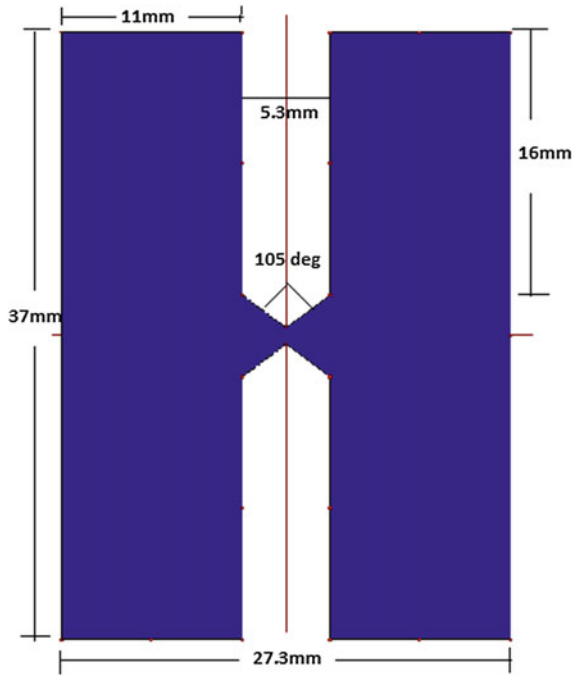
Method of Moments (MoM)

Analysis of various MSAs done by IE3D software is based on MoM. In this, the surface currents and volume polarization currents are utilized for modelling the microstrip patch as well as to model fields in the dielectric slab. The unknown currents for the feed lines and their images in ground plane as well as the microstrip patches are obtained using an integral equation. These integral equations are easily solved by a computer after they are transformed into algebraic equations. This method provides a more exact solution as it takes into account the fringing fields outside the physical boundary of the two-dimensional patch.

Coaxial Probe Feed Technique

The outer part of the conductor in the SMA connector is attached to the ground plane of antenna, while the inner conductor extends all the way through the dielectric and is soldered to radiating patch of the antenna.

Fig. 1 Modified single layer patch



Antenna Design

We considered a rectangular patch of dimension 27.3 mm × 37 mm with two equal biangular slots of dimension 5.3 mm × 16 mm subtending an angle of 105° at centre. The patch is designed on FR4 substrate with z top as 1.6 and loss tangent 0.025. Figure 1 represent modified single layer microstrip patch antenna.

The design of microstrip patch is presented in Fig. 1.

This particular antenna is resonant at three frequencies 5.5, 5.7 and 7.1 GHz with respective bandwidths of 10.89 and 11.17 %.

Simulated return loss curve for multilayer patch is shown in Fig. 2.

The best result yet achieved by single layer microstrip patch antenna was a dual band broadband antenna with peak bandwidth of 11.26 % and peak gain of 4.52 dBi. Since the bandwidth of single layer configuration was still not enough, we shifted our work from single layer to multilayer configuration.

In multilayer geometry, we started with studying a conventional multilayer microstrip patch antenna. Dimensions of this patch were taken as 27.3 mm × 37 mm and that of top patch is 30 mm × 40 mm. The air-gap provided is 1.8 mm. We used the same substrate to design this patch. Figure 3 shows multilayer conventional patch.

Simulated return loss curve for multilayer conventional patch is illustrated in Fig. 4.

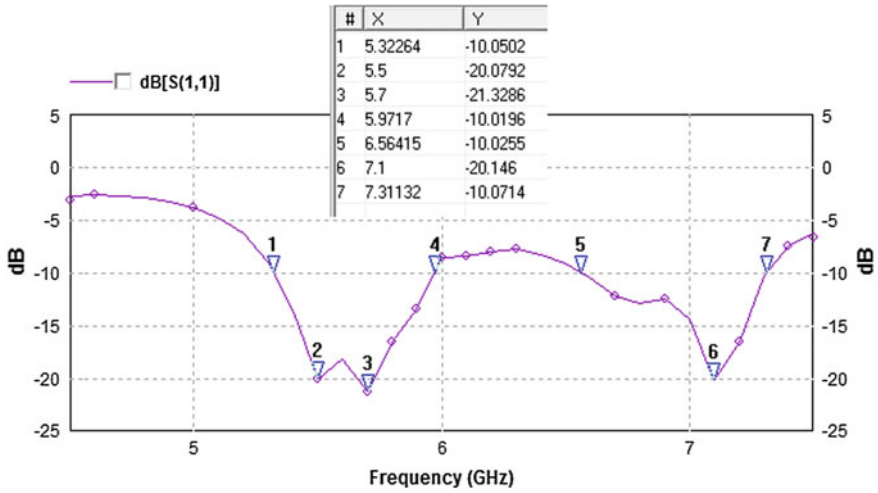
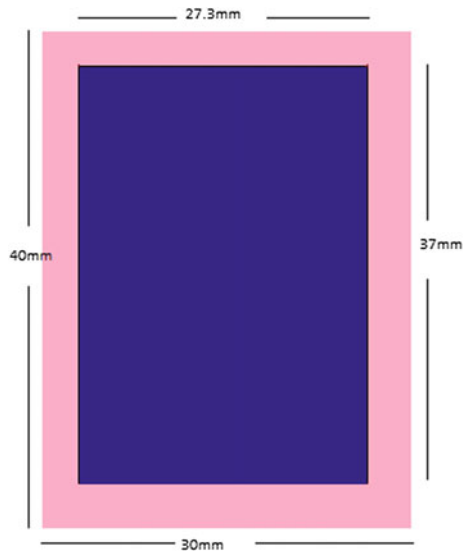


Fig. 2 Simulated return loss of modified single layer patch antenna

Fig. 3 Multilayer conventional patch



Conventional patch is resonant at two frequencies 7.1 GHz with 13.7 % bandwidth. This patch can be referred as single band single frequency antenna.

To obtain the best results on multilayer we use the single layer configuration patch shown in Fig. 1, so now we designed it on multilayer configuration. Top conventional patch length is 30 mm and width is 40 mm and the multilayer

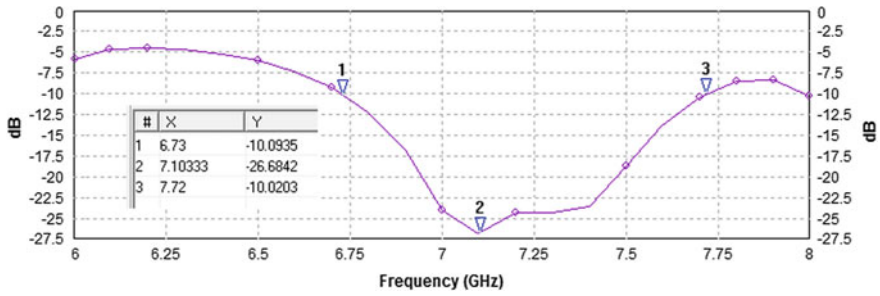
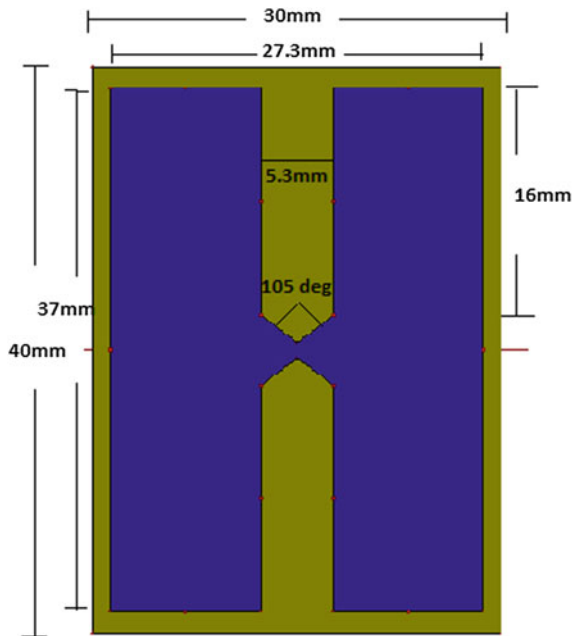


Fig. 4 Return loss curve for multilayer conventional patch

Fig. 5 Modified multilayer microstrip antenna



modified patch dimensions are taken as same as in single layer. The substrate which is used to design the antenna is FR4 substrate. The thickness of FR4 substrate used is 1.6 mm and Dielectric constant for the substrate is 4.4. Because of FR4 substrate is a lossy substrate, we take loss tangent as 0.025. For getting enhanced bandwidth and gain on compact size antenna, multilayer configuration fed by electromagnetic coupling is used. In this antenna we propose multi layer design with three layers. Air-gap between two substrate layers are taken as 1.6 mm. The antenna geometry is illustrated in Fig. 5.

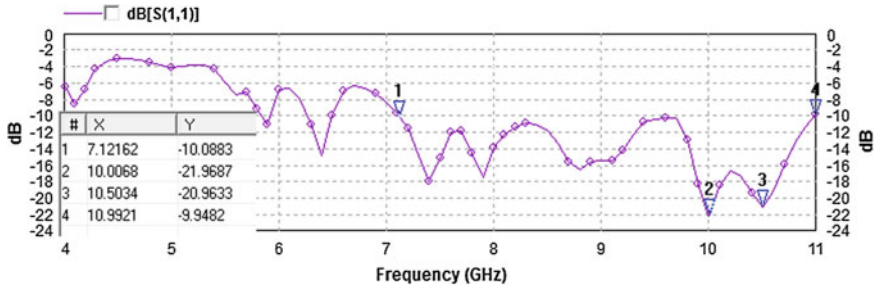


Fig. 6 Return loss for designed patch

Results and Discussions

Return loss curve for designed Patch is shown in Fig. 6. As from the return loss, we can see that our designed patch is resonant at two frequencies 10.0 and 10.5 GHz. This antenna covers the frequency range from 7.12 to 11.0 GHz with a bandwidth of 42.76 %, so this antenna covers a wide portion of X-band.

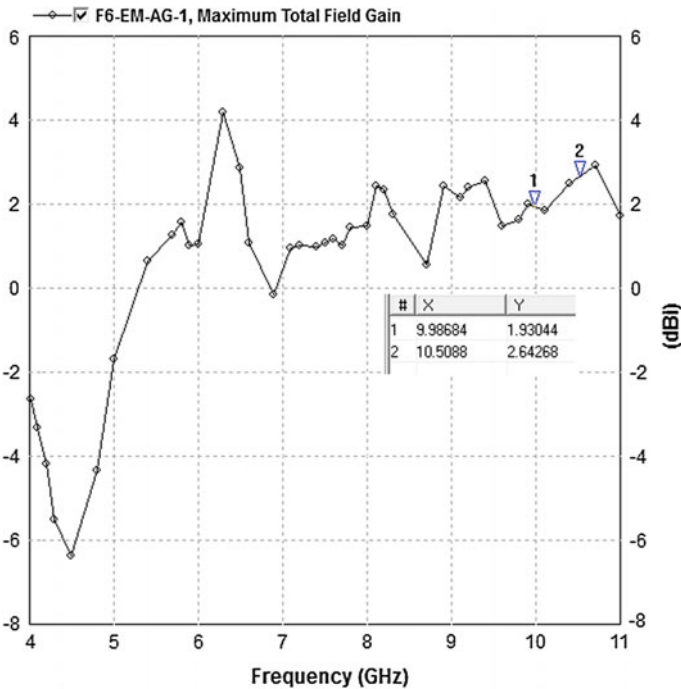


Fig. 7 Variation of gain versus resonance frequency

Fig. 8 2D radiation pattern of designed patch at 10 GHz

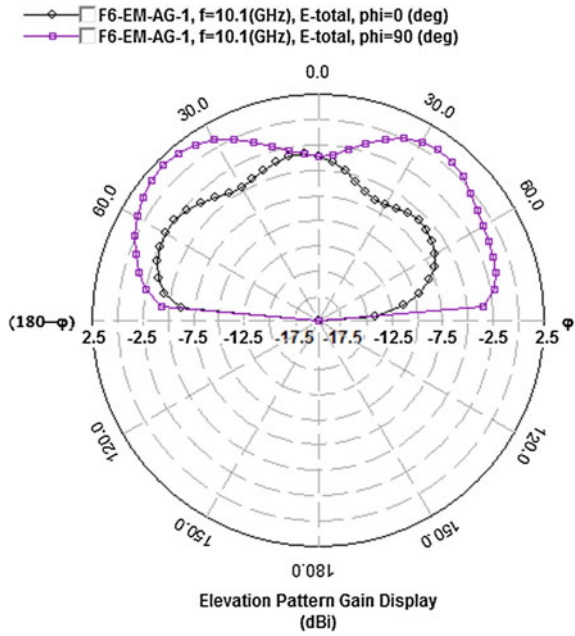


Fig. 9 2D radiation pattern of designed patch at 10.5 GHz

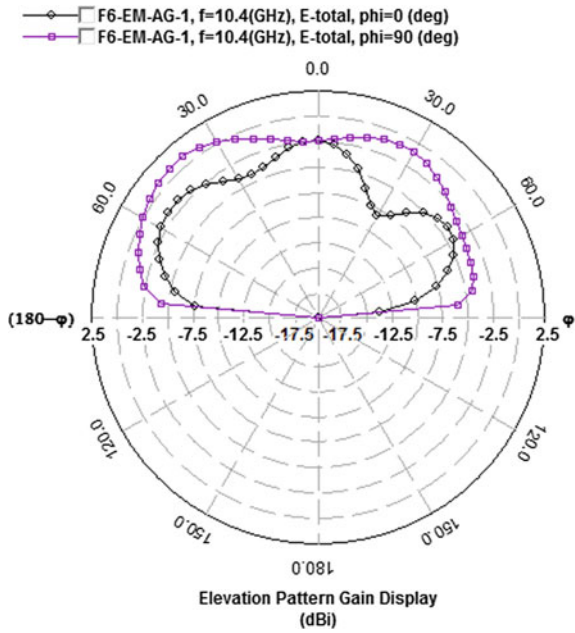


Table 1 Variation of antenna parameters of modified single layer MSA with angle variation

Dimension (mm)	Angle	Feed location (x, y)	Resonating frequency	Impedance	Bandwidth (%)	Gain (dB)	Directivity	Efficiency (%)	VSWR
	90	(12, 2)	5.8	54-j8.4	6.4	-2.3	12.93	21.32	1.23
	100	(12, 2.5)	5.5, 5.9	55-j3.2	4.9	0.73	10.34	12.33	1.21
				47-j3.5	8.4	1.23	10.94	15.67	1.20
				49+j2.2	9.2	-0.3	10.23	18.3	1.20
L = 27.3	105	(12, 2.5)	5.5	53.92-j9.56	10.6	4.52	9.49	32.21	1.21
W = 37			5.7	42.13-j0.82	10.6	4.00	9.20	29.77	1.20
a = 9			7.1	45.42+j8.23	11.26	0.27	9.27	13.09	1.23
b = 16									
	120	(12, 2.5)	5.6, 5.7	55+j2.3	9.8	2.07	10.32	28.71	1.21
				48-j0.9	12.2	1.94	11.21	23.49	1.23

Table 2 Variation of antenna parameters of modified multilayer MSA with air-gap width

Air-gap width (mm)	Resonating frequency (GHz)	Bandwidth (%)	Gain (dBi)	Efficiency (%)
0.0	7.9	13.29	2.03	26.62
0.6	5.6	27.01	1.54	29.43
	6.5	27.01	2.03	26.47
1.6	10.0	42.76	1.93	26.58
	10.5	42.76	2.64	24.31
2.2	7.0	14.87	3.22	32.98
	7.3	14.87	2.45	28.74

Table 3 Comparison of single layer and multilayer microstrip patch antennas

Patch	Frequency (GHz)	Impedance (Ω)	Gain (dBi)	Directivity (dBi)	Bandwidth (%)
Modified single layer MSA	5.5	53.92-j8.84	4.53	9.49	10.7
	5.7	42.72-j0.67	4.00	9.20	10.7
	7.1	45.42+j0.23	0.28	9.27	11.26
Modified multilayer MSA	10.0	46.10-j7.18	1.93	7.64	42.76
	10.5	48.01-j8.51	2.64	8.75	42.76

From the gain curve in Fig. 7, both our bandwidths are completely useful, because the gain is positive in entire bandwidths. Gain at both resonant frequencies is 1.93 dB and 2.64 dBi which is positive.

Radiation pattern at the two resonating frequencies 10.0 and 10.5 GHz is shown in Figs. 8 and 9, respectively. The variations of various antenna parameters of Modified Single layer MSA with angle variation and Modified Multi layer MSA with Air-gap width has been compared and shown in Tables 1 and 2. Comparison of Single layer and Multilayer Microstrip Patch Antennas also shown in Table 3.

Conclusions

The designed dual resonator broadband rectangular multilayer microstrip patch antenna is operating at two resonating frequencies 10.0 and 10.5 GHz in range 7.12–11.5 GHz covering X-band as well as satellite application standards. The presented antenna enhances gain up to 2.64 dBi with the multilayer configuration. This antenna also has better performance in terms of directivity and radiation pattern. The work requires extensive experimentation before reaching any possible thought for its application. The patch antenna was simulated first using EM simulation IE3D software.

Acknowledgments The authors express their sincere thanks to Professor Deepak Bhatnagar for providing the simulation facilities at their research laboratory.

References

1. Girish Kumar, Ray, K.P.: *Broadband Microstrip Antennas*. Artech House (2003)
2. Balasnis, C.A.: *Antenna Theory Analysis and Design*. Wiley, New York (1997)
3. Sarkar, I., Sarkar, P.P., Chowdhury, S.K.: A new compact printed antenna for mobile communication. In: 2009 Lough borough Antennas and Propagation Conference, 16–17 Nov 2009, pp. 109–112
4. Chatterjee, S., Chakraborty, U., Sarkar, I., Chowdhury, S.K., Sarkar, P.P.: A compact microstrip antenna for mobile communication. In: IEEE Annual Conference. Paper ID: 510
5. Wu, J.-W., Hsiao, H.-M., Lu, J.-H., Chang, S.-H.: Dual broadband design of rectangular slot antenna for 2.4 and 5 GHz wireless communication. *IEE Electron. Lett.* **40**(23) (2004)
6. Chakraborty, U., Chatterjee, S., Chowdhury, S.K., Sarkar, P.P.: A compact microstrip patch antenna for wireless communication. *Prog. Electromagnet. Res. C* **18**, 211–220 (2011)
7. Raj, R.K., Joseph, M., Anandan, C.K., Vasudevan, K., Mohanan, P.: A new compact microstrip-fed dual-band coplaner antenna for WLAN applications. *IEEE Trans. Antennas Propag.* **54**(12), 3755–3762 (2006)
8. Zhang, Z., Iskander, M.F., Langer, J.-C., Mathews, J.: Dual-band WLAN dipole antenna using an internal matching circuit. *IEEE Trans. Antennas Propag.* **53**(5), 1813–1818 (2005)
9. Jan, J.-Y., Tseng, L.-C.: Small planar monopole antenna with a shorted parasitic inverted-wire for Wireless communications in the 2.4, 5.2 and 5.8 GHz bands. *IEEE Trans. Antennas Propag.* **52**(7), 1903–1905 (2004)
10. Chatterjee, S., Paul, J., Ghosh, K., Sarkar, P.P., Chowdhury, S.K.: A printed patch antenna for mobile communication. In: *Convergence of Optics and Electronics Conference*, 2011, Paper ID: 15, pp. 102–107
11. Dheeraj Bhardwaj, Nidhi Jain, Komal Sharma: Broadband dual resonator uniform H-shaped microstrip patch antenna for C-band applications. In: 2014 National Conference NSAWAO-2014
12. Dheeraj Bhardwaj, Nidhi Jain, Komal Sharma: On radiation from H-shaped microstrip patch antenna with central rectangular slot for C-band applications. In: 2014 National Seminar on Innovations in Science and Technology
13. Dheeraj Bhardwaj, Nidhi Jain, Komal Sharma: Dual frequency broadband H-shaped microstrip patch antenna with vertical dual notch for C-band applications, University of Rajasthan
14. Dheeraj Bhardwaj, Nidhi Jain, Komal Sharma: Bandwidth enhancement of broadband dual resonator I-shaped antenna for C-band applications. *Int. J.*
15. Dheeraj Bhardwaj, Nidhi Jain, Komal Sharma: Comparison of simulated radiation performance of uniform and nonuniform H-shaped microstrip patch antenna using IE3D simulation software. In: 2014 National conference ECTME-2014

An Environment Aware Frequency Selective Headset

Sambit Mohapatra, G.V. Swathi and Vijayaraghavan Sundararaman

Abstract A common problem associated with the use of conventional headsets is that all or most of the external audio signals are prevented from reaching the user which makes him unaware of the environment. Many times, accidents occur due to the user not being able to hear people calling them or trying to make them aware of a potential threat. To overcome this drawback of headsets, this paper proposes a novel technique that allows the user to hear and respond to certain frequencies such as human voice without having to take off the headset.

Keywords Selective noise filtering · Active band pass filter · Audio application

Introduction

In this paper, we have chosen only the frequencies produced by the human voices to be allowed into the headset assuming the case when someone is calling from outside.

Human voice frequency typically ranges from 70 to 300 Hz (including both male and female voices) [1].

Current Scenario and Proposed Development

Existing headsets mainly aim at cancelling the external noise from reaching the users of the headset [2]. However, every external sound may not be a noise such as an alarm, a distress call, etc.

Sambit Mohapatra (✉)
National Institute of Electronics and IT, Calicut, India
e-mail: mohapatra.sambit8467@gmail.com

G.V. Swathi · Vijayaraghavan Sundararaman
Nagarjuna College of Engineering and Technology, Bangalore, India

Inability to respond properly and quickly to such calls or alarms causes inconvenience and even accidents, very often.

Hence, we felt the need of proposing a scheme that could be implemented on an existing headset which allows only a particular set of sound waves to be passed into the headset.

Of all the external sounds, we have assumed the most important are the human voices. Hence, we have chosen the band of frequencies produced by human vocal cord to be allowed to pass into the headset.

Implementation

A microphone is mounted on the outside of the headset [3]. The output of this external microphone serves as input to the system.

The output of the microphone is of very low voltage which needs to be amplified before further processing.

Hence, the output of the microphone is fed to an amplifying circuit which uses a TL082 operational amplifier to amplify the signal.

This amplified signal is then fed to a Chebyshev band pass filter.

The filter has a lower cutoff frequency of 90 Hz and upper cutoff frequency of 250 Hz.

This allows only the human voices to pass rejecting all other noises.

The filter output is then conditioned to get the signal into a level that can drive a speaker mounted on the inside of the headset.

Microphone and Amplifying Circuit

Figures 1 and 2 show the microphone connected to the amplifying circuit. The LED lights up when a sound is picked up by the microphone.

The Filter Circuit

A filter is a circuit that passes signals of certain frequencies without much attenuation while attenuating or blocking signals of other frequencies.

Filters can be of low pass, high pass, band pass, band stop or notch types.

We have used an active band pass filter.

Fig. 1 Microphone and amplifier circuit

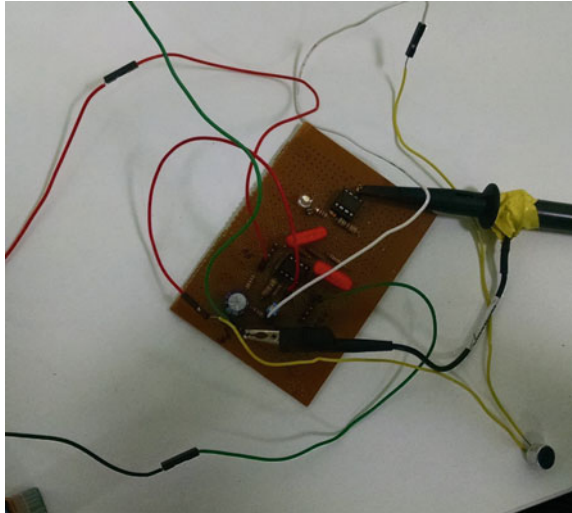
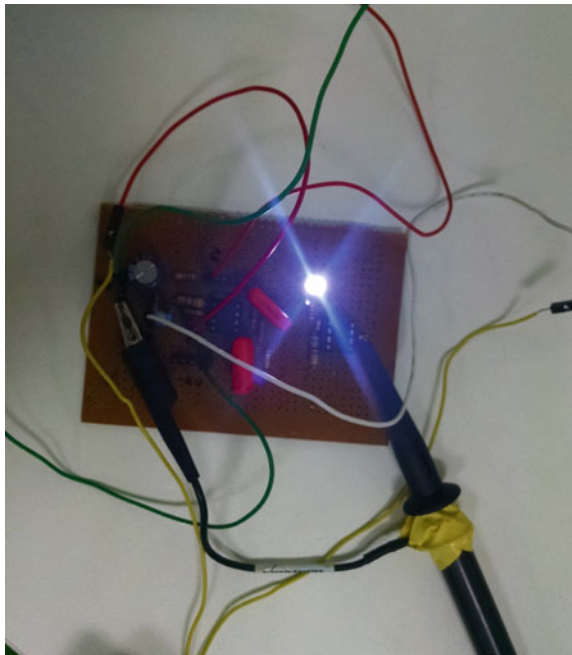


Fig. 2 Microphone picking up sound and amplifier output drives LED



A band pass filter can again be of the following types [4]:

- (1) *Butterworth filter*:

This has a flat magnitude response in its pass band. However, it does not have a very sharp cut off in the stop band.

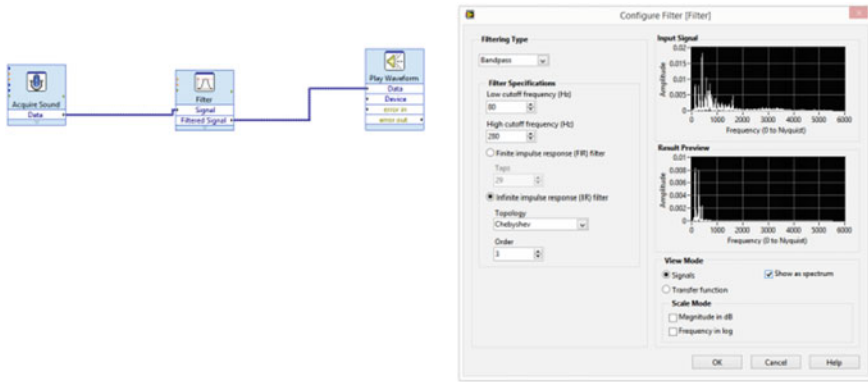


Fig. 3 LabView model and frequency response

(2) *Chebyshev filter:*

This filter has the steepest cut off among all analog active filters. However, it has ripples in its pass band which is allowable in our application.

(3) *Bessel filter:*

This is the least suitable for our application and hence not explained here.

A band pass filter can be considered as a cascading of a high pass filter, an amplifier and a low pass filter.

It is characterized by a lower cutoff frequency (FL), a higher cutoff frequency (FH), 3-dB bandwidth, Q factor and centre frequency (FC) [5].

$$FC = \sqrt{FH \times FL}$$

3-dB Bandwidth = FH – FL

In our experiment,

FH = 240 Hz

FL = 90 Hz

FC = 146.96 Hz

BW = 150 Hz

The filter was modelled in MATLAB Simulink and the entire circuit was modelled in Lab View and satisfactory results were obtained.

Figure 3 shows the Lab View modelling of the system.

The filter circuit was designed using MultiSim as shown below.

Simulations and Results

Figures 4 and 5 show the schematic and the actual circuit for implementing the band pass filter.

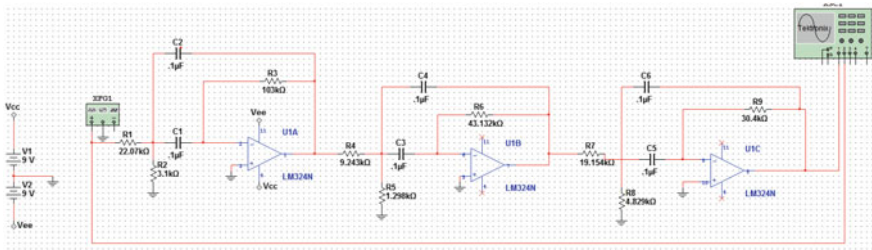
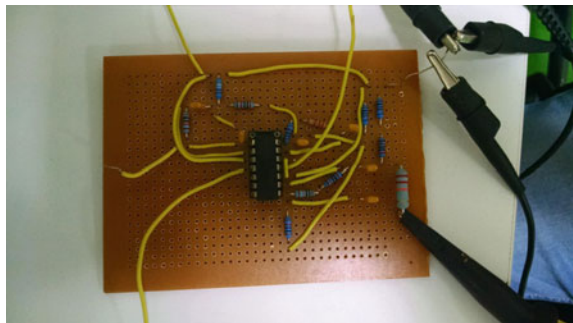


Fig. 4 Bandpass Chebyshev filter schematic

Fig. 5 The filter circuit



The circuit was tested as frequencies lesser than FL (90 Hz) and greater than FH (240 Hz) and the filter produced satisfactory attenuation. It was also tested at frequencies lying within the pass band and it produced satisfactory result.

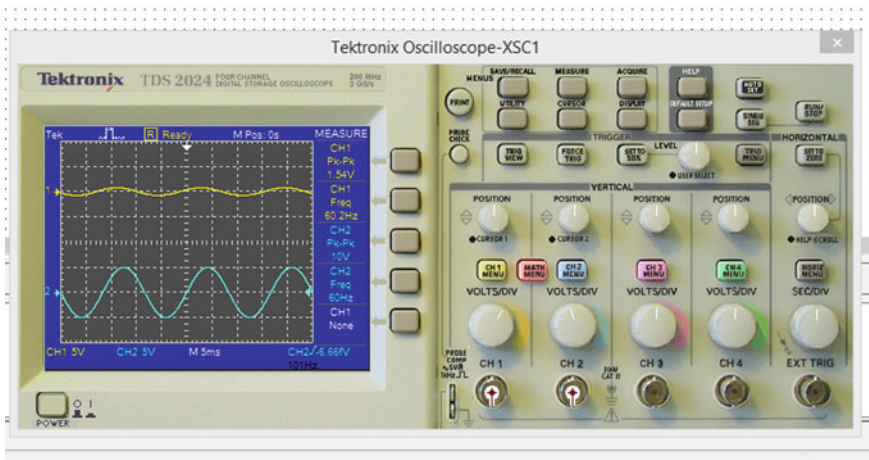


Fig. 6 Filter response at signal frequency of 60 Hz

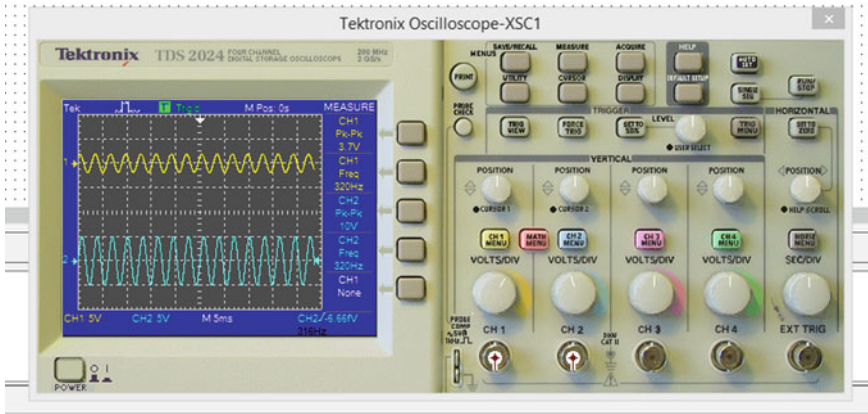


Fig. 7 Filter response at signal frequency of 320 Hz

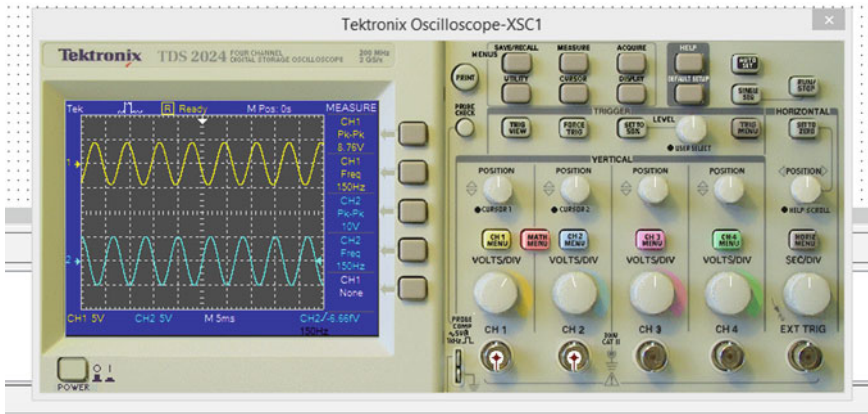


Fig. 8 Filter response at signal frequency of 150 Hz

Figures 6, 7 and 8 show the response of the filter circuit for an input frequency lesser than the cutoff frequency, higher than the cutoff frequency and a frequency lying within the pass band of the filter, respectively. The blue lines correspond to input signal and the signals in yellow are the outputs in each case.

References

1. <https://en.wikipedia.org>
2. Denenberg, J.N.: Anti-noise—Quieting the environment with active noise cancellation technology. *IEEE Potentials* **11**, 36–40 (1992)

3. Zangi, K.C.: A New Two Sensor Active Noise Cancellation Algorithm. unpublished
4. Thede, L.: Practical Analog and Digital Filter Design. Artech House, Inc (2004)
5. Kugelstadt, T.: Active Filter Design Techniques, Literature Number SLOAD006A, Texas Instruments

Performance Analysis and Optimization of 40 Gbps Transmission System over 4000 km with FBG

Mukesh Kumar Gupta, Jyoti Agarwal, Anila Dhingra
and Ghanshyam Singh

Abstract In this paper, we analyze the performance of the single channel transmission system for different lengths of fiber using dispersion compensated fiber (DCF) and fiber Bragg grating (FBG). A system with high data rate of 40 Gbps is simulated and analyzed to study effects of factors like dispersion and nonlinearity for different modulation techniques. The analysis is done in terms of bit error rate (BER) and quality factor (Q) for a comparative study of different level coding. The simulation results depict that FBG works as a better dispersion compensator as compared to DCF, also provides improved performance in optical fiber network with symmetrical compensation. The observation results that duo-binary coding schemes depict good performance with FBG (Fiber bragg Grating) up to a length of 4000 km.

Keywords FBG · DCF · MDRZ · DB · BER · Q factor

Introduction

To fulfill the increasing demand of bandwidth, transmission capacity, and high speed performance, passive long reach optical network is the best choice in optical communication system. The system designed for long-haul transmission requires coding for spectral efficiency, high bit rate and transmission quality to increase bandwidth. The existing system works on 2.5 and 10 Gbps data rate for transmission and the recent developments for the future system demand the transmission rates as high as 40 Gbps bit [1–5].

M.K. Gupta · Ghanshyam Singh
Department of Electronics and Communication Engineering,
Malaviya National Institute of Technology, Jaipur, India
e-mail: mkgupta06@gmail.com

Jyoti Agarwal (✉) · Anila Dhingra
Department of Electronics and Communication Engineering,
Yagyavalkya Institute of Technology, Jaipur, India
e-mail: agarwal15jyoti@gmail.com

The performance of the future systems with such high data transmission rates for long distance might face few challenges due to dispersion, nonlinearity, and other losses. Challenges due to dispersion and nonlinearity can be taken care by using different coding format, and the use of erbium-doped fiber amplifier (EDFA) helps to minimize the losses. The spreading of pulse due to intersymbol interference leads to one of the major problems of dispersion in communication system. There are several techniques to reduce the problem of dispersion, two widely used techniques are DCF and FBG [5–7].

DCF is used to compensate the dispersion that occurs in standard single mode fiber (SSMF) because negative dispersion of DCF removes positive dispersion of SSMF from the whole optical communication system. FBG is also used to compensate the dispersion and nonlinearity in communication system with large bandwidth, a part of that, FBG and DCF both can be used for pre, post, and symmetric configuration. These techniques use different modulation formats at transmitter side to mitigate the effect of nonlinearity [6, 8, 9].

In this paper, we have studied the effects of two dispersion compensation techniques with symmetrical configuration to minimize the spreading of the pulse for long-haul optical link transmission. The performance of FBG and DCF is observed for the comparative study of data rate of 40 Gbps for different length.

Dispersion Compensation Techniques

Dispersion is introduced as broadening of pulse in which different pulses of light is transmitted with different bit rates and received at different times in optical communication system and produces loss and distortion. It increases complexity and nonlinear effects in optical transmission system. Dispersion can be divided, such as group velocity dispersion (GVD), material dispersion, waveguide dispersion, higher order dispersion, and polarization mode dispersion (PMD). These limit the performance of fiber in communication system [7, 10–12].

To overcome effect of nonlinearity and remove the pulse broadening, different techniques are used. These techniques are dispersion compensating fiber (DCF), electronic dispersion compensation (EDC), fiber Bragg grating (FBG), and digital filters. In optical communication system, mainly two techniques, DCF and FBG are used for minimum dispersion.

Dispersion compensating fiber (DCF) compensates and manages group velocity dispersion with minimum optical power. DCF allows high speed optical signal to transmit over hundreds and thousands of kilometers in long-haul transmission system. Nonlinearity of the fiber and system performance depends on signal power in DCF. The radius of the core is decreased to get high negative dispersion. But it improves nonlinearity and loss in system. It provides high insertion loss with noise and the effective mode area of DCF increases the nonlinearity effects in optical fiber communication system [8, 11, 13].

Fiber Bragg grating (FBG) is an optical filter which reflects back incident light due to the stop band. It is used to mitigate the dispersion for high speed transmission with low insertion loss. FBG is placed in line with large bandwidth to enhance the transmission distance. Grating length is used for dispersion compensation in uniform FBG. In chirped FBG, it has wide stop band and optical period and Bragg wavelength changes with length which is used in broadband services [5, 9, 11, 14–16].

Simulation Setup

Figure 1a and b depict the simulation setup of DCF and FBG with symmetrical compensation for long distance optical transmission link. In this setup, a 40 Gbps single channel with center frequency 1550 nm is simulated with both compensators, i.e., FBG and DCF at different transmission distance using different modulation formats. Figure 1 shows the simulation setup of DCF consisting of transmitter, transmission channel, and receiver.

Transmitter includes PRBS generator, electrical signal generator, continuous wave (CW) laser, and Mach–Zehnder modulator (MZM). The pseudorandom binary sequence (PRBS) of length $2^7 - 1$ is used as data. It produces binary sequence at 40 Gbps bit rate and used to generate electrical pulse with NRZ/RZ/DB/MDRZ modulation formats. Optical input signal is generated by modulation of electric pulse and light beam using Mach–Zehnder modulator. The optical input signal feeds into the loop controller which controls the length of optical link. In transmission channel, two standard single mode fibers of 25 km each are used which gives positive dispersion and DCF of 10 km with negative dispersion is used to compensate dispersion. It provides minimum optical power and reduces the positive dispersion in the whole system. Erbium-doped fiber amplifier (EDFA) with constant noise figure is used as optical amplifier which is placed after fiber is used to reduce loss occurred from optical fiber. The signal is transmitted over N spans of single

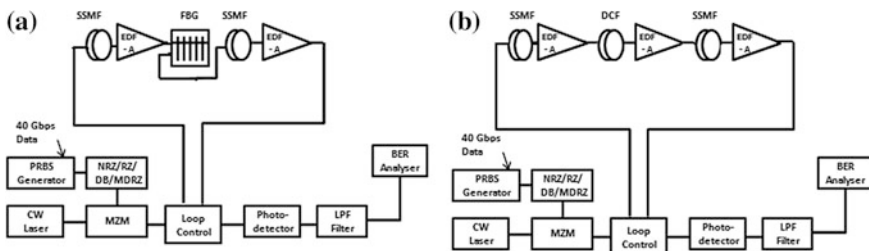


Fig. 1 Simulation setup of **a** DCF **b** FBG symmetrical compensation, SSMF: standard single mode fiber, DCF: dispersion compensating fiber, FBG: fiber Bragg grating, EDFA: erbium-doped fiber amplifier, MZM: Mach–Zehnder modulator, CW: continuous wave, LPF: low pass filter, BER: bit error rate 4000 km transmission distance with **(a)** DCF and **(b)** FBG

mode fiber and received at the receiver. At the receiver, photodetector is used to convert optical signal into electrical signal and LPF filters electrical signal by removing unwanted signal and noise. Bit error rate analyzer observes the output signal in terms of Q factor and bit error rate.

Due to the nonlinearity and high insertion loss, DCF is replaced by FBG as shown in Fig. 1b. FBG is used to compensate nonlinearity and dispersion. It has low insertion loss and large bandwidth for long distance transmission compared to DCF. FBG is the best solution for dispersion compensation and improve performance of FBG is measured in terms of BER and Q factor over 4000 km.

Result and Discussion

In long distance transmission optical link, Q factor and BER are the important parameters to analyze the whole performance of optical networks. We have evaluated both the compensators, i.e., FBG and DCF at different length from Fig. 2 and we have found that FBG has improved BER compared to DCF with different modulation formats.

Figure 2 shows the comparative performance of NRZ, RZ, DB, and MDRZ as shown above. Figure 3 shows when distance increases, value of Q factor decreases. In case of NRZ format, Q factor goes to zero which is not acceptable. We get higher value of Q factor in duo-binary (DB) modulation format for FBG compensator. The value of Q factor in DB modulation for FBG is 4.79 and bit error rate (BER) is 10^{-8} while for DCF, Q factor is 4.27 and BER is 10^{-7} .

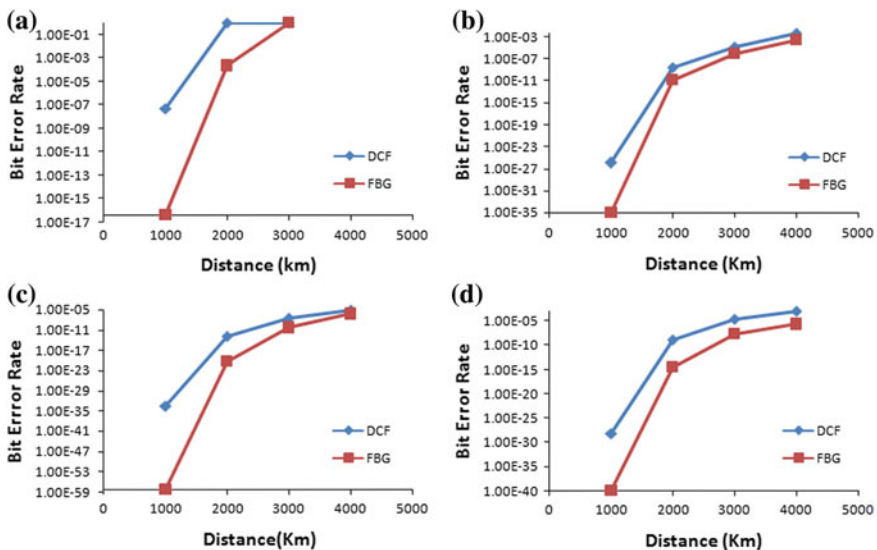


Fig. 2 Performance of a NRZ, b RZ, c DB, and d MDRZ

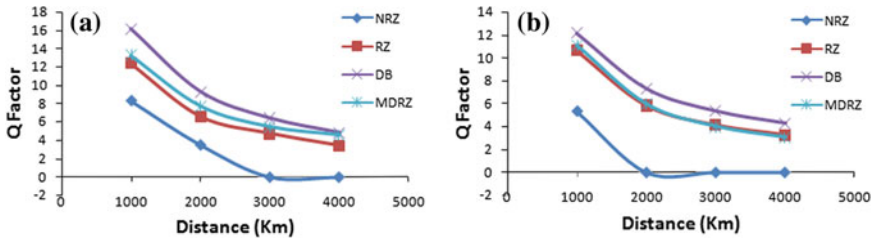


Fig. 3 Comparison of Q factor for different modulation formats with different distance for **a** FBG and **b** DCF

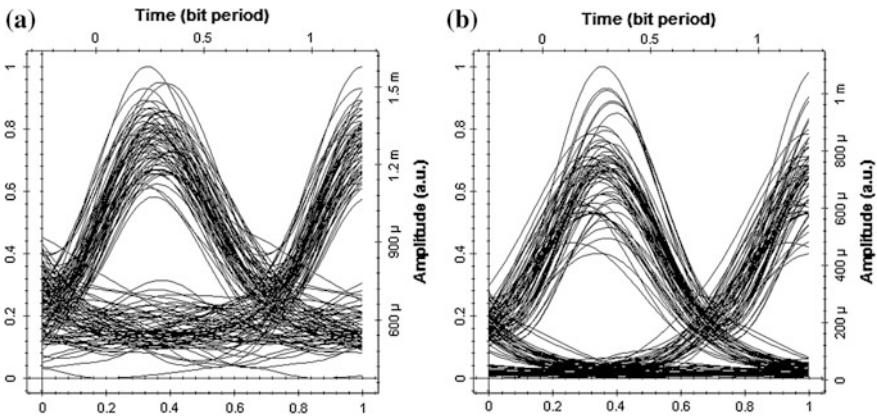
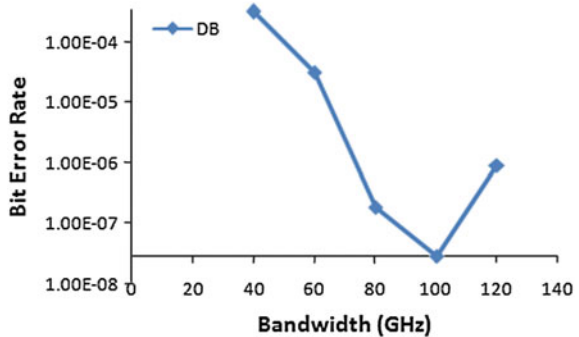


Fig. 4 Eye diagrams of DB modulation format for symmetrical compensation at 4000 km transmission distance with **a** DCF and **b** FBG

Fig. 5 Bit error rate with bandwidth (GHz) for DB modulation



The eye diagrams for duo-binary (DB) modulation formats for symmetrical compensation at 4000 km with DCF and FBG are shown in Fig. 4. We optimize FBG bases system by deviating the FBG bandwidth for DB modulation from 40 to 120 GHz at 4000 km as shown in Fig. 5. FBG bandwidth plays an important role for

dispersion compensation in optical link. We obtain minimum BER with maximum Q factor at 100 GHz so we get optimized bandwidth of FBG, which is 100 GHz.

Conclusion

In this paper, we have analyzed and optimized the simulation results of DCF and FBG of symmetrical compensation which is transmitted at 40 Gbps for single channel optical link using NRZ, RZ, DB, and MDRZ modulation formats up to 4000 km. From the simulated results, we have obtained that FBG gives better result at symmetrical compensation and DB with FBG shows improved result in BER and Q factor compared to other modulation formats. DB circuit complexity is less compared to other modulation format such as DPSK and DQPSK. In future, FBG can compensate the dispersion after 4000 km for long transmission optical link with minimum cost.

References

1. Bobrovs, V., Spolitis, S., Ivanovs, G.: Comparison of chromatic dispersion compensation techniques for WDM-PON solution. In: IEEE 2nd Baltic Congress on Future Internet Communications, pp. 64–67, Apr 2012
2. Yina, A., Zhanga, X.: Analysis of modulation format in the 40 Gbit/s optical communication system. *Optik* **121**, 1550–1557 (2010)
3. Lee, J.-H., Han, D.-W., Ahn, J.-Y.: Simulation of 40 Gbps WDM systems using single mode fiber. In: IEEE International Symposium on Science and Technology, pp. 777–780 (2005)
4. Gnanagurunathan, G., Rahman, F.A.: Comparing FBG and DCF as dispersion compensators in the long haul narrowband WDM systems. In: IEEE International Conference on Wireless and optical Communications Networks, pp. 4 (2006)
5. Pei, L., Ning, T., Yan, F., Dong, X., Tan, Z., Liu, Y., Jian, S.: Dispersion compensation of fiber Bragg gratings in 3100 km high speed optical fiber transmission system. *Front. Optoelectron. China* **2**(2), 163–169 (2009)
6. Landolsi, T., El-Tarhuni, M.: Optimization of DCF location for WDM systems using RZ, chirped RZ and carrier-suppressed RZ Modulations. In: IEEE 4th International Conference on Innovations in Information Technology, pp. 646–649 (2008)
7. Hu, B.-N., Jing, W., Wei, W., Zhao, R.-M.: Analysis on dispersion compensation with DCF based on optisystem. In: IEEE 2nd International Conference on Industrial and Information Systems, pp. 40–43 (2010)
8. Patel, A.V., Prof. Patel, R.B. Prof. Mehta, K.A.: Comparative analysis of single span high speed 40 Gbps long haul optical link using different modulation formats in the presence of Kerr nonlinearity. *IEEE Students' Technology Symposium*, pp. 132–137 (2014)
9. Suman, P.N., Chandan, R., Singh, D.: Optimization of WDM PON System for Long Haul optical communication based on FBG. *Int. J. Sci. Eng. Technol.* **2**(7), 749–751 (2013)
10. Faiyaz, N.M., Omi, A.I., Faisal, M.: Optimization of apodization profile of chirped fiber Bragg grating for chromatic dispersion compensation: dispersion compensation using chirped FBG. In: IEEE International Conference on Electrical Engineering and Information and Communication Technology, pp. 1–5, Apr 2014

11. Agrawal, G.P.: *Fiber-Optic Communications Systems*, 3rd edn. John Wiley & Sons (2002)
12. Garrett, L.D.: Survey of systems experiments demonstrating dispersion compensation technologies. *J. Opt. Fiber. Commun.* **3**, 340–398 (2006)
13. Sheetala, A., Sharma, A.K., Kaler, R.S.: Simulation of high capacity 40 Gb/s long haul DWDM system using different modulation formats and dispersion compensation schemes in the presence of Kerr's effect. *Optik* **121**,739–749 (2010)
14. Dochhan, A., Smolorz, S., Rohde, H., Rosenkranz, W.: FBG dispersion compensation in a 43 Gbit/s WDM system: comparing different FBG types and modulation formats. *IEEE International Conference on Transparent Optical Networks*, pp. 1–4 (2009)
15. Yousaf, K. et al.: Generation and transmission of dispersion tolerant 10-Gbps RZ-OOK signal for radio over fiber link. *Front. Optoelectron.* **5**(3), 306–310 (2012)
16. Kahlon, N.K., Kaur, G.: Various dispersion compensation techniques for optical system: a survey. *Open J. Commun. Soft.* **1**(1), pp. 64–73, May 2014

Broadband Modified U-Shaped Patch Antenna for Wireless Communication

Devendra Mehra and Sanyog Rawat

Abstract This paper presents a novel single-patch broadband microstrip patch antenna that is obtained by cutting a modified U-shaped slot on patch. The proposed antenna also has slots on ground plane. The length, width, and position of ground plane slots are so optimized to achieve wide bandwidth. The substrate material of proposed antenna is FR4-lossy and simulated on a CST-microwave design tool. The proposed antenna provides a bandwidth of 2.33 GHz centered at 4.73 GHz frequency with stable gain in the impedance bandwidth range.

Keywords Broadband · Microstrip patch antenna · U slot antenna

Introduction

In recent years, wireless communication is the best way of communication. Wireless communication provides the services of long distance as well as short distance communication that is impossible to implement by use of wires. Wireless communication systems and networks are installed in many towns and cities everyday throughout the world [1]. Now, because of the modern communication industry the demand for broadband antennas has amplified for use in high frequency and rapid data communication. Reference [2] broadband antenna has quite a few good qualities like good data transfer rate, compact size, conformal in nature, and easy to mount [3]. Antennas play a pivotal role in modern communication systems and are required to create a communication link. Antennas are the best choice of requirement for miniaturization and large bandwidth in the modern wireless network. The various kinds of antennas used in wireless communication systems are electrically small antennas, resonant antennas, broadband antennas, and aperture antennas [4].

Devendra Mehra (✉) · Sanyog Rawat
Amity University Rajasthan, Jaipur, India
e-mail: mehradevendra26@yahoo.com

Sanyog Rawat
e-mail: sanyog.rawat@gmail.com

Microstrip patch antenna is one of the low profile, lightweight, and has low power handling capacity antenna that is conformable to planar and nonplanar surfaces [5]. It is a type of resonant antenna. It is simple and inexpensive to fabricate using modern printed circuit technology [6]. In this paper, we introduce a microstrip feed with modified U-shaped patch, and for enhancement of the impedance bandwidth the slots are etched in the ground structure. The proposed geometry has an uncomplicated design.

Antenna Geometry

The initial geometry of proposed patch antenna is shown in Fig. 1. The proposed patch antenna designed using FR-4(lossy) material has a height (thickness) of nearly 1.59 mm. The proposed geometry has dimensions of 14 mm \times 14 mm.

In Fig. 1, the initial structure of proposed patch design in modified U-shaped with length $L1$ is 17 mm and $L2$ is 5 mm. The elevation and dimension of the patch, the substrate permittivity, and position of cuts on ground plane can vividly change the antenna's conduct, and for obtaining wider bandwidth and better radiation parameters there are two slots on ground plan with the change in height of the patch. The final structure of proposed antenna is shown in Fig. 2.

The parameter value of final proposed antenna structure is shown in Table 1 and all the parameters are in mm.

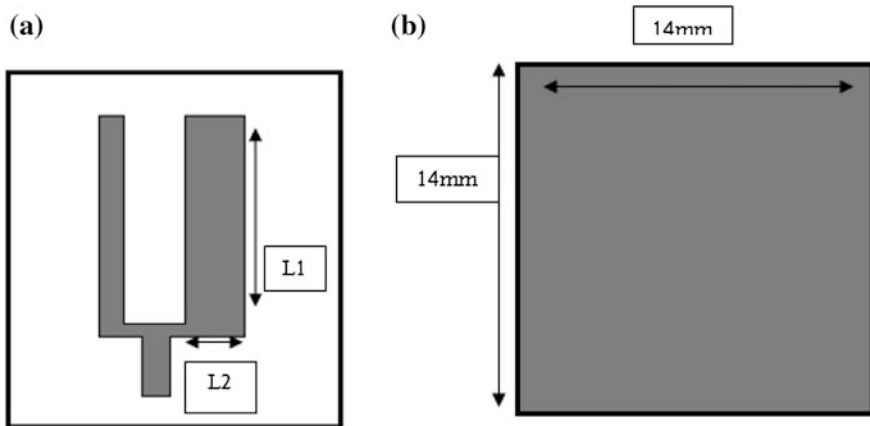


Fig. 1 **a** Front view of proposed antenna with initial patch structure. **b** Back view of proposed antenna with initial ground plane

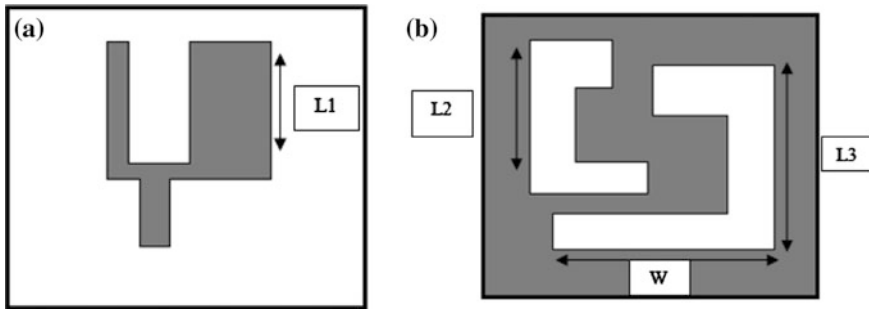


Fig. 2 Front view of proposed antenna with final patch structure. **b** Back view of proposed antenna with final ground plane

Table 1 Parameter value of final proposed antenna structure

<i>L1</i>	<i>L2</i>	<i>L3</i>	<i>W1</i>
11 mm	17 mm	21 mm	23 mm

Simulation and Result Analysis

The proposed antenna simulated on CST-tool software Fig. 3 shows the simulated result of proposed antenna by taking initial geometry of patch antenna. In Fig. 2 the *S11* parameter in terms of reflection coefficient as a function of frequency curve having value -14.7 dB at frequency of 8.2 GHz with little bandwidth value is shown.

The simulated result of final geometry structure is shown in Fig. 4. In Fig. 4 the return loss (*S11*) parameter in terms of frequency and reflection coefficient is -70.05 dB at frequency of 4.73 with 2.33 GHz as operating bandwidth is shown. Figure 5 depicts gain in the function of frequency and Fig. 6a, b shows that the

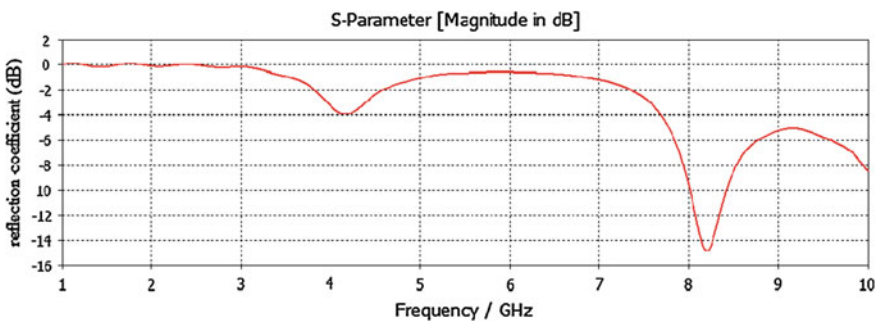


Fig. 3 Return loss graph by initial geometry of patch antenna

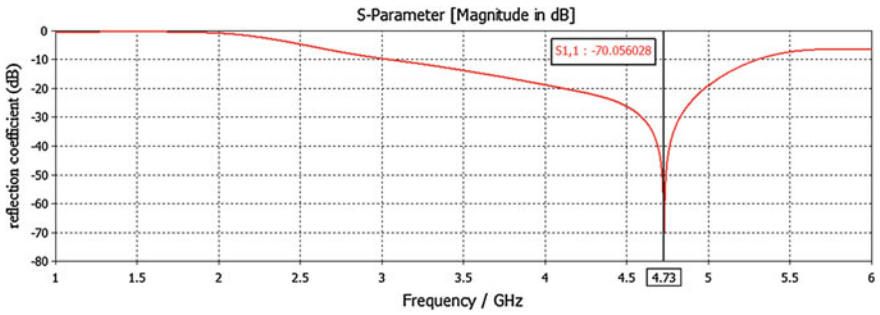


Fig. 4 Return loss graph by final geometry of patch antenna

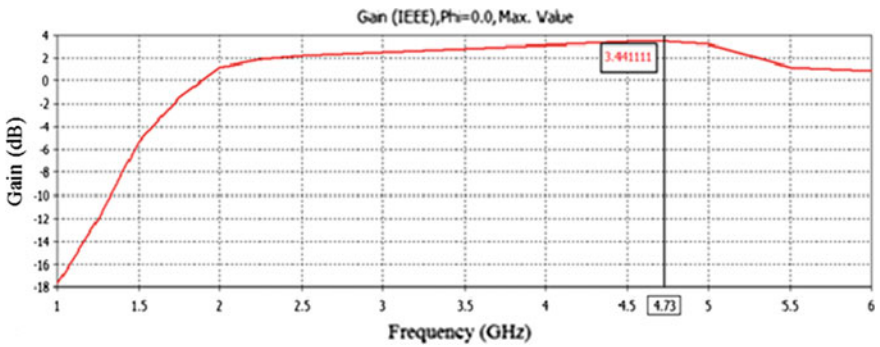


Fig. 5 Graph of stable gain

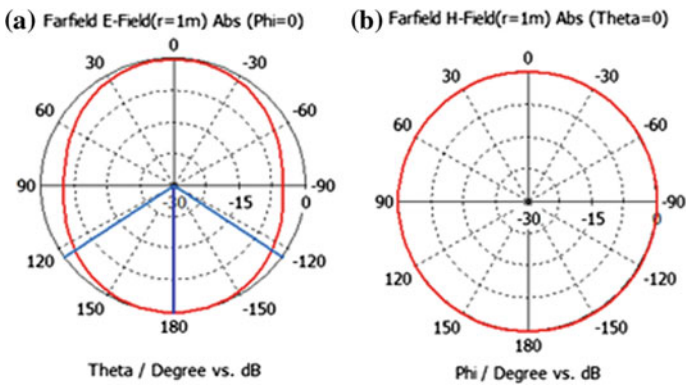


Fig. 6 a Normalized *E* field pattern of antenna operating at 4.73 GHz frequency. b Normalized *H* field pattern of antenna operating at 4.73 GHz frequency

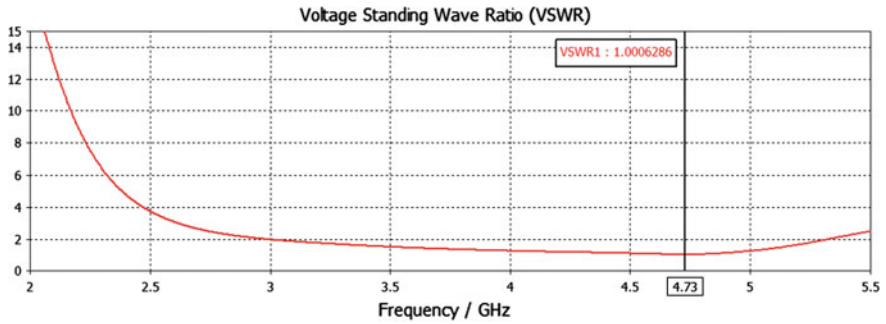
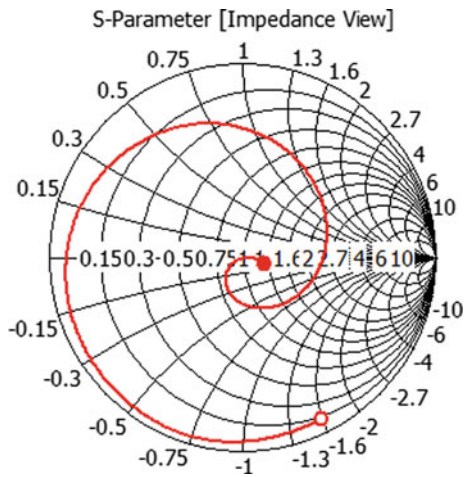


Fig. 7 VSWR graph unity at operating frequency 4.73 GHz

Fig. 8 Smith chart for proposed antenna



radiation pattern in both e field and h field are normalized to the patch. In Fig. 7 is shown, the VSWR is uniform and equal to unity at operating frequency range.

The Smith chart of proposed modified U-shaped patch antenna is shown in Fig. 8

Conclusion

A novel geometry of compact microstrip antenna is proposed for wireless communication applications with modified U-shaped patch and successfully implemented, and it is fulfilled that slot in ground plane provides a bandwidth of nearly 2.33 GHz with 3.44 dB of uniform and stable gain and about 1.004 VSWR value. This proposed microstrip antenna enhanced the impedance bandwidth and provided good matching. This antenna is simulated by CST. This proposed antenna is used in all wireless communication application.

References

1. Story, A.T.: *A Story of Wireless Telegraphy*. D. Appleton and Co, New York (1904)
2. Kraus, J.D.: Antennas since hertz and marconi. *IEEE Trans. Antennas Propag.* **33**(2), 131–136 (1985)
3. James, J.R., Hall, P.S.: *Handbook of Microstrip Antennas*. Peter Peregrinus
4. Huynh, T., Lee, K.F.: Single-layer single-patch wideband microstrip antenna. *Electron. Lett.* **31**(16), 1310–1312 (1995)
5. Rafferty, W., Dessouky, K., Sue, M.: NASA's mobile development program. In: *Proceedings of the Mobile Conference*, pp. 11–22 (1988)
6. Lee, R.Q., Lee, K.F., Bobinchak, J.: Characteristics of a two-layer electromagnetically coupled rectangular patch antenna. *Electron. Lett.* **23**(20), 1070–1072 (1987)

Performance Improvement of Epidemic Routing Protocol of Delay Tolerant Networks Using Improved Buffer Management

Harminder Singh Bindra

Abstract Large quantum of work has already been carried out by researchers in the field of delay tolerant networks (DTN). Most of the past work is related to designing and formulating routing strategies for DTN, managing the buffer using various queuing model, and securing the message bundle. In this work, we have analyzed the removal and accommodation of messages at the node, and observed that there are certain cases in which some messages that are removed from the node to accommodate new messages again arrive at the node through some other node, which in turn initiates the process of removal of the message from the buffer to accommodate this message. This leads to the circular loop of message removal/accommodation which in turn increases the overhead linked with the routing protocol and lowers the delivery probability. So, in this work we have proposed and analyzed the extension to this basic epidemic routing principle to avoid this message accommodation and removal loop. The results that were obtained clearly show that the extension applied to the epidemic routing protocol has a significant impact on the performance of the routing protocol and hence it is to be applied in the working environment.

Keywords Delay tolerant networks · Epidemic routing · Buffer management · Opportunistic network environment · Intermittent connectivity

Introduction

Delay tolerant networks (DTN) have been proposed as an issue to fabricate the system base by irregularly associated portable nodes with high impact by dynamic topology changes and node intermittent connectivity. The communication in such a scenario is carried out using “store-carry-forward” model. In such model, the constituent nodes

H.S. Bindra (✉)

Department of Information Technology, Malout Institute
of Management & Information Technology, Malout, Punjab, India
e-mail: Bindra.harminder@gmail.com

© Springer India 2016

N. Afzalpulkar et al. (eds.), *Proceedings of the International Conference on Recent Cognizance in Wireless Communication & Image Processing*, DOI 10.1007/978-81-322-2638-3_86

773

store the messages in their buffer and hand over the message to the next node when the two nodes come in communication range of each other [1].

In DTN, mobile nodes act as a router that can be configured with finite buffer space, energy, and processing power. The DTN environment experiences restricted system assets, for example, energy, data transfer capacity, and data holding space [2]. Taking into account these stipulations, the DTN routing conventions can be ordered into two plans: (i) Single Copy and (ii) Multi-Copy directing conventions. The single copy directing method [3, 4] forwards the single copy of the message along one unique path. This decreases the system assets, however it endures long defer and abates the conveyance likelihood. So as to minimize the conveyance delay, multi-copy [5–8] forwarding conventions were proposed, where a node spreads numerous duplicates of each message along diverse ways. The numerous transmissions can result in the overhead on system assets.

In multi-copy forwarding conventions, the high volumes of system assets, for example, data holding space and data transfer capacity can be minimized by changing the transmission and buffer management procedures.

The rest of the paper is organized as follows: section “[Related Work](#)” discusses the brief related work. Section “[Methodology](#)” elaborates the mechanism proposed in this work for buffer management and performance improvement of epidemic routing protocol. In section “[Simulation and Results](#)”, the simulation environment and simulation results are discussed, and section “[Conclusion](#)” concludes the paper.

Related Work

A number of research findings are present in the literature for efficient routing of data packets in DTN. The area that needs to be addressed is the impressive buffer management policies which should target to devise a mechanism to evaluate the procedure to drop a message from the buffer. Numerous buffer management techniques, for example, drop-oldest (DOA), drop random (DR), LIFO/DL, FIFO/DF are employed in the DTN. The above-mentioned methods are those that reduce the waiting time of the message in the buffer and because of this reason these methods are not applicable in DTNs.

Lindgren et al. [9] worked by studying the different buffer management techniques, for example, Most Forwarded First (MOFO), Most Favorably Forwarded first (MOPR), Shortest Lifetime First (SHLI), and Least Probable First (LEPR). In his study, the MOFO gave excellent results for varying buffer size. Other researchers worked on algorithms like global-based drop (GBD) in which working of the mechanism is based on the knowledge of the entire network state. However, this type of algorithm cannot be implemented in DTN as in the case of DTN, the knowledge about the network state cannot be built due to excessive network delays and intermittent connectivity pattern. In a continuation of this work, the author proposed History-Based Drop (HBD) policy. This is the modified version of the GBD.

Another approach N-Drop was proposed in which the message that is forwarded N number of times is selected to be removed from the buffer. In case there is no message that is transmitted N number of times, then the message that is present at the end of the queue is the one to be removed to free the buffer space.

Some of the drop policies available in the literature tackle the process of message deletion with the help of acknowledgment [10]. It uses the node movement behavior to transfer the acknowledgments that in turn are used to remove the useless message copies from the buffer space. These types of policies are hard to implement in DTN as it is difficult to maintain the central network state (message delivery information).

A few works proposed recently, which manage the issue of congestion, e.g., lifetime ASC (ascending) [11] request drop strategy confirms to the messages decided to be tossed are those whose remaining TTL terminates closer; drop largest (DLA), [12] substantial size message are chosen to drop. T-DROP [13] drops the message that lies in the limit size scope of buffer and E-DROP [14]. It drops the message of equivalent size from the node buffer when the node is congested. All these plans have a few advantages and disadvantages and still more research discoveries are progressing.

In our study and analysis, we found that at the contact opportunity, the message copy is forwarded to the next intermediate node depending on the availability of buffer space at the next node. If the buffer space is available, then the message is forwarded to the node but if the buffer space is not available in the next hop node then the space is created at the next hop node using some buffer management scheme. In this process, some of the messages are removed from the buffer so as to accommodate the new message at the node.

But if we analyze the removal and accommodation of the messages at the node, we observe that there are certain cases in which some messages that are removed from the node to accommodate new messages again arrive at the node through some other node. This mechanism creates a loop in which again the same message is accommodated by the node which has removed it to accommodate some other message in some previous time instance. This loop increases the overhead associated with the routing protocol and lowers the delivery probability of the same. There are a large number of schemes that manage buffers to accommodate the new incoming message, but we did not find any scheme that deals with the issue mentioned above. So the gap that we analyzed is the need of the mechanism to deal with this message removal and accommodation loop.

Methodology

The overall message forwarding mechanism followed by the epidemic routing protocol is shown in Fig. 1. When the transmission range of the two nodes overlaps, the two nodes exchange the summary vector (list of messages in message collection). From the summary vector, the current node generates the list of messages to

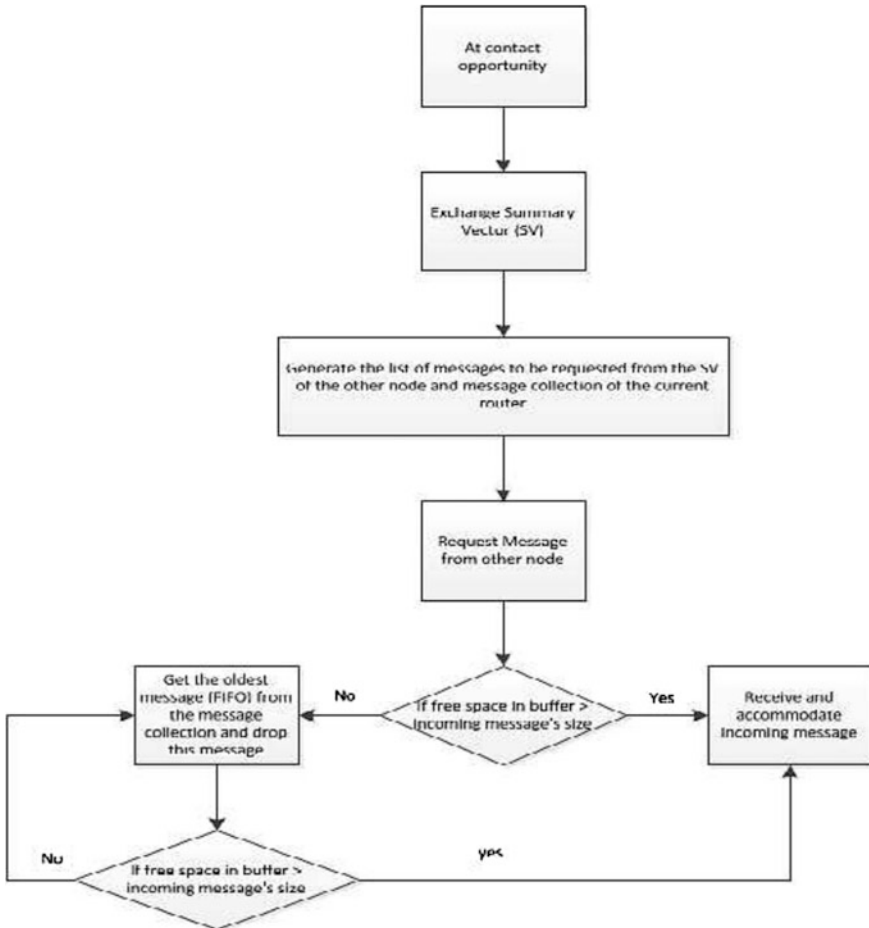


Fig. 1 Normal behavior of router with epidemic routing protocol in DTN

be requested from the other node. This list is exchanged to the other node. When a message arrives at a node, if the buffer space is available, the message is received by the node. But if the buffer space is not available, some messages from the message collection are removed depending on the buffer management scheme being followed (FIFO). This freed space is used to accommodate the message present in the message collection of the other node.

But the drawback of this behavior is message accommodation and dropping the loop as mentioned in the research gap section. So the extension is applied to the normal behavior as shown in Fig. 2.

In the extension used, each node maintains the list of dropped messages. When a message arrives at the node, the routing module first checks the presence of the incoming message in the dropped message list. If the message is present in the

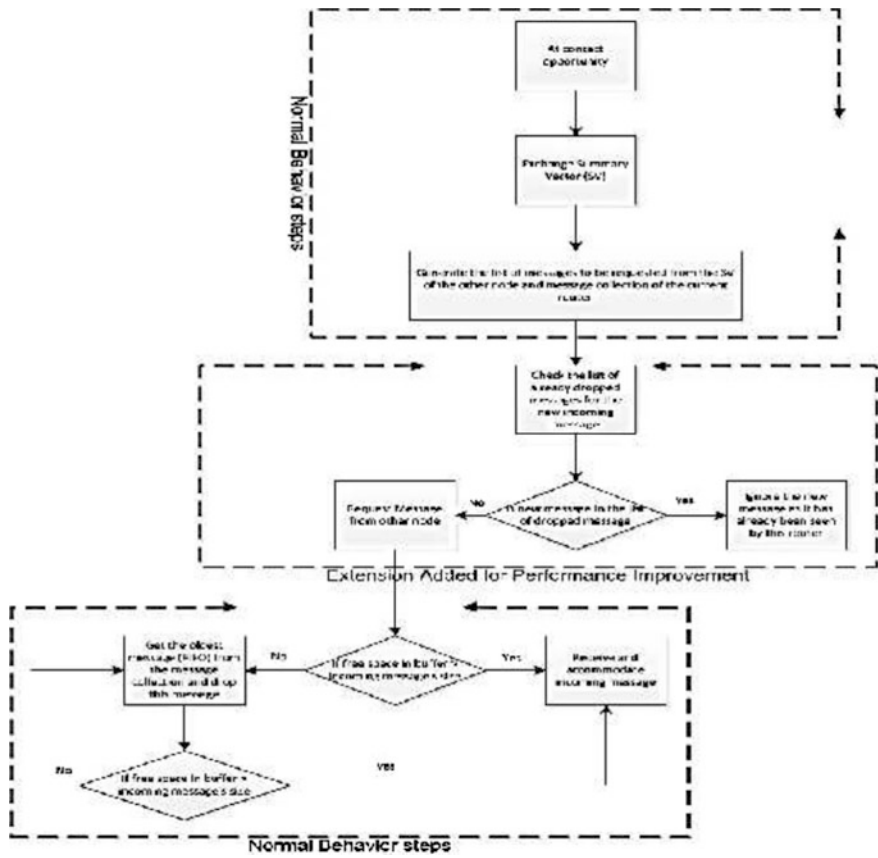


Fig. 2 Extended behavior of router with epidemic routing protocol in DTN

dropped message list, the new incoming message is discarded as this message has already got enough time in the buffer for being forwarded to the other node. If the message is not present in the dropped message list, then the normal routing protocol routine proceeds.

Simulation and Results

We have simulated a 12 h period and evaluated the different metrics used to compare the performance of epidemic routing protocol under normal behavior (defined in Fig. 1) and under the proposed extension (defined in Fig. 2). This routing protocol is implemented in Java-based opportunistic network environment (ONE) simulator [15]. The flow model of the underlying routing process as applied in ONE is depicted in Fig. 1.

In the considered scenario, the movement of nodes is governed through shortest path map-based movement model. Each node has to wait for a random time period when it reached the destination location. This random time period varies between lower bound and upper bound value of 5 to 15 min. After the wait period, the node selects the new location which is again a random selection and then it moves to this selected location with a speed varying between the lower bound and upper bound value of 30–50 km/h. The buffer size of the nodes is varied from 5 to 35 Mbytes and performance of the considered protocol is evaluated w. r. t. different buffer size. It is assumed that there is no prior information about the node movement or message creation is available with the nodes/network. Connections among the nodes are created using IEEE 802.11b interface. The transmission rate and transmission range for this interface is set to 2 Mbits/s and 30 meters, respectively.

Also, an extension mechanism proposed in this work is implemented by adding code to the ActiveRouter class and MessageRouter class defined above.

Figure 3 shows the delivery probability results for the normal and extended epidemic routing protocol for the described scenario. At the node density of 40 nodes per group, the delivery probability improves by 31 %, i.e., it improves from 0.29 to 0.38 at 7 M buffer size.

Thus, it is evident from Fig. 3 that the proposed extension when applied to the epidemic routing protocol has great impact on its delivery probability under the defined network scenario. When we increase the node density, the delivery probability of the considered routing protocol increases. As the node density increases the replication level or the chances of the message replication increases, thereby increasing the delivery probability.

The response of the overhead ratio to the proposed extension of the buffer management at the node density 40 nodes per group is shown in Fig. 4. From the data shown in Fig. 4, it can be interpreted that there is a significant improvement in

Fig. 3 Delivery probability of epidemic routing protocol under normal and proposed extension with node density of 40 nodes per group

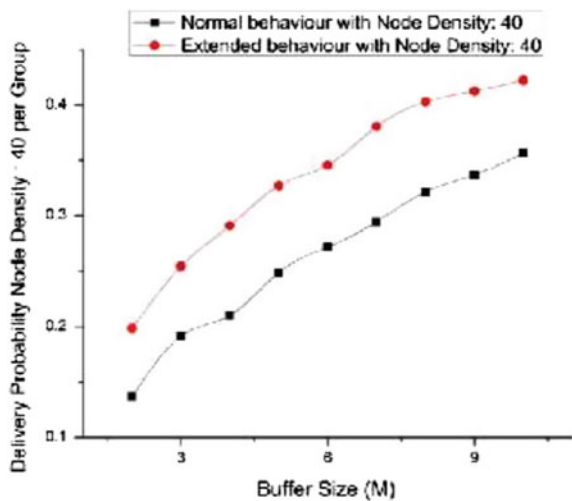
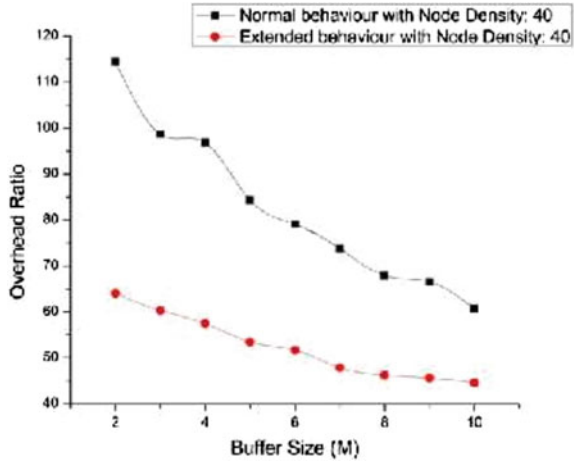


Fig. 4 Overhead ratio of epidemic routing protocol under normal and proposed extension with node density of 40 nodes per group



the overhead ratio of the epidemic routing protocol with the extension applied. At 2 M buffer size this value drops from 114.42 to 63.98, i.e., 44 % reduction in the overhead ratio. This improvement is the main contribution of our work, which is a very significant value. Similarly at 4 M buffer size, overhead ratio value improves by 41% at the same node density.

From Fig. 5, it is clear that there is not much drop or increase in the average latency of the epidemic routing protocol in the presence of the extension of the protocol. This response of the routing protocol clearly shows that the replications of the packets that are avoided by the extension were useless and were not contributing to the delivery of the data packets to the final destination. The packets that were earlier being delivered are still being delivered and hence there is not much change in average latency value.

Fig. 5 Average latency of epidemic routing protocol under normal and proposed extension with node density of 40 nodes per group

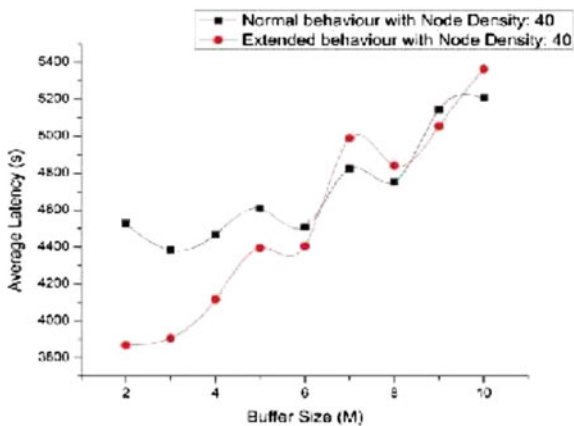


Fig. 6 Energy consumption in normal and extended epidemic routing protocol

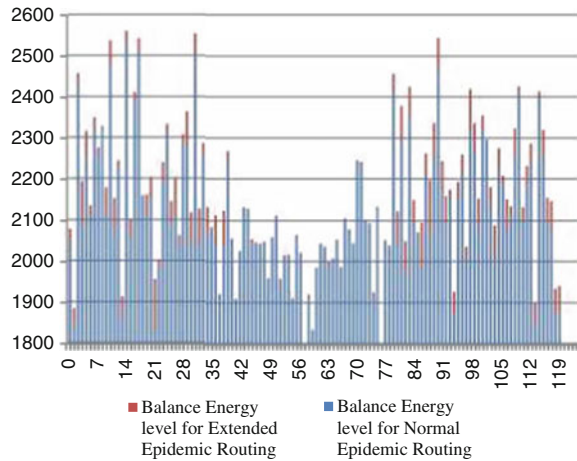


Figure 6 shows the balance energy of the nodes after the 43200 s of simulation. The simulation started with the nodes having the 4097 units of energy. With the passage of time energy gets consumed for scanning of the nodes, packets management, and other routing relating activities. The graph shows that the nodes when simulated with the extended epidemic routing protocol consumes less amount of energy, as thus after 43200 s (12 h) of simulation are left with much more balance energy. Thus, the proposed extension improves the energy consumption of the nodes. For example, if we consider the p21 node in the simulation, the balance energy after 12 h of simulation improves to 1825.4 units from 1694.52 units when the proposed extension is applied to the considered routing protocol. Thus, it saves 130.88 units of energy in 12 h of simulation. This clearly is a huge saving in the energy consumption of the node, which is the most valuable resource for wireless networks.

Conclusion

We have evaluated, analyzed, and compared the performance of epidemic routing protocol with the base configuration and the proposed extension applied. This comparative study is carried out for having a clear understanding of the considered routing protocol (i.e., epidemic routing) and also to study the impact of the extension proposed in this paper on the considered routing protocol. The results given in this paper clearly show that the extension applied to the epidemic routing protocol has a significant impact on the performance of the routing protocol and hence it is to be applied in the working environment.

References

1. Khabbaz, M.J., Assi, C.M., Fawaz, W.F.: Disruption-tolerant networking: a comprehensive survey on recent developments and persisting challenges. *Commun. Surveys Tutorials, IEEE* **14**(2), 607–640 (2011)
2. Farrell, S., et al.: When TCP breaks: delay- and disruption- tolerant networking. *Internet Comput. IEEE* **10**(4), 72–78 (2006)
3. Spyropoulos, T., Psounis, K., Raghavendra, C.S.: Single-copy routing in intermittently connected mobile networks. In: *First Annual IEEE Communications Society Conference on Sensor and Ad Hoc Communications and Networks, 2004. IEEE SECON 2004* (2004)
4. Shah, R.C., et al.: Data MULEs: modeling and analysis of a three-tier architecture for sparse sensor networks. *Ad Hoc Netw.* **1**(2–3), 215–233 (2003)
5. Ramanathan, R., et al.: Prioritized epidemic routing for opportunistic networks. In: *Proceedings of the 1st international MobiSys Workshop on Mobile Opportunistic Networking*, pp. 62–66 (2007). ACM, San Juan, Puerto Rico
6. Spyropoulos, T., Psounis, K., Raghavendra, C.S.: Spray and wait: an efficient routing scheme for intermittently connected mobile networks. In: *Proceedings of the 2005 ACM SIGCOMM Workshop on Delay-Tolerant Networking, 2005*, pp. 252–259. ACM, Philadelphia, Pennsylvania, USA
7. Spyropoulos, T., Psounis, K., Raghavendra, C.S.: Spray and focus: efficient mobility-assisted routing for heterogeneous and correlated mobility. In: *Fifth Annual IEEE International Conference on Pervasive Computing and Communications Workshops, 2007. PerCom Workshops '07* (2007)
8. Burgess, J., et al.: MaxProp: routing for vehicle-based disruption-tolerant networks. In: *INFOCOM 2006. 25th IEEE International Conference on Computer Communications. Proceedings* (2006)
9. Lindgren, A., et al.: Probabilistic routing in intermittently connected networks. *SIGMOBILE Mob. Comput. Commun. Rev.* **7**(3), 19–20 (2003)
10. Feng Cheng, L., Weihan, G., Chai-Kiat, Y.: A queuing mechanism to alleviate flooding attacks in probabilistic delay tolerant networks. In: *Sixth Advanced International Conference on Telecommunications (AICT)* (2010)
11. Soares, V.N.G.J., et al.: Improvement of messages delivery time on vehicular delay-tolerant networks. In: *International Conference on Parallel Processing Workshops. ICPPW '09* (2009)
12. Rashid, S., Ayub, Q.: Efficient buffer management policy DLA for DTN routing protocols under congestion. *Int. J. Comput. Netw. Secur.* **2**(9), 118–121 (2010)
13. Ayub, Q., Rashid, S.: T-drop: An optimal buffer management policy to improve QOS in DTN routing protocols. *J. Comput.* **2**(10), 46–50 (2010)
14. Sulma, R., Qaisar, A.: E-DROP an effective drop buffer management policy for DTN routing protocols. *Int. J. Comput. Appl.* **13**(7), 8–13 (2011)
15. Keranen, A., Ott, J., Karkkainen, T.: The ONE simulator for DTN protocol evaluation. In: *Proceedings of the 2nd International Conference on Simulation Tools and Techniques, 2009, ICST (Institute for Computer Sciences, Social-Informatics and Telecommunications Engineering)*, pp. 1–10. Rome, Italy

Elliptically Slotted Self-affine 8-Shaped Fractal Multiband Antenna

Rohit Gurjar, Ravi Singh and Saurabh Kumar

Abstract Antennas in modern telecommunication systems require smaller dimensions and wider bandwidth. The authors have presented the self-affined multiband elliptically slotted 8-shaped fractal antenna. The elliptically slotted 8-shaped fractal antenna has been designed by iterated function system (IFS) up to the second iteration. The resonance frequencies of the second iteration of (K_2) fractal antenna are 2.462, 3.329, 3.827, and 4.775 GHz with VSWR 1.359, 1.339, 1.221, and 1.911, respectively. The proposed fractal antenna (K_2) size is reduced to 19.5 % from base structure (K_0). Proposed fractal antenna (K_2) obtained a bandwidth of 592 MHz. IE3D software has been used for simulation in this paper.

Keywords Fractal antenna · 8-shaped antenna · Elliptically slotted antenna · Microstrip antenna · Self-affine antenna

Introduction

The modern science of fractal offers us new interesting possibilities for designing lesser broadband and effective antennas for restricted space. So in this, we emphasize on nature-based antenna design concepts to employ fractal geometry. Fractal structures are available in nature; numerous examples of natural fractals are

Rohit Gurjar (✉)
Department of Electronics & Communication Engineering,
Anand Engineering College, Agra 282007, India
e-mail: gurjarsgi@gmail.com

Ravi Singh · Saurabh Kumar
AEC, Agra, India
e-mail: ravisinghec09@gmail.com

Saurabh Kumar
e-mail: ersaurabhkumar@yahoo.com

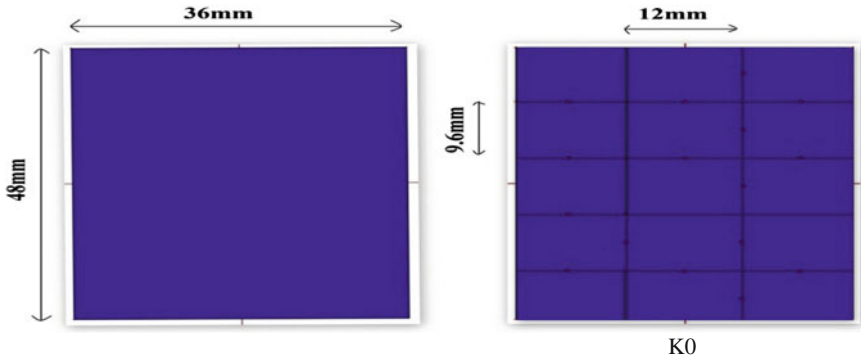


Fig. 1 Scaling rectangular patch by self-affine property

plants, leaves, shores, alp ranges, etc. [1]. Fractals are space-filled structures; these structures are electrically large, and can be packed efficiently in smaller areas. So, these antennas are compact in size with multiband characteristics [2].

Fractal means irregular or broken fragments. Benoit Mandelbrot used it initially [1] to explain self-similar or self-affined type complex structures. If any structure is scaled equally along horizontal and vertical sides then it is called as self-similar structure [3], otherwise called as self-affine structure [3]. This concept of self-affinity is used in this paper. We scaled base structure (*K0*) unequally in horizontal and vertical sides.

Proposed Antenna

In this paper, self-affined elliptically slotted 8-shaped fractal antenna is considered. This structure is formed by dividing the base structure (*K0*) horizontally into three parts and vertically in five parts using self-affine property [4]. Then, the structure (*K0*) is drawn by using an iterated function system (IFS) as shown in Fig. 1 and IFS coefficients as shown in Table 1. IFS is explained by the equation [3, 5, 6]

$$W \begin{bmatrix} x \\ y \end{bmatrix} = \begin{bmatrix} a & b \\ c & d \end{bmatrix} \begin{bmatrix} x \\ y \end{bmatrix} + \begin{bmatrix} e \\ f \end{bmatrix} \tag{1}$$

Then, out of which the two central rectangles are slotted in an ellipse shape to make an 8-shape as shown in Fig. 2 (*K1*). It is the first iteration (*K1*). Then, again self-affine property is applied to the remaining rectangles of the iterated structure (*K1*) by same scaling factors. Then, IFS and elliptically slotting concept are used to generate second iterated structure (*K2*) as shown in Fig. 2.

Table 1 IFS Transformation coefficients for the self-affine fractal

W	a	b	c	d	e	f
1	0.3333	0	0	0.20	0	0
2	0.3333	0	0	0.20	0.3333	0
3	0.3333	0	0	0.20	0.6666	0
4	0.3333	0	0	0.20	0	0.2
5	0.3333	0	0	0.20	0.3333	0.2
6	0.3333	0	0	0.20	0.6666	0.2
7	0.3333	0	0	0.20	0	0.4
8	0.3333	0	0	0.20	0.3333	0.4
9	0.3333	0	0	0.20	0.6666	0.4
10	0.3333	0	0	0.20	0	0.6
11	0.3333	0	0	0.20	0.3333	0.6
12	0.3333	0	0	0.20	0.6666	0.6
13	0.3333	0	0	0.20	0	0.8
14	0.3333	0	0	0.20	0.3333	0.8
15	0.3333	0	0	0.20	0.6666	0.8

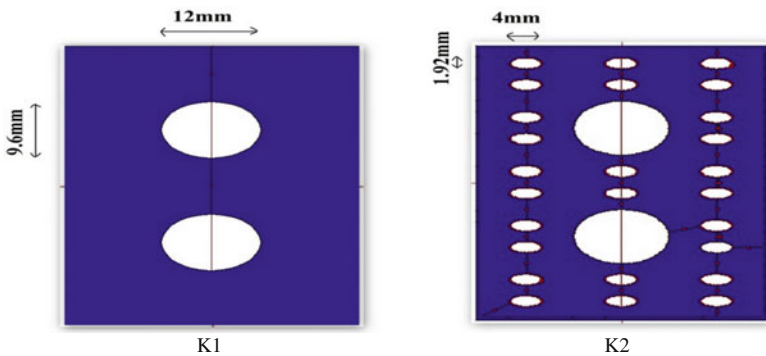
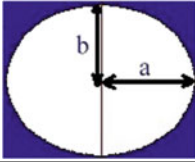


Fig. 2 First two iterations of the fractal geometry

For an ellipse, the eccentricity lies between 0 and 1. It is observed in Table 2, that both the slots are elliptical and in shape of $K2$ structure. There are 2 larger and 26 smaller slots in iterated fractal geometry $K2$. Hence, the total slotted area for $K2$ is 337.76 mm^2 .

We used the Teflon (PTFE) material as a substrate. Then, the following parameters are taken into account for the design of fractal antenna for resonant frequency of 2.6 GHz: the thickness of the substrate is 4.8 mm, dielectric constant of PTFE is 2.1, and calculated dimensions of the rectangular patch fractal antenna are $36 \text{ mm} \times 48 \text{ mm}$ (without iteration). The Zeland IE3D simulation software has been used for antenna designing. This structure provides a multiband behavior and is fabricated using a coaxial probe feed. The feed point is located on the patch such that it has the input impedance of 50Ω for the resonant frequency. Therefore, a method called trial and error is used to locate the feed point.

Table 2 Parameters of iterated fractal geometry (K_2)

	Parameters	Larger slot	Smaller slot
	Semimajor axis (a)	6 mm	2 mm
	Semiminor axis (b)	4.8 mm	0.96 mm
	Area of elliptically slotted part ($A = \pi ab$)	90.477 mm ²	6.031 mm ²
	Eccentricity, $e = \frac{\sqrt{a^2 - b^2}}{a}$	0.6	0.877

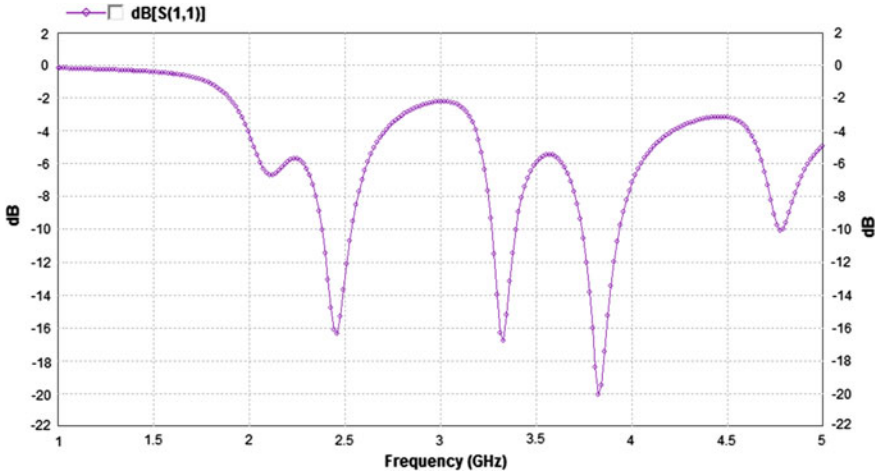


Fig. 3 Simulated return loss of second iterated (K_2) fractal antenna

Table 3 Simulated results of second iterated (K_2) proposed fractal antenna

S. no.	Resonant frequency (GHz)	Return loss (dB)	Bandwidth (MHz)	VSWR
1	2.462	-16.35	166	1.359
2	3.329	-16.79	136	1.339
3	3.827	-20.06	210	1.221
4	4.775	-10.09	80	1.911

Simulation Results and Discussions

The proposed antenna (K_2) simulation is done by Zeland Inc.’s IE3D software based on the method of moment (MoM). The MoM is a very powerful technique which can be applied to the analysis of three-dimensional structures. Fig. 3 shows proposed antenna’s return loss graph.

The patch antenna base structure K_0 was designed for 2.6 GHz resonance frequency. It is observed that resonant frequency reduces as one move from K_0 to K_2 fractal antenna. It is observed that on applying iterations in patch antenna, the

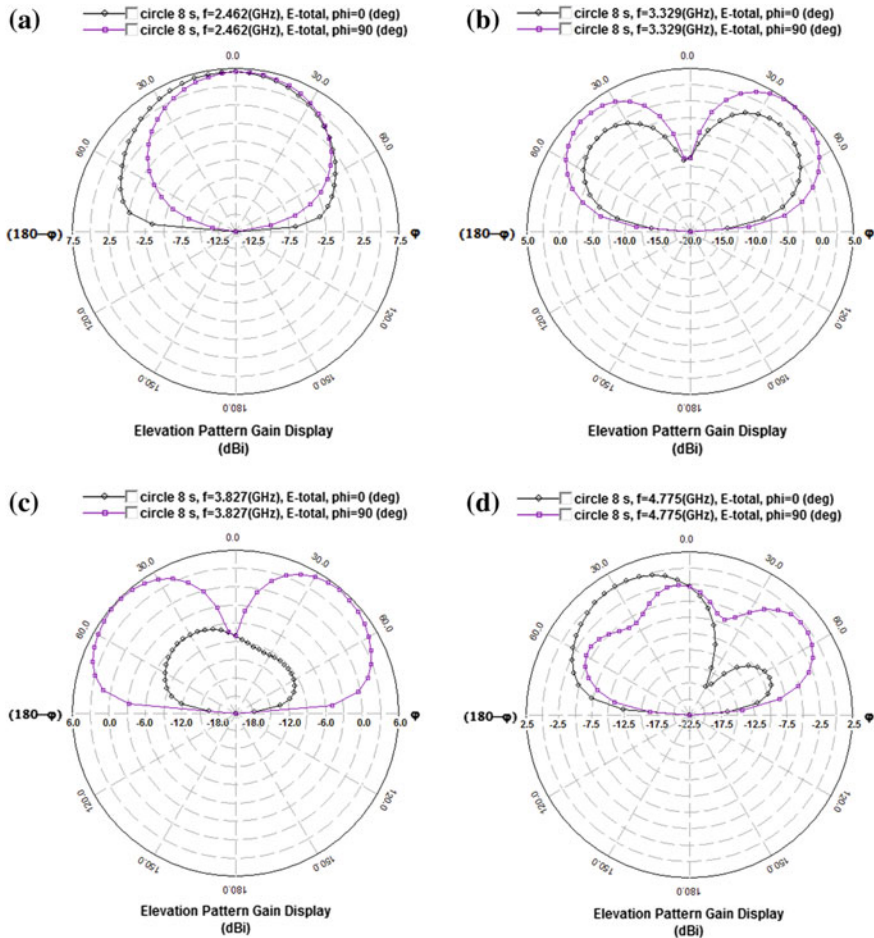


Fig. 4 Elevation pattern gains display (dBi) of second iterated (K_2) fractal antenna. **a** 2.462 GHz. **b** 3.329 GHz. **c** 3.827 GHz. **d** 4.775 GHz

resonant frequencies are increased. This shows that fractal antenna has multiband behavior. The resonant frequencies obtained for iterated fractal geometry K_2 are listed in Table 3.

Figure 4 shows radiation patterns for four frequencies, including 2.462, 3.329, 3.827, and 4.775 GHz for proposed elliptically slotted self-affine 8-shaped fractal multiband fractal antennas (K_2).

The proposed antenna resonates at (2.462, 3.329, 3.827, and 4.775) GHz frequencies as shown in Fig. 3 with the VSWR of (1.359, 1.339, 1.221, and 1.911) as shown in Fig. 5 for respective resonance frequencies. Figure 6 shows the smith chart of the proposed antenna (K_2).

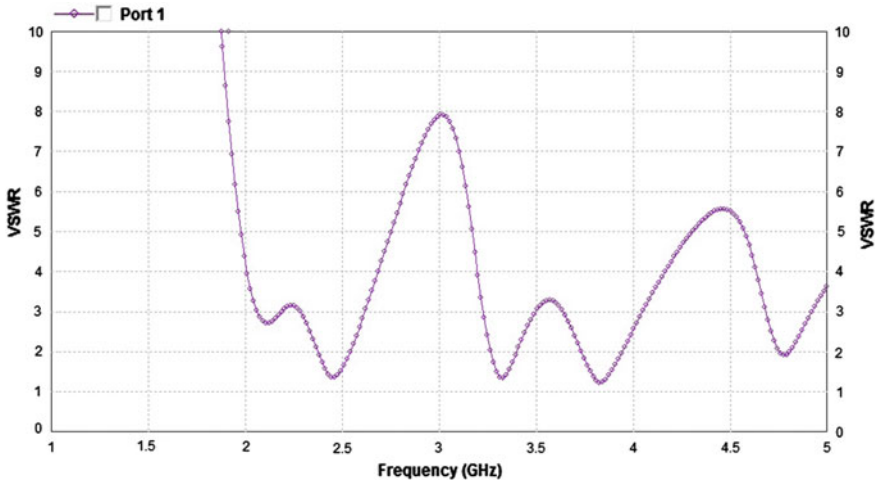
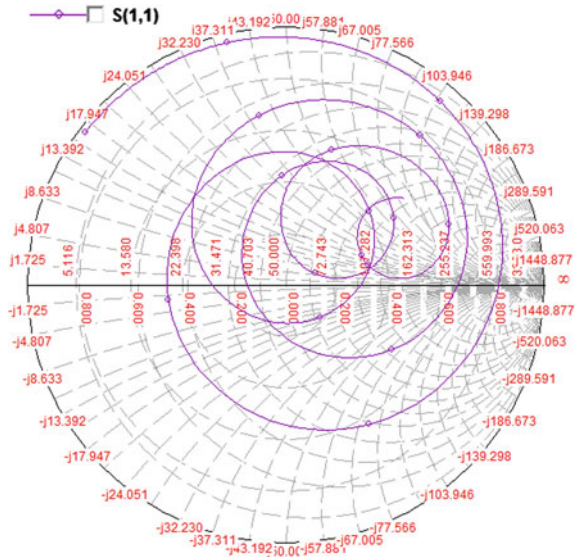


Fig. 5 VSWR versus frequency characteristics of second iterated (K_2) fractal antenna

Fig. 6 Smith chart of antenna



Conclusion

It is observed that self-affine elliptically slotted 8-shaped fractal antenna possesses multiband characteristics similar to a Sierpinski gasket antenna [7]. This paper has presented a new 8-shaped multiband fractal antenna. This proposed antenna has been designed for multiband frequencies (2.462, 3.329, 3.827, and 4.775) GHz. The

proposed antenna shows a significant size reduction compared to base antenna ($K0$). At the second iteration, antenna size is reduced by 19.5 % from conventional rectangular microstrip patch antenna.

References

1. Mandelbrot, B.B.: The Fractal Geometry of Nature. W. H. Freeman, New York (1983)
2. Gianvittorio, J., Rahmat-Samii, Y.: Fractal antennas: a novel antenna miniaturization technique, and applications. *IEEE Antenna's Propag. Mag.* **44**(1), Feb 2002
3. Peitgen, H.O., Jurgens, H., Saupe, D.: *Chaos and Fractals, New Frontiers in Science*. Springer, New York (1992)
4. Gurjar, R., Dwivedi, S., Thakur, S., Jain, M.: A self-affine 8-shaped fractal multiband antenna for wireless applications. *Int. J. Electron. Commun. Eng. Technol. (IJECET)* **4**(2), 103–108 (2013). ISSN Print: 0976-6464, ISSN Online: 0976–6472
5. Barnsley, M.F.: *Fractals Everywhere*, 2nd edn. Academic, San Diego, CA (1993)
6. Sinha, S.N. (Senior Member IEEE), Jain, M.: A self-affine fractal multiband antenna. *IEEE Antennas Wireless Prop. Lett.* **6** (2007)
7. Puente, C., Romeu, J., Pous, R., Cardama, A.: On the behavior of the Sierpinski multi-band fractal antenna. *IEEE Trans. Antennas Prop.* **46**, 517–524 (1998)

Design of Compact Triangular Patch Antenna for WiMax Applications

Manisha Gupta and Vinita Mathur

Abstract This paper presents a design of triangular microstrip patch antenna with varying substrate heights. The operating frequency used is in the range 1–3 GHz for wireless communication systems. Microstrip patch antenna with triangular shape is fabricated on FR-4 substrate which has a relative permittivity of 4.4 and mounted at a height above ground plane. Important parameters of antenna like return loss, input impedance, antenna gain, and VSWR are observed and comparison is done among the different antenna widths.

Keywords Microstrip antenna · Triangular patch · Resonant frequency · Return loss · Radiation pattern · VSWR · Antenna gain

Introduction

Antennas have a wide range of applications in the advancement of mobile communication systems like (mobile phone, personal digital assistants, notebook computer, etc.). The frequency bands for which they are entitled are GSM, GPS, Wi-Fi, and distant communication WiMAX bands. A single antenna cannot operate in all of these frequency bands, so multiband is required. So, most antenna designers preferred microstrip patch antenna for various wireless communication applications according to Balanis [1–4].

In the context of microstrip antennas, which are simpler to design and require low cost to manufacture, and consist of a very thin metallic patch below substrate and ground. Conducting material is used for the fabrication of patch and ground.

Manisha Gupta

Department of Physics, IEEE, JECRC University, Jaipur 303905, India
e-mail: drguptamanisha@gmail.com

Vinita Mathur (✉)

Department of Electronics and Communication, JECRC University,
Jaipur 303905, India
e-mail: vinitamathur12@gmail.com

© Springer India 2016

N. Afzalpulkar et al. (eds.), *Proceedings of the International Conference on Recent Cognizance in Wireless Communication & Image Processing*, DOI 10.1007/978-81-322-2638-3_88

791

Patch can have any shape like rectangular, square, or circular [5–8] but here analysis has been done using triangular patch because it occupies smaller surface area than other geometries. Certain advantages like reduced cost, size, and weight have increased the patch antenna capability to add with microwave integrated circuits, which add its applications in wired and wireless communication systems, mobile phones, and laptops.

There are many important constraints that need to be considered while designing microstrip patch antenna such as gain, bandwidth, directivity, and radiation pattern been mentioned. In this paper, more analysis is being done with bandwidth. It depends upon two main parameters, first by increasing substrate thickness (h) and second by decreasing the value of dielectric constant of the material. In this paper, analysis will be only done considering the thickness of the substrate [9, 10]. Due to integration and miniaturization, thickness cannot be increased beyond a certain extremity, and if increased beyond $0.1\lambda_0$, it results in degradation in antenna performance due to surface-wave propagation and lastly with an increase in h , the probe inductance increases and probe compensation techniques have to be employed to obtain impedance matching [11, 12].

A new standard by IEEE 802.16 has been established popularly known as worldwide interoperability for microwave access abbreviated as WiMax. It covers a range of 50 km and provides us with a transmission rate of 70 Mbps. For proper transmission and receiving of information in this band, antennas are required in its subdivided three allocation bands. [13–15]. The bands are low band (2.5–2.69 GHz), middle band (3.2–3.8 GHz), and upper band (5.2–5.8 GHz). As triangular patch antenna has advantages therefore, it is designed in this band and results are observed by varying the substrate thickness.

Paper is organized as follows: In section “[Antenna Design](#),” design of the novel triangular patch antenna is done. Section “[Results and Discussion](#)” shows the results and compares them with triangular patch antenna with various substrate heights. Finally, the results are presented in section “[Conclusion](#)”. The whole simulation is performed using CST microwave studio tool.

Antenna Design

Figure 1 shows the physical dimension of the design antenna. The design is based on the single-feed dual-frequency equilateral triangular [15, 16]. The dielectric constant of the substrate used for the FR-4 antenna is $\epsilon_r = 4.4$; loss tangent 0.019 and the thickness is varied. The thickness of the ground material is 0.035 mm. Furthermore, a single probe feed located along the center line is used for good impedance matching which is 50Ω . By determining the operating frequency at 1.5 GHz, we obtained the triangle side as 55 mm.

Fig. 1 Schematic diagram of the triangular patch antenna



Basic antenna shape is an equilateral triangle with a strip line feeder. The length of the side of an equilateral triangle microstrip antenna can be determined using the following equation [16].

$$a = \frac{2c}{3f_{10}\sqrt{\epsilon_r}}$$

where

f_{10} = lowest order resonant frequency, c = speed of light, a = length of a side of equilateral triangle, and ϵ_{eff} = effective dielectric constant

Results and Discussion

The proposed antenna has been simulated using the CST microwave studio tool (CST) software. Figure 2 shows the simulated return loss of the antenna with different substrate heights and keeping resonant frequency as 1.5 GHz.

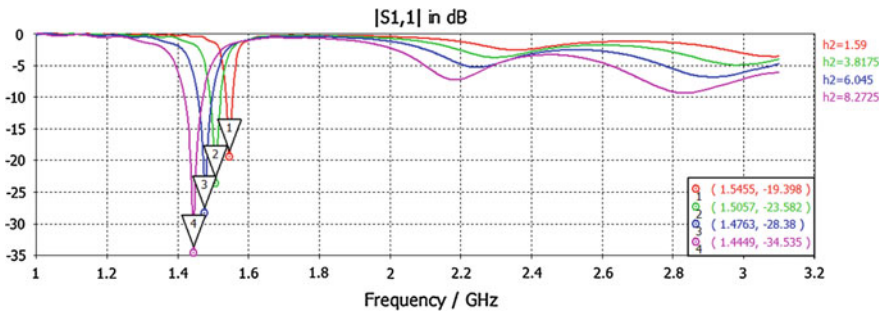


Fig. 2 Simulation result of the triangular patch antenna return loss versus frequency for different substrate heights

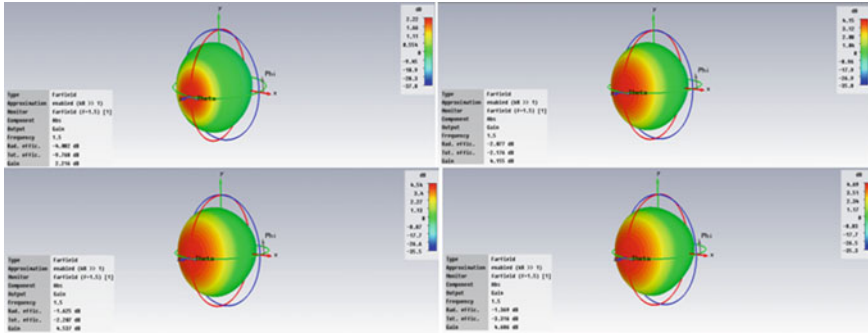


Fig. 3 The 3D Radiation pattern of the triangular patch antenna for different substrate heights

Table 1 Comparison between different substrate thicknesses

Parameters	Substrate thickness			
	1.5 mm	3.8175 mm	6.045 mm	8.275 mm
Resonant frequency (GHz)	1.5	1.5	1.5	1.5
Return loss (S_{11}) (dB)	-19.398	-23.582	-28.38	-34.535
Bandwidth (MHz)	16.8	28.9	40.9	51.3
Gain (dB)	2.216	4.155	4.537	4.686
Directivity (dBi)	6.307	6.231	6.160	6.049
VSWR	1.2781	1.1794	1.1229	1.0525
Input impedance (Ω)	19.465	41.361	57.654	70.974

Taking substrate height as 1.5 mm in the first case, the return loss obtained is -19.398 dB, increasing the substrate height to 3.8175 mm return loss reduces to -23.582 dB, return loss is -28.38 dB and -34.535 dB at substrate height 6.045 mm and 8.2725 mm, respectively.

The value of VSWR 2:1 is considered as a good bandwidth measurement for small antennas. 3D radiation pattern for different substrate heights is as shown in Fig. 3. It is observed that by increasing the substrate height, gain in dB also increases from 1.935 to 4.710 dB.

Following Table 1 shows the comparison between different substrate thicknesses with different parameters of triangular patch antenna.

Conclusion

This paper presents a design of triangular microstrip patch antenna with varying substrate heights. The operating frequency used is in the range 1–3 GHz for wireless communication systems. Triangular patch antenna is designed on FR-4 substrate with relative permittivity of 4.4 and mounted above ground plane. Return

loss, input impedance, antenna gain, and VSWR are observed for the antenna and comparison is done among different antenna widths. It is observed that by increasing the substrate height, gain, return loss and bandwidth increases, while input impedance is best obtained with substrate height 6.166 mm.

Acknowledgements Authors gratefully acknowledge the JECRC University for providing the platform to conduct this research.

References

1. Singh, I., Tripathi, V.S.: *Microstrip Patch Antenna and Its Applications: A Survey* (2011)
2. Balanis, C.A.: *Antenna Theory, Analysis and Design*. John Wiley & Son, New York (1997)
3. Chitra, R.J., Suganya, A., Nagarajan, V.: Enhanced gain of double U-slot microstrip patch antenna array for WiMAX application. In: *IEEE International Conference on Communications and Signal Processing*, Chennai, pp. 141–144 (2012)
4. Tlili, B.: Design of double C-slot microstrip patch antenna for WiMax application. In: *IEEE International Symposium on Antennas and Propagation Society*, Toronto, ON, pp. 1–4 (2010)
5. Mehranpour, M., Nourinia, J., Ghobadi, Ch., Ojaroudi, M.: Dual band-notched square monopole antenna for ultra wide applications. *IEEE Antennas Wireless Propog. Lett.* **11**, 172–175 (2012)
6. Noghabaei, M., Rahim, S.K.A., Sabran, M.I.: Dual band single layer microstrip antenna with circular polarization for WiMAX application. In: *6th European Conference on Antennas and Propagation*, 1996–1999 (2011)
7. Caso, R., Buffi, A., Pino, M.R., Nepa, P., Manara, G.: A novel dual-feed slot-coupling feeding technique for circularly polarized patch arrays. *IEEE Antennas Wireless Propag. Lett.* **9**, 183–186 (2010)
8. Mathur, V., Gupta, M.: Morphology of Koch Fractal Antenna. *Int. J. Comput. Technol.* **13**(2), 4157–4163 (2014)
9. Singh, N., Yadav, D.P., Singh, S., Sarin, R.K.: Compact corner truncated triangular patch antenna for WiMax application. In: *Mediterranean Microwave Symposium*, Guzelurt, pp. 163–165 (2010)
10. Bhatnagar, D., et al.: Microwave related activities in India: an overview. In: *41st European Microwave Conference*, Manchester, pp. 1356–1359 (2011)
11. Bhatnagar, D., Bhardwaj, V., Saini, J.S., Sharma, K.B., Gupta, M.: On radiations from right triangular microstrip antennas. *IEEE Antennas and Propag. Soc. Int. Symp.* **2**, 898–901 (2002)
12. Shukla, A., Biswas, M.: CAD model to compute the input impedance of cavity backing triangular patch antenna for wireless application. In: *2011 International Conference on Communication and Industrial Application (ICCIA)*, Kolkata, pp. 1–3 (2011)
13. Dam, M., Biswas, M.: Fast and Accurate Model to Compute the Resonant Frequency of Triangular Patch Antenna on Suspended and Composite Substrates, pp. 220–223. *IEEE* (2012)
14. Liu, L., Zhu, S., Langley, R.: Dual-band triangular patch antenna with modified ground plane. *Electron. Lett.* **43**(3) (2007)
15. Li, F., Ren, J., Yin, Y., Lei, J., Lian, R.: Design of wideband triangular patch antenna with modified ground plane. In: *International Workshop on Microwave and Millimeter Wave Circuits and System Technology*, pp. 123–126 (2013)
16. Sharma, L.N., Das, S., Gogoi, A.K.: ISM band traingular patch antenna on FR4 substrate with ‘U’ pattern slots. *IEEE Indicon Conference*, Chennai, pp. 184–187 (2005)

Post-accident Assistance Using On-Board Diagnostics and Smartphones

Arghya Biswas and Abhishek Pal

Abstract Today, we have reached a stage where we humans cannot imagine a life without automobiles. With considerable increase in the use of automobiles in our day-to-day life there is a proportional rise in the safety requirement in the vehicular network. Medical services are required to reach the accident location in minimal amount of time. Thus, we propose a system to accelerate the process of medical assistances and emergency services, reaching to the victims involved in a road accident. Smartphones give us a mean to establish wireless communication with the on-board diagnostics (OBD-II) and provide us with the computation power to monitor and detect various accident scenarios. The system determines the accident location using Global Positioning System (GPS) and broadcasts the location of the accident to the emergency services in the vicinity using the available GSM cellular network.

Keywords Emergency system · OBD-II · GPS system · Smartphones · Accident detection · ELM 327

Introduction

Automobiles have become an integral part of our life. India records one of the highest numbers of road accidents in the world. Statistics released by the Ministry of Road Transport and Highway in 2011 says there were 497,000 road accidents that left 145,485 people dead [1]. A major percentage of the deaths are due to lack of proper medical assistance reaching them in time. Based on a survey, it takes 10 min on an average for the emergency services to dispatch an ambulance to the

Arghya Biswas (✉) · Abhishek Pal
Under Graduate Pursuing Bachelor of Engineering in Computer, South Indian Education Society Graduate School of Technology, Nerul, Navi Mumbai, India
e-mail: biswas.arghya721@gmail.com

Abhishek Pal
e-mail: abhishekp.al@gmail.com

accident location. Thus, there exists a requirement of a system that minimizes this time delay. The proposed system consists of smartphones interfaced with the OBD-II of the vehicle via wireless connection using ELM327. Today, smartphones are common communication equipment readily available to everyone. The system is designed to detect possible accident scenarios, retrieving the accident location using GPS and broadcast the message to various emergency services in the vicinity of the accident.

Related Work

(a) *Smartphone sensors*: Today, smartphones come with a set of inbuilt sensors for better user experience. To detect the changes in the movement of the vehicle the system can rely on the motion sensors available in these smartphone. Keeping the device steady, the system can use a combination of these sensors like accelerometer and magnetometer to observe the changes in motion of the vehicle [2]. To have accurate readings from these sensors the smartphone is required to be steady inside the vehicle. Minor changes in orientation and calibration of these sensors lead to inaccuracy in the system. On testing in real-time scenarios, the system was incapable of detecting changes in speed and corresponding change in direction accurately. The dependency on the smartphone sensors for monitoring changes in movement and computation increased the load on the smartphone processor.

(b) *On-board diagnostics*: On-board diagnostic-II being a self-diagnostic system is commonly available in most of the cars. OBD-II is primarily designed to detect any faults in the vehicle by itself. Using this system the designed architecture is able to retrieve real-time values for various factors from the OBD-II. The communication between the OBD-II and smartphones is established by passing parameter IDs (PID) for the specific entity. Among the various modes of the OBD-II we use the current mode (0x01) which provides instantaneous data without freezing any frames. As the OBD-II codes are hexadecimal codes written in ASCII format, the responses for the OBD-II are later on converted to decimal format for further evaluation.

Speed PID is 0D:	RPM PID is 0C:	Torque PID is 63:
> 010D	> 010C	> 0163
410D 3E	410C 0F A0	416301 FF

Consider the above instance for retrieving speed of the vehicle, the response from the OBD-II is split into three blocks. The first two bytes (0x40 + 0x01) represent as the response for mode 1 of OBD-II. 0D represents the response for the specific PID (speed) and 3E represents the hexadecimal value for the speed of the vehicle.

(c) *ELM327*: ELM327 is a microcontroller used for interfacing on-board diagnostics with the smartphones via wireless Bluetooth connection.

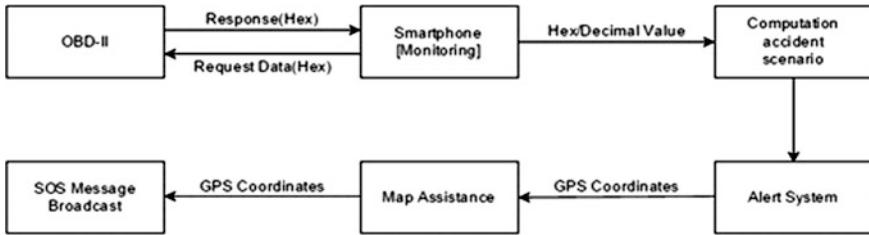


Fig. 1 Proposed architecture

Proposed System

Figure 1 represents how various modules of the proposed system interact with each other. The system consists of the ELM327 plugged into the OBD-II connector present below the dashboard of the vehicle. Thus, ELM327 provides the necessary wireless connectivity to the smartphone in the vehicle. The application in the smartphone retrieves and monitors the data from OBD-II by passing specific PID codes. Plotting this data with respect to time, the system can detect various accident scenarios. Once the accident is detected the longitude and latitude coordinates are determined via GPS module of the smartphone application. Then the longitude and latitude coordinates are embedded in a link and sent to the emergency services such as ambulances.

Implementation

As mentioned earlier the connection with the OBD-II is established by Bluetooth connectivity using ELM327. To establish an ‘Rfcomm socket connection’ the UUID of the application is changed to ‘UUID-00001101-0000-1000-8000-00805F9B34FB’. This ensures that the application detects devices such as ELM327, thus making the smartphone as the master in the Bluetooth connection. Once the connection has been established the system automates the process of passing the parameters to the ELM327 [3].

Detecting Accident Scenarios

The system is designed to detect various accident scenarios. By judging the intensity of the accident the application will result in either giving an alert message or broadcast the location details of the accident. The parameters considered for accident detection are mentioned below. The collected data from the sensors are at

the rate of one unit per 0.1 s. This gives 10 readings of data per second making it significantly capable to mark minute changes in motion of the vehicle with respect to the following parameters [4]:

- (1) Deceleration of the vehicle
- (2) RPM
- (3) Torque at the wheels

When the engine clutch is pressed the engine load is released. At this point the engine check unit (ECU) provides us with the speed and RPM of the vehicle as a varying factor.

Based on the reading from OBD-II, three scenarios are considered:

- 1. Hard breaking or head-on collision (heavy deceleration): Fig. 2 represents the experiment involving a hard breaking. From Fig. 2 it is observed that the vehicle’s speed reduced within few seconds, which resulted in a deceleration of more than 13 m/s^2 (-1.32 g). It is also observed that the RPM of the engine reduces, while the torque remains constant for that instant.
- 2. Sideways or rear collision: In this case it is observed that the torque at the wheel with respect to the engine output changes. In case of a rear collision the torque at the wheel increases substantially whereas engine’s RPM remains steady as seen in Fig. 3. Thus monitoring the torque of the engine with respect to time the system can detect a rear/sideways collision.

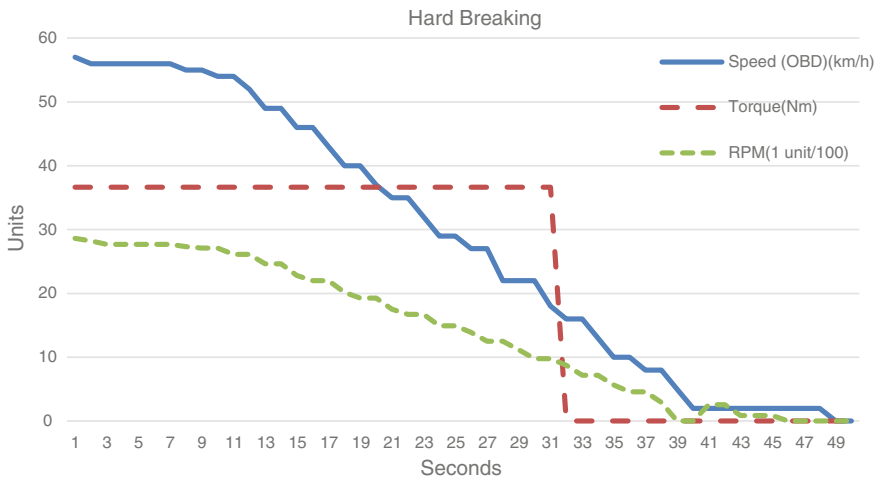


Fig. 2 Subset of the data collected for the hard breaking scenario

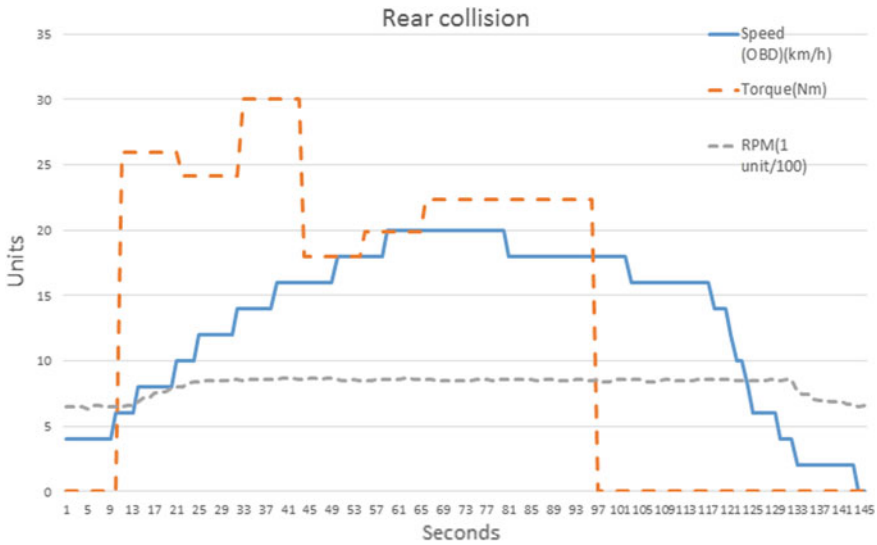


Fig. 3 Subset of the data collected for rear collision scenario

SOS Message Broadcast

On detection of a positive accident scenario the system retrieves the longitude and latitude coordinates using GPS module and embeds the coordinates in a google map’s link. In case the GPS module fails to retrieve the location, the system uses the last known location of the device. Using the ‘GOOGLE PLACE API’ the system can determine the emergency service in the nearby location and broadcast the message using the existing GSM architecture [5]. This activity can also be triggered using human intervention in case of a medical emergency faced by the passengers.

Map Assistance

In case the driver/passengers avoids a fatal injury then they can skip the SOS message broadcast and use GOOGLE MAPS for self-assistance. ‘GOOGLE PLACE API’ plays an important role in determining the nearby medical facilities and emergency services.

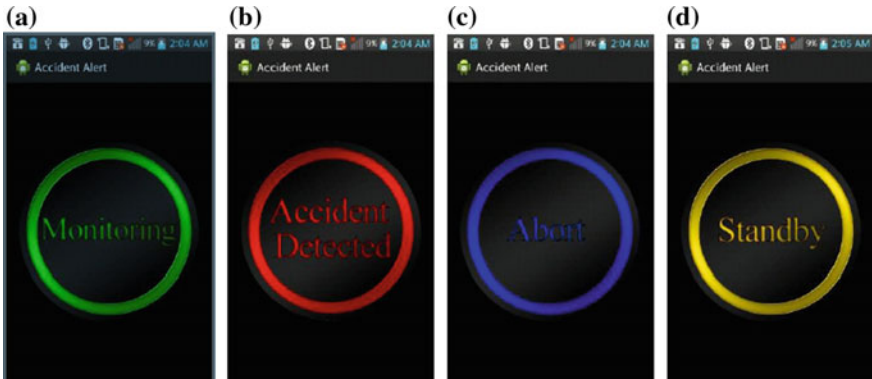


Fig. 4 Graphic user interface

GUI Design

The basic user interface consists of a single centralized button which changes colour to represent the different states of the system. Figure 4a represents application monitoring the sensors properly, Fig. 4b represents accident detected, Fig. 4c represents message sequence aborted, and Fig. 4d represents standby. The user can check the menu to see the sensors which are being monitored at that point.

Conclusion and Future Work

The system is build using the existing architecture of OBD-II on vehicles and smartphones thus making the system cost-efficient. The data retrieved from the OBD-II increases the precision of the system and overcomes the drawbacks of systems based on smartphone sensor. The computation power of the smartphone is able to process the data and give a response in milliseconds; this is the desired response to detect accident scenarios. On survey it was found that it takes 10 min or more for an ambulance to be dispatched to an accident location. Using our system it was found that this time window was reduced on an average of 2 min, based on the factors such as signal strength of the phone and propagation delay. The system fails in case the phone is out of network coverage area. As part of our future work we intend to test the system in real-time environment.

Acknowledgements Authors gratefully acknowledge Prof. Preeti Godabole and Mr. Shubhash Malge for believing in us, believing in the idea, and extending their support, guiding and helping us in everyway possible.

References

1. Open Government Data (OGD) Platform India: Accidental deaths in India. <http://data.gov.in/keywords/indian-road-accident-data>
2. Johnson, D.A., Trivedi, M.M. (Laboratory for Intelligent and Safe Automobiles (LISA), University of California, San Diego): Driving style recognition using a smartphone as a sensor platform. In: 2011 14th International IEEE Conference on Intelligent Transportation Systems, Washington, DC, USA, 5–7 Oct 2011
3. Android Developers: Bluetooth devices. <http://developers.android.com/reference/android/Bluetooth/BluetoothDevice.html>
4. Shaout, A.K., Bodenmiller, A.E. (The Electrical and Computer Engineering Department. The University of Michigan-Dearborn): A Mobile Application for Monitoring Inefficient and Unsafe Driving Behaviour
5. Android Developers. Google places: <https://developers.google.com/places/documentation/>
6. Zaldivar, J., Calafate, C.T., Cano, J.C., Manzoni, P. (Department of Computer Engineering, Universitat Politècnica de València): Providing accident detection in vehicular networks through OBD-II devices and android-based smartphones. In: 5th IEEE Workshop on User Mobility and Vehicular Networks
7. Outils OBD Facile. www.outlisobdfacile.com/obd-mode-pid.php

Digital Image Forensics and Counter Anti-forensics

Neha Singh and Sandeep Joshi

Abstract The use of digital images in journalism and as evidence in the court of law for crime investigation and law enforcement are some application areas where it is extremely important to ensure authenticity of the images being used. Wide availability of sophisticated image processing software has simplified image manipulation. Image forensics deals with the study of the images to reconstruct their history and detect if it has undergone some intentional or unintentional modifications. This paper presents an introductory overview of the digital image forensics and its counterpart aiming to help the beginners understand their alliance so as to develop robust forensic tools against intentional and unintentional attacks on the multimedia. A brief look into counter anti-forensics is also presented in this paper.

Keywords Digital image forensics · Anti-forensics · Counter anti-forensics · Image tampering

Introduction

With the advent of new technologies, the creation and exchange of digital images has become easier. But this has also made tampering of digital images easy, resulting in reduced trust in authenticity of digital images. The solution is to develop techniques which are able to judge if the image is intentionally or unintentionally manipulated and establish their authenticity as well as ownership. Digital image watermarking and image forensics are relied upon widely to reestablish the lost trust in digital images [1].

Neha Singh (✉) · Sandeep Joshi
Department of CSE, Manipal University Jaipur, Jaipur, India
e-mail: nneha.singh01@gmail.com

Sandeep Joshi
e-mail: sandeep.joshi@jaipur.manipal.edu

Digital image watermarking [1, 2] is the technique where self-authenticating information is embedded in the digital media with the main concern of establishing ownership of the content. Any deviation in the embedded information at the time of recovery will confirm manipulation of the data. Various possibilities for the choice and amount of information to be hidden, location for hiding and methods to conceal the information in the data imperceptibly are being explored by the researcher community. The hidden information and the method employed for hiding it imperceptibly within the data are expected to resist deliberate attacks like: compression, filtering, histogram equalization, rotation, cropping, addition of noise, etc. Digital image watermarking falls under the category of active techniques of image authentication and tamper detection because it requires addition to the data either during capturing or storage of digital data. This presents a disadvantage that the original data is manipulated before saving. Image forensics [1] is a passive technique to validate the authenticity of digital images by detecting tampering and recovering information about their history. Digital image forensics aims to identify if the image is computer generated or originally captured using a camera, authenticate or identify the image capturing device, detect tampering or identify if something is hidden in the image [3]. Most of the literature on image forensics deals with the image source identification and tampering detection of the digital images with cloning, splicing and retouching as the major concerns. Cloning refers to intentional image manipulation by copying some region from the image itself and pasting it to new locations (after being rotated and/or scaled) generally to conceal the original image contents. When regions from an image are pasted into a different image to produce a new image which retains the majority of one image for detail, it is referred to as image splicing. Image retouching refers to tampering where images with poor quality are modified for enhanced appeal. Image forensics has given rise to its counterpart, anti-forensics [4, 5] or counter forensics, which aim to remove forensically significant indicators of various processing steps which an image has gone through.

This paper presents an elementary overview of image forensic and anti-forensics and is organized as follows: section “[Digital Image Forensics](#)” presents a short introduction about some of the digital image forensic techniques for tampering detection in digital images followed by section “[Anti-forensics](#)” which sheds light on anti-forensics which counters for image forensics followed by section “[Countering Anti-forensics](#)” presenting a brief review of work done by the researchers to counter anti-forensics. Section “[Conclusion](#)” finally concludes the paper.

Digital Image Forensics

Many processing operations, both within and outside digital cameras, leave distinct traces or marks on digital images. These distinct traces are generally referred to as intrinsic fingerprints [4, 5] which account for the originality of digital image. Image forensic tools are based on the fact that image tampering disturbs these fingerprints

present within the images. The intrinsic fingerprints introduced during in-camera processing characterize the make and model of the imaging device and any discrepancy in these patterns is identified as a proof of post-production manipulation being done. The dearth of these fingerprints suggests that the image is computer generated and not originally captured by a camera or imaging device.

Surveys and studies on image forensics [6–9] as passive-blind technique for tamper detection are widely available in literature with cloning detection as the major concern. Figure 1 depicts the basic approach employed for cloning or copy-move forgery. The image is divided into nonoverlapping blocks for which features are extracted and sorted using a stable sort. This will put the similar features close to each other and the similar features imply similarity in the corresponding image regions.

The techniques for detection of cloning in images are either based on the key features of the image or image blocks [6]. The key-point-based methods detect similar features based on the Euclidean distance between the features of the image regions with high entropy. Block-based techniques divide the image under test into overlapping blocks. Features for individual blocks are calculated and stored in a row matrix which is then sorted. Sorting brings similar features closer to each other. Similar features imply similar blocks. Major work in the text belongs to the class of block-based technique with the major aim to reduce the time complexity by reducing either the image size to be analyzed [10, 11], number of image blocks to be tested [11], or choosing a suitable feature vector. Time complexity is further reduced by choosing radix sort over lexicographical sort. Attempts have been made to combine the key feature-based and block-based techniques for tamper detection [12, 13]. Various features based on moments, dimensionality reduction approaches, intensity, and frequency domain were analyzed for block approaches in [6] which were compared with key-point-based algorithms to evaluate their performance. Different key-point-based methods like scale invariant feature transform (SIFT), speeded up robust feature (SURF), and block-based methods like discrete cosine transform (DCT), principal component analysis (PCA), and discrete wavelet transform (DWT) are shown to perform well. It is further suggested that they can be combined to get better results. SIFT and SURF methods excelled when the copied region undergoes several rotations and scaling operations before pasting. These methods were found to be efficient in terms of time complexity but they lack in accuracy to detect forgery when the copied image is very much self-similar to the background. Block-based methods overcome this problem and perform well for Gaussian noise and Joint Photographic Experts Group (JPEG) compression attacks but are computationally costly and fail to detect forgery for large rotation and scaling.

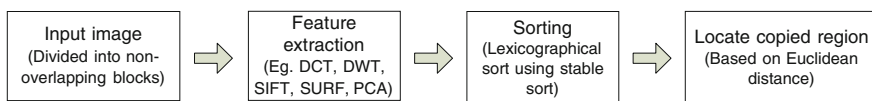


Fig. 1 Basic approach for copy-move forgery detection

Anti-forensics

Together with forensic techniques, anti-forensics or counter forensics techniques have evolved to defeat the detection of fingerprints. Anti-forensics is defined as “the research field that challenges digital forensics and systematically explores its limitations against intelligent counterfeiters” in [14]. The counter forensic techniques are classified as targeted or universal depending on whether the technique removes the traces detectable with either a specific forensic technique or even any unknown technique, respectively. Also these tamper hiding techniques are classified as: integrated if they are used with image tampering operations, and post-processing if the manipulations are hidden later. *Targeted* and *post-processing* counter forensic techniques have been focused on much of the published works. Image compression has been widely explored for anti-forensics [15–19]. Targeting to fool DCT quantization artifacts-based classifier, [16] proposed addition of noise to the DCT coefficients to hide the JPEG compression history of a digital image. JPEG compression introduces two important artifacts. First, DCT coefficients are closer to the multiples of the step size due to quantization which is visible on histogram of the DCT coefficients. Second, pixel value discontinuities occur across block boundaries. Anti-forensic technique to remove artifacts of wavelet-based image compression technique, presented in [17], adds anti-forensic dither to the wavelet coefficients of the compressed image so as to match the coefficient distribution of the uncompressed image. An anti-forensic technique against the blocking artifacts of JPEG compression is proposed in [18]. It uses DCT coefficients histogram and blocking artifact measure to detect if an image under test has undergone JPEG compression. The work proposed in [19] is an extension of what is presented in [16]. It employs smoothing followed by the addition of low-power white Gaussian noise to hide statistical traces of JPEG blocking artifacts without affecting DCT coefficient distribution. To fool the forensic examination, it was proposed to add anti-forensic dither to the DCT coefficients after initial JPEG compression but before the second pass of JPEG compression. This will reflect as if the image has undergone JPEG compression just once. Not only compression has been studied for anti-forensics but median filtering is studied too. Median filtering is characterized by high probability of adjacent pixels being similar. In other words, median filtering is more likely to put the difference between the adjacent pixels to zero. The characteristic traces of median filtering in uncompressed images are hidden by modifying suitable random pixels based on the occurrence of block center gray level and distribution of block median in [20]. Another approach to conceal traces of median filtering has been presented in [21] which use linear convolution filters of size 3×3 to produce another image from the median filtered image such that the fidelity between the median filtered image and that obtained after convolution filtering is maximized. A survey on anti-forensics operation has been presented in [22].

Countering Anti-forensics

The use of anti-forensics by the forgers to hide the tampering has resulted in the study of fingerprints that might be introduced due to their use. Digital image compression has been studied in [16–19] for anti-forensics to be developed to hide the compression history. An attempt to detect anti-forensic operation performed on spliced JPEG image has been made in [23]. The decision to confirm tampering is based on the forensic and counter anti-forensic analysis of the image. The forger is assumed to hide the traces of splicing using two anti-forensic tools for the work and the image is classified as tampered if either of the tools identifies the fingerprints of tampering or anti-forensic operation. JPEG compression is mostly studied to identify the traces of compression. Anti-forensics for JPEG compression is countered by the work in [24] which uses inter- and intra-block correlations. Anti-forensics developed for wavelet-based compression techniques is countered in [25] by analyzing relations between DWT coefficients across different levels. Hough transform is applied to the joint DWT histogram to derive the feature vector using a support vector machine (SVM). A short review of anti-forensics for median filtering is presented in the last section of the paper which is countered by the work presented in [26]. To detect the fingerprints of anti-forensics for median filtering, the difference between adjacent pixels in horizontal direction is determined using which ratio of zero for each row is found. If discrete Fourier transform of these ratio of zero for each row exhibits periodicity, it is expected to confirm that the image has been modified by an anti-forensic method.

Conclusion

Digital image forensic researchers are continuously developing techniques to detect various types of image tampering. Block-based methods are time-consuming as they require comparison of each block of image with every other block to find similarity. This time complexity is reduced either by reducing the image dimension or by reducing the feature dimension by many researchers but the computational time is still an issue to be improved. Not only image forensics but anti-forensics is also developing in parallel as the other side of the same coin because anti-forensics aims at revealing the weakness of forensic technology. Anti-forensic techniques are required to be explored by the forensic researcher community so as to understand which forensic techniques can be deceived, with the aim to reduce the probability of false classification of the anti-forensic processed images as the true images and thereby increasing the reliability of the forensic techniques. Anti-forensics can be used to protect reverse engineering. Also researchers need to study if these techniques themselves leave behind some fingerprints which can be used to detect the use of anti-forensic operations.

References

1. Guojuan, Z., Dianji, L.: An overview of digital watermarking in image forensics. In: IEEE Proceedings of Fourth International Joint Conference on Computational Sciences and Optimization, pp. 332–335 (2011)
2. Mohammad, N., Sun, X., Yang, H.: An adaptive visible watermarking algorithm for BTC compressed images. *Inf. Technol. J.* **13**(3), 536–541 (2014)
3. Qazi, T., Hayat, K., Khan, S.U., Madani, S.A., Khan, I.A., Kołodziej, J., Li, H., Lin, W.Y.K. C., Xu, C.Z.: Survey on blind image forgery detection. *IET Image Process.* **7**(7), 1–11 (2013)
4. Abhitha, E., Karthick, V.J.A.: Forensic technique for detecting tamper in digital image compression. *Int. J. Adv. Res. Comput. Commun. Eng.* **2**(3), 1325–1330 (2013)
5. Swaminathan, A., Wu, M., Liu, K.J.R.: Digital image forensics via intrinsic fingerprints. *IEEE Trans. Inf. Forensics Secur.* **3**(1), 101–117 (2008)
6. Christlein, V., Riess, C., Jordan, J., Riess, C., Angelopoulou, E.: An evaluation of popular copy-move forgery detection approaches. *IEEE Trans. Inf. Forensics Secur.* **7**(6), 1–26 (2012)
7. Bayram, S., Sencar, H.T., Memon, N.: A survey of copy-move forgery detection techniques. In: Proceedings of the IEEE Western New York Image Processing Workshop, pp. 538–542, IEEE (2008)
8. Weiqi, L., Zhenhua, Q., Feng, P., Jiwu, H.: A survey of passive technology for digital image forensics. Review article. *Front. Comput. China* (2007)
9. Lin, H.J., Wang, C.W., Kao, Y.T.: Fast copy-move forgery detection. *WSEAS Trans. Signal Process.* **5**(5), 188–197 (2009)
10. Singh, V.K., Tripathi, R.C.: Fast and efficient region duplication detection in digital images using sub-blocking method. *Int. J. Adv. Sci. Technol.* **35**, 93–102 (2011)
11. Yang, B., Sun, X., Chen, X., Zhang, J., Li, X.: An efficient forensic method for copy-move forgery detection based on DWT-FWHT. *Radioengineering* **22**(4), 1098–1105 (2013)
12. Kaur, A., Sharma, R.: Optimization of copy-move forgery detection technique. *Int. J. Adv. Res. Comput. Sci. Software Eng.* **3**(4), 576–578 (2013)
13. Kaur, A., Sharma, R.: Copy-move forgery detection using DCT and SIFT. *Int. J. Comput. Appl.* **70**(7) (2013)
14. Böhme, R., Kirchner, M.: Counter-forensics: attacking image forensics. In: *Digital Image Forensics*. Springer, New York (2012)
15. Manimurugan, S., Kaimal, A.B.: A tailored anti-forensic technique for digital image applications. *Int. J. Comput. Appl.* **53**(9) (2012)
16. Stamm, M.C., Tjoa, S.K., Lin, W.S., Liu, K.J.R.: Anti-forensics of JPEG compression. In: Proceedings of IEEE conference on ICASSP 2010, pp. 1694–1697 (2010)
17. Stamm, M.C., Liu, K.J.R.: Wavelet-based image compression anti-forensics. In: Proceedings of 2010 IEEE 17th International Conference on Image Processing, Hong Kong, pp. 1737–1740 (2010)
18. Sreelakshmi, M.S., Venkataraman, D.: Image compression using anti-forensics method. *Int. J. Comput. Sci. Eng. Appl.* **3**(1), 81–89 (2013)
19. Stamm, M.C., Tjoa, S.K., Lin, W.S., Liu, K.J.R.: Undetectable image tampering through JPEG compression anti-forensics. In: Proceedings of 2010 IEEE 17th International Conference on Image Processing, Hong Kong, pp. 2109–2112 (2010)
20. Dang-Nguyen, D.T., Gebru, I.D., Conotter, V., Boato, G., De Natale, F.G.B.: Counter-forensics of median filtering. In: IEEE 15th International Workshop on Multimedia Signal Processing (MMSP), pp. 260–265 (2013)
21. Fontani, M., Barni, M.: Hiding traces of median filtering in digital images. In: *EUSIPCO*, pp. 1239–1243 (2012)
22. Pandit, P.D., Rajput, M.: Survey on anti-forensics operations in image forensics. *Int. J. Comput. Sci. Inf. Technol.* **5**(2), 1570–1573 (2014)
23. Fontani, M., Bonchi, A., Piva, A., Barni, M.: Countering anti-forensics by means of data fusion. In: Proceedings of SPIE Electronic Imaging Conference, 2–6 Feb 2014

24. Li, H., Luo, W., Huang, J.: Countering anti-JPEG compression forensics. In: 19th IEEE International Conference on Image Processing (ICIP), pp. 241–244 (2012)
25. Wang, M., Chen, Z., Fan, W., Xiong, Z.: Countering anti-forensics to wavelet-based compression. In: Proceedings of the IEEE International Conference on Image Processing (ICIP), Paris, France, pp. 5382–5386 (2014)
26. Zeng, H., Qin, T., Kang, X., Liu, L.: Countering anti-forensics of median filtering. In: IEEE International Conference on Acoustic, Speech and Signal Processing, pp. 2723–2727 (2014)

Can We Use Mass-Based Similarity Measure in Classification?

Ashish Kumar, Roheet Bhatnagar and Sumit Srivastava

Abstract Similarity measures are very much essential in solving many data mining tasks such as clustering, information retrieval, and classification. A large number of the similarity measures directly or indirectly depend upon distance. Recently developed mass-based similarity measure, Massim, is well established in information retrieval task with algorithm MassIR. This paper will examine the probable uses of mass-based similarity measure in classification tasks.

Keywords Classification · Data mining · Similarity measure

Introduction

Recent developments in information technology have made possible the collection and analysis of millions of transactions consist of private data. These data have criminal records, debit and credit records, shopping habits, and medical histories among others. This progress in the storage and analysis of data has led individuals and organizations to face the challenge of turning such data into useful information and knowledge. Data mining is a promising approach to meet this challenging constraint. Data mining itself comprises different tasks and many data mining tasks engage the comparison of objects and determining with regard to their similarities (or dissimilarities) like nearest neighbor search, clustering, automatic categorization, prediction and classification, characterization and discrimination, and correlation analysis. Among these tasks, classification is the process of finding a model

Ashish Kumar (✉) · Roheet Bhatnagar · Sumit Srivastava
Department of Computer Science & Engineering, Manipal University Jaipur,
Jaipur 303007, India
e-mail: aishshub@gmail.com

Roheet Bhatnagar
e-mail: roheet.bhatnagar@jaipur.manipal.edu

Sumit Srivastava
e-mail: sumit.srivastava@jaipur.manipal.edu

which describes and distinguishes data classes or concepts, with the end goal of having the capacity to use the model to anticipate the class of objects whose class is unknown. There are many techniques to find a classification model such as decision trees, naive Bayesian classification, support vector machines, k-nearest neighbor classification, artificial neural networks, and genetic algorithm. Some of these are directly or indirectly based on similarity measures. To measure the similarity between two instances, lots of similarity measures are established and the majority of them are developed in consonance with their uses or domain in which they are used. Nonmetric dissimilarities or similarities are very general in the domains like information retrieval, bioinformatics, and natural language processing (NLP) [1–3].

The simplest technique for similarity-based classification is the k-nearest neighbor classification technique which is one of determining the similarity between each training instance in the dataset and the test instance and then classifies the test instance as the class of instances to which it is more similar. In reality, nearest neighbor classification models based on similarity measures have been demonstrated to achieve lower error than metric-based k-nearest neighbor classification models [4, 5].

Ting et al. [6] proposed concept of mass-based similarity measure, Massim, can substitute the distance-based similarity measures and has shown its utility in information retrieval through MassIR, a new information retrieval system. In this paper, we will discuss about how we can use Massim in classification and in which classification techniques it can be used.

Rest of the paper is organized as follows: section “[Similarity Measures](#)” will discuss about similarity measures. Section “[Mass-Based Similarity Measure: Massim](#)” will discuss about currently developed mass-based similarity measure, Massim. In section “[Similarity Based Classification](#)”, discussion around the classification techniques that are indirectly or directly based on similarity measures will be done. Last section will discuss about how we can use Massim in classification and in which classification techniques it can be used.

Similarity Measures

After Jaccard suggested a similarity measure to categorize biological species in 1901, various similarity measures have been suggested in various fields over a hundred years. Similarity measures alias similarity functions is real-valued function which measures similarity between two objects or instances. This value should be higher if the instances are more identical to each other. The use of a similarity measure depends upon available measures of instances. In data mining tasks such as clustering and classification, distance-based similarity measures are frequently used as a critical role player. All the existing distance-based similarity measures are binary functions and they fulfill all four distance axioms (reflexivity, nonnegativity, symmetry, triangle inequality). On the other hand, Skopal and Bustos [7] have been

challenged the triangle inequality axiom by proposing nonmetric similarity measures. A brief and critical survey of 76 binary similarity and distances measures has been done by Choi et al. [8].

Mass-Based Similarity Measure: Massim

Massim is essentially different from every one of the similarity measures because it depends on the concept of mass, which is cardinality of the data cloud, rather than distance. The concept of mass and mass estimation is introduced by Ting et al. [9]. Ting et al. [10] discussed mass estimation in more detail. It can be used as a substitute of density estimation to work out various data mining tasks. Mass is a unary function but Massim is a binary function to determine similarity between two instances. Table 1 issues you a thought regarding mass-based and distance-based similarity measures. Massim not satisfy all four distance axioms, as given in Table 2 that is quite different from distance-based similarity measure which satisfies all the four axioms. It also gives us guarantee that two similar instances must be in same local neighborhood [6]. It is principally based on data distribution in local region and does not calculate distance, which is core calculation of distance-based similarity measures.

Table 1 Mass-based similarity measure versus distance-based similarity measure [6]

	Mass-based similarity measure	Distance-based similarity measure
Computation	Mass(x, y) is primarily based on data distribution in the local region of the feature space	dist(x, y) is solely based on the positions of x and y in the feature space
Definition	Mass based function M(x, y) measures the cardinality of the smallest local region covering both x and y	dist(x, y) measures the length of the shortest path from x to y
Inequality	similarity(x, y) > similarity(x, z) \equiv Mass(x, y) < Mass(x, z)	similarity(x, y) > similarity(x, z) \equiv dist(x, y) < dist(x, z)
Metric	The measure does not satisfy some distance axiom	All distance axioms usually hold

Table 2 Axioms used for Mass-based similarity and distance-based similarity [6]

	Mass-based similarity	Distance-based similarity	
Axiom 1	Mass(x, y) \geq 1	dist(x, y) \geq 0	(Nonnegativity)
Axiom 2	i. $\forall x, y$ Mass(x, x) \leq Mass(x, y) ii. $\exists x \neq y$ Mass(x, x) \neq Mass(y, y)	dist(x, y) = 0 \Leftrightarrow x = y	(Identity of indiscernibles)
Axiom 3	Mass(x, y) = Mass(y, x)	dist(x, y) = dist(y, x)	(Symmetry)
Axiom 4	Mass(x, z) < Mass(x, y) + Mass(y, z)	dist(x, z) \leq dist(x, y) + dist(y, z)	(Triangle inequality)

Similarity-Based Classification

Similarity-based classification is a technique in which a test instance is classified based on the pairwise similarities among the test instance and a set of class-labeled training instances. This term, similarity-based classification, is also referred as same when the pairwise connection between test instance and training instances is either dissimilarity or similarity. There is no requirement of any explicit portrayal of the features of training instances for this approach. The heart and soul of any similarity-based classification approach is the similarity measure used to estimate pairwise similarity among test instance and training instances. A brief review of similarity measures applicable to the task of classification is done by Santini and Jain [11]. The approaches used in this technique are multidimensional scaling (MDS), similarities as kernels in support vector machine (SVM), use of similarities to training instances as features, k-nearest neighbor (k-NN), similarity discriminant analysis (SDA) (see Fig. 1).

Multidimensional Scaling (MDS)

Multidimensional scaling (MDS) is a technique used to visualize the (dis)similarities. The main outcome of an MDS is a dimensional arrangement, in which instances are pictured as points. These points in this arrangement are organized like their distances that correspond to the similarities of the instances: Similar instances are pictured by the points which are near to each other and dissimilar instances by the points which are far away from each other. The application of MDS is not only restricted to psychology but it is in a broad area of practices, like archeology, biology, chemistry, economics, sociology, and pattern reorganization. It is utilized as a technique for analyzing the data. Borg and Groenen [12] have written a comprehensive textbook on multidimensional scaling.

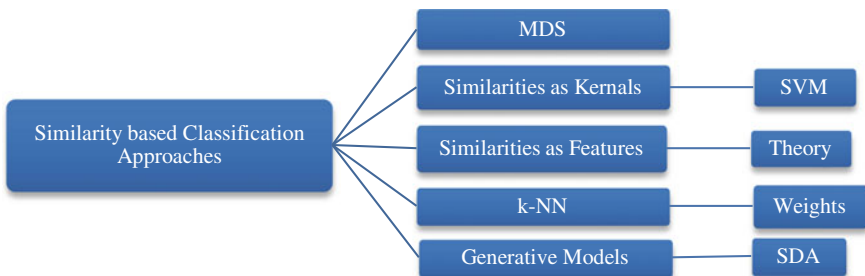


Fig. 1 Similarity-based classification approaches

Similarities as Kernels

Even though in mathematical meaning, kernel is inner product in any Hilbert space, in regular explanation kernel is a similarity measure between different instances [13]. That is the reason numerous researchers have been utilized similarities measure as kernel and practised the classifiers that trust on inner products. A comprehensive analysis was done by Wu et al. [14] about the transformation of similarity measures into kernels. Some of the methods for this task are spectrum clip, spectrum flip, spectrum shift, and spectrum square. As we all know that the support vector machines (SVM) are well-known representative of kernel-based classification techniques, so they can be a better choice for similarity-based classification if the similarity measure is symmetric and positive definite or conditionally positive definite as characterized by Schölkopf [15]. A potential support vector machine (PSVM) was developed which can be utilized with several similarity measures [3, 16].

Similarities as Features

Similarity-based classification can be transformed into Euclidean-based classification by considering similarity measure between test instance and training instances as features. Pelaska et al. [2] considered different generative classification techniques for this approach and proposed Fisher linear discriminant classifier and Duin et al. [17] proposed quadratic discriminant classifier for the same. Using this approach, Graepel et al. [18] and Graepel et al. [19] put forward a “Separating Hyperplane Classification Model” by implementing a linear SVM over similarity features. Liao and Noble [20] also implemented an SVM over similarity features using Gaussian radial basis function kernel. A problem with using similarity measures as features is that the number of features will increase as the number of training instances will increase and it will cause Bellman’s curse of dimensionality for the classifier [21]. Pelaska et al. [2] has suggested some solution to this problem.

k-Nearest Neighbor

The majority of the research works on learning for nearest neighbor classification is based on dissimilarities (distance) measure [22–24]. But several experimental works have shown that the use of similarity measure can be preferred over the distance measure in nontextual datasets like Balance, Wine, and Iris [25]. Also in practical circumstances like text classification, similarities (e.g., cosine similarity) can be favored over dissimilarities (distances, e.g., Euclidean distance). Researchers have been also shown that nearest neighbor classification can give better

performance on similarity-based classification problems [4, 5]. Many researchers have deliberated approaches to condense nearest neighbors for similarity-based classification to reduce required memory and enhance classification speed for achieving better performance [1, 26, 27]. Chen et al. [13] have discussed some of the design goals like affinity and diversity and proposed two different approaches termed as kernel ridge interpolation and kernel ridge regression for similarity-based weighted nearest neighbors.

Generative Classification Model

Generative classification model provide either joint probability or likelihood as probabilistic outcomes and utilized Bayes' rule to proffer final prediction [21]. One approach to utilize similarity measures in generative classification model is same as utilizing similarity measures as features to portray an n-dimensional feature vector, and then applying typical generative models [2]. Another technique termed as similarity discriminant analysis (SDA) simulates class conditional distribution of similarity statistics based on maximum entropy architecture [28]. Chen et al. [13] has proposed a mixture SDA model to remove the bias problem of basic SDA model.

Discussion

As discussed in section “[Similarities as Kernels](#)”, there are two fundamental conditions for a similarity measure to be used as a kernel in SVM. The first condition is, it ought to be symmetric and the second one is, either positive definite or conditionally positive definite. Massim already assures symmetry (see Table 2). But it also needs to be positive definite and with the help of spectrum shift technique suggested by Wu et al. [14], we can do so. After this, we can use Massim as kernel in any typical SVM.

One approach suggested by Pekalska et al. [2] to solve the Bellman's curse of dimensionality is to use simply a subset of training instances to determine feature vector. Massim already uses subset of dataset to produce similarity forest (sForest), define as the collection of balanced tree, and is a nonmetric so it does not require dimension reduction [6]. That is the reason it can be utilized as features.

As similarity measures are directly used in k-nearest neighbor classifiers. So, with little modification, Massim can easily be used in k-nearest neighbor classification. Massim-based classifier using k-NN classification technique has been already proposed in its implementation phase. After this, the evaluation of the proposed classifier will be done with state-of-the-art classifiers on well-defined classification problems and datasets.

References

1. Jacobs, D.W., Weinshall, D., Gdalyahu, Y.: Classification with non-metric distances: image retrieval and class representation. *IEEE Trans. Pattern Anal. Mach. Intell.* **22**(6), 583–600 (2000)
2. Pekalska, E., Pačič, P., Duin, R.P.W.: A generalized kernel approach to dissimilarity-based classification. *J. Mach. Learn. Res.* **2**, 175–211 (2001)
3. Hochreiter, S., Obermayer, K.: Support vector machines for dyadic data. *Neural Comput.* **18**(6), 1472–1510 (2006)
4. Simard, P., Cun, Y.L., Denker, J.: Efficient pattern recognition using a new transformation distance. *Adv. Neural Inf. Process. Syst.* **5**, 50–68 (1993)
5. Belongie, S., Malik, J., Puzicha, J.: Shape matching and object recognition using shape contexts. *IEEE Trans. Pattern Anal. Mach. Intell.* **24**(4), 509–522 (2002)
6. Ting, K.M., Fernando, T.L., Webb, G.I.: Mass-Based Similarity Measure: An Effective Alternative to Distance-Based Similarity Measures, Technical report 2013/276, Calyton School of IT, Monash University, Australia (2013)
7. Skopal, T., Bustos, B.: On nonmetric similarity search problems in complex domains. *ACM Comput. Surv. (CSUR)* **43**(4), 34 (2011)
8. Choi, S.S., Cha, S.H., Tappert, C.C.: A survey of binary similarity and distance measures. *J. Syst. Cybern. Inf.* **8**(1) (2010)
9. Ting, K.M., Zhou, G.T., Liu, F.T., Tan, J.S.C.: Mass estimation and its applications. In: *Proceedings of the 16th ACM SIGKDD International Conference on Knowledge Discovery and Data Mining*, ACM, pp. 989–998 (2010)
10. Ting, K.M., Zhou, G.T., Liu, F.T., Tan, S.C.: Mass estimation. *Mach. Learn.* **90**(1), 127–160 (2013)
11. Santini, S., Jain, R.: Similarity measures. *IEEE Trans. Pattern Anal. Mach. Intell.* **21**(9), 871–883 (1999)
12. Brog, I., Gronen, P.J.F.: *Modern Multidimensional Scaling: Theory and Applications*, 2nd edn. Springer, New York (2005)
13. Chen, Y., Garcia, E.K., Gupta, M.R., Rahimi, A., Caazzanti, L.: Similarity-based classification: concepts and algorithms. *J. Mach. Learn. Res.* **10**, 747–776 (2009)
14. Wu, G., Chang, E.Y., Zhang, Z.: An Analysis of Transformation on Non-Positive Semi Definite Similarity Matrix for Kernel Machines. Technical report, University of California, Santa Barbara, March 2005
15. Schölkopf, B.: The kernel trick for distances. In: *Advances in Neural Information Processing Systems*, vol. 13 (2001)
16. Hochreiter, S., Mozer, M.C., Obermayer, K.: Coulomb classifiers: generalizing support vector machines via an analogy to electrostatic systems. In: *Advances in Neural Information Processing Systems*, vol. 15, pp. 545–552 (2003)
17. Duin, R.P.W., Pekalska, E., de Ridder, D.: Relational discriminant analysis. *Pattern Recogn. Lett.* **20**, 1175–1181 (1999)
18. Graepel, T., Herbrich, R., Bollmann-Sdorra, P., Obermayer, K.: Classification on pairwise proximity data. In: *Advances in Neural Information Processing Systems*, pp. 438–444 (1998)
19. Graepel, T., Herbrich, R., Schölkopf, B., Smola, A., Bartlett, P., Müller, K.-R., Obermayer, K., Williamson, R.: Classification on proximity data with LP-machines. In: *Proceedings of the International Conference on Artificial Neural Networks* (1999)
20. Liao, L., Noble, W.S.: Combining pairwise sequence similarity and support vector machines for detecting remote protein evolutionary and structural relationships. *J. Comput. Biol.* **10**(6), 857–868 (2003)
21. Hastie, T., Tibshirani, R., Friedman, J.: *The Elements of Statistical Learning*. Springer, New York (2001)
22. Weinberger, K.Q., Saul, L.K.: Distance metric learning for large margin nearest neighbor classification. *J. Mach. Learn. Res.* **10**, 207–244 (2009)

23. Shalev-Shwartz, S., Singer, Y., Ng, A.Y.: Online and batch learning of pseudo-metrics. In: Proceedings of the Twenty-first International Conference on Machine learning, ACM, p. 94 (2004)
24. Baoli, L., Qin, L., Shiwen, Y.: An adaptive k-nearest neighbor text categorization strategy. *ACM Trans. Asian Lang. Inf. Process. (TALIP)* **3**(4), 215–226 (2004)
25. Qamar, A.M., Gaussier, E., Chevallet, J.P., Lim, J.H.: Similarity learning for nearest neighbor classification. In: Eighth IEEE International Conference on Data Mining, ICDM'08, pp. 983–988. IEEE (2008)
26. Pekalska, E., Duin, R.P.W., Paclík, P.: Prototype selection for dissimilarity based classifiers. *Pattern Recogn. Lett.* **39**, 189–208 (2006)
27. Lozano, M., Sotoca, J.M., Sánchez, J.S., Pla, F., Pekalska, E., Duin, R.P.W.: Experimental study on prototype optimisation algorithms for prototype based classification in vector spaces. *Pattern Recogn.* **39**, 1827–1838 (2006)
28. Cazzanti, L., Gupta, M.R., Koppal, A.J.: Generative models for similarity-based classification. *Pattern Recogn.* **41**(7), 2289–2297 (2008)

CNT-Based Biomedical Sensor for Cancer Detection

Argha Sarkar, B. Madhuri, Shivam Kumar and Santanu Maity

Abstract This paper proposes on simulation and characterization of sensing layer for biosensor application. Prostate cancer becomes critical for human being, when it is not detected at an early stage. So biosensor can play a vital role to detect initially. New generation sensor includes carbon nanotube (CNT). It could be better solution for sensing. This paper details biosensor and this aspect single-wall carbon nanotube with 20 Å is analyzed. And the functionalization, surface immobilization, as well as strict monitoring of physical and chemical features of single-wall carbon nanotube are described. These are necessary successful implementation for biomedical sensor. The chirality control, band gap control (semiconducting and metallic) properties along with some unique characteristics are also described with the help of Ninithi software.

Keywords Chirality · SWCNT (Single-wall carbon nanotube) · PSA (Prostate specific antigen) · PCa (Prostate cancer)

Introduction

Cancer detection is very important because it becomes worsened if it is not diagnosed at earlier stage. Carbon nanotube for electromechanical biosensor would be a fruitful solution with reliability for cancer detection. Sensing of prostate cancer detection using nanoelectric sensor is done by a field effect transistor where single-walled carbon nanotube will act as a semiconducting channel [1]. Some ideal

Argha Sarkar
Computer Science and Engineering, National Institute of Technology,
Arunachal Pradesh 791112, India
e-mail: argha15@gmail.com

B. Madhuri · Shivam Kumar · Santanu Maity (✉)
Electronics and Communication Engineering, National Institute of Technology,
Arunachal Pradesh 791112, India
e-mail: santanu.ece@nitap.in

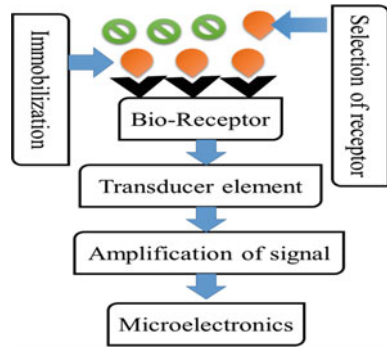
structures of carbon nanotube depending upon chiral value shows some unique properties like chemical and electrical properties and has caught the attention of researchers to go for carbon nanotube for the design purpose of highly sensitive biosensor [2]. When the wall of carbon nanotube absorbs specific biomolecules, then it is conductance that changes rapidly. Since carbon nanotube has a great level of adsorptive capacity, large surface-to-area ratio, and fast response time, it is used as a good sensing element. Thus the electrical properties like conductance capacitance changes [3] significantly for ionic cells. And also other effective feature of carbon nanotube is the low power consumption while operating as a transistor which is near about 10 nW [4]. So the carbon nanotube is optimized and the specialty of single-wall carbon nanotube is realized for the sensing channel as well as the transducer element. The schematic block diagram and the model of biosensor are designed for future implementation.

Prostate Cancer and Biosensor

BRICS are the developing countries and India is one of them. As the country is developing, the life style, food habits are also changing. As a result, noncommunicable diseases like cardiovascular problem, diabetes as well as cancer are on rise. Prostate cancer (PCa) is the second most cancer from the variety of causes and sixth leading cause of cancer death in man globally [5]. Previously, it was believed that mainly western countries suffer from prostate cancer but the scenario is totally changed. The recent population-based cancer registries (PBCR) of different cities in India during 2008–2011 estimated that leading sites of cancer includes Bangalore, Barshi, Bhopal, Chennai, Delhi, Mumbai, Kamrup, Ahmedabad, Kolkata, Nagpur, Thiruvananthapuram [6]. Prostate cancer is mostly seen in the elderly men mostly around 65 years of age. Industrialization is increasing significantly during the recent decades of twentieth century.

Practice of PSA is the main reason to increase the prostate cancer. The carcinogen develops in the prostate gland and if it is not detected at the right time, then definitely it causes death. PSA is an enzyme that is in the blood. PSA is formed in the duct of prostate gland in the male reproductive system. According to the PSA concentration in the serum normal (0–4 ng/ml), critical stage is determined [7]. So, sensor should be implemented for PSA detection. The ultrasensitive carbon nanotube-based field effect transistor biosensor is suitable to detect and differentiate various forms of isoforms [8]. Biosensor is a bioanalytical device having two basic elements, bioreceptor and transducer. The bioreceptor recognizes the target analyte. This is basically the reaction with the presence of cell or molecule present in an analyte (shown in Fig. 1). And the transducer converts the biological changes into a measurable signal. The sensor for prostate cancer detection should differentiate the target analyte and the similar molecule rapidly as well as must have great level of selectivity and specificity for real-time environment.

Fig. 1 Schematic block diagram of biosensor

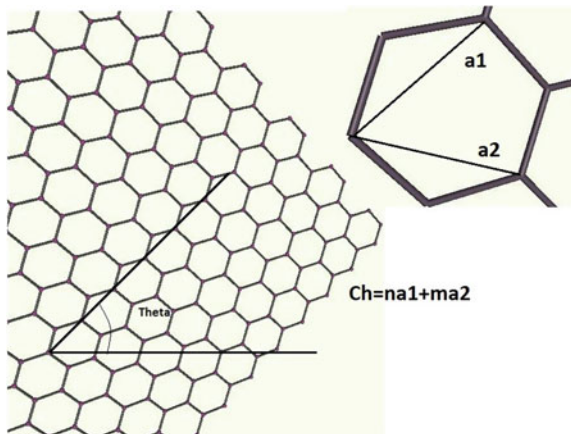


Characterization and Simulation Carbon Nanotube

NANO HUB is a novel resource for nanotechnology-related simulation. FETTOY, MONTECARLO are very useful spice solutions. These are the distributed computing. These are run in real time. Ninithi from nanohub is open source software which overcomes the problems of the distributed computing. This is a good tool to visualize and analyze widely used carbon allotropes in nanotechnology, graphene, carbon nanoribbons, fullerenes, and carbon nanotube. 3D views of molecular configuration and the corresponding graphs show electrical properties [9]. Carbon nanotube is basically carbon in a tubular form having diameter as small as 1 nm and it is configured by rolling a grapheme sheet into a tube. It is characterized by chirality and chirality may be defined by chiral indices (n, m) . Figure 2 shows the chiral vector and chiral angle on the graphene sheet.

$$C_h = n\bar{a}_1 + m\bar{a}_2 \tag{1}$$

Fig. 2 Graphene sheet with basic vector of hexagonal lattice



where, \bar{a}_1, \bar{a}_2 are the 2D grapheme lattice vectors. The indices can be managed with respect to d_t and θ , where d_t implies the diameter of the nanotube and θ is the chiral angle and it is basically the angle with respect to zigzag axis [10].

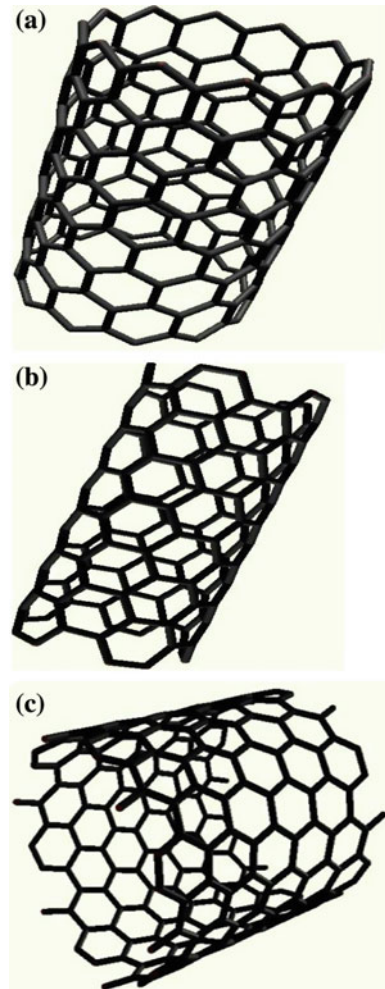
Mathematically,

$$d_t \approx (a/\pi)\sqrt{(n^2 + m^2 + nm)} \quad (2)$$

and

$$\theta = \tan^{-1} \sqrt{3}m/(2n + m) \quad (3)$$

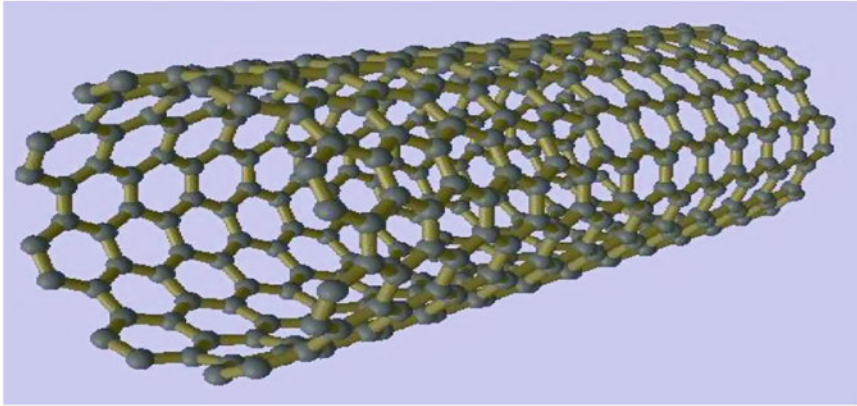
Fig. 3 Different structure from different chiral vector
a Zigzag (0, 12) **b** Armchair (5, 5) **c** Chiral (12, 6)



Based on the chiral angle and chiral indices zigzag ($\theta = 0; m = 0$), arm chair ($\theta = \pi/6; n = m$), and chiral ($0 < \theta < \pi/6; n \neq m \neq 0$) are simulated. Here in Fig. 3, outer end of the tubes shows the different structural configuration like zigzag, arm chair, etc.

CNT can be modeled based on chiral indices (m, n) and depending upon indices it shows metallic or semiconducting behaviors. The CNT is metallic and

(a)



(b) Energy(eV)

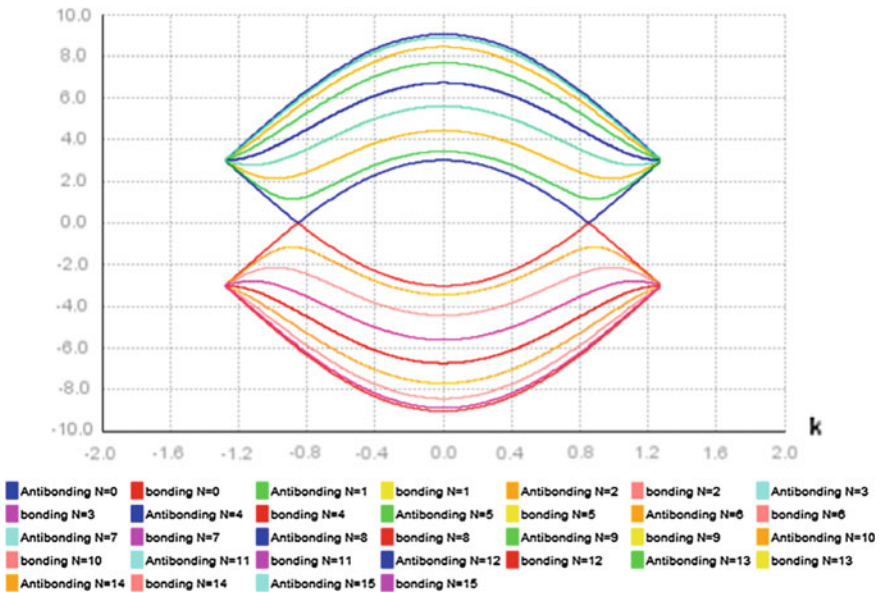


Fig. 4 a CNT (8,8), length 20 Å, C-C bond length 1.42 Å, C-C transfer energy 3.013 eV, b E-K diagram

semiconducting in nature [5] if the difference between chiral indices is zero or a multiple of three. Electronic band gap of single-wall CNT is, $E_g \approx (2a^-)/(\sqrt{3}d_t)$ eV [11], where hopping tight-binding parameter for pi orbital to ≈ 2.6 eV. In the simulated Fig. 4 the difference between m and n is zero and has small band gap, $E_g \approx 14/d_t^2$ MeV [12], is not an ideal metallic, it is basically small band gap semiconducting single-wall CNT. CNT (8, 8) is shown in Fig. 4.

The E-K diagram provides the necessary relation between energy–wave momentum for carriers and band structure. Figure 5 shows the single-wall carbon

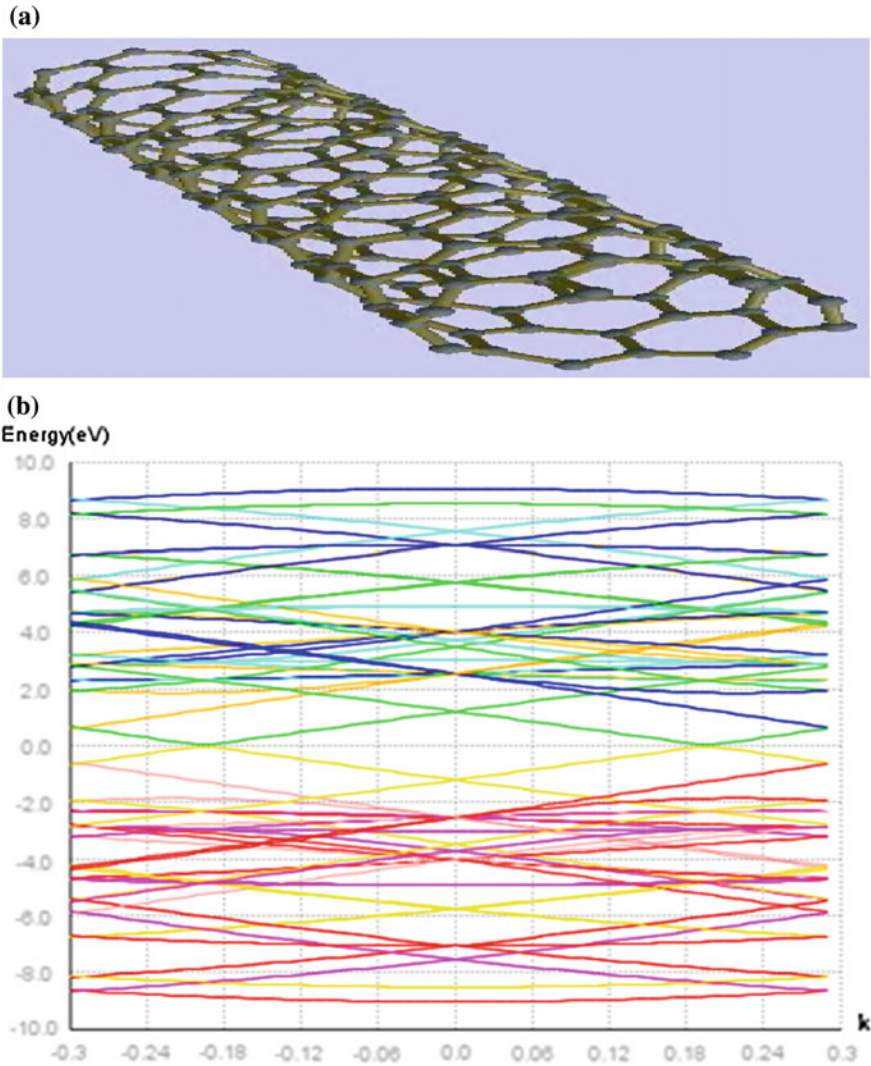


Fig. 5 Single-wall CNT (7, 1) and corresponding E-K diagram

nanotube with chiral indices (7, 1) and having length 20 Å, the bond length 1.42 Å, C-C transfer energy 3.013 eV.

Figure 5 shows E-K diagram of semiconducting CNT. A phase factor to the electron wave function in the direction of circumference is produced due to magnetic field. Result is that magnetic field changes the electronic properties of CNT. The electrical conductivity of CNT is almost six times higher and for that the CNT is highly acceptable in sensing application [11].

Single-Wall Carbon Nanotube Field Effect Transistor

Single-walled carbon nanotubes (SWCNT) are highly acceptable for sensing application because of its cylindrical shape where C atom is exposed to its neighborhood [13]. Carbon nanotube field effect transistor provides good solution for miniaturization [14].

The simulated SWCNT will be effectively used as the semiconducting channel in a transistor configuration [15] and interacts with specific analytes and charge transfer occurs in analytes to CNT or analytes can create scattering potential across CNTs. Change of potential or conductance is sensed and it produces the output of prostate cancer detection. Figure 6 drawn on Microsoft word shows the proposed functional setup. Linker 1pyrene butanoic acid succinimidyl ester and spacer 1 pyrene butanol are very efficient to keep desired linker-to-spacer ratio on single-wall carbon nanotube, so that conductance could be highly increased [16].

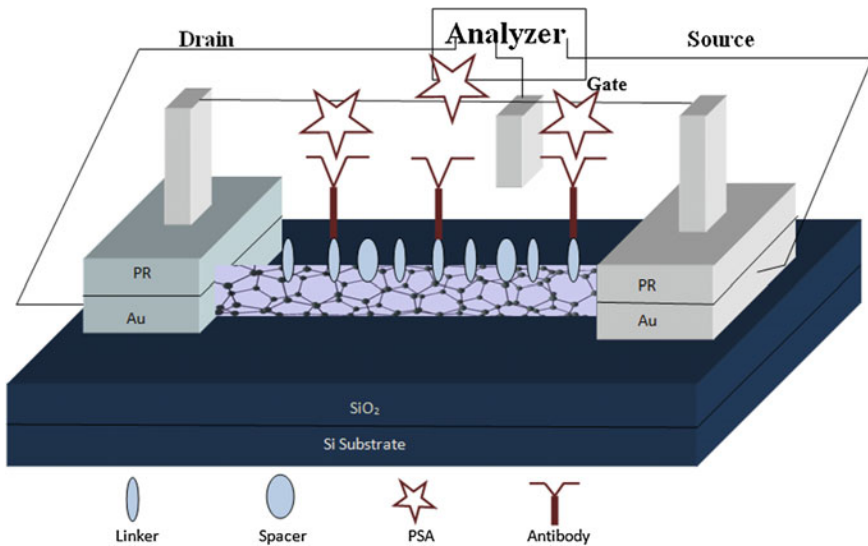


Fig. 6 Model of proposed CNT-based field effect transistor

Conclusion

The structural differences between zigzag, armchair, and chiral carbon nanotube are depicted and the properties of SWCNTs have been analyzed with the help of Ninithi software. The semiconducting and metallic properties are also realized from the electrical properties and energy band diagram. The simulated SWCNT (7, 1) is excellent for sensing application and it could be implemented in the sensor devices. CNT-based sensor model for prostate cancer detection is proposed for future work of fabrication.

References

1. Chgen, R., Choi, H., Bangsaruntip, S., Yenilmez, E., Tang, X., Wang, Q., Chang, Y., Dai, H.: An investigation of the mechanisms of electronic sensing of protein adsorption on carbon anotube devices. *J. Am. Chem. Soc.* **126**, 1563–1568 (2004)
2. Li, J., Meyyappan, M.: Biomolecular sensing for cancer diagnostics using carbon nanotubes. In: *BioMEMS and Biomedical Nanotechnology*, vol. 1, pp. 1–19 (2006)
3. Thai, T.T., Yang, L., DeJean, G.R., Tentzeris, M.M.: Nanotechnology enable wireless gas sensing. *IEEE Microw. Mag.* **12**, 84–95 (2011)
4. Roman, C., Helbling, T., Hierold, C.: Single-walled carbon nanotube sensor concepts. In: *MEMS/NEMS and BioMEMS/NEMS*, part B, pp. 403–425 (2010)
5. Lalitha, K., Suman, G., Pruthvish, S., Mathew, A., Murthy, N.S.: Estimation of time trends of incidence of prostate cancer—an Indian Scenario. *Asian Pac. J. Cancer Prev.* **13**, 6245–6250 (2012)
6. Jain, S., Saxena, S., Kumar, A.: Epidemiology of prostate cancer in India. *Meta Gene* **2**, 596–605 (2014)
7. Stenman, U.H, Leinomen, J., Zhang, W.-H., Finne, P.: Fabrication of silicon nanowire devices for ultrasensitive, label free, real time detection of biological and chemical species. In: *Seminars in Cancer Biology*, vol. 9, pp. 83–93 (1999)
8. Shobha, B.N., Muniraj, N.J.R.: Design, modelling and performance analysis of carbon nanotube with DNA strands as biosensor for prostate cancer. *Microsoft Technol.* (2014). doi:10.1007/s00542-014-2281-x
9. Rupasinghe, C.S., Raskin, M.: “ninithi”. <https://nanohub.org/resources/8987> (2010)
10. Li, S., Yu, Z., Rutherglen, C., Burke, P.J.: Electrical properties of 0.4 cm long single-walled carbon nanotubes. *Nano Lett.* **4**, 2003–2007 (2004)
11. White, C.T., Mintmire, J.W.: Density of states reflects diameter in nanotubes. *Nature* **394**, 29–30 (1998)
12. Kleiner, A., Eggert, S.: Curvature, hybridization, and STM images of carbon nanotubes. *Phys. Rev. B* **64**, 113402–1–113402–4 (2001)
13. Acosta, N.G., (Electrical Engineering, Temple University), Advisor, Dr. Johnson, A.T.: Nanoelectronic sensor for detection of prostate cancer biomarkers. In: *Sunfest Summer Undergraduate Fellowship in Sensor Technologies*
14. Sedra, A.S., Smith, K.C.: *Microelectronic Circuits*, 5th edn. Oxford University Press, New York (2004)
15. Star, A., Gabriel, J.C.P., Bradley, K., Gruner, G.: Electronic detection of specific protein binding using nanotube FET devices. *Nano Lett.* **3**(4), 459–463 (2003)
16. Choi, Y.-E., Kwak, J., Park, J.W.: Nanotechnology for early cancer detection. *Sensors* **10**(1), 428–455 (2010). doi:10.3390/s100100428

Effective Role of Thrashing in Load Balancing During VM Live Migration

Pradeep Kumar Tiwari and Sandeep Joshi

Abstract Virtualization is an important component of cloud computing. Researchers are paying attention in the field of virtualization for last many years. Researchers are taking much attention in load balance for proper resource migration (e.g., computing, storage and networking) and they proposed static, dynamic, linear, and heuristic algorithms in different ways with concept of time and energy efficiency. Proposed paper focused on thrashing mechanism to manage the resources during live migration in different virtual machines (VMs). This paper presents the different aspects of effective resource management mechanism.

Keywords Virtual machine · Load balance · Thrashing · Migration

Introduction

There are many reasons to go for virtualization but the most common reasons are resource sharing, isolation, aggregation, and management. Virtualization introduces extra layer in cloud computing infrastructure. Live migration with load management, multitenancy, and multitasking features are managed by extra layer. Virtualization can convert single physical server into multiple isolate virtual machines and same is possible with operating systems (OS). Multiple OS can reside in single physical machine without inferring each other [1]. Each VM have own memory space, applications, and operating system separately and it can reside over particular physical server.

Many IT players (e.g., Amazon, Microsoft, IBM, HP, and Google) provide features of hypervisor or virtual machine monitor (VMM). Hypervisor gives abstraction mechanism in multitenancy situations while utilizing the heterogeneous

P.K. Tiwari (✉) · Sandeep Joshi
Department of Computer Science & Engineering, Manipal University, Jaipur 303007, India
e-mail: pradeeptiwari.mca@gmail.com

Sandeep Joshi
e-mail: sandeep.joshi@jaipur.manipal.edu

OS and applications aloof VMs and these VMs can dwell with the same physical machine. Single hypervisor can oversee desktop virtualization, physical machine virtualization, and administration of resource component (e.g., Application, OS, and memory) in multitenant environment [2]. Management of resources among different users in different VMs is not easy-going task. Researchers have common goal to how to utilize computing resources (e.g., storage and network resource) within effective time. Load management is highly bonded to handle the VMs with respect to allocation of CPU and memory and it also manages by different load balancing algorithms [3].

The load balance algorithm is based on four components (a) Selection—How to choose VM for transfer load? (b) Transfer—How to shift the load? (c) Location—Find both highly and underloaded VM for transfer load? (d) Information—Collect all VM information and manage the sending and receiving policy during load transfer. Proper use of these components produces intelligent load identification policy and effective load balance algorithm. Researchers allude two types of methodologies: First one combines the upper thrash hold and lower thrash hold values and store in host machine, another is estimating host machine thrash hold work load to predict subsequent work load [4]. Researchers also approach static consolidation for load management but it is effective when thrash value and available resources are previously recognized. During frequently changing environment, resource requirements may be different but fixed load does not be constant for all time, so dynamic or heuristic approaches are best [4, 5]. Paper proposed thrash hold policy during frequently changing environments. This approach presents thrashing mechanism be a good approach to load distribution over frequently changing environment.

In section “[Live Migration of Virtual Machines](#)”, we discuss the live migration of VMs. In section “[Requirements of an Effective Thrashing Algorithm](#)”, we present the flow chart and algorithm for management of load. In section “[Challenges in Resource Mangement](#)”, challenges in resource management are discussed and in section “[Conclusion](#)”, we conclude the paper work.

Live Migration of Virtual Machines

Live VMs migration system have control over all running VMs and migrate load from one VM to another VM during live running environment without any breach in services with best response time. VMs which are hosted in physical server must have the ability to respond to users’ request and time of load balance is very short and effective. Migration of CPU states and input–output devices are simple but their migration in frequently changing environment with high load possibly will be time intensive and difficult to manage [6].

Management of live migration technique must follow these two polices: (a) Energy efficient migration technique and (b) Load balanced with fault tolerance technique.

(a) Energy efficient migration technique

Servers usually consume 70 % of total access energy. Live migration technique must follow the energy efficient mechanism. If VMs load in ideal situation and no need to use other VMs, at this situation remaining VMs should go in sleep (energy saving) mode [8].

(b) Load balance with fault tolerance technique

VMs loads should be scalable and monitored during load transfer and when resources are being utilized. VMs must be able to take loads of crashed VMs or not working VMs. Fault tolerance should give assurance to clients, if any machine or system will be crashed than it must handle client's jobs in consonance with SLA. Fault tolerance enhances productivity of VMs and makes an effective, robust mechanism during crashes of VMs [7, 8].

Requirements of an Effective Thrashing Algorithm

Improvement of load balance mechanism should follow these objectives:

(a) Scalability

Make an effective mechanism to large number of VMs and also capable to scale load of all VMs with respect to average thrash hold value (Atv) and map with respect to high thrash hold value (Htv). $Htv > Atv$ and under thrash value $Utv < Atv$.

(b) Location transparency

In live migration VMs locations should be hidden from cloud users and also hide the queue length and memory status and check the high load Htv and Utv and transfer load with respect to this condition [$ok = Utv < Atv < Uthv$].

(c) Determination

Load of all VMs should be specifying after load transfer from Htv to Utv and also have record of current thrash value (Tv) with respect to Atv. It should determine VMs, Tv value after every load balance and specify a specific ID of VMs.

(c) Preemption

VMs must be equally load balanced. If any VM is crashed then it should be removed from list and load of this particular machine should be transferred to other VM without disturbance to services. It should be also able to supervise risk and recovery management with proper policy. Resources ought to be available in every disaster circumstances.

(e) Heterogeneity

VM migration system must be able to work in heterogeneous environments. It must manage heterogeneous architecture machine, heterogeneous operating systems (OS), and heterogeneous applications in single physical machine with many VMs.

Algorithm Discription

Transfer of load in trash hold policy depends on VM queue length. Transfer policy is triggered when new resource requirements arrived. Actual load capacity of VMs be as equal to average thrash value.

VM queue length (Atv) == Null.

If VM has lower average load the lower average load (Ltv) < Atv. And if VM has high load (Htv) > Atv.

Underloaded VM can take load of overload VM but it should satisfy [ok = Ltv < Atv < Utv].

If condition is satisfied then transfer the load. When VM have high load then Htv shows [Htv = = 1].

After the load transfer it shows the value zero. Underloaded VM shows the value [Utv = = 0].

Value of [Htv = = 1] VM is overloaded and value [Utv = = 0] shows VM is underloaded.

After transfer the load value should be changed in respect of Atv. If VM is Htv = = 1 then select the Htv VM for transfer load.

Host machine find Utv = = 0 and select Utv machine to transfer load.

Check the condition [ok = Utv < Atv < Htv]

Transfer the load Htv to Utv and check the condition Htv <=Atv change the ID and value of Htv

After the load balance also change ID and value of Utv and check Utv <= Atv.

Thrash hold value = Tv

Average thrash hold value = Atv Under thrash hold value = Utv High Thrash hold value = Htv

Suppose every VM queue length = 1, Then Atv = 1, with respect to Atv = 1, Utv < Atv, and Htv > Atv. Utv <=0 and Htv >=2

1. Coming load should go on VM queue = Tv.
2. Check load if Htv then find Utv
3. Select Htv to transfer load and also select Utv to accept load
4. Check the condition [ok = Utv < Atv < Htv.
5. Transfer the load Htv to Utv.

If Htv <=Atv

Then exit go to Step 6

else if Htv > = Atv and current Utv < Atv goto Step 5

else

goto Step 3

6. Change Htv and Utv, value of Tv

7. Remove ID from list if Htv <= Atv and Utv <=Atv

8. Update all ID when load balance is done.

Load balance work should be managed by host machine. It should have all information of VMs and separately stored thrash hold valves of Htv, Atv, and Utv

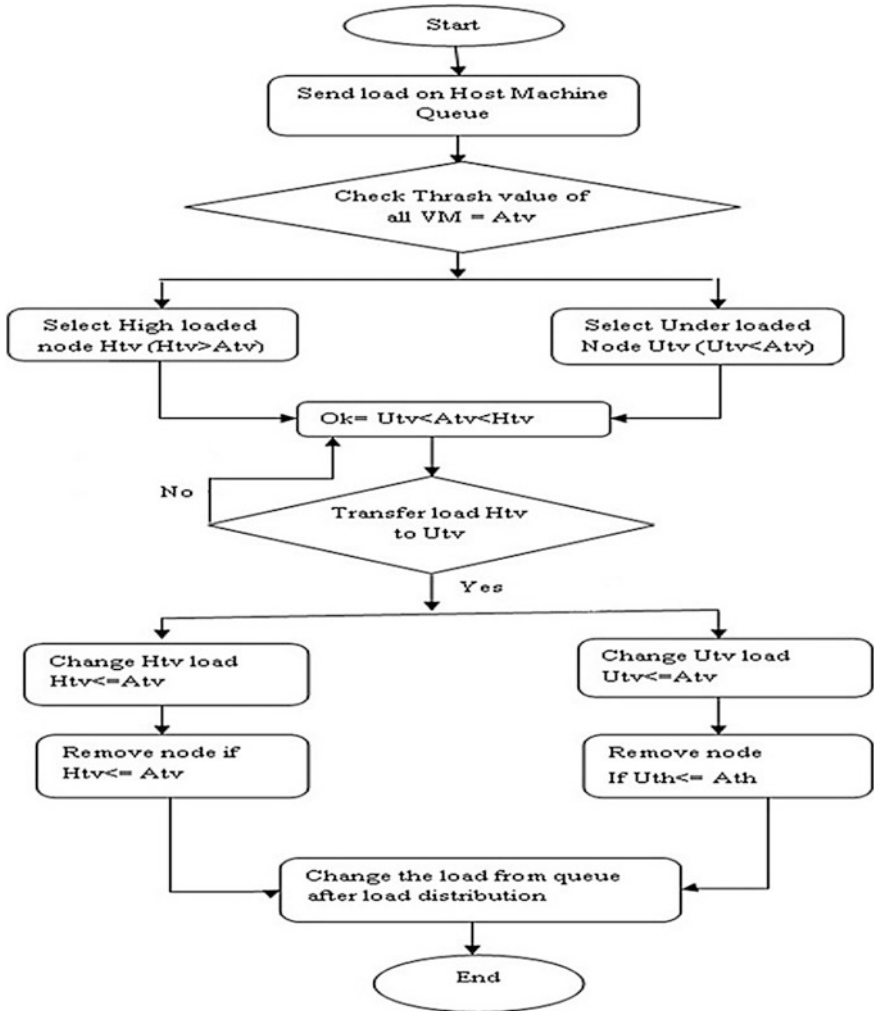


Fig. 1 Flow chart of load balance mechanism

and change the ID and load information when load is transferred from Htv to Utv. It also ensures that dead lock and bottleneck problem do not occur during the load migration. Host machine should be able to manage disaster management and any type of failure of VMs. Figure 1 shows the load management among VMs. High load machine ($Htv > Atv$) can transfer the load to underload machine ($Utv < Atv$). Load transfer will be under the condition of $OK = Utv < Atv < Htv$. Figure 1 load balance process can be determined by the above algorithm procedure.

Challenges in Resource Mangement

Some challenges in resource management are as follows:

Can measure all the available resources, when resources are already utilized and how to know when resources will be free and how to scale all reserved and unreserved resources?

Which are mostly frequently used resources and how to be available in short of availability?

Do users get the resources according to SLA and how to implement load balance mechanism with respect to SLA?

If all VMs are highly overloaded and access queue is also highly overloaded that time how to manage resources?

How to make energy efficient live migration machine when most of the machines are underloaded?

Conclusion

Traditional computing system mostly uses centralized server system but cloud system uses distributed and grid computing systems to manage resources with effective time and energy. Management of resources in effective time and energy saving mechanism both are not easy to manage simultaneously. Researchers have already done lots of works in live VM migration but there is still need of improvements. Paper has included challenges of load balance during live migration. Load balanced policy should be monitored and scalable during VMs migration. Load migration should be proper scheduled, synchronized, and also able to run multiple processes simultaneously.

This paper proposed effective load balance algorithm. Algorithm proposed a way to find overloaded VMs and underloaded VMs with load transfer mechanism in live migration. This algorithm would be helpful for finding overloaded VMs and underloaded VMs and also able to relocate loads from high loaded VMs to underloaded VMs by utilizing thrashing mechanism. Thrashing mechanism is an efficient energy saving load management policy to transfer load in live VM migration.

References

1. Xiao, Z., Xiao, Y.: Security and privacy in cloud computing. *Commun. Surv. Tutor., IEEE* **15** (2), 843–859 (2013)
2. Denz, R., Taylor, S.: A survey on securing the virtual cloud. *J. Cloud Comput.* **2**(1), 1–9 (2013)

3. Wickboldt, J.A., Esteves, R.P., de Carvalho, M.B., Granville, L.Z.: Resource management in IaaS cloud platforms made flexible through programmability. *Comput. Netw.* (2014)
4. Liu, Y., Gong, B., Xing, C., Jian, Y.: A virtual machine migration strategy based on time series workload prediction using cloud model. *Math. Probl. Eng.* (2014)
5. Ferreto, T.C., Netto, M.A., Calheiros, R.N., De Rose, C.A.: Server consolidation with migration control for virtualized data centers. *Future Gener. Comput. Syst.* **27**(8), 1027–1034 (2011)
6. Hu, L., Zhao, J., Xu, G., Ding, Y., Chu, J.: A survey on data migration management in cloud environment. *J. Digital Inf. Manage.* **10**(5) (2012)
7. Vinothina, V., Sridaran, R., Ganapathi, P.: A survey on resource allocation strategies in cloud computing. *Int. J. Adv. Comput. Sci. Appl.* **3**(6) (2012)
8. Zhang, Q., Cheng, L., Boutaba, R.: Cloud computing: state-of-the-art and research challenges. *J. Internet Serv. Appl.* **1**(1), 7–18 (2010)

Real-Time Abandoned Object Detection Using Video Surveillance

Aditya Gupta, V.R. Stapute, K.D. Kulat and Neeraj Bokde

Abstract Due to increase of attacks in public places, security has now become a major issue in public places. In this paper, we have proposed an abandoned object detection through video surveillance with real-time alarming. We use dual background subtraction method to find out the static object. It is been assumed that object which is part of foreground for longer period of time slowly turns as part of background. Background modelling is done using approximate median model. For foreground processing background subtracting method is followed by ANDing operation of frames to find out the static object. The system is simple to design and not having complexity of filters or complex calculation. PETS 2006 database is used for testing algorithm. The result shows satisfactory performance even under complex condition of shadow, moving crowd, and lightning condition. MATLAB R2013a is used for compilation of system.

Keywords Abandoned object · Video surveillance · Dual background subtraction

Introduction

From last decades, there had been rise of attacks on public places, even though video surveillance systems are installed at such places. All these are manually monitored, then also proves inefficient. Hence there is need of automatic surveillance system which can identify abandoned object in such places. These systems

Aditya Gupta (✉) · V.R. Stapute · K.D. Kulat · Neeraj Bokde
Department of Electronics and Communication, VNIT, Nagpur, India
e-mail: adityagupta2590@gmail.com

V.R. Stapute
e-mail: vrsatpute@ece.vnit.ac.in

K.D. Kulat
e-mail: kdkulat@ece.vnit.ac.in

Neeraj Bokde
e-mail: Neerajdhanraj@gmail.com

can able to detect such objects and even can track the person to which it belongs. Due to development of high processing devices and need of security, this field becomes the field of research in recent years. Various methods have been proposed [1, 2] in past years for abandoned object detection but are less efficient. Problem like people's occlusion, makes it complex. Other difficulties like change in lighting condition and shadows make this subject more complex. In abandoned object detection we have to find out the objects that are being left alone with intention of giving harm to society. We proposed an abandoned object detection algorithm which works efficiently on complex environment like crowd, changing lightning condition, shadow. Here, we have used dual background subtraction algorithm for detection purpose. In recent past many people try to find solution in different ways. Each of past algorithms has its own advantages and limitations on parameters of accuracy and complexity. Adaptive background subtraction is one of the popular methods for finding out the object detection. Auvinet and Grossmann used adaptive background method for object detection. But these ABS base systems have problem in integration of foreground object into background [3]. Singh [4] uses dual background base for object detection. The advantage of this algorithm is it is more immune to lightning condition and other problems of shadow change. For dual background initial background modelling has to be done using different methods. The most popular one is Gaussian mixture models, proposed by Friedman and Russell [5] later modified by several authors [6]. The disadvantage of this algorithm is large computation which generally takes time. Wren [7] proposes a running Gaussian average method for background modelling which uses last n frames for background modelling. Here, a weighted average is used where more weightage is given to newer frame, which varies according to Gaussian distribution. Problem related to this is always we have to calculate mean and variance so every time complex calculation is involved. McFarlane [8] uses adaptive median method for background modelling. For background modelling median of previous n frames is taken. An alternative has been done for this algorithm.

In these papers, we have used dual background subtraction method which maintains current (BC) and buffer background. Adaptive median is used for background modelling. The paper is arranged as follows: (i) Proposed methodology, (ii) result, (iii) conclusion followed by references.

Proposed Methodology

Our aim is to differentiate between object belongs to foreground and background in video. The basic idea of implementation is process foreground to find out static object which is slowly becoming part of background. After object detection raises the alarm it remains present for certain period of time. Flow chart in Fig. 1 shows the proposed algorithm. Initially, frames from video have been taken and converted to grayscale. For initial 500 frames background modelling is been done. For background modelling we compare the current frames with previous frames. Assign

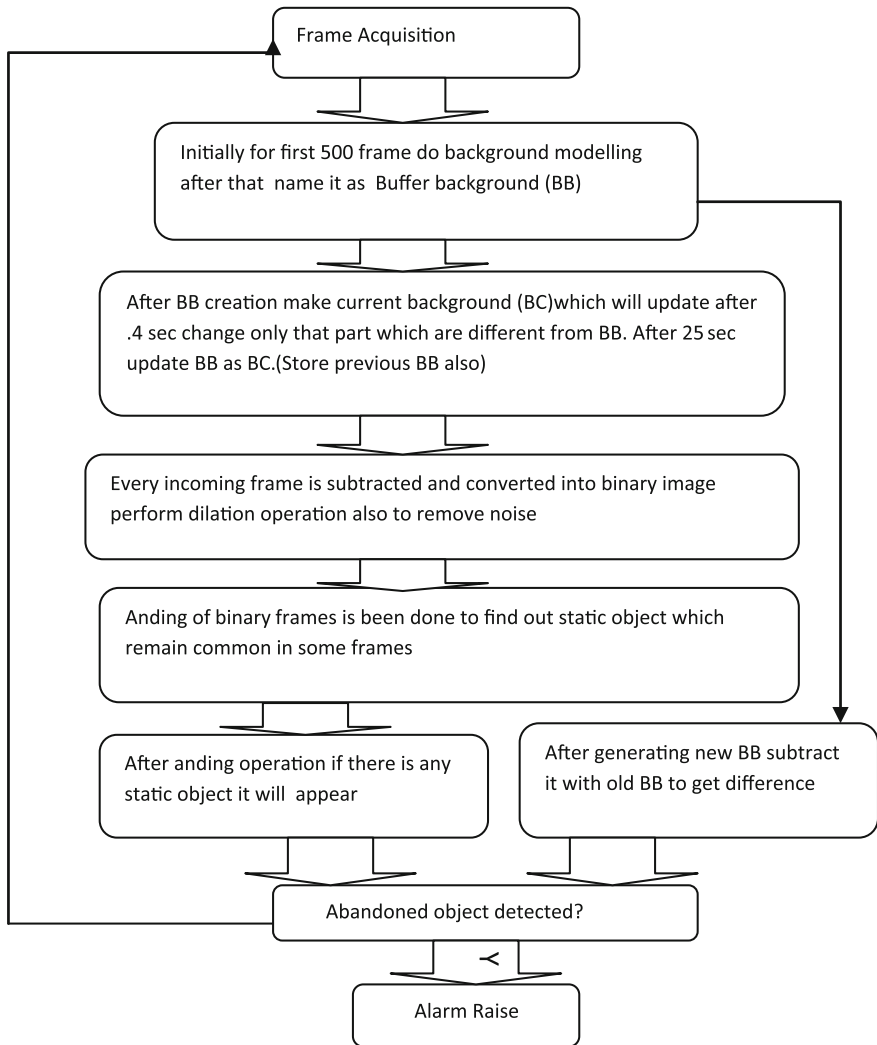


Fig. 1 Shows the flow chart of proposed algorithm

first frame as variable 'B'. If intensity of pixel value of nth frame is more than (n - 1)th frame then value of intensity of that pixel value 'B' is increased by 1 if intensity is less, then its value decreases by 1. If pixel value remains same then there is no change in value of 'B'. After initial 500 frames assign value of B as BB which is buffer background. After initializing BB, frame is taken one by one; frame is subtracted from BB to get the frame difference. This is again converted to binary image to void changes due to lightning condition. There is change in pixel value of current background (B) for the pixel value which is different than BB. The current

background is thus updated after every 4 s. AND ing operation is done between two consecutive binary converted frame differences.

$$A_n = A_{n-1} \&\& (I_n - BB) \quad \text{here } A_n \text{ is initialized as matrix containing all 1}$$

If object remains static throughout then it is supposed to be common in all frame differences hence after 25 s when BB is going to get updated, the value of A_n tells the static object. But if due to occlusion that static object is missing in one frame then its result is zero. So to avoid such condition we come up with solution of two consecutive buffer background differences.

It is assumed that if any object remains constant in foreground then slowly it will start converting to background. So any static object which is constant in all foregrounds becomes part of BB during next upgradation of BB. So binary frame difference between BB_m and BB_{m-1} gives the abandoned object. Morphological operation that is dilation operation is being done on that image of frame difference to get the proper static image. Logical OR operation is done on image to get the final result.

$$(BB_m - BB_{m-1}) || A_n$$

where $(BB_m - BB_{m-1})$ is frame difference between two consecutive buffer backgrounds. A_n is frame obtaining from AND ing operation of frames.

Background Modelling: Initially 500 frames are used for background modelling. First frame is initialized with B. Increment or decrement the value of pixel of B depends upon the equation.

Adaptive Median: This BGS method, described in [1], works under the assumption that the foreground is more likely to appear at any given pixel over a period of time. This leads to supposition that the pixel stays in the background for more than half the value in its history. The median of previous n frames can therefore be used as the background model. Due to the high memory requirements of the iterative version, a recursive version of this algorithm is more practically feasible. Following is the update equation for the background model in this approach:

$$B_t = \begin{cases} B_t - 1 & \text{if } (B_{t-1} > I_t), \\ B_t + 1 & \text{if } (B_{t-1} < I_t), \\ B_t & \text{if } (B_{t-1} = I_t) \end{cases}$$

Here, B_t and I_t , respectively, refer to the intensity values in background model and the current frame at time t.

Foreground Analysis: After background subtraction there is some noisy portion left due to sudden lightning change and shadow. Further existence of these shadow and light change leads to holes creation. This noise must be removed. Morphological operation is being performed to remove the holes.

Figure 2a, b shows the buffer background and current frames. This current frame is subtracted with background shown in Fig. 2c. We can see that there is shadow effect in it so binarization is done followed by morphology operation shown in Fig. 2d.

Figure 3a–e shows the subtracted image of buffer background and current frame. Figure 3f shows AND ing operation of frame (Fig. 3a–e). It is seen that an object which remains static in all such frames reflected in this image which is abandoned object.

Figure 4a, b shows the two consecutive buffer backgrounds and it can be noted that as object remains static during foreground for longer period so it becomes part of background only.

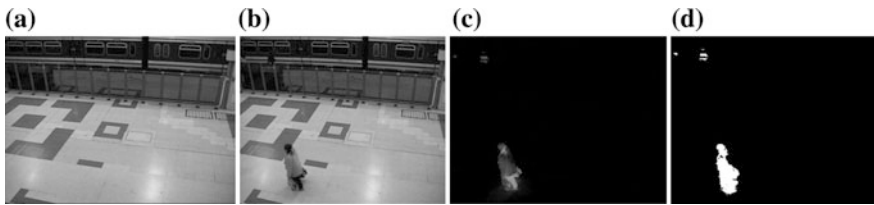


Fig. 2 a Buffer background, b current frame, c subtracted frame, d binary equivalent of this image

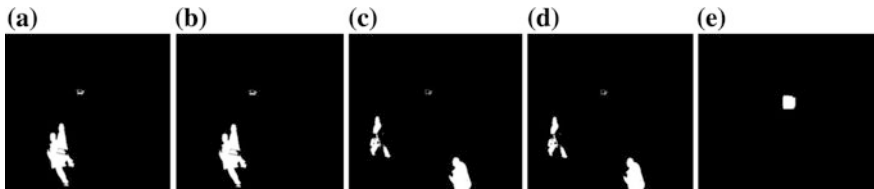


Fig. 3 a–e Subtracted background 2 e AND ing of all the frames which gives static or abandoned object

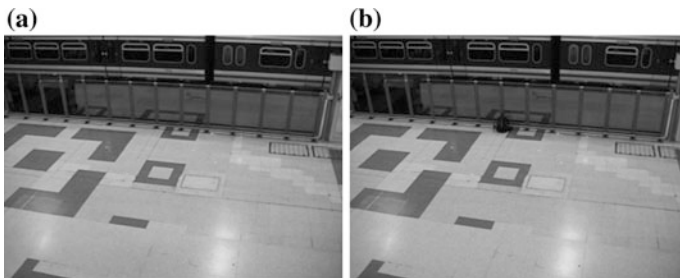


Fig. 4 a Previous buffer background, b Buffer background

Table 1 Test results on PETS Database 2006 [9]

Sequence	Abandoned object present	Abandoned object detected
S1	Yes	Yes
S2	Yes	Yes
S3	Yes	Yes
S4	Yes	Yes
S5	No	Yes
S6	Yes	Yes
S7	Yes	Yes

The result shows that system works efficiently in finding out the abandoned object

Result

The proposed algorithm in previous section has been implemented as real-time system. The algorithm was performed on standard database named as PETS 2006 [9, 10]. MATLAB version 2013 is used for these purposes. The proposed algorithms performed on desktop having Intel core i3 processor, 8 GB RAM on Windows 7 platform (Table 1).

Conclusion

In these papers, we have proposed a system which can be used for automatic abandoned object detection without any human interference. Such system proves to be efficient in public place for providing security. Here to provide efficiency we have used two methods for finding out object and from AND ing operation of frames and other is from consecutive buffer background difference. The system is quite immune to complex condition but has to be more immune to shadows and lighting condition. Here, there is one false detection in sequence S5, to avoid this object classification can be done. The important outcome is the operation is in real time so we can design the system and use in human life for security purpose.

Future Scope

In future, we can go for object classification to avoid false detection as we have found in sequence S5. We can implement tracking algorithm also so that we can find out the person who is caring that abandoned object. This can be done using histogram matching algorithm. The system can be implemented in hardware using low-cost devices such as Beagleboard.

References

1. Mathew, R., Yu, Z., Zhang, J.: Detecting new stable objects in surveillance video. In: Proceedings of the IEEE 7th Workshop on Multimedia Signal Processing, pp. 1–4 (2005)
2. Bird, N., Atev, S., Caramelli, N., Martin, R., Masoud, O., Papanikolopoulos, N.: Real time, online detection of abandoned objects in public areas. In: Proceedings of IEEE International Conference on Robotics and Automation, pp. 3775–3780 (2006)
3. Singh, A., Hanmandlu, M., Madasu, V.K., Lovell, B.C.: An abandoned object detection system based on dual background segmentation. In: Proceedings of Sixth IEEE International Conference on Advanced Video and Signal Based Surveillance, pp. 352–357 (2009)
4. Auvinet, E., Grossmann, E., Rougier, C., Dahmane, M., Meunier, J.: Left-luggage detection using homographies and simple heuristics. In: Proceedings of IEEE International Workshop on Performance Evaluation of Tracking and Surveillance (PETS), New York, pp. 51–58 (2006)
5. Friedman, N., Russell, S.: Image segmentation in video sequences: a probabilistic approach. In: Proceedings of 13th Annual Conference on Uncertainty in Artificial Intelligence, pp. 175–181 (1997)
6. Stauffer, C., Grimson, W.: Adaptive background models for realtime tracking. In: Proceedings of IEEE Conference on Computer Vision and Pattern Recognition, vol. 2, pp. 246–252 (1999)
7. Wren, C., Azarbayejani, A., Darrell, T., Pentland, A.: Pfunder: real time tracking of the human body. *IEEE Trans. Pattern Anal. Mach. Intell.* **19**(7), 780–785 (1997)
8. McFarlane, N., Schofield, C.: Segmentation and tracking of piglets in images. *Mach. Vis. Appl.* **8**(3), 187–193 (1995)
9. www.ftp.PETS.rdg.ac.uk/PETS2006
10. www.cv.rdg.ac.uk/PETS2006/data.html

Request Allocation and Resource Management Techniques in Cloud Computing

Swati Khemka and Mehul Mahrishi

Abstract Cloud computing raises capacity by providing resources as a service; there is no need to purchase new resources. Popularity of cloud computing systems has been increasing, which rents computing resources on user demand. Many users must be provided services by cloud simultaneously as per their requirements. In this, it is difficult for the cloud to process requests of all and allocates resources to the users in a mutually optimal way at the same time. So, this paper is a review of certain papers on request processing and resource allocation techniques or algorithms in cloud computing and proposes a new user defined dynamic priority scheduling algorithm.

Keywords Cloud computing · Cloud service provider

Introduction

The cloud has introduced a new way of using the software and hardware. Companies can speedup their business and decrease their expenses if they use cloud computing. The basic model of a cloud environment is shown in Fig. 1. Users can get software and hardware facility from “cloud” anywhere anytime as they require only “pay per use”. Cloud computing always tries to increase the gain and decrease the execution time. But cloud service providers (CSPs) have the problem of allocating resources dynamically.

Swati Khemka (✉) · Mehul Mahrishi
Department of Computer Science Engineering, SKIT, Jaipur 301027,
Rajasthan, India
e-mail: swati.khemka001@gmail.com

Mehul Mahrishi
e-mail: mehul@skit.ac.in

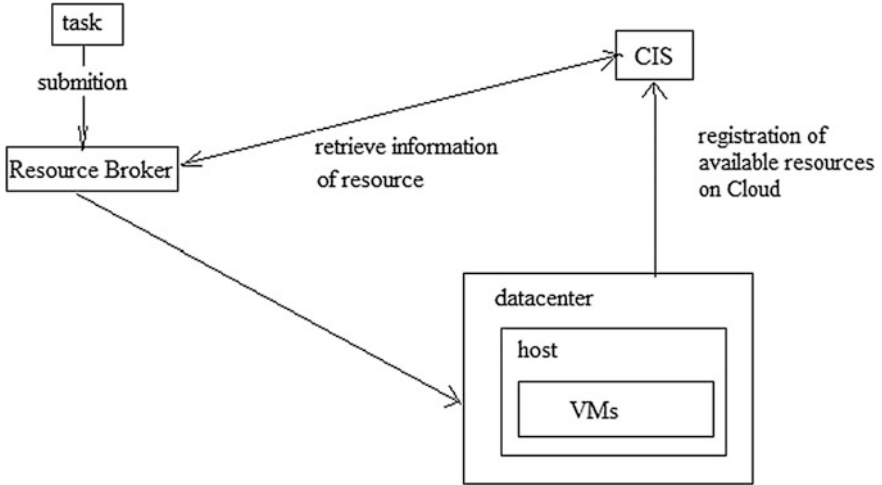


Fig. 1 Basic cloud environment

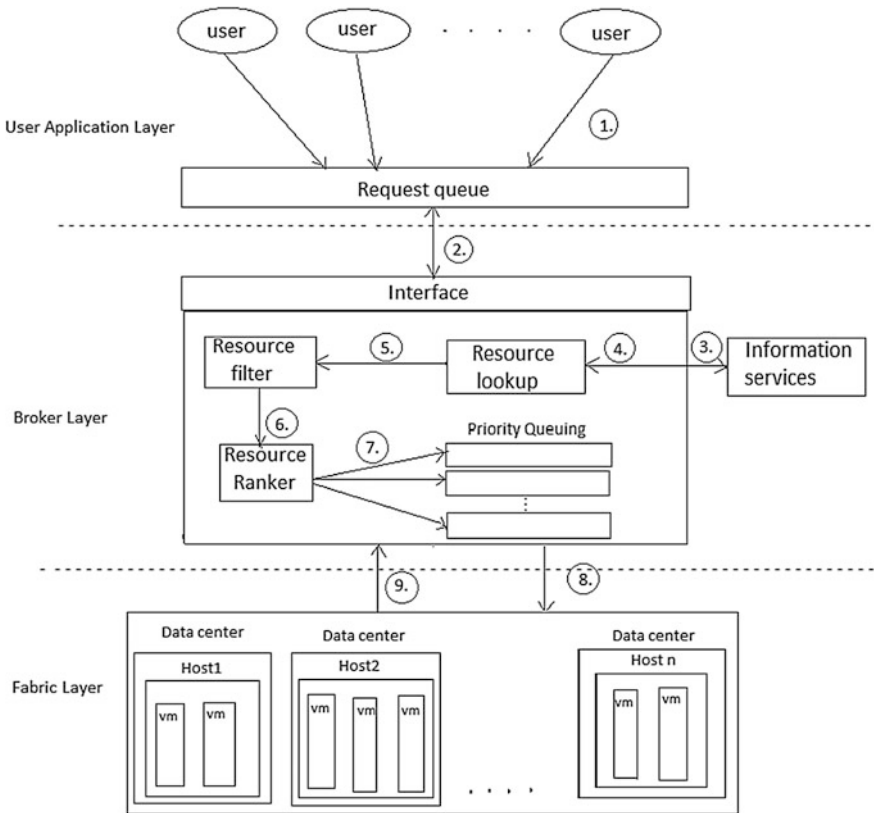


Fig. 2 User defined dynamic priority workflow

Need for Request Allocation and Management of Resources in Cloud Computing

When many users want to access the cloud at the same time then allocation of resource to all users becomes difficult for cloud computing. Moreover, how the user requests will be processed is also a challenging task. At this point, the cloud has to provide resources to its users on time as well as without any allocation failure. Resource utilization with maximum users' satisfaction becomes harder for cloud. To provide cost efficient resources to the user the cloud has to perform calculation on resource allocation.

Literature Study of Request Allocation and Resource Management

Recently, many researchers have worked on request allocation and resource management. The scheduling problem in distributed cloud for context-aware applications is a complicated task because there are many alternative computers with varying capacities. So, providing a suitable one on time to gain profit becomes complicated to providers. In [1] the giFIFO scheduling algorithm is proposed. In this algorithm, all the context aware applications (i.e., each request that arrives at a datacenter contains a context id) are allocated dynamically to appropriate endserver (resources) of datacenter. It divides all the coming requests in different classes depending on their context id. Final allocation of endserver is based on compatibility check of context id and id of endserver. This giFIFO algorithm finally provides dynamic request allocation with minimum response time and maximum profit gained by the cloud.

Priority queuing techniques are emerged in cloud computing. Nan et al. [2] used queuing model to prioritize the request on the basis of their requested services in multimedia cloud. The main consideration is on minimization of execution time and cost, which is handled by optimize resource allocation. This queuing model contains three queues. The master server sends the requests (which are in the scheduling queue) to the computing server. Computing server schedules the user requests on the basis of priority. After this, transmission server delivers results back to the customers. This model finally achieves minimum service response time and resource cost.

Another approach for priority queuing was introduced by Li [3], a non-preemptive priority M/G/1 queuing model. First, differentiation in the QoS requirement is done. Differentiating the QoS requirements provides different

priorities to classify jobs in different classes to schedule them. Each class has different priority from 1 to N . Smaller the number, higher the priority. The higher priority class is scheduled first. This model is based on non-preemptive scheduling (i.e., a job scheduled on a resource will release that resource after its completion or termination). This reduces scheduling overhead.

In previous work on cloud computing, all the scheduling algorithms are for one workflow and only for one or two QoS parameters, as considering more QoS parameters for scheduling will be challenging. In [4] a scheduling policy which is based on multi QoS, parameters for multiple workflows are introduced. The system contains three main parts. The first is the preprocessor which calculates four QoS parameters of user requests and sends user requests to the scheduler. Recomputation of QoS parameters is done by scheduler and it rearranges the requests. Finally, executer executes the requests. Due to this, probability of allocation of the best suitable resource increases. The average success rate of MWMQ algorithm is up to 92 %.

In [5], a three-tier architecture (cloud users, CSPs, and resource provider) is introduced with a scheduling algorithm, i.e., DPSA. The resource provider provides the resources to the CSPs. CSPs create dynamic instances of the resources and allocate them to the users. The basic components are classifier, scheduler, and summary component. All requests first pass to classifier, where each request is divided into small units and priority is assigned according to system state and task itself. After that task units are sent to the scheduler. Scheduler contains scheduling units (queue), where each queue is assigned a threshold value A_k , i.e., time limit assigned to a queue means that a task can only stay in that queue for A_k time whether it is scheduled or not, and after that the task switches to upper priority queue. At the end of task, units are sent to summary component. Results of DPSA are compared with FCFS and SPSA, which showed that the DPSA is effective in implementation of user tasks and with better fairness.

Warneke and Kao [6] proposed a framework and Nephele introduced, which was the first data processing framework. It mainly uses IaaS clouds to process user requests. Nephele provides parallel data processing framework in heterogeneous system which overcomes the problem of static and homogeneous computation system. Its scheduler always ensures that instances that are required in a stage must be allocated when processing of that stage starts. And before processing of next stage starts intermediate results of all its previous stages are stored. Deallocation of an instance is done if it is not required in coming stages. So, Nephele improves the average resource utilization and processing cost reduction is done. Experimental results of MapReduce programs on Nephele and on Hadoop are compared. Finally, the experiments in Nephele gave the best result. The main objective of today's CSPs is to increase credits. It shows the self-centered nature of CSPs that makes adverse effects on the user. In this type of situation, how can a consumer fully trust

a CSP? A trustworthy mechanism for scheduling of single tasks and suitable pricing model is proposed in [7]. The scheduling algorithm is auction-based dynamic scheduling which minimizes the response time and cost for workflows. Every workflow is in DAG form. Each node in DAG represents a user task. On the basis of this workload a rank is provided to each task. According to this rank, tasks are scheduled on the resources. Every resource has its pricing model and according to that the cost of the used resource is calculated depending on their scheduling.

Different users have different service and QoS requirements. Liu et al. [8] proposed a scheduling model for these service requests with various QoS requirements. To optimize this scheduling model, ant colony optimization algorithm is used. The running condition of the service request is represented by SLA monitoring. The final experimental results proposed are efficient.

When cloud users use the services of the cloud they only consider the execution time. They ignore execution cost and data transferring cost between resources on network. So, in [9] a POS-based heuristic scheduling approach is proposed. It provides an experimental setup for calculation of communication cost and computation cost. Finally this approach achieves (1) three times more cost saving over BRS (best resource selection) and (2) load balancing over cloud resources.

An approach is introduced by Tripathy and Patra [10] for reduction of communication time and response time. A scheduling technique is proposed to minimize the makespan. This technique is priority-based and parallel processing. Highest priority job is scheduled first. It results in decreased completion time of MapReduce jobs. Another approach in [11] a task scheduling model based on fuzzy genetic optimizations algorithm was proposed. This method totally depends on prediction of response time. This method provides not only load balancing but also increases resource utilization.

Proposed Work

We proposed a time and cost weightage-based scheduling algorithm, i.e., user defined dynamic priority scheduling algorithm which decides the priority of scheduling either on the basis of cost or on the basis of time. The time and cost constraints are submitted by user along with the request. Workflow of proposed algorithm is shown in Fig. 2

User Defined Dynamic Priority Scheduling Algorithm

Input - User request (tasks) with (w_t , w_c and t)

Output – A schedule for all the tasks

```

if(inputQueue(Q) == empty)
{
    Do nothing;
}
end if
else
    for all  $i \in Q$  do
        if(  $w_{ti} + w_{ci} = 1$  )
        {
            Select R a subset of resources for the task i on the basis of  $w_{ti}$  and  $w_{ci}$  from
            available resource list.
        }
        end if
        Calculate for each  $R_j$ 
         $TH_{ij} = w_{ti}t_i + w_{ci}c_j$ 
        Min( $TH_{ij}$ )
        Send the i with min( $TH_{ij}$ ) resource in priority queue (TPQ or CPQ)
    end for
end else
    TPQ – time priority queue
    CPQ – cost priority queue

```

Resources are provided to the user on the basis of their requirement with the parameters such as time and cost. User can request either for time optimization or cost optimization by giving weightage factors.

Conclusion

Cloud computing is a most extensive research which provides facilities regarding software, platform, and resources for computation. Cloud computing mainly aims at providing the best resources to its users. Many researchers tried to fulfill this objective of request allocation and resource management for cloud computing. In this paper, the literature study of many algorithms for this objective is done. Through this research we proposed a user-based time and cost optimization scheduling in cloud using standard CloudSim simulator.

References

1. Bolor, K., Chirkova, R., Viniotis, Y.: Dynamic request allocation and scheduling for context aware applications subject to a percentile response time SLA in a distributed cloud. In: 2nd IEEE International Conference on Cloud Computing Technology and Science, pp. 464–472 (2010)
2. Nan, X., He, Y., Guan, L.: Optimal resource allocation for multimedia cloud in priority service scheme. In: International Symposium on Circuits and Systems (ISCAS), pp. 1111–1114. IEEE (2012)
3. Li, L.: An optimistic differentiated service job scheduling system for cloud computing service users and providers. In: IEEE 3rd International Conference on Multimedia and Ubiquitous Engineering, pp. 295–299 (2009)
4. Xu, M., Cui, L., Wang, H., Bi, Y.: A multiple QoS constrained scheduling strategy of multiple workflows for cloud computing. In: IEEE International Symposium on Parallel and Distributed Processing with Applications, pp. 629–634 (2009)
5. Lee, Z., Wang, Y., Zhou, W.: A dynamic priority scheduling algorithm on service request scheduling in cloud computing. In: IEEE International Conference on Electronic & Mechanical Engineering and Information Technology, pp. 4665–4669 (2011)
6. Warneke, D., Kao, O.: Exploiting dynamic resource allocation for efficient parallel data processing in the cloud. In: IEEE Transactions on Parallel and Distributed systems, pp. 985–997 (2011)
7. Fard, H.M., Prodan, R., Fahringer, T.: A truthful dynamic workflow scheduling mechanism for commercial multi-cloud environments. In: IEEE Transactions on Parallel and Distributed systems (2012)
8. Liu, H., Xu, D., Miao, H.K.: Ant colony optimization based service flow scheduling with various QoS requirements in cloud computing. In: IEEE First ACIS International Symposium on Software and Network Engineering, pp. 53–58 (2011)
9. Pandey, S., Wu, L., Guru, S.M., Buyya, R.: A particle swarm optimization-based heuristic for scheduling workflow applications in cloud computing environments. In: 24th IEEE International Conference on Advanced Information Networking and Applications, pp. 400–407 (2010)
10. Tripathy, L., Patra, R.R.: Scheduling in cloud computing. In: IJCCSA, pp. 21–27 (2014)
11. Tayal, S.: Tasks scheduling optimization for the cloud computing system. In: IJAEST, pp. 11–15 (2011)

Blind Image Watermarking of Variable Block Size for Copyright Protection

Amit M. Joshi, Monica Bapna and Manisha Meena

Abstract The development of multimedia technology has paved a way for rapid and fast communication. Various multimedia objects are transmitted through Internet once they have been captured. This has lifted up the concern over secure communication and also copyright protection issue. It is likely a case for the creator to be in dilemma whether the data had reached the intended person with all its imbibes integrity or not. Watermarking is an art of hiding owner's signature in terms of text, audio, video, or image to prove the authenticity of an owner. This serves as safeguard for the originator in case of any misshape. In this paper, an efficient and blind watermark embedding method has been developed using Haar wavelet. The binary logo is used as a watermark that carries a sequence of zeros and ones. The single bit of watermark is embedded in k block size of the original image. The proposed scheme shows an excellent performance and has admirable robustness against various attacks.

Keywords Block size · Discrete wavelet transform · Frequency domain · Level of decomposition · Normalized correlation

Introduction

With the growth of technology, multimedia objects such as video, image, audio, speech are exchanged easily once they have been encapsulated [1]. The main concern is the integrity of these objects after they have been transmitted over the

A.M. Joshi (✉)

Electronics & Communication Department, MNIT, Jaipur 302017, India
e-mail: amjoshi.ece@mnit.ac.in

Monica Bapna

Physics Department, IIT Bombay, Bombay, India
e-mail: monica.bapna13@gmail.com

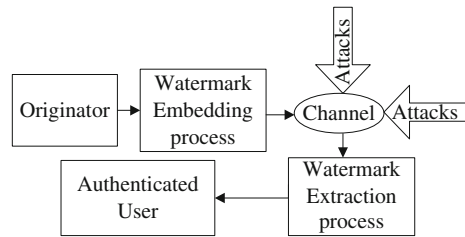
Manisha Meena

Pipelines division, Indian Oil Corporation Ltd, Rajkot, India
e-mail: manishaderwal@gmail.com

© Springer India 2016

N. Afzalpulkar et al. (eds.), *Proceedings of the International Conference on Recent Cognizance in Wireless Communication & Image Processing*, DOI 10.1007/978-81-322-2638-3_96

Fig. 1 General digital watermark system



channel. Digital image watermarking is the technique where the watermark (may be image, text, logo, etc.,) is inserted in the original image [2]. The watermark carries ownership to provide the authenticity and/or copyright of the owner whenever it is required. The algorithm requires some essential features as perceptibility, robustness, security, and payload [3]. To have copyright protection, the digital watermark algorithm should have all the above features [4]. The general block diagram of digital watermarking is shown in Fig. 1.

The system has two main processes, first is watermark embedding process and the other is watermark extraction process. The concept of image watermarking is applied in either spatial domain or frequency domain [5]. Spatial domain techniques are easier for implementation but they fail to withstand any attacks. The process of embedding the watermark in frequency domain has greater robustness which uses various transformation methods known as discrete Fourier transform (DFT), wavelet transform, discrete cosine transform, etc. [6]. DWT-based watermarking is an ideal choice as it provides different frequency bands according to their energy information which helps during watermark embedding process.

From the past two decades, there has been substantial work carried out in digital watermarking for different image applications [7]. Proposed algorithm uses the concept of variable block size for copyright protection application. The watermark uses binary logo as watermark and is embedded in original image by replacing either minimum or maximum value of the block. The block value ‘k’ is adaptively selected during the watermark embedding. The algorithm is tested against all common signal processing attacks. The organization of paper is as follows: section “[Proposed Image Watermarking Algorithm](#)” explains the proposed image watermarking algorithm with watermark embedding and watermark extraction process. Section “[Results and its Analysis](#)” covers the result analysis, and finally the work is concluded in section “[Conclusion](#)”.

Proposed Image Watermarking Algorithm

Proposed image watermarking scheme uses Haar wavelet-based frequency domain transformation. Haar is the most popular wavelet transform method and uses simple arithmetic computation [8]. The watermark is embedded in low frequency

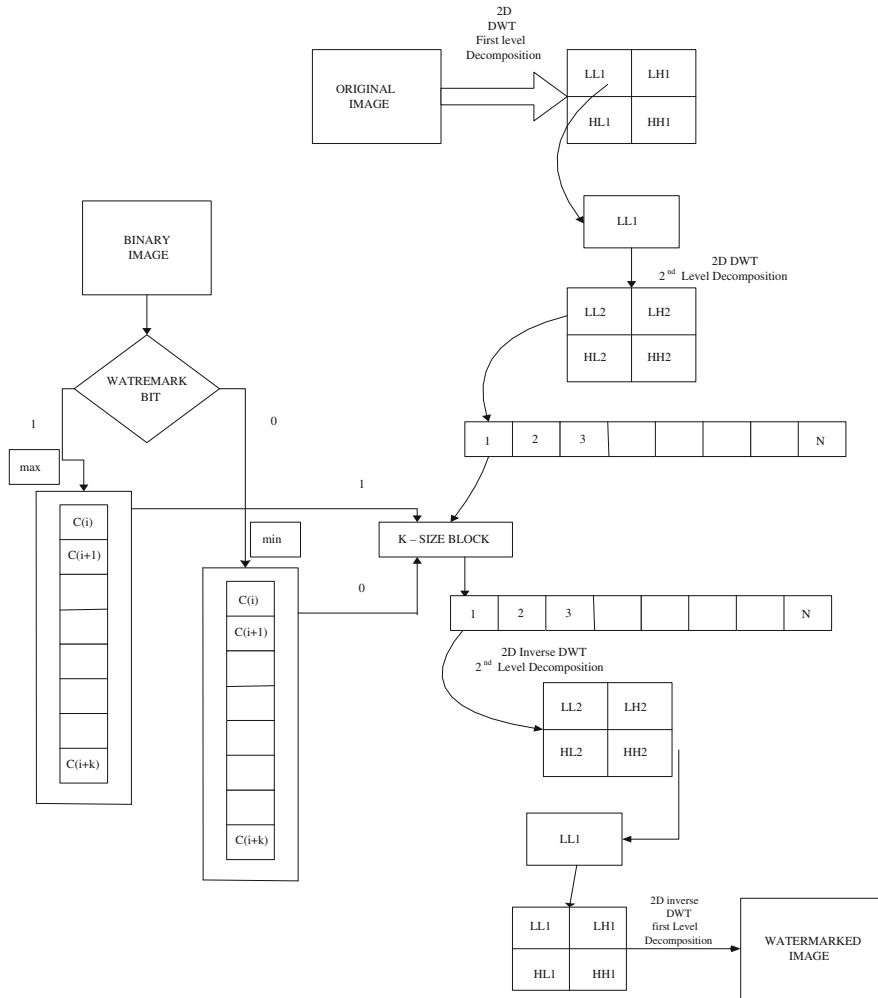


Fig. 2 Block-based digital watermarking algorithm

(LL) band to increase the robustness against severe attacks. If the watermark is inserted at high frequency band, then it is more likely that compression and/or the low pass filter destroys the watermark [9]. Thus, watermark is inserted in low frequency components. The flow of the proposed watermarking algorithm is shown in Fig. 2. The detailed explanation of watermark embedding and extraction process is carried out in following section.

Watermark Embedding Steps

- Step 1: First the original color image is converted to YUV format. Y plane is used for watermark embedding. U and V planes are sensitive to human visual system (HVS). Thus, they are not chosen to insert the watermark.
- Step 2: Y plane is transformed using Haar wavelet with two levels of decomposition for the host image. The watermark is embedded in LL₂ band.
- Step 3: The watermark is binary logo which carries the sequence of 1's and 0's.
- Step 4: LL₂ band is divided in the block size of 'k'. The watermark is inserted in wavelet coefficients of the particular block according to a watermark bit. The rule of embedding as per Eq. (1):

if $(W(m) = 1)$,

$$C(n) = \text{Max} (C(n), C(n + 1), C(n + 2), \dots, C(n + k));$$

Else,

$$C(n) = \text{Min}(C(n), C(n + 1), C(n + 2), \dots, C(n + k)); \tag{1}$$

Here, k is the last element of block, where $C(n)$ is the n th wavelet coefficient of the original image and $W(m)$ is the m th pixel of the watermark image.

Step 5: Once the watermark is embedded the inverse discrete wavelet transform is carried out to get watermarked image.

Watermark Extraction Steps

The retrieval process of watermark is blind, where there is no requirement of the original image. First watermarked image is transformed using Haar wavelet with second level of decomposition. The watermark is extracted as follows:

$$\text{If, } WC(n) > \text{median} (WC(n), WC(n + 1), \dots, WC(n + k)) \\ W(m) = 1$$

Else,

$$W(m) = 0 \tag{2}$$

where, $W_C(n)$ is the n th wavelet coefficient of the watermarked image and $W(m)$ is m th pixel of the extracted watermark.

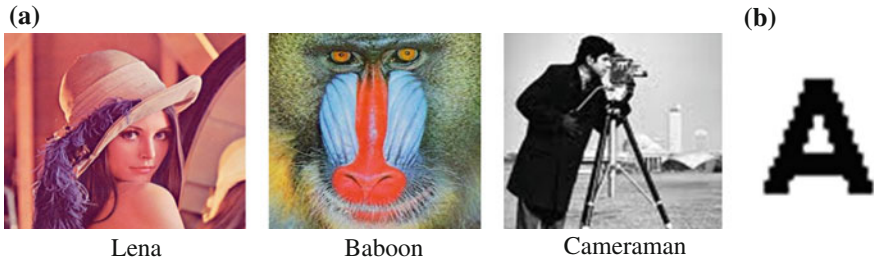


Fig. 3 Test Images **a** Original Images **b** Original Watermark

Results and Its Analysis

‘Lena’, ‘Baboon’, and ‘Cameraman’ (RGB image of size $512 \times 512 \times 3$) is considered as original image and binary logo (size of 128×128) is used as original watermark. They are shown in Fig. 3a and b respectively.

The watermark should be inserted to satisfy an invisibility criterion. The visibility of the watermarked image is verified using peak signal-to-noise ratio (PSNR) and mean square error (MSE) that are as per Eqs. (3) and (4).

$$MSE = \frac{1}{N_1 * N_2} \sum_{x=0}^{X-1} \sum_{y=0}^{Y-1} [I(x,y) - I_w(x,y)]^2 \tag{3}$$

$$PSNR = 20 \log_{10} \frac{255}{\sqrt{MSE}} \tag{4}$$








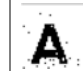



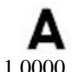
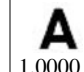
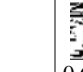

$I(x,y)$ = original image $I_w(x,y)$ = watermarked image N_1, N_2 = size of the image.

To verify the perceptual distortion introduced in watermarked image after the insertion of watermark, MSE and PSNR are calculated. MSE should be low or PSNR should be high and are calculated between the original and watermarked image [10]. The algorithm is tested against different attacks to check the robustness. Robustness of an algorithm is quantified with normalized correlation (NC) as in Eq. (5)

$$NC(w,w') = \frac{\sum_{i=1}^{N-1} w_{org} \times w'_{exct}}{\sqrt{\sum_{i=1}^{N-1} w_{org}^2} \sqrt{\sum_{i=1}^{N-1} w'_{exct}^2}} \tag{5}$$

W_{org} = original image of watermark, W'_{exct} = extracted image of watermark and N = size of watermark.

Table 1 Extraction of watermark

Variable block size (Payload)	Parameter	Without attack	Salt and pepper (0.02 density)	Compression (10 %)	Rotation (1°Anticlock)	Median filter (3 × 3)
Block size = 4 4096	MSE	0.0012	16.162	0.0025	490.535	0.7127
	PSNR	77.3390	36.045	74.147	21.224	49.601
	Retrieved watermark NC	 0.9094	 0.8973	 0.9101	 0.4460	 0.8392
Block size = 8 2048	MSE	0.0008	19.3995	0.0023	489.129	0.7119
	PSNR	79.1000	35.252	74.5135	21.236	49.606
	Retrieved watermark NC	 0.9871	 0.9773	 0.9849	 0.5728	 0.937
Block size = 16 1024	MSE	0.0005	9.4711	0.0019	483.380	0.7119
	PSNR	81.1411	38.366	75.3433	21.2432	49.606
	Retrieved watermark NC	 1.0000	 1.0000	 1.0000	 0.6291	 0.9938

In copyright application, the acceptable value of NC should be at least 0.75–0.80 (75–80 %). Table 1 shows the performance of algorithm in terms of NC against various attacks. NC is measured between the original and extracted watermark whereas MSE and PSNR are calculated between original image and watermarked image. The results are tabulated in Table 1 with the consideration of ‘Lena’ color image as host image and logo of ‘A’ as binary watermark.

Conclusion

The paper presents blind and robust image watermarking algorithm for copyright protection application. The algorithm uses the concept of variable block size to embed one bit of binary watermark. Different block sizes have been considered and results are calculated using MATLAB. The different values of ‘k’ are decided with consideration of various payloads. The results confirm the robustness property of the proposed algorithm, and thus is useful to prove the ownership of original content.

Acknowledgement We are thankful for each and everyone who helped to successfully complete of this paper.

References

1. Joshi, A.M., Darji, A., Mishra, V.: Design and implementation of real-time image watermarking. In: IEEE International Conference on Signal Processing, Communications and Computing (ICSPCC), pp. 1–5, September 2011
2. Bousslimi, D., Coatrieux, G., Cozic, M., Roux, C.: A Joint encryption/ watermarking system for verifying the reliability of medical images. *IEEE Trans. Inf. Technol. Biom.* **16**(5), 13–16 (2012)
3. Joshi, A.M., Patrikar, R.M., Mishra, V.: Design of low complexity video watermarking algorithm based on Integer DCT. In: IEEE International Conference on Signal Processing and Communications (SPCOM), pp. 1–5, July 2012
4. Wang, S., Zheng, D., Zhao, J., Tam, W., Speranza, F.: Adaptive watermarking and tree structure based image quality estimation. In: *IEEE Trans. Multimed.* **16**(2), 311–325 (2014)
5. Joshi, A.M., Patrikar, R.M., Mishra, V.: Real time implementation of digital watermarking algorithm for image and video application. In: Gupta, M.D. (ed.) *Watermarking*, vol 2, ISBN: 978-953-51-0619-7
6. Potdar, V.M., Han, S., Chang, E.: A survey of digital image watermarking techniques. In: 3rd IEEE International Conference on Industrial Informatics, INDIN'05, pp. 709–716, August 2005
7. Fu, Y.G., Wang, H.R.: A novel discrete wavelet transform based digital watermarking scheme. In: 2nd IEEE International Conference on Anti-counterfeiting, Security and Identification, ASID 2008, pp. 55–58, August 2008
8. Yeh, J.P., Lu, C.W., Lin, H.J., Wu, H.H.: Watermarking technique based on DWT associated with embedding rule. In: *Int. J. Circuits Syst. Signal Process.* **4**(2) 2010
9. Fang, Y., Tian, L.: An improved Blind Watermarking Algorithm for Image based on DWT Domain. *J. Theor. Appl. Inf. Technol.* **15**(1), 168–173 (2012)
10. Kashyap, N., Sinha, G.: Image watermarking using 3 level discrete wavelet transform. *Int. J. Mod. Educ. Comput. Sci.* **3**, 50–56 (2012)

Compact Goblet-Shaped Single Band-Notched UWB Antenna

Rajesh Kumar Raj, Krishna Rathore, Bhavana Peswani,
Roopkishor Sharma and H.R. Chaudhary

Abstract A compact planar monopole antenna with band-notched characteristics suitable for ultra-wide band operation is presented. The antenna consists of a goblet-shaped patch with a wide bandwidth ranging from 2.6 to 11.7 GHz. A good band reject performance is obtained by suitably placing the vertical strip on one of the lower sides of goblet-shaped radiating patch. The specialty in the design is its simplicity and compactness. Antenna occupies a very small size of $20(W) \times 33(L) \times 1.6(H)$ mm³. Because of its compactness and good radiation performance; it can be easily integrated with mobile wireless devices for UWB applications.

Keywords Goblet antenna · Band-notched · Ultra-wide band (UWB)

Introduction

UWB has attracted much attention over the past decade. There are two reasons for its popularity. First, in the year 2002, Federal Communication Commission (FCC) allowed the usage of frequency band 3.1–10.6 GHz. Second, UWB

R.K. Raj (✉)

Department of ECE, Government Engineering College, Ajmer, India
e-mail: raj_raj2002@rediffmail.com

Krishna Rathore · Roopkishor Sharma
Government Engineering College, Ajmer, India
e-mail: rathore65@gmail.com

Roopkishor Sharma
e-mail: roopkishorbtp@gmail.com

Bhavana Peswani
Government Women Engineering College, Ajmer, India
e-mail: bhavnapesswani21@gmail.com

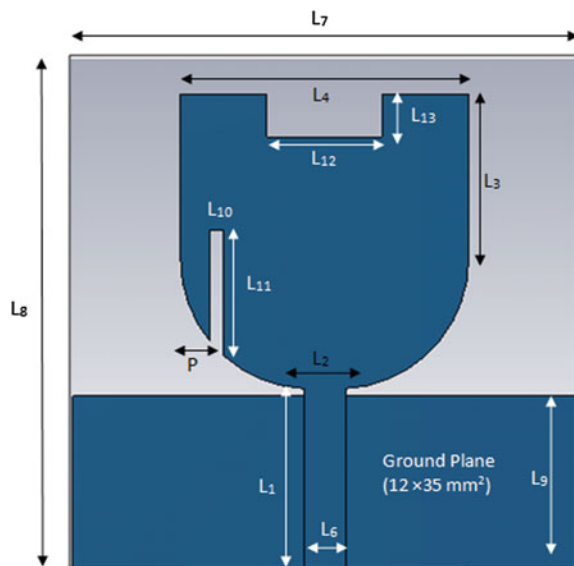
H.R. Chaudhary
Department of CSE, Government Engineering College, Ajmer, India
e-mail: roopkishorbtp@gmail.com

communication possesses several advantages such as high data rate, less interference, small emission power and low cost [1]. The problem of frequency interference rose because there are several wireless technologies such as WLAN/HiperLAN (5.15–5.85 GHz), WiMax (3.3–3.85 GHz) operating in UWB band. To deal with the effect caused by frequency interference, many UWB antennas with band-notched characteristics have been reported [2–10]. These papers have presented many techniques to obtain band notch like parasitic inverted U strip [2], conducting strips [3, 4], defected ground structures [5], complementary split ring resonators [6], I-shaped multi slots [7] and U-shaped slots [8–10]. However, all of these designs are quite complex but the idea here is that a simple design with the same band-notched performance can be produced. In this paper, we thus propose an antenna that simply employs a thin vertical slot with its optimized length, width and position. The antenna is compact and at the same time gives stable radiation performance hence, it is easy to integrate it with wireless portable devices.

Antenna Design

The antenna structure is shown in Fig. 1. The antenna uses FR4 substrate with dielectric constant 4.4 and loss tangent 0.0023. The thickness of the substrate is 1.6 mm. This antenna is fed by a $50\ \Omega$ microstrip line having width of 2.9 mm. The patch is in the form of a goblet shape with a vertical thin slot at the lower side of the patch and a notch in the centre at the upper side of the patch. The overall dimension of the antenna is merely $20(W) \times 33(L)$ mm². A partial ground plane is used with

Fig. 1 Geometry of the proposed UWB band-notched antenna



length 12 mm and width 35 mm. Slots has been cut on goblet-shaped patch structure. The goblet shape is formed using two circles of radius 9 mm(R) with centres 2 mm apart from the original centre in x direction and with a rectangular strip ($L_3 \times L_4$) extended from the x -axis into the y -direction [11]. A vertical thin slot has been cut from the sensitive portion of the patch.

In our antenna design, the length and position of the vertical slot plays a critical role in deciding the centre-rejected frequency. Optimum design parameters are listed below. When antennas are implemented practically, the stopband frequency of the antenna gets shifted. To overcome this effect, the stopband characteristics of the antenna can be controlled by flexibly tuning either the width (L_{10}), length (L_{11}) or the position (P) of the vertical slot.

The optimum dimensions of the proposed antenna are $L_1 = 12.5$ mm, $L_2 = 4$ mm, $L_3 = 11.5$ mm, $L_4 = 20$ mm, $L_5 = 33$ mm, $L_6 = 2.9$ mm, $L_7 = 35$ mm, $L_8 = 35$ mm, $L_9 = 12$ mm, $L_{10} = 1$ mm, $L_{11} = 2$ mm, $L_{12} = 2$ mm, $L_{13} = 1$ mm, $R = 9$ mm, $P = 2$ mm.

Results and Discussions

Computer simulation technology (CST) 2011 is used to design and simulate the proposed antenna. The return loss curve of the proposed antenna for optimized parameters is shown in Fig. 2. The curve shows that the impedance bandwidth of the antenna ranges from 2.6 to 11.7 GHz. There is a band notch from 4.9 to 6.1 GHz. This efficiently excludes the WLAN region (5.15–5.85 GHz), so the effects due to frequency interference can be avoided well.

To easily visualize the band notch characteristics, the surface current distribution of the antenna at the centre-rejected frequency of 5.6 GHz has been simulated in Fig. 3. We see that a major portion of current is flowing through vertical slot as compared to the complete surface area of patch. This is in accordance with the frequency rejection property of band-notched antennas.

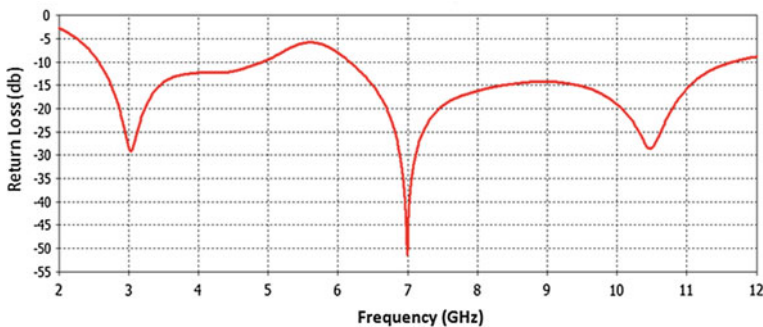


Fig. 2 Simulated return loss of the proposed antenna

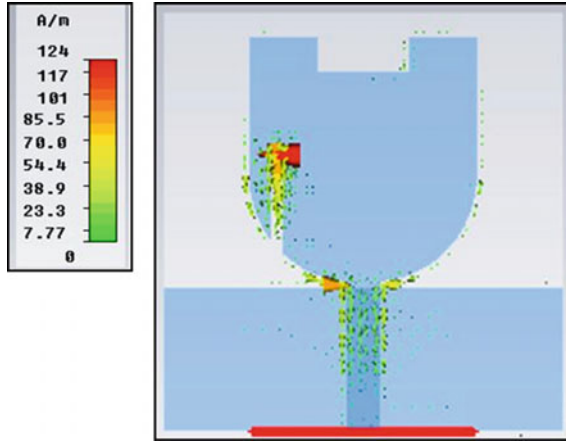


Fig. 3 Simulated surface current distribution at the centre-rejected frequency of 5.6 GHz for the proposed antenna

Further, we observed the operation of antenna for different valued parameters of vertical slot. First, the length (L_{11}) of the slot is varied from 1 to 4 mm as shown in Fig. 4a. It is seen that as the length increases, when the notched band shifts towards left. For the length of 4 mm, the notched region covers 3.5–5.5 GHz. Second, the

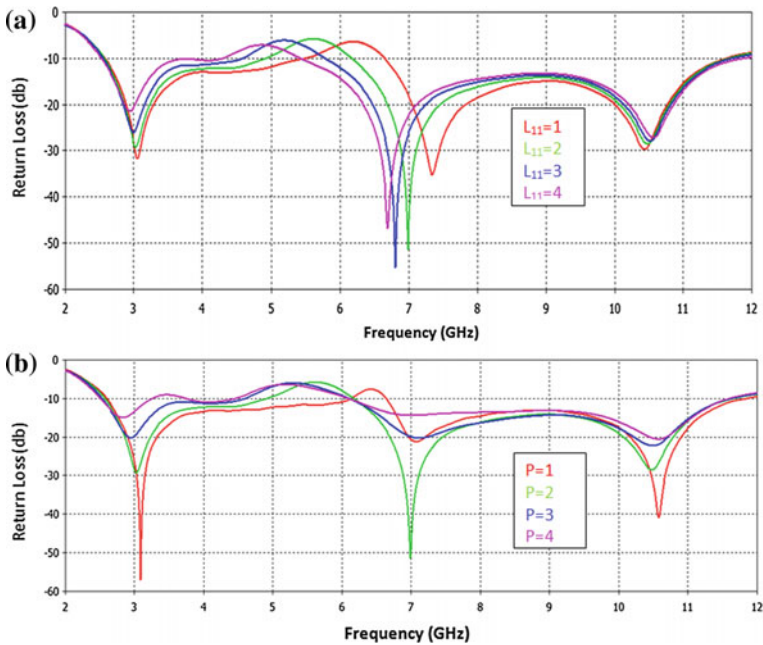


Fig. 4 Simulated return loss for different design parameters regarding the stop band property **a** Slot length L_{11} **b** Slot position P

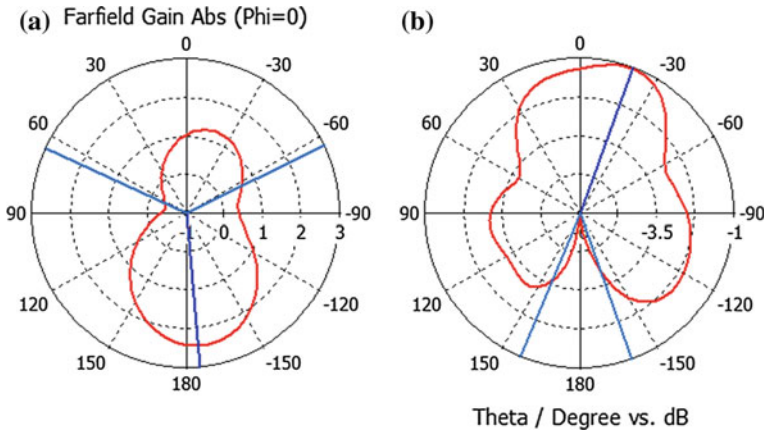


Fig. 5 Simulated radiation pattern of the proposed antenna at a 4 GHz b 8 GHz

position (P) of the slot is varied with respect to the left side of the goblet. The simulation result is shown in Fig. 4b. We see that as the slot is shifted right, the notched band widens up and slightly shifts towards left. The optimized position of the slot was taken as 1 mm plus the width of the slot. It is further observed that antenna is capable of achieving a tunable stopband range from 3.5 to 6.5 GHz.

Figure 5a, b shows the far field radiation pattern at the frequencies of 4 and 8 GHz. The antenna shows slightly bidirectional radiation patterns at the frequencies 4 GHz and omnidirectional radiation pattern can be seen for 8 GHz frequency. Thus, a good and uniform coverage can be obtained through this antenna design.

Figure 6 shows the VSWR result for the proposed antenna design. The value of VSWR is below 2 for the entire operating band except for the rejected frequency

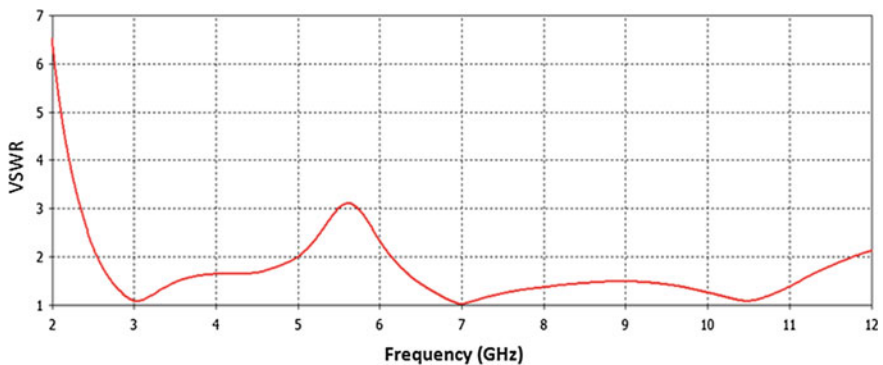
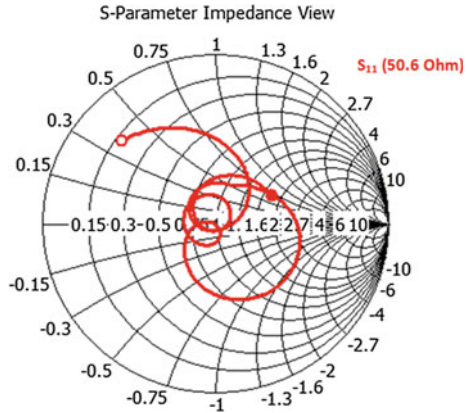


Fig. 6 Simulated VSWR characteristics of the proposed antenna

Fig. 7 S-parameter impedance graph of the proposed antenna



band. It is properly matching with the theoretical concepts of band notching. Figure 7 gives a proof that the microstrip feed line impedance in our antenna is well matched to 50 Ω , as it is easier to get 50 Ω port connectors in the market.

Conclusion

A compact goblet-shaped monopole antenna with band-notched characteristics for UWB operation is studied. The antenna possesses compactness, simplicity and good radiation performance. Compared to other conventional designs, this antenna structure is very simple at the same time gives better band-notched performance. Besides this, the notched band can be easily tuned so the frequency interference issues could be handled well. Furthermore, because of stable transmission characteristics and compact size of the antenna, it is well suited to be integrated with different wireless portable devices.

References

1. Jung, J., Choi, W., Choi, J.: A small wideband microstrip-fed monopole antenna. *IEEE Microwave Wirel. Compon. Lett.* **15**(10) (2005)
2. Fallahi, R., Kalteh, A.A., Golparvar, M.: A novel UWB elliptical slot antenna with band-notched characteristics. *Prog. Electromagn. Res. PIER*, **82**, 127–136 (2008)
3. Ryu, K.S., Kishk, A.A.: UWB antenna with single or dual band-notches for lower WLAN band and upper WLAN band. *IEEE Trans. Antennas Propag.* **57**(12), (2009)
4. Liu, H.-W., Ku, C.-H., Wang T.-S., Yang, C.-F.: Compact monopole antenna with band-notched characteristics for UWB applications. *IEEE Antennas Wirel. Propag. Lett.* **9** (2010)
5. Liu, W.-C., Wu, C.-M., Dai Y.: Design of triple frequency microstrip fed monopole antenna using defected ground structure. *IEEE Trans. Antenna Propag.* **59**(7), (2011)

6. Kamma, A., Reddy, G.S., Parmar, R.S., Mukherjee, J.: Reconfigurable dual- band notch UWB antenna. *IEEE* (2014)
7. Abdollahvand, M., Dadashzadeh, G., Mostafa, D.: Compact dual band- notched printed monopole antenna for UWB application. *IEEE Antennas Wirel. Propag. Lett.* **9** (2010)
8. Zhou, H.J., Sun, B.H., Liu, Q-Z., Deng, J.-Y.: Implementation and investigation of U-shaped aperture UWB antenna with dual band-notched characteristics. *Electron. Lett.* **44**(24), 1387–1388 (2008)
9. Dissanayake, T., Esselle, K.P.: Prediction of the notch frequency of slot loaded printed UWB antennas. *IEEE Trans. Antenna Propag.* **55**(11), 3320–3325 (2007)
10. Jang, J.W., Hwang, H.Y.: An improved band-rejection UWB antenna with resonant patches and a slot. *IEEE Antennas Wirel. Propag. Lett.* **8**, 299–302 (2009)
11. Lodi, G.A., Zafar, R.I., Bilal, M.: A novel goblet shaped patch antenna for ultra wide band applicayions. *IEEE* (2010)

An Application of Firefly Algorithm for Clustering in Wireless Sensor Networks

Arshad Nadeem, T. Shankar, Rakesh Kumar Sharma
and Sourabh K. Roy

Abstract Wireless sensor network gained popularity during the past few decades due to the ad hoc nature, which makes it easy to install in a landscape where human may not be able to approach. Wireless Sensor Network (WSN) is considered for networks consisting of many tiny sensor devices running on batteries. This type of wireless sensor networks are deployed to fulfil a specific objective for a long period of time, hence the energy consumed in communication should be optimized to prolong the network. This paper presents the energy optimization method using Firefly algorithm to prolong network lifetime. Firefly algorithm is a nature inspired optimization technique that is based on the behaviour of an insect known as “Firefly” that produces the flashing light mainly to attract the pray and to attract the mating partner. The proposed algorithm for effective communication is compared with LEACH and ABC (Artificial Bee Colony) optimization for cluster-based sensor network and the simulated result shows the better performance.

Keywords Wireless sensor network · Clustering · Firefly · Optimization · Radio model

Critical Review of Literature

Wireless sensor network is a scenario where a base station collects all the sensed data from sensor nodes distributed randomly in the field. The typical applications [1] of wireless sensor network are in temperature, pressure, humidity, in military

Arshad Nadeem (✉)

Department of ECE, Poornima Group of Institutions, Jaipur, India
e-mail: arshad.nadeem@poornima.org

T. Shankar

School of Electronics Engineering, VIT University, Vellore, India
e-mail: tshankar77@gmail.com

R.K. Sharma · S.K. Roy

Computer Science Engineering, Poornima Group of Institutions, Jaipur, India

© Springer India 2016

N. Afzalpulkar et al. (eds.), *Proceedings of the International Conference on Recent Cognizance in Wireless Communication & Image Processing*,
DOI 10.1007/978-81-322-2638-3_98

applications to sense the motion in hostile environment and many more. These sensor nodes are easily configurable, ready to install and works with limited battery power. Clustering [2] is one of the preferred approaches to improve the network life time and performance. Clustering provides the better resource utilization and better management of wireless sensor nodes also it provides the load sharing. LEACH [3] protocol performs better than conventional routing like direct transmission. LEACH protocol is a self organized and adaptive clustering protocol for selecting proper cluster head for the single hop [2] networks. Later some variants of LEACH was introduced, i.e. LEACH-C, ALEACH [4], etc. Although LEACH provides good method of communication but it has several disadvantages discussed in the further sections of the paper.

Distance between the communicating nodes is the major factor of energy dissipation [5] apart from the internal signal processing by electronics. Also the energy dissipation is depending upon the square of the distance between source and sink, which is a non linear dependency. There are few nature inspired optimization algorithm was used recently for proper cluster head selection in order to provide energy efficient communication. Some energy optimization algorithms are PSO (Particle Swarm Optimization), ABC (Artificial Bee Colony) algorithm [6] which is used for energy optimization. These algorithms are complex in nature but it provides better performance than LEACH protocol. The protocol running on the network should be real time and fast executing. To perform better the proposed protocol is satisfactorily functional while it was also used in many other optimization problems [7, 8]. This paper implements the Firefly optimization [4] to increase the network life time. The proposed algorithm is compared with LEACH and ABC algorithm. Further sections of this paper describe the first order radio model, Firefly algorithm, proposed method for selecting cluster heads and the simulations.

First Order Radio Model

The first order radio model describes the function of a sensor node as shown in Fig. 1. A sensor node basically has a transmitter electronics which perform the task of modulation, coding and various signal conditioning while the receiver perform the reverse process of it hence the energy consumed by both the blocks will remain same.

The energy consumed by transmit amplifier depends on the distance of communication. An assumption has made that the radio electronics consume $E_{elec} = 70$ nJ/bit [3] for transmission and reception of data and the transmitter amplifier need $\epsilon_{amp} = 120$ pJ/bit/m² energy to make suitable transmission as mentioned in Table 1.

A sender node transmits the signal ensuring that the antenna of the receiver node is in the range of the signal reception. According to Friis transmission equation shown in Eq. 1, the received power is inversely proportional to the square of the distance between transmitter and receiver.

Fig. 1 First order radio model

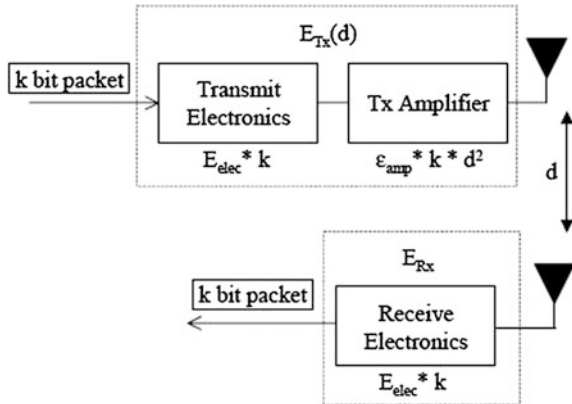


Table 1 Parameters of first order radio model

Process	Energy dissipation
Transmitter electronics ($E_{Tx_{elec}}$)	70 nJ/bit
Receiver electronics ($E_{Rx_{elec}}$) ($E_{Tx_{elec}} = E_{Rx_{elec}} = E_{elec}$)	
Transmit amplifier (ϵ_{amp})	120 pJ/bit/m ²

$$P_r = \frac{P_s \cdot A_s \cdot A_r \cdot \lambda^2}{(4 \cdot \pi \cdot d)^2} \tag{1}$$

where P_r , P_s , A_r , A_s , λ , d , represents the received power, sender power, receiver antenna gain, sender antenna gain, wavelength of signal, distance between receiver and sender, respectively. The received signal strength P_r must be greater than the radio sensitivity S as mentioned in Eq. 2.

$$P_r \geq S \tag{2}$$

$$S \leq \frac{P_s \cdot A_s \cdot A_r \cdot \lambda^2}{(4 \cdot \pi)^2 \cdot d^2} \tag{3}$$

Equation (3) can be written from Eqs. (1) and (2). Consider the limiting case that received power P_r is equal to the radio sensitivity of the receiver S , also for the given wave length λ , other parameters A_r , A_s , P_s , will remain constant which is represented with the symbol Ω in Eq. (4).

$$\Omega = \frac{S \cdot (4\pi)^2}{A_s A_r \lambda^2} \tag{4}$$

It can be concluded from Eqs. (3) and (4) as follow Eq. (5).

$$P_s \geq \Omega.d^2 \quad (5)$$

Above Eq. (5) clearly shows that the power consumed by the transmit amplifier is directly proportional to the distance between communicating sensor nodes.

Energy Analysis

According to the above described first order radio model the energy consumption is highly dependent on distance between communicating element. Due to the communication overhead the network may drain out quickly hence our objective is to analysis the equations for energy consumption and to provide the solution to reduce energy consumption. Transmitter requires the energy for transmitting a frame of k bits as below.

$$\begin{aligned} E_{tx}(k, d) &= E_{txelec}(k) + E_{txamp}(k, d) \\ E_{tx}(k, d) &= E_{elec} * k + E_{amp} * k * d^2 \end{aligned} \quad (6)$$

And, at the receiver

$$\begin{aligned} E_{rx}(k) &= E_{rxelec}(k) \\ E_{rx}(k) &= E_{elec} \end{aligned} \quad (7)$$

The above Eqs. (6) and (7) describes the cost of communication is depending mainly on the communication distance hence the protocol must avoid the redundant transmission and optimize the distance between transmitter and receiver.

Clustering Algorithms

Nodes in the WSN transmit data to base station by relying each other in cooperative manner. The clustering algorithm should be dynamic for better performance of network and distributive hence some time nodes may function as router as well. As we discussed earlier clustering is the preferred approach in WSN for data transmission. LEACH protocol effectively provides better load sharing and better management of sensor nodes.

(a) *LEACH Algorithm*: LEACH is a dynamic clustering routing method where nodes are selected as cluster head randomly based on a threshold equation [3] given in Eq. (8). In the beginning the selection of cluster head is done based on the priori, then all the nodes in the network joins one cluster head at a time for the given round

which consumes least energy based on distance. When nodes are organized in clusters, every cluster head creates a time division schedule, providing entire bandwidth to a member node for an allotted time meanwhile other member nodes remain silent and wait for their turn to transmit to cluster head.

$$T(n) = \begin{cases} \frac{p}{1-p^{*(r \bmod \frac{1}{p})}} & \text{if } n \in G \\ 0 & \text{otherwise} \end{cases} \tag{8}$$

At the beginning of each round “r” every node determines whether it become cluster head or a member node based on the prior percentage “p” of nodes to be cluster head. To make the decision each node generates a random number between 0 and 1. If the generated number is less than the Threshold T(n), then the node become cluster head for the current round. Equation (8) shows the value of T(n) is depending on the rounds which repeats the value after every 1/p rounds, where G is the set of node which have not been elected as cluster head within last 1/p rounds.

Artificial Bee Colony (ABC) optimization: Artificial Bee Colony (ABC) algorithm is a nature inspired optimization algorithm based on the food search method used by honey bees. ABC optimization method was used in wireless sensor networks [6] to find the solution or to select the appropriate cluster heads. The ABC algorithm evaluates the fitness function given by Eq. (9) for each cluster head and then performs the iterative optimization for certain number of optimization cycles.

Fitness Function

The fitness function is defined as the fitness value which is inversely proportional to the energy consumed for a round. Consider the “t” time required for signal to reach at destination then the sender would require energy given by Eq. (9), using the Eq. (5) as follow.

$$E = \sum_i^m (Ps_i.t) \geq \Omega \left[\sum_i^m d_i^2 + b^2 \right].t \tag{9}$$

where i is the index for member nodes for total m number of members in a cluster, d is the distance from member node to the cluster head and b represents the distance from cluster head to base station. Let’s take $\Omega.t = q$ in Eq. (9) and rewrite it as follow.

$$E \geq q. \left[\sum_i^m d_i^2 + b^2 \right] \tag{10}$$

The individual fitness of a cluster head can be given as

$$f_i = \left[q \cdot \left[\sum_i^m d_i^2 + b^2 \right] \right]^{-1} \quad (11)$$

For multiple clusters the minimum energy consumption can be written as below by Eq. (11), where j is the index for a cluster and c is the total number of cluster heads in the network.

$$\sum_{j=1}^c E \geq q \cdot \sum_j^c \left[\sum_i^{m_j} d_{ij}^2 + b_j^2 \right] \quad (12)$$

It is evident from the above Eq. (12), for selecting the appropriate cluster head the sum of the distances between member nodes to cluster head should be minimize also the distance between cluster head to base station, which gives the minimum energy consumption for a round, likewise the optimization process to be done up to the maximum number of optimization cycles. The fitness function can be written as

$$f = \left[q \cdot \sum_j^c \left\{ \sum_i^{m_j} d_{ij}^2 + b_j^2 \right\} \right]^{-1} \quad (13)$$

However, the ABC optimization technique is optimizing the distances, which is the major factor for energy consumption but still it has drawback. While selecting the cluster head the residue energy of the node is not taken into consideration, thereby the chance of early death is possible.

(b) Firefly Algorithm: The firefly is an insect which produce shining light to attract other insects as food source also to attract opposite sex for copulation. The illuminative behaviour of firefly is used to solve the optimization problem in [8, 9]. It is a unique feature of firefly to illuminate glow for signalling purpose, however, it is still a topic of debate, but with few assumption [4] this property of firefly is used successfully for optimization. (i) All the fireflies are independent of gender, hence any firefly can attract to any other. (ii) The attractiveness of the firefly modifies with the distance, however, the attractiveness is proportional to the brightness of other fireflies, the less brighter firefly attract towards the more brighter firefly, as the distance increases the attractive decreases. (iii) If the entire firefly has similar brightness then there will be random motion of fireflies. Brightness of the firefly is evaluated by the objective function $f(x)$. Each firefly is attracted by the brighter neighbour and occupies the new location as per the Eq. (15). Each firefly has a distinct value of relative attractiveness $\beta(r)$ depending upon the Euclidian distance r , between them as given in Eq. (14)

$$\beta(r) = \beta_0 \cdot e^{-(\gamma \cdot r^2)} \tag{14}$$

where β_0 is the attractiveness at the $r = 0$, and γ is the light absorption coefficient varying as $[0, \infty)$. The movement of firefly i located at x_i towards brighter firefly j located at x_j is given as

$$x_i(t + 1) = x_i(t) + \beta_0 \cdot e^{-(\gamma \cdot r^2)} (x_j - x_i) \tag{15}$$

The optimization problem can be solved as per the pseudo code below.

```

Objective function  $f(x)$ , where  $x = (x_1, x_2 \dots x_d)$ 
Initialization of population of fireflies  $x_i (i=1, 2 \dots n)$ 
Calculate the light intensity  $I_i$  at  $x_i$  by  $f(x_i)$ 
Initialize the value of  $\gamma$ 
while ( $t < \text{MaxCycle}$ )
    for  $i=1:n$  all fireflies
        for  $j=1:n$  all fireflies
            if ( $I_j > I_i$ )
                move firefly  $i$  towards  $j$ 
            end if
            Adjust attractiveness with distance  $r$ 
            Calculate new solution and update light intensity
        end for  $j$ 
    end for  $i$ 
    Rank the fireflies and find the current best
end while
    
```

Cluster Head Selection Using Firefly Algorithm: Proposed Approach

This section describes the implementation of energy efficient routing using firefly algorithm. The objective of the algorithm is to select the appropriate cluster head to reduce the energy consumption for each round and to increase the network life time. The clustering mechanism of the proposed algorithm is based on the LEACH also the calculation of fitness function is based on the ABC algorithm discussed in previous section. The major advantage of proposed approach is the consideration on residue energy while selecting the cluster heads. The cluster head selection algorithm is implemented at the base station, which maintain the table of current cluster heads and the inter distance.

Assume that n is the total number of nodes deployed randomly in the monitoring zone. For k number of clusters the cluster head selection algorithm is implemented as below:

Step 1: Initialize the population with randomly selected k number of cluster heads. Create the clusters by assigning non cluster head nodes to the selected cluster heads as per the minimum distances.

Step 2: Calculate the fitness function of each cluster head by Eq. (11).

Step 3: Perform the cluster head update according to firefly algorithm.

- (i) Select the member nodes which is having higher energy as cluster head in each cluster, discard the previous one.
- (ii) Create the new clusters according to newly elected cluster heads.

Step 4: Calculate the fitness of newly elected cluster heads and find out the best cluster heads comparing with step 2.

Step 5: Repeat the steps from step 2 to step 5, until the maximum number of cycle is reached.

Simulations and Result

The proposed algorithm is simulated on MATLAB with various parameters. In the simulation, 100 nodes are considered which are distributed randomly in the field of 100×100 as shown in Fig. 2 while the base station is located at (100, 150). It is assumed that all the nodes are in the range of communication to base station and the nodes are TDMA synchronized within the cluster with cluster head. The radio parameters for transmitter and receiver is taken as per given in Table 1 and the energy consumption is calculated as discussed in the previous section. The nodes has probability of being elected as cluster is $p = 10\%$ for LEACH and we set the number of cluster heads as 10% of alive nodes (active nodes) for ABC and Firefly algorithm.

Fig. 2 First node death

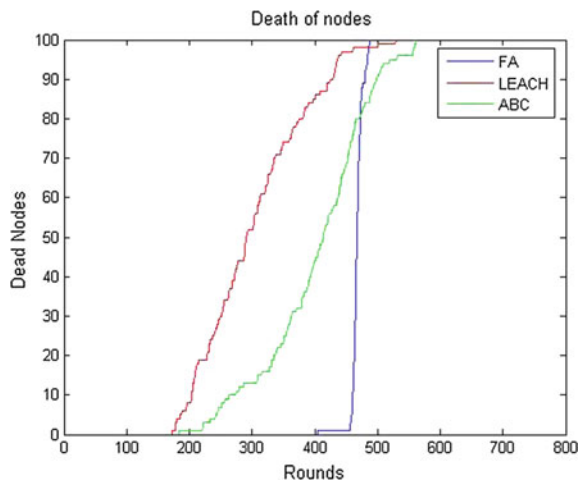


Fig. 3 Residual energy of the network

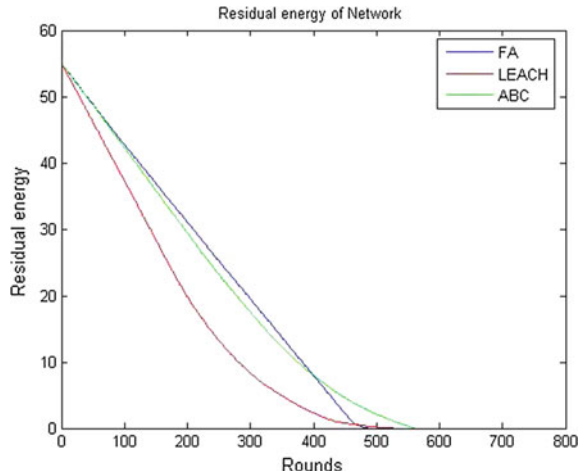


Table 2 Occurrence of first node death

Protocols	First node death (round)
Proposed firefly clustering algorithm	404
ABC clustering algorithm	183
LEACH	170

To accomplish the simulation we prepared a discrete model in which all the nodes are sending fixed amount of data $k = 4096$ bits periodically in each round. To verify the proposed algorithm the simulation is compared with LEACH and ABC algorithm for cluster head selection with similar parameters. In simulation the initial energy level for normal nodes are set to 0.5 Joule and for the 10 % advanced nodes it is set to 1 Joule for each advance nodes.

The simulated comparison for the first node death is shown in Fig. 2. It is clear from Fig. 3 the proposed algorithm increased the first node death occurrence significantly as compare to LEACH & ABC clustering. Table 2 contains the occurrence of First Node Death (FND) which specifies the beginning of decay of nodes.

Figure 3 shows the residue energy of the entire network, the energy left out in the nodes which are higher in the proposed method. The throughput of the sensor network is defined as the bits transferred to the base station in each round.

Conclusion

The main task of a sensor network is to gather the information periodically which needs the longer lifetime of the network. The proposed clustering method has improved the life time of the network and the throughput as demonstrated in above

section. The occurrence of first node death in firefly clustering method is achieved lately as compared to ABC clustering algorithm and LEACH, hence the proposed method give about 40 % improvement in the first node death.

References

1. Akyildiz, I.F., Su, W., Sankarasubramaniam, Y., Cayirci, E.: Wireless sensor networks: a survey. *Comput. Netw.* **38**, 393–422, (2002)
2. Younis, O., Krunz, M., Ramasubramanian, S.: Node clustering in wireless sensor networks: recent developments and deployment challenges, *IEEE* (2006)
3. Heinzelman, W.R., Chandrakasan, A., Balakrishnan, H.: Energy-Efficient Communication Protocol for Wireless Microsensor Networks. In: *Proceedings of the 33rd Hawaii International Conference on System Sciences* (2000)
4. Ali, M.S. Dey, T., Biswas, R.: ALEACH: Advanced LEACH routing protocol for wireless microsensor networks. In: *5th International Conference on Electrical and Computer Engineering*, *IEEE* (2008)
5. Zhang, W., Liang, Z., Hou, Z., Tan, M.: A power efficient routing protocol for wireless sensor network. In: *Proceedings of the IEEE International Conference, Networking, Sensing and Control*, London, UK, 15–17 April 2007
6. Karaboga, D., Okdem, S., Ozturk, C.: cluster based wireless sensor network routings using artificial bee colony algorithm, *IEEE* (2010)
7. Bian, Q., Zhang, Y., Zhao, Y.: Research on clustering routing algorithms in wireless sensor networks. In: *International Conference on Intelligent Computation Technology and Automation*, *IEEE* (2010)
8. Senthilnath, J., Omkar, S.N., Mani, V.: *Clustering using firefly algorithm: performance study*, Elsevier (2011)
9. Sulaiman, M.H., Mustafa, M.W., Zakaria, Z. N., Aliman, O., Abdul Rahim, S.R.: Firefly algorithm technique for solving economic dispatch problem. In: *IEEE International Power Engineering and Optimization Conference (PEOCO2012)*, Melaka, Malaysia, 6–7 June 2012

Microstrip Antenna with Defected Ground Structure (DGS) for Multiband Operation

Vinay Sharma and Rajesh Kumar Vishwakarma

Abstract In this paper, a microstrip feeding rectangular MPA using DGS structure into ground plane is presented. In the absence of a slot, a conventional rectangular MPA is also considered for confirming the validity of designed antenna. This conventional antenna design was found to resonate on 7.0611 GHz frequency at -23.70 dB return loss. When introducing the combination of two L-shaped DGS structures into the ground plane, then the frequency shift from 7.0611 GHz to 3.2012 GHz is observed. The main involvement of this antenna design is the multiband responses. Further, the end result confirms that the designed DGS antenna has return loss at -14.0170 dB on 3.2012 GHz, -16.5623 dB on 4.4505 GHz, -17.8874 dB on 5.1952 GHz, and -17.5474 dB on 8.9349 GHz.

Keywords Multiband antenna · MPA (microstrip patch antenna) · DGS (defected ground structure)

Introduction

The wireless communication's predominant growth forces the researchers to design a low profile, small in size, and low cost antenna for multifrequency operation. Telecommunication technology is only one technical field which has great concern in many applications like military, professional, and civil sphere. Due to commercial increment of multifarious electrical devices, antenna devices of recent

Vinay Sharma (✉) · R.K. Vishwakarma
Department of Electronics and Communication Engineering,
Jaypee University of Engineering and Technology, Guna, India
e-mail: vinaysharma.y7@gmail.com

R.K. Vishwakarma
e-mail: rkv.786@gmail.com

communication have to be capable to receive and transmit electromagnetic waves in different frequency bands associated with different communication services [1]. The performance parameter of the single band MPA only works properly at the design frequency.

Now, we turn our attention toward multiband microstrip antenna meant for multifrequency operation of numerous applications. Multiband antenna works in several bands with slight modification. Conventionally, a single band antenna cannot work at all bands of frequency for mobile communication; multiple band antennas can cover these bands separately. To achieve multiband response several strategies have been developed. In [2], a multiband microstrip antenna was presented with a defects ground structure which is conventionally conformal and appropriate for WLAN applications. In [3], the authors mainly focus on the basic concept and characteristics of DGS structure. DGS structure is basically formed in periodic/nonperiodic configuration defect etched into ground plane. A rectangular MPA with slots on patch and DGS structure into ground plane level was introduced. Without slots and DGS, the MPA was found to resonate on 5.22 GHz and by introducing slots and DGS frequency shift from 5.22 GHz to 1.56 GHz was observed [4]. In [5], microstrip antenna using periodic cross strip-line gaps as DGS structure is created. The suitable comparison between the outcome of conventional antenna and DGS antenna has been present. In [6], a compact multiband MPA using DGS was introduced. The design for the MPA consist an H-shaped slot on top of the patch along with DGS structure of U and L shape into ground plane level. This antenna design operates on multifrequency bands. A planar array MPA in [7] using DGS structure for multiband operations is presented. The combination of I-shape DGS structure is etched out into ground plane level. The outcomes of this planar array microstrip antenna by the use of DGS and without DGS have been taken into consideration. In [8], MPA with I-shaped DGS is introduced for improved bandwidth of 118 % compared to conventional design.

This antenna design also confirms additional improvement in parameters like gain, return loss and radiating patch size. In [9], the paper presents a L-shaped loaded multiband microstrip antenna designed for wireless, DCS, and WLAN applications.

Antenna Configuration

In this paper, MPA (microstrip patch antenna) is designed and analyzed with the help of ANSOFT HFSS software [10]. For explicit comparison, it is essential to propose a conventional MPA as a reference. This conventional antenna designed on FR4 epoxy dielectric material of 1.6 mm thickness having ϵ_r (relative permittivity)

Fig. 1 Conventional MPA (microstrip patch antenna)

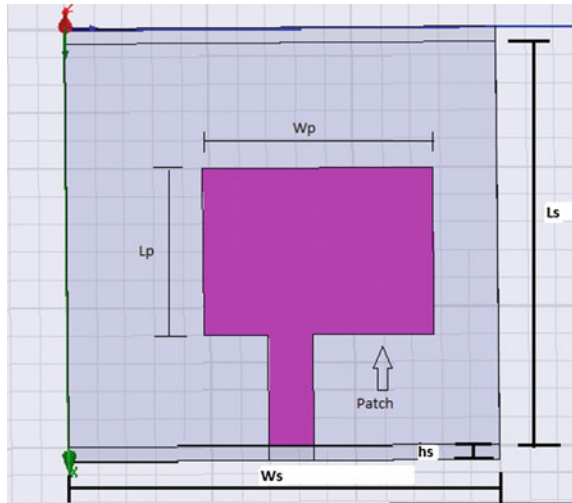


Table 1 Common design specification for both antennas

S. no	Specification	Dimensions
1	Ground plane	$W_g = 30 \text{ mm}$, $L_g = 30 \text{ mm}$
2	Substrate	$W_s = 30 \text{ mm}$ $L_s = 30 \text{ mm}$ $h_s = 1.6 \text{ mm}$
3	Rectangular patch	$W_p = 12.67 \text{ mm}$ $L_p = 9.29 \text{ mm}$
4	Permittivity of substrate material	4.4

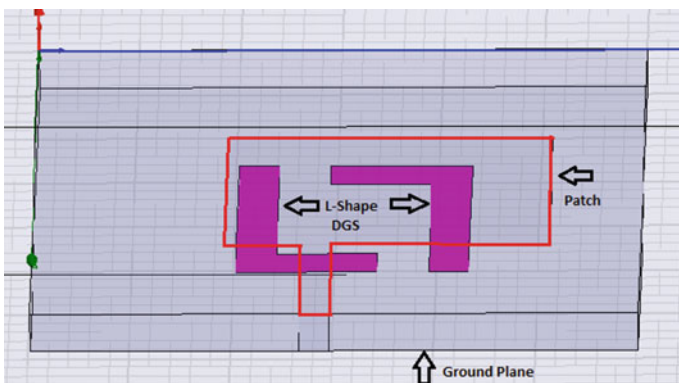


Fig. 2 L-shaped DGS MPA (microstrip patch antenna)

of 4.4 and design frequency of 7.2 GHz. In Fig. 1 front view of the reference conventional MPA is present. Width and length of MPA are simply given in [11]. This conventional antenna operates at 7.0611 GHz frequency of single band with 192.2 MHz bandwidth. Table 1 explains the appropriate detail about the parameter dimension of the designed antenna.

In Fig. 2 the DGS MPA configuration is present, in which the patch is considered as without slot. Two L-shaped DGS structures are etched into ground plane level. These two L-shaped DGS are integrated in the center of ground plane. This geometry, forces the current to split in multiple paths and we observed multiband frequency response. Design specification of DGS antenna without defects is similar to conventional antenna as given in Table 1.

Fig. 3 a Return loss (S11) versus frequency. b Return loss (S11) versus frequency

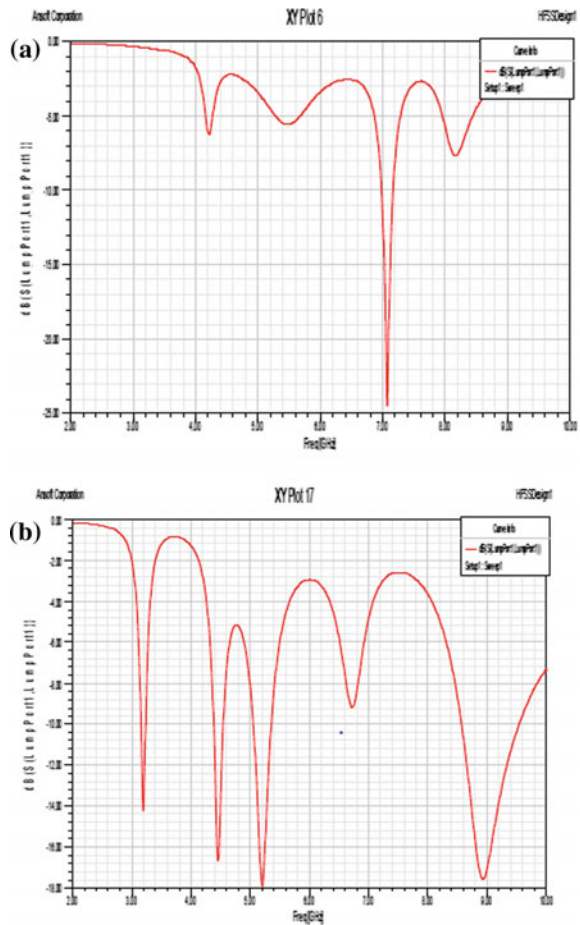
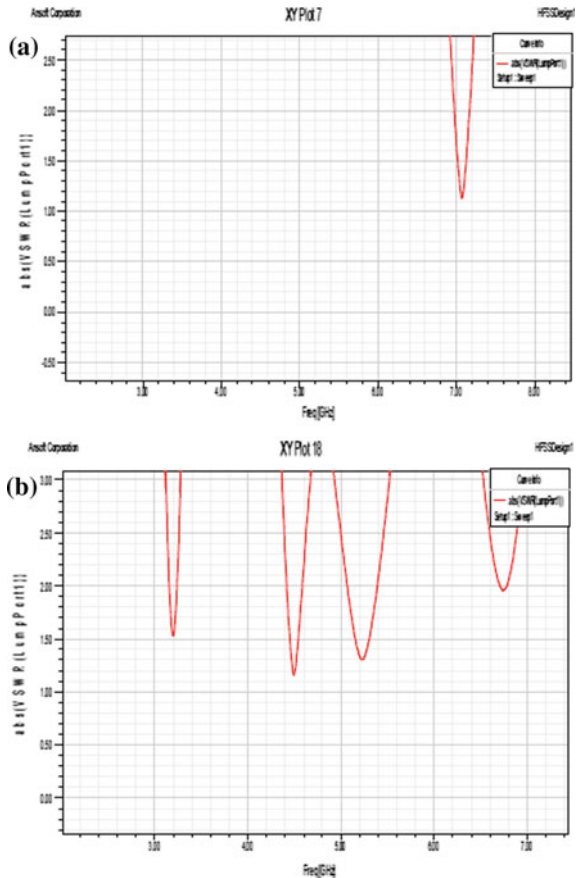


Table 2 Comparison of simulated results for both antennas

S. no	Parameters	Conventional antenna	L-shaped DGS antenna
1.	Resonating frequency (GHz)	$f_1 = 7.0611$	$f_1 = 3.2012$
			$f_2 = 4.4505$
			$f_3 = 5.1952$
			$f_4 = 8.9349$
			$BW1 = 80$
2.	Bandwidth (MHz)	$BW1 = 192.2$	$BW2 = 152.1$
			$BW3 = 304.3$
			$BW4 = 960.9$
			-14.017 at f_1
3.	Return loss (dB)	-23.70 at f_1	-16.562 at f_2
			-17.887 at f_3
			-17.547 at f_4
4.	VSWR	1.1468	1.2907
5.	Gain	1.5386	5.0128

Fig. 4 **a** VSWR versus frequency. **b** VSWR versus frequency



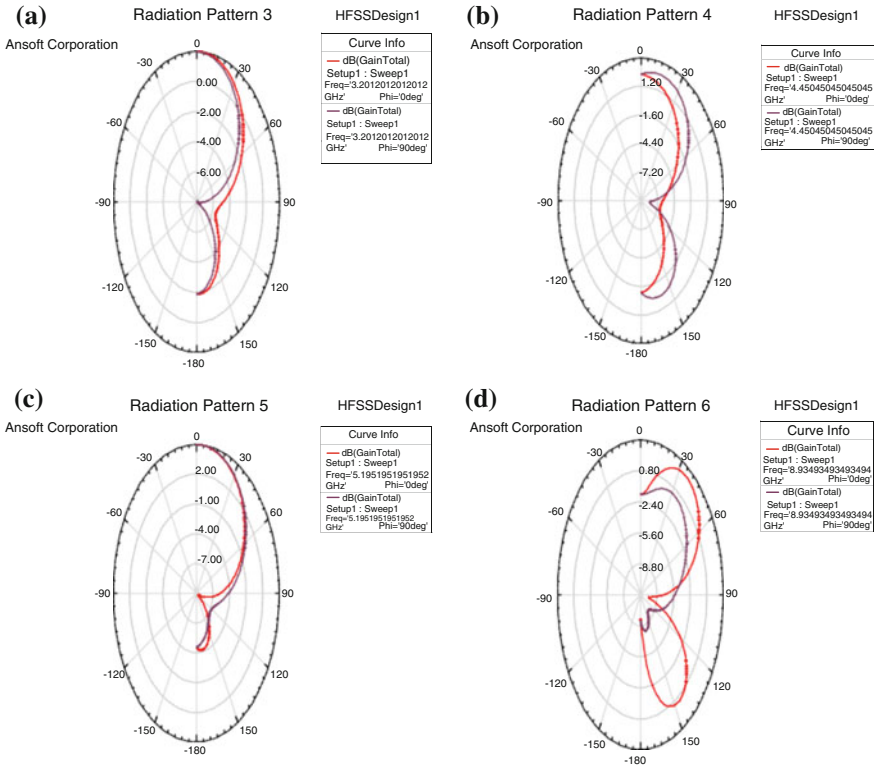


Fig. 5 a 2D radiation pattern for E-plane at 3.20 GHz. b 2D radiation pattern for E-Plane at 4.45 GHz. c 2D radiation pattern for E-plane at 5.19 GHz. d 2D radiation pattern for E-plane at 8.93 GHz

Results and Discussion

The outcome shown here is simulated on HFSS software to determine the characteristic parameters of design antenna such as VSWR, return loss, and impedance bandwidth.

Return Loss and Impedance Bandwidth

The graphs of Fig. 3 confirm a relative comparison between the conventional antenna and the L-shaped DGS antenna. Graph 3a indicates that the conventional antenna is resonating on frequency of 7.0611 GHz with -23.7098 dB return loss for single band with the bandwidth of 192.2 MHz, while Graph 3b indicates that the resonating frequency of DGS MPA is shifted down from 7.0611 GHz to

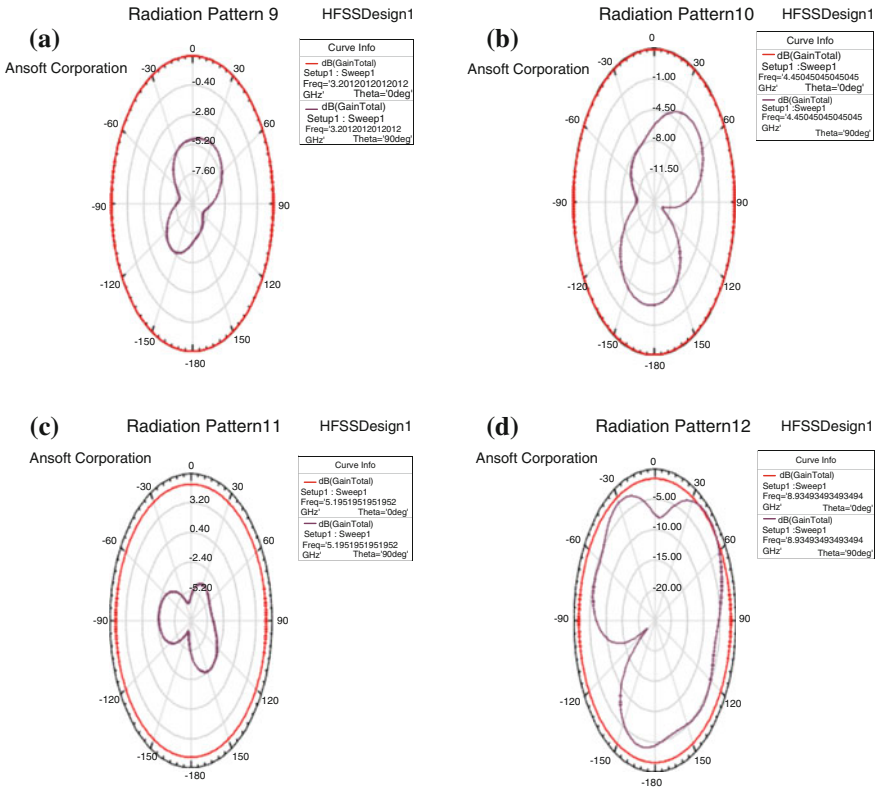


Fig. 6 a 2D radiation pattern for H-plane at 3.20 GHz. b 2D radiation pattern for H-plane at 4.45 GHz. c 2D radiation pattern for H-plane at 5.19 GHz. d 2D radiation pattern for H-plane at 8.93 GHz

3.2012 GHz due to increase in the capacitance of slots incorporated in ground plane. Graph 3b also specifies that the designed DGS MPA is resonating on multiple frequencies which means we get the multiband response due to suitable DGS into ground plane level. Our antenna design shows four resonating frequencies with satisfactory impedance bandwidth concluded in Table 2. So from the graphs and Table 2, it is confirmed that our proposed L-shaped DGS antenna has satisfactory bandwidth and sufficient return loss for all the bands. So this antenna design can cover many applications for wireless communication.

VSWR

One more necessary parameter to measure how well matched the antenna to transmission line is known as voltage standing wave ratio. Figure 4a, b show the

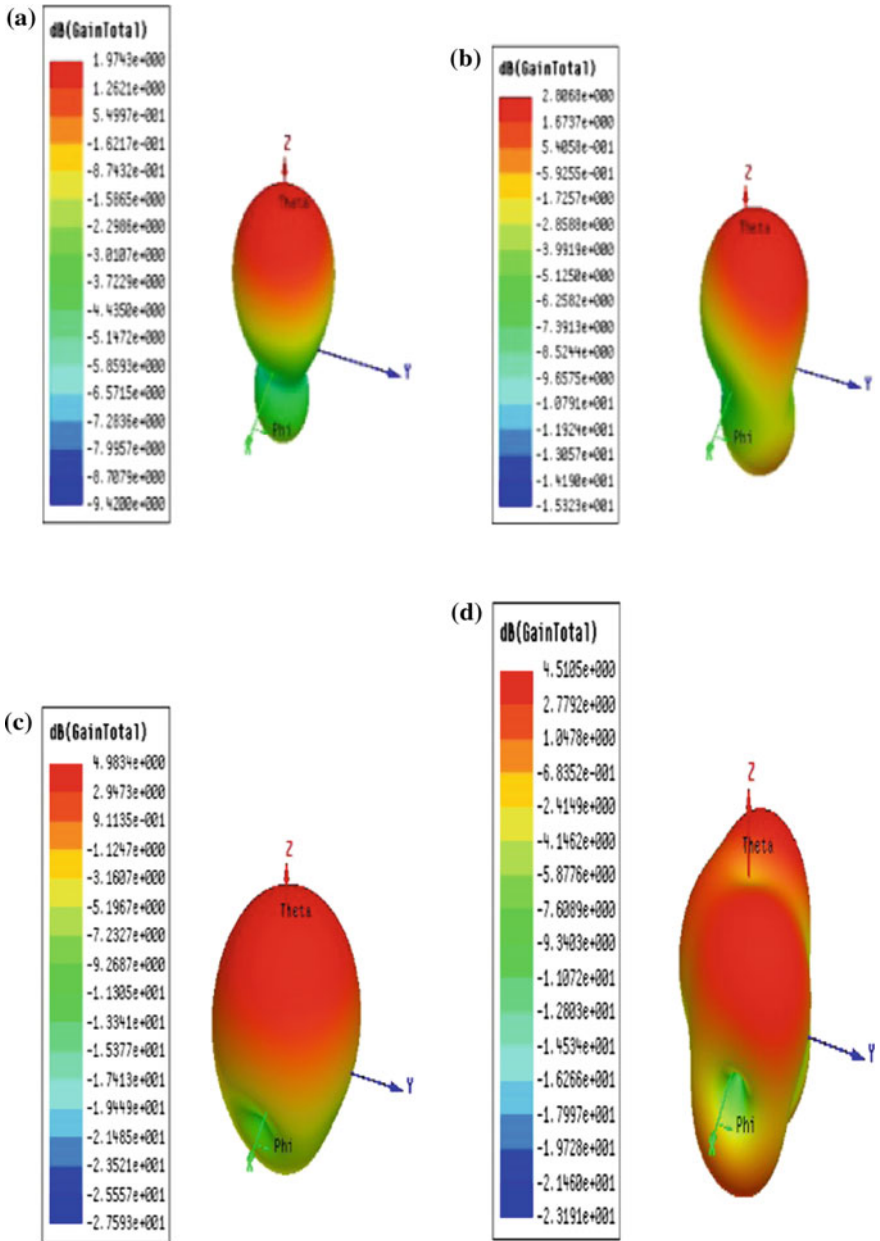


Fig. 7 a 3D Radiation pattern at 3.2012 GHz. b 3D Radiation pattern at 4.4505 GHz. c 3D radiation pattern at 5.1952 GHz. d 3D radiation pattern at 8.9349 GHz

VSWR of conventional antenna and L-shaped DGS antenna, respectively. VSWR < 2 is indicated by the graphs and normally this is adequate margin.

Radiation Pattern

The E-plane and H-plane are defined as the electric field and the magnetic field vector, respectively, with the directions of maximum radiations. Principle E-Plane is X-Z plane elevation with φ (azimuth angle). While the principle H-plane is X-Y plane azimuth with θ (elevation angle). The graphs of Figs. 5 and 6 show the 2D E-plane and H-plane radiation patterns, respectively at different operating frequencies.

The graphs of Fig. 7 indicate the 3D radiation pattern for different frequencies in the band.

Table 2 shows the conclusion of the obtained simulation results of considered antennas.

Conclusion

The technique for the multiband operation of microstrip antenna is investigated with DGS (defected ground structure). The DGS is produced by the combination of two L-shaped structures incorporated into ground plane level. Projected antenna offers multiband response at a satisfactory return loss and ample impedance bandwidth. This kind of multiband antenna is basically suitable for wireless applications.

References

1. Balanis, C.A.: *Antenna Theory, Analysis and Design*. Wiley, New York (1982)
2. Geng, J.P., Li, J.J., Jin, R.H., Ye, S., Liang, X.L., Li, M.Z.: The development of curved microstrip antenna with defected ground structure. *Progress Electromagnet. Res., PIER* **98**, 53–73 (2009)
3. Weng, L.H., Guo, Y.C., Shi, X.W., Chen, X.Q.: An overview on defected ground structure. *Progres Electromagnet. Res. B* **7**, 173–189 (2008)
4. Chakraborty, M., Rana, B., Sarkar, P.P., Das, A.: Design and analysis of a compact rectangular microstrip antenna with slots using defective ground structure. *Procedia Technol.* **4**, 411–416 (2012)
5. Zhao, Y., Qiu, J., Wang, W.: A microstrip antenna based on the defected ground structure. In: *TENCON 2013 IEEE Region 10 Conference* (31194), pp. 1–4 (2013)
6. Shah, I.H., Bashir, S., Shah, S.D.H.: Compact multiband microstrip patch antenna using defected ground structure (DGS). *The 8th European Conference on Antennas and Propagation*, pp. 2367–2370 (2014)

7. Chawla, P., Khanna, R.: Microstrip planar array antenna with improved DGS structure for multiband operation. In: IEEE International Conference on Signal Processing, Computing and Control (ISPCC), pp. 1–6 (2013)
8. Ripin, N., Yusoff, S.N.C., Sulaiman, A.A., Rashid, N.E.A., Hussin, M.F.: Enhancement of bandwidth through i-shape defected ground structure. In: IEEE International Conference on RF and Microwave (RFM), pp. 477–481 (2013)
9. Afzal, W., Ahmed, M.M., Mughal, F.A.: L-Shaped multiband microstrip patch antenna for DCS and WLAN applications. In: IEEE 9th International Conference on Emerging Technologies (ICET), pp. 1–5 (2013)
10. Ansoft HFSS: Pittsburg PA 15219, USA
11. Bahl, I.J., Bhartia, P.: Microstrip Antennas. Artech House, New Delhi (1980)

Design of a Compact Novel Planar Dual Band-Notched UWB Antenna

Sanjiv Tomar and Ajay Kumar

Abstract In this paper, a compact planar ultra-wideband (UWB) antenna with double band-notched characteristics has been presented. The design involves a lamp post-shaped planar radiator fed through a microstrip line of width 2.6 mm, with a U-shaped slot and a C-shaped slot etched on the radiator, with a slotted ground plane on the other side of the substrate. The proposed antenna has been realized using CST MWS SuiteTM. The antenna has a size of $30 \times 30 \times 1.6 \text{ mm}^3$ prototyped on FR4 substrate. The proposed antenna exhibited a bandwidth of more than 7.5 GHz, i.e., 2.68–11.75 GHz for $VSWR \leq 2$ over the entire range except at two notched bands for WiMax systems at 3.3–3.7 GHz and WLAN systems at 5.15–5.85 GHz. The average gain of the antenna is 4.5 dBi with a variation of ± 1.8 dBi over the entire impedance bandwidth. The proposed antenna has demonstrated nearly omnidirectional radiation pattern over the entire impedance bandwidth except for the two notched bands centered at 3.5 and 5.5 GHz.

Keywords Ultra-wideband (UWB) · Dual band-notched antenna · Planar UWB antenna · Slotted ground plane · C-shaped slot · U-shaped slot

General

Ever since Federal Communications Commission (FCC) in March 2002 approved the release of $S_{11} \leq -10$ dB unlicensed bandwidth of 7.5 GHz ranging from 3.1 to 10.6 GHz with an effective isotropic radiated power (EIRP) spectral density of

Sanjiv Tomar (✉)

Department of Electronics and Communication Engineering,

Manipal University, Jaipur 302026, India

e-mail: sanjivtomar@gmail.com

Ajay Kumar

Department of Mechatronics, School of Automobile,

Mechanical and Mechatronics Engineering, Jaipur, India

e-mail: ajay.kumar@jaipur.manipal.edu

© Springer India 2016

N. Afzalpulkar et al. (eds.), *Proceedings of the International Conference on Recent Cognizance in Wireless Communication & Image Processing*, DOI 10.1007/978-81-322-2638-3_100

889

−41.3 dBm/MHz for commercial use in radio communication, intense research in the field of UWB communication has been reported for enhanced data rate and for variety of other purposes. The interest of researchers in UWB communication also emanates from the inherent advantage of small size, low power consumption, simple structure, and ease of integration together with high transmission rate and relatively good omnidirectional properties.

While this bandwidth of 7.5 GHz is the core motivation for developing high data rate devices, there exist other narrowband services which may potentially interfere with UWB communication such as WiMax communication at 3.5 GHz (3.3–3.7 GHz) and WLAN IEEE 802.11/a operating at 5.5 GHz (5.15–5.35 GHz and 5.725–5.875 GHz). In order to avoid interference from existing narrowband applications, it is incumbent to have antenna with band-notched functions. While integrating filters with the UWB antenna may increase the complexity and cost of manufacturing [1], antenna filtering techniques may be employed since these techniques are simple to execute and inexpensive.

Till now, a number of methods has been reported for band-notched functions which includes etching C-shaped slots as investigated by Chu and Yang [2] and Hong et al. [3]. Lin and Hung [4] in their work have investigated a T-shaped slot for band-notched function. Some researchers have also investigated L-shaped slots for band-notched function [5, 6]. Pi-shaped slots have been investigated by Xie et al. [7] for dual band-notched characteristic. Use of inverted cup, cap, and U-shaped slot have been investigated by Lee et al. [8]. Use of embedded stubs having different shapes and resonating strips has also been investigated [9–11]. Use of split ring resonator (SRR) or stepped impedance resonator (SIR) close to feed line has also been investigated extensively [12, 13].

Use of above-mentioned techniques in different combinations can yield single-notched band, double-notched band or triple-notched band capability. A large number of such antennas have been reported in various research works till date. However, the size of the antennas is found to be relatively large and the notched bands are quite wide in terms of bandwidth and the usable bandwidth is reduced to a large percentage. As a result, intense simulation is needed to make the structure compatible having low profile, stable gain, and radiation pattern.

This paper is based on the simulation of a novel design of a triple-notched band antenna having a unique lamp post-shaped structure using CST Microwave Studio Suite, which utilizes finite integration technique. In this proposed design, use of one inverted U-shaped slot and one C-shaped slot etched on the radiating patch have led to achieve double band-notched characteristics. The length of the slot is taken to be one half of the guided wavelength of the center frequency of the respective notched bands. The length of the each slot can be calculated using the expression (1) given below:

$$f_{notch} = \frac{c}{2L_{slot}\sqrt{\epsilon_{eff}}}, \quad (1)$$

$$\epsilon_{eff} = (\epsilon_r + 1)/2$$

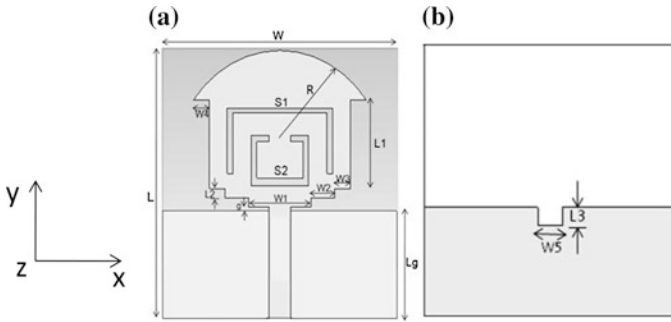


Fig. 1 a Geometry of front end of antenna. b Geometry of back end with slotted ground plane

Where f_{notch} is the center frequency of the notched band, L_{slot} is the length of the slot, ϵ_{eff} is the effective dielectric constant, and c is the velocity of light.

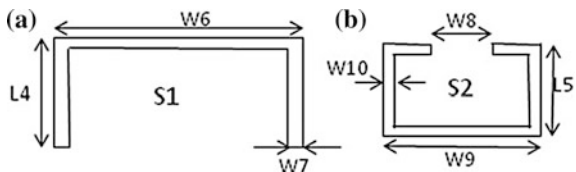
The position and dimensions of each slot can be altered independently and optimized. The proposed antenna is compact in size having $L \times G$ as $30\text{ mm} \times 30\text{ mm}$ with -10 dB impedance bandwidth of more than 7.5 GHz with two notched bands for avoiding interference from respective narrow band services.

Design of a Compact Planar Monopole Antenna with Double-Notched Bands Slots

The geometry of the proposed UWB antenna is shown in Fig. 1. The dimension of the proposed antenna is $30\text{ mm} \times 30\text{ mm}$. It has been prototyped on FR4 substrate of 1.6 mm thickness with dielectric constant ϵ_r as 4.4 and loss tangent of 0.02 . The antenna is fed through a $50\ \Omega$ microstrip feedline having a rectangular ground plane. An inverted U-shaped slot and a C-shaped slot have been etched on the radiating patch while the ground plane has a square notch to increase the impedance bandwidth, as shown in the Fig. 2 An initial estimation of the slot dimension was done using the expression (1).

The inverted U-shaped slot S1 is designed to notch the frequency band covering $3.3\text{--}3.7\text{ GHz}$ with center frequency at 3.5 GHz . The second C-shaped slot S2 is

Fig. 2 Geometry of a Slot S1
b Slot S2



designed for center frequency of 5.5 GHz encompassing a range of 5.15–5.85 GHz. After extensive simulation, the achieved optimized antenna parameters are as follows: $L = 30$ mm, $W = 30$ mm, $L_g = 12$ mm, $R = 8$ mm, $W_1 = 8$ mm, $W_2 = 3$ mm, $W_3 = 2$ mm, $W_4 = 8$ mm, $L_1 = 9.5$ mm, $L_2 = 1$ mm, $g = 0.5$ mm, $L_3 = 2$ mm, $W_5 = 2.8$ mm.

Initially, the estimation of the dimensions has been done using the expression (1) and later optimized through simulation. The design of the slots is given in Fig. 2 and dimensions of the slots after optimization process are as follows: $W_6 = 13.5$ mm, $W_7 = 0.75$ mm, $L_4 = 13.5$ mm, $W_8 = 2.5$ mm, $W_9 = 7$ mm, $W_{10} = 0.65$ mm, $L_5 = 5.5$ mm.

Result and Discussion

In this section, the results of the double-notched band antenna are presented. The simulated return loss characteristic of the antenna is shown in Fig. 3. The overall characteristic shows the wideband behavior of the antenna stretching from 2.68 to 11.75 GHz for $S_{11} \leq -10$ dB which is well over the FCC designated band width.

It is observed that the antenna is able to generate two notched bands through slot S1 and S2 with central rejection frequency centered at 3.5 and 5.5 GHz. The VSWR of the simulated antenna is shown in Fig. 4 which again establishes the fact that each slot creates a corresponding notched band and we are able to generate a compact antenna with double-notched band features with $VSWR \leq 2$ at passband frequencies.

In order to further analyze the band-notched properties, it is important to look at the surface current distribution at notched bands and also at passband frequencies.

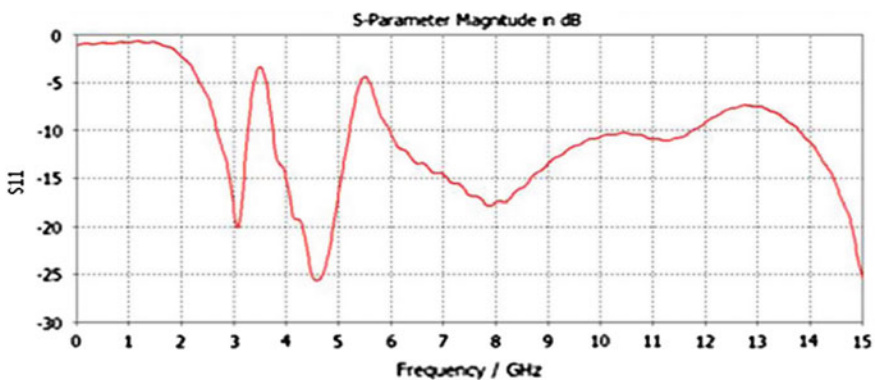


Fig. 3 Simulated S_{11} parameters of the antenna with two band-notched slots

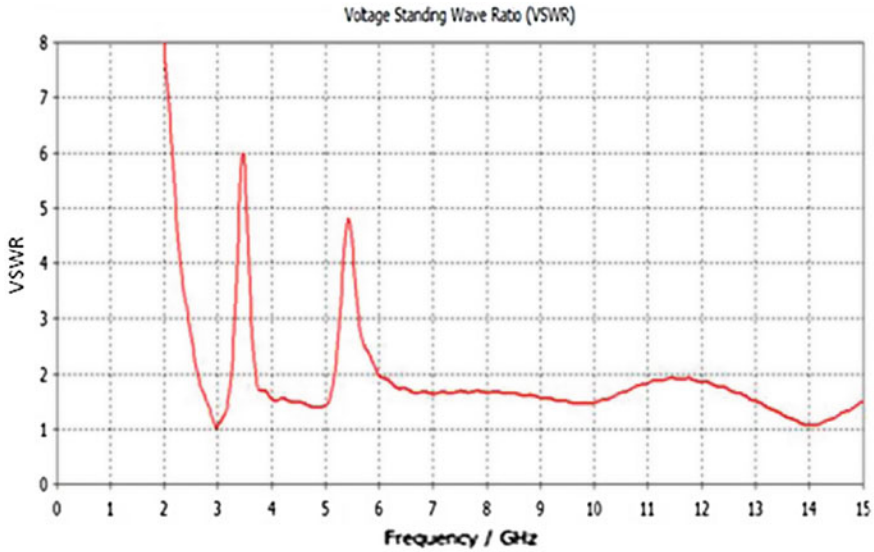


Fig. 4 Simulated VSWR of the antenna with band-notched characteristic

The simulated current distribution at pass band frequencies 3 GHz and 9.5 GHz is shown in Fig. 5a, b. The weak current distribution near the two slots S1 and S2 indicates that at passband frequencies the slots have negligible effect. While it can be observed as shown Fig. 5c, d that the current distribution at center frequency of stop bands (3.5 and 5.5 GHz) is concentrated around the slots. The strong current distribution indicates that the slots are resonating at respective center frequencies, and thus the energy is not being radiated out in an efficient manner.

The simulated plot of the far field pattern of the proposed compact antenna with double band-notched features is plotted in H-plane (xoz) and E-plane (yoz) at three passband frequencies at 3, 6.5, and 9.5 GHz as shown in Figs. 6, 7 and 8. On investigating the normalized radiation pattern, it is seen that the proposed antenna is having an omnidirectional properties in H-plane at lower frequencies with a little variation at higher frequencies. The E-plane radiation pattern is bidirectional in nature at lower frequency and a slight variation is noticed at higher frequencies, however, overall the radiation patterns are in agreement with the radiation pattern of a conventional monopole antenna.

The simulated gain of the antenna is shown in Fig. 9. The gain pattern indicates that the antenna has a stable gain over the entire UWB except at notched bands where a sharp decrease in gain is observed. The gain increases steadily from 2 dBi to 5 dBi and decreases to -3.5 dBi near the notched bands.

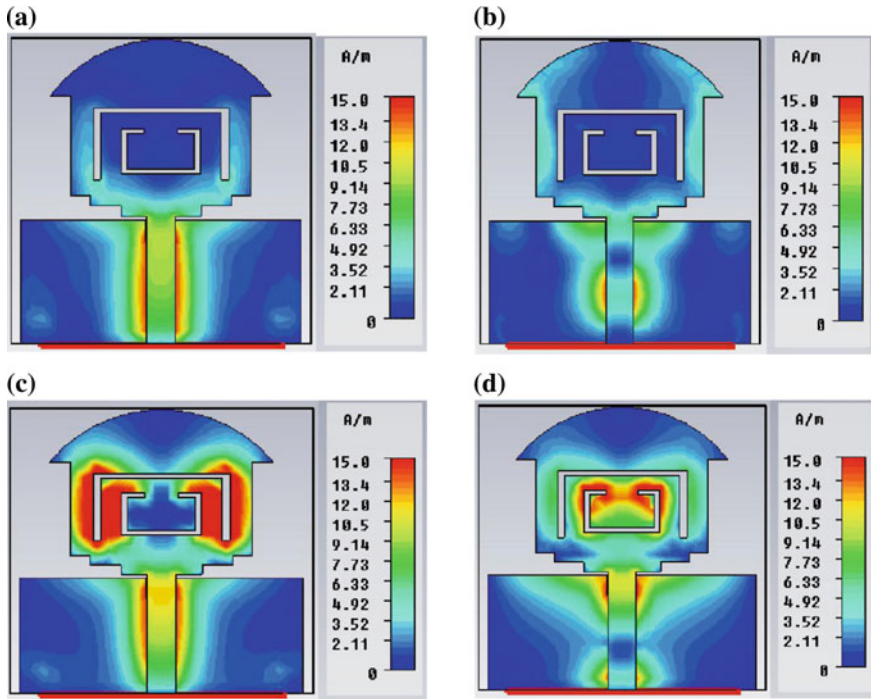


Fig. 5 Surface current distribution at radiating patch at **a** a passband frequency of 3 GHz, **b** a passband frequency of 9.5 GHz, **c** the first notched band at 3.5 GHz, **d** the second notched band at 5.5 GHz

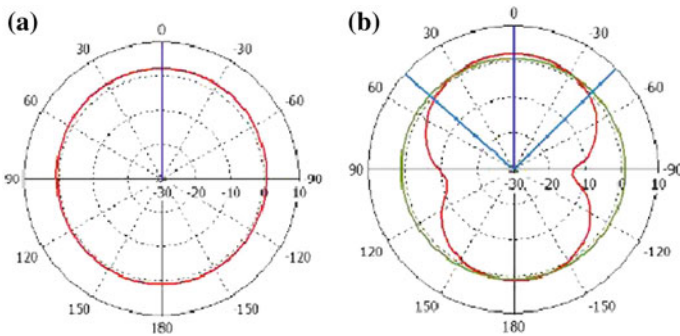


Fig. 6 Radiation patterns of the proposed antenna at 3 GHz **a** H-plane, **b** E-plane

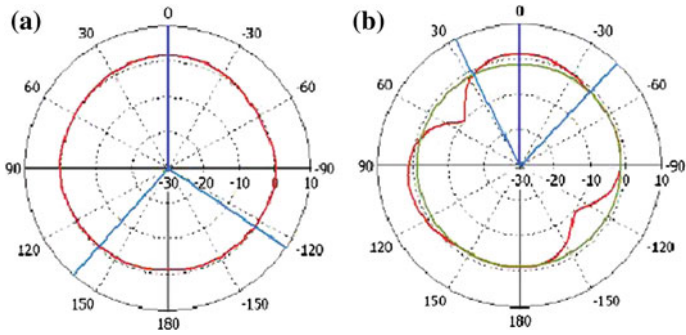


Fig. 7 Radiation patterns of the proposed antenna at 6.5 GHz **a** H-plane. **b** E-plane

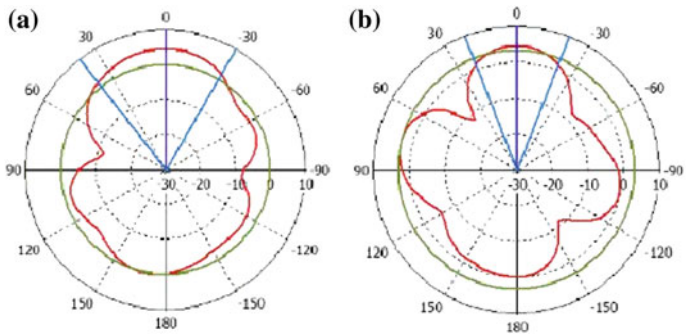


Fig. 8 Radiation patterns of the proposed antenna at 9.5 GHz **a** H-plane. **b** E-plane

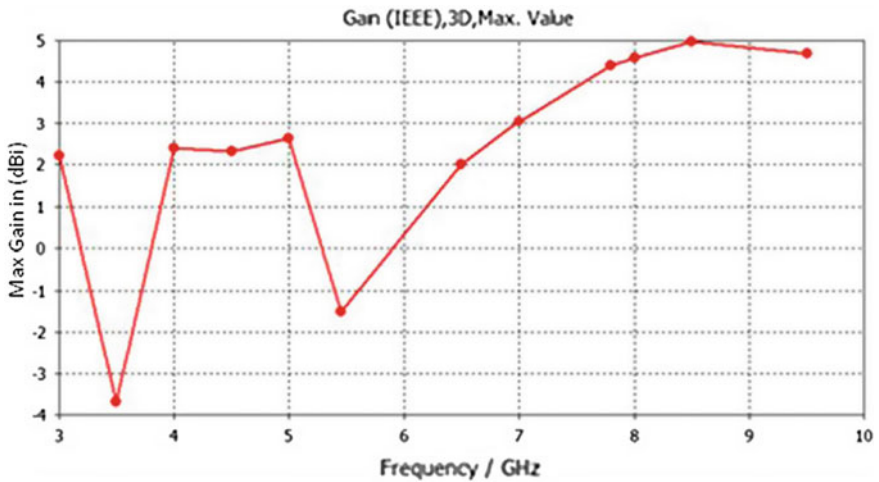


Fig. 9 Simulated peak gain of the proposed antenna

Conclusion

This paper presents a novel compact antenna of size 30 mm × 30 mm with double band-notched features. The proposed antenna is able to cover entire UWB spectrum except at two notched bands. The two notched bands at 3.5 and 5.5 GHz have been obtained by incorporating one U-shaped slot and also an inverted C-shaped slot in radiating patch. U-shaped slot has been used for avoiding interference with WiMax band while a C-shaped slot is used for avoiding interference with WLAN band. The length of the slots is taken to be one half of the guided wavelength of the center frequency of notched band. The H-plane radiation pattern is omnidirectional in nature, while E-plane is almost bidirectional over the entire bandwidth. The strength of the antenna lies in its compact design with stable radiation pattern and gain over the entire UWB which makes it a good candidate for UWB applications.

References

1. Mishra, S.K., Mukherjee, J.: Compact printed dual band-notched U-shaped UWB antenna. *Prog. Electromagnet. Res. C* **27**, 169–181 (2012)
2. Chu, Q.X., Yang, Y.Y.: A compact ultrawide band antenna with 3.4/5.5 GHz dual band-notched characteristics. *IEEE Trans. Antennas Propag.* **56**(12), 3637–3644 (2008)
3. Hong, C.Y., Ling, C.W., Tarn, I.Y., Chung, S.J.: Design of a planar ultra wideband antenna with a new band-notch structure. *IEEE Trans. Antennas Propag.* **55**(12), 3391–3397 (2007)
4. Lin, Y.C., Hung, K.J.: Compact ultra-wideband rectangular aperture antenna and band-notched designs. *IEEE Trans. Antennas Propag.* **54**(11), 3075–3081 (2006)
5. Zaker, R., Ghobadi, C., Nourinia, J.: Bandwidth enhancement of novel compact single and dual band-notched printed monopole antenna with a pair of L-shaped slots. *IEEE Trans. Antennas Propag.* **57**(12), 3978–3983 (2009)
6. Mehranpour, M., Nourinia, J., Ghobadi, C., Ojaroudi, M.: Dual band-notched square monopole antenna for ultra-wideband applications. *IEEE Antennas Wirel. Propag. Lett.* **11**, 172–175 (2012)
7. Xie, L., Zhao, G., Jiao, Y.C., Zhang, F.S.: Ultra-wideband antenna using meandered slots for dual band-notched characteristic. *Prog. Electromagnet. Res. Lett.* **16**, 171–180 (2010)
8. Lee, W.S., Kim, D.Z., Kim, K.J., Yu, J.W.: Wideband planar monopole antennas with dual band-notched characteristics. *IEEE Trans. Microwave Theor. Technol.* **54**(3), 2800–2806 (2008)
9. Kim, K.-H., Park, S.-O.: Design of the band-rejected UWB antenna with the ring-shaped parasitic patch. *Microwave Opt. Technol. Lett.* **48**(7), 1310–1313 (2006)
10. Liu, X.L., Yin, Y.Z., Liu, P.G., Wang, J.H., Xu, B.: A CPW-fed dual band-notched UWB antenna with a pair of bended dual-L shape parasitic branches. *Prog. Electromagnet. Res.* **136**, 623–634 (2013)
11. Emadian, S.R., Ghobadi, C., Nourinia, J., Mirmozafari, M.H., Pourahmadazar, J.: Bandwidth enhancement of CPW-fed circle-like slot antenna with dual band-notched characteristic. *IEEE Antennas Wirel. Propag. Lett.* **11**, 543–546 (2012)
12. Zhang, Y., Hong, W., Yu, C., Kuai, Z.-Q., Don, Y.-D., Zhou, J.-Y.: Planar ultrawide band antennas with multiple notched bands based on etched slots on the patch and/or split ring resonators on the feed line. *IEEE Trans. Antennas Propag.* **56**(9), 3063–3068 (2008)
13. Zhang, Y., Hong, W., Yu, C., Zhou, J.-Y., Kuai, Z.-Q.: Design and implementation of planar ultra-wideband antennas with multiple notched bands based on stepped impedance resonators. *IET Microwaves Antennas Propag.* **3**(7), 1051–1059 (2009)

X-Band and Ku-Band Patch Antenna for Radio Location Applications

Amit Singh Bhadouria, Suman Kumari and Mithilesh Kumar

Abstract Simple and compact microstrip patch antenna for radiolocation application in X-band and Ku-band is proposed. Using three rectangular and two cylindrical slots in patch, we get one frequency band (9.8–10.3 GHz) in X-band and another band (13.23–13.60 GHz) in Ku-band and both the bands are used for radiolocation applications. The proposed antenna is designed on Rogers R04350 substrate with dielectric constant 3.66 and thickness 1.5 mm and its overall size is $10 \times 10 \times 1.57 \text{ mm}^3$ with patch size $7 \times 8 \times 0.035 \text{ mm}^3$. The results of the proposed antennas like return loss, VSWR, and radiation pattern (gain, directivity, and efficiency) are simulated and analyzed using commercial computer simulation technology microwave studio (CST MWS). By simulating this antenna structure using the above EM tool, we are getting two resonant frequencies 10.12 and 13.5 GHz. The return loss at these frequencies is -34.19 dB and -32.75 dB which is very good. The gain at the first resonant frequency is 4.76 dB and at second resonant frequency it is 5.14 dB and the efficiency at both the resonant frequencies is 93 and 72.2 %. The value of VSWR ≤ 1.5 for both the resonant frequencies. The main application of the proposed antenna is to make it compatible with radiolocation applications in X-band (8–12 GHz) and Ku-band (12–18 GHz).

Keywords Ku-band · MSP (microstrip patch) · RADAR (radio detection and ranging) · Radiolocation · VSWR (voltage standing wave ratio) · X-band

A.S. Bhadouria (✉) · Suman Kumari · Mithilesh Kumar
Electronics Engineering Department, UCE, RTU, Kota, India
e-mail: aamit05singh@gmail.com

Suman Kumari
e-mail: sumannehra15891@gmail.com

Mithilesh Kumar
e-mail: mith_kr@yahoo.com

Introduction

In radio determination, the velocity, position, or other characteristics of an object are determined or obtain the information relating to these parameters by means of propagation properties of radio waves. Radiolocation radars in the X-band are primarily used for detection of airborne objects. Radiolocation has wide applications in industry, military, biomedical [1], radiology, and in cellular telephony at base station. The patch of MSP antenna is made of conducting material such as copper or gold, and can take any possible shapes (generally square, rectangular, circular, and triangular) [2].

The MSP antenna has more advantages when compared with the conventional antennas; they are lighter, low volume, low cost, and smaller in dimension and easy to fabricate [3]. These advantages of MSP antennas make them popular in many wireless communication applications such as satellite communication, radar, medical application, etc. [4]. To develop efficient MSP antenna for deep satellite communication, the antenna needs to be designed at particular frequency ranges involving S, C, Ka, Ku, and X-bands with a specific dielectric constant at specific feeding techniques [5]. Different MSP antennas with different shapes of slots in patch for X-band and Ku-band application are reported [6–9]. In this paper, a new compact MSP antenna for radiolocation operations in X and Ku-band is designed. Feeding is provided in these MSP antennas using microstrip line feeding technique. By introducing three rectangular slots and two cylindrical slots on patch, we get the required bands.

Antenna Design

The proposed antenna is designed on Rogers RO4350 substrate with dielectric constant 3.66 and thickness 1.5 mm. A very thin layer of copper material is used for ground plane and patch with thickness 0.035 mm. We are providing microstrip line feed to this rectangular patch with length L_4 and width W_4 . For designing proposed antenna, three rectangular slots (R1, R2, and R3) and two cylindrical slots (C1 and C2) are cut in patch for getting required results. This proposed antenna is designed in five steps which are explained as:

Firstly, simple rectangular-shaped MSP antenna is designed with dimension $10 \times 10 \times 1.57 \text{ mm}^3$ as shown in Fig. 1a. The patch dimensions are $7 \times 8 \times 0.035 \text{ mm}^3$. By simulating this simple patch antenna, we were getting two frequency bands with resonant frequencies 10.3 and 16.4 GHz. In second step, we cut two rectangular slots R1 and R2 with identical dimensions $L_2 \times W_2$ on patch and these are introduced vertically in patch as shown in Fig. 1b. From second structure, two frequency bands are received with resonant frequencies 10.3 and 14.6 GHz. Then, in third step one more rectangular slot R3 with dimensions $L_3 \times W_3$ is introduced as shown in Fig. 2a and this is placed in patch horizontally.

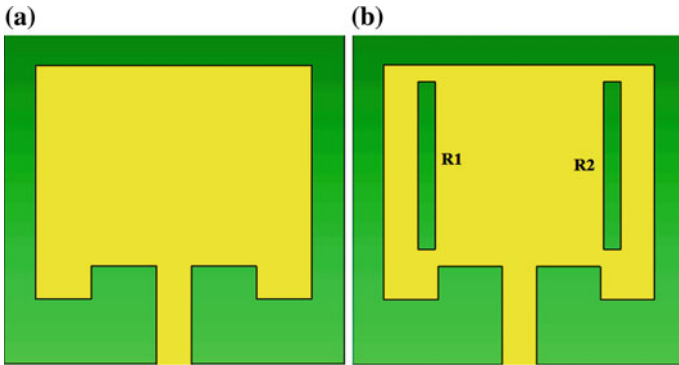


Fig. 1 a Simple MSP antenna. b MSP with slot R1 and R2

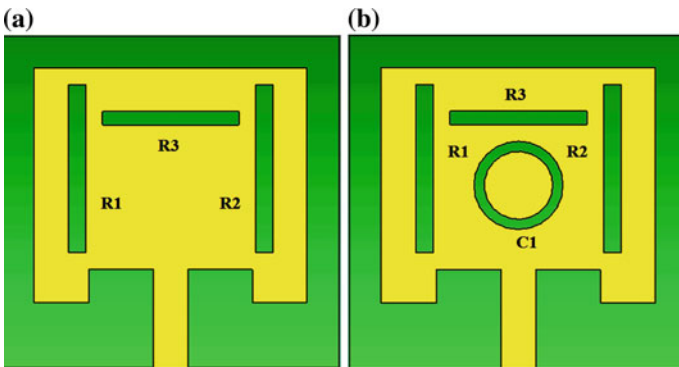


Fig. 2 a MSP antenna with three rectangular slots (R1, R2, and R3). b MSP antenna with slot (R1, R2, and R3) and one cylindrical slot C1

After simulating this design, two bands are achieved with resonant frequencies 10.3 and 13.55 GHz, respectively. From these three steps, we see that first resonant frequency is same for all three steps but by introducing a new slot every time, our second frequency is shifted toward lower Ku-band. The range of return loss for all the resonant frequencies we get till third step is $-23.24 \text{ dB} \leq \text{return loss} \leq -16.10 \text{ dB}$.

As the return loss is not that much good, for improving it, we introduced two cylindrical slots C1 and C2 in patch; first, hollow cylindrical slot C1 with inner radius r_1 and outer radius r_2 is used as shown in Fig. 2b. And using this, return loss is improved in the range $-37.9 \text{ dB} \leq \text{return loss} \leq -21.36 \text{ dB}$. But using slot C1, only the return loss of second resonant frequency is improved. But still the return loss of the first frequency was not good; Hence, to improve it, we cut one simple cylindrical slot C2 in patch with radius 0.5 mm and by this our return loss is improved for both the resonant frequencies; for the first resonant frequency at 10.12 GHz it is

Table 1 Dimensions of proposed MSP antenna design

Antenna parameter	Value (mm)	Antenna parameter	Value (mm)
L	10	W	10
L1	7	W1	8
L2	5	W2	0.5
L3	4	W3	0.4
L4	3	W4	1
r1	1.3	r2	1
W5	1.6	W6	1.9

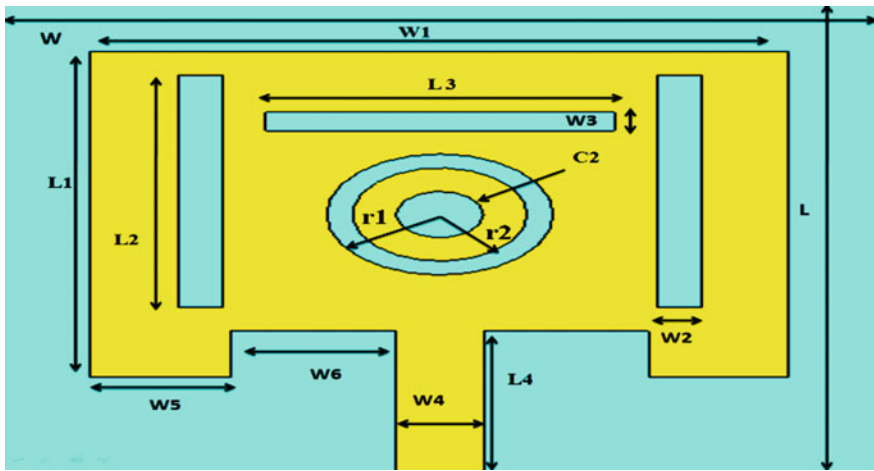


Fig. 3 Modified MSP antenna with two cylindrical slots (C1 and C2) and three rectangular slot (R1, R2, and R3)

−34.19 dB and for the second resonant frequency at 13.5 GHz it is −32.75 dB. The dimensions of the proposed antenna are tabulated in Table 1 (Fig. 3).

Simulation Results and Discussion

Figure 4a, b show the return loss graph for simple rectangular microstrip patch antenna and MSP with different slots R1, R2, R3, and C1. As shown in graph, we see that by increasing the number of rectangular slots the second resonant frequency shifted towards lower Ku-band. Figure 4c shows final return loss graph of proposed antenna. As the graph shows that return is improved for resonant frequencies using the cylindrical slots, but there is a small variation in resonant frequencies. The frequency bands, return loss, and resonant frequencies of this proposed antenna are tabulated in Table 2. VSWR for two resonant frequencies achieved by proposed

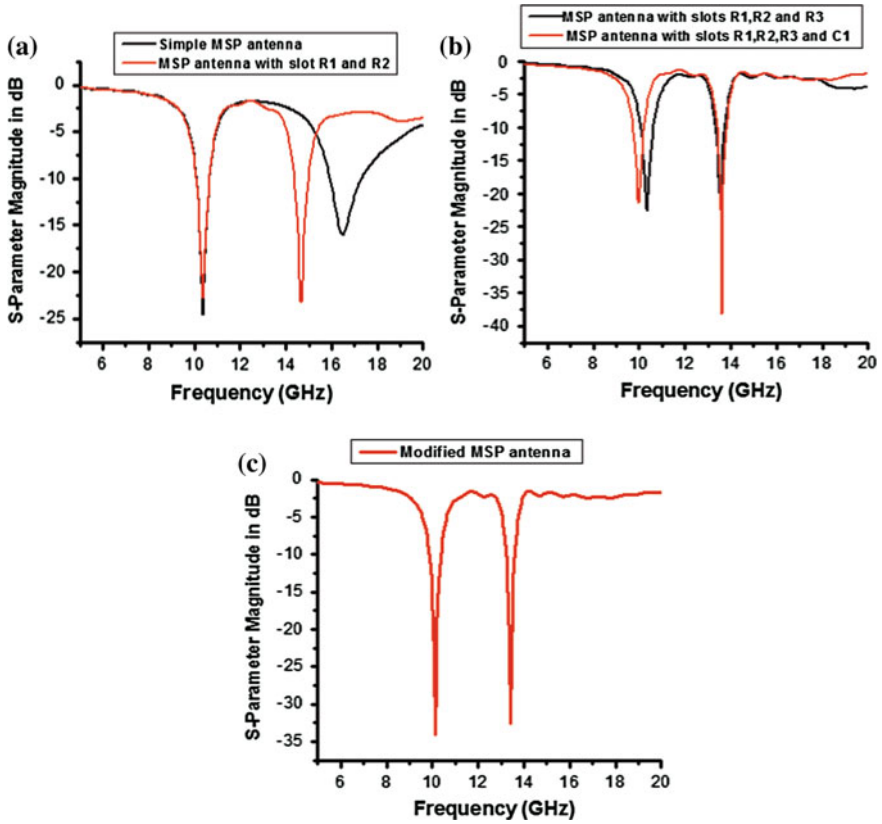


Fig. 4 Return loss of a simple and MSP antenna with two rectangular slots, b MSP antenna with four and five rectangular slots, c final modified MSP antenna with cylindrical slots

Table 2 Comparison of variation in return loss due to different slots

Type of antenna	Bands (GHz)	Resonant frequency (GHz)	Return loss (dB)
Simple MSP antenna	10.09–10.65	10.3	-24.57
	15.9–17.32	16.48	-16.10
MSP with slots R1 and R2	10.07–10.65	10.3	-22.71
	14.36–14.98	14.66	-23.24
MSP with slot R1, R2, and R3	10.09–10.62	10.3	-22.58
	13.34–13.75	13.55	-19.93
MSP with slot R1, R2, R3, and C1	9.75–10.22	10	-21.36
	13.40–13.81	13.6	-37.90
Modified MSP antenna	9.8–10.3	10.12	-34.19
	13.23–13.60	13.5	-32.75

structures is ≤ 1.5 . The comparison of VSWR graphs of all designing step structures is shown in Fig. 5. Figure 6a, b show far-field gain Abs (Theta = 90°) of proposed antenna at resonant frequencies. The values of far-field radiation pattern are tabulated in Table 3. The values of gain, directivity, and radiation efficiency of design structure at their resonant frequencies are tabulated in Table 4.

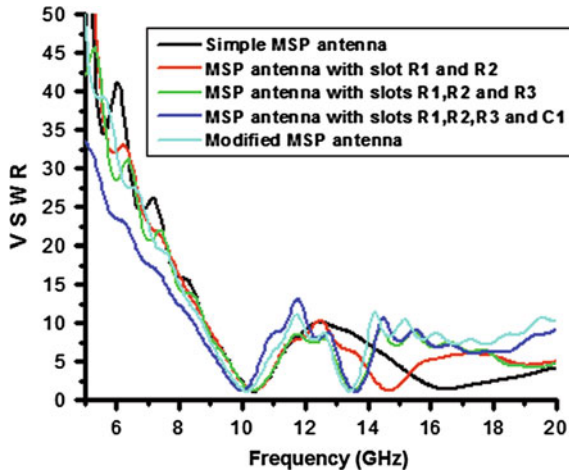


Fig. 5 Comparison of variation in VSWR due to using different slots

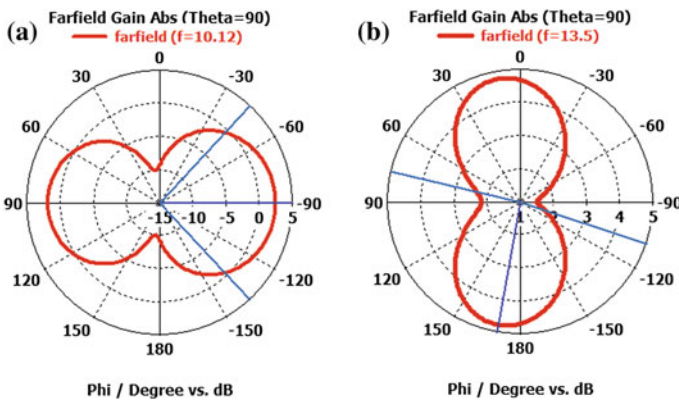


Fig. 6 Simulated Radiation pattern of proposed antenna at resonant frequencies, a 10.12 GHz, b 13.5 GHz

Table 3 Far-field parameters of proposed antenna

Antenna structure	Resonant frequencies (GHz)	Main lobe magnitude (dB)	Main lobe direction (deg)	Angular width (3 dB) (deg)
MSP with slot R1, R2, R3 and C1	10	3.1	-90.0	96.8
	13.6	6.6	171.0	130.4
Modified MSP antenna	10.12	2.4	-90.0	94.3
	13.5	4.8	170.0	174.6

Table 4 Radiation parameters of proposed antenna

Antenna structure	Resonant frequencies (GHz)	Gain (dB)	Directivity (dB)	Radiation efficiency (%)
MSP with slot R1, R2, R3 and C1	10	4.76	5.6	82
	13.6	5.14	6.7	69
Modified MSP antenna	10.12	5.23	5.54	92
	13.5	4.98	6.40	72.2

Conclusion

Simple and compact dual-band MSP antenna for X-band and Ku-band radiolocation applications is proposed. Proposed antenna is compact with overall size $10 \times 10 \times 1.57 \text{ mm}^3$. For designing this antenna, Rogers RO4350 substrate with dielectric constant 3.66 and thickness 1.5 mm is used. By using three rectangular slots, two resonant frequencies 10.3 and 13.55 GHz are achieved. For improving the return loss and other characteristics of antenna, two cylindrical slots are used. From final design structure, two frequency bands with return loss -34.19 and -32.75 dB at resonant frequencies 10.12 and 13.5 GHz are achieved. At resonant frequencies VSWR ≤ 1.5 , gain is 5.23 and 4.98 dB, directivity is 5.54 and 6.40 dB and radiation efficiency is 92 and 72.2 %. The main application of the proposed antenna is to make it compatible with radiolocation applications in X-band and Ku-band and radiolocation has wide applications in industry, military services, biomedical, and radiology.

References

1. Liu, L., Liu, Z., Barrowes, B.E.: Through-wall bio-radiolocation with UWB impulse radar: observation, simulation and signal extraction. *IEEE J. Sel. Top. Appl. Earth Obs. Remote Sens.* **4**(4), 791–798 (2011)
2. Gupta, S., Khera, P., Dhillon, S.S., Marwaha, A.: Dual band U-slotted microstrip patch antenna for C band and X band radar applications. In: *5th International Conference on Computational Intelligence and Communication Networks*. IEEE (2013)

3. Balanis, A.: *Antenna Theory: Analysis and Design*, pp. 722–783. Wiley, New York (1997)
4. Jegan, G., Kumar, G.A., Juliet, A.V.: Multi band microstrip patch antenna for satellite communication. 978-1-4244-9182-7/10 ©2010 IEEE
5. Motin, M.A., Hasan, M.I., Islam, M.S.: Design and simulation of a low cost three band microstrip patch antenna for the X-band, Ku-band and K-band applications. In: 2012 7th International Conference on Electrical and Computer Engineering
6. Younssi, M., Jaoujal, A., El Moussaoui, A., Aknin, N.: Miniaturized probe-fed elliptical microstrip patch antenna for radiolocation applications. *Int. J. Eng. Technol. (IJET)* **4**(5), Oct–Nov 2012. ISSN:0975-4024
7. Motin, M.A., Hasan, M.I., Islam, M.S.: Design and simulation of a low cost three band microstrip patch antenna for the X-band, Ku-band and K-band applications. In: 2012 7th International Conference on Electrical and Computer Engineering
8. Dubey, S.K., Pathak, S.K., Modh, K.K.:. High gain multiple resonance Ku-band microstrip patch antenna. 978-1-4577-1099-5/11/\$26.00 ©2011 IEEE
9. Prasad, P.C., Chattoraj, N.: Design of compact Ku band microstrip antenna for satellite communication. In: *International Conference on Communication and Signal Processing*, 3–5 Apr 2013, India (2013)

Procuring Wireless Sensor Actuator Network Security

Jasminder Kaur Sandhu and Sharad Saxena

Abstract Wireless Sensor Actuator Networks (WSANs) are large-scale innovative networks. The dynamic, reconfigurable, and self-adjustment nature of these networks make them distinctive from rest of the networks using wireless medium for communication. This is because these networks are basically placed in hostile environments like—surveillance, forest fire detection, flood detection; it has many applications and defense is the most prominent one. Hence security forms the basis of this paper which includes attack detection and mitigation using various schemes. A vision on denial-of-service (DoS) attack and its preventive measures for WSAN are in particular. The preeminent objective of this paper is to identify various intruder attacks in WSANs and to propose a new optimal solution for the prevention of DoS attacks (flooding attack) in WSAN. There are various mechanisms to eliminate the malicious node that carry out an attack. These mechanisms are used to safe guard against intruder attacks. In this paper, we have simulated flooding attack in wireless sensor actuator networks, computed a mitigation system and tested the validity of our results.

Keywords DoS · NORMDIS · Flooding attack

Introduction

Wireless sensor actuator network focuses on environment interaction and is embedded in the environment itself. Wireless sensor nodes are called motes. The main functions of a node are sensing, actuation, processing, and communicating information wireless. Hence, are prominently called wireless sensor actuator networks (WSAN). These networks use radio signals for communication. These networks are vulnerable to different types of attacks by the adversaries [7]. Also

J.K. Sandhu (✉) · Sharad Saxena
School of Mathematics and Computer Applications, Thapar University, Patiala 147004,
Punjab, India
e-mail: jasminder.kaur@thapar.edu

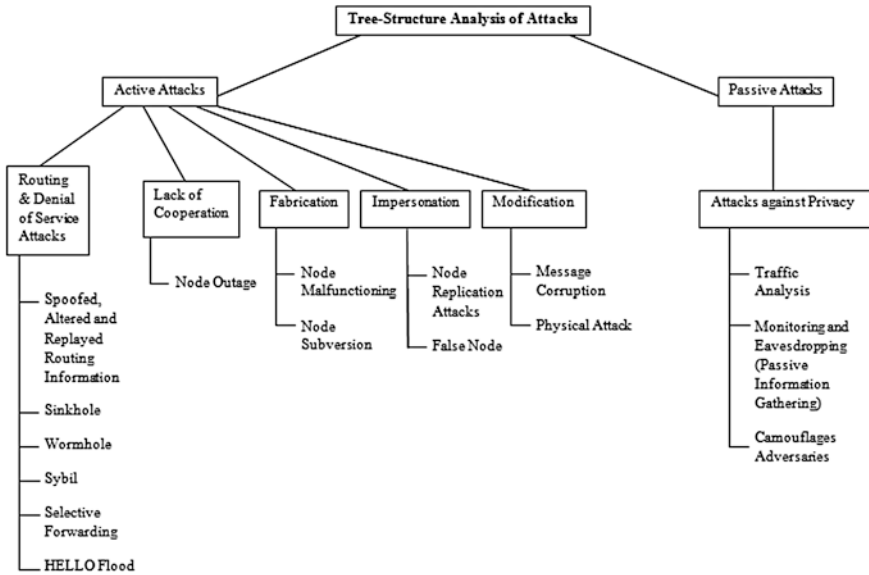


Fig. 1 Tree-structured analysis of attacks [2, 25, 27]

security is critical for sensor network applications whether it be under water exploration, terrestrial deployment.

There are two types of attacks: Active attacks results in alteration of the data files. A passive attack is the disclosure of information without the knowledge of user [11]. The tree-structure analysis of attacks is shown in Fig. 1.

Attacks on Different Layers of WSN

A holistic approach or layered approach [1, 20, 32] targets the improvement of performance of wireless sensor actuator networks with reference to the certain conditions pertaining to the environment in which they have been deployed. These conditions include connectivity, protection from attacks and lifetime. This holistic approach related to the security aims at all the layers of the network. This will henceforth ensure the over all security in a network.

In this layered approach, security is cinched for every layer of a WSN. If by any chance one layer is captured say the physical layer, security of the system will degradefully. Hence, by constructing these security layers, protection is ensured for entire network. Enlisted below in the Table 1 are various threats based on layering scheme [14, 23, 26, 36]:

Table 1 Typical threats in WSAN

Layer	Threat
Physical	Jamming
	Tampering
Data link	Exhaustion
	Collision
Network	Route information manipulating
	Selective forwarding
	Sybil attack
	Sinkhole attack
	Wormhole attack
	Hello Flood attack
Transport	Flooding
Application	Clone/Node

- *Jamming Attack:* Sensor network uses radio signals for communication. In this attack, these signals are infringed so as to disrupt the network fully or partially [24]. To solve the problem of this attack the malicious node can be blacklisted.
- *Tampering:* In this physical harm is made to a particular affected node. The node is compromised or tampered by an attacker who makes a physical access to the node. The attacker gaining physical access to the node can extract extremely useful data such as the cryptographic keys [10]. The solution to this attack is implementing protection, usage of tamper-proof nodes and changing of keys.
- *Exhaustion:* Intruder repeatedly sends messages making the resource exhaust. This leads to collisions which would in turn lead to retransmission of data. Repeated collisions thus lead to resource exhaustion. Time-division multiplexing could provide a solution to this problem. Another solution would be applying rate limitation at which data should be sent across a communication channel [5].
- *Collision:* Simultaneous transmissions at the same frequency lead to a collision. Due to collision, data gets altered leading to erroneous data transmission through a communication channel. The prescribed solution in the text is usage of error-correcting codes like CRC (cyclic redundancy code).
- *Route information manipulation:* This means changing the data being sent on a communication channel. To prevent this, proper authentication mechanism can be used to identify the intended receiver [4]. Also, encryption technique can be used to render the actual text unreadable, so that an eavesdropper is not able to intercept this text.
- *Selective forwarding:* In a multi-hop network the adversary node when being a part of this network, selectively forwards only certain messages while dropping others. This is called selective forwarding [6, 21]. Solution is to find the attacker node and pre-assume that it has failed and traverse through an alternative path to the destination [13].

- *Sybil attack*: Here, one node presents multiple identities to a network, i.e., a particular node duplicates itself and is shown in multiple locations. Authentication techniques [9] can be useful in preventing this attack.
- *Sinkhole attack*: Here, an intruder makes the malicious node look more attractive to its neighbors. So selective forwarding would become very simple and data transfer would hence take place through this affected node. The solution to this problem involves techniques like authentication, monitoring, and redundancy [33].
- *Wormhole attack*: An intruder reads the data packet from a location, tunnels it, and retransmits the packet onto the network which leads to wormhole attack. The solution to this problem involves variant and flexible routing scheme, monitoring the network [17].
- *Hello Flood attack*: An attacker transmits a packet to the sensor network saying HELLO. This gives an illusion that the intruder is the neighbor [3]. Hence transmittal of data is made through malicious node. Transmittal of information to the base station through the attacker nodes which is its neighbor makes data unsafe to use. Two-way authentication procedure is required as a solution to this problem.
- *Flooding attack*: Malicious node makes multiple connection requests until the resource reaches a maximum limit. Thus any further legitimate requests made will also be ignored [35]. The solution involves limiting total connections making resource request in the network.
- *Clone attack*: An intruder copies a nodes unique ID to replicate a node. In this attack, the node ID is same whereas the location on which a clone is placed is different from the actual location and this degrades the sensor network performance. It is also called the node replication attack [29]. The solution of this problem is using a unique pairwise key that is a cryptographic measure.

Denial-of-Service Attack

Attack which degrades a systems capacity to perform its normal functioning is termed as DoS attack. Like the WSN-layered attacks, these attacks also take place on various layers of the network [19, 31]. DoS attacks can be categorized as [30]:

- *Routing traffic attack*: Can be launched in two ways, i.e., by dissipating bogus information dealing with the routes. Hence, paths constructed for communicating information are not valid. And the second way is when an attacker ejects a handsome amount of traffic into the network to choke it.
- *Attack on data traffic*: This implies monitoring, retransmitting, or altering the data being communicated on a transmission channel.

In both the above attacks beneficial network resources like bandwidth, node resources like memory or computation power are either consumed or wasted.

Table 2 DoS attacks and their solutions

DoS attack	Possible solutions
Interference with radio signals	Spread spectrum
Tampering	Tamper-resistant node
Denying channel	Error correction codes
Black holes	Multiple routing paths
Misdirection	Source authorization
Flooding	Limiting connections

A primitive attack on WSAAN is called jamming [18, 22], which incorporates a single node or certain group of nodes. This attack can be categorized as follows:

- *Constant Jamming*: No message can be sent or received, i.e., the complete network is jammed.
- *Intermittent Jamming*: Messages are exchanged between nodes periodically but not consistently. Attacks are possible on the link layer itself. In this case the attacker may intentionally violate the communication protocol like, the IEEE 801.11 b (Wi-Fi) protocol or the ZigBee [8], and continuously carry out the transmission in order to create collisions resulting in re-transmittal of affected data. This retransmission will lead to a huge wastage of the power supply.

When considering the routing layer, a node has a benefit of single-hop communication or multi-hop communication to route messages from source to destination constantly or on intermediate levels which would result in transmittal of data through an adversary node, hence, making data unavailable to entire network. Another variant is misdirection which means intentionally routing messages to incorrect nodes [15, 34].

The threats encountered by the transport layer are somewhat similar to the flooding attack [28]. In this, many connections request are made to the susceptible node. Thus, resources need to be allocated to handle the connection request. This results in exhaustion of resources thus making node useless [12]. The various DoS attacks discussed above are summarized in Table 2.

Simulation and Experimental Results

The performance can be evaluated with the help of a Network Simulator Version 2 [16]. The traffic generated is done using CBR (constant bitrate) to transmit packets at 0.25 (rate of transmittal). This rate corresponds to the transmittal of 4 packets per second.

CBR is connectionless and creates an unreliable connection. There is no feedback available which is also known as acknowledgments. Queue with FIFO is being maintained by each node using Drop Tail mechanism. Sensors are deployed in an area of 726 m × 698 m in a random way. Listed in Table 3 are certain parameters:

Table 3 Parameters to be set at the time of simulation

Parameter	Value
Channel type	Wireless
Antenna	Omnidirectional
Routing protocol	AODV
Number of mobile nodes	6
Queue type	Drop tail

Figure 2 shows a scenario of six nodes, red is the malicious node. Transmittal of data is from node 0 to 3 and from node 1 to 4. Node 5 is a malicious node introduced in the network to add an attack in the scenario below.

Figure 3 shows a scenario of six nodes, red colored node again being the malicious node. Data are being sent from Node 0 to Node 4. This scenario has been modified by applying normal distribution (NORMDIS mechanism) on all the nodes in the network.

The results are analyzed for performance based on certain parameters which have been explained as under:

Packet Drop: The attack took place at time 3 s. After that packet drop has increased considerably to 38.86 %, thereby degrading the effectiveness of the

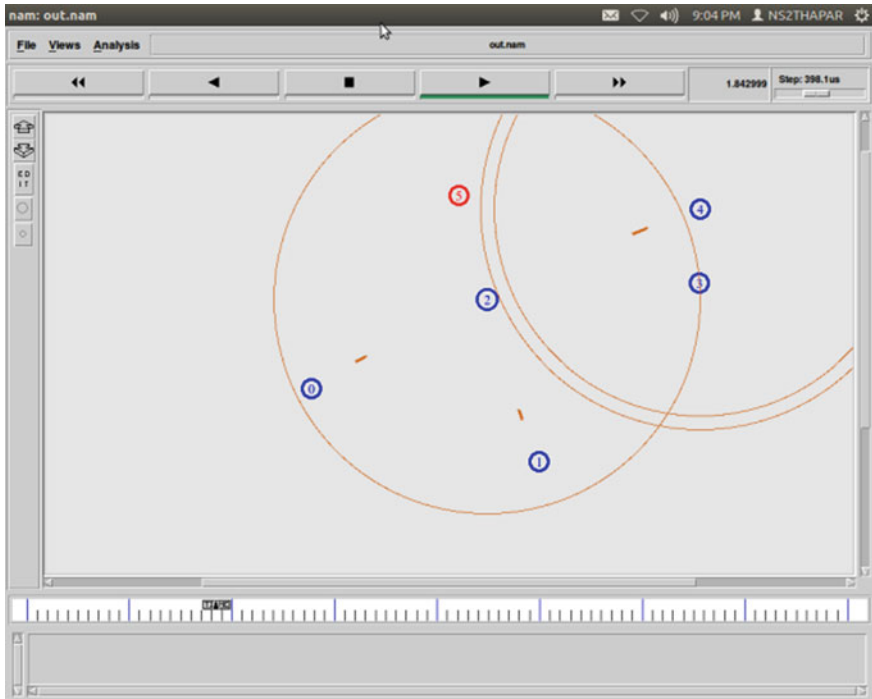


Fig. 2 Flooding scenario

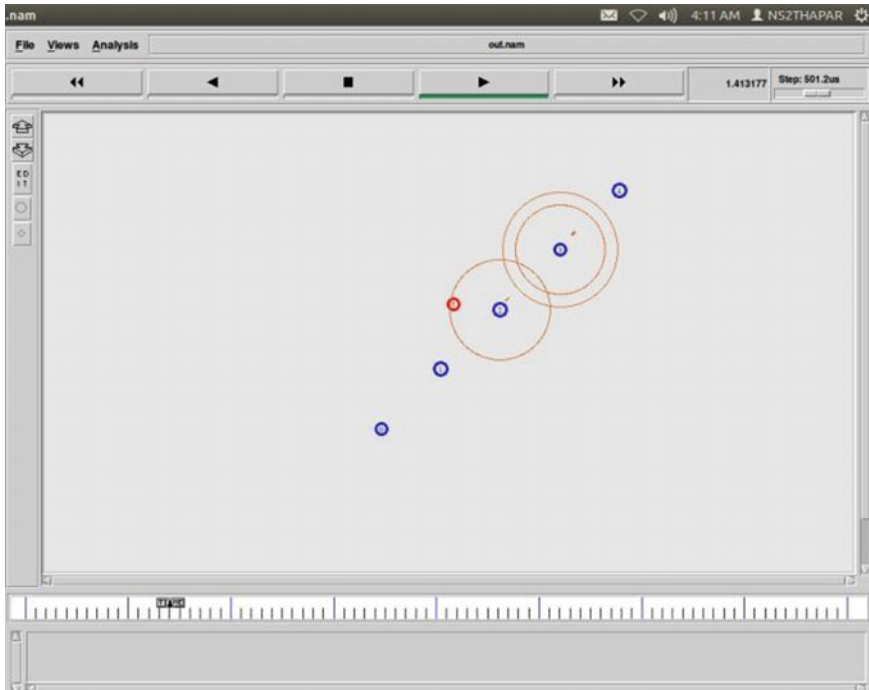


Fig. 3 Normalization scenario

system. When NORMDIS scheme is applied for the network scenario, this packet drop decreases and comes to 18.60 %, thereby improving system performance as shown by the green line Fig. 4 shows the computation result of the packet drop.

Packet Delivery Fraction: It is the number of packets reached till the destination divided by the number of packets transmitted. It is popularly known as PDF. Figure 5 shows the computation result of the packet delivery fraction. The red line depicts scenario with attack and green line without attack.

After applying the NORMDIS mechanism, we are able to achieve a stable PDF depicted by the green line.

Delay Computation: The average time taken for packets to reach destination computes delay. The red line depicts a gradual increase in delay after the attack at 3 s. In order to improve this parameter NORMDIS mechanism is applied which yields the improved green line. Figure 6 shows the computation result of the delay.

PDF decides the effectiveness of the network. The effectiveness of the network was 61.13 % which has increased to 81.39 % after applying the NORMDIS mechanism.

Average Throughput: It is the amount of data delivered from one node to another per unit time. As the malicious node (indicated in red) is inserted into the network, the throughput degrades. As a result, the performance of the network is affected

Fig. 4 Time versus packet drop

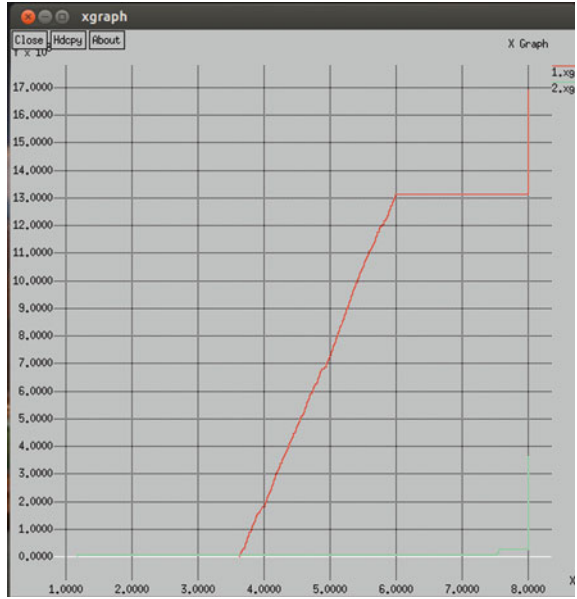


Fig. 5 Time versus packet delivery fraction (PDF)

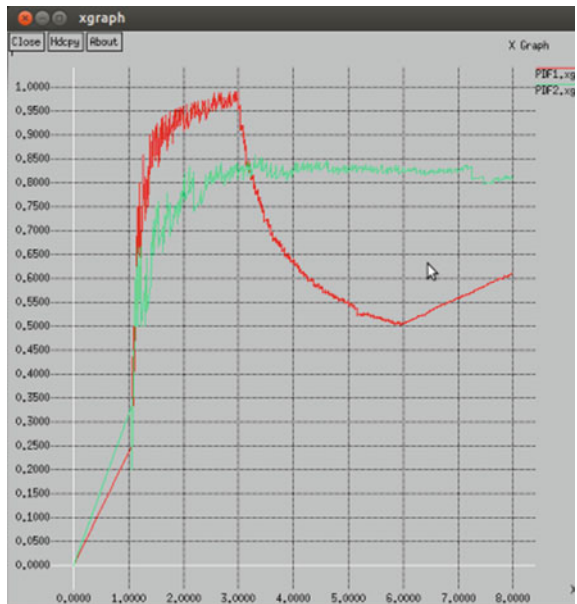


Fig. 6 Time versus delay computation

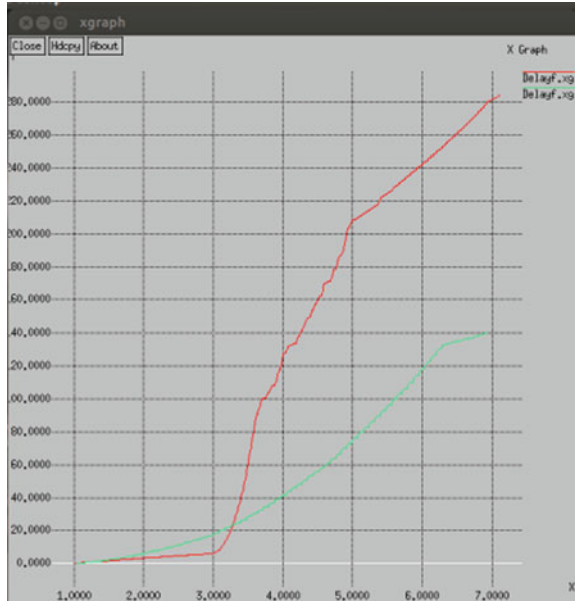
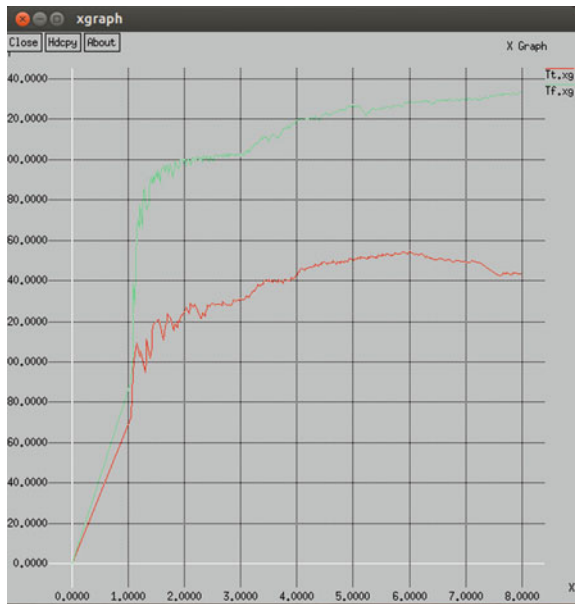


Fig. 7 Time versus throughput computation



badly. The graph in Fig. 7 shows the degraded throughput, i.e., 143.53 Kbps represented by the red line, whereas, the green line depicts the throughput after applying the NORMDIS mechanism, i.e., 233.43 Kbps.

Conclusion

Security is a vital issue in wireless sensor actuator networks. In this research work, we focused on the various types of attacks in the WSN. Then, a detailed study of the denial-of-service attacks have been carried out. We have proposed a NORMDIS mechanism for mitigating the flooding attack. With the results of trace graph, it can be concluded that in the case of the flooding attack, delay of delivered packets increases as compared to our normalization technique. Also packet drop is more in case of flooding. The packet delivery fraction in this attack is considerably low as compared to our normalize mechanism.

Future scope is to devise new techniques for prevention of attack on various other layers of the wireless sensor actuator network-layered framework which have been discussed earlier and applying few more mathematical distributions to decrease the effect of attacks on these sensor networks. Also, the energy constraint to be added to compute the net energy required for efficient communication. Hence, achieving much more energy-efficiency and security in transmittal of data is an upcoming area of research.

Acknowledgment This research and findings are supported by Thapar University, Patiala under Seed Grant Project Scheme. I thank Dr. Sharad Saxena for sharing his pearls of wisdom with me during the work.

References

1. Akyldiz, I.F., Su, W., Sankarasubramaniam, Y., Cayirci, E.: Wireless sensor networks: a survey. *Comput. Netw.* **38**(4), 394–422. Elsevier Science (2002)
2. Anand, M., Cronin, E., Sherr, M., Blaze, M., Ives, Z., Lee, I.: Sensor network security: more interesting than you think. In: *HOTSEC'06: Proceedings of First USENIX Workshop on Hot Topics in Security*, USENIX Association, Berkeley, CA, USA, pp. 25–30 (2006)
3. Baig, Z.A.: Pattern recognition for detecting distributed node exhaustion attacks in wireless sensor networks. *Comput. Commun.* **34**(3) (2010)
4. Bhende, M., Wagh, S.J., Utpat, A.: A quick survey of wireless sensor networks. In: *IEEE 4th International Conference on Communication Systems and Network Technologies*, pp. 160–167 (2014)
5. Bojkovic, Z.S., Bakmaz, B.M., Bakwaz, M.R.: Security issues in wireless sensor network. *Int. J. Commun.* **2**(1), 106–115 (2008)
6. Bysani, L.K., Turuk, A.K.: A survey on selective forwarding attack in wireless sensor network. In: *IEEE* (2011)
7. Chan, H., Perrig, A.: Security and privacy in sensor networks. In: *IEEE*, pp. 103–105, October 2003

8. Chong, C., Kumar, S.P.: Sensor networks: evolution, opportunities, and challenges. In: Proceedings of the IEEE, vol. 91, no. 8, (2003)
9. Curia, D.-I., Plasto, M., Bani, O., Volosencu, C., Tudoroiu, R., Doboli, A.: Combined malicious node discovery and self-destruction technique for wireless sensor networks. In: International Conference on Sensor Technologies and Applications, pp. 436–441 (2009)
10. Du, X., Chen, H.-H.: Security in wireless sensor network. *IEEE* **15**(4), 60–66 (2008)
11. Du, X., Chen, H.-H.: Security in wireless sensor networks. *IEEE Wirel. Commun.* **15**(4), 60–66 (2008)
12. Estrin, D., Govindan, R., Heidemann, J., Kumar, S.: Next century challenges: scalable coordination in sensor networks. In: *MobiCom 99*, Seattle, USA (1999)
13. Gaubatz, G., Kaps, J., Sunar, B.: *Public Key Cryptography in Sensor Networks—Revisited*. Springer, Berlin/Heidelberg (2005)
14. Hai, T.H., Huh, E.-N.: Detecting selective forwarding attacks in wireless sensor networks using two-hop neighbor knowledge. *IEEE International Symposium on Network Computing and Applications*, pp. 325–331 (2008)
15. Intanagonwiwat, C., Govindan, R., Estrin, D., Heidemann, J., Silva, F.: Directed Diffusion for WSN. *IEEE/ACM*, vol. 11 (2003)
16. Issariyakul, T., Hossain, E.: *Introduction to Network Simulator NS2*. Springer, USA (2009)
17. Jokhio, S.H., Jokhio, I.A., Kemp, A.H.: Node capture attack detection and defence in wireless sensor networks. *IET* **2**(3), 161–169 (2011)
18. Karl, H., Willig, A.: *Protocols and Architectures for Wireless Sensor Networks*. Wiley, New York (2005)
19. Latre, B., Braem, B., Moerman, I., Blondia, C., Demeester, P.: A survey on wireless body area networks. *Wirel. Netw.* **17**(1), 1–18 (2011)
20. Li, Y.-X., Qin, L., Liang, Q.: Research on wireless sensor network security. In: *IEEE, International Conference on Computational Intelligence and Security*, pp. 493–496 (2010)
21. Liu, S., Tang, Y., Liu, Y.: A survey of transport protocols for wireless sensor networks. In: *IEEE*, pp. 2338–2341 (2012)
22. Olariu, S.: Information assurance in wireless sensor networks. Sensor Network Research Group, Old Dominion University, New York, NY, USA, pp. 259–268. *ACM* (2004)
23. Padmavathi, G., Shanmugapriya, D.: A survey of attacks, security mechanisms and challenges in wireless sensor networks. *Int. J. Comput. Sci. Inf. Secur. (IJCSIS)* **4**(1), 1–9 (2009)
24. Pathan, A.-S.K., Lee, H.-W., Hong, C.S.: Security in wireless sensor networks: issues and challenges. In: *ICACT* (2006)
25. Qian, Y., Lu, K., Tipper, D.: Towards survivable and secure wireless sensor networks. In: *IEEE*, pp. 442–448 (2007)
26. Sharma, G., Bala, S., Verma, A.K.: Security frameworks for wireless sensor networks—review. In: *2nd International Conference on Communication, Computing & Security (ICCCS-2012)*
27. Singal, T.L.: *Wireless Communications*. New Delhi, Tata Mc Graw Hill (2010)
28. Sohrabi, K.: Protocols for self-organization of a wireless sensor network. *IEEE Pers. Commun.* **7**(5), 16–27 (2000)
29. Verma, A.K., Singh, A.: Simulation and analysis of AODV, DSDV, ZRP in VANET. *IJFCST* **3**(5), (2013)
30. Verma, A.K.: Comparison of flooding and directed diffusion for wireless sensor network. In: *IEEE*, pp. 1–4 (2009)
31. Verma, A.K.: Promising key management schemes in wireless sensor networks: a review. In: *IEEE*, pp. 1061–1066 (2009)
32. Wang, Y., Attebury, G., Ramamurthy, B.: A survey of security issues in wireless sensor networks. *IEEE Commun. Surv. Tuts.* **8**(2), 2–22 (2006)
33. Wood, A.D., Stankovic, J.A.: Denial of service in sensor network. *IEEE* **35**(10), 54–62 (2002)
34. Yen, W., Chen, C., Yang, C.: Single Gossiping with Directional Flooding Routing Protocol in WSNs. In: *IEEE* (2008)

35. Zhang, Y., Li, X., Liu, Y.: The detection and defence of DoS attack for wireless sensor network. *J. China Univ. Posts Telecommun.* **19**, 52–56 (2012)
36. Zhou, Y., Fang, Y., Zhang, Y.: Securing wireless sensor networks: a survey. *IEEE Comm. Surv. Tuts.* **10**(3), 6–28 (2008)

Performance Analysis of VoIP Over WiMAX Networks Under Nodes Failure

Jinia and Jarnail Singh

Abstract WiMAX stands for Worldwide Interoperability for Microwave Access. Multimedia applications are gaining much of the user attention with the introduction of new broadband technologies. VoIP is the most well-known service of WiMAX and is a growing rapidly in world of telecommunication. Not only for improved quality but for also a wide range we prefer wireless networks. As in wireless networks nodes are mobile meaning they can move freely so in my thesis we do study on the performance under nodes failure, and its effect on the entire performance of the network. Various codecs have been used to check the performance. In this Paper, the performance of WiMAX for Voice over IP (VoIP) by varying no. of nodes failure is analyzed for two transmitter techniques MIMO and SISO. The performance is analyzed by using OPNET Modeller. The performance is compared in terms of throughput, end-to-end delay, and traffic sent.

Keywords WiMAX · MIMO · Codec · VoIP · SISO

Introduction

WiMAX is the short form for Worldwide Interoperability for Microwave Access. Basically WiMAX is a wireless technology that provides high data range over longer distances to give benefits to more and more users and used as an alternative to cable and DSL to fulfill the mobile access needs [1]. The IEEE 802.16 has a quite wide range configured in miles, conveying data at the rate of 75 megabits per second. WiMAX [2] supports rigid and portable Internet access. VoIP stands for Voice over Internet protocol; it is used for transporting the voice data over

Jinia (✉)

Department of Computer Science Engineering, BFCET, Bathinda 151001, India
e-mail: goyal.jinia33@gmail.com

Jarnail Singh

Department of IT, BFCET, Bathinda, India
e-mail: er.jarnailrathor@gmail.com

© Springer India 2016

N. Afzalpulkar et al. (eds.), *Proceedings of the International Conference on Recent Cognizance in Wireless Communication & Image Processing*, DOI 10.1007/978-81-322-2638-3_103

917

Internet-based networks. WiMAX network provides a better way to utilize various applications like Internet Protocol television (IPTV), video conferencing by providing better Internet network facility to facilities the use of VoIP [3]. The basic output of the WiMAX network that is in terms of signals and Internet services lies between the WiFi and 4G mobility [4]. With the help of VoIP user can easily make an audio and video call over Internet. VoIP protocols act like a bridge between Internet network and voice [5].

Literature Review

Halepovic et al. [6] in their research they studied the multimedia applications over WiMAX network with the help of VoIP and video streaming and they found WiMAX network supports VoIP for varying duration of calls where as the quality of calls is compared to high speed Ethernet. The result shows WiMAX network can easily come in trends with currently on going multimedia Internet applications like gtalk, video call [6].

Alshomrani et al. [7] here authors have studied the codec schemes and statistical distribution of codec scheme. Simulation has been performed to understand the WiMAX network over various QoS services like delay, jitter, MOS and their results show better choice of voice codec effect the VoIP performance [7].

Elechi Onyekachi et al. [8] adopted a simulation-based network performance analysis to examine the effects of the application of different voice encoder schemes on QoS of VoIP system over WiMAX network [8] by using voice jitter, voice packet ETE delay, packet-sent-packet-received, WiMAX network delay, voice packet delay variation, and throughput as QoS parameters and in result they show that codec scheme and the number of voice frame size per packet have a significant impact over VoIP when it is set up within a WiMAX Network.

Simulation Results

In this analytical work there are two experiments being performed by creating different scenarios.

Experiment 1: Here we used scenarios simulation to study the effect of different codecs on VoIP services over WiMAX networks without nodes failure. Then we make scenario with nodes failure to study the effect of different codecs on VoIP services over WiMAX networks by varying nodes failure. The number of nodes failure taken is 4 and 6 in different scenarios the encoder schemes used for the investigation include ITU-T g711 (default encoder scheme), g723 and g729 with voice frame size used per packet set to “7”. These experiments are repeated for two transmitter techniques 2×1 MIMO and SISO.

Experiment 2: Here we used scenarios simulation to study the effect of different codecs on VoIP services over WiMAX networks without nodes failure. Then we make scenario with nodes failure to study the effect of different codecs on VoIP services over WiMAX networks by varying nodes failure. The number of nodes failure taken is 4 and 6 in different scenarios the encoder schemes used for the investigation include ITU-T g711 (default encoder scheme), g723 and g729 with voice frame size used per packet set to “13”. These experiments are repeated for two transmitter techniques STC 2×1 MIMO and SISO (Fig. 1).

The effect of VoIP over WiMAX under nodes failure by using various modulation techniques is being analyzed. The comparison is done in terms of throughput, end-to-end delay, and traffic sent.

Throughput: In this the result for voice packet for 7, 13 when the node failure is increased the throughput also increase but it is still less than when there is no failure of node. The result also shows that the performance of g711 is better than other.

End-to-End Delay: We did the nodes failure and analyses for the end-to-end delay to find out how it affects the voice quality. It shows that when we increase the node failure end-to-end delay decreases; the result shows that the end-to-end delay for g711 is lesser than other so performance of g711 is better than other.

Traffic Sent: In this the result for voice packet for 7, 13. It shows that as we add the node failure, nodes the traffic sent decreases. It also shows that when we increase node failure the traffic sent decreases. The result shows that the traffic received for g711 is more than other. So the performance of g711 is better than other. Table 1 shows the different analyzed values on throughput, end-to-end delay, and traffic sent.

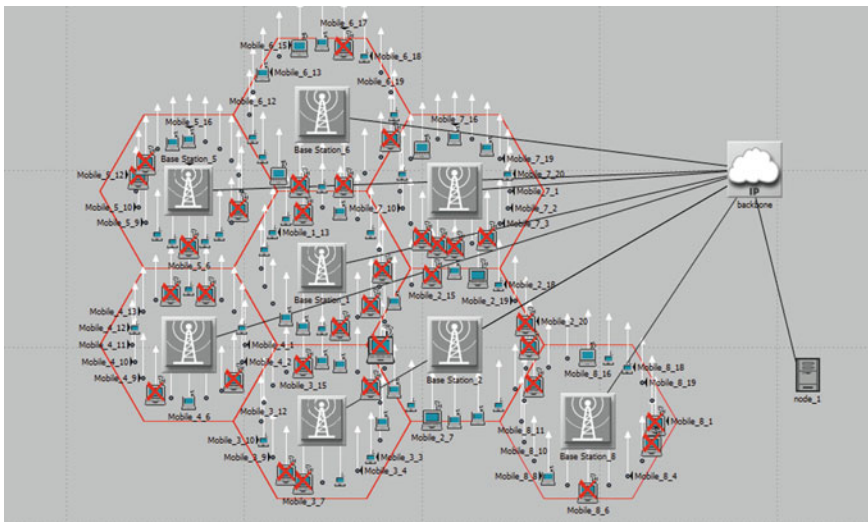


Fig. 1 WiMAX Network

Table 1 Comparison table of End-to-End Delay, throughput, traffic sent

Packet size	Voice codecs	Number of nodes failure	End-to-End Delay (s)	Traffic sent (bytes/s)	Throughput (bits/s)	MIMO traffic sent (bytes/s)	MIMO End-to-End delay (s)	MIMO throughput (bits/s)	
7	g711	0	0.216361	12,90,860	72474.1	12,90,990	0.22	69,999	
		4	0.24621	1.05E + 06	59008.9	10,20,000	0.239	55,000	
		6	0.22	9,10,000	70,000	9,00,010	0.22	71,000	
	g723	0	0.506817	109,000	9,990	1,09,000	0.501	10,010	
		4	0.55	89,000	6,000	88,900	0.5501	7500	
		6	0.49	78,500	8,500	78,950	0.499	9,990	
	g729	0	0.22	1,61,100	15,000	1,61,000	0.2198	11,500	
		4	0.25	1,30,000	9,980	1,30,000	0.2501	10,100	
		6	0.2198	118,890	14,950	1,18,500	0.2198	15,000	
	13	g711	0	0.3468	1.29E + 06	69436.4	12,99,990	0.35	68,000
			4	0.3711	9,01,100	53,000	10,10,000	0.3601	6500
			6	0.3511	10,10,010	65,200	8,10,000	0.38	86,000
g723		0	0.888	1,09,090	9,990	1,19,000	0.86	9,000	
		4	0.889	86,050	8,000	88,000	0.91	5700	
		6	0.928	78,800	4,800	77,000	0.87	8000	
g729	0	0.35	1,61,010	13,000	1,60,010	0.3499	14,500		
	4	0.376	1,28,000	3500	1,30,000	0.38	10,700		
	6	0.3499	1,18,900	12,000	1,16,500	0.3499	12,000		

The following graphs show the different analyzed values on throughput, end-to-end delay, and traffic sent, in the same way for MIMO (Figs. 2 and 3).

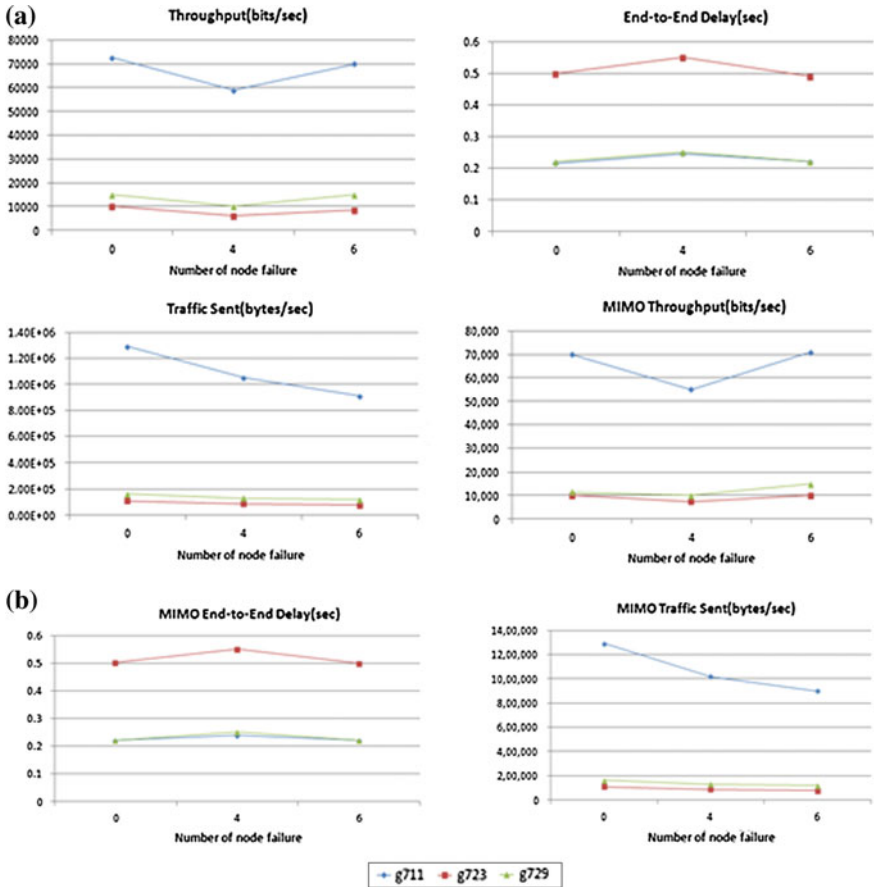


Fig. 2 a Result graphs of Throughput, End-to-End Delay, Traffic Sent and MIMO Throughput, for packet per frame size 7. b Result graphs of MIMO End-to-End Delay and MIMO Traffic Sent for packet per frame size 7

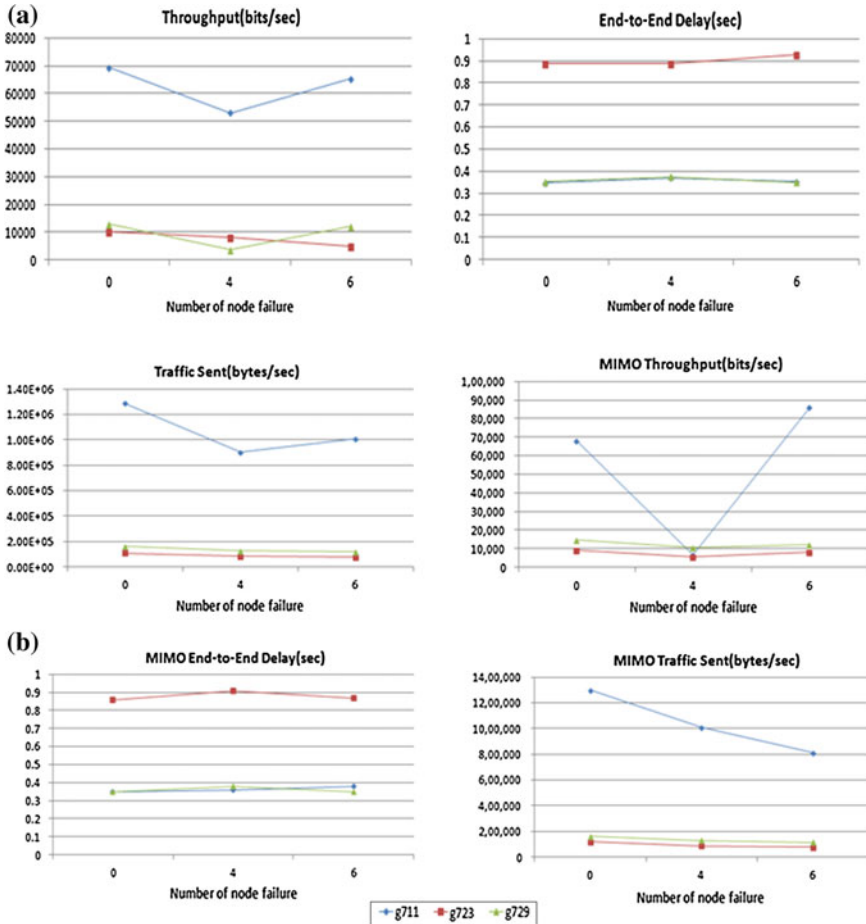


Fig. 3 a Result graphs of Throughput, End-to-End Delay, Traffic Sent and MIMO Throughput for packet per frame size 13. b Result graphs of MIMO End-to-End Delay and MIMO Traffic Sent for packet per frame size 13

Conclusion and Future Scope

In this research analyses the performance of VoIP over WiMAX by altering number of nodes failure in terms of end-to-end delay, traffic sent, and throughput are carried out for two types of transmitter techniques STC 2×1 MIMO and SISO under using the three voice codecs namely g711, g723, and g729. The results showed that with increase in nodes failure end-to-end delay increases and throughput and traffic sent decreases. The result also shows that the performance of g711 is better than other in

terms of end-to-end relay, traffic sent, and throughput. The result shows that for SISO Traffic sent is less and delay is more than MIMO. As a result the performance of MIMO is better than SISO.

Future Scope

In this research analysis the performance of VoIP over WiMAX under nodes failure has been evaluated by taking end-to-end delay, traffic sent, and throughput. We have done our work on various voice codecs and transmitters. In future one can analyze the VoIP over WiMAX by varying different parameters like network area, varying the number of nodes to be failed, using different transmitters. One can also evaluate the performance by varying the properties of nodes failure. Various other modulation techniques can also be used and the best can be chosen for practical implementation.

References

1. Cicconetti, C., Ert, A., Lenzini, L., Mingozi, E.: Performance evaluation of the IEEE 802.16 MAC for QoS support. *IEEE Trans. Mob. Comput.* **6**(1), 26–38 (2007)
2. Lee, B.G., Choi, S.: *Broadband Wireless Access and Local Networks: Mobile WiMAX and WiFi*. Artech House, Boston, London (2007)
3. WiMAX (802.16) specialized model, OPNET. <http://www.opnet.com/WiMAX/index.html>
4. Malik, G., Singh, A.: Performance Evaluation of WiFi and WiMAX Using Opnet. *Int. J. Adv. Res. Comput. Sci. Softw. Eng.* **3**(6), (2002)
5. Sengupta, S., Chatterjee, M., Ganguly, S.: Improving quality of VoIP streams over WiMAX. *IEEE Trans. Comput.* **57**(2), (2008)
6. Halepovic, E., Ghaderi, M., Williamson, C.: *Multimedia application performance on a WiMAX network* (2008)
7. Alshomrani, S., Qamar, S., Jan, S., Khan, I., Shah, I.A.: QoS of VoIP over WiMAX access networks. *Int. J. Comput. Sci. Telecommun.* **3**(4), (2012)
8. Elechi Onyekachi, O., et al.: Investigating the QoS of Voice over IP using WiMAX Access Networks in a Campus Network. *Comput. Eng. Intell. Syst.* **4**(5), (2013) www.iiste.org ISSN 2222-1719 (Paper) ISSN 2222-2863
9. Singh, P., Kaur, R.: VoIP Over Wimax: a comprehensive review. (*IJCSIT*) *Int. J. Comput. Sci. Inf. Technol.* **5**(4), 5533–5535 (2014)

Design of Reduced Order Controller for Mechanical System

Jyoti Kataria, Manish Kumar Madhav and Sunny Kumar Verma

Abstract Most of control system designing methods are based on mathematical model of the object. Consequently, it is very thorny to design the controller when containing high order. For this purpose, the system is modelled as linear time invariant system using well-known laws of mechanics, and then use model order reduction techniques for reducing the system. Using the state derivative feedback and reduction methods a reduced state derivative feedback controller is designed and used for a mechanical system. In addition comparison is done with state feedback controller and state derivative feedback controller.

Keywords Mathematical modelling · Feedback gain matrix · Reduced controller design

Introduction

The estimates of a high-order system by a low-order model have a momentous importance in controller design and control system analysis [1–9]. The mathematical modelling of the system is used in study and analysis of any physical system such as mechanical system, control systems (temperature control, missile direction control, etc.). The main approach of mathematical modelling is converting the system dynamics using simple laws of physics into linear differential equation.

Jyoti Kataria (✉)

KIIT College of Engineering, Gurgaon, Haryana, India

e-mail: kataria.jyoti315@gmail.com

M.K. Madhav

Sri Ramswaroop Memorial University, Lucknow, Uttar Pradesh, India

e-mail: manishh.madhav@gmail.com

S.K. Verma

MITRC College of Engineering, Alwar, Rajasthan, India

e-mail: kumarvsunny5@gmail.com

© Springer India 2016

N. Afzalpulkar et al. (eds.), *Proceedings of the International Conference*

On Recent Cognizance in Wireless Communication & Image Processing,

DOI 10.1007/978-81-322-2638-3_104

And it may be possible that the order of linear differential equation may be extremely high. Or we can state that system is made by interconnection of different subsystems, because of that the system model goes too high. Usually, analysis of such system is extremely thorny and this causes model of system reduced by various reduction techniques. The estimates of a high-order system by a low-order model have a significant meaning in controller design and control system analysis [1–9].

All the physical system is a set of physical substances related jointly to serve up a function. Examples of physical system may be a communication satellite, a steam turbine, an electronics amplifier, drives, etc. No physical system can be modelled by its absolute physical details available and subsequently idealizing assumptions are at all times organized for the explanation of assessment and creation of systems. A physical model means an idealized physical system. A same physical system can be modelled in various traditions depending upon study.

In this research paper modelling of the system for vibration control as linear time invariant system, due to this reason non-linearities present in the system are absent. In this research paper the design of a reduced controller for mechanical system is presented. For designing purpose, we have taken an example of a vibration control system.

Mathematical Modelling of Physical System

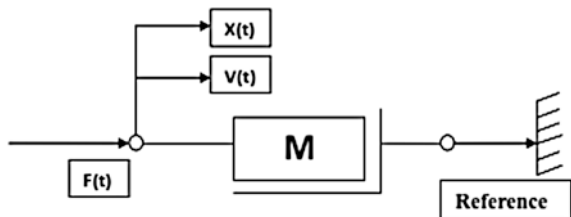
Any mechanical systems can be modelled by means of three ideal elements [10]; the mass element, damper element and spring element. All three are discussed below one by one in Figs. 1, 2 and 3.

(1) THE MASS ELEMENT

Physical governing equation is

$$F = M \frac{dv}{dt} = M \frac{d^2x}{dt^2} \tag{1}$$

Fig. 1 Mass Element



(2) THE SPRING ELEMENT

Physical governing equation is

$$\begin{aligned}
 F &= K(x_1 - x_2) = Kx \\
 &= K \int_{-\infty}^t (v_1 - v_2) = K \int_{-\infty}^t v dt
 \end{aligned}
 \tag{2}$$

(3) THE DAMPER ELEMENT

Physical governing equation is

$$\begin{aligned}
 F &= f(v_1 - v_2) = fv \\
 &= f(x_1 - x_2) = fx
 \end{aligned}
 \tag{3}$$

In the above three elements mass, damper and spring, damper is energy dissipating element and the mass as well as spring are energy-storing elements.

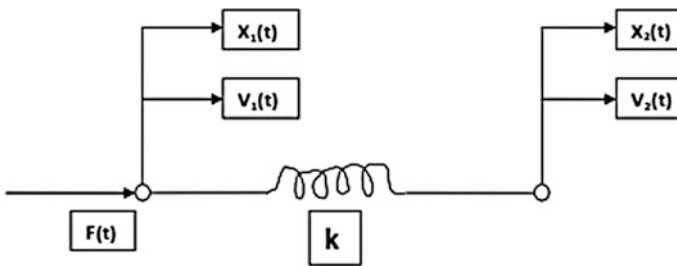


Fig. 2 Spring Element

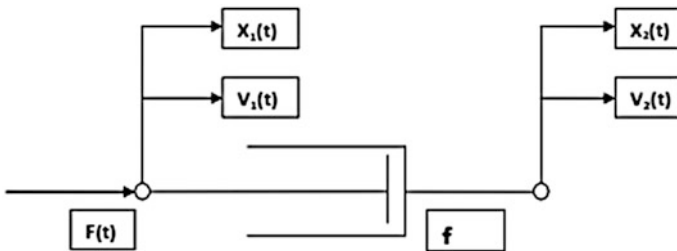


Fig. 3 Damper Element

A mathematical differential equation results when a mechanical system which is modelled using the above three ideal elements and then further Laplace transforming it gives transfer function of the system (taking initial conditions zero).

Design of Reduced Order Controller for Mechanical System

For designing a reduced controller for mechanical system, first, the above rules for modelling the system as a transfer function model are used then a reduced controller is designed using the algorithm.

Designing steps of reduced controller procedure [11].

Step 1—Take the system transfer function given as

$$H(s) = \frac{b_1s^{n-1} + \dots + b_n}{a_0s^n + a_1s^{n-1} + \dots + a_n} \tag{4}$$

Step 2—Convert it into state space form (controllable canonical form) given as

$$\dot{z}(t) = \begin{bmatrix} 0 & 1 & 0 & \dots & 0 \\ 0 & 0 & 1 & \dots & 0 \\ \vdots & \vdots & \vdots & \ddots & \vdots \\ 0 & 0 & 0 & \dots & 1 \\ -a_0 & -a_1 & -a_2 & \dots & -a_{n-1} \end{bmatrix} z + \begin{bmatrix} 0 \\ 0 \\ \vdots \\ 0 \\ 1 \end{bmatrix} u$$

Step 3—Solve it for state derivative feedback controller, where desired poles location is given by solving Riccati equation and desired poles are given by

$$D(s) = (s - \lambda_1)(s - \lambda_2) \dots (s - \lambda_n) = s^n + d_{n-1}s^{n-1} + \dots + d_1s + d_0 \tag{5}$$

Step 4—Now applying the procedure given by [12]; find feedback gain matrix K, given as

$$K = [K_1 \quad K_2 \quad \dots \quad K_n]$$

Step 5—Now applying feedback, we found the reference model for reduced methods which are used reduced controller design

Step 6—Applying reduction methods, which are explained by [1–9], one by one to the system model (1), and find Kth order reduced model of the system. $R_k(s) = A_k(s)/B_k(s)$. And find the poles of reduced model, which are preserved in the reduced model.

Step 7—Now on the basis of dominant pole behaviour preserves the k number of poles from desired poles location and then applying the same above procedure from (1) to (4) and find the reduced controller as

$$K_r = [K_1 \quad K_2 \quad \dots \quad K_k \quad \dots \quad 00]$$

Step 8—This is the required reduced controller. All these steps can be easily implemented by using a numerical analysis.

Numerical Analysis

In this paper, design of reduced order controller for mechanical system is discussed by using an example of a vibration control system in Fig. 4.

Example: Vibration control system [10]

After using the above rules, the transfer function of the system

$$G(S) = \frac{X_2(s)}{F(s)} = \frac{sB_{12}}{(s^2M_1 + sB_{12} + sf_{c1} + k_1)(s^2M_2 + sB_{12} + sf_{c2} + k_2) - s^2B_{12}^2} \quad (6)$$

For simulation, let the parameters are as follows:

$$M_1 = 10 \text{ kg}; M_2 = 100 \text{ kg}; k_1 = 360 \frac{kN}{m}; k_2 = 36 \frac{kN}{m}; f_{c1} = 70 \frac{Ns}{m};$$

$$f_{c2} = 50 \frac{Ns}{m}; B_{12} = 60Ns/m.$$

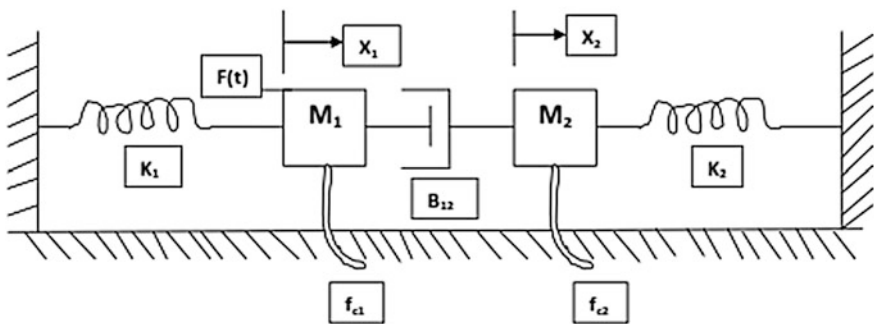


Fig. 4 Vibration control system

This yields

$$G(s) = \frac{60s}{10^3s^4 + 14100s^3 + 36370700s^2 + 44280000s + 12960 * 10^6} \tag{7}$$

Converting it into canonical controllable form as

$$\dot{x}(t) = \begin{bmatrix} 0 & 1 & 0 & 0 \\ 0 & 0 & 1 & 0 \\ 0 & 0 & 0 & 1 \\ -12960 * 10^3 & -44280 & -36370.7 & -14.1 \end{bmatrix} x(t) + \begin{bmatrix} 0 \\ 0 \\ 0 \\ 1 \end{bmatrix} u(t)$$

$$y(t) = [0.0600]x(t)$$

Second-order reduced model of system using RA method

$$R(s) = \frac{1.8608 * 10^{-6}s}{s^2 + 1.3733s + 401.94} \tag{8}$$

Now, solving the Riccati equation for, we found the desired poles equation

$$-1136.3 + 1169.8i, -1136.3 - 1169.8i, -292.4, -1.0$$

Now, using reduction methods reduced controller is

$$K_{rRA} = [401.941 \quad 0.3747 \quad 0 \quad 0]$$

Using the procedure full state derivative feedback controller is found as

$$K = [12998319.85 \quad 19184.91 \quad 28.7522 \quad -0.9833]$$

For this system state feedback controller

$$K_{state} = [764709885.1 \quad 780949723 \quad 3290312.27 \quad 2551.9]$$

Conclusion and Result

The comparison graph (from Figs. 5, 6 and 7) and different values of K , feedback gain matrix (from above discussed result) concluded that both state derivative controller and state feedback controller can remove vibrations for a vibration control system. But the state derivative controller required a lesser amount of

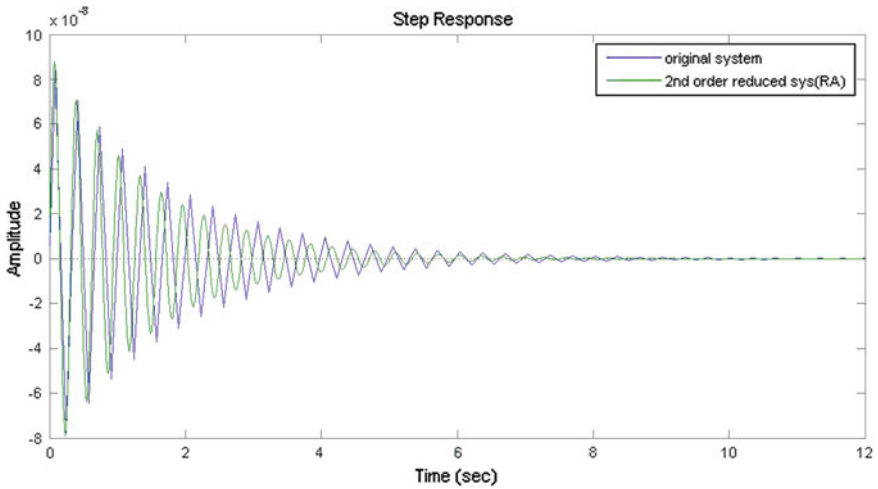


Fig. 5 Comparison of step response without controller

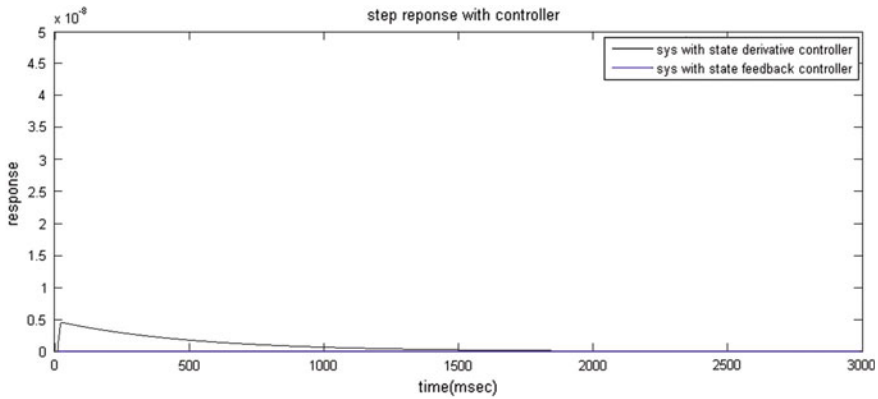


Fig. 6 Vibration control with state derivative control and state feedback control

energy in association with state feedback controller for the reason that coefficient f feedback matrix has less K in comparison with K_{state} . And reduced controller (design with help of Routh approximation reduction method) cannot eliminate vibration completely. The comparison plots are exposed in Figs. 5, 6 and 7.

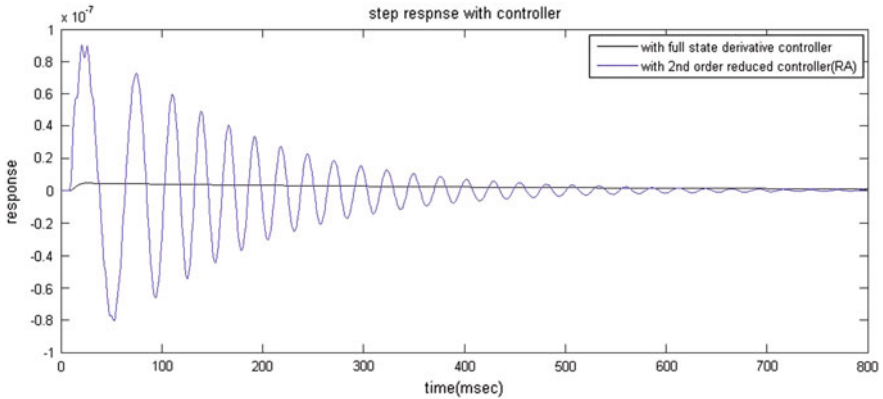


Fig. 7 Vibration control with full state derivative control and second-order reduced controller

References

1. Hutton, M.F., Friendland, B.: Routh approximation for reducing order of linear, time-invariant system. *IEEE Trans. Autom. Control*, **ac-20**(3), (1975)
2. Singh, V.: Improved stable approximants using the Routh array. *IEEE Trans.* **AC-26**, 581–583 (1981)
3. Lamba, S.S., Bandyopadhyay, B.: An improvement on Routh approximation technique. *IEEE Trans.* **AC-31**, 1047–1050 (1986)
4. Bandyopadhyay, B., Rao, A., Singh, H.: On pade approximation for multivariable systems. *IEEE Trans. Circuits Syst.* **36**(4), 638–639 (1989)
5. Hsieh, C. A., Hwang, C.: Model reduction of continuous-time systems using a modified Routh approximation method. In: *IEE Proceeding D. Control Theory Applications*, vol. 136, no 4, pp. 151–156 (1989)
6. Choo, Y.: Improvement to modified Routh approximation method. *Electron. Lett.* **35**(7), (1999)
7. Choo, Y.: Direct method for obtaining modified Routh approximants. *Electron. Lett.* **35**(79), (1999)
8. Jamshidi, M.: An overview on the aggregation of large scale systems (1981)
9. Janardhanan, J.: Model order reduction and controller design techniques **42** (2005)
10. Nagrath, I.J., Gopal, M.: *Control System Engineering*, Third Edition, New Delhi (1999)
11. Nguyen, C.H.: Designing controller by state space techniques using reduced order model algorithm. In: *Fourth International Conference on Intelligent Computation Technology and Automation*, pp. 530–992. *IEEE* (2011)
12. Abdelaziz, T.H.S., Valášek, M.: Pole-placement for SISO linear systems by state-derivative feedback. In: *IEE Proceedings-Control Theory Applications*, vol. 151, No. 4, July 2004

A Survey on Black Hole Attack in MANET

Shruti Singh, Abhishek Bajpai and Suryambika

Abstract Security is a primary goal in order to provide data transmission or communication among mobile hops in hostile wireless environment. MANET is self-configuration and decentralized-type network and it is different from wired one. Some unique characteristics of MANET are dynamic topology, self-configuration, and strict resources and shared medium; make it different from wired infrastructure. All nodes in mobile ad hoc network perform their task in associative way. These characteristics become also challenges for MANET to some extent and make a situation to build a solution that provides broad protection and efficient performance. Security is a very important characteristic during implementation of MANET or other network. MANET is widely used in our daily life like meeting, conference, medical field emergency situations like flood, earthquake, and military operation. In this chapter we discuss on the security services in MANET. We also discuss security attack at different layers and our major concern about network layer attack is especially on black hole attack and its existing solution.

Keywords MANET · Black hole attack · Tunneling attack · Dynamic topology

Introduction

In recent years ad hoc network is used commonly, everywhere, likes PDAs, mobile phones, GPS, laptops, etc. In addition, these devices create a wireless network environment because microprocessors and sensors inbuilt in it. Wireless networks

Shruti Singh (✉) · Suryambika
Department of Computer Science & Engineering, SRMU,
Barabanki 225003, India
e-mail: srt0701@gmail.com

Suryambika
e-mail: Suryambikasingh12@gmail.com

Abhishek Bajpai
Faculty of Computer Science & Engineering, SRMU, Barabanki 225003, India
e-mail: Abhishek_vajpayee@hotmail.com

are very popular due to use of multi-hop communication networks (MCNs). By using MCNs, wireless networks become more flexible and provide easy debugging and less cost of maintenance. The wireless network system is distributed in such manner where the communication between sensors and actuators is done by wireless multi-hop communication network [1].

There are many applications in mobile ad hoc network which does not support fixed infrastructure, for example, defense, natural disaster, military tank in battle-field, conference and meeting and information sharing, etc., so these applications need a different type of network which does depend on fixed infrastructure or centralized environment. This need will lead to emergence of Ad hoc network. There is no requirement of central authority because it is a decentralized [2]. The lifespan of MANET is short in comparison to wired network because in such network devices equipped very limited resources and battery power [3]. There is an issue of free riding in MANET, which affects its performance. Free riding means participating node only consume the resources not contribute or share their resources [4]. There are some distinct characteristics are shown by MANET such as weaker security, size limitation of battery, limited battery life, dynamic topology, and limited bandwidth. Above-mentioned characteristics are the security constrained from MANET [5].

As we know MANET is highly adaptable so it is very useful in different applications like meeting, video conferencing, rescue, military operation, natural disaster, polling system, and many more [6]. MANET security solution provides some security services to its user like authenticity, confidentiality, integrity, and availability. Various protocols used in MANET and some of them are AODV, HSR, etc. [7]. MANET is dynamic network [8].

The layout of the paper is arranged as follows. Section “[Routing in MANET](#)” describes the different routing technique of MANET. Section “[Security Threats](#)” illustrates about the security threats of MANET, which occurred due to its unique characteristics. In section “[Challenges in MANET](#),” we talk about the security constraint. Network layer attack is illustrated in section “[Network Layer Attack](#).” Section [Black Hole Attack](#) elaborates about the black hole attack and its related work. And finally we talk about the conclusion and future work regarding topic in section “[Conclusion and Future Work](#)”.

Routing in MANET

As dynamic nature of MANET whose structure is shown in Fig. 1, nodes do not have any prior knowledge about the topology; therefore, they have to assume topology. All nodes in MANET advertise its presence characteristics, RREQ and RREP to all participating node, this way by which all nodes are able to find the path from source to destination. However, routing is a major challenge in MANET because of redundant migration of nodes [6, 9]. When we are designing a protocol for ad hoc network we have to consider some factors, and these factors are mentioned below [10].

Fig. 1 Structure of MANET [18]

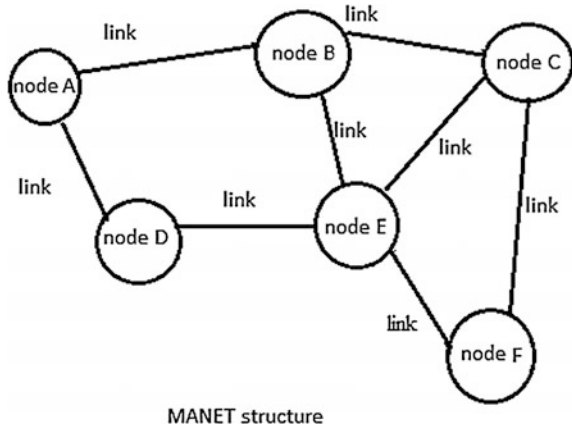


Table 1 Kind of routing protocol

Protocol type	Example
Table-based (Proactive)	DSDV, OLSR, FSR
On-demand (Reactive)	AODV, DSR etc.
Hybrid	ZRP, HSR, CGSR etc.

A. Distributed nature operation

Protocol must be in distributed nature because all nodes in MANET distributed at different location and are mobile in nature.

B. Loop-free operation

MANET protocol must be route-free, i.e., when a node cannot find the route then it avoids spinning from node to node in continuous manner.

C. Reactive operation versus Proactive operation

In MANET, both types of routing done are on-demand need and predefined need; so routing protocol is either demands based, i.e., reactive or predefined need based, i.e., proactive.

D. "Sleep" interval operation

All protocols have to be designed in order to conserve energy means when a node has not actively participated in network then it must be in sleep mode so energy of that node is conserved for future use. Different kinds of protocol are shown in Table 1.

Security Threats

Security is a major concern in every network, either wireless or wired network, but wireless network is more prone to attack in comparison to wired one. And we know that connectivity among mobile nodes and multimode wireless channel in MANET is provided by data link layer protocol.

Absences of trusted central administration, limited amount of energy, dynamic topology are some restriction that leads to security attack. Intruders in MANET have same purpose, i.e., either drop all data or alter the parameter of message. Intruder also tries to burn out the battery backup by misguiding the routing message. For example sending wrong message to wrong direction leads to energy wastage [11]. Active attack is easy to detect because it disturbs the network but passive attack is not easy to detect because it obtains data in sleep mode without disturbing network [12].

Routing attack is an attack which does not follow the guidelines of routing protocol, but their behavior related to the routing protocol. Example in term of distance source routing (DSR) [13] the attacker node alter the sender node route mentioned in the RREQ or RREP packets by removing a node from list, swapping the order of node in the list and supplementing a new node in the list. But when we talk about distance vector routing protocol such as AODV [14] it is different from DSR, in this attacker node promote itself as it has the shortest and valid path to destination with the highest sequence number but actually it does not have. Packet forwarding attack lies under denial of service attack. In this attack intruder node insert a huge amount of trash packet and these packets waste important portion of data and lead to congestion. Classification of attacks is given below [15]. There are various kinds of attacks at layers as mentioned above in Table 2.

A. Basic security attack

These are further classified into active attack and passive attack.

1. *Active Attack*: In this attack, malicious node needs extra energy to perform attack and disturb the network during attack.
2. *Passive Attack*: In this attack attacker only listens to the traffic, observes silently, and does not disturb the network.

B. Other common attack

There are some more attacks in MANET other than basic attack and they are mentioned below.

Table 2 Attacks on different layer

Layers	Issues	Example
Application layer	Prevention and detection virus worms and malicious code	•Repudiation •Malicious code
Transport layer	Authenticating and securing end-to-end communication	•Session hijacking
Network layer	Protects routing and forwarding message	•DoS attacks
Data link layer	Provides link layer security	•Traffic analysis •Traffic monitoring
Physical layer	Prevents signal jamming DoS attack	•Eavesdropping

1. *Denial of services*: In this attack, a malicious node is trying to make resources unavailable to its neighboring node and interrupts the network for some duration [16].
2. *Impersonation*: An attacker successfully gets the identity of one of legal participating nodes in the communication system [17].
3. *Eavesdropping*: It is a type of attack in which an attacker is trying to listen in the confidential data like password, pin, session key, etc., during communication. It is an illegal interception of secure communication like phone calls, video, or many more [18, 19].

In this paper our major focus is on black hole attack, which lies under network layer attack. Table 2 shows the various type of security threats at different layer with issues arise at each layer [6, 9].

Challenges in MANET

There are different challenges of wireless infrastructure like strict resources, decentralized infrastructure, limited power backup, limited bandwidth, etc. In MANET, each device is connected virtually not physically, so there is no fix point where we can apply a single security solution. So this is also a challenge for MANET infrastructure. The strict resources constrain one of critical challenge to security design in mobile ad hoc networks. Resources like bandwidth, computation capability, and limited power are constrained in MANET [7].

Decentralized infrastructure is also a security constrained in MANET because in such type of network every hop behave as a host, a destination, and a router. Each hop manages its resources and failure. In this network new hop can easily be added or removed so maintaining hop information become overhead. So we can say mobility is also a challenge in MANET [7]. So the above-mentioned challenges show that we have to protect mobile ad hoc network from different constraints and issues. The security scheme should provide security at each layer and span throughout the protocol stack of all layers and security scheme should provide prevention from both type of threats, i.e., insider and outsider. So, we can say that security scheme should follow these three steps—prevention, detection, and reaction [7].

Network Layer Attack

Network layer is a very important layer and responsible for routing. There are some set of functions performed by network layer like host addressing connection less and connection-oriented communication, packet forwarding. At this layer malicious

node disrupts the network by sending false message. This layer is also prone to threat [14]. So making network layer as attack free is a very robust task.

There are various kinds of attack at network layer as mentioned below in Table 3, here we discuss DoS attack (black hole, wormhole, gray hole, rushing attack), routing attack (routing table overflow, packet replication).

A. Wormhole attack

Wormhole attack is refers as tunneling attack which is severely dangerous because it can damage also those data which is very confidential [13]. In this attack, two intruders launch attack in coordinative way. These two nodes linked with each other through wired or wireless link and link called wormhole tunnel [20].

B. Gray hole attack

Nodes behavior is unpredictable in this attack. In gray hole attack, malicious node may drop the packet with some certainty and may behave as malicious node for certain period of time and also for certain node.

C. Rushing hole attack

In rushing hole attack, malicious node is trying to damage the RREQ, alter the list of node and rushing nodes packet to its neighbor node. As we know in reactive protocol, only one RREQ packet forwarded, so if the packet sent by attacker first reaches the destination node then attack node makes a path to source easily, and easily discovers route to other node [20, 21].

D. Routing table flow attack

In this attack, an attacker announces or discloses a route from authorized node to the node which does not exist in the network. The main idea behind this attack is to create overflow in the routing table [22].

E. Packet replication

It is an attack which occurs on network layer and a type of internal attack. The attacker and the victim node both are inside the network and attacker node is try to intrude the inside resources. When this attack performed, a replica created by attacker node of delayed node and forwards them to provoke network. The outcome of this attack is that attacker node start consuming battery and resources of node [23].

Table 3 Comparison of different attacks

Name of attack	Type	Action	Effect
Black hole	DoS	Drop the packet	Misguide route
Worm hole	DoS	Either drop the packet or send	Confidentiality affected
Gray hole	DoS	Node either drops packet or behaves normally	Tear down the performance
Rushing hole	DoS	Misguide to source	Overhead
Routing table overflow	Routing attack	Create false route	Overflow in network
Packet replication	Routing attack	Replica table is created	More battery consumption

Black Hole Attack

In this attack an intruder node shows itself as having authentic and nearest path to destination but actually not. Intruder node drops all packets when it gets data. Side by side, attacker node observes the network traffic to monitor the activity of each participating node [7].

A. Working in black hole

We have shown the working of black hole attack in Fig. 2 [24]. Let source S want to communicate with node source start route finding process by broadcasting RREQ packet to its all-neighboring node. After getting RREQ, destination (D) node or any intermediate node gives reply back by RREP packet to a node having fresh route to source. X is a malicious node, it does not forward RREQ packet, and it replies source by announcing itself having a short and valid path to destination. When reply from X reaches S, S considers it a valid path and sends packet via X to destination (D) but node X drops all packet instead of forward packet to D.

B. Categories of black hole

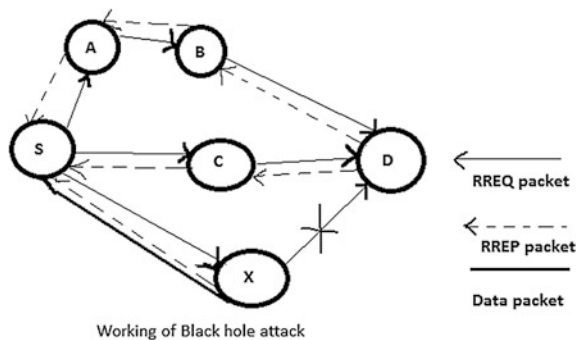
1. *Single black hole*: In this attack single node performs attack and reacts as it having the smallest route to destination [20].
2. *Cooperative black hole*: In this attack, two or more nodes cooperate with each other. This attack is tough to catch [20].

C. Existed solutions regarding black hole attack

There are various solutions presented in many research papers, but in this paper we discuss some of them.

- In article [25], reply packet authenticity approach is used. In this approach authenticity of node is verified by sending reply packet and wait for reply from two or more than two nodes. But there is one limitation for this, i.e., longer delay.
- In article [26], MOSAODV approach is used. In this source node after receiving first RREP packet wait for particular time, during this period source node all previously received RREP message in table. The packet when having very high

Fig. 2 Working of black hole attack [2]



sequence number is discarded but limitation of this technique is raised in end-to-end delivery.

- In [27], author used DPRAODV approach. A threshold value is taken for verification, if RREP packet has sequence number greater than threshold value, then node is considered as a malicious node.
- In article [28], checking for information is done by FREP and REQ. In this approach modified version of AODV is used. This approach is used to identify cooperative black hole node between source and destination. It uses further REQ (REQ) and further REP(FREP) for cross-checking. Limitation of this approach is that this solution is better only when more percentage of black hole nodes are present.
- In article [11], unique sequence number for receive and sent packet approach is used. This approach checks the authenticity of node by comparing the sequence number; if the node has higher value than current node, then it is considered as a secure node otherwise it is considered as malicious node. The disadvantage is that it is not much secure.
- In [29], author used fuzzy logic, which is based on mamdani fuzzy inference system approach. It first checks the Varsity level of participating node then this Varsity level is compared with threshold value; if the value is less than the threshold then the node is considered as malicious node.

Conclusion and Future Work

MANET is a type of wireless network which is easily deployable anywhere or in any critical situation like natural disaster, military operation, etc. Therefore, it is very useful and important in today's scenario. Using mobile ad hoc network is quite beneficial but it has many challenges like mobility, security, and many more. Security is a very essential characteristic of any network during deployment. In this article, we discuss about MANET and its challenges and security attack especially about black hole attack with its existing solutions, but there are still many attacks for future work. Gray hole attack, Sybil attack, and its solution can also be considered.

References

1. D'Innocenzo, A., Di Benedetto, M.D., Smarra, F.: Fault detection and isolation of malicious nodes in MIMO multi-hop control networks. In: IEEE 52nd Annual Conference on Decision and Control (CDC). IEEE (2013)
2. Djenouri, D., Khelladi, L., Badache, N.: A survey of security issues in mobile ad hoc networks. *IEEE Commun. Surv.* **7**(4), 2–28 (2005)
3. Lo, N.-W., Liu, F.-L.: A secure routing protocol to prevent cooperative black hole attack in MANET. In: *Intelligent Technologies and Engineering Systems*, pp. 59–65. Springer, New York (2013)

4. Mundinger, J., Le Boudec, J.-Y.: Analysis of a reputation system for mobile ad-hoc networks with liars. *Perform. Eval.* **65**(3), 212–226 (2008)
5. Sharma, K., Khandelwal, N., Prabhakar, M.: An overview of security problems in MANET. In: *Proceedings of the International Conference on Network Protocols (ICNP)* (2010)
6. Jhaveri, R.H., Patel, S.J., Jinwala, D.C.: DoS attacks in mobile ad hoc networks: a survey. In: *Second International Conference on Advanced Computing & Communication Technologies (ACCT)*. IEEE (2012)
7. Yang, H., et al.: Security in mobile ad hoc networks: challenges and solutions. *IEEE Wireless Commun.* **11**(1) 38–47 (2004)
8. Rai, P., Singh, S.: A review of ‘MANET’s security aspects and challenges’. *Int. J. Comput. Appl. IJCA* **4**, 162–166 (2010)
9. Qasim, N., Said, F., Aghvami, H.: Performance evaluation of mobile ad hoc networking protocols. In: *Advances in Electrical Engineering and Computational Science*, pp. 219–229. Springer, The Netherlands (2009)
10. Gupta, R.: Mobile adhoc network (MANETS): proposed solution to security related issues. *Indian J. Comput. Sci. Eng. (IJCSE)* **2**(5), 748–46 (2011)
11. Sharma, N., Sharma, A.: The Black-hole node attack in MANET. In: *Second International Conference on Advanced Computing and Communication Technologies (ACCT)*. IEEE (2012)
12. Perkins, C.E., Royer, E.M.: Ad-hoc on-demand distance vector routing. In: *Proceedings of Second IEEE Workshop on Mobile Computing Systems and Applications, WMCSA’99*. IEEE (1999)
13. Jhaveri, R. H., et al.: MANET routing protocols and wormhole attack against AODV. *Int. J. Comput. Sci. Netw. Secur.* **10**(4), 12–18 (2010)
14. Nadeem, A., Howarth, M.P.: A survey of MANET intrusion detection & prevention approaches for network layer attacks. *IEEE Commun. Surv. Tut.* **15**(4), 2027–2045 (2013)
15. Darji, D., Thakkar, N.B.: Challenges in mobile ad hoc networks: security threats and its solutions. *Indian J. Appl. Res.* (2013)
16. http://www.webopedia.com/TERM/D/DoS_attack.html. Accessed Nov 2014
17. <http://www.springerreference.com/docs/html/chapterdbid/317115.html>. Accessed Nov 2014
18. <http://searchfinancialsecurity.techtarget.com/definition/eavesdropping>. Accessed Nov 2014
19. https://www.owasp.org/index.php/Network_Eavesdropping. Accessed Nov 2014
20. <https://sites.google.com/site/securezrp/routingattacks>. Accessed Nov 2014
21. www.wikipedia.com. Accessed Nov 2014
22. <http://www.informit.com/articles/article.aspx?p=361984&seqNum=10> (2014)
23. http://www.answers.com/Q/What_is_Packet_Replication_Attack. Accessed Nov 2014
24. Tamilselvan, L., Sankaranarayanan, V.: Prevention of blackhole attack in MANET. In: *The 2nd International Conference on Wireless Broadband and Ultra Wideband Communications, AusWireless 2007*. IEEE (2007)
25. Al-Shurman, M., Yoo, S.-M., Park, S.: Black hole attack in mobile ad hoc networks. In: *Proceedings of the 42nd Annual Southeast Regional Conference*. ACM (2004)
26. Mistry, N., Jinwala, D.C., Zaveri, M.: Improving AODV protocol against blackhole attacks. In: *Proceedings of the International Multi Conference of Engineers and Computer Scientists*, vol. 2 (2010)
27. Raj, P.N., Swadas, P.B.: Dpraodv: a dyanamic learning system against blackhole attack in aodv based manet (2009). arXiv preprint [arXiv:0909.2371](https://arxiv.org/abs/0909.2371)
28. Weerasinghe, H., Fu, H.: Preventing cooperative black hole attacks in mobile ad hoc networks: simulation implementation and evaluation. In: *Future generation communication and networking (fgcn 2007)*, vol. 2. IEEE (2007)
29. Chaudhary, A., Kumar, A., Tiwar, V.N.: A reliable solution against packet dropping attack due to malicious nodes using fuzzy logic in MANETs. In: *International Conference on Optimization, Reliability, and Information Technology (ICROIT)*. IEEE (2014)

Area-Efficient FPGA Model of LMS Filtering Algorithm

Devendra Goyal and Manish Singhal

Abstract Present technical scenario of communication system, adaptive filters has been widely used, in several applications such as adaptive interference cancellation, beamforming, prediction equalization, and plant identification. This research work proposes an area-efficient design of FPGA based least mean square. A control approach is used to minimize the state diagram of the FSM of the proposed filter design. Least mean square algorithm is usually used for low computational complexity, simplification, and better performance in different running environments.

Keywords Adaptive filters · LMS · FPGA · FSM

Introduction

The term filter is designed to take out data of prescribed quantity of interest from noisy data or mix data which is selective information for user, so a filter is a process which removes undesirable data from noisy data. An adaptive filter system has a transfer function that is controlled by variable parameters and these parameters are optimized according to an optimization algorithm. An adaptive filter has the key property of self-qualifying its frequency response to modify the behaviour in time, permitting the filter to accommodate the response of the input signal features update.

Devendra Goyal (✉)
Poornima College of Engineering, Jaipur, India
e-mail: devagoyal87@gmail.com

Manish Singhal
Department of Electronics and Communication,
Poornima College of Engineering, Jaipur, India
e-mail: manishsinghal@poornima.org

An adaptive filter is explained by the following:

- Which signal is being processed by the filter.
- Filter’s signal output is calculated from its signal input.
- Parametric quantities of filter’s architecture are changed by using series of iterations to change the relationship of input and output signals.
- Filter algorithm depicts about the adjustment of parameters at specific instant of time and application. Basic building blocks of adaptive filter are shown in Fig. 1.

Least Mean Square Filtering Algorithm

The stochastic gradient algorithm starts with an optimization principle which is named as method of steepest descent. In this method, the process starts with some initial value for tap weight vector and this value improves as the number of iteration increases. According to incoming data adaptive filter weights are used by LMS algorithm. Because of adaptive nature LMS algorithm is robust for different kinds of signal conditions (Fig. 2).

The resulting gradient-based algorithm is called least mean square (LMS) algorithm with update Eq. 1 [1]

$$w(k + 1) = w(k) + 2\mu e(k)x(k) \tag{1}$$

Fig. 1 Block diagram of adaptive filter

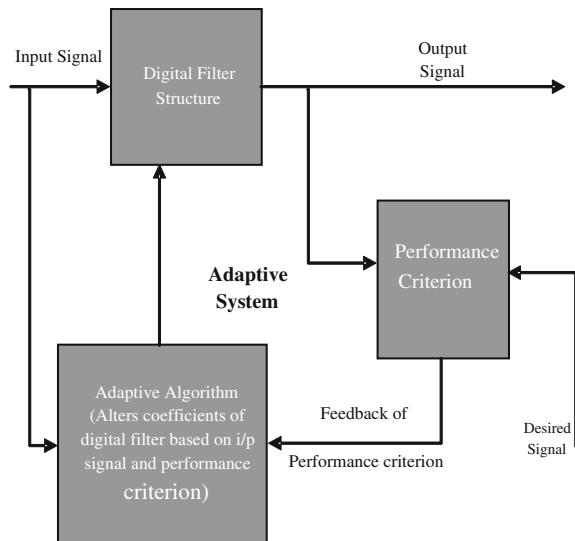
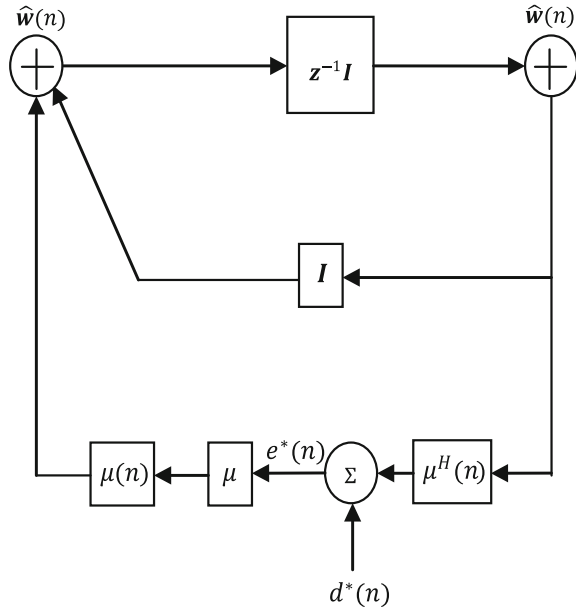


Fig. 2 Signal-flow graph representation of the least mean square algorithm [2]



In addition [3], to ensure the stability (or convergent) of the LMS algorithm, the step-size parameter is bounded by the Eq. 2

$$0 < \mu < \frac{1}{\text{Tap input power}} \tag{2}$$

where tap input power is the sum of the mean-squared values of all tap inputs in transversal filter, given by $\sum_{k=0}^{N-1} E[|x(n-k)|^2]$. Note that the upper bound is dependent on the statistics of filter input signals.

FPGA Modal of LMS Filter Algorithm

FPGA boards are planned to be assembled by a design engineers after manufacturing so that these boards called ‘Field-Programmable’. Hardware description language is used to specify FPGA configuration. To implement complex digital computations FPGAs have prominent resources of logic gates and RAM blocks [4]. The appropriate VHDL design of the LMS filter is shown in Fig. 3.

(a) FSM for Conventional LMS Filter Design

The control path FSM for the LMS filter design is implemented. The working of the two parallel pipeline data paths is controlled by the FSM controls. Figure 4

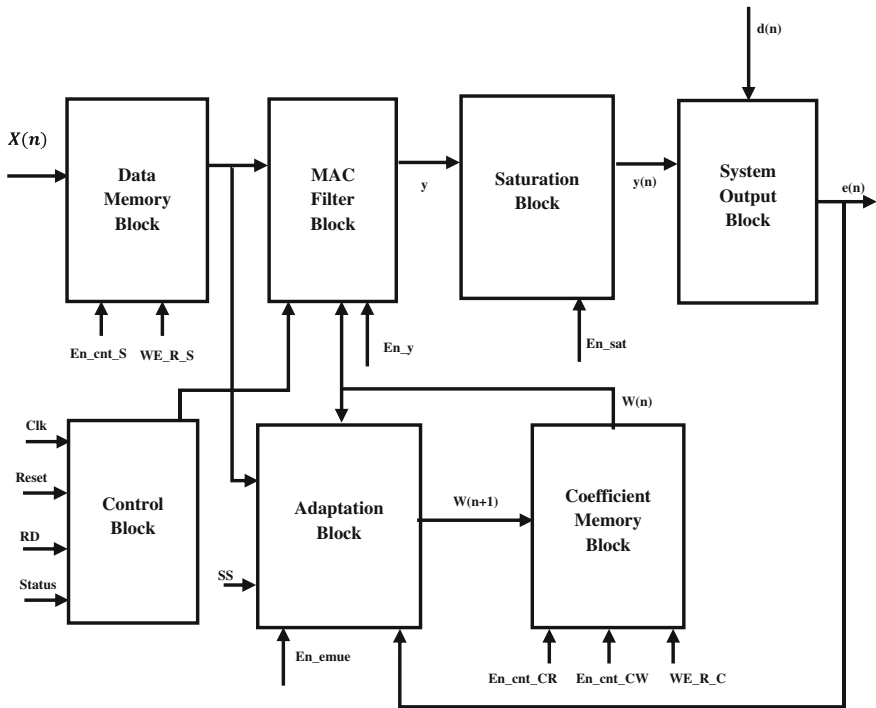


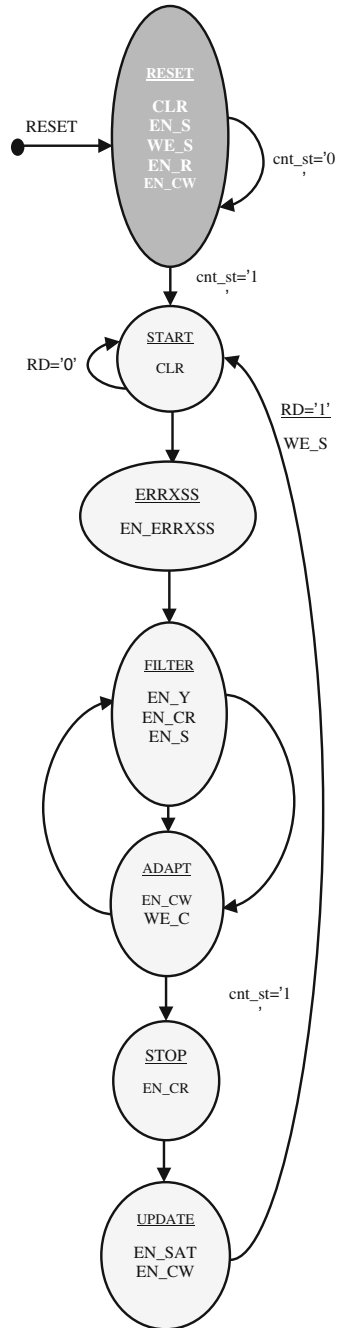
Fig. 3 VLSI modal of LMS filter

shows a FSM in which succession iteration is initiated with new input taste pair Err & XN . There are seven steps described for FSM as follows [5]:

The following sequences of FSM:

- **START:** In this state, all registers clears their previous value. The signal WE_S is used to store a new sample XN in RAM using an input RD .
- **ERRXSS:** It performs multiplication operation between step size factor SS & error signal Err and then store in register Reg_ErrxSS .
- **FILTER:** The parallel execution of two pipeline operation is done in this step. Updation of input sample, coefficient, outputting memory and accumulation of a product from sample and coefficient, then saves in register Reg_Y , such operations are performed by the filter.
- **ADAPT:** For adaptation of coefficients the pipeline performs updating operations for input sample data, coefficients, updating address for writing, outputting memory, accumulating the product from Ref_Fir & $ErrxSS$ on present coefficients.
- **STOP:** Stop is the final multiply operation of sample & coefficient and collection of result by the signal En_Y and then for the transition to a next state, read the address of coefficient from memory.

Fig. 4 FSM for the conventional LMS filter design



- **UPDATE:** The accumulation result is stored by the signal En_sat in output register and directed to saturation block and executes modification of RAM address.
- **RESET:** This state reset all registers and content of RAMs.

(b) FSM for Proposed LMS Filter Design

The updated FSM of the LMS filter design is implemented. Figure 5 describes a succession which is initiated with input sample XN and stored in RAM. There are five states described for FSM as follows:

The following sequences of FSM:

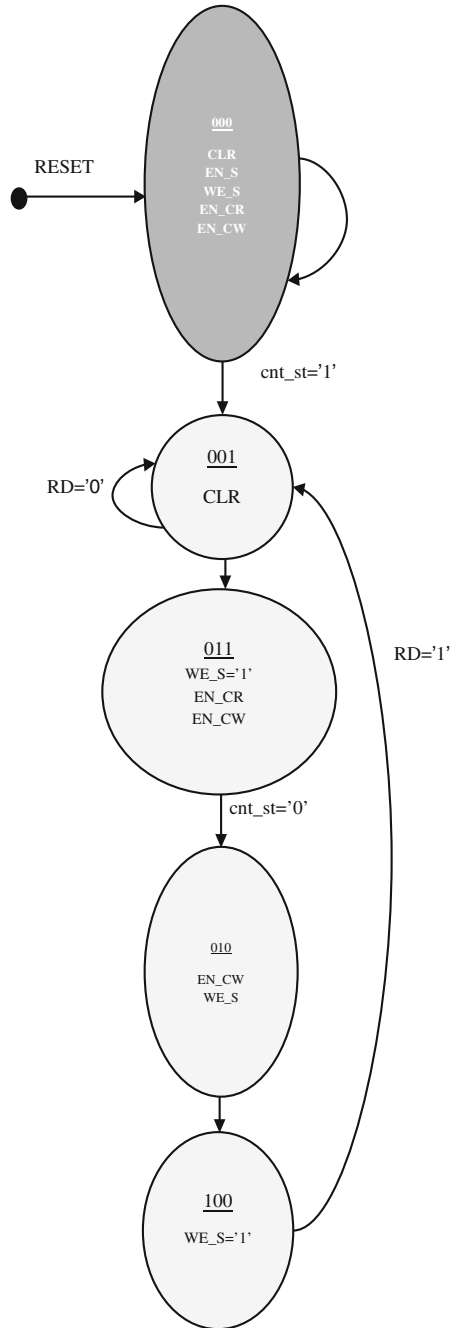
- **START (000):** All registers clear their previous value in this state with M multipliers and $M-1$ adders. This block is designed as three-stage operation round. The signal read from the data RAM block which is multiplied by WE_S is used to store input sample XN in RAM.
- **Wait State (001):** When coefficient memory is not written completely then it will wait for that state only.
- **Filter and Adaptation Block (011):** The filter block executes functioning of updating address for reading input sample, coefficient, output memory and accumulation of a product from sample & coefficient and then saves in register Reg_Y . The adaptation block performs updating reading input sample data, coefficient, updating address for writing, outputting memory, accumulating the product from ReC_Fir & $ErrxSS$ on present coefficient and storage of adapted coefficients.
 - **Update Block (010):** It is triggered if $En_cw = 1$. The accumulation result stored in the output register.
 - **Stop (100):** If $we_s = 1$, final data is written back to memory and it is return back to start state.

Synthesis Report

By using Xilinx 9.2 ISE and Modelsim 6.5e simulator; conventional LMS, Proposed LMS Filter are simulated. To develop RTL schematic of desired circuit, hardware is designed in a VHDL IDE to develop the RTL Schematic of desired circuit. This representation (.ngr file) is produced by Xilinx Synthesis Technology. Synthesis is the reverse process of simulation and acquires the designing of hardware from hardware description language.

In this process a physical system is designed using a pre-defined set of basic building blocks like logic gates, flip-flops, latches, small blocks of memory, LUTs in FPGA. The synthesis tool generalizes hardware architecture from the VHDL model. Then VHDL is compiled and mapped into an implementation technology such as an FPGA. Here Synthesis has been carried out using Xilinx9.2 ISE in which Spartan3 FPGA family is used.

Fig. 5 Modified FSM for the LMS filter design



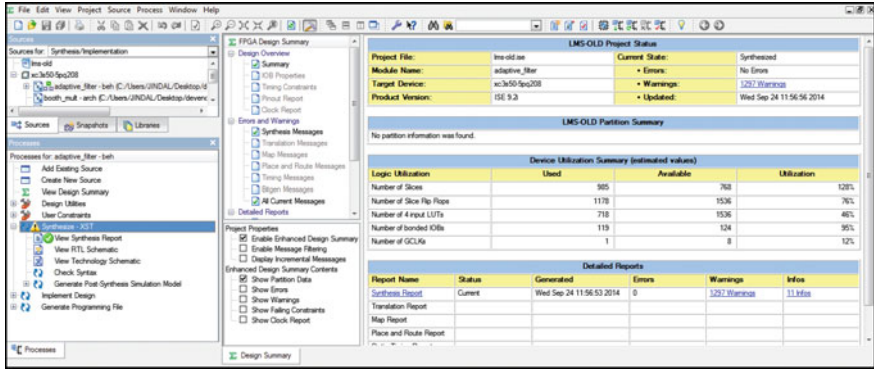


Fig. 6 Synthesis report for conventional LMS filter

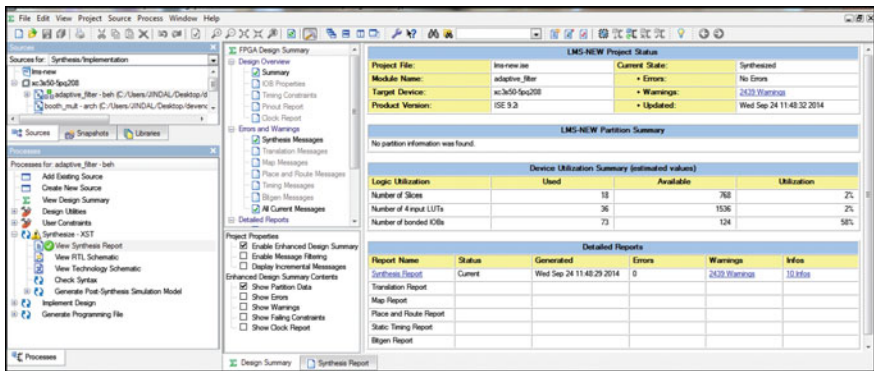


Fig. 7 Synthesis report for proposed LMS filter

Following Figs. 6 and 7 show the synthesis implementation of conventional LMS, Proposed LMS filters respectively [6].

Result Analysis

The comparative synthesis report of optimized area is described in between conventional LMS and proposed LMS. As the resultant table (Table 1) shows the improvement in the area reduction of LMS algorithm for different four parameters.

Table 1 Comparison between conventional LMS and proposed LMS

S.No.	Items	% Use Conventional LMS	% Use Proposed LMS
1.	No. of slices	128	2
2.	No. of. 4 input LUTs	46	2
3.	No. of. bonded IOBs	95	58
4.	No. of GCLKs	12	12

Conclusion

In DSP, adaptive digital signal processing is a necessary field. FPGA implementation of least mean square (LMS) algorithm is designed using VHDL. When the step-size parameter increases, the LMS algorithm converges faster with a larger final misadjustment. Similarly, when the step-size parameter decreases, the LMS algorithm converges slower with a smaller final misadjustment. So, we designed normalized least mean square (NLMS) with variable step-size which increases the stability of filter.

The proposed system is area efficient as compared to the existing schemes and the control mechanism has been modified. Simulation results indicate that the proposed method can improve the performance of the system.

Future Scope

The use of adaptive filtering algorithm in digital signal processing field is vast and further research and development in this area can show more improvement. Still there is a scope of advancement in this algorithm, which reduces complexity & satisfies stringent conditions for stability. For future work, it can be implemented with following aspects:

- This system can be implemented with adaptive filtering with averaging (AFA) algorithm which converges rapidly with lower complexity.
- For improvement, the existing time domain adaptive filters can be replaced with frequency domain adaptive filters.
- Adaptive filtering algorithms such as LMS, NLMS and modified NLMS used in this dissertation can also be implemented for infinite impulse response filters for better performance.

References

1. Hadei, S.: A family of adaptive filter algorithms in noise cancellation for speech enhancement, IEEE 2 (2010)
2. Hayking, S.: Adaptive Filtering Theory, Pearson (2012). ISBN: 978-81-317-0869-9

3. Rekha, K.R., Nagabushan, B.S., Nataraj, K.R.: FPGA implementation of NLMS algorithm for identification of unknown system. *Int. J. Eng. Sci. Technol.* **2**(11), (2010). ISSN: 6391-6407
4. Subudhi, A.K., Mishra, B., Mohanty, M.N.: VLSI design and implementation for adaptive filter using LMS algorithm. *Int. J. Comput. Commun. Technol. (IJCCT)*, **2**
5. Diggikar, A.B., Ardhapurkar, S.S.: Design and implementation of adaptive filtering algorithm for noise cancellation in speech signal on FPGA. In: *IEEE, International Conference on Computing, Electronics and Electrical Technologies (ICCEET)* (2012)
6. Kartheek, B.V, Manojkumar, S.B, Anandaraju, M.B.: Design and Implementation of Modified Adaptive Filtering Algorithm for Noise Cancellation in Speech Signal on FPGA for Minimum Resource Usage. *Int. J. Invent. Eng. Sci. (IJIES)*, **1**(7), (2013). ISSN: 2319-9598

Authors Biography

Devendra Goyal has received his B.E. Degree in 2009 Electronics & Communication Engineering from MIT, KOTA & now pursuing M. Tech in VLSI DESIGN from Poornima College of Engineering Jaipur. His current area of research includes Adaptive Filter, VHDL and currently working on the project related to it.

Mr. Manish Singhal passed B.E. in 2001 and M.Tech in 2011 from MNIT, Jaipur with specialization in VLSI Design. He has one year industry experience and after that he joined Poornima College of Engineering, Jaipur as a lecturer. He has written two books Microprocessor & Microcontroller and Microcontroller & Embedded System Design. He has published several papers in national and international journals and has guided 6 M.Tech students. His research areas include Microprocessor, Microcontroller, Embedded System Design, Digital VLSI Design and Image Processing.

An Efficient Hybrid-Cascaded Framework for Emission Computed Tomography Using OSEM Image Reconstruction Algorithm

Shailendra Tiwari and Rajeev Srivastava

Abstract In the literature, it is well established that the ordered subset expectation maximization (OSEM) algorithm, is an accelerated version of original maximum likelihood expectation maximization (MLEM) method, which performs better than MLEM in terms of processing speed. But, the quality of the reconstructed image with OSEM still remains same as MLEM and it also suffers from the problem of initialization and ill-posedness. To address these issues, in this paper a hybrid-cascaded framework of OSEM is proposed. This framework consists of breaking the reconstruction process into two parts, viz., primary and secondary. In the primary part, simultaneous algebraic reconstruction technique (SART) is applied to overcome the problems of slow convergence and initialization. SART provides fast convergence and produce good reconstruction results with lesser number of iterations than other iterative methods. The task of primary part is to provide an enhanced image to secondary part to be used as an initial estimate for reconstruction process. The secondary part is a hybrid combination of two parts namely, the reconstruction part and the prior part. The reconstruction is done using OSEM algorithm while anisotropic diffusion (AD) is used prior to deal with ill-posedness. A comparative analysis of the proposed model with some other standard methods in the literature is presented both qualitatively and quantitatively for a phantom test data and standard medical image. The proposed model yields significant improvements in reconstruction quality from the projection data.

Keywords Reconstruction algorithms · Emission computed tomography (ECT) · Ordered subset expectation maximization algorithms (OSEM) · Simultaneous algebraic reconstruction technique (SART) · Anisotropic diffusion (AD) · Acceleration techniques

Shailendra Tiwari (✉) · Rajeev Srivastava
Department of Computer Science and Engineering, Indian Institute
of Technology (BHU), Varanasi 221005, India
e-mail: stiwari.rs.cse@iitbhu.ac.in

Rajeev Srivastava
e-mail: rajeev.cse@iitbhu.ac.in

Introduction

Nowadays, OSEM (ordered subset expectation maximization) has become the most widely used iterative methods in emission computed tomography (ECT) [1]. The use of various noninvasive techniques [5] has greatly reduced risks to patients and has increased our understanding of how the body works. Image reconstruction algorithms play a significant role in many ECT devices. ECT image quality is dependent on a number of parameters in the acquisition of the projectional raw data, such as the intrinsic resolution of the camera, choice of collimator, geometry of the gantry setup, timing of the study acquisition, and patient-derived factors such as body habitus and movement during study acquisition [1]. ECT produces an accurate measure of spatial distribution of radioactive substances throughout the patient to extract physiological or functional information. The rate of radioactive emissions can best be described by a Poisson process [2]. Therefore, the noise properties of emission tomography are also spatial-variant in nature.

A huge number of image reconstruction methods have been developed over the past few decades for ECT, which can generally be divided into two major categories; analytic reconstruction (AR) methods and iterative reconstruction (IR) methods. The AR methods, such as filtered back projection (FBP) [3], are based on direct inversion of the mathematical Radon transformation and it requires complete projection data with low noise level. In case of low radiation dose, where noisy and under-sampled projection data are considered, the resulting image produced by the conventional analytical filtered back projection (FBP) method may be severely degraded due to excessive noise.

Another method is iterative reconstruction, which is divided into two categories: First, algebraic iterative method such as the Algebraic Reconstruction Technique (ART) [5], Simultaneous Algebraic Reconstruction Technique (SART) [4], the Simultaneous Iterative Reconstruction Technique (SIRT) [5], and others. It requires less data than FBP methods and is more robust to the effects of noise, but needs much more computation. Second, Statistical Iterative Reconstruction (SIR) techniques such as maximum likelihood expectation maximization (MLEM) [6], median root prior (MRP) [7], ordered subsets expectation maximization (OSEM) [8] algorithms and their variants [9, 10] which play an important role on the quality of the images produced by ECT, since they can provide accurate system model and as an alternative to the filtered back projection and Algebraic Reconstruction Technique, being less sensitive to noise and sparse view inputs.

A major drawback of the SIR method such as MLEM is that it produces images with better quality than other analytical and algebraic techniques; however, images become noisier after a large number of iterations. Another issue is the computational burden associated with the multiple forward and back projection operation cycles through the image domain. It increases the number of iterations, and slow convergence speed of the reconstructed image. As a further development to this, Hudson and Larkin (1994) [8] proposed an alternative version of maximum likelihood approach called OSEM and it is widely used by modern ECT clinical

scanners together with MLEM. They showed that their refinements accelerate the iteration process by a factor proportional to the number of subsets. But, the quality of the reconstructed image with OSEM still remains same as MLEM and it also suffers from the problem of initialization and ill-posedness. So, there has to be an optimum starting point and optimum stopping rules are needed, which stops the reconstruction process well in time before we over run the algorithm as well as to maintain the visual quality of the reconstructed images.

To address the above mentioned issues of initialization and ill-posedness, in this paper, an efficient hybrid-cascaded framework is proposed for improving the quality of medical images. This framework consists of breaking the reconstruction process into two parts, viz., primary and secondary. Primary and secondary reconstruction parts work in a cascaded manner. Output from primary reconstruction is fed into secondary reconstruction. This allows us to use more than one algorithm for reconstruction and extract the benefits of both. With a cascaded network, we attain performance superior than either of the two algorithms used alone.

Rest of the paper is organized as follows: section “**Methods and Model**” presents the methods and model; section “**Results and Discussions**” presents the results and discussions, and section “**Conclusion**” presents the conclusion of the paper.

Methods and Model

The proposed hybrid model consists of two parts namely, primary reconstruction and secondary reconstruction as shown in Fig. 1.

Primary Reconstruction

During primary part, SART [4] is used as an initialization stage for OSEM [8]. SART-based reconstruction approaches converges faster than any other iterative methods but the only drawback of SART is that the quality of reconstructed images

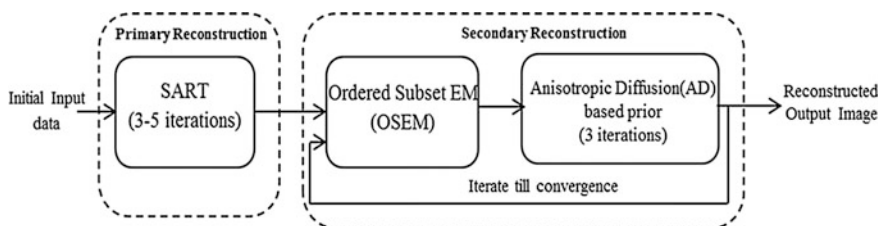


Fig. 1 The proposed hybrid model

produced by it are inferior to EM-based approaches. Hence, in this paper we exploit the advantage of faster convergence of SART and incorporate it in our hybrid approach during primary reconstruction to accelerate the OSEM. In particular, choosing a suitable initial value for the OSEM algorithm in such a manner to remove the noise or error as well as improvised the slow convergence problem significantly.

The SART reconstruction technique uses simultaneous error correction. Such a procedure leads to reduced noise levels in lesser number of iterations. Thus by running a few iterations of SART, we obtain an image in which all regions are enhanced and noise elements are diminished by some amount. This image serves as an optimum initial estimate for MLEM and other superior iterative methods as it will be closer to the best estimate. This reduces the chances of running into stagnant regions in the reconstruction process. Further we show that, using SART to provide initial image will lead to lesser number of iterations of OSEM algorithm and thus speeding up the convergence. The basic SART algorithm begins with an arbitrary $x^{(0)}$ and then begins to iterate until convergence, the initial solution is defined as

$$x_j^k = x_j^{k-1} + \frac{\lambda}{\sum_{i=1}^N a(i,j)} \sum_{i=1}^N \left(\frac{e_j^k a(i,j)}{\sum_{j=1}^M a(i,j)} \right) \quad (1)$$

where M is the total number of rays and N is the total number of pixels. λ is the relaxation parameter which can lead to the better qualities of reconstructions [4]. Here, we choose the value of λ as less than one, and find good convergence with small number of iterations. The error e_j^k is calculated in projections using $e_j^k = P_j - p_j^k$, where P is true projections and p_j^k is calculated projections at k th iteration.

Secondary Reconstruction

The secondary reconstruction is a hybrid combination of iterative reconstruction and a prior part as shown in Fig. 1. They both work in conjunction to provide one iterative cycle of secondary part. This is repeated a number of times till we get the required result. The use of prior knowledge within the secondary reconstruction enables us to tackle noise at every step of reconstruction and hence noise is tackled in an efficient manner. Using anisotropic diffusion (AD) prior [11] inside reconstruction part gives better results than working after the reconstruction is over. It has been widely used for image restoration and tomographic reconstruction [12] which can produce better image quality than other methods. The output of the k th SART iteration is used as an initial input of an OSEM and then updating the reconstructed

images by n th projections. If the required accuracy for numerical convergence has been achieved then stop the iteration process.

Hence, modified OSEM = OSEM (Initial guess image $x^{(0)}$ given by k th SART iteration):

$$x(i)_j^{n+1} = x(i)_j^n \left(\frac{1}{\sum_{j \in S_n} a(i,j)} \sum_{j \in S_n} \frac{y(j)a(i,j)}{\sum_{i'=1}^I x(i')^{(n)} a(i',j)} \right), \text{ for pixels } i = 1, 2, \dots, I. \quad (2)$$

where $x_j^{(n+1)}$ is the value of pixel j after the n th iteration of OSEM correction step.

Unregularized image reconstruction in Eq. (2) is ill-posed nature. So, converged OSEM images may be still noisy. Recently, anisotropic diffusion (AD) as a non-linear partial differential equation (PDE)-based diffusion process [11] is introduced into tomography reconstruction that purports to filter the noise without blurring edges. Overcoming the undesirable effects of linear smoothing filter, such as blurring or dislocating the useful edge information of the images, AD and its variant has been widely used in image smoothing, image reconstruction and image segmentation [12]. Therefore, we can add an AD regularizer to Eq. (2):

$$\frac{\partial x}{\partial t} = \text{div}[C(|\nabla x|) \cdot \nabla x] \quad (3)$$

where x is the image at time t iteration step, ∇x is the local gradient of the image and $C(\nabla x)$ is the diffusion coefficient. The diffusion model in Eq. (3), will reduce to isotropic process if the value of $C(\nabla x)$ is tuned to be constant, if it is set to large values in the regions so that intra-region in an image become smooth while edges of inter-region are preserved. The following diffusion functions were proposed by [11]:

$$C_1(|\nabla x|) = \frac{1}{1 + \left(\frac{|\nabla x|}{K}\right)^a}, \quad a > 1, \quad C_2(|\nabla x|) = \exp \left[-\left(\frac{|\nabla x|}{K}\right)^2 \right] \quad (4)$$

where K is a gradient threshold that controls the edge sensitivity of the model. Mostly these priors are used at the end of reconstruction when all the data is available for the noise removal and missing/faulty data. Here, using diffusion on images within the reconstruction process, we get higher SNR values for the final image. Moreover, since noise is tackled in each iteration of secondary reconstruction, the number of iterations required to reach the result are also reduced by great amount and the resulting image is visually enhanced:

$$x_j^{k+1} = x_j^k + \Delta t \sum_{j' \in N_j} \left(C \left(\left| \nabla x_{j,j'}^k \right| \right) \nabla x_{j,j'}^k \right) \tag{5}$$

For the discretized version of Eq. (5) to be stable, the von Neumann analysis [2] shows that we require $\frac{\Delta t}{(\Delta x)^2} < 1/4$. If the grid size is set to $\Delta x = 1$ then $\Delta t < 1/4$, i.e., ($\Delta t < 0.25$), Therefore, the value of Δt is set to 0.25 for stability of equation.

Results and Discussions

For simulation study MATLAB 2013b software was used on a Personal Computer with Intel(R) Core (TM) 2 Duo CPU U9600 @ 1.6 GHz, 4.00 GB RAM, and 64-bit operating system. The comparative analysis of the proposed method is presented with other standard methods available in the literature such as MLEM [6], MLEM + AD [10], MRP [7] and OSEM [8]. For quantitative analysis various performance measures such as signal-to-noise ratio (SNR), the root-mean-square error (RMSE), and the correlation parameter (CP) [2] are used. The SNR and RMSE give the error measures in reconstruction process. The correlation parameter is a measure of edge preservation in the reconstructed image. The brief descriptions of the two test cases are as follows: The first test case is a modified Shepp–Logan Phantom of size 64×64 and 120 projection angles was used. The simulated data was all Poisson distributed and all assumed to be 128 radial bins and 128 angular views evenly spaced over 1800. The second test case used for simulation was a gray-scale standard medical thorax image of size 128×128 . For this test case, the projections are calculated mathematically with coverage angle ranging from 0° to 360° with rotational increment of 2° to 10° . (Fig. 2)

For both the test cases, we simulated the sinograms with total counts amount 6×10^5 . A Poisson noise of magnitude 15 % is added to projections. During the primary reconstruction of the proposed method, SART was run for 3–5 iterations to produce the initial estimate of the image to be used in secondary reconstruction step of the proposed algorithm. In secondary reconstruction the value of diffusion coefficient (Kappa) used by AD was set to 0.0033 within each OSEM step. The proposed algorithm was run for 500–1000 iterations for simulation purposes and the convergence trend of the proposed method and other methods were recorded.

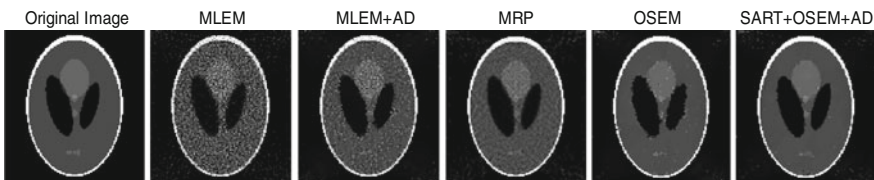


Fig. 2 The modified Shepp–Logan phantom with different reconstruction methods

However, the proposed and other algorithms converged in less than 500 iterations. Also, this was done to ensure that the algorithm has only single maxima and by stopping at the first instance of stagnation or degradation, we are not missing any further maxima which might give better results. The corresponding graphs are plotted for SNR, PSNR, RMSE, and CP. The graphs support the fact as shown in Figs. 3, 4, and 5. Thus we can say that using SART for primary reconstruction brings the convergence earlier and fetches better results. Similarly for AD in secondary reconstruction, the SNR output is highly enhanced. Further, the proposed model preserves the edges and other radiometric information such as luminance and contrast of the images, the plot correlation parameter (CP) as shown in Figs. 3 and 5, respectively.

The visual results of the resultant reconstructed images for both the test cases obtained from different algorithms are shown in Figs. 2 and 4. The experiment reveals the fact that proposed hybrid framework effectively eliminated Poisson

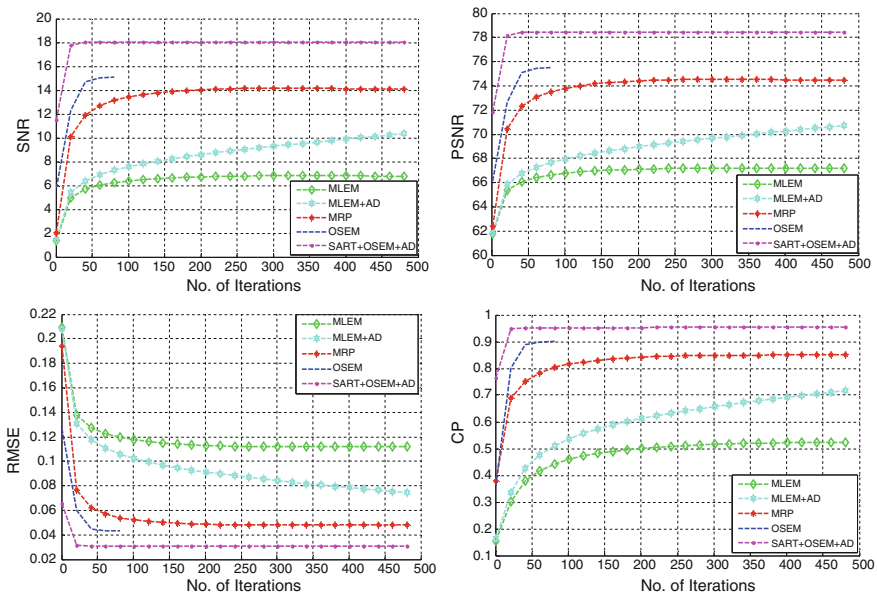


Fig. 3 The plots of SNR, PSNR, RMSE, and CP along with number. of iterations for test case 1

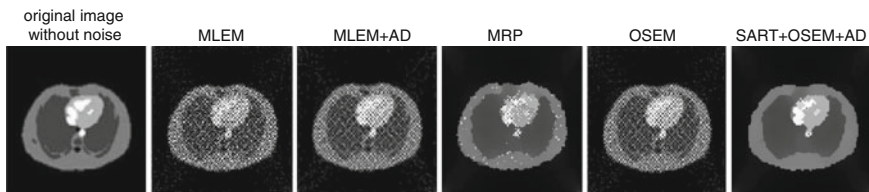


Fig. 4 The standard medical thorax image with different reconstruction methods

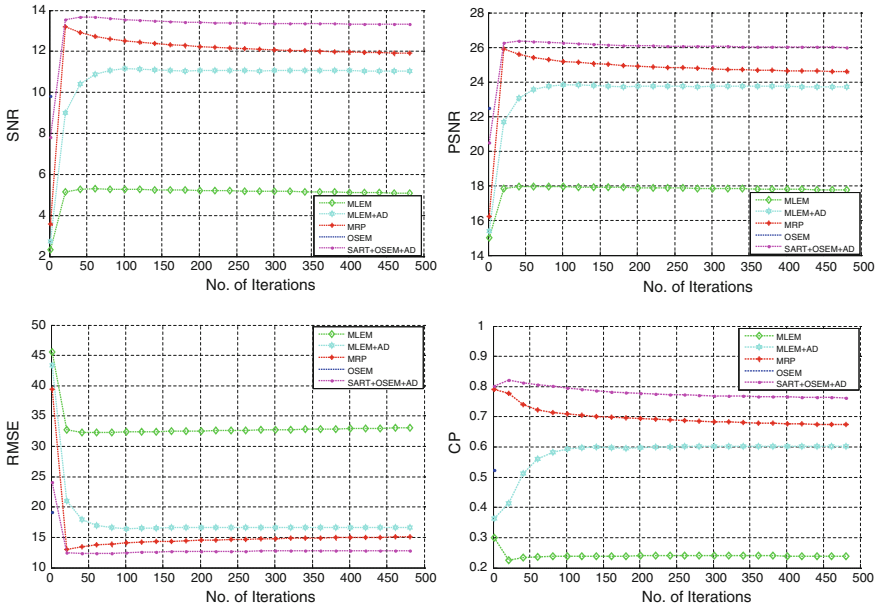


Fig. 5 The plots of SNR, PSNR, RMSE, and CP along with no. of iterations for test case 2

noise and it performs better even at limited number of projections in comparison to other standard methods and has better quality of reconstruction in term of SNRs, PSNRs, RMSEs, and CPs. Tables 1 and 2 show the quantification values of SNRs, PSNRs, RMSEs, and CPs. in for both the test cases, respectively. The comparison

Table 1 Different performance measures for the reconstructed images in Fig. 1

Performance measures	MLEM [6]	MLEM + AD [10]	MRP [12]	OSEM [8]	SART + OSEM + AD (The proposed method)
SNR	12.3355	15.9454	19.4039	19.4279	22.7114
RMSE	0.0933	0.0616	0.0414	0.0412	0.0283
PSNR	68.7649	72.3748	75.8333	75.8573	79.1408
CP	0.6962	0.8555	0.9299	0.9533	0.9923

Table 2 Different performance measures for the reconstructed images in Fig. 4

Performance measures	MLEM [6]	MLEM + AD [10]	MRP [12]	OSEM [8]	SART + OSEM + AD (The proposed method)
SNR	5.2971	11.1649	13.2200	10.0488	13.6744
RMSE	32.2868	16.4301	12.9683	18.6827	12.3073
PSNR	17.9843	23.8520	25.9071	22.7360	26.3615
CP	0.3007	0.6032	0.8107	0.5324	0.8228

Fig. 6 Line plot of Shepp–Logan phantom

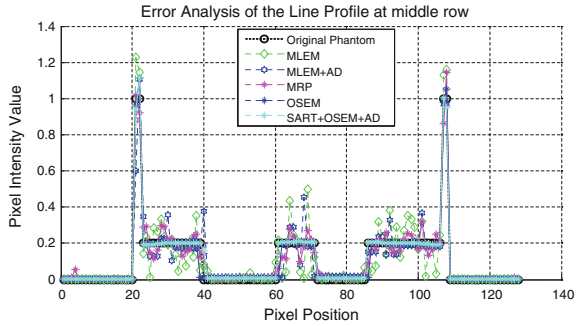


Fig. 7 Line plot of standard medical thorax image

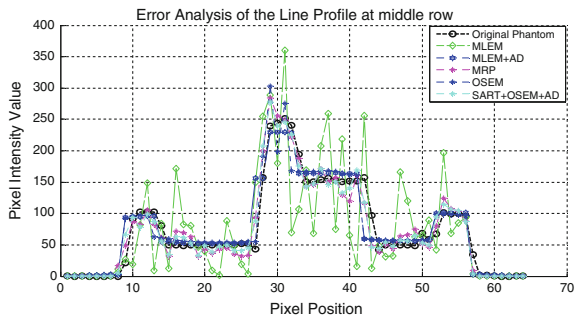


table indicates the proposed reconstruction method produces images with perfect quality than other reconstruction methods in consideration.

Figures 6 and 7 indicate the error analysis of the line profile at the middle row for two different test cases. To check the accuracy of the proceeding reconstructions, line plots for two test cases were drawn, where x-axis represents the pixel position and y-axis represents pixel intensity value. Line plots along the mid-row line through the reconstructions produced by different methods show that the proposed method can recover image intensity effectively in comparison to other methods. Both the visual displays and the line plots suggest that the proposed model is preferable to the existing reconstruction methods. From all the above observations, it may be concluded that the proposed model is performing better in comparison to its other counterparts and provide a better reconstructed image.

Conclusion

In this paper, an efficient hybrid-cascaded framework (here referred to as: SART + OSEM + AD) to reduce the number of iterations as well as to improve the quality of reconstructed images is proposed. This method speedup the process by using a fast algebraic iterative reconstruction algorithm (SART) first and then

switch to more precise accelerated version of statistical EM algorithm (OSEM). Additionally, regularization term anisotropic diffusion proposed by Perona and Malik (1990) is combined to maximize the likelihood function. The proposed method reduced the computational time, and solves the problem of slow convergence as well as ill-conditioned. Numerical simulation experience demonstrates that proposed method is superior to the MLEM, MRP, OSEM, and SART alone in performing iterative image reconstruction. Finally, hybrid method is applied to PET/SPECT tomography for obtaining optimal solutions. The qualitative and quantitative analyses clearly show that this framework can be used for image reconstruction and is a suitable replacement for standard iterative reconstruction algorithms.

References

1. Qi, J., Leahy, R.M.: Iterative reconstruction techniques in emission computed tomography. *Phys. Med. Biol.* **51**, R541 (2006)
2. Srivastava, Rajeev, Srivastava, Subodh: Restoration of poisson noise corrupted digital images with nonlinear PDE based filters along with the choice of regularization parameter estimation. *Pattern Recogn. Lett.* **34**, 1175–1185 (2013)
3. Zeng, G.L.: Comparison of a noise-weighted filtered backprojection algorithm with the standard MLEM algorithm for poisson noise. *J. Med. Technol.* **41**(4), 283–288 (2013)
4. Anderson, A.H., Kak, A.C.: Simultaneous Algebraic Reconstruction Technique (SART): A Superior Implementation of the ART Algorithm. Academia press, New York (1984)
5. Hansen, P.C., Saxild-Hansen, M.: AIR tools, A MATLAB package of algebraic iterative reconstruction methods. *J. Comput. Appl. Math.* **236**(8), 2167–2178 (2012)
6. Shepp, L.A., Vardi, Y.: Maximum likelihood reconstruction for emission tomography. *IEEE Trans. Med. Imaging* **1**(2), 113–122 (1982)
7. Alenius, S., Ruotsalainen, U.: Generalization of median root prior reconstruction. *IEEE Trans. Med. Imaging* **21**, 1413–1420 (2002)
8. Hudson, H.M., Larkin, R.S.: Accelerated image reconstruction using ordered subsets of projection data. *IEEE Trans. Med. Imaging* **13**(4), 601–609 (1994)
9. Zhang, Quan, Liu, Yi, Shu, Huazhong, Gui, Zhiguo: Application of regularized maximum likelihood algorithm in PET image reconstruction combined with nonlocal fuzzy anisotropic diffusion. *Optik—Int. J. Light Electron. Opt.* **124**(20), 4561–4565 (2013)
10. He, Q., Huang, L.: Penalized maximum likelihood algorithm for positron emission tomography by using anisotropic median-diffusion. *Math. Prob. Eng.* **2014**, 7 (2014). Article ID 491239
11. Perona, P., Malik, J.: Scale-space and edge detection using anisotropic diffusion. *IEEE Trans. Pattern Anal. Mach. Intell.* **12**, 629–639 (1990)
12. Chan, C., Fulton, R., Feng, D.D., Meikle, S.: Regularized image reconstruction with an anatomically adaptive prior for positron emission tomography. *Phys. Med. Biol.* **54**(24), 7379 (2009)

A Review of Energy-Efficient Routing Protocols in Wireless Sensor Networks

Simerjeet Kaur, Rajni and Barinder Paul Singh

Abstract Wireless Sensor Networks (WSNs) are collection of randomly distributed minute devices mainly named as nodes which interact with each other and base station to transmit the required information to the controller via Internet. These networks sense or track the phenomenon, occurring at an unattended place. The major constraint of the WSN is limited life of sensor nodes due to loss of energy. Several routing protocols are developed to transfer the information or data among these nodes in an efficient way and to enlarge the lifetime of nodes. A thorough review of different categories of routing protocols has been discussed in the presented paper.

Keywords Wireless sensor network (WSN) · Low-energy adaptive clustering hierarchy (LEACH) · Base station (BS) · Power efficient gathering in sensor information system (PEGASIS)

Introduction

Wireless Sensor Network (WSN) is a network composed of finite quantity of small and inexpensive devices or nodes that can sense an event, process, and send out the sensed data over a wireless medium. These nodes are densely deployed around the event. The position or arrangement of sensor nodes is not predetermined. This

Simerjeet Kaur (✉) · B.P. Singh
Department of Electronics and Communication Engineering,
Ferozepur College of Engineering and Technology, Ferozeshah, Punjab, India
e-mail: Sonia_27585@yahoo.in

B.P. Singh
e-mail: barinder.singh88@gmail.com

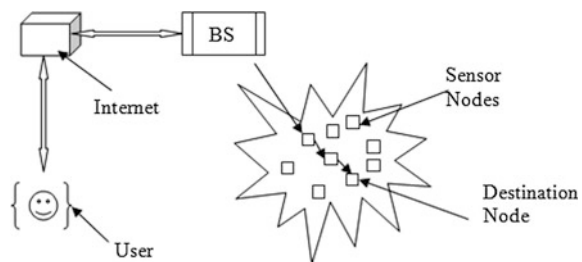
Rajni
Department of Electronics and Communication Engineering,
Shaheed Bhagat Singh State Technical Campus, Ferozepur, Punjab, India
e-mail: rajni_c123@yahoo.co.in

allows random deployment of sensor nodes around the event. Sensor nodes generally drive their energy from attached batteries [1]. Each node consists of mainly a microcontroller, transceiver, memory devices, and power source. The microcontrollers are used for data processing and to do the logical functions. Memory device is used for the storage of data while the combination of transmitter and receiver functions is integrated into the transceiver [2]. These sensor devices or nodes make interaction to each other and pass the messages or data to BS which in turn transmits this collected information to the user through Internet [3]. The WSN finds its applications in various domains such as agriculture or ecological sensing, tracking of an object, monitoring of wildlife, health care, home automation and security [4–6]. Figure 1 shows the systematic structure of WSN. The different types of topologies used for the transmission of data are Star, Mesh, and Hybrid topologies [7].

A star network is a topology which works on the concept of communication where a single BS can send or accept a message to remote nodes. The remote nodes are capable to transmit or receive a message only from BS. The benefit of this type of network is that the design of topology is uncomplicated and capable to maintain the remote node’s power consumption to a least quantity. Further it permits for small latency exchanges among nodes and the base station. Mesh network allows the nodes to interact with each other within its radio transmission range. That make network similar as that of multi-hop communications, in which whenever a node desires to convey information to another node which is not situated in the communications range, it employs a node as an intermediate for the transmission of message to the destination node. A hybrid topology consisting of the star and mesh network offers a dynamic and flexible communication network.

WSNs are also classified on the basis of three different modes of data transference named as Time, Event, and Query-driven type of networks [8]. In Time-driven network, every node transmits data at regular periods, whereas in Event-driven nature of network a node forwards the data or message simply when it senses any occurrence. The final or third class is the network which is based on Query where the sensors transmit the data at the condition only when it receives a query message from the BS. In addition to this, the hybrid networks are also used that combine all the previous three models. These aspects are significant because of the guidelines given by them to design an algorithm or a protocol for WSNs. The energy difference among the nodes increases with time resulting in deterioration of

Fig. 1 WSN structure



network performance [9–12]. Main focus while designing WSN protocols should be on power management. A research challenge in WSNs is to cope with little communication of power. In this regard, the routing protocols play an essential role in efficient energy consumption. An appropriate choice of an exact direction to send data from node to BS is necessary which tends to minimize the energy consumption. In the presented paper, section “[Routing Protocols](#)” represents classification of routing protocol. Section “[Various Design Issues of Wireless Sensor Networks](#)” discusses various design issues in WSN and section “[Conclusion](#)” concludes the discussion.

Routing Protocols

Routing protocols are generally classified on the concept of structure of network and operations of protocol. On the basis of structure of network, the protocols are again categorized as flat routing, hierarchal routing, location-based routing, and chain routing.

FLAT Routing

FLAT routing is basically data-centric routing. Each node is assumed to equally participate into sensing task and is excited through queries generated by BS upon requirement of the user.

(a) *SPIN*

Heinzelman et al. [13] developed a category of protocols known as Sensor Protocols for Information via Negotiation (SPIN). These protocols are resource conscious and adaptive in nature. These are designed to overcome the difficulties arises in older flooding protocols. Each sensor node in the network is recognized as potential member that has enough data that can be accessed by BS through queries. SPIN-1 is developed to minimize the amount of wireless sensor devices within the network. SPIN-2 is developed to reduce the consumption of energy of the nodes. SPIN can be used for mobile application [14].

(b) *Direct Diffusion*

Directed diffusion is flooding routing protocol. When BS generates some queries or requires some information it sends queries in the network and sets up gradient for data flow from nodes to BS. When BS receives information from the source node, it evaluates and sends it back to network with gradient level (evaluation of received information level with the required information level). Nodes upon receiving the query from BS retrieve their database and evaluate the information with gradient level, if available information is of high level then response is sent back to BS [15, 16].

(c) Rumor Routing

Rumor routing is basically agent-based routing, which is long-lived packet of information. The agent travels the whole network and exchanges the information regarding events occurred in the network with the nodes. When detail of any event is required by a particular node or BS, it can directly interact with the node where event has occurred by retrieving the information exchange by the agent. Using this protocol flooding or roaming the entire network is eliminated [17].

(d) Cougar

It is optimized data-centric routing protocol. It assists the user by providing programs used for various applications consisting of declarative queries of collected or sensed data from the source node. User does not know how the required information is obtained. This approach incorporates a query layer between application and network layer. When a query is generated from gate way node it is well entertained by query proxy service that is linked with sensor nodes [18].

(e) Acquire

Acquire is more optimized technique to respond a query. It is enhanced version of Cougar and it deals with complex queries. The generated queries from the BS are divided into subqueries and are transferred within sensor nodes. When a node receive a query it looks into its database to respond to query, if available data is not sufficient to satisfy the received query it uses its look ahead of d hops for systematically and stepwise forwarding the query to surrounding nodes that can have sufficient data to satisfy the request. It cannot be mixed with directed diffusion because the query is forwarded to limited number of nodes not to entire network. It depends upon d factor of Acquire if d becomes equal to network then it behaves as directed diffusion [19].

Hierarchical Routing

Hierarchical routing is the most energy efficient routing technique. It is also known as cluster base routing. Hierarchical routing involves the dividing of the entire network into minute blocks which are mainly named as cluster. The Cluster Head (CH) is then allocated to every cluster. It greatly reduces the traffic towards the BS. The structured way of sensing task is being performed by low energy level clusters and transformation of that data is done by high-level clusters. It greatly reduces the energy utilization and increase the network life.

(a) Low-Energy Adaptive Clustering Hierarchy

Low-Energy Adaptive Clustering Hierarchy (LEACH) is the very first protocol of hierarchical routing [20]. LEACH divides the total operation into two segments, setup, and steady state segment. In first segment, the clusters get generated and each cluster is assigned with CH. In steady state, transmission of information takes place from cluster to CH and from CH to BS done. LEACH cannot be used in the area of large vicinity due to its drawbacks [21, 22]. To sustain data aggregation via proficient network association, the nodes get split up into a few numbers of tiny groups

known as clusters. Each cluster is then composed of coordinator, called CH, and a few collection member nodes. Clustering works under an efficient hierarchy called two-tier hierarchy where the assigned CHs generates the higher tier and the member nodes give rise to lower tier. Clustering improves the lifetime of a network which results to enhance the performance of sensor network.

(b) *Two Level Low Energy Adaptive Clustering Hierarchy (TL-LEACH)*

Two levels LEACH is an enhanced version of traditional LEACH protocol. It engages the formation of primary and secondary CH. To reduce the consumption of energy and transmission of data in an effective manner, secondary CH interacts with Primary CH and primary interact with BS [23].

(c) *LEACH-Centralized (LEACH-C)*

Wu [24] introduced LEACH-C called LEACH-Centralized. In LEACH protocol, all sensor nodes choose their cluster heads by themselves and the result will be a number of Cluster heads. In LEACH-Centralized, the authors made advancement over traditional LEAH protocol such that throughout the procedure of selection of CH the BS should be conscious regarding the remaining energy of sensor nodes and their locations. Therefore, the BS chooses the most appropriate nodes to act as the role of CH, and split up the rest of the sensor nodes between CH for the formation of clusters. The improvement in energy of LEACH-C protocol is confined by simulation results depends on the foremost dead node as compared to conventional LEACH as well as conventional routing protocols.

(d) *Heterogeneous Energy-Efficient Distributed Protocol*

Sensor nodes within the network are mainly of quasi-stationary form. The location of nodes are uninformed which means to say that they are not equipped with any of GPS proficient antenna. The signal processing and communication abilities of all the nodes are also identical to each other. The position of nodes left unattended after their deployment. The remaining energy of each and every node primarily plays the role of selection of CHs. To manage the ties, the intra-cluster communication expenses are predictable as the less imperative parameter. The meaning of tie is that the node might be felt inside the range of more than one CH. The CH having lower intra-cluster communication cost is preferential under the presence of variety of cluster heads. The less important parameter of clustering, intra-cluster communication expenses, is a (i) purpose of properties of cluster like dimension of cluster and (ii) whether or not random levels of power is acceptable for interactions intra-cluster activities [25].

(e) *Hierarchical Power-Aware Routing (HPAR)*

In HPAR, the collections of sensor nodes are created within the network. The collections of wireless sensor nodes in similar geographic regions are grouped collectively as a region. Each region is then considered as an entity. Each region independently decides how the message received from BS is to travel among the other zones. Message is directed to that path which has high power remaining among the other routes [26].

Location-Based Routing

In this routing, the sensor nodes are attended to by their respective locations. The distance among the nodes is sensed by the strength of received signal.

(a) Geographic Adaptive Fidelity (GAF)

The protocol is basically designed for MANETs but later used for WSNs because of less energy consumption. GAF greatly reduces the energy consumption by switching off the idle sensors when required information is continuously receiving from the network. In this protocol, the network structure is split up into grid type squares and every node consumes its information of location given by Global Positioning System (GPS) so as to connect itself with a particular grid in which it resides [27, 28].

(b) Geographic and Energy-Aware Routing (GEAR)

This protocol is an energy-effective routing protocol which is presented to aim a particular area within a network. Each sensor node is equipped with location aware hardware like GPS and is attentive of their initial and residual energy. They are also aware regarding the energies of their neighboring node. So, data is transmitted through the high energy path. GEAR implements energy-aware scenarios which depend on geographical information to choose sensors for the routing of a packet toward its target region [29].

(c) Geographic Random Forwarding (GeRaF)

This protocol was presented by Zorzi and Rao [30], employs the concept of geographic routing. In this process, a sensor which acts as relay is not identified a priori by correspondent. No any assurance is provided regarding the correspondent will be capable of promoting the information in the direction of its final aim which is named as sink node for all time. GeRaF is also called as best-effort forwarding protocol for this reason. GeRaF protocol presumes that all of the sensor nodes have knowledge regarding their physical location and also of sink node. Even though GeRaF combines an algorithm depends on geographical routing and awake-sleep scheduling mechanism, the sensor nodes are not necessitate to keep path of the positions of neighboring nodes and awake-sleep schemes. The sensor node checks the channel first, through which it has to transmit the data to sink node. This avoids the collisions and makes the efficient routing. The source sensor node transmits a message called request to send (RTS) to all of the neighbor nodes under the idle conditions of channel.

Chain Routing

The concept of chain routing is entirely different from the concept of flat, location-based, and hierarchical routing. In chain routing, the formation of cluster head is not necessary like hierarchical routing. In chain routing, the transference of messages or data takes place by the formation of leader in the chain which again

makes contact with the other nearest node. Therefore, all the nodes become the leader node according to their turn in the chain so that the data can be transferred. The chain routing is an efficient way to make contact with the other nodes within a network because of no overhead on nodes.

(a) *Power-Efficient Gathering in Sensor Information System*

It is a proficient and effective protocol which works on the concept of chain routing for its operation. In PEGASIS a continuous chain of node is formed so as to send out the required information to BS. Nodes that have relevant data interact with its neighbor node which further with its neighbor and so on, resulting continues chain to transfer the data from the source node to sink node. Every node become a leader and pass the information to adjacent node, so continues process of becoming a leader is taken out [31].The effectiveness of the PEGASIS protocol can be enhanced by using the greedy algorithms [32].

Various Design Issues of Wireless Sensor Networks

(a) *Hardware Design*

Range of network devices should be high ranging from 1 to 6 km. Establishing the connection between the networks is difficult and depends upon the node. Battery life should be high and power consumption should be low so that life of the sensor node increased [33].

(b) *Operating System for Network*

It is used to compute, manipulate, and route the data. Various operating systems are used like Tiny OS, Mantis OS, and Nano Q Plus. Operating system must be hardware-independent, application-specific, and easy programmed so that effectively transmit the data to sink from source [34–36].

(c) *Deployment*

Deployment means to set up the sensor node in the practical environment. The deployment may be deterministic and randomly. Deterministic deployment involves proper positioning of sensor node in a predetermined way. Random deployment involves randomly or by dropping it from plane [39]. Congestion is also result due to deployment because so many nodes transmit the data at the same time [37].

(d) *Localization*

It is the geographical issue to properly deploy the nodes in network so that there is little effort to trace a source of relevant data that is required. It arises due to improper deployment of the nodes in network. It results in using the localization algorithm to satisfy the various requirements [38].

Quality of Service

QoS is major issue in WSN. QoS must be of high level so that data is of high value is reached at the receiver point. WSNs are used in various application like military, weather, and nuclear points.

(e) Production Costs

WSNs consist of predetermined quantity of small sensor nodes, single node's cost is considerable to justify the total cost of networks and therefore the cost of each sensor node should be kept low.

Conclusion

In the presented paper, we presented a comprehensive study of various techniques of routing in WSNs presented in the literature. Although all above routing techniques put into enhance the lifetime of WSN, but there are still many aspects to be considered in WSNs. We concluded all those confronts and identified guidelines for future research to this regard.

References

1. Zhang, J., Liu, D., Xu, Y.: An efficient power and coverage algorithm in WSNs. In: Proceedings of International Multi Symposiums on Computer and Computational Sciences 2011, pp. 102–105 (2008)
2. Ramli, S.: Design of Wireless Sensor Network for Environmental Monitoring (WISNEM) (2008)
3. Mhatre, V., Rosenberg, C.: Design guidelines for wireless sensor networks: communication, clustering and aggregation. *Ad Hoc Netw.* **2**(1), 45–63 (2004)
4. Ruizhong, L., Zhi, W., Youxian, S.: Wireless sensor networks solutions for real time monitoring of nuclear power plant. In: Proceedings of the 5th World Congress on Intelligent Control and Automation, Hangzhou, P.R. China, pp. 3663–3667 (2004)
5. Romer, K.: The design space of wireless sensor networks. *IEEE Wirel. Commun.* **2004**, 54–61 (2004)
6. Yoneki, E., Bacon, J.: A survey of wireless sensor network technologies research trends and middle wares role. Technical report (2005)
7. Poe, W.Y., Schmitt, J.B.: Node deployment in large wireless sensor networks: coverage, energy consumption, and worst-case delay. In: Proceeding AINTEC'09 Asian Internet Engineering College 2009, pp. 77–84 (2009)
8. Singh, B.P., Rajni, Singh, G.: Investigation of efficient energy coverage problem in wireless sensor networks with ACO and ACB-SA. In: Proceeding of International Conference on Emerging Research in Computing, Information, Communication and Application, ERCICA, pp. 559–563. Elsevier (2014)
9. Chen, Y., Zhao, Q.: On the lifetime of wireless sensor networks. *Commun. Lett. IEEE* **9**(11), 976–978 (2005)

10. Heinzelman, W.R., Chandrakasan, A., Balakrishnan, H.: Energy-efficient communication protocol for wireless microsensor networks. In: IEEE Proceedings of the 33rd Annual Hawaii International Conference on System Sciences (2000)
11. Israr, N., Awan, I.: Multihop clustering algorithm for load balancing in wireless sensor networks. *Int. J. Simul. Syst. Sci. Technol.* **8**(1), 13–25 (2007)
12. Singh, B.P., Rajni, Singh, G.: Comparative analysis of efficient energy coverage problem of WSN with ACO and ACB-SA. *Int. J. Recent Trends Eng. Technol. (IJRTET)* **11**(2), 371–377 (2014). ACEEE (a subdivision of IDES)
13. Heinzelman, W.R., Kulik, J., Balakrishnan, H.: Adaptive protocols for information dissemination in wireless sensor networks. In: Proceedings of 5th ACM/IEEE Mobicom Conference (MobiCom '99), Seattle, WA, 1999, pp. 174–185 (1999)
14. Kulik, J., Heinzelman, W.R., Balakrishnan, H.: Negotiation-based protocols for disseminating information in wireless sensor networks. *Wirel. Netw.* **8**(2/3), 169–185 (2002)
15. Intanagonwiwat, C., Govindan, R., Estrin, D.: Directed diffusion: a scalable and robust communication paradigm for sensor networks. In: Proceedings ACM MobiCom'00, Boston, MA, Aug 2000, pp. 56–67 (2000)
16. Intanagonwiwat, C., Govindan, R., Estrin, D., Heidemann, J., Silva, F.: Directed diffusion for wireless sensor networking. *IEEE/ACM Trans. Netw.* **11**(1), 2–16 (2003)
17. Braginsky, D., Estrin, D.: Rumor routing algorithm in sensor networks. In: Proceedings ACM WSN, in Conjunction with ACM MobiCom'02, Atlanta, GA, Sept 2002, pp. 22–31 (2002)
18. Yao, Y., Gehrke, J.: The cougar approach to in-network query processing in sensor networks. *SGIMOD Rec.* **31**(3), 9–18 (2002)
19. Sadagopan, N., Krishnamachari, B., Helmy, A.: The ACQUIRE mechanism for efficient querying in sensor networks. in: Proceedings SNPA'03, Anchorage, AK, May 2003, pp. 149–155 (2003)
20. Heinzelman, W.R., Chandrakasan, A., Balakrishnan, H.: Energy-efficient communication protocol for wireless microsensor networks. In: IEEE Computer Society Proceedings of the Thirty Third Hawaii International Conference on System Sciences (HICSS '00), Washington, DC, USA (2000)
21. Bhattacharyya, D., Kim, T., Pal, S.: A comparative study of wireless sensor networks and their routing protocols. *MDPI J. Sens.* **10**, 10506–10523 (2010)
22. Pal, S., Bhattacharyya, D., Tomar, G.S., Kim, T.: Wireless sensor networks and its routing protocols: a comparative study. In: Proceedings of International Conference on Computational Intelligence and Communication Networks (CICN) 2010, pp. 314–319 (2010)
23. Al-karaki, J.N.: routing techniques in wireless sensor networks. *IEEE Wirel. Commun.* **11**(6), 6–28 (2004)
24. Wu, X.H., Wang, S.: Performance comparison of LEACH and LEACH-C protocols by NS2. In: Proceedings of 9th International Symposium on Distributed Computing and Applications to Business, Engineering and Science. Hong Kong, China, pp. 254–258 (2010)
25. Pal, S., Bhattacharyya, D., Tomar, G.S., Kim, T.: Wireless sensor networks and its routing protocols: a comparative study. In: Proceedings of International Conference on Computational Intelligence and Communication Networks (CICN), pp. 314–319 (2010)
26. Li, Q., Aslam, J., Rus, D.: Hierarchical power-aware routing in sensor networks. In: Proceedings of the DIMACS Workshop on Pervasive Networking, May 2001 (2001)
27. Xu, Y., Heidemann, J., Estrin, D.: Geography-informed energy conservation for ad-hoc routing. In: Proceedings ACM/IEEE MobiCom'01, Rome, Italy, pp. 70–84 (2001)
28. Stemm, M., Katz, R.H.: Measuring and reducing energy consumption of network interfaces in handheld devices. *IEICE Trans. Commun.* **E80-B** (8), pp. 1125–1131
29. Yu, Y., Govindan, R., Estrin, D.: Geographical and energy aware routing: a recursive data dissemination protocol for wireless sensor networks, Technical report UCLA/CSD-TR-01-0023, UCLA Computer Science Department, May 2001 (2001)
30. Zorzi, M., Rao, R.R.: Geographic random forwarding (GeRaF) for ad hoc and sensor networks: multihop performance. *IEEE Trans. Mob. Comput.* **2**(4), 337–348 (2003)

31. Lindsey, S., Raghavendra, C.S.: PEGASIS: power efficient gathering in sensor information systems. In: Proceedings of IEEE Aerospace Conference, 2002, pp. 1–6 (2002)
32. Khan, A.G.: A comparative analysis: routing protocols for wireless sensor networks. MAIREC Int. J. Res. IT Manage. (IJRIM) **2**, 516–534 (2012)
33. Zhang, P., Sadler, M., Lyon, A., Martonosi, M.: Hardware design experiences in ZebraNet. In: Proceedings of SenSys'04, 3–5 Nov, Baltimore, USA (2004)
34. Abrach, H., Bhatti, S.: MANTIS: system support for multimodal networks of in-situ sensors. In: 2nd ACM International Workshop on Wireless Sensor Networks and Applications, pp. 50–59 (2003)
35. Park, S., Kim, J.W.: Embedded sensor networked operating system. In: Proceedings of the Ninth IEEE International Symposium on Object and Component-Oriented Real-Time Distributed Computing, pp. 117–124 (2006)
36. Ringwald, M., Romer, K.: Deployment of sensor networks: problems and passive inspection. In: Proceedings of Fifth International Workshop on Intelligent Solutions in Embedded Systems, Madrid, Spain (2007)
37. Li, J., Bai, Y., Ji, H., Qian, D.: POWER: planning and deployment platform for wireless sensor networks. In: Proceedings of the Fifth International Conference on Grid and Cooperative Computing Workshops (GCCW'06). IEEE (2006)
38. Patro, R.K.: Localization in wireless sensor networks with mobile beacons. In: 23rd IEEE Convention of Electrical and Electronics Engineers in Israel, pp. 22–24 (2004)

A Study of Phase Shifting Surface

Neha Singh and Kamal Kishor Choure

Abstract This paper presents a study of phase-shifting surface (PSS). The phase-shifting surface (PSS) is a free-standing surface or screen that allows for shifting, controlled, or changing of the phase of an electromagnetic (EM) wave propagating through it. PSS dielectric surface is divided into a lattice of unit cells which are rectangular or square, each unit cell designed to provide a predetermined phase shift. A high-gain, low-cost and lightweight antenna for microwave region is required in various applications. For achieving that goal PSS concept is used.

Keywords Phase shifting surface · Unit cell · Conductive strip · Frequency selective surface

Introduction

The phase-shifting surface (PSS) is a free-standing surface or screen that allows for shifting, controlled or changing of the phase of an electromagnetic (EM) wave propagating through it. For transform a radiated beam from a feeder antenna to achieve some characteristics such as gain enhancement this concept is very useful. The PSS is made non-uniform, so that every location on its surface achieves different phase shifts. In PSS dielectric surface is divided into a regular repeated three-dimensional arrangement of unit cells which are square or rectangular, each of these unit cells designed to give a predetermined phase shift. Because of this reason, the physical parameters of unit cell are having great importance. The analysis of different unit cells is done by EM simulations; the process is described in more

Neha Singh (✉) · K.K. Choure
Department of Electronics and Communication Engineering,
Poomima Group of Colleges, Jaipur, Rajasthan, India
e-mail: nehasingh10.05.88@gmail.com

K.K. Choure
e-mail: kamal.choure@poomima.org

detail in next sections. The regular pattern of many different unit cells makes a final PSS design [1].

In traditional designs, such as lenses or phase gratings, phase shifting is achieved by varying the thickness of a dielectric slab over the aperture of the device. This approach is not good for optical regime, because in this regime wavelengths are short and these traditional approaches result in physically compact designs. As we know that the physical size which is needed to achieve a given phase shift is proportional to the wavelength. As we know that the physical size of the phase shifting structure will increase when wavelength is increase, which causes bulky designs at millimetre and microwave wavelengths. In various applications we require a high-gain, low-cost and lightweight antenna for microwave region. For achieving that object PSS concept is used. In PSS different layers of different dielectric material are used. Multiple layers of dielectric material can be used, but number of layers would have to be limited so that fabrication complexity of structure, thickness of the device and the overall weight of the device can be reduced [2]. This concept is different from the previous concepts which can introduce a phase shift, although some previous alternative technologies were based on a similar approach [1].

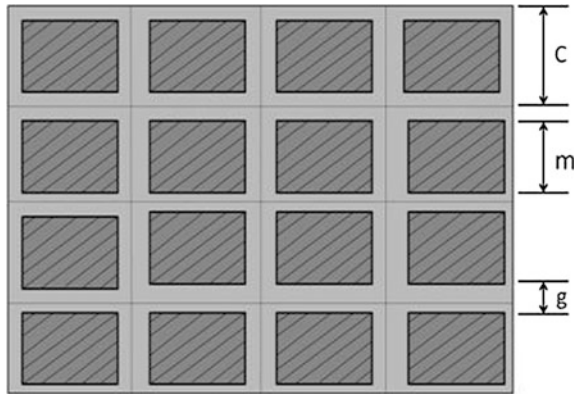
The idea of generating different phase shifts from a thin and flat dielectric sheet and a photolithographic (wet chemical) conductor etching process is come from newspaper printing, where the grey colour tones are obtained from different sizes of small black dots in a given, predetermined array. The ink on paper in the newspaper printing process becomes the metal on dielectric in the PSS structure [3].

Unit Cell Design

This section describes the unit cell design of the PSS. The unit cell design is the most important parameter of the PSS structure. The dimensions of the conducting elements of the unit cell are varied in order to obtain different values of phase. The arrangement of different unit cell elements over the area of the PSS gives a free-standing device that is used to achieve high gain [4]. Each unit cell on dielectric sheet has unique physical dimensions of conductor printed on the different layers; these unique physical dimensions provide a unique phase. The transverse cross-sectional location in the XY -plane of the PSS of the different unit cells allows for achieving gain enhancement [5]. The different unit cells used in a PSS are analysed in the context of a periodic structure, similar to the one shown in Fig. 1 (where c is cell size, m is size of metal patch and g is gap between two metallic patches). A periodic structure analysis allows reduction in computer memory (RAM) and time [6].

The conductive elements on the different dielectric sheets constituting the PSS have to be selected very carefully. The first EM simulations were conducted on square unit cells partially covered with centred square patches [5], similar to those shown in Fig. 1. To perform analysis, it is assumed that the PSS structure is

Fig. 1 Front view of the square uniform periodic structure composed of square unit cells with square metallic patches (the dielectric is shown in *light colour* and the metal is shown in *dark colour* by *hatched line*)



infinitely periodic since it constitutes a good way for obtaining behaviour of the unit cell. This kind of analysis assumes that the neighbouring cells are identical to the single cell being studied. Since the PSS structure becomes large, it is impractical to analyze the full structure using numerical methods due to the large memory storage and computational time requirements [7]. In analysis, it is not possible to consider an infinite structure in the simulations. So that periodic structure can be truncated to a finite size containing a large number of cells [8]. Cell size is chosen from the equation given below [4]:

$$c < \lambda_0 / (1 + |\sin \theta_{\max}|) \tag{1}$$

where c is the unit cell size, λ_0 is the free-space wavelength and $\sin \theta_{\max}$ is the maximum angle of the incident wave measured normal to the surface, i.e. from the z -axis. For a normal incident plane wave, $\theta_{\max} = 0^\circ$ and $c < \lambda_0$; in the worst case, $\theta_{\max} = 90^\circ$ and $c < \lambda_0/2$. m is size of metal patch and g is gap between two metallic patches.

For the simulations, the PSS structure is positioned in the XY -plane, the EM waves which are incident on the structure are assumed to be plane waves propagating in the $+z$ -direction, the incident electric field is selected to be polarized along the y -axis and the incident magnetic field is selected to be polarized along the x -axis. The incoming wave onto the structure of PSS is not plane and the angle of incidence is not necessarily normal, this is only an assumption [5]. The simulations of the structure were performed using commercially available full-wave simulation package employing the finite integral technique [4].

Choice of Basic Parameters

For designing a final PSS structure various parameters are taken in account. In this section we have discussed some of them.

(A) Frequency of operation

For providing PSS practical advantages, a frequency band is selected at which PSS design can show significant improvement in terms of size, weight and cost compared to conventional technologies. For example, if frequency of operation is chosen 30 GHz; at this frequency the free-space wavelength λ_0 is approximately equal to 10 mm. It is worth mentioning though that the above selection does not mean that the PSS concept is strictly limited to this frequency band. In fact, the PSS could potentially be scaled to be used at higher and lower frequencies.

(B) Unit cell size

Cell size is calculated from the Eq. (1); it is $0.1\lambda_0 - 0.5\lambda_0$. If cell size was small, i.e. it was selected 1 mm ($0.1\lambda_0$), then it can be possible to reduce quantisation error as much as possible [2]. It was also found that, for a small cell size c , the tolerance of the photolithographic (wet chemical) etching process used to fabricate the structure could not allow for small enough gaps g (see Fig. 1) between the patches to obtain a wide range of phases. It was then confirmed to increase the value of *cell size* in order to overcome this problem; *cell size* was selected in central range, i.e. $0.3\lambda_0$ [4].

One problem which arise with $c = 0.3\lambda_0$ is that the number of unknowns in the simulation problem is high and the simulations require a large amount of memory and a high computer processor (CPU) speed [6].

(C) Relative permittivity and thickness

For the PSS, the thickness and relative permittivity must be chosen in such a manner that the amplitude of the transmission coefficient is high when the sample is bare and also to ensure that the amplitude of the transmission coefficient will remain high for the large range of patch sizes needed to provide the required range of phase shifts. Large thickness has the potential for obtaining a large phase shift range while maintaining a high amplitude transmission coefficient. But, large thickness is not recommended because they are bulky, heavy, and more material is required [6]. After some preliminary studies, the dielectric constant was selected 2–8 and the thickness is $0.2\lambda - 0.4\lambda$ [4].

(D) Unit cell etching pattern

As previously mentioned, the initial unit cell etching pattern studied was that of a square conductive patch within a square unit cell. In this section, this approach is revisited and a new etching pattern based on a conductive strip is presented.

(a) Conductive square patch

The conductive square patch in a square unit cell lattice is shown in Fig. 2a, it is a logical choice, due to their symmetry, square elements can support orthogonal polarizations. The conductive square patch can be easily modified into a conductive rectangular patch, as shown in Fig. 2b, while keeping the unit cell square. Such configuration also support orthogonal polarizations, but the amplitude and phase of the transmission coefficient would be different for the two polarizations. This is an interesting concept that can bring polarization-independent behavior. It is not possible to obtain a significant phase shift range from a single layer of conductive pattern [5].

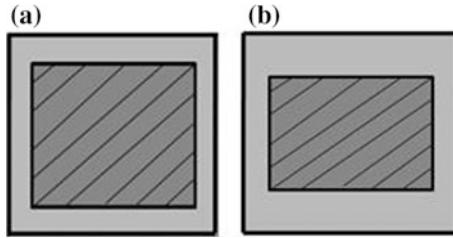


Fig. 2 Front view of the square unit cells with **a** square metallic patches, **b** rectangular metallic patches (the dielectric is shown in *light colour* and the metal is shown in *dark colour* by *hatched line*)

For improving phase shifting performance, more layers of conductive patches in the same square lattice are added on the back of the dielectric sheet and inserted between dielectric materials; no additional dielectric material is added. This arrangement gives significant phase shift range [2].

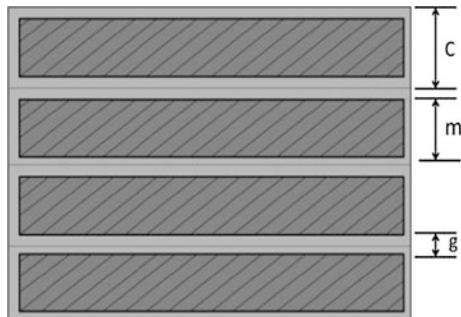
(b) Conductive strip

In order to reduce the simulation time as well as the memory requirement, horizontal conductive strip elements are used in place of conductive patch elements. Since there is no variation of the incident field or the geometry along the *x*-axis, strip repeats itself along the *y*-axis only; so that the result is a one-dimensional unit cell rather than a two-dimensional unit cell. However, the structure can be assumed to be periodic along the *x*-axis also. Since the length of the strip can be infinitely long [4]. When the strip element used for the unit cell, the uniform periodic structure is represented in Fig. 3. In case of continuous strip fields are more uniformly filled compared to a discrete patch, so that this type of arrangement gives more bandwidth [9].

(E) Strip Unit Cell

This section presents the different cases for the strip elements [4]. As previously mentioned a single layer of conductive strip is not sufficient to provide large range of phase shift. So that more than one layers are used for broad range of phase shift. In this section behavior of phase shift is given with number of conductive strip. For

Fig. 3 Front view of the uniform periodic structure composed of strip elements (the dielectric is shown in *light colour* and the metal is shown in *dark colour* by *hatched line*)



the simulation purpose, the conductive layers of design were assumed to be perfectly conducting and infinitesimally thin while the dielectric material was assumed to be lossless.

(a) Single layer

The simplest configuration consists of a single layer of metallic strips on the surface of dielectric material on front side. In this case, the arrangement is similar to Fig. 3 with strips on the front layer only, as shown in Fig. 4a. In the simulation, the strips are assumed to be etched on a dielectric sheet. For this setup phase shift range obtained is around 60°.

(b) Double layer

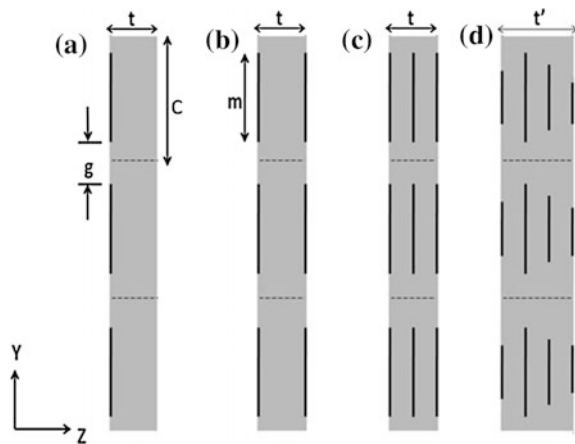
It is possible to etch layers of metallic strips on the front and back side of a single dielectric sheet, as shown in Fig. 4b. The phase shift range obtained for two layer cases is significantly better than for the single layer case, but it is still not sufficient to cover the desired range of 360°. Phase shift range for two layer case is around 135°.

(c) Symmetrical three independent layers

It is possible to insert conductive strips not only on the front and backside, but also between the dielectric sheets, as shown in Fig. 4c. It is also assumed that the front, back and middle layers have the same strip width of m ; maximum phase shift range is 305°. Consequently, it is to be noted that the complete 360° phase shift range is not achieved for this configuration. However, this configuration is very useful and practical, and it will be used for designing many phase shifting components.

Before proceeding to next Section, which examines the four-layer structure shown in Fig. 4d, the electric field of the three-layer structure is studied in some detail. As mentioned previously, the electric field incident on the PSS is polarized along the y -axis, i.e. $E_x = 0, E_y \neq 0, E_z = 0$. The introduction of conductive strips will result in a component of the electrical field parallel to the z -axis (E_z) close to

Fig. 4 Side views of different configurations of periodic structures composed of strip elements, **a** single layer, **b** symmetrical double layer, **c** symmetrical three independent layers, **d** four fully independent layers (the dielectric is shown in light colour and the metal is shown in black colour)



the conductor. Away from the conductor, the electric field is purely polarized along the y -axis. Electric field along the x -axis, i.e. E_x is initially null and will remain null.

(d) Four fully independent layers

The number of layers can be increased for improving the range of phase shifts. However, using too many layers will significantly add to the fabrication complexity of the structure and may become unattractive due to the extra thickness and weight. When too many layers of conductive material are used, bandwidth of the final structure will suffer. As we know from the previous discussion that three conductive layers are not sufficient for complete 360° phase shift. For that reason four conductive layers can be used for designing PSS structure. A four-layer model of PSS can be shown in Fig. 4d. For this particular case, the strip width m is independent for each layer. This four-layer configuration allows the achievement of a phase shift range of a full 360°.

Equivalent Circuit Model

In this section, an equivalent circuit model for the PSS is derived from layer diagram of PSS structure. Visual inspection of the geometry of the PSS in Fig. 4 [4], intuitively suggests an equivalent circuit model for the unit cell of the PSS. Considering Fig. 4c for a three-layer symmetrical PSS, and assuming that a normal incidence plane wave is propagating along the z -direction with electric field polarized along the y -axis, and magnetic field polarized along x -axis, the equivalent circuit shown in Fig. 5.

The shunt capacitance C_1 results from the charge accumulation at the edge of the strips of two adjacent unit cells, located on the same layer, but separated by a gap along the y -axis. The shunt capacitance C_1 depends on the front, back and middle strip width, m . Shunt inductances, in series with these capacitances, should also be present because current flowing along the y -axis on the metallic strips generates inductance; however, values of these inductances are negligible for the frequencies of interest and consequently are of importance only at much higher frequencies. Because of that reason, these shunt inductances were not included in the equivalent circuit model.

Fig. 5 Equivalent circuit model for the unit cell of a three-layer PSS

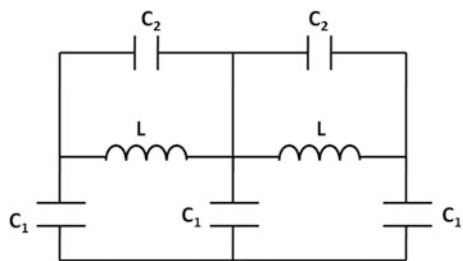


Table 1 Influence of the physical parameters on the electric components of the equivalent circuit model

Parameters	ϵ_r	μ_r	t	c	m or g
C_1	✓		✓	✓	✓
C_2	✓		✓	✓	✓
L		✓	✓	✓	

The shunt capacitances C_1 and series inductance L , also model the transmission line like characteristics of the dielectric layers. The inductance L is easily approximated theoretically [9].

$$L = \mu W = \mu_r \mu_0 W \tag{2}$$

Where μ is the permeability, μ_r is the relative permeability, μ_0 is the free-space permeability and w is the layer thickness, which corresponds to half the total thickness t for the case of a three-layer PSS. The capacitance between the strips in the unit cell is represented by series capacitance C_2 but on different layers (i.e. with different z -values). The capacitance C_2 depends on the size of m of two layers. If structure of PSS is physically symmetrical, the equivalent circuit is also symmetrical. Table 1 shows the effect of the physical parameters on the components of the equivalent circuit model.

At this point, it is important to note that the behaviour of the PSS structure appears to be very similar to that of a low-pass filter, for which the filter order is related to the number of layers. In this case, three conductive layers are separated by two dielectric layers, so that resulting filter order is 5. The analogy with a low-pass filter should not be a surprise since the equivalent circuit model of Fig. 5 is indeed similar to a low-pass filter, except for the series capacitances C_2 [10]. However, it was found that if simulation bandwidth is extending far beyond the frequency of operation reveals that the structure is not a perfect low-pass filter. This is also not a surprise since the circuit model which was obtained here is only for a given bandwidth. The important thing is to keep in mind that, although the equivalent circuit model presented in Fig. 5 behaves like a low-pass filter, it does not mean that PSS final structure also behaving like a low pass filter [4].

Further Considerations of the PSS Structures

In this section some further discussion on the performance of the PSS structure is provided.

(A) Number of layers and bandwidth

It was already discussed that when few layers (single or double) are used, the PSS structure cannot achieve a large enough phase shift range. Consequently, it is necessary to increase the number of layers, which provide a broader phase shift range. From filter theory, it is clear that increasing the order of a filter results in a smaller transition band between stop band and pass band, which corresponds to a more abrupt slope between stop band and pass band [11]. However, increasing the number of layers (beyond three or four) results in bandwidth limitations, since the transition region becomes smaller. The optimum number of layers for the design of a PSS is probably around 3 or 4 layers since fewer layers (one or two) do not result in a large enough phase shift range and more layers (beyond three or four) will present a significant bandwidth reduction.

(B) Use of PSS concept at other frequency bands

As operating frequency increases, the transmission amplitude of EM wave decreases, even though for some band the transmission amplitude is unity or very close to it. Note that these bands are not predicted by the equivalent circuit model of Fig. 5. As stated in the previous section, the PSS is designed to operate near and at the transition region between the pass band and the stop band. Consequently, it is not possible to use the same PSS structure with the same dimensions of unit cell size c and thickness t at another frequency. Alternatively, the same PSS configuration can be work at other frequency bands by performing minor modifications to it, such as scaling. Scaling is done on the basis of operating frequency [6].

Furthermore, operating the PSS at low frequencies would lead to large unit cells with respect to the wavelength, which would have more quantisation error as well as potential problems regarding the unit cell size, as stated by Eq. (1). From filter theory, it is clear that for the case of a low-pass filter, all electric components of the filter can be scaled up in values in order to lower the cutoff frequency. This can be accomplished here for the PSS. From Eq. (2), the only way to increase L is by increasing the thickness t of the PSS structure. However, when value of L is increasing, it will reduce the value of the series capacitance C_2 . For increase C_2 , either the strip or patch size has to be increased, or the dielectric constant has to be increased, or both. If the size of patch is increased, this requires increasing the unit cell size as well. Furthermore, in order to scale the shunt capacitances C_1 and C_2 as well, there may not be any other option than increasing the size of the unit cell c . The same method can be performed for a PSS structure which is made to operate at higher frequencies. Therefore, it is shown that the scaling of the electric components, and the scaling in frequency, is intuitively done by changing the size of the physical parameters [12].

(C) Electromagnetic wave type and oblique incidence

Up to this point in the analysis and electromagnetic simulations performed on the PSS structure, it has been assumed that a normal incident plane wave with the electric field vertically polarized on the structure is used. However, this is only rigorously true if the incident electromagnetic fields are actually normally incident, of the plane-wave type and vertically polarized. This assumption is the same as that

made in the designing of reflect arrays, but it remains an assumption and does not fully represent about actual situation.

The reader can be convinced of that statement by considering any such structure, feed by a closely located feed antenna, to figure out that, although the polarization statement is true, the wave incident on the structure, here the PSS structure, is generally neither of the plane-wave nor normally incident. In fact, the angle of incidence of the rays increases away from the middle of the lens structure. As for the type of wave, before the electromagnetic simulation tools became widely available, all lens and reflector antenna were designed using the geometrical optics approximation, where any point on the structure was treated locally using ray tracing, i.e. localised plane wave [4]. The angle of incidence is another parameter that could be taken in account for generating a database for PSS designs. Nevertheless, for small focal length to diameter ratios (F/D), the angle of incidence can be a critical factor, it may not be neglected.

Comparison of PSS with Other Technology

This section shows the uniqueness of the PSS concept and how it is different to other technology.

(A) PSS versus Artificial dielectric

Artificial dielectrics have been used in the past for realizing gain enhancement structures such as lenses [13]. The artificial dielectric material has some useful characteristics such as harmonic rejection, surface wave suppression, and band suppression. The artificial dielectric material enhances radiation performance, bandwidth, gain and efficiency of the designed antenna [14]. Artificial dielectrics lens consist of a series of thin, parallel dielectric layers containing two-dimensional arrays of small metallic implants whose size and spacing are small compared to the wavelength. The size of the metallic implants and their spacing is designed in such a way that a desired effective dielectric constant is achieved [15]. A slab of high relative permittivity has been perforated to reduce the resulting relative permittivity in some area of the lens antenna [16]. For all cases of the artificial dielectric, the implants are repeated periodically along the direction of propagation and the thickness is significantly larger with a significant number of repetition or layer s . The PSS structure is too thin, as compared to an artificial dielectric and the metallic implants are not repeated along the direction of propagation. An artificial dielectric implies an equivalent relative permittivity [17]. The PSS structure is simply converted to an equivalent circuit model of lumped elements instead of an equivalent relative permittivity (and relative permeability).

(B) PSS versus Metamaterial

A metamaterial is an engineered material that displays a behaviour which is usually not found in nature. It generally refers to a left-handed material, i.e. a material which has negative permittivity and permeability [18]. Basic concept of

metamaterial was first introduced in the late 1960s [19], but brings back by Pendry in late 1990s [20], and now it has been the interesting research area since the beginning of the twenty-first century. Metamaterials are controversial, because there is no clear proof whether the negative permittivity and permeability behaviour truly occurs or not, and whether metamaterials are could really exist in nature [21]. PSS is not to be a metamaterial [4]. The behaviour of the PSS can be explained easily by using a circuit model [22]. In section “Equivalent Circuits Model”, it was clearly demonstrated that the behaviour of the PSS could be explained by a simple circuit model over a reasonable frequency band, PSS structure works as a filter; therefore it is clear that PSS is not a metamaterial.

(C) PSS versus Artificial impedance surface

An artificial impedance surface is a surface, which is designed with specific impedance using a periodic structure approach backed with a ground plane. The concept of artificial impedance surface has been used in surface wave applications. Artificial impedance surface was first introduced in the late 1990s [23]. With the help of artificial impedance surfaces a method is developed to control the radiation from surface currents on metallic bodies. The artificial impedance surface is usually a high impedance surface or it is designed to reproduce a magnetic conductor, with a reflection phase of 0° , which is different from the 180° reflection phase obtained from a uniform sheet of metal. This arrangement has several advantages for various antenna applications, such as a dipole over a ground plane, for which the overall thickness of the antenna can be reduced [9]. The artificial impedance surface requires a very small unit cell size with respect to a wavelength for efficient operation (typically $0.1\lambda_0$), whereas the unit cell size of the PSS structure can work efficiently for any size (as long as it is less than half a free-space wavelength, in order to avoid grating lobes). The PSS and the artificial impedance surface could be similar at first sight, but it is not true, they are actually quite different [23]. The major difference between them is that the artificial impedance surface is a reflective-type surface, with a conductive layer on the back, whereas the PSS is a transmissive type surface. The reflection of the artificial impedance surface is always unity (if no losses are present).

(D) PSS versus Frequency selective surface (FSS)

A frequency selective surface is a resonant structure that allows for transmitting the wave energy over some specific frequencies while blocking it at other undesired frequency [24]. An FSS (frequency selective surface) is a periodic array of aperture or patch elements that behave like a filter [25]. It consists of a structure that is designed to control the amplitude of an incoming wave, as a function of frequency. The PSS is not designed for frequency selectiveness, it is designed to provide amplitude and phase transformation to an incident wave front. Unlike FSS the PSS is a non-resonant structure [4]. At microwave wavelengths, FSS structures were easy to manufacture and easily employ in antenna design. However, at near-infrared wavelengths, the size of FSS is of the order of a micrometre, making such FSS structures much more difficult to manufacture [26]. PSS is working on reactive coupling principle between the different layers. This is not the case for FSS [27].

The complexity in the design of existing FSS structure and their required size and sensitivity to the angle of incidence limits their functionality in many areas [28]. FSS controls the flow of the electromagnetic energy, and it acts as a band pass of band-stop filter [24]. From above discussion it is clear that PSS is not FSS.

Conclusion

In this paper we have discussed PSS concept in detail. PSS is a novel concept used for providing phase shift to the incident wave. This concept is used for designing thin lens antennas. For PSS designing selection of cell size and metallic patch are very important issues. For PSS designing basically two types of cells are used, i.e. rectangular and square, both cell types are discussed with their advantages and disadvantages. The behaviour of the PSS was fully explained, with equivalent circuit model. The uniqueness of the PSS concept was validated by comparison with other concepts that could be thought to be the same.

References

1. Singh, N., Choure, K.K., Kumari, M.: A survey on free-standing phase correcting gain enhancement devices. *Int. J. Sci. Eng. Res. (IJSER)* **4**(7), 109–115 (2013). ISSN:2229-5518
2. Gagnon, N., Petosa, A., McNamara, D.A.: Thin microwave phase-shifting surface (PSS) lens antenna made of square elements. *IET Electron. Lett.* **46**(5), 327–329 (2010)
3. Waters, W.M.: An electronic half-tone image recording technique. *Proc. IEEE* **54**(2), 319–320 (1966)
4. Gagnon, N.: Phase shifting surface (PSS) and phase and amplitude shifting surface (PASS) for microwave applications, Ph.D. thesis. University of Ottawa, Canada (2011)
5. Gagnon, N., Petosa, A., McNamara, D.: Phase hologram composed of square patches on a thin dielectric sheet. In: *Proceedings of the International Symposium on Antennas and Propagation (ISAP 2008)*, Taipei, Taiwan, pp. 678–681 (2008)
6. Gagnon, N., Petosa, A., McNamara, D.A.: thin microwave quasi-transparent phase-shifting surface (PSS). *IEEE Trans. Antennas Propag.* **58**(4), 1193–1201 (2010)
7. Huang, J., Encinar, J.A.: *Reflectarray antennas*. Wiley-IEEE Press, Hoboken (2007)
8. Cwik, T.: Frequency-selective screens. In: Balanis, C.A. (ed.) *Modern Antenna Handbook*. Wiley, Hoboken (2008). Chap. 16
9. Sievenpiper, D.F.: Artificial impedance surfaces for antennas. In: Balanis, C.A. (ed.) *Modern Antenna Handbook*. Wiley, Hoboken (2008). Chap. 15
10. Bode, H.W.: *Network Analysis and Feedback Amplifier Design*. Van Nostrand, New York (1945)
11. Rorabaugh, C.B.: *Digital Filter Designer's Handbook: with C++ Algorithms*. McGraw-hill, New York (1997)
12. Pozar, D.M.: *Microwave Engineering*, 2nd edn. Wiley, New York (1998)
13. Siisskind, C.: Obstacle-type artificial dielectrics for microwaves. *J. Br. Inst. Radio Eng. Univ. Coll.* **24**, 49–60 (1951)

14. Sun, J.S., Chen, G.Y., Lin, C.H., Tiong, K.K., Chen, Y.D.: Application of artificial dielectric material for a PIFA antenna. In: Progress in Electromagnetics Research Symposium, Hangzhou, China, pp. 24–28 (2008)
15. Kock, W.E.: Metallic delay lenses. *Bell Syst. Tech. J.* **27**, 58–82 (1948)
16. Petosa, A., Ittipiboon, A., Thirakoune, S.: Shadow blockage improvement using a perforated dielectric fresnel lens. In: IEEE AP-S International Symposium, Columbus, vol. 4, pp. 514–517 (2003)
17. Brown, J., Jackson, W.: The relative permittivity of tetragonal arrays of perfectly conducting thin disks. *Proc. IEEE—Part B: Radio Electron. Eng.* **102**(1), 37–42 (1955)
18. Singh, N, Choure, K.K., Kochar, A., Singh, H.: A study of significance of metamaterial in antenna array elements design. *Int. J. Adv. Res. Comput. Sci. Softw. Eng. (IJARCSSE)* **4**(3), 237–241 (2014). ISSN:2277-128X
19. Veselago, V.G.: The electrodynamics of substances with simultaneously negative values of ϵ and μ . *Soviet Phys.-USPEKHI* **10**(4), 509–514 (1968)
20. Pendry, J.B., et al.: Magnetism from conductors, and enhanced non-linear phenomena. *IEEE Trans. Microw. Theor. Tech.* **47**(11), 2075–2084 (1999)
21. Munk, B.A.: *Metamaterials: Critique and Alternatives*. Wiley, New York (2009)
22. Spielman, B.E., et al.: Metamaterials face-off. *IEEE Microw. Mag.* **10**(3), 8–42 (2009)
23. Sievenpiper, D., et al.: High-impedance electromagnetic surfaces with a forbidden frequency band. *IEEE Trans. Microw. Theor. Tech.* **47**(11), 2059–2074 (1999)
24. Munk, B.A.: *Frequency selective surfaces: theory and design*. Wiley, New York (2000)
25. Sung, H.-H.: Frequency selective wallpaper for mitigating indoor wireless interference, Ph.D. thesis. University of Auckland (2006)
26. Reed, J.A.: Dissertation proposal: frequency selective surfaces with multiple periodic elements, Ph.D. thesis. University of Texas at Dallas (1997)
27. Birbir, F., Shaker, J., Antar, Y.M.M.: Chebishev bandpass spatial filter composed of strip gratings. *IEEE Trans. Antennas Propag.* **56**(12), 3707–3713 (2008)
28. Bayatpur, F.: Metamaterial-inspired frequency-selective surfaces, Ph.D. thesis University of Michigan (2009)

Review on Student Attendance Maintenance System: A Discontentment

Anshuman Kalla and Dileep Kumar Tiwari

Abstract In many countries including India, monitoring student attendance, in almost all the educational sectors be it schools, institutes, college or universities, is still a tedious, time-consuming, error-prone, unmanageable and manual process. The above fact is hard to fathom in the present era where technological developments are on the cutting-edge and technology-driven solutions have served as primary key to unlock doors to trouble free quality life. Thus the paper aims to bring in lime light the importance of careful monitoring of student attendance, hardship associated with prevailing ways of monitoring student attendance, typical nature of problem of student attendance maintenance (as compared other problems with innate identification requirement), RFID as a promising technology, salient features (and needs) to which student attendance systems should be tailored. The paper reviews of some of the work done so far in the field of RFID based student attendance maintenance systems. The paper aims to lay foundation for focused research to develop and deploy not just feasible but broadly acceptable technical solution for maintenance of student attendance in all educational sectors.

Keywords RFID · Student attendance maintenance system · Attendance monitoring system

Introduction

Education forms the foundation of human lives and almost everyone spends significant portion of his/her lifetime at educational institutes. Thus scientific and technological advancements should fully intervene to simplify numerous issues involved and to improvise the quality of teaching. One basic but highly perplexing

Anshuman Kalla (✉) · D.K. Tiwari

Department of Electronics and Communication, Jaipur National University, Jaipur, India
e-mail: kallajnu@gmail.com

D.K. Tiwari

e-mail: dil.371987@gmail.com

© Springer India 2016

N. Afzalpulkar et al. (eds.), *Proceedings of the International Conference on Recent Cognizance in Wireless Communication & Image Processing*,
DOI 10.1007/978-81-322-2638-3_110

987

academic chore, that still lacks technological elegance in its conduction, is student attendance maintenance system. Various indispensable steps involved in managing student attendance system are scanning, storing, analyzing, and sharing. There are several reasons that validate importance of monitoring student attendance and are discussed as follows:

- i. Many courses, specially technical courses, require students to regularly attend the lectures and perform experiments in laboratories. Guidelines/norms regarding minimum student attendance have been put forward by various apex bodies for example by All India Council of Technical Education (AICTE) in India. Student's attendance should be above this minimum criterion in order to be eligible to write exams pertaining to a course. Thus monitoring and maintaining student attendance becomes essential and integral part of academics activities.
- ii. Many professors allocate some percentage of final grades to student attendance in order to create better academic environment that promotes interactions and discussions leading to the better understanding of the subject & thereby improves lecture delivery.
- iii. Many schools, institutes and universities strongly consider student attendance during classes as one of the prominent performance indexes. In fact, higher student attendance (above the minimum criterion) directly implies willingness of students to attend classes and thus indicates quality of teaching of a particular educational institute.
- iv. Educational institutes may also take into account student attendance as one of the parameters for evaluating performance of faculty members during annual appraisal.
- v. Student attendance might also work as one of the pivotal input data for department(s) of basic and higher education to understand current educational scenario and accordingly develop and roll-out strategies to empower education.

From the above discussion it is quite evident that student attendance is crucial but unfortunately till today conventional ways (which were prevalent about several decades ago) are being followed. Surprisingly not a single technical solution has been so developed such that it could be fully deployed in all the educational sectors like schools, colleges, universities etc.

Student Attendance and Related Problems

The existing two variants of conventional way of marking student attendance are (i) students signing an attendance sheet at the end of class and instructor preserving that sheet in a file (ii) students replying verbally to the roll-calls made in class by the instructor and simultaneously marking of either presence or absence in a register,

i.e., book-keeping. Such orthodox ways of maintaining attendance has several associated entangled problems which are discussed as follow:

1. Most noticeable is the reduction in effective lecture duration. As experienced by every instructor and mentioned in [1], the traditional ways of marking student attendance nibble about 10 min of the total lecture duration for a class of 60 students. Thus if the total lecture duration is 1 h then total wastage is around 15–20 %. The time wastage would increase if the total lecture duration is lesser as attendance scanning time is only dependent on total number of students.
2. Nowadays, in significant number of educational institutes, it is mandatory to digitize the attendance recorded during the class by manually entering the attendance from paper register or attendance sheet in software. The attendance database so created could be easily used for analyzing, understanding, deciding, and sharing of records. Thus instructors further need to devote some more time off-class (sitting in their cabins/offices) for the same which subsequently increases percentage of effective time wastage for maintaining student attendance records.
3. The entire process of attendance (i.e., recording attendance during lecture duration and then uploading it to software) is error-prone. Student(s) may sign attendance sheet or reply to roll-call for other students intentionally or accidentally. In former case it results in hoax (proxy) attendance and later case results in loss of attendance.
4. In institutes where digitization (i.e., uploading attendance to software) is not performed, preservability is an issue since attendance is recorded only in paper sheets or paper registers. In addition, absence of software requires manual analysis to be carried out before each examination so as to prepare a list of eligible students and debarred students.
5. In case of occasional mistake made by the instructor while marking attendance during lectures may either lead to permanent errors or untidy register/sheet (as instructor tires to correct errors by overwriting).
6. Last but not least; if class is big in term of number of students then registering attendance could be quite troublesome as during that time normally students get themselves engage in chatting with each other.

Nature of Problem of Student Attendance Maintenance

Maintaining attendance records is inevitable and mandatory part of day-to-day working of any organization be it a business enterprise or an educational institute. But there is subtle difference between monitoring attendance (requiring individual's identification) at a business enterprise and at an educational institute. People working in an average-scale business enterprise might be significantly less than the students studying in an average-scale educational institute. Also, what is important for business enterprise is to monitor entry time and exit time of every employee

each day, whereas in any institute, attendance has to be recorded during each lecture provided that there could be many lectures per day. It would be sufficient to install one identification reader at the entry gate of each building of business enterprise but for educational institute there should be one identification reader available in each class room. Hence it could be well understood that both number of identification readers and number of identification tags (that carries individual's identification) required are more in educational institute. It is worth noticing that increase in percentage of identification readers is much more alarming than number of identification tags since the cost per unit reader is much higher than the cost per unit tag. Thus the cost of deploying an attendance maintenance system, which is primarily governed by number of reader required, would be tremendously high for educational institute. The situation is exacerbated by the fact that money seems not to be an issue for business enterprises but is certainly a great concern for educational institutes.

From the above discussion it is clear that fundamental requirement for a successful technical solution for student attendance maintenance system, would be low overall cost. In other words the solution should offer low CAPital EXpenditure (CAPEX) as well as marginally low OPERating EXpenditure (OPEX). The other requirements will be discussed shortly.

RFID Technology

Among several competing identification technologies like barcode, optical character recognition (OCR), voice recognition, RFID, biometric identification (fingerprint, iris, ear, face), smart card, etc., the RFID technology seems to be the most promising for current problem of monitoring student attendance. The numerous advantage [2] of RFID over the other technologies are (i) Technology is quite mature today, (ii) Ability to read in hostile environments, (iii) Real time reading capability, (iv) Fast reading of RFID tags (cards), i.e., around 0.5 s [2], (v) No physical contact between RFID reader and tag thus no wear and tear (vi) RFID when used with passive tags than operational expenditure (OPEX) is low as replacement of battery within a tag is not required, (vii) Reading of RFID tags is not affected by orientation or position provided they are within the reading range, (viii) Reading is not affected by dirt or damp, (ix) Cost of RFID tag is very cheap, (x) Data density is very high, etc. Thus present paper has focused on the work done so far for student attendance maintenance system using RFID technology.

Salient Feature of Student Attendance System

Due to typical nature of student attendance problem there are some salient features that should be preferably incorporated when designing a technical solution that could be globally accepted and deployed. Such requirements are discussed below:

1. **Cost:** As discussed before the cost is the preminent concern for educational institutes. For complete deployment of any technical solution for student attendance maintenance system the cost per unit system should be very low so that even small schools could effortlessly afford it.
2. **Portable:** The device should be portable so that faculty members could carry it in classrooms as sometimes it is not good idea to install it in each classroom for many reasons like increase in cost, security of device, etc. Thus the device should preferably a handheld device.
3. **Power Efficient:** In case student attendance device is handheld device then most probably it is driven by (rechargeable) DC power supply. Thus the circuitry must draw as much less power supply as possible as it would add to operating expenses which should be minimized.
4. **Compact:** The device (and its printed circuit board) should be designed in such a way that minimum numbers of components should be used and they should be placed in an optimum and compact way.
5. **Light Weight:** It is an apparent need for a handheld device that it should be light in weight so that instructors could effortlessly carry it in classroom and if needed could be circulated among the students for scanning attendance.
6. **Authorization:** Attendance system should allow only faculty members to scan attendance, upload it to central database, refresh the internal memory of device, etc. Students on the other hand should be allowed only to mark their attendance by their ID cards.
7. **Audio and Visual Acknowledgment:** It is necessary to provide students with some kind of acknowledgment when they flash their ID cards over a device for marking attendance. The acknowledgment would signify students that their attendance is scanned successfully by the attendance system.
8. **Simple and Elegant Circuit Design:** This feature would allow easy large scale production and repairing of devices.

Review of Related Work

Authors in [3] have proposed RFID based attendance management system. The designed hardware comprises of off-the-shelf Intersoft RFID Demokit-1 that offers serial data transmission facility and within which there is TR-RO1-OEM RFID reader module operating at 125 kHz. The communication between RFID reader and computer is realized with help of USB-to-RS-232 serial converter. The link between RFID reader module and USB-to-RS-232 serial converter is established by using RS-232 serial cable (male to female, DE-9 type) whereas USB cable (one end standard—A and another end standard—B) is used between USB-to-RS-232 serial converter (standard—B, end is connected) and USB port of computer (standard—A, end is connected). Further, 9 V battery is used to supply power to RFID reader module. Software part is developed using Microsoft Visual C# for programming

and Microsoft SQL Server for database management system. Authors recommended installing RFID reader at the gate of every classroom. Students need to flash their ID cards while entering and exiting classroom. On successful reading of ID cards, RFID reader sends the data containing arrival and departure timings to server (running on connected computer). For sharing the recorded attendance SMS and email facility is also being incorporated through which weekly summary of attendance could be send to concerned people. Since installing RFID reader at gates of class rooms leaves possibility of impersonation thus authors proposed to use biometric security along with RFID in future to circumvent the problem.

In [1] authors developed RFID technology based attendance managements systems and propose to analyze the scalability and efficiency of such attendance systems. Software has been developed which intends to provide facility to generate attendance report for a given course, to manage large records and to securely store data. Visual Basic 6.0 has been used for programming and Microsoft Access for providing database. The hardware section consists of readymade RFID module from NSK Electronics which works on the 125 kHz and has reading sensitivity of 10 cm. The middleware is equipped with AT89S52 microcontroller from Atmel Corporation, external EEPROM to store the data and 16×2 LCD for display. Authors concluded that for a class of 60 students, RFID enabled attendance system takes 12 s to record attendance as compared to 120 s by bar code enabled attendance system and 600 s by using conventional way of marking attendance. Authors advocate that RFID technology could be best suitable technology for student attendance system provided the cost of RFID tag and RFID reader is reduced.

The paper [4] introduced RFID based time attendance management system for companies (with large number of working employees), primarily to maintain attendance database along with entry and exit times. The system is also used to make the entry restricted by controlling the opening of gate based on scanning of RFID cards. The proposed system consists of both hardware and software sections. Hardware part includes RFID reader (operating at 125 kHz frequency, reading range of 7 cm, of make Seeed Company and supports UME4100 protocol enabled RFID tags), Atmel AT89S52 microcontroller, motor to drive opening and closing of entry/exit gate and RS-232 serial-to-USB converter. If scanned tag is found to be authorized then microcontroller actuates the motor to open the entry gate. Authors used Microsoft Visual Studio 2008 and Microsoft.Net framework for programming and creating graphical user interface (GUI). In addition Microsoft Access 2007 has been utilized for database management. Two databases used are register database and attendance database. Register database holds identification of all the registered employees and is used as backhand database to identify authorized users whereas attendance database holds all the attendance records. Authors suggest using LCD to display identification details and IP camera to avoid impersonation in future.

In [5] authors employed multiple technologies for creating a smart attendance maintenance system; RFID technology to scan ID cards of students, biometric finger print technology to enhance security and GSM (Global System for Mobile Communication) to convey student attendance to their parents/guardians. Authors have advised to install a RFID scanning device at the main entry point of the

institute's campus. Student on entering institute flashes his/her RFID card and the entry in institute is marked. Simultaneously SMS is being sent to the registered guardian. Further, biometric finger print module is also being installed at each block (within campus) where again second level of verification is performed by scanning finger prints of students. Thus student's presence could be tracked at two levels. Authors have developed a webpage over ASP.Net which facilitates an easy access to students, guardians and instructors with different privilege levels. Software part is developed using VB.Net and database is managed over MS SQL. In future, authors expect to use GPS for exact location tracking and suggest installing one RFID reader at entry point of each classroom.

Authors in [6] advocated that combination of RFID technology with cloud computing has potential to permanently fix some of the prevailing hurdles for student attendance monitoring. Further, they envisage that collaborative usage of RFID technology and cloud computing would render time management as prime advantage. The recorded data from RFID readers is sent to cloud servers instead of local servers. MS Access and Visual Basic have been used for building backend database and developing user interface respectively. Hardware section uses readymade RFID module (operating frequency 125 kHz) from NSK Electronics, microcontroller, liquid crystal display, level converter and buzzer. RFID reader module is fixed at the entry point of each classroom. In future author propose to add SMS facility and augment biometric system for avoiding faulty attendance.

In [7] authors put forward a design of student attendance monitoring system which is web-based and uses RFID technology. The entire system is composed of three parts; (i) RFID reader module, (ii) data reporter module and (iii) server module. RFID reader module used is Mifare (AC900) operating at 125 kHz and is connected to hub (layer-1) or switch (layer-2) with help of RJ45 connector. Thus authors connected various RFID readers installed at different classrooms via layer-2 switch which is further connected to router. The data reporter module reads tag values through RFID reader module and conveys it to online server every 30 min. Web pages are developed in PHP and database is developed using MySQL. For testing and debugging purpose, XAMPP server is being used. Three types of login privileges have been allowed namely admin, lecturer, and student based on the obvious needs.

In [8] researchers developed a software for online student supervision using passive RFID by using MS Visual Basic 6.0 for programming, MS Access for storage information system (database management), Macromedia Dreamweaver MX for interfacing between LAN and server. Further, website is being developed using Active Server Pages (ASP) and it runs over Internet Information Services (IIS) server. Author tested performance of tag under high and low level noise with moisture in air.

Paper [9] built software for automation of attendance. The software is provisioned with numerous features like fetching from hardware the clock time at which card is scanned, marking of attendance and removing incorrect attendance, weightage calculation which shows eligibility of students to appear for opted

course, generating warning for non-eligible students, updating attendance by sending emails and SMS, etc.

Lim et al. in [10] designed a prototype for RFID based attendance system. The fundamental components of prototype are Microcontroller (PIC18F4550), RFID reader (EM4095 IC based), Real Time Clock (1307), MMC (Multi Media Card), 16×2 Liquid Crystal Display (LCD), Dual Driver Transceiver (MAX 232) and two types of power supplies AC and DC with rating 220 V and 12 V respectively. Microcontroller being the heart of circuitry reads a tag value by making use of reader and further stores the value in its internal electrical erasable read-only memory (EEPROM). The values being read is also displayed over LCD thus provides visual acknowledgement to user. Computer is interfaced with hardware section for data communication by using dual driver transceiver IC. The software used is Hyper-Terminal (available in windows operating system). The circuit normally works on AC but in absence of AC voltage, supply is automatically driven from 12 V standby battery. In Circuit Serial Programmer (ICSP) is being used to update microcontroller's program without removing in from circuit. The hardware supports serial programmer (JDM) which supports programmable interface controller (PIC) microcontrollers. Authors assert that their design is compact, low cost, portable, and light weight. Though not mentioned in the paper but a quick analysis would reveal that total cost of designed hardware should be around 450 INR which is still high for any attendance maintenance system in educational institutes. Perhaps there is still room for cost reduction as the cost of microcontroller used is very high.

In [11], authors made use of RFID reader YHU638 from EHUOYAN with operating frequency of 13.56 MHz for hardware section. The software part is built using JAVA. Researchers intend to install one RFID reader in each classroom. At the beginning of lecture, instructor enters his/her login and password to activate entire hardware, i.e., RFID reader and webcam to record attendance. Students then flash their RFID enabled ID cards, photo of individual student is clicked and attendance is recorded. The instructor then clicks the submit button to lock and upload the attendance data (tag values plus photos) to database. For future work authors propose to introduce GPS and GSM technology to the designed system.

Authors in [12] designed the software part and used off-the-shelf RFID reader operating at 125 kHz frequency. The software is developed based on client server model. RFID reader reads tag values and sends it to attached client computer. The client further sends the attendance data to the database. ASP.Net is used to develop the software and MySQL server 2008 is used for database handling. The client access the software through web browser to upload attendance to server. In future authors propose to use LCD display and IP camera to avoid proxy attendance.

Paper [13] developed software module to maintain student attendance system. ASP.NET is used for programming, SQL server for database management and C# is used to develop an application with GUI. The hardware part is composed of IR sensors, LPC-2148 microcontroller, LCD display, RFID reader, MAX-232 Dual Driver Transceiver, GSM/GPRS module. IR sensor mounted at gate is used to count the number of students (users) entering in classroom. Microcontroller

performs several tasks, out of which displaying the count from IR sensor on LCD display is one task. RFID reader reads the tag value when student flashes RFID enabled ID card over it and sends it to microcontroller. Further, microcontroller pushes this tag value to computer attached via dual driver IC. GSM/GPRS module connected to microcontroller is used to send the attendance data to web server.

In paper [14] authors published an attendance system which offers facility to be remotely monitored by using GSM network. The hardware section comprises of RFID reader with inbuilt dual driver transceiver, GSM module (SIM 300) and computer. MS Visual Basic 6.0 is being used for programming and configuring communication port whereas MS Access is used for database management. When user flashes the RFID tag over reader then attendance is recorded and simultaneously SMS is being sent to the registered user(s) who are interested in monitoring attendance.

Gopala Krishna et al. [15] designed an intelligent Campus Security Tracking (iCST) system for attendance and security purpose. For circuit designing authors used RFID reader to scan ID cards, Zigbee module to send data from hardware section to computer, GSM module to send SMS and make predefined voice call to registered guardians/parents and microprocessor (Freescale MC9S12XS128) to control overall process.

Das et al. [16] devised a RFID based time attendance system where RFID reader with inbuilt serial communication port is directly connected to computer with help of USB-to-RS-232 converter. C# is being used for programming and MS Access for database. The developed software provides registration facility to new users and allows attendance report generation in MS Excel and portable document format (pdf).

In [2] Ranjan Patel et al. worked on online attendance monitoring system which consists of RFID readers installed in each class room. These readers are connected to server through local area network (LAN). The server stores attendance records in a database and publishes them over Internet so that users can take a look.

Ademola et al. in [17] developed RFID based attendance system and introduced the use of pictorial database management. When a student swaps RFID enabled ID card over a reader then a successful reading and correct matching of tag value results in displaying a stored image of that student along with name, RFID tag value, current data and percentage of attendance. For hardware part authors used RFID- μ RW-USB (operating frequency 125 kHz) which can read and write EM4100, EM4205, EM305, Hitags and T55xx/67/xx tags/transponder value. MS Access is used for database management and Visual Studio 2012 IDE C++ is used programming.

Parvathy et al. in [18] devised a RFID based attendance management system for examination hall. The hardware part consists of readymade RFID reader (operating frequency 125 kHz) from NSK electronics, Liquid Crystal Display (16×2 LCD), buzzer for sound acknowledgment, Atmel AT89S52 microcontroller and dual driver transceiver (MAX-232). RFID reader supports UNIQUE or TK5530 protocol and FSK decoding is used to read tag value. Further, the reader section consists of PIC16F628 microcontroller, three shunted inverter gates, push-pull amplifier, voltage divider resistor, and filter capacitors for the required functioning. When

students swap their ID cards then their seating arrangement is shown on the LCD display.

Conclusion

Attendance monitoring is an intrinsic activity pertaining to any educational institute but till date conventional ways are being used in almost all the sectors of education. In the paper, an overview of various research work done so far in the area of RFID enabled student attendance maintenance system has been presented. It could easily be observed that most of researchers have focused on designing the software part and comparatively lesser efforts have been made to design and develop, equally important, hardware section while keeping in mind essential features like low cost, high power efficiency, handheld portability, etc. Like, in the case of computers the cost of operating system is a small percentage of overall cost of a computer, in the same way, for automation of student attendance, one would need to purchase single copy of a software (with required number of users) but number of hardware devices to be purchased would be very large in number. Thus the paper tries to pinpoint the increasing importance of designing and deploying a simple yet elegant technical solution with necessity to pay special attention on hardware part as well.

Authors hope that this paper would turn out to be a starting point for young researchers who desire to work on (application based problem of) student attendance maintenance system. At the same time the paper is expected to be a source of information for academicians (and related people) wishing to keep their knowledge updated.

References

1. Nainan, S., Parekh, R., Shah, T.: RFID technology based attendance management system. *IJCSI Int. J. Comput. Sci. Issues* **10**(1), No 1 (2013)
2. Patel, R., Patel, N., Gajjar, M.: Online students' attendance monitoring system in classroom using radio frequency identification technology: a proposed system framework. *Int. J. Emerg. Technol. Adv. Eng.* **2**(2) Feb 2012
3. Arulogun, O.T., Olatunbosun, A., Fakolujo, O.A., Olaniyi, O.M.: RFID-based students attendance management system. *Int. J.Sci. Eng. Res.* **4**(2) (2013)
4. Chiagozie, O.G., Nwaji, O.G.: Radio Frequency Identification (RFID) based attendance system with automatic door unit. *Acad. Res. Int.* **2** (2012)
5. Rasagna, B., Rajendra, C.: SSCM: A Smart System for College Maintenance. *Int. J. Adv. Res. Comput. Eng. Technol.* **1**(3) (2012)
6. Parvathy, A., Rajasekhar, B., Nithya, C., Thenmozhi, K., Rayappan, J.B.B., Raj, P., Amirtharajan, R.: RFID in cloud environment for attendance monitoring system. *Int. J. Eng. Technol. (IJET)* **5**(3) (2013)
7. Kassim, M., Mazlan, H., Zaini, N., Salleh, M.K.: Web-based student attendance system using RFID technology. *IEEE Control Syst. Graduate Res. Colloquium (ICSGRC)* (2012)

8. Herdawatie binti Abdul Kadir, Siti Nurul Aqmariah binti Mohd Kanafiah, Mohd Helmy bin Abd. Wahab, Zarina Tukiran, Zulida bte Abdul Kadir.: Online Students Supervision (OSS) systems using passive RFID. In: International Conference on Electronic Design, Malaysia, Dec 2008
9. Qaiser, A., Khan, S.A.: Automation of time and attendance using RFID systems. In: 2nd International Conference on Emerging Technologies, Pakistan, Nov 2006
10. Lim, T.S., Sim, S.C., Mansor, M.M.: RFID based attendance system. In: IEEE Symposium on Industrial Electronics and Applications (ISIEA 2009), Malaysia, Oct 2009
11. Saparkhojayev1, N., Guvercin, S.: Attendance control system based on RFID-technology. IJCSI Int. J. Comput. Sci. Issues, **9**(3), No 1 (2012)
12. Shukla, S., Shah, S., Save, P.: RFID Based attendance management system. Int. J. Electr. Comput. Eng. (IJECE) **3**, 784–790 (2013)
13. Mohammed, A.A., Jyothi Kameswari, U.: Web-server based student attendance system using RFID technology. Int. J. Eng. Trends Technol. (IJETT) **4**(5) (2013)
14. Singhal, Z., Gujral, R.K.: Anytime anywhere—remote monitoring of attendance system based on RFID using GSM network. Int. J. Comput. Appl. **39** (2012)
15. Gopala Krishna, V.B., Chandra Sekhar, S., Rajesh Babu, N.: The design of intelligent campus security & attendance system based on RFID, GSM and Zig-Bee. IOSR J. Eng. (IOSRJEN) **2** (6), 16–22 (2012)
16. Das, S.K., Jena, S.: RFID based time attendance system. In: National Conference on VLSI and Embedded System, CEERI, Pilani, India, Oct 2011
17. Abdulkareem, A., Ike, D.U., Olowononi, F.: Development of a radio frequency identification based attendance management application with a pictorial database framework. IJRIT Int. J. Res. Inf. Technol. **2**(4), 621–628 (2014)
18. Parvathy, A., Raj, V.R., Venumadhav, M.: RFID based exam hall maintenance system. IJCA Special Issue on Artificial Intelligence Techniques—Novel Approaches & Practical Applications, AIT 2011

Author Index

A

Aayush Dwivedi, 741
Abhishek Bajpai, 249, 933
Abhishek Pal, 797
Aditya Gupta, 837
Agarwal, Madan Mohan, 599
Agrawal, Atul Kumar, 463
Ajay Khunteta, 9, 671
Ajay Kumar, 889
Ajay Tiwari, 695
Ajay Yadav, 645
Ajeet Kumar, 201
Akanksha Deo, 399
Amit Limba, 399
Amritpal Singh, 123
Amruth, V., 627
Anila Dhingra, 759
Anil Boyal, 399
Anjali Agarwal, 31
Ankita Nirankari, 391
Ankur Choudhary, 21
Ankur Dalmiya, 559
Ansari, Mohd Samar, 151, 159
Anshuman Kalla, 59, 987
Anupma Marwaha, 573
Apoorva Khandelwal, 391
Archana Agarwal, 93
Argha Sarkar, 821
Arghya Biswas, 797
Arshad Nadeem, 869
Arun, Goswami Siddhant, 543
Aruna Rani, 209
Arvind Kumar, 21
Ashish Khare, 481
Ashish Kumar, 39, 813
Ashish Sharma, 511
Atesh Kumar, 501

B

Badve, Omkar P., 683
Bansal, Ajay Kumar, 535
Bhadouria, Amit Singh, 51, 897
Bhatnagar, D., 695
Bhatnagar, S.K., 107
Bhavana Peswani, 861
Bhim Singh, 381
Bhunia, C.T., 317, 367
Bhunia, Chandan Tilak, 133
Bhushan Dhengale, 543
Bindra, Harminder Singh, 773
Binh, Nguyen Thanh, 481
Brajraj Sharma, 695

C

Chakraborty, P., 367
Chandankhede, Pankaj H., 115
Chaudhary, H.R., 861
Chhagan Doot, 99
Chhipa, Mayur Kumar, 193
Choure, Kamal Kishor, 973

D

Darshana Upadhyay, 305
Debashis De, 435
Deepak Bhatia, 463
Deepa Modi, 241
Deepti Mittal, 175
Devendra Goyal, 943
Devendra Mehra, 767
Devi, Ngasepam Monica, 347
Dharmanna Lamani, 69
Dheeraj Bhardwaj, 729, 741
Dhruba Ghosh, 167
Dinesh Sethi, 645
Dusad, Lalit Kumar, 193
Dutta, Manash P., 317

G

Garima Yadav, 31
 Gaurav Sharma, 635
 Ghanshyam Singh, 107, 409, 415, 759
 Gitansh Gulati, 729
 Govil, M.C., 599
 Gupta, B.B., 523, 683
 Gupta, Manisha, 81
 Gupta, Mukesh Kumar, 759
 Gupta, R.A., 381
 Gurwinder Singh, 573, 703

H

Harsh Gupta, 441
 Harshita, 471
 Heena Shahani, 187
 Himanshu Jindal, 1
 Hiroyuki Tsuda, 415
 Hunagund, P.V., 263

J

Jain, Bharat Bhushan, 381
 James Eke, 415
 Janmoni Borah, 581
 Jarnail Singh, 917
 Jaya Krishna, R., 627
 Jhankal, Anuj Kumar, 599
 Jinia, 917
 Jitendra Vaswani, 635
 Joshi, Amit M., 853
 Joydeep Kundu, 435
 Jyoti Agarwal, 759
 Jyoti Kataria, 925

K

Kalpana Sharma, 271
 Kanika Sahni, 373
 Karia, Deepak C., 543
 Kasana, Singara Singh, 1
 Kaur, Jashan Preet, 589
 Khan, A. Mohsin, 657
 Khanapurkar, M.M., 115
 Khanna, R.K., 619, 645
 Kiran Rawat, 373
 Komal Sharma, 729, 741
 Koushik Majumder, 435
 Krishna Joshi, 223, 297
 Krishna Rathore, 711, 861
 Kulat, K.D., 837
 Kumar, Arun, 81
 Kumar, M. Ravi, 427
 Kuriakose, Jeril, 627

L

Lakshit Bhardwaj, 729
 Latha, C.P., 657
 Lipi Sarkar, 339

M

M. Mahesh, 69
 Madhav, Manish Kumar, 925
 Madhuri, B., 821
 Madhuri Sahal, 663
 Maity, S., 367
 Manisha Gupta, 791
 Manisha Meena, 853
 Manish Khare, 481
 Manish Singhal, 943
 Manish Tiwari, 409
 Manjunath, T.C., 69
 Manjunatha, M.B., 657
 Mann, Gurpreet Singh, 589
 Manoj Thosar, 619
 Mehul Mahrishi, 489, 845
 Mithilesh Kumar, 51, 897
 Monica Bapna, 853
 Monika Mathur, 107
 Monika Saini, 39
 Mushtaq Ahmed, 233
 Muzzammil Hussain, 287

N

Nagaraja, H.N., 359
 Neelam Choudhary, 695
 Neeraj Bokde, 837
 Neeta Nain, 233, 241
 Neha Janu, 99
 Neha Singh, 805, 973
 Nehra, Maninder Singh, 233
 Nidhi Bhartiya, 609
 Nidhi Jain, 741
 Nidhi Tiwari, 391
 Niraj Kumar, 501
 Nirma Kumawat, 711

O

Om Prakash, 481

P

Pandey, Abhishek Kumar, 581
 Pandey, Amit Kr., 399
 Paras Bassi, 489
 Parveen, 123
 Patidar, Dipesh Kumar, 175
 Patil, Rajendra R., 263

Poonam Malpani, 489
 Poonia, Yogendra Singh, 175
 Pradeep Kumar, 141
 Pragya Agarwal, 21
 Priyanka Jain, 93
 Priyanka Rahi, 645
 Priyanka Sharma, 305
 Priyank Dubey, 501

R

Rahul Kumar, 523
 Raj, Rajesh Kumar, 861
 Rajdeep Kaur, 589
 Rajeev Srivastava, 953
 Rajesh Saha, 133, 339, 353
 Rajni, 573, 703, 963
 Ramteke, R.J., 451
 Raushan, R., 367
 Ravi Singh, 783
 Rekha Mehra, 187
 Richa Sharma, 99
 Rijita Poddar, 353
 Rimpi Goyal, 719
 Ritu Sharma, 193
 Roheet Bhatnagar, 813
 Rohit Gurjar, 783
 Rookkishor Sharma, 861
 Roy, Sourabh K., 869
 Ruchika Solanki, 271

S

Sahadev Roy, 133, 353, 581
 Sahu, P.P., 367
 Saini, J.S., 695
 Saini, Than Singh, 201
 Sakshi Bhatnagar, 441
 Sambit Mohapatra, 217, 751
 Sandeep Joshi, 805, 829
 Sandeep Vyas, 409
 Sandhu, Jasminder Kaur, 905
 Sanjay Sharma, 567
 Sanjeev Dewra, 209
 Sanjiv Tomar, 889
 Santanu Maity, 279, 339, 347, 821
 Santosh Kumawat, 9
 Sanyog Rawat, 567, 767
 Sarvesh Tanwar, 471
 Saurabh Kumar, 783
 Saurabh Maheshwari, 31, 271
 Saurabh Mishra, 501
 Shadab Siddiqui, 223, 297
 Shagun Maheshwari, 93
 Shahin Fatima, 223, 297
 Shailendra Tiwari, 953

Shankar Bhattacharjee, 279
 Sharad Saxena, 1, 905
 Sharma, Om Prakash, 559
 Sharma, Rakesh Kumar, 869
 Sharma, T.P., 223
 Sheikh, Tasher Ali, 581
 Shirish Nagar, 671
 Shivam Kumar, 821
 Shruti Singh, 249, 933
 Shruti Thapar, 59
 Simarpreet Kaur, 703
 Simerjeet Kaur, 963
 Singh, Barinder Paul, 963
 Singh, Bishal Kumar, 317
 Sinha, Ravindra Kumar, 201
 Soma Kumawat, 427
 Sran, Sukhwinder Singh, 719
 Srishti Gusain, 391
 Srivastava, Devesh Kumar, 511, 627
 Stanley, A.I., 415
 Stapute, V.R., 837
 Subhasish Banerjee, 317
 Subramanya Bhat, 359
 Suditi Choudhary, 287
 Sujata Pandey, 141, 167, 373
 Suman Kumari, 51, 897
 Sumit Srivastava, 813
 Sunkaria, Ramesh Kumar, 175
 Surabhi Chakravorty, 391
 Suryambika, 249, 933
 Swapnil Jain, 441
 Swathi, G.V., 217, 751
 Swati Khemka, 845
 Swati Mathur, 535

T

T. Shankar, 869
 Takasumi Tanabe, 409
 Taruna, S., 609
 Thosar, Ashwini Joshi, 619
 Tiwari, Dileep Kumar, 987
 Tiwari, Pradeep Kumar, 829
 Tiwari, V.N., 663
 Tripathi, S.K., 159
 Tripathy, Malay Ranjan, 167
 Trishla Shah, 305

V

Vani, R.M., 263
 Verma, Sunny Kumar, 925
 Vijayalakshmi, T.G., 217
 Vijayaraghavan Sundararaman, 217, 751
 Vikash Mishra, 325
 Vikram Singh, 325

Vinay Sharma, [879](#)
Vineet Khanna, [271](#)
Vinita Mathur, [791](#)
Vipin Jain, [489](#)
Vipul Bhatnagar, [141](#)
Vishwajit Nandi, [353](#)
Vishwakarma, Rajesh Kumar, [879](#)

Y
Y.S. Nijagunarya, [69](#)

Z
Ziauddin Ahmad, [373](#)
Zinjore, Ranjana S., [451](#)